

Artificial intelligence applications in chronic ocular diseases

Edited by

Wei Chi, Weihua Yang, Peirong Lu, Yanwu Xu
and Huiying Liu

Published in

Frontiers in Cell and Developmental Biology



FRONTIERS EBOOK COPYRIGHT STATEMENT

The copyright in the text of individual articles in this ebook is the property of their respective authors or their respective institutions or funders. The copyright in graphics and images within each article may be subject to copyright of other parties. In both cases this is subject to a license granted to Frontiers.

The compilation of articles constituting this ebook is the property of Frontiers.

Each article within this ebook, and the ebook itself, are published under the most recent version of the Creative Commons CC-BY licence. The version current at the date of publication of this ebook is CC-BY 4.0. If the CC-BY licence is updated, the licence granted by Frontiers is automatically updated to the new version.

When exercising any right under the CC-BY licence, Frontiers must be attributed as the original publisher of the article or ebook, as applicable.

Authors have the responsibility of ensuring that any graphics or other materials which are the property of others may be included in the CC-BY licence, but this should be checked before relying on the CC-BY licence to reproduce those materials. Any copyright notices relating to those materials must be complied with.

Copyright and source acknowledgement notices may not be removed and must be displayed in any copy, derivative work or partial copy which includes the elements in question.

All copyright, and all rights therein, are protected by national and international copyright laws. The above represents a summary only. For further information please read Frontiers' Conditions for Website Use and Copyright Statement, and the applicable CC-BY licence.

ISSN 1664-8714
ISBN 978-2-8325-4839-4
DOI 10.3389/978-2-8325-4839-4

About Frontiers

Frontiers is more than just an open access publisher of scholarly articles: it is a pioneering approach to the world of academia, radically improving the way scholarly research is managed. The grand vision of Frontiers is a world where all people have an equal opportunity to seek, share and generate knowledge. Frontiers provides immediate and permanent online open access to all its publications, but this alone is not enough to realize our grand goals.

Frontiers journal series

The Frontiers journal series is a multi-tier and interdisciplinary set of open-access, online journals, promising a paradigm shift from the current review, selection and dissemination processes in academic publishing. All Frontiers journals are driven by researchers for researchers; therefore, they constitute a service to the scholarly community. At the same time, the *Frontiers journal series* operates on a revolutionary invention, the tiered publishing system, initially addressing specific communities of scholars, and gradually climbing up to broader public understanding, thus serving the interests of the lay society, too.

Dedication to quality

Each Frontiers article is a landmark of the highest quality, thanks to genuinely collaborative interactions between authors and review editors, who include some of the world's best academicians. Research must be certified by peers before entering a stream of knowledge that may eventually reach the public - and shape society; therefore, Frontiers only applies the most rigorous and unbiased reviews. Frontiers revolutionizes research publishing by freely delivering the most outstanding research, evaluated with no bias from both the academic and social point of view. By applying the most advanced information technologies, Frontiers is catapulting scholarly publishing into a new generation.

What are Frontiers Research Topics?

Frontiers Research Topics are very popular trademarks of the *Frontiers journals series*: they are collections of at least ten articles, all centered on a particular subject. With their unique mix of varied contributions from Original Research to Review Articles, Frontiers Research Topics unify the most influential researchers, the latest key findings and historical advances in a hot research area.

Find out more on how to host your own Frontiers Research Topic or contribute to one as an author by contacting the Frontiers editorial office: frontiersin.org/about/contact

Artificial intelligence applications in chronic ocular diseases

Topic editors

Wei Chi — Sun Yat-sen University, China

Weihua Yang — Jinan University, China

Peirong Lu — The First Affiliated Hospital of Soochow University, China

Yanwu Xu — Baidu, China

Huiying Liu — Institute for Infocomm Research (A*STAR), Singapore

Citation

Chi, W., Yang, W., Lu, P., Xu, Y., Liu, H., eds. (2024). *Artificial intelligence applications in chronic ocular diseases*. Lausanne: Frontiers Media SA.

doi: 10.3389/978-2-8325-4839-4

The Topic Editor Dr. Yanwu Xu is employed by Baidu, China, and Topcon Healthcare, China. All other Topic Editors declare no competing interests concerning the present Research Topic.

Table of contents

06	Editorial: Artificial intelligence applications in chronic ocular diseases Yanwu Xu and Weihua Yang
12	Accuracy and feasibility with AI-assisted OCT in retinal disorder community screening Jianhao Bai, Zhongqi Wan, Ping Li, Lei Chen, Jingcheng Wang, Yu Fan, Xinjian Chen, Qing Peng and Peng Gao
24	Artificial intelligence-based pathologic myopia identification system in the ophthalmology residency training program Zhi Fang, Zhe Xu, Xiaoying He and Wei Han
33	Choroidal layer segmentation in OCT images by a boundary enhancement network Wenjun Wu, Yan Gong, Huaying Hao, Jiong Zhang, Pan Su, Qifeng Yan, Yuhui Ma and Yitian Zhao
49	Orbital and eyelid diseases: The next breakthrough in artificial intelligence? Xiao-Li Bao, Ying-Jian Sun, Xi Zhan and Guang-Yu Li
60	Effectiveness of reducing corneal astigmatism after combined high-frequency LDV Z8 femtosecond laser-assisted phacoemulsification and arcuate keratotomy Hung-Yuan Lin, Shuan Chen, Ya-Jung Chuang, Suhua Zhang, Steven Wei-Hsin Chang, Pi-Jung Lin and Zhe Zhang
71	Meibomian gland morphological changes in ocular herpes zoster patients based on AI analysis Xinxin Yu, Xu Jia, Zuhui Zhang, Yana Fu, Jing Zhai, Naimei Chen, Qixin Cao, Zhentao Zhu and Qi Dai
80	Is histogram manipulation always beneficial when trying to improve model performance across devices? Experiments using a Meibomian gland segmentation model Xianyu Deng, Lei Tian, Yinghuai Zhang, Ao Li, Shangyu Cai, Yongjin Zhou and Ying Jie
91	Reduced macula microvascular densities may be an early indicator for diabetic peripheral neuropathy Xiaoyu Deng, Shiqi Wang, Yan Yang, Aizhen Chen, Jinger Lu, Jinkui Hao, Yufei Wu and Qinkang Lu
101	Advances in artificial intelligence applications for ocular surface diseases diagnosis Yuke Ji, Sha Liu, Xiangqian Hong, Yi Lu, Xingyang Wu, Kunke Li, Keran Li and Yunfang Liu
114	Artificial intelligence technology for myopia challenges: A review Juzhao Zhang and Haidong Zou

- 125 **Prospective clinical study of retinal microvascular alteration after ICL implantation**
Chuhao Tang, Yu Zhang, Tong Sun, Jianyang Xie, Yiyun Liu, Rongjun Liu, Zhengze Sun and Hong Qi
- 132 **Research progress and application of artificial intelligence in thyroid associated ophthalmopathy**
Jiale Diao, Xinxin Chen, Ya Shen, Jian Li, Yuqing Chen, Linfeng He, Sainan Chen, Pei Mou, Xiaoye Ma and Ruili Wei
- 141 **Artificial intelligence-assisted diagnosis of ocular surface diseases**
Zuhui Zhang, Ying Wang, Hongzhen Zhang, Arzigul Samusak, Huimin Rao, Chun Xiao, Muhetaer Abula, Qixin Cao and Qi Dai
- 160 **Automatic measurement of exophthalmos based orbital CT images using deep learning**
Yinghuai Zhang, Jing Rao, Xingyang Wu, Yongjin Zhou, Guiqin Liu and Hua Zhang
- 171 **Retinal fluid is associated with cytokines of aqueous humor in age-related macular degeneration using automatic 3-dimensional quantification**
Siyuan Song, Kai Jin, Shuai Wang, Ce Yang, Jingxin Zhou, Zhiqing Chen and Juan Ye
- 181 **Effects of exogenous retinoic acid on ocular parameters in Guinea pigs with form deprivation myopia**
Yajun Wu, Yuliang Feng, Jiasong Yang, Hua Fan, Zitong Yu, Xiaolin Xie, Yumeng Dai, Xin Huang and Wensheng Li
- 195 **Research progress on diagnosing retinal vascular diseases based on artificial intelligence and fundus images**
Yuke Ji, Yun Ji, Yunfang Liu, Ying Zhao and Liya Zhang
- 208 **Using a smartphone app in the measurement of posture-related pupil center shift on centration during corneal refractive surgery**
Wenbo Cheng, Li Li, Gang Luo and Yan Wang
- 215 **Quantitative assessment of retinal microvascular remodeling in eyes that underwent idiopathic epiretinal membrane surgery**
Yingjiao Shen, Xin Ye, Jiwei Tao, Chenhao Zhao, Zhaokai Xu, Jianbo Mao, Yiqi Chen and Lijun Shen
- 225 **Advances in artificial intelligence models and algorithms in the field of optometry**
Suyu Wang, Yuke Ji, Wen Bai, Yun Ji, Jiajun Li, Yujia Yao, Ziran Zhang, Qin Jiang and Keran Li
- 242 **The application of artificial intelligence in glaucoma diagnosis and prediction**
Linyu Zhang, Li Tang, Min Xia and Guofan Cao

- 255 **Joint conditional generative adversarial networks for eyelash artifact removal in ultra-wide-field fundus images**
Jiong Zhang, Dengfeng Sha, Yuhui Ma, Dan Zhang, Tao Tan, Xiayu Xu, Quanyong Yi and Yitian Zhao
- 268 **Attention-guided cascaded network with pixel-importance-balance loss for retinal vessel segmentation**
Hexing Su, Le Gao, Yichao Lu, Han Jing, Jin Hong, Li Huang and Zequn Chen
- 282 **Oxygen-saturation-related functional parameter as a biomarker for diabetes mellitus—extraction method and clinical validation**
Jinze Zhang, Zhongzhou Luo, Gengyuan Wang, Yuancong Huang, Keyi Fei, Yushuang Liu, Jiaxiong Li, Jin Yuan and Peng Xiao
- 289 **Disrupted dynamic amplitude of low-frequency fluctuations in patients with active thyroid-associated ophthalmopathy**
Zhi Wen, Yan Kang, Yu Zhang, Huaguang Yang, Yilin Zhao, Xin Huang and Baojun Xie
- 299 **A bibliometric analysis of artificial intelligence applications in macular edema: exploring research hotspots and Frontiers**
Haiwen Feng, Jiaqi Chen, Zhichang Zhang, Yan Lou, Shaochong Zhang and Weihua Yang
- 311 **Impacts of gender and age on meibomian gland in aged people using artificial intelligence**
Binge Huang, Fangrong Fei, Han Wen, Ye Zhu, Zhenzhen Wang, Shuwen Zhang, Liang Hu, Wei Chen and Qinxiang Zheng
- 321 **Relationships between quantitative retinal microvascular characteristics and cognitive function based on automated artificial intelligence measurements**
Xu Han Shi, Li Dong, Rui Heng Zhang, Deng Ji Zhou, Sai Guang Ling, Lei Shao, Yan Ni Yan, Ya Xing Wang and Wen Bin Wei
- 339 **Effects of orthokeratology lenses on tear film and tarsal glands and control of unilateral myopia in children**
Li Li, Taichen Lai, Jing Zou, Linling Guo, Zhiming Lin, Jiawen Lin and Ying Xue
- 350 **Deep learning for detecting visually impaired cataracts using fundus images**
He Xie, Zhongwen Li, Chengchao Wu, Yitian Zhao, Chengmin Lin, Zhouqian Wang, Chenxi Wang, Qinyi Gu, Minye Wang, Qinxiang Zheng, Jiewei Jiang and Wei Chen



OPEN ACCESS

EDITED BY

Bin Sheng,
Shanghai Jiao Tong University, China

REVIEWED BY

Tao Tan,
Eindhoven University of Technology,
Netherlands
Xiangning Wang,
Shanghai Sixth People's Hospital, China
Yang Wen,
Shenzhen University, China

*CORRESPONDENCE

Weihua Yang,
✉ benben0606@139.com

RECEIVED 17 September 2023

ACCEPTED 28 November 2023

PUBLISHED 07 December 2023

CITATION

Xu Y and Yang W (2023), Editorial:
Artificial intelligence applications in
chronic ocular diseases.
Front. Cell Dev. Biol. 11:1295850.
doi: 10.3389/fcell.2023.1295850

COPYRIGHT

© 2023 Xu and Yang. This is an open-access article distributed under the terms of the [Creative Commons Attribution License \(CC BY\)](#). The use, distribution or reproduction in other forums is permitted, provided the original author(s) and the copyright owner(s) are credited and that the original publication in this journal is cited, in accordance with accepted academic practice. No use, distribution or reproduction is permitted which does not comply with these terms.

Editorial: Artificial intelligence applications in chronic ocular diseases

Yanwu Xu^{1,2} and Weihua Yang^{3*}

¹School of Future Technology, South China University of Technology, Guangzhou, Guangdong Province, China, ²Pazhou Lab, Guangzhou, Guangdong Province, China, ³Shenzhen Eye Institute, Shenzhen Eye Hospital, Jinan University, Shenzhen, Guangdong Province, China

KEYWORDS

artificial intelligence, deep learning, machine learning, chronic ocular diseases, diagnosis, ocular structures analysis

Editorial on the Research Topic

Artificial intelligence applications in chronic ocular diseases

Introduction

Chronic ocular diseases are eye health conditions that develop slowly over an extended period, typically without showing noticeable symptoms in the short term. These conditions can progressively affect vision and overall ocular health, potentially causing significant disruptions to a patient's life quality if not promptly diagnosed and treated. Common chronic ocular diseases include glaucoma (Morgan and Drance, 1975), cataracts, dry eye syndrome (Schaumberg et al., 2002), diabetic retinopathy, age-related macular degeneration, myopia (Singh et al., 2022), and hyperopia (Sharafeldin et al., 2018). It is essential for individuals with chronic ocular diseases to receive regular eye examinations and appropriate medical care to manage and mitigate the long-term effects of these conditions on their eye health and vision.

Artificial intelligence (AI) is a cutting-edge technology in computer science that aims to enable computers to learn, reason, and make decisions like humans. AI technology has already achieved great success in many fields, including automatic driving, financial forecasting, natural language processing applications, and medical diagnostics. Among the field of medical diagnostics, AI technology has significantly contributed to clinical research in various areas. These include AI-assisted diagnosis of intracranial tumors from magnetic resonance (MR) imaging scans (Anaraki et al., 2019), AI-supported analysis of vascular stenosis in coronary computed tomography (CT) imaging (Han et al., 2020), AI-assisted evaluation of head and neck CT angiography images (Fu et al., 2023), AI-powered diagnosis of fundus lesions from fundus imaging (Li et al., 2022), and AI-driven analysis of pneumonia in CT imaging (Chassagnon et al., 2021). Especially in eye imaging research, AI can be utilized to conduct studies in various areas. This includes retinal disease screening based on fundus color photographs (Orlando et al., 2020; Li et al., 2022), cataract grading based on AS-OCT images (Zhang et al., 2022), and glaucoma grading based on multi-modal ophthalmic examination images (Wu et al., 2023), such as fundus color photos and OCT images. AI can also be employed for the segmentation of ocular structures or lesions in

different modal eye examination images, including optic cup and disc segmentation (Fu et al., 2018), retinal blood vessel segmentation (Hu et al., 2022), lesion segmentation (Fang et al., 2022) in fundus color images, and segmentation of ocular structural layers and lesions in OCT images (Li et al., 2021; Farshad et al., 2022).

Moreover, the application of AI technology in the management and treatment of chronic ocular diseases also holds significant importance. It can offer support and improvements across various aspects, including early diagnosis and prediction, disease progression monitoring, personalized treatment, etiological analysis and research, precise surgical assistance, and patient health management (Yang et al., 2023). AI techniques will be employed for intelligent image analysis, disease classification and diagnosis, surgical assistance, and etiological research.

Hence, a Research Topic dedicated to the research on the application of AI in chronic ocular diseases has been initiated. During this Research Topic, we received a total of 53 submissions. These submissions underwent rigorous evaluation, resulting in the inclusion of 30 selected papers. The overall download count reached more than 7,600, with a combined total of 53k views and downloads. We have categorized the studies in this Research Topic according to the corresponding types of chronic diseases based on the structure of the eyeball from front to back, as illustrated in Figure 1; Table 1.

The ocular surface and orbital diseases involve structural lesions of the orbit, eyelids, cornea, and so forth. The orbit is the bony cavity within the skull that houses the eyeball, primarily serving to protect the eye. The eyelids are movable folds of skin that cover the eyeball, capable of opening and closing to protect the eye from external harm, regulate the entry of light, and secrete tears. The cornea is the transparent tissue on the front surface of the eye, allowing light to enter the eye. Myopia-related diseases may involve lesions on the cornea and the crystalline lens. The crystalline lens is a transparent biconvex structure within the eye, responsible for adjusting focal length. Glaucoma is related to structural changes in the anterior chamber and optic nerve

pathology. The anterior chamber is a fluid-filled area located in the front part of the eye, between the iris and the cornea, responsible for maintaining the shape of the eye, supplying oxygen and nutrients, and regulating eye pressure. Cataract diseases exhibit significant abnormalities in the lens. Diseases of the retina involve lesions in areas such as the retina, macula, central fovea, and so forth. The primary function of retina is to perceive light, process visual information, and transmit this information to the brain. The macula is a critical area for vision, especially in detail resolution, color perception, and direct gaze. The central fovea is the most sensitive area of the retina, allowing us to achieve the highest resolution central vision. Fundus vasculature disorders are conditions caused by alterations in the retinal blood vessels. The primary function of retinal blood vessels is to supply the ocular tissues with the oxygen and nutrients.

Ocular surface and orbital diseases

Ocular surface and orbital diseases are a group of eye conditions that impact the structure and function of the eye's surface. Articles related to this topic in the Research Topic involve the studies of various aspects, including eye orbit, eyelids, meibomian glands, and cornea, as well as related diseases.

Eye orbit and eyelids

Bao et al. and Diao et al. primarily focus on the orbital and eyelid images collected during clinical diagnostics for **Thyroid-Associated Ophthalmopathy (TAO)**. Bao et al. mainly discuss the application of AI technology in the analysis of orbital CT/MR images. For instance, AI methods can automatically identify and quantify orbital anatomical structures such as bone structures, fat, and abscesses using image segmentation techniques.

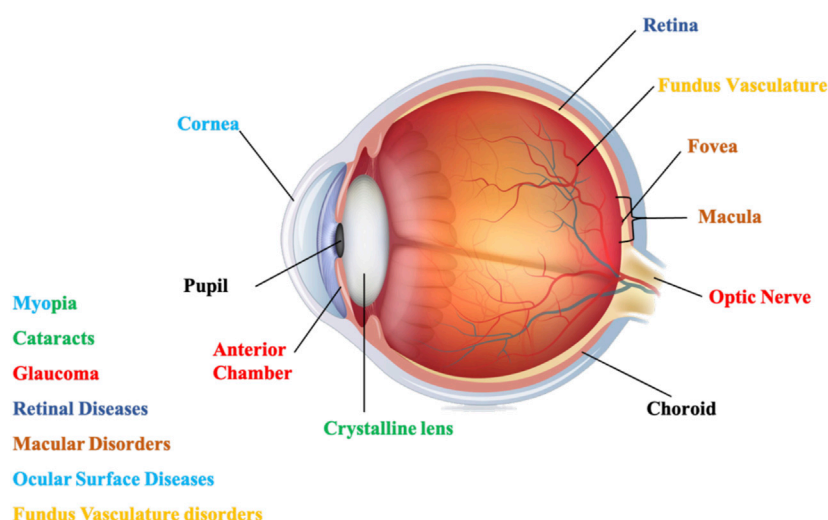


FIGURE 1

The structure of the eyeball, and chronic ocular diseases those can be caused by degeneration in different structures.

TABLE 1 Summary of the papers in the Research Topic of Artificial Intelligence Applications in Chronic Ocular Diseases.

Disease	Ocular structure	Paper	Main findings
Ocular Surface and orbital Diseases	Eye orbit and eyelids	Bao et al.	AI methods can automatically identify and quantify orbital anatomical structures
		Zhang et al.	
		Diao et al.	AI methods can provide applications in the clinical diagnosis, activity, severity grading, and treatment outcome prediction
		Wen et al.	
	Meibomian gland	Deng et al.	Using U-Net or its variants for the segmentation of the meibomian gland, followed by morphological parameter measurement, and subsequently applying the measured parameters for medical statistics on different diseases
		Yu et al.	
		Li et al.	
		Huang et al.	
	Cornea	Lin et al.	Using AI method to discuss the effects of cataract surgery and corneal incisions on corneal astigmatism
		Cheng et al.	Using deep learning method to measure the deviation of the pupil center during corneal refractive surgery
		Ji et al.	AI methods can automatically diagnosis ocular surface diseases
		Zhang et al.	
Myopia	Cornea	Wang et al.	Using AI methods for myopia risk prediction, diagnosis, screening, etc., and discussing the demonstrative role of AI methods in education
	Crystalline lens	Zhang et al.	
		Bai et al.	
	Choroid layer	Wu et al.	Designing a new boundary-enhanced encoder-decoder architecture for choroid layer segmentation
		Wu et al.	Employing AI methods to investigate the impact of drugs on the eye structure of myopia patients
Glaucoma	Anterior chamber	Zhang et al.	Introducing various diagnostic models for glaucoma based on different examine images. (Random forest models and VGG networks based on visual field test results; ResNet classifier based on fundus images; ResNet classifier based on OCT)
	Optic nerve		
Cataracts	Crystalline lens	Xie et al.	Developing a deep learning method for screening visually impaired cataract cases using fundus images
Retinal Diseases	Retina	Bai et al.	Using AI methods to screen and analyze various retinal diseases, especially multiple macular-related diseases, and also employing AI methods to analyze the biological significance of cytokines in the retina
	Macula	Song et al.	
	Fovea	Feng et al.	
Fundus Vasculature Disorders	Fundus vasculature	Ji et al.	Applying AI methods in the diagnosis and grading of retinal vascular diseases
		Shi et al.	Using AI methods to segment blood vessels in different modal images, measure related parameters, and then analyze changes in microvascular parameters before and after disease onset or surgical intervention using medical statistics
		Deng et al.	
		Zhang et al.	
		Shen et al.	
		Tang et al.	
		Su et al.	Proposing an attention-guided cascade network for retinal vessel segmentation
		Zhang et al.	Using AI method eliminating eyelash artifacts from ultra-wide-field fundus images, aiming to improve the visibility of retinal vasculature and enhance the quality of images

Additionally, they summarize the applications of AI in TAO. Similarly, [Diao et al.](#) conduct research on the application of AI technology in the diagnosis dimension concerning TAO. They provide an overview of recent AI applications in the clinical diagnosis, activity, severity grading, and treatment outcome prediction. The study also discusses current challenges and future prospects in the application of AI in the treatment of

TAO. [Wen et al.](#) study the difference of dynamic low-frequency amplitude between patients with TAO and normal people based on resting brain functional MR images (fMRI), laying a foundation for subsequent automatic diagnosis of thyroid-associated eye disease based on dynamic low-frequency amplitude. Based on eye orbit CT images, [Zhang et al.](#) focus on measuring eyeball protrusion by calculating eyeball

protrusion distance using segmentation models in artificial intelligence.

Meibomian gland

Four articles focus on meibomian gland analysis, all involving segmentation of the meibomian glands and subsequently performing different downstream tasks. [Deng et al.](#) segment the meibomian gland area to analyze the meibomian gland conditions in patients with meibomian gland dysfunction. [Yu et al.](#) conduct structural segmentation and morphological analysis of the meibomian glands to discuss the differences in meibomian gland morphology between patients with ophthalmic herpes zoster and a normal control group. Similarly, [Li et al.](#) analyze glandular model parameters, automatically calculating the glandular deformation coefficient to explore the impact of orthokeratology lenses (OK lenses) on tear film, meibomian glands, and myopia control in monocular myopic children. [Huang et al.](#) use a deep learning model to analyze images, measuring meibomian gland area, density, quantity, height, width, and curvature, and use a deep learning system to analyze the effects of age, gender, and behavior on meibomian gland morphology.

Cornea

Among the intelligent analysis of the corneal structure, [Lin et al.](#) discuss the effects of cataract surgery and corneal incisions on corneal astigmatism. [Cheng et al.](#) mainly use deep learning technology to measure the deviation of the pupil center during corneal refractive surgery. The application, limitations, and challenges of AI in the diagnosis of ocular surface diseases (such as keratitis, keratoconus, dry eye, pterygium, and other ocular surface diseases), as well as the prospects of future applications are summarized by [Ji et al.](#) and [Zhang et al.](#)

Myopia

The papers on this topic cover various aspects of myopia, including high myopia, pathological myopia, strabismus, amblyopia, and the effects of drugs on myopia. Specifically, [Wang et al.](#) provide a comprehensive review of the advancements in the application of different AI models and algorithms in optometry (for issues such as myopia, strabismus, amblyopia, keratoconus, and artificial lenses) and discussed the associated limitations and challenges in this field. [Zhang et al.](#) conduct a review and elaborated on the technical details of AI methods in myopia risk prediction, screening, diagnosis, pathogenesis, and treatment. [Bai et al.](#) discuss the application of AI-based myopia automatic recognition systems in the training of resident physicians, validating the role of artificial intelligence in medical education. [Wu et al.](#) employ AI technology to investigate the impact of drugs on the eye structure of myopia patients, particularly on choroidal thickness and retinal thickness. Additionally, [Wu et al.](#) conduct research on choroid layer segmentation in optical coherence tomography (OCT) images, introducing a new

boundary-enhanced encoder-decoder architecture. This architecture aims to precisely extract choroid layer information from images with blurred edges, assisting in choroidal thickness calculations.

Glaucoma

Glaucoma is a condition that gradually damages the optic nerve, often associated with elevated intraocular pressure. If left uncontrolled, glaucoma may lead to permanent vision loss. Zhang et al. introduce various diagnostic models for glaucoma based on different examined images, for example, random forest models and VGG networks based on visual field test results, ResNet classifier based on fundus images, and ResNet classifier based on OCT. In view of the difficulty of creating standard data sets and standardization guidelines, it is suggested that we should optimize data sets and build multi-center, large sample, and high-efficiency data sets. Finally, the clinical application rules are more standardized, and the diagnosis and prediction tools for glaucoma are simplified in a single direction, benefiting multiple ethnic groups.

Cataracts

Cataracts involve the gradual clouding of the lens, resulting in decreased vision clarity and difficulty seeing objects. While cataracts can be treated through surgery, untreated cases can severely impair vision. [Xie et al.](#) develop a deep learning method for screening visually impaired cataract cases using fundus images. A total of 8,395 fundus images (5,245 subjects) from three clinical centers and corresponding visual function parameters were collected to develop and evaluate the deep learning method for classifying non-cataract, mild cataract, and vision-impaired cataract. They used three deep learning algorithms (DenseNet121, Inception V3, and ResNet50) to train the model to get the best model of the system. The performance of the system is evaluated by the area under the receiver operating characteristic curve (AUC), sensitivity, and specificity. On the internal test dataset as well as two external test datasets, the optimal algorithm was DenseNet121, and the system performed better in detecting visually impaired cataracts than cataract specialists ($p < 0.05$). Research shows that a function-focused screening tool has the potential to identify visually impaired cataracts in fundus images, leading to timely referral of patients to tertiary eye hospitals.

Retinal diseases

The retina, a thin layer at the back of the eye, plays a vital role in converting light into signals that our brain interprets as vision. Retinal diseases are various medical conditions that affect the retina's structure or function. Early detection and treatment are crucial for preserving eye health. [Bai et al.](#) evaluate the accuracy and reliability of AI approaches using OCT images to achieve community screening for 15 retinal diseases. The OCT scans cover an area of 12 mm × 9 mm at the posterior pole retina

involving the macular and optic disc. The 15 retinal diseases include pigment epithelial detachment, posterior vitreous detachment, epiretinal membranes, sub-retinal fluid, choroidal neovascularization, drusen, retinoschisis, cystoid macular edema, exudation, macular hole, retinal detachment, ellipsoid zone disruption, focal choroidal excavation, choroid atrophy, and retinal hemorrhage. Song et al. explore the biological significance of cytokines in the eye using OCT images. They analyze the correlation between cytokine levels in aqueous humor and retinal fluid, shedding light on the potential role of cytokines in the development of neovascular age-related macular degeneration. Moreover, Feng et al. provide comprehensive overviews of the application of AI technologies in macular edema.

Fundus vasculature disorders

Fundus vascular disorders are a group of medical diseases related to the vascular structure at the base of the eye. Ji et al. discuss the application of AI in the diagnosis and grading of retinal vascular diseases, such as diabetic retinopathy, retinal vein occlusion, and retinopathy of prematurity, based on color fundus photographs. A significant portion of the research in this topic of our Research Topic focuses on examining alterations in microvasculature before and after the onset of disease or following surgical interventions. Shi et al. segment and measure retinal vessels in fundus color photographs, followed by exploring the relationship between vascular parameters, including retinal vessel branching angle, vessel fractal dimension, vessel diameter, vessel tortuosity, vessel density, and cognitive impairment. Deng et al. use OCT angiography (OCTA) images to compare differences in macular microvasculature between type II diabetes patients with and without peripheral neuropathy. Zhang et al. calculate functional parameters related to retinal vessel oxygen saturation based on fundus color photographs to investigate changes in retinal vessel oxygen saturation in type II diabetes patients. Shen et al. use OCTA images to discuss the condition of macular microvasculature and the recovery of visual function in patients after idiopathic epiretinal membrane surgery. Tang et al. discuss changes in retinal microvasculature in patients with moderate to high myopia after implantable collamer lens (ICL) implantation.

In addition to the aforementioned studies on the clinical application of AI, Su et al. propose an attention-guided cascade network for retinal vessel segmentation, aiming to accurately segment retinal vessels from fundus images. Moreover, Zhang et al. conduct research on eliminating eyelash artifacts from ultra-wide-field fundus images, aiming to improve the visibility of retinal vasculature and enhance the quality of eye examination images. These studies enable more precise quantitative analysis of retinal vasculature, which can enhance the accuracy of vascular-related research.

Conclusion

Research on this topic has covered a wide range of chronic ocular diseases, including ocular surface and orbital diseases,

myopia, glaucoma, cataracts, retinal diseases, and vascular diseases, providing us with a comprehensive understanding of chronic ocular conditions. Additionally, the studies within this topic effectively encompass various applications of AI technology in chronic ocular disease research. These applications include the automatic diagnosis of chronic ocular diseases using AI, the exploration of the relationship between changes in ocular structures and diseases or treatments using AI, and the enhancement of medical education and work efficiency using AI. These research efforts have offered valuable insights into the use of AI in the clinical diagnosis, treatment, and management. We are confident that we will continue to make better use of AI technology in the future.

Author contributions

YX: Conceptualization, Supervision, Writing—original draft, Writing—review and editing. WY: Conceptualization, Funding acquisition, Supervision, Validation, Writing—original draft, Writing—review and editing.

Funding

The author(s) declare(s) that no financial support was received for the research, authorship, and/or publication of this article. WY Supported by Shenzhen Fund for Guangdong Provincial High-level Clinical Key Specialties (SZGSP014), Sanming Project of Medicine in Shenzhen (SZSM202011015) and Shenzhen Science and Technology Planning Project (JCYJ20220818103207015).

Acknowledgments

We are grateful for the contribution of every participant in this Research Topic.

Conflict of interest

The authors declare that the research was conducted in the absence of any commercial or financial relationships that could be construed as a potential conflict of interest.

The author(s) declared that they were an editorial board member of Frontiers, at the time of submission. This had no impact on the peer review process and the final decision.

Publisher's note

All claims expressed in this article are solely those of the authors and do not necessarily represent those of their affiliated organizations, or those of the publisher, the editors and the reviewers. Any product that may be evaluated in this article, or claim that may be made by its manufacturer, is not guaranteed or endorsed by the publisher.

References

- Anaraki, A. K., Ayati, M., and Kazemi, F. (2019). Magnetic resonance imaging-based brain tumor grades classification and grading via convolutional neural networks and genetic algorithms. *J. Biocybern. Biomed. Eng.* 39 (1), 63–74. doi:10.1016/j.bbe.2018.10.004
- Chassagnon, G., Vakalopoulou, M., Battistella, E., Christodoulidis, S., Hoang-Thi, T. N., Dangeard, S., et al. (2021). AI-driven quantification, staging and outcome prediction of COVID-19 pneumonia. *Med. image Anal.* 67, 101860. doi:10.1016/j.media.2020.101860
- Fang, H., Li, F., Fu, H., Sun, X., Cao, X., Lin, F., et al. (2022). Adam challenge: detecting age-related macular degeneration from fundus images. *IEEE Trans. Med. Imaging* 41 (10), 2828–2847. doi:10.1109/TMI.2022.3172773
- Farshad, A., Yeganeh, Y., and Gehlbach, P. (2022). *Y-Net: a spatio-spectral dual-encoder network for medical image segmentation*[C]//International Conference on Medical Image Computing and Computer-Assisted Intervention. Cham: Springer Nature Switzerland, 582–592.
- Fu, F., Shan, Y., Yang, G., Zheng, C., Zhang, M., Rong, D., et al. (2023). Deep learning for head and neck CT angiography: stenosis and plaque classification. *Radiology* 307 (3), e220996. doi:10.1148/radiol.220996
- Fu, H., Cheng, J., Xu, Y., Wong, D. W. K., Liu, J., and Cao, X. (2018). Joint optic disc and cup segmentation based on multi-label deep network and polar transformation. *IEEE Trans. Med. imaging* 37 (7), 1597–1605. doi:10.1109/TMI.2018.2791488
- Han, D., Liu, J., Sun, Z., Cui, Y., He, Y., and Yang, Z. (2020). Deep learning analysis in coronary computed tomographic angiography imaging for the assessment of patients with coronary artery stenosis. *Comput. Methods Programs Biomed.* 196, 105651. doi:10.1016/j.cmpb.2020.105651
- Hu, J., Wang, H., Wu, G., Cao, Z., Mou, L., Zhao, Y., et al. (2022). Multi-scale interactive network with artery/vein discriminator for retinal vessel classification. *IEEE J. Biomed. Health Inf.* 26 (8), 3896–3905. doi:10.1109/JBHI.2022.3165867
- Li, F., Pan, J., Yang, D., Wu, J., Ou, Y., Li, H., et al. (2022). A multicenter clinical study of the automated fundus screening algorithm. *Transl. Vis. Sci. Technol.* 11 (7), 22. doi:10.1167/tvst.11.7.22
- Li, J., Jin, P., Zhu, J., Zou, H., Xu, X., Tang, M., et al. (2021). Multi-scale GCN-assisted two-stage network for joint segmentation of retinal layers and discs in peripapillary OCT images. *Biomed. Opt. Express* 12 (4), 2204–2220. doi:10.1364/BOE.417212
- Morgan, R. W., and Drance, S. M. (1975). Chronic open-angle glaucoma and ocular hypertension. An epidemiological study. *Br. J. Ophthalmol.* 59 (4), 211–215. doi:10.1136/bjo.59.4.211
- Orlando, J. I., Fu, H., Breda, J. B., van Keer, K., Bathula, D. R., Diaz-Pinto, A., et al. (2020). Refuge challenge: a unified framework for evaluating automated methods for glaucoma assessment from fundus photographs. *Med. image Anal.* 59, 101570. doi:10.1016/j.media.2019.101570
- Schaumberg, D. A., Sullivan, D. A., and Dana, M. R. (2002). "Epidemiology of dry eye syndrome," in *Lacrimal Gland, Tear Film, and Dry Eye Syndromes 3: Basic Science and Clinical Relevance Part A and B*, 989–998. doi:10.1007/978-1-4615-0717-8_140
- Sharafeldin, N., Kawaguchi, A., Sundaram, A., Campbell, S., Rudnisky, C., Weis, E., et al. (2018). Review of economic evaluations of teleophthalmology as a screening strategy for chronic eye disease in adults. *Br. J. Ophthalmol.* 102 (11), 1485–1491. doi:10.1136/bjophthalmol-2017-311452
- Singh, H., Singh, H., Latief, U., Tung, G. K., Shahtaghi, N. R., Sahajpal, N. S., et al. (2022). Myopia, its prevalence, current therapeutic strategy and recent developments: a Review. *Indian J. Ophthalmol.* 70 (8), 2788–2799. doi:10.4103/ijo.IJO_2415_21
- Wu, J., Fang, H., Li, F., Fu, H., Lin, F., Li, J., et al. (2023). Gamma challenge: glaucoma grading from multi-modality images. *Med. Image Anal.* 90, 102938. doi:10.1016/j.media.2023.102938
- Yang, W., Shao, Y., Xu, Y., and Expert Workgroup of Guidelines on Clinical Research Evaluation of Artificial Intelligence in Ophthalmology 2023, Ophthalmic Imaging and Intelligent Medicine Branch of Chinese Medicine Education Association, Intelligent Medicine Committee of Chinese Medicine Education Association (2023). Guidelines on clinical research evaluation of artificial intelligence in ophthalmology (2023). *Int. J. Ophthalmol.* 16 (9), 1361–1372. doi:10.18240/ijo.2023.09.02
- Zhang, X., Xiao, Z., Fu, H., Hu, Y., Yuan, J., Xu, Y., et al. (2022). Attention to region: region-based integration-and-recalibration networks for nuclear cataract classification using AS-OCT images. *Med. Image Anal.* 80, 102499. doi:10.1016/j.media.2022.102499



OPEN ACCESS

EDITED BY

Weihua Yang,
Shenzhen Eye Hospital, Jinan University,
China

REVIEWED BY

Xuefei Song,
Shanghai Ninth People's Hospital, China
Zongyuan Ge,
Monash University, Australia
Xiao Huang,
Second Military Medical University,
China

*CORRESPONDENCE

Xinjian Chen,
xjchen@suda.edu.cn
Qing Peng,
pengqing@tongji.edu.cn
Peng Gao,
neocloudy@hotmail.com

[†]These authors have contributed equally
to this work

SPECIALTY SECTION

This article was submitted to Molecular
and Cellular Pathology,
a section of the journal
Frontiers in Cell and Developmental
Biology

RECEIVED 25 September 2022

ACCEPTED 18 October 2022

PUBLISHED 03 November 2022

CITATION

Bai J, Wan Z, Li P, Chen L, Wang J, Fan Y,
Chen X, Peng Q and Gao P (2022),
Accuracy and feasibility with AI-assisted
OCT in retinal disorder
community screening.
Front. Cell Dev. Biol. 10:1053483.
doi: 10.3389/fcell.2022.1053483

COPYRIGHT

© 2022 Bai, Wan, Li, Chen, Wang, Fan,
Chen, Peng and Gao. This is an open-
access article distributed under the
terms of the [Creative Commons
Attribution License \(CC BY\)](https://creativecommons.org/licenses/by/4.0/). The use,
distribution or reproduction in other
forums is permitted, provided the
original author(s) and the copyright
owner(s) are credited and that the
original publication in this journal is
cited, in accordance with accepted
academic practice. No use, distribution
or reproduction is permitted which does
not comply with these terms.

Accuracy and feasibility with AI-assisted OCT in retinal disorder community screening

Jianhao Bai^{1†}, Zhongqi Wan^{1†}, Ping Li¹, Lei Chen¹,
Jingcheng Wang², Yu Fan², Xinjian Chen^{3*}, Qing Peng^{1*} and
Peng Gao^{1*}

¹Department of Ophthalmology, Shanghai Tenth People's Hospital of Tongji University, Tongji
University School of Medicine, Shanghai, China, ²Suzhou Big Vision Medical Technology Co Ltd,
Suzhou, China, ³School of Electronic and Information Engineering, Soochow University, Suzhou,
China

Objective: To evaluate the accuracy and feasibility of the auto-detection of
15 retinal disorders with artificial intelligence (AI)-assisted optical coherence
tomography (OCT) in community screening.

Methods: A total of 954 eyes of 477 subjects from four local communities were
enrolled in this study from September to December 2021. They received OCT
scans covering an area of 12 mm × 9 mm at the posterior pole retina involving
the macular and optic disc, as well as other ophthalmic examinations performed
using their demographic information recorded. The OCT images were analyzed
using integrated software with the previously established algorithm based on
the deep-learning method and trained to detect 15 kinds of retinal disorders,
namely, pigment epithelial detachment (PED), posterior vitreous detachment
(PVD), epiretinal membranes (ERMs), sub-retinal fluid (SRF), choroidal
neovascularization (CNV), drusen, retinoschisis, cystoid macular edema
(CME), exudation, macular hole (MH), retinal detachment (RD), ellipsoid zone
disruption, focal choroidal excavation (FCE), choroid atrophy, and retinal
hemorrhage. Meanwhile, the diagnosis was also generated from three
groups of individual ophthalmologists (group of retina specialists, senior
ophthalmologists, and junior ophthalmologists) and compared with those by
the AI. The area under the receiver operating characteristic curve (AUC),
sensitivity, and specificity were calculated, and kappa statistics were performed.

Results: A total of 878 eyes were finally enrolled, with 76 excluded due to poor
image quality. In the detection of 15 retinal disorders, the ROC curve
comparison between AI and professors' presented relatively large AUC
(0.891–0.997), high sensitivity (87.65–100%), and high specificity
(80.12–99.41%). Among the ROC curve comparisons with those by the
retina specialists, AI was the closest one to the professors' compared to
senior and junior ophthalmologists ($p < 0.05$).

Conclusion: AI-assisted OCT is highly accurate, sensitive, and specific in auto-
detection of 15 kinds of retinal disorders, certifying its feasibility and
effectiveness in community ophthalmic screening.

KEYWORDS

artificial intelligence (AI), optical coherence tomography (OCT), retinal disorders, community ophthalmic screening, accuracy

Introduction

With the rapid progress in population aging and the escalating prevalence of systemic diseases like hypertension and diabetes mellitus, as well as the increasing incidence of myopia in contemporary society, the morbidity rate of multiple ophthalmic diseases, especially with various retinal disorders, has ascended consequently. It caused visual impairment and even blindness in both developed and developing countries (Hong et al., 2013; Wolfram et al., 2019; Li et al., 2022b). Among them, the age-related macular degeneration (AMD), diabetic retinopathy (DR), and myopic retinopathy, as well as other macular disorders like epiretinal membranes (ERMs) and macular holes, were the significant components and chief culprits for visual loss in most populations (Mitchell et al., 2018; Wang and Lo, 2018; Ruiz-Medrano et al., 2019).

Early diagnosis and prompt treatment were essential to achieve the best possible visual prognosis (Mitchell et al., 2018; Wang and Lo, 2018; Ruiz-Medrano et al., 2019). Therefore, early detection at the initial stages and positive screening at the pre-hospital level were necessary, indicating the importance of effective and efficient community screening. A notable and challenging fact exists on the insufficient medical human resources allocated in the community and the inadequately experienced ophthalmologists in primary hospitals, forging a considerable gap and actual bottleneck toward the enormous demand for community screening (Feng et al., 2018).

With tremendous progress in recent years, artificial intelligence (AI) has been integrated with various fields of science and taken to practical engineering in multiple scenes. The deep-learning (DL) algorithm is an advanced type of machine learning (ML) with a multi-layered convolutional neural network (CNN) model. It is capable of learning and detecting image features and recognizing patterns from a large dataset. The application of DL in medicine has fulfilled the function of automated lesion recognition and prognosis prediction in various diseases (Gulshan et al., 2016; Zhang Q. et al., 2021). In the field of ophthalmology, different AI algorithms have been developed and applied for auto-detection of diverse diseases like glaucoma (Keel et al., 2019; Camara et al., 2022), ocular surface diseases (Zhang Y. Y. et al., 2021), and multiple retinal disorders, like DR, AMD, and myopic retinopathy, and have exhibited relatively high accuracy and reliable performance in clinical diagnosis as well as the pre-hospital community screening, providing a promising solution for the challenge mentioned previously (Rajalakshmi et al., 2018; He et al., 2020; Xie et al., 2020; Cen et al., 2021).

One disadvantage of AI algorithms trained to detect retinal disorders is that they are mainly based on the features from fundus photography images, which could not offer a comprehensive message of deep layers of the retina and the choroid (He et al., 2020; Xie et al., 2020; Cen et al., 2021). Meanwhile, the optical coherence tomography (OCT) technique can provide the cross-sectional images of the retina with high resolution realizing *in vivo* visualization of cellular tissue microstructure *via* interferometry and has been widely utilized in the clinical practice of ophthalmology. By providing the morphological features and quantitative measurement data of the different layers of the retina, especially at the macular and around the optic head, and the certain depth of the choroid, OCT shows its advantage in detecting multiple retinal diseases superior to utilizing fundus image only. One emerging trend is to develop AI algorithms based on OCT images to diagnose some retinal diseases. At the same time, several studies have shown its feasibility and revealed its accuracy in clinical application (Sandhu et al., 2018; Treder et al., 2018; Sandhu et al., 2020; Sogawa et al., 2020; Wang et al., 2020).

Another major disadvantage of current AI software was that it mostly focuses only on one specific retinal disorder. In comparison, a very considerable proportion of patients suffer from more than one retinal disorder, which restricts the practical application of this AI software in a real clinical setting (Sandhu et al., 2018; Treder et al., 2018; Sandhu et al., 2020; Sogawa et al., 2020; Wang et al., 2020). Therefore, the impending demand rising from clinical practice and community screening work is to develop AI algorithms that can recognize multiple retinal disorders simultaneously in single detection.

In view of the aforementioned requirement, this study involved the utilization of an AI-assisted OCT instrument to examine the retina in a community screening, with the acquired images analyzed using a pre-designed DL algorithm that could detect 15 retinal disorders simultaneously, aiming to evaluate its accuracy and feasibility in the practical application.

Materials and methods

Participants' enrollment

The inhabitants of four local communities (DaNing Road community, GongHe Road community, PengPu Town community, and Linfen Road community, all of which are located in Jing'an District, Shanghai) participated in the study. The study period was from September to December 2021.

The inclusion criteria were: 1) age > 18 years; 2) co-operation with the ophthalmic examinations; and 3) voluntary

participation in the study. The exclusion criteria were as follows: 1) patients with ophthalmic disease causing severe refractive media opacity like keratoleukoma, cataract, and vitreous or within ophthalmic emergency situations; 2) patients with other severe uncontrolled systemic diseases; and 3) patients during pregnancy or lactation period.

The study was approved by the Ethical Committee of Shanghai Tenth People's Hospital and conducted in accordance with the tenets of the Declaration of Helsinki, with the written informed consent forms signed by all the participants voluntarily.

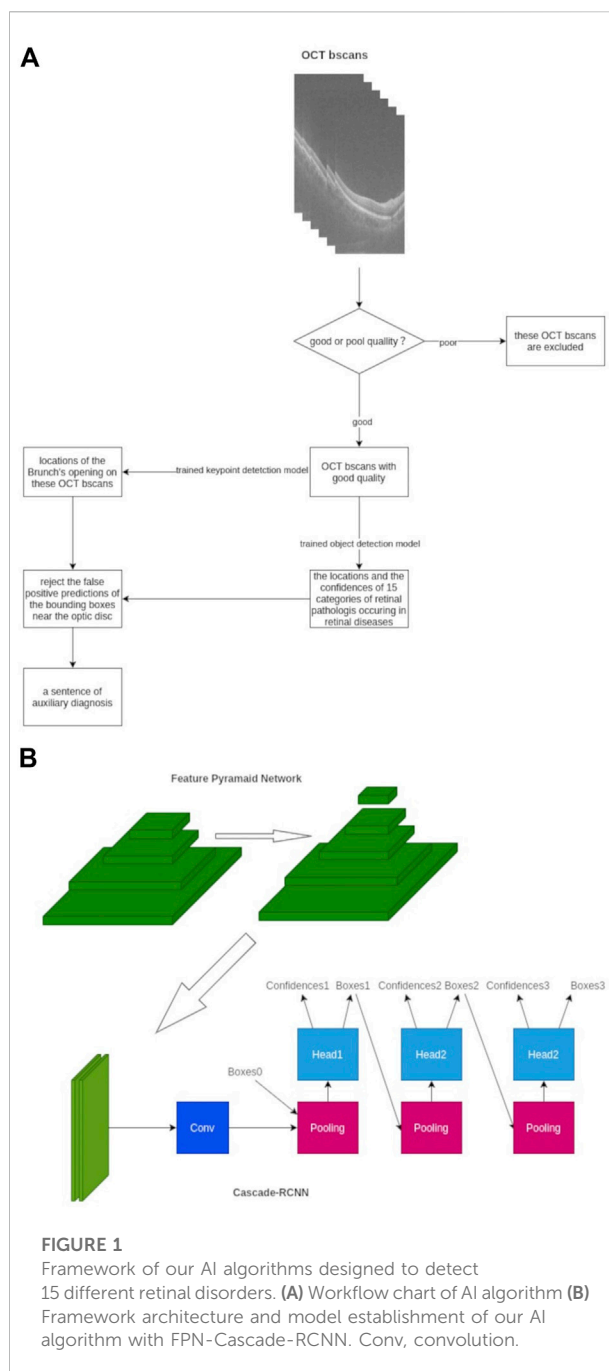
Community screening

All the participants underwent the following ophthalmic examinations: 1) best-corrected visual acuity (BCVA); 2) intraocular pressure (IOP), performed using an iCare tonometer device (iCare IC 100, Icare Oy, Vantaa, Finland); 3) slit-lamp examination (YZ5X, Suzhou 66 Vision, Suzhou, China); 4) automatic nonmydriatic fundus photography (TRC-NW400, Topcon, Tokyo, Japan), images captured with both macula-centered and disc-centered; and 5) spectral domain-OCT scan (SD-OCT, BV1000, Bigvision Inc., Jiangxi, China). Meanwhile, the demographic information of the participants and their general medical history of systemic diseases, such as hypertension and diabetes mellitus, were recorded.

The OCT scan covered an area of 12 mm × 9 mm at the posterior pole of the retina involving the macular and optic disc in one image view and extended to a depth of 2.3mm, with the axial resolution of 5 μm and the horizontal resolution of 20 μm in tissues. Owing to the maximum A-scan speed at 45,000 times per second and the automated voice prompt operating system, the process of the examination was convenient and fast. The images were then transmitted to the AI algorithm, which was integrated into the instrument to generate an analysis of multiple retinal disorders. During the process, the time duration for the OCT examination for one eye (starting from the participant placing their head and chin at the bracket to terminating at the end of the scan for one eye) and the output time of the AI report were also recorded.

AI auto-detection

The inference pipeline was as follows: first, the quality of collected OCT images was assessed using an AI algorithm. The OCT b-scans with poor quality, such as heavy noise, severe artifacts, low contrast, or low brightness, were excluded to avoid the analysis results with low confidence. The module of quality assessment is a trained binary classification model, which is composed of ResNet-50. Then, the OCT b-scans with good quality were imputed into a trained object detection model to detect up to 15 categories of retinal pathologies, and the detection model was based on the deep-learning convolutional neural



network. Subsequently, the trained key-point detection model extracted the Bruch's membrane opening locations on OCT b-scans, and the false optimistic predictions of the bounding boxes near the site of the optic disc would be eliminated. Finally, a probability ratio (0–1) of auxiliary diagnosis based on all considerations and lesion locations of 15 categories of retinal disorders on OCT b-scans was calculated and applied (Figure 1).

As for the development strategy of the AI algorithm, a multi-stage object detection model based on the adjusted

TABLE 1 Demographic information and baseline characteristics of the participants.

Characteristic	Data
Participants' eyes, right, n (%)	439 (50%)
Age (years), mean \pm SD	53.16 \pm 17.14
Gender, male, n (%)	213 (48.5%)
Hypertension, n (%)	75 (17.1%)
Diabetes, n (%)	48 (10.9%)
OCT scan (seconds), mean \pm SD	18.4 \pm 0.11
AI outputting time (minutes), mean \pm SD	4.01 \pm 0.03

Cascade-RCNN was adopted (Essa et al., 2011). The feature pyramid network architecture was used to extract the multi-scale features of each b-scan image to enhance the ability of the model to detect large-size retinal and tiny-size pathologist such as retinal detachment and exudation. We trained the model for 48 epochs, and the SGD optimizer was used (Zhang Z. et al., 2021). The Smooth L1 loss function was used in the regression of the region proposal network and cascade-head network, and the cross-entropy loss was used in classification parts. The online hard example mining mechanism was used to improve the convergence speed due to the unbalanced ratio between the foreground and background, and the tremendous differences in learning difficulty among 15 categories of retinal disorders were observed (Chen et al., 2021). As for the datasets, 1311 cubes were collected and divided into the training set, validation set, and test set with a ratio of 6:2:2. The distribution of the datasets is presented in Supplementary Table 1, which shows 363 cubes are normal, and most of the retinal disorders are PVD. Three or more typical b-scans slices were selected from cubes, and these selected slices contained various lesions of retinal disorders, which contributed to the better learning and adaptive ability of AI algorithm. Subsequently, the external test was performed, and the results of the external test set can be used as evidence of the generalization ability of the AI model.

Ophthalmologist diagnosis

Three groups of ophthalmologists were organized to perform manual annotation with the selection criteria as follows:

The junior group (OP1) consists of three resident doctors who had worked in the Department of Ophthalmology for more than 3 years. The senior group (OP2) consists of three attending ophthalmologists with more than 8 years of experience in clinical practice. The retinal specialist's group (OP3) consists of three retinal professors who have dedicated to working in the field of retinal diseases for more than 12 years. The ophthalmologists were all from the Department of Ophthalmology of Shanghai

Tenth People's Hospital and trained together before the task. If the conclusions of three doctors in each group were inconsistent, a panel discussion and vote inside the group would be arranged to reach a consensus and generate a standard conclusion.

A manual review and final diagnosis of the 15 retinal disorders were prepared according to all the participant's medical information, including slit-lamp examination, fundus photography, OCT images, demographic information, and systemic medical history. Doctors in each group carried out an independent diagnosis and were masked to AI diagnosis results from doctors in the same group as well as in other groups. The manual diagnosis and AI algorithm outputs were compared according to the recognized diagnostic criteria, noting that a combination of various pathologies could coexist in one participant.

Statistical analysis

To evaluate the performance of the AI algorithm compared with three different levels of ophthalmologists, the receiver operating characteristic curve (ROC) was generated using the diagnosis results given by the retinal specialist (OP3) regarded as the reference standard. The area under ROC (AUC), sensitivity and specificity, and Youden index with 95% confidence intervals (95% CIs) were calculated. Paired comparisons were performed between the AUC of AI to OP3, junior ophthalmologist (OP1) to OP3, and senior ophthalmologist (OP2) to OP3 to assess their difference toward the reference standard. Kappa (κ) statistics were used to quantify and evaluate the degree of agreement between AI and three different level group ophthalmologists (OP1, OP2, and OP3). To transfer the AI grading score to a binary decision for analysis, the cut-off value was set at 0.7 based on the pre-setting data during model establishment, which means that a value equal to or larger than 0.7 in AI calculated results as positive, while less than 0.7 is recognized as negative. The threshold value 0.7 was selected on the validation set, which means that the AI gained the maximum value of the F1 score on the validation set when the threshold value was set at 0.7. The F1 score is an index that could balance the false detection rate and missed detection rate, and it is a commonly used index for selecting the threshold of the algorithm model. A p -value < 0.05 was considered statistically significant. All data generated were analyzed using SPSS version 21.0 (IBM Inc., Chicago, Illinois, United States).

Results

From September to December 2021, 477 subjects (954 eyes) from four local communities mentioned previously participated in the study. However, after image quality control, only 878 eyes (from 439 subjects) were finally enrolled, while 76 eyes were

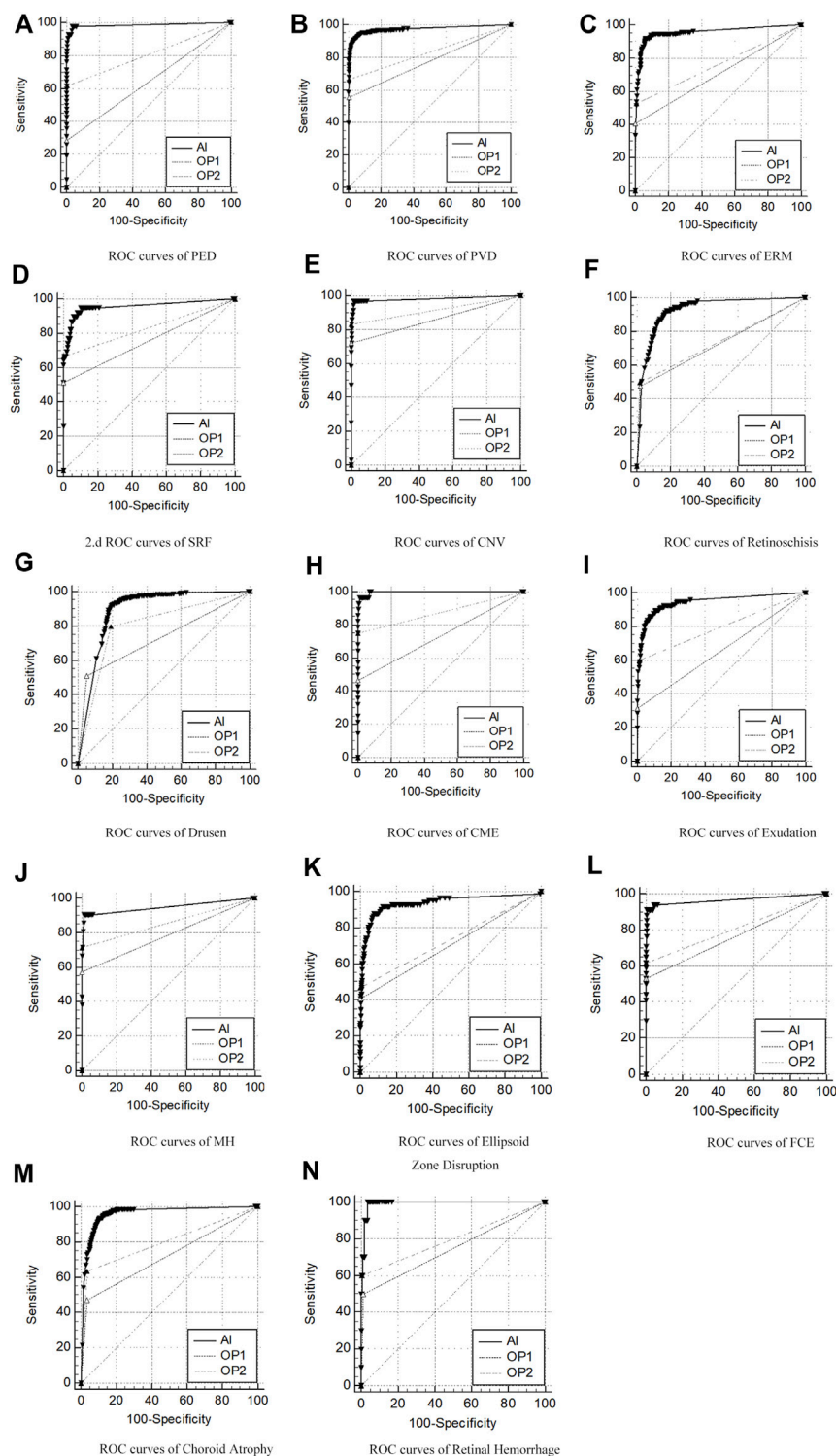


FIGURE 2

ROC curves of AI/group of junior ophthalmologists (OP1)/group of senior ophthalmologists (OP2) compared to the group of retinal specialists (OP3, as the golden standard) in diagnosis of 14 retinal disorders. (A–N) Pigment epithelial detachment (PED), posterior vitreous detachment (PVD), epiretinal membranes (ERMs), sub-retinal fluid (SRF), choroidal neovascularization (CNV), drusen, retinoschisis, cystoid macular edema (CME), exudation, macular hole (MH), ellipsoid zone disruption, focal choroidal excavation (FCE), choroid atrophy, and retinal hemorrhage.

TABLE 2 AUC (with 95% CI), Youden index, specificity, and sensitivity in ROC of AI/group of junior ophthalmologists (OP1)/group of senior ophthalmologists (OP2) compared to the group of retinal specialists (OP3, as the golden standard).

	AI vs. OP3						OP1 vs. OP3			OP2 vs. OP3			<i>p</i> (AUC, AI–OP3 vs. OP1–OP3)	<i>p</i> (AUC, AI–OP3 vs. OP2–OP3)
	AUC	95% CI	<i>p</i>	Youden index	Sensitivity (%)	Specificity (%)	AUC	95% CI	<i>p</i>	AUC	95% CI	<i>p</i>		
PED	0.985	0.974–0.992	<0.0001	0.9391	97.62	96.29	0.643	0.610–0.675	0.0001	0.808	0.780–0.833	<0.0001	<0.0001	<0.0001
PVD	0.973	0.960–0.983	<0.0001	0.8743	91.83	95.60	0.775	0.745–0.802	<0.0001	0.830	0.804–0.855	<0.0001	<0.0001	<0.0001
ERM	0.955	0.940–0.968	<0.0001	0.8552	91.84	93.68	0.704	0.673–0.734	<0.0001	0.759	0.730–0.787	<0.0001	<0.0001	<0.0001
SRF	0.956	0.940–0.968	<0.0001	0.8450	94.87	89.63	0.756	0.727–0.784	<0.0001	0.833	0.807–0.857	<0.0001	<0.0001	= 0.0003
CNV	0.983	0.972–0.990	<0.0001	0.9556	97.22	98.34	0.860	0.835–0.882	<0.0001	0.917	0.896–0.934	<0.0001	= 0.0007	= 0.0227
Retinoschisis	0.926	0.906–0.942	<0.0001	0.7456	92.23	82.32	0.727	0.696–0.756	<0.0001	0.739	0.708–0.767	<0.0001	<0.0001	<0.0001
Drusen	0.891	0.868–0.911	<0.0001	0.7222	92.10	80.12	0.728	0.698–0.758	<0.0001	0.803	0.775–0.828	<0.0001	<0.0001	<0.0001
CME	0.997	0.991–0.999	<0.0001	0.9537	96.43	98.94	0.732	0.702–0.761	<0.0001	0.875	0.851–0.896	<0.0001	<0.0001	= 0.0028
Exudation	0.944	0.927–0.959	<0.0001	0.7856	89.57	88.99	0.657	0.624–0.688	<0.0001	0.793	0.764–0.819	<0.0001	<0.0001	<0.0001
MH	0.948	0.931–0.962	<0.0001	0.8931	90.48	98.83	0.785	0.756–0.811	<0.0001	0.857	0.832–0.880	<0.0001	= 0.0020	= 0.0376
Ellipsoid zone disruption	0.935	0.916–0.950	<0.0001	0.8000	87.65	92.35	0.704	0.672–0.734	<0.0001	0.734	0.703–0.763	<0.0001	<0.0001	<0.0001
FCE	0.967	0.953–0.978	<0.0001	0.9058	91.18	99.41	0.764	0.735–0.792	<0.0001	0.808	0.781–0.834	<0.0001	<0.0001	= 0.0001
Choroid atrophy	0.959	0.943–0.971	<0.0001	0.8288	93.62	89.26	0.718	0.687–0.748	<0.0001	0.799	0.771–0.825	<0.0001	<0.0001	<0.0001
Retinal hemorrhage	0.991	0.982–0.996	<0.0001	0.9631	100.00	96.31	0.744	0.714–0.773	0.0034	0.798	0.770–0.824	0.0003	= 0.0022	= 0.0136

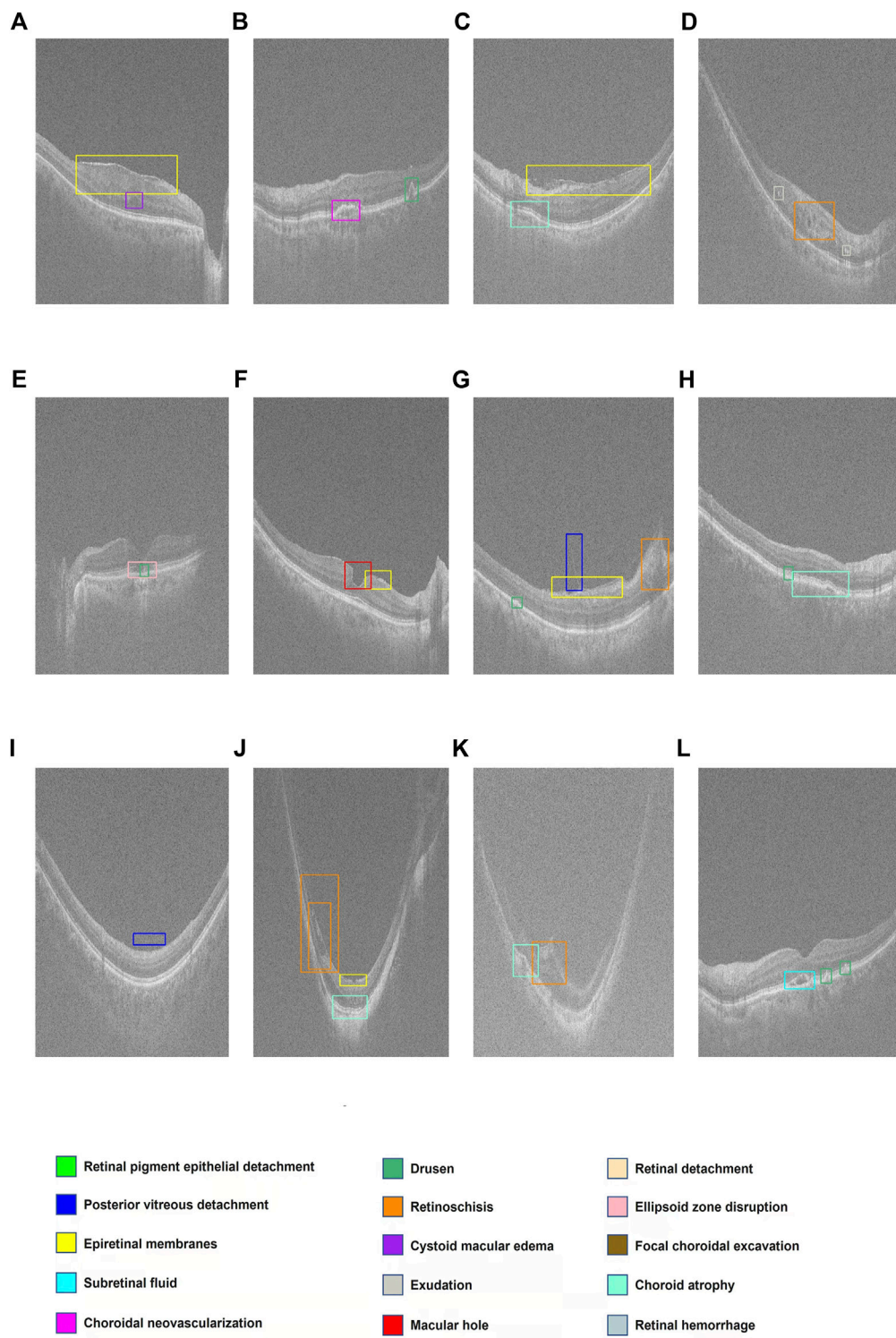


FIGURE 3
Display of multiple retinal disorders and their locations. (A–L) Fifteen categories of retinal disorders are marked by rectangles with specific colors on OCT images.

TABLE 3 Kappa analysis results.

Diagnosis	Kappa value		
	AI vs. OP1	AI vs. OP2	AI vs. OP3
PED	0.608	0.816	0.774
PVD	0.657	0.763	0.873
ERM	0.452	0.584	0.834
SRF	0.440	0.539	0.580
CNV	0.824	0.860	0.843
Drusen	0.383	0.751	0.720
Retinoschisis	0.424	0.426	0.520
CME	0.809	0.847	0.803
Exudation	0.373	0.616	0.709
MH	0.555	0.630	0.709
RD	NA	NA	NA
Ellipsoid zone disruption	0.627	0.669	0.669
FCE	0.767	0.803	0.807
CA	0.553	0.690	0.792
RH	0.635	0.899	0.595
Average	0.579	0.707	0.731

excluded due to poor OCT image quality, mainly due to small pupils, keratoleukoma, cataracts, vitreous opacity, *etc.* The 439 subjects consisted of 213 males and 226 females, aging from 34 to 72 (53.16 ± 17.14), among whom 75 (17.1%) had a history of hypertension and 48 (10.9%) had a history of diabetes mellitus. The demographic information, average time for the OCT scan, and AI output are presented in Table 1.

The overall ROC curve comparison between AI diagnosis and the group of retinal specialists (OP3) represented a large AUC (0.891–0.997), high sensitivity (87.65–100%), and high specificity (80.12–99.41%). Since no case of RD was detected in the whole participants' screening either by doctors or by AI software, the data related to RD were unavailable beyond any comparison or discussion. Among the rest 14 retinal disorders, the best performance was revealed in the diagnosis of CME and retinal hemorrhage, with the AUC, sensitivity, and specificity at 0.997, 96.43%, and 98.94%, and 0.991, 100%, and 96.31%, respectively. Also, high accuracy with a relatively large AUC was acquired in the diagnosis of PED, PVD, ERM, FCE, and CNV, with the AUC, sensitivity, and specificity at 0.985, 97.62%, and 96.29% in PED; 0.973, 91.83%, and 95.60% in PVD, and 0.955, 91.84%, and 93.68% in ERM, respectively. As for the diagnosis in FCE, the AUC was 0.967 with a sensitivity of 91.18% and specificity of 99.41%, while the result was 0.983, 97.22%, and 98.34%, relatively for CNV, respectively. The lower results were generated in the detection of exudation (AUC of 0.944, sensitivity of 89.57%, and specificity of 88.99%) and retinoschisis (AUC of 0.926, sensitivity of 92.23%, and specificity of 82.32%). The lowest AUC appeared in the

recognition of drusen, which still reached 0.891, with a sensitivity of 92.10% and a specificity of 80.12%.

The ROC curve comparisons between the groups of junior (OP1) or senior (OP2) ophthalmologists and AI to the group of retinal specialists (OP3) were generated and compared. The paired comparison showed that the AUC of AI–OP3 was larger than that of OP1–OP3 or OP2–OP3 with a significant difference, indicating that the AI results were much closer to OP3 taken as the golden standard, surpassing OP1 or OP2.

The ROC curves for 14 retinal disorders are shown in Figure 2, and comparisons of AUC, Youden index, specificity, and sensitivity with 95% CI are shown in Table 2. At the same time, representing images with lesions labeled at the specific location of the retina are illustrated in Figure 3.

The results of the kappa analysis are shown in Table 3. The consistency between AI and retinal specialists was relatively high, with the average value of 0.731, while the average value was 0.579 between AI and OP1 and 0.707 between AI and OP2.

Discussion

To relieve the conflict between the enormous demand for early screening of multiple retinal diseases with rising prevalence and the lack of human medical resources, the application of AI algorithms, especially the DL models as auxiliary tools for diagnosis provided a feasible and promising solution (He et al., 2020; Xie et al., 2020; Cen et al., 2021). Taking the retinal OCT image rather than fundus photography only as the diagnosis reference proof was a new trend in this field (Treder et al., 2018; Sogawa et al., 2020; Wang et al., 2020). However, most current software was designed to detect one single category of retinal disease, which hindered its application in real-world practice. Our study utilized an AI algorithm that can recognize 15 retinal disorders at one time with features extracted from OCT images and evaluated its accuracy and feasibility in community screening.

In this study, the demographic information showed equivalence in gender but possessed a relatively elder population age, which conformed to the actual characteristic of the four communities involved. The prevalence of hypertension (17%) and diabetes mellitus (11%) among our participants was similar to that of the general population (Wang et al., 2018; Sun et al., 2022). Except for the retinal detachment with no case occurred in the study, the incidence rate of the rest 14 retinal disorders was close to the natural scale in the general population (Hong et al., 2013; Mitchell et al., 2018; Wang and Lo, 2018; Wolfram et al., 2019; Li et al., 2022b).

According to our data, the overall ROC curve comparison between AI diagnosis and the group of retinal specialists (OP3) exhibited large AUC (0.891–0.997), high sensitivity (87.65–100%), and high specificity (80.12–99.41%). Also, the AUC of AI–OP3 was larger than that of OP1–OP3 or

OP2–OP3 with a significant difference, while the average value generated from kappa analysis representing the consistency between AI and retinal specialists (OP3) was larger than AI–OP1 and AI–OP2, which in all supported that AI results were much closer to OP3 as the golden standard, exceeding the performance of OP1 or OP2, and certified the accuracy of the AI auto-detection system we utilized.

Compared to the function of other AI software developed for a specific category of retinal disorders (AMD, DR, or ERM solely) in previous studies, our system also demonstrated equal or even better performance in the corresponding specific disease. As for the detection of AMD, one of the leading causes of visual impairment in elderly patients, several deep-learning algorithms have been developed to recognize relative lesions and perform machine discrimination. Treder et al. (2018) developed an AI algorithm based on an open-source multi-layer deep CNN model to diagnose AMD and the generated sensitivity, specificity, and accuracy were 100%, 92%, and 96%, respectively. However, the size of the test was relatively small ($n = 50$). The DL model of Lee et al. (2017) achieved an area under the ROC curve of 92.78% with an accuracy of 87.63% at the image level, while at the patient level, the data were 97.45% and 93.69%, respectively. However, neither the classifiers could detect the specified lesion nor the position of AMD, which was fulfilled in our algorithm (Lee et al., 2017; Treder et al., 2018). Elsharkawy et al. (2021) reviewed several studies using DL models for AMD diagnosis in a qualitative and quantitative manner and found that despite the positive results generated from different algorithms, most of them could not identify or grade each type of AMD. Also, the majority of the testing was conducted on preselected individuals' sample only, rather than real-world validation in our study. Mantel et al. (2021) developed a DL algorithm for the automated identification, localization, and volume measurement of exudative manifestations of intraretinal fluid (IRF), sub-retinal fluid (SRF), and pigment epithelium detachment (PED) in neovascular age-related macular degeneration (nAMD). The results showed that the AUC, sensitivity, and specificity were 0.97, 0.95, and 0.99, respectively, with accurate measurement of the volumes, despite a limited number of included OCT volumes, advancing the aspect of AI from quantitation to quantification.

As for the automated diagnosis of DR, the prevalence of which was ascending worldwide and causing a visual loss for a large population, and previous studies were carried out using fundus photographs as image sources. In contrast, recent studies were conducted utilizing OCT images (Sandhu et al., 2018; Sandhu et al., 2020; Lakshminarayanan et al., 2021). Lakshminarayanan et al. (2021) reviewed different ML models on DR diagnosis published within 6 years (2016–2021) and concluded that although some of the recent CNN-based models exhibited high performance in terms of the standard

metrics, the lack of validation for real-life clinical applications remained as defects, with difficulty in detecting specific lesion like exudation and microaneurysms.

Previous studies also involved auto-detection of myopic macular diseases using AI algorithm due to the rising prevalence of myopia and multiple vision-threatening retinal damages (Sogawa et al., 2020; Choi et al., 2021; Ye et al., 2021; Li et al., 2022a). Ye et al. (2021) engineered the deep-learning (DL) model to identify myopic maculopathy, including macular choroidal thinning, macular Bruch membrane (BM) defects, sub-retinal hyper-reflective material (SHRM), myopic traction maculopathy (MTM), and dome-shaped macula (DSM), and the result showed that the AUC was 0.927–0.974 for five myopic maculopathies. Choi et al. (2021) trained and validated three DL models to identify myopia and generated a result of the absolute agreement with retina specialists which was 99.11%. However, the specific lesion associated with myopia could not be detected, and validation with an external dataset was needed. Li et al. (2022a) developed four independent CNN models to identify retinoschisis, macular hole, retinal detachment, and pathological myopic choroidal neovascularization and acquired satisfactory results with a high AUC for all conditions (0.961–0.999), revealing that the sensitivity and specificity of the AI system were equal to or even better than those of retina specialists.

Among the literature, we reviewed another two specific retinal disorders: ERM and PED (Sun et al., 2016; Lo et al., 2020). Lo et al. (2020) proposed a deep-learning model to identify the epiretinal membrane (ERM) in OCT. Also, the results showed that the diagnostic accuracy was 98.1% and the AUC was 0.999, implying that the model's performance was slightly better than the average non-retinal specialized ophthalmologists. Sun et al. (2016) proposed an automated framework to segment serous PED in SD-OCT images. The average true-positive volume fraction (TPVF), false-positive volume fraction (FPVF), dice similarity coefficient (DSC), and positive predictive value (PPV) were calculated as 90.08%, 0.22%, 91.20%, and 92.62%, respectively. However, the test dataset consisted of only 25 patients.

No literature was found concerning AI auto-detection based on OCT images of the following specific retinal disorders: ellipsoid zone disruption, FCE, PVD, and RD.

Through the aforementioned literature review, we saw a different performance of various AI models, as well as compared our results. The underlying reason may include: 1) different models and architecture; 2) variant resources and sizes of the dataset for training and testing; 3) inconsistent standards for lesion labeling, as well as the difference in definition and classification of a specific disease; 4) different procedures of image quality control, as the quality of an image may affect the results of AI output; and 5) different methodology of evaluation, as with image view

(only judge the image) or patient view (with consideration to other clinical information.)

A common disadvantage of the aforementioned studies was that their AI models focused on only one specific retinal disorder leaving others unable to be recognized, which reduced their feasibility and availability in real-world practice as community screening (Kuwayama et al., 2019; Wang et al., 2020; Guo et al., 2021; Liu et al., 2022). Our AI model could identify multiple retinal disorders simultaneously in single detection, which was more appropriate for the scene of community screening with the unpredicted situations and comprehensive diseases and saved more time and occupied fewer human resources. In addition to the AUC and specificity, our results revealed a relatively high sensitivity, which ensured its potency as a screening tool in the early stage. In the procedure of the OCT scan, the average examination time was 18.4 s for one eye and the average output time of the AI report was 4 min. The high accuracy and efficiency were proposed due to 1) the strategy in architecture and model establishment, as well as the online hard example mining mechanism utilized to improve the convergence speed due to the unbalanced ratio between the foreground and background; 2) accumulated experience and advanced technology in OCT image analysis with AI algorithms (Sun et al., 2016; Zhu et al., 2017; Shi et al., 2019; Shi et al., 2021; Wang et al., 2022); 3) the integrated design of the OCT instrument and AI algorithm; 4) the high performance of the OCT instrument with a maximum A scan speed at 45,000 times per second as well as the high resolution of the images. The aforementioned issues all guaranteed the accuracy and speed of the community screening work.

However, there are still some limitations to our study. First, the images were acquired from one type of the OCT instrument, and the procedure was carried out in one district by one single medical center. To certify the accuracy of the AI system about images from other OCT instruments and the participants from other communities with other medical centers, we will further promote the study. The second issue was that the detection of RD was not verified due to the limitation of the participants in our study. Further evaluation may be performed with specified patients. Finally, for some retinal disorders, the performance of specificity and sensitivity still needs to be improved with the further imperfection of the algorithm.

Conclusion

To the best of our knowledge, this was the first study carried out in real-world community screening utilizing the SD-OCT and integrated AI algorithm to auto-detect 15 different retinal disorders simultaneously, with its accuracy compared to three different levels of ophthalmologists judging from the patient aspects. Positive results revealed that the accuracy of AI was close to that of the retinal specialist, surpassing that of junior and senior ophthalmologists, indicating a promising prospect of the

application of the OCT instrument and AI software in clinical practice and community screening.

Data availability statement

The original contributions presented in the study are included in the article/[Supplementary Material](#); further inquiries can be directed to the corresponding author/s.

Ethics statement

The studies involving human participants were reviewed and approved by the Ethics Review Committee of Shanghai Tenth Peoples Hospital, Shanghai, China. The patients/participants provided their written informed consent to participate in this study. Written informed consent was obtained from the individual(s) for the publication of any potentially identifiable images or data included in this article.

Author contributions

JB and ZW participated in the data analysis and writing of the manuscript. PL, LC, and JW participated in data collection and revised the manuscript. YF participated in the data analysis. PG, QP, and XC designed the study and wrote and revised the manuscript. All authors contributed to the article and approved the submitted version.

Funding

This work was supported by the National Natural Science Foundation of China [grant number 81470025] and the Shanghai Municipal Science and Technology Commission (research project number 21142201800).

Conflict of interest

JW and YF was employed by Suzhou Big Vision Medical Technology Co., Ltd.

The remaining authors declare that the research was conducted in the absence of any commercial or financial relationships that could be construed as a potential conflict of interest.

Publisher's note

All claims expressed in this article are solely those of the authors and do not necessarily represent those of their

affiliated organizations, or those of the publisher, the editors, and the reviewers. Any product that may be evaluated in this article, or claim that may be made by its manufacturer, is not guaranteed or endorsed by the publisher.

References

- Camara, J., Neto, A., Pires, I. M., Villasana, M. V., Zdravetski, E., and Cunha, A. (2022). Literature review on artificial intelligence methods for glaucoma screening, segmentation, and classification. *J. Imaging* 8 (2), 19. doi:10.3390/jimaging8020019
- Cen, L. P., Ji, J., Lin, J. W., Ju, S. T., Lin, H. J., Li, T. P., et al. (2021). Automatic detection of 39 fundus diseases and conditions in retinal photographs using deep neural networks. *Nat. Commun.* 12 (1), 4828. doi:10.1038/s41467-021-25138-w
- Chen, Z. M., Jin, X., Zhao, B. R., Zhang, X., and Guo, Y. (2021). Hce: Hierarchical context embedding for region-based object detection. *IEEE Trans. Image Process.* 30, 6917–6929. doi:10.1109/tip.2021.3099733
- Choi, K. J., Choi, J. E., Roh, H. C., Eun, J. S., Kim, J. M., Shin, Y. K., et al. (2021). Deep learning models for screening of high myopia using optical coherence tomography. *Sci. Rep.* 11 (1), 21663. doi:10.1038/s41598-021-00622-x
- Elsharkawy, M., Elrazzaz, M., Ghazal, M., Alhalabi, M., Soliman, A., Mahmoud, A., et al. (2021). Role of optical coherence tomography imaging in predicting progression of age-related macular disease: A survey. *Diagn. (Basel)* 11 (12), 2313. doi:10.3390/diagnostics11122313
- Essa, I., Kang, S. B., and Pollefeys, M. (2011). Guest editors' introduction to the special section on award-winning papers from the IEEE conference on computer vision and pattern recognition 2009 (CVPR 2009). *IEEE Trans. Pattern Anal. Mach. Intell.* 33 (12), 2339–2340. doi:10.1109/tpami.2011.215
- Feng, J. J., An, L., Wang, Z. F., Zhan, L. L., and Xu, X. (2018). Analysis on ophthalmic human resource allocation and service delivery at county level in Mainland China in 2014. *Zhonghua. Yan Ke Za Zhi* 54 (12), 929–934. doi:10.3760/cma.j.issn.0412-4081.2018.12.011
- Gulshan, V., Peng, L., Coram, M., Stumpe, M. C., Wu, D., Narayanaswamy, A., et al. (2016). Development and validation of a deep learning algorithm for detection of diabetic retinopathy in retinal fundus photographs. *Jama* 316 (22), 2402–2410. doi:10.1001/jama.2016.17216
- Guo, C., Yu, M., and Li, J. (2021). Prediction of different eye diseases based on fundus photography via deep transfer learning. *J. Clin. Med.* 10 (23), 5481. doi:10.3390/jcm10235481
- He, J., Cao, T., Xu, F., Wang, S., Tao, H., Wu, T., et al. (2020). Artificial intelligence-based screening for diabetic retinopathy at community hospital. *Eye (Lond)* 34 (3), 572–576. doi:10.1038/s41433-019-0562-4
- Hong, T., Mitchell, P., Rochtchina, E., Fong, C. S., Chia, E. M., and Wang, J. J. (2013). Long-term changes in visual acuity in an older population over a 15-year period: The blue mountains eye study. *Ophthalmology* 120 (10), 2091–2099. doi:10.1016/j.ophtha.2013.03.032
- Keel, S., Wu, J., Lee, P. Y., Scheetz, J., and He, M. (2019). Visualizing deep learning models for the detection of referable diabetic retinopathy and glaucoma. *JAMA Ophthalmol.* 137 (3), 288–292. doi:10.1001/jamaophthalmol.2018.6035
- Kuwayama, S., Ayatsuka, Y., Yanagisano, D., Uta, T., Usui, H., Kato, A., et al. (2019). Automated detection of macular diseases by optical coherence tomography and artificial intelligence machine learning of optical coherence tomography images. *J. Ophthalmol.* 2019, 6319581. doi:10.1155/2019/6319581
- Lakshminarayanan, V., Kheradfallah, H., Sarkar, A., and Jothi Balaji, J. (2021). Automated detection and diagnosis of diabetic retinopathy: A comprehensive survey. *J. Imaging* 7 (9), 165. doi:10.3390/jimaging7090165
- Lee, C. S., Baughman, D. M., and Lee, A. Y. (2017). Deep learning is effective for the classification of OCT images of normal versus Age-related Macular Degeneration. *Ophthalmol. Retina* 1 (4), 322–327. doi:10.1016/j.oret.2016.12.009
- Li, Y., Feng, W., Zhao, X., Liu, B., Zhang, Y., Chi, W., et al. (2022a). Development and validation of a deep learning system to screen vision-threatening conditions in high myopia using optical coherence tomography images. *Br. J. Ophthalmol.* 106 (5), 633–639. doi:10.1136/bjophthalmol-2020-317825
- Li, Y., Hu, Q., Li, X., Hu, Y., Wang, B., Qin, X., et al. (2022b). The fujian eye cross sectional study: Objectives, design, and general characteristics. *BMC Ophthalmol.* 22 (1), 112. doi:10.1186/s12886-022-02346-6
- Liu, X., Zhao, C., Wang, L., Wang, G., Lv, B., Lv, C., et al. (2022). Evaluation of an OCT-AI-based telemedicine platform for retinal disease screening and referral in a primary care setting. *Transl. Vis. Sci. Technol.* 11 (3), 4. doi:10.1167/tvst.11.3.4
- Lo, Y. C., Lin, K. H., Bair, H., Sheu, W. H., Chang, C. S., Shen, Y. C., et al. (2020). Epiretinal membrane detection at the ophthalmologist level using deep learning of optical coherence tomography. *Sci. Rep.* 10 (1), 8424. doi:10.1038/s41598-020-65405-2
- Mantel, I., Mosinska, A., Bergin, C., Polito, M. S., Guidotti, J., Apostolopoulos, S., et al. (2021). Automated quantification of pathological fluids in neovascular age-related macular degeneration, and its repeatability using deep learning. *Transl. Vis. Sci. Technol.* 10 (4), 17. doi:10.1167/tvst.10.4.17
- Mitchell, P., Liew, G., Gopinath, B., and Wong, T. Y. (2018). Age-related macular degeneration. *Lancet* 392 (10153), 1147–1159. doi:10.1016/s0140-6736(18)31550-2
- Rajalakshmi, R., Subashini, R., Anjana, R. M., and Mohan, V. (2018). Automated diabetic retinopathy detection in smartphone-based fundus photography using artificial intelligence. *Eye (Lond)* 32 (6), 1138–1144. doi:10.1038/s41433-018-0064-9
- Ruiz-Medrano, J., Montero, J. A., Flores-Moreno, I., Arias, L., García-Layana, A., and Ruiz-Moreno, J. M. (2019). Myopic maculopathy: Current status and proposal for a new classification and grading system (ATN). *Prog. Retin. Eye Res.* 69, 80–115. doi:10.1016/j.preteyeres.2018.10.005
- Sandhu, H. S., Elmoghy, M., Taher Sharafelddeen, A., Elsharkawy, M., El-Adawy, N., Eltanboly, A., et al. (2020). Automated diagnosis of diabetic retinopathy using clinical biomarkers, optical coherence tomography, and optical coherence tomography angiography. *Am. J. Ophthalmol.* 216, 201–206. doi:10.1016/j.ajo.2020.01.016
- Sandhu, H. S., Eltanboly, A., Shalaby, A., Keynton, R. S., Schaal, S., and El-Baz, A. (2018). Automated diagnosis and grading of diabetic retinopathy using optical coherence tomography. *Invest. Ophthalmol. Vis. Sci.* 59 (7), 3155–3160. doi:10.1167/jovs.17-23677
- Shi, F., Cai, N., Gu, Y., Hu, D., Ma, Y., Chen, Y., et al. (2019). DeSpecNet: A CNN-based method for speckle reduction in retinal optical coherence tomography images. *Phys. Med. Biol.* 64 (17), 175010. doi:10.1088/1361-6560/ab3556
- Shi, F., Cheng, X., Feng, S., Yang, C., Diao, S., Zhu, W., et al. (2021). Group-wise context selection network for choroid segmentation in optical coherence tomography. *Phys. Med. Biol.* 66 (24), 245010. doi:10.1088/1361-6560/ac3a23
- Sogawa, T., Tabuchi, H., Nagasato, D., Masumoto, H., Ikuno, Y., Ohsugi, H., et al. (2020). Accuracy of a deep convolutional neural network in the detection of myopic macular diseases using swept-source optical coherence tomography. *PLoS One* 15 (4), e0227240. doi:10.1371/journal.pone.0227240
- Sun, H., Saeedi, P., Karuranga, S., Pinkepank, M., Ogurtsova, K., Duncan, B. B., et al. (2022). IDF Diabetes Atlas: Global, regional and country-level diabetes prevalence estimates for 2021 and projections for 2045. *Diabetes Res. Clin. Pract.* 183, 109119. doi:10.1016/j.diabres.2021.109119
- Sun, Z., Chen, H., Shi, F., Wang, L., Zhu, W., Xiang, D., et al. (2016). An automated framework for 3D serous pigment epithelium detachment segmentation in SD-OCT images. *Sci. Rep.* 6, 21739. doi:10.1038/srep21739
- Treder, M., Lauermann, J. L., and Eter, N. (2018). Automated detection of exudative age-related macular degeneration in spectral domain optical coherence tomography using deep learning. *Graefes Arch. Clin. Exp. Ophthalmol.* 256 (2), 259–265. doi:10.1007/s00417-017-3850-3
- Wang, L., Wang, G., Zhang, M., Fan, D., Liu, X., Guo, Y., et al. (2020). An intelligent optical coherence tomography-based system for pathological retinal cases identification and urgent referrals. *Transl. Vis. Sci. Technol.* 9 (2), 46. doi:10.1167/tvst.9.2.46
- Wang, M., Zhu, W., Shi, F., Su, J., Chen, H., Yu, K., et al. (2022). MsTGANet: Automatic drusen segmentation from retinal OCT images. *IEEE Trans. Med. Imaging* 41 (2), 394–406. doi:10.1109/tmi.2021.3112716
- Wang, W., and Lo, A. C. Y. (2018). Diabetic retinopathy: Pathophysiology and treatments. *Int. J. Mol. Sci.* 19 (6), E1816. doi:10.3390/ijms19061816

Supplementary material

The Supplementary Material for this article can be found online at: <https://www.frontiersin.org/articles/10.3389/fcell.2022.1053483/full#supplementary-material>

Wang, Z., Chen, Z., Zhang, L., Wang, X., Hao, G., Zhang, Z., et al. (2018). Status of hypertension in China: Results from the China hypertension survey, 2012–2015. *Circulation* 137 (22), 2344–2356. doi:10.1161/circulationaha.117.032380

Wolfram, C., Schuster, A. K., Elflein, H. M., Nickels, S., Schulz, A., Wild, P. S., et al. (2019). The prevalence of visual impairment in the adult population. *Dtsch. Arztebl. Int.* 116 (17), 289–295. doi:10.3238/arztebl.2019.0289

Xie, Y., Nguyen, Q. D., Hamzah, H., Lim, G., Bellemo, V., Gunasekaran, D. V., et al. (2020). Artificial intelligence for teleophthalmology-based diabetic retinopathy screening in a national programme: An economic analysis modelling study. *Lancet. Digit. Health* 2 (5), e240–e249. doi:10.1016/s2589-7500(20)30060-1

Ye, X., Wang, J., Chen, Y., Lv, Z., He, S., Mao, J., et al. (2021). Automatic screening and identifying myopic maculopathy on optical coherence tomography images using deep learning. *Transl. Vis. Sci. Technol.* 10 (13), 10. doi:10.1167/tvst.10.13.10

Zhang, Q., Li, J., Bian, M., He, Q., Shen, Y., Lan, Y., et al. (2021a). Retinal imaging techniques based on machine learning models in recognition and prediction of mild cognitive impairment. *Neuropsychiatr. Dis. Treat.* 17, 3267–3281. doi:10.2147/ndt.S333833

Zhang, Y. Y., Zhao, H., Lin, J. Y., Wu, S. N., Liu, X. W., Zhang, H. D., et al. (2021b). Artificial intelligence to detect meibomian gland dysfunction from *in-vivo* laser confocal microscopy. *Front. Med.* 8, 774344. doi:10.3389/fmed.2021.774344

Zhang, Z., Qiu, X., and Li, Y. (2021c). Sefpn: Scale-equalizing feature Pyramid network for object detection. *Sensors (Basel)* 21 (21), 7136. doi:10.3390/s21217136

Zhu, S., Shi, F., Xiang, D., Zhu, W., Chen, H., and Chen, X. (2017). Choroid neovascularization growth prediction with treatment based on reaction-diffusion model in 3-D OCT images. *IEEE J. Biomed. Health Inf.* 21 (6), 1667–1674. doi:10.1109/jbhi.2017.2702603



OPEN ACCESS

EDITED BY
Huiying Liu,
Institute for Infocomm Research
(A*STAR), Singapore

REVIEWED BY
Jinhai Huang,
Fudan University, China
Wei Li,
National Institutes of Health (NIH),
United States

*CORRESPONDENCE
Wei Han,
hanweidr@zju.edu.cn

SPECIALTY SECTION
This article was submitted to Molecular
and Cellular Pathology,
a section of the journal
Frontiers in Cell and Developmental
Biology

RECEIVED 25 September 2022
ACCEPTED 19 October 2022
PUBLISHED 03 November 2022

CITATION
Fang Z, Xu Z, He X and Han W (2022),
Artificial intelligence-based pathologic
myopia identification system in the
ophthalmology residency
training program.
Front. Cell Dev. Biol. 10:1053079.
doi: 10.3389/fcell.2022.1053079

COPYRIGHT
© 2022 Fang, Xu, He and Han. This is an
open-access article distributed under
the terms of the [Creative Commons
Attribution License \(CC BY\)](https://creativecommons.org/licenses/by/4.0/). The use,
distribution or reproduction in other
forums is permitted, provided the
original author(s) and the copyright
owner(s) are credited and that the
original publication in this journal is
cited, in accordance with accepted
academic practice. No use, distribution
or reproduction is permitted which does
not comply with these terms.

Artificial intelligence-based pathologic myopia identification system in the ophthalmology residency training program

Zhi Fang^{1,2}, Zhe Xu^{1,2}, Xiaoying He^{1,2} and Wei Han^{1,2*}

¹Department of Eye Center, The Second Affiliated Hospital, Zhejiang University School of Medicine, Hangzhou, Zhejiang, China, ²Zhejiang Provincial Key Lab of Ophthalmology, Hangzhou, Zhejiang, China

Background: Artificial intelligence (AI) has been successfully applied to the screening tasks of fundus diseases. However, few studies focused on the potential of AI to aid medical teaching in the residency training program. This study aimed to evaluate the effectiveness of the AI-based pathologic myopia (PM) identification system in the ophthalmology residency training program and assess the residents' feedback on this system.

Materials and Methods: Ninety residents in the ophthalmology department at the Second Affiliated Hospital of Zhejiang University were randomly assigned to three groups. In group A, residents learned PM through an AI-based PM identification system. In group B and group C, residents learned PM through a traditional lecture given by two senior specialists independently. The improvement in resident performance was evaluated by comparing the pre-and post-lecture scores of a specifically designed test using a paired *t*-test. The difference among the three groups was evaluated by one-way ANOVA. Residents' evaluations of the AI-based PM identification system were measured by a 17-item questionnaire.

Results: The post-lecture scores were significantly higher than the pre-lecture scores in group A ($p < 0.0001$). However, there was no difference between pre-and post-lecture scores in group B ($p = 0.628$) and group C ($p = 0.158$). Overall, all participants were satisfied and agreed that the AI-based PM identification system was effective and helpful to acquire PM identification, myopic maculopathy (MM) classification, and "Plus" lesion localization.

Conclusion: It is still difficult for ophthalmic residents to promptly grasp the knowledge of identification of PM through a single traditional lecture, while the AI-based PM identification system effectively improved residents' performance in PM identification and received satisfactory feedback from residents. The application of the AI-based PM identification system showed advantages in promoting the efficiency of the ophthalmology residency training program.

KEYWORDS

artificial intelligence, pathologic myopia, myopic maculopathy, "Plus" lesion, ophthalmology residency training

Introduction

Artificial intelligence (AI) models have shown equal or better performance in disease diagnosis and management based on the medical image, such as diabetic retinopathy (Ruamviboonsuk et al., 2022), glaucoma (Medeiros et al., 2021; Ibrahim et al., 2022), age-related macular degeneration (Yan et al., 2021; Potapenko et al., 2022), congenital cataract (Lin et al., 2019), central serous chorioretinopathy (Xu et al., 2021; Jin and Ye, 2022), and papilledema (Milea et al., 2020). AI-based teaching can improve students' or junior residents' performance and satisfaction during ophthalmology clerkship, especially showing an advantage in deepening understanding of signs and morphological features (Wu et al., 2020; Han et al., 2022). Previous surveys showed the majority of medical staff or ophthalmologists believed AI will improve the practice of ophthalmology and should be incorporated into medical school and residency curricula (Valikodath et al., 2021a; Valikodath et al., 2021b; Zheng et al., 2021).

With the rapid increase of myopia prevalence, the incidence in high myopia was significantly raised as well (Grzybowski et al., 2020). Myopic maculopathy (MM) is a group of severe sight-threatening complications among pathologic myopia (PM) patients, which usually need extensive examination and evaluation by retinal specialists. The meta-analysis of a pathologic myopia system (META-PM) defined PM and provided a photographic classification and grading system for MM (Ohno-Matsui et al., 2015). The morphological and functional characteristics in eyes with high myopia were positively correlated with the severity classified by META-PM (Zhao et al., 2020; Li et al., 2021). However, it usually takes a long time to cultivate a qualified or experienced retinal specialist. Therefore, we are always facing a shortage of retinal specialists, especially in primary healthcare and community medical service institutes. It is also a heavy task to teach PM knowledge to relevant clinicians like residents of ophthalmology. The shortage of specialist manpower leads to the potential application of AI technology in clinical teaching and training tasks.

A series of deep learning systems were designed to detect PM and MM classification based on color fundus images with comparable performance to the general ophthalmologist and retinal specialist (Lu et al., 2021b). We further developed an AI-based system for automatic PM identification, MM classification, and "Plus" lesion detection based on retinal color fundus images (namely Ophthalmology-client), which achieved excellent accuracy (Lu et al., 2021a). AI-based models have been proven to be a potential resolution to aid diagnosis and classification based on fundus photography. In this study, we aim to evaluate the effectiveness of the AI-aided teaching model in a group of ophthalmology residents using our AI-based PM identification system. The performance of the AI system is also compared with that of the traditional lecture-based teaching model.

Materials and methods

Participant enrollment and assignment

Ninety residents participating in the ophthalmology residency training program at the Second Affiliated Hospital of Zhejiang University were enrolled in June 2022. The participants were randomly assigned into three groups (1:1:1 ratio) and parallelly finished the training on the same day. In group A, the residents were instructed to learn the PM knowledge through an AI-based PM identification system by exploring and operating an AI-aided diagnosis platform-Ophthalmology-client. In groups B and C, the residents learned PM fundus image features through the traditional lecture given by two senior specialists respectively. All the procedures in this study were arranged strictly with the approval of the ethics committee of the Second Affiliated Hospital, School of Medicine, Zhejiang University. Written informed consent was given by every participant.

The flowchart of the study was shown in Figure 1. All three groups received a pre-lecture test, a 45-minute lecture, and a post-lecture test. The same specific designed test was used for pre-and post-lecture tests including three parts: part I was the recognition of PM, part II was the MM classification, and part III was the "Plus" lesion detection.

Group A and group B were guided by an experienced instructor 1 (Dr. Zhi Fang). Group C was guided by another experienced instructor 2 (Dr. Zhe Xu) following the same working flow. Both instructors are physicians from the eye center of the Second Affiliated Hospital of Zhejiang University.

Ophthalmology-client, the AI-aided diagnosis platform for PM

Ophthalmology-client is an AI-aided PM diagnosis and classification platform developed by our team. This AI platform can identify PM or non-PM, classify the MM, and detect "Plus" lesions based on retinal fundus images. The AI platform also can automatically localize the "Plus" lesions based on retinal fundus images with comparable performance to retinal experts after being trained with a large number of retinal fundus images.

AI-based PM identification system

The residents in group A learned the contents including the introduction of Ophthalmology-client as well as the criteria for diagnosis of PM and the META-PM system 1 day before the class. Besides, the instructor encouraged them to discuss the key points of the retinal fundus image before the class. In the class, 10 min were given to allow the residents to finish the pre-lecture

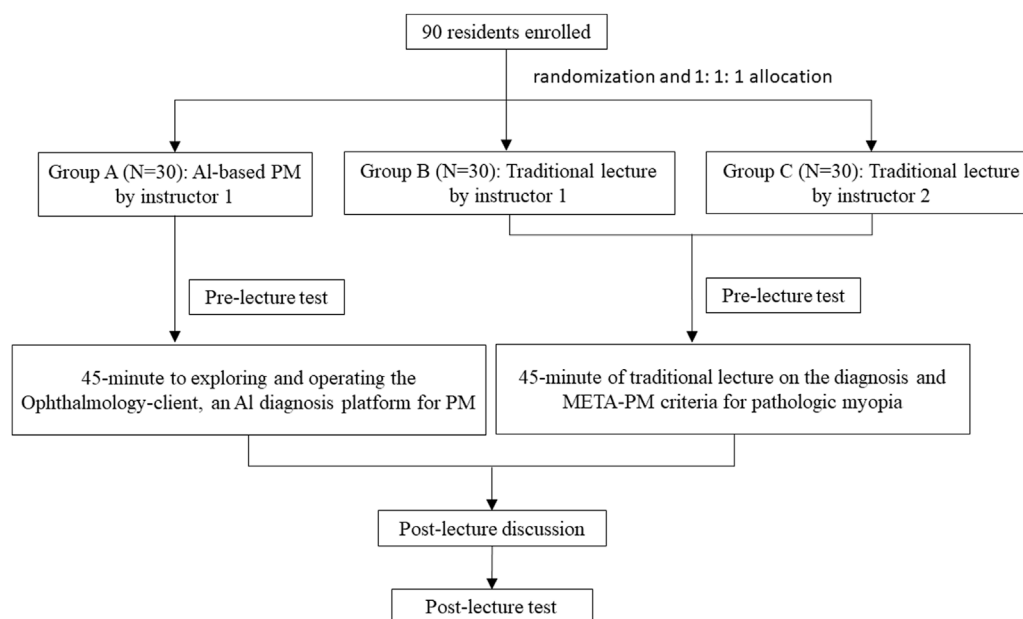


FIGURE 1
Flowchart of the study.

test. Then the residents had 45 min to explore and operate the AI-aided platform of Ophthalmology-client. The content of AI training regarding the PM topic included fundus images from a database on the website involving typical PM at different categories or non-PM and a report from the Ophthalmology-client. The contents of the output report included the category of PM according to the META-PM classification system if it is a PM, the location of the specific lesion with labels if there is a PM “Plus” lesion, and a brief introduction of PM. A 10-minute discussion regarding the key points and “Plus” lesions of PM fundus image was conducted. Finally, 10 min were given to finish the post-lecture test.

Conduction of the traditional lecture

The residents in group B learned the knowledge of PM diagnosis and the META-PM system 1 day before class. The instructor encouraged them to discuss the key points of the retinal fundus image before the class. During the class, 10 min were given to residents to finish the pre-lecture test. Subsequently, the instructor gave a 45-minute traditional lecture on the topic of PM. The content of the traditional lecture regarding the PM topic included the brief introduction and typical fundus image of PM, the META-PM classification, and relevant typical fundus with the indication of chorioretinal atrophy, macular atrophy, and “Plus” lesion (lacquer cracks, choroidal neovascularization, or Fuchs spot). A 10-minute

discussion regarding the key points and “Plus” lesions of PM fundus image was conducted. Finally, 10 min were given to finish the post-lecture test.

Residents’ evaluations

The residents’ evaluations of the AI-based PM identification system were measured by a 17-item questionnaire, including 16 one-choice questions and one open-ended question (Table 1). The questionnaire in our study was designed based on previous studies of medical education, which rated on a 4-point scale ranging from “strongly agree” (with the highest score) to “strongly disagree” (with the lowest score) (Huang et al., 2016; Wu et al., 2020). The questionnaire was conducted in group A after class to collect and assess residents’ satisfaction with the AI-based PM identification system. Information of the questionnaire had several topics, including knowledge acquisition (2 items), motivational dimension (3 items), group cooperation (1 item), creative and critical thinking (1 item), instructor performance (3 items), organization (1 item), overall rating (2 items), recommendations (2 items).

Data analysis

All data from the survey questionnaire were gathered by Questionnaire Star anonymously. We described categorical

TABLE 1 Seventeen-item questionnaire.

No.	Question
One-choice questions (A, strongly agree; B, agree; C, disagree; D, strongly disagree)	
1	AI-based PM identification system helped me to acquire a higher level of knowledge
2	AI-based PM identification system is more effective and motivate compared with traditional didactic lecture
3	AI-based PM identification system challenged me to do my best
4	AI-based PM identification system promoted the learning of essential concepts or skills
5	AI-based PM identification system promoted effective cooperative learning
6	AI-based PM identification system promoted increased reading of the textbook by the students
7	Overall, I am very satisfied with the AI-based PM identification system
8	AI-based PM identification system should be offered more frequently in the curriculum
9	I will recommend the AI-based PM identification system to other residents
10	This activity was preferable to the traditional lecture
11	AI-based PM identification system is easy to operate and well-designed
12	I study with colleagues frequently
13	The instructor highly facilitated the learning process of AI-based PM identification system
14	The instructor can well answer the residents' questions
15	The instructor encouraged and provided opportunities for discussion
16	AI-based PM identification system is beneficial to help develop creative thinking and self-learning ability
17	Compared with the traditional teaching method, what do you think are the advantages and disadvantages of the AI-based PM identification system?

AI, artificial intelligence; PM, pathologic myopia.

variables as frequencies and percentages. The effects of the AI-based platform on residents' performance were measured by comparing pre-and post-lecture scores using a paired *t*-test. The difference among the three groups was evaluated by one-way ANOVA. Furthermore, an independent *t*-test was used to compare the improvement in performance between the three groups. A subgroup analysis was conducted between senior residents (3rd year) and junior residents (1st–2nd year) in both groups. It was considered statistically significant when $p < 0.05$. All data were analyzed by SPSS version 22.0 software (SPSS Inc., Chicago, IL, United States).

Results

Baseline characteristics

All participants finished the class and completed the pre-and post-lecture tests. There was no significant difference in the baseline characteristics between the three groups including gender, educational background, grade, and age ($p = 0.610$) (Table 2). The percentage of the male was 33.3%, 33.3%, and 30%; the percentage with a postgraduate degree was 66.7%, 63.3%, and 63.3%; the percentage of senior residents (3rd year) was 36.7%, 33.3%, and 30%; the age was 27.53 ± 3.48 years, 27.97 ± 3.06 years, and 27.10 ± 3.55 years respectively in groups A, B, and C.

Pre-lecture scores of residents' performance in each group

The total and three parts of pre-lecture scores were similar between three groups with no significant difference (Table 3). Subgroup analysis showed there was no obvious difference in the total, part II, and part III of pre-lecture scores between the senior and junior residents. However, the pre-lecture scores of part I were significantly higher among the senior residents' than the junior residents (Table 4, $p = 0.030$).

Improvement of residents' performance in each group

One-way ANOVA detected significant difference in the total ($p < 0.0001$), part I ($p = 0.024$), part II ($p < 0.0001$), and part III ($p < 0.0001$) of post-lecture scores among three groups. Further *t*-test found the total, part II, and part III of post-lecture scores were significantly higher than the pre-lecture scores in group A (Table 5, $p < 0.01$). However, we found no improvement of part I in group A (Table 5, $p = 0.199$). In group B, the improvement was not obvious in total ($p = 0.302$), part I ($p = 0.087$), and part II ($p = 0.504$) (Table 5). In group C, the improvement was also not significant in total ($p = 0.158$), part I ($p = 0.808$), and part II ($p = 0.594$) (Table 5). However, significant improvement of part III about the "Plus" lesion detection was observed in both group B and group C (Table 5, $p < 0.05$). The total, part I, part II, and part

TABLE 2 Baseline characteristics of participants.

Characteristics	Group A	Group B	Group C	<i>p</i> Value
Male (n, %)	10, 33.3%	10, 33.3%	9, 30%	
Postgraduate (n, %)	20, 66.7%	19, 63.3%	19, 63.3%	
3rd year resident (n, %)	11, 36.7%	10, 33.3%	9, 30%	
Age (years, mean \pm SD)	27.53 \pm 3.48	27.97 \pm 3.06	27.10 \pm 3.55	0.610

SD, standard deviation.

TABLE 3 Pre-lecture scores of three groups.

	Group A (mean \pm SD)	Group B (mean \pm SD)	Group C (mean \pm SD)	<i>p</i> Value
Part I	15.43 \pm 2.06	15.23 \pm 1.92	14.93 \pm 2.12	0.634
Part II	7.67 \pm 2.09	8.57 \pm 2.31	8.33 \pm 1.58	0.207
Part III	12.20 \pm 3.03	11.77 \pm 2.77	11.70 \pm 2.82	0.767
Total	35.30 \pm 5.72	35.57 \pm 5.22	34.97 \pm 4.62	0.905

SD, standard deviation.

TABLE 4 Pre-lecture scores between junior and senior residents.

	Junior (1st–2nd year, mean \pm SD)	Senior (3rd year, mean \pm SD)	<i>p</i> Value
Part I	14.83 \pm 1.96	15.80 \pm 1.95	0.030*
Part II	7.95 \pm 1.99	8.63 \pm 2.08	0.133
Part III	11.70 \pm 2.84	11.93 \pm 2.57	0.705
Total	34.48 \pm 5.04	36.37 \pm 5.01	0.097

**p* < 0.05. SD, standard deviation.

TABLE 5 Improvement of residents' performance of three groups.

		Part I	Part II	Part III	Total
Group A (mean \pm SD)	Pre-lecture	15.43 \pm 2.06	7.67 \pm 2.09	12.20 \pm 3.03	35.30 \pm 5.72
	Post-lecture	16.00 \pm 1.91 ^{**}	14.27 \pm 3.54 ^{***}	15.47 \pm 1.80 ^{***}	45.73 \pm 5.00 ^{***}
Group B (mean \pm SD)	Pre-lecture	15.23 \pm 1.92	8.57 \pm 2.31	11.77 \pm 2.77	35.57 \pm 5.22
	Post-lecture	14.53 \pm 2.06	8.90 \pm 1.97	13.20 \pm 2.33*	36.63 \pm 4.48
Group C (mean \pm SD)	Pre-lecture	14.93 \pm 2.12	8.33 \pm 1.58	11.70 \pm 2.82	34.97 \pm 4.62
	Post-lecture	15.07 \pm 2.23	8.47 \pm 1.78	12.27 \pm 2.46*	35.80 \pm 4.78

Compared with pre-lecture scores: **p* < 0.05; ***p* < 0.01. Compared with group B: ****p* < 0.01. SD, standard deviation.

III of post-lecture scores in group A were significantly higher than those in group B (Table 5, *p* < 0.01). However, there was no significant difference of post-lecture scores between group B and group C (Table 5, *p* = 0.489 for total scores, *p* = 0.340 for part I scores, *p* = 0.375 for part II scores, *p* = 0.137 for part III scores), which indicated a similar effect of training by different instructors.

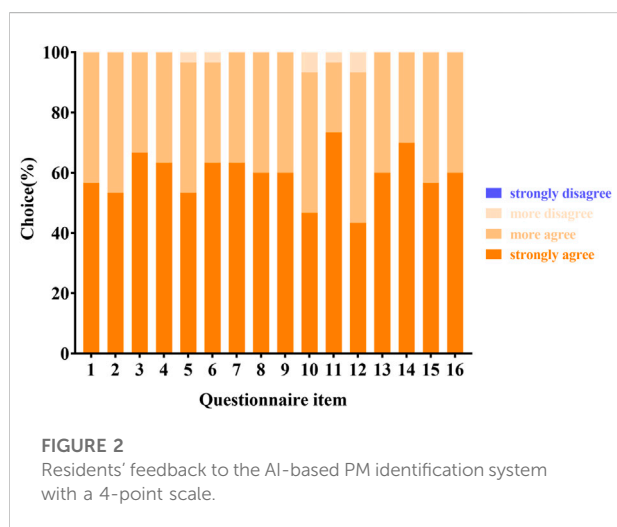
Comparison of junior and senior residents' performance between three groups

One-way ANOVA showed significant difference of post-lecture scores both in junior (*p* < 0.0001 for total, *p* = 0.033 for part I, *p* < 0.0001 for part II, and *p* < 0.0001 for part III) and senior residents (*p* < 0.0001 for total, *p* < 0.0001 for part II,

TABLE 6 Comparison of post-lecture scores between junior and senior residents.

	Junior (1st–2nd year, mean \pm SD)			Senior (3rd year, mean \pm SD)		
	Group A	Group B	Group C	Group A	Group B	Group C
Part I	15.89 \pm 2.00**	14.00 \pm 2.25	14.90 \pm 2.32	16.18 \pm 1.83	15.60 \pm 1.07 [#]	15.44 \pm 2.07
Part II	14.00 \pm 3.90**	9.05 \pm 1.96	8.43 \pm 1.60	14.73 \pm 2.94**	8.60 \pm 2.07	8.56 \pm 2.24
Part III	15.58 \pm 1.57**	13.05 \pm 2.52	12.29 \pm 2.49	15.27 \pm 2.20**	13.50 \pm 1.96	12.22 \pm 2.54
Total	45.47 \pm 5.43**	36.10 \pm 5.00	35.62 \pm 4.26	46.18 \pm 4.35**	37.70 \pm 3.16	36.22 \pm 6.10

Compared with Group B: * $p < 0.05$; ** $p < 0.01$. Compared with junior residents: * $p < 0.05$. SD, standard deviation. SD, standard deviation.



and $p = 0.017$ for part III) between three groups. Only the part I of senior residents showed no significant difference between three groups ($p = 0.591$). Subgroup analysis showed that both junior and senior residents in group A achieved significantly higher post-lecture scores than those in group B (Table 6, $p < 0.01$). Further analysis showed that three parts in junior residents, and part II, part III in senior residents were significantly improved (Table 6, $p < 0.01$). Besides, the part I scores among senior residents were significantly higher in group B, which was consistent with pre-lecture scores (Table 6, $p < 0.05$). There was no significant difference between senior and junior residents in total, part II, and part III of group B, total and three parts of group C (Table 6).

Residents' satisfaction

All residents in group A responded to the questionnaire. Overall, all respondents were satisfied with the AI-based PM identification system and agreed that the system was helpful, effective, innovative, and beneficial for them to develop the skill of fundus image identification for PM and

an extensive understanding of the META-PM classification (Figure 2).

Meanwhile, they also believed that the instructor played an important role in guiding the AI-based PM identification system (Figure 2). We collected residents' answers to the open-ended question: What are the advantages and disadvantages of the AI-based PM identification system? Many residents confirmed that the AI-based PM identification system benefits them, in terms of efficiency, convenience, innovative design, flexible learning style, self-learning ability, and self-motivation. However, some residents expressed concerns about the hardware requirement, accuracy, and website stability of the AI-based platform.

Discussion

Standardization is essential for the ophthalmology residency training program. However, significant regional discrepancy among training programs still exist and may result in the variable competency of ophthalmology residents (Wang et al., 2020). AI model showed the potential to provide trainees equal opportunity and minimize the regional difference due to the self-learning model and timely feedback (Fischetti et al., 2022). Particularly, due to the COVID-19 pandemic, routine clinical practice maybe disrupted. Hence, the clinical teaching can also be substantially influenced (Ferrara et al., 2020; Silva et al., 2020). Instead, the AI-assisted education system based on the web platform or mobile devices has broad prospect and has been recommended to make up the theory classes (Pradeep et al., 2021). Moreover, medical students or trainees showed a positive attitude toward AI and high acceptance of the AI-aided medical training (Bisdas et al., 2021). Efforts have been made to develop visual AI courses for further difficult AI courses (Wang et al., 2022) or introductory curriculum into AI in radiology titled AI-RADS for residents education (Lindqwister et al., 2021). This study applied an AI-based PM identification system developed by our team to the residency training program and achieved excellent performance. Our data demonstrated a striking improvement in the residents enrolled in the AI group. This was in consistent with the previous study that AI model could

improve the students' performance in sign and diagnosis part significantly (Wu et al., 2020). Notably, the improvement was significant in total, part II, and part III while no difference was detected in part I. Also, a significant higher scores of part I was observed in senior residents compared with junior residents. These results indicated that the PM diagnosis based on typical fundus images can be improved by residents through self-learning or traditional teaching activity. In one of our traditional lecture groups, no difference in total scores was found while part III was significantly improved. Part III was about the "Plus" lesions detection from fundus images including lacquer cracks, choroidal neovascularization, and Fuchs spot. The improvement in part III in both traditional and AI training groups indicated that it might be relatively easier for the trainees to identify the "Plus" lesions compared with the mission of categorizing the PM macular lesions according to the META-PM grading system. Overall, the MM classification was the most difficult, followed by the "Plus" lesion detection for residents to fully understand and improve through the didactic lecture solely. In this study, AI model showed better efficiency and great potential help to acquire difficult tasks, shorten the learning curve and training period.

The AI training exhibited better performance as it can provide the huge and multiple fundus images as learning materials in the online database and effectively facilitate the trainees to deepen their understanding of PM signs and morphological features. The database allows the trainees to learn the relevant knowledge efficiently and improve their performance in a short period instead of long-term clinical practice to gain experience. Moreover, our AI system also can archive one-to-many and interactive teaching mode. Due to the merits of efficiency, convenience, flexible learning style, and timely feedback, all residents were satisfied with the system.

Previous study reported the better performance of AI technique in junior residents compared with that of medical students (Han et al., 2022). However, adjunctive tool like ultra-widefield retinal imaging had a better performance in junior residents than senior residents (Lin et al., 2021). Thus, the performance of a new teaching model or adjunct tool may vary during different training stage. Junior and senior residents' performance even fluctuated during different months of a year (Ali et al., 2022). In our study, both senior and junior residents using AI model achieved significantly higher scores than traditional lecture group, indicating that AI model is worthy for all residents and has great potential for the standardized residency training. However, part I in senior residents showed no difference between groups A and B, which may due to the previous clinical training. Given these results, we believe that a well-designed AI-assisted teaching model can provide an effective learning and practice platform to make up the weakness of the traditional teaching mode in ophthalmology residency training program.

The efficiency of traditional lectures by different instructors were also evaluated in this study. The results showed no significant difference in both pre-and post-lecture scores between groups B and C. Subgroup analysis of post-lecture showed significantly higher scores of senior residents compared to junior residents in group B, but not in group C. These results suggested the comparable effect between two experienced instructors only with minor difference and further confirmed the results of the superiority of AI-based teaching mode compared with the traditional lecture.

The free discussion after the lectures was arranged to fully discuss the content of the lecture. However, the discussions between the three groups were highly related to the their own teaching content of each group with no crosstalk. For example, the traditional lecture group only discussed the relevant content mentioned by the instructor, while the AI-based group only discussed the operating experience of AI platform and the output of the AI platform. Moreover, the results showed no significant improvement in scores of the total, part I, and Part II after the post-lecture free discussion in traditional lecture group. Given the reasonability and results above, the free discussion after the lectures will not have a significant impact on our results.

Our questionnaire also gave an intact feedback evaluation of our AI-based PM identification system from the residents. All of the participants were satisfied with the AI-based PM identification system and confirmed the positive role of instructor. Comments mainly included efficiency, convenience, innovative design, flexible learning style and higher requirement of hardware.

Compared to previous studies, the present study enrolled more numbers of participants using a new in-house designed AI-based platform. The difference between senior and junior residents was also analyzed. However, the contents regarding the treatment for PM or MM was not included, as the AI model at this stage mainly focuses in the PM identification and MM classification. Further studies are desirable to evaluate the role of AI-based PM identification system on residency training program in more comprehensive respects, including diagnosis, management of disease and even human-machine interaction.

In conclusion, we found the AI-based PM identification system effectively improved the residents' performance of PM identification, while the group receiving the single traditional lecture showed no significant improvement. Further stratification analysis showed the similar results between the senior and junior residents in both groups, prompting the request for the efficient clinical teaching model to help trainees grasp complex and difficult tasks. Overall, application of the AI-based PM identification system showed advantages in promoting the efficiency of

ophthalmology residency training and received positive feedback from residents as well.

Data availability statement

The raw data supporting the conclusions of this article will be made available by the authors, without undue reservation.

Ethics statement

The study was approved by the ethics committee of the Second Affiliated Hospital, School of Medicine, Zhejiang University. Written informed consent was obtained from each participant before the study.

Author contributions

ZF designed, performed research, and wrote the manuscript. ZX performed part of the research. XH collected and analyzed the data. WH revised the manuscript and supervised the study.

References

- Ali, S. A., Riaz, Q., Mushtaq, Z. M., Awan, S., and Tariq, M. (2022). Low performance of internal medicine senior residents in in-service examinations. *Postgrad. Med. J.* 98 (1158), 246–250. doi:10.1136/postgradmedj-2020-138476
- Bidas, S., Topriceanu, C. C., Zakrzewska, Z., Irimia, A. V., Shakallis, L., Subhash, J., et al. (2021). Artificial intelligence in medicine: A multinational multi-center survey on the medical and dental students' perception. *Front. Public Health* 9, 795284. doi:10.3389/fpubh.2021.795284
- Ferrara, M., Romano, V., Steel, D. H., Gupta, R., Iovino, C., van Dijk, E. H. C., et al. (2020). Reshaping ophthalmology training after COVID-19 pandemic. *Eye (Lond)* 34 (11), 2089–2097. doi:10.1038/s41433-020-1061-3
- Fischetti, C., Bhatner, P., Frisch, E., Sidhu, A., Helmy, M., Lungren, M., et al. (2022). The evolving importance of artificial intelligence and radiology in medical trainee education. *Acad. Radiol.* 29 (5), S70–S75. doi:10.1016/j.acra.2021.03.023
- Grzybowski, A., Kancierz, P., Tsubota, K., Lanca, C., and Saw, S. M. (2020). A review on the epidemiology of myopia in school children worldwide. *BMC Ophthalmol.* 20 (1), 27. doi:10.1186/s12886-019-1220-0
- Han, R., Yu, W., Chen, H., and Chen, Y. (2022). Using artificial intelligence reading label system in diabetic retinopathy grading training of junior ophthalmology residents and medical students. *BMC Med. Educ.* 22 (1), 258. doi:10.1186/s12909-022-03272-3
- Huang, Z., Li, M., Zhou, Y., Ao, Y., Xin, W., Jia, Y., et al. (2016). Modified team-based learning in an ophthalmology clerkship in China. *PLoS One* 11 (4), e0154250. doi:10.1371/journal.pone.0154250
- Ibrahim, M. H., Hacibeyoglu, M., Agaoglu, A., and Ucar, F. (2022). Glaucoma disease diagnosis with an artificial neural network-based deep learning algorithm. *Med. Biol. Eng. Comput.* 60 (3), 785–796. doi:10.1007/s11517-022-02510-6
- Jin, K., and Ye, J. (2022). Artificial intelligence and deep learning in ophthalmology: Current status and future perspectives. *Adv. Ophthalmol. Pract. Res.* 2 (3). doi:10.1007/s11517-022-02510-6
- Li, J., Zhao, X., Chen, S., Liu, B., Li, Y., Lian, P., et al. (2021). Patterns of fundus autofluorescence in eyes with myopic atrophy maculopathy: A consecutive case series study. *Curr. Eye Res.* 46 (7), 1056–1060. doi:10.1080/02713683.2020.1857780
- Lin, H., Li, R., Liu, Z., Chen, J., Yang, Y., Chen, H., et al. (2019). Diagnostic efficacy and therapeutic decision-making capacity of an artificial intelligence

Funding

This study was supported by the Science and Technology Project of Zhejiang Province (Grant No. 2019C03046) and the Natural Science Foundation of Zhejiang Province under Grant (Grant No. LQ20H120007).

Conflict of interest

The authors declare that the research was conducted in the absence of any commercial or financial relationships that could be construed as a potential conflict of interest.

Publisher's note

All claims expressed in this article are solely those of the authors and do not necessarily represent those of their affiliated organizations, or those of the publisher, the editors and the reviewers. Any product that may be evaluated in this article, or claim that may be made by its manufacturer, is not guaranteed or endorsed by the publisher.

- platform for childhood cataracts in eye clinics: A multicentre randomized controlled trial. *EClinicalMedicine* 9, 52–59. doi:10.1016/j.eclinm.2019.03.001
- Lin, I. H., Chien, C. C., Chen, Y. H., Pao, S. I., Chen, J. T., and Chen, C. L. (2021). Ultra-widefield retinal imaging for adjunctive resident training in retinal break detection. *PLoS One* 16 (6), e0253227. doi:10.1371/journal.pone.0253227
- Lindqwister, A. L., Hassanpour, S., Lewis, P. J., and Sin, J. M. (2021). AI-RADS: An artificial intelligence curriculum for residents. *Acad. Radiol.* 28 (12), 1810–1816. doi:10.1016/j.acra.2020.09.017
- Lu, L., Ren, P., Tang, X., Yang, M., Yuan, M., Yu, W., et al. (2021a). AI-model for identifying pathologic myopia based on deep learning algorithms of myopic maculopathy classification and "plus" lesion detection in fundus images. *Front. Cell. Dev. Biol.* 9, 719262. doi:10.3389/fcell.2021.719262
- Lu, L., Zhou, E. L., Yu, W. S., Chen, B., Ren, P. F., Lu, Q. Y., et al. (2021b). Development of deep learning-based detecting systems for pathologic myopia using retinal fundus images. *Commun. Biol.* 4 (1), 1225. doi:10.1038/s42003-021-02758-y
- Medeiros, F. A., Jammal, A. A., and Mariottoni, E. B. (2021). Detection of progressive glaucomatous optic nerve damage on fundus photographs with deep learning. *Ophthalmology* 128 (3), 383–392. doi:10.1016/j.ophtha.2020.07.045
- Milea, D., Najjar, R. P., Zhuho, J., Ting, D., Vasseneix, C., Xu, X., et al. (2020). Artificial intelligence to detect papilledema from ocular fundus photographs. *N. Engl. J. Med.* 382 (18), 1687–1695. doi:10.1056/NEJMoa1917130
- Ohno-Matsui, K., Kawasaki, R., Jonas, J. B., Cheung, C. M., Saw, S. M., Verhoeven, V. J., et al. (2015). International photographic classification and grading system for myopic maculopathy. *Am. J. Ophthalmol.* 159 (5), 877–883. doi:10.1016/j.ajo.2015.01.022
- Potapenko, I., Thiesson, B., Kristensen, M., Hajari, J. N., Ilginis, T., Fuchs, J., et al. (2022). Automated artificial intelligence-based system for clinical follow-up of patients with age-related macular degeneration. *Acta Ophthalmol.* doi:10.1111/aos.15133
- Pradeep, T. G., Sundaresh, D. D., and Ramani, S. (2021). Adoption of newer teaching methods to overcome challenges of training in ophthalmology residency during the COVID-19 pandemic. *Indian J. Ophthalmol.* 69 (5), 1292–1297. doi:10.4103/ijo.IJO_3063_20
- Ruamviboonsuk, P., Tiwari, R., Sayres, R., Nganthavee, V., Hemarat, K., Kongprayoon, A., et al. (2022). Real-time diabetic retinopathy screening by deep learning in a multisite

national screening programme: A prospective interventional cohort study. *Lancet. Digit. Health* 4 (4), e235–e244. doi:10.1016/S2589-7500(22)00017-6

Silva, N., Laiginhas, R., Meireles, A., and Barbosa Breda, J. (2020). Impact of the COVID-19 pandemic on ophthalmology residency training in Portugal. *Acta Med. Port.* 33 (10), 640–648. doi:10.20344/amp.14341

Valikodath, N. G., Al-Khaled, T., Cole, E., Ting, D. S. W., Tu, E. Y., Campbell, J. P., et al. (2021a). Evaluation of pediatric ophthalmologists' perspectives of artificial intelligence in ophthalmology. *J. AAPOS* 25 (3), 164 e1–e164164.e5. doi:10.1016/j.jaapos.2021.01.011

Valikodath, N. G., Cole, E., Ting, D. S. W., Campbell, J. P., Pasquale, L. R., Chiang, M. F., et al. (2021b). Impact of artificial intelligence on medical education in ophthalmology. *Transl. Vis. Sci. Technol.* 10 (7), 14. doi:10.1167/tvst.10.7.14

Wang, C. J., Zhong, H. X., Chiu, P. S., Chang, J. H., and Wu, P. H. (2022). Research on the impacts of cognitive style and computational thinking on college students in a visual artificial intelligence course. *Front. Psychol.* 13, 864416. doi:10.3389/fpsyg.2022.864416

Wang, Y. E., Zhang, C., Chen, A. C., Pineles, S., and Hou, J. (2020). Current status of ophthalmology residency training in China: The experience from well-structured centers around the country. *Asia. Pac. J. Ophthalmol.* 9 (4), 369–373. doi:10.1097/APO.0000000000000284

Wu, D., Xiang, Y., Wu, X., Yu, T., Huang, X., Zou, Y., et al. (2020). Artificial intelligence-tutoring problem-based learning in ophthalmology clerkship. *Ann. Transl. Med.* 8 (11), 700. doi:10.21037/atm.2019.12.15

Xu, F., Wan, C., Zhao, L., Liu, S., Hong, J., Xiang, Y., et al. (2021). Predicting post-therapeutic visual acuity and OCT images in patients with central serous chorioretinopathy by artificial intelligence. *Front. Bioeng. Biotechnol.* 9, 649221. doi:10.3389/fbioe.2021.649221

Yan, Y., Jin, K., Gao, Z., Huang, X., Wang, F., Wang, Y., et al. (2021). Attention-based deep learning system for automated diagnoses of age-related macular degeneration in optical coherence tomography images. *Med. Phys.* 48 (9), 4926–4934. doi:10.1002/mp.15002

Zhao, X., Ding, X., Lyu, C., Li, S., Liu, B., Li, T., et al. (2020). Morphological characteristics and visual acuity of highly myopic eyes with different severities of myopic maculopathy. *Retina* 40 (3), 461–467. doi:10.1097/IAE.0000000000002418

Zheng, B., Wu, M. N., Zhu, S. J., Zhou, H. X., Hao, X. L., Fei, F. Q., et al. (2021). Attitudes of medical workers in China toward artificial intelligence in ophthalmology: A comparative survey. *BMC Health Serv. Res.* 21 (1), 1067. doi:10.1186/s12913-021-07044-5



OPEN ACCESS

EDITED BY

Weihua Yang,
Jinan University, China

REVIEWED BY

Guang Yang,
Imperial College London,
United Kingdom
Lei Wang,
Wenzhou Medical University, China
Zhili Chen,
Shenyang Jianzhu University, China

*CORRESPONDENCE

Qifeng Yan,
yanqifeng@nimte.ac.cn
Yuhui Ma,
mayuhui@nimte.ac.cn

*These authors have contributed equally
to this work

SPECIALTY SECTION

This article was submitted to Molecular
and Cellular Pathology,
a section of the journal
Frontiers in Cell and Developmental
Biology

RECEIVED 03 October 2022

ACCEPTED 25 October 2022

PUBLISHED 10 November 2022

CITATION

Wu W, Gong Y, Hao H, Zhang J, Su P,
Yan Q, Ma Y and Zhao Y (2022),
Choroidal layer segmentation in OCT
images by a boundary
enhancement network.
Front. Cell Dev. Biol. 10:1060241.
doi: 10.3389/fcell.2022.1060241

COPYRIGHT

© 2022 Wu, Gong, Hao, Zhang, Su, Yan,
Ma and Zhao. This is an open-access
article distributed under the terms of the
[Creative Commons Attribution License
\(CC BY\)](https://creativecommons.org/licenses/by/4.0/). The use, distribution or
reproduction in other forums is
permitted, provided the original
author(s) and the copyright owner(s) are
credited and that the original
publication in this journal is cited, in
accordance with accepted academic
practice. No use, distribution or
reproduction is permitted which does
not comply with these terms.

Choroidal layer segmentation in OCT images by a boundary enhancement network

Wenjun Wu^{1,2†}, Yan Gong^{3†}, Huaying Hao¹, Jiong Zhang¹,
Pan Su⁴, Qifeng Yan^{1*}, Yuhui Ma^{1*} and Yitian Zhao^{1,5}

¹Ningbo Cixi Institute of Biomedical Engineering, Ningbo Institute of Materials Technology and Engineering, Chinese Academy of Sciences, Ningbo, China, ²University of Chinese Academy of Sciences, Beijing, China, ³The Affiliated Ningbo Eye Hospital of Wenzhou Medical University, Ningbo, China, ⁴School of Control and Computer Engineering North China Electric Power University, Baoding, China, ⁵Zhejiang Engineering Research Center for Biomedical Materials, Ningbo Cixi Institute of Biomedical Engineering, Ningbo Institute of Materials Technology and Engineering, Chinese Academy of Sciences, Ningbo, China

Morphological changes of the choroid have been proved to be associated with the occurrence and pathological mechanism of many ophthalmic diseases. Optical Coherence Tomography (OCT) is a non-invasive technique for imaging of ocular biological tissues, that can reveal the structure of the retinal and choroidal layers in micron-scale resolution. However, unlike the retinal layer, the interface between the choroidal layer and the sclera is ambiguous in OCT, which makes it difficult for ophthalmologists to identify with certainty. In this paper, we propose a novel boundary-enhanced encoder-decoder architecture for choroid segmentation in retinal OCT images, in which a Boundary Enhancement Module (BEM) forms the backbone of each encoder-decoder layer. The BEM consists of three parallel branches: 1) a Feature Extraction Branch (FEB) to obtain feature maps with different receptive fields; 2) a Channel Enhancement Branch (CEB) to extract the boundary information of different channels; and 3) a Boundary Activation Branch (BAB) to enhance the boundary information via a novel activation function. In addition, in order to incorporate expert knowledge into the segmentation network, soft key point maps are generated on the choroidal boundary, and are combined with the predicted images to facilitate precise choroidal boundary segmentation. In order to validate the effectiveness and superiority of the proposed method, both qualitative and quantitative evaluations are employed on three retinal OCT datasets for choroid segmentation. The experimental results demonstrate that the proposed method yields better choroid segmentation performance than other deep learning approaches. Moreover, both 2D and 3D features are extracted for statistical analysis from normal and highly myopic subjects based on the choroid segmentation results, which is helpful in revealing the pathology of high myopia. Code is available at <https://github.com/iMED-Lab/Choroid-segmentation>.

KEYWORDS

choroidal layer, optical coherence tomography, boundary segmentation, deep learning, high myopia

1 Introduction

The choroid is a dense vascular layer posterior of the uvea, the middle membrane of the ocular posterior segment. It plays a critical role in thermoregulation, adjustment of retinal position, and secretion of growth factor (Nickla and Wallman, 2010). The high blood flow in the choroid makes it immune to environmental conditions with various extreme temperatures. Choroidal thickness has become one of the diagnostic indicators of many ophthalmic diseases, such as high myopia, glaucoma, age-related macular degeneration, and diabetic retinopathy (Regatieri et al., 2012; Chen et al., 2014; Wang et al., 2015; Yiu et al., 2015). Taking high myopia as an example, the percentage of Asian young people with high myopia increased by 6.8%–21.6% over the period 2010 to 2014 (Wong and Saw, 2016). Individuals with high myopia are highly susceptible to developing pathological myopia, which is one of the leading causes of low vision and blindness (Oduntan, 2005; Cedrone et al., 2006). Therefore, choroid segmentation and choroidal thickness analysis are crucial in determining the pathogenesis and treatment strategy of ophthalmopathy.

The development of Optical Coherence Tomography (OCT) (Huang et al., 1991) has made analysis of retinal and choroidal morphology convenient and accurate for clinical research and application. With the emergence of new OCT techniques such as spectral domain OCT (SD-OCT) (Yaqoob et al., 2005), enhanced depth imaging OCT (EDI-OCT) (Wong et al., 2011) and swept-source OCT (SS-OCT) (Choma et al., 2003), the choroid can be clearly visible. Because of the characteristics of non-invasive 3D imaging, these new OCT techniques have become the primary choice for clinicians to diagnose ophthalmic diseases. Figure 1 shows an OCT volume acquired from a healthy eye, which can be divided into three parts: from top to bottom (retina, choroid

and sclera). In addition, the 2D B-scans can be extracted from the 3D volume for further study of the choroidal morphology.

Based on the B-scans, various methods have been proposed for choroidal layer segmentation. Previous methods were mainly based on graph theory (Zhang et al., 2012; Hu et al., 2013; Mazzaferri et al., 2017). These methods rely on manual parameter settings, and usually yield low efficiency, which limits their segmentation accuracy and makes them difficult to apply in clinical practice. With the emergence and development of deep learning, several Convolutional Neural Network (CNN) models have been applied to choroidal layer segmentation (Chen et al., 2015; Sui et al., 2017; He et al., 2021; Yan et al., 2022). The powerful feature learning capability of CNN has significantly improved choroid segmentation accuracy and efficiency over the last decade. In addition, end-to-end networks have enabled models to take original images as direct input, and output segmentation results without handcrafted operations (Mao et al., 2020; Zhang et al., 2020).

Many current studies have explored possible improvements of segmentation efficiency and model optimization, but only a few have focused on the structural characteristics of the choroidal layer. Due to the low contrast of OCT images (as shown in Figure 1), the boundary between choroid and sclera is ambiguous, which for many algorithms leads to inaccurate boundary localization. However, the issue of vagueness in imaging the Choroidal Scleral Interface (CSI) has been little investigated. Moreover, choroidal thickness, as an alternative and important biological indicator strongly associated with several ocular diseases, has been quantified in much recent work on the basis of 2D B-scans only (Regatieri et al., 2012; Kim et al., 2013; Agrawal et al., 2020). In contrast, the 3D morphological characteristics of the choroid and its thickness in different regions, such as the nasal side and the foveal region, may provide more indicative and accurate information for

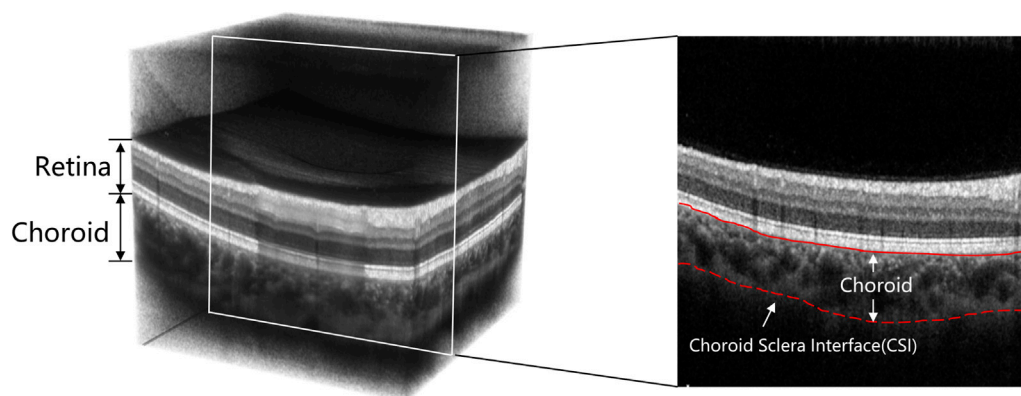


FIGURE 1

Examples of a 3D OCT volume and 2D OCT B-scan image. The choroid-sclera interface (indicated by the red dashed line) is ambiguous and difficult to extract compared to the other boundaries.

diagnosis of ocular diseases. But few research works have investigated choroid characteristics derived from 3D morphology.

In this paper, we focus on tackling the following two issues in choroid segmentation and morphological analysis. Firstly, since it is difficult to extract the boundary between choroid and sclera due to low contrast in OCT, existing segmentation methods usually perform ineffectively and produce poor definition of the choroidal boundary. Secondly, there is a lack of choroid-related biomarkers in highly myopic subjects, especially three-dimensional biomarkers, which are more conducive to the diagnosis and treatment of diseases.

To this end, we propose a fully automated choroid segmentation framework with boundary feature enhancement. Initially, in order to extract accurate boundary information, we design a new Boundary Enhancement Module (BEM). This consists of three parallel branches. One branch is a Feature Extraction Branch (FEB), which uses dilated convolution (Yu and Koltun, 2015) with different dilation rates to acquire relevant image features under different receptive fields, so that the boundary features are fully retained. The second branch is a Channel Enhancement Branch (CEB), which exploits and enhances the boundary characteristics of different channels through global average pooling and convolution operations. The third branch is a Boundary Activation Branch (BAB), which strengthens the boundary information from the spatial perspective *via* one-dimensional convolution and a specific activation function to further enhance boundary features. The BEM can be integrated with different encoder-decoder networks, such as the U-Net and FCN. In addition, for each B-scan, a soft point map is generated based on the extracted points on the choroidal boundary by using a boundary strengthen point selection algorithm. Based on these boundary soft point maps, we introduce the Boundary Perceptual Loss (BP-Loss) to provide feedback on the boundary enhancement effect of the output segmentation result. Finally, we extract and analyze both 2D and 3D morphological features of the choroid in the highly myopic population, based on the segmentation results.

In brief, our main contributions are listed as follows:

- We propose a novel BEM module for reinforcing information on the choroidal boundary from three perspectives including feature, channel and space, which can be integrated with major encoder-decoder architectures such as U-Net, FCN, etc.
- A boundary perceptual loss is introduced to incorporate expert knowledge into our segmentation network. This new loss provides the flexibility to learn a prior boundary information from a soft point map.
- We extract 3D edge point cloud features and reconstructed the 3D structure of the choroid based on the 2D segmentation results of all B-scans. In addition, we statistically analyze choroidal thickness and 3D

characteristics in different subfields to further determine the correlation between choroidal morphological changes and high myopia.

2 Related work

2.1 Choroid segmentation

Existing methods for choroid segmentation in OCT are mainly divisible into two categories: traditional methods, and machine learning methods. Zhang et al. (Zhang et al., 2012) first attempted to extract the choroidal layer in 3D SD-OCT by adapting a graph-based method, which produced a relatively accurate choroidal surface. However, this method was tested on normal subjects only, and it is difficult to achieve the expected segmentation performance for some patients, especially those with large changes of choroidal morphology. In order to overcome this limit, Hu et al. (Hu et al., 2013) improved the graph-based multi-layer segmentation method by applying various smoothness and interaction constraints to different choroidal layer structures. This method has been validated on OCT images collected from both healthy subjects and non-neovascular AMD subjects, revealing great similarities with manual segmentation.

With the emergence of Enhanced Depth Imaging OCT (EDI-OCT) technology, its high-resolution imaging made the choroidal layer structure more clearly displayed in OCT B-scans, which is more conducive to choroid segmentation. Tian et al. (Tian et al., 2013) adopted Dijkstra's algorithm to seek the shortest path, and the choroidal surface was quickly and accurately detected. Similarly, Danesh et al. (Danesh et al., 2014) proposed a segmentation method based on the Gaussian mixture model, to obtain the choroidal structure in EDI-OCT images. However, this still requires handcrafted features, and is sensitive to noise artifacts existing in EDI-OCT images. In addition, Chen et al. (Chen et al., 2015) introduced a new pipeline composed of a progressive intensity distance image generation algorithm and graph search method for the problem of noise and boundary ambiguity. Wang et al. (Wang et al., 2017) used a Markov Random Field (MRF) method to connect adjacent pixels, and a level set method to regularize the distance of uneven textures.

Since graph search technology is greatly affected by manual parameter settings, deep learning-based methods have been developed to obtain the choroidal structure. Sui et al. (2017) proposed a convolutional neural network (CNN)-based method that learns a graph-edge weight directly from raw OCT pixels. The network structure can be divided into two parts: one detects the CSI boundary, and the other detects the BM boundary. This method has revealed good adaptability to 3D EDI-OCT images collected from both healthy subjects and patients with macular edema. He et al. (2021) combined CNN and a l_2 - l_q ($0 < q < 1$) fitter to segment the outer choroidal surface, in which the CNN is

used to generate predicted values, and the l_2 - l_q fitter is employed to maintain the stability of the fitting function. The OCT image is partitioned into small patches to form the input of the CNN, and post-processing is required to discard irrelevant information, which leads to relative inefficiency compared to end-to-end architectures. Similarly, Masood et al. (2019) used deep learning methods to establish a new segmentation structure to obtain the outer choroidal surface. Before being fed into the CNN, the OCT image needs to be divided into patches for data sampling and conversion. This method reduces the average segmentation error, but it is still not as efficient as end-to-end architectures.

As a result, several end-to-end deep learning approaches have been proposed more recently. Zhang et al. (2020) proposed an end-to-end method, consisting of a global multi-layer segmentation block, a choroidal layer segmentation block, and a regularization block. This first segments all the inner retinal layers, and then utilizes global information to detect the choroidal layer. For 3D OCT images collected from healthy subjects, the thickness difference obtained by this method (4.30 ± 0.02 pixels) is more accurate than those obtained by other state-of-the-art methods. Chai et al. (2020) proposed a method that can effectively segment the choroidal boundary by minimizing the differences between different regions, and takes into account the differences between different OCT acquisition equipment. It feeds OCT images from different domains into a U-Net-based network, and uses both adversarial and perceptual loss for domain adaptation.

2.2 Choroidal thickness analysis

Examining the choroidal layer as extracted from OCT images, ophthalmologists can analyze choroidal variations from different perspectives. In particular, choroidal thickness is of great interest, as it often indicates the presence or even severity of some ophthalmic diseases. Yiu et al. (2015) extracted choroidal thickness from EDI-OCT images collected from subjects with Age-related Macular Degeneration (AMD). Employing on a semi-automatic segmentation method, they analyzed the similarities and differences in choroidal thickness between normal individuals and patients with AMD. Wang et al. (2015) compared choroidal thickness between patients with high myopia and healthy people. By analyzing the experimental results, they found that choroidal thickness in healthy individuals is significantly thicker than that of individuals with high myopia. Regatieri et al. (2012) examined choroidal thickness in diabetic patients and found that the change of choroidal thickness was related to the severity of diabetes. More recently, several studies have shown that choroidal thickness as revealed by retinal OCT images is associated with certain neurodegenerative diseases. Moschos and Chatziralli (2018) extracted the retinal thickness and choroidal thickness of patients with Parkinson's Disease (PD) from spectral domain OCT, and compared the results with those from healthy individuals. The

differences between people with, and without PD were statistically significant. Similarly, Satue et al. (2018) used swept-source OCT to measure retinal and choroidal thickness of patients with PD. They found that the retina of patients with PD became thinner, while choroidal thickness might increase. Similar to our work, Chen et al. (2022) segmented the choroidal layer of highly myopic patients and non highly myopic people and compared the thickness, while they lacked the analysis of three-dimensional features, and the segmentation performance needs to be improved.

To this end, the automatic and accurate quantification of choroidal thickness is potentially crucial to diagnosis of these diseases. However, most quantification approaches of choroidal thickness can only provide two-dimensional measurements at a fixed location, which limits the practicability. Therefore, we proposed to use 3D edge point cloud features to produce a three-dimensional reconstruction of the choroidal layer.

2.3 Boundary segmentation

Boundary segmentation in images remains a research hotspot, not only in the fields of medical image analysis but also in many fields of other computer vision such as remote sensing. The mainstream boundary segmentation approaches may be divided into two categories: filtering-based methods, and learning-based methods. Wang et al. (2018) introduced an interactive geodesic method based on CNN into medical image segmentation: a manual correction of boundary information is required to improve the accuracy of boundary segmentation. Lee et al. (2020) proposed a novel network with boundary preserving blocks to retain the boundary information via learning proper weights of boundary features. Wei et al. (2021) proposed a concentric loop CNN with a boundary detector and a refinement block to improve the effect of boundary segmentation in remote sensing images. Dang and Lee (2021) improved the effect of boundary segmentation in document images by sharing the weights of boundary features and global features, and using adversarial loss to strengthen the learning of boundary information. Wang et al. (2021) combined a transformer with CNN to enhance the segmentation of skin lesions, and used an attention mechanism to boost the performance of boundary segmentation. Recently, Yu et al. (2022) proposed FBCU-Net, which uses boundary semantic features to segment medical images, but it is mainly used for region segmentation and the performance of layer structure segmentation still needs to be improved.

3 Methods

In this paper, we propose a novel encoder-decoder network with boundary feature enhancement for choroid segmentation. The proposed choroid segmentation framework is presented in

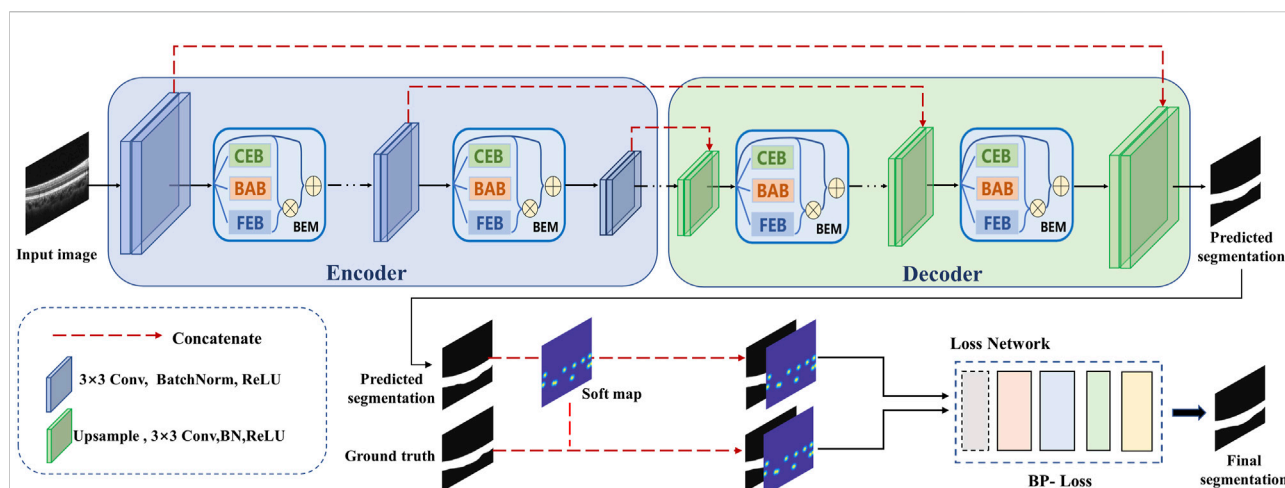


FIGURE 2

An overview of the proposed boundary enhancement framework for choroid segmentation. A novel BEM is incorporated into each encoder/decoder layer of the proposed framework. In addition, a pre-trained VGG network is utilized to calculate the specific boundary perceptual loss to improve the choroidal boundary segmentation with the guidance of the soft point map generated from ground truth.

Figure 2. The proposed framework adopts U-Net (Ronneberger et al., 2015) as the baseline encoder-decoder network, and incorporates a novel module, termed a BEM into each encoder/decoder layer. The BEM consists of three parallel branches: FEB, CEB and BAB. In addition, pre-trained VGG-19 is utilized to calculate the specific boundary perceptual loss, which guides the segmentation framework in reducing the gap at boundary feature level between the predicted segmentation map and ground truth.

In order to train the proposed framework, a soft point map is constructed for each B-scan as another ground truth for extra supervision. Boundary enhancement points are first extracted using the boundary enhancement point selection algorithm. To allow tolerance of the key points' position in the training phase, we generate Gaussian distributed disks based on all extracted points for each B-scan to construct the corresponding soft point map. The details are illustrated in the following subsections.

3.1 Soft point map construction

Inspired by Lee et al. (2020), we employed the boundary enhancement point selection algorithm to select several key points, then generated a point map for each B-scan as another ground truth for training. By contrast with the binary disks generated on the selected points in (Lee et al., 2020), we adopted a two-dimensional Gauss function to generate a point map with soft boundaries for more effective guidance with boundary information to segmentation. This modification is mainly based on the following

considerations: a binary disk allocates undifferentiated attention to all pixels in the neighborhood of the corresponding selected point, which creates vulnerability to deviation of boundary localization. The soft point map can be expressed as follows:

$$S_{i,j} = \max_{k \in \{1, \dots, K\}} \exp\left(-\frac{(i - x_k)^2 + (j - y_k)^2}{2\sigma^2}\right) \quad (1)$$

where (i, j) represent the coordinates of one pixel of the generated soft point map matrix S ; (x_k, y_k) represent the coordinates of k th selected key point (total K selected key points); σ represents the standard deviation of the Gauss function. The differences between the original point map and the proposed soft point map are illustrated in Figure 3.

3.2 Boundary enhancement module

The proposed choroid segmentation architecture incorporates our novel BEMs into its encoder/decoder layers, as shown in Figure 2. Figure 4 presents the architecture of the BEM, which consists of three branches including FEB, CEB and BAB. The BEM can be embedded in various layers in the segmentation network. The BEM embedded in the i th layer takes the feature maps $f^i \in R^{w^i \times h^i \times c^i}$ as input, where w^i , h^i , and c^i respectively represent the width, height and channels of the feature maps at the i th layer. The FEB produces the boundary-enhanced point map $M^i \in R^{w^i \times h^i \times 1}$. The CEB generates a channel-wise weighting vector $N^i \in R^{c^i}$. The BAB outputs a

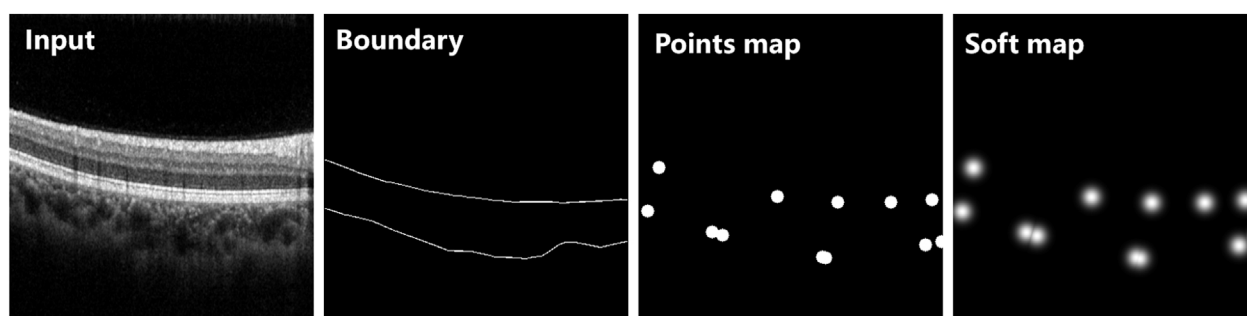
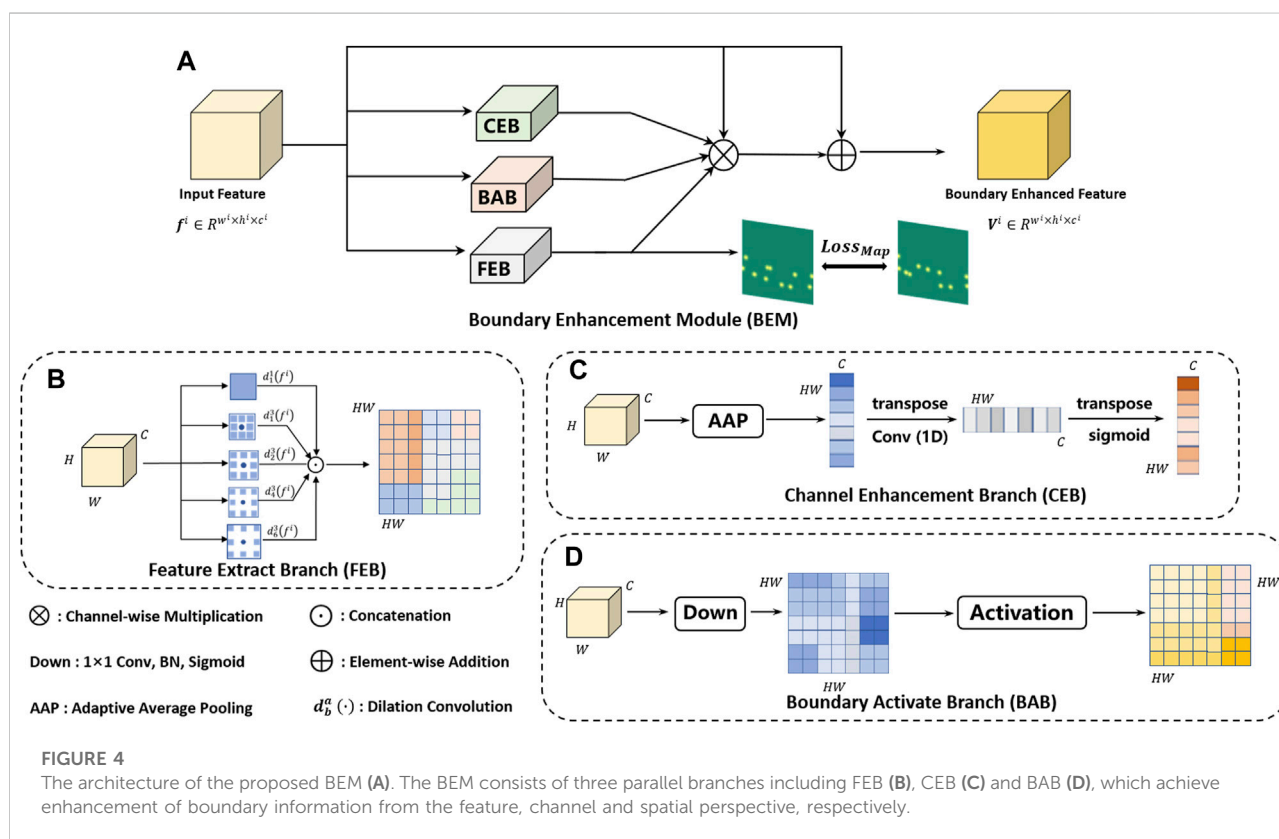


FIGURE 3

Two different types of point maps extracted from the same OCT B-scan. The original points map was generated using binary disk as (Lee et al., 2020), while the soft map was generated based on a two-dimensional Gauss function. All points were extracted from the same boundary of ground truth.



single-channel activation map $Q^i \in R^{w^i \times h^i \times 1}$. Then, the final output feature maps $v^i \in R^{w^i \times h^i \times c^i}$ is calculated as follows:

$$v^i = f^i \oplus (f^i \otimes M^i \otimes Q^i \otimes N^i), \quad (2)$$

where \oplus represents element-wise addition; \otimes represents multiplication (pixel-wise multiplication for single-channel maps M^i and Q^i , and channel-wise multiplication for the weighting vector N^j).

3.2.1 Feature extraction branch

The gray section in Figure 4 shows the architecture of the FEB, which is designed for extracting a boundary-enhanced point map with different receptive fields. Multiple receptive fields integrate global context information and local detailed information, which is beneficial to accurate localization of boundary key points. We adopted convolution with different

dilation rates to obtain the features with different receptive fields. Finally, the features with different receptive fields are concatenated and then fed into a single 1×1 convolutional layer with a Sigmoid function. Let $d_r^s(f^i)$ be the encoded feature maps of input feature maps f^i using $s \times s$ convolution with dilation rate r . Then the generated boundary-enhanced point map can be expressed as:

$$M^i = \mathcal{S}(d_1^1[f^i] \odot d_1^3(f^i) \odot d_2^3(f^i) \odot d_4^3(f^i) \odot d_6^3(f^i)), \quad (3)$$

where \odot and \mathcal{S} denote a concatenation operation, and a Sigmoid function, respectively.

3.2.2 Channel enhancement branch

Each channel of a feature map may be regarded as a specific-class response. However, there are also some differences in the importance of different feature classes to a specific task (e.g., choroid segmentation). In order to selectively enhance features useful for choroid segmentation, a CEB is designed to calculate channel-wise weighting vectors for extracted feature maps. The detailed structure of CEB is shown in the green section of Figure 4. The branch first adopts global average pooling (*gap*) to generate channel-wise statistics of the input feature maps f^i , then applies one-dimensional convolution of kernel size 3 to obtain the final channel-wise weighting vectors N^i , which can be denoted as follows:

$$N^i = \mathcal{S}(C1D_3(f_{gap}(f^i))), \quad (4)$$

where f_{gap} denotes global average pooling; $C1D_3$ denotes the one-dimensional convolution of kernel size 3; \mathcal{S} denotes a Sigmoid function.

3.2.3 Boundary activation branch

In order to further improve detection of the choroidal boundary, we introduced an extra branch called the BAB, as detailed in by the red section of Figure 4. The channel number of the feature maps is reduced to 1 via a 1×1 convolutional layer followed by a Sigmoid function: a specific activation function is then applied to the obtained single-channel feature map, which can be formulated as follows:

$$\begin{cases} Q^i = e^{(x^i - 0.5)^2} + 1 - e^{-0.25}, \\ x^i = \mathcal{S}(C2D_1(f^i)), \end{cases} \quad (5)$$

where f^i represents the input feature maps; $C2D_1$ represents the 1×1 convolutional layer; \mathcal{S} denotes a Sigmoid function.

It is worth noting that the specific activation function was designed based on the observation that choroidal boundary pixels generally have a value around 0.5 in the obtained

feature maps, while interior of choroid and background pixels have values near 1 and 0, respectively. To this end, the activation map is utilized to adjust each feature map spatially for the choroid segmentation task, by assigning higher weights for choroidal boundary pixels (close to $2 - e^{-0.25}$), and lower weights for interior of choroid and background pixels (close to 1) (Simonyan and Zisserman, 2014). In this way, the boundary information is highlighted after activation.

3.3 Loss function

In order to effectively train the proposed choroid segmentation network, we introduced a novel loss called boundary perceptual loss (BP-Loss), which embeds the soft point map into the segmentation network. The complete joint loss function is formed after incorporating segmentation loss.

3.3.1 Segmentation loss

First, we adopted Binary Cross Entropy Loss as the segmentation loss in order to reduce the difference between the ground-truth segmentation map and the predicted segmentation map, which is defined as:

$$Loss_{Seg} = - \sum_i \left((1 - S_{GT}^i) \cdot \log(1 - \hat{S}_{Pred}^i) + S_{GT}^i \cdot \log(\hat{S}_{Pred}^i) \right), \quad (6)$$

where S_{GT}^i and \hat{S}_{Pred}^i represent the i th pixel of ground truth segmentation map, and the corresponding predicted segmentation map, respectively.

3.3.2 Boundary perceptual loss

Unlike general semantic segmentation tasks, medical images require strong expert knowledge to achieve better segmentation performance. Therefore, we concatenated the generated soft point map with the predicted result and ground-truth to form the input of the VGG network, in order to constrain their geometrical relationship. To maintain consistency between the output of the FEB and ground truth. We adopted mean square error (MSE) loss and defined boundary point loss as:

$$Loss_{Map}^i = \frac{1}{h^i \times w^i} \sum_{j=1}^{h^i} \sum_{k=1}^{w^i} (M_{j,k}^i - M_{GT,j,k}^i)^2, \quad (7)$$

where M^i and M_{GT}^i respectively represent the output point map and the ground truth soft point map for the FEB in the i th layer, and h^i and w^i represent the corresponding height and width, respectively.

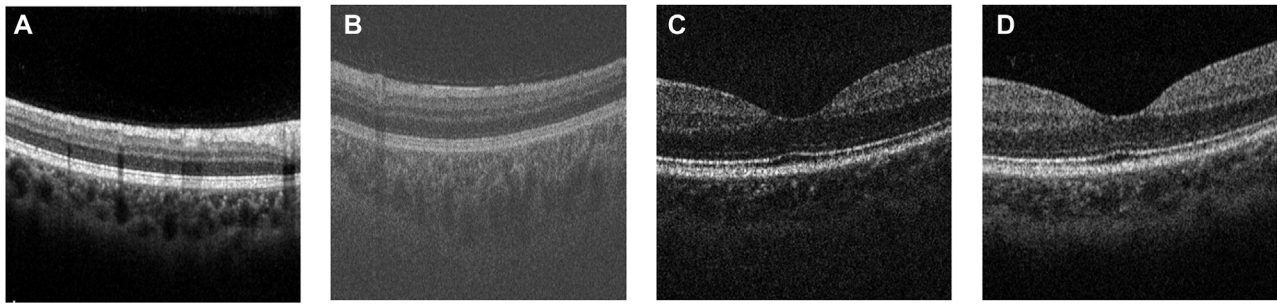


FIGURE 5

Examples of the original OCT images from (A) COSTA-H dataset, (B) COSTA-T dataset, (C) COSTA-B dataset (6 bit-depth), and (D) COSTA-B dataset (12 bit-depth).

$$Loss_{GF} = \sum_i \frac{1}{N_i} \|\phi_i(S_{GT} \odot M_{GT}) - \phi_i(\hat{S}_{Pred} \odot M_{GT})\|_1, \quad (8)$$

where $\phi_i(\cdot)$ denotes the feature maps from the i th layer of the VGG-19 network pre-trained on the ImageNet; S_{GT} denotes ground truth segmentation map; M_{GT} denotes ground truth soft point map; \hat{S}_{Pred} denotes the predicted segmentation map; \odot denotes concatenation operation; and N_i denotes the element number of feature maps from the i th layer of VGG-19.

The Boundary Perceptual Loss is defined as:

$$Loss_{BP} = Loss_{GF} + \sum_i^n Loss_{Map}^i \quad (9)$$

where n indicates the number of BEMs in the proposed choroid segmentation network.

Finally, the total loss function is defined as:

$$Loss_{Total} = \lambda_{Seg} Loss_{Seg} + \lambda_{BP} Loss_{BP} \quad (10)$$

where λ_{Seg} and λ_{BP} are set as 0.5 and 0.5 in our task.

4 Experiment settings

4.1 Datasets

In this work, a new Choroidal OCT image for SegmenTation (COSTA) dataset, which consists of three subsets named COSTA-H, COSTA-T and COSTA-B, was constructed for our proposed approach. These subsets were acquired from different devices or adopted different bit depths, as illustrated in Figure 5.

- **COSTA-H** consists of 10 OCT volumes from 10 healthy subjects. Each volume was captured by the Heidelberg Spectralis system, and contains 384 non-overlapping B-scans, each covering a $3 \times 3 \times 2 \text{ mm}^3$ region. Two groups of ophthalmologists were invited to independently make manual annotations of the upper and lower boundaries of the choroidal layer (BM and CSI), and their consensus were used as ground truth after discussion. In order to reduce the

number of manual annotations, we asked these ophthalmologists to annotate one B-scan every six consecutive B-scans, due to the high similarity between adjacent B-scans in an OCT volume. Finally, we obtained a total of $384/6 \times 10 = 640$ B-scans with manually annotated choroid boundaries.

- **COSTA-T** was captured by the Topcon DRI-OCT-1 system, containing a total of 20 OCT volumes from 20 healthy human eyes. Each volume contains 256 B-scans with a resolution of 512×992 pixels covering a $6 \times 6 \times 2 \text{ mm}^3$ region. This dataset was also annotated by the same protocol as COSTA-H, yielding a total of $256/4 \times 20 = 1280$ B-scans with annotated choroid boundaries.

Both COSTA-H and COSTA-T datasets were used for training and testing, where the ratio of data volume between the training and testing sets is 3:1. To more accurately and credibly evaluate the proposed network, we adopted the 4-fold cross-validation strategy, i.e., randomly dividing all samples into 4 equal pieces and taking each piece as the validation set and others as the training set in turn. After 4 groups of tests, different validation sets are replaced each time. That is, the results of four groups of models are obtained, and the average value is taken as the final result.

- **COSTA-B** was captured by a homemade 70-Khz SD-OCT system with different bit depths, and all this data was selected from Hao et al. (Hao et al., 2020). It contains 199 annotated B-scans with a resolution of 270×450 pixels from one normal subject. By contrast with COSTA-H and COSTA-T, COSTA-B was only used to test the robustness of the proposed method with respect to imaging quality. For the same B-scan, we also made a comparison of segmentation results based on different bit depths. The higher bit depth represents the better image quality, which makes for easier choroid segmentation.

4.2 Implementation

All deep learning approaches in the experiments were implemented with PyTorch (Paszke et al., 2019) and ran on a single NVIDIA GeForce GTX 3090 GPU with 24 GB memory

under an Ubuntu 16.04 system. The proposed network was trained with 400 epochs, and some hyper-parameters were set as follows: Adam optimization, with an initial learning rate of 0.0005 and batch size of 8. For other comparison methods, we adopted the same training strategy in the original paper.

4.3 Quantitative evaluation metrics

In order to compare the performance of the proposed method with other state-of-the-art deep learning networks, the following routine metrics for image segmentation were adopted and calculated:

- Dice Coefficient (Dice) = $\frac{2 \times TP}{2 \times TP + FP + FN}$;
- Intersection over Union (IoU) = $\frac{TP}{TP + FP + FN}$;
- Accuracy (Acc) = $\frac{TP + TN}{TP + TN + FP + FN}$;
- Sensitivity (Sen) = $\frac{TP}{TP + FN}$;

where TP is true positive, FP is false positive, TN is true negative, and FN is false negative.

In addition, we adopted Average Unsigned Surface Detection Error (AUSDE) (Xiang et al., 2018) based on BM and CSI:

$$AUSDE = \frac{1}{m} \sum_{i=1}^m |y^{(i)} - \hat{y}^{(i)}| \quad (11)$$

where m represents the width of the B-scan, $y^{(i)}$ and $\hat{y}^{(i)}$ represent vertical coordinates of the i th point in the horizontal direction of BM or CSI in the predicted segmentation map and ground truth, respectively. Based on $y^{(i)}$ and $\hat{y}^{(i)}$ of BM and CSI (respectively denoted as $y_{BM}^{(i)}$, $\hat{y}_{BM}^{(i)}$ and $y_{CSI}^{(i)}$, $\hat{y}_{CSI}^{(i)}$), average Thickness Difference (TD) can also be calculated as:

$$TD = \frac{1}{m} \sum_{i=1}^m \|y_{CSI}^{(i)} - y_{BM}^{(i)}\| - \|\hat{y}_{CSI}^{(i)} - \hat{y}_{BM}^{(i)}\| \quad (12)$$

5 Results

In this section, we performed training, validation as well as testing on COSTA-H and COSTA-T datasets, and compared them with the state-of-the-art choroid segmentation methods from both qualitative and quantitative perspectives. In addition, we applied the model trained on COSTA-H to COSTA-B to validate the robustness of the proposed method. Furthermore, we applied the proposed method to high myopia subjects. Segmentation results of all B-scans were then utilized for 3D reconstruction, which extracts 3D features for clinical correlation analysis.

5.1 Qualitative results

Figure 6 shows the visualization of the results of training and testing on Heidelberg, and we compare them with other popular

methods that use deep learning to segment the choroid layer, including the U-Net (Ronneberger et al., 2015), FCN (Long et al., 2015), DeepLab v3+ (Chen et al., 2018), SegNet (Badrinarayanan et al., 2017), CE-Net (Gu et al., 2019), CS-Net (Mou et al., 2019), and SCA-CENet (Mao et al., 2020). In Figure 7, the BM and CSI are located by blue and red lines, respectively. In both the overall segmentation and the boundary extraction (shown by the zoomed-in part of Figure 7), the proposed BEM performed better than its counterparts, which shows that our reinforcement of boundary characteristics is useful and efficient.

The testing results on the COSTA-B dataset are presented in Figure 8, which shows three OCT B-Scans with different bit depths, including 6, 8, and 12 (the best image quality) bits. The model with the best segmentation results on the COSTA-H dataset was used to segment these images. The segmentation results show the excellent robustness of the proposed model. Common segmentation methods that focus on global information and lack detailed features have difficulty in fully segmenting all the choroid layers. In contrast, the proposed method, which benefits from its ability to enhance boundary characteristics and extract different features from different perceptual fields and channels, shows good robustness across images of differing qualities.

5.2 Quantitative results

In order to verify the advantages of our method from a quantitative perspective, we selected the Dice, IoU, AUSDE and TD as evaluation metrics. For the COSTA-B test, only two metrics, Dice and IoU, were selected for evaluation, as the segmentation results of many methods could not form clear boundary lines (as shown in Figure 8).

Table 1 shows the quantitative comparison of various deep learning methods applied to the COSTA-H dataset. As is shown in Table 1, our method achieved 97.06% of the Dice coefficient and 94.31% of the IoU value, with a Boundary Error of 0.9496 for AUSDE of the BM and a Detection Error of 3.0029 for the lower boundary CSI, outperforming other methods. After adding BEM and BP-Loss to UNet, the value of AUSDE of CSI is improved by 2.57 pixels and that of TD is improved by 2.68 pixels, demonstrating the value of boundary extraction.

In order to further evaluate our proposed method, we conducted additional tests on the COSTA-T dataset and the results are shown in Table 2. With the help of BEM, our method achieves 92.87% of the Dice coefficient and 86.91% of the IoU value: after adding the BEM and BP-Loss, this improves to 2.02% and 2.39% on the Dice and IoU values, respectively.

We also select 6, 8, 10, and 12 bit depth images in the COSTA-B dataset for evaluation on the DICE and IoU metrics. For each network, both the best trained and validated models on the COSTA-H dataset were tested. It may be seen from Figure 9, by contrast with our proposed method, the segmentation results

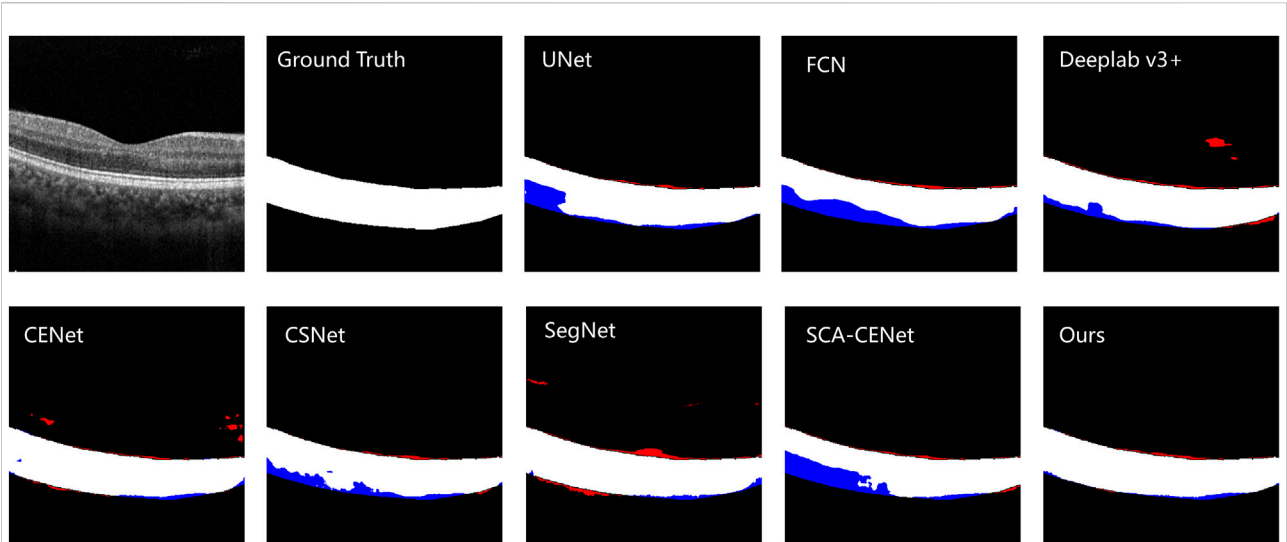


FIGURE 6
The visualization of the example result of choroid segmentation on the COSTA-H dataset. The first image is the original image, the second image is the ground truth, and the next few images are the results of different methods of segmentation: the specific methods are marked in the upper left corner of the image. White denotes a correctly segmented choroidal area, red denotes over-segmentation, and blue denotes under-segmentation.

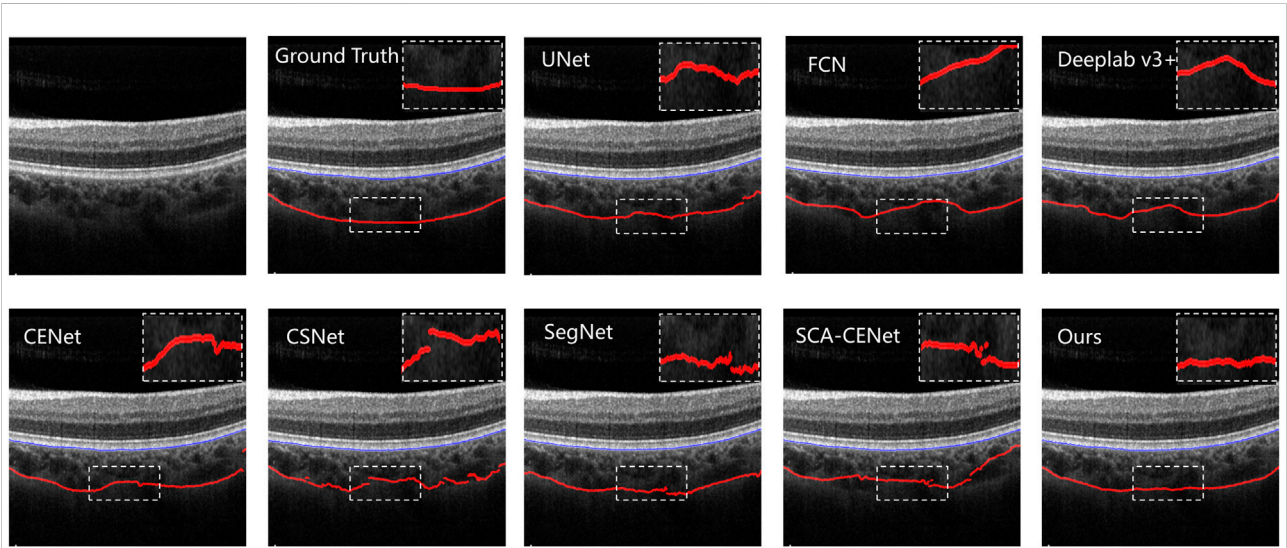


FIGURE 7
Results of different choroid segmentation methods in boundary detection. The name of the method is shown at the upper left corner of each image.

of the other networks degrade significantly over decreased depths of the same image. Specifically, all of the tested algorithms obtain better segmentation results on the 12-bit depth map than those on the 6 and 8-bit depths. This further validates the robustness of the proposed method.

5.3 Ablation study

In order to verify that each branch in the BEM and the BP-Loss are effective, we conducted ablation experiments by removing each branch separately and performing the experiments on the same

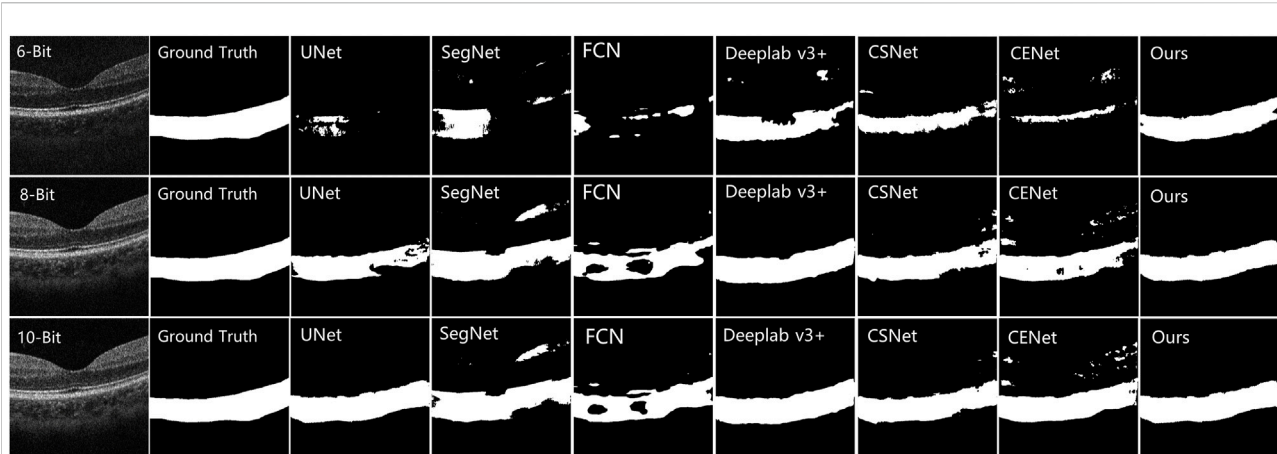


FIGURE 8

Comparison results of other choroid segmentation methods in boundary detection. The specific methods are marked in the upper left corner of the image.

TABLE 1 Quantitative segmentation results of different deep learning methods on the COSTA-H dataset.

COSTA-H							
Methods	Acc(%)	Sen(%)	Dice (%)	AUSDE (pixels)		TD (pixels)	Size (Mb)
				BM	CSI		
U-Net	99.04 ± 0.92	95.52 ± 3.87	96.10 ± 3.96	1.01 ± 1.07	5.57 ± 5.58	5.92 ± 7.01	53.7
CE-Net	99.09 ± 0.88	96.05 ± 5.12	96.30 ± 3.08	1.05 ± 0.25	3.95 ± 5.03	4.19 ± 4.89	116.2
FCN	99.00 ± 0.95	96.33 ± 5.51	96.04 ± 3.26	1.25 ± 0.46	3.93 ± 4.82	4.24 ± 4.57	134.4
SegNet	98.86 ± 0.70	96.70 ± 2.97	95.68 ± 1.84	1.33 ± 0.73	4.72 ± 3.22	4.99 ± 3.12	176.8
DeepLab v3+	98.78 ± 0.99	95.30 ± 5.40	95.23 ± 3.29	1.37 ± 0.89	5.36 ± 5.08	5.52 ± 4.94	368.1
SCA-CENet	99.14 ± 0.80	96.11 ± 4.65	96.41 ± 3.23	1.01 ± 0.30	4.11 ± 5.15	4.40 ± 5.00	116.2
CS-Net	99.00 ± 0.85	95.31 ± 4.92	96.03 ± 2.85	1.03 ± 0.50	4.32 ± 4.45	4.46 ± 4.26	35.8
Our method	99.27 ± 0.27	97.07 ± 2.01	97.06 ± 0.90	0.95 ± 0.59	3.00 ± 1.48	3.24 ± 1.37	54.1

The values in bold represent the best of all the comparative experimental results.

TABLE 2 Quantitative segmentation results of different deep learning methods on the COSTA-T dataset.

COSTA-T							
Methods	Acc(%)	Sen(%)	Dice (%)	AUSDE (pixels)		TD (pixels)	Size (Mb)
				BM	CSI		
U-Net	97.20 ± 1.47	91.32 ± 6.25	90.85 ± 4.29	1.99 ± 0.97	11.99 ± 7.48	11.98 ± 7.45	53.7
CE-Net	97.52 ± 1.46	93.00 ± 5.85	91.77 ± 4.70	1.96 ± 0.81	10.06 ± 6.35	10.18 ± 6.49	116.2
FCN	97.19 ± 1.47	91.49 ± 6.53	90.61 ± 5.04	2.72 ± 3.56	12.17 ± 7.54	11.97 ± 8.32	134.4
SegNet	97.37 ± 1.35	92.01 ± 6.11	91.38 ± 4.04	2.12 ± 1.17	11.43 ± 6.67	11.57 ± 6.61	176.8
DeepLab v3+	96.87 ± 1.64	87.00 ± 9.05	88.95 ± 6.01	3.22 ± 4.35	13.75 ± 9.18	13.92 ± 8.71	368.1
SCA-CENet	97.62 ± 1.52	93.30 ± 5.93	92.21 ± 4.78	1.94 ± 0.70	9.56 ± 6.56	9.77 ± 6.65	116.2
CS-Net	97.31 ± 1.52	90.65 ± 6.74	91.12 ± 4.58	1.76 ± 0.59	11.16 ± 7.74	11.20 ± 7.76	35.8
Our method	97.85 ± 1.25	92.47 ± 6.13	92.87 ± 3.70	1.88 ± 1.07	9.11 ± 6.19	9.23 ± 6.28	54.1

The values in bold represent the best of all the comparative experimental results.

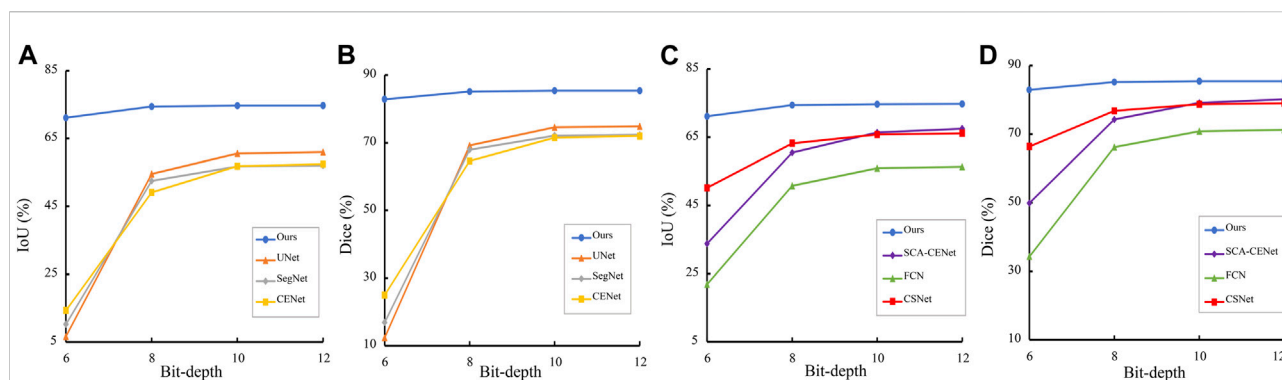


FIGURE 9

Trend of Dice and IoU results of different segmentation methods in different bit depth images. (A), (C) are the result on the COSTA-H dataset, and (B), (D) are the result on the COSTA-T dataset.

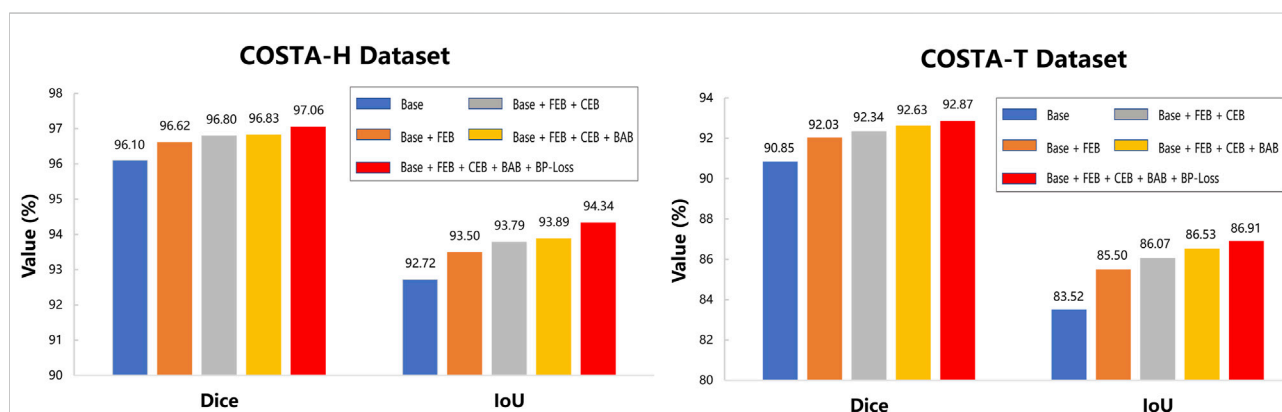


FIGURE 10

Ablation results on COSTA-H and COSTA-T datasets. The blue bars denote the quantitative results of the baseline network U-Net. The orange bars denote the segmentation results of the network with FEB. The gray bars denote the segmentation results of the network with FEB and CEB. The yellow bars denote the segmentation results of the network with FEB, CEB, and BAB. The red bars denote the segmentation results of the network with FEB, CEB, BAB, and BP-Loss.

dataset, and the results are shown in Figure 10. It can be seen that the dice and IoU metrics gradually increase with the addition of different branches, both in COSTA-T and COSTA-H datasets. It is obvious that the segmentation result benefits from every branch of the BEM.

After adding BEM, the IoU of the segmentation result on COSTA-T dataset reaches 86.53%, which is 3.01% higher than the baseline. With the help of BP-Loss, the segmentation result reaches 86.91%, which further improves the segmentation effect. Similarly, each module and branch plays a role on the COSTA-H dataset.

6 Clinic applications

High myopia is a common visual impairment worldwide. The mechanical pulling of the growing eye axis in high myopia

leads to retinal and choroidal thinning, as well as to a variety of pathological changes in the fundus, which can easily evolve into pathological myopia (Read et al., 2019; Scherm et al., 2019; Singh et al., 2019). Previous studies have shown that choroidal thickness is significantly higher in highly myopic patients than that in the healthy subjects, but no correlation has been found in other features such as volume, surface area, curvature of the BM and CSI, and other 3D features. Encouraged by the good performance of the proposed method demonstrated in the experimentation, we applied the segmentation method to a prospective clinical study, in which the choroidal thickness of different regions are extracted and the 3D morphology of choroidal structures reconstructed using point clouds.

1) Dataset: We collected 20 volunteers aged between 20 and 30 years with high myopia. The right and left eyes of all

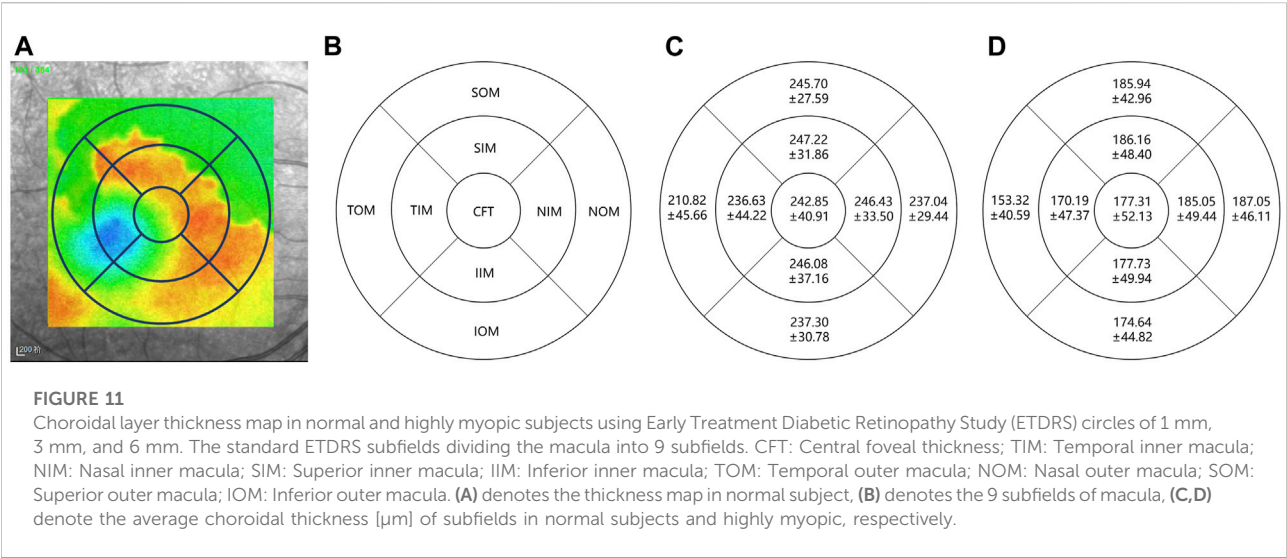


TABLE 3 Average choroidal thickness and 95% CI of different Early Treatment Diabetic Retinopathy Study (ETDRS) subfields in normal and highly myopic subjects.

ETDRS subfield	Normal		High Myopia		Mean Difference (μm)*	95%CI (μm)		p-value
	Mean	SD	Mean	SD		Lower Bound	Upper Bound	
	(μm)	(μm)	(μm)	(μm)				
Center point thickness	235.93	45.54	180.94	50.72	−54.99	28.13	81.85	<0.001
Central foveal thickness	242.85	40.91	177.31	52.13	−65.54	12.82	39.81	<0.001
Superior inner macula	247.22	31.86	186.16	48.40	−61.06	38.97	83.16	<0.001
Nasal inner macula	246.43	33.50	185.05	49.44	−61.38	38.55	84.22	<0.001
Inferior inner macula	246.08	37.16	177.73	49.94	−68.36	44.32	92.39	<0.001
Temporal inner macula	236.63	44.22	170.19	47.37	−66.44	40.79	92.08	<0.001
Superior outer macula	245.70	27.59	185.94	48.96	−59.76	38.20	81.32	<0.001
Nasal outer macula	237.04	29.44	187.05	46.11	−49.99	29.19	70.78	<0.001
Inferior outer macula	237.30	30.78	174.64	44.82	−62.67	41.85	83.49	<0.001
Temporal outer macula	210.82	45.66	153.32	40.59	−57.50	32.83	82.16	<0.001
Global average	230.41	28.92	177.31	42.35	−53.09	33.47	72.72	<0.001

* Normal group as reference, SD, means Standard Deviation.

volunteers were scanned by the Heidelberg Spectralis system device for data acquisition, and volume data were extracted within a $4.5 \times 4.5 \times 2 \text{ mm}^3$ area centered on the macula. Each volume contained 512 B-scans.

2) Result: Figure 11 shows the distribution of choroidal layer thickness in different areas across the volume, in both normal and highly myopic subjects. Table 3 shows the quantitative results of the average choroidal thickness in different subfields of the macula. The average choroidal thickness in the highly myopic subjects was significantly thinner than that in the normal subjects in all regions, with an average choroidal thickness of

$230.41 \pm 28.92 \mu\text{m}$ in the normal population and $177.31 \pm 42.35 \mu\text{m}$ in the highly myopic subjects, while the specific thickness distribution in the other regions is shown in Table 3, with *p*-values less than 0.001 after *t*-test, which is consistent with the results reported in (Wang et al., 2015) recently.

Current studies on the correlation between choroidal morphology and diseases rarely involve the 3D features of the choroid. To fill this gap, we reconstructed the 3D morphology of the choroid and extracted the 3D features of choroidal volume, surface area and surface curvature using 3D point clouds. The

TABLE 4 Results of choroidal 3D features in normal and highly myopic subjects.

	Normal		High Myopia		Mean Difference *	p-value
	Mean	SD	Mean	SD		
BM Curvature (mm^{-1})	0.027	0.011	0.029	0.006	0.002	0.538
CSI Curvature (mm^{-1})	0.091	0.024	0.115	0.141	0.024	0.474
Inner Volume (mm^3)	2.211	0.656	1.304	0.441	-0.907	<0.001
Inner Surface Area (mm^2)	1.166	0.258	0.804	0.436	-0.362	<0.001

* Normal group as reference.

average volume of the choroid in the central macular notch $3 \times 3 \times 2 \text{ mm}^3$ in the normal subjects was $2.211 \pm 0.656 \text{ mm}^3$, whereas the average volume of the choroid in the same range in the highly myopic subjects was $1.304 \pm 0.441 \text{ mm}^3$, with a *p*-value less than 0.001. This is also consistent with the relevant research results reported in (Barteselli et al., 2012).

In addition, we also calculated the surface area and the curvature of the upper and lower choroid: the results are shown in Table 4. It may be seen from Table 4 that the choroidal surface areas of highly myopic subjects and normal subjects are significantly different, while differences of curvature between highly myopic subjects and normal subjects are not as significant.

7 Discussion and conclusion

With the emergence and popularity of deep learning methods, several choroidal layer segmentation methods have been developed during the last decade and many have been applied to choroidal segmentation tasks. However, due to the low depth and low contrast of the early OCT techniques, the applications of deep learning methods to retinal segmentation tasks have been limited. Since the continuous innovation of OCT equipment means that the choroid can now be rendered intact in B-scan, it is straightforward that the previous methods for segmenting the retinal layer should be applied to the task of choroidal layer segmentation. However, even when using the most recent technical improvements in OCT imaging, the CSI layer of the choroid is still not as clear as the boundaries of the retina. Therefore, the models developed for retinal layer segmentation tend to generate ambiguous results when applied to the choroidal boundary.

Recognizing the limitations of existing models, the goal of our work is to develop a method to automatically segment the choroidal layers, while dealing with the ambiguous boundary. We enable the segmentation network to focus on the boundary features by adding a boundary enhancement module to the major segmentation network. The module has three branches to

enhance boundary features via different perspectives: expanding the perceptual field using dilated convolution, activating a boundary features using the boundary activation function and extracting the boundary features of different channels using channel convolution.

In order to embed expert knowledge into the proposed choroidal automatic segmentation model, we extract boundary enhancement points from the boundary of ground truth and generate a soft point map, then introduce a boundary perceptual loss, so that the boundary region information can be fed back to the segmentation network based on ground truth, following which the accurate segmentation of the choroidal layer can be performed.

In addition, in order to further validate the clinical application of this method, compared with previous studies, we investigated not only from the two-dimensional perspective of thickness, but also from a three-dimensional perspective. The differences of choroidal 3D morphological structures between highly myopic and normal subjects are compared. This paper demonstrates the effectiveness of the proposed method, which has the potential to promote understanding the pathogenesis of some eye diseases (e.g., high myopia) related to morphological changes of the choroid, so as to support early screening and intervention.

However, this work has limitations. For example, the volunteer normal subjects may have a certain degree of myopia, yet still not reach the definition of high myopia, which may affect the statistical analysis of final results. The dataset employed for validation might be extended, not only in terms of data volume but also in terms of disease types, such as glaucoma and pathological myopia. Another limitation of our method is that it is less useful for tackling multi-layer (multi-class) segmentation tasks. Since the selected boundary enhancement points have not been further classified by different layers, soft point map construction and boundary enhancement module in the proposed method might not be suitable for multi-layer segmentation in retinal OCT images. In future work, the proposed model may be improved by setting different weights to the boundary points, which would change the type and number of points adaptively. In this way, the proposed

model might then be applied to both binary and multiclassification tasks.

Data availability statement

The original contributions presented in the study are included in the article/supplementary material, further inquiries can be directed to the corresponding author.

Ethics statement

The studies involving human participants were reviewed and approved by Ningbo Institute of Materials Technology and Engineering, Chinese Academy of Sciences. The patients/participants provided their written informed consent to participate in this study. Written informed consent was obtained from the individual(s) for the publication of any potentially identifiable images or data included in this article.

Author contributions

QY and YM designed this study, analyzed the data and revised the manuscript, they are both the corresponding authors. WW and YG carried out this study, performed the research and wrote the manuscript. HH and YZ helped to analyze part of the data. JZ and PS developed the computational pipeline and revised the manuscript. All authors read, edited and approved the final manuscript.

References

- Agrawal, R., Ding, J., Sen, P., Rousselot, A., Chan, A., Nivison-Smith, L., et al. (2020). Exploring choroidal angioarchitecture in health and disease using choroidal vascularity index. *Prog. Retin. Eye Res.* 77, 100829. doi:10.1016/j.preteyeres.2020.100829
- Badrinarayanan, V., Kendall, A., and Cipolla, R. (2017). Segnet: A deep convolutional encoder-decoder architecture for image segmentation. *IEEE Trans. Pattern Anal. Mach. Intell.* 39, 2481–2495. doi:10.1109/TPAMI.2016.2644615
- Barteselli, G., Chhablani, J., El-Emam, S., Wang, H., Chuang, J., Kozak, I., et al. (2012). Choroidal volume variations with age, axial length, and sex in healthy subjects: A three-dimensional analysis. *Ophthalmology* 119, 2572–2578. doi:10.1016/j.ophtha.2012.06.065
- Cedrone, C., Nucci, C., Scuderi, G., Ricci, F., Cerulli, A., and Culasso, F. (2006). Prevalence of blindness and low vision in an Italian population: A comparison with other European studies. *Eye* 20, 661–667. doi:10.1038/sj.eye.6701934
- Chai, Z., Zhou, K., Yang, J., Ma, Y., Chen, Z., Gao, S., et al. (2020). “Perceptual-assisted adversarial adaptation for choroid segmentation in optical coherence tomography,” in 2020 IEEE 17th International Symposium on Biomedical Imaging (ISBI), Iowa City, IA, United States, April 3–7, 2020 (IEEE), 1966.
- Chen, H.-J., Huang, Y.-L., Tse, S.-L., Hsia, W.-P., Hsiao, C.-H., Wang, Y., et al. (2022). Application of artificial intelligence and deep learning for choroid segmentation in myopia. *Transl. Vis. Sci. Technol.* 11, 38. doi:10.1167/tvst.11.2.38
- Chen, L.-C., Zhu, Y., Papandreou, G., Schroff, F., and Adam, H. (2018). Encoder-decoder with atrous separable convolution for semantic image segmentation. In

Funding

This work was supported in part by the Zhejiang Postdoctoral Scientific Research Project (ZJ2022118), in part by General research program of Zhejiang Provincial Department of health (2021PY073), in part by Traditional Chinese Medicine project of Zhejiang Province (2021ZB268), in part by the National Science Foundation Program of China (61906181, 62272444 and 62103398), in part by the Zhejiang Provincial Natural Science Foundation of China (LR22F020008), in part by the Ningbo Natural Science Foundation (2022Z127), in part by the Key Research and Development Program of Zhejiang Province (2020C03036).

Conflict of interest

The authors declare that the research was conducted in the absence of any commercial or financial relationships that could be construed as a potential conflict of interest.

Publisher's note

All claims expressed in this article are solely those of the authors and do not necessarily represent those of their affiliated organizations, or those of the publisher, the editors and the reviewers. Any product that may be evaluated in this article, or claim that may be made by its manufacturer, is not guaranteed or endorsed by the publisher.

- Proceedings of the European conference on computer vision (ECCV), Munich, Germany, September 8–14, 2018. 801
- Chen, Q., Fan, W., Niu, S., Shi, J., Shen, H., and Yuan, S. (2015). Automated choroid segmentation based on gradual intensity distance in hd-oct images. *Opt. Express* 23, 8974–8994. doi:10.1364/OE.23.008974
- Chen, S., Wang, W., Gao, X., Li, Z., Huang, W., Li, X., et al. (2014). Changes in choroidal thickness after trabeculectomy in primary angle closure glaucoma. *Investig. Ophthalmol. Vis. Sci.* 55, 2608–2613. doi:10.1167/iovs.13-13595
- Choma, M. A., Sarunic, M. V., Yang, C., and Izatt, J. A. (2003). Sensitivity advantage of swept source and Fourier domain optical coherence tomography. *Opt. Express* 11, 2183–2189. doi:10.1364/oe.11.002183
- Danesh, H., Kafieh, R., Rabbani, H., and Hajizadeh, F. (2014). Segmentation of choroidal boundary in enhanced depth imaging ocs using a multiresolution texture based modeling in graph cuts. *Comput. Math. Methods Med.* 2014, 479268. doi:10.1155/2014/479268
- Dang, Q.-V., and Lee, G.-S. (2021). Document image binarization with stroke boundary feature guided network. *IEEE Access* 9, 36924–36936. doi:10.1109/access.2021.3062904
- Gu, Z., Cheng, J., Fu, H., Zhou, K., Hao, H., Zhao, Y., et al. (2019). Ce-net: Context encoder network for 2d medical image segmentation. *IEEE Trans. Med. Imaging* 38, 2281–2292. doi:10.1109/TMI.2019.2903562
- Hao, Q., Zhou, K., Yang, J., Hu, Y., Chai, Z., Ma, Y., et al. (2020). High signal-to-noise ratio reconstruction of low bit-depth optical coherence tomography using deep learning. *J. Biomed. Opt.* 25, 123702. doi:10.1117/1.JBO.25.12.123702

- He, F., Chun, R. K. M., Qiu, Z., Yu, S., Shi, Y., To, C. H., et al. (2021). Choroid segmentation of retinal OCT images based on CNN classifier and l_2 - l_q fitter. *Comput. Math. Methods Med.* 2021, 8882801. doi:10.1155/2021/8882801
- Hu, Z., Wu, X., Ouyang, Y., Ouyang, Y., and Sadda, S. R. (2013). Semiautomated segmentation of the choroid in spectral-domain optical coherence tomography volume scans. *Investig. Ophthalmol. Vis. Sci.* 54, 1722–1729. doi:10.1167/iov.12-10578
- Huang, D., Swanson, E. A., Lin, C. P., Schuman, J. S., Stinson, W. G., Chang, W., et al. (1991). Optical coherence tomography. *science* 254, 1178–1181. doi:10.1126/science.1957169
- Kim, J. T., Lee, D. H., Joe, S. G., Kim, J.-G., and Yoon, Y. H. (2013). Changes in choroidal thickness in relation to the severity of retinopathy and macular edema in type 2 diabetic patients. *Investig. Ophthalmol. Vis. Sci.* 54, 3378–3384. doi:10.1167/iov.12-11503
- Lee, H. J., Kim, J. U., Lee, S., Kim, H. G., and Ro, Y. M. (2020). “Structure boundary preserving segmentation for medical image with ambiguous boundary,” in Proceedings of the IEEE/CVF Conference on Computer Vision and Pattern Recognition, Seattle, Online, United States, June 14–19, 2020, 4817–4826.
- Long, J., Shelhamer, E., and Darrell, T. (2015). “Fully convolutional networks for semantic segmentation,” in Proceedings of the IEEE conference on computer vision and pattern recognition, Boston, MA, United States, June 7–12, 2015, 3431
- Mao, X., Zhao, Y., Chen, B., Ma, Y., Gu, Z., Gu, S., et al. (2020). “Deep learning with skip connection attention for choroid layer segmentation in oct images,” in 2020 42nd Annual International Conference of the IEEE Engineering in Medicine & Biology Society (EMBC), Montreal, QC, Canada, July 20–24, 2020 (IEEE), 1641.
- Masood, S., Fang, R., Li, P., Li, H., Sheng, B., Mathavan, A., et al. (2019). Automatic choroid layer segmentation from optical coherence tomography images using deep learning. *Sci. Rep.* 9, 3058–3118. doi:10.1038/s41598-019-39795-x
- Mazzaferri, J., Beaton, L., Hounye, G., Sayah, D. N., and Costantino, S. (2017). Open-source algorithm for automatic choroid segmentation of oct volume reconstructions. *Sci. Rep.* 7, 42112–42210. doi:10.1038/srep42112
- Moschos, M. M., and Chatziralli, I. P. (2018). Evaluation of choroidal and retinal thickness changes in Parkinson's disease using spectral domain optical coherence tomography. *Seminars Ophthalmol.* 33, 494. doi:10.1080/08820538.2017.1307423
- Mou, L., Zhao, Y., Chen, L., Cheng, J., Gu, Z., Hao, H., et al. (2019). “Cs-Net: channel and spatial attention network for curvilinear structure segmentation,” in International Conference on Medical Image Computing and Computer-Assisted Intervention, Shenzhen, China, October 13–17, 2019 (Springer), 721
- Nickla, D. L., and Wallman, J. (2010). The multifunctional choroid. *Prog. Retin. Eye Res.* 29, 144–168. doi:10.1016/j.preteyeres.2009.12.002
- Oduntan, A. (2005). Prevalence and causes of low vision and blindness worldwide. *Afr. Vis. eye health* 64, 44–57. doi:10.4102/aveh.v64i2.214
- Paszke, A., Gross, S., Massa, F., Lerer, A., Bradbury, J., Chanan, G., et al. (2019). “Pytorch: An imperative style, high-performance deep learning library,” in The Conference in NeurIPS 2019, Vancouver Convention Center, Canada, November 8–14, 2019 32, 8026. Available at: <http://papers.neurips.cc/paper/9015-pytorch-an-imperative-style-high-performance-deep-learning-library.pdf>.
- Read, S. A., Fuss, J. A., Vincent, S. J., Collins, M. J., and Alonso-Caneiro, D. (2019). Choroidal changes in human myopia: Insights from optical coherence tomography imaging. *Clin. Exp. Optom.* 102, 270–285. doi:10.1111/cxo.12862
- Regatieri, C. V., Branchini, L., Carmody, J., Fujimoto, J. G., and Duker, J. S. (2012). *Choroidal thickness in patients with diabetic retinopathy analyzed by spectral-domain optical coherence tomography*, 32. Philadelphia, Pa: Retina, 563.
- Ronneberger, O., Fischer, P., and Brox, T. (2015). “U-net: Convolutional networks for biomedical image segmentation,” in International Conference on Medical image computing and computer-assisted intervention, Munich, Germany, October 5–9, 2015 (Springer), 234
- Satue, M., Obis, J., Alarcia, R., Orduna, E., Rodrigo, M. J., Vilades, E., et al. (2018). Retinal and choroidal changes in patients with Parkinson's disease detected by swept-source optical coherence tomography. *Curr. Eye Res.* 43, 109–115. doi:10.1080/02713683.2017.1370116
- Scherm, P., Pottenkofer, M., Maier, M., Lohmann, C. P., and Feucht, N. (2019). Choriocapillary blood flow in myopic subjects measured with oct angiography. *Ophthalmic Surg. Lasers Imaging Retina* 50, e133–e139. doi:10.3928/23258160-20190503-13
- Simonyan, K., and Zisserman, A. (2014). *Very deep convolutional networks for large-scale image recognition*. Oxford, United Kingdom: Cornell University. *arXiv preprint arXiv:1409.1556*.
- Singh, S. R., Vupparaboina, K. K., Goud, A., Dansingani, K. K., and Chhablani, J. (2019). Choroidal imaging biomarkers. *Surv. Ophthalmol.* 64, 312–333. doi:10.1016/j.survophthal.2018.11.002
- Sui, X., Zheng, Y., Wei, B., Bi, H., Wu, J., Pan, X., et al. (2017). Choroid segmentation from optical coherence tomography with graph-edge weights learned from deep convolutional neural networks. *Neurocomputing* 237, 332–341. doi:10.1016/j.neucom.2017.01.023
- Tian, J., Marziliano, P., Baskaran, M., Tun, T. A., and Aung, T. (2013). Automatic segmentation of the choroid in enhanced depth imaging optical coherence tomography images. *Biomed. Opt. Express* 4, 397–411. doi:10.1364/BOE.4.000397
- Wang, C., Wang, Y. X., and Li, Y. (2017). Automatic choroidal layer segmentation using markov random field and level set method. *IEEE J. Biomed. Health Inf.* 21, 1694–1702. doi:10.1109/JBHI.2017.2675382
- Wang, G., Zuluaga, M. A., Li, W., Pratt, R., Patel, P. A., Aertsen, M., et al. (2018). Deepigeos: A deep interactive geodesic framework for medical image segmentation. *IEEE Trans. Pattern Anal. Mach. Intell.* 41, 1559–1572. doi:10.1109/TPAMI.2018.2840695
- Wang, J., Wei, L., Wang, L., Zhou, Q., Zhu, L., and Qin, J. (2021). Boundary-aware transformers for skin lesion segmentation,” in International Conference on Medical Image Computing and Computer-Assisted Intervention, Strasbourg, France, September 27–October 1, 2021. Springer, 206
- Wang, S., Wang, Y., Gao, X., Qian, N., and Zhuo, Y. (2015). Choroidal thickness and high myopia: A cross-sectional study and meta-analysis. *BMC Ophthalmol.* 15, 70–10. doi:10.1186/s12886-015-0059-2
- Wei, S., Zhang, T., and Ji, S. (2021). A concentric loop convolutional neural network for manual delineation level building boundary segmentation from remote sensing images. *IEEE Trans. Geosci. Remote Sens.* 60, 1–11. doi:10.1109/tgrs.2021.3126704
- Wong, I. Y., Koizumi, H., and Lai, W. W. (2011). Enhanced depth imaging optical coherence tomography. *Ophthalmic Surg. Lasers Imaging* 42, S75–S84. doi:10.3928/15428877-20110627-07
- Wong, Y.-L., and Saw, S.-M. (2016). Epidemiology of pathologic myopia in Asia and worldwide. *Asia. Pac. J. Ophthalmol.* 5, 394–402. doi:10.1097/APO.0000000000000234
- Xiang, D., Tian, H., Yang, X., Shi, F., Zhu, W., Chen, H., et al. (2018). Automatic segmentation of retinal layer in oct images with choroidal neovascularization. *IEEE Trans. Image Process.* 27, 5880–5891. doi:10.1109/TIP.2018.2860255
- Yan, Q., Gu, Y., Zhao, J., Wu, W., Ma, Y., Liu, J., et al. (2022). Automatic choroid layer segmentation in oct images via context efficient adaptive network. *Appl. Intell. (Dordr)*. 1–13. doi:10.1007/s10489-022-03723-w
- Yaqoob, Z., Wu, J., and Yang, C. (2005). Spectral domain optical coherence tomography: A better oct imaging strategy. *Biotechniques* 39, S6–S13. doi:10.2144/000112090
- Yiu, G., Chiu, S. J., Petrou, P. A., Stinnett, S., Sarin, N., Farsiu, S., et al. (2015). Relationship of central choroidal thickness with age-related macular degeneration status. *Am. J. Ophthalmol.* 159, 617–626. doi:10.1016/j.ajo.2014.12.010
- Yu, F., and Koltun, V. (2015). *Multi-scale context aggregation by dilated convolutions*. Princeton, United States: Cornell University. *arXiv preprint arXiv:1511.07122*.
- Yu, M., Pei, K., Li, X., Wei, X., Wang, C., and Gao, J. (2022). Fbcu-net: A fine-grained context modeling network using boundary semantic features for medical image segmentation. *Comput. Biol. Med.* 150, 106161. doi:10.1016/j.combiomed.2022.106161
- Zhang, H., Yang, J., Zhou, K., Li, F., Hu, Y., Zhao, Y., et al. (2020). Automatic segmentation and visualization of choroid in oct with knowledge infused deep learning. *IEEE J. Biomed. Health Inf.* 24, 3408–3420. doi:10.1109/JBHI.2020.3023144
- Zhang, L., Lee, K., Niemeijer, M., Mullins, R. F., Sonka, M., and Abramoff, M. D. (2012). Automated segmentation of the choroid from clinical sd-oct. *Investig. Ophthalmol. Vis. Sci.* 53, 7510–7519. doi:10.1167/iov.12-10311



OPEN ACCESS

EDITED BY
Weihua Yang,
Jinan University, China

REVIEWED BY
Jing Rao,
Shenzhen Eye Hospital, China
Yongjin Zhou,
Shenzhen University, China
Kun Liu,
Shanghai First People's Hospital, China

*CORRESPONDENCE
Guang-Yu Li,
liguangyu@aliyun.com

SPECIALTY SECTION
This article was submitted to Molecular
and Cellular Pathology,
a section of the journal
Frontiers in Cell and Developmental
Biology

RECEIVED 13 October 2022
ACCEPTED 08 November 2022
PUBLISHED 18 November 2022

CITATION
Bao X-L, Sun Y-J, Zhan X and Li G-Y
(2022), Orbital and eyelid diseases: The
next breakthrough in artificial
intelligence?
Front. Cell Dev. Biol. 10:1069248.
doi: 10.3389/fcell.2022.1069248

COPYRIGHT
© 2022 Bao, Sun, Zhan and Li. This is an
open-access article distributed under
the terms of the [Creative Commons
Attribution License \(CC BY\)](#). The use,
distribution or reproduction in other
forums is permitted, provided the
original author(s) and the copyright
owner(s) are credited and that the
original publication in this journal is
cited, in accordance with accepted
academic practice. No use, distribution
or reproduction is permitted which does
not comply with these terms.

Orbital and eyelid diseases: The next breakthrough in artificial intelligence?

Xiao-Li Bao¹, Ying-Jian Sun¹, Xi Zhan² and Guang-Yu Li^{3*}

¹Department of Ophthalmology, Second Hospital of Jilin University, Changchun, China, ²Department of Engineering, The Army Engineering University of PLA, Nanjing, China, ³The Eye Hospital, School of Ophthalmology & Optometry, Wenzhou Medical University, Wenzhou, China

Orbital and eyelid disorders affect normal visual functions and facial appearance, and precise oculoplastic and reconstructive surgeries are crucial. Artificial intelligence (AI) network models exhibit a remarkable ability to analyze large sets of medical images to locate lesions. Currently, AI-based technology can automatically diagnose and grade orbital and eyelid diseases, such as thyroid-associated ophthalmopathy (TAO), as well as measure eyelid morphological parameters based on external ocular photographs to assist surgical strategies. The various types of imaging data for orbital and eyelid diseases provide a large amount of training data for network models, which might be the next breakthrough in AI-related research. This paper retrospectively summarizes different imaging data aspects addressed in AI-related research on orbital and eyelid diseases, and discusses the advantages and limitations of this research field.

KEYWORDS

artificial intelligence, deep learning, orbital and eyelid diseases, ophthalmic plastic surgery, orbital computed tomography, orbital magnetic resonance imaging

Introduction

Artificial Intelligence (AI) simulates and extends human intelligence, and has been hailed as “the Future of Employment” (Yang et al., 2021). Long before the mid-twentieth century, the British scientist Alan Turing first predicted that machines could become intelligent (Li et al., 2019), and in 1956, McCarthy introduced “AI” at the Dartmouth Conference (Dzobo et al., 2020). At the time, “AI” was actualized via a static computer program that controlled a machine, which is unlike the AI we currently know (Mintz and Brodie, 2019). In 1959, Samuel developed the theory of AI and proposed “machine learning (ML)” (Finlayson et al., 2019), which denotes the capability of a computer to learn by itself without explicit program instructions (Nichols et al., 2019). In ML large amounts of data are analyzed to make predictions on real-world events using supervised and unsupervised algorithms. ML has spawned variants such as conventional machine learning (CML) and deep learning (DL) (Brehar et al., 2020; Ye et al., 2020). DL has exhibited a remarkable ability to analyze high-dimensional data with multiple processing layers, gradually becoming the mainstream of ML modeling (Finlayson et al., 2019). In particular, DL-based technologies display excellent abilities to extract image features and

associate various types of data, which plays an active role in the automatic recognition of image, sound, and text data (Cai et al., 2020). Ting et al. (2017) reported that AI could automatically diagnose diabetic retinopathy from more than 100,000 retinal photographs. In recent years, DL has gradually become a new tool in the automatic diagnosis of glaucoma and cataracts (Lin et al., 2019; Wu et al., 2019; Wang et al., 2020a; Girard and Schmetterer, 2020). Some commercial software applications related to DL are used to assist in the diagnosis of retinal diseases in clinical practice (van der Heijden et al., 2018; Girard and Schmetterer, 2020).

Imaging data, including orbital computed tomography (CT), orbital magnetic resonance imaging (MRI), and external ocular photographs, play a crucial role in the diagnosis and treatment of orbital and eyelid diseases (Bailey and Robinson, 2007; Abdullah et al., 2010). Currently, AI automatically diagnoses and grades some orbital and eyelid diseases, such as orbital blowout fractures and thyroid-associated ophthalmopathy (TAO) (Li et al., 2020; Song et al., 2021a). Automatic measurement of eyelid morphological parameters and automatic surgical decision-making based on AI technology are two recent research hotspots (Bahceci Simsek and Sirolu, 2021; Chen et al., 2021; Lou et al., 2021; Hung et al., 2022). Compared to traditional medical models, AI can rapidly analyze large sets of patient data, achieving healthcare cost savings and assisting in the construction of teleconsultation platforms (Bi et al., 2020). Automatic measurement of eyelid morphological parameters based on AI technology could correct artifactual errors to maintain objectivity and repeatability in patient data evaluation, which might be a new tool in the assessment of oculoplastic surgery (Lou et al., 2021). However, because of the small amount of standard imaging data and the imbalance in categories, ensuring a highly-efficient algorithm training is still a challenge. In addition, the development of methods for obtaining high-quality imaging data of orbital and eyelid diseases should also be considered.

In this paper, we comprehensively review the application of AI-based technology to the diagnosis and treatment of orbital and eyelid diseases by analyzing various types of image data. The advantages and limitations of AI in this field are also discussed to explore its potential targets in detecting and treating orbital and eyelid diseases.

What is artificial intelligence?

AI is a branch of computer science, in which “artificial” indicates that the systems are man-made and “intelligence” denotes features such as consciousness and thinking (Thrall et al., 2018). The major purpose of AI is to simulate human thinking processes by learning from existing experiences to solve problems that cannot be solved through traditional computer programming (Bischoff et al., 2019). ML is a subset of AI that has become the mainstream of AI technology (Shin et al., 2021). ML extracts and analyzes the features of input samples to classify new homogeneous samples (Totschnig, 2020). ML automatically improves and optimizes computer algorithms and programs by analyzing the data rather than relying on explicit

program instructions (Nichols et al., 2019; Cho et al., 2021). Among the various ML models that have emerged, neural networks simulate the synaptic structure of human neurons and improve the computational ability of ML by adjusting the parameters of network models (Starke et al., 2021). Convolutional neural networks (CNNs), which have an encoding structure similar to that of visual cortical neurons (Hou et al., 2019), have become one of the most popular neural network models (Mintz and Brodie, 2019).

In human vision, each neuron in the visual cortex responds to stimulation by activating specific regions in the visual space that form the entire visual field (Figure 1) (Brachmann et al., 2017). Similarly, CNNs extract features from the input image and output a feature map using convolution and pooling operations (Le et al., 2020). A convolution layer consists of a set of two-dimensional numerical matrices that are also known as filters. The CNN obtains the pixel value of the output images by multiplying the value in the filter by the value of the corresponding pixel in the image and summing the product, that is, *via* convolution operations (Brachmann et al., 2017). To avoid similar sizes of the output pixels after the convolution operation, the CNN changes the size of the output pixels by reducing the input values through the pooling operation. By repeating the convolution and pooling operations, the CNN continuously self-corrects so that the output values become closer to the human ratings (Larentzakis and Lygeros, 2021). New neural network models, such as UNet and ResNet, have been developed to overcome the difficulty of training CNNs with deep layers. These neural network models improve the framework of a CNN by expanding its depth, convolutional layer, or pooling layer. For example, while traditional CNN models can only classify images and output the labeling of an entire image, UNet can achieve pixel-level classification and output the class of each pixel, which makes it well-suited for image segmentation tasks (Yin et al., 2022). ResNet solves the gradient vanishing and gradient exploding problems of traditional CNNs by adding a residual block (He et al., 2020).

To process large amounts of data, multilayer neural networks have been cascaded to form DL algorithms (Kaluvarachchi et al., 2021). Compared with traditional ML algorithms, DL has a greater ability to analyze large-scale matrix data (Jalali et al., 2021). The relationship between AI, ML, and DL is shown in Figure 2. Currently, DL-based technologies are widely used in the diagnosis of certain ophthalmic diseases, such as cataracts (Wu et al., 2019) and glaucoma (Sudhan et al., 2022), and the segmentation of medical images, including those of retinal vessels (van der Heijden et al., 2018).

Artificial intelligence technology applied to orbital computed tomography/magnetic resonance imaging images

Orbital CT and MRI are important tools for the diagnosis and monitoring of orbital and eyelid diseases (Weber and

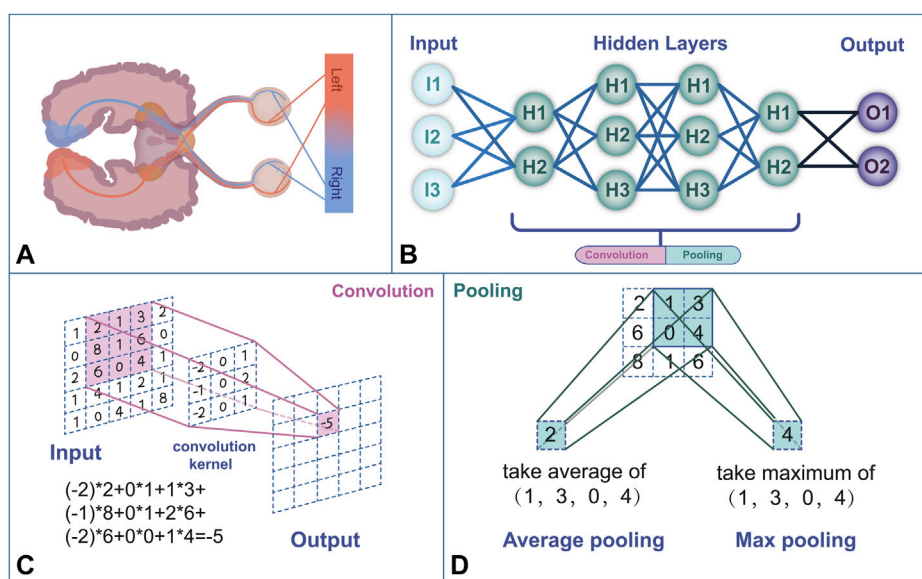
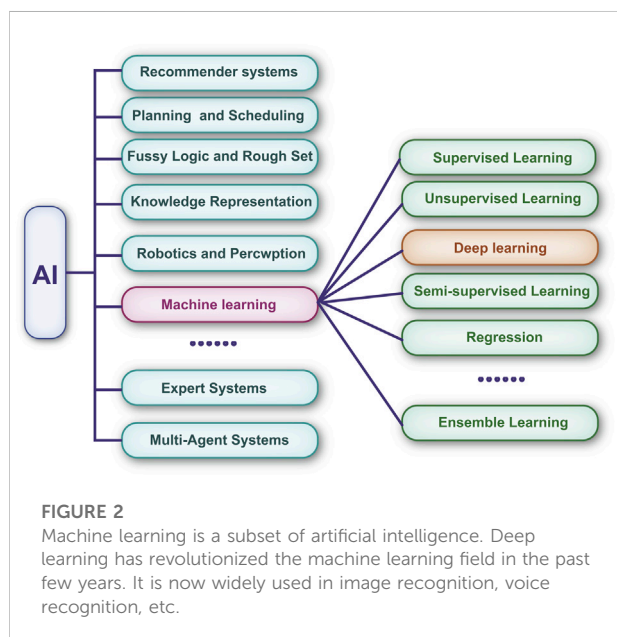


FIGURE 1

(A) Human visual feedback pathway. (B) Neural network structure framework mimics the human neural network. (C) The convolution process performs a linear transformation at each position of the image and maps it to a new value. (D) Pooling is a computational process that reduces the data size. The commonly used pooling methods are max pooling and average pooling.



Sabates, 1996). MRI and CT rely on magnetic fields and radio wave energy to provide images within the orbit (Russell et al., 1985; Langer et al., 1987). MRI is suitable for imaging soft tissue, whereas CT is commonly used to image bony structures (Hou et al., 2019). CT and MRI images are suitable as training data for AI-based research as they have less background occupation and noise (Thrall et al., 2018; Jalali et al., 2021).

Automatic identification and segmentation of anatomical structures from orbital computed tomography/magnetic resonance imaging

Automatic recognition and labeling of anatomical structures of the eye orbit can be achieved through the segmentation of medical images based on AI technology (Hou et al., 2019). Furthermore, AI can segment bony structures from orbital CT/MRI images. Hamwood et al. (2021) developed a DL system for the segmentation of bony regions from orbital CT/MRI images that exhibited excellent efficiency, particularly in terms of computational time. Li et al. (2022a) extracted bony orbit features and analyzed Asian aging characteristics through the popular deep CNN (DCNN) model. Some commercial software can also automatically segment orbital regions from CT images (Hamwood et al., 2021). In addition, using AI-based technology, irregular soft tissues, such as fat and abscesses, have been reliably segmented from orbital CT/MRI images. Brown et al. (2020) used a UNet-like CNN to segment orbital septal fat from orbital MRI images, and the results showed that AI segmentation was consistent with manual segmentation. Fu et al. (2021) trained and evaluated a context-aware CNN (CA-CNN) to segment orbital abscess regions from CT images of patients with orbital cellulitis, with the AI results being similar to those obtained by medical experts.

In addition, AI can automatically quantify certain anatomical structures based on image segmentation. Umapathy et al. (2020)

established an MRes-UNet model to segment and quantify the volume of the eyeball based on orbital CT images. Pan et al. (2022) achieved automatic calculation of the size and height of the bony orbit regions using a U-Net++ based on pre-3D images reconstructed from orbital CT images.

Automatic diagnosis and grading of orbital and eyelid diseases based on orbital computed tomography/magnetic resonance imaging images

Orbital CT/MRI images are crucial in the preliminary diagnosis of orbital diseases such as orbital wall fractures, orbital tumors, and TAO (Griffin et al., 2018). Orbital blowout fractures are one of the most common injuries caused by orbital trauma. Li et al. (2020) used the Inception V3 DCNN to automatically classify CT images exhibiting orbital burst fractures. Song et al. (2021a) proposed a 3D-ResNet to automatically detect TAO from orbital CT images, and the trained AI algorithm showed excellent performance in a real clinical setting. Lin et al. (2021) used a DCNN to grade TAO based on orbital MRI images, resulting in a labeling of disorder areas that was consistent with that made manually through an occlusion test. Hanai et al. (2022) developed a deep neural network to assess the enlarged extraocular muscles (EEM) of patients with Graves' ophthalmopathy (GO) from orbital CT images. When applied to the test data, the area under the receiver operating curve (AUC) was 0.946, indicating that the deep neural network could effectively detect EEM in GO patients. Lee et al. (2022) used 288 orbital CT scans from patients with mild and moderate-to-severe GO and healthy controls to train a neural network for diagnosing and assessing the severity of GO. The developed neural network yielded an AUC of 0.979 in diagnosing patients with moderate-to-severe GO. Han et al. (2022) automatically identified the differences in the orbital cavernous venous malformations (OCVM) from orbital CT images by training 13 ML models, including support vector machines (SVMs) and random forests. Nakagawa et al. (2022) implemented a VGG-16 network to determine from CT images whether a nasal or sinus tumor invades the periorbital area. The network model achieved a diagnostic accuracy of 0.920, indicating that CNN-based DL techniques can be a useful supporting tool for assessing the presence of orbital infiltration on CT images.

In addition to diagnosing and grading diseases, AI can extract and determine subtle features from images to differentiate confusing diseases. Orbital cavernous hemangioma and schwannoma differ in terms of surgical strategy but have similar MRI features. Bi et al. (2020) developed a database of orbital MRI images of patients with cavernous hemangioma and schwannoma from 45 hospitals in China and used AI to identify and classify the affected eye, tumor location, and tumor category.

The AI system was validated, showing an accuracy greater than 0.900 on a multicenter database. Xie et al. (2022) developed a DL model that combines multimodal radiomics with clinical and imaging features to distinguish ocular adnexal lymphoma (OAL) from idiopathic orbital inflammation (IOI). The diagnosing results yielded an AUC of 0.953, indicating that the DL-based analysis may successfully help distinguish between OAL and IOI. Hou et al. (2021) used an SVM classifier and the bag-of-features (BOF) technique to distinguish OAL from IOI based on orbital MRI images. During an independent verification test, the proposed method with augmentation achieved an AUC of 0.803, indicating that BOF-based radiomics might be a new tool for the differentiation between OAL and IOI. Early detection of hypothyroid optic neuropathy (TON) is crucial in clinical decision-making. Wu et al. (2022) built an AI predictive model to distinguish between TAO and TON by extracting radiomic features from optic-nerve T2-weighted water-fat images from a cohort of patients with TAO and a cohort of patients with TON. Table 1 summarizes the discussed AI-related studies on orbital CT/MRI images.

Artificial intelligence technology based on external ocular photographs

Owing to features such as easy and convenient delivery and storage, external ocular photographs are unique imaging data for diagnosing orbital and eyelid diseases. External ocular photographs show abnormalities and deformities in the orbital and eyelid appearance caused by trauma, tumors, inflammation, and other factors (Fukuda et al., 2005). With the development of face recognition technology, AI could locate and extract ocular information from faces, which lays the foundation for AI research based on external ocular photographs.

Automatic measurements of eyelid morphologic parameters from external ocular photographs

The accurate measurement of eyelid morphological parameters is crucial in developing an individual eyelid surgery strategy. However, manual measurement of eyelid morphological parameters is difficult to replicate because of subjective errors induced by head movements and changes in facial expressions. AI provides a more objective and convenient tool for quantifying eyelid morphological parameters by parameterizing facial structures and automatically measuring length, area, and volume. Moriyama et al. (2006) achieved eye motion tracking based on the eyelid structure parameters and iris position. Van Brummen et al. (2021) utilized a ResNet-50 model to segment regions, such as the iris and eyebrow, to measure the

TABLE 1 AI-related studies utilizing orbital CT/MRI images.

Authors	Study goals	Imaging data type	Dataset	Network model	Accuracy	AUC	Dice
Hamwood et al. (2021)	Segmentation of the bony orbital regions	Orbital CT and MRI images	Training set ($n = 443$ slices). Test set ($n = 363$ slices)	Two full convolutional neural networks (CNNs) in series followed by a graph-search method	—	—	Dice (CT images) = 0.813 and 0.975. Dice (MRI images) = 0.930 and 0.995
Li et al. (2022a)	Analysis of Asian aging characteristics by extracting features of the bony orbit	Orbital CT images	595 people	UNet	0.979 (Male) and 0.992 (Female)	—	—
Brown et al. (2020)	Segmentation of orbital septal fat	Orbital MRI images	1,018 scans from 256 participants	UNet-like CNN	—	—	—
Fu et al. (2021)	Segmentation of orbital abscess regions	Orbital CT images	67 patients	Context-aware CNN (CA-CNN)	—	—	Dice = 0.780. Jaccard = 0.120. Hausdorff = 0.650
Umapathy et al. (2020)	Segmentation and quantification of eyeball volume	Orbital CT images	80 patients	MRes-UNet	—	—	Dice = 0.940
Pan et al. (2022)	Segmentation of the bony orbit regions	Orbital CT images	595 Chinese people	UNet	—	—	IoU = 0.954
Li et al. (2020)	Classification of orbital CT images with orbital blowout fractures	Orbital CT images	94 patients and 94 normal people	Inception V3 deep CNN (DCNN)	0.920	0.957	—
Song et al. (2021a)	Detection of patients with thyroid-associated ophthalmopathy (TAO)	Orbital CT images	193 patients and 715 normal people	3D-ResNet	0.870	0.919	—
Lin et al. (2021)	Grading of TAO disease	Orbital MRI images	160 patients (80% for training, 20% for testing)	DCNN	0.863	0.922	—
Hanai et al. (2022)	Assessment of the enlarged extraocular muscles of patients with Graves' ophthalmopathy	Orbital CT images	371 participants	—	—	0.946	—
Lee et al. (2022)	Diagnosis and severity assessment of Graves' ophthalmopathy	Orbital CT images	288 cases; 80% for training and 20% for testing	A developed CNN.	Moderate-to-severe GO: 0.930 mild GO: 0.826	0.979 0.895	—
Han et al. (2022)	Distinguishing orbital cavernous venous malformations	Orbital CT images	215 patients with OCVM and 96 non-OCVM patients	13 ML models	—	—	—
Nakagawa et al. (2022)	Determination of whether a tumor invades the periorbital area in a nasal or sinus tumor	Orbital CT images	Training set ($n = 119$). Test set ($n = 49$)	Pre-trained CNN algorithm devoted to image classification	0.920	0.940	—
Bi et al. (2020)	Identification and classification of the affected eye, tumor location, and tumor category	Orbital MRI images	11,489 images of cavernous hemangioma and 3,478 images of schwannoma	RCNN ResNet-101	0.911	0.954	—
Xie et al. (2022)	Distinguishing ocular adnexal lymphoma (OAL) from idiopathic orbital inflammation (IOI)	Orbital CT images	OAL ($n = 39$) and IOI ($n = 50$)	VGG-16	0.920	0.953	—
Hou et al. (2021)	Differentiating OAL and IOI	Orbital contrast-enhanced MRI (CE-MRI)	IOI ($n = 28$ patients) and OAL ($n = 28$ patients)	Support vector machine (SVM)	—	0.803	—
Wu et al. (2022)	Distinguishing hypothyroid optic neuropathy from TAO patients	Orbital MRI images (optic-nerve T2-weighted water-fat images)	Training set ($n = 163$). Test set ($n = 72$)	Radiomics nomogram	—	Test set: 0.880 vs. 0.750	—

marginal reflex distance (MRD) in static and dynamic external ocular photographs. Simsek and Sirolu used computer vision algorithms to automatically measure pupillary distance (PD), eye area (EA), and average eyebrow height (AEBH) from external ocular photographs for evaluating the surgical effect of patients who had undergone Muller's muscle-conjunctival resection (MMCR) surgery (Bahceci Simsek and Sirolu, 2021). The automated measurement of eyelid morphology parameters based on AI technology helps assess eyelid status and improves the accuracy of eyelid surgery.

Compared with other types of imaging data, external ocular photographs can be taken and shared by patients and physicians through smartphones and the internet, which provides sufficient data for AI research on external ocular photographs. Chen et al. (2021) compiled CNN algorithms using the software MAIA to build DL models for the automatic measurement of MRD1, MRD2, and levator muscle strength based on external ocular photographs taken with smartphones. This study was the first smartphone-based DL model for the automatic measurement of eyelid morphological parameters. Compared to those obtained manually, measurements taken with the aid of AI are more objective.

Ptosis is a common eyelid disorder in which a drooping eyelid obscures the pupil, hindering vision in severe cases. Ptosis is generally diagnosed by measuring eyelid morphological parameters, such as the levator muscle strength, lid fissure height, and limbal reflex distance, based on typical clinical symptoms. Surgical therapy is the main treatment for ptosis (Mahroo et al., 2014). Tabuchi et al. (2022) performed an automatic diagnosis of ptosis using a pre-trained MobileNetV2 CNN applied to photos of patients taken with an iPad Mini. Hung et al. (2022) realized the automatic identification of monocular appearance photos of ptosis patients based on a VGG-16 neural network, and the results showed that AI outperformed GPs in diagnosing ptosis. Combined with devices such as smartphones, the analysis of eye appearance based on AI can be useful in further clinical scenarios. AI provides an objective tool for measuring eyelid morphological parameters and planning surgery strategies instead of relying on the experience of surgeons. Song et al. (2021b) developed a gradient-boosted decision tree (GBDT) for choosing ptosis surgery strategies and trained it with 3D models created by photographing and scanning the eyes of ptosis patients with a structured light camera. The AI model evaluates the external ocular photographs and the 3D model to determine whether surgery is required and establish the surgery strategy to follow. Lou et al. (2021) evaluated the outcome of ptosis surgery by comparing pre- and postoperative values of eyelid morphological parameters, such as MRD1 and MRD2, which were automatically measured by a UNet from ocular appearance photographs of the patients.

Artificial intelligence diagnosis and prediction based on external ocular photographs

Oculoplastic surgery involves the aesthetic restoration and predicting postoperative outcomes through AI can help the surgeon develop a personalized plastic surgery plan. The major purpose of oculoplastic surgery is to realize the expected aesthetic goals. However, it is hard to judge the expected aesthetic results due to a variety of subjective factors (Swanson, 2011). Establishing an objective facial beauty standard is still controversial. Zhai et al. (2019) proposed a new facial detection method based on a transfer learning CNN, which has better classification accuracy than previous geometric assessment methods, laying a foundation for the prediction of oculoplastic surgery effects. Yixin et al. explored the effect of the eyelid on oculoplastic surgery and aesthetic outcomes by comparing the postoperative metrics of oculoplastic patients assessed by the CNN model with those assessed only artificially. The CNN assessment group had better postoperative extent, lower eyelid skin wrinkles, eyelid tear troughs, skin shine, and aesthetic scores than the control group, suggesting that CNN is a beneficial tool for evaluating oculoplastic surgery (Yixin et al., 2022).

Eyelid and periocular skin tumors seriously affect the health and aesthetics of patients (Silverman and Shinder, 2017). Early preliminary screening through external photography helps detect and monitor these tumors. Seeja and Suresh (2019) trained a UNet to automatically segment skin lesions and differentiate melanoma from benign skin lesions, achieving reliable results in the segmentation and diagnosis of melanoma. Li et al. (2022b) used a faster region-based CNN and a DL classification network to build an AI system that automatically detects malignant eyelid tumors from ocular external photographs, obtaining positive performance on both internal and external test sets (AUC ranging from 0.899 to 0.955). CNNs could fully mine image information and distinguish deep features from external photography to detect subtle eyelid and skin tumors that are elusive to the naked eye, thus helping reduce misdiagnosis and missed diagnosis.

Changes in ocular appearance, such as retraction of the upper eyelid, strabismus, and proptosis, are crucial in the diagnosis of TAO (Hodgson and Rajaii, 2020). Huang et al. (2022) used the ResNet-50 model to obtain an automatic diagnosis of TAO based on external ocular photographs. Karlin J et al. (2022) developed a DL model for detecting TAO based on external ocular photographs. A set comprising 1944 photographs from a clinical database was used for training, and a test set of 344 additional images was used to evaluate the trained DL network. The accuracy of the model on the test set was 0.892, and heatmaps showed that the model could identify pixels corresponding to the clinical features of TAO. Orbital decompression surgery can alleviate the symptoms of eye protrusion and repair the appearance of patients with TAO. According to the 2021-EUGOGO guidelines, orbital decompression surgery is the recommended treatment strategy for patients with severe TAO (Smith, 2021). Yoo et al. (2020) trained a

TABLE 2 AI-related studies utilizing external ocular images.

Authors	Study goals	Imaging data type	Dataset	Network model	Accuracy	AUC
Moriyama et al. (2006)	Eye motion tracking	External ocular images	—	Generative eye region model	—	—
Van Brummen et al. (2021)	Segmentation of regions such as iris and eyebrow	Photographs of periorbital areas	418 images	ResNet-50	—	—
Bahceci Simsek and Sirolu, (2021)	Evaluation of postoperative changes	Full-face photographs	55 patients	DLIBML toolkit	—	—
Chen et al. (2021)	Measurement of eyelid paraments	External ocular images	411 participants	MAIA software	—	—
Tabuchi et al. (2022)	Classification of images taken with a tablet device of patients with blepharoptosis diagnosis	Eyelid images	1,276 images	Pre-trained MobileNetV2 CNNi	0.828	0.900
Hung et al. (2022)	Identification of monocular appearance photos of ptosis patients	External ocular images	782 images	VGG-16	0.90	0.987
Song et al. (2021b)	Determination of the choices of ptosis surgery strategies	External ocular images	152 eyes	Gradient-boosted decision tree (GBDT)	0.826	0.795
Lou et al. (2021)	Evaluation of ptosis surgery outcome	External ocular images	103 patients (135 ptotic eyes)	U-Net (Attention R2U-Net)	—	—
Yixin et al. (2022)	Exploration of the effect of eyelid on oculoplastic surgery and aesthetic outcomes	External ocular images	64 patients	Multichannel CNN	0.988	—
Huang et al. (2022)	Diagnosis of TAO	Facial images	3,120 eyes	ResNet-50 U-Net	Eye location: 0.980. Cornea: 0.930. Sclera segmentation: 0.870	Over 0.850
Li et al. (2022b)	Automatic detection of malignant eyelid tumors	External ocular images	Development set ($n = 1,258$). External test set ($n = 309$)	Faster-RCNN	—	AUCs ranged from 0.899 to 0.955
Karlin J et al. (2022)	Detection of thyroid eye disease	External ocular images	Training set ($n = 1994$). Test set ($n = 344$)	ResNet-18	0.892	—
Yoo et al. (2020)	Synthesis of realistic postoperative appearance for orbital decompression surgery	External ocular images	500 preoperative images and 500 postoperative images	Generative adversarial network (GAN)	—	0.957

conditional generative adversarial network (GAN) using pre- and postoperative external ocular photographs of patients with orbital decompression. The trained GAN could convert the preoperative external ocular photographs into predictive postoperative images, which were similar to the real postoperative condition, suggesting that GAN might be a new tool for the prediction of oculoplastic surgery results. Table 2 summarizes the aforementioned AI-related studies on external ocular images.

Artificial intelligence-based techniques using other image data types

Tear spillage is a major symptom of lacrimal duct obstruction (LDO), and its incidence in rural areas is gradually increasing (Brendler et al., 2013). The use of anterior segment optical coherence tomography (AS-OCT) to assess the tear meniscus

is considered a more objective non-invasive diagnostic procedure. Imamura et al. used DenseNet-169 and pooled DL models (VGG-16, ResNet-50, DenseNet-121, DenseNet-169, Inception ResNet-V2, and Inception-V3) to detect patients with LDO from AS-OCT images. The trained network models exhibited remarkable reliability in marking the areas of the tear meniscus (Imamura et al., 2021).

Pathological examination is the gold standard for diagnosing the nature of ocular tumors. However, traditional pathological examination results are influenced by the experience of the physician, which takes a large amount of time from specimen submission to result confirmation (Heran et al., 2014). AI is not influenced by subjective factors and can process a large number of specimens in a short time. Wang et al. (2020b) used AI technology to automatically diagnose malignant melanoma of the eyelid from pathological sections. They also developed a random forest model to grade tumor malignancy, suggesting that

AI may be a future tool for the rapid screening and grading of tumor pathology.

Jiang et al. (2022) proposed a DL framework for the automatic detection of malignant melanoma (MM) of the eyelid based on self-supervised learning (SSL). The framework consisted of a self-supervised model for detecting MM regions at the patch level and another model for classifying lesion types at the slide level. Considering that the differential diagnosis of basal cell and sebaceous carcinomas of the eyelid is highly dependent on the experience of the pathologist, Luo et al. (2022) proposed a fully automated differential diagnostic method based on whole slide images (WSIs) and DL classification, achieving an accuracy of 0.983 for the trained network model.

In addition, AI-decision models can be established based on various types of patient information. Song et al. (2022) trained an ML model using a database that contained both ocular surface characteristics and demographic information (gender, age) of patients with lacrimal sacculitis. Tan et al. (2017) established an alternating decision tree to predict the risk of reconstructive surgery after eyelid basal cell carcinoma (pBBC) resection which provides a new prediction model based on a database with various patient information.

Discussion

The acquisition and analysis of imaging data are crucial in the treatment of orbital and eyelid diseases. In this paper, we discuss the advantages and limitations of AI technology for diagnosing orbital and eyelid diseases by analyzing the different characteristics of image data and the current problems and potential approaches to promote the development of AI-based technology in this field.

Orbital and eyelid diseases are primarily caused by inflammatory (Lutt et al., 2008), metabolic, and traumatic factors (Li et al., 2020). The anatomy integrity of the orbital and eyelid not only protects and supports important structures, such as the eyeball and optic nerve, but is also critical to the aesthetic appearance of the patient's face (Huggins et al., 2017). AI converts traditional medical images into matrix data and supports clinical decision-making by developing models and analyzing the matrix data (Mintz and Brodie, 2019). Structural segmentation of orbital CT/MRI images using AI might assist in endoscopic and 3D-print surgery and lay a foundation for robotic surgery (Wang et al., 2022). In addition, the automatic measurement of eyelid morphological parameters based on external ocular photographs provides a new tool for developing individualized eyelid surgical strategies (Bahceci Simsek and Sirolu, 2021). Thus, AI technology for diagnosing and treating orbital and eyelid diseases, which remains in its infancy, has great potential for broad clinical application.

Imaging data play an important role in the diagnosis and treatment of orbital and eyelid diseases, providing an adequate

source of data for AI training. Non-invasive Orbital CT examination is easy and fast to perform (Lee et al., 2004). Orbital MRI examination is free of ionizing radiation damage and is superior in revealing soft tissue. Compared with MRI examinations, CT images are noisier (Hamwood et al., 2021). Therefore, the traditional UNet algorithm is better suited to training with CT images because it extracts rich feature scales and can effectively filter local noise (Pan et al., 2022). External ocular photographs serve as a unique type of imaging data for orbital and eyelid diseases and provide information for eyelid surgery decisions. Compared with other types of medical images, external ocular photographs are non-invasive and can be easily taken by doctors and patients with smartphones, which breaks the barrier of expensive image equipment and facilitates the application of AI (Chen et al., 2021). Furthermore, automatic facial recognition and eye-tracking technology, which have been widely used in safety inspection, instrument development, etc., could also be applied to AI research based on external ocular photographs (Asaad et al., 2020). In addition, visual field tests, OCT, and CT of the optic-nerve canal also play an active role in the diagnosis of orbital and eyelid diseases. The multimodal diagnostic images provide adequate raw datasets for training AI models and validating their performance.

Although AI analysis of imaging data of orbital and eyelid diseases has, there are some limitations in its development (Mintz and Brodie, 2019; Yang et al., 2021). Uneven disease prevalence and small sample sizes for certain rare diseases cause oversampling when training AI models for specific types of diseases, resulting in poor generalization and a lack of adaptability to new data. Several studies have shown that the category imbalance problem can be solved by weighting the data differently when computing the loss function (Liu et al., 2021; Luo et al., 2021). Moreover, the current AI datasets of orbital and eyelid diseases are generally obtained from the same medical institution. However, it is difficult to obtain standardized data because of the differences in the examination equipment used by different medical institutions. Image-based AI research requires large sets of standard, annotated imaging data, which are still scarce in the case of orbital and eyelid diseases as compared, for instance, with ImageNet. Transfer learning may offer a good solution to the lack of imaging data. When obtaining a large dataset or labeling the data is difficult, learning can be transferred from a task with sufficient data that is easily labeled and similar to the target task. Liu et al. (2020) modified ResNet-152, which was pre-trained on ImageNet, through transfer learning to classify left and right optic discs with an accuracy of 0.988, thus demonstrating a new solution to the lack of data in orbital and eyelid diseases. In addition, we can increase the amount of data through data augmentation by rotating, panning, zooming, or changing the brightness or contrast of the images. For example, Song et al. (2021a) performed 200 rotations on the training data for a CNN to increase the dataset size and reduce overfitting. When verified, the overfitting of the trained CNN remarkably decreased. There are also some drawbacks regarding the quality of imaging data in orbital and eyelid diseases, which have limited the

development of AI-related research. For example, it is difficult to obtain standardized orbital CT/MRI images due to the long scanning time, different equipment, and variable experience of the operators. Zhai et al. (2021) developed a method based on a signed distance field for the automatic calibration and quantitative error evaluation when processing orbital CT images, which provides a new tool to standardize CT/MRI images. Moreover, lighting variations prevent high-quality standardized external ocular photography. To address this problem, some studies have attempted to model the illumination templates and establish illumination-invariant algorithms (Li et al., 2007; Lu et al., 2017), whose main purpose is to make shapes and textures independent of illumination variations. Lastly, ethical considerations and patient privacy issues associated with external ocular photography also require in-depth deliberation.

Overall, although there are still some limitations to the advance of AI-based research on orbital and eyelid diseases, as large databases are established and shared and as new neural networks that more closely resemble biological neurons are developed, further development of such AI applications is expected to occur, leading to the next breakthrough in ophthalmology.

Conclusion

AI technology has a significant potential for application in the automatic diagnosis and precise quantification of orbital and eyelid diseases. AI is more objective than manual methods, can process large amounts of data in a short time, and, thus, could assist physicians in clinical decision-making and surgical design. The predictive capabilities of AI may also play an active role in assessing the outcome of oculoplastic surgery. As computer algorithms are updated and high-quality datasets become available, AI will play a broader role in the assessment of orbital and eyelid disorders in the future.

References

- Abdullah, A., Elsomaloty, H., Patel, Y., and Chang, J. (2010). CT and MRI findings with histopathologic correlation of a unique bilateral orbital mantle cell lymphoma in Graves' disease: A case report and brief review of literature. *J. Neurooncol.* 97 (2), 279–284. doi:10.1007/s11060-009-0019-x
- Asaad, M., Dey, J. K., Al-Mouakeh, A., Manjouna, M. B., Nashed, M. A., Rajesh, A., et al. (2020). Eye-tracking technology in plastic and reconstructive surgery: A systematic review. *Aesthet. Surg. J.* 40 (9), 1022–1034. doi:10.1093/asj/sjz328
- Bahceci Simsek, I., and Siroglu, C. (2021). Analysis of surgical outcome after upper eyelid surgery by computer vision algorithm using face and facial landmark detection. *Graefes Arch. Clin. Exp. Ophthalmol.* 259 (10), 3119–3125. doi:10.1007/s00417-021-05219-8
- Bailey, W., and Robinson, L. (2007). Screening for intra-orbital metallic foreign bodies prior to MRI: Review of the evidence. *Radiogr. (Lond)* 13 (1), 72–80. doi:10.1016/j.radi.2005.09.006
- Bi, S., Chen, R., Zhang, K., Xiang, Y., Wang, R., Lin, H., et al. (2020). Differentiate cavernous hemangioma from schwannoma with artificial intelligence (AI). *Ann. Transl. Med.* 8 (11), 710. doi:10.21037/atm.2020.03.150

Author contributions

X-LB and G-YL prepared the first draft of the document. All authors contributed to the writing and editing of the manuscript and agreed to its submission.

Funding

The study was funded by the National Natural Science Foundation of China (grant No. 82171053 and No. 81570864), and the Natural Science Foundation of Jilin Province (grant No. 20200801043GH and No. 20190201083JC).

Acknowledgments

We thank Editage (<https://www.editage.com>) for English language editing during the preparation of this manuscript.

Conflict of interest

The authors declare that the research was conducted in the absence of any commercial or financial relationships that could be construed as a potential conflict of interest.

Publisher's note

All claims expressed in this article are solely those of the authors and do not necessarily represent those of their affiliated organizations, or those of the publisher, the editors and the reviewers. Any product that may be evaluated in this article, or claim that may be made by its manufacturer, is not guaranteed or endorsed by the publisher.

- Bischoff, F., Koch, M. d. C., and Rodrigues, P. P. (2019). Predicting blood donations in a tertiary care center using time series forecasting. *Stud. Health Technol. Inf.* 261, 135–139.
- Brachmann, A., Barth, E., and Redies, C. (2017). Using CNN features to better understand what makes visual artworks special. *Front. Psychol.* 8, 830. doi:10.3389/fpsyg.2017.00830
- Brehar, R., Mitrea, D. A., Vancea, F., Marita, T., Nedevschi, S., Lupsor-Platon, M., et al. (2020). Comparison of deep-learning and conventional machine-learning methods for the automatic recognition of the hepatocellular carcinoma areas from ultrasound images. *Sensors (Basel)* 20 (11), E3085. doi:10.3390/s20113085
- Brendler, C., Pour AryaNN.Rieger, V., Klinger, S., and Rothermel, A. (2013). A substrate isolated LDO for an inductively powered retinal implant. *Biomed. Tech.* 58, 4367. doi:10.1515/bmt-2013-4367
- Brown, R. A., Fetco, D., Fratila, R., Fadda, G., Jiang, S., Alkhawajah, N. M., et al. (2020). Deep learning segmentation of orbital fat to calibrate conventional MRI for longitudinal studies. *Neuroimage* 208, 116442. doi:10.1016/j.neuroimage.2019.116442

- Cai, L., Gao, J., and Zhao, D. (2020). A review of the application of deep learning in medical image classification and segmentation. *Ann. Transl. Med.* 8 (11), 713. doi:10.21037/atm.2020.0244
- Chen, H. C., Tzeng, S. S., Hsiao, Y. C., Chen, R. F., Hung, E. C., and Lee, O. K. (2021). Smartphone-based artificial intelligence-assisted prediction for eyelid measurements: Algorithm development and observational validation study. *JMIR Mhealth Uhealth* 9 (10), e32444. doi:10.2196/32444
- Cho, S. M., Austin, P. C., Ross, H. J., Abdel-Qadir, H., Chicco, D., Tomlinson, G., et al. (2021). Machine learning compared with conventional statistical models for predicting myocardial infarction readmission and mortality: A systematic review. *Can. J. Cardiol.* 37 (8), 1207–1214. doi:10.1016/j.cjca.2021.02.020
- Dzobo, K., Adotey, S., Thomford, N. E., and Dzobo, W. (2020). Integrating artificial and human intelligence: A partnership for responsible innovation in biomedical engineering and medicine. *OMICS* 24 (5), 247–263. doi:10.1089/omi.2019.0038
- Finlayson, S. G., Bowers, J. D., Ito, J., Zittrain, J. L., Beam, A. L., and Kohane, I. S. (2019). Adversarial attacks on medical machine learning. *Science* 363 (6433), 1287–1289. doi:10.1126/science.aaw4399
- Fu, R., Leader, J. K., Pradeep, T., Shi, J., Meng, X., Zhang, Y., et al. (2021). Automated delineation of orbital abscess depicted on CT scan using deep learning. *Med. Phys.* 48 (7), 3721–3729. doi:10.1002/mp.14907
- Fukuda, Y., Fujimura, T., Moriawaki, S., and KiTahara, T. (2005). A new method to evaluate lower eyelid sag using three-dimensional image analysis. *Int. J. Cosmet. Sci.* 27 (5), 283–290. doi:10.1111/j.1467-2494.2005.00282.x
- Girard, M. J. A., and Schmetterer, L. (2020). Artificial intelligence and deep learning in glaucoma: Current state and future prospects. *Prog. Brain Res.* 257, 37–64. doi:10.1016/bs.pbr.2020.07.002
- Griffin, A. S., Hoang, J. K., and Malinzak, M. D. (2018). CT and MRI of the orbit. *Int. Ophthalmol. Clin.* 58 (2), 25–59. doi:10.1097/HIO.0000000000000218
- Hamwood, J., Schmutz, B., Collins, M. J., Allenby, M. C., and Alonso-Caneiro, D. (2021). A deep learning method for automatic segmentation of the bony orbit in MRI and CT images. *Sci. Rep.* 11 (1), 13693. doi:10.1038/s41598-021-93227-3
- Han, Q., Du, L., Mo, Y., Huang, C., and Yuan, Q. (2022). Machine learning based non-enhanced CT radiomics for the identification of orbital cavernous venous malformations: An innovative tool. *J. Craniofac. Surg.* 33 (3), 814–820. doi:10.1097/SCS.00000000000008446
- Hanai, K., Tabuchi, H., Nagasato, D., Tanabe, M., Masumoto, H., Miya, S., et al. (2022). Automated detection of enlarged extraocular muscle in Graves' ophthalmopathy with computed tomography and deep neural network. *Sci. Rep.* 12 (1), 16036. doi:10.1038/s41598-022-20279-4
- He, F., Liu, T., and Tao, D. (2020). Why ResNet works? Residuals generalize. *IEEE Trans. Neural Netw. Learn. Syst.* 31 (12), 5349–5362. doi:10.1109/TNNLS.2020.2966319
- Heran, F., Berges, O., BlustaJn, J., Boucenna, M., Charbonneau, F., Koskas, P., et al. (2014). Tumor pathology of the orbit. *Diagn. Interv. Imaging* 95 (10), 933–944. doi:10.1016/j.diii.2014.08.002
- Hodgson, N. M., and Rajaii, F. (2020). Current understanding of the progression and management of thyroid associated orbitopathy: A systematic review. *Ophthalmol. Ther.* 9 (1), 21–33. doi:10.1007/s40123-019-00226-9
- Hou, R., Zhou, D., Nie, R., Liu, D., and Ruan, X. (2019). Brain CT and MRI medical image fusion using convolutional neural networks and a dual-channel spiking cortical model. *Med. Biol. Eng. Comput.* 57 (4), 887–900. doi:10.1007/s11517-018-1935-8
- Hou, Y., Xie, X., Chen, J., Lv, P., Jiang, S., He, X., et al. (2021). Bag-of-features-based radiomics for differentiation of ocular adnexal lymphoma and idiopathic orbital inflammation from contrast-enhanced MRI. *Eur. Radiol.* 31 (1), 24–33. doi:10.1007/s00330-020-07110-2
- Huang, X., Ju, L., Li, J., He, L., Tong, F., Liu, S., et al. (2022). An intelligent diagnostic system for thyroid-associated ophthalmopathy based on facial images. *Front. Med.* 9, 920716. doi:10.3389/fmed.2022.920716
- Huggins, A. B., Latting, M. W., Marx, D. P., and Giacometti, J. N. (2017). Ocular adnexal reconstruction for cutaneous periocular malignancies. *Semin. Plast. Surg.* 31 (1), 22–30. doi:10.1055/s-0037-1598190
- Hung, J. Y., Chen, K. W., Perera, C., Chiu, H. K., Hsu, C. R., Myung, D., et al. (2022). An outperforming artificial intelligence model to identify referable blepharoptosis for general practitioners. *J. Pers. Med.* 12 (2), 283. doi:10.3390/jpm12020283
- Imamura, H., Tabuchi, H., Nagasato, D., Masumoto, H., Baba, H., Furukawa, H., et al. (2021). Automatic screening of tear meniscus from lacrimal duct obstructions using anterior segment optical coherence tomography images by deep learning. *Graefes Arch. Clin. Exp. Ophthalmol.* 259 (6), 1569–1577. doi:10.1007/s00417-021-05078-3
- Jalali, Y., Fateh, M., Rezvani, M., Abolghasemi, V., and Anisi, M. H. (2021). ResBCDU-net: A deep learning framework for lung CT image segmentation. *Sensors (Basel)* 21 (1), E268. doi:10.3390/s21010268
- Jiang, Z., Wang, L., Wang, Y., Jia, G., Zeng, G., Wang, J., et al. (2022). A self-supervised learning based framework for eyelid malignant melanoma diagnosis in whole slide images. *IEEE/ACM Trans. Comput. Biol. Bioinform.* 2022, 1–15. doi:10.1109/TCBB.2022.3207352
- Kaluarachchi, T., Reis, A., and Nanayakkara, S. (2021). A review of recent deep learning approaches in human-centered machine learning. *Sensors (Basel)* 21 (7), 2514. doi:10.3390/s21072514
- Karlin, J. G. L., LaPierre, N., Danesh, K., Farajzadeh, J., Palileo, B., Taraszka, K., Zheng, J., et al. (2022). Ensemble neural network model for detecting thyroid eye disease using external photographs. *Br. J. Ophthalmol.* 2022, 321833. doi:10.1136/bjo-2022-321833
- Langer, B. G., Mafee, M. F., Pollack, S., Spigos, D. G., and Gyi, B. (1987). MRI of the normal orbit and optic pathway. *Radiol. Clin. North Am.* 25 (3), 429–446. doi:10.1016/s0033-8389(22)02253-9
- Larentzakos, A., and Lygeros, N. (2021). Artificial intelligence (AI) in medicine as a strategic valuable tool. *Pan Afr. Med. J.* 38, 184. doi:10.11604/pamj.2021.38.184.28197
- Le, W. T., Maleki, F., Romero, F. P., Forghani, R., and Kadoury, S. (2020). Overview of machine learning: Part 2: Deep learning for medical image analysis. *Neuroimaging Clin. N. Am.* 30 (4), 417–431. doi:10.1016/j.nic.2020.06.003
- Lee, H. J., Jilani, M., Frohman, L., and Baker, S. (2004). CT of orbital trauma. *Emerg. Radiol.* 10 (4), 168–172. doi:10.1007/s10140-003-0282-7
- Lee, J., Seo, W., Park, J., Lim, W. S., Oh, J. Y., Moon, N. J., et al. (2022). Neural network-based method for diagnosis and severity assessment of Graves' orbitopathy using orbital computed tomography. *Sci. Rep.* 12 (1), 12071. doi:10.1038/s41598-022-16217-z
- Li, L., Song, X., Guo, Y., Liu, Y., Sun, R., Zou, H., et al. (2020). Deep convolutional neural networks for automatic detection of orbital blowout fractures. *J. Craniofac. Surg.* 31 (2), 400–403. doi:10.1097/SCS.0000000000000609
- Li, L., Zheng, N. N., and Wang, F. Y. (2019). On the crossroad of artificial intelligence: A revisit to alan turing and norbert wiener. *IEEE Trans. Cybern.* 49 (10), 3618–3626. doi:10.1109/TCYB.2018.2884315
- Li, S. Z., Chu, R., Liao, S., and Zhang, L. (2007). Illumination invariant face recognition using near-infrared images. *IEEE Trans. Pattern Anal. Mach. Intell.* 29 (4), 627–639. doi:10.1109/TPAMI.2007.1014
- Li, Z., Chen, K., Yang, J., Pan, L., Wang, Z., Yang, P., et al. (2022). Deep learning-based CT radiomics for feature representation and analysis of aging characteristics of asian bony orbit. *J. Craniofac. Surg.* 33 (1), 312–318. doi:10.1097/SCS.00000000000008198
- Li, Z., Qiang, W., Chen, H., Pei, M., Yu, X., Wang, L., et al. (2022). Artificial intelligence to detect malignant eyelid tumors from photographic images. *NPJ Digit. Med.* 5 (1), 23. doi:10.1038/s41746-022-00571-3
- Lin, C., Song, X., Li, L., Li, Y., Jiang, M., Sun, R., et al. (2021). Detection of active and inactive phases of thyroid-associated ophthalmopathy using deep convolutional neural network. *BMC Ophthalmol.* 21 (1), 39. doi:10.1186/s12886-020-01783-5
- Lin, H., Li, R., Liu, Z., Chen, J., Yang, Y., Chen, H., et al. (2019). Diagnostic efficacy and therapeutic decision-making capacity of an artificial intelligence platform for childhood cataracts in eye clinics: A multicentre randomized controlled trial. *EClinicalMedicine* 9, 52–59. doi:10.1016/j.eclinm.2019.03.001
- Liu, T. Y. A., Ting, D. S. W., Yi, P. H., Wei, J., Zhu, H., Subramanian, P. S., et al. (2020). Deep learning and transfer learning for optic disc laterality detection: Implications for machine learning in neuro-ophthalmology. *J. Neuroophthalmol.* 40 (2), 178–184. doi:10.1097/WNO.0000000000000827
- Liu, Y., Li, Q., Wang, K., Liu, J., He, R., Yuan, Y., et al. (2021). Automatic multi-label ECG classification with category imbalance and cost-sensitive thresholding. *Biosens. (Basel)* 11 (11), 453. doi:10.3390/bios11110453
- Lou, L., Cao, J., Wang, Y., Gao, Z., Jin, K., Xu, Z., et al. (2021). Deep learning-based image analysis for automated measurement of eyelid morphology before and after blepharoptosis surgery. *Ann. Med.* 53 (1), 2278–2285. doi:10.1080/07853890.2021.2009127
- Lu, L., Zhang, X., Xu, X., and Shang, D. (2017). Multispectral image fusion for illumination-invariant palmprint recognition. *PLoS One* 12 (5), e0178432. doi:10.1371/journal.pone.0178432
- Luo, X., Yang, L., Cai, H., Tang, R., Chen, Y., and Li, W. (2021). Multi-classification of arrhythmias using a HCRNet on imbalanced ECG datasets. *Comput. Methods Programs Biomed.* 208, 106258. doi:10.1016/j.cmpb.2021.106258

- Luo, Y., Zhang, J., Yang, Y., Rao, Y., Chen, X., Shi, T., et al. (2022). Deep learning-based fully automated differential diagnosis of eyelid basal cell and sebaceous carcinoma using whole slide images. *Quant. Imaging Med. Surg.* 12 (8), 4166–4175. doi:10.21037/qims-22-98
- Lutt, J. R., Lim, L. L., Phal, P. M., and Rosenbaum, J. T. (2008). Orbital inflammatory disease. *Semin. Arthritis Rheum.* 37 (4), 207–222. doi:10.1016/j.semarthrit.2007.06.003
- Mahroo, O. A., Hysi, P. G., Dey, S., Gavin, E. A., Hammond, C. J., and Jones, C. A. (2014). Outcomes of ptosis surgery assessed using a patient-reported outcome measure: An exploration of time effects. *Br. J. Ophthalmol.* 98 (3), 387–390. doi:10.1136/bjophthalmol-2013-303946
- Mintz, Y., and Brodie, R. (2019). Introduction to artificial intelligence in medicine. *Minim. Invasive Ther. Allied Technol.* 28 (2), 73–81. doi:10.1080/13645706.2019.1575882
- Moriyama, T., Kanade, T., Xiao, J., and Cohn, J. F. (2006). Meticulously detailed eye region model and its application to analysis of facial images. *IEEE Trans. Pattern Anal. Mach. Intell.* 28 (5), 738–752. doi:10.1109/TPAMI.2006.98
- Nakagawa, J., Fujima, N., Hirata, K., Tang, M., Tsuneta, S., Suzuki, J., et al. (2022). Utility of the deep learning technique for the diagnosis of orbital invasion on CT in patients with a nasal or sinonasal tumor. *Cancer Imaging* 22 (1), 52. doi:10.1186/s40644-022-00492-0
- Nichols, J. A., Herbert Chan, H. W., and Baker, M. A. B. (2019). Machine learning: Applications of artificial intelligence to imaging and diagnosis. *Biophys. Rev.* 11 (1), 111–118. doi:10.1007/s12551-018-0449-9
- Pan, L., Chen, K., Zheng, Z., Zhao, Y., Yang, P., Li, Z., et al. (2022). Aging of Chinese bony orbit: Automatic calculation based on UNet++ and connected component analysis. *Surg. Radiol. Anat.* 44 (5), 749–758. doi:10.1007/s00276-022-02933-8
- Russell, E. J., Czervionke, L., HuckmanM.Daniels, D., and McLachlan, D. (1985). CT of the inferomedial orbit and the lacrimal drainage apparatus: Normal and pathologic anatomy. *AJR. Am. J. Roentgenol.* 145 (6), 1147–1154. doi:10.2214/ajr.145.6.1147
- Seeja, R. S., and Suresh, A. (2019). Deep learning based skin lesion segmentation and classification of melanoma using support vector machine (SVM). *Asian pac. J. Cancer Prev.* 20 (5), 1555–1561. doi:10.31557/APJCP.2019.20.5.1555
- Shin, S., Austin, P. C., Ross, H. J., Abdel-Qadir, H., Freitas, C., Tomlinson, G., et al. (2021). Machine learning vs. conventional statistical models for predicting heart failure readmission and mortality. *Esc. Heart Fail.* 8 (1), 106–115. doi:10.1002/ehf2.13073
- Silverman, N., and Shinder, R. (2017). What's new in eyelid tumors. *Asia. Pac. J. Ophthalmol.* 6 (2), 143–152. doi:10.22608/APO.201701
- Smith, T. J. (2021). Comment on the 2021 EUGOGO clinical practice guidelines for the medical management of Graves' orbitopathy. *Eur. J. Endocrinol.* 185 (6), L13–L14. doi:10.1530/EJE-21-0861
- Song, X., Li, L., Han, F., Liao, S., and Xiao, C. (2022). Noninvasive machine learning screening model for dacryocystitis based on ocular surface indicators. *J. Craniofac. Surg.* 33 (1), e23–e28. doi:10.1097/SCS.00000000000007863
- Song, X., Liu, Z., Gao, Z., Fan, X., Zhai, G., Guangtao, Z., et al. (2021). Artificial intelligence CT screening model for thyroid-associated ophthalmopathy and tests under clinical conditions. *Int. J. Comput. Assist. Radiol. Surg.* 16 (2), 323–330. doi:10.1007/s11548-020-02281-1
- Song, X., Tong, W., Lei, C., Huang, J., Fan, X., Zhai, G., et al. (2021). A clinical decision model based on machine learning for ptosis. *BMC Ophthalmol.* 21 (1), 169. doi:10.1186/s12886-021-01923-5
- Starke, G., De Clercq, E., Borgwardt, S., and Elger, B. S. (2021). Why educating for clinical machine learning still requires attention to history: A rejoinder to gauld et al. *Psychol. Med.* 51 (14), 2512–2513. doi:10.1017/S0033291720004766
- Sudhan, M. B., Sinthuja, M., Pravinth Raja, S., Amutharaj, J., Charlyn Pushpa Latha, G., Sheeba Rachel, S., et al. (2022). Segmentation and classification of glaucoma using U-net with deep learning model. *J. Healthc. Eng.* 2022, 1601354. doi:10.1155/2022/1601354
- Swanson, E. (2011). Objective assessment of change in apparent age after facial rejuvenation surgery. *J. Plast. Reconstr. Aesthet. Surg.* 64 (9), 1124–1131. doi:10.1016/j.bjps.2011.04.004
- Tabuchi, H., Nagasato, D., Masumoto, H., Tanabe, M., Ishitobi, N., Ochi, H., et al. (2022). Developing an iOS application that uses machine learning for the automated diagnosis of blepharoptosis. *Graefes Arch. Clin. Exp. Ophthalmol.* 260 (4), 1329–1335. doi:10.1007/s00417-021-05475-8
- Tan, E., LinF.Sheck, L., Salmon, P., and Ng, S. (2017). A practical decision-tree model to predict complexity of reconstructive surgery after periocular basal cell carcinoma excision. *J. Eur. Acad. Dermatol. Venereol.* 31 (4), 717–723. doi:10.1111/jdv.14012
- Thrall, J. H., Li, X., Li, Q., Cruz, C., Do, S., Dreyer, K., et al. (2018). Artificial intelligence and machine learning in radiology: Opportunities, challenges, pitfalls, and criteria for success. *J. Am. Coll. Radiol.* 15 (3), 504–508. doi:10.1016/j.jacr.2017.12.026
- Ting, D. S. W., Cheung, C. Y. L., Lim, G., Tan, G. S. W., Quang, N. D., Gan, A., et al. (2017). Development and validation of a deep learning system for diabetic retinopathy and related eye diseases using retinal images from multiethnic populations with diabetes. *JAMA* 318 (22), 2211–2223. doi:10.1001/jama.2017.18152
- Totschnig, W. (2020). Fully autonomous AI. *Sci. Eng. Ethics* 26 (5), 2473–2485. doi:10.1007/s11948-020-00243-z
- Umapathy, L., Winegar, B., MacKinnon, L., HillM.Altbach, M. I., Miller, J. M., et al. (2020). Fully automated segmentation of globes for volume quantification in CT images of orbits using deep learning. *AJNR. Am. J. Neuroradiol.* 41 (6), 1061–1069. doi:10.3174/ajnr.A6538
- Van Brummen, A., Owen, J. P., Spaide, T., Froines, C., Lu, R., Lacy, M., et al. (2021). PeriorbitAI: Artificial intelligence automation of eyelid and periorbital measurements. *Am. J. Ophthalmol.* 230, 285–296. doi:10.1016/j.ajo.2021.05.007
- van der Heijden, A. A., Abramoff, M. D., Verbraak, F., van Hecke, M. V., Liem, A., and Nijpels, G. (2018). Validation of automated screening for referable diabetic retinopathy with the IDX-DR device in the Hoorn Diabetes Care System. *Acta Ophthalmol.* 96 (1), 63–68. doi:10.1111/aos.13613
- Wang, L., Ding, L., Liu, Z., Sun, L., Chen, L., Jia, R., et al. (2020). Automated identification of malignancy in whole-slide pathological images: Identification of eyelid malignant melanoma in gigapixel pathological slides using deep learning. *Br. J. Ophthalmol.* 104 (3), 318–323. doi:10.1136/bjophthalmol-2018-313706
- Wang, M., Shen, L. Q., Pasquale, L. R., Wang, H., Li, D., Choi, E. Y., et al. (2020). An artificial intelligence approach to assess spatial patterns of retinal nerve fiber layer thickness maps in glaucoma. *Transl. Vis. Sci. Technol.* 9 (9), 41. doi:10.1167/tvst.9.9.41
- Wang, Y., Sun, J., Liu, X., Li, Y., Fan, X., and Zhou, H. (2022). Robot-assisted orbital fat decompression surgery: First in human. *Transl. Vis. Sci. Technol.* 11 (5), 8. doi:10.1167/tvst.11.5.8
- Weber, A. L., and Sabates, N. R. (1996). Survey of CT and MR imaging of the orbit. *Eur. J. Radiol.* 22 (1), 42–52. doi:10.1016/0720-048x(96)00737-1
- Wu, H., Luo, B., Zhao, Y., Yuan, G., Wang, Q., Liu, P., et al. (2022). Radiomics analysis of the optic nerve for detecting dysthyroid optic neuropathy, based on water-fat imaging. *Insights Imaging* 13 (1), 154. doi:10.1186/s13244-022-01292-7
- Wu, X., Huang, Y., Liu, Z., Lai, W., Long, E., Zhang, K., et al. (2019). Universal artificial intelligence platform for collaborative management of cataracts. *Br. J. Ophthalmol.* 103 (11), 1553–1560. doi:10.1136/bjophthalmol-2019-314729
- Xie, X., Yang, L., Zhao, F., Wang, D., Zhang, H., He, X., et al. (2022). A deep learning model combining multimodal radiomics, clinical and imaging features for differentiating ocular adnexal lymphoma from idiopathic orbital inflammation. *Eur. Radiol.* 32 (10), 6922–6932. doi:10.1007/s00330-022-08857-6
- Yang, L. W. Y., Ng, W. Y., Foo, L. L., Liu, Y., Yan, M., Lei, X., et al. (2021). Deep learning-based natural language processing in ophthalmology: Applications, challenges and future directions. *Curr. Opin. Ophthalmol.* 32 (5), 397–405. doi:10.1097/ICU.0000000000000789
- Ye, Y., Xiong, Y., Zhou, Q., Wu, J., Li, X., and Xiao, X. (2020). Comparison of machine learning methods and conventional logistic regressions for predicting gestational diabetes using routine clinical data: A retrospective cohort study. *J. Diabetes Res.* 2020, 4168340. doi:10.1155/2020/4168340
- Yin, X. X., Sun, L., Fu, Y., Lu, R., and Zhang, Y. (2022). U-Net-Based medical image segmentation. *J. Healthc. Eng.* 2022, 4189781. doi:10.1155/2022/4189781
- Yixin, Q., Bingying, L., Shuiling, L., Xianchai, L., Zhen, M., Xingyi, L., et al. (2022). Effect of multichannel convolutional neural network-based model on the repair and aesthetic effect of eye plastic surgery patients. *Comput. Math. Methods Med.* 2022, 5315146. doi:10.1155/2022/5315146
- Yoo, T. K., Choi, J. Y., and Kim, H. K. (2020). A generative adversarial network approach to predicting postoperative appearance after orbital decompression surgery for thyroid eye disease. *Comput. Biol. Med.* 118, 103628. doi:10.1016/j.combiomed.2020.103628
- Zhai, G., Yin, Z., Li, L., Song, X., and Zhou, Y. (2021). Automatic orbital computed tomography coordinating method and quantitative error evaluation based on signed distance field. *Acta Radiol.* 62 (1), 87–92. doi:10.1177/0284185120914029
- Zhai, Y., Cao, H., Deng, W., Gan, J., Piuri, V., and Zeng, J. (2019). BeautyNet: Joint multiscale CNN and transfer learning method for unconstrained facial beauty prediction. *Comput. Intell. Neurosci.* 2019, 1910624. doi:10.1155/2019/1910624



OPEN ACCESS

EDITED BY
Huiying Liu,
Institute for Infocomm Research
(A*STAR), Singapore

REVIEWED BY
Ye Xiangyu,
Xiamen University, China
Yong Wang,
Wuhan Aier Eye Hospital, China

*CORRESPONDENCE
Zhe Zhang,
whyotato@126.com

SPECIALTY SECTION
This article was submitted to Molecular
and Cellular Pathology,
a section of the journal
Frontiers in Cell and
Developmental Biology

RECEIVED 04 September 2022
ACCEPTED 08 November 2022
PUBLISHED 21 November 2022

CITATION
Lin H-Y, Chen S, Chuang Y-J, Zhang S,
Chang SW-H, Lin P-J and Zhang Z
(2022), Effectiveness of reducing
corneal astigmatism after combined
high-frequency LDV Z8 femtosecond
laser-assisted phacoemulsification and
arcuate keratotomy.
Front. Cell Dev. Biol. 10:1036469.
doi: 10.3389/fcell.2022.1036469

COPYRIGHT
© 2022 Lin, Chen, Chuang, Zhang,
Chang, Lin and Zhang. This is an open-
access article distributed under the
terms of the [Creative Commons
Attribution License \(CC BY\)](https://creativecommons.org/licenses/by/4.0/). The use,
distribution or reproduction in other
forums is permitted, provided the
original author(s) and the copyright
owner(s) are credited and that the
original publication in this journal is
cited, in accordance with accepted
academic practice. No use, distribution
or reproduction is permitted which does
not comply with these terms.

Effectiveness of reducing corneal astigmatism after combined high-frequency LDV Z8 femtosecond laser-assisted phacoemulsification and arcuate keratotomy

Hung-Yuan Lin^{1,2,3}, Shuan Chen¹, Ya-Jung Chuang⁴,
Suhua Zhang⁵, Steven Wei-Hsin Chang⁶, Pi-Jung Lin⁷ and
Zhe Zhang^{8,9,10*}

¹Universal Eye Center, Zhong-Li, Taiwan, ²Department of Ophthalmology, Shanghai Ruidong Hospital, Shanghai, China, ³Department of Ophthalmology, Fujian Medical University, Fuzhou, China, ⁴Universal Eye Center, Long-Tan, Taiwan, ⁵Taiyuan Central Hospital of Shanxi Medical University, Taiyuan, China, ⁶Department of Biomedical Engineering, I-Shou University, Kaohsiung, Taiwan, ⁷Universal Eye Center, Taipei, Taiwan, ⁸Shenzhen Eye Hospital, Shenzhen Eye Institute, Jinan University, Shenzhen, China, ⁹The First Hospital of Shanxi Medical University, Taiyuan, China, ¹⁰Shanxi Eye Hospital, Taiyuan, China

Purpose: In this retrospective study, the efficacy of the FEMTO LDV Z8 Femtosecond Laser-Assisted Cataract Surgery (Femto Z8 FLACS) and the Femtosecond laser Arcuate Keratotomy (FSAK) in decreasing the corneal astigmatism was investigated.

Methods: During FLACS, FSAK was positioned with the help of the FEMTO LDV Z8 laser at a diameter of 8.5 mm and an 80% depth. Before and 3 months after surgery, the astigmatism of the cornea was measured with the aid of Pentacam. The variables influencing the efficacy of FSAK were assessed using the multiple regression analysis technique. Vector analyses were carried out. To determine the net corneal alterations, the with-the-wound and against-the-wound variations were computed along the FSAKs' meridian.

Results: This study investigated 80 eyes from 62 participants. The average keratometric astigmatism value was 0.92 ± 0.44 diopters (D). The average keratometric astigmatism decreased to 0.61 ± 0.45 D 3 months following FSAK compared to preoperative corneal astigmatism ($p < 0.05$). Additionally, there was a considerable decline in the percentage of eyes with ± 0.5 D and ± 1.0 D astigmatism, which reduced 3 months after surgery by 58% and 85%, respectively ($p < 0.05$).

Conclusion: The FEMTO LDV Z8 laser can create an effective and precise arcuate keratotomy with an excellent safety profile, rapid recovery, and vision stability.

KEYWORDS

high-frequency femtosecond laser-assisted phacoemulsification, arcuate keratotomy, corneal astigmatism, nomogram, cataract surgery

Introduction

The advancements in Femtosecond Laser-Assisted Cataract Surgery (FLACS) allowed ophthalmologists to achieve very accurate, safe, and predictable refractive results. At the same time, patients' high expectations regarding "spectacle independence" have made astigmatism correction an increasingly important component of cataract surgery (Pager et al., 2004; Hawker et al., 2005). Recent large-scale retrospective surveys showed that approximately 40%–47% of eyes preparing for cataract surgery exhibit the minimal astigmatism value of 1.0 Diopter (D) (Khan and Muhtaseb, 2011; Yuan et al., 2014). Furthermore, Ferrer-Blasco et al. have reported that approximately 22% of cataract patients have 1.50 D or higher (Ferrer-Blasco et al., 2009). Villegas et al. (2014) observed a decrease in visual quality when patients showed refractive astigmatism of 0.5 D (Villegas et al., 2014). Hence, less than 0.5 D would be recommended for the visual benefit of precise astigmatism correction.

Although arcuate relaxing keratotomy is a well-established technique to manage astigmatism, most surgeons are uncomfortable with performing manual arcuate keratotomy during cataract surgery (Duffey and Leaming, 2005; Yeu et al., 2013). The femtosecond laser features precise incisions taking the depth, shape, and angulation of arcuate incisions into account, giving surgeons the ability to titrate the incision instead of creating these manually.

Notably, the femtosecond laser has received widespread recognition for its high dependability, consistency, and effectiveness in eliminating corneal astigmatism in patients suffering from mild to moderate astigmatism (Alió et al., 2014; Grewal et al., 2016; Vickers and Gupta, 2016; Baharozian et al., 2017; Roberts et al., 2018). In this review paper, Chang concluded that intrastromal FSAK is a great alternative for native eyes undergoing FLACS to correct the issue like low astigmatism (<1.5 D) and that most cuts are carried out at the optical zone of ≥ 7.5 mm to prevent dysphotopsia (Chang, 2018).

In planning astigmatism management, it is important to obtain reliable and consistent astigmatism measurements. Nomograms can be used to calculate arc length and optical zone required to obtain the astigmatism correction once the degree of astigmatism has been established.

Nomograms for FLACS FSAK can readily be found in recent literature (Medical; Wang et al., 2016). However, Most of the nomogram was established for high-pulses (μ J) coupled with low-frequency (kHz) laser systems, such as LenSx (Alcon Laboratories). A modified Donnenfeld nomogram has been presented by Wang et al. (2016) to support the application of the high-energy femtosecond laser platform, i.e., LenSx to correct astigmatism during cataract surgery.

The Femto LDV Z8 (Ziemer Ophthalmic Systems AG, Port, Switzerland) is a novel low-energy pulses (nJ) paired with a high-frequency (MHz) femtosecond laser system having a small spot size that pinpoints the exact location of the ocular surfaces intraoperatively. Because of this, the cutting processes in both

systems are different. High-pulse energy facilitates wider spot spacing as the mechanical force applied to the expanding bubbles propels the cutting action. The low-pulse energy laser, on the other hand, allows for an increasing number of overlapping smaller-sized spots that directly vaporize the tissue inside the plasma volume, thereby successfully separating tissue without the need for the secondary mechanical tearing effects (Pepose 2008; Latz et al., 2021). As a result, the cuts achieved by low-energy pulses with high-frequency lasers, such as Femto LDV Z8 (Ziemer) system, create a smooth surface without damaging the adjacent tissues (Riau et al., 2014; Lin et al., 2021).

However, the efficacy of FSAK combined with FLACS of low-energy high-frequency laser platforms and a nomogram has not been established yet. In this study, Wang's modified Donnenfeld nomogram was used for the purpose of estimating the number and arc length of FSAK. This study assessed the effectiveness of FSAK performed during Femto LDV Z8 FLACS. Meanwhile, a nomogram based on age and the type of astigmatism (WTR and ATR) was developed. This could be the first study that assessed the effectiveness of FSAK performed during Femto LDV Z8 FLACS (Z8 FLACS).

Patients and methods

Patients

In this single-center retrospective study, 80 eyes in total from 62 cataract patients who underwent the FLACS treatment between January 2019 and August 2021 were included. A skilled surgeon (HYL) at the universal Eye Center in Zhong-Li, Taiwan carried out the surgeries. The Institutional Review Board at Antai Tian-Sheng Memorial Hospital in Taiwan (21-088-B) approved the study after waiving the permission since the data was collected during routine patient care. This study was carried out following the principles of the Declaration of Helsinki for human research.

The participants who were included in this study had to fulfill the following inclusion criteria: aged ≥ 45 years, able to cooperate with the requirements of the docking system for femtosecond laser, should not have undergone any ocular trauma or surgery, absence of any ocular surface disease, presence of clear corneal media, ability to achieve full pupil dilation (> 7 mm), and they should be able to come back for their scheduled follow-up tests. The following exclusion criteria were used in the study: minimal K-value < 37 D; maximum K-value of > 58 D; corneal disease or pathology with the exception of senile cataract, and a total corneal irregular astigmatism index $> 0.4 \mu$ m as determined by Pentacam.

Corneal astigmatism measurements

Keratometry measurements were estimated preoperatively from Pentacam (Oculus, Wetzlar, Germany). The simulated

keratometry of steep K-value, flat K-value, steep K meridian, and Km of Pentacam were measured 1 and 3 months postoperatively.

Preoperative femtosecond laser arcuate keratotomy planning

For phacoemulsification-induced astigmatism, 0.1 D was set in the system based on an earlier analysis conducted by the same surgeon (Lin, HY M.D., data to be published). The location of the incision was the temporal side of the eyes (left eye/0° or right eye/180°). If the FSAK were closer to the primary cut, its location would be shifted 30° away from the temporal side. The arc length and number of FSAK were calculated using the Wang nomogram and were entered into the program for femtosecond laser treatment (Wang et al., 2016).

Surgical technique

1 VERION-guided marking and manual meridian adjustment:

To prevent the effects of cyclotorsion, limbus registration was carried out with the help of a Verion image-guided system with the patients asked to sit upright. Then, a Verion system-guided 27-gage needle and ink were used and 2 endpoints of the 0°–180° horizontal axis were inscribed on the corneal limbus. When the Femto LDV Z8 image was captured after docking experiments, two blue marks at the limbus that were 180° apart could be noted clearly. The operator screen was used to project the horizontal Femto LDV Z8 reference line onto the cornea. Cyclotorsion was the cause of the angular difference between the two. The surgeon carefully set the two lines in alignment (Lin et al., 2019).

2 FLACS + FSAK technique:

Phenylephrine and tropicamide eye drops (Mydrin-P Eye Drop, Santen) were injected into the eye for 30, 25, 20, 15, and 10 min Before the procedure to help dilate the pupils. For 3 days before surgery, the patients received 4 daily injections of ketorolac 0.5% ophthalmic solution (Acular LS; Allergan, Inc., Irvine, CA). The mobile arm of the laser system was anchored over the corneal apex after the suction ring was filled with a balanced salt solution so as to form a fluid-filled interface. The femtosecond laser was used to generate a 5.5 mm capsulotomy. The lens was divided into either 4 quadrants (cataract grade II) or into 6 quadrants (cataract grade III). Following the recommendations by the manufacturer of the femtosecond laser, paired or single penetrating FSAK with a preset length were placed at an 8.5 mm diameter and a depth of 80% of the corneal thickness. The femtosecond laser produced a 1.0 mm single-plane paracentesis and a 2.2 mm primary 2-plane clean

corneal incision (+40°/50°). The intraocular lenses were successfully inserted into the capsular bag.

In the paired FSAK group, the eyes were divided into two subgroups: With The Rule astigmatism (WTR) and Against The Rule astigmatism (ATR). For the eyes affected by WTR astigmatism, the paired FSAK was carried out around 90° and 270° based on the steep axis of corneal astigmatism ($\pm 30^\circ$). However, for eyes affected by ATR astigmatism, the paired FSAK were implemented around 0° and 180° according to the corneal astigmatism steep axis ($\pm 30^\circ$). Meanwhile, the corneal incision was shifted to 210° (OD) or 30° (OS). In a single FSAK group, for eyes affected by WTR astigmatism, one FSAK was done around 0° meridian (OD) or 180° (OS), and a clear corneal incision of FLACS was done at 180° (OD) or 0° (OS). Figure 1 depicts the animation derived from the FEMTO LDV Z8 program demonstrating the position of clear corneal incision (purple dots), paired arcuate keratotomy (yellow dots), and paracentesis (light blue dots) of FLACS with FSAK on the right eye.

Data and statistical analysis

Changes in keratometry

The percentage of eyes with keratometric astigmatism that was determined with the aid of Pentacam at 0 ± 0.25 D, ± 0.50 D, ± 0.75 D, ± 1.00 D, ± 1.50 D, ± 2.00 D, and ± 3.00 D before and after surgery has also been listed.

Astigmatism vector analysis

The Alpins method, which was included in the ASSORT software, was used to measure three vectors and their relationships while taking into consideration the differences (variations) in the keratometric astigmatism axis to study the changes occurring during the surgery (Alpins, 2001). The anticipated astigmatic modification following surgery was a target-induced astigmatism vector (TIA). Furthermore, surgically induced astigmatism (SIA) was seen to be an astigmatic change brought about by surgery. Postoperative corneal astigmatism is similar to the difference vector (DV). The ratio of SIA to TIA (SIA/TIA) is used to determine the correction index (CI). The arithmetic difference noted between the angles of the SIA and TIA is known as the angle of error (AE). The magnitude of error (ME) is the arithmetic difference between the SIA and TIA.

The flattening index (FI) shows the percentage of SIA that effectively reduces astigmatism at the target meridian ($FI = SIA \cos 2AE/TIA$).

FSAK nomograms

The Holladay-Cravy-Koch formula was used for estimating the with-the-wound (WTW) and against-the-wound (ATW) variations (Holladay et al., 1992). The Pentacam HR was used to obtain the preoperative and postoperative simulated K in

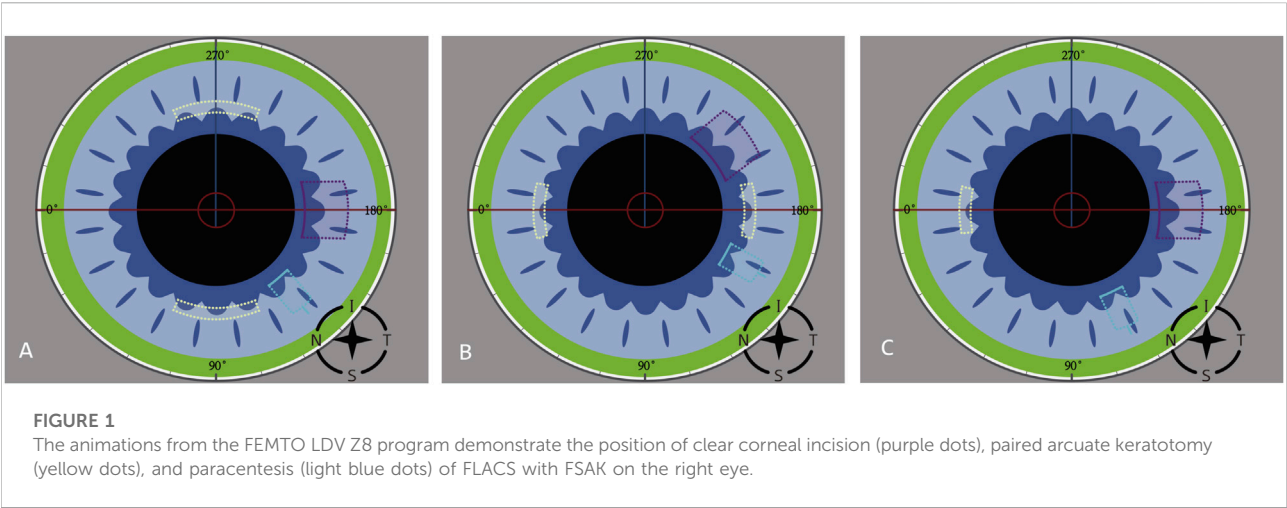


TABLE 1 Preoperative patient characteristics and biometric parameters.

	Mean \pm SD	Range
Age (y)	65 \pm 7	47 to 85
Axial length (mm)	24.4 \pm 1.5	29 to 22
Pachymetry (mm)	555.9 \pm 29.8	646 to 490
Pentacam Sim K		
Km vaule (D)	43.6 \pm 1.4	39.5 to 47.9
Astigmatism magnitude (D)	0.9 \pm 0.4	0.2 to 2.3

K, corneal power; Km, simulated keratometry; D, diopter.

addition to their axes for these computations. A WTW demonstrates the astigmatic effects along the steep corneal meridian, while an ATW reveals the astigmatic effect at 90° from the steep meridian. The WTW-ATW difference illustrates the total net effect or net corneal change induced by the incision alongside the meridian of the relaxing incision.

TABLE 2 Percentage of eye within certain levels of corneal astigmatism measured by Pentacam (*n* = 80).

Keratometric Astigmatism (D)	Pre-OP keratometric Astigmatism		Post-OP 3 months keratometric Astigmatism	
	Num Eyes	%	Num Eyes	%
≤0.25	2	3%	15	19%
0.26 to 0.50	8	10%	31	39%
0.51 to 0.75	23	29%	14	18%
0.76 to 1.00	22	28%	7	9%
1.01 to 1.25	7	9%	5	6%
1.26 to 1.50	11	14%	4	5%
1.51 to 2.00	5	6%	4	5%
2.01 to 3.00	2	3%	0	0%

Statistical analysis

SPSS software was used for all descriptive statistical analyses (version 23.0, SPSS, Inc.). The percentage data were presented in %, whereas numerical data were expressed as mean \pm SD. The Kolmogorov-Smirnov test was carried out to determine whether the data distribution was normal. To assess corneal astigmatism before surgery and 3 months after surgery, a paired-sample *t*-test was employed. Statistical significance was described as a *p*-value<0.05. The net corneal changes estimated by deducting the ATW changes from WTW changes that indicate the effectiveness of FSAK were evaluated using the multiple regression analysis technique.

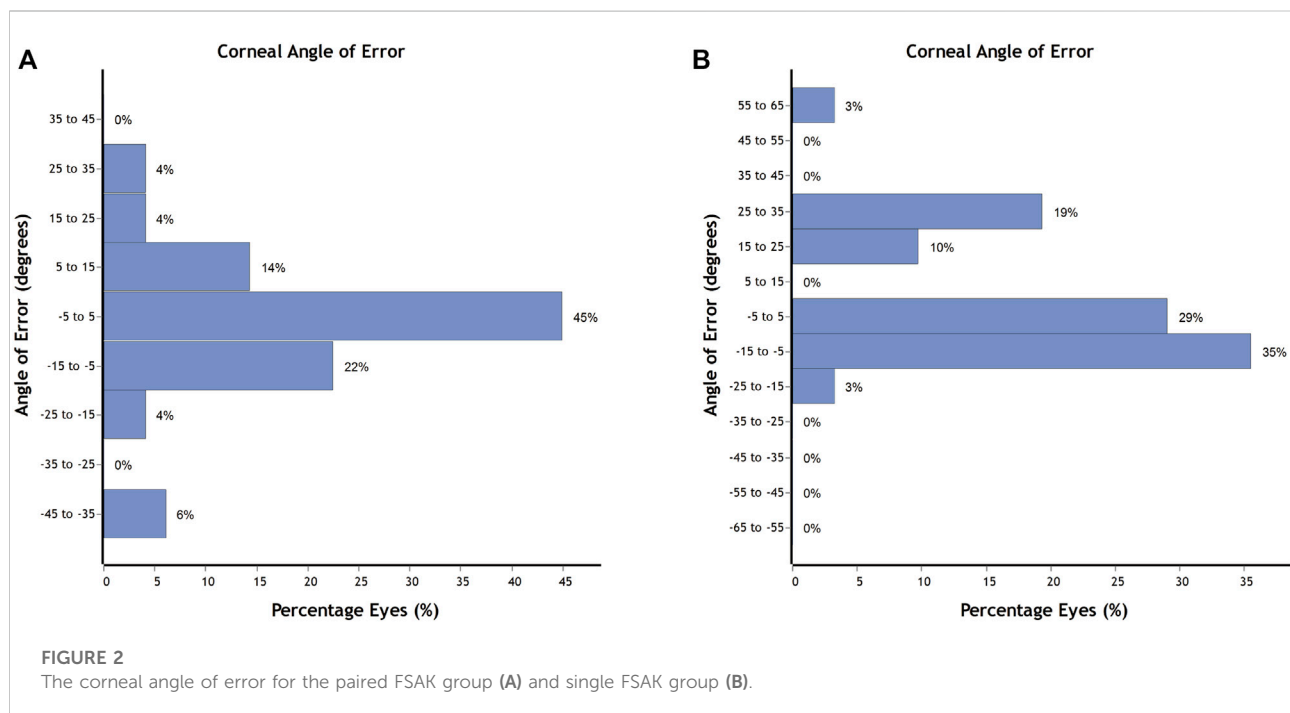
Results

In total, 62 patients and 80 eyes were involved in this study. With arc lengths that ranged between 25 and 55°, 49 of the 80 eyes underwent a paired FSAK, while 31 underwent a single FSAK

TABLE 3 Vector analysis of keratometric astigmatism after femto Z8 FLACS and FSAK using the alpins method.

Vector Analysis Parameters	Pair FSAKs				
	Total (n = 80)	Total (n = 49)	WTR group (n = 34)	ATR group (n = 15)	Single FSAK (n = 31)
TIA Arithmetic mean \pm SD, D Range, D	0.92 \pm 0.44 0.2 to 2.3	0.93 \pm 0.35 0.4 to 1.8	0.91 \pm 0.34 0.5 to 1.8	0.99 \pm 0.39 0.4 to 1.6	0.89 \pm 0.57 0.2 to 2.3
SIA Arithmetic mean \pm SD, D Range, D	0.95 \pm 0.60 0.1 to 2.69	0.89 \pm 0.54 0.1 to 2.57	0.72 \pm 0.41 0.1 to 2.07	1.26 \pm 0.61 0.33 to 2.57	1.05 \pm 0.69 0.23 to 2.69
DV Arithmetic mean \pm SD, D Range, D	0.61 \pm 0.45 0 to 2.0	0.47 \pm 0.30 0 to 1.3	0.46 \pm 0.24 0.1 to 1.2	0.49 \pm 0.40 0 to 1.3	0.83 \pm 0.56 0.1 to 2.0
CI Arithmetic mean \pm SD Geometric mean Range	1.17 \pm 0.80 0.94 0.11 to 3.97	0.96 \pm 0.51 0.84 0.17 to 3.17	0.80 \pm 0.37 0.71 0.17 to 1.64	1.31 \pm 0.63 1.21 0.67 to 3.17	-0.16 \pm 0.89-1.99 to 1.77
ME Arithmetic mean \pm SD, D Range, D	-0.03 \pm 0.65-2.35 to 1.61	0.05 \pm 0.43-1.27 to 1.15	0.19 \pm 0.34-0.57 to 1.15	-0.27 \pm 0.45-1.27 to 0.2	1.50 \pm 1.04 1.14 0.11 to 3.97
AE Arithmetic mean \pm SD, ° Range, °	1.00 \pm 16.38-41.50 to 58.87	-1.78 \pm 13.97-41.50 to 27.07	-2.69 \pm 15.80-41.50 to 27.07	0.29 \pm 8.60-15.96 to 14.57	5.39 \pm 19.04-19.56 to 58.87
Absolute AE Arithmetic mean \pm SD, ° Range, °	11.43 \pm 11.72 0 to 58.87	9.54 \pm 10.27 0 to 41.5	10.88 \pm 11.63 0 to 41.5	6.49 \pm 5.37 0 to 15.96	14.41 \pm 13.33 0 to 58.87
FI Arithmetic mean \pm SD, D Range, D	-1.03 \pm 0.84-3.89 to 0.61	-0.87 \pm 0.54-3.13 to -0.03	-0.70 \pm 0.39-1.62 to -0.03	-1.26 \pm 0.62-3.13 to -0.67	-1.28 \pm 1.14-3.89 to 0.61
WTW-ATW Arithmetic mean \pm SD, ° Range	-0.86 \pm 0.63-2.67 to 0.18	-0.82 \pm 0.55-2.55 to -0.02	-0.64 \pm 0.43-2.01 to -0.02	-1.21 \pm 0.60-2.55 to -0.32	-0.93 \pm 0.74-2.67 to 0.18

TIA, target induced astigmatism; SIA, surgically induced astigmatism; DV, difference vector; ME, magnitude of error; CI, correction index; AE, angle of error; Absolute AE, absolute angle of error; FI, flattening index; WTW-ATW, net corneal change induced by the incision; SD, standard deviation.



with arc lengths that ranged between 20 and 55°. During surgery, the average patient age was 65 ± 7 years. The average axial length was seen to be 24.4 ± 1.5 mm. The patients' characteristics and ocular biometric parameters are listed in Table 1. No significant intraoperative or postoperative complications occurred during the surgery.

Changes in keratometric astigmatism

The percentage of eyes within ± 0.5 D and ± 1.0 D of keratometric astigmatism measured by Pentacam significantly increased 3 months after surgery to 58% and 85%, as shown in Table 2.

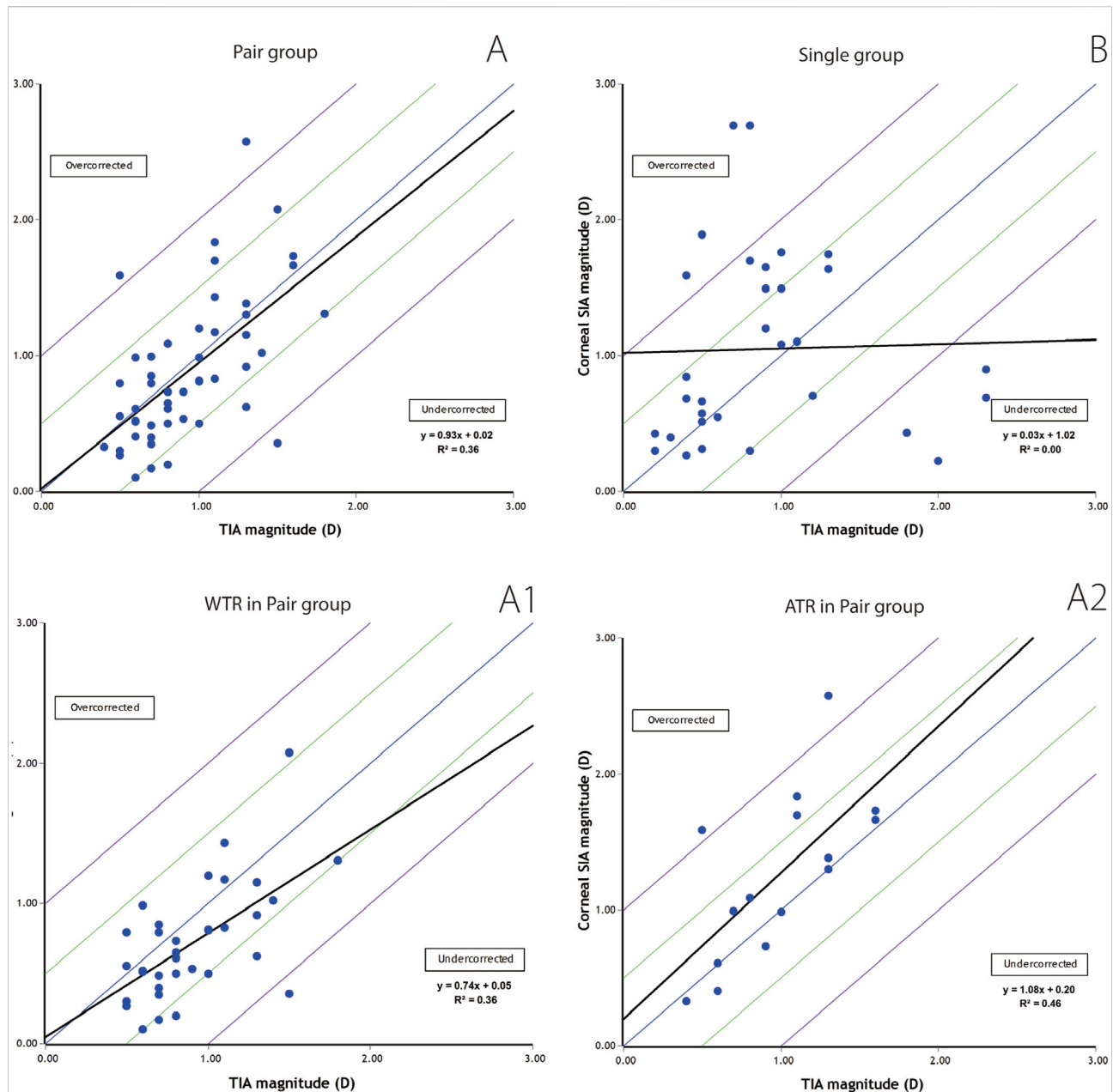


FIGURE 3

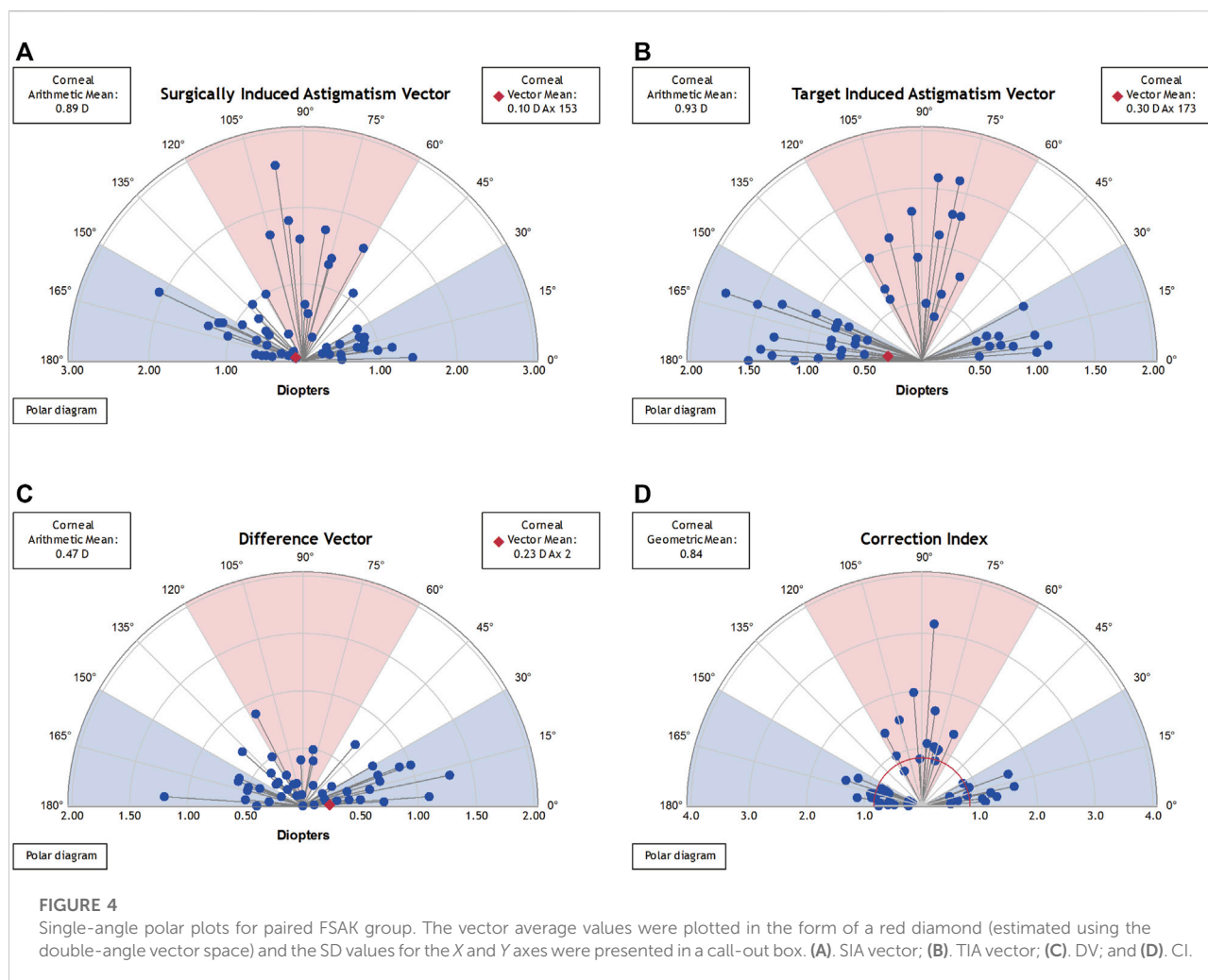
Scatterplots depicting target-induced astigmatism (TIA) vs. the surgically induced astigmatism (SIA). (A). Cases of paired FSAK group; A1. Cases of WTR in paired FSAK group; A2. Cases of ATR in paired FSAK group and (B). cases of single FSAK group.

Astigmatism vector analysis

This study showed a significant decrease in keratometric astigmatism post-surgery. Preoperative average keratometric astigmatism or TIA value was 0.92 ± 0.44 D, which was significantly decreased to 0.61 ± 0.45 D or presented as DV 3 months postoperatively ($p < 0.001$). In paired FSAK group, the mean keratometric astigmatism was decreased from 0.93 ± 0.35 D to 0.47 ± 0.30 D at 3 months

postoperatively ($p < 0.001$). However, in the single FSAK group, the mean keratometric astigmatism reduced from 0.89 ± 0.57 D to 0.83 ± 0.56 D ($p = 0.53$), with no statistical difference.

Table 3 displays the outcomes of vector analysis using the Alpins approach, including SIA, TIA, ME, DV, AE, CI, and absolute AE. In the paired FASK group, the arithmetic mean SIA magnitude was recorded to be 0.89 ± 0.54 D, which was lower than the arithmetic mean TIA in the single FSAK group. CI,



which refers to the ratio of the SIA to TIA, presents the overcorrection when it is greater than one or an under correction if it is less than one. The geometric mean of CI values for paired FSAK groups was 0.84, which can be interpreted as mild under-correction, whereas the single FSAK group was 1.14, which means overcorrection.

The ME (arithmetic difference present between the SIA and TIA) was -0.03 ± 0.65 D, which indicated a near-zero value or a slight under-correction. AE refers to the arithmetic variation between the angles of SIA and TIA. The corneal AE for both groups is shown in Figure 2. A total of 45% of eyes received paired FSAK during FLACS surgery and had AE within -5 to 5° , indicating no significant systematic error for the misaligned treatment. However, only 29% of eyes in the single FSAK groups had AE within $\pm 5^\circ$, which revealed different factors, like healing or alignment at the individual level.

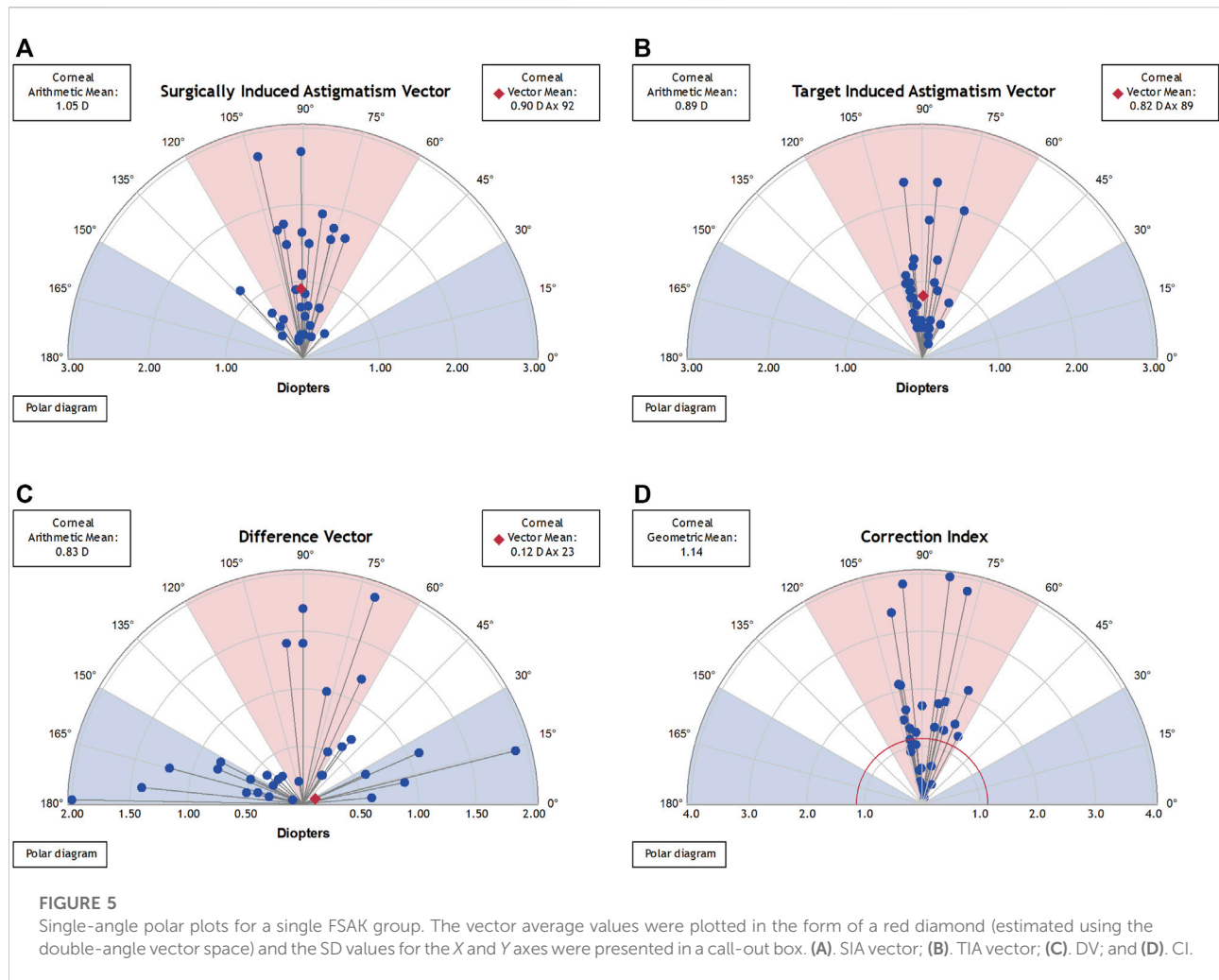
The FI shows the amount of astigmatism that was decreased at the intended meridian. FI shows an ideal value of -1 . Here, the calculations showed an effective FI of -1.03 ± 0.84 D, which

shows that astigmatism correction at that targeted orientation is effective. Significant mean net corneal changes (WTW-ATW) were -0.82 ± 0.55 D in the paired FSAK group and -0.93 ± 0.74 D in the single FSAK group, 3 months post-surgery. Whereas the magnitude of WTW-ATW astigmatism of WTR in paired FSAK group was -0.64 ± 0.43 D, ATR in the paired FSAK group was -1.21 ± 0.60 D.

A scatterplot of SIA vs. TIA after combined Femto LDV Z8 Femto and FSAK is illustrated in Figure 3. As mentioned above, overcorrection occurred when $SIA/TIA > 1$, and under-correction occurred when $SIA/TIA < 1$.

In paired FSAK group, the preoperative TIA and SIA values, 3 months after surgery, showed a significant relationship ($r = 0.93, p < 0.01$). However, the correlation between TIA and SIA in the single group was very low ($r = 0.03, p = 0.886$).

Figures 4, 5 present the single-angle polar plots for vector TIA, DV, vector SIA, and CI for both groups. The standard deviation for the X and Y axes was visualized in the call-out box, and vector means are represented as red diamonds (measured in the double-angle vector space).



Femtosecond laser arcuate keratotomy nomograms

The net corneal changes (WTW-ATW) were derived for nomogram development using the corneal simulated variations that were estimated using the Pentacam 3 months following surgery (Table 4). According to the age and length of the paired FSAK, the following regression formulas were used for eyes having WTR and ATR corneal astigmatism:

Paired group:

a) WTR

$$\text{Net corneal changes} = -0.01601507 \times \text{age (years)} - 0.0413699 \times \text{length (degrees)} + 1.98254955$$

b) ATR

$$\text{Net corneal changes} = -0.01601507 \times \text{age (years)} - 0.0413699 \times \text{length (degrees)} - 0.66906866 + 1.98254955.$$

In the single FSAK group, the correlation between TIA and SIA was very low. Therefore, a nomogram for the single FSAK was not designed ($r = 0.03$, $p = 0.886$).

Discussion

Two alternative laser parameter patterns are used by FLACS: high-energy pulses (μJ) coupled with a low-frequency (kHz); low-energy pulses (nJ) coupled with a high-frequency (MHz). Because of this, the cutting processes used by both systems are different. A particularly smooth surface is produced by the Femto LDV Z8 (Ziemer) system without damaging the surrounding tissues (Riau et al., 2014; Lin et al., 2021). This is important for the FSAK because it offers smoother corneal incisions during surgery. The other difference between the LenSx and Femto LDV Z8 systems is the docking interface. Femto LDV Z8 system employs a liquid-

TABLE 4 Nomogram: total net corneal change (WTW-ATW changes) based on age and length of FSAKs in paired group with WTR and ATR corneal astigmatism.

Paired Incision Length	Age						
	50 years	55 years	60 years	65 years	70 years	75 years	80 years
WTR eyes							
25°	0.15	0.07	−0.01	−0.09	−0.17	−0.25	−0.33
30°	−0.06	−0.14	−0.22	−0.30	−0.38	−0.46	−0.54
35°	−0.27	−0.35	−0.43	−0.51	−0.59	−0.67	−0.75
40°	−0.47	−0.55	−0.63	−0.71	−0.79	−0.87	−0.95
45°	−0.68	−0.76	−0.84	−0.92	−1.00	−1.08	−1.16
50°	−0.89	−0.97	−1.05	−1.13	−1.21	−1.29	−1.37
55°	−1.09	−1.17	−1.25	−1.33	−1.41	−1.49	−1.57
60°	−1.30	−1.38	−1.46	−1.54	−1.62	−1.70	−1.78
ATR eyes							
25°	−0.52	−0.60	−0.68	−0.76	−0.84	−0.92	−1.00
30°	−0.73	−0.81	−0.89	−0.97	−1.05	−1.13	−1.21
35°	−0.94	−1.02	−1.10	−1.18	−1.26	−1.34	−1.42
40°	−1.14	−1.22	−1.30	−1.38	−1.46	−1.54	−1.62
45°	−1.35	−1.43	−1.51	−1.59	−1.67	−1.75	−1.83
50°	−1.56	−1.64	−1.72	−1.80	−1.88	−1.96	−2.04
55°	−1.76	−1.84	−1.92	−2.00	−2.08	−2.16	−2.24
60°	−1.97	−2.05	−2.13	−2.21	−2.29	−2.37	−2.45

filled interface, where the vacuum ring improves the contact with the sclera, and the center is filled with liquid. LenSx system uses an applanating curved interface, which directly touches the cornea. Though during the surgery, the mechanical contact interface significantly stabilizes the cornea, the use of a liquid-filled interface has been found to prevent corneal folds that may cause incomplete capsulotomy.

Yet, as mentioned above, the efficacy of FSAK combined with FLACS of low-energy high-frequency laser platforms could be different. Each platform has developed its recommendations to minimize unwanted problems during the FSAK procedure. According to the manufacturer's instructions, the paired FSAK was placed for the Femto LDV Z8 at a diameter of 8.5 mm and a corneal thickness depth of 80%. The modified Donnenfeld nomogram proposed by Wang et al. (2016) was used to calculate the number and length of FSAK since there was no calculator available to do so during FLACS.

In this study, vector analysis showed that the mean keratometric astigmatism measured by Pentacam was decreased in the 3rd month after surgery. The vector analysis was conducted to estimate the WTW and ATW changes that denote the overall net effect caused by the incisions. At 3 months

after surgery, the average WTW and ATW changes in the paired FSAK group were recorded to be -0.82 ± 0.55 D.

The multiple regression analysis revealed that age, FSAK location, and FSAK arc length were found to significantly influence total net corneal modifications (WTW-ATW changes). Age, larger incisions, horizontal incisions (0° or 180°), corneal astigmatism, and preoperative ATR all contribute to the amount of net corneal modifications that arise in eyes with preoperative ATR. In this study, the main incision of FLACS was at the temporal side of the cornea, which is more stable and predictable than the oblique angle, such as 120° or 60° .

Based on the results obtained in this study, the effectiveness of FSAK alongside the horizontal meridian is greater than the vertical meridian within the same age groups. This could be attributed to corneal biomechanical factors linked to temporal incision. As a result, it was seen that the length of arcuate incision needed for ATR cornea is less than WTR cornea for the same correction of astigmatism. Previous studies have shown that the amplitude of refractive cylinder increases with increasing age, and its orientation also shifts from WTR to ATR (Saunders, 1986; Gudmundsdottir et al., 2000; Navarro et al., 2013; Rozema et al., 2019). Thus, for long-term FLACS and FSAK surgical outcomes, it is suggested that it is better to have overcorrection than under-correction when dealing with ATR corneal astigmatism.

In terms of the single FSAK group in this study, as the correlation between TIA and SIA was very low and did not show statistical significance, there is no reliable astigmatism reduction. When considering the effectiveness, the asymmetrical incisions created by FSAK and FLACS could lead to variable biomechanical responses, and therefore, variable effectiveness in reducing ATR astigmatism in a single FSAK group. The incisions of FSAK and FLACS could result in variable influences on several aspects, such as the angle of the corneal incision, full/partial depth, and one/two plans.

This study has a few drawbacks. Firstly, the sample size is small, necessitating more extensive patient follow-up visits. The purpose of this study was to present the preliminary findings and recommend a Z8 nomogram. More patients will be included in the trial with a longer follow-up duration, and the nomogram's performance will be assessed further. Secondly, the keratometric and refractive results of a small subset of eyes that underwent single FSAK were merged with those of the eyes that experienced paired FSAK. These conclusions sum up the outcomes of these related cases. Eyes were separated into single FSAK and paired FSAK groups to compute and visualize the WTW and ATW alterations induced by the FSAK.

In conclusion, low-energy high-frequency femtosecond laser arcuate keratotomy performed during cataract surgery can reduce the pre-existing low-grade corneal astigmatism in a short-term observation. Long-term observation of refractive stability is needed. Furthermore, our nomogram needs to be refined, requiring more cases to be enrolled in the future. It is necessary to evaluate the length and depth of the incisions and determine the role played by the corneal biomechanical factors to assess the long-term benefits.

Data availability statement

The raw data supporting the conclusion of this article will be made available by the authors, without undue reservation.

Ethics statement

The studies involving human participants were reviewed and approved by the Institutional Review Board of Antai Tian-Sheng

Memorial Hospital, Taiwan (21-088-B). Written informed consent for participation was not required for this study in accordance with the national legislation and the institutional requirements.

Author contributions

H-YL and SC: Conception and design, analysis, and interpretation of data, writing the manuscript, critical revision of the manuscript, given final approval; Y-JC, SZ, SW-HC, and P-JL: Data collection, critical revision of the manuscript, given final approval; ZZ: Conception and design, writing the manuscript, critical revision of the manuscript, given final approval.

Funding

The work was supported by the Shanxi Provincial Department of Science and Technology Research Grant (No. 201601D021142); Partially supported by the Sanming Project of Medicine in Shenzhen (No. SZSM201812091); Partially supported by Shanxi Provincial Health Care Committee Research Fund (No. 2020039). Partially supported by Shenzhen Science and Technology Program (JCYJ20220530153604010).

Conflict of interest

The authors declare that the research was conducted in the absence of any commercial or financial relationships that could be construed as a potential conflict of interest.

Publisher's note

All claims expressed in this article are solely those of the authors and do not necessarily represent those of their affiliated organizations, or those of the publisher, the editors and the reviewers. Any product that may be evaluated in this article, or claim that may be made by its manufacturer, is not guaranteed or endorsed by the publisher.

References

- Alió, J. L., Abdou, A. A., Puente, A. A., Zato, M. A., and Nagy, Z. (2014). Femtosecond laser cataract surgery: Updates on technologies and outcomes. *J. Refract. Surg.* 30 (6), 420–427. doi:10.3928/1081597X-20140516-01
- Alpins, N. (2001). Astigmatism analysis by the Alpins method. *J. Cataract. Refract. Surg.* 27 (1), 31–49. doi:10.1016/s0886-3350(00)00798-7
- Baharozian, C. J., Song, C., Hatch, K. M., and Talamo, J. H. (2017). A novel nomogram for the treatment of astigmatism with femtosecond-laser arcuate incisions at the time of cataract surgery. *Clin. Ophthalmol.* 11, 1841–1848. doi:10.2147/OPTH.S141255
- Chang, J. S. M. (2018). Femtosecond laser-assisted astigmatic keratotomy: A review. *Eye Vis.* 5, 6. doi:10.1186/s40662-018-0099-9
- Duffey, R. J., and Leaming, D. (2005). US trends in refractive surgery: 2004 ISRS/AAO survey. *J. Refract. Surg.* 21 (6), 742–748. doi:10.3928/1081-597X-20051101-14
- Ferrer-Blasco, T., Montés-Micó, R., Peixoto-De-Matos, S. C., González-Méijome, J. M., and Cerviño, A. (2009). Prevalence of corneal astigmatism before cataract surgery. *J. Cataract. Refract. Surg.* 35 (1), 70–75. doi:10.1016/j.jcrs.2008.09.027

- Grewal, D. S., Schultz, T., Basti, S., and Dick, H. B. (2016). Femtosecond laser-assisted cataract surgery—current status and future directions. *Surv. Ophthalmol.* 61 (2), 103–131. doi:10.1016/j.survophthal.2015.09.002
- Gudmundsdottir, E., Jonasson, F., Jonsson, V., Stefánsson, E., Sasaki, H., and Sasaki, K. (2000). With the rule' astigmatism is not the rule in the elderly. Reykjavik eye study: A population based study of refraction and visual acuity in citizens of reykjavik 50 years and older. Iceland-Japan Co-working study groups. *Acta Ophthalmol. Scand.* 78 (6), 642–646. doi:10.1034/j.1600-0420.2000.078006642.x
- Hawker, M. J., Madge, S. N., Baddeley, P. A., and Perry, S. R. (2005). Refractive expectations of patients having cataract surgery. *J. Cataract. Refract. Surg.* 31 (10), 1970–1975. doi:10.1016/j.jcrs.2005.03.065
- Holladay, J. T., Cravy, T. V., and Koch, D. D. (1992). Calculating the surgically induced refractive change following ocular surgery. *J. Cataract. Refract. Surg.* 18 (5), 429–443. doi:10.1016/s0886-3350(13)80095-8
- Khan, M. I., and Muhtaseb, M. (2011). Prevalence of corneal astigmatism in patients having routine cataract surgery at a teaching hospital in the United Kingdom. *J. Cataract. Refract. Surg.* 37 (10), 1751–1755. doi:10.1016/j.jcrs.2011.04.026
- Latz, C., Asshauer, T., Rathjen, C., and Mirshahi, A. (2021). Femtosecond-laser assisted surgery of the eye: Overview and impact of the low-energy concept. *Micromachines (Basel)* 12 (2), 122. doi:10.3390/mi12020122
- Lin, H. Y., Chuang, Y. J., Lin, P. J., and Ho, Y. J. (2019). Novel method for preventing cyclorotation in Ziemer Femto LDV Z8 femtosecond laser-assisted cataract surgery with Verion image-guided system. *Clin. Ophthalmol.* 13, 415–419. doi:10.2147/OPTH.S177219
- Lin, H. Y., Chuang, Y. J., and Lin, P. J. (2021). Surgical outcomes with high and low pulse energy femtosecond laser systems for cataract surgery. *Sci. Rep.* 11 (1), 9525. doi:10.1038/s41598-021-89046-1
- Medical A Optics Inc. Iriculator.com. Available at: <http://www.Iriculator.com>.
- Navarro, R., Rozema, J. J., and Tassignon, M. J. (2013). Orientation changes of the main corneal axes as a function of age. *Optom. Vis. Sci.* 90 (1), 23–30. doi:10.1097/OPX.0b013e3182780f88
- Pager, C. K., Mccluskey, P. J., and Retsas, C. (2004). Cataract surgery in Australia: A profile of patient-centred outcomes. *Clin. Exp. Ophthalmol.* 32 (4), 388–392. doi:10.1111/j.1442-9071.2004.00843.x
- Pepose, J. L. H. (2008). Comparing femtosecond lasers. *Cataract Refract. . Surg. Today* 10, 45–51.
- Riau, A. K., Liu, Y. C., Lwin, N. C., Ang, H. P., Tan, N. Y., Yam, G. H., et al. (2014). Comparative study of nJ- and μ J-energy level femtosecond lasers: Evaluation of flap adhesion strength, stromal bed quality, and tissue responses. *Invest. Ophthalmol. Vis. Sci.* 55 (5), 3186–3194. doi:10.1167/iovs.14-14434
- Roberts, H. W., Wagh, V. K., Sullivan, D. L., Archer, T. J., and O'brart, D. P. S. (2018). Refractive outcomes after limbal relaxing incisions or femtosecond laser arcuate keratotomy to manage corneal astigmatism at the time of cataract surgery. *J. Cataract. Refract. Surg.* 44 (8), 955–963. doi:10.1016/j.jcrs.2018.05.027
- Rozema, J. J., Hershko, S., and Tassignon, M. J. (2019). The components of adult astigmatism and their age-related changes. *Ophthalmic Physiol. Opt.* 39 (3), 183–193. doi:10.1111/opo.12616
- Saunders, H. (1986). A longitudinal study of the age-dependence of human ocular refraction--I. Age-dependent changes in the equivalent sphere. *Ophthalmic Physiol. Opt.* 6 (1), 39–46. doi:10.1016/0275-5408(86)90116-x
- Vickers, L. A., and Gupta, P. K. (2016). Femtosecond laser-assisted keratotomy. *Curr. Opin. Ophthalmol.* 27 (4), 277–284. doi:10.1097/ICU.0000000000000267
- Villegas, E. A., Alcón, E., and Artal, P. (2014). Minimum amount of astigmatism that should be corrected. *J. Cataract. Refract. Surg.* 40 (1), 13–19. doi:10.1016/j.jcrs.2013.09.010
- Wang, L., Zhang, S., Zhang, Z., Koch, D. D., Jia, Y., Cao, W., et al. (2016). Femtosecond laser penetrating corneal relaxing incisions combined with cataract surgery. *J. Cataract. Refract. Surg.* 42 (7), 995–1002. doi:10.1016/j.jcrs.2016.04.020
- Yeu, E., Reeves, S. W., Wang, L., and Randleman, J. B. (2013). Resident surgical experience with lens and corneal refractive surgery: Survey of the ASCRS young physicians and residents membership. *J. Cataract. Refract. Surg.* 39 (2), 279–284. doi:10.1016/j.jcrs.2012.09.029
- Yuan, X., Song, H., Peng, G., Hua, X., and Tang, X. (2014). Prevalence of corneal astigmatism in patients before cataract surgery in northern China. *J. Ophthalmol.* 2014, 536412. doi:10.1155/2014/536412



OPEN ACCESS

EDITED BY

Yanwu Xu,
Baidu, China

REVIEWED BY

Bei Zhang,
Sir Run Run Shaw Hospital, China
Ningning Tang,
People's Hospital of Guangxi Zhuang
Autonomous Region, China
Yang Jiang,
Peking Union Medical College Hospital
(CAMS), China

*CORRESPONDENCE

Qixin Cao,
cq6785@163.com
Zhentao Zhu,
jshayzzt@163.com
Qi Dai,
dq@mail.eyec.ac.cn†These authors have contributed equally
to this work

SPECIALTY SECTION

This article was submitted to Molecular
and Cellular Pathology,
a section of the journal
Frontiers in Cell and Developmental
Biology

RECEIVED 09 November 2022

ACCEPTED 21 November 2022

PUBLISHED 01 December 2022

CITATION

Yu X, Jia X, Zhang Z, Fu Y, Zhai J, Chen N,
Cao Q, Zhu Z and Dai Q (2022),
Meibomian gland morphological
changes in ocular herpes zoster patients
based on AI analysis.
Front. Cell Dev. Biol. 10:1094044.
doi: 10.3389/fcell.2022.1094044

COPYRIGHT

© 2022 Yu, Jia, Zhang, Fu, Zhai, Chen,
Cao, Zhu and Dai. This is an open-
access article distributed under the
terms of the [Creative Commons
Attribution License \(CC BY\)](https://creativecommons.org/licenses/by/4.0/). The use,
distribution or reproduction in other
forums is permitted, provided the
original author(s) and the copyright
owner(s) are credited and that the
original publication in this journal is
cited, in accordance with accepted
academic practice. No use, distribution
or reproduction is permitted which does
not comply with these terms.

Meibomian gland morphological changes in ocular herpes zoster patients based on AI analysis

Xinxin Yu^{1†}, Xu Jia^{1†}, Zuhui Zhang¹, Yana Fu¹, Jing Zhai¹,
Naimei Chen², Qixin Cao^{3*}, Zhentao Zhu^{2*} and Qi Dai^{1*}¹School of Ophthalmology and Optometry, The Eye Hospital of Wenzhou Medical University, Wenzhou, China, ²Department of Ophthalmology, Huaian Hospital of Huaian City, Huaian, China, ³Huzhou Traditional Chinese Medicine Hospital Affiliated to Zhejiang University of Traditional Chinese Medicine, Huzhou, China

Varicella-zoster virus (VZV) infections result in a series of ophthalmic complications. Clinically, we also discover that the proportion of dry eye symptoms was significantly higher in patients with herpes zoster ophthalmicus (HZO) than in healthy individuals. Meibomian gland dysfunction (MGD) is one of the main reasons for dry eye. Therefore, we hypothesize that HZO may associate with MGD, affecting the morphology of meibomian gland (MG) because of immune response and inflammation. The purpose of this study is to retrospectively analyze the effect of HZO with craniofacial herpes zoster on dry eye and MG morphology based on an Artificial intelligence (AI) MG morphology analytic system. In this study, 26 patients were diagnosed as HZO based on a history of craniofacial herpes zoster accompanied by abnormal ocular signs. We found that the average height of all MGs of the upper eyelid and both eyelids were significantly lower in the research group than in the normal control group ($p < 0.05$ for all). The average width and tortuosity of all MGs for both upper and lower eyelids were not significantly different between the two groups. The MG density of the upper eyelid and both eyelids were significantly lower in the HZO group than in the normal control group ($p = 0.020$ and $p = 0.022$). Therefore, HZO may lead to dry eye, coupled with the morphological changes of MGs, mainly including a reduction in MG density and height. Moreover, it is important to control HZO early and timely, which could prevent potential long-term severe ocular surface injury.

KEYWORDS

varicella-zoster virus, herpes zoster ophthalmicus, artificial intelligence, convolutional neural network, meibomian gland morphology

Introduction

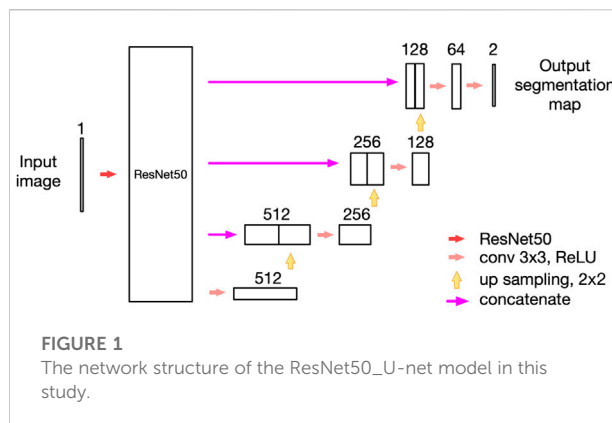
Herpes zoster (HZ) is caused by the reactivation of the latent varicella-zoster virus (VZV) within the sensory ganglia. VZV is a member of the Herpesviridae family that affects sensory neurons following a varicella infection in childhood (chickenpox) (Jeng, 2018). VZV tends to be reactivated when immunosuppression is caused by medication,

illness, or advanced age. Different degrees of eye lesions can occur when the virus invades the ocular branch of the trigeminal nerve. VZV infections result in a series of ophthalmic complications, including involvement of the skin and cornea, as well as the iris, retina, optic nerve, and other cranial nerves. An estimated 10%–20% of people with HZ will develop herpes zoster ophthalmicus (HZO) (Johnson et al., 2015), such as ptosis, blepharitis, keratitis, scleritis, uveitis, glaucoma, diffuse or focal choroiditis, and acute retinal necrosis (Davis and Sheppard, 2019; Niederer et al., 2021). These manifestations are considered to be related to active infection as well as to the host's immune response and inflammation. In addition, HZO is chronic and recurrent, which is different from cutaneous herpes zoster mostly occurs only once in a lifetime.

Clinically, we also found that the proportion of dry eye symptoms, such as dryness, foreign body sensation, redness, and burning, was significantly higher in patients with HZO than in healthy individuals. A case-control study confirmed that patients with a history of herpes simplex (HS) keratitis often experience ocular dryness (Simard-Lebrun et al., 2010; Jabbarvand et al., 2015; Roozbahani and Hammersmith, 2018). We consider that the underlying mechanisms of dry eye owing to HZ infection are the same as those of HS infection, including corneal nerve function abnormalities, chronic inflammation of the ocular surface, and so on.

The Tear Film and Ocular Surface Dry Eye Workshop II in 2017 defined dry eye disease (DED) as a multifactorial disease of the ocular surface characterized by a loss of homeostasis of the tear film and accompanied by ocular symptoms. Tear film instability and hyperosmolarity, ocular surface inflammation and damage, and neurosensory abnormalities play etiological roles in DED (Craig et al., 2017). Evaporative dry eye accounts for the majority of dry eye and is most often caused by meibomian gland dysfunction (MGD). The meibomian gland (MG) is an important sebaceous gland located in the eyelid that secretes lipids, an important component of the tear film (Yu et al., 2016; Stapleton et al., 2017). Abnormalities in the quantity and quality of lipids can damage the lipid layer of the tear film, severely affecting the physicochemical properties of the tear film and reducing its stability, which can lead to evaporative dry eye (Bron et al., 2004; Yeotikar et al., 2016). The function of MG is closely related to its morphology. Studies have shown that the morphology of MG is a sensitive early diagnostic indicator of MGD (Yeotikar et al., 2016; Adil et al., 2019). We hypothesize that HZO may be associated with MGD, similar to many inflammatory diseases, such as Sjögren syndrome, rheumatoid arthritis, and rosacea (Wang et al., 2018), affecting the morphology of MGs because of immune response and inflammation.

Artificial intelligence (AI) analytic system based on a convolutional neural network (CNN) is a relatively new technology in the field of computer vision. CNN is a feedforward neural network that can reduce manual analysis errors and save time when used to manipulate MG images (Rajkomar et al., 2017; Chen et al., 2018a; Deng et al., 2021). Our previous study confirmed that a



CNN-based AI system could be used to analyze MG morphological characteristics efficiently and effectively (Zhang et al., 2022). Therefore, the purpose of this study was to retrospectively analyze the effect of HZO with craniofacial herpes zoster on dry eye and MG morphology based on AI MG morphology analytic system. To the best of our knowledge, this is the first study to investigate the change of MGs morphology after craniofacial herpes zoster.

Materials and methods

Subjects

We conducted a retrospective, self-control study at the Affiliated Eye Hospital of Wenzhou Medical University from December 2018 to May 2021. This study was approved by the Research Ethics Committee of the Eye Hospital, Wenzhou Medical University. All the procedures adhered to the tenets of the Declaration of Helsinki. Informed consent to publish was obtained from all participants before including them in the study.

The patients were diagnosed as HZO based on a history of craniofacial herpes zoster accompanied by herpes zoster keratitis. Participants wearing contact lenses, with chalazion, active nasolacrimal infections, severe systemic diseases, and a history of ocular trauma or surgery were excluded from the study. Basic information was collected, including patients' age at diagnosis of craniofacial herpes zoster, patient age at diagnosis of HZO, interval time from diagnosis of craniofacial herpes zoster to the diagnosis of HZO, duration of follow-up, HZO eye, and gender. The HZO eye was used as the research group, whereas, the contralateral eye was used as the control group.

AI model and morphology analysis

A Keratograph 5M (K5M; Oculus, Wetzlar, Germany) was used to perform meibography scans of the upper and lower

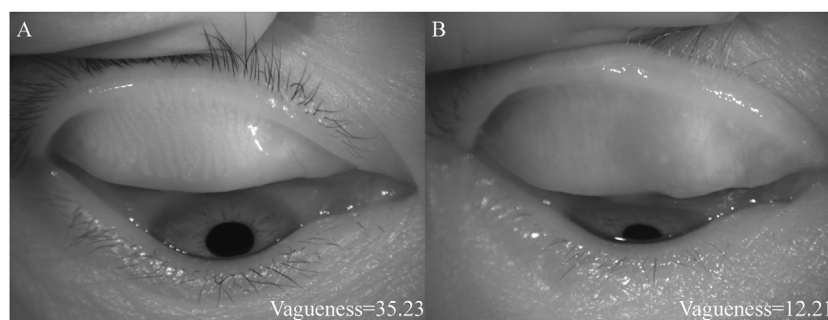


FIGURE 2

The diagrams of different vagueness values. (A) showed the higher vagueness value, (B) showed the lower vagueness value.

eyelids of both eyes. An AI analytical system for MG morphology was used to automatically analyze and calculate the morphological parameters of MGs. The AI model used in this study was a revision of our previously published model (Figure 1) (Zhang et al., 2022). We replaced the 50-layer ResNet (ResNet50) with the max-pooling layers of the U-net model, however, the up-sampling layer remained the same. We called it ResNet50_U-net model, and the AI system achieved 92% accuracy (IoU) and 100% repeatability in MG segmentation for both upper and lower eyelids.

1) Vagueness value (Yin and Gong, 2019)

MGs display intensity in meibography. Firstly, grayscale values of each pixel of meibography were measured by a computer. Secondly, the algorithm of the vagueness value is as follows:

Average grayscale value of MGs = Total grayscale values of MGs/Total pixels of MGs

Average grayscale value of background = (Total grayscale values of tarsus–Total grayscale values of MGs)/(Total pixels of tarsus–Total pixels of MGs)

Vagueness value = Average grayscale value of MGs–Average grayscale value of background

Figure 2 shows the different vagueness values. The higher the value, the clearer the picture.

2) MG morphological indexes

The morphological parameters of MGs included height, width, tortuosity, and density. MG height was the vertical difference between the top and bottom pixels of the MG, and MG width is the area divided by height. The MG density was defined as the ratio of the sum of the area of the MGs to the total area of the tarsus, as follows:

MG density = Sum pixels of all MGs/Total pixels of the tarsus

We defined MG tortuosity as the ratio of the imaginary straight length between the two nodes and the actual length of each MG. The MG perimeter was a pixel at the edge of the MG. Because the outlines of the MGs were irregular, some of them were tilted. Therefore, we used the minimum external rectangle to frame the outline of the MGs and calculate their height.

MG tortuosity = MG perimeter/(2 × height of the minimum external rectangle of the MG)–1

Statistical analysis

Statistical analysis was performed using IBM SPSS 26.0 statistical software. Sample characteristics were summarized using descriptive statistics including means and SD for continuous measures, and frequencies and percentages for categorical measures. The normality of all datasets was tested using the Kolmogorov-Smirnov test. The paired *t*-test or the Wilcoxon signed-rank test was used to compare the differences between HZO eyes and normal eyes. A *p* value < 0.05 was considered significant.

Results

This study included 26 patients who had been diagnosed with HZO. The demographic features were presented in Table 1. The mean age was 54.16 ± 18.59 years when diagnosed as HZO and the majority was male (76.9%). Age stratification into 10-year increments revealed that HZO could occur at any age and increase with age (Figure 3). The mean interval time from craniofacial herpes zoster to HZO was 6.50 months. The tear break-up time (TBUT) and tear meniscus height (TMH) were not statistically different between the research group and the control group.

TABLE 1 Demographic features and baseline characteristics.

Parameters

Age at diagnosis of HZO (years, mean \pm SD)	54.16 \pm 18.59
Gender (n, male/female)	20/6
Eye involved (n, OD/OS)	9/17
Interval time from diagnosis of craniofacial herpes zoster to a diagnosis of HZO (months)	6.50 (3.00, 12.25)
TBUT (seconds)	
Research group	5.76 \pm 2.86
Control group	7.68 \pm 4.92
TMH (mm)	
Research group	0.22 (0.18, 0.26)
Control group	0.19 (0.16, 0.23)

HZO, herpes zoster ophthalmicus; TBUT, tear break-up time; TMH, tear meniscus height.

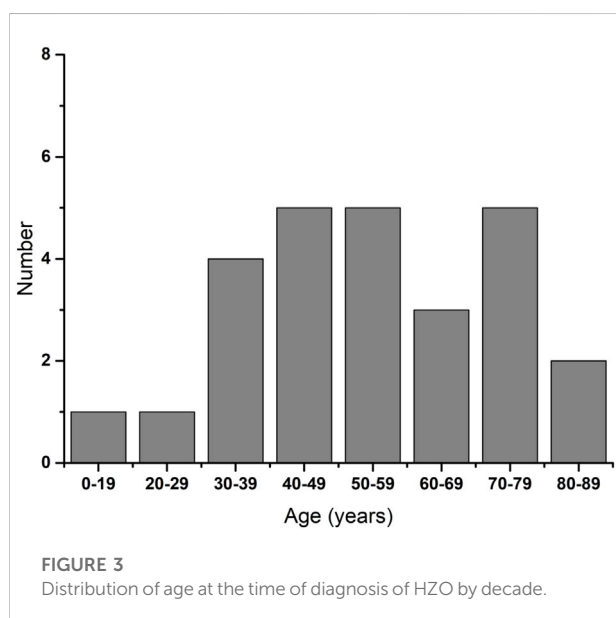
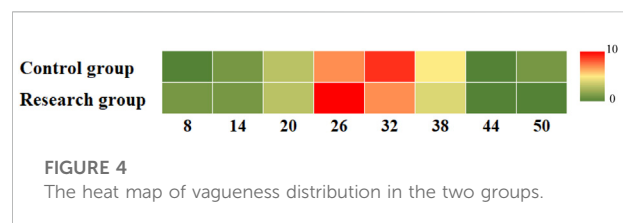


Table 2 showed the MG vagueness value in the research group and normal control group. The vagueness value of the upper eyelid was lower in the research group (27.24 ± 10.32) than in the normal control group (30.54 ± 11.51), but there was no statistical difference ($p > 0.05$). The results of the lower eyelid and both eyelids were consistent with those of the upper eyelid. Figure 4 shows the heat map of vagueness distribution in the two groups.

To understand the effect of VZV infection on MG morphology, we calculated the average height, width, tortuosity, and density of all MGs. The results were presented in Table 3. The average height of all the MGs of the upper eyelid and both eyelids were significantly lower in the research group than in the normal control group ($p < 0.05$ for



all). However, the average height of all MGs of the lower eyelid in the research group (87.52 ± 19.13) was not significantly lower than in the control group (89.90 ± 19.38 ; $p = 0.603$). Except for the average width of all MGs of both eyelids, the average width of all MGs and the average tortuosity of all MGs of the upper eyelid, lower eyelid, and both eyelids were not significantly different between the two groups. The MG density of the upper eyelid and both eyelids was significantly lower in the research group than in the normal control group ($p = 0.020$ and $p = 0.022$, respectively).

We also compared the changes in the average height of all MGs, the average width of all MGs, the average tortuosity of all MGs, and MG density between the two groups during follow-up visits (Figure 5). The results showed that the parameters of MG morphology, such as the average height of all MGs, the average width of all MGs, the average tortuosity of all MGs, and MG density, decreased over time. Although there was no significant difference between the research group and the control group for parameters of MG morphology over time, the parameters of MG morphology in the research group were lower than those in the normal control group as time went on. The results were shown in Figure 5 and Table 4.

The MG morphology parameters, including the average height, width, tortuosity, and MG density, had no significant correlations with TBUT and TMH in either the research group or the control group ($p > 0.05$ for all).

TABLE 2 MG vagueness value in the research group and normal control group.

	Research group	Control group	<i>p</i> value
Vagueness value of the upper eyelid	27.24 ± 10.32	30.54 ± 11.51	0.208
Vagueness value of the lower eyelid	22.76 ± 10.18	23.90 ± 11.92	0.693
Vagueness value of both eyelids	25.00 ± 6.85	27.22 ± 7.49	0.270

TABLE 3 MG parameters of the two study groups.

	Parameters	Research group	Control group	<i>p</i> value
Upper eyelid	Average height of all mgs	126.46 ± 43.81	149.92 ± 41.44	0.014
	Average width of all mgs	21.26 ± 4.76	24.76 ± 8.78	0.058
	Average tortuosity of all mgs	0.43 ± 0.10	0.50 ± 0.23	0.485
	MG density	0.19 ± 0.08	0.22 ± 0.08	0.020
Lower eyelid	Average height of all mgs	87.52 ± 19.13	89.90 ± 19.38	0.603
	Average of all mgs	26.50 ± 5.89	28.00 ± 5.25	0.338
	Average tortuosity of all mgs	0.53 ± 0.15	0.58 ± 0.14	0.174
	MG density	0.16 ± 0.07	0.19 ± 0.08	0.088
Both eyelids	Average height of all mgs	107.07 ± 26.58	119.91 ± 25.76	0.038
	Average width of all mgs	23.93 ± 4.58	26.39 ± 5.43	0.039
	Average tortuosity of all mgs	0.48 ± 0.10	0.52 ± 0.12	0.139
	MG density	0.17 ± 0.06	0.21 ± 0.06	0.022

Figure 6 showed the follow-up results of a child. We investigated the photograph of MG in the early stage of HZO and 2 years after infection. In the early stage, the photograph of MG in the eye with HZO was blurry. However, the photograph of MG became clear when the inflammation was under control. However, it was still more twisted and fragmented than the other eye.

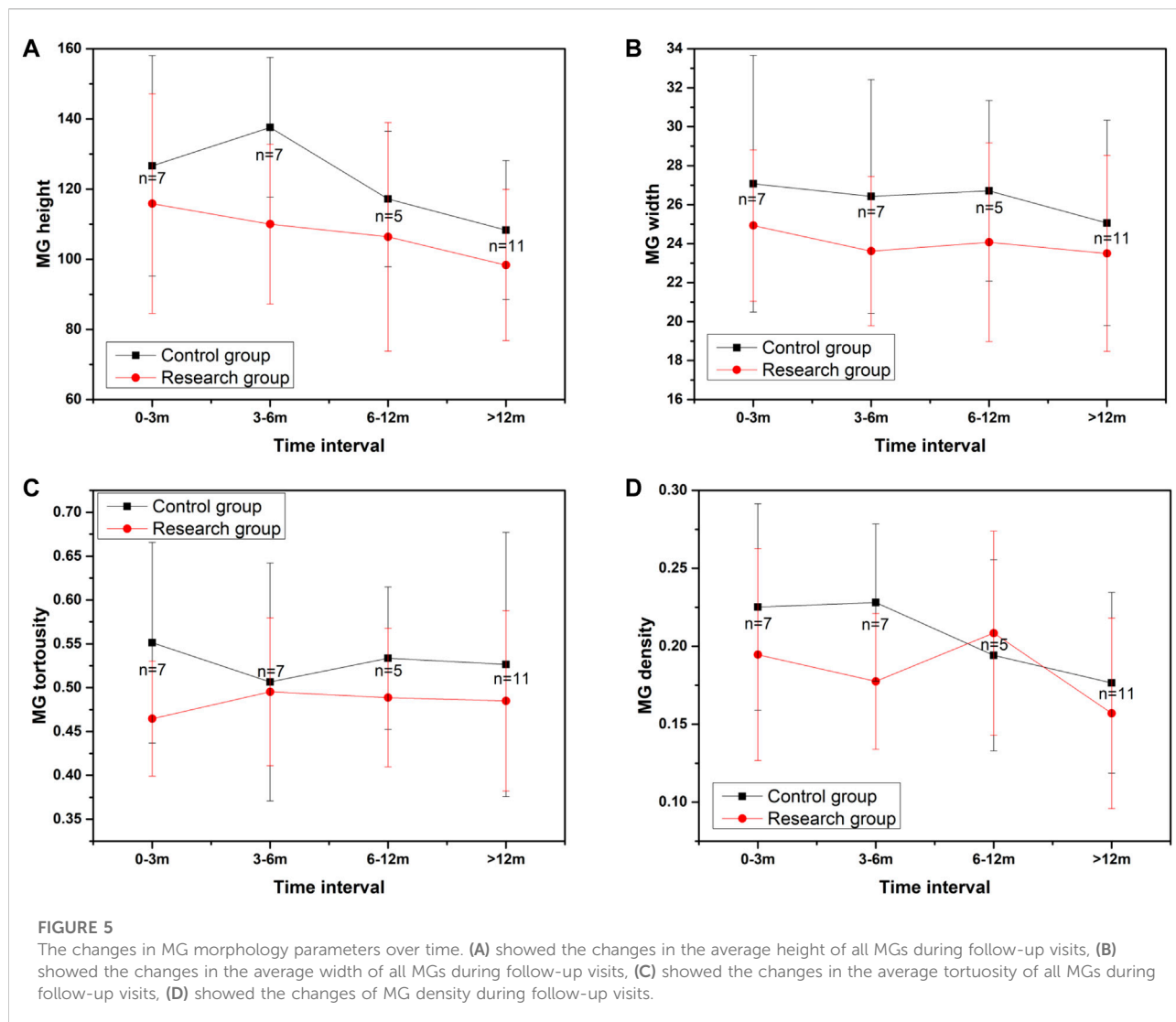
We also investigated the photographs of MG before and after HZO (Figure 7). There was no significant difference between the sides before HZO for the photograph of MG. The MG after HZO became more twisted, and swelled with more fragmentation than the status before HZO.

Discussion

Ocular inflammation may cause typical ocular surface changes in patients with HZO and craniofacial herpes zoster. Additionally, the nerve damage inherent to VZV infection results in a neurotrophic keratopathy with diminished corneal sensation, loss of corneal epithelial integrity, and tear dysfunction (Liesegang, 2008; Ghaznawi et al., 2011). Many studies have shown a strong association between MGD and ocular surface inflammation (Wang et al., 2018). Mathers et al. reported that patients with chronic inflammation, such as blepharitis and conjunctivitis, experienced a greater loss of

MGs (Mathers et al., 1991; Mathers and Billborough, 1992). Thus, we hypothesized that HZ infection associated ocular surface inflammation might cause peri-glandular inflammation and subsequent MG loss.

MG atrophy causes abnormalities in the quantity and quality of lipids, which can damage the lipid layer of the tear film and lead to MGD. A detailed analysis of MGs morphology is important to determine the extent and severity of MGD (Deng et al., 2021). Most AI-assisted morphologic studies of the MGs have focused on the MGs grading system, and few have quantitatively discussed the various morphological characteristics, such as tortuosity and density. The present study utilized an AI system based on a convolutional neural network, to automatically analyze MG morphology, including the height, width, tortuosity, density, and vagueness value of the MGs. Currently, studies on MG morphology have focused on the tortuosity of MGs, whereas studies on MG density are relatively rare. Xiao et al. (2019) found that meiboscore, gland distortion, and MG length had an excellent ability to differentiate between patients with MGD and healthy subjects. They considered that structural MG changes were closely associated with MGD progression. Shirakawa et al. (2013) compared MG morphology between children and adults and confirmed that MG density in the upper eyelid was significantly greater in children than in adults. Shirakawa et al. (2013) defined MG



density as the number of MGs divided by eyelid width. In our study, MG density was calculated as the ratio of the sum of the area of the MGs to the total area of the tarsus, which is a continuous, objective, quantitative index that is more accurate than MG grading and avoids subjective errors. We compared the MG morphology (height, width, tortuosity, density, and vagueness value of the MGs) with and without HZO using this novel AI system.

Some morphological characteristics of MGs, such as length, width, and shape irregularity, have been suggested to be valuable for assessing MGD. We found the average height of all MGs and MG density in the upper eyelid and both eyelids were significantly decreased in the research group compared to the normal controls (Table 3). Similar to our study, some research groups had described other changes in MG morphology, such as MG thickness and length, in patients with dry eye. A related study found that the number of distorted glands and MG thickness, density, and length were

inversely correlated with meibum expressibility (Xiao et al., 2019). However, in our study, the average width of all MGs and average tortuosity of all MGs of the upper eyelid, the lower eyelid, and both eyelids were not significantly different between the research group and the normal control group (Table 3). In our previous study, the early stage of MGD showed an increase in tortuosity, while in patients with more severe MGD, the change in tortuosity was no longer noticeable and the density decreased significantly (Lin et al., 2020). In the present study, we assumed that ocular inflammation caused by HZO was severe, thus leading to severe MGD associated MGs shortening and decreased MGs density, rather than increased MG tortuosity. Furthermore, conjunctival inflammation and edema could affect vagueness value by reducing transmission of infrared light. We also calculated the vagueness value in the research group and normal control group. The research group was lower than the normal control group, but there was no statistical difference. We speculated the cause that some

TABLE 4 The changes in MG morphology parameters over time.

Parameters	Time interval	Research group	Control group	<i>p</i> value
MG height	0–3 min	115.85 ± 31.32	126.62 ± 31.41	0.270
	3–6 min	110.02 ± 22.78	137.60 ± 19.91	0.058
	6–12 min	106.39 ± 32.61	117.20 ± 19.31	0.344
	>12 min	98.34 ± 21.53	108.31 ± 19.81	0.347
MG width	0–3 min	24.93 ± 3.88	27.07 ± 6.58	0.247
	3–6 min	23.62 ± 3.83	26.43 ± 6.00	0.280
	6–12 min	24.07 ± 5.10	26.71 ± 4.63	0.343
	>12 min	23.50 ± 5.03	25.06 ± 5.27	0.484
MG tortuosity	0–3 min	0.46 ± 0.07	0.55 ± 0.11	0.075
	3–6 min	0.50 ± 0.08	0.51 ± 0.14	0.870
	6–12 min	0.49 ± 0.08	0.53 ± 0.08	0.333
	>12 min	0.48 ± 0.10	0.53 ± 0.15	0.439
MG density	0–3 min	0.19 ± 0.07	0.23 ± 0.07	0.067
	3–6 min	0.18 ± 0.04	0.23 ± 0.05	0.108
	6–12 min	0.21 ± 0.07	0.19 ± 0.06	0.666
	>12 min	0.16 ± 0.06	0.18 ± 0.06	0.383

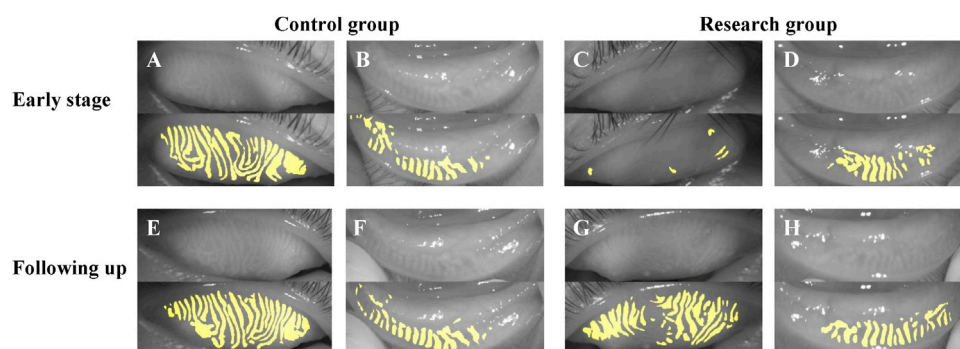


FIGURE 6

The follow-up results of a child. (A–D) showed the photograph of MG in the early stage of HZO, and (E–H) showed the photographs of MG following 2 years after HZ infection. (A,B,E,F) were the control eyes without HZ infection, and (C,D,G,H) were the research eyes with HZ infection.

patients had a certain period of time from the onset of the disease and the conjunctival inflammation had subsided when the meibographs were taken. This phenomenon was clearly observed in meibographs of some patients followed from the early stage of the disease.

In addition, we also compared the changes in MG morphology parameters over time, such as the average height of all MGs, the average width of all MGs, the average tortuosity of all MGs, and MG density. The results showed that the parameters of MG morphology were decreasing as time went on. Although there was no statistical difference regardless of the presence or absence of

HZO, the parameters of MG morphology in the research group were always lower than those in the normal control at different periods. We considered the possible reason was the insufficient sample size for each period. We plan to include patients with ocular herpes simplex in further studies. The population of ocular herpes simplex patients similar to HZO is larger and more common.

What's more, we observed two special cases (Figures 6, 7). Figure 6 showed the follow-up results for a child. In the early stages of HZO, the photograph of MG on the side of the HZO was blurry. However, the meibography images became clear when inflammation was controlled. This suggests that

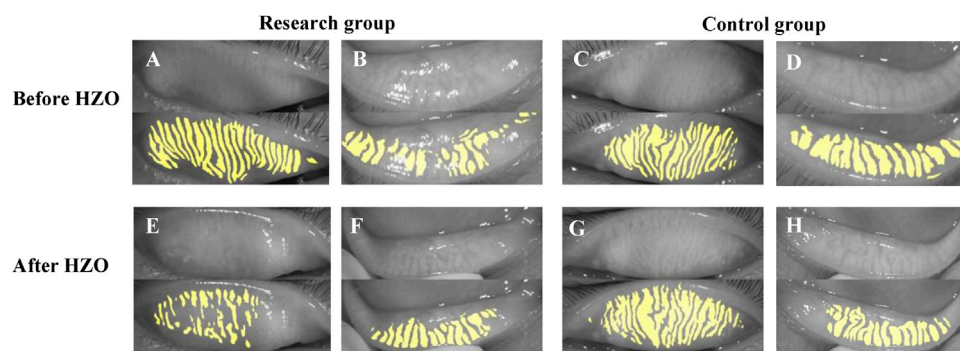


FIGURE 7

The photograph of MG before and after HZO. (A–D) showed the photograph of MG before HZO, and (E–H) showed the photograph of MG after HZO. (A,B,E,F) were the research eyes with HZ infection, and (C,D,G,H) were the control eyes without HZ infection.

palpebral conjunctival edema caused by inflammation, leading to blurred meibography images and lower optical density also plays an important role in MG density decrease (Chen et al., 2018b). Figure 7 showed that there was no significant difference between the eye with HZO and the normal contralateral eye in the photograph of MG before the attack of craniofacial herpes zoster. After the onset of craniofacial herpes zoster, the MGs became twisted, swollen, and fragmented in the HZO eye. Comparing these two cases, we believe it is important to control HZO early. Early and timely control of inflammation could prevent potential complications, such as peri-glandular inflammation, loss of MGs, dry eye, and so on.

The present study has some limitations. The sample size was small and the age span of the patients was large, which might be the reason for the lack of statistically significant differences in parameters between the research group and the normal control group. The changes in MGs over time in HZO patients should be verified in a future study with a larger sample.

Conclusion

In conclusion, similar to many ocular surface inflammatory diseases, HZO may lead to dry eye, and be accompanied by morphological changes of MGs, mainly including a reduction in MG density and height. Moreover, it is important to control HZO early and timely, which could prevent potential long-term severe ocular surface injury.

Data availability statement

The raw data supporting the conclusion of this article will be made available by the authors, without undue reservation.

Ethics statement

The studies involving human participants were reviewed and approved by the Research Ethics Committee of the Eye Hospital, Wenzhou Medical University. Written informed consent to participate in this study was provided by the participants' legal guardian/next of kin.

Author contributions

XY and XJ contributed equally to this work. XY drafted the manuscript and collected patient information, XJ analyzed and interpreted the patient data, ZZ and YF collected data, JZ and NC edited the patients' meibography images, QD, ZZ, and QC critically revised the manuscript for intellectual content and supervised the project. All authors read and approved the final manuscript.

Funding

This work was supported in part by the Zhejiang Provincial Medical and Health Science Technology Program of Health and Family Planning Commission under Grant (2022PY074 and 2020KY191), and the Project Supported by the Scientific Research Fund of Zhejiang Provincial Education Department (Y202147994).

Conflict of interest

The authors declare that the research was conducted in the absence of any commercial or financial relationships that could be construed as a potential conflict of interest.

Publisher's note

All claims expressed in this article are solely those of the authors and do not necessarily represent those of their affiliated

organizations, or those of the publisher, the editors and the reviewers. Any product that may be evaluated in this article, or claim that may be made by its manufacturer, is not guaranteed or endorsed by the publisher.

References

- Adil, M. Y., Xiao, J., Olafsson, J., Chen, X., Lagali, N. S., Raeder, S., et al. (2019). Meibomian gland morphology is a sensitive early indicator of meibomian gland dysfunction. *Am. J. Ophthalmol.* 200, 16–25. doi:10.1016/j.ajo.2018.12.006
- Bron, A. J., Tiffany, J. M., Gouveia, S. M., Yokoi, N., and Voon, L. W. (2004). Functional aspects of the tear film lipid layer. *Exp. Eye Res.* 78 (3), 347–360. doi:10.1016/j.exer.2003.09.019
- Chen, L. C., Papandreou, G., Kokkinos, I., Murphy, K., and Yuille, A. L. (2018a). DeepLab: Semantic image segmentation with deep convolutional nets, atrous convolution, and fully connected CRFs. *IEEE Trans. Pattern Anal. Mach. Intell.* 40 (4), 834–848. doi:10.1109/TPAMI.2017.2699184
- Chen, W., Deng, Y., Jiang, H., Wang, J., Zhong, J., Li, S., et al. (2018b). Microvascular abnormalities in dry eye patients. *Microvasc. Res.* 118, 155–161. doi:10.1016/j.mvr.2018.03.015
- Craig, J. P., Nichols, K. K., Akpek, E. K., Caffery, B., Dua, H. S., Joo, C. K., et al. (2017). TFOS DEWS II definition and classification report. *Ocul. Surf.* 15 (3), 276–283. doi:10.1016/j.jtos.2017.05.008
- Davis, A. R., and Sheppard, J. (2019). Herpes zoster ophthalmicus review and prevention. *Eye Contact Lens* 45 (5), 286–291. doi:10.1097/ICL.0000000000000591
- Deng, Y., Wang, Q., Luo, Z., Li, S., Wang, B., Zhong, J., et al. (2021). Quantitative analysis of morphological and functional features in meibography for meibomian gland dysfunction: Diagnosis and grading. *EClinicalMedicine* 40, 101132doi:10.1016/j.eclinm.2021.101132
- Ghaznawi, N., Virdi, A., Dayan, A., Hammersmith, K. M., Rapuano, C. J., Laibson, P. R., et al. (2011). Herpes zoster ophthalmicus: Comparison of disease in patients 60 years and older versus younger than 60 years. *Ophthalmology* 118 (11), 2242–2250. doi:10.1016/j.ophtha.2011.04.002
- Jabbarvand, M., Hashemian, H., Khodaparast, M., Rafatnejad, A., Beheshtnejad, A., and Salami, A. (2015). Do unilateral herpetic stromal keratitis and neurotrophic ulcers cause bilateral dry eye? *Cornea* 34 (7), 768–772. doi:10.1097/ICO.0000000000000425
- Jeng, B. H. (2018). Herpes zoster eye disease: New ways to combat an old foe? *Ophthalmology* 125 (11), 1671–1674. doi:10.1016/j.ophtha.2018.08.029
- Johnson, J. L., Amzat, R., and Martin, N. (2015). Herpes zoster ophthalmicus. *Prim. Care* 42 (3), 285–303. doi:10.1016/j.pop.2015.05.007
- Liesegang, T. J. (2008). Herpes zoster ophthalmicus natural history, risk factors, clinical presentation, and morbidity. *Ophthalmology* 115 (2), S3–S12. doi:10.1016/j.ophtha.2007.10.009
- Lin, X., Fu, Y., Li, L., Chen, C., Chen, X., Mao, Y., et al. (2020). A novel quantitative index of meibomian gland dysfunction, the meibomian gland tortuosity. *Transl. Vis. Sci. Technol.* 9 (9), 34. doi:10.1167/tvst.9.9.34
- Mathers, W. D., and Billborough, M. (1992). Meibomian gland function and giant papillary conjunctivitis. *Am. J. Ophthalmol.* 114 (2), 188–192. doi:10.1016/s0002-9394(14)73983-2
- Mathers, W. D., Shields, W. J., Sachdev, M. S., Petroll, W. M., and Jester, J. V. (1991). Meibomian gland dysfunction in chronic blepharitis. *Cornea* 10 (4), 277–285. doi:10.1097/00003226-199107000-00001
- Niederer, R. L., Meyer, J. J., Liu, K., and Danesh-Meyer, H. V. (2021). Herpes zoster ophthalmicus clinical presentation and risk factors for loss of vision. *Am. J. Ophthalmol.* 226, 83–89. doi:10.1016/j.ajo.2021.02.002
- Rajkumar, A., Lingam, S., Taylor, A. G., Blum, M., and Mongan, J. (2017). High-throughput classification of radiographs using deep convolutional neural networks. *J. Digit. Imaging* 30 (1), 95–101. doi:10.1007/s10278-016-9914-9
- Rozebani, M., and Hammersmith, K. M. (2018). Management of herpes simplex virus epithelial keratitis. *Curr. Opin. Ophthalmol.* 29 (4), 360–364. doi:10.1097/ICU.0000000000000483
- Shirakawa, R., Arita, R., and Amano, S. (2013). Meibomian gland morphology in Japanese infants, children, and adults observed using a mobile pen-shaped infrared meibography device. *Am. J. Ophthalmol.* 155 (6), 1099–1103. doi:10.1016/j.ajo.2013.01.017
- Simard-Lebrun, A., Boisjoly, H., Al-Saadi, A., Choremis, J., Mabon, M., and Chagnon, M. (2010). Association between unilateral quiescent stromal herpetic keratitis and bilateral dry eyes. *Cornea* 29 (11), 1291–1295. doi:10.1097/ICO.0b013e3181cbf9f5
- Stapleton, F., Alves, M., Bunya, V. Y., Jalbert, I., Lekhanont, K., Malet, F., et al. (2017). TFOS DEWS II epidemiology report. *Ocul. Surf.* 15 (3), 334–365. doi:10.1016/j.jtos.2017.05.003
- Wang, C. Y., Ho, R. W., Fang, P. C., Yu, H. J., Chien, C. C., Hsiao, C. C., et al. (2018). The function and morphology of meibomian glands in patients with thyroid eye disease: A preliminary study. *BMC Ophthalmol.* 18 (1), 90. doi:10.1186/s12886-018-0763-9
- Xiao, J., Adil, M. Y., Olafsson, J., Chen, X., Utheim, O. A., Raeder, S., et al. (2019). Diagnostic test efficacy of meibomian gland morphology and function. *Sci. Rep.* 9 (1), 17345doi:10.1038/s41598-019-54013-4
- Yeotikar, N. S., Zhu, H., Markoulli, M., Nichols, K. K., Naduvilath, T., and Papas, E. B. (2016). Functional and morphologic changes of meibomian glands in an asymptomatic adult population. *Invest. Ophthalmol. Vis. Sci.* 57 (10), 3996–4007. doi:10.1167/iops.15-18467
- Yin, Y., and Gong, L. (2019). The quantitative measuring method of meibomian gland vagueness and diagnostic efficacy of meibomian gland index combination. *Acta Ophthalmol.* 97 (3), 403–409. doi:10.1111/aos.14052
- Yu, T., Shi, W. Y., Song, A. P., Gao, Y., Dang, G. F., and Ding, G. (2016). Changes of meibomian glands in patients with type 2 diabetes mellitus. *Int. J. Ophthalmol.* 9 (12), 1740–1744. doi:10.18240/ijo.2016.12.06
- Zhang, Z., Lin, X., Yu, X., Fu, Y., Chen, X., Yang, W., et al. (2022). Meibomian gland density: An effective evaluation index of meibomian gland dysfunction based on deep learning and transfer learning. *J. Clin. Med.* 11 (9), 2396. doi:10.3390/jcm11092396



OPEN ACCESS

EDITED BY
Weihua Yang,
Jinan University, China

REVIEWED BY
Bilian Ke,
Shanghai General Hospital, China
Qi Dai,
Wenzhou Medical University, China

*CORRESPONDENCE
Yongjin Zhou,
yjzhou@szu.edu.cn
Ying Jie,
jie_yingcn@aliyun.com

[†]The first two authors,
Deng and Tian, contributed equally to
this work

SPECIALTY SECTION
This article was submitted to Molecular
and Cellular Pathology,
a section of the journal
Frontiers in Cell and Developmental
Biology

RECEIVED 12 October 2022
ACCEPTED 14 November 2022
PUBLISHED 05 December 2022

CITATION
Deng X, Tian L, Zhang Y, Li A, Cai S,
Zhou Y and Jie Y (2022), Is histogram
manipulation always beneficial when
trying to improve model performance
across devices? Experiments using a
Meibomian gland segmentation model.
Front. Cell Dev. Biol. 10:1067914.
doi: 10.3389/fcell.2022.1067914

COPYRIGHT
© 2022 Deng, Tian, Zhang, Li, Cai, Zhou
and Jie. This is an open-access article
distributed under the terms of the
[Creative Commons Attribution License
\(CC BY\)](https://creativecommons.org/licenses/by/4.0/). The use, distribution or
reproduction in other forums is
permitted, provided the original
author(s) and the copyright owner(s) are
credited and that the original
publication in this journal is cited, in
accordance with accepted academic
practice. No use, distribution or
reproduction is permitted which does
not comply with these terms.

Is histogram manipulation always beneficial when trying to improve model performance across devices? Experiments using a Meibomian gland segmentation model

Xianyu Deng^{1,2†}, Lei Tian^{3,4†}, Yinghuai Zhang^{1,2}, Ao Li^{3,4},
Shangyu Cai^{1,2}, Yongjin Zhou^{1,2*} and Ying Jie^{3,4*}

¹Health Science Center, School of Biomedical Engineering, Shenzhen University, Shenzhen, China, ²Marshall Laboratory of Biomedical Engineering, Shenzhen, China, ³Beijing Ophthalmology and Visual Sciences Key Laboratory, Beijing Tongren Eye Center, Beijing Tongren Hospital, Beijing Institute of Ophthalmology, Capital Medical University, Beijing, China, ⁴Ophthalmology and Visual Sciences Key Laboratory, Beijing, China

Meibomian gland dysfunction (MGD) is caused by abnormalities of the meibomian glands (MG) and is one of the causes of evaporative dry eye (DED). Precise MG segmentation is crucial for MGD-related DED diagnosis because the morphological parameters of MG are of importance. Deep learning has achieved state-of-the-art performance in medical image segmentation tasks, especially when training and test data come from the same distribution. But in practice, MG images can be acquired from different devices or hospitals. When testing image data from different distributions, deep learning models that have been trained on a specific distribution are prone to poor performance. Histogram specification (HS) has been reported as an effective method for contrast enhancement and improving model performance on images of different modalities. Additionally, contrast limited adaptive histogram equalization (CLAHE) will be used as a preprocessing method to enhance the contrast of MG images. In this study, we developed and evaluated the automatic segmentation method of the eyelid area and the MG area based on CNN and automatically calculated MG loss rate. This method is evaluated in the internal and external testing sets from two meibography devices. In addition, to assess whether HS and CLAHE improve segmentation results, we trained the network model using images from one device (internal testing set) and tested on images from another device (external testing set). High DSC (0.84 for MG region, 0.92 for eyelid region) for the internal test set was obtained, while for the external testing set, lower DSC (0.69–0.71 for MG region, 0.89–0.91 for eyelid region) was obtained. Also, HS and CLAHE were reported to have no statistical improvement in the segmentation results of MG in this experiment.

KEYWORDS

Meibomian gland, segmentation, histogram, image, model performance

Introduction

Meibomian glands (MG) are special sebaceous gland located on the tarsal plate of eye (Erich et al., 2011). They produce meibum to prevent tear from over evaporation (Nichols et al., 2011), maintain the surface tension of the tear film, and trap tears between its oily edge and the eyeball. Healthy MG are elongated in shape, arrange in parallel and throughout the entire tarsal plate (Djalilian, 2018). Functional and/or structural problem of MG may cause meibomian gland dysfunction (MGD) (Driver and Lemp, 1996). MGD is a chronic, diffuse abnormality of the meibomian glands, commonly characterized by terminal duct obstruction and/or qualitative/quantitative changes in the glandular secretion (Den et al., 2011; Nichols et al., 2011). MGD often leads to tear film alteration, ocular surface disease, and is the leading cause of evaporative dry eye (Turgut et al., 2018), which can seriously affect the patient's life and increase the global public health and financial burden (McDonald et al., 2016).

Meibomian gland area loss is an important index to evaluate MGD (Arita et al., 2014). MGD can be directly observed using meibography, which is an optical imaging technique allowing visualizing MG morphology *in vivo* (Pult and Nichols, 2012). Recently, many non-contact infrared meibography methods were developed, making the MGD diagnosis process more patient-friendly and less time-consuming (Pult and Riede-Pult, 2012; Wong et al., 2019; Xiao et al., 2020; Hwang et al., 2021). These devices allow users to capture high-resolution images of meibomian glands in a short period of time, which can provide sufficient experimental material for MG analysis. Quantification of the area of meibomian glands loss is of importance when assessing MGD. To date, automatic methods based on image processing techniques have been developed for the automated assessment and classification of MGD (Arita et al., 2014; Celik et al., 2013; Koprowski et al., 2016; Koprowski et al., 2017; Liang et al., 2017; Llorens-Quintana et al., 2019; Pult and Riede-Pult, 2013; Xiao et al., 2021). In recent years, MGD automatic analysis methods based on convolutional neural network (CNN) have been developed rapidly. These works automatically segment the eyelid and MG, and calculate the loss rate and analyze the morphological parameters of MG (Wang et al., 2019). In order to promote the segmentation performance of MG, contrast limited adaptive histogram equalization (CLAHE) will be used as an image preprocessing step to enhance the contrast of MG images (Prabhu et al., 2020; Dai et al., 2021).

However, the MG images used in these works were acquired from a single device. The preset parameters of the method or the trained model are for the specific data domain used in the experiment. When testing these methods with images from other distribution domains (such as different image modalities, or different acquisition devices), a lower performance is usually obtained (Yan et al., 2019). Such

problem is called "distribution shift" (Jo and Bengio, 2017). To reduce the performance gap, an effective method is to reduce the distribution domain distance of the data. Training a generative adversarial network (GAN) to generate fake images between two different domains is a common method to improve the generalization of the model to data from different domains (Perone et al., 2019; Yan et al., 2019); but it requires a large number of training samples. In some medical image processing tasks, histogram specification (HS) has been reported as an effective method for contrast enhancement and improving model performance on images of different modalities, such as between MRI and CT images (Naseem et al., 2021).

In this study, we focus on two open questions in the field of automated meibomian gland analysis:

- 1) In the CNN-based MG analysis method, does CLAHE improve the network performance?
- 2) Can HS improve the performance of models trained with data collected from a single device on cross-device data?

This study aims at developing and validating an MG segmentation method based on CNN. Whether HS and CLAHE as preprocessing methods can effectively improve the segmentation performance of the CNN model was also investigated in this study. MG images captured from different devices were divided into different testing sets based on different preprocessing methods, and then segmented by CNN model to calculate MG loss rate. All the results will be compared with the ground-truth by the clinicians.

Related works

Histogram specification (HS) enhances the brightness and contrast of the input image and transforms the input image into an image with a similar shape to the template histogram. HS has the advantage of simplicity and low computational cost (Xiao et al., 2018). HS is very common in the preprocessing stage of medical images. HS is used to match the histogram of the input image to the template image to initialize and avoid gradient explosion before using CNN to segment the kidney based on CT images (da Cruz et al., 2020). Naseem et al. (2021) based on HS to enhance images of different modalities. They enhance low-contrast CT images based on MRI images based on the second-order distribution.

The raw MG image often has low contrast. In other word, the pixel intensity of glands and background have little difference, as a result, it is difficult for the observer to separate the glands from background, especially when the image is blur. CLAHE is applied for the meibography image enhancement. CLAHE enhances an image by limiting the height of the local region histogram, such as a 64 pixels neighborhood block, thereby overcome the global uneven illumination and noise amplification problem. CLAHE is

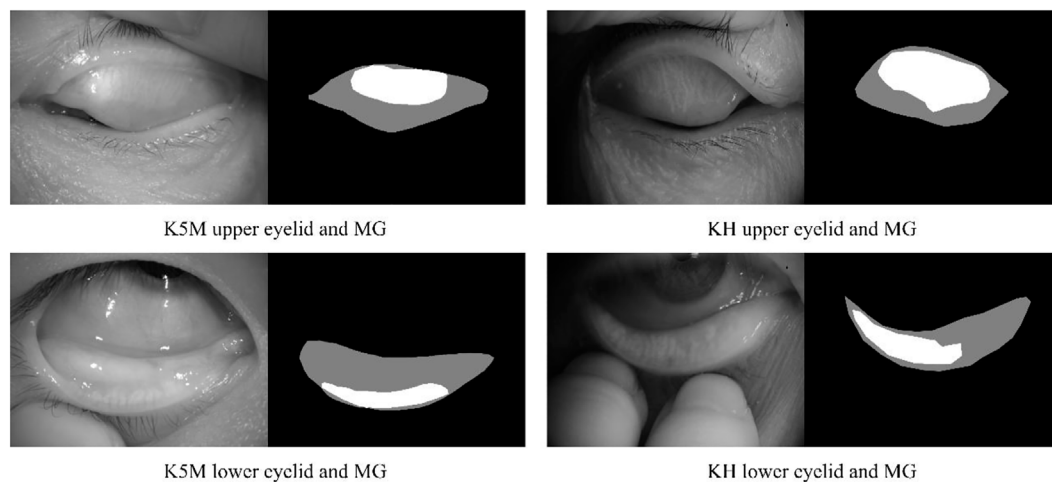


FIGURE 1

Examples of upper and lower eyelids and MG, and ground-truth for segmentation mask. Black, gray, and white pixel represent the background, eyelid region and MG region, respectively.

often used as a preprocessing method to enhance the performance of MG segmentation (Prabhu et al., 2020; Dai et al., 2021).

Materials

This study involves 287 subjects (age: 56.1 ± 17.2 years old, 83 men and 204 women) collected by Beijing Tongren Hospital. The purpose and possible consequences of the study were explained to all involved subjects. Exclusion criteria included 1) ocular allergies, 2) history of ocular surgery, 3) history of ocular trauma, 4) other eye diseases, 5) long term or frequent contact lens use and 6) Any other eye or systemic disease known to affect the tear film. Excluded images include: 1) Images included something other than the eyelids and their surrounding tissues were, 2) Images were not sufficiently clear for automatic analysis were excluded. 3) Patients' eyes exhibited excessive meibomian lipid secretion. The study was approved by the Ethical Committee of the Beijing Tongren Hospital and was conducted in accordance with the tenets of the Declaration of Helsinki. A total of 1,074 images were collected by professional clinicians, including 888 MG images collected from Keratograph 5M (K5M; OCULUS Optikgeräte GmbH, Wetzlar, Germany) and 186 from KANGHUA DED-1L (KH). Note that I_{k5m} is used to represent the image set collected from K5M, and I_{kh} is used to represent the image collected from KH. Then, I_{k5m} was divided into two sets, 648 for training set used for neural networks training, and 240 for testing set to appraise the algorithm performance. And I_{kh} is used as an external testing set to test the performance of our models on data from different device. It should be noted that as a retrospective study, some of the

287 patients have received treatment and collected follow-up data at different times, therefore there are more meibomian gland images than the subject number.

The ground-truth annotation was completed by a senior clinician using imageLabeler application in MATLAB (9.5.0.944444, R2018b, Java 1.8.0_152-b16). For labeling the eyelid region, the upper edge is defined at the opening of the gland, the lower edge is defined at the edge of proximal tarsal plate, and the horizontal borders is defined at the top and bottom borders intersected (Wang et al., 2019). Value 1 and 2 are used to denote the eyelid region and the MG region, respectively. Examples are shown in Figure 1.

Methods

Image preprocessing

Images I_{kh} and I_{k5m} acquired by two different devices are involved in this study. The grayscale histograms of the two image sets are significantly different, as shown in the figure. HS is applied to convert the grayscale density so that I_{kh} can be matched to the histogram of I_{k5m} . Specifically, the brightness distribution of each image in I_{k5m} is counted, and the results are averaged to obtain an average histogram H_{k5m} representing I_{k5m} . Then, each image of I_{kh} is matched to H_{k5m} using HS, resulting in a similar pixel distribution to I_{k5m} , as shown. I_{kh-HS} is used to represent I_{kh} after HS preprocessing. To explore the effect of CLAHE on segmentation performance, I_{k5m} , I_{kh} and I_{kh-HS} were preprocessed with CLAHE. $I_{k5m-CLAHE}$, $I_{kh-CLAHE}$ and $I_{kh-HS-CLAHE}$ are used to represent each set of images processed using CLAHE.

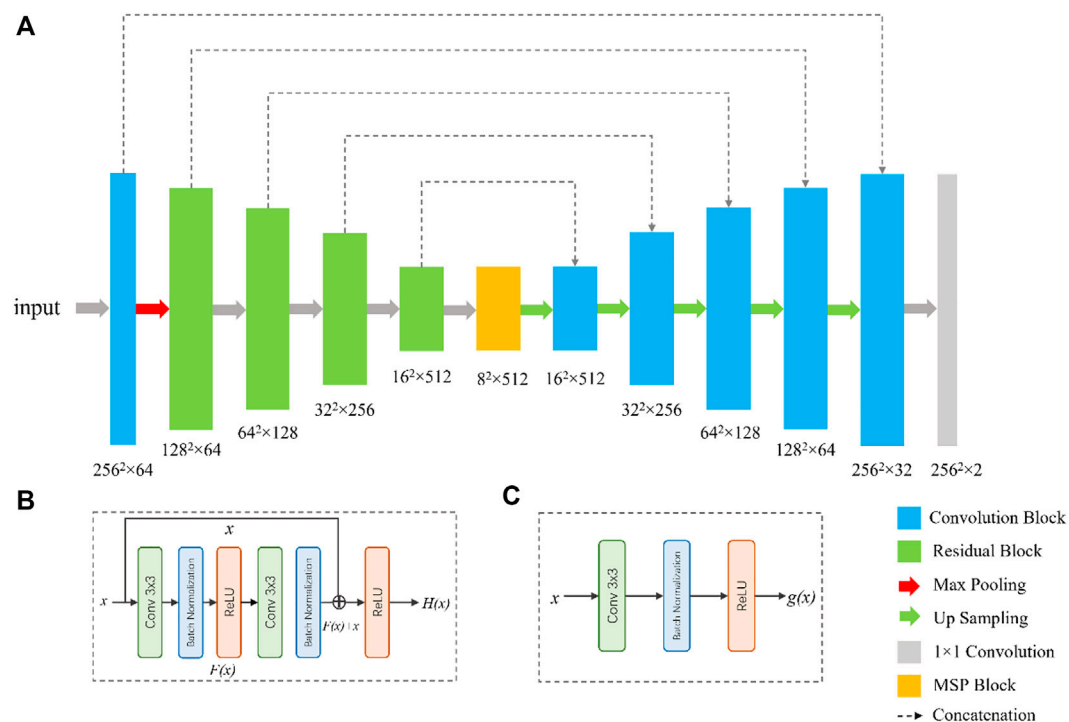


FIGURE 2

Network architecture for the segmentation of tear meniscus. The network (A) is a U-Net-like architecture with a modified ResNet-34 as encoder. The bottom of the network is multi-scale perception block (MSP). (B) and (C) are the illustrations of the residual block and convolution block, respectively.

MG segmentation network

To segment the eyelid region and MG region, we constructed a compact CNN based on U-Net architecture (Ronneberger et al., 2015). The segmentation network contains an encoder and a decoder, as shown in Figure. Specifically, we use ResNet-34 and remove its fully connection layers as the backbone of our network (He et al., 2016). Residual blocks in ResNet-34 use shortcuts to extract features more efficiently, transfer gradients and prevent gradients vanishing in deep layers. A residual block is consisted of convolution layers, batch normalization layers and rectified linear unit (ReLU), as shown in Figure 2.

Inspired by CE-Net (Zaiwang et al., 2019), we add a multi-scale perception block (MSP) between encoder and decoder, as shown in Figure 3. In order to save calculation cost, MSP realizes multi-scale convolution operation through dilated convolution, as shown in Figure 3. Convolution kernels of different sizes have different receptive fields, allowing more features to be captured. In this study, MSP contains 3×3 , 5×5 , and 7×7 convolution layers, which are realized by 3×3 dilatation convolution with dilated rate 1, 2, and 3, respectively. Finally, the feature graph is integrated by 1×1 convolution. After each convolutional layer, ReLU is added as activation function to increase the nonlinearity of the network.

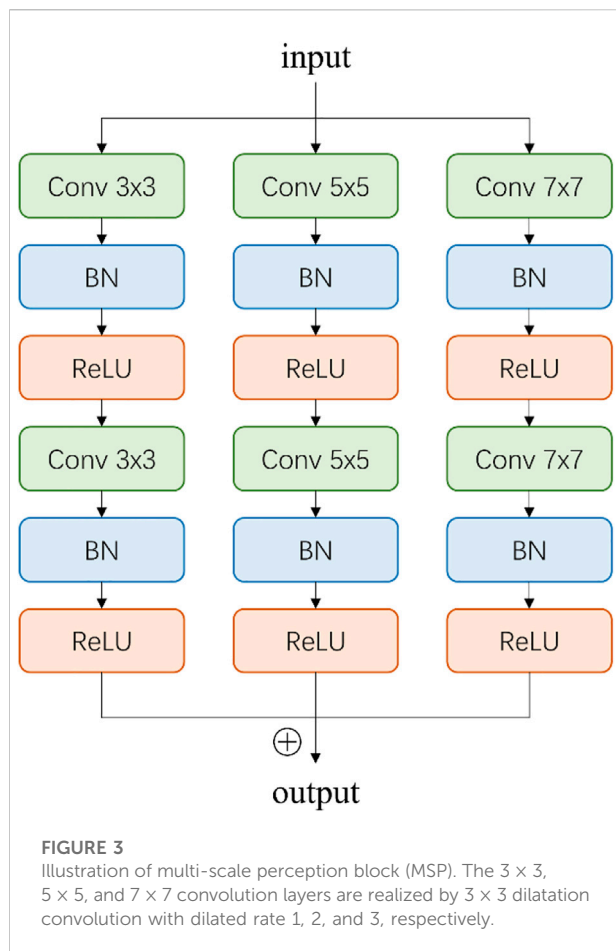
In the decoder, each step consists of a bilinear interpolation operation, which is responsible for upscaling the feature map resolution by four times, followed by two convolutional blocks (Figure 2) and a concatenation with the corresponding feature maps from the encoder. At the final layer, a 1×1 padded convolutional layer was used to map the multi-channel feature maps to three classes that are belonged to eyelid region, MG region, and background region. The output of network was converted to a grayscale segmentation map, in which value 0, 1, and 2 are responding to background pixel, eyelid pixel, and MG region pixel, respectively.

MG loss rate calculation

MG loss rate is the ratio of the area of meibomian gland loss to the total eyelid area. Therefore, the MG loss rate is a positive real number in the range [0,1]. The loss rate can be expressed by Eq. 1.

$$MG \text{ atrophy rate} = 1 - \frac{MG \text{ area}}{Eyelid \text{ area}} \quad (1)$$

MG loss rate is a parameter directly related to the severity of MGD and is the most used in clinic. When the meibomian gland



atrophied by 33%, the severity of MGD increased by one grade, which is known as meiboscore (Arita et al., 2014; Arita et al., 2008).

Results

Two models were trained with the training set, including: 1) the model was trained with the k5m generation graph; 2) K5M images enhanced by CLAHE were used for training. Each training image and its corresponding mask were resized to 256×256 and augmented by gamma transformation, rotation, blur, noise addition, and image flip. The data augmentation increased the training images by 12 times. Training and evaluating of the proposed models were performed on a computer with an Nvidia GeForce GTX 3090 GPU. The deep learning models were implemented based on PyTorch (version 1.1.0) package in Python. All models were trained using the Adam optimizer ($\alpha = 0.9$, $\beta = 0.999$), with an initial learning rate of 0.0003 and decays 0.8 times every five epochs. The batch size is set to 32 and the maximum epoch number of 50. L1 regulation was applied to prevent over-

fitting (Hawkins, 2004). The loss function used in the experiment is Dice loss function (Jadon, 2020), which is represented by Eq. 2.

$$L_{Dice} = 1 - \frac{2 \cdot |y \cap y'|}{|y| + |y'|} \quad (2)$$

To explore the influence of HS and CLAHE on model performance, k5m images and KH images were divided into different testing sets, which were: 1) I_{k5m} and I_{kh} ; 2) apply HS to KH image with I_{k5m} as the guide images; 3) preprocessed I_{k5m} and I_{kh} using CLAHE. The specific division is shown in Table 1.

The performance of the MG segmentation models was assessed by dice similarity coefficient (DSC), recall, and precision. These results were reported in Table 1 and Table 2. The results in Table 1 show that all images have close results. The maximum value of each indicator is marked in bold. Table 3 shows the comparison between segmentation results of different preprocessing methods on two image set. Note that there is no statistical difference in all different testing sets, except that the precision between the $I_{kh-CLAHE}$ and $I_{kh-HS-CLAHE}$ is statistically different. Similar results can also be found in the I_{k5m} and $I_{k5m-CLAHE}$, with no statistically significant difference between the evaluation results of the segmentation model regardless of whether the images were processed with CLAHE or not.

Figure 4 shows some visualization of MG segmentation results. Most of the images in both the internal testing set and the external testing set have segmentation results with high DSC score, and the network predicted segmentation masks and ground-truth masks have high similarity and coincidence. But some images in the external testing set have very low segmentation results, as shown in Figure 5, both the eyelid region and the MG region are under-segmented, with rough edges and anomalous masks. These under-segmented images have dissimilar features when compared with the predicted results on average level.

Figure 6 and Figure 7 show the direct comparison results between the MG loss rate and GT for the external and internal testing sets. Most of the predicted MG loss rates are distributed near the ideal line (predicted MG loss rate equals to ground-truth MG loss rate), which indicates that the MG loss rates calculated according to the predicted segmentation results of the network are relatively close to the ground-truth. Root Mean Squared Error (RMSE) in Table 4 was used to quantify and compare the MG loss rate with the ground-truth. Testing set $I_{k5m-CLAHE}$ has the smallest RMSE when compared with ground-truth (RMSE = 0.09).

Discussion

Meibomian gland morphology analysis is an important index to evaluate MGD. However, the current manual grading methods have

TABLE 1 Segmentation results of testing images from KH.

	MG region			Eyelid region		
	DSC	Recall	Precision	DSC	Recall	Precision
I_{kh}	0.70 ± 0.26	0.75 ± 0.29	0.67 ± 0.27	0.90 ± 0.10	0.89 ± 0.12	0.92 ± 0.07
I_{kh-HS}	0.69 ± 0.27	0.73 ± 0.29	0.67 ± 0.27	0.89 ± 0.10	0.88 ± 0.12	0.92 ± 0.08
$I_{kh-CLAHE}$	0.71 ± 0.26	0.75 ± 0.27	0.69 ± 0.26	0.90 ± 0.06	0.89 ± 0.10	0.92 ± 0.07
$I_{kh-HS-CLAHE}$	0.70 ± 0.25	0.72 ± 0.27	0.71 ± 0.27	0.91 ± 0.05	0.91 ± 0.08	0.91 ± 0.07

I_{kh} : Testing images from KH without any preprocessing.

I_{kh-HS} : Testing images from KH with HS.

$I_{kh-CLAHE}$: Testing images from KH with CLAHE.

$I_{kh-HS-CLAHE}$: Testing images from KH with HS and CLAHE.

Bold values are indicates the best performance.

TABLE 2 Segmentation results of testing images from K5M.

	MG region			Eyelid region		
	DSC	Recall	Precision	DSC	Recall	Precision
I_{k5m}	0.84 ± 0.11	0.79 ± 0.15	0.93 ± 0.07	0.92 ± 0.05	0.87 ± 0.08	0.97 ± 0.08
$I_{k5m-CLAHE}$	0.84 ± 0.11	0.79 ± 0.15	0.92 ± 0.07	0.92 ± 0.05	0.87 ± 0.08	0.98 ± 0.03

I_{k5m} : Testing images from K5M without any preprocessing.

$I_{k5m-CLAHE}$: Testing images from K5M with CLAHE.

Bold values are indicates the best performance.

TABLE 3 Comparison between segmentation results of different preprocessing methods.

	MG region			Eyelid region		
	DSC	Recall	Precision	DSC	Recall	Precision
	<i>p</i> -value	<i>p</i> -value	<i>p</i> -value	<i>p</i> -value	<i>p</i> -value	<i>p</i> -value
$I_{kh}-I_{kh-HS}$	0.36	0.12	0.16	0.42	0.16	0.41
$I_{kh}-I_{kh-CLAHE}$	0.38	0.20	0.16	0.39	0.17	0.0004
$I_{k5m}-I_{k5m-CLAHE}$	0.40	0.38	0.43	0.37	0.40	0.34

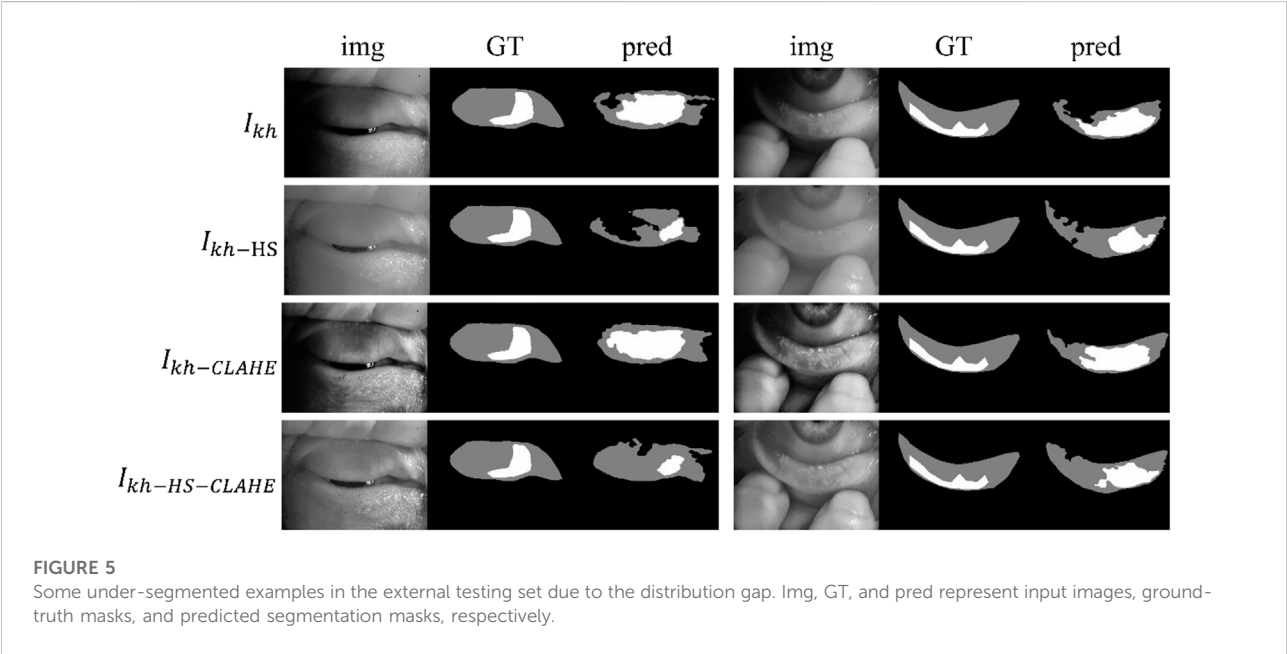
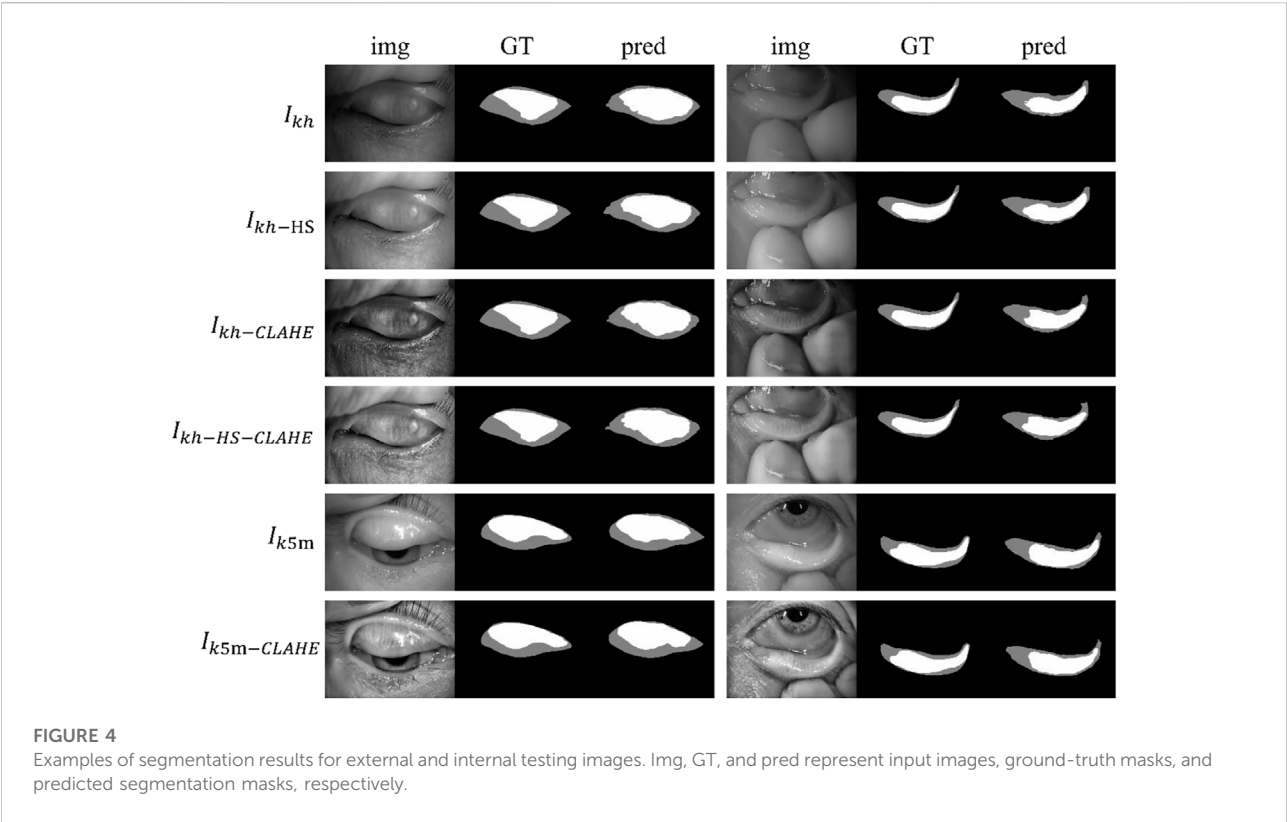
$p < 0.01$ is considered a statistical difference (Mann-Whitney U test).

The bold value here means that the p value less that 0.05 which indicates a statistical difference.

the problems of heavy workload, low efficiency and large error, which is not conducive to the standardized diagnosis and treatment of MGD and dry eye. In this study, we developed and evaluated the automatic segmentation method of the eyelid area and the MG area based on CNN and automatically calculated MG loss rate. This method is evaluated in the internal and external testing sets from the two meibography devices. In addition, we also tested that the pre-processing method of HS and CLAHE as MG images has not improved significantly.

In this experiment, the segmentation results of the external testing set (I_{kh} , I_{kh-HS} , $I_{kh-CLAHE}$, and

$I_{kh-HS-CLAHE}$) from another device are lower than the internal testing set (I_{k5m} and $I_{k5m-CLAHE}$). Such performance gap is common in segmentation tasks based on CNN. Even though data augmentation was used in the training phase, data augmentation in the distribution domain of the training set (I_{k5m} and $I_{k5m-CLAHE}$) cannot close the distribution gap, because domain shift is systematic. As shown in the histogram in Figure 8, I_{kh} and I_{k5m} have very different pixel distributions. These image differences lead to a performance gap in the segmentation performance of the model between the two different testing sets. We used HS



to make the histograms much more similar, but the obtained network segmentation results did not improve significantly. t-SNE (Van der Maaten and Hinton, 2008) was used to gain

insight into the difference between the two sets of images before and after using HS, as shown in Figure 9A. The images are applied dimensionality reduction and projected onto a 2D

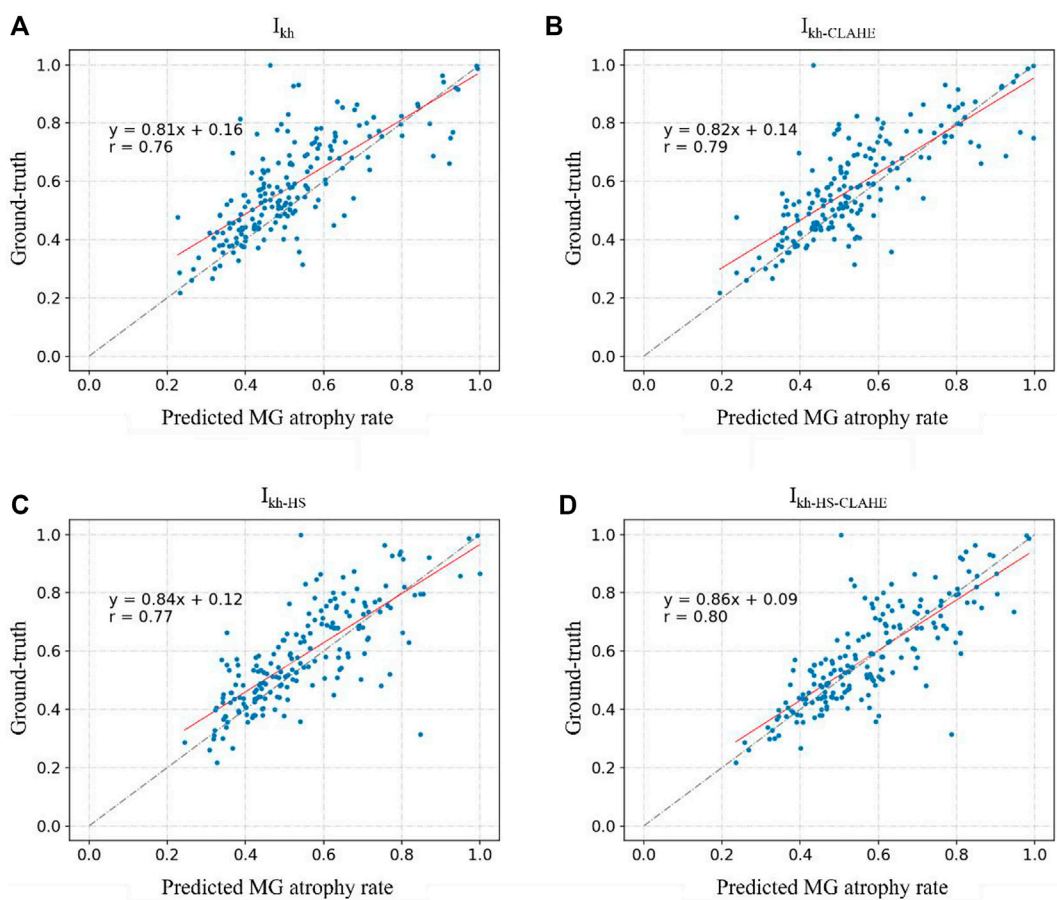


FIGURE 6
(A–D) represent the direct comparison of the ground truth and predicted MG atrophy rates of the unprocessed image set I_{kh} , image set $I_{kh-CLAHE}$ processed with CLAHE, image set I_{kh-HS} processed with HS, and image set $I_{kh-HS-CLAHE}$ processed with HS and CLAHE, respectively.

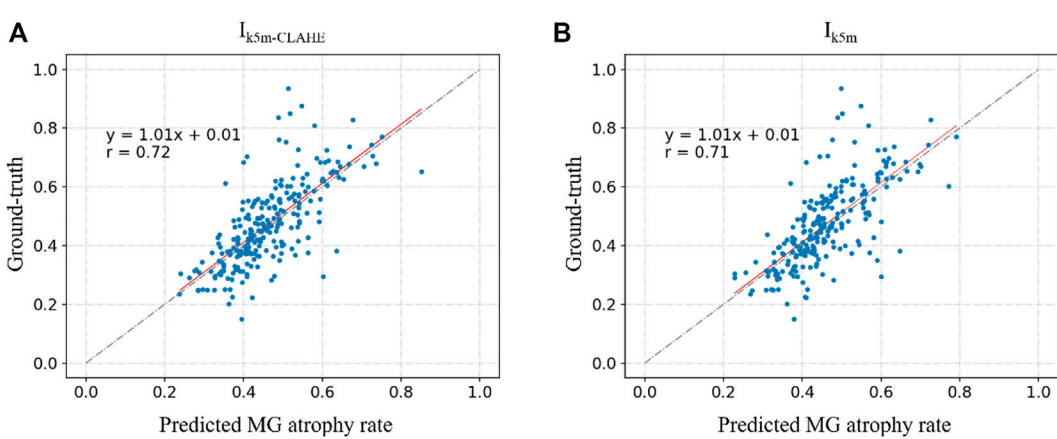


FIGURE 7
(A) and (B) represent the direct comparison of the ground real and predicted MG atrophy rates of the unprocessed image set I_{k5m} , image set $I_{k5m-CLAHE}$ processed with CLAHE, respectively.

TABLE 4 RMSE of internal and external testing set compared with ground-truth.

	I_{kh}	I_{kh-HS}	$I_{kh-CLAHE}$	$I_{kh-HS-CLAHE}$	I_{k5m}	$I_{k5m-CLAHE}$
RMSE	0.12	0.12	0.13	0.11	0.10	0.09

The bold value here means the smallest RMSE and the best performance.

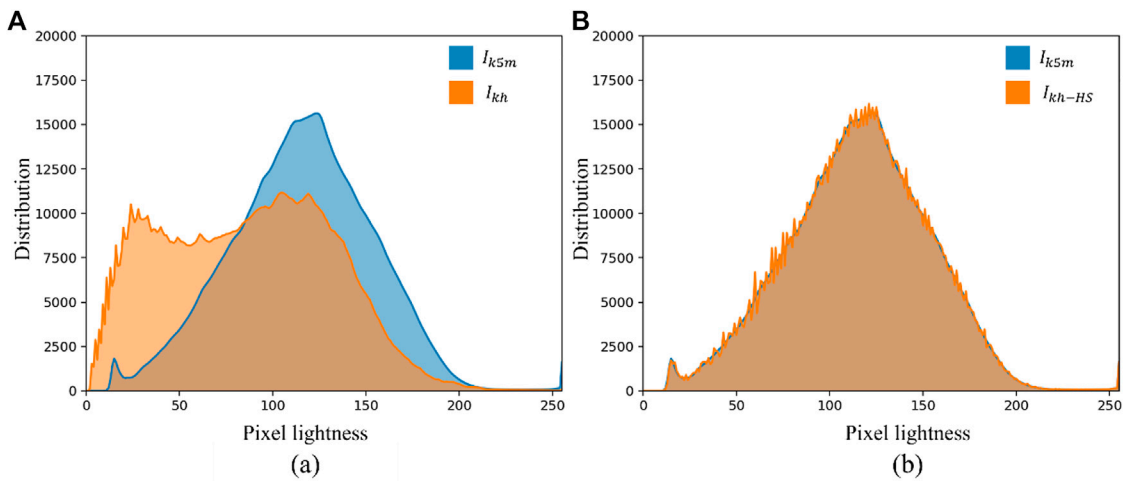


FIGURE 8
Histogram comparison of internal and external test sets. (A) Shows the histograms of I_{kh} and I_{k5m} ; (B) Shows the histograms of I_{k5m} and I_{kh-HS} .

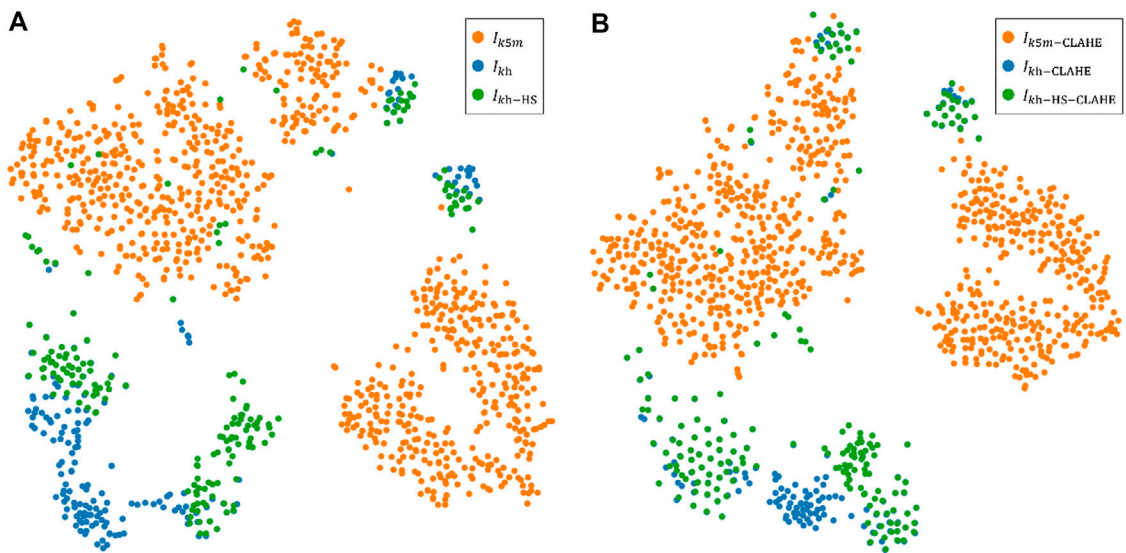


FIGURE 9
Execution of t-SNE algorithm for images from two different devices. Colors represent data from different devices. (A) A visualization of the t-SNE 2D non-linear embedding projection for the images without CLAHE. (B) A visualization of the t-SNE 2D non-linear embedding projection for the images with CLAHE for contrast enhancement.

plane. There is a large gap between the distributions of I_{k5m} and I_{kh} . Also, HS does not effectively reduce the distribution gap, although the histograms had been matched. Changing the low-dimensional image feature of gray distribution will not affect CNN to extract and learn the high-dimensional semantic information of the image.

CLAHE can effectively enhance the visual effect of MG images, which is beneficial for doctors to read and measure MG images manually. However, CLAHE does not significantly improve the segmentation results of neural networks, because CLAHE also fails to close the distribution gap between the distributions of I_{k5m} and I_{kh} , as shown in Figure 9B. CNN have been shown to be feasible in medical image segmentation tasks, but when used in practice, network models can suffer huge performance degradations if image data from other distributed domains are involved. Such performance gap can be explained using the independent and identically distributed (i.i.d.) assumption of statistical learning: a network model that is well-trained in the source distribution domain does not necessarily achieve similar high performance on datasets with the same distribution as the source distribution domain performance (Zhu et al., 2017). Adjusting the pixel distribution of images by HS and CLAHE did not improve the prediction results of the network model, although the images were visually very similar to the source distribution domain. Through tsne-2D visualization, it can be found that HS and CLAHE do not close the distribution gap.

Conclusion

In this study, we developed and validated a CNN-based automatic MG analysis method based on MG images acquired by two different devices, K5M and KH. Predictions of MG loss rates were in high agreement with the gold standard obtained by physicians. We also found that in this study HS and CLAHE do not significantly improve the performance of CNN for segmenting MG, which may indicate that in future deep learning-based MG analysis tasks, no

additional computational cost is required for image preprocessing phase.

Data availability statement

The raw data supporting the conclusion of this article will be made available by the authors, without undue reservation.

Ethics statement

The studies involving human participants were reviewed and approved by the Beijing Tongren Hospital. The patients/participants provided their written informed consent to participate in this study.

Author contributions

YoZ and YJ developed the plot and designed the experiments, which were executed by YiZ and AL; XD and LT did the discussion and wrote the manuscript.

Conflict of interest

The authors declare that the research was conducted in the absence of any commercial or financial relationships that could be construed as a potential conflict of interest.

Publisher's note

All claims expressed in this article are solely those of the authors and do not necessarily represent those of their affiliated organizations, or those of the publisher, the editors and the reviewers. Any product that may be evaluated in this article, or claim that may be made by its manufacturer, is not guaranteed or endorsed by the publisher.

References

- Arita, R., Itoh, K., Inoue, K., and Amano, S. (2008). Noncontact infrared meibography to document age-related changes of the meibomian glands in a normal population. *Ophthalmology* 115, 911–915. doi:10.1016/j.ophtha.2007.06.031
- Arita, R., Suehiro, J., Haraguchi, T., Shirakawa, R., Tokoro, H., and Amano, S. (2014). Objective image analysis of the meibomian gland area. *Br. J. Ophthalmol.* 98, 746–755. doi:10.1136/bjophthalmol-2012-303014
- Celik, T., Lee, H. K., Petznick, A., and Tong, L. (2013). Bioimage informatics approach to automated meibomian gland analysis in infrared images of meibography. *J. Optometry* 6, 194–204. doi:10.1016/j.optom.2013.09.001
- da Cruz, L. B., Araújo, J. D. L., Ferreira, J. L., Diniz, J. O. B., Silva, A. C., de Almeida, J. D. S., et al. (2020). Kidney segmentation from computed tomography images using deep neural network. *Comput. Biol. Med.* 123, 103906. doi:10.1016/j.compbiomed.2020.103906
- Dai, Q., Liu, X., Lin, X., Fu, Y., Chen, C., Yu, X., et al. (2021). A novel meibomian gland morphology analytic system based on a convolutional neural network. *IEEE Access* 9, 23083–23094. doi:10.1109/ACCESS.2021.3056234
- Den, S., Danielson, J., McCulley, J. P., Shimazaki, J., Craig, J., Benitez-Del-Castillo, J. M., et al. (2011). The international workshop on meibomian gland dysfunction: Report of the definition and classification subcommittee. *Invest. Ophthalmol. Vis. Sci.* 52, 1930–1937. doi:10.1167/iovs.10-6997b
- Djalilian, A. R. (2018). "Ocular surface disease," in *Update in the diagnosis and management of meibomian gland dysfunction* (Berlin, Germany: Springer), 17–29. doi:10.1007/978-3-319-15823-5

- Driver, P. J., and Lemp, M. A. (1996). Meibomian gland dysfunction. *Surv. Ophthalmol.* 40, 343–367. doi:10.1016/s0039-6257(96)80064-6
- Erich, K., Nadja, K., Thomas, M., Hiroto, O., and Sullivan, D. A. (2011). The international workshop on meibomian gland dysfunction: Report of the subcommittee on anatomy, physiology, and pathophysiology of the meibomian gland. *Invest. Ophthalmol. Vis. Sci.* 52, 1938–1978. doi:10.1167/iovs.10-6997c
- Hawkins, D. M. (2004). The problem of overfitting. *J. Chem. Inf. Comput. Sci.* 44, 1–12. doi:10.1021/ci0342472
- He, K., Zhang, X., Ren, S., and Sun, J. (2016). “Deep residual learning for image recognition,” in Proceedings of the IEEE Conference on Computer Vision and Pattern Recognition, Las Vegas, NV, USA, 27–30 June 2016, 770–778.
- Hwang, H. S., Mikula, E., Xie, Y., Brown, D. J., and Jester, J. V. (2021). A novel transillumination meibography device for *in vivo* imaging of mouse meibomian glands. *Ocul. Surf.* 19, 201–209. doi:10.1016/j.jtos.2020.08.012
- Jadon, S., 2020. A survey of loss functions for semantic segmentation. arXiv preprint arXiv:2006.14822.
- Jo, J., and Bengio, Y., 2017. Measuring the tendency of cnns to learn surface statistical regularities. arXiv preprint arXiv:1711.11561.
- Koprowski, R., Tian, L., and Olczyk, P. (2017). A clinical utility assessment of the automatic measurement method of the quality of Meibomian glands. *Biomed. Eng. Online* 16, 82. doi:10.1186/s12938-017-0373-4
- Koprowski, R., Wilczyński, S., Olczyk, P., Nowińska, A., Węglarz, B., and Wylęgała, E. (2016). A quantitative method for assessing the quality of meibomian glands. *Comput. Biol. Med.* 75, 130–138. doi:10.1016/j.compbiomed.2016.06.001
- Liang, F., Xu, Y., Li, W., Ning, X., Liu, X., and Liu, A. (2017). Recognition algorithm based on improved FCM and rough sets for meibomian gland morphology. *Appl. Sci.* 7, 192. doi:10.3390/app7020192
- Llorens-Quintana, C., Rico-del-Viejo, L., Syga, P., Madrid-Costa, D., and Iskander, D. R. (2019). A novel automated approach for infrared-based assessment of meibomian gland morphology. *Trans. Vis. Sci. Tech.* 8, 17. doi:10.1167/tvst.8.4.17
- McDonald, M., Patel, D. A., Keith, M. S., and Snedecor, S. J. (2016). Economic and humanistic burden of dry eye disease in europe, north America, and asia: A systematic literature review. *Ocul. Surf.* 14, 144–167. doi:10.1016/j.jtos.2015.11.002
- Naseem, R., Khan, Z. A., Satpute, N., Beghdadi, A., Cheikh, F. A., and Olivares, J. (2021). Cross-modality guided contrast enhancement for improved liver tumor image segmentation. *IEEE Access* 9, 118154–118167. doi:10.1109/ACCESS.2021.3107473
- Nichols, K. K., Foulks, G. N., Bron, A. J., Glasgow, B. J., Dogru, M., Tsubota, K., et al. (2011). The international workshop on meibomian gland dysfunction: Executive summary. *Invest. Ophthalmol. Vis. Sci.* 52, 1922–1929. doi:10.1167/iovs.10-6997a
- Perone, C. S., Ballester, P., Barros, R. C., and Cohen-Adad, J. (2019). Unsupervised domain adaptation for medical imaging segmentation with self-ensembling. *NeuroImage* 194, 1–11. doi:10.1016/j.neuroimage.2019.03.026
- Prabhu, S. M., Chakiat, A., S. S., Vunnava, K. P., and Shetty, R. (2020). Deep learning segmentation and quantification of Meibomian glands. *Biomed. Signal Process. Control* 57, 101776. doi:10.1016/j.bspc.2019.101776
- Pult, H., and Nichols, J. J. (2012). A review of meibography. *Optom. Vis. Sci.* 89, E760–E769. doi:10.1097/OPX.0b013e3182512ac1
- Pult, H., and Riede-Pult, B. (2013). Comparison of subjective grading and objective assessment in meibography. *Cont. Lens Anterior Eye* 36, 22–27. doi:10.1016/j.clae.2012.10.074
- Pult, H., and Riede-Pult, B. H. (2012). Non-contact meibography: Keep it simple but effective. *Cont. Lens Anterior Eye* 35, 77–80. doi:10.1016/j.clae.2011.08.003
- Ronneberger, O., Fischer, P., and Brox, T. (2015). “U-net: Convolutional networks for biomedical image segmentation,” in International Conference on Medical Image Computing and Computer-Assisted Intervention, Berlin, Germany, 18 November 2015 (Springer), 234–241.
- Turgut, B., Çatak, O., and Demir, T. (2018). Meibomian gland dysfunction: An overlooked eyelid disease. *Adv. Ophthalmol. Vis. Syst.* 8. doi:10.15406/aovs.2018.08.00295
- Van der Maaten, L., and Hinton, G. (2008). Visualizing non-metric similarities in multiple maps. *Mach. Learn.* 9, 33–55. doi:10.1007/s10994-011-5273-4
- Wang, J., Yeh, T. N., Chakraborty, R., Yu, S. X., and Lin, M. C. (2019). A deep learning approach for meibomian gland atrophy evaluation in meibography images. *Trans. Vis. Sci. Tech.* 8, 37. doi:10.1167/tvst.8.6.37
- Wong, S., Srinivasan, S., Murphy, P. J., and Jones, L. (2019). Comparison of meibomian gland dropout using two infrared imaging devices. *Cont. Lens Anterior Eye* 42, 311–317. doi:10.1016/j.clae.2018.10.014
- Xiao, B., Tang, H., Jiang, Y., Li, W., and Wang, G. (2018). Brightness and contrast controllable image enhancement based on histogram specification. *Neurocomputing* 275, 2798–2809. doi:10.1016/j.neucom.2017.11.057
- Xiao, J., Adil, M. Y., Chen, X., Utheim, Ø. A., Ræder, S., Tønseth, K. A., et al. (2020). Functional and morphological evaluation of meibomian glands in the assessment of meibomian gland dysfunction subtype and severity. *Am. J. Ophthalmol.* 209, 160–167. doi:10.1016/j.ajo.2019.09.005
- Xiao, P., Luo, Z., Deng, Y., Wang, G., and Yuan, J. (2021). An automated and multiparametric algorithm for objective analysis of meibography images. *Quant. Imaging Med. Surg.* 11, 1586–1599. doi:10.21037/qims-20-611
- Yan, W., Wang, Y., Gu, S., Huang, L., Yan, F., Xia, L., et al. (2019). “The domain shift problem of medical image segmentation and vendor-adaptation by unet-GAN,” in *Medical image computing and computer assisted intervention – MICCAI 2019, lecture notes in computer science*. Editors D. Shen, T. Liu, T. M. Peters, L. H. Staib, C. Essert, S. Zhou, et al. (Cham: Springer International Publishing), 623–631. doi:10.1007/978-3-030-32245-8_69
- Zaiwang, G., Jun, C., Huazhu, F., Kang, Z., Huaying, H., Yitian, Z., et al. 2019, CE-Net: Context encoder network for 2D medical image segmentation. arXiv:1903.02740v1.
- Zhu, J.-Y., Park, T., Isola, P., and Efros, A. A. (2017). “Unpaired image-to-image translation using cycle-consistent adversarial networks,” in Proceedings of the IEEE International Conference on Computer Vision, Venice, Italy, 22–29 October 2017, 2223–2232.



OPEN ACCESS

EDITED BY

Weihua Yang,
Jinan University, China

REVIEWED BY

Keran Li,
Fourth Affiliated Hospital of Nanjing
Medical University, China
Pan Su,
North China Electric Power University,
China
Ruoxiu Xiao,
University of Science and Technology
Beijing, China
Lichao Yang,
Cranfield University, United Kingdom

*CORRESPONDENCE

Yufei Wu,
yufei_wu211@163.com
Qinkang Lu,
luqinkang@163.com

[†]These authors have contributed to the
work equally

SPECIALTY SECTION

This article was submitted to Molecular
and Cellular Pathology,
a section of the journal
Frontiers in Cell and
Developmental Biology

RECEIVED 27 October 2022

ACCEPTED 22 November 2022

PUBLISHED 09 December 2022

CITATION

Deng X, Wang S, Yang Y, Chen A, Lu J,
Hao J, Wu Y and Lu Q (2022), Reduced
macula microvascular densities may be
an early indicator for diabetic
peripheral neuropathy.
Front. Cell Dev. Biol. 10:1081285.
doi: 10.3389/fcell.2022.1081285

COPYRIGHT

© 2022 Deng, Wang, Yang, Chen, Lu,
Hao, Wu and Lu. This is an open-access
article distributed under the terms of the
[Creative Commons Attribution License
\(CC BY\)](https://creativecommons.org/licenses/by/4.0/). The use, distribution or
reproduction in other forums is
permitted, provided the original
author(s) and the copyright owner(s) are
credited and that the original
publication in this journal is cited, in
accordance with accepted academic
practice. No use, distribution or
reproduction is permitted which does
not comply with these terms.

Reduced macula microvascular densities may be an early indicator for diabetic peripheral neuropathy

Xiaoyu Deng^{1†}, Shiqi Wang^{1†}, Yan Yang¹, Aizhen Chen¹,
Jinger Lu¹, Jinkui Hao², Yufei Wu^{1*} and Qinkang Lu^{1*}

¹The Affiliated People's Hospital of Ningbo University, Ningbo, China, ²Cixi Institute of Biomedical Engineering, Ningbo Institute of Materials Technology and Engineering, Chinese Academy of Sciences, Ningbo, China

Purpose: To assess the alteration in the macular microvascular in type 2 diabetic patients with peripheral neuropathy (DPN) and without peripheral neuropathy (NDPN) by optical coherence tomography angiography (OCTA) and explore the correlation between retinal microvascular abnormalities and DPN disease.

Methods: Twenty-seven healthy controls (42 eyes), 36 NDPN patients (62 eyes), and 27 DPN patients (40 eyes) were included. OCTA was used to image the macula in the superficial vascular complex (SVC) and deep vascular complex (DVC). In addition, a state-of-the-art deep learning method was employed to quantify the microvasculature of the two capillary plexuses in all participants using vascular length density (VLD).

Results: Compared with the healthy control group, the average VLD values of patients with DPN in SVC ($p = 0.010$) and DVC ($p = 0.011$) were significantly lower. Compared with NDPN, DPN patients showed significantly reduced VLD values in the SVC ($p = 0.006$) and DVC ($p = 0.001$). Also, DPN patients showed lower VLD values ($p < 0.05$) in the nasal, superior, temporal and inferior sectors of the inner ring of the SVC when compared with controls; VLD values in NDPN patients were lower in the nasal section of the inner ring of SVC ($p < 0.05$) compared with healthy controls. VLD values in the DVC (AUC = 0.736, $p < 0.001$) of the DPN group showed a higher ability to discriminate microvascular damage when compared with NDPN.

Conclusion: OCTA based on deep learning could be potentially used in clinical practice as a new indicator in the early diagnosis of DM with and without DPN.

KEYWORDS

diabetic retinopathy, microvasculature, optical coherence tomography angiography, vascular length density, diabetic peripheral neuropathy

Introduction

The incidence of diabetes has been rising worldwide in recent years. The number of people diagnosed with diabetes is expected to reach 800 million by 2045 (Sun et al., 2022). Vascular complications (including microvascular and macrovascular) are the main reasons for the increase in morbidity and mortality in diabetic patients (Sarwar et al., 2010; Kim et al., 2021). Long-term hyperglycemia may lead to large and small vessel abnormalities; some of the major complications include cardiovascular disease, diabetic nephropathy, diabetic retinopathy, and neuropathy (Cole and Florez 2020). Although some of the studies showed that intensive blood glucose control could reduce the risk of microvascular

complications in diabetic patients, such as diabetic retinopathy (Chew et al., 2010) and diabetic peripheral neuropathy (DPN) (Callaghan et al., 2012), the beneficial effects of intensive control on macrovascular and cardiovascular endpoints in patients with type 2 diabetes are vague. Therefore, early detection of complications related to diabetes and further understanding of their underlying pathology are of crucial importance.

DPN is one of the most common complications of type 1 and type 2 diabetes. More than half of diabetic patients suffer from peripheral nerve injury (Kazamel et al., 2021). DPN mainly leads to chronic neuropathic pain, numbness and tingling of extremities, paresthesia, and foot ulcer. Its diagnosis commonly relies on traditional measurement methods of neuropathy, such as nerve conduction studies, skin biopsy

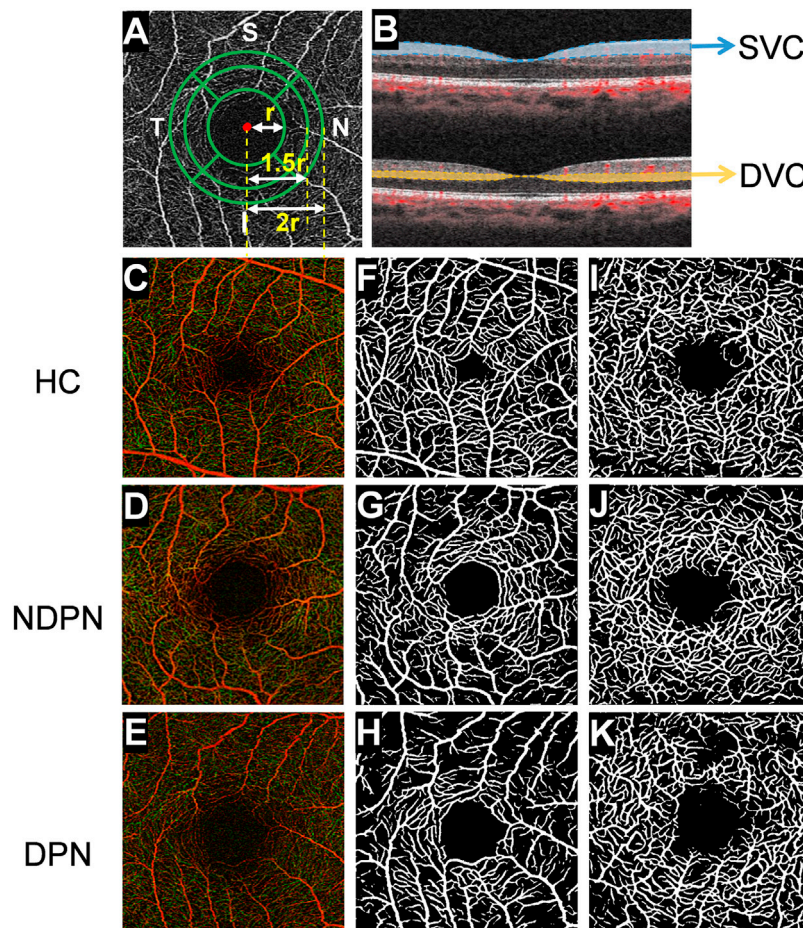


FIGURE 1

OCTA image analysis of macular fovea and artificial intelligence algorithm for layered analysis of images. (A) Using OCTA to scan the macula area of the subject within the range of $3 \times 3 \text{ mm}^2$, and the images of capillaries around the fovea are obtained. Then, using deep learning software, FAZ was used to fit a circle with radius r , after which three concentric circles with radius r , $1.5r$, and $2r$ were drawn. With further partitioning, the retina was divided into inner and outer rings: nasal area, superior area, temporal area, and inferior area, and there were 8 areas in total. (B) The retina was segmented into SVC (from the internal limiting membrane to $10 \mu\text{m}$ above the inner plexiform layer) and DVC (from $10 \mu\text{m}$ above the inner plexiform layer to the $10 \mu\text{m}$ below the outer plexiform layer) images with different depths. The images (C–K) show retinal microvascular in a different layer of HC, NDPN, and DPN groups. (C–E) The images show the full-thickness retinal microvasculature produced by OCTA in HC, NDPN, and DPN groups. (F–H) Capillaries in the SVC by deep learning software. (I–K) Capillaries in the DVC by deep learning software.

evaluation, Michigan Neuropathy Symptom Inventory (MNSI), and the Utah Early Neuropathy Scale (UENS) (Singleton et al., 2008; Iqbal et al., 2018). Yet, these diagnostic methods have low repeatability, poor sensitivity (especially in detecting early-stage disease), and certain hysteresis in early clinical diagnosis (Malik 2014). If not timely treated, DPN develops into a diabetic foot, leading to amputation. Previous studies have shown that the 5-year survival rate of diabetic patients after amputation is even lower than that of prostate cancer and breast cancer (Selvarajah et al., 2019).

The recent development of new ophthalmological examination methods allows the evaluation of systemic vascular and nerve damage by using the changes in ocular vascular and nerve microstructures. Because the retina is suggested as a site of diabetic damage, prior studies suggested that the retinal nerve fiber layer (RNFL) changes are associated with the presence of DPN (Shahidi et al., 2012; Salvi et al., 2016; Dehghani et al., 2017). A recent report suggested a close link between microcirculation dysfunction and DPN (Hu et al., 2021). In addition, several studies using fundus photography have shown significant retinal vascular changes in DPN patients compared with healthy controls (Ding et al., 2012; Hu et al., 2021). However, retinal photography imaging rarely gives information about deeper retinal microstructure, so subtle microvascular changes that occur at the capillary level may be missed.

OCTA is a non-invasive, non-contact imaging technology that enables the high-resolution visualization of the retinal microvasculature network in different retina layers. Cumulative reports using OCTA (Kim A et al., 2016; Chen et al., 2017) show that the retinal microvascular density of diabetic patients is lower than that of healthy controls. However, little is known about the retinal microvascular changes in DPN patients. In this study, we used an automated framework based on the state-of-the-art deep learning approach to extract retinal microvasculature to characterize the macula microvascular alterations that occur in type 2 diabetic patients with DPN and those without DPN. We also determined the ability of the deep learning approach to find the changes in the retinal microvascular network at different levels in different subareas and to look for indicators that can prompt the diagnosis of DPN patients so as to improve the diagnostic rate of DPN patients.

Materials and methods

Participants

This was an observational cross-sectional study. Subjects admitted to the Affiliated People's Hospital of Ningbo University were enrolled between November 2019 and August 2021. The study was approved by the Ethics Committee of The

Affiliated People's Hospital of Ningbo University and followed the Declaration of Helsinki. All participants provided informed consent.

Diabetes mellitus patients with and without DPN and healthy controls were included in our study. Patients with type 2 diabetes mellitus were diagnosed according to WHO standards (Alberti and Zimmet 1998). A retinal specialist (YW) used a modified Airlie House classification (Wu et al., 2013) to select DM patients with retinopathy.

Basic information, such as medical history and symptoms, was collected from all participants. Besides, neurological examination of the nervous system and nerve conduction tests were also performed. Neurological examinations included pain sensation, temperature sensation, tactile sensation, vibration sensation, and ankle reflex. According to the comprehensive analysis of peripheral symptoms, signs, and nerve conduction test results (Tesfaye et al., 2010; Lipsky et al., 2012), the DPN diagnosis was confirmed by a neurologist (AC). Therefore, we classified possible and probable DPN into the NDPN group, and subclinical and confirmed DPN into the DPN group (Sloan et al., 2021).

The healthy controls were in good health in the past, with no history of diabetes and no history of eye diseases or surgery. Clinical information such as diabetes and hypertension were recorded for all participants. Controls were excluded if they had the following: trauma or toxic disorder affecting the brain, optic nerve, or retina, current or previous drug abuse, uncontrolled hypertension, hypotension, and any neuro-ophthalmic disease which could affect the retina, patients with diabetic retinopathy in the proliferative phase and non-proliferative phase in which the retinal structures were affected by bleeding, edema, and other reasons.

Ophthalmic examinations

All the enrolled subjects underwent complete binocular examination, including best corrected visual acuity, intraocular pressure, anterior segment slit lamp examination, ultra-wide angle fundus photography, and OCTA examination. Type 2 diabetes mellitus (primary and long-term) patients were 30–80 years old, with ametropia between +3.00 D and −3.00 D, intraocular pressure between 10 and 21 mmHg, no obvious turbid refractive media, no history of glaucoma, no diffuse or focal sheath thinning, no retinal hemorrhage or macular defect, and no treatment history of active eye disease. Participants with the following conditions were excluded: 1) serious cardiovascular and cerebrovascular diseases, malignant tumors, immunological diseases, etc.; 2) history of intraocular surgery (exception: cataract extraction within 12 months); 3) ocular disease affecting the retina that has been diagnosed in the past, including macular edema, the onset of glaucoma, optic nerve disease, and choroidal

TABLE 1 Demographic characteristics of all subjects.

Parameters	Control, <i>n</i> = 27	NDPN, <i>n</i> = 36	DPN, <i>n</i> = 27	<i>p</i>
Eyes	42	62	40	
Age, y	57.12 ± 13.36	55.50 ± 10.11	59.63 ± 8.53	0.324
Sex, M/F	10:17	22:14	16:11	0.129
BMI	21.97 ± 1.68	24.50 ± 2.92	22.84 ± 3.61	0.003
MAP, mmHg	91.69 ± 7.12	92.44 ± 8.97	91.99 ± 8.98	0.944
SE, diopter	−0.41 ± 1.10	−0.29 ± 1.72	−0.12 ± 0.93	0.628
BCVA, logMAR	0.01 ± 0.03	0.01 ± 0.04	0.06 ± 0.13	0.003
IOP, mmHg	15.40 ± 2.89	15.83 ± 2.90	16.74 ± 3.70	0.148
Duration, y	NA	6.40 ± 6.81	9.93 ± 6.47	0.043
HbA1c	—	9.75 ± 2.19	9.36 ± 2.14	0.499
BG	—	9.36 ± 3.55	9.55 ± 4.19	0.843
TG	—	2.18 ± 2.90	2.12 ± 1.54	0.917
T-CHOL	—	4.83 ± 1.27	4.53 ± 1.48	0.388
HDL-C	—	1.15 ± 0.32	1.07 ± 0.30	0.272
LDL	—	3.01 ± 0.75	2.77 ± 1.04	0.314

Values for continuous variables are means ± standard deviations for all subjects in each group. HC, healthy control; NDPN, Diabetic patients without DPN; DPN, diabetic patients with peripheral neuropathy; —, not performed; NA, not applicable; BCVA, best-corrected visual acuity. One-way ANOVA, for numerical data.

neovascularization; 4) image quality affected by abnormal refractive medium or poor fixation (<8); 5) a patient with diabetic retinopathy greater than NPDR2 grade 2 or diabetic retinopathy affecting the fovea; 6) poor control of hypertension causes hypertensive retinopathy.

OCTA imaging

Zeiss Cirrus 5000-HD-OCT Angioplex (Carl Zeiss Meditec, Dublin, CA, United States) with a scanning rate of 68,000 A-scans/s was used for retinal imaging. Each B-scan consisted of 350 A-scans in the horizontal and vertical directions. OCTA equipment includes three-dimensional projection artifact elimination (3D PAR) technology, which can minimize the artifacts in images while keeping the authenticity of the images.

Both eyes of all participants were examined and imaged. The macula was analyzed using B-scans covering an area of 3 × 3 mm² repeated horizontally and vertically. Images of good quality (signal quality ≥ 8) were selected for further analysis. Angiograms with irregular patterns of vessels or irregular vascular segmentation were excluded. Retinal layer segmentation of the macula was done commercially by an inbuilt algorithm in the OCTA tool (Spaide et al., 2014). The retina in the macular region was divided into the superficial vascular complex (SVC, from the internal limiting membrane to 10 μm above the inner plexiform layer) and deep vascular complex (DVC, from 10 μm above the inner plexiform layer to the 10 μm below the outer plexiform layer) for microstructure analysis.

Deep learning algorithm on macular microvasculature

A state-of-the-art OCTA-Net algorithm was used for the microvasculature segmentation (Ma et al., 2020). To construct this model, we used a coarse-to-fine segmentation method, in which the initial confidence map for the retinal microvascular network was generated first, followed by the outline of the macular microvasculature. The OCTA-Net was trained on the public OCTA Segmentation Dataset (ROSE); its effectiveness has been well documented in a previous report (Ma et al., 2020). Vascular length density (VLD) was used to assess the macular microvasculature; VLD is defined as the ratio of the total number of pixels on microvascular centerlines to the measurement area. VLD in the SVC and the DVC was calculated using MATLAB software.

The VLD value of the nine quadrant sectors (center, superior inner, temporal inner, inferior inner, nasal inner, superior outer, temporal outer, inferior outer, and nasal outer) was analyzed to give the mean value. To generate the sub-sectors, we first fit a circle with radius *r* using the foveal avascular zone (FAZ) and then drew three concentric circles with radius *r*, 1.5 *r*, and 2*r*, respectively, as shown in Figure 1 to exclude the potential influence of the FAZ (Figure 1).

Statistical analysis

IBM SPSS Statistics 23 software (version 23; SPSS, Inc. Chicago, IL, United States) was used for statistical analysis. The Kolmogorov-Smirnov test was applied to assess the normality of the data. Quantitative variables were expressed as mean ±

TABLE 2 Comparison of VLD value among the three groups.

		HC	NDPN	DPN	P1	P2	P3
SVC							
Average		7.61 ± 0.73	7.50 ± 0.84	6.89 ± 0.98	0.868	0.010	0.006
Inner	Nasal	11.38 ± 0.83	10.90 ± 1.19	10.35 ± 1.04	0.04	<0.001	0.023
	Superior	11.47 ± 1.03	11.16 ± 0.98	10.30 ± 1.17	0.311	<0.001	<0.001
	Temporal	11.10 ± 1.02	10.79 ± 1.06	10.22 ± 1.21	0.203	0.002	0.033
	Inferior	11.63 ± 1.07	11.32 ± 1.17	10.70 ± 1.22	0.189	0.001	0.019
Outer	Nasal	25.01 ± 2.59	24.76 ± 3.03	23.12 ± 2.78	0.499	0.003	0.007
	Superior	24.93 ± 3.15	24.61 ± 3.51	22.70 ± 3.16	0.918	0.009	0.005
	Temple	24.33 ± 3.08	24.16 ± 2.70	23.23 ± 3.09	0.805	0.169	0.198
	Inferior	24.29 ± 3.16	24.35 ± 3.15	23.33 ± 3.56	0.97	0.219	0.181
DVC							
Average		8.07 ± 0.41	8.07 ± 0.63	7.60 ± 0.57	0.286	0.011	0.001
Inner	Nasal	9.02 ± 1.74	9.07 ± 1.60	8.84 ± 1.67	0.985	0.506	0.448
	Superior	11.02 ± 0.97	10.87 ± 1.26	10.19 ± 1.24	0.554	0.003	0.006
	Temporal	9.38 ± 1.47	9.12 ± 1.65	9.11 ± 1.63	0.426	0.452	0.962
	Inferior	10.64 ± 1.40	10.48 ± 1.70	10.32 ± 1.54	0.6	0.354	0.607
Outer	Nasal	28.92 ± 2.42	28.37 ± 3.11	27.43 ± 3.00	0.336	0.056	0.237
	Superior	28.45 ± 2.22	28.55 ± 2.80	26.48 ± 3.01	0.796	0.002	<0.001
	Temple	28.89 ± 2.29	28.71 ± 3.31	27.09 ± 4.09	0.738	0.037	0.046
	Inferior	28.47 ± 2.47	28.06 ± 3.10	26.84 ± 3.24	0.69	0.065	0.096

P1: comparison between HC, and NDPN; P2: comparison between HC, and DPN; P3: comparison between NDPN, and DPN., data were adjusted for age, gender; MAP, and signal quality of angiograms; SVC, superficial vascular complex; DVC, deep vascular complex.

standard deviation (SD). Refraction data were converted to spherical equivalent (SE). The best corrected visual acuity was expressed as the logarithm of the minimum resolution angle (LogMAR). Generalized estimating equations (GEE) were used to assess the differences among the groups while adjusting for age, gender, mean arterial pressure, and signal quality of angiograms. The subjects' receiver operating characteristic (ROC) curve was used to assess the diagnostic capability of the VLD calculated by the artificial intelligence recognition system for diabetes with DPN. Larger areas under the ROC curve (AUROC) indicated higher diagnostic values. A *p*-value <0.05 was considered statistically significant.

Results

Demographic characteristics among three groups

We initially enrolled 30 healthy controls and 66 DM patients; three healthy controls were excluded due to age macular

degeneration (AMD) and three DM patients because of uncooperativeness during retinal imaging using the OCTA. Finally, 27 healthy controls (42 eyes), 36 DM patients without DPN (62 eyes), and 27 DM patients with DPN (40 eyes) were included in data analysis. There was no significant difference among the three groups in age, sex, and MAP (all *p* > 0.05, Table 1). Yet, there was a significant difference in visual acuity between the three groups (*p* = 0.003, Table 1) and the visual acuity was significantly lower in the DPN group vs the other two groups. As far as the duration of diabetes is concerned, the disease duration in the DPN group was obviously longer than that of the NDPN group (*p* = 0.043, Table 1).

Changes in VLD among the three groups

To further explore the correlation between DPN and microvascular changes in the retina, we used OCTA to collect fundus blood vessels from three groups of subjects and used the intelligent recognition system trained on the public ROSE dataset to segment the vascular. There was no significant difference in the

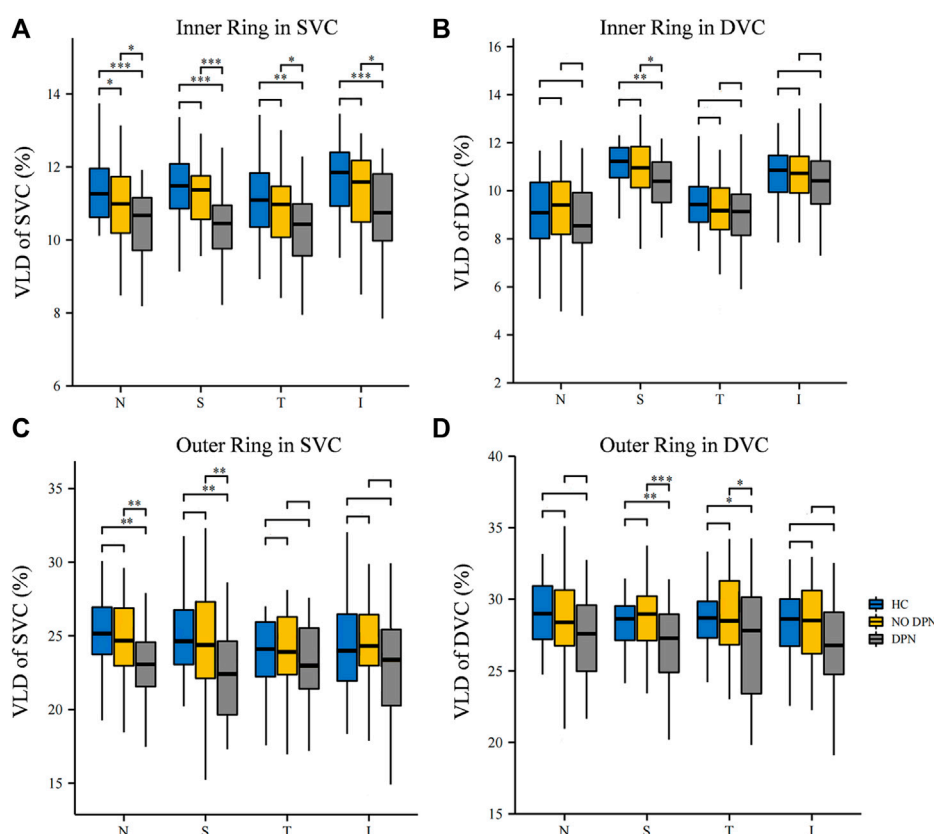


FIGURE 2

Comparison of VLD in different sectors between HC, NDPN, and DPN groups. (A) Describe the VLD of the SVC in four inner quadrant sectors (nasal inner, superior inner, temporal inner, and inferior inner). (B) VLD of DVC in four inner sectors. (C) VLD of SVC in four outer quadrant sectors (nasal outer, superior outer, temporal outer, and inferior outer). (D) VLD of DVC in four outer quadrant sectors. VLD is defined as the ratio of the total number of pixels on microvascular centerlines to the area of measurement.

average VLD values of the SVC ($p = 0.868$, Table 2) and DVC ($p = 0.286$, Table 2) in NDPN when compared with healthy controls; yet, DPN patients showed significantly lower SVC ($p = 0.010$, Table 2) and DVC ($p = 0.011$, Table 2) average VLD values when compared with healthy controls. Also, compared with NDPN, DPN showed significantly lower SVC ($p = 0.006$, Table 2) and DVC ($p = 0.001$, Table 2) average VLD values.

Next, the VLD values of the SVC and DVC in the eight sections around the fovea were compared among the three groups. Figure 2 shows the comparison of VLD values in the eight sections of the SVC and DVC among the three groups. DPN patients showed significantly lower VLD values ($p < 0.05$, Figure 2) in the nasal, superior, temporal and inferior sectors of the inner ring of the SVC when compared with controls; likewise, VLD values in NDPN patients were significantly lower in the nasal section of the inner ring of the SVC ($p < 0.05$, Figure 2) compared with controls. Importantly, DPN patients showed significantly lower VLD values ($p < 0.05$, Figure 2) in the four inner ring sections of the

SVC compared with NDPN. As for DVC, we found that the VLD values coming from the DPN group were significantly decreased in superior sectors of the inner ring, as well as superior and temporal sectors of the outer ring ($p < 0.05$, Figure 2) when compared with healthy controls and NDPN groups.

ROC curve analysis was carried out to determine the ability of VLD to detect alterations in microvascular of DPN and NDPN (Figure 3). The VLD values in the DVC of the DPN group showed a higher ability to discriminate microvascular damage when compared with the NDPN group (Figure 3). The results showed that the area under the curve (AUC) of SVC in the diagnosis of DPN was 0.729 ($p < 0.001$), while the cutoff point of 8.01 showed a sensitivity of 95%, a specificity of 40.48% (Table 3). On the other hand, the AUC of DVC for DPN development was 0.736 ($p < 0.001$), with a cutoff point of 7.47, showing a sensitivity of 47.50% and a specificity of 92.86%. SVC (AUC = 0.519, $p > 0.05$) and DVC (AUC = 0.520, $p > 0.05$) had poor diagnostic values for NDPN (Table 3).

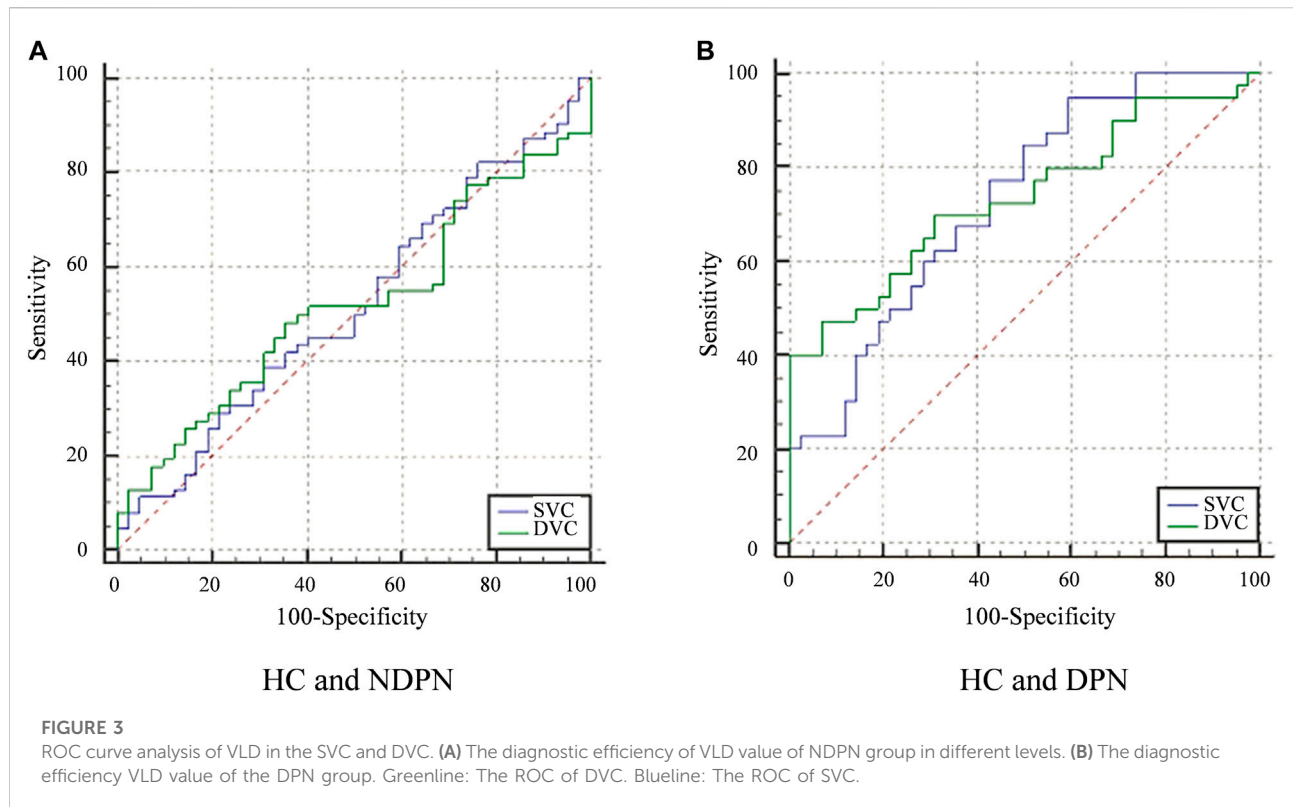


TABLE 3 ROC curve analysis of VLD in different layers of DM with or without DPN.

	AUC (95%CI)	Cutoff	Sen, %	Spe, %	<i>p</i>
NDPN					
SVC	0.519	7.41	38.71	69.05	0.740
DVC	0.520	8.18	48.39	64.29	0.721
DPN					
SVC	0.729	8.01	95.00	40.48	<0.001
DVC	0.736	7.47	47.50	92.86	<0.001

AUC, area under the curve; CI, confidence interval; Cut Off, the magnitude of the analyte to be detected; Sen, sensitivity; Spe: specificity.

Discussion

It would be beneficial to gain a better understanding of the neurodegeneration and vascular complications in both normal and DPN patients in order to determine the characteristics and progression of this disease. Traditional neurodegenerative indicators are not sensitive enough to detect early DPN and identify disease progression (Iqbal et al., 2018). As a result, half of the diabetic patients have DPN in the course of their disease development, but only about 20% of them have typical clinical

manifestations of neuropathy at the time of diagnosis (Deli et al., 2013; Hosseini and Abdollahi 2013; Verrotti et al., 2014). Our research provides a new method for diagnosing DPN, which is expected to become an objective biomarker for predicting which patients may develop from NDPN to DPN in the future.

Previous cross-sectional studies (Ding et al., 2012; Hu et al., 2021) showed that DPN patients have a retinal microvascular abnormality, which is not seen in healthy controls. However, these reports used fundus photography, which limits the resolution of the retinal microvasculature to the superficial vessels. In this study, we used OCTA to image the macular microvasculature and utilized a deep learning approach to assess the VLD in DPN and NDPN when compared with healthy controls and determined the diagnostic ability of the deep learning approach to identify the macular capillary changes. DPN was significantly altered in SVC and DVC when compared with healthy controls and NDPN. The SVC layer is responsible for the metabolic supply of the ganglion cell. A previous study observed degeneration of retinal ganglion cells and axons in SVC in diabetic patients (Kim K et al., 2016; Kim et al., 2018). Changes in the SVC seen in our report complement the already reported OCT structural markers (Shahidi et al., 2012; Sangeetha et al., 2016). On the other hand, DVC lies beneath the SVC and is important for the nutrition of the inner nuclear layer. This microvascular plexus consists of bipolar cells, horizontal cells,

and amacrine cells found in the deeper portion of the inner retina. The DVC is supplied by vertical anastomoses of the SVC (Campbell et al., 2017), indicating that changes in the SVC may affect the DVC. The microvascular changes seen in our current study are in line with previous OCTA studies (Nesper et al., 2017; Conti et al., 2019; Dai et al., 2020), which used different quantitative programs to characterize the microvascular changes suggesting that peripheral neuropathy may lead to microvascular impairment.

Patients with DM can exhibit microvascular damage (Thrainsdottir et al., 2003), endothelial cell proliferation, and intimal thickening, which results in blockage of the vessel lumen, ultimately leading to hypoperfusion and dysfunction of nerve cells (Malik et al., 1993). Microvascular impairment progresses into neuropathy and is one of the hallmarks of DPN (Gibbons and Shaw 2012). In the early phase, microvascular impairment and peripheral neuropathy are principally asymptomatic, and few tests are accessible for diagnosis. Interestingly, we found that the VLD in DPN patients' nasal and superior areas was more susceptible and pronounced than in other areas. Similarly, Radi et al. found that the retina vessel density in the superficial of the macular region was significantly reduced, and the decrease in the superior and temporal sectors was the most obvious in the early stage of DR (Radi et al., 2019). In addition, Li et al. (2020) performed fundus angiography and fundus photography on patients with diabetic retinopathy at different stages and found that the exudation and microvascular lesions on the nasal side of the posterior pole increased significantly in the early phase of diabetic retinopathy and the microvessels on the nasal side were significantly damaged. However, some scholars found that diabetic microvascular abnormalities were more common on the temporal side than on the nasal side in the early stage of retinopathy in diabetic patients (Silva et al., 2013; Matsunaga et al., 2015). This phenomenon of uneven distribution of lesions may be related to the uneven physiological or metabolic processes in different regions, such as abnormal expression and distribution of biochemical substances such as caspase-1 (Glut1), and inducible nitric oxide synthase (iNOS) and PKCE (Tang et al., 2003). Other scholars believe that the differences in microvascular changes in different sections may be related to the different anatomical structures of retinal microcirculation (Chaher et al., 2022). However, the specific mechanism is still unclear.

Importantly, we analyzed the ability of the macular microvasculature density to detect the early changes in DPN and NDPN groups. Our ROC curve analysis showed the ability of VLD in SVC and DVC to discriminate between HC and DPN, HC, and NDPN; however, the DVC showed a higher discriminating power than the SVC. Noteworthy, the DVC has a thinner and smaller microvascular structure making it more sensitive to the progression of the disease than the SVC (Wang et al., 2018); thus, we suggest that this plexus may be more sensitive to the microvascular damage

associated with the disease cascade. This implies a close connection between neurodegeneration and microvasculature in these patients. Since retinal microvascular has been suggested to reflect microvascular diseases in other parts of the body (Cankurtaran et al., 2020; Zhang et al., 2021), we suggest that assessment of retinal microvasculature could be a route for the early detection of microvascular degenerates as indirect pointers of DPN. Such *in vivo* quantitative means allow monitoring of DPN and may enable the assessment of treatments. Therefore, endocrinologists should comprehensively consider the retinal structure and microvasculature in estimating and treating the early DPN of DM patients.

There are several limitations in the present study. First, six participants were excluded due to movement during OCTA imaging. Moreover, healthy control subjects were not examined for HbA1c. Although the history of past medical conditions was obtained from each patient, we cannot rule out the possibility of underlying diseases. Second, this cross-sectional study did not comprehensively analyze retinal microvascular parameters over time and disease progression in patients with DPN. Finally, the sample size is relatively small. The relationship between the development of retinal vascular changes over time and DPN should be further explored through a multi-center longitudinal study with larger samples.

Conclusion

Our results showed that DM patients with DPN had significantly lower SVC and DVC VLD, and the VLD in the nasal and superior sectors of DPN patients was more susceptible and more pronounced. We also found that the AUCs for VLD of the SVC and DVC could discriminate between DPN patients and controls to a certain extent and may serve as an early pointer of microangiopathy. OCTA based on deep learning could be potentially used in clinical practice as a new indicator in the early diagnosis of DM with and without DPN.

Data availability statement

The raw data supporting the conclusion of this article will be made available by the authors, without undue reservation.

Ethics statement

The studies involving human participants were reviewed and approved by the Ethics Committee of The Affiliated People's Hospital of Ningbo University. The patients/participants provided their written informed consent to participate in this study.

Author contributions

Design of the study QL, YW; conduct of the study, data collection, analysis, and interpretation XD, YY, SW, JH, AC, and JL; manuscript preparation and review YW, XD, and QL.

Funding

This study was supported by research grants from Ningbo Major Science and Technology Task Project (2021Z054); Ningbo Clinical Research Center for Ophthalmology.

References

- Alberti, K. G., and Zimmet, P. Z. (1998). Definition, diagnosis and classification of diabetes mellitus and its complications. Part 1: Diagnosis and classification of diabetes mellitus provisional report of a WHO consultation. *Diabet. Med.* 15 (7), 539–553. doi:10.1002/(SICI)1096-9136(199807)15:7<539:AID-DIA668>3.0.CO;2-S
- Callaghan, B. C., Little, A. A., Feldman, E. L., and Hughes, R. A. (2012). Enhanced glucose control for preventing and treating diabetic neuropathy. *Cochrane Database Syst. Rev.* 6 (6), CD007543. doi:10.1002/14651858.CD007543.pub2
- Campbell, J. P., Zhang, M., Hwang, T. S., Bailey, S. T., Wilson, D. J., Jia, Y., et al. (2017). Detailed vascular anatomy of the human retina by projection-resolved optical coherence tomography angiography. *Sci. Rep.* 7 (1), 42201. doi:10.1038/srep42201
- Cankurtaran, V., Inanc, M., Tekin, K., and Turgut, F. (2020). Retinal microcirculation in predicting diabetic nephropathy in type 2 diabetic patients without retinopathy. *Ophthalmologica*. 243 (4), 271–279. doi:10.1159/000504943
- Chaher, A., Fajnkuchen, F., Tabary, S., and Giocanti-Auregan, A. (2022). Reduced vessel density in the mid-periphery and peripapillary area of the superficial capillary plexus in non-proliferative diabetic retinopathy. *J. Clin. Med.* 11 (3), 532. doi:10.3390/jcm11030532
- Chen, Q., Ma, Q., Wu, C., Tan, F., Chen, F., Wu, Q., et al. (2017). Macular vascular fractal dimension in the deep capillary layer as an early indicator of microvascular loss for retinopathy in type 2 diabetic patients. *Invest. Ophthalmol. Vis. Sci.* 58 (9), 3785–3794. doi:10.1167/iovs.17-21461
- Chew, E. Y., Ambrosius, W. T., Davis, M. D., Danis, R. P., Gangaputra, S., Greven, C. M., et al. (2010). Effects of medical therapies on retinopathy progression in type 2 diabetes. *N. Engl. J. Med.* 363 (3), 233–244. doi:10.1056/NEJMoa1001288
- Cole, J. B., and Florez, J. C. (2020). Genetics of diabetes mellitus and diabetes complications. *Nat. Rev. Nephrol.* 16 (7), 377–390. doi:10.1038/s41581-020-0278-5
- Conti, F. F., Qin, V. L., Rodrigues, E. B., Sharma, S., Rachitskaya, A. V., Ehlers, J. P., et al. (2019). Choriocapillaris and retinal vascular plexus density of diabetic eyes using split-spectrum amplitude decorrelation spectral-domain optical coherence tomography angiography. *Br. J. Ophthalmol.* 103 (4), 452–456. doi:10.1136/bjophthalmol-2018-311903
- Dai, Y., Zhou, H., Chu, Z., Zhang, Q., Chao, J. R., Rezaei, K. A., et al. (2020). Microvascular changes in the choriocapillaris of diabetic patients without retinopathy investigated by swept-source OCT angiography. *Invest. Ophthalmol. Vis. Sci.* 61 (3), 50. doi:10.1167/iovs.61.3.50
- Dehghani, C., Srinivasan, S., Edwards, K., Pritchard, N., Russell, A. W., Malik, R. A., et al. (2017). Presence of peripheral neuropathy is associated with progressive thinning of retinal nerve fiber layer in type 1 diabetes. *Invest. Ophthalmol. Vis. Sci.* 58 (6), BIO234–BIO239. doi:10.1167/iovs.17-21801
- Deli, G., Bosnyak, E., Puschi, G., Komoly, S., and Feher, G. (2013). Diabetic neuropathies: Diagnosis and management. *Neuroendocrinology* 98 (4), 267–280. doi:10.1159/000358728
- Ding, J., Cheung, C. Y., Ikram, M. K., Zheng, Y. F., Cheng, C. Y., Lamoureux, E. L., et al. (2012). Early retinal arteriolar changes and peripheral neuropathy in diabetes. *Diabetes care* 35 (5), 1098–1104. doi:10.2337/dc11-1341
- Gibbons, G. W., and Shaw, P. M. (2012). Diabetic vascular disease: Characteristics of vascular disease unique to the diabetic patient. *Semin. Vasc. Surg.* 25 (2), 89–92. doi:10.1053/j.semvascsurg.2012.04.005
- Hosseini, A., and Abdollahi, M. (2013). Diabetic neuropathy and oxidative stress: Therapeutic perspectives. *Oxid. Med. Cell. Longev.* 2013, 168039. doi:10.1155/2013/168039
- Hu, G., Wu, H., Kuang, L., Zee, B. C., Huang, Y., Huang, Z., et al. (2021). Clinical study of diabetic peripheral neuropathy screening by retinal vascular geometric parameters. *Sci. Rep.* 11 (1), 6784. doi:10.1038/s41598-021-85831-0
- Iqbal, Z., Azmi, S., Yadav, R., Ferdousi, M., Kumar, M., Cuthbertson, D. J., et al. (2018). Diabetic peripheral neuropathy: Epidemiology, diagnosis, and pharmacotherapy. *Clin. Ther.* 40 (6), 828–849. doi:10.1016/j.clinthera.2018.04.001
- Kazamel, M., Stino, A. M., and Smith, A. G. (2021). Metabolic syndrome and peripheral neuropathy. *Muscle Nerve* 63 (3), 285–293. doi:10.1002/mus.27086
- Kim, A. Y., Chu, Z., Shahidzadeh, A., Wang, R. K., Puliafito, C. A., Kashani, A. H., et al. (2016). Quantifying microvascular density and morphology in diabetic retinopathy using spectral-domain optical coherence tomography angiography. *Invest. Ophthalmol. Vis. Sci.* 57 (9), T362–T370. doi:10.1167/iovs.15-18904
- Kim, J. H., Lee, M. W., Byeon, S. H., Kim, S. S., Koh, H. J., Lee, S. C., et al. (2018). Associations between individual retinal layer thicknesses and diabetic peripheral neuropathy using retinal layer segmentation analysis. *Retina Phila. Pa* 38 (11), 2190–2196. PMID: 28902096. doi:10.1097/IAE.0000000000001835
- Kim, K. K., Yu, S., Kwak, H. W., and Kim, E. S. (2016). Retinal neurodegeneration associated with peripheral nerve conduction and autonomic nerve function in diabetic patients. *Am. J. Ophthalmol.* 170, 15–24. doi:10.1016/j.ajo.2016.06.038
- Kim, K. J., Choi, J., Bae, J. H., Kim, K. J., Yoo, H. J., Seo, J. A., et al. (2021). Time to reach target glycosylated hemoglobin is associated with long-term durable glycemic control and risk of diabetic complications in patients with newly diagnosed type 2 diabetes mellitus: A 6-year observational study (diabetes metab J 2021;45:368-78). *Diabetes Metab. J.* 45 (4), 617–618. doi:10.4093/dmj.2021.0152
- Li, X., Xie, J., Zhang, L., Cui, Y., Zhang, G., Wang, J., et al. (2020). Differential distribution of manifest lesions in diabetic retinopathy by fundus fluorescein angiography and fundus photography. *BMC Ophthalmol.* 20 (1), 471. doi:10.1186/s12886-020-01740-2
- Lipsky, B. A., Berendt, A. R., Cornia, P. B., Pile, J. C., Peters, E. J., Armstrong, D. G., et al. (2012). 2012 Infectious Diseases Society of America clinical practice guideline for the diagnosis and treatment of diabetic foot infections. *Clin. Infect. Dis.* 54 (12), e132–e173. doi:10.1093/cid/cis346
- Ma, Y., Hao, H., Xie, J., Fu, H. F., Zhang, J., Yang, J., et al. (2020). Rose: A retinal OCT-angiography vessel segmentation dataset and new model. *IEEE Trans. Med. Imaging* 40 (3), 928–939. doi:10.1109/TMI.2020.3042802
- Malik, R. A., Tesfaye, S., Thompson, S. D., Veves, A., Sharma, A. K., Boulton, A. J., et al. (1993). Endoneurial localisation of microvascular damage in human diabetic neuropathy. *Diabetologia* 36 (5), 454–459. doi:10.1007/BF00402283
- Malik, R. A. (2014). Which test for diagnosing early human diabetic neuropathy? *Diabetes* 63 (7), 2206–2208. doi:10.2337/db14-0492

Conflict of interest

The authors declare that the research was conducted in the absence of any commercial or financial relationships that could be construed as a potential conflict of interest.

Publisher's note

All claims expressed in this article are solely those of the authors and do not necessarily represent those of their affiliated organizations, or those of the publisher, the editors and the reviewers. Any product that may be evaluated in this article, or claim that may be made by its manufacturer, is not guaranteed or endorsed by the publisher.

- Matsunaga, D. R., Yi, J. J., De, Koo, L. O., Ameri, H., Puliafito, C. A., and Kashani, A. H. (2015). Optical coherence tomography angiography of diabetic retinopathy in human subjects. *Ophthalmic Surg. Lasers Imaging Retina* 46 (8), 796–805. doi:10.3928/23258160-20150909-03
- Nesper, P. L., Roberts, P. K., Onishi, A. C., Chai, H., Liu, L., Jampol, L. M., et al. (2017). Quantifying microvascular abnormalities with increasing severity of diabetic retinopathy using optical coherence tomography angiography. *Invest. Ophthalmol. Vis. Sci.* 58 (6), BIO307–BIO315. doi:10.1167/iops.17-21787
- Radi, A. H., Mohamed, M. A. A., and Attia, A. M. (2019). Macular vessels density in diabetic retinopathy: Quantitative assessment using optical coherence tomography angiography. *Int. Ophthalmol.* 39 (8), 1845–1859. doi:10.1007/s10792-018-1013-0
- Salvi, L., Plateroti, P., Balducci, S., Bollanti, L., Conti, F. G., Vitale, M., et al. (2016). Abnormalities of retinal ganglion cell complex at optical coherence tomography in patients with type 2 diabetes: A sign of diabetic polyneuropathy, not retinopathy. *J. Diabetes Complicat.* 30 (3), 469–476. doi:10.1016/j.jdiacomp.2015.12.025
- Sangeetha, S., Nicola, P., Dimitrios, V., Katie, E., Sampson, G. P., Russell, A. W., et al. (2016). Retinal tissue thickness is reduced in diabetic peripheral neuropathy. *Curr. Eye Res.* 41 (10), 1359–1366. doi:10.3109/02713683.2015.1119855
- Sarwar, N., Gao, P., Seshasai, S. R., Gobin, R., Kaptoge, S., Di Angelantonio, E., et al. (2010). Diabetes mellitus, fasting blood glucose concentration, and risk of vascular disease: A collaborative meta-analysis of 102 prospective studies. *Lancet* 375 (9733), 2215–2222. doi:10.1016/S0140-6736(10)60484-9
- Selvarajah, D., Kar, D., Khunti, K., Davies, M. J., Scott, A. R., Walker, J., et al. (2019). Diabetic peripheral neuropathy: Advances in diagnosis and strategies for screening and early intervention. *Lancet. Diabetes Endocrinol.* 7 (12), 938–948. doi:10.1016/S2213-8587(19)30081-6
- Shahidi, A. M., Sampson, G. P., Pritchard, N., Edwards, K., Vagenas, D., Russell, A. W., et al. (2012). Retinal nerve fibre layer thinning associated with diabetic peripheral neuropathy. *Diabet. Med.* 29 (7), e106–e111. doi:10.1111/j.1464-5491.2012.03588.x
- Silva, P. S., Cavallerano, J. D., Sun, J. K., Soliman, A. Z., Aiello, L. M., Aiello, L. P., et al. (2013). Peripheral lesions identified by mydriatic ultrawide field imaging: Distribution and potential impact on diabetic retinopathy severity. *Ophthalmology* 120 (12), 2587–2595. doi:10.1016/j.ophtha.2013.05.004
- Singleton, J. R., Bixby, B., Russell, J. W., Feldman, E. L., Peltier, A., Goldstein, J., et al. (2008). The Utah early neuropathy Scale: A sensitive clinical scale for early sensory predominant neuropathy. *J. Peripher. Nerv. Syst.* 13 (3), 218–227. doi:10.1111/j.1529-8027.2008.00180.x
- Sloan, G., Selvarajah, D., and Tesfaye, S. (2021). Pathogenesis, diagnosis and clinical management of diabetic sensorimotor peripheral neuropathy. *Nat. Rev. Endocrinol.* 17 (7), 400–420. doi:10.1038/s41574-021-00496-z
- Spaide, R. F., Klancnik, J. M., and Cooney, M. J. (2014). Retinal vascular layers imaged by fluorescein angiography and optical coherence tomography angiography. *JAMA Ophthalmol.* 133 (1), 45–50. doi:10.1001/jamaophthalmol.2014.3616
- Sun, H., Saeedi, P., Karuranga, S., Pinkepank, M., Ogurtsova, K., Duncan, B. B., et al. (2022). IDF Diabetes Atlas: Global, regional and country-level diabetes prevalence estimates for 2021 and projections for 2045. *Diabetes Res. Clin. Pract.* 183, 109119. doi:10.1016/j.diabres.2021.109119
- Tang, J., Mohr, S., Du, Y. D., and Kern, T. S. (2003). Non-uniform distribution of lesions and biochemical abnormalities within the retina of diabetic humans. *Curr. Eye Res.* 27 (1), 7–13. doi:10.1076/ceyr.27.2.7.15455
- Tesfaye, S., Boulton, A. J., Dyck, P. J., Freeman, R., Horowitz, M., Kempler, P., et al. (2010). Diabetic neuropathies: Update on definitions, diagnostic criteria, estimation of severity, and treatments. *Diabetes care* 33 (10), 2285–2293. doi:10.2337/dc10-1303
- Thrainsdottir, S., Malik, R. A., Dahlin, L. B., Wiksell, P., Eriksson, K. F., Rosén, I., et al. (2003). Endoneurial capillary abnormalities presage deterioration of glucose tolerance and accompany peripheral neuropathy in man. *Diabetes* 52 (10), 2615–2622. doi:10.2337/diabetes.52.10.2615
- Verrotti, A., Prezioso, G., Scattoni, R., and Chiarelli, F. (2014). Autonomic neuropathy in diabetes mellitus. *Front. Endocrinol.* 5, 205. doi:10.3389/fendo.2014.00205
- Wang, L., Murphy, O., Caldito, N. G., Calabresi, P. A., and Saidha, S. (2018). Emerging applications of optical coherence tomography angiography (OCTA) in neurological research. *Eye Vis.* 5, 11. doi:10.1186/s40662-018-0104-3
- Wu, L., Fernandez-Loaiza, P., Sauma, J., Hernandez-Bogantes, E., and Masis, M. (2013). Classification of diabetic retinopathy and diabetic macular edema. *World J. Diabetes* 4 (6), 290–294. doi:10.4239/wjd.v4.i6.290
- Zhang, K., Liu, X., Xu, J., Yuan, J., Cai, W., Chen, T., et al. (2021). Deep-learning models for the detection and incidence prediction of chronic kidney disease and type 2 diabetes from retinal fundus images. *Nat. Biomed. Eng.* 5 (6), 533–545. doi:10.1038/s41551-021-00745-6



OPEN ACCESS

EDITED BY

Yanwu Xu,
Baidu, China

REVIEWED BY

Yongjin Zhou,
Shenzhen University, China
Zhi Fang,
Zhejiang University, China
Gangjin Kang,
The Affiliated Hospital of Southwest
Medical University, China

*CORRESPONDENCE

Yunfang Liu,
✉ panle0701@139.com
Keran Li,
✉ kathykeran860327@126.com
Kunke Li,
✉ likunke@foxmail.com

[†]These authors have contributed equally
to this work and share first authorship

SPECIALTY SECTION

This article was submitted to Molecular
and Cellular Pathology,
a section of the journal
Frontiers in Cell and Developmental
Biology

RECEIVED 25 November 2022

ACCEPTED 05 December 2022

PUBLISHED 20 December 2022

CITATION

Ji Y, Liu S, Hong X, Lu Y, Wu X, Li K, Li K
and Liu Y (2022), Advances in artificial
intelligence applications for ocular
surface diseases diagnosis.
Front. Cell Dev. Biol. 10:1107689.
doi: 10.3389/fcell.2022.1107689

COPYRIGHT

© 2022 Ji, Liu, Hong, Lu, Wu, Li, Li and
Liu. This is an open-access article
distributed under the terms of the
[Creative Commons Attribution License
\(CC BY\)](https://creativecommons.org/licenses/by/4.0/). The use, distribution or
reproduction in other forums is
permitted, provided the original
author(s) and the copyright owner(s) are
credited and that the original
publication in this journal is cited, in
accordance with accepted academic
practice. No use, distribution or
reproduction is permitted which does
not comply with these terms.

Advances in artificial intelligence applications for ocular surface diseases diagnosis

Yuke Ji^{1†}, Sha Liu^{1†}, Xiangqian Hong², Yi Lu², Xingyang Wu²,
Kunke Li^{2*}, Keran Li^{1*} and Yunfang Liu^{3*}

¹The Laboratory of Artificial Intelligence and Bigdata in Ophthalmology, Affiliated Eye Hospital of Nanjing Medical University, Nanjing, China, ²Shenzhen Eye Hospital, Jinan University, Shenzhen, China, ³Department of Ophthalmology, First Affiliated Hospital of Huzhou University, Huzhou, China

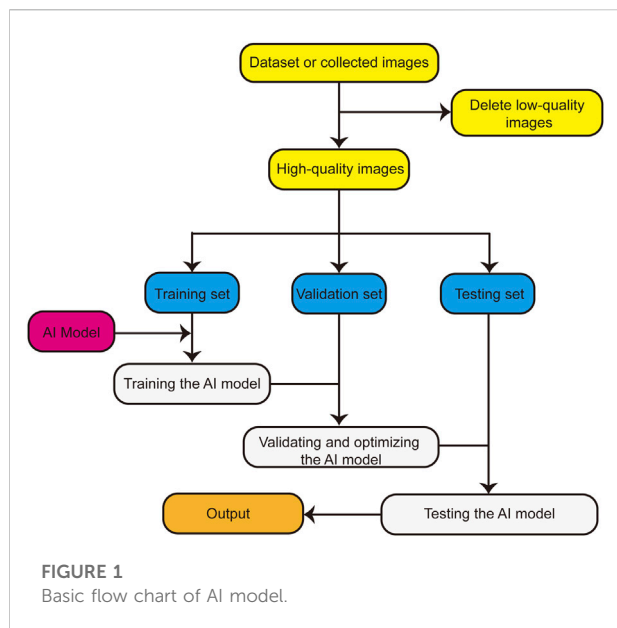
In recent years, with the rapid development of computer technology, continual optimization of various learning algorithms and architectures, and establishment of numerous large databases, artificial intelligence (AI) has been unprecedentedly developed and applied in the field of ophthalmology. In the past, ophthalmological AI research mainly focused on posterior segment diseases, such as diabetic retinopathy, retinopathy of prematurity, age-related macular degeneration, retinal vein occlusion, and glaucoma optic neuropathy. Meanwhile, an increasing number of studies have employed AI to diagnose ocular surface diseases. In this review, we summarize the research progress of AI in the diagnosis of several ocular surface diseases, namely keratitis, keratoconus, dry eye, and pterygium. We discuss the limitations and challenges of AI in the diagnosis of ocular surface diseases, as well as prospects for the future.

KEYWORDS

artificial intelligence, ocular surface disease, disease diagnosis, keratitis, keratoconus, dry eye, pterygium

1 Introduction

Since the beginning of the 21st century, significant changes have occurred in daily life with the rapid development of science and technology, including computer science. In 2018, the US Food and Drug Administration approved the launch of IDx-DR, which is the first ophthalmic artificial intelligence (AI) device that can automatically diagnose and grade diabetic retinopathy. Since then, there has been an upsurge in the application of AI technology in the field of ophthalmology and various research results continue to emerge. AI is a branch of computer science that mainly studies and develops new technical science to simulate and extend the theory, methods, technology, and application systems of human intelligence. Machine learning (ML), deep learning (DL), artificial neural networks, deep neural networks (DNNs), convolution neural networks (CNNs), and transfer learning all belong to this category. At present, a series of research achievements have been made in AI technology for the diagnosis and treatment of eye diseases such as diabetic retinopathy (Raman et al., 2019; Ai et al., 2021; Bhardwaj et al., 2021), retinopathy of prematurity (Redd et al., 2018; Attallah, 2021; Wang et al., 2021a), age-related macular



degeneration (Burlina et al., 2018; Yan et al., 2020; Yim et al., 2020), retinal vein occlusion (Nagasato et al., 2018; Nagasato et al., 2019; Xu et al., 2022), and glaucoma (Christopher et al., 2018; Hood and De Moraes, 2018; Medeiros et al., 2021).

In general, ocular surface diseases are diseases that damage the normal structure and function of the cornea, conjunctiva, and ocular surface. In recent years, increasing studies have applied AI to assist in the diagnosis of ocular surface diseases. In this review, we summarize the application of AI in the diagnosis of four common ocular surface diseases: keratitis, keratoconus, dry eye, and pterygium. Moreover, we discuss the limitations and challenges of AI in clinical applications and future prospects. The term “diagnosis” used in this article has a broad meaning, including the designation or detection of a specific disease and

other diagnostic decisions (for example, identification and screening of different disease states, subtypes, stages or degrees, and the prediction of disease progression).

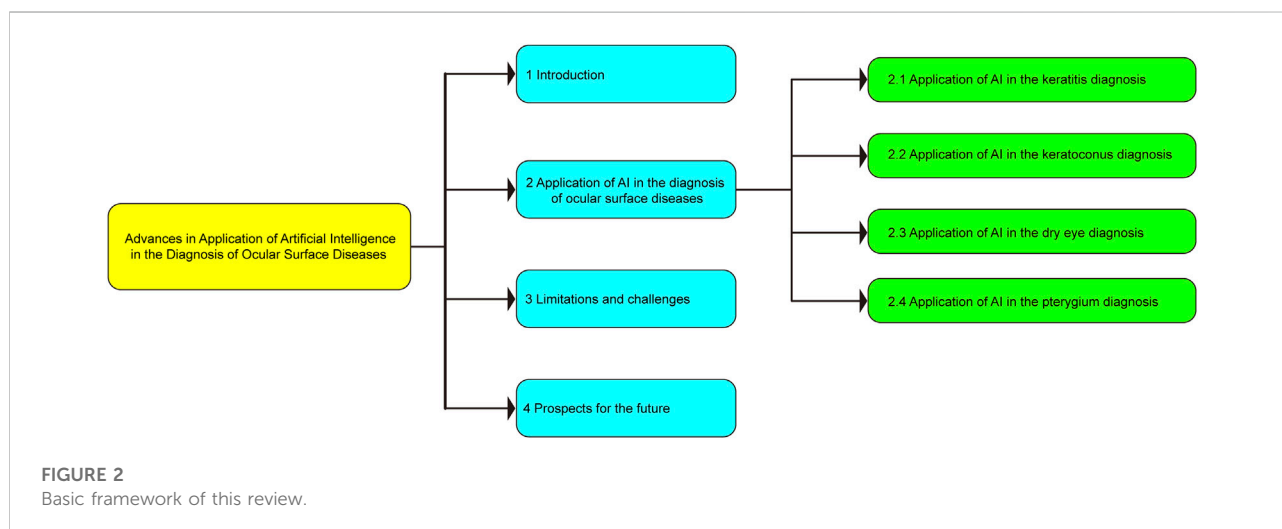
The basic research flow of an AI model for such an application is presented in Figure 1. First, the dataset is organized, low-quality images are deleted, and the remaining high-quality images are divided into the training, verification, and testing sets. Subsequently, the AI model is trained using the training set, validated using the verification set, and optimized according to the results. Finally, the optimized AI model is tested using the testing set, and the application performance of the AI model is obtained.

The basic framework of this review, which is divided into four parts, is depicted in Figure 2. The first part focuses the current status of AI and its application in ophthalmic diseases; the second part presents the research progress of AI in the diagnosis of ocular surface diseases; the third part introduces the limitations and challenges of AI in the diagnosis of ocular surface diseases; the fourth part provides an overview of the future application prospects of AI in the diagnosis of ocular surface diseases.

2 Application of AI in ocular surface disease diagnoses

2.1 Application of AI in keratitis diagnosis

Keratitis, which is the fifth most common cause of human blindness (Pascolini and Mariotti, 2012; Flaxman et al., 2017), refers to the weakening of the corneal defense ability and inflammation of the corneal tissue as a result of exogenous or endogenous pathogenic factors. The etiology of keratitis is complex; it can be caused not only by pathogenic microorganisms (such as bacteria, fungi, viruses, and



chlamydia), but also by autoimmune diseases such as rheumatoid arthritis. The inflammation of adjacent tissues (such as conjunctivitis, scleritis, and iridocyclitis) may also lead to keratitis (Chidambaram et al., 2018; Khor et al., 2018). At present, the classification of keratitis has not been unified. It can be categorized as infectious, immune, malnourished, neuromyolytic, and exposed keratitis, according to its pathogenic causes. Infectious keratitis can be further subdivided into bacteria, viruses, fungi, chlamydia, and so on, according to different pathogenic microorganisms (Tena et al., 2019).

Although the etiology of keratitis is varied, the pathological processes of different types usually exhibit common characteristics. The classical pathological process can be divided into four stages: the infiltration, ulcer formation, ulcer regression, and healing stages (Li et al., 2021). The most common symptoms of keratitis in clinical manifestations include eye pain, photophobia, tears, and blepharospasm, which can persist until the inflammation subsides (Austin et al., 2017). Keratitis is often accompanied by varying degrees of vision loss. Typical signs of keratitis include ciliary hyperemia, corneal infiltration, and corneal ulcer formation. Moreover, it is often accompanied by varying degrees of vision loss. The shape and location of corneal infiltration and ulcers also differ according to the location, size, and nature of the lesion (Ting et al., 2018; Ting et al., 2021). Although keratitis exhibits typical characteristics, its diagnosis is challenging owing to its diverse clinical manifestations and atypical symptoms and signs in the early stages, and especially if the appropriate equipment is unavailable. Applying AI technology to assist in keratitis diagnosis can aid the treatment of keratitis and reduce the blindness rate (Li et al., 2021; Tahvildari et al., 2021).

Kuo et al. (Kuo et al., 2021) constructed a model for the diagnosis of bacterial keratitis based on several DL algorithms (ResNet-50, ResNeXt-50, DenseNet-121, SE-ResNet50, EfficientNet B0, EfficientNet B1, EfficientNet B2, and EfficientNet B3). They collected 1,512 slit lamp images for the training, modification, and verification of the diagnostic model. Following verification, the EfficientNet B3 model exhibited the best performance, with a sensitivity of 0.741, a specificity of 0.643, and an accuracy of 0.703. Lv et al. (Lv et al., 2020) constructed an AI model that can automatically diagnose keratitis based on the ResNet algorithm, and collected 2,088 confocal microscope images to train and test the model. Following testing, the AUC value, sensitivity, specificity, and accuracy of the model were 0.9875, 0.9186, 0.9834, and 0.9626, respectively. Kuo et al. (Kuo et al., 2020b) constructed a DL model for the diagnosis of fungal keratitis based on the DenseNet algorithm, and used 288 collected corneal images to train and test the DL model. The sensitivity, specificity, and accuracy of the diagnostic model were 0.711, 0.684, and 0.694, respectively. Liu et al. (Liu et al., 2020) proposed a DL model that can diagnose keratitis using two CNNs (AlexNet and VGGNet), and improved the diagnostic

performance of the model using data enhancement and image fusion. They collected 1,213 confocal microscope images to train and validate the model. The experimental results revealed that the accuracies of the AlexNet and VGGNet models were 0.9995 and 0.9989, respectively. According to the aforementioned research, intelligent diagnosis models based on DL have exhibited good performance for keratitis diagnosis and significant application potential. Keratitis can be diagnosed as early as possible with limited medical resources, thereby reducing the occurrence of corneal blindness.

Gu et al. (Gu et al., 2020) proposed a method to distinguish infectious and non-infectious keratitis based on the Inception v3 algorithm. They collected 5,325 slit lamp images for training and testing. Following testing, the AUC values of the model for diagnosing infectious and non-infectious keratitis were 0.930 and 0.934, respectively. Hung et al. (Hung et al., 2021) constructed an AI model that can distinguish different types of keratitis using various CNNs (DenseNet-121, DenseNet-161, DenseNet-169, DenseNet-201, EfficientNet B3, Inception v3, ResNet-101, and ResNet-50). They used 1,330 slit lamp images for training and verification. The average accuracy was 0.80 and the performance of DenseNet-161 was the best, with an AUC value of 0.85. Li et al. (Li et al., 2021) presented a system using three classical DL algorithms (DenseNet-121, Inception v3, and ResNet-50) to distinguish different types of keratitis. They collected 13,557 slit lamp images for training and verification of the classification system. The DenseNet-121 model exhibited the best performance, with a sensitivity of 0.977, a specificity of 0.982, and an accuracy of 0.980. Ghosh et al. (Ghosh et al., 2022) combined three CNNs (VGG-19, ResNet-50, and DenseNet-121) to create an AI model that can distinguish bacterial keratitis from fungal keratitis. They used 2,167 slit lamp images for training and testing. The results demonstrated that the model sensitivity was 0.77, the F1 score was 0.83, and the AUC value was 0.904. The above AI model exhibits good performance in the classification of keratitis, which is close to that of clinical practice, and is expected to become a powerful auxiliary tool in clinical work.

Xu et al. (Xu et al., 2021a) developed an AI model that can automatically detect and evaluate corneal inflammatory cells in patients with keratitis using five DL algorithms (VGG-16, ResNet-101, Inception v3, Xception, and Inception-ResNet v2). They used 4,011 confocal microscope images to train and verify the model. The Inception-ResNet v2 model exhibited the best performance, with an AUC value of 0.9646, an accuracy of 0.9767, a sensitivity of 0.9174, and a specificity of 0.9931. Tiwari et al. (Tiwari et al., 2022) constructed an AI model based on a CNN that can distinguish active keratitis from scar healing. They collected 2,445 corneal images for the model training and verification. Following verification, the F1 score of the model was 0.843, the sensitivity was 0.935, the specificity was 0.8442, and the AUC value was 0.9731. The above results suggest that AI

TABLE 1 Summary of application of AI models in keratitis.

Authors	Task	Sample size	AI algorithms	Diagnostic performance
Kuo et al. (2021)	Diagnosis	1,512 images	ResNet-50, ResNeXt-50, DenseNet-121, SE-ResNet-50, EfficientNet B0, EfficientNet B1, EfficientNet B2, EfficientNet B3	Sensitivity = 0.741, Specificity = 0.643, Accuracy = 0.703
Lv et al. (2020)	Diagnosis	2,088 images	ResNet	AUC = 0.9875 Sensitivity = 0.9186 Specificity = 0.9834 Accuracy = 0.9626
Kuo et al. (2020b)	Diagnosis	288 images	DenseNet	Sensitivity = 0.711 Specificity = 0.684 Accuracy = 0.694
Liu et al. (2020)	Diagnosis	1,213 images	AlexNet	Accuracy of AlexNet = 0.9995
			VGGNet	Accuracy of VGGNet = 0.9989
Gu et al. (2020)	Classification	5,325 images	Inception v3	AUC of infectious keratitis = 0.930
				AUC of non-infectious keratitis = 0.934
Hung et al. (2021)	Classification	1,330 images	DenseNet-121, DenseNet-161, DenseNet-169, DenseNet-201, EfficientNet B3, Inception v3, ResNet-101, ResNet-50	Average accuracy = 0.80, AUC of DenseNet-161 = 0.85
Li et al. (2021)	Classification	13,557 images	DenseNet-121, Inception v3, ResNet-50	Sensitivity = 0.977 Specificity = 0.982 Accuracy = 0.980
Ghosh et al. (2022)	Classification	2,167 images	VGG19, ResNet-50, DenseNet-121	Sensitivity = 0.77, F1 score = 0.83, AUC = 0.904
Xu et al. (2021a)	Detection	4,011 images	VGG-16, ResNet-101, Inception v3, Xception, Inception-ResNet v2	AUC = 0.9646, Accuracy = 0.9767, Sensitivity = 0.9174, Specificity = 0.9931
Tiwari et al. (2022)	Classification	2,445 images	CNNs	F1 score = 0.843, Sensitivity = 0.935, Specificity = 0.8442, AUC = 0.9731

technology also offers good application potential in evaluating the activity of keratitis. The above studies are summarized in [Table 1](#).

2.2 Application of AI in keratoconus diagnosis

Keratoconus is a congenital developmental disorder that is characterized by localized conical protuberances with thinning of the corneal stroma in the protuberant area. Conus protuberances may lead to severe irregular astigmatism and high myopia, thereby resulting in severe vision loss ([Pinero et al., 2012](#); [Hashemi et al., 2020](#)). The disease generally occurs before and after puberty and occurs in both eyes, with a progressive decline in visual acuity ([Chatzis and Hafezi, 2012](#)). It can be corrected by myopic lenses in the early stages and contact lenses need to be worn owing to irregular astigmatism in the later stages ([Papali'i-Curtin et al., 2019](#)). The typical characteristics of the disease are central or paracentric conic dilatation, whereby the cone may be large or small, round or oval, and the thinning area of the corneal stroma is most obvious at the top of the cone. Patients with advanced keratoconus can see Munson's sign, Vogt's striae, or Fleischer's ring and other clinical signs, which can aid in diagnosing keratoconus ([de Sanctis et al., 2008](#); [Gordon-Shaag](#)

[et al., 2012](#); [Chan et al., 2021](#)). Although clinical diagnosis is straightforward for obvious keratoconus, it is difficult to diagnose atypical early keratoconus. At present, the most effective method for the early diagnosis of the disease is corneal topography, which reveals that the central corneal topography is distorted and the lower quadrant becomes steep. The corneal steepness expands to the subnasal, superior temporal, and superior nasal quadrants with the progression of the disease. Other examination methods include keratometers, retinography, and Placido discs ([Brunner et al., 2018](#); [Mohammadpour et al., 2018](#); [Rocha-de-Lossada et al., 2021](#)). Patients with early keratoconus can wear frame glasses or keratoplasty lenses according to the optometry results to improve their visual acuity ([Goh et al., 2020](#)). Moreover, intracorneal ring implants and corneal cross-linking or other methods can be used to delay the progress of the disease ([Ferdin et al., 2019](#)). If patients with early keratoconus do not receive effective intervention, the late stage will lead to severe vision loss, requiring keratoplasty, or even blindness. Therefore, the early screening, detection, and effective intervention of keratoconus are particularly important.

Tan et al. ([Tan et al., 2022](#)) proposed a diagnostic model for keratoconus based on the 5-FNN neural network model. They collected corneal videos of 354 eyes for the model training and testing. The results revealed that the diagnostic accuracy, sensitivity, and specificity of the model were 0.996, 0.993, and 1.000, respectively. Kamiya et al. ([Kamiya et al., 2019](#)) developed

a diagnostic classification model based on ResNet-18 to assist in the diagnosis and classification of keratoconus. They collected 543 anterior segment optical coherence tomography (As-OCT) images for the model training and testing. According to the results, the diagnostic accuracy of the model was 0.991 and the classification accuracy was 0.874. Dos Santos et al. (Dos Santos et al., 2019) designed an AI model that can diagnose keratoconus based on U-Net. They collected and marked 20,160 images for the model training and testing. Following testing, the accuracy of the model was 0.9956. The high accuracy and excellent performance of the above AI models demonstrate that AI technology can be used extensively in the clinical diagnosis and treatment of keratoconus, thereby greatly reducing the work stress of clinicians.

As early keratoconus often exhibits no typical symptoms and signs, screening to distinguish patients with keratoconus will help them to receive earlier treatment. Kuo et al. (Kuo et al., 2020a) constructed an AI model that can screen keratoconus based on three CNNs (VGG-16, Inception v3, and ResNet-152), and collected 354 corneal topographic maps for model training and external testing. The results revealed that the ResNet-152 model achieved the best performance, with an accuracy of 0.958, a sensitivity of 0.944, a specificity of 0.972, and an AUC value of 0.995. Chen et al. (Chen et al., 2021) presented a model that can detect coning modeling using CNNs. The model was trained and tested using the whole Liverpool (United Kingdom) and New Zealand (NZ) datasets. The results demonstrated that the model accuracy was 0.9785. Lavric et al. (Lavric and Valentin, 2019) constructed a screening model that can rapidly screen keratoconus based on CNNs, and collected 4,350 corneal topographic maps to train and test the model. The results indicated that the model accuracy was 0.9933. Al-Timemy et al. (Al-Timemy et al., 2021) developed a detection model that can recognize keratoconus based on the EfficientNet B0 DL algorithm. They collected 4,844 corneal topography maps for the training, debugging, and verification of the model. The AUC value, F1 score, and accuracy of the model were 0.99, 0.99, and 0.985, respectively. Abdelmotaal et al. (Abdelmotaal et al., 2020) constructed an AI model that can recognize keratoconus based on CNNs, and used 19,310 corneal topographic maps for training and testing. The test results demonstrated that the model accuracy was 0.958. In view of the good results of the above AI models in keratoconus identification and screening, timely diagnosis and treatment is possible.

Castro-Luna et al. (Castro-Luna et al., 2021) developed a model that can classify subclinical keratoconus using the random forest (RF) model. They collected clinical data of 81 eyes to train and verify the model. Kamiya et al. (Kamiya et al., 2021) presented a neural network prediction model to predict the progression of keratoconus, and collected 218 As-OCT images for training and verification. The results revealed that the prediction accuracy of the model was 0.794. Kato et al. (Kato et al., 2021) constructed an AI model that can predict the

progression of keratoconus based on the VGG-16 neural network model, and collected 274 corneal tomography images for training and verification. According to the results, the AUC value, sensitivity, and specificity of the model were 0.814, 0.778, and 0.696, respectively. Yousefi et al. (Yousefi et al., 2018) developed an AI model using ML to predict the severity of keratoconus. They collected and processed 3,156 corneal topographic maps for the model training and verification. The specificity and sensitivity of the model were 0.941 and 0.977, respectively. Herber et al. (Herber et al., 2021) presented an AI model that can predict the severity of keratoconus through two types of ML (linear discriminant analysis (LDA) and RF algorithms), and collected clinical data of 434 eyes for training and verification. Following verification, the accuracies of the LDA and RF models were 0.71 and 0.78, respectively. The above studies demonstrate that AI models can achieve satisfactory results in the classification and prediction of the progression of keratoconus. Thus, such models can be used to create effective treatment plans for keratoconus patients. The above studies are summarized in Table 2.

2.3 Application of AI in the diagnosis of dry eye

Dry eye, which is also known as keratoconjunctivitis sicca, refers to the decline in tear film stability caused by an abnormal quality and quantity of tears or abnormal dynamics resulting from any cause. It is accompanied by eye discomfort, resulting in ocular surface tissue lesions of various diseases (Craig et al., 2017a; Craig et al., 2017b). Dry eye disease is caused by many complex pathological processes. It can be roughly divided into abnormal tear dynamics and an abnormal ocular surface epithelium (Hu et al., 2021), both of which often play a role overall. Recent studies have demonstrated that changes in the eye surface, immune-based inflammatory response, apoptosis, decreased levels of sex hormones, and meibomian gland dysfunction are the main causes of xerophthalmia (Cardona et al., 2011; Argiles et al., 2015; Rodriguez et al., 2018; DeAngelis et al., 2019). However, the relationship or causal relationship between the factors is not yet fully understood. At present, no consensus exists on the diagnostic classification criteria of dry eye. According to the etiology, dry eye is mainly divided into water sample deficiency dry eye, mucin deficiency dry eye, lipid deficiency dry eye, and dry eye caused by abnormal tear dynamics. The most common symptoms of dry eye are eye fatigue, foreign body sensation, dryness, burning, eye distension, eye pain, photophobia, and eye redness (Tepelus et al., 2017). Dry eyes slightly affect visual acuity in the early stage. Filamentous keratitis may occur after the development of the disease. Corneal ulcers, corneal thinning, perforation, and occasional secondary bacterial infection may occur in the late stage, and visual acuity will be seriously affected after the formation of corneal scar,

TABLE 2 Summary of application of AI models in keratoconus.

Authors	Task	Sample size	AI algorithms	Diagnostic performance
Tan et al. (2022)	Diagnosis	354 eyes	5-FNN	Accuracy = 0.996, Sensitivity = 0.993, Specificity = 1.000
Kamiya et al. (2019)	Diagnosis	543 images	ResNet-18	Accuracy = 0.991
				Accuracy = 0.874
Dos Santos et al. (2019)	Diagnosis	20,160 images	U-Net	Accuracy = 0.9956
Kuo et al. (2020a)	Detection	354 maps	VGG-16, Inception v3, ResNet-152	Accuracy = 0.958, Sensitivity = 0.944
				Specificity = 0.972
				AUC = 0.995
Chen et al. (2021)	Detection	Liverpool and New Zealand datasets	CNNs	Accuracy = 0.9785
Lavric and Valentin, (2019)	Detection	4,350 maps	CNNs	Accuracy = 0.9933
Al-Timemy et al. (2021)	Detection	4,844 maps	EfficientNet B0	AUC = 0.99
				F1 score = 0.99
				Accuracy = 0.985
Abdelmotaal et al. (2020)	Detection	19,310 maps	CNNs	Accuracy = 0.958
Castro-Luna et al. (2021)	Classification	81 eyes	RF	Accuracy = 0.89
Kamiya et al. (2021)	Prediction	218 images	Neural network	Accuracy = 0.794
Kato et al. (2021)	Prediction	274 images	VGG-16	AUC = 0.814
				Sensitivity = 0.778, Specificity = 0.696
Yousefi et al. (2018)	Prediction	3,156 maps	ML	Specificity = 0.941
				Sensitivity = 0.977
Herber et al. (2021)	Prediction	434 eyes	LDA, RF	Accuracy of LDA = 0.71
				Accuracy of RF = 0.78

thereby resulting in a decline in the quality of life of patients (Nichols et al., 2011; Stapleton et al., 2017). The main clinical examination methods for dry eye include the tear secretion test, tear film rupture time, tear river height measurement, Schirmer test, tear osmotic pressure, and fluorescein staining (Nichols et al., 2004; Sullivan et al., 2010; Zeev et al., 2014; Vehof et al., 2020). Doctors need to spend more time and energy on examination and analysis in the clinical diagnosis of dry eye. Numerous research data have shown that dry eye has a high incidence and consumes substantial manpower and financial resources every year; thus, it is necessary to improve the diagnosis and treatment efficiency of dry eye.

AI has been increasingly applied to dry eye with remarkable effects. Chase et al. (Chase et al., 2021) constructed a DL model for the diagnosis of dry eye. They collected 27180 As-OCT images for the model training and testing. The results demonstrated that the accuracy, sensitivity, and specificity of

the model in the diagnosis of dry eye were 0.8462, 0.8636, and 0.8235, respectively. Zhang et al. (Zhang et al., 2022) established a dry eye diagnosis model using a U-Net image segmentation algorithm and ResNet image classification algorithm. The models were trained and evaluated using blinking videos of 357 patients with dry eye and 152 normal persons, and the accuracies were 0.963 and 0.960, respectively. Da Cruz et al. (da Cruz et al., 2020a) used six DL models (the support vector machine (SVM), RF, naive Bayes, multilayer perceptron, random tree, and radial basis function network) for the classification of tear film images to assist in the diagnosis of dry eye. They used the VOPTICAL_GCU database for training and verification. The RF model achieved the best classification effect, with an accuracy of 0.990, an AUC value of 0.999, a kappa value of 0.995, and an F-measure of 0.996. Da Cruz et al. (da Cruz et al., 2020b) also used the six DL models to classify tear film lipid layers automatically for the diagnosis of dry eye. They trained

TABLE 3 Summary of application of AI models in dry eye.

Authors	Task	Sample size	AI algorithms	Diagnostic performance
Chase et al. (2021)	Diagnosis	27,180 images	DL	Accuracy = 0.8642, Sensitivity = 0.8636, Specificity = 0.8235
Zhang et al. (2022)	Diagnosis	507 videos	U-Net	Accuracy of U-Net = 0.963
			ResNet	Accuracy of ResNet = 0.960
da Cruz et al. (2020a)	Diagnosis	VOPTICAL_GCU database	SVM, RF, naive Bayes, multilayer perceptron, random tree, radial basis function network	Accuracy = 0.990
				AUC = 0.999
				Kappa = 0.995
				F-measure = 0.996
da Cruz et al. (2020b)	Diagnosis	VOPTICAL_GCU database	SVM, RF, naive Bayes, multilayer perceptron, random tree, radial basis function network	Accuracy = 0.97
				AUC = 0.99
Koprowski et al. (2016)	Assessment	172 images	DL	Sensitivity = 0.993
				Specificity = 0.975
Wang et al. (2019)	Assessment	706 images	DNNs	Accuracy of meibomian gland atrophy segmentation = 0.954
				Overall grading accuracy = 0.956
Maruoka et al. (2020)	Detection	137 images	DL	AUC = 0.966
				Sensitivity = 0.942
				Specificity = 0.821
Setu et al. (2021)	Detection	728 images	DL	Accuracy = 0.83
				Recall = 0.81
				F1 score = 0.84

and tested various DL models on the VOPTICAL_GCU datasets. The results revealed that the classification effect of the RF model was the best, with an accuracy of 0.97 and an AUC value of 0.99. Based on the above research, AI models exhibit high accuracy and superior performance in the diagnosis of dry eye, and can be used in the clinical diagnosis and treatment of dry eye in the future.

Koprowski et al. ([Koprowski et al., 2016](#)) developed a method for the automatic quantitative assessment of meibomian gland dysfunction (MGD) based on DL, and used 172 images (upper and lower eyelid images of 86 participants) for training and verification. The results revealed that the sensitivity of this method was 0.993 and the specificity was 0.975, which was faster and more accurate than an ophthalmologist. Wang et al. ([Wang et al., 2019](#)) proposed a method that can accurately evaluate meibomian gland atrophy based on a DNN. They collected 706 upper eyelid images for the model

training, adjustment, and verification. The results demonstrated that the segmentation accuracy of the meibomian gland atrophy was 0.954 and the overall grading accuracy was 0.956. Waruoka et al. ([Maruoka et al., 2020](#)) constructed various DL models to detect obstructive MGD. Following training and verification using 137 images, the performance of DenseNet-201 was the best, with an AUC value of 0.966, a sensitivity of 0.942, and a specificity of 0.821. Setu et al. ([Setu et al., 2021](#)) constructed an algorithm for meibomian gland segmentation based on DL. A total of 728 clinical images were used to train and evaluate the model. According to the results, the average precision, recall, and F1 score were 0.83, 0.81, and 0.84, respectively. The function of the meibomian gland is closely related to the incidence of dry eye. These studies, which are summarized in [Table 3](#), demonstrate that AI technology can be used to effectively evaluate the function of the meibomian gland, reduce the analysis time, and improve the diagnostic accuracy of doctors.

2.4 Application of AI in pterygium diagnosis

Pterygium is a chronic inflammatory disease named for its insect wing shape. It is mainly characterized by fibrovascular hyperplasia of conjunctival tissue and the invasion of the surrounding corneal tissue, which is also known as proliferative disease (Yue and Gao, 2019; Wang et al., 2021b). Pterygium usually consists of three parts: the head, neck, and body, which often invade the cornea and limbus cornea (Seet et al., 2012). Its incidence is closely related to the geographical latitude, especially near the equator between 30 and 35 degrees. Furthermore, the disease is more common in outdoor working people (such as fishermen and farmers) (Coroneo, 2011; Delic et al., 2017). However, the specific cause of the disease remains unknown and it may be related to ultraviolet exposure, smoke, viral infections, ocular degeneration, sex, and age (Sjo et al., 2007; Huang et al., 2013; Rezvan et al., 2018). Clinically, the disease occurs in both eyes, especially on the nasal side. In the early stage, there are generally no obvious symptoms or only a slight foreign body sensation. When the lesion invades the corneal pupil area, corneal astigmatism or direct occlusion of the pupil area will occur, thereby resulting in a decline in visual acuity (Kampitak et al., 2016). Pterygium can be divided into the progressive and static types according to the development of abnormal tissue (Safi et al., 2016). Progressive pterygium exhibits protuberance of the head and infiltration at the front, Stocker lines at times, and hyperemia and hypertrophy of the body, with gradual growth into the cornea. Static pterygium exhibits a flat head, thin body, and static non-development (Mohd Radzi et al., 2019). At present, the clinical diagnosis of pterygium is mainly dependent on anterior segment photography (Abdani et al., 2022). Surgery is the main treatment for the disease. Small and static pterygium generally do not require treatment, but sand, sunlight, and other stimulation should be reduced as far as possible. Furthermore, when the pterygium invades the pupil area, it should be resected in time (Graue-Hernandez et al., 2019). However, surgical resection may still result in postoperative complications in patients with advanced pterygium, such as a high recurrence rate, corneal scarring, and astigmatism (Hirst, 2003; Mahar and Manzar, 2013; Resnikoff et al., 2020). Therefore, it is very important to screen pterygium and evaluate the timing of surgery in the early stage.

In recent years, with the rapid development of AI, it has been increasingly applied to assist in the clinical screening, diagnosis, and prognosis of pterygium. Zheng et al. (Zheng et al., 2021) constructed two diagnostic models (MobileNet 1 and MobileNet 2) that can aid in the diagnosis of pterygium. They collected 436 images of the anterior segment of the eyes for the testing and training of the diagnostic models. The

MobileNet 2 model achieved the best performance, with a sensitivity of 0.8370, a specificity of 0.9048, and an F1 score of 0.8250. Wan et al. (Wan et al., 2022) constructed a diagnosis system for pterygium using U-Net, which was employed to assist doctors in creating surgical treatment strategies for pterygium patients. They collected 489 anterior segment images to test and verify the diagnosis system. The experimental results revealed that the Dice coefficients of the pterygium and corneal segmentation were 0.9020 and 0.9620, respectively, and the kappa consistency coefficient between the diagnosis results of the system and those of doctors was 0.918, which indicates that the system offers practical application significance. Xu et al. (Xu et al., 2021b) studied a diagnostic system that can intelligently diagnose pterygium using a DL algorithm. They collected 1,220 anterior segment images for the system training and testing. Compared with the expert diagnosis results, the diagnostic accuracy of the system was 0.9468 and the specificity was high. The above research demonstrates that AI technology can be used as an auxiliary diagnostic tool to assist clinicians with diagnosing pterygium, thereby significantly reducing their work stress and improving their efficiency.

Zaki et al. (Wan Zaki et al., 2018) built a system for pterygium screening based on a DL algorithm, and evaluated the system using a SVM and an artificial neural network. They used the UBIRIS, MILES, and Brazil Pterygium databases to train, modify and test the system. The results demonstrated that the accuracy, sensitivity, specificity, and AUC value of the system were 0.9127, 0.887, 0.883, and 0.956, respectively. Abdani et al. (Abdani et al., 2021) developed a system that can automatically screen pterygium through the DL algorithm, and used 328 images of the anterior segment of the eye for training and verification. The accuracy of the system was 0.9330. Fang et al. (Fang et al., 2021) created a pterygium detection model based on DL, and collected 9443 images of the anterior segment of the eye for the model training and testing. The AUC value, sensitivity, and specificity of the model were 0.995, 0.985, and 0.990, respectively. These studies demonstrate that AI models have exhibited good performance in pterygium screening. It is expected that such approaches can be used in pterygium screening in areas where medical resources are scarce or the economy is challenged to achieve early diagnosis and timely medical treatment for pterygium patients.

Jais et al. (Jais et al., 2021) developed a model that can predict the best corrected visual acuity of patients with pterygium using four different ML algorithms (the decision tree, SVM, logistic regression, and naive Bayes). They used the data of 93 patients with different types of pterygium as the dataset for the model. The final results showed that the SVM model achieved the best performance, with an accuracy of $94.44\% \pm 5.86\%$, a specificity of 100%, and a sensitivity of $92.14\% \pm 8.33\%$. Hung et al. (Hung et al., 2022) developed a DL system for grading pterygium and

TABLE 4 Summary of application of AI models in pterygium.

Authors	Task	Sample size	AI algorithms	Diagnostic performance
Zheng et al. (2021)	Diagnosis	436 images	MobileNet 1, MobileNet 2	Sensitivity = 0.8370, Specificity = 0.9048
				F1 score = 0.8254
				AUC = 0.8720
Wan et al. (2022)	Diagnosis	489 images	U-Net	Dice of pterygium = 0.9020
				Dice of cornea = 0.9620, Kappa = 0.918
Xu et al. (2021b)	Diagnosis	1,220 images	DL	Accuracy = 0.9468
Wan Zaki et al. (2018)	Detection	UBIRIS, MILES, and Brazil Pterygium databases	SVM, neural network	Accuracy = 0.9127, Sensitivity = 0.887, Specificity = 0.883
				AUC = 0.956
Abdani et al. (2021)	Detection	328 images	DL	Accuracy = 0.9330
Fang et al. (2021)	Detection	9,443 images	DL	AUC = 0.995
				Sensitivity = 0.985, Specificity = 0.990
Jais et al. (2021)	Prognosis and recurrence	93 patients	Decision tree, SVM, logistic regression, naive Bayes	Accuracy = 94.44% \pm 5.86%
				Specificity = 100%
				Sensitivity = 92.14% \pm 8.33%
Hung et al. (2022)	Prognosis and recurrence	237 images	DL	Sensitivity = 0.6667
				Specificity = 0.8182

predicting postoperative recurrence. The system used 237 images for training and testing. According to the results, the sensitivity, F1 score, and accuracy for the pterygium grading were 0.8000–0.9167, 0.8182 to 0.9434, and 0.8667 to 0.9167, respectively, whereas the sensitivity and specificity for predicting the postoperative recurrence of pterygium were 0.6667 and 0.8182, respectively. Thus, AI models can aid in predicting the recurrence and prognosis of pterygium, and can help clinicians to deal with various postoperative complications better, so as to create the most effective treatment plan. The above studies are summarized in Table 4.

3 Limitations and challenges

According to the aforementioned diverse applications of AI in ocular surface disease diagnoses, AI has shown considerable advantages for ocular surface and other ophthalmic disease diagnoses, especially through data and image analysis. However, although many studies on the application of AI to the diagnosis of ocular surface diseases have exhibited satisfactory results, they still have numerous limitations and challenges. 1) Datasets suffer from image quality problems (Ghosh et al., 2022; Dong et al., 2022). Some of the images in

the training, verification, and test sets used in some AI studies suffered from quality problems, such as unclear or incomplete images, which significantly impacted the research results. 2) The external verification of algorithms face many challenges (Tan et al., 2022; Martins et al., 2022). The DL algorithms in several studies was verified and tested on open datasets. When they are applied to actual clinical diagnosis and treatment, their performance will be reduced owing to the differences in image quality, shooting equipment, patient cooperation etc. 3) The sample size used in some studies was small (Zhang et al., 2022; Kang et al., 2022). The datasets used in some studies contained small sample sizes, resulting in unstable performance of the AI models and large differences in results. 4) Heterogeneity of patients (Wan et al., 2022; Sheng et al., 2022). Every person is different, and most individuals have considerable differences among each other. This human heterogeneity is likely to result in a decline in the accuracy of AI model verification and testing for clinical diagnosis and treatment. 5) Biases exist in AI model datasets (Hung et al., 2022; Keel et al., 2018; Pur et al., 2022). The AI models are most likely to be successful when they are trained and validated using high-quality datasets. However, many studies used small or common datasets (wherein some data may be biased), which caused certain biases in their results, resulting in low external applicability of AI models.

4 Prospects for the future

Although the application of AI to the clinical diagnosis of ophthalmic diseases, such as ocular surface diseases, still faces numerous challenges. The current AI studies on ocular surface disease diagnoses indicate that AI can obtain the disease characteristics from the training set and apply them to the verification or testing set to diagnose the corresponding disease. AI can classify images into different types according to the disease characteristics, such as disease classification and stage. Additionally, AI can also detect and segment the anatomical structure in the image, such as lesion shape, to realize the automatic quantization of image biomarkers and perform auxiliary diagnosis. Therefore, based on these advantages, the application of AI technology in clinical diagnosis and treatment offers infinite potential and significant prospects. With the continual progress of science and technology, the ongoing improvements in AI, and the establishment and improvement of relevant legal systems, AI will be better applied to the clinical diagnosis and treatment of ophthalmology, especially in economically challenged areas and those that lack medical resources, in the near future. The application of AI will greatly improve the level of diagnosis and treatment in such areas, thereby aiding more patients to detect diseases as soon as possible, which is essential for early diagnosis and treatment. Moreover, if clinical diagnosis and treatment course can be entirely established through AI, the work stress of clinical medical staff will be significantly reduced and their work efficiency will improve, allowing them to perform the best diagnosis and offer the best treatment plan for patients.

AI offers the potential to improve the diagnosis level of ophthalmic diseases significantly. In the future, with the expansion of AI in the field of ophthalmology, in addition to image processing technology, other AI technologies will be researched and applied in the field of ophthalmology. The full application of AI will result in

fundamental changes in the clinical ophthalmology diagnosis and treatment.

Author contributions

YJ and SL conceived and designed the research and wrote the manuscript; XH, YL, and XW wrote the manuscript; KUL, KEL, and YL designed the research, acquired the article information, and revised the manuscript. All authors contributed to the article and approved the submitted version.

Funding

This study was supported by Shenzhen Fund for Guangdong Provincial High-level Clinical Key Specialties (SZGSP014), Sanming Project of Medicine in Shenzhen (SZSM202011015), Shenzhen Fundamental Research Program (JCYJ20220818103207015) and Scientific Research Project of Chinese Medicine Education Association (2022KTM028).

Conflict of interest

The authors declare that the research was conducted in the absence of any commercial or financial relationships that could be construed as a potential conflict of interest.

Publisher's note

All claims expressed in this article are solely those of the authors and do not necessarily represent those of their affiliated organizations, or those of the publisher, the editors and the reviewers. Any product that may be evaluated in this article, or claim that may be made by its manufacturer, is not guaranteed or endorsed by the publisher.

References

- Abdani, S. R., Zulkifley, M. A., Shahrimin, M. I., and Zulkifley, N. H. (2022). Computer-assisted pterygium screening system: A review. *Diagn. (Basel)* 12, 639. doi:10.3390/diagnostics12030639
- Abdani, S. R., Zulkifley, M. A., and Zulkifley, N. H. (2021). 11. Basel, 1104. doi:10.3390/diagnostics11061104Group and shuffle convolutional neural networks with pyramid pooling module for automated pterygium segmentation *Diagnostics*
- Abdelmotaal, H., Mostafa, M. M., Mostafa, A. N. R., Mohamed, A. A., and Abdelazeem, K. (2020). Classification of color-coded scheimpflug camera corneal tomography images using deep learning. *Transl. Vis. Sci. Technol.* 9, 30. doi:10.1167/tvst.9.13.30
- Ai, Z., Huang, X., Fan, Y., Feng, J., Zeng, F., and Lu, Y. (2021). DR-IIXRN : Detection algorithm of diabetic retinopathy based on deep ensemble learning and attention mechanism. *Front. Neuroinform.* 15, 778552. doi:10.3389/fninf.2021.778552
- AL-Timemy, A. H., Mosa, Z. M., Alyasseri, Z., Lavric, A., Lui, M. M., Hazarbasanov, R. M., et al. (2021). A hybrid deep learning construct for detecting keratoconus from corneal maps. *Transl. Vis. Sci. Technol.* 10, 16. doi:10.1167/tvst.10.14.16
- Argiles, M., Cardona, G., Perez-Cabre, E., and Rodriguez, M. (2015). Blink rate and incomplete blinks in six different controlled hard-copy and electronic reading conditions. *Invest. Ophthalmol. Vis. Sci.* 56, 6679–6685. doi:10.1167/iovs.15-16967
- Attallah, O. (2021). Diarop: Automated deep learning-based diagnostic tool for retinopathy of prematurity. *Diagnostics* 11, 2034. doi:10.3390/diagnostics1112034
- Austin, A., Lietman, T., and Rose-Nussbaumer, J. (2017). Update on the management of infectious keratitis. *Ophthalmology* 124, 1678–1689. doi:10.1016/j.ophtha.2017.05.012
- Bhardwaj, C., Jain, S., and Sood, M. (2021). Deep learning-based diabetic retinopathy severity grading system employing quadrant ensemble model. *J. Digit. Imaging* 34, 440–457. doi:10.1007/s10278-021-00418-5

- Brunner, M., Czanner, G., Vinciguerra, R., Romano, V., Ahmad, S., Batterbury, M., et al. (2018). Improving precision for detecting change in the shape of the cornea in patients with keratoconus. *Sci. Rep.* 8, 12345. doi:10.1038/s41598-018-30173-7
- Burlina, P., Joshi, N., Pacheco, K. D., Freund, D. E., Kong, J., and Bressler, N. M. (2018). Utility of deep learning methods for referability classification of age-related macular degeneration. *JAMA Ophthalmol.* 136, 1305–1307. doi:10.1001/jamaophthalmol.2018.3799
- Cardona, G., Garcia, C., Seres, C., Vilaseca, M., and Gispets, J. (2011). Blink rate, blink amplitude, and tear film integrity during dynamic visual display terminal tasks. *Curr. Eye Res.* 36, 190–197. doi:10.3109/02713683.2010.544442
- Castro-Luna, G., Jimenez-Rodriguez, D., Castano-Fernandez, A. B., and Perez-Rueda, A. (2021). Diagnosis of subclinical keratoconus based on machine learning techniques. *J. Clin. Med.* 10, 4281. doi:10.3390/jcm10184281
- Chan, E., Chong, E. W., Lingham, G., Stevenson, L. J., Sanfilippo, P. G., Hewitt, A. W., et al. (2021). Prevalence of keratoconus based on scheinplufg imaging: The raine study. *Ophthalmology* 128, 515–521. doi:10.1016/j.ophtha.2020.08.020
- Chase, C., Elsayw, A., Eleiwa, T., Ozcan, E., Tolba, M., and Abou Shousha, M. (2021). Comparison of autonomous AS-OCT deep learning algorithm and clinical dry eye tests in diagnosis of dry eye disease. *Clin. Ophthalmol.* 15, 4281–4289. doi:10.2147/OPTH.S321764
- Chatzis, N., and Hafezi, F. (2012). Progression of keratoconus and efficacy of pediatric [corrected] corneal collagen cross-linking in children and adolescents. *J. Refract. Surg.* 28, 753–758. doi:10.3928/1081597X-20121011-01
- Chen, X., Zhao, J., Iselin, K. C., Borroni, D., Romano, D., Gokul, A., et al. (2021). Keratoconus detection of changes using deep learning of colour-coded maps. *BMJ Open Ophthalmol.* 6, e000824. doi:10.1136/bmjophth-2021-000824
- Chidambaram, J. D., Venkatesh Prajna, N., Srikanthi, P., Lanjewar, S., Shah, M., Elakkiya, S., et al. (2018). Epidemiology, risk factors, and clinical outcomes in severe microbial keratitis in South India. *Ophthalmic Epidemiol.* 25, 297–305. doi:10.1080/09286586.2018.1454964
- Christopher, M., Belghith, A., Bowd, C., Proudfoot, J. A., Goldbaum, M. H., Weinreb, R. N., et al. (2018). Performance of deep learning architectures and transfer learning for detecting glaucomatous optic neuropathy in fundus photographs. *Sci. Rep.* 8, 16685. doi:10.1038/s41598-018-35044-9
- Coroneo, M. (2011). Ultraviolet radiation and the anterior eye. *Eye Contact Lens* 37, 214–224. doi:10.1097/ICL.0b013e318223394e
- Craig, J. P., Nelson, J. D., Azar, D. T., Belmonte, C., Bron, A. J., Chauhan, S. K., et al. (2017a). TFOS DEWS II report executive summary. *Ocul. Surf.* 15, 802–812. doi:10.1016/j.jtos.2017.08.003
- Craig, J. P., Nichols, K. K., Akpek, E. K., Caffery, B., Dua, H. S., Joo, C. K., et al. (2017b). TFOS DEWS II definition and classification report. *Ocul. Surf.* 15, 276–283. doi:10.1016/j.jtos.2017.05.008
- Da Cruz, L. B., Souza, J. C., DE Paiva, A. C., DE Almeida, J. D. S., Junior, G. B., Aires, K. R. T., et al. (2020a). Tear film classification in interferometry eye images using phylogenetic diversity indexes and ripley's K function. *IEEE J. Biomed. Health Inf.* 24, 3491–3498. doi:10.1109/JBHI.2020.3026940
- Da Cruz, L. B., Souza, J. C., DE Sousa, J. A., Santos, A. M., DE Paiva, A. C., DE Almeida, J. D. S., et al. (2020b). Interferometric eye image classification for dry eye categorization using phylogenetic diversity indexes for texture analysis. *Comput. Methods Programs Biomed.* 188, 105269. doi:10.1016/j.cmpb.2019.105269
- DE Sanctis, U., Loiacono, C., Richiardi, L., Turco, D., Mutani, B., and Grignolo, F. M. (2008). Sensitivity and specificity of posterior corneal elevation measured by Pentacam in discriminating keratoconus/subclinical keratoconus. *Ophthalmology* 115, 1534–1539. doi:10.1016/j.ophtha.2008.02.020
- Deangelis, K. D., Rider, A., Potter, W., Jensen, J., Fowler, B. T., and Fleming, J. C. (2019). Eyelid spontaneous blink analysis and age-related changes through high-speed imaging. *Ophthalmic Plast. Reconstr. Surg.* 35, 487–490. doi:10.1097/IOP.0000000000001349
- Delic, N. C., Lyons, J. G., DI Girolamo, N., and Halliday, G. M. (2017). Damaging effects of ultraviolet radiation on the cornea. *Photochem. Photobiol.* 93, 920–929. doi:10.1111/php.12686
- Dong, L., He, W., Zhang, R., Ge, Z., Wang, Y. X., Zhou, J., et al. (2022). Artificial intelligence for screening of multiple retinal and optic nerve diseases. *JAMA Netw. Open* 5, e229960. doi:10.1001/jamanetworkopen.2022.9960
- Dos Santos, V. A., Schmetterer, L., Stegmann, H., Pfister, M., Messner, A., Schmidinger, G., et al. (2019). CorneaNet: Fast segmentation of cornea OCT scans of healthy and keratoconic eyes using deep learning. *Biomed. Opt. Express* 10, 622–641. doi:10.1364/BOE.10.000622
- Fang, X., Deshmukh, M., Chee, M. L., Soh, Z. D., Teo, Z. L., Thakur, S., et al. (2021). Deep learning algorithms for automatic detection of pterygium using anterior segment photographs from slit-lamp and hand-held cameras. *Br. J. Ophthalmol.* 106, 1642–1647. doi:10.1136/bjophthalmol-2021-318866
- Ferdí, A. C., Nguyen, V., Gore, D. M., Allan, B. D., Rozema, J. J., and Watson, S. L. (2019). Keratoconus natural progression: A systematic review and meta-analysis of 11 529 eyes. *Ophthalmology* 126, 935–945. doi:10.1016/j.ophtha.2019.02.029
- Flaxman, S. R., Bourne, R. R. A., Resnikoff, S., Ackland, P., Braithwaite, T., Cicinelli, M. V., et al. VISION LOSS EXPERT GROUP OF THE GLOBAL BURDEN OF DISEASE, S (2017). Global causes of blindness and distance vision impairment 1990–2020: A systematic review and meta-analysis. *Lancet. Glob. Health* 5, e1221–e1234. doi:10.1016/S2214-109X(17)30393-5
- Ghosh, A. K., Thammasudjarit, R., Jongkhajornpong, P., Attia, J., and Thakkestian, A. (2022). Deep learning for discrimination between fungal keratitis and bacterial keratitis: DeepKeratitis. *Cornea* 41, 616–622. doi:10.1097/ICO.0000000000002830
- Goh, Y. W., Gokul, A., Yadegarfar, M. E., Vellara, H., Shew, W., Patel, D., et al. (2020). Prospective clinical study of keratoconus progression in patients awaiting corneal cross-linking. *Cornea* 39, 1256–1260. doi:10.1097/ICO.0000000000002376
- Gordon-Shaag, A., Millodot, M., Ifrah, R., and Shneor, E. (2012). Aberrations and topography in normal, keratoconus-suspect, and keratoconic eyes. *Optom. Vis. Sci.* 89, 411–418. doi:10.1097/OPX.0b013e318249d727
- Graue-Hernandez, E. O., Cordoba, A., Jimenez-Corona, A., Ramirez-Miranda, A., Navas, A., Serna-Ojeda, J. C., et al. (2019). Practice patterns in the management of primary pterygium: A survey study. *Cornea* 38, 1339–1344. doi:10.1097/ICO.0000000000002091
- Gu, H., Guo, Y., Gu, L., Wei, A., Xie, S., Ye, Z., et al. (2020). Deep learning for identifying corneal diseases from ocular surface slit-lamp photographs. *Sci. Rep.* 10, 17851. doi:10.1038/s41598-020-75027-3
- Hashemi, H., Heydarian, S., Hooshmand, E., Saatchi, M., Yekta, A., Aghamirsalam, M., et al. (2020). The prevalence and risk factors for keratoconus: A systematic review and meta-analysis. *Cornea* 39, 263–270. doi:10.1097/ICO.0000000000002150
- Herber, R., Pillunat, L. E., and Raiskup, F. (2021). Development of a classification system based on corneal biomechanical properties using artificial intelligence predicting keratoconus severity. *Eye Vis.* 8, 21. doi:10.1186/s40662-021-00244-4
- Hirst, L. W. (2003). The treatment of pterygium. *Surv. Ophthalmol.* 48, 145–180. doi:10.1016/s0039-6257(02)00463-0
- Hood, D. C., and DE Moraes, C. G. (2018). Efficacy of a deep learning system for detecting glaucomatous optic neuropathy based on color fundus photographs. *Ophthalmology* 125, 1207–1208. doi:10.1016/j.ophtha.2018.04.020
- Hu, J. W., Zhu, X. P., Pan, S. Y., Yang, H., and Xiao, X. H. (2021). Prevalence and risk factors of dry eye disease in young and middle-aged office employee: A xi'an study. *Int. J. Ophthalmol.* 14, 567–573. doi:10.18240/ijo.2021.04.14
- Huang, Y., He, H., Sheha, H., and Tseng, S. C. (2013). Ocular demodicosis as a risk factor of pterygium recurrence. *Ophthalmology* 120, 1341–1347. doi:10.1016/j.ophtha.2013.01.001
- Hung, K. H., Lin, C., Roan, J., Kuo, C. F., Hsiao, C. H., Tan, H. Y., et al. (2022). Application of a deep learning system in pterygium grading and further prediction of recurrence with slit lamp photographs. *Diagn. (Basel)* 12, 888. doi:10.3390/diagnostics12040888
- Hung, N., Shih, A. K., Lin, C., Kuo, M. T., Hwang, Y. S., Wu, W. C., et al. (2021). Using Slit-Lamp Images for Deep Learning-Based Identification of Bacterial and Fungal Keratitis: Model Development and Validation with Different Convolutional Neural Networks, 11. *Diagn. (Basel)*.
- Jais, F. N., Che Azemin, M. Z., Hilmi, M. R., Mohd Tamrin, M. I., and Kamal, K. M. (2021). Postsurgery classification of best-corrected visual acuity changes based on pterygium characteristics using the machine learning technique. *ScientificWorldJournal*. 2021, 6211006. doi:10.1155/2021/6211006
- Kamiya, K., Ayatsuka, Y., Kato, Y., Shoji, N., Miyai, T., Ishii, H., et al. (2021). Prediction of keratoconus progression using deep learning of anterior segment optical coherence tomography maps. *Ann. Transl. Med.* 9, 1287. doi:10.21037/atm-21-1772
- Kamiya, K., Ayatsuka, Y., Kato, Y., Fujimura, F., Takahashi, M., Shoji, N., et al. (2019). Keratoconus detection using deep learning of colour-coded maps with anterior segment optical coherence tomography: A diagnostic accuracy study. *BMJ Open* 9, e031313. doi:10.1136/bmjopen-2019-031313
- Kampitak, K., Leelawongtawun, W., Leamornsiri, S., Suphachearaphan, W., and Thitiwichienklert, S. (2016). A comparative study of higher order aberrations between pterygium and non-terygium eyes. *J. Med. Assoc. Thai* 99 (4), S178–S181.
- Kang, L., Ballouz, D., and Woodward, M. A. (2022). Artificial intelligence and corneal diseases. *Curr. Opin. Ophthalmol.* 33, 407–417. doi:10.1097/ICU.0000000000000885

- Kato, N., Masumoto, H., Tanabe, M., Sakai, C., Negishi, K., Torii, H., et al. (2021). Predicting keratoconus progression and need for corneal crosslinking using deep learning. *J. Clin. Med.* 10, 844. doi:10.3390/jcm10040844
- Keel, S., Lee, P. Y., Scheetz, J., Li, Z., Kotowicz, M. A., Macisaac, R. J., et al. (2018). Feasibility and patient acceptability of a novel artificial intelligence-based screening model for diabetic retinopathy at endocrinology outpatient services: A pilot study. *Sci. Rep.* 8, 4330. doi:10.1038/s41598-018-22612-2
- Khor, W. B., Prajna, V. N., Garg, P., Mehta, J. S., Xie, L., Liu, Z., et al. (2018). The asia cornea society infectious keratitis study: A prospective multicenter study of infectious keratitis in asia. *Am. J. Ophthalmol.* 195, 161–170. doi:10.1016/j.ajo.2018.07.040
- Koprowski, R., Wilczynski, S., Olczyk, P., Nowinska, A., Weglarz, B., and Wylegala, E. (2016). A quantitative method for assessing the quality of meibomian glands. *Comput. Biol. Med.* 75, 130–138. doi:10.1016/j.combiomed.2016.06.001
- Kuo, B. I., Chang, W. Y., Liao, T. S., Liu, F. Y., Liu, H. Y., Chu, H. S., et al. (2020a). Keratoconus screening based on deep learning approach of corneal topography. *Transl. Vis. Sci. Technol.* 9, 53. doi:10.1167/tvst.9.2.53
- Kuo, M. T., Hsu, B. W., Lin, Y. S., Fang, P. C., Yu, H. J., Chen, A., et al. (2021). Comparisons of deep learning algorithms for diagnosing bacterial keratitis via external eye photographs. *Sci. Rep.* 11, 24227. doi:10.1038/s41598-021-03572-6
- Kuo, M. T., Hsu, B. W., Yin, Y. K., Fang, P. C., Lai, H. Y., Chen, A., et al. (2020b). A deep learning approach in diagnosing fungal keratitis based on corneal photographs. *Sci. Rep.* 10, 14424. doi:10.1038/s41598-020-71425-9
- Lavric, A., and Valentin, P. (2019). KeratoDetect: Keratoconus detection algorithm using convolutional neural networks. *Comput. Intell. Neurosci.* 2019, 8162567. doi:10.1155/2019/8162567
- Li, Z., Jiang, J., Chen, K., Chen, Q., Zheng, Q., Liu, X., et al. (2021). Preventing corneal blindness caused by keratitis using artificial intelligence. *Nat. Commun.* 12, 3738. doi:10.1038/s41467-021-24116-6
- Liu, Z., Cao, Y., Li, Y., Xiao, X., Qiu, Q., Yang, M., et al. (2020). Automatic diagnosis of fungal keratitis using data augmentation and image fusion with deep convolutional neural network. *Comput. Methods Programs Biomed.* 187, 105019. doi:10.1016/j.cmpb.2019.105019
- Lv, J., Zhang, K., Chen, Q., Chen, Q., Huang, W., Cui, L., et al. (2020). Deep learning-based automated diagnosis of fungal keratitis with *in vivo* confocal microscopy images. *Ann. Transl. Med.* 8, 706. doi:10.21037/atm.2020.03.134
- Mahar, P. S., and Manzar, N. (2013). Pterygium recurrence related to its size and corneal involvement. *J. Coll. Physicians Surg. Pak.* 23, 120–123. doi:10.2.2013/JCPS.120123
- Martins, T., Schor, P., Mendes, L. G. A., Fowler, S., and Silva, R. (2022). Use of artificial intelligence in ophthalmology: A narrative review. *Sao Paulo Med. J.* 140, 837–845. doi:10.1590/1516-3180.2021.0713.R1.22022022
- Maruoka, S., Tabuchi, H., Nagasato, D., Masumoto, H., Chikama, T., Kawai, A., et al. (2020). Deep neural network-based method for detecting obstructive meibomian gland dysfunction with *in vivo* laser confocal microscopy. *Cornea* 39, 720–725. doi:10.1097/ICO.0000000000002279
- Medeiros, F. A., Jammal, A. A., and Mariottoni, E. B. (2021). Detection of progressive glaucomatous optic nerve damage on fundus photographs with deep learning. *Ophthalmology* 128, 383–392. doi:10.1016/j.optha.2020.07.045
- Mohammadpour, M., Heidari, Z., and Hashemi, H. (2018). Updates on managements for keratoconus. *J. Curr. Ophthalmol.* 30, 110–124. doi:10.1016/j.joco.2017.11.002
- Mohd Radzi, H., Khairidzan, M. K., Mohd Zulfaezal, C. A., and Azrin, E. A. (2019). Corneo-ptyerygium total area measurements utilising image analysis method. *J. Optom.* 12, 272–277. doi:10.1016/j.optom.2019.04.001
- Nagasato, D., Tabuchi, H., Ohsugi, H., Masumoto, H., Enno, H., Ishitobi, N., et al. (2018). Deep neural network-based method for detecting central retinal vein occlusion using ultrawide-field fundus ophthalmoscopy. *J. Ophthalmol.* 2018, 1875431. doi:10.1155/2018/1875431
- Nagasato, D., Tabuchi, H., Ohsugi, H., Masumoto, H., Enno, H., Ishitobi, N., et al. (2019). Deep-learning classifier with ultrawide-field fundus ophthalmoscopy for detecting branch retinal vein occlusion. *Int. J. Ophthalmol.* 12, 94–99. doi:10.18240/ijo.2019.01.15
- Nichols, K. K., Foulks, G. N., Bron, A. J., Glasgow, B. J., Dogru, M., Tsubota, K., et al. (2011). The international workshop on meibomian gland dysfunction: Executive summary. *Invest. Ophthalmol. Vis. Sci.* 52, 1922–1929. doi:10.1167/iov.10-6997a
- Nichols, K. K., Mitchell, G. L., and Zadnik, K. (2004). The repeatability of clinical measurements of dry eye. *Cornea* 23, 272–285. doi:10.1097/00003226-200404000-00010
- Papali'I-Curtin, A. T., Cox, R., Ma, T., Woods, L., Covello, A., and Hall, R. C. (2019). Keratoconus prevalence among high School students in New Zealand. *Cornea* 38, 1382–1389. doi:10.1097/ICO.0000000000002054
- Pascolini, D., and Mariotti, S. P. (2012). Global estimates of visual impairment: 2010. *Br. J. Ophthalmol.* 96, 614–618. doi:10.1136/bjophthalmol-2011-300539
- Pinero, D. P., Nieto, J. C., and Lopez-Miguel, A. (2012). Characterization of corneal structure in keratoconus. *J. Cataract. Refract. Surg.* 38, 2167–2183. doi:10.1016/j.jcrs.2012.10.022
- Pur, D. R., Krance, S. H., Pucchio, A., Miranda, R. N., and Felfeli, T. (2022). Current uses of artificial intelligence in the analysis of biofluid markers involved in corneal and ocular surface diseases: A systematic review. *Eye (Lond)*. doi:10.1038/s41433-022-02307-9
- Raman, R., Srinivasan, S., Virmani, S., Sivaprasad, S., Rao, C., and Rajalakshmi, R. (2019). Fundus photograph-based deep learning algorithms in detecting diabetic retinopathy. *Eye (Lond)* 33, 97–109. doi:10.1038/s41433-018-0269-y
- Redd, T. K., Campbell, J. P., Brown, J. M., Kim, S. J., Ostmo, S., Chan, R. V. P., et al. (2018). IMAGING & INFORMATICS IN RETINOPATHY OF PREMATURITY RESEARCH, CEvaluation of a deep learning image assessment system for detecting severe retinopathy of prematurity. *Br. J. Ophthalmol.* 103, 580–584. doi:10.1136/bjophthalmol-2018-313156
- Resnikoff, S., Lansingh, V. C., Washburn, L., Felch, W., Gauthier, T. M., Taylor, H. R., et al. (2020). Estimated number of ophthalmologists worldwide (international council of ophthalmology update): Will we meet the needs? *Br. J. Ophthalmol.* 104, 588–592. doi:10.1136/bjophthalmol-2019-314336
- Rezvani, F., Khabazkhoob, M., Hooshmand, E., Yekta, A., Saatchi, M., and Hashemi, H. (2018). Prevalence and risk factors of pterygium: A systematic review and meta-analysis. *Surv. Ophthalmol.* 63, 719–735. doi:10.1016/j.survophthal.2018.03.001
- Rocha-DE-Lossada, C., Prieto-Godoy, M., Sanchez-Gonzalez, J. M., Romano, V., Borroni, D., Rachwani-Anil, R., et al. (2021). Tomographic and aberrometric assessment of first-time diagnosed paediatric keratoconus based on age ranges: A multicentre study. *Acta Ophthalmol.* 99, e929–e936. doi:10.1111/aos.14715
- Rodriguez, J. D., Lane, K. J., Ousler, G. W., 3R. D., Angioli, E., Smith, L. M., and Abelson, M. B. (2018). Blink: Characteristics, controls, and relation to dry eyes. *Curr. Eye Res.* 43, 52–66. doi:10.1080/02713683.2017.1381270
- Safi, H., Kheirkhah, A., Mahbod, M., Molaei, S., Hashemi, H., and Jabbarvand, M. (2016). Correlations between histopathologic changes and clinical features in pterygia. *J. Ophthalmic Vis. Res.* 11, 153–158. doi:10.4103/2008-322X.183917
- Seet, L. F., Tong, L., Su, R., and Wong, T. T. (2012). Involvement of SPARC and MMP-3 in the pathogenesis of human pterygium. *Invest. Ophthalmol. Vis. Sci.* 53, 587–595. doi:10.1167/iov.11-7941
- Setu, M. A. K., Horstmann, J., Schmidt, S., Stern, M. E., and Steven, P. (2021). Deep learning-based automatic meibomian gland segmentation and morphology assessment in infrared meibography. *Sci. Rep.* 11, 7649. doi:10.1038/s41598-021-87314-8
- Sheng, B., Chen, X., Li, T., Ma, T., Yang, Y., Bi, L., et al. (2022). An overview of artificial intelligence in diabetic retinopathy and other ocular diseases. *Front. Public Health* 10, 971943. doi:10.3389/fpubh.2022.971943
- Sjo, N. C., VON Buchwald, C., Prause, J. U., Norrild, B., Vinding, T., and Heegaard, S. (2007). Human papillomavirus and pterygium. Is the virus a risk factor? *Br. J. Ophthalmol.* 91, 1016–1018. doi:10.1136/bjo.2006.108829
- Stapleton, F., Alves, M., Bunya, V. Y., Jalbert, I., Lekhanont, K., Malet, F., et al. (2017). TFOS DEWS II epidemiology report. *Ocul. Surf.* 15, 334–365. doi:10.1016/j.jtos.2017.05.003
- Sullivan, B. D., Whitmer, D., Nichols, K. K., Tomlinson, A., Foulks, G. N., Geerling, G., et al. (2010). An objective approach to dry eye disease severity. *Invest. Ophthalmol. Vis. Sci.* 51, 6125–6130. doi:10.1167/iov.10-5390
- Tahvildari, M., Singh, R. B., and Saeed, H. N. (2021). Application of artificial intelligence in the diagnosis and management of corneal diseases. *Semin. Ophthalmol.* 36, 641–648. doi:10.1080/08820538.2021.1893763
- Tan, Z., Chen, X., Li, K., Liu, Y., Cao, H., Li, J., et al. (2022). Artificial intelligence-based diagnostic model for detecting keratoconus using videos of corneal force deformation. *Transl. Vis. Sci. Technol.* 11, 32. doi:10.1167/tvst.11.9.32
- Tena, D., Rodriguez, N., Toribio, L., and Gonzalez-Praetorius, A. (2019). Infectious keratitis: Microbiological review of 297 cases. *Jpn. J. Infect. Dis.* 72, 121–123. doi:10.7883/yoken.JJID.2018.269
- Tepelus, T. C., Chiu, G. B., Huang, J., Huang, P., Sadda, S. R., Irvine, J., et al. (2017). Correlation between corneal innervation and inflammation evaluated with confocal microscopy and symptomatology in patients with dry eye syndromes: A preliminary study. *Graefes Arch. Clin. Exp. Ophthalmol.* 255, 1771–1778. doi:10.1007/s00417-017-3680-3

- Ting, D. S. J., Foo, V. H., Yang, L. W. Y., Sia, J. T., Ang, M., Lin, H., et al. (2021). Artificial intelligence for anterior segment diseases: Emerging applications in ophthalmology. *Br. J. Ophthalmol.* 105, 158–168. doi:10.1136/bjophthalmol-2019-315651
- Ting, D. S. J., Settle, C., Morgan, S. J., Baylis, O., and Ghosh, S. (2018). A 10-year analysis of microbiological profiles of microbial keratitis: The north east england study. *Eye (Lond)* 32, 1416–1417. doi:10.1038/s41433-018-0085-4
- Tiwari, M., Piech, C., Baitemirova, M., Prajna, N. V., Srinivasan, M., Lalitha, P., et al. (2022). Differentiation of active corneal infections from healed scars using deep learning. *Ophthalmology* 129, 139–146. doi:10.1016/j.optha.2021.07.033
- Vehof, J., Utheim, T. P., Bootsma, H., and Hammond, C. J. (2020). Advances, limitations and future perspectives in the diagnosis and management of dry eye in Sjogren's syndrome. *Clin. Exp. Rheumatol.* 38 (126), 301–309.
- Wan, C., Shao, Y., Wang, C., Jing, J., and Yang, W. (2022). A novel system for measuring pterygium's progress using deep learning. *Front. Med.* 9, 819971. doi:10.3389/fmed.2022.819971
- Wan Zaki, W. M. D., Mat Daud, M., Abdani, S. R., Hussain, A., and Mutalib, H. A. (2018). Automated pterygium detection method of anterior segment photographed images. *Comput. Methods Programs Biomed.* 154, 71–78. doi:10.1016/j.cmpb.2017.10.026
- Wang, J., Ji, J., Zhang, M., Lin, J. W., Zhang, G., Gong, W., et al. (2021a). Automated explainable multidimensional deep learning platform of retinal images for retinopathy of prematurity screening. *JAMA Netw. Open* 4, e218758. doi:10.1001/jamanetworkopen.2021.8758
- Wang, J., Yeh, T. N., Chakraborty, R., Yu, S. X., and Lin, M. C. (2019). A deep learning approach for meibomian gland atrophy evaluation in meibography images. *Transl. Vis. Sci. Technol.* 8, 37. doi:10.1167/tvst.8.6.37
- Wang, Y. C., Zhao, F. K., Liu, Q., Yu, Z. Y., Wang, J., and Zhang, J. S. (2021b). Bibliometric analysis and mapping knowledge domain of pterygium: 2000–2019. *Int. J. Ophthalmol.* 14, 903–914. doi:10.18240/ijo.2021.06.17
- Xu, F., Qin, Y., He, W., Huang, G., Lv, J., Xie, X., et al. (2021a). A deep transfer learning framework for the automated assessment of corneal inflammation on *in vivo* confocal microscopy images. *PLoS One* 16, e0252653. doi:10.1371/journal.pone.0252653
- Xu, W., Jin, L., Zhu, P. Z., He, K., Yang, W. H., and Wu, M. N. (2021b). Implementation and application of an intelligent pterygium diagnosis system based on deep learning. *Front. Psychol.* 12, 759229. doi:10.3389/fpsyg.2021.759229
- Xu, W., Yan, Z., Chen, N., Luo, Y., Ji, Y., Wang, M., et al. (2022). Development and application of an intelligent diagnosis system for retinal vein occlusion based on deep learning. *Dis. Markers* 2022, 4988256. doi:10.1155/2022/4988256
- Yan, Q., Weeks, D. E., Xin, H., Swaroop, A., Chew, E. Y., Huang, H., et al. (2020). Deep-learning-based prediction of late age-related macular degeneration progression. *Nat. Mach. Intell.* 2, 141–150. doi:10.1038/s42256-020-0154-9
- Yim, J., Chopra, R., Spitz, T., Winkens, J., Obika, A., Kelly, C., et al. (2020). Predicting conversion to wet age-related macular degeneration using deep learning. *Nat. Med.* 26, 892–899. doi:10.1038/s41591-020-0867-7
- Yousefi, S., Yousefi, E., Takahashi, H., Hayashi, T., Tampo, H., Inoda, S., et al. (2018). Keratoconus severity identification using unsupervised machine learning. *PLoS One* 13, e0205998. doi:10.1371/journal.pone.0205998
- Yue, X. L., and Gao, Z. Q. (2019). Identification of pathogenic genes of pterygium based on the Gene Expression Omnibus database. *Int. J. Ophthalmol.* 12, 529–535. doi:10.18240/ijo.2019.04.01
- Zeev, M. S., Miller, D. D., and Laskany, R. (2014). Diagnosis of dry eye disease and emerging technologies. *Clin. Ophthalmol.* 8, 581–590. doi:10.2147/OPTH.S45444
- Zhang, Z. Z., Kuang, R. F., Wei, Z. Y., Wang, L. Y., Su, G. Y., Ou, Z. H., et al. (2022). Detection of the spontaneous blinking pattern of dry eye patients using the machine learning method. *Zhonghua. Yan Ke Za Zhi.* 58, 120–129. doi:10.3760/cma.j.cn112142-20211110-00537
- Zheng, B., Liu, Y., He, K., Wu, M., Jin, L., Jiang, Q., et al. (2021). Research on an intelligent lightweight-assisted pterygium diagnosis model based on anterior segment images. *Dis. Markers* 2021, 7651462. doi:10.1155/2021/7651462



OPEN ACCESS

EDITED BY

Yanwu Xu,
Baidu (China), China

REVIEWED BY

Weihua Yang,
Jinan University, China
Pan Su,
North China Electric Power University,
China
Heng Li,
Southern University of Science and
Technology, China

*CORRESPONDENCE

Haidong Zou,
✉ zouhaidong@sjtu.edu.cn

SPECIALTY SECTION

This article was submitted to
Molecular and Cellular Pathology,
a section of the journal
Frontiers in Cell and
Developmental Biology

RECEIVED 14 December 2022

ACCEPTED 10 January 2023

PUBLISHED 17 January 2023

CITATION

Zhang J and Zou H (2023), Artificial
intelligence technology for myopia
challenges: A review.
Front. Cell Dev. Biol. 11:1124005.
doi: 10.3389/fcell.2023.1124005

COPYRIGHT

© 2023 Zhang and Zou. This is an open-
access article distributed under the terms
of the [Creative Commons Attribution
License \(CC BY\)](#). The use, distribution or
reproduction in other forums is permitted,
provided the original author(s) and the
copyright owner(s) are credited and that
the original publication in this journal is
cited, in accordance with accepted
academic practice. No use, distribution or
reproduction is permitted which does not
comply with these terms.

Artificial intelligence technology for myopia challenges: A review

Juzhao Zhang¹ and Haidong Zou^{1,2,3,4*}

¹Department of Ophthalmology, Shanghai General Hospital, Shanghai Jiao Tong University School of Medicine, Shanghai, China, ²Shanghai Eye Diseases Prevention and Treatment Center, Shanghai Eye Hospital, Shanghai, China, ³National Clinical Research Center for Eye Diseases, Shanghai, China, ⁴Shanghai Engineering Center for Precise Diagnosis and Treatment of Eye Diseases, Shanghai, China

Myopia is a significant global health concern and affects human visual function, resulting in blurred vision at a distance. There are still many unsolved challenges in this field that require the help of new technologies. Currently, artificial intelligence (AI) technology is dominating medical image and data analysis and has been introduced to address challenges in the clinical practice of many ocular diseases. AI research in myopia is still in its early stages. Understanding the strengths and limitations of each AI method in specific tasks of myopia could be of great value and might help us to choose appropriate approaches for different tasks. This article reviews and elaborates on the technical details of AI methods applied for myopia risk prediction, screening and diagnosis, pathogenesis, and treatment.

KEYWORDS

artificial intelligence, machine learning, deep learning, risk prediction, myopia, classification, semantic segmentation

Introduction

Artificial intelligence (AI), first proposed by John McCarthy in 1956, refers to the science and engineering of making intelligent computer programs and is considered one of the key technologies of the fourth industrial revolution. Due to its great potential for automated analysis of medical information and imaging, AI is rapidly developing in the medical field (Gupta et al., 2020). This pattern of automated screening, diagnosis, or risk assessment based on clinical and imaging data has proven to be applicable to a wide range of clinical diseases such as cardiovascular diseases (Wang et al., 2017), neurological diseases (Sarraf and Tofighi, 2016), respiratory diseases (Zech et al., 2018), and malignancies (Coudray et al., 2018), and has a tendency to be translated into real clinical practice. For ocular diseases such as diabetic retinopathy (DR) (Gulshan et al., 2016), age-related macular degeneration (AMD) (Peng et al., 2019), and cataracts (Gutierrez et al., 2022), AI has been used for screening, diagnosis, and other aspects. However, there are relatively few applications of AI in myopia.

Myopia is one of the most common refractive errors. In myopic eyes, the high corneal curvature and long eye axis cause distant objects to be imaged in front of the retina, resulting in blurred vision at a distance and affecting human visual function (Morgan et al., 2012). The current global prevalence of myopia is estimated to be about 28.3%, and this number will grow to 49.8% by 2050 (Holden et al., 2016). The situation is even worse in East Asia (Edwards and Lam, 2004; Han et al., 2019; Ueda et al., 2019; Dong et al., 2020). Online remote learning and working styles have led to a further increase in myopia rates, especially among school-age adolescents (Liang et al., 2021). If left uncontrolled, myopia can progress to high myopia. This will increase the likelihood of developing irreversible fundus lesions or pathologic myopia and is one of the main causes of low vision or even vision loss. In China, myopia prevention and control has become a national strategy, but there are still many challenges to overcome to achieve this goal, which needs the help of novel technology.

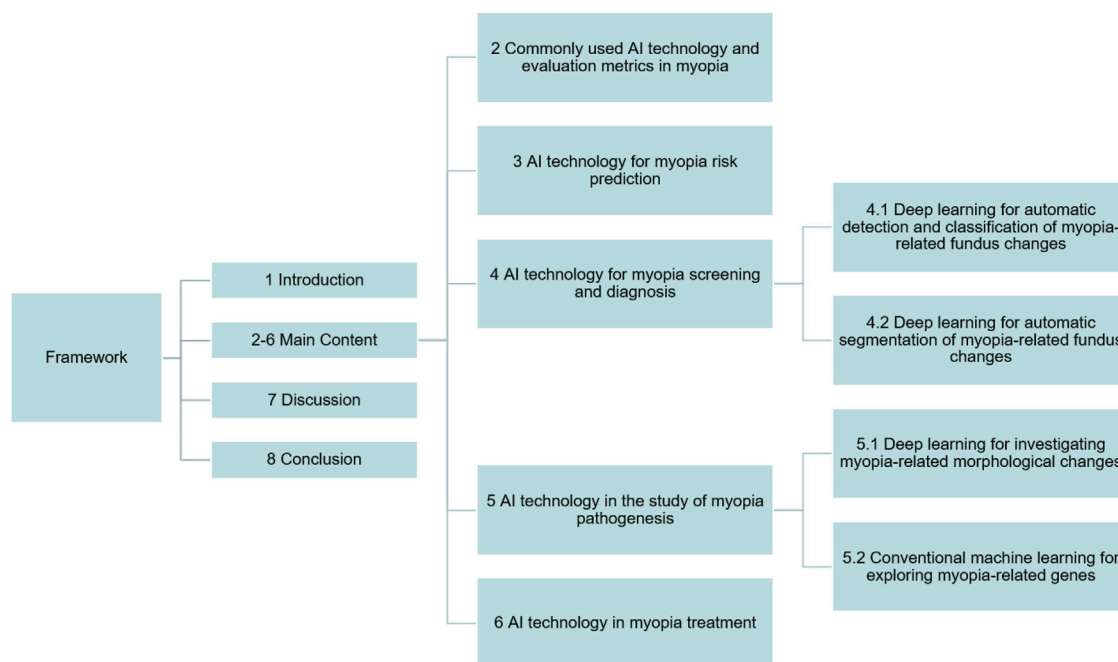


FIGURE 1
Overview diagram of this review.

Currently, the main challenges faced in myopia are: A) Unclear pathogenesis. It is difficult to objectively quantify the role of many impact factors on myopia, such as genetics, environment, and lifestyle. The morphological changes in eyes are also uncertain; B) Large screening workload. Myopia can only be prevented but not cured, and currently the most effective way is mass screening and follow-up. However, an insufficient number of relevant equipment and ophthalmologists makes it impossible to achieve large population coverage; C) Difficulties in risk prediction. The lack of reliable risk prediction model for high and pathologic myopia, as well as individual differences in the progression of myopia makes it difficult to provide timely intervention; and D) Uncertain efficacy. There is a range of myopia prevention and control methods including outdoor activities, spectacles, corneal contact lenses, atropine, and surgical treatments. Emerging methods include low-intensity red light irradiation. However, it is still a question of how to choose the most appropriate method for each individual.

Various works have been proposed to review the research of AI in myopia (Foo et al., 2021; Du and Ohno-Matsui, 2022; Zhang et al., 2022). To our knowledge, none of the existing work has elaborated technical details of the discussed work, thus fail to make readers more aware of strengths and limitations of each AI method in specific tasks of myopia. This could be of great value to readers with a technical background who are interested in ophthalmic data analysis and myopia. Therefore, our review investigates how AI methods can be applied to address important challenges in the field of myopia and their technical details, with the hope of informing relevant researchers including ophthalmologists and computer scientists.

The basic framework of this review is depicted in Figure 1. In the second part, we summarize widely used AI technology and evaluation metrics in myopia at present; the following four parts focus on the research progress and technical details of different AI technology in myopia risk

prediction, myopia screening and diagnosis, myopia pathogenesis, and myopia treatment, respectively; the seventh part provides a comprehensive discussion of the challenges and future prospects of AI in myopia.

Commonly used AI technology and evaluation metrics in myopia

In the absence of a universal evaluation benchmark, existing research in myopia does not start with a single AI method, but usually tries several models at the same time and selects the best performing one after parameter tuning and inter-model comparison. Machine learning (ML) is an important branch of AI that refers to methods for training computers to automatically learn relationships between inputs and outputs without explicitly programming them for each situation, and is suitable for analyzing large-scale medical data (Deo, 2015). Conventional machine learning (CML) methods (Chauhan and Singh, 2018) such as linear regression, support vector machine (SVM), and random forest (RF) have been applied in myopia. Newly proposed integrated learning methods such as XGBoost and Gradient Boosting can also be seen (Balyen and Peto, 2019). On the other hand, with breakthroughs in computing power and the introduction of convolutional neural networks (CNNs), deep learning (DL) methods are performing well in the analysis of medical images (Albawi et al., 2017). Some basic deep learning network structures including ResNet, DenseNet, Inception V3, MobileNet, UNet, and VGGNet are widely used in solving problems in the field of myopia. In addition, due to data privacy issues, most myopia studies can only train models based on data from a single center or several centers in the same region, so pre-trained models or transfer learning methods are often utilized to achieve better performance on relatively small datasets.

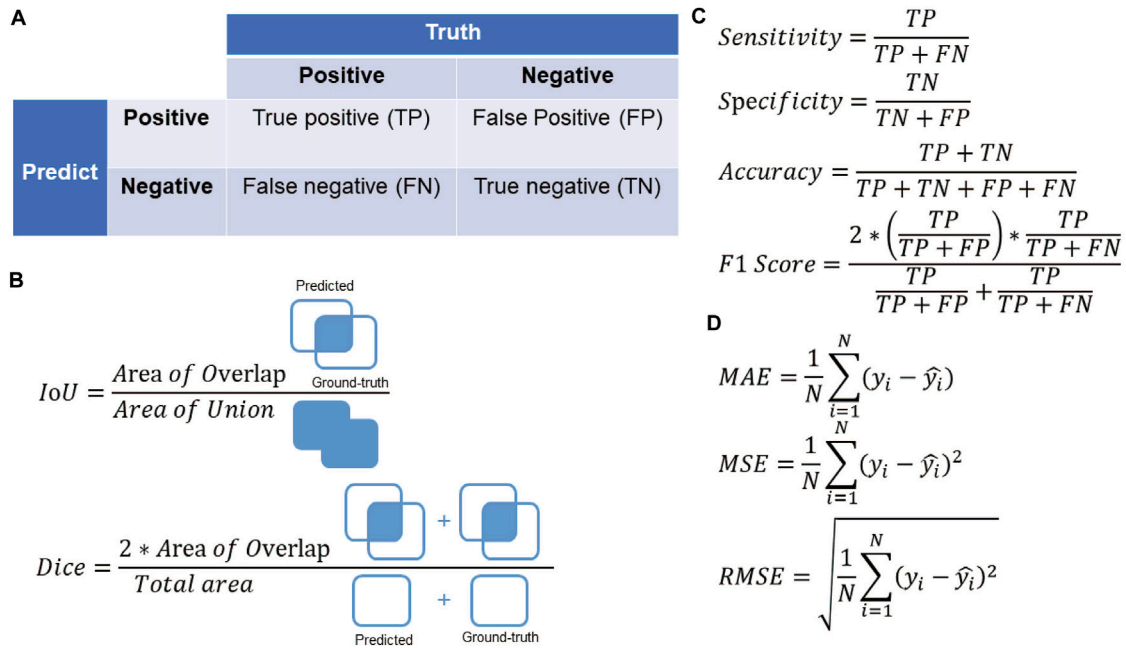


FIGURE 2

(A) The confusion matrix. (B) Evaluation metrics for segmentation tasks in the field of myopia. (C) Evaluation metrics for classification tasks in the field of myopia. (D) Evaluation metrics for regression tasks in the field of myopia. y_i is the ground-truth value of sample i and \hat{y}_i is the predicted value of sample i .

When evaluating the performance of a model, AI research in myopia often uses the following metrics: For classification tasks such as disease detection and prognosis prediction, metrics calculated from the confusion matrix such as accuracy, sensitivity, specificity, and F1 score are usually used for evaluation. Area under the receiver operating characteristic curve (AUROC) and area under the precision-recall curve (AUPRC) are also commonly used and give a more general idea about the classifier performance, for they do not require a cut-off point; When the task is to derive a prediction region, such as lesion segmentation of fundus pictures, it is often evaluated by Intersection of union (IoU) and Dice similarity coefficient (DSC). These two metrics measure the overlap area between the predicted region and the ground truth; While for regression tasks such as refraction prediction and axial length prediction, the evaluation is often performed using mean absolute error (MAE), mean square error (MSE) and root mean square error (RMSE). The detailed calculation method of these evaluation metrics is presented in Figure 2.

AI technology for myopia risk prediction

In clinical work of myopia, it is often necessary to evaluate and follow up patients with low to moderate myopia, especially to monitor the visual acuity of the pediatric and adolescent population. This will generate a series of data and records including (Chen et al., 2021): myopia-related risk factors (e.g., near work time, outdoor activity time, genetics, race, gender, etc.), best-corrected visual acuity, refraction, axial length, and some ocular metrics (e.g., intraocular pressure, ocular surface conditions). Analyzing and interpreting these data is a challenge: on the one hand, there is a lack of reliable risk prediction models to determine the progression of myopia patients and their prognosis. On the other hand, given the size of the data and

the complexity of a disease like myopia, it is difficult to perform manual analysis.

Conventional machine learning methods have the ability to process large amounts of data in a non-linear way and to extract a large number of potential predictor variables, even though their number may exceed the number of observed variables. This characteristic is suitable for analyzing myopic data (Obermeyer and Emanuel, 2016). Based on the eye and behavioral data from more than three thousand elementary school students, a study by Yang et al. (2020) provided a systematic solution that included feature selection, data cleaning, and model training. A series of protective and risk factors for myopia were screened, and a risk prediction model based on SVM was highly accurate in predicting the occurrence of myopia in the future. Compared to using a single model, Li et al. (2022a) introduced the idea of ensemble learning and constructed a strong classifier by integrating a large number of decision trees as the basic unit. However, there was no significant improvement in the results, which may be related to the dataset and the selection of predictor variables. In addition, the number of samples available for machine learning algorithms has greatly increased in the era of big data, enabling us to train models with sufficient samples. A study that included data from more than 600,000 refractive examinations confirmed the value of large data volume in improving machine learning performance (Lin et al., 2018). However, clinical data collected in real-world settings are often biased, and different studies set up validation sets in different ways. Reasonable evaluation of the performance of different models and improving their generality are issues that need to be solved.

Besides predicting refractive data, the choice of the target variable can also vary according to clinical need. For children wearing orthokeratology lens, changes in corneal curvature make refractive examinations inaccurate in assessing myopia progression, while axial

TABLE 1 Summary of CML methods for myopia risk prediction.

Research	Tasks	AI technology	Accuracy	Sensitivity	Specificity	AUC	MAE	R ²
Yang et al. (2020)	Prediction of the onset of myopia in primary school students	GBRT, SVM	0.93	0.94	0.94	0.97	—	—
Li et al. (2022)	Prediction of the progression of myopia	RF	0.8–0.9	—	—	—	<0.05D	—
Lin et al. (2018)	Prediction of the onset of myopia in adolescents	RF	—	—	—	0.802–0.888 (8 years in advance)	0.678–0.879 (8 years in advance)	0.743–0.912 (8 years in advance)
Tang et al. (2020)	Prediction of axial length growth	Robust linear regression	—	—	—	—	0.293	0.86

GBRT, gradient boosting regression tree; SVM, support vector machine; RF, random forest.

length is more reliable. Tang et al. (2020) showed that robust regression model was able to achieve an accurate prediction of axial length growth. Also, with the use of electronic medical records at all levels of medical institutions and the establishment of standardized information management systems, information and data interoperability will be realized among institutions. With more information that can be mined, not only can the model performance be improved, but also more application scenarios will emerge. Table 1 summarizes the discussed conventional machine learning methods for myopia risk prediction.

AI technology for myopia screening and diagnosis

As myopia progresses further, the axial length (AL) increases, the optic disc begins to tilt and twist, and irreversible retinal chorioretinopathy may develop. These are some of the fundus lesions associated with high myopia. Among these patients, about 3.1% eventually develop different types of myopic maculopathy with a characteristic set of pathological changes (Chang et al., 2013). Pathologic myopia and its complications have become the leading cause of blindness in China (Duan et al., 2021) and there are some urgent needs in this area. First, early identification of fundus changes is important. About 14% of myopic patients are highly myopic and at least one fundus examination is recommended annually to assess the condition of central and peripheral retina (Gifford et al., 2019). However, manual interpretation of these images is laborious and even unfeasible. Second, myopia-related fundus lesions are not obvious in their early stages and are difficult to describe or quantify. Doctors with different experience will give different judgments. This is a matter of concern in those districts with little medical care and is not suitable for the promotion of large-scale and standardized screening at the community level.

Deep learning for automatic detection and classification of myopia-related fundus changes

The detection of fundus lesions and myopia-related complications in high myopia is an important need, for which deep learning methods

such as CNNs already have high accuracy (Shao et al., 2021; Sun et al., 2021). Compared to the manual, deep learning methods take only a few hours to a few days in the training phase of the model and can produce instant results when interpreting images. It is even possible to achieve “offline prediction” based on smartphones (Natarajan et al., 2019). The structure of CNNs consists of four parts: preprocessing, feature extraction, classification and special modules representing various novel ideas. The preprocessing part includes noise reduction, enhancement of FP, OCT or other pictures, unifying resolution, focusing on regions of interest (ROIs), etc. The feature extraction part, also known as backbone network, is the core of CNNs. Convolutional kernels are selected to extract image features by convolutional operation on the original input image. The classification part consists of fully connected layers, which convert the output feature map of the last convolutional layer into a one-dimensional vector. The probability of having a certain myopic fundus lesion is obtained using functions such as Sigmoid or Softmax, and compared with a threshold to output the result. There is no fixed definition of special modules, and it is up to the researcher to choose which modules to use and how to use them. Commonly used modules in ophthalmic image processing include attention mechanisms, residual connectivity, and bottleneck structures. In general, the current CNN models applied to myopia are not novel. The fact that in fundus image analysis, the number of pixels in target structures such as lesions, optic cups optic discs and blood vessels is much less than the background and the curved structure of blood vessels (especially capillaries) is often complicated. These traits in ophthalmology imaging result in a difficult sampling problem. Proposing customized backbone networks or special modules based on the characteristics of myopia-related tasks could be a way to further improve the model performance.

Not only the detection, but also the differentiation of diverse classes of myopia-related fundus lesions is challenging. As the difficulty of the task increases, it is generally necessary to increase the depth of the backbone network to ensure that deep features in fundus pictures can be better extracted. However, traditional convolutional neural networks such as AlexNet and VGG16 may suffer from gradient explosion or disappearance when the depth is increased. New methods represented by ResNet (Tan et al., 2021; Ye et al., 2021; Park et al., 2022), InceptionNet (Choi et al., 2021; Li et al., 2022b), and DenseNet (Sogawa et al., 2020) have effectively addressed this problem. Lu et al. (Lu et al., 2021) used ResNet18 as the backbone

TABLE 2 Summary of DL methods for classification tasks in myopia.

Research	Tasks	AI technology	Accuracy	Sensitivity	Specificity	AUC
Lu et al. (2021)	Detection of PM and classification of MM	ResNet18; FPN-based Faster R-CNN	0.970–0.994	0.684–0.978	0.970–0.995	0.979–0.995
Du et al. (2021)	Classification of MM	EfficientNet	0.875–0.975	0.370–0.872	0.945–0.983	0.881–0.982
Tan et al. (2021)	Detection of high myopia and MM	ResNet101	—	—	—	0.913–0.978
Li et al. (2022)	Detection of tessellated fundus and PM	Dual-stream DCNNs	—	0.811–0.988	0.959–0.996	0.970–0.998
Sogawa et al. (2020)	Detection of MM	VGG16/19; ResNet50; Inception V3; InceptionResNetV2; Xception; DenseNet121/169/210	0.676–0.965	0.906–1.000	0.942–1.000	0.970–1.000
Li et al. (2022)	Detection of four myopic vision-threatening conditions	InceptionResNetV2	—	—	—	0.961–0.999
Choi et al. (2021)	Detection of high myopia	ResNet50; InceptionV3; VGG-16	—	—	—	0.860–0.900
Ye et al. (2021)	Detection of MM	ResNet101	—	—	—	0.927–0.974
Park et al. (2022)	Detection of PM	ResNet18/50; EfficientNet	0.860–0.950	0.850–0.930	0.880–0.960	0.950–0.980

PM, pathologic myopia; MM, myopic maculopathy.

network to classify lesions in patients with high myopia based on color fundus images. The results showed that the classification accuracy for each lesion specified in META-PM, a widely accepted classification standard for pathologic myopia, was comparable to that of experts, reaching 97.03%–99.41%. On this basis, it is meaningful to engineer relevant algorithms so that these results can truly contribute to clinical and healthcare screening of myopic patients.

In addition to training deeper networks to solve more complex tasks, the application of AI in ophthalmology is mostly carried out by clinicians, focusing more on clinical application value than on algorithms themselves. That is to say, a flexible model that can reduce parameter tuning efforts and match with specific tasks is needed. Google's EfficientNet (Tan and Le, 2019), proposed in 2019, is a solution based on which Du et al. (Du et al., 2021) trained four bicategorical models to detect four fundus lesions in highly myopic patients, namely diffuse atrophy, patchy atrophy, macular atrophy, and choroidal neovascularization. With EfficientNet-B0 used as basis, models with different parameters can be easily constructed by adjusting depth, width and resolution simultaneously. At the same time, the included MBConv module introduces an attention mechanism that forces the network to pay more attention to the “critical regions” of the image. The results showed that the detection accuracy of this auxiliary classification system for all lesions except choroidal neovascularization was more than 84%, and the overall detection accuracy for myopic macular degeneration was up to 87.53%, whereas the classification accuracy of ophthalmology specialists on the same task was merely 89%. A study by Li et al. (2022c) showed similar results, further confirming the effectiveness of EfficientNet. However, according to Du et al. (2021), the detection of choroidal neovascularization was only 37.07%, which might be related to the poor visualization of blood vessels in color fundus images (Jiang et al., 2020; Láíns et al., 2021). OCTA can image blood vessels better, but there are currently no studies using AI methods to analyze OCTA images in myopic eyes. Table 2 summarizes the above-presented methods for automatic detection and classification of myopia-related fundus changes.

Deep learning for automatic segmentation of myopia-related fundus changes

Besides the above-mentioned research with direct outcomes, completing semantic segmentation tasks on fundus images of myopic eyes helps us better comprehend the morphological changes (Read et al., 2019). It can also aid in the training of physicians to interpret images (Fang et al., 2022). In labeling the choroid and the layers of the retina in OCT images, Cahyo et al. (2020) took advantage of the multi-scale feature fusion characteristic of UNet, thus preserving more information. UNet is one of the most commonly used models for semantic segmentation of medical images (Ronneberger et al., 2015; Li et al., 2021). It proposes a novel structure called “Decoder-Encoder”: the decoder is used for feature extraction, and the encoder is used for up-sampling and feature fusion, which is very suitable for medical images with simple semantics and fixed structure. The results showed that by fusing shallow features with little semantic information but accurate target location and deep features with rich semantic information but coarse target location, the IoU could reach above 0.90. Accurate segmentation results were obtained even for the thin choroid of highly myopic patients. By using the upgraded version of UNet, namely UNet++, the segmentation of optic disc, retinal atrophy lesions, and retinal detachment lesions was also satisfactory (Hemelings et al., 2021). However, UNet is a standalone network structure that is difficult to combine with other networks. In view of this, Feature Pyramid Networks (FPNs), a module that can be added after many network structures, was proposed in 2017 (Lin et al., 2017). The core idea consists of two: up-sampling deep features and fusing features from each layer at different depths, and performing prediction independently at different feature layers. Lu et al. (2021) applied FPN to the focal segmentation task of myopic macular lesions and showed that the performance could be substantially improved without changing the structure of the original model and with essentially no increase in computational load.

Completing classification or other tasks on the basis of semantic segmentation is a new direction of current research (Shao et al., 2021). Based on the segmentation results of the choroid and retina, Chen

TABLE 3 Summary of DL methods for segmentation tasks in myopia.

Research	Tasks	AI technology	Accuracy	Sensitivity	Specificity	IoU	Dice score	F1 score
Cahyo et al. (2020)	Segmentation of choroid in myopic eyes	U-Net	0.99	—	—	0.92	—	—
Lu et al. (2021)	Segmentation of myopic “Plus” lesions	ResNet50; FPN	0.656–0.789	—	—	—	—	0.688–0.889
Chen et al. (2022)	Segmentation and quantification of the choroid in myopic eyes	Mask R-CNN	—	—	—	—	0.938	—
Li et al. (2021)	Segmentation of choroidal sublayers and vessels	U-Net	0.980–0.987	0.699–0.962	0.990–0.999	—	0.699–0.959	—
Shao et al. (2021)	Segmentation of tessellated fundus and calculating FTD	ResNet18; FCN	0.965	0.725	0.961	—	—	—
Hemelings et al. (2020)	Segmentation of myopia-related fundus changes	U-Net++	—	—	—	—	0.93 (optic disc), 0.80 (retinal atrophy), 0.80 (retinal detachment)	0.98 (optic disc), 0.91 (retinal atrophy), 0.70 (retinal detachment)

FTD, fundus tessellated density.

(Chen et al., 2022) quantified the thickness of each layer by adding an additional fully connected layer. The retina is histologically divided into ten layers that are only 400–500 microns thick at their thickest point and may be even thinner in myopic eyes. Therefore, their results can help physician improve the accuracy of interpretation. Notably, while not common currently in AI research in myopia, this type of application is widespread in diabetic retinopathy and can change the “end-to-end” workflow (i.e., prediction directly based on entire images). Table 3 summarizes the above-mentioned studies for automatic segmentation of myopia-related fundus changes.

AI technology in the study of myopia pathogenesis

Deep learning for investigating myopia-related morphological changes

Artificial intelligence can provide new ideas for morphological changes in myopic eyes. On tasks that ophthalmologists cannot perform (e.g., predicting refraction based on fundus images), deep learning methods can be done with low mean square error based on FP, UWF FP, or OCT images (Varadarajan et al., 2018; Shi et al., 2021; Yoo et al., 2022). One explanation is that the model automatically learns fundus changes that are not visible in the early stages of myopia and uses them for prediction. Considering this, Shi et al. (2021) introduced the gradient-weighted class activation mapping (Grad-CAM) method to find the region most essential for model prediction. The core idea is to calculate the gradient of the previous layer of the fully connected layer (i.e.: the last convolutional layer) with respect to each pixel in the input image, and to draw a heatmap from it. The pixels that have a higher impact on the model prediction are closer to the red color in the heatmap, and the pixels with less impact are closer to the blue color. The results showed that the area of interest was concentrated around the optic disc as well as the macula, suggesting a potential relationship between early morphological changes in this region and myopia.

In many mammalian models, choroidal thickness (ChT) can rapidly change in both directions when images are focused anteriorly (myopia) or posteriorly (hyperopia) to the retina before axial changes (Read et al., 2019). Studies have confirmed that the choroid undergoes histological changes before the retina in highly myopic eyes (Jonas and Xu, 2014; Zhou et al., 2017). The choroid can also influence choroidal neovascularization and scleral growth through the secretion of growth factors (Nickla and Wallman, 2010; Scherm et al., 2019) which in turn affects the progression of myopia. However, the choroid is the middle layer of the eye wall and cannot be viewed with the naked eye through fundus images. To investigate the choroidal changes, Sun et al. (2021) applied radiomics methods to the optic disc region. Features were automatically extracted from fundus images using PyRadiomics program, followed by LASSO regression to filter the most predictive features and eventually, a novel optic disc imaging metrics was constructed. The results showed that AI methods can effectively predict ChT based on fundus images rather than OCT images, which facilitates the assessment of early pathological changes in highly myopic eyes and guides early diagnosis and treatment.

Conventional machine learning for exploring myopia-related genes

Through the use of molecular techniques such as linkage analysis, candidate gene analysis, genome-wide association studies (GWAS) and next-generation sequencing (NGS), many new genes and chromosomal loci associated with myopia have now been identified. Representative studies include CREAM (Verhoeven et al., 2013) and 23andME (Tedja et al., 2018). However, these genes can currently explain less than 10% of the genetic variation in myopia (Han et al., 2022). Considering the size and high dimensional characteristics of this data type, conventional machine learning methods are suitable to transform it into valuable knowledge. Ghorbani Mojarad et al., 2018 used data from CREAM and 23andME

to screen for differential genes and calculate a genetic risk score (GRS), which was used as a variable to construct linear models. The results showed that the inclusion of the GRS significantly improved the performance of models in determining the occurrence of myopia compared with using the number of myopic relatives (NMP) alone ($p < 0.0001$). The model incorporating GRS better estimated refractive error at 7 ($R^2 = 3.0\%$ vs. 3.7%) and 15 ($R^2 = 2.6\%$ vs. 7.0%) years old compared to using only age, sex, and NMP, but the improvement was still unsatisfactory, as supported by the results of [Chen et al. \(2019\)](#). One possible reason is that the current understanding of myopia-related single nucleotide polymorphisms (SNPs) and gene-environment interactions is still limited. As for deep learning methods, deep neural networks (DNNs) and recurrent neural networks (RNNs) can be used for tasks such as variant calling, genome annotation, mutation classification, and “phenotype-genotype” correspondence ([Dias and Torkamani, 2019](#)) but have not yet been applied in myopia.

AI technology in myopia treatment

As mentioned above, the mechanisms of myopia onset and progression are still unclear, thus the methods of myopia prevention and treatment are constantly being updated. For non-progressive myopia (i.e., people with slow progression of myopia and progression ≤ 0.50 D/year), available correction methods include spectacles, corneal contact lenses, and surgery (e.g., laser keratomileusis, implantable collamer lens (ICL), posterior scleral reinforcement). For progressive myopia (i.e., those with rapid myopic progression and progression ≥ 0.75 D/year), available control measures include orthokeratology lens, spectacles with multi-point myopic defocus technique or point diffusion technique, medications (e.g., atropine, pirenzepine, 7-methylxanthine), low-energy red light irradiation, and a combination of above methods.

When choosing orthokeratology lens, less trials can help reduce the chance of ocular infections ([Kam et al., 2017](#)). The use of conventional machine learning methods can provide an accurate estimate of the proper alignment curve (AC) curvature of the lens. The results of [Fan et al. \(2022\)](#) showed that models such as SVM and Gaussian process had a better fitness with R-squared (R^2) up to 0.73–0.91. By using different kernel functions, SVM can also assist in the prediction of two important parameters of orthokeratology lens: return zone depth (RZD) and landing zone angle (LZA). The R^2 can reach above 0.80 and 0.90, respectively ([Fan et al., 2022](#)). AI technology also have applications in refractive surgery. Methods like random forest, gradient boosting, XGBoost, and SVM regression (SVR) can assist in implant size selection and arch height prediction in ICL surgery ([Kamiya et al., 2021](#); [Kang et al., 2021](#); [Shen et al., 2021](#)). Proper sizing ensures a safe postoperative ICL dome and reduces complications such as angle-closure glaucoma and anterior subcapsular cataract. Using an artificial neural network (ANN) containing dual hidden layers and boosting strategy, [Cui et al. \(2020\)](#) developed an assistance system for the design of SMILE surgical parameters. The postoperative corrected distance visual acuity (CDVA) is similar to the preoperative CDVA, but the postoperative uncorrected distance visual acuity (UDVA) is greater than the preoperative one. This result demonstrated that while AI did not significantly differ from experts in terms of safety, they did

increase in terms of effectiveness. However, these studies have made simplifications to clinical need, such as considering only two ICL sizes and converting the regression problem into a classification problem. This may improve model performance but also results in some limitations.

In addition, [Wu et al. \(2020\)](#) retrospectively analyzed a cohort of patients with topically applied atropine for myopia control. They used multiple conventional machine learning methods to predict IOP at the endpoint based on 19 variables, and the best performing XGBoost algorithm had an RMSE of up to 2.2604 mmHg, showing potential in predicting efficacy as well as potential side effects of atropine. Fewer studies have used AI in this area, possibly because cohort data for myopia are more difficult to collect compared to cross-sectional studies. [Table 4](#) summarizes the aforementioned AI-related studies for myopia treatment.

Discussion

Artificial intelligence-enabled intelligent ophthalmic devices are an important solution to the lack of ophthalmic medical resources (especially in primary hospitals), but the area of healthcare has its unique concerns. To apply AI methods in the process of real myopia clinical practice, we believe that the following aspects should be focused on.

Firstly, physician and patient acceptance is a challenge. [Scheetz et al. \(2021\)](#) showed a high rate of patient satisfaction with AI technology for ophthalmic screening, but [Lin et al. \(2022\)](#) found that residents were “algorithm aversion” and expected more physician involvement in eye screening services. Explainable artificial intelligence (XAI) is a potential solution to open the “black box” and gain the trust of patients. When detecting myopic macular lesions using OCT images, deep learning models can be trained using soft labels and output the probability of belonging to each lesion category rather than predicting a particular category, which has been shown to yield satisfying results ([Du et al., 2022](#)). Other visualization methods, such as the occlusion test ([Zeiler and Fergus, 2014](#)), saliency maps ([Simonyan et al., 2013](#)) and gradient-weighted class activation maps (Grad-CAMs) ([Selvaraju et al., 2017](#)) can also retrospectively analyze the prediction process of neural networks and highlight important regions relevant to decision making, thus improving interpretability. AI studies on other ocular diseases often choose to publish their heatmap results ([Brown et al., 2018](#); [Keel et al., 2019](#)) and many current studies in myopia are gradually starting to take this on board.

Secondly, it is important to accurately evaluate the performance of AI methods from a technical point of view. Existing AI studies in myopia do not have directly comparable results due to the difference in datasets and the way training set/test set were selected. In this regard, some studies have thought beyond the perspective of clinical applications to the perspective of computer science and have done some “benchmark work” in diabetic retinopathy ([Li et al., 2019](#)): by establishing a multicenter, well-labeled dataset and conducting repetitive tests using several state-of-the-art algorithms on same tasks, a benchmark of algorithm performance could be established and serves as a reference for further development of relevant evaluation systems. This can be borrowed to myopic AI research to help address the critical question of how to evaluate whether the performance of an AI method is good enough.

TABLE 4 Summary of AI technology for myopia treatment.

Research	Tasks	AI technology	Accuracy	AUC	MAE	RMSE	R ²
Fan et al. (2022)	Estimation of the AC curvature in orthokeratology lens fitting	Robust linear regression; SVM; Bagging decision trees; Gaussian process	—	—	0.263–0.507	0.373–0.680	0.73–0.91
Fan et al. (2021)	Prescribing CRT lens parameters in adolescents with myopia	Gaussian process; Robust linear regression; SVM	—	—	0.386–0.979 (for LZA); 5.326–8.644 (for RZD)	0.556–1.214 (for LZA); 6.883–10.998 (for RZD)	0.693–0.866 (for LZA); 0.964–0.975 (for RZD)
Shen et al. (2021)	Prediction of the postoperative ICL vault	RF; Gradient Boosting; XGBoost	0.802–0.828 (vault prediction); 0.815–0.822 (ICL size prediction)	0.718–0.765	—	159.03–162.53	0.285–0.315
Kang et al. (2021)	Prediction of the postoperative ICL vault	XGBoost; Light GBM; RF; SVM	0.759 (internal validation); 0.674 (external validation)	—	106.88 (internal validation); 143.69 (external validation)	140.14 (internal validation); 186.29 (external validation)	—
Kamiya et al. (2021)	Prediction of postoperative ICL vault	SVR; Gradient Boosting; RF	—	—	99.6–131.4	—	—
Cui et al. (2020)	Prediction of SMILE nomogram	ANN	—	—	0.066–0.114	—	0.9645
Wu et al. (2020)	Prediction of IOP in children with myopia treated with topical atropine	MARS; CART; RF; XGBoost	—	—	0.778–0.867	2.260–2.432	—

AC, alignment curve; CRT, corneal refractive therapy; LZA, landing zone angle; RZD, return zone depth; SVR, support vector regressor; SMILE, small incision lenticule extraction; ANN, artificial neural network; MARS, multivariate adaptive regression splines; CART, classification and regression tree.

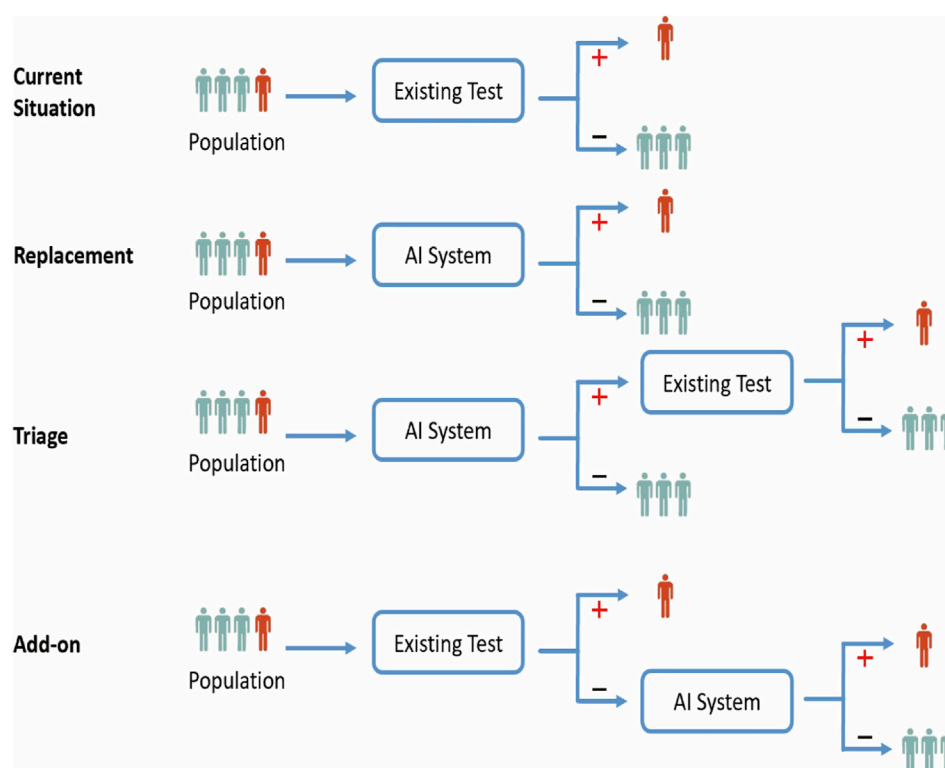


FIGURE 3
Three ways to integrate AI technology into existing clinical practices.

Lastly, AI should not only continue to improve its performance on evaluation metrics, but also be organically integrated with clinical practice in myopia to achieve a better visual health system. Regarding how to integrate a new technology into existing clinical practice, Bossuyt et al. (2006) summarized three possible ways (Figure 3): replacement, triage, and add-on. For the application of AI in myopia, we believe that the “Triage” and “Add-on” ways are viable and valuable: the former uses AI as the most basic diagnostic classification tool that can serve as a referral for large-scale primary ophthalmology screening or as an “opportunistic screening” in non-ophthalmology clinical work; The latter uses AI in parallel with or after the clinician’s diagnosis to serve as an assistant in tasks like segmenting the layers of the retina or measuring thickness on OCT images for classifying pathologic myopia, as mentioned earlier. As for the “Replacement”, AI algorithms are used to replace clinicians in clinical diagnostic tasks, which is generally only applicable to tasks that are simple enough or where the AI performs absolutely better than the physician. This requires rigorous validation and is not common in the field of myopia.

Conclusion

The application of AI in the field of myopia is impressive, and its performance holds promise to replace traditional computer-aided diagnostic systems (CADs). The results of this review suggest that AI has been applied to tackle some of the key challenges in myopia clinical practice. However, AI research should not simply be about applying models to various tasks and more attention needs to be paid to those technical problems that have yet to be solved. In the future, more technical approaches need to be proposed according to the characteristics of each task. It is promising that more AI approaches will be deployed as stable and efficient diagnostic systems for practical clinical diagnosis.

References

- Albawi, S., Mohammed, T. A., and Al-Zawi, S. (2017). “Understanding of a convolutional neural network,” in 2017 International Conference on Engineering and Technology (ICET), Antalya, Turkey, 21–23 Aug. 2017.
- Balyen, L., and Peto, T. (2019). Promising artificial intelligence-machine learning-deep learning algorithms in ophthalmology. *Asia Pac J. Ophthalmol. (Phila)*. 8 (3), 264–272. doi:10.22608/APO.2018479
- Bossuyt, P. M., Irwig, L., Craig, J., and Glasziou, P. (2006). Comparative accuracy: Assessing new tests against existing diagnostic pathways. *Bmj* 332 (7549), 1089–1092. doi:10.1136/bmj.332.7549.1089
- Brown, J. M., Campbell, J. P., Beers, A., Chang, K., Ostmo, S., Chan, R. V. P., et al. (2018). Automated diagnosis of plus disease in retinopathy of prematurity using deep convolutional neural networks. *JAMA Ophthalmol.* 136 (7), 803–810. doi:10.1001/jamaophthalmol.2018.1934
- Cahyo, D. A. Y., Wong, D. W. K., Yow, A. P., Saw, S. M., and Schmetterer, L. (2020). Volumetric choroidal segmentation using sequential deep learning approach in high myopia subjects. *Annu. Int. Conf. IEEE Eng. Med. Biol. Soc.* 2020, 1286–1289. doi:10.1109/EMBC44109.2020.9176184
- Chang, L., Pan, C. W., Ohno-Matsui, K., Lin, X., Cheung, G. C., Gazzard, G., et al. (2013). Myopia-related fundus changes in Singapore adults with high myopia. *Am. J. Ophthalmol.* 155 (6), 991–999. doi:10.1016/j.ajo.2013.01.016
- Chauhan, N. K., and Singh, K. (2018). “A review on conventional machine learning vs deep learning,” in 2018 International Conference on Computing, Power and Communication Technologies (GUCON), Greater Noida, India, 28–29 Sept. 2018.
- Chen, H. J., Huang, Y. L., Tse, S. L., Hsiao, W. P., Hsiao, C. H., Wang, Y., et al. (2022). Application of artificial intelligence and deep learning for choroid segmentation in myopia. *Transl. Vis. Sci. Technol.* 11 (2), 38. doi:10.1167/tvst.11.2.38
- Chen, Y., Han, X., Guo, X., Li, Y., Lee, J., and He, M. (2019). Contribution of genome-wide significant single nucleotide polymorphisms in myopia prediction: Findings from a 10-year cohort of Chinese twin children. *Ophthalmology* 126 (12), 1607–1614. doi:10.1016/j.ophtha.2019.06.026
- Chen, Y. X., Liao, C. M., Tan, Z., and He, M. G. (2021). Who needs myopia control? *Int. J. Ophthalmol.* 14 (9), 1297–1301. doi:10.18240/ijo.2021.09.01
- Choi, K. J., Choi, J. E., Roh, H. C., Eun, J. S., Kim, J. M., Shin, Y. K., et al. (2021). Deep learning models for screening of high myopia using optical coherence tomography. *Sci. Rep.* 11 (1), 21663. doi:10.1038/s41598-021-00622-x
- Coudray, N., Ocampo, P. S., Sakellaropoulos, T., Narula, N., Snuderl, M., Fenyö, D., et al. (2018). Classification and mutation prediction from non-small cell lung cancer histopathology images using deep learning. *Nat. Med.* 24 (10), 1559–1567. doi:10.1038/s41591-018-0177-5
- Cui, T., Wang, Y., Ji, S., Li, Y., Hao, W., Zou, H., et al. (2020). Applying machine learning techniques in nomogram prediction and analysis for SMILE treatment. *Am. J. Ophthalmol.* 210, 71–77. doi:10.1016/j.ajo.2019.10.015
- Deo, R. C. (2015). Machine learning in medicine. *Circulation* 132 (20), 1920–1930. doi:10.1161/CIRCULATIONAHA.115.001593
- Dias, R., and Torkamani, A. (2019). Artificial intelligence in clinical and genomic diagnostics. *Genome Med.* 11 (1), 70. doi:10.1186/s13073-019-0689-8

Author contributions

JZ and HZ contributed to the study conception and design. JZ made the figures, the tables and wrote the initial draft, HZ revised the manuscript and obtained funding. Both authors read and approved the final manuscript.

Funding

The study was funded by the Chinese National key research and development program (Project number 2021YFC2702100) and the Project of Shanghai Shen Kang Hospital Development Centre (Grant No. SHDC2020CR30538).

Acknowledgments

We thank Prof. Rui Feng and Xiangui He for their advices on this manuscript.

Conflict of interest

The authors declare that the research was conducted in the absence of any commercial or financial relationships that could be construed as a potential conflict of interest.

Publisher’s note

All claims expressed in this article are solely those of the authors and do not necessarily represent those of their affiliated organizations, or those of the publisher, the editors and the reviewers. Any product that may be evaluated in this article, or claim that may be made by its manufacturer, is not guaranteed or endorsed by the publisher.

- Dong, L., Kang, Y. K., Li, Y., Wei, W. B., and Jonas, J. B. (2020). Prevalence and time trends of myopia in children and adolescents in China: A systemic review and meta-analysis. *Retina* 40 (3), 399–411. doi:10.1097/IAE.0000000000002590
- Du, R., and Ohno-Matsui, K. (2022). Novel uses and challenges of artificial intelligence in diagnosing and managing eyes with high myopia and pathologic myopia. *Diagn. (Basel)* 12 (5), 1210. doi:10.3390/diagnostics12051210
- Du, R., Xie, S., Fang, Y., Hagino, S., Yamamoto, S., Moriyama, M., et al. (2022). Validation of soft labels in developing deep learning algorithms for detecting lesions of myopic maculopathy from optical coherence tomographic images. *Asia Pac J. Ophthalmol. (Phila)* 11 (3), 227–236. doi:10.1097/APO.0000000000000466
- Du, R., Xie, S., Fang, Y., Igarashi-Yokoi, T., Moriyama, M., Ogata, S., et al. (2021). Deep learning approach for automated detection of myopic maculopathy and pathologic myopia in fundus images. *Ophthalmol. Retina* 5 (12), 1235–1244. doi:10.1016/j.oret.2021.02.006
- Duan, H. Y., Ma, B. K., Yang, T. T., Hu, C. X., Tang, C. H., Sun, T., et al. (2021). Research advances of morphological changes of the choroid in high myopia. *Zhonghua Yan Ke Za Zhi* 57 (6), 459–464. doi:10.3760/cma.j.cn112142-20201121-00767
- Edwards, M. H., and Lam, C. S. (2004). The epidemiology of myopia in Hong Kong. *Ann. Acad. Med. Singap* 33 (1), 34–38.
- Fan, Y., Yu, Z., Tang, T., Liu, X., Xu, Q., Peng, Z., et al. (2022). Machine learning based strategy surpasses the traditional method for selecting the first trial Lens parameters for corneal refractive therapy in Chinese adolescents with myopia. *Cont. Lens Anterior Eye* 45 (3), 101330. doi:10.1016/j.clae.2020.05.001
- Fang, Z., Xu, Z., He, X., and Han, W. (2022). Artificial intelligence-based pathologic myopia identification system in the ophthalmology residency training program. *Front. Cell Dev. Biol.* 10, 1053079. doi:10.3389/fcell.2022.1053079
- Foo, L. L., Ng, W. Y., Lim, G. Y. S., Tan, T. E., Ang, M., and Ting, D. S. W. (2021). Artificial intelligence in myopia: Current and future trends. *Curr. Opin. Ophthalmol.* 32 (5), 413–424. doi:10.1097/ICU.0000000000000791
- Ghorbani Mojarad, N., Williams, C., and Guggenheim, J. A. (2018). A genetic risk score and number of myopic parents independently predict myopia. *Ophthalmic Physiol. Opt.* 38 (5), 492–502. doi:10.1111/opo.12579
- Gifford, K. L., Richdale, K., Kang, P., Aller, T. A., Lam, C. S., Liu, Y. M., et al. (2019). Imi - clinical management guidelines report. *Invest. Ophthalmol. Vis. Sci.* 60 (3), M184–m203. doi:10.1167/iiov.18-25977
- Gulshan, V., Peng, L., Coram, M., Stumpe, M. C., Wu, D., Narayanaswamy, A., et al. (2016). Development and validation of a deep learning algorithm for detection of diabetic retinopathy in retinal fundus photographs. *Jama* 316 (22), 2402–2410. doi:10.1001/jama.2016.17216
- Gupta, P. C., Kumar, M. P., and Ram, J. (2020). COVID-19 pandemic from an ophthalmology point of view. *Indian J. Med. Res.* 151 (5), 411–418. doi:10.4103/ijmr.IJMR_1369_20
- Gutierrez, L., Lim, J. S., Foo, L. L., Ng, W. Y., Yip, M., Lim, G. Y. S., et al. (2022). Application of artificial intelligence in cataract management: Current and future directions. *Eye Vis. (Lond)* 9 (1), 3. doi:10.1186/s40662-021-00273-z
- Han, S. B., Jang, J., Yang, H. K., Hwang, J. M., and Park, S. K. (2019). Prevalence and risk factors of myopia in adult Korean population: Korea national health and nutrition examination survey 2013–2014 (KNHANES VI). *PLoS One* 14 (1), e0211204. doi:10.1371/journal.pone.0211204
- Han, X., Liu, C., Chen, Y., and He, M. (2022). Myopia prediction: A systematic review. *Eye (Lond)* 36 (5), 921–929. doi:10.1038/s41433-021-01805-6
- Hemelings, R., Elen, B., Blaschko, M. B., Jacob, J., Stalmans, I., and De Boever, P. (2021). Pathological myopia classification with simultaneous lesion segmentation using deep learning. *Comput. Methods Programs Biomed.* 199, 105920. doi:10.1016/j.cmpb.2020.105920
- Holden, B. A., Fricke, T. R., Wilson, D. A., Jong, M., Naidoo, K. S., Sankaridurg, P., et al. (2016). Global prevalence of myopia and high myopia and temporal trends from 2000 through 2050. *Ophthalmology* 123 (5), 1036–1042. doi:10.1016/j.ophtha.2016.01.006
- Jiang, Z., Huang, Z., Qiu, B., Meng, X., You, Y., Liu, X., et al. (2020). Comparative study of deep learning models for optical coherence tomography angiography. *Biomed. Opt. Express* 11 (3), 1580–1597. doi:10.1364/BOE.387807
- Jonas, J. B., and Xu, L. (2014). Histological changes of high axial myopia. *Eye (Lond)* 28 (2), 113–117. doi:10.1038/eye.2013.223
- Kam, K. W., Yung, W., Li, G. K. H., Chen, L. J., and Young, A. L. (2017). Infectious keratitis and orthokeratology lens use: A systematic review. *Infection* 45 (6), 727–735. doi:10.1007/s15010-017-1023-2
- Kamiya, K., Ryu, I. H., Yoo, T. K., Kim, J. S., Lee, I. S., Kim, J. K., et al. (2021). Prediction of phakic intraocular lens vault using machine learning of anterior segment optical coherence tomography metrics. *Am. J. Ophthalmol.* 226, 90–99. doi:10.1016/j.ajo.2021.02.006
- Kang, E. M., Ryu, I. H., Lee, G., Kim, J. K., Lee, I. S., Jeon, G. H., et al. (2021). Development of a web-based ensemble machine learning application to select the optimal size of posterior chamber phakic intraocular lens. *Transl. Vis. Sci. Technol.* 10 (6), 5. doi:10.1167/tvst.10.6.5
- Keel, S., Wu, J., Lee, P. Y., Scheetz, J., and He, M. (2019). Visualizing deep learning models for the detection of referable diabetic retinopathy and glaucoma. *JAMA Ophthalmol.* 137 (3), 288–292. doi:10.1001/jamaophthalmol.2018.6035
- Lains, I., Wang, J. C., Cui, Y., Katz, R., Vingopoulos, F., Staurengi, G., et al. (2021). Retinal applications of swept source optical coherence tomography (OCT) and optical coherence tomography angiography (OCTA). *Prog. Retin Eye Res.* 84, 100951. doi:10.1016/j.preteyeres.2021.100951
- Li, J., Wang, L., Gao, Y., Liang, Q., Chen, L., Sun, X., et al. (2022). Automated detection of myopic maculopathy from color fundus photographs using deep convolutional neural networks. *Eye Vis. (Lond)* 9 (1), 13. doi:10.1186/s40662-022-00285-3
- Li, J., Zhu, L., Zhu, R., Lu, Y., Rong, X., Zhang, Y., et al. (2021). Automated analysis of choroidal sublayer morphologic features in myopic children using EDI-OCT by deep learning. *Transl. Vis. Sci. Technol.* 10 (13), 12. doi:10.1167/tvst.10.13.12
- Li, S. M., Ren, M. Y., Gan, J., Zhang, S. G., Kang, M. T., Li, H., et al. (2022). Machine learning to determine risk factors for myopia progression in primary school children: The anyang childhood eye study. *Ophthalmol. Ther.* 11 (2), 573–585. doi:10.1007/s40123-021-00450-2
- Li, T., Gao, Y., Wang, K., Guo, S., Liu, H., and Kang, H. (2019). Diagnostic assessment of deep learning algorithms for diabetic retinopathy screening. *Inf. Sci.* 501, 511–522. doi:10.1016/j.ins.2019.06.011
- Li, Y., Feng, W., Zhao, X., Liu, B., Zhang, Y., Chi, W., et al. (2022). Development and validation of a deep learning system to screen vision-threatening conditions in high myopia using optical coherence tomography images. *Br. J. Ophthalmol.* 106 (5), 633–639. doi:10.1136/bjophthalmol-2020-317825
- Liang, J. H., Chen, Y. C., Zhao, Y., Kakaer, A., Jiang, N., Huang, S., et al. (2021). Prevalence of visual impairment among students before and during the COVID-19 pandemic, findings from 1,057,061 individuals in guangzhou, southern China. *Front. Pediatr.* 9, 813856. doi:10.3389/fped.2021.813856
- Lin, H., Long, E., Ding, X., Diao, H., Chen, Z., Liu, R., et al. (2018). Prediction of myopia development among Chinese school-aged children using refraction data from electronic medical records: A retrospective, multicentre machine learning study. *PLoS Med.* 15 (11), e1002674. doi:10.1371/journal.pmed.1002674
- Lin, S., Li, L., Zou, H., Xu, Y., and Lu, L. (2022). Medical staff and resident preferences for using deep learning in eye disease screening: Discrete choice experiment. *J. Med. Internet Res.* 24 (9), e40249. doi:10.2196/40249
- Lin, T. Y., Dollár, P., Girshick, R., He, K., Hariharan, B., and Belongie, S. (2017). “Feature Pyramid networks for object detection,” in 2017 IEEE Conference on Computer Vision and Pattern Recognition (CVPR), Hawaii Convention Center, 21–26 July 2017.
- Lu, L., Ren, P., Tang, X., Yang, M., Yuan, M., Yu, W., et al. (2021). AI-model for identifying pathologic myopia based on deep learning algorithms of myopic maculopathy classification and “plus” lesion detection in fundus images. *Front. Cell Dev. Biol.* 9, 719262. doi:10.3389/fcell.2021.719262
- Morgan, I. G., Ohno-Matsui, K., and Saw, S. M. (2012). Myopia. *Lancet.* 379 (9827), 1739–1748. doi:10.1016/S0140-6736(12)60272-4
- Natarajan, S., Jain, A., Krishnan, R., Rogye, A., and Sivaprasad, S. (2019). Diagnostic accuracy of community-based diabetic retinopathy screening with an offline artificial intelligence system on a smartphone. *JAMA Ophthalmol.* 137 (10), 1182–1188. doi:10.1001/jamaophthalmol.2019.2923
- Nickla, D. L., and Wallman, J. (2010). The multifunctional choroid. *Prog. Retin Eye Res.* 29 (2), 144–168. doi:10.1016/j.preteyeres.2009.12.002
- Obermeyer, Z., and Emanuel, E. J. (2016). Predicting the future - big data, machine learning, and clinical medicine. *N. Engl. J. Med.* 375 (13), 1216–1219. doi:10.1056/NEJMp1606181
- Park, S. J., Ko, T., Park, C. K., Kim, Y. C., and Choi, I. Y. (2022). Deep learning model based on 3D optical coherence tomography images for the automated detection of pathologic myopia. *Diagn. (Basel)* 12 (3), 742. doi:10.3390/diagnostics12030742
- Peng, Y., Dharssi, S., Chen, Q., Keenan, T. D., Agrón, E., Wong, W. T., et al. (2019). DeepSeeNet: A deep learning model for automated classification of patient-based age-related macular degeneration severity from color fundus photographs. *Ophthalmology* 126 (4), 565–575. doi:10.1016/j.ophtha.2018.11.015
- Read, S. A., Fuss, J. A., Vincent, S. J., Collins, M. J., and Alonso-Caneiro, D. (2019). Choroidal changes in human myopia: Insights from optical coherence tomography imaging. *Clin. Exp. Optom.* 102 (3), 270–285. doi:10.1111/cxo.12862
- Ronneberger, O., Fischer, P., and Brox, T. (2015). *U-Net: Convolutional networks for biomedical image segmentation*. New York: Springer International Publishing.
- Sarraf, S., and Tofghi, G. (2016). “Deep learning-based pipeline to recognize Alzheimer’s disease using fMRI data,” in 2016 Future Technologies Conference, San Francisco, CA, USA, 6–7 Dec. 2016.
- Scheetz, J., Koca, D., McGuinness, M., Holloway, E., Tan, Z., Zhu, Z., et al. (2021). Real-world artificial intelligence-based opportunistic screening for diabetic retinopathy in endocrinology and indigenous healthcare settings in Australia artificial intelligence-based opportunistic screening for diabetic retinopathy in endocrinology and indigenous healthcare settings in Australia. *Sci. Rep.* 11 (1), 15808. doi:10.1038/s41598-021-94178-5
- Scherm, P., Pettenkofer, M., Maier, M., Lohmann, C. P., and Feucht, N. (2019). Choroidal capillary blood flow in myopic subjects measured with OCT angiography. *Ophthalmic Surg. Lasers Imaging Retina* 50 (5), e133–e139. doi:10.3928/23258160-20190503-13

- Selvaraju, R. R., Cogswell, M., Das, A., Vedantam, R., Parikh, D., and Batra, D. (2017). "Grad-CAM: Visual explanations from deep networks via gradient-based localization," in 2017 IEEE International Conference on Computer Vision (ICCV), Venice, Italy, 22–29 Oct. 2017.
- Shao, L., Zhang, Q. L., Long, T. F., Dong, L., Zhang, C., Da Zhou, W., et al. (2021). Quantitative assessment of fundus tessellated density and associated factors in fundus images using artificial intelligence. *Transl. Vis. Sci. Technol.* 10 (9), 23. doi:10.1167/tvst.10.9.23
- Shen, Y., Wang, L., Jian, W., Shang, J., Wang, X., Ju, L., et al. (2021). Big-data and artificial-intelligence-assisted vault prediction and EVO-ICL size selection for myopia correction. *Br. J. Ophthalmol.* 2021, 319618. doi:10.1136/bjophthalmol-2021-319618
- Shi, Z., Wang, T., Huang, Z., Xie, F., and Song, G. (2021). A method for the automatic detection of myopia in Optos fundus images based on deep learning. *Int. J. Numer. Method Biomed. Eng.* 37 (6), e3460. doi:10.1002/cnm.3460
- Simonyan, K., Vedaldi, A., and Zisserman, A. (2013). "Deep inside convolutional networks: Visualising image classification models and saliency maps,". arxiv:1312.6034 [csCV].
- Sogawa, T., Tabuchi, H., Nagasato, D., Masumoto, H., Ikuno, Y., Ohsugi, H., et al. (2020). Accuracy of a deep convolutional neural network in the detection of myopic macular diseases using swept-source optical coherence tomography. *PLoS One* 15 (4), e0227240. doi:10.1371/journal.pone.0227240
- Sun, D., Du, Y., Chen, Q., Ye, L., Chen, H., Li, M., et al. (2021). Imaging features by machine learning for quantification of optic disc changes and impact on choroidal thickness in young myopic patients. *Front. Med. (Lausanne)*. 8, 657566. doi:10.3389/fmed.2021.657566
- Tan, M., and Le, Q. V. (2019). "EfficientNet: Rethinking model scaling for convolutional neural networks,". arxiv:1905.11946[csLG,csCV,statML].
- Tan, T. E., Anees, A., Chen, C., Li, S., Xu, X., Li, Z., et al. (2021). Retinal photograph-based deep learning algorithms for myopia and a blockchain platform to facilitate artificial intelligence medical research: A retrospective multicohort study. *Lancet Digit. Health* 3 (5), e317–e329. doi:10.1016/S2589-7500(21)00055-8
- Tang, T., Yu, Z., Xu, Q., Peng, Z., Fan, Y., Wang, K., et al. (2020). A machine learning-based algorithm used to estimate the physiological elongation of ocular axial length in myopic children. *Eye Vis. (Lond)*. 7, 50. doi:10.1186/s40662-020-00214-2
- Tedja, M. S., Wojciechowski, R., Hysi, P. G., Eriksson, N., Furlotte, N. A., Verhoeven, V. J. M., et al. (2018). Genome-wide association meta-analysis highlights light-induced signaling as a driver for refractive error. *Nat. Genet.* 50 (6), 834–848. doi:10.1038/s41588-018-0127-7
- Ueda, E., Yasuda, M., Fujiwara, K., Hashimoto, S., Ohno-Matsui, K., Hata, J., et al. (2019). Trends in the prevalence of myopia and myopic maculopathy in a Japanese population: The hisayama study. *Invest. Ophthalmol. Vis. Sci.* 60 (8), 2781–2786. doi:10.1167/iovs.19-26580
- Varadarajan, A. V., Poplin, R., Blumer, K., Angermueller, C., Ledsam, J., Chopra, R., et al. (2018). Deep learning for predicting refractive error from retinal fundus images. *Invest. Ophthalmol. Vis. Sci.* 59 (7), 2861–2868. doi:10.1167/iovs.18-23887
- Verhoeven, V. J., Hysi, P. G., Wojciechowski, R., Fan, Q., Guggenheim, J. A., Höhn, R., et al. (2013). Genome-wide meta-analyses of multiethnic cohorts identify multiple new susceptibility loci for refractive error and myopia. *Nat. Genet.* 45 (3), 314–318. doi:10.1038/ng.2554
- Wang, J., Ding, H., Bidgoli, F. A., Zhou, B., Iribarren, C., Molloy, S., et al. (2017). Detecting cardiovascular disease from mammograms with deep learning. *IEEE Trans. Med. Imaging* 36 (5), 1172–1181. doi:10.1109/TMI.2017.2655486
- Wu, T. E., Chen, H. A., Jhou, M. J., Chen, Y. N., Chang, T. J., and Lu, C. J. (2020). Evaluating the effect of topical atropine use for myopia control on intraocular pressure by using machine learning. *J. Clin. Med.* 10 (1), 111. doi:10.3390/jcm10010111
- Yang, X., Chen, G., Qian, Y., Wang, Y., Zhai, Y., Fan, D., et al. (2020). Prediction of myopia in adolescents through machine learning methods. *Int. J. Environ. Res. Public Health* 17 (2), 463. doi:10.3390/ijerph17020463
- Ye, X., Wang, J., Chen, Y., Lv, Z., He, S., Mao, J., et al. (2021). Automatic screening and identifying myopic maculopathy on optical coherence tomography images using deep learning. *Transl. Vis. Sci. Technol.* 10 (13), 10. doi:10.1167/tvst.10.13.10
- Yoo, T. K., Ryu, I. H., Kim, J. K., and Lee, I. S. (2022). Deep learning for predicting uncorrected refractive error using posterior segment optical coherence tomography images. *Eye (Lond)*. 36 (10), 1959–1965. doi:10.1038/s41433-021-01795-5
- Zech, J. R., Badgeley, M. A., Liu, M., Costa, A. B., Titano, J. J., and Oermann, E. K. (2018). Variable generalization performance of a deep learning model to detect pneumonia in chest radiographs: A cross-sectional study. *PLoS Med.* 15 (11), e1002683. doi:10.1371/journal.pmed.1002683
- Zeiler, M. D., and Fergus, R. (2014). *Visualizing and understanding convolutional networks*. New York: Springer International Publishing.
- Zhang, C., Zhao, J., Zhu, Z., Li, Y., Li, K., Wang, Y., et al. (2022). Applications of artificial intelligence in myopia: Current and future directions. *Front. Med. (Lausanne)* 9, 840498. doi:10.3389/fmed.2022.840498
- Zhou, L. X., Shao, L., Xu, L., Wei, W. B., Wang, Y. X., and You, Q. S. (2017). The relationship between scleral staphyloma and choroidal thinning in highly myopic eyes: The Beijing Eye Study. *Sci. Rep.* 7 (1), 9825. doi:10.1038/s41598-017-10660-z



OPEN ACCESS

EDITED BY

Yanwu Xu,
Baidu, China

REVIEWED BY

Heng Li,
Southern University of Science and
Technology, China
Guoying Mu,
Shandong Provincial Hospital affiliated to
Shandong First Medical University, China
Yi Shao,
Nanchang University, China

*CORRESPONDENCE

Hong Qi,
✉ doctorqihong@hotmail.com

[†]These authors have contributed equally to
this work and share first authorship

SPECIALTY SECTION

This article was submitted to Molecular
and Cellular Pathology,
a section of the journal
Frontiers in Cell and Developmental
Biology

RECEIVED 04 December 2022

ACCEPTED 10 January 2023

PUBLISHED 19 January 2023

CITATION

Tang C, Zhang Y, Sun T, Xie J, Liu Y, Liu R,
Sun Z and Qi H (2023), Prospective clinical
study of retinal microvascular alteration
after ICL implantation.
Front. Cell Dev. Biol. 11:1115822.
doi: 10.3389/fcell.2023.1115822

COPYRIGHT

© 2023 Tang, Zhang, Sun, Xie, Liu, Liu, Sun
and Qi. This is an open-access article
distributed under the terms of the [Creative
Commons Attribution License \(CC BY\)](#).
The use, distribution or reproduction in
other forums is permitted, provided the
original author(s) and the copyright
owner(s) are credited and that the original
publication in this journal is cited, in
accordance with accepted academic
practice. No use, distribution or
reproduction is permitted which does not
comply with these terms.

Prospective clinical study of retinal microvascular alteration after ICL implantation

Chuhao Tang^{1†}, Yu Zhang^{1†}, Tong Sun¹, Jianyang Xie², Yiyun Liu¹,
Rongjun Liu¹, Zhengze Sun¹ and Hong Qi^{1*}

¹Department of Ophthalmology, Peking University Third Hospital, Beijing Key Laboratory of Restoration of Damaged Ocular Nerve, Beijing, China, ²Cixi Institute of BioMedical Engineering, Ningbo Institute of Materials Technology and Engineering, Chinese Academy of Sciences, Ningbo, China

Purpose: To evaluate the retinal microvascular alteration after implantable collamer lens (ICL) implantation in moderate to high myopia patients using quantitative optical coherence tomography angiography (OCTA).

Methods: This prospective cohort study included 50 eyes of 25 patients with preoperative spherical equivalent ≥ -3.00 D. Patients underwent bilateral ICL implantation at the Department of Ophthalmology, Peking University Third Hospital, from November 2018 to July 2019. OCTA was used to image the superficial and deep retinal capillary plexuses before ICL implantation surgery and at 3 months follow-up.

Results: There was no significant difference in the microvascular density within each annular zone and all quadrantal zones of the superficial and deep layers found in myopia patients before and after ICL surgery.

Conclusion: Levels of microvascular density in retinal capillary plexuses were stable, as detected by the OCTA, showing the high security of ICL implantation, which would not leave adverse effects on retinal microvasculature in myopia patients.

KEYWORDS

implantable collamer lens implantation surgery, myopia, optical coherence tomography angiography, retinal microvasculature, vessel density, visual acuity

1 Introduction

With the increase in educational pressure and limited time outdoors, myopia has become the most common vision problem (Morgan et al., 2018). Recent epidemiological studies indicated a prevalence of myopia as high as 80%–90% in young adults in East Asia (Foster and Jiang, 2014; Wu et al., 2016). It is estimated that, in 2050, half of the world's population will be affected with myopia and 10% of people will be at a relevant risk of becoming blind as a result of high myopia (Holden et al., 2016; Hopf and Pfeiffer, 2017). With the elongation of the eyeball that occurs with the progression of myopia, the retinal microvascular decrease was observed in the myopia subjects (Yang et al., 2016; Al-Sheikh et al., 2017; Li et al., 2017).

Since the introduction of the Implantable Collamer Lens (ICL; Staar Surgical, Nidau, Switzerland) in 1993, refractive surgery has entered a new era of myopia treatment (Assetto et al., 1996). Because it significantly increased best-corrected visual acuity (BCVA) while reducing caused higher-order aberrations and improving postoperative contrast sensitivity (Wang and Zhou, 2016), the ICL is most frequently used to correct high and extreme myopia. In addition, the ICL performs superbly in the treatment of low to moderate myopia (Kamiya et al., 2012; Dougherty and Priver, 2017; Kamiya et al., 2018).

However, multiple studies revealed that intraocular refractive surgery, such as cataract surgery, may lead to early retinal ischemia, hypoxia, or even retinal vasculitis (Alnawaiseh et al., 2018; Kim et al., 2018; Pilotto et al., 2019; Liu J et al., 2021). Retinal complications would cause a potential or substantial threat to patients' vision. So, it is vital to monitor retinal microvascular alteration after intraocular refractive surgery. ICL implantation is also a kind of intraocular refractive surgery. However, it is still unknown whether the ICL implantation surgery will affect the retinal microvasculature of myopic eyes.

Optical coherence tomography angiography (OCTA) is a new, non-invasive imaging technique with wide application potential for retinal vascular disease (de Carlo et al., 2015; Gao et al., 2016; Wylegala, 2018). In 2006, Optical Coherence Angiography was first performed to visualize the vasculature in the human eyes (Makita et al., 2006). OCTA can produce high-resolution, three-dimensional images and measure the microvascular network in different layers of the retina structure without the use of contrast agents (Gao et al., 2016; Zhang Q et al., 2016). This study aimed to use OCTA to uncover potential retinal capillary network alterations induced by ICL implantation surgery.

2 Materials and methods

2.1 Participants

This study includes a total of 50 eyes from 25 participants with moderate and high myopia. All subjects underwent ICL implantation surgery at the Department of Ophthalmology, Peking University Third Hospital between November 2018 and July 2019. Inclusion criteria: 21–45 years old, binocular myopia, with a spherical equivalent of greater than −3.00 diopters (D), anterior chamber depth (ACD) ≥ 2.8 mm, corneal endothelial cell count (cECC) ≥ 2000 cells/mm², SE remained unchanged for more than 1 year, unsatisfactory vision with contact lenses or spectacles. All patients included in this study had no history of intraocular surgery and showed no other ocular pathologies (uveitis, glaucoma, cataract, keratoconus, severe dry eye, etc.) or serious systemic diseases (diabetes, uncontrolled hypertension, severe hyperthyroidism, etc.).

The method of this study was approved by the Ethics Committee of Peking University Third Hospital (M2020240). In addition, this study was registered and approved on Clinical Trials.gov (NCT04443231). Each subject was given informed consent after an adequate study explanation.

Before surgery, each subject got a full ocular examination: The ACD (measured from the endothelium to the crystalline lens) was measured using anterior segment Optical Coherence Tomography (Visante-OCT; Carl Zeiss Meditec, Jena, Germany), the horizontal white-to-white (WTW) distance and axial length (AL) were measured by optical biometry (IOL Master 700; Carl Zeiss Meditec, Jena, Germany), cECC was obtained from each eye, using a corneal endothelial microscope (SP-2000; Topcon, Tokyo, Japan). Additionally, each eye was subjected to slit-lamp biomicroscopic examination, corneal topography, and funduscopic examination.

The size of the ICL was calculated with a STAAR sizing formula, based on the result of WTW and ACD. Myopia patients are planned for standard ICL implantation surgeries by the same surgeon (QH) under similar settings. Preoperatively, in all patients, 0.5% levofloxacin

eye drops were used 3 days before the operation, four times daily and topical anesthesia (4% lidocaine) was administered 30 min before the operation. Through a 3.0-mm temporal corneal incision, the ICL was slowly inserted into the anterior chamber following the implantation of hyaluronic acid (ViscAid, Beijing, China), under visualization with OPMI Lumera 700 surgical microscope (Carl Zeiss Meditec, Germany), and the Toric ICL implantation surgery was completed with the help of the Callisto Eye System (Carl Zeiss Meditec, Germany). Any remaining viscosurgical device was washed out of the anterior chamber with the balanced salt solution. Antibiotic eye drops, steroidal eye drops, and artificial tear drops were used postoperatively.

Moreover, each patient's eye was assessed for uncorrected visual acuity (UCVA), BCVA, intraocular pressure (IOP), and manifest refraction before surgery as well as 1 day, 1 week, 1 month, and 3 months afterward. For statistical analysis, the decimal Snellen evaluation of UCVA and BCVA was converted to the logarithm of the minimum angle of resolution (logMAR). With the aid of a non-contact tonometer (CT-80; Topcon, Tokyo, Japan), the IOP was measured. The central vault of the ICL (distance from the posterior surface of the ICL to the crystalline lens) was measured using OCT 3 months after surgery.

2.2 OCT angiography

After the ocular examination, AngioVue (Optovue, Fremont, CA, United States), was used to capture the OCTA images in all participants from 8:00 a.m. to 12:00 a.m. The system has an A-scan rate of 70 kHz scans per second, with a light source centered on 840 nm and a bandwidth of 45 nm. The scan area was centered on the fovea with a field of view of 6 mm × 6 mm. The resolution of the exported OCT images was 400 × 400 pixels and images with scan quality ≥ 6 were included for analysis. Automatic segmentation was performed by the software to generate images of the superficial retinal capillary plexus (SCP), and deep retinal capillary plexus (DCP). The SCP was segmented from 3 μm beneath the inner limiting membrane (ILM) to 15 μm beneath the inner plexiform layer (IPL), representing the outer boundary of the ILM to the outer boundary of the IPL. The DCP was segmented from 15 μm beneath the IPL to 70 μm beneath the IPL, representing the outer boundary of the IPL to the outer boundary of the outer plexiform layer (OPL) (Yang et al., 2016).

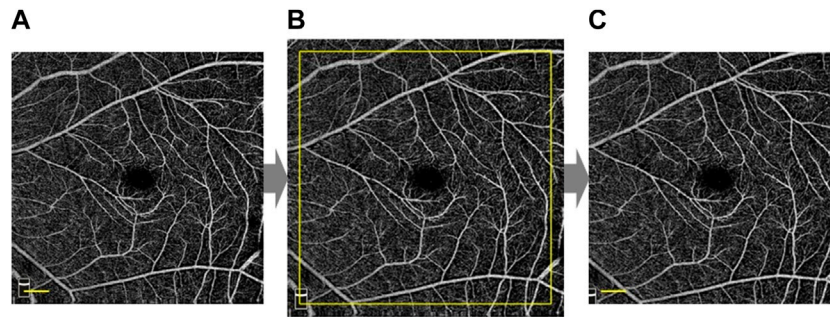
Due to the elongation of the eye, the magnification for imaging the fundus using fundus photography and OCT differs in the myopic eye (Li et al., 2017). As a result, Bennett's formula (Figure 1) (Bennett et al., 1994) was used to correct magnification in photographs taken with highly myopic eyes. The correction formula of the image is:

$$t = p \times q \times s \quad (1)$$

Where t represents the actual scan length, p is the magnification factor determined by the OCTA imaging system, and s represents the original measurement value obtained from the OCTA. The formula of the correction factor q is:

$$q = 0.01306 \times (AL - 1.82) \quad (2)$$

The AL is the axial length as mentioned above. The foveal avascular zone (FAZ) centroid was determined using Matlab (The Mathworks, Inc., Natick, MA, United States) and the image was

**FIGURE 1**

Magnification correction of OCTA high myopia image. According to Bennett's formula, the original image (A) was magnified $\times 1.10$ to obtain the magnified image (B) based on AL = 26.17mm, and then further cropped to the size of the original image (C). Scale bar: 600 μm . (A), (B), and (C) were based on the same OCTA image.

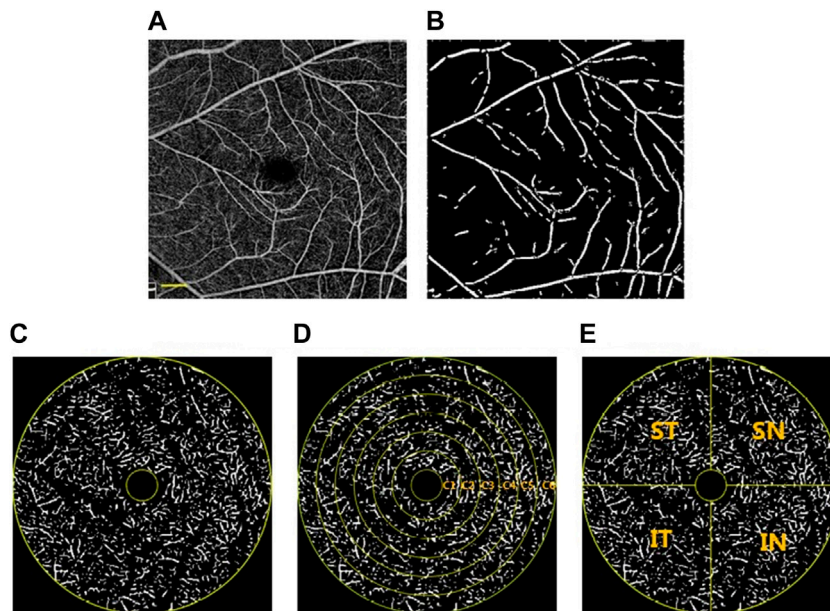
**FIGURE 2**

Image partitioning and processing methods. (A) OCTA image after magnification correction. The OCTA image was skeletonized and large blood vessels with a diameter $> 30 \mu\text{m}$ were extracted (B) and divided. The annular zone with a diameter of 0.6–5 mm (C) was divided into 6 annuli (C1–C6) for analysis after the removal of the avascular zone (D). In addition, four quadrants centered on the fovea were generated (E). ST, superior temporal; SN, superior nasal; IN, inferior nasal; IT, inferior temporal. Scale bar: 600 μm . (A), (B), (C), (D), and (E) were based on the same OCTA image, which was the same sample as used for Figure 1.

skeletonized. Since large blood vessels in the deep retinal vascular plexus were considered to be projection artifacts of superficial blood vessels (Zhang M et al., 2016), our custom algorithm separated the vessels with diameters $> 30 \mu\text{m}$ in both the superficial and deep layers. The images were then converted to binary images. The partition method for the macular retinal region was shown in Figure 2.

Fractal dimension (FD) analysis was commonly used in the objective quantification of retinal capillary complexity (Ab Hamid et al., 2016). Photoshop was used to crop the image of each area separately, and then the box-counting method with FracLab 2.1 toolbox was used to quantitatively analyze the FD (representing blood vessel density) of each area. FracLab (Paris,

France) is designed for digital image analysis and is a plug-in for Matlab.

2.3 Statistical analysis

The data were presented as the mean \pm standard deviation (SD). The differences between the means were evaluated using independent sample t-tests (for patients preoperatively and postoperatively) and analyzed using SPSS Statistics 24 (SPSS Inc., Chicago, IL, United States). $p < 0.05$ was considered significantly different.

TABLE 1 Preoperative demographics of the myopia patients underwent implantable collamer lens implantation in this study.

Characteristic	Mean ± SD
Number, people/eyes	25/50
Sex, male/female	5/20
Age (years)	27.0 ± 3.8 (range 21–36)
MRSE (D)	−8.50 ± 2.68
LogMAR BCVA	0.02 ± 0.06
AL (mm)	26.63 ± 1.06
WTW (mm)	11.90 ± 0.31
ACD (mm)	3.26 ± 0.25
cECC (cells/mm ²)	2913.00 ± 218.86
ICL size (mm)	12.9 ± 0.3
ICL power (D)	−9.38 ± 2.70 (−4.00 to −14.00)

MRSE, manifest refraction spherical equivalent; LogMAR, logarithm of the minimal angle of resolution; BCVA, best corrected visual acuity; AL, axial length; WTW, white-to-white; ACD, anterior chamber depth; cECC, corneal endothelial cell count.

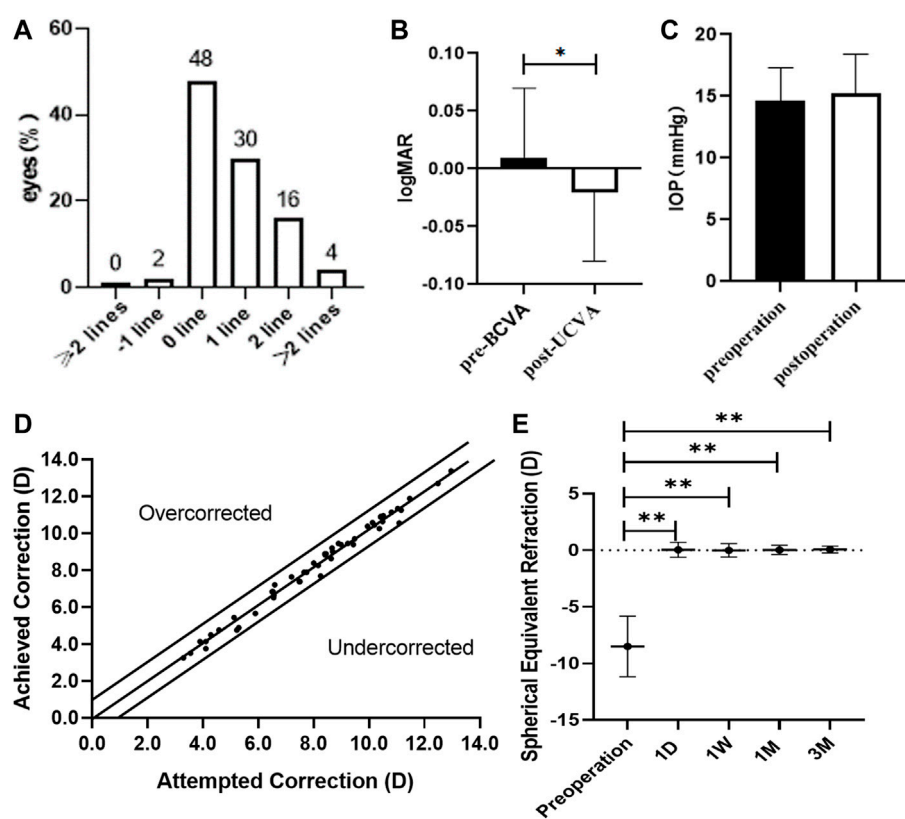


FIGURE 3 Clinical examinations of myopia patients after ICL implantation surgery. **(A)** Changes in Snellen lines of BCVA at 3 months after ICL implantation. **(B)** Changes between BCVA 3 months after ICL implantation and UCVA Preoperatively. **(C)** Changes in intraocular pressure 3 months after ICL implantation. **(D)** A scatter plot of the attempted versus the achieved manifest spherical equivalent correction 3 months after ICL implantation. **(E)** Time course of manifest spherical equivalent after ICL implantation. The asterisks indicate statistically significant differences between pre-surgery and post-surgery. D, day; W, week; M, month(s).

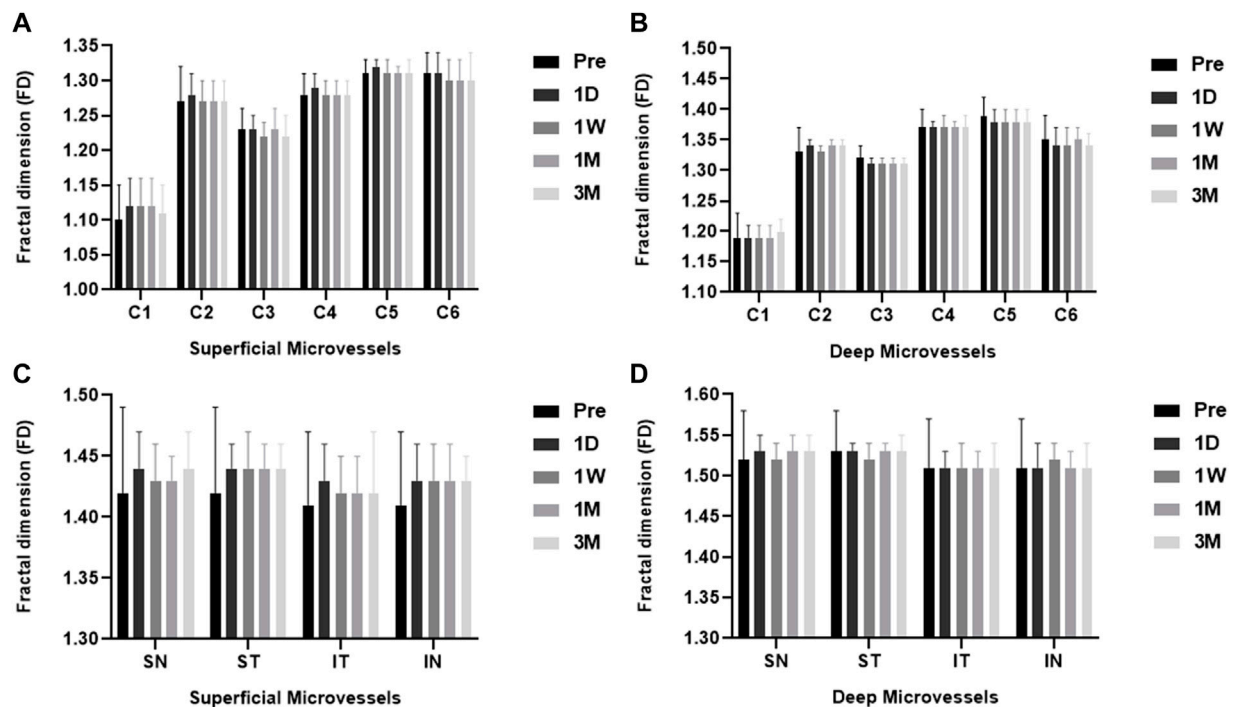


FIGURE 4

The FD (representing retinal microvascular density) of ICL patients pre- and post-surgery for each layer. Among the six individual annular zones (A, B), the microvascular density in the (A) superficial and (B) deep layers showed no significant difference in myopia patients pre- and post-surgery (all $p > 0.05$). The microvascular density was also not significantly different in all quadrantal zones of the superficial (C) and deep (D) layers in myopia patients pre- and post-surgery. (all $p > 0.05$). ST, superior temporal; SN, superior nasal; IN, inferior nasal; IT, inferior temporal.

3 Result

The demographics of the enrolled subjects are summarized in Table 1. The mean patient age at the time of surgery was 27.0 ± 3.8 years (ranging from 21 to 36 years). The preoperative manifest refraction spherical equivalent (MRSE) was -8.50 ± 2.68 D (ranging from -3.50 D to -13.88 D). The preoperative manifest sphere was -7.95 ± 2.57 D (ranging from -3.00 D to -13.75 D). The preoperative manifest refractive cylinder was -1.16 ± 0.92 D (ranging from 0.00 to -3.25 D). The IOP was 14.60 ± 2.71 mmHg. AL was 26.63 ± 1.06 mm (ranging from 24.87 to 29.50 mm). WTW was 11.90 ± 0.31 mm (ranging from 11.3 mm to 12.7 mm). ACD was 3.26 ± 0.25 mm (ranging from 2.92 mm to 3.80 mm).

All surgical procedures were uneventful, and no postoperative complications, such as cataract formation, pigment dispersion syndrome, pupillary block, or axis rotation, were seen throughout the observation period. Visual acuity improved for all patients on the first day after surgery. Three months postoperatively, 2% of eyes lost one line of vision and 98% of eyes maintained or gained BCVA (Figure 3A). The efficacy index was 1.11 ± 0.24 (preoperative BCVA: 0.01 ± 0.06 logMAR and postoperative UCVA: -0.02 ± 0.06 logMAR, $p < 0.05$; Figure 3B). The mean preoperative IOP and postoperative IOP (14.6 ± 2.7 versus 15.2 ± 3.2 , $p > 0.05$; Figure 3C) were not significantly different. At 3 months postoperatively, 90% and 100% were within ± 0.5 and 1.0 D of the attempted correction, respectively (Figure 3D). The time course changes in the manifest refraction were shown in Figure 3E. Changes in the manifest refraction from

1 day to 3 months were 0.02 ± 0.68 D. Three months postoperatively, the vault was 0.64 ± 0.20 mm.

Preoperative versus postoperative retinal microvascular density for myopia patients, with p values for comparison. The total annular zone was divided into four quadrantal zones and six annular zones (bandwidth = 0.73 mm). No significant difference in the microvascular density within each annular zone and all quadrantal zones of the superficial and deep layers was found in myopia patients between pre-surgery and post-surgery (Figure 4).

4 Discussion

Myopia is one of the most prevalent eye disorders, and the epidemic of high myopia, in particular, is a serious hazard to public health, such as financial, psychological, quality of life, and direct and indirect risks of blindness. ICL implantation is one of the methods to treat myopia. According to our data, ICL implantation is a safe and effective treatment for both moderate and high myopia. No eye loses two or more lines of vision after ICL implantation. All eyes were within ± 1.0 D of the attempted correction and both refractive status and IOP remained stable for 3 months after surgery. Its performance in safety, effectiveness, stability, and predictability is even better than the results of Sanders et al. (2004) due to the advancement of surgical techniques and the update of ICL.

Retinopathy is the most common complication of high myopia, which is a slowly progressive and sight-threatening condition. Several studies have investigated the retinal microvascular in patients with

myopia, revealing the retinal microvascular network alterations in myopic eyes. The structural elongation of the eyeball mechanically stretches the retinal tissue, resulting in the straightening and narrowing of the microvessels and consequently the decrease of the retinal microvascular density and perfusion in myopic eyes (Li et al., 2017; Leng et al., 2018; Li et al., 2018; Milani et al., 2018; Gołębiewska et al., 2019; Guo et al., 2019). Jiang et al. (2021) found that the superficial and deep macular microvascular density in high myopia was significantly higher than that in non-high myopia by using OCTA; Liu M et al. (2021) also reached the same conclusion in a larger sample study and found a negative correlation between microvascular density and axial length.

OCT angiography, as an advanced imaging technique characterized by non-invasiveness, quantification, and reliability, which can detect blood flow signals in the retina, has superior advantages over traditional angiography techniques. OCTA is widely used in the evaluation and diagnosis of eye diseases, such as high myopia retinopathy (Grudzińska and Modrzejewska, 2018), glaucoma optic nerve damage (Rao et al., 2020), retinal vein occlusion (Hirano et al., 2021) and diabetic retinopathy (Sun et al., 2021). Using OCTA, images from different layers of the retina can be projected clearly due to its high resolution. In the present study, by using OCT angiography, superficial and deep retinal capillary density were measured in moderate and high myopia patients who underwent ICL implantation between pre-surgery and post-surgery. The OCTA provided the macular perfusion of a 6 mm × 6 mm area, we calculated the microvascular density in each region through the box-counting method after correcting for magnification. Our data showed that ICL implantation surgery would not leave adverse effects on the retinal capillary network.

Moreover, clinical evidence suggests that eye surgery would cause the alteration of retinal microcirculation (Alnawaiseh et al., 2018; Kim et al., 2018; Liu J et al., 2021). Pilotto et al. (2019) found that the perfusion of the retinal microvascular plexus in the deeper layers of the macula increased after uncomplicated cataract surgery, which may be related to the early postoperative local inflammatory response. Analogously, Chen et al. (2017) used a retinal oximeter to detect retinal oxygen desaturation due to retina oxygen deficiency after ICL implantation. ICL implantation surgery as a safe and effective refractive surgery plays an important role in correcting moderate and high myopia. However, due to the unusual anatomy and physiology of the retina in high myopia eyes, it deserves our attention for any microcirculation abnormality inherent to ICL implantation surgery. Using OCTA, ophthalmologists can easily assess patients' retinal microvascular health and disease, which might be beneficial for pre-operative evaluation of ICL implantation surgery and the detection of postoperative complications.

There were a few limitations to this study. Since the levels of microvascular density in the retinal capillary plexuses after ICL surgery detected by OCTA were stable in this study, the sample size could not be calculated. Although we have included as many participants as possible in this study, the number of patients was relatively small and the follow-up period was only 3 months. In bigger populations and during longer follow-up periods, retinal microvascular change may be seen. Besides, because most of the patients who underwent ICL implantation were young people, this study did not include children and the elderly, whose preoperative retinal microcirculation is slightly different (Leng et al., 2018; Golebiewska et al., 2019), and might respond differently to ICL implantation surgery. Moreover, the OCTA scan area

used in this study is 6 mm × 6 mm around the macula. Although it has a wider scan range, it has not achieved the best presentation on retinal microvasculature.

In conclusion, this study demonstrates that ICL implantation is an effective treatment for both moderate and high myopia in young patients, with excellent safety, predictability, and stability. Simultaneously, using OCTA, this research provides evidence that ICL implantation has no adverse effects on retinal microvascular. Further larger sample sizes and longer-term studies are warranted to confirm the conclusions presented herein.

Data availability statement

The raw data supporting the conclusion of this article will be made available by the authors, without undue reservation.

Ethics statement

The studies involving human participants were reviewed and approved by Ethics Committee of Peking University Third Hospital. The patients/participants provided their written informed consent to participate in this study.

Author contributions

The authors confirm contribution to the paper as follows: Study conception and design: CT, YZ, and HQ; data collection: CT, TS, and YL; analysis and interpretation of results: RL and JX; original draft preparation: CT; review and editing: YZ, HQ, and ZS. All authors reviewed the results and approved the final version of the manuscript.

Funding

The study was supported by National Natural Science Foundation of China (82171022, 81974128) and The Capital Health Research and Development of Special (2020-2-4097).

Acknowledgments

We thank all participants for their contribution to the present study.

Conflict of interest

The authors declare that the research was conducted in the absence of any commercial or financial relationships that could be construed as a potential conflict of interest.

Publisher's note

All claims expressed in this article are solely those of the authors and do not necessarily represent those of their affiliated

organizations, or those of the publisher, the editors and the reviewers. Any product that may be evaluated in this article, or

claim that may be made by its manufacturer, is not guaranteed or endorsed by the publisher.

References

- Ab Hamid, F., Che Azemin, M. Z., Salam, A., Aminuddin, A., Mohd Daud, N., and Zahari, I. (2016). Retinal vasculature fractal dimension measures vessel density. *Curr. Eye Res.* 41 (6), 823–831. doi:10.3109/02713683.2015.1056375
- Al-Sheikh, M., Phasukkijwatana, N., Dolz-Marco, R., Rahimi, M., Iafe, N. A., Freund, K. B., et al. (2017). Quantitative OCT angiography of the retinal microvasculature and the choriocapillaris in myopic eyes. *Invest. Ophthalmol. Vis. Sci.* 58 (4), 2063–2069. doi:10.1167/iovs.16-21289
- Alnawaiseh, M., Müller, V., Lahme, L., Merté, R. L., and Eter, N. (2018). Changes in flow density measured using optical coherence tomography angiography after iStent insertion in combination with phacoemulsification in patients with open-angle glaucoma. *J. Ophthalmol.* 2018, 2890357. doi:10.1155/2018/2890357
- Assetto, V., Benedetti, S., and Pesando, P. (1996). Collamer intraocular contact lens to correct high myopia. *J. Cataract. Refract. Surg.* 22 (5), 551–556. doi:10.1016/s0886-3350(96)80007-1
- Bennett, A. G., Rudnicka, A. R., and Edgar, D. F. (1994). Improvements on Littmann's method of determining the size of retinal features by fundus photography. *Graefes Arch. Clin. Exp. Ophthalmol.* 232 (6), 361–367. doi:10.1007/BF00175988
- Chen, P., Cai, X., Xu, L., Zhang, J., Yang, Y., Gao, Q., et al. (2017). Assessing oxygen saturation in retinal vessels in high myopia patients pre- and post-implantable collamer lens implantation surgery. *Acta Ophthalmol.* 95 (6), 576–582. doi:10.1111/aos.13368
- de Carlo, T. E., Romano, A., Waheed, N. K., and Duker, J. S. (2015). A review of optical coherence tomography angiography (OCTA). *Int. J. Retina Vitre.* 1, 5. doi:10.1186/s40942-015-0005-8
- Dougherty, P. J., and Priver, T. (2017). Refractive outcomes and safety of the implantable collamer lens in young low-to-moderate myopes. *Clin. Ophthalmol.* 11, 273–277. doi:10.2147/oph.S120427
- Foster, P. J., and Jiang, Y. (2014). Epidemiology of myopia. *Eye (Lond)* 28 (2), 202–208. doi:10.1038/eye.2013.280
- Gao, S. S., Jia, Y., Zhang, M., Su, J. P., Liu, G., Hwang, T. S., et al. (2016). Optical coherence tomography angiography. *Invest. Ophthalmol. Vis. Sci.* 57 (9), Oct27–36. doi:10.1167/iovs.15-19043
- Golebiewska, J., Biala-Gosek, K., Czeszyk, A., and Hautz, W. (2019). Optical coherence tomography angiography of superficial retinal vessel density and foveal avascular zone in myopic children. *PLoS One* 14 (7), e0219785. doi:10.1371/journal.pone.0219785
- Grudzińska, E., and Modrzejewska, M. (2018). Modern diagnostic techniques for the assessment of ocular blood flow in myopia: Current state of knowledge. *J. Ophthalmol.* 2018, 4694789. doi:10.1155/2018/4694789
- Guo, Y., Sung, M. S., and Park, S. W. (2019). Assessment of superficial retinal microvascular density in healthy myopia. *Int. Ophthalmol.* 39 (8), 1861–1870. doi:10.1007/s10792-018-1014-z
- Hirano, Y., Suzuki, N., Tomiyasu, T., Kurobe, R., Yasuda, Y., Esaki, Y., et al. (2021). Multimodal imaging of microvascular abnormalities in retinal vein occlusion. *J. Clin. Med.* 10 (3), 405. doi:10.3390/jcm10030405
- Holden, B. A., Fricke, T. R., Wilson, D. A., Jong, M., Naidoo, K. S., Sankaridurg, P., et al. (2016). Global prevalence of myopia and high myopia and temporal trends from 2000 through 2050. *Ophthalmology* 123 (5), 1036–1042. doi:10.1016/j.ophtha.2016.01.006
- Hopf, S., and Pfeiffer, N. (2017). Epidemiology of myopia. *Ophthalmologie* 114 (1), 20–23. doi:10.1007/s00347-016-0361-2
- Jiang, Y., Lou, S., Li, Y., Chen, Y., and Lu, T. C. (2021). High myopia and macular vascular density: An optical coherence tomography angiography study. *BMC Ophthalmol.* 21 (1), 407. doi:10.1186/s12886-021-02156-2
- Kamiya, K., Igarashi, A., Shimizu, K., Matsumura, K., and Komatsu, M. (2012). Visual performance after posterior chamber phakic intraocular lens implantation and wavefront-guided laser *in situ* keratomileusis for low to moderate myopia. *Am. J. Ophthalmol.* 153 (6), 1178–1186. doi:10.1016/j.ajo.2011.12.005
- Kamiya, K., Shimizu, K., Igarashi, A., Kitazawa, Y., Kojima, T., Nakamura, T., et al. (2018). Posterior chamber phakic intraocular lens implantation: Comparative, multicentre study in 351 eyes with low-to-moderate or high myopia. *Br. J. Ophthalmol.* 102 (2), 177–181. doi:10.1136/bjophthalmol-2017-310164
- Kim, J. A., Kim, T. W., Lee, E. J., Girard, M. J. A., and Mari, J. M. (2018). Microvascular changes in peripapillary and optic nerve head tissues after trabeculectomy in primary open-angle glaucoma. *Invest. Ophthalmol. Vis. Sci.* 59 (11), 4614–4621. doi:10.1167/iovs.18-25038
- Li, M., Yang, Y., Jiang, H., Gregori, G., Roisman, L., Zheng, F., et al. (2017). Retinal microvascular network and microcirculation assessments in high myopia. *Am. J. Ophthalmol.* 174, 56–67. doi:10.1016/j.ajo.2016.10.018
- Leng, Y., Tam, E. K., Falavarjani, K. G., and Tsui, I. (2018). Effect of age and myopia on retinal microvasculature. *Ophthalmic Surg. Lasers Imaging Retina* 49 (12), 925–931. doi:10.3928/23258160-20181203-03
- Li, Y., Miara, H., Ouyang, P., and Jiang, B. (2018). The comparison of regional RNFL and fundus vasculature by OCTA in Chinese myopia population. *J. Ophthalmol.* 2018, 3490962. doi:10.1155/2018/3490962
- Liu, J., Liu, Q., Yu, H., Xia, Y., Zhang, H., Geng, C., et al. (2021). Microvascular changes in macular area after phacoemulsification and its influencing factors assessed by optical coherence tomography angiography. *Ther. Clin. Risk Manag.* 17, 405–414. doi:10.2147/tcrm.S309679
- Liu, M., Wang, P., Hu, X., Zhu, C., Yuan, Y., and Ke, B. (2021). Myopia-related stepwise and quadrant retinal microvascular alteration and its correlation with axial length. *Eye (Lond)* 35 (8), 2196–2205. doi:10.1038/s41433-020-01225-y
- Makita, S., Hong, Y., Yamanari, M., Yatagai, T., and Yasuno, Y. (2006). Optical coherence angiography. *Opt. Express* 14 (17), 7821–7840. doi:10.1364/oe.14.007821
- Milani, P., Montesano, G., Rossetti, L., Bergamini, F., and Pece, A. (2018). Vessel density, retinal thickness, and choriocapillaris vascular flow in myopic eyes on OCT angiography. *Graefes Arch. Clin. Exp. Ophthalmol.* 256 (8), 1419–1427. doi:10.1007/s00417-018-4012-y
- Morgan, I. G., French, A. N., Ashby, R. S., Guo, X., Ding, X., He, M., et al. (2018). The epidemics of myopia: Aetiology and prevention. *Prog. Retin Eye Res.* 62, 134–149. doi:10.1016/j.preteyeres.2017.09.004
- Pilotto, E., Leonardi, F., Stefanon, G., Longhini, E., Torresin, T., Deganello, D., et al. (2019). Early retinal and choroidal OCT and OCT angiography signs of inflammation after uncomplicated cataract surgery. *Br. J. Ophthalmol.* 103 (7), 1001–1007. doi:10.1136/bjophthalmol-2018-312461
- Rao, H. L., Pradhan, Z. S., Suh, M. H., Moghimi, S., Mansouri, K., and Weinreb, R. N. (2020). Optical coherence tomography angiography in glaucoma. *J. Glaucoma* 29 (4), 312–321. doi:10.1097/ijg.0000000000001463
- Sanders, D. R., Doney, K., and Poco, M. (2004). United States food and drug administration clinical trial of the implantable collamer lens (ICL) for moderate to high myopia: Three-year follow-up. *Ophthalmology* 111 (9), 1683–1692. doi:10.1016/j.ophtha.2004.03.026
- Sun, Z., Yang, D., Tang, Z., Ng, D. S., and Cheung, C. Y. (2021). Optical coherence tomography angiography in diabetic retinopathy: An updated review. *Eye (Lond)* 35 (1), 149–161. doi:10.1038/s41433-020-01233-y
- Wang, X., and Zhou, X. (2016). Update on treating high myopia with implantable collamer lenses. *Asia Pac J. Ophthalmol. (Phila)* 5 (6), 445–449. doi:10.1097/apo.0000000000000235
- Wu, P. C., Huang, H. M., Yu, H. J., Fang, P. C., and Chen, C. T. (2016). Epidemiology of myopia. *Asia Pac J. Ophthalmol. (Phila)* 5 (6), 386–393. doi:10.1097/apo.0000000000000236
- Wylegala, A. (2018). Principles of OCTA and applications in clinical neurology. *Curr. Neurol. Neurosci. Rep.* 18 (12), 96. doi:10.1007/s11910-018-0911-x
- Yang, Y., Wang, J., Jiang, H., Yang, X., Feng, L., Hu, L., et al. (2016). Retinal microvasculature alteration in high myopia. *Invest. Ophthalmol. Vis. Sci.* 57 (14), 6020–6030. doi:10.1167/iovs.16-19542
- Zhang, M., Hwang, T. S., Campbell, J. P., Bailey, S. T., Wilson, D. J., Huang, D., et al. (2016). Projection-resolved optical coherence tomographic angiography. *Biomed. Opt. Express* 7 (3), 816–828. doi:10.1364/boe.7.000816
- Zhang, Q., Lee, C. S., Chao, J., Chen, C. L., Zhang, T., Sharma, U., et al. (2016). Wide-field optical coherence tomography based microangiography for retinal imaging. *Sci. Rep.* 6, 22017. doi:10.1038/srep22017



OPEN ACCESS

EDITED BY
Yanwu Xu,
Baidu (China), China

REVIEWED BY
Kai Jin,
Zhejiang University, China
Huasheng Yang,
Sun Yat-sen University, China
Ming Lin,
Shanghai Jiao Tong University, China

*CORRESPONDENCE
Ruili Wei,
✉ ruliwei@smmu.edu.cn

†These authors have contributed equally to
this work and share first authorship

SPECIALTY SECTION
This article was submitted to Molecular
and Cellular Pathology,
a section of the journal
Frontiers in Cell and Developmental
Biology

RECEIVED 15 December 2022
ACCEPTED 12 January 2023
PUBLISHED 24 January 2023

CITATION
Diao J, Chen X, Shen Y, Li J, Chen Y, He L,
Chen S, Mou P, Ma X and Wei R (2023),
Research progress and application of
artificial intelligence in thyroid
associated ophthalmopathy.
Front. Cell Dev. Biol. 11:1124775.
doi: 10.3389/fcell.2023.1124775

COPYRIGHT
© 2023 Diao, Chen, Shen, Li, Chen, He,
Chen, Mou, Ma and Wei. This is an open-
access article distributed under the terms
of the [Creative Commons Attribution
License \(CC BY\)](https://creativecommons.org/licenses/by/4.0/). The use, distribution or
reproduction in other forums is permitted,
provided the original author(s) and the
copyright owner(s) are credited and that
the original publication in this journal is
cited, in accordance with accepted
academic practice. No use, distribution or
reproduction is permitted which does not
comply with these terms.

Research progress and application of artificial intelligence in thyroid associated ophthalmopathy

Jiale Diao[†], Xinxin Chen[†], Ya Shen[†], Jian Li, Yuqing Chen, Linfeng He, Sainan Chen, Pei Mou, Xiaoye Ma and Ruili Wei*

Department of Ophthalmology, Changzheng Hospital of Naval Medicine University, Shanghai, China

Thyroid-associated ophthalmopathy (TAO) is a complicated orbitopathy related to dysthyroid, which severely destroys the facial appearance and life quality without medical interference. The diagnosis and management of thyroid-associated ophthalmopathy are extremely intricate, as the number of professional ophthalmologists is limited and inadequate compared with the number of patients. Nowadays, medical applications based on artificial intelligence (AI) algorithms have been developed, which have proved effective in screening many chronic eye diseases. The advanced characteristics of automated artificial intelligence devices, such as rapidity, portability, and multi-platform compatibility, have led to significant progress in the early diagnosis and elaborate evaluation of these diseases in clinic. This study aimed to provide an overview of recent artificial intelligence applications in clinical diagnosis, activity and severity grading, and prediction of therapeutic outcomes in thyroid-associated ophthalmopathy. It also discussed the current challenges and future prospects of the development of artificial intelligence applications in treating thyroid-associated ophthalmopathy.

KEYWORDS

thyroid-associated ophthalmopathy, artificial intelligence, deep learning, automated diagnosis, facial images

Introduction

Artificial intelligence (AI) has gradually become a part of each aspect of our lives, especially medicine, with the rapid development of computer technologies and smart devices. This term did not emerge recently but was first proposed at a conference in 1956 (Russell and Norvig, 2010). The early achievement of AI applications in medicine was the automated recognition of electrocardiograms, which was based on programmed medical knowledge (Kundu et al., 2000). Machine learning (ML), a subfield of computer science, endowed AI with the ability to independently discern patterns from data. The training set, containing several inputs and relevant outputs, is critical for ML methods to analyze the underlying patterns, which help obtain correct outputs from new inputs (Deo, 2015). Further, deep learning (DL) has given a major boost to the AI renaissance in recent decades. DL methods generally build an artificial neural network with many layers to analyze colossal datasets, such as numerous medical images (LeCun et al., 2015; Schmidhuber, 2015).

The application of integrated AI-ML-DL algorithms, combined with advanced medical imaging and data transmission systems, has grown rapidly in the medical field, such as ophthalmic healthcare (Balyen and Peto, 2019). For instance, diabetic retinopathy (DR) can be detected by screening the retina using fundus photography and optical coherence tomography as a representative chronic ocular disease. It was found that multiple AI applications in retinal images had significant benefits in the early detection of DR (Gulshan et al., 2016; Ting et al.,

2017; Tufail et al., 2017). Recent studies also revealed that the detection of glaucoma could be promoted using AI-ML-DL algorithms with high accuracy, sensitivity, and specificity (Li et al., 2018a; Devalla et al., 2018).

Thyroid-associated ophthalmopathy (TAO), an intricate autoimmune disease, is associated with the highest incidence of the orbital disorder in adults, affecting approximately 2.9 men and 16 women per hundred thousand people every year (Bartley et al., 1995; Wiersinga and Bartalena, 2002). Severe cases tend to develop in male and older patients, accompanied by disfiguring proptosis and optic neuropathy (Bahn, 2010). The clinical manifestations of TAO include chemosis, eyelid retraction, exophthalmos, periorbital pain, and strabismus. Besides, the course of the disease is described as Rundle's curve, which is composed of a one- to 3-year active phase and a subsequent chronic stable phase (Khong et al., 2016). This characteristic of TAO can be graded according to the clinical activity score and the severity grading identified by European Group on Graves' orbitopathy (EUGOGO) (Bartalena et al., 2021). Variations of patterns in patients make TAO diagnosis, evaluation, and management challenging, which immensely depend on the profession and experience of well-trained ophthalmologists. AI applications may act as a supporting role in TAO clinical practice.

This review summarized the research progress and prospective application of AI in TAO diagnosis and management. The available studies focused on the identification of characteristic signs, disease grades, and dysthyroid optic neuropathy (DON); prediction of TAO progression; therapeutic response to glucocorticoids (GCs) and decompression surgery; and even protocol formulation of orbital radiotherapy. Given the prosperity of this "Big Data" era, we believe that this review could comprehend the current achievements and accelerate the promising AI applications in clinical practice, which may help ophthalmologists and endocrinologists with limited experience.

Application of AI algorithms in detecting the signs and symptoms of TAO

As mentioned earlier, TAO generally starts with an active course. In this stage, patients suffer from ocular pain, redness and swelling of the conjunctiva and eyelids, and, most importantly, progressive proptosis and vision loss (Mourits et al., 1989). Early intervention, such as GC pulse therapy, can lead to premature termination of the active course and the start of a stable phase (Kauppinen-Mäkelin et al., 2002). Therefore, the early and accurate diagnosis of TAO can benefit the following management and prognosis. However, a large proportion of patients with TAO do not approach the department of ophthalmology, but the department of endocrinology, at the first visit because of thyroid dysfunction. Also, a few symptoms and signs of TAO are insidious enough to be missed during the examination. Thus, an automated diagnostic system assisted by AI algorithms can significantly increase the clinical efficiency of TAO diagnosis.

Grus et al. (1998) first tested an artificial neural network (ANN) in TAO. This ANN, a kind of probabilistic neural network, contained input, pattern, summation and output layers, which could recognize the possible class of samples after training, thus possessing the diagnostic value. The sera samples were collected from patients with or without TAO ($n = 16:11$), Western blot analysis was performed, and densitometric data were collected. After training,

96.3% of test samples were correctly classified using an ANN, exceeding the multivariate statistical technique with 85% accuracy. This initial research enlightened the diagnostic potential provided by AI methods in TAO, though the autoantibodies detected in this study were not useful in TAO diagnosis. A few years later, Salvi et al. focused on the clinical signs and specialist examination of patients with TAO in two analogical studies (Salvi et al., 2002a; Salvi et al., 2002b). The samples were both divided into two groups based on disease progression. The ANN applied in two studies was a back-propagation model used for the classification and progression prediction of TAO, which was constructed with 13 input variables derived from ophthalmic examinations. The accuracy of classification and progression prediction was 78.3%–86.2% and 67%–69.2%, respectively. As to the fundamentals of AI application in TAO diagnosis, these DL methods still need manual parameters measured by ophthalmologists or physicians.

After 2 decades of technological updating, advanced face recognition and automated image processing systems have increased the possibility for AI application in TAO. An intelligent diagnostic system for TAO was invented using multiple task-specific models based on facial images (Huang et al., 2022). Briefly, an entire facial image was analyzed and cropped into the eye part using Module I. Ocular dyskinesia and special signs of TAO were subsequently detected using Modules II and III. This study recruited 21,840 images from 1560 patients, of which 20% were used as the test set. The accuracy of eye location and cornea and sclera segmentation, conducted using Modules I and II, was 0.98, 0.93, and 0.87, respectively. The area under the receiver-operating characteristic curve (AUROC), sensitivity, and specificity of detecting signs were 0.93, 87%, and 88% for eyelid retraction; 0.90, 79%, and 86% for eyelid edema; 0.94, 89%, and 90% for eyelid congestion; 0.91, 83%, and 85% for conjunctival congestion; and 0.91, 85%, and 79% for ocular dyskinesia, respectively. Besides, the AUROC of DL networks (ResNet-50, ResNet-101, and InceptionV3) was 0.91, 0.92, and 0.89, respectively. Compared with previous models, this automated diagnostic system detected TAO signs highly accurately just with facial images. Besides, this system could also be loaded into mobile devices, thus showing the potential to help patients in areas lacking veteran ophthalmologists and medical resources.

Karlin et al. (2022) developed another AI platform based on a DL model to identify TAO using ocular photographs. The training set contained 1944 facial images, and the testing depended on additional 344 photographs. In line with the testing results, the accuracy, specificity, precision, recall, and F1 score of the proposed platform reached 89.2%, 86.9%, 79.7%, 93.4%, and 86.0%, respectively. The specific signs of TAO were not separated but integrated into a component model, thus generating heatmaps to present the pathological regions in facial images. This DL model was also compared with a cohort of ophthalmologists in the diagnosis of TAO. Interestingly, compared with the expert cohort, the DL ensemble model had higher accuracy (86% vs. 78%) and recall (89% vs. 58%), whereas the specificity was lower (84% vs. 90%).

In clinical practice, doctors usually spend a lot of time confirming TAO diagnosis at their first ophthalmologic visits. Even with an expert with abundant experience in orbital diseases, a TAO diagnosis can only be confirmed by the comprehensive assessment of the chief complaints of patients, ocular signs, medical history of dysthyroid, and

imageological examination (Dolman, 2012). To a certain extent, the aforementioned studies indicated that the DL classifier using external ocular photographs might substitute the specialists to provide the initial diagnosis for patients with TAO and even accurately grade the activity and severity.

Application of AI algorithms in the orbital imaging of TAO

Orbital imaging has provided substantial support since the 1980s in the clinical evaluation of TAO (Hosten et al., 1989). Computed tomography (CT) scanning and magnetic resonance imaging (MRI) hold the same importance with their own merits. CT can clearly present the degree of extraocular muscle enlargement and the condition of the optic nerve in the orbital apex. The delineated anatomy of the orbital wall and periorbital structures such as adjacent sinuses are essential for decompression surgery design (Cubuk et al., 2018). The benefits of MRI rely on its capacity for better resolution between muscles and orbital fat, which can help identify the specific pattern of TAO without radiation (Higashiyama et al., 2017). These characteristics have promoted the widespread use of CT and MRI in TAO, and abundant image data have become the hotbed of AI algorithms.

The research team of Shanghai Jiao Tong University explored the diagnostic value of two AI models for TAO using CT and MRI images. Lin et al. (2021) constructed DL algorithms into networks A and B, which inherited from the Visual Geometry Group (VGG) network and the Residual Neural Network (ResNet). By recruiting 160 MRI images, the accuracy, specificity, and sensitivity of network A were 0.863 ± 0.055 , 0.896 ± 0.042 , and 0.750 ± 0.136 , respectively, for differentiating between active and inactive statuses of patients with TAO. After optimizing, the sensitivity of network B improved (0.821 ± 0.021), and the AUC of both networks was 0.922. In another study, 1,435 CT scans were used for a TAO screening 3D-ResNet model training, validation, and testing (Song et al., 2021). The results demonstrated that the AUC, accuracy, sensitivity, and specificity of this AI model were 0.919, 0.868, 0.878, and 0.865, respectively. Besides, the performance of this screening algorithm was also satisfactory in the diagnostic test.

Hanai et al. (2022) focused on extraocular muscle (EOM) enlargement in patients with TAO. The proposed diagnostic system was constructed based on deep neural networks including ResNet-50 and VGG-16. A total of 371 participants were recruited in this study with their coronal scans, including about 60% for training, 20% for validation, and the remaining 20% for test data. The results showed that the AUC, sensitivity, and specificity of this model for detecting EOM enlargement were 0.946, 92.5%, and 88.6%, respectively, indicating that the thickness of EOM could be detected using AI algorithms with high accuracy and speed in TAO.

Lee et al. (2022) developed a convolutional neural network-based model to assess the severity of TAO by analyzing the axial, coronal, and sagittal planes of CT images. A total of 288 CT images comprised mild TAO, moderate-to-severe TAO, and normal controls, which were divided into four comparable groups. Compared with controls, the diagnostic AUC of this model was 0.979 ± 0.020 for moderate-to-severe TAO, 0.895 ± 0.052 for mild TAO, and 0.905 ± 0.029 for three

comparisons. The performance of the proposed model was also better than that of VGG-16, GoogleNet, and ResNet-50, and even of three oculo-plastic specialists.

DON is significant with respect to the vision-threatening condition in TAO (Saeed et al., 2018). The optic nerve is suppressed by pathologically thickened tissues in the orbital apex, leading to several symptoms such as blurred vision, decreased color vision, and defect of field vision (Victores and Takashima, 2016). Early detection and intervention improve the prognosis. A hybrid model based on a deep convolutional neural network was proposed to predict DON using CT scans (Wu et al., 2022). In this model, a specific module was used to preprocess the image and extract the meaningful features for DON pathologies. The samples were divided into 87 healthy controls and 91 patients with TAO, including 42 patients with DON. After training and testing, the accuracy, specificity, sensitivity, and F1-score were 96%, 99.5%, 94%, and 96.4%, respectively. In this study, a DL model displayed significant advantages in predicting DON in patients with TAO.

The orbital CT scans and MRI images are the most common images examined in patients with TAO, as they can be not only evaluated by radiologists and ophthalmologists but also preprocessed into available data and then submitted to AI algorithms for further screening or predicting. The diagnosis, activity and severity grading, and DON prediction all have important clinical implications for patients with TAO patients, and AI algorithms, especially DL models, can provide satisfactory assistance to optimize this complex process in the future. The summarization of aforementioned studies in diagnosis and grading of TAO is presented in Table 1.

Application of AI algorithms in treating TAO

GC pulse therapy

In accordance with the 2021 EUGOGO guidelines (Bartalena et al., 2021), intravenous GCs combined with mycophenolate sodium were nominated as the first-line treatment for moderate-to-severe and active TAO. The pulse therapy of GCs has been used in TAO management for decades, and many studies have demonstrated substantial benefits. Still, about 20%–30% of patients in clinical trials were unresponsive to GC treatment, even with unbearable adverse effects (Vannucchi et al., 2014; Zhu et al., 2014). The general method in a clinic is closely monitoring the initial outcomes of GC treatment, which determine the subsequent remedies, to avoid the unworthy risk of overdosed GCs. Thus, a practical method for response prediction before GC therapy is required.

Coronal T₂-weighted MRI images with fat suppression can clearly show the cross-sectional morphology and radiomics features of EOMs. Hu et al. (2022) developed three ML-based models to analyze the radiomics data of patients with TAO. In this retrospective study, 110 samples were selected, and GC-responsive ($n = 62$) and unresponsive ($n = 48$) cases were equally split into training and validation sets. A semi-quantitative imaging model was also built by two experienced doctors, in which the absolute signal intensities of

TABLE 1 AI algorithms in diagnosis and grading of TAO.

Authors (Year)	Task	Input data type	Samples dataset	AI model	Accuracy	AUC
Grus et al. (1998)	Diagnostic classification of TAO	IgG autoantibody repertoires	Sera TAO: 16, controls: 11	The probabilistic neural network	96.3%	-
Salvi et al. (2002a)	Classification and progression prediction of TAO	13 clinical eye signs	246 patients with absent or inactive TAO and 152 patients with active TAO	A back-propagation neural model	Classification: 86.2%, progression prediction: 67%	-
Salvi et al. (2002b)	Classification and progression prediction of TAO	13 clinical eye signs and age, gender, smoking and follow-up interval	129 patients with absent or inactive TAO and 113 patients with active TAO, 103 normal subjects	A back-propagation neural model	Classification: 78.3%, progression prediction: 69.2%	-
Huang et al. (2022)	Diagnostic system of TAO and its special signs	Facial images	21,840 facial images from 1560 patients (3120 eyes)	ResNet-50, ResNet-101 and InceptionV3	Eye location: 0.98, cornea: 0.93, sclera: 0.87	ResNet-50: 0.91, ResNet-101: 0.92, InceptionV3: 0.89
Karlin et al. (2022)	Detecting TAO	Single front facing photograph	1944 photographs for training and 344 images for testing	ResNet-18	89.2%, 86% (compared to expert cohort)	-
Lin et al. (2021)	Detecting the active and inactive phase of TAO	Orbital MRI images	160 images from 108 patients	Deep convolutional neural network (DCNN)	0.863	0.922
Song et al. (2021)	Screening TAO	Orbital CT images	1,435 CT scans from 193 patients and 715 healthy subjects	3D-ResNet	0.868	0.919
Hanai et al. (2022)	Detection of EOM enlargement in TAO	Orbital CT images	371 participants (60% for training, 20% for validation and 20% for testing)	ResNet-50 and VGG-16	-	0.946
Lee et al. (2022)	Diagnosis and severity evaluation of TAO	Orbital CT images	288 CT scans from 200 patients and 100 controls	CNN	Mild TAO: 0.826, moderate-to-severe TAO: 0.930, three comparisons: 0.842	0.895 0.979 0.905
Wu et al. (2022)	Prediction of dysthyroid optic neuropathy (DON) in TAO	Orbital CT images	178 participants (42 DON, 49 TAO without DON, 87 controls)	DCNN	96%	-

EOM, extraocular muscle; DCNN, deep convolutional neural network; DON, dysthyroid optic neuropathy.

EOMs were manually measured and normalized to values of ipsilateral temporal muscle. The AUCs of the three ML-based models in two sets (0.968 and 0.916; 0.933 and 0.857; 0.919 and 0.855) were all better than the performance of the semi-quantitative method (0.805). Additionally, including the disease duration of TAO into AI algorithms enhanced the diagnostic ability in their validation (AUC: 0.952 vs. 0.916), indicating the advantage of the AI model in predicting the response of patients with TAO to GCs.

Besides the use of MRI, a prospective and observational protocol was proposed by Wang et al. (2021) for developing a new prediction model. A total of 278 untreated patients with moderate-to-severe and active TAO will be recruited into this trial based on the events per variable method and previous models. The clinical data and AI-related parameters will be collected from these volunteers before their standard 12-week GC pulse therapy. After treatment, the patients will be divided into GC-responsive/unresponsive groups based on their outcomes of therapy. The facial morphological changes and traditional clinical data will be used to develop a new AI model, which can recognize the best variables for GC-response prediction. This study is an ongoing project, and the findings can guide on the individualized GC treatment for TAO.

Orbital radiotherapy

Orbital radiotherapy in alliance with GCs was recommended as the second-line treatment (Bartalena et al., 2021). The therapeutic effect of regional irradiation, which seems to have a mutual promoting effect with GCs (Bartalena et al., 1983; Oeverhaus et al., 2017), was demonstrated by several randomized controlled trials in TAO (Prummel et al., 2004). Conventionally, a low dose of 20 Gy was given for about 2 weeks (Tanda and Bartalena, 2012). Although adverse events were relatively rare in orbital radiotherapy (Marcocci et al., 2003), the irradiation target still needs to be precisely delineated to avoid possible damage to organs at risk (OARs).

Jiang et al. (2021) developed a DL model based on a fully convolutional network (FCN) to realize the auto-segmentation of the clinical target volume (CTV) for patients with TAO. Briefly, CT images from 121 patients with TAO undergoing radiotherapy were collected for training and testing. The outcomes were set as the Dice similarity coefficient (DSC) and Hausdorff distance (HD). Because of two orbits, Jiang et al. suggested treating the two-part CTV as one target, which was demonstrated to have higher HD values than the separate method (8.23 ± 2.80 vs. 9.03 ± 2.78). The dosimetric comparison showed that both algorithms based on the FCN model

TABLE 2 AI algorithms in treatment of TAO.

Authors (Year)	Task	Input data type	Samples dataset	AI model	Accuracy	AUC
Hu et al. (2022)	Prediction of therapeutic response to GCs in TAO	Orbital T ₂ -weighted MRI images	Training (n = 78) and validation (n = 32) cohorts	LR DT SVM	-	0.968, 0.916 0.933, 0.857 0.919, 0.855
Wang et al. (2021)	Developing a prediction model for identifying intravenous GCs response	Traditional clinical information and PPVs output by four AI models	278 untreated patients with moderate-to-severe and active TAO	Ongoing study	Ongoing study	Ongoing study
Jiang et al. (2021)	Auto-segmentation of CTV for TAO patients	Orbital CT images	121 patients undergoing radiotherapy	FCN	-	-
Jiang et al. (2020)	Improving the auto-segmentation accuracy of CTV in TAO	Orbital CT images	120 cases with moderate-to-severe TAO	Stacked neural network	-	-
Zhang et al. (2021)	Detecting positioning error in TAO radiotherapy	Radiomics analysis from EPID	Treatment plans of 40 patients with TAO	SVM KNN XGBoost	-	Positioning errors: all above 0.90; direction classification: 0.76, 0.91, 0.80
Dai et al. (2021)	Identifying positioning error in TAO radiotherapy	Radiomics data from EPID transmission maps	40 TAO patient radiotherapy plans	SVM KNN XGBoost CNN	ML 1: 0.532-0.889 ML 2: 0.491-0.949 ML 3: 0.671-0.931 CNN: 0.689-0.949	ML 1: 0.778-0.945 ML 2: 0.682-0.989 ML 3: 0.779-0.990 CNN: 0.832-0.992
Liu et al. (2022)	Position error classification in radiotherapy of TAO	EPID fluence maps	2240 EPID fluence maps	DNN	0.722	-

LR, logistic regression; DT, decision tree; SVM, support vector machine; PPV, positive predictive values; FCN, fully convolutional network; EPID, electronic portal imaging device; KNN, k-nearest neighbors.

performed better than manual segmentation. In another study (Jiang et al., 2020), a stacked neural network using adjacent anatomy for target location was proposed to improve the accuracy of CTV. Compared with the FCN model, this stacked network increased the bilateral DSC by 1.7% and 3.4%, but reduced the HD value by 0.6.

Position errors caused by manual or mechanical misconduct are probable in the actual delivery, except for planned contours before irradiation (Ezzell et al., 2003). The electronic portal imaging device (EPID) dosimetry was established for real-time supervision. Zhang et al. (2021) conducted an interesting study for integrating EPID measurements and AI algorithms. First, the irradiation plans were duplicated from 40 patients with TAO to a solid head phantom, and position errors combined with varying translation errors in different directions were added to the protocols. The radiomics of EPID measurements were extracted and analyzed using 3 ML models. Their AUC values were all above 0.90 for position error detection and relatively lower (0.76, 0.80, and 0.91) for direction identification. The research team classified all the position and direction errors into three types (Dai et al., 2021). The aforementioned ML models plus a CNN model were also applied to recognize these errors using radiomics data from EPID transmission maps as inputs. The classification accuracies of the CNN model performed well in this competition. Additionally, Liu et al. (2022) developed a deep neural network (DNN) algorithm with structural similarity difference and orientation-based loss, which could provide more features and information from EPID images. A total of 2240 EPID fluence maps were enrolled and subjected to the DNN model for training and testing. The proposed model outperformed with a better prediction accuracy (0.722) than other ML models and previous study results.

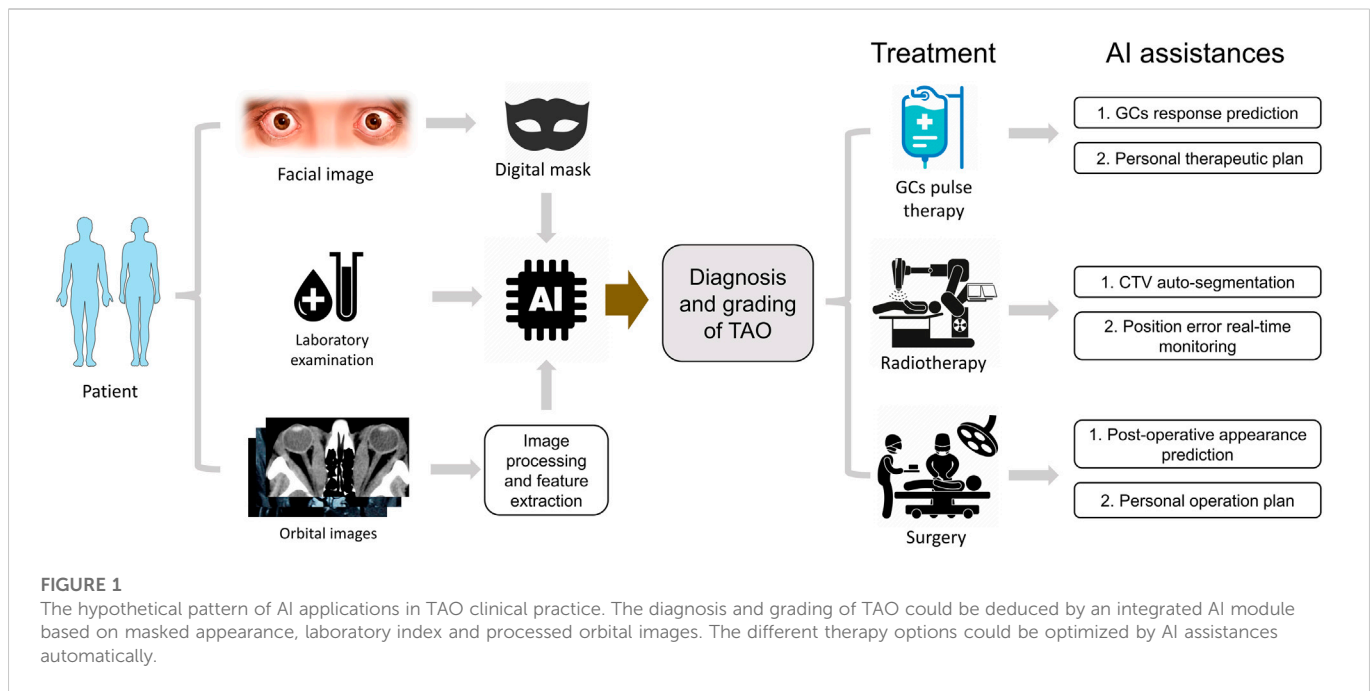
The OARs contain lenses, optic nerves, retina, and lacrimal glands during orbital radiotherapy. AI-based algorithms can optimize the

procedure of restricted irradiation and reduce the potential risks, which may be beneficial for TAO treatment. Other orbital diseases requiring radiotherapy, such as mucosa-associated lymphoid tissue lymphoma and optic nerve sheath meningioma, may also benefit from AI applications.

Orbital decompression surgery

Orbital decompression surgery was introduced to solve the conflict between excessive orbital contents and relatively inadequate orbital volumes by removing parts of the orbital bony wall and fat (Roncovic and Jackson, 1989). This surgery would serve as a salvage operation only for uncontrollable exposure keratopathy or DON with unresponsive GCs (Bartalena et al., 2021). It performs during a later course of TAO management, when patients step into the inactive phase with stable disfigurements (Limone et al., 2021).

Yoo et al. (2020) introduced a generative adversarial network (GAN) model to predict postoperative appearance before decompression surgery. A GAN could automatically synthesize medical images by a generator module, which learns to map samples from a random distribution to the specific distribution (Iqbal and Ali, 2018). This transformation was conducted based on the preoperative facial images. In brief, 109 pairs of matched images were augmented for the proposed GAN model training. These AI-synthesized images were semblable after their evaluation compared with the actual postoperative facial images, whereas the image quality was unsatisfactory. Besides, an additional training set, containing 76 paired datasets and 1000 GAN-generated datasets, was used to enhance the ability of the DL classifier (based on VGG-16) for TAO identification (AUC, 0.872 vs.



0.957). The overview of discussed studies in treatment of TAO is exhibited in [Table 2](#).

Application of AI algorithms in privacy safeguard of TAO

The physiognomic changes in patients can be crucial for a real-time evaluation of the disease stage in the clinical diagnosis and management of TAO. The storage of facial images is important, which can also be used in AI training as mentioned earlier ([Huang et al., 2022](#); [Karlin et al., 2022](#)). The facial privacy of patients was commonly anonymized by cropping images into a restricted area in the overwhelming majority of data collection and literature reports. Regarding ophthalmology, the retained field generally ranged from the supraorbital arch to the infraorbital margin. However, this pattern could not elude advanced facial recognition, while dropping some meaningful clinical information ([Clover et al., 2010](#)).

Recently, a creative study on AI-assisted privacy protection was published in *Nature Medicine*. [Yang et al. \(2022\)](#) introduced a novel technology named the digital mask. This mask could be synthesized with diagnostic information and without recognizable characteristics in the original face depending on DL algorithms and three-dimensional reconstruction. They carried out a prospective clinical trial to evaluate the feasibility of this mask. A total of 420 patients (from departments dealing with strabismus, pediatric ophthalmology, TAO, and oculoplasty) were recruited, and 253 were confirmed with associated ocular diseases through facial diagnosis. According to their results, all the pixel errors in eyeball and eyelid reconstruction were about 1%. Cohen's κ values between 12 ophthalmologists and digital masks demonstrated high consistency ($\kappa = 0.801$ for TAO and $0.845\text{--}0.934$ for other diseases). In the recognition-removal experiments, the accuracy of recognition by respondents between cropped pictures and masked images was 91.3% versus 27.3%.

Regarding AI recognition systems, Rank-1 was <0.02 for the three AI models, indicating the extremely low possibility for the correct identification of digital masked images. Besides, Yang et al. also investigated the willingness of patients to share facial images, and the result confirmed that the proposed digital mask did help.

Discussion

AI applications occupy an increasing important part in clinical practice owing to their rapidity, precision, and economy. In ophthalmology, many AI applications have achieved satisfactory performance in diagnosing and predicting several retinal diseases based on the contribution of widely used fundus images ([Li et al., 2018b](#); [Nagasato et al., 2018](#); [Peng et al., 2019](#)). Unlike the majority of ocular diseases, TAO is more specialized and has gained the attention of fewer ophthalmologists, implying inadequate medical resources for such patients. The burgeoning AI represents a promising future for solving this problem.

The diagnosis and grading of TAO are highly comprehensive, including the summarization of chief complaints and symptoms, examination of external ocular signs, detection of thyroid function and immunology, and assessment of orbital images ([Smith and Hegedüs, 2016](#)). Facial images can be easily acquired using smartphones, and automated AI algorithms can help identify meaningful signs and provide diagnostic advice. Orbital CT and MRI scans are broadly used, and the conventional images can be converted into precise data for AI analysis, thus avoiding variable subjective interpretation between observers. The response to GC therapy and the occurrence of DON can also be predicted by AI-aided image processing with digital standards.

Among these aforementioned studies, we found that developing AI models to predict the postoperative appearance of orbital decompression may worth more discussion. In a recent study,

Wickwar et al. (2018) conducted a qualitative study about patients' expectations of orbital decompression surgery. It found that the inability to completely imagine post-operative appearance caused some anxieties, which may be greatly ameliorated by AI-synthesized images. On the other hand, there were different feelings on whether outcomes of surgery had met patients' expectations. And possible strabismus or asymmetry may worsen the situation (Del Monte, 2002). Thus, it would be more reasonable for this kind of AI-assisted prediction to take these factors into consideration. Overall, predicting postoperative appearance by AI models does help propagandize orbital decompression but still needs to be improved.

AI development in TAO has some challenges. Firstly, the incidence of TAO can hardly be comparable to other ocular diseases, especially cataracts and diabetes retinopathy (Shah and Patel, 2022). CT and MRI examinations are also not as simple as fundus photography and optical coherence tomography. Attributed to these two factors the sample size of TAO-related data is relatively low, substantially hindering the advance of AI models in this field. Secondly, the exophthalmometry values and orbital depths are significantly different between races (de Juan et al., 1980; Tsai et al., 2006), implying that the AI model trained based on Caucasian data may not be practicable for Chinese Asians, and extra data collection is needed. Thirdly, some common problems still exist. Many clinicians are reluctant to use AI models in their practice due to the lack of understanding and trust (Maddox et al., 2019), while most patients also prefer to meet a doctor in reality (Keel et al., 2018). The AI-relevant laws and social supervision cannot match the present technology. Under this situation, we suggested that a TAO-related database collaborated by domestic and international centers would play a vital role in AI development. Establishing some AI pilot schemes in expert clinics of TAO could also help the verification and generalization of AI applications in TAO. Regarding the privacy of patients, the novel introduced digital mask (Yang et al., 2022) can provide us an admirable start to build the safeguard.

Although several challenges and problems stand in the way of AI development in TAO, we still need to embrace this promising technology. For further studies, it is foreseeable that the integration of AI models using clinical signs and orbital images can create more reliable AI-based systems for TAO diagnosis. Using AI algorithms, we may separate the standard 12-week GC therapy and record changes from intervals. The AI prediction for GC response can be more precise with these data and help formulate the individual treatment options for each patient with TAO. Through all-around

integration, the future scenario of AI applications in TAO may develop as the flow chart in Figure 1.

Conclusion

In summary, the emerging AI algorithms may potentially improve the accuracy of TAO diagnosis and reduce the economic costs for patients to access qualified healthcare resources. This automated technology can instantly help optimize therapeutic strategies and surgical design during the long course of TAO management. We believe that AI algorithms may become vital in TAO clinical practice soon with the continuous accumulation of TAO data and an improvement in computing capacity.

Author contributions

JD and XC prepared the first draft of the manuscript. All authors contributed to the writing and editing of the manuscript and agree to be accountable for the content of the work. RW approved the submitted manuscript.

Funding

This study was funded by the National Natural Science Foundation of China (grant No. 81770959 and No. 81570885).

Conflict of interest

The authors declare that the research was conducted in the absence of any commercial or financial relationships that could be construed as a potential conflict of interest.

Publisher's note

All claims expressed in this article are solely those of the authors and do not necessarily represent those of their affiliated organizations, or those of the publisher, the editors and the reviewers. Any product that may be evaluated in this article, or claim that may be made by its manufacturer, is not guaranteed or endorsed by the publisher.

References

- Bahn, R. S. (2010). Graves' ophthalmopathy. *N. Engl. J. Med.* 362 (8), 726–738. doi:10.1056/NEJMra0905750
- Balyen, L., and Peto, T. (2019). Promising artificial intelligence-machine learning-deep learning algorithms in ophthalmology. *Asia Pac J. Ophthalmol. (Phila)* 8 (3), 264–272. doi:10.22608/APO.2018479
- Bartalena, L., Kahaly, G. J., Baldeschi, L., Dayan, C. M., Eckstein, A., Marcocci, C., et al. (2021). The 2021 European Group on Graves' orbitopathy (EUGOGO) clinical practice guidelines for the medical management of Graves' orbitopathy. *Eur. J. Endocrinol.* 185 (4), G43–g67. doi:10.1530/eje-21-0479
- Bartalena, L., Marcocci, C., Chiovato, L., Laddaga, M., Lepri, G., Andreani, D., et al. (1983). Orbital cobalt irradiation combined with systemic corticosteroids for graves' ophthalmopathy: Comparison with systemic corticosteroids alone. *J. Clin. Endocrinol. Metab.* 56 (6), 1139–1144. doi:10.1210/jcem-56-6-1139
- Bartley, G. B., Fatourehchi, V., Kadrmas, E. F., Jacobsen, S. J., Ilstrup, D. M., Garrity, J. A., et al. (1995). The incidence of graves' ophthalmopathy in olmsted county, Minnesota. *Am. J. Ophthalmol.* 120 (4), 511–517. doi:10.1016/s0002-9394(14)72666-2
- Clover, A. J., Fitzpatrick, E., and Healy, C. (2010). Analysis of methods of providing anonymity in facial photographs: a randomised controlled study. *Ir. Med. J.* 103 (8), 243–245.
- Cubuk, M. O., Konuk, O., and Unal, M. (2018). Orbital decompression surgery for the treatment of graves' ophthalmopathy: Comparison of different techniques and long-term results. *Int. J. Ophthalmol.* 11 (8), 1363–1370. doi:10.18240/ijo.2018.08.18
- Dai, G., Zhang, X., Liu, W., Li, Z., Wang, G., Liu, Y., et al. (2021). Analysis of EPID transmission fluence maps using machine learning models and CNN for identifying position errors in the treatment of GO patients. *Front. Oncol.* 11, 721591. doi:10.3389/fonc.2021.721591
- de Juan, E., Jr., Hurley, D. P., and Sapira, J. D. (1980). Racial differences in normal values of proptosis. *Arch. Intern. Med.* 140 (9), 1230–1231. doi:10.1001/archinte.140.9.1230

- Del Monte, M. A. (2002). 2001 an ocular odyssey: Lessons learned from 25 years of surgical treatment for graves eye disease. *Am. Orthopt. J.* 52, 40–57. doi:10.3368/aoj.52.1.40
- Deo, R. C. (2015). Machine learning in medicine. *Circulation* 132 (20), 1920–1930. doi:10.1161/circulationaha.115.001593
- Devalla, S. K., Chin, K. S., Mari, J. M., Tun, T. A., Strouthidis, N. G., Aung, T., et al. (2018). A deep learning approach to digitally stain optical coherence tomography images of the optic nerve head. *Invest. Ophthalmol. Vis. Sci.* 59 (1), 63–74. doi:10.1167/iovs.17-22617
- Dolman, P. J. (2012). Evaluating graves' orbitopathy. *Best. Pract. Res. Clin. Endocrinol. Metab.* 26 (3), 229–248. doi:10.1016/j.beem.2011.11.007
- Ezzell, G. A., Galvin, J. M., Low, D., Palta, J. R., Rosen, I., Sharpe, M. B., et al. (2003). Guidance document on delivery, treatment planning, and clinical implementation of IMRT: Report of the IMRT subcommittee of the AAPM radiation therapy committee. *Med. Phys.* 30 (8), 2089–2115. doi:10.1118/1.1591194
- Grus, F. H., Augustin, A. J., and Toth-Sagi, K. (1998). Diagnostic classification of autoantibody repertoires in endocrine ophthalmopathy using an artificial neural network. *Ocul. Immunol. Inflamm.* 6 (1), 43–50. doi:10.1076/ocii.6.1.43.8082
- Gulshan, V., Peng, L., Coram, M., Stumpe, M. C., Wu, D., Narayanaswamy, A., et al. (2016). Development and validation of a deep learning algorithm for detection of diabetic retinopathy in retinal fundus photographs. *Jama* 316 (22), 2402–2410. doi:10.1001/jama.2016.17216
- Hanai, K., Tabuchi, H., Nagasato, D., Tanabe, M., Masumoto, H., Miya, S., et al. (2022). Automated detection of enlarged extraocular muscle in Graves' ophthalmopathy with computed tomography and deep neural network. *Sci. Rep.* 12 (1), 16036. doi:10.1038/s41598-022-20279-4
- Higashiyama, T., Iwasa, M., and Ohji, M. (2017). Quantitative analysis of inflammation in orbital fat of thyroid-associated ophthalmopathy using MRI signal intensity. *Sci. Rep.* 7 (1), 16874. doi:10.1038/s41598-017-17257-6
- Hosten, N., Sander, B., Cordes, M., Schubert, C. J., Schörner, W., and Felix, R. (1989). Graves ophthalmopathy: MR imaging of the orbits. *Radiology* 172 (3), 759–762. doi:10.1148/radiology.172.3.2772184
- Hu, H., Chen, L., Zhang, J. L., Chen, W., Chen, H. H., Liu, H., et al. (2022). T2-weighted MR imaging-derived radiomics for pretreatment determination of therapeutic response to glucocorticoid in patients with thyroid-associated ophthalmopathy: Comparison with semiquantitative evaluation. *J. Magn. Reson. Imaging* 56 (3), 862–872. doi:10.1002/jmri.28088
- Huang, X., Ju, L., Li, J., He, L., Tong, F., Liu, S., et al. (2022). An intelligent diagnostic system for thyroid-associated ophthalmopathy based on facial images. *Front. Med. (Lausanne)* 9, 920716. doi:10.3389/fmed.2022.920716
- Iqbal, T., and Ali, H. (2018). Generative adversarial network for medical images (MI-GAN). *J. Med. Syst.* 42 (11), 231. doi:10.1007/s10916-018-1072-9
- Jiang, J., Luo, Y., Wang, F., Fu, Y., Yu, H., and He, Y. (2021). Evaluation on auto-segmentation of the clinical target volume (CTV) for graves' ophthalmopathy (GO) with a fully convolutional network (FCN) on CT images. *Curr. Med. Imaging* 17 (3), 404–409. doi:10.2174/1573405616666200910141323
- Jiang, J., Zhou, L., He, Y., Jiang, X., and Fu, Y. (2020). Using stacked neural network to improve the auto-segmentation accuracy of Graves' ophthalmopathy target volumes for radiotherapy. *Sheng Wu Yi Xue Gong Cheng Xue Za Zhi* 37 (4), 670–675. doi:10.7507/1001-5515.202002025
- Karlin, J., Gai, L., LaPierre, N., Danesh, K., Farajzadeh, J., Palileo, B., et al. (2022). Ensemble neural network model for detecting thyroid eye disease using external photographs. *Br. J. Ophthalmol.* 2022, 2022–321833. doi:10.1136/bjo-2022-321833
- Kauppinen-Mäkelin, R., Karma, A., Leinonen, E., Löytyniemi, E., Salonen, O., Sane, T., et al. (2002). High dose intravenous methylprednisolone pulse therapy versus oral prednisone for thyroid-associated ophthalmopathy. *Acta Ophthalmol. Scand.* 80 (3), 316–321. doi:10.1034/j.1600-0420.2002.800316.x
- Keel, S., Lee, P. Y., Scheetz, J., Li, Z., Kotowicz, M. A., MacIsaac, R. J., et al. (2018). Feasibility and patient acceptability of a novel artificial intelligence-based screening model for diabetic retinopathy at endocrinology outpatient services: A pilot study. *Sci. Rep.* 8 (1), 4330. doi:10.1038/s41598-018-22612-2
- Khong, J. J., McNab, A. A., Ebeling, P. R., Craig, J. E., and Selva, D. (2016). Pathogenesis of thyroid eye disease: Review and update on molecular mechanisms. *Br. J. Ophthalmol.* 100 (1), 142–150. doi:10.1136/bjophthalmol-2015-307399
- Kundu, M., Nasipuri, M., and Basu, D. K. (2000). Knowledge-based ECG interpretation: A critical review. *Pattern Recognit.* 33 (3), 351–373. doi:10.1016/s0031-3203(99)00065-5
- LeCun, Y., Bengio, Y., and Hinton, G. (2015). Deep learning. *Nature* 521 (7553), 436–444. doi:10.1038/nature14539
- Lee, J., Seo, W., Park, J., Lim, W. S., Oh, J. Y., Moon, N. J., et al. (2022). Neural network-based method for diagnosis and severity assessment of Graves' orbitopathy using orbital computed tomography. *Sci. Rep.* 12 (1), 12071. doi:10.1038/s41598-022-16217-z
- Li, Z., He, Y., Keel, S., Meng, W., Chang, R. T., and He, M. (2018a). Efficacy of a deep learning system for detecting glaucomatous optic neuropathy based on color fundus photographs. *Ophthalmology* 125 (8), 1199–1206. doi:10.1016/j.ophtha.2018.01.023
- Li, Z., Keel, S., Liu, C., He, Y., Meng, W., Scheetz, J., et al. (2018b). An automated grading system for detection of vision-threatening referable diabetic retinopathy on the basis of color fundus photographs. *Diabetes Care* 41 (12), 2509–2516. doi:10.2337/dc18-0147
- Limone, P. P., Mellano, M., Rufo Redda, M. G., Macera, A., Ferrero, V., Sellari Franceschini, S., et al. (2021). Graves' orbitopathy: A multidisciplinary approach. *Q. J. Nucl. Med. Mol. Imaging* 65 (2), 157–171. doi:10.23736/s1824-4785.21.03350-1
- Lin, C., Song, X., Li, L., Li, Y., Jiang, M., Sun, R., et al. (2021). Detection of active and inactive phases of thyroid-associated ophthalmopathy using deep convolutional neural network. *BMC Ophthalmol.* 21 (1), 39. doi:10.1186/s12886-020-01783-5
- Liu, W., Zhang, L., Dai, G., Zhang, X., Li, G., and Yi, Z. (2022). Deep neural network with structural similarity difference and orientation-based loss for position error classification in the radiotherapy of graves' ophthalmopathy patients. *IEEE J. Biomed. Health Inf.* 26 (6), 2606–2614. doi:10.1109/JBHI.2021.3137451
- Maddox, T. M., Rumsfeld, J. S., and Payne, P. R. O. (2019). Questions for artificial intelligence in health care. *Jama* 321 (1), 31–32. doi:10.1001/jama.2018.18932
- Marcocci, C., Bartalena, L., Rocchi, R., Marinò, M., Menconi, F., Morabito, E., et al. (2003). Long-term safety of orbital radiotherapy for Graves' ophthalmopathy. *J. Clin. Endocrinol. Metab.* 88 (8), 3561–3566. doi:10.1210/jc.2003-030260
- Mourits, M. P., Koornneef, L., Wiersinga, W. M., Prummel, M. F., Berghout, A., and van der Gaag, R. (1989). Clinical criteria for the assessment of disease activity in graves' ophthalmopathy: A novel approach. *Br. J. Ophthalmol.* 73 (8), 639–644. doi:10.1136/bjo.73.8.639
- Nagasato, D., Tabuchi, H., Ohsugi, H., Masumoto, H., Enno, H., Ishitobi, N., et al. (2018). Deep neural network-based method for detecting central retinal vein occlusion using ultrawide-field fundus ophthalmoscopy. *J. Ophthalmol.* 2018, 1875431. doi:10.1155/2018/1875431
- Oeverhaus, M., Witteler, T., Lax, H., Esser, J., Führer, D., and Eckstein, A. (2017). Combination therapy of intravenous steroids and orbital irradiation is more effective than intravenous steroids alone in patients with graves' orbitopathy. *Horm. Metab. Res.* 49 (10), 739–747. doi:10.1055/s-0043-116945
- Peng, Y., Dharssi, S., Chen, Q., Keenan, T. D., Agrón, E., Wong, W. T., et al. (2019). DeepSeeNet: A deep learning model for automated classification of patient-based age-related macular degeneration severity from color fundus photographs. *Ophthalmology* 126 (4), 565–575. doi:10.1016/j.ophtha.2018.11.015
- Prummel, M. F., Terwee, C. B., Gerding, M. N., Baldeschi, L., Mourits, M. P., Blank, L., et al. (2004). A randomized controlled trial of orbital radiotherapy versus sham irradiation in patients with mild Graves' ophthalmopathy. *J. Clin. Endocrinol. Metab.* 89 (1), 15–20. doi:10.1210/jc.2003-030809
- Roncevic, R., and Jackson, I. T. (1989). Surgical treatment of thyrotoxic exophthalmos. *Plast. Reconstr. Surg.* 84 (5), 754–760. doi:10.1097/0006534-198911000-00006
- Russell, S., and Norvig, P. (2010). *Artificial intelligence: A modern approach*. New Jersey: Prentice-Hall.
- Saeed, P., Tavakoli Rad, S., and Bisschop, P. (2018). Dysthyroid optic neuropathy. *Ophthalmic Plast. Reconstr. Surg.* 34, S60–S67. doi:10.1097/iop.0000000000001146
- Salvi, M., Dazzi, D., Pellistri, I., and Neri, F. (2002a). Prediction of the progression of thyroid-associated ophthalmopathy at first ophthalmologic examination: Use of a neural network. *Thyroid* 12 (3), 233–236. doi:10.1089/105072502753600197
- Salvi, M., Dazzi, D., Pellistri, I., Neri, F., and Wall, J. R. (2002b). Classification and prediction of the progression of thyroid-associated ophthalmopathy by an artificial neural network. *Ophthalmology* 109 (9), 1703–1708. doi:10.1016/s0161-6420(02)01127-2
- Schmidhuber, J. (2015). Deep learning in neural networks: An overview. *Neural Netw.* 61, 85–117. doi:10.1016/j.neunet.2014.09.003
- Smith, T. J., and Hegedüs, L. (2016). Graves' disease. *N. Engl. J. Med.* 375 (16), 1552–1565. doi:10.1056/NEJMra1510030
- Song, X., Liu, Z., Li, L., Gao, Z., Fan, X., Zhai, G., et al. (2021). Artificial intelligence CT screening model for thyroid-associated ophthalmopathy and tests under clinical conditions. *Int. J. Comput. Assist. Radiol. Surg.* 16 (2), 323–330. doi:10.1007/s11548-020-02281-1
- Tanda, M. L., and Bartalena, L. (2012). Efficacy and safety of orbital radiotherapy for graves' orbitopathy. *J. Clin. Endocrinol. Metab.* 97 (11), 3857–3865. doi:10.1210/jc.2012-2758
- Ting, D. S. W., Cheung, C. Y., Lim, G., Tan, G. S. W., Quang, N. D., Gan, A., et al. (2017). Development and validation of a deep learning system for diabetic retinopathy and related eye diseases using retinal images from multiethnic populations with diabetes. *Jama* 318 (22), 2211–2223. doi:10.1001/jama.2017.18152
- Tsai, C. C., Kau, H. C., Kao, S. C., and Hsu, W. M. (2006). Exophthalmos of patients with graves' disease in Chinese of taiwan. *Eye (Lond)* 20 (5), 569–573. doi:10.1038/sj.eye.6701925
- Tufail, A., Rudisill, C., Egan, C., Kapetanakis, V. V., Salas-Vega, S., Owen, C. G., et al. (2017). Automated diabetic retinopathy image assessment software: Diagnostic accuracy and cost-effectiveness compared with human graders. *Ophthalmology* 124 (3), 343–351. doi:10.1016/j.ophtha.2016.11.014
- Vannucchi, G., Covelli, D., Campi, I., Origo, D., Currò, N., Cirello, V., et al. (2014). The therapeutic outcome to intravenous steroid therapy for active Graves' orbitopathy is influenced by the time of response but not polymorphisms of the glucocorticoid receptor. *Eur. J. Endocrinol.* 170 (1), 55–61. doi:10.1530/eje-13-0611

- Victores, A. J., and Takashima, M. (2016). Thyroid eye disease: Optic neuropathy and orbital decompression. *Int. Ophthalmol. Clin.* 56 (1), 69–79. doi:10.1097/ijo.000000000000101
- Wang, Y., Wang, H., Li, L., Li, Y., Sun, J., Song, X., et al. (2021). Novel observational study protocol to develop a prediction model that identifies patients with Graves' ophthalmopathy insensitive to intravenous glucocorticoids pulse therapy. *BMJ Open* 11 (12), e053173. doi:10.1136/bmjopen-2021-053173
- Wickwar, S., McBain, H., Edmunds, M. R., Ezra, D. G., Rose, G. E., and Newman, S. P. (2018). Patients' expectations for the functional and psychosocial outcomes of orbital decompression surgery for thyroid eye disease: A qualitative study. *Psychol. Health Med.* 23 (4), 475–484. doi:10.1080/13548506.2017.1356930
- Wiersinga, W. M., and Bartalena, L. (2002). Epidemiology and prevention of Graves' ophthalmopathy. *Thyroid* 12 (10), 855–860. doi:10.1089/105072502761016476
- Wu, C., Li, S., Liu, X., Jiang, F., and Shi, B. (2022). DMs-MAFM+EfficientNet: A hybrid model for predicting dysthyroid optic neuropathy. *Med. Biol. Eng. Comput.* 60 (11), 3217–3230. doi:10.1007/s11517-022-02663-4
- Yang, Y., Lyu, J., Wang, R., Wen, Q., Zhao, L., Chen, W., et al. (2022). A digital mask to safeguard patient privacy. *Nat. Med.* 28 (9), 1883–1892. doi:10.1038/s41591-022-01966-1
- Yoo, T. K., Choi, J. Y., and Kim, H. K. (2020). A generative adversarial network approach to predicting postoperative appearance after orbital decompression surgery for thyroid eye disease. *Comput. Biol. Med.* 118, 103628. doi:10.1016/j.compbiomed.2020.103628
- Zhang, X., Dai, G., Zhong, R., Zhou, L., Xiao, Q., Wang, X., et al. (2021). Radiomics analysis of EPID measurements for patient positioning error detection in thyroid associated ophthalmopathy radiotherapy. *Phys. Med.* 90, 1–5. doi:10.1016/j.ejmp.2021.08.014
- Zhu, W., Ye, L., Shen, L., Jiao, Q., Huang, F., Han, R., et al. (2014). A prospective, randomized trial of intravenous glucocorticoids therapy with different protocols for patients with graves' ophthalmopathy. *J. Clin. Endocrinol. Metab.* 99 (6), 1999–2007. doi:10.1210/jc.2013-3919



OPEN ACCESS

EDITED BY

Yanwu Xu,
Baidu, China

REVIEWED BY

Tae Keun Yoo,
B&VIIT Eye center/Refractive surgery & AI
Center, Republic of Korea
Peifang Ren,
Zhejiang University, China
Peng Gao,
Tongji University, China

*CORRESPONDENCE

Qixin Cao,
✉ cqx6785@163.com
Qi Dai,
✉ dq@mail.eye.ac.cn

[†]These authors share first authorship

SPECIALTY SECTION

This article was submitted to Molecular
and Cellular Pathology,
a section of the journal
Frontiers in Cell and Developmental
Biology

RECEIVED 29 December 2022

ACCEPTED 08 February 2023

PUBLISHED 17 February 2023

CITATION

Zhang Z, Wang Y, Zhang H, Samusak A,
Rao H, Xiao C, Abula M, Cao Q and Dai Q
(2023), Artificial intelligence-assisted
diagnosis of ocular surface diseases.
Front. Cell Dev. Biol. 11:1133680.
doi: 10.3389/fcell.2023.1133680

COPYRIGHT

© 2023 Zhang, Wang, Zhang, Samusak,
Rao, Xiao, Abula, Cao and Dai. This is an
open-access article distributed under the
terms of the [Creative Commons
Attribution License \(CC BY\)](#). The use,
distribution or reproduction in other
forums is permitted, provided the original
author(s) and the copyright owner(s) are
credited and that the original publication
in this journal is cited, in accordance with
accepted academic practice. No use,
distribution or reproduction is permitted
which does not comply with these terms.

Artificial intelligence-assisted diagnosis of ocular surface diseases

Zuhui Zhang^{1,2†}, Ying Wang^{1†}, Hongzhen Zhang¹,
Arzigul Samusak¹, Huimin Rao¹, Chun Xiao¹, Muhetaer Abula¹,
Qixin Cao^{3*} and Qi Dai^{1,2*}

¹The First People's Hospital of Aksu District in Xinjiang, Aksu City, China, ²National Clinical Research Center for Ocular Diseases, Eye Hospital, Wenzhou Medical University, Wenzhou, China, ³Huzhou Traditional Chinese Medicine Hospital Affiliated to Zhejiang University of Traditional Chinese Medicine, Huzhou, China

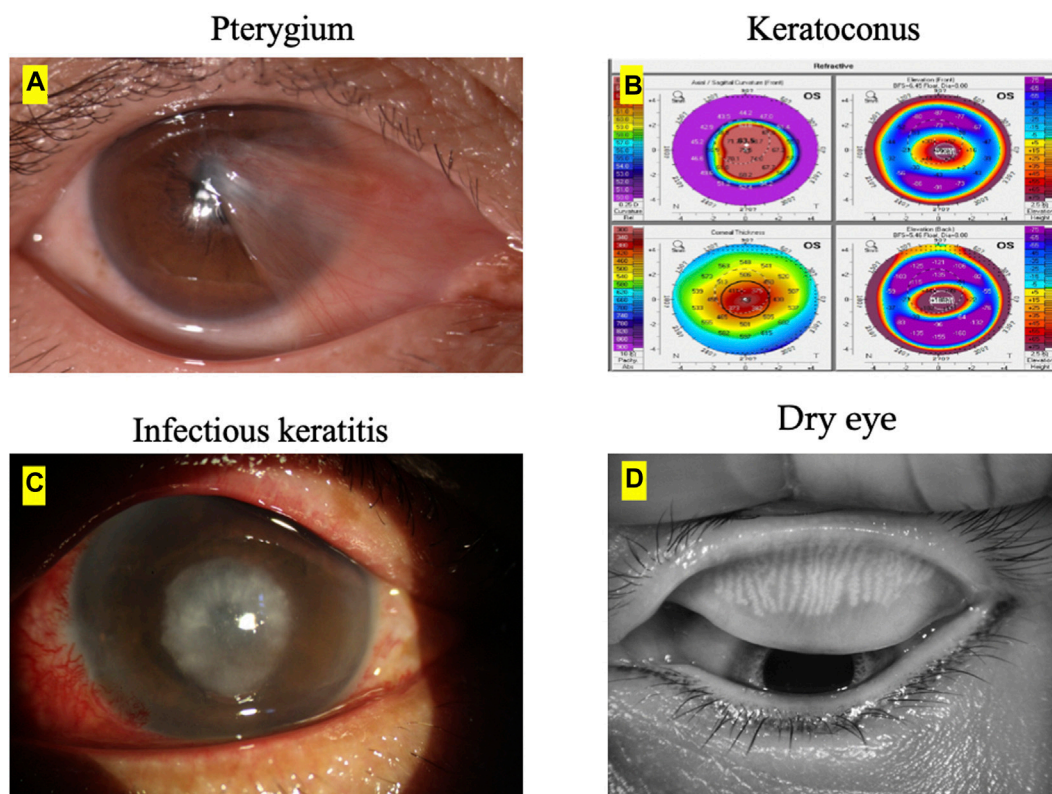
With the rapid development of computer technology, the application of artificial intelligence (AI) in ophthalmology research has gained prominence in modern medicine. Artificial intelligence-related research in ophthalmology previously focused on the screening and diagnosis of fundus diseases, particularly diabetic retinopathy, age-related macular degeneration, and glaucoma. Since fundus images are relatively fixed, their standards are easy to unify. Artificial intelligence research related to ocular surface diseases has also increased. The main issue with research on ocular surface diseases is that the images involved are complex, with many modalities. Therefore, this review aims to summarize current artificial intelligence research and technologies used to diagnose ocular surface diseases such as pterygium, keratoconus, infectious keratitis, and dry eye to identify mature artificial intelligence models that are suitable for research of ocular surface diseases and potential algorithms that may be used in the future.

KEYWORDS

artificial intelligence, deep learning, machine learning, ocular surface diseases, convolutional neural network

1 Introduction

Artificial intelligence (AI) is a frontier field of computer science whose goal is to use computers to solve practical issues (Rahimy, 2018). The concept was introduced at a workshop at Dartmouth College in 1956 (Lawrence et al., 2016). The conference discussed the relevant theories and principles of machine simulation intelligence. Since then, the development of AI has been unstable due to limited technical conditions and levels. Nevertheless, with the rapid development of computer technology, the application of AI in medical research has become a hot topic in modern technology. Recently, healthcare has become one of the frontiers of AI applications, particularly for image-centric subspecialties such as ophthalmology (Ting et al., 2019), cardiology (Dey et al., 2019), radiology (Saba et al., 2019), and oncology (Niazi et al., 2019), among others. They adopt big data technology to collect massive clinical data and images and apply big medical data to AI to guide or assist doctors in clinical decision-making through the supercomputing power and data mining ability of cloud computing. AI can obtain disease characteristics from the training set and apply them to a verification or test set to diagnose the corresponding disease. AI can segment anatomical structures such as abnormal shapes in the images. AI can also classify images into different types according to the characteristics of diseases. The algorithms of AI include

**FIGURE 1**

Ocular surface diseases and image modalities. (A) The main imaging modality of pterygium is anterior segment photograph. (B) The main imaging modality of keratoconus is pentacam. (C) The main imaging modality of infectious keratitis is slit-lamp images. (D) The main imaging modality of dry eye is Keratograph 5M.

traditional machine learning (ML) algorithm and deep learning (DL) algorithm. The traditional ML algorithms mainly include linear regression, logical regression, support vector machine (SVM), decision tree and random forest (RF) algorithms, and usually do not involve large-scale neural networks. DL algorithm mainly uses multimedia data sets (such as images, videos, and sounds), and usually involves the application of large-scale neural networks, including artificial neural network (ANN), convolutional neural network (CNN), and recurrent neural network (RNN).

Previously, most studies on the application of AI in ophthalmology focused on glaucoma (Devalia et al., 2018; Kucur et al., 2018; Asaoka et al., 2019; Wang M. et al., 2019), fundus diseases (Gulshan et al., 2016; Burlina et al., 2017; Ting et al., 2017; Venhuizen et al., 2018; Nagasato et al., 2019), and cataracts (Gao et al., 2015; Yang et al., 2016; Long et al., 2017; Wu et al., 2019; Xu et al., 2020). Compared to diagnosing retinal diseases, which largely depend on fundus images acquired from ophthalmoscopy or fundus photography, multiple examinations are required to diagnose ocular surface diseases, considering the complexity of their structural and physiological functions. In recent years, with the expansion of AI in ophthalmology, increasing research has applied AI to ocular surface diseases such as pterygium, keratoconus (KC), infection keratitis, and dry

eye. Herein, we reviewed research on the application of AI in the field of ocular surface-related diseases to guide clinical work. The remainder of this paper consists of the following: Sections 2–7 provides the efficiency of AI in diagnosing ocular surface diseases, pterygium, KC, infectious keratitis, dry eye, and other ocular surface diseases.

The image examples of ocular surface diseases and image modalities to diagnose each corneal disease is presented in Figure 1. The main image modalities of ocular surface diseases include anterior segment photograph, pentacam, slit-lamp images and Keratograph 5M, etc.

2 Search methods

A systematic literature search was performed in PubMed and Web of science. The goal was to retrieve as many studies as possible applying ML to ocular surface disease related data. The following keywords were used: All combinations of “ocular surface,” “pterygium,” “keratoconus,” “keratitis,” “dry eye,” and “meibomian gland dysfunction (MGD)” with “artificial intelligence,” “machine learning,” “deep learning,” “convolutional neural network,” “decision tree.” No time period limitations were applied for any of the searches.

TABLE 1 Summary of studies focused on computer-aided pterygium diagnosis.

Year	Authors	Imaging modality	Image size	Databases	AI algorithms	AUC (%)	Accuracy (%)	Sensitivity (%)	Specificity (%)	IoU (%)
2018	Wan Zaki et al. (2018)	ASP	3,017	Normal and pterygium	SVM/ANN	95.60	91.27	88.70	88.30	—
2018	Zhang et al. (2018)	ASP	1,513	Normal, pterygium, keratitis, subconjunctival hemorrhage, and cataract	CNN/Faster-RCNN	95.95	>95.00	97.45	71.15	—
2019	Zulkifley et al. (2019)	ASP	120	Normal and pterygium	FCNN	97.0	81.10	95.0	98.3	—
2020	Abdani et al. (2020)	ASP	328	Ranging from early to late stage of pterygium	CNN	—	92.02	—	—	92.02
2021	Xu W. et al. (2021)	ASP	1,220	Normal, observation (pterygium) and operation (pterygium)	DL (EfficientNet-B6)	>93.00	94.68	>90.00	>95.00	—
2021	Abdani et al. (2021)	ASP	328	Ranging from early to late stage of pterygium	CNN	—	93.30	—	—	86.40
2021	Fang et al. (2022)	ASP	9,443	Pterygium and referable pterygium	CNN	≥98.50	≥95.2	≥94.0	≥95.30	—
2022	Hung et al. (2022)	SLI	237	Normal, primary and recurrent pterygium	DL	—	80.00	66.67	81.82	—
2022	Wan et al. (2022)	ASP	489	Normal, observation (pterygium) and operation (pterygium)	DL(U-Net++)	95.86	92.37	90.24	93.51	—
>86.40	AUC, area under the curve; IoU, intersection over union; ASP, anterior segment photograph; SVM, support vector machine; ANN, artificial neural networks; CNN, convolutional neural network; Faster-RCNN, faster-region based convolutional neural network; FCNN, fully convolutional neural networks; DL, deep learning; SLI, slit-lamp images.									

3 AI application in pterygium

Pterygium is a common eye disorder in which abnormal fibrovascular tissue protrudes from the inner side of the eyes toward the corneal area (Zulkifley et al., 2019). Since it is directly linked to excessive exposure to ultraviolet radiation, farmers and fishermen are the two high-risk groups (Gazzard et al., 2002; Abdani et al., 2019). This condition can be better managed when patients know about this disease early. Moreover, pterygium tissues or lesions encroach on the pupil area at the latter stage, possibly causing vision impairment (Tomidokoro et al., 2000; Clearfield et al., 2016; Wang F. et al., 2021). Currently, the grading of pterygium is mainly based on the subjective evaluation of doctors. Therefore, AI can be used to develop an efficient automatic grading system for pterygium (Hung et al., 2022). In vast rural and remote areas that lack professional medical resources for ophthalmology, AI diagnostic technology can provide local patients with a convenient pterygium screening method, prevent the rush of patients to county or prefectural hospitals for medical care, and reduce the burden on patients. Furthermore, it suggests treatment methods, clarifies the indications for further surgical treatment, facilitates the timely referral of patients needing surgery at the grassroots level, and rationally allocates medical resources. Table 1 mainly reviews AI applications for the diagnosis of pterygium.

In 2012, Gao et al. (2012) proposed a pterygium detection system based on color information. Interestingly, the pupil detection technique, which uses corneal images, achieved 85.38% accuracy. Similarly, Mesquita and Figueiredo (2012) applied a circle hough transform to segment the iris. Subsequently, a region-growing algorithm based on Otsu's algorithm is applied to the iris's segmented area to segment the pterygium tissue. Wan Zaki et al. (2018) developed an image-processing method based on ASP using the following four modules to differentiate pterygium from normal: preprocessing, corneal segmentation, feature extraction, and classification. Image-processing method performance was evaluated using a SVM and an ANN. The performance of the proposed image-processing method generated results of 88.7%, 88.3%, and 95.6% for sensitivity, specificity, and area under the curve (AUC), respectively. However, the imperfect image setup should also be noted as a limitation. Abdani et al. (2020) and Abdani et al. (2021) proposed an automatic pterygium tissue segmentation using CNN. This is useful for detecting pterygium from the early stage to the late stage. The overall accuracy of both studies is high [92.20% (Abdani et al., 2020), 93.30% (Abdani et al., 2021)].

Zhang et al. (2018) also used a deep DL diagnosis system that can automatically diagnose various eye diseases based on the patient's ASP and provide diagnosis-based targeted treatment recommendations. Specifically, the last stage provides treatment advice based on medical experience and AI strictly associated

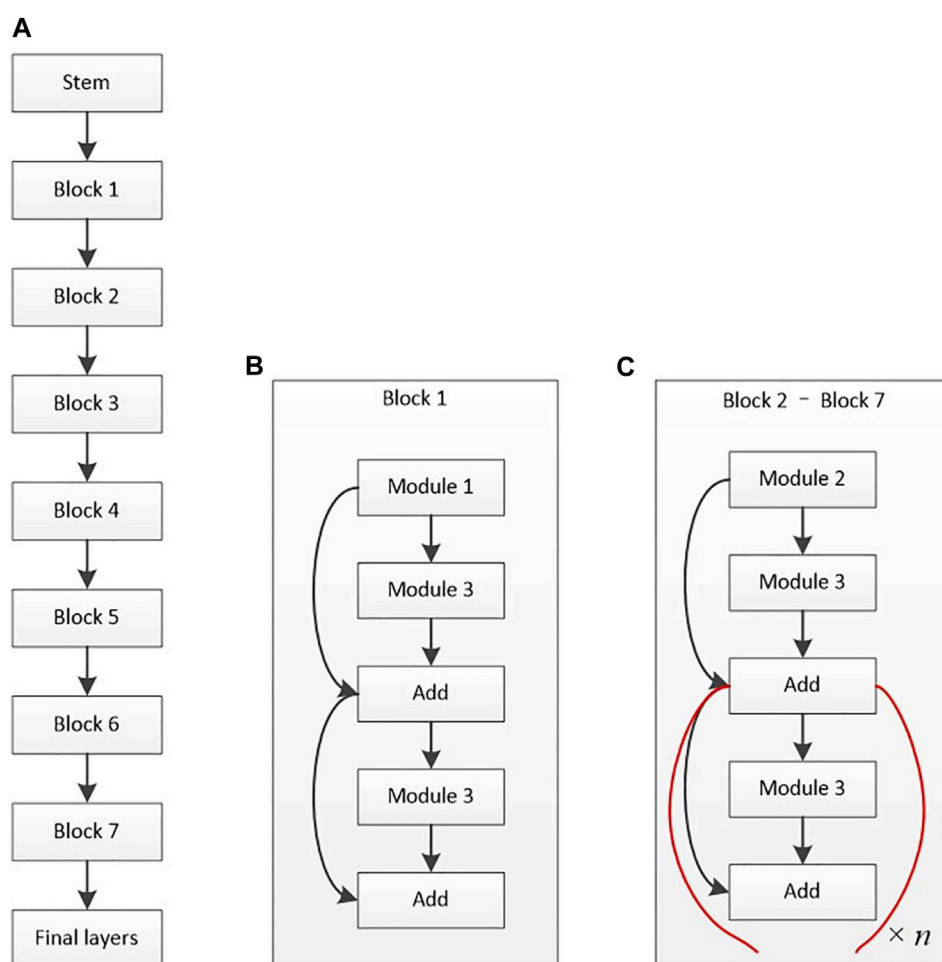


FIGURE 2

Architectural diagram of EfficientNet-B6 (Xu W. et al., 2021). (A) Basic architecture. (B) Structure of block 1. (C) Structure of blocks 2–7.

with pterygium (accuracy, >95%). Zulkifley et al. (2019) proposed a DL approach (Pterygium-Net) based on fully convolutional neural networks (FCNN) with the help of transfer learning to detect and localize the pterygium automatically. Pterygium-Net produces high average detection sensitivity and specificity of 0.95 and 0.983, respectively. As for pterygium tissue localization, the algorithm achieves 0.811 accuracies with a meager failure rate of 0.053. Xu W. et al. (2021) developed a unique intelligent diagnosis system based on DL to diagnose pterygium (Figure 2 depicts the architectural diagram of EfficientNet-B6, created by Xu et al.). Experts and the AI diagnosis system categorized the images into the following three categories: normal, pterygium observation, and pterygium surgery. Moreover, the accuracy rate of the AI diagnosis system on the 470 tested images was 94.68%, diagnostic consistency was high, and kappa values of the three groups were above 85%. The AI, pterygium diagnosis system, can not only judge the presence of pterygium but also classify the severity of pterygium. Fang et al. (2022) evaluated the performance of a DL algorithm for the detection of the presence and extent of pterygium based on ASP taken from

slit-lamp and handheld cameras. The AI algorithm could detect the presence of referable-level pterygium with optimal sensitivity and specificity. A handheld camera might be a simple screening tool for detecting reference pterygium.

Hung et al. (2022) proposed a DL system to predict pterygium recurrence. The AI algorithm shows high specificity (80.00%) but low sensitivity (66.67%) in predicting pterygium recurrence. Wan et al. (2022) proposed a DL system for measuring the pathological progression of pterygium. These are essential for achieving accurate medical diagnosis and can conveniently assist ophthalmologists in timely detecting pterygium status and arranging surgery strategies. In addition to the abovementioned application of AI to the segmentation and diagnosis of pterygium, Kim et al. (2022) developed AI software for quantitative analysis of the immunochemical image of pterygium. They concluded that the AI software might improve the reliability and accuracy of evaluating histopathological specimens obtained after ophthalmological surgery. The above research shows that the AI model can achieve satisfactory results in the diagnosis and classification prediction of pterygium.

TABLE 2 Summary of studies focused on computer-aided KC diagnosis.

Year	Authors	Imaging modality	Image size	Databases	AI algorithms	AUC (%)	Accuracy (%)	Sensitivity (%)	Specificity (%)	IoU (%)
1997	Smolek and Klyce (1997)	TMS-1	300	KC, KCS, and others	CNN	—	100.00	100.00	100.00	—
2002	Accardo and Pensiero (2002)	EyeSys	396	Normal, KC, and others	CNN	—	96.70	94.10	97.60	—
2005	Twa et al. (2005)	Keratron	244	Normal and KC	MLC	97.00	92.00	92.00	93.00	—
2010	Souza et al. (2010)	Orbscan II	318	Normal, astigmatism, KC, and PRK	SVM/MLP/RBFNN	>98.00	—	100.00	98.00	—
2012	Arbelaez et al. (2012)	Sirius	3,502	Normal, SKC, KC and PRK	SVM	—	98.20	95.00	99.30	—
2013	Smadja et al. (2013)	Galilei	372	Normal, FFKC, and KC	MLC	—	—	99.50	100.00	—
2016	Ruiz Hidalgo et al. (2016)	Pentacam	860	Normal, astigmatism, FFKC, KC, and PRK	SVM/MLC	99.80	98.90	99.10	98.50	—
2016	Kovács et al. (2016)	Pentacam	135	Normal fellow eyes with unilateral KC, bilateral KC, and PRK	CNN/MLC	99.00	—	100.00	95.00	—
2018	Yousefi et al. (2018)	CASIA AS-OCT	3,156	Normal, FFKC, mild KC, and advanced KC	Unsupervised ML	—	—	97.70	94.10	—
2019	Zou et al. (2019)	Pentacam	2018	Normal, SKC, and KC	SVM-RFE/GBDT	99.82	98.91	76.92	100	—
2019	Dos Santos et al. (2019)	UHR-OCT	20,160	Normal and KC	CNN (CorneaNet)	—	99.56	>99.30	—	>98.50
2019	Issarti et al. (2019)	Pentacam	838	Normal and KCS and mild-moderate KC	FFN	—	96.56	97.78	95.56	—
2019	Kamiya et al. (2019)	CASIA AS-OCT	304	Normal and grade 1–4 KC	CNN	—	99.10	100	98.40	—
2019	Lavric and Valentin (2019)	SyntEyes	400	Normal and KC	CNN	—	99.33	—	—	—
2020	Kuo B. I et al. (2020)	TMS-4+ Pentacam + Corvis ST	354	Normal, SKC, and KC	CNN	99.50	95.80	94.40	97.20	—
2020	Abdelmotaal et al. (2020)	Pentacam	3,218	Normal, SKC, and KC	CNN/SVM	—	>95.50	>92.00	>92.00	—
2020	Shi et al. (2020)	Pentacam + UHR-OCT	121	Normal, SKC, and KC	MLC	100	—	100	100	—
2020	Xie et al. (2020)	Pentacam	6,465	Normal, suspected irregular cornea, early KC, KC, and PRK	CNN/TL	99.90	95.0	97.80	99.20	—
2020	Cao et al. (2020)	Pentacam	88	Normal and SKC	RF	96.00	87.00	88.00	85.00	—
2021	Cao et al. (2021)	Pentacam	267	Normal and SKC	RF	—	98.00	97.00	98.00	—
2021	Al-Timemy et al. (2021)	Pentacam	3,794	Normal, KCS, and KC	CNN/SVM	99.00	97.70	—	—	—

(Continued on following page)

TABLE 2 (Continued) Summary of studies focused on computer-aided KC diagnosis.

Year	Authors	Imaging modality	Image size	Databases	AI algorithms	AUC (%)	Accuracy (%)	Sensitivity (%)	Specificity (%)	IoU (%)
2021	Herber et al. (2021)	Pentacam + Corvis ST	434	Normal, mild, moderate, and advanced KC eyes	RF	97.00	93.00	91.00	94.00	—
2021	Castro-Luna et al. (2021)	Pentacam + Corvis ST	81	Normal and SKC	RF	—	89.00	86.00	93.00	—
2021	Kamiya et al. (2021a)	TMS-4	349	Normal and grade 1–4 KC	CNN	99.70	96.60	98.80	94.40	—
2021	Chen et al. (2021)	Pentacam	1926	Normal and grade 1–4 KC	CNN	94.23	97.85	98.46	90.00	—
2021	Malyugin et al. (2021)	Pentacam	800	Normal and grade 1–4 KC	ML/QDA	97.00	97.00	—	—	—
2021	Ghaderi et al. (2021)	Pentacam	450	Normal and grade 1–3 KC	MLP/ANFIS	—	98.20	99.10	96.20	—
2021	Kamiya et al. (2021b)	CASIA AS-OCT	218	Non-progressive and progressive KC	CNN	—	84.90	95.50	58.10	—
2021	Kato et al. (2021)	Pentacam	274	Non-progressive and progressive KC	CNN	81.40	—	77.80	69.60	—
2021	Kundu et al. (2021)	MS-39	1,122	Normal, VAE, and KC	RF/ZP	99.70	99.10	98.70	—	—
2021	Aatila et al. (2021)	CASIA AS-OCT	12, 242	Normal, FFKC, mild KC, and advanced KC	RF	100	98.00	98.00	—	—
2022	Mohammadpour et al. (2022)	Pentacam, Sirius and OPD-Scan III	212	Normal, SKC, and KC	MLC	—	91.24	80.00	96.60	—
2022	Tan et al. (2022)	Corvis ST	354	Normal and KC	FFN	—	99.60	99.30	100	—
2022	Ahn et al. (2022)	Pentacam	1,246	Normal, SKC, and KC	Ensemble	—	85.40	96.40	83.10	—
2022	Xu et al. (2022)	Pentacam	1,108	Normal, AKC, and KC	CNN	100	98.77	98.48	98.96	—

KC, keratoconus; KCS, keratoconus suspect; MLC, machine learning classification; PRK, photorefractive keratectomy; MLP, multi-layer perceptron; RBFNN, radial basis function neural network; SKC, subclinical keratoconus; FFKC, forme fruste keratoconus; AS-OCT, anterior segment optical coherence tomography; ML, machine learning; RFE, recursive feature elimination; GBDT, gradient boosting decision tree; UHR-OCT, ultra-high-resolution optical coherence tomography; FFN, feedforward neural network; TL, transfer learning; RF, random forest; QDA, quadratic discriminant analysis; ANFIS, adaptive network-based fuzzy inference system; VAE, very asymmetric ectasia; ZP, zernike polynomials; AKC, asymmetric keratoconus. TMS: A computer-assisted videokeratoscope (Tomey Corporation, Nagoya, Japan). MS-39: A hybrid tomographer (CSO, Florence, Italy).

4 AI application in KC

KC is a non-inflammatory, asymmetric, ectatic corneal disorder characterized by progressive thinning and impaired vision ([Henein and Nanavaty, 2017](#); [Mas Tur et al., 2017](#)). Since the signs of intermediate and advanced KC are quite common, clinical diagnosis is straightforward ([Gomes et al., 2015](#)). Atypical KC includes KC suspect (KCS), forme fruste KC (FFKC), and subclinical KC (SKC). Unfortunately, these atypical KC symptoms and signs are not obvious and are difficult to diagnose based on general examination results. However, most of the KC studies analyzed the corneal morphological metrics from Pentacam. AI-based corneal morphological metrics can provide early KC detection. Moreover, early AI research on KC relied on corneal

topography data for neural network training to distinguish KC from other corneal abnormalities such as astigmatism, corneal transplantation, and post-photorefractive keratectomy (PRK). [Table 2](#) mainly reviews AI applications for the diagnosis of KC.

The advantage of these AI algorithms lies in the potential to help clinicians differentiate between KC and normal eyes. In 1997, [Smolek and Klyce \(1997\)](#) designed a classification neural network for KC screening to detect the existence of KC or KCS. In total, 10 topographic indices were used as the network inputs. The AI model showed 100% accuracy, specificity, and sensitivity for the test set. [Accardo and Pensiero \(2002\)](#) proposed an ANN method to identify KC from corneal topographies. The results showed a global sensitivity and specificity of 94.1% (with a KC sensitivity of 100%) and 97.6% (98.6% for KC alone) in the test set, respectively. This

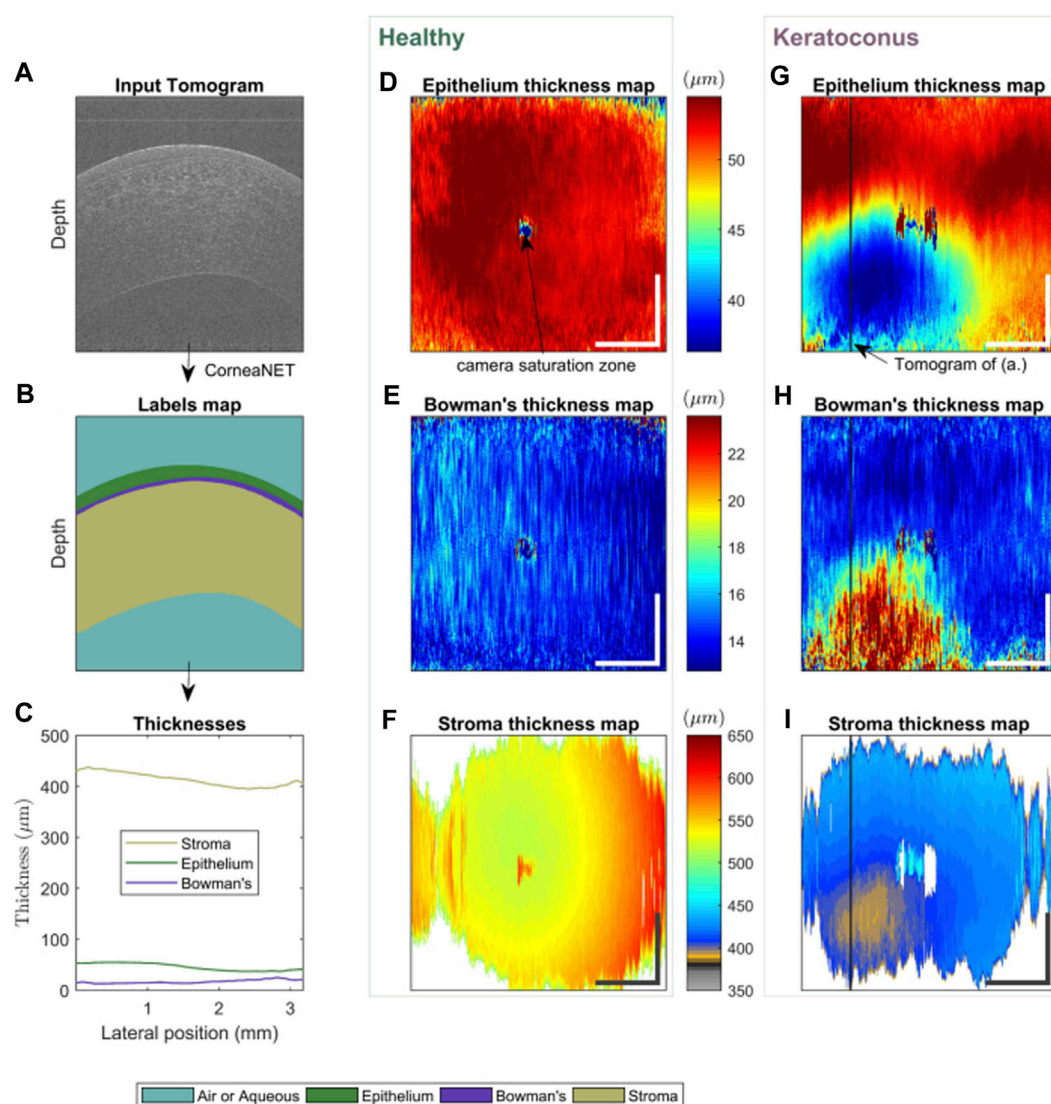


FIGURE 3

Using CorneaNet, the thicknesses of the epithelium, stroma, and Bowman's layer were computed in a normal and a KC case (Dos Santos et al., 2019). The healthy case shows close to uniform thicknesses for all three layers. In contrast, for the KC case, the epithelium and stroma are thinner in a specific region of the cornea, and Bowman's layer is thicker. (A–C) Thickness calculation in one tomogram. (A) UHR-OCT tomogram of a keratoconus patient, (B) corresponding labels map computed using CorneaNet. (C) Thicknesses of the three corneal layers computed using the label maps. (D–F) Thickness maps in a healthy subject case. (G–I) Thickness maps in a keratoconus case. The thickness scale bar is shared by the maps horizontally. Scale bar: 1 mm.

study elevates the potential of AI for the automatic screening of early KC, pointing out that simultaneously using the topographic parameters of both eyes improves the discriminative capability of the ANN. Twa et al. (2005) described applying decision tree induction, an automated machine learning classification (MLC) approach, to objectively and quantitatively differentiate between normal and KC corneal shapes. The results showed an accuracy of 92% and an area under the receiver operating characteristic (ROC) curve of 0.97. Arbelaez et al. (2012) employed the SVM algorithm to integrate data from the corneal surfaces and pachymetry into the model. Interestingly, precision was improved the most when posterior corneal surface data were included, particularly in SKC cases. Additionally, this AI approach increases its sensitivity from 89.3% to 96.0%, 92.8% to 95.0%, 75.2% to 92.0%, and 93.1% to 97.2% in abnormal eyes, eyes with KC, those with SKC, and normal eyes,

respectively. Therefore, the diagnostic accuracy of the AI approach was further improved by including the posterior corneal surface and corneal thickness data. Smadja et al. (2013) applied an MLC to discriminate between normal eyes and KC with 100% sensitivity and 99.5% specificity and between normal and FFKC with 93.6% sensitivity and 97.2% specificity. The MLC showed excellent performance in discriminating between normal eyes and FFKC, thus providing a tool closer to automated medical reasoning. This AI might undoubtedly enable clinicians to detect FFKC before refractive surgery. However, its effect requires further validation since only 372 eyes of 197 patients were included. Similarly, Ruiz Hidalgo et al. (2016) classified 860 eyes into five groups by combining 22 parameters obtained from Pentacam measurements and conducted MLC training. Consequently, the accuracy of the FFKC versus normal task was 93.1%, with 79.1% sensitivity and

97.9% specificity for the FFKC discrimination. Considering the difference between eyes, Kovács et al. (2016) included a “bilateral data” parameter and used a neural network algorithm for modeling. This system on bilateral data of the index of height decentration had a higher accuracy than a single unilateral parameter in differentiating the eyes of all patients with KC from control eyes (area under ROC, 0.96 versus 0.88). Yousefi et al. (2018) developed an unsupervised ML algorithm and applied it to identify and monitor KC stages. Four hundred and twenty corneal topographies, elevations, and pachymetric parameters were also measured. Notably, the specificity of this AI method for identifying normal eyes from those with KC was 94.1%, and the sensitivity for identifying KC in normal eyes was 97.7%. Therefore, this technique can be adopted in corneal clinics and research settings to better diagnose and monitor changes and improve our understanding of corneal changes in KC. Zou et al. (2019) also investigated the diagnosis of healthy corneas, SKC, and KC through ML modeling using Pentacam data of participants in 2018. The diagnostic accuracy of this model for SKC and normal corneas was 95.53% and 96.67%, respectively, and the AUC of the validation set was 99.36%. Conversely, the accuracy of diagnosis of KC and normal corneas was 98.91%, and the AUC of the validation set was 99.82%. The diagnostic accuracy of the model was 95.53%, which was significantly better than the resident’s with 93.55%. Dos Santos et al. (2019) employed a custom-built ultra-high-resolution OCT (UHR-OCT) system to scan 72 and 70 normal and KC eyes, respectively. Overall, 20,160 images were labeled and used for training in a supervised learning approach. A custom neural network architecture, CorneaNet [Figure 3 depicts CorneaNet, created by Dos Santos et al. (2019)], was designed and trained. This study revealed that CorneaNet could segment both normal and KC images with high accuracy (validation accuracy, 99.56%). Interestingly, CorneaNet could detect KC early and, more generally, examine other diseases that change corneal morphology. Issarti et al. (2019) established a stable, low-cost computer-aided diagnosis (CAD) system for early KC detection. CAD combines a custom-made mathematical model, feedforward neural network (FFN), and Grossberg-Runge Kutta architecture to detect and suspect KC clinically. The final diagnostic accuracy was >95% for KCS, mild KC, and moderate KC. The algorithm also provides a 70% reduction in computation time while increasing stability and convergence regarding traditional ML techniques.

Some studies have focused on staging KC severity. Kamiya et al. (2019) applied the DL of color-coded maps, measured using swept-source AS-OCT, to evaluate the diagnostic accuracy of KC. They included a total of 304 eyes [grades 1 (108 eyes), 2 (75 eyes), 3 (42 eyes), and 4 (79 eyes)] according to the Amsler-Krumeich classification and 239 age-matched healthy eyes. This AI system effectively discriminated KC from normal corneas (99.1% accuracy) and further classified the grade of the disease (87.4% accuracy). Two studies used topography images to detect and stage KC (Kamiya et al., 2021a; Chen et al., 2021). Both studies had high overall accuracies [78.5% (Kamiya et al., 2021a), 93% (Chen et al., 2021)], with better performance on color-coded maps than the raw topographic indices. Malyugin et al. (2021) trained an ML model using topography images and visual acuity to classify KC stages based on the Amsler-Krumeich classification system. The model’s overall classification accuracy was 97%, highest for stage

4 KC and lowest for FFKC. Another study trained an ensemble CNN on Pentacam measurements to differentiate between normal eyes and early, moderate, and advanced KC with a staging accuracy of 98.2% (Ghaderi et al., 2021). Other studies have focused on detecting KC progression, though each study had varying definitions of disease progression. The first study trained a CNN model on AS-OCT images, achieving an 84.9% accuracy in discriminating KC with and without progression (Kamiya et al., 2021b). Another study trained an AI model to predict KC progression and the need for corneal crosslinking using tomography maps and patient age with an AUC of 0.814 (Kato et al., 2021).

Lavric and Valentin (2019) proposed a corneal detection algorithm using CNN to analyze and detect KC and obtained an accuracy rate of 99.33%. Kuo B. I et al. (2020) developed a DL algorithm for detecting KC based on a computer-assisted videokeratoscope (TMS-4), Pentacam and Corvis ST. The AI model has high sensitivity and specificity in identifying KC. Abdelmotaal et al. (2020) used a domain-specific CNN to implement DL. The CNN performance was assessed using standard metrics and detailed error analyses, which include network activation maps. Accordingly, the CNN categorized four map-selectable display images, with average accuracies of 0.983 and 0.958 for the training and test sets, respectively. Furthermore, Shi et al. (2020) created an automated classification system that used MLC to distinguish clinically unaffected eyes in patients with KC from a normal population by combining Scheimpflug camera images and UHR-OCT imaging data. Interestingly, this AI model dramatically improved the differentiable power to discriminate between normal eyes and those with SKC (AUC = 0.93). The epithelial features extracted from the OCT images were the most valuable for the discrimination process. Cao et al. (2021) developed a new clinical decision-making system based on ML, automatically detecting SKC with high accuracy, specificity and sensitivity. Mohammadpour et al. (2022) developed a classifier based on AI, which can help detect early keratoconus. Al-Timemy et al. (2021) trained a hybrid-CNN model to identify features and then used it to train an SVM to detect KC. The final AI model had a 97.70% accuracy in differentiating normal from KC eyes and 84.40% in differentiating normal, KCS, and KC based on the merged development subset and independent validation subset. Kundu et al. (2021) established a universal architecture of combining AS-OCT and AI. It achieves an excellent classification of normal and KC. This AI model effectively classified very asymmetric ectasia (VAE) eyes as SKC and FFKC. Tan et al. (2022) developed a novel method based on biomechanical parameters calculated from raw corneal dynamic deformation videos to quickly and accurately diagnose KC using ML (99.6% accuracy). Ahn et al. (2022) developed and validated a novel AI model to determine a diagnosis of KC based on basic ophthalmic examinations, including visual impairment, best-corrected visual acuity, intraocular pressure (IOP), and autokeratometry. Xu et al. (2022) developed a deep learning-derived classifier (KerNet) that is helpful for distinguishing clinically unaffected eyes in patients with asymmetric keratoconus (AKC) from normal eyes.

Other studies have compared AI algorithms to detect KC. Souza et al. (2010) used three algorithms: SVM, multi-layer perceptron, and radial basis function neural networks. Notably, the three selected classifiers performed optimally, with no significant

TABLE 3 Summary of studies focused on computer-aided infection keratitis diagnosis.

Year	Authors	Imaging modality	Image size	Databases	AI algorithms	AUC (%)	Accuracy (%)	Sensitivity (%)	Specificity (%)	IoU (%)
2003	Saini et al. (2003)	Clinical data	63	Fungal ulcers/ Bacterial ulcers	ANN	—	90.70	76.47/100.00	100.00/76.47	—
2017	Sun et al. (2017)	FSI	48	Corneal ulcers	DCNN	—	86.00 (Dice)	82.00	99.00	—
2018	Wu et al. (2018)	CM	378	Normal and FK	ARBP/SVM	99.01	99.74	100.00	99.45	—
2019	Liu et al. (2020)	CM	1,213	Normal and FK	DCNN/HMF	—	99.95	99.90	100.00	—
2020	Lv et al. (2020)	CM	2088	Normal and FK	ResNet	97.69	93.64	82.56	98.89	—
2020	Kuo M. T et al. (2020)	SLI	288	FK and others	CNN (DenseNet)	65.00	69.40	71.10	68.40	—
2021	Mayya et al. (2021)	SLI	540	FK, BK, HSK, AK, and others	MS-CNN	—	88.96	90.67	87.57	—
2021	Xu F. et al. (2021)	CM	1,089	FK and BK	CNN	98.30	94.20	92.70	95.50	—
2021	Xu Y. et al. (2021)	SLI	115, 408	FK, BK, HSK, and others	CNN/TL	≥92.00	80.00	—	—	—
2021	Li Z. et al. (2021)	SLI	13, 557	Normal, keratitis, and others	DL (DenseNet121)	99.80	98.0	97.70	98.20	—
2021	Hung et al. (2021)	SLI	1,330	FK and BK	CNN (DenseNet161)	85.00	78.60	65.80	87.3	—
2021	Koyama et al. (2021)	SLI/FSI	4,306	FK, BK, HSK, and AK	DL/GBDT	≥94.60	≥90.7	—	—	—
2022	Zhang et al. (2022a)	SLI	4,830	FK, BK, HSK, and AK	CNN	≥86.00	≥70.27	≥70.00	—	—
2022	Ghosh et al. (2022)	SLI	2,167	FK and BK	CNN	90.40	83.00	77.00	—	—

FSI, fluorescein staining image; DCNN, deep convolutional neural network; CM, confocal microscopy; FK, fungal keratitis; ARBP, adaptive robust binary pattern; HMF, histogram matching fusion; SLI, slit-lamp images; BK, bacterial keratitis; HSK, herpes simplex virus stromal keratitis; AK, acanthamoeba keratitis; MS-CNN, multi-scale convolutional neural network.

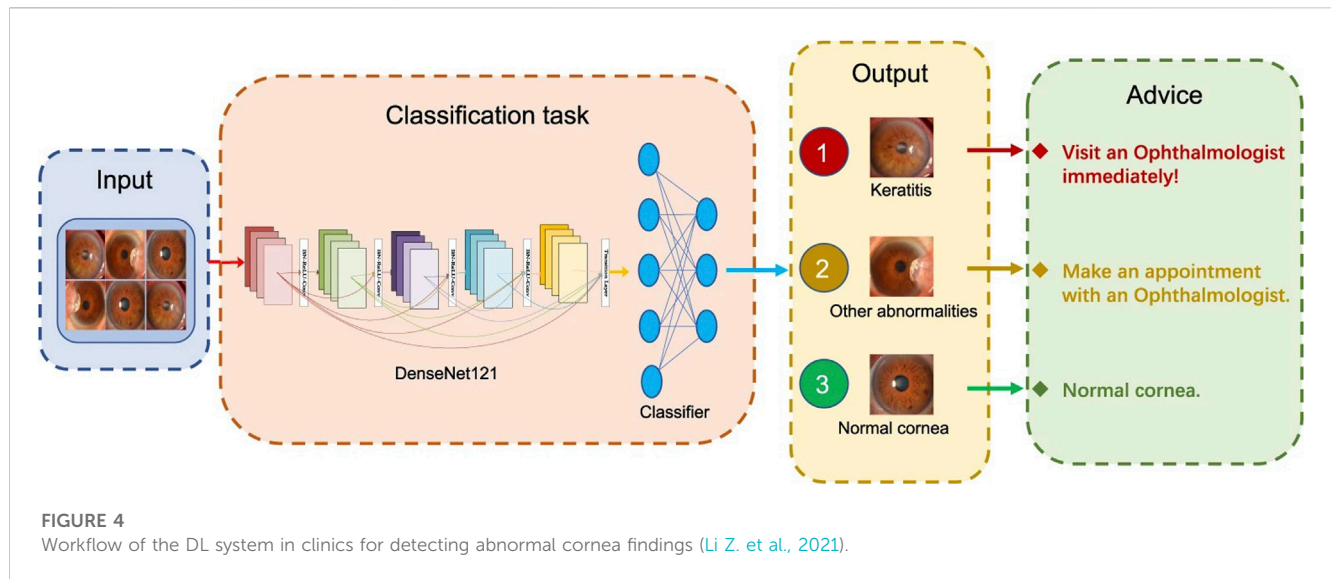
differences between their performance. [Cao et al. \(2020\)](#) found the RF model outperformed other ML algorithms using tomographic and demographic data. [Herber et al. \(2021\)](#) found that the RF model had good accuracy in predicting healthy eyes and various stages of KC. The accuracy was superior to that of the linear discriminant analysis model. [Castro-Luna et al. \(2021\)](#) also found that the RF outperformed the decision tree model (89% accuracy vs. 71%, respectively), while [Aatila et al. \(2021\)](#) found the RF model to have the highest accuracy when compared with other ML models in detecting all classes of KC.

AI has been used to screen potential candidates for refractive surgery besides detecting KC. For example, [Xie et al. \(2020\)](#) established a system centered on the AI model Pentacam InceptionResNetV2 Screening System (PIRSS) to screen normal corneas, suspected irregular corneas, early stage KC, KC, and PRK corneas. The PIRSS system achieved an overall detection accuracy of 95%, similar to that of specialists who were refractive surgeons (92.8%). Recently, [Hosoda et al. \(2020\)](#) have identified KC-susceptibility loci by integrating genome-wide association study (GWAS) with AI, demonstrating that computational techniques combined with GWAS can help identify hidden relationships

between disease susceptibility genes and potential susceptibility genes. The above research shows that the AI model is close to an experienced ophthalmologist in the classification and grading of KC.

5 AI application in infectious keratitis

Infectious keratitis is one of the most common corneal diseases that significantly causes visual impairment ([Papaioannou et al., 2016](#); [Austin et al., 2017](#); [Flaxman et al., 2017](#); [Ung et al., 2019](#)). The disease can be categorized into different types, such as bacterial keratitis (BK) ([Tuft et al., 2022](#)), fungal keratitis (FK) ([Sharma et al., 2022](#)), herpes simplex virus stromal keratitis (HSK) ([Banerjee et al., 2020](#)), or Acanthamoeba keratitis (AK) ([de Lacerda and Lira, 2021](#)). Early detection and timely medical intervention of keratitis can prevent the disease progression, thus attaining a better prognosis ([Austin et al., 2017](#); [Lin et al., 2019](#)). However, if not diagnosed and treated promptly, keratitis may lead to significant vision loss and corneal perforation ([Watson et al., 2018](#)). The diagnosis of infectious keratitis mostly depends on discriminatively identifying the visual



features of the infectious lesion in the cornea by a skilled ophthalmologist. AI analysis has been introduced into the field of keratitis diagnosis for automatic real-time identification of abnormal components in corneal images, thereby assisting ophthalmologists in rapidly diagnosing infectious keratitis. Table 3 mainly reviews AI applications for the diagnosis of infectious keratitis.

In 2003, Saini et al. (2003) assessed the usefulness of ANN for classifying infective keratitis. The trained ANN correctly classified all 63 and 39 of 43 corneal ulcers in the training and test sets, respectively. Specificity for bacterial and fungal categories was 76.47% and 100%, respectively. The accuracy of the ANN was 90.7% and was significantly better than that of the ophthalmologist's predictions (62.8%). These preliminary results suggest that using neural networks to interpret corneal ulcers requires further development. In 2017, Sun et al. (2017) established a new technique to automatically identify corneal ulcer sites using fluorescein staining images based on a CNN that labels each pixel in the staining image as an ulcer or a non-ulcer. The AI method had a mean Dice overlap of 0.86 compared with the manually delineated gold standard. In 2018, Patel et al. (2018) evaluated the variability of corneal ulcer measurements between cornea specialists and reduced clinician-dependent variability using semi-automated segmentation of ulcers from photographs. Wu et al. (2018) classified normal and FK images based on the newly proposed texture analysis method, adaptive robust binary pattern (ARBP), and the SVM, preprocessed abnormal images to enhance targets and employed the line segment detector algorithm to detect hyphae. Interestingly, it could perfectly separate abnormal from normal corneal images with an accuracy of 99.74%. Liu et al. (2020) proposed a new CNN framework for automatically diagnosing FK using data augmentation and image fusion. This study indicated that the accuracy of conventional AlexNet and VGGNet were 99.35% and 99.14%, those of AlexNet and VGGNet based on mean fusion were 99.80% and 99.83%, and those of AlexNet and VGGNet based on histogram matching fusion (HMF) were 99.95% and 99.89%. Additionally, this novel CNN framework perfectly balances

diagnostic performance and computational complexity and can improve real-time performance in diagnosing FK.

Lv et al. (2020) developed an AI system based on the DL algorithm for the automated diagnosis of FK in IVCN images. The AI system exhibited satisfactory diagnostic performance (93.64% accuracy) and effectively classified FK in various IVCN images. Xu F. et al. (2021) established an interpretable AI (XAI) system based on Gradient-weighted Class Activation Mapping (Grad-CAM) and Guided Grad-CAM and used IVCN images for FK detection. With better interpretability and explainability, XAI-assistance increased the accuracy (94.2%) and sensitivity (92.7%) of competent and novice ophthalmologists significantly without reducing specificity (95.5%). Two studies used SLI images to detect FK (Kuo M. T et al., 2020; Mayya et al., 2021). The diagnostic rate of FK in one study is 69.40% (Kuo M. T et al., 2020), while that of the other study is 88.96% (Mayya et al., 2021). Xu Y. et al. (2021) designed a sequential-level deep model to discriminate infectious corneal diseases effectively by classifying clinical images based on more than 1,10,000 SLI. The model achieved a diagnostic accuracy of 80%, much better than the 49.27% diagnostic accuracy of 421 ophthalmologists. Furthermore, Li Z. et al. (2021) developed an AI system for the automated classification of keratitis, other corneal abnormalities, and normal corneas based on 6,567 SLI (Figure 4 depicts the workflow of the DL system in clinics, which was created by Li et al.). This AI system showed remarkable performance in cornea images captured by different digital slit-lamp cameras and a smartphone with the super macro mode (all AUCs >0.96). Additionally, the system performed similarly to that of ophthalmologist specialists in classifying keratitis, cornea with other abnormalities, and normal corneas.

Furthermore, Hung et al. (2021) applied different CNN to differentiate between BK and FK using SLI. The DL algorithm achieved an average accuracy of 80.0%. Additionally, the diagnostic accuracy for BK and FK ranged from 79.6% to 95.9% and 26.3% to 65.8%, respectively. Koyama et al. (2021) adopted a DL architecture for facial recognition and applied it to determine the

TABLE 4 Summary of studies focused on computer-aided dry eye diagnosis.

Year	Authors	Imaging modality	Image size	Databases	AI algorithms	AUC (%)	Accuracy (%)	Sensitivity (%)	Specificity (%)	IoU (%)
2017	Peteiro-Barral et al. (2017)	Tearscope plus	105	Tear film classification	SVM/MLC	≥92.00	≥94.00	≥84.00	≥96.00	—
2018	Su et al. (2018)	Digital camera	80	Break-up, non-break-up, eyelid, eyelash, and sclera (TBUT)	DCNN	96.00	98.00	83.00	95.00	—
2019	Wang J. et al. (2019)	Keratograph 5M	706	MG trophy area	CNN	—	97.60	—	—	95.40
2020	Maruoka et al. (2020)	CM	137	Normal and obstructive MGD	Ensemble DL	98.10	—	92.10	98.80	—
2020	Stegmann et al. (2020)	OCT	6,658	Tear meniscus segmentation	DCNN	—	≥99.20	≥96.36	≥99.86	≥93.16
2021	Chase et al. (2021)	AS-OCT	27,180	Normal and dry eye	CNN	—	84.62	86.36	82.35	—
2021	Deng et al. (2021)	Keratograph 5M	528	Tear meniscus segmentation	FCNN	—	—	≥84.40	—	82.50
2021	Zhang et al. (2021)	CM	8,311	Normal, obstructive and atrophic MGD	CNN	≥97.30	≥97.30	≥88.80	≥95.40	—
2021	Setu et al. (2021)	Keratograph 5M	728	MG segmentation and morphology assessment	DL/TL	96.00	84.00 (Dice)	81.00	—	—
2021	Wang J. et al. (2021)	Keratograph 5M	1,443	MG segmentation and ghost glands assessment	DL	—	—	84.40	71.70	63.00
2021	Dai et al. (2021)	Keratograph 5M	120	MG morphologic	CNN	—	—	—	—	90.77
2022	Zhang et al. (2022b)	Keratograph 5M	4,006	MG density and meiboscore	Mask R-CNN/TL	90.00	—	88.00	81.00	93.00
2022	Vyas et al. (2022)	TOPCON DV3 camera	30	Normal, break-up, blink, or noise (TBUT)	CNN/TL	80.00	83.00	87.00	89.00	—

TBUT, tear film break-up time; MG, meibomian gland; MGD, meibomian gland dysfunction; FCNN, fully convolutional neural networks. Keratograph 5M: (OCULUS, Arlington, WA), a clinical instrument that uses an infrared light with wavelength 880 nm for MG imaging.

probability score for specific pathogens that cause keratitis. 4,306 SLI were studied, including 312 images from internet publications on keratitis caused by bacteria, fungi, acanthamoeba, and HSV. The developed algorithm had a high overall accuracy; for diagnosis, the accuracy/AUC for AK, BK, FK, and HSK was 97.9%/0.995, 90.7%/0.963, 95.0%/0.975, and 92.3%/0.946, respectively. [Zhang et al. \(2022a\)](#) constructed an early IK-aided diagnosis model (KeratitisNet) based on DL. The accuracy of KeratitisNet for diagnosing BK, FK, AK, and HSK was 70.27%, 77.71%, 83.81%, and 79.31%, and AUC was 0.86, 0.91, 0.96, and 0.98, respectively. [Ghosh et al. \(2022\)](#) found that compared with the single architecture model, the CNN with ensemble learning performs best in distinguishing FK from BK.

In addition to the abovementioned discrimination between different keratitis types, there is also a study of a fully-automatic DL-based algorithm for segmenting ocular structures and microbial keratitis biomarkers on SLI ([Loo et al., 2021](#)). [Tiwari et al. \(2022\)](#)

trained a CNN to differentiate active corneal ulcers from healed scars from SLI. The AI model was tested on internal (India) and external (the United States) data sets and achieved high performance (AUCs > 0.94). [Koo et al. \(2021\)](#) reported that the model detects hyphae more quickly, conveniently, and consistently through DL using CM images in real-world practice. The performance of this AI model showed high sensitivity and specificity. The above research shows different performances in the diagnosis and classification of different keratitis by AI model, but basically the accuracy is gradually improving.

6 AI application in dry eye

Dry eye is one of the most common ocular surface diseases in clinical practice, characterized by a loss of homeostasis of the tear film and accompanied by ocular abnormalities, such as tear film

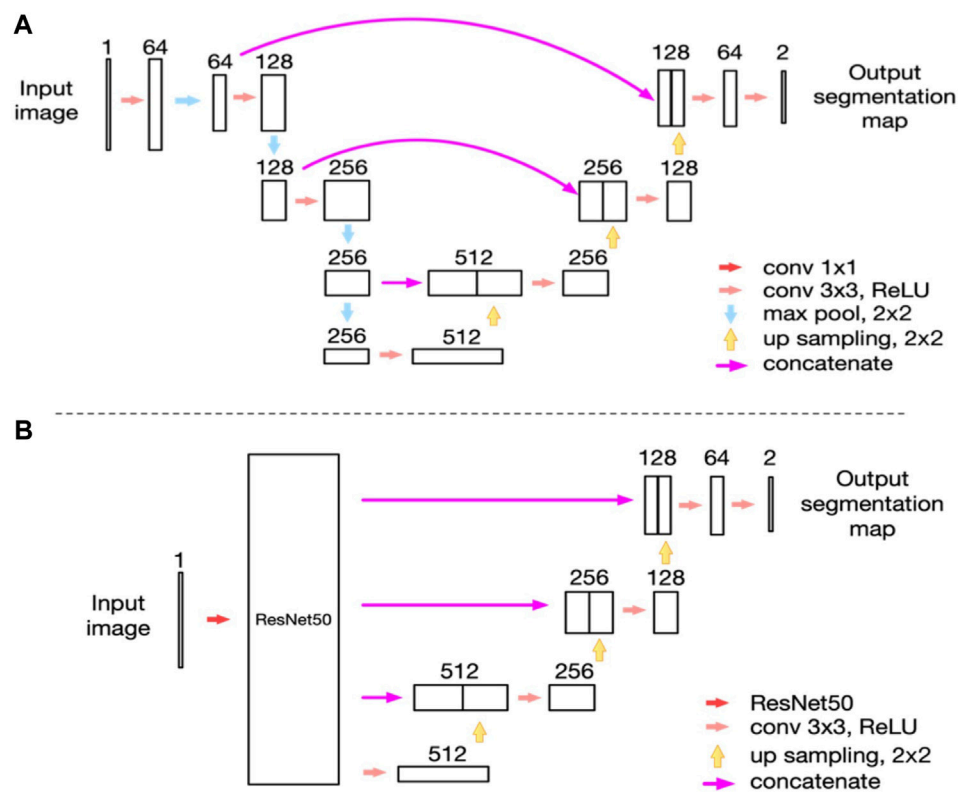


FIGURE 5

Network structure (Zhang et al., 2022b). (A) The network structure of the modified U-net model as we reported previously; (B) The network structure of the ResNet50_U-net model in this study.

instability and hyperosmolarity, ocular surface inflammation and damage, and neurosensory abnormalities (Craig et al., 2017a; Craig et al., 2017b; Stapleton et al., 2017). As the most common trigger of dry eye (Craig et al., 2017b), MGD is associated with many other ocular diseases (Sullivan et al., 2018; Lekhanont et al., 2019; Llorens-Quintana et al., 2020) and systemic factors (Arita et al., 2019; Sandra Johanna et al., 2019; Wang et al., 2020), which affect patients' quality of life, causing ocular irritation, ocular surface inflammation, and visual impairment (Sabeti et al., 2020). Therefore, evaluating the function of meibomian glands (MGs) in patients with dry eyes is essential. Furthermore, MG morphology is closely associated with the severity of MGD, and the MG image index indicates their health (Giannaccare et al., 2018). Recently, researchers have started employing image processing and image analysis software such as ImageJ to perform morphological analysis of the structure of MGs. However, semi-quantitative analysis requires manual labeling of each image, which is labor-intensive and inefficient. The efficiency of AI technology in image recognition is much higher than that of manual analysis, and the cost is significantly reduced. Table 4 mainly reviews AI applications for the diagnosis of dry eye.

In 2019, Wang J. et al. (2019) established a DL approach to digitally segment the MG atrophy area and compute the percentage atrophy in meibography images. In total, 497 meibography images were used to train and adjust the DL model, while the remaining 209 images were applied for evaluation. The AI algorithm achieves 95.6% meiboscore grading accuracy on average, significantly

outperforming the specialist by 16.0% and the clinical team by 40.6%. This study presents an accurate and consistent gland atrophy evaluation method for meibography images based on deep neural networks and may contribute to an improved understanding of MGD. However, this AI system could only predict the MG atrophy region rather than individual MG morphology. In 2020, Maruoka et al. (2020) evaluated the ability of DL models to detect obstructive MGD using *in vivo* confocal microscopy (IVCM) images. For the single DL model, the AUC, sensitivity, and specificity of diagnosing obstructive MGD were 0.966%, 94.2%, and 82.1%, respectively, and for the ensemble DL model, 0.981%, 92.1%, and 98.8%, respectively. Zhang et al. (2021) developed a DL algorithm to check and classify IVCM images of MGD automatically. By optimizing the AI algorithm, the classifier model displayed excellent accuracy. The sensitivity and specificity of the AI model for obstructive MGD were 88.8% and 95.4%, respectively, and for atrophic MGD, 89.4% and 98.4%, respectively. Furthermore, Zhou et al. (2020) used the transfer-learning mask R-CNN to build a model. The model evaluated each image in 0.499 s, whereas the average time for clinicians was more than 10 s. This study also included 2,304 MG images to construct an MG image database. The proportion of MGs marked by the model was $53.24\% \pm 11.09\%$, and the artificial marking was $52.13\% \pm 13.38\%$. Therefore, this model can improve the accuracy of examinations, save time, and be used for clinical auxiliary diagnosis and screening of diseases related to MGD. Prabhu et al. (2020) proposed an automated algorithm

TABLE 5 Comparison table of MG density and meiboscore (Zhang et al., 2022b).

	MG density					
	Upper eyelid (1,620)			Lower eyelid (2,386)		
	Median (IQR)	H-value	P	Median (IQR)	H-value	P
Meiboscore 0	0.30 (0.25–0.33)	882.932	<0.001	0.19 (0.14–0.23)	596.815	<0.001
Meiboscore 1	0.25 (0.21–0.29)			0.17 (0.13–0.21)		
Meiboscore 2	0.15 (0.12–0.18)			0.13 (0.10–0.17)		
Meiboscore 3	0.10 (0.06–0.12)			0.07 (0.04–0.11)		

MG, meibomian gland; IQR, interquartile range.

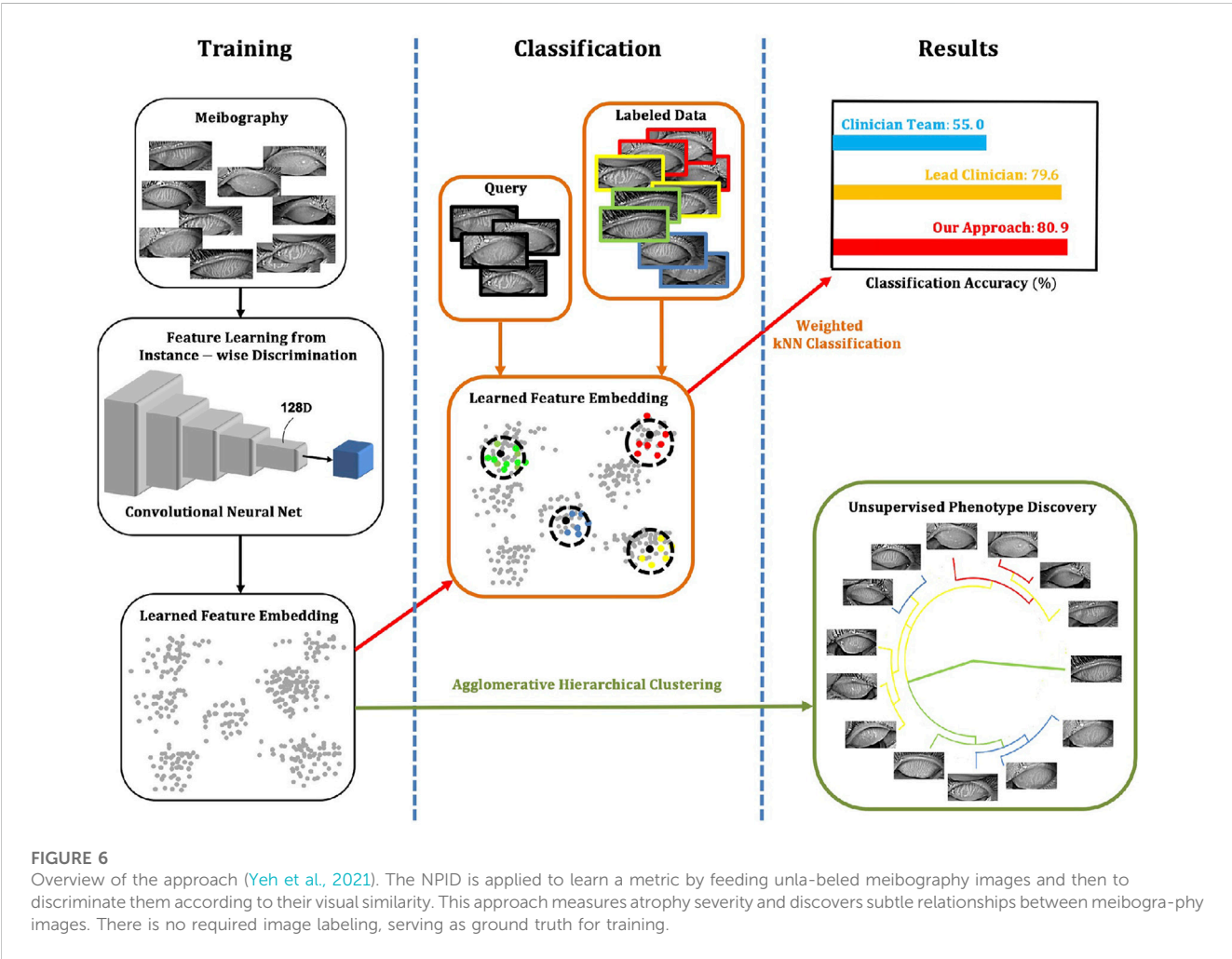


FIGURE 6 Overview of the approach (Yeh et al., 2021). The NPID is applied to learn a metric by feeding unlabeled meibography images and then to discriminate them according to their visual similarity. This approach measures atrophy severity and discovers subtle relationships between meibography images. There is no required image labeling, serving as ground truth for training.

based on DL to segment MGs and evaluated various features for quantifying these glands. This study also analyzed five clinically relevant metrics in detail and found that they represented changes associated with MGD.

In 2021, we proposed a novel MGs extraction method based on CNN (Dai et al., 2021) with an enhanced mini U-Net. Consequently, the IoU achieved 0.9077, and repeatability was 100%. The processing time for each image was 100 ms. We identified a significant and

linear correlation between MG morphology and clinical parameters using this method. This study provided a new method for quantifying morphological features of MG obtained by meibography. Furthermore, we used an advanced AI system based on ResNet_U-net (Figure 5 depicts the network structure created by Zhang et al.) to assess the effect of MG density in diagnosing MGD (Zhang et al., 2022b). The updated AI system achieved 92% accuracy (IoU) and 100% repeatability in MG

segmentation. The AUC was 0.900 for MG density in all eyelids. Sensitivity and specificity were 88% and 81%, respectively, at a cutoff value of 0.275. We compared the correspondence between MG density and meiboscore, as shown in Table 5. Thus, MG density is an effective index for MGD, particularly supported by the AI system, which could replace the meiboscore.

In 2021, Khan et al. (2021) established a model based on adversarial learning, a conditional generative adversarial network (C-GAN), to accurately detect, segment, and analyze MG. This technique significantly improved the inability of existing methods to quantify irregularities in infrared images of the MG regions. Additionally, this technique outperformed state-of-the-art results for detecting and analyzing the dropout area of the MGD. Setu et al. (2021) proposed an automatic infrared MG segmentation method based on DL (U-Net). The model was trained and evaluated using 728 anonymized clinical meibography images. The average precision, recall, and F1 scores were 83%, 81%, and 84% on the testing dataset, with an AUC value of 0.96, based on the ROC curve and the Dice coefficient of 84%. Single-image segmentation and morphometric parameter evaluations had an average of 1.33 s. Wang J. et al. (2021) developed an automated AI method to segment individual MG regions in an infrared meibography image and analyzed their morphological features. The AI algorithm, on average, achieved 63% mean IoU in segmenting glands, 84.4% sensitivity and 71.7% specificity in identifying ghost glands. Yeh et al. (2021) established an unsupervised feature learning method based on non-parametric instance discrimination (NPID) to automatically measure MG atrophy (Figure 6 illustrates an overview of the approach created by Yeh et al.). 497 meibography images were used for network learning and tuning, and the remaining 209 images were applied for network model evaluations. The proposed NPID achieved an average 80.9% meiboscore grading accuracy, outperforming the clinical team by 25.9%. Therefore, this method may aid in diagnosing and managing MGD without prior image annotations, which require time and resources.

Dry eye is complicated to diagnose since there is no single characteristic symptom or diagnostic measure. Other studies have employed AI to detect tear film, tear meniscus height (TMH), corneal morphology and blinking to diagnose dry eye besides the abovementioned assessment of dry eye by AI detection of MGs morphology. Diego et al. (Peteiro-Barral et al., 2017) proposed a method that automatically assessed tear film classification and demonstrated its effectiveness. This method applied class binarization and feature selection for optimization purposes. Su et al. (2018) proposed an automatic method to detect the fluorescent tear film break-up area using a CNN model and to define its appearance as CNN-BUT. The sensitivity and specificity of CNN-BUT in screening patients with dry eye were 0.83 and 0.95, respectively. Vyas et al. (2022) proposed a tear film break-up time (TBUT)-based dry eye detection method that detects the presence/absence of dry eye from TBUT video. This AI system exhibits high performance in classifying TBUT frames, detecting dry eye, and severity grading of TBUT video with an accuracy of 83%.

Further, Stegmann et al. (2020) evaluated lower TMH using OCT by automatically segmenting the image data using AI algorithms. The AI segmentation times were approximately two orders of magnitude faster than the previous algorithms.

Chase et al. (2021) developed a CNN algorithm to detect dry eye using AS-OCT images with good performance (accuracy = 84.62%, sensitivity = 86.36%, specificity = 82.35%). The epithelial layer and tear film were the learned areas of the AS-OCT images that differentiated images with dry eye from normal. The AI model had a significantly higher accuracy detecting dry eye than corneal staining, conjunctival staining, and Schirmer's testing. Deng et al. (2021) established a method for the automatic quantitation of lower TMH with FCNN. These neural networks have high performance owing to the modified encoder with a residual block, which has better feature extraction than the original U-Net. Additionally, the overall average IoU for tear meniscus segmentation was 82.5%. Therefore, the algorithm results of the TMH had a higher correlation with the ground truth than manually obtained results. Su et al. (2020) proposed training a deep CNN model to detect superficial punctate keratitis (SPK) automatically, and this AI method can be used to reliably grade the severity of SPK to improve the efficiency (97% accuracy) of dry eye diagnosis. Through AI analysis, Jing et al. (2022) have found a significant correlation between corneal nerve morphological changes in patients with dry eyes and intrinsic corneal aberrations, particularly higher-order aberrations. Zheng et al. (2022) established a blink analysis model using AI to generate a blink profile, which provides a new method for evaluating incomplete blinking and diagnosing dry eye. The above research shows that the AI model has achieved remarkable results in the segmentation of MG morphology in patients with dry eye.

7 AI application in other ocular surface diseases

AI has also led to many achievements in the auxiliary diagnosis and treatment of corneal edema, corneal endothelial dystrophy, corneal nerves, corneal epithelial defects, posterior elastic layer detachment, corneal perforation, corneal foreign bodies, and other ocular surface diseases. Veli and Ozcan (2018) established a cost-effective and portable platform based on contact lenses for the non-invasive detection of *Staphylococcus aureus* using a three-dimensional (3D) holographic reconstruction combined with an SVM-based ML algorithm. Interestingly, the method is characterized by low cost and portability, although the study did not include participants for clinical trials. Eleiwa et al. (2020) created and validated a DL model based on VGG19 and transferred learning to diagnose Fuchs endothelial corneal dystrophy. Additionally, Wei et al. (2020) proposed a DL model for automated sub-basal corneal nerve fiber segmentation and evaluation using IVCN. The model achieved an AUC, sensitivity, and specificity of 0.96, 96%, and 75%, respectively. However, this AI model had limitations in that it was not externally validated and could consider all parameters in the IVCN images. Zéboulon et al. (2021) established and verified a novel automated tool for detecting and visualizing corneal edema using OCT. This study trained a CNN to classify each pixel in the corneal OCT images as "normal" or "edema" and to generate colored heat maps of the result. Additionally, the optimal threshold for differentiating normal from edematous corneas was 6.8%, with an accuracy, sensitivity, and specificity of 98.7%, 96.4%, and 100%, respectively. However, the AI model could not quantitatively analyze the severity of edema, and the principle of

the model training process output results remains invisible. Li D. F et al. (2021) developed an image analysis system for AS-OCT examination results based on DL technology and evaluated its influence on identifying various corneal pathologies and quantified indices. Furthermore, the labeled AS-OCT images were used to train corneal pathology detection and stratification models based on the deep CNN algorithm. Interestingly, the average sensitivity and specificity of the corneal pathology detection model were 96.5% and 96.1%, compared with the results of manual labeling. Additionally, the average Dice coefficients of the corneal stratification model for the corneal epithelium and stroma were 0.985 and 0.917, respectively. Deshmukh et al. (2021) developed an automated segmentation DL algorithm for corneal stromal deposits in patients with corneal stromal dystrophy. Segmentation on corneal deposits was accurate *via* the DL algorithm in the well-controlled dataset and showed reasonable performance in a real-world setting. Yoo et al. (2021) developed an AI model to detect conjunctival melanoma using a digital imaging device such as smartphone camera. It showed an accuracy of 94.0% using 3D melanoma phantom images captured using a smartphone camera.

8 Discussion

With the development of modern society and the economy, people's health awareness is gradually improving, and the pressure on ophthalmologists to diagnose and treat will increase. However, although over 2,00,000 ophthalmologists exist worldwide, there is currently a severe shortfall in developing countries (Resnikoff et al., 2012). Furthermore, the number of ophthalmologists is declining in 12% of low-income countries with the lowest ophthalmologist densities and highest population growth rates (Resnikoff et al., 2020). The timely emergence of AI has given rise to optimism in the field of ophthalmology, particularly in areas involving big data and image-based analysis. DL is a branch of ML that employs multi-layer neurons with high-dimensional non-linear transformations in performing high-dimensional data abstraction to extract hidden features (Lecun et al., 2015). Therefore, with the help of DL, we can input many images as samples to the computer and allow the computer to automatically learn the high-dimensional features of the images to determine the intrinsic relationship between the images and the results. DL establishes an intrinsic relationship between input and output through multi-layer CNN mapping, similar to the human learning process. Thus far, various AI models have been developed, such as CNN, deep neural networks, deep belief networks, and RNN. These models have been applied in computer vision, speech recognition, natural language processing, audio recognition, and bioinformatics with excellent results (Lecun et al., 1998; Taigman et al., 2014; He et al., 2016). Additionally, using DL to process and analyze images of ocular surface diseases can significantly improve accuracy and efficiency, reduce manual analysis costs, and overcome errors between different experienced annotators. Currently, different AI models are used for AI applications for different ocular surface diseases. Among them, CNN model accounts for the majority of the AI applications for pterygium, keratitis and dry eye, while RF model has good accuracy in predicting healthy eyes and KC in all stages in the AI application for KC.

DL established a method for computers to automatically learn the hidden features in images and integrate feature learning into

building models, thereby reducing the incompleteness caused by artificially designed features. Patterns that are invisible to the naked eye can be picked out. For example, Kermany et al. (2018) trained a DL system to identify retinal OCT images of patients. Surprisingly, the system also accurately identified several other characteristics, including risk factors for heart disease, age, and sex. No one had previously noticed sex variations in the human retina. However, we cannot fully understand its feature extraction logic, leading to the AI "black box" since the DL neural network is very complex and has poor interpretability challenges (Ahuja and Halperin, 2019). Therefore, Kermany et al. (2018) used "occlusion testing" in their study of AI recognition of OCT retinopathy images to study the logic of AI diagnosis. This involved occluding different parts of OCT images of the fundus of patients with retinopathy. The AI erroneously categorized the lesion image as normal after considering the features of a specific section, implying that these features are the basis for the AI's judgment. Similarly, in analyzing ocular surface diseases using DL models, we can also use occlusion testing to learn the judgment basis of AI to discover new morphological evaluation indicators of ocular surface diseases. An ophthalmic multi-modal diagnostic platform using multiple modules for targeted examination of target tissues has been established and applied clinically. With advances in technology, it may be possible in the future to acquire global three-dimensional data of the eye simultaneously. Correct reading, analysis and diagnosis of acquired data require a more comprehensive and in-depth knowledge base. Compared with human beings, AI has absolute superiority in integrating information, processing data, diagnosis speed, etc.

At present, AI still has certain limitations. 1) Most ML methods have insufficient training and validation sets; therefore, more image data training is needed to improve accuracy, sensitivity, and specificity further. 2) The inspection equipment used by different countries, regions, and medical institutions differ, as do the images obtained by different inspection equipment regarding color and resolution, which will inevitably affect image acquisition and diagnostic accuracies. 3) Current ML methods cannot explain disease diagnosis, of which the output results are learned only from the training set. 4) AI cannot learn effectively for some difficult and rare ocular surface diseases with insufficient data. Therefore, it is difficult to obtain an effective and correct diagnosis rate. Although AI still faces certain challenges in model building, it can assist doctors with objective clinical decisions and lay the foundation for the accurate treatment of patients. These issues must be adequately addressed before AI can be translated into clinical applications in ophthalmology.

In conclusion, AI has great potential to improve the diagnostic efficiency of ocular surface diseases. The novelty of this study is evidenced by its contribution to the existing literature, as it is one of the studies to provide information on research hotspots and trends in the application of AI in diagnosing ocular surface diseases. Furthermore, the results reveal that although AI still faces certain challenges in model building, it can assist doctors with objective clinical decisions and lay the foundation for the accurate treatment of patients. Ultimately, AI algorithms and tools in development for ocular surface disease are helping us to understand disease pathogenesis, identify disease biomarkers, and develop novel treatments for ocular surface disease.

Author contributions

Writing—original draft preparation, ZZ; Formal analysis, YW and HZ; Writing—review, AS and HR; Editing, CX and MA; Supervision, QC; Conceptualization, QD. All authors have read and agreed to the published version of the manuscript.

Funding

This research was funded by the Zhejiang Provincial Medical and Health Science Technology Program of Health and Family Planning Commission (grant number: 2022PY074; grant number: 2022KY217), and by the Scientific Research Fund of Zhejiang Provincial Education Department (Y202147994).

References

- Aatila, M., Lachgar, M., Hamid, H., and Kartit, A. (2021). Keratoconus severity classification using features selection and machine learning algorithms. *Comput. Math. Methods Med.* 2021, 9979560. doi:10.1155/2021/9979560
- Abdani, S. R., Zulkifley, M. A., and Hussain, A. (2019). "Compact convolutional neural networks for pterygium classification using transfer learning," in IEEE International Conference on Signal and Image Processing Applications, Kuala Lumpur, Malaysia, 17–19 September 2019, 140–143. doi:10.1109/ICSIPA45851.2019.8977757
- Abdani, S. R., Zulkifley, M. A., and Moubark, A. M. (2020). "Pterygium tissues segmentation using densely connected DeepLab," in Proceedings of the 2020 IEEE 10th Symposium on Computer Applications Industrial Electronics (ISCAIE), Malaysia, April 18–19 2020, 229–232. doi:10.1109/ISCAIE47305.2020.9108822
- Abdani, S. R., Zulkifley, M. A., and Zulkifley, N. H. (2021). Group and shuffle convolutional neural networks with pyramid pooling module for automated pterygium segmentation. *Diagn. (Basel)* 11 (6), 1104. doi:10.3390/diagnostics11061104
- Abdelmotaal, H., Mostafa, M. M., Mostafa, A. N. R., Mohamed, A. A., and Abdelazeem, K. (2020). Classification of color-coded Scheimpflug camera corneal tomography images using deep learning. *Transl. Vis. Sci. Technol.* 9 (13), 30. doi:10.1167/tvst.9.13.30
- Accardo, P. A., and Pensiero, S. (2002). Neural network-based system for early keratoconus detection from corneal topography. *J. Biomed. Inf.* 35 (3), 151–159. doi:10.1016/S1532-0464(02)00513-0
- Ahn, H., Kim, N. E., Chung, J. L., Kim, Y. J., Jun, I., Kim, T. I., et al. (2022). Patient selection for corneal topographic evaluation of keratoconus: A screening approach using artificial intelligence. *Front. Med. (Lausanne)* 9, 934865. doi:10.3389/fmed.2022.934865
- Ahuja, A. S., and Halperin, L. S. (2019). Understanding the advent of artificial intelligence in ophthalmology. *J. Curr. Ophthalmol.* 31 (2), 115–117. doi:10.1016/j.joco.2019.05.001
- Al-Timemy, A. H., Mosa, Z. M., Alyasseri, Z., Lavric, A., Lui, M. M., Hazarbassanov, R. M., et al. (2021). A hybrid deep learning construct for detecting keratoconus from corneal maps. *Transl. Vis. Sci. Technol.* 10 (14), 16. doi:10.1167/tvst.10.14.16
- Arbelaez, M. C., Versaci, F., Vestri, G., Barboni, P., and Savini, G. (2012). Use of a support vector machine for keratoconus and subclinical keratoconus detection by topographic and tomographic data. *Ophthalmology* 119 (11), 2231–2238. doi:10.1016/j.optha.2012.06.005
- Arita, R., Mizoguchi, T., Kawashima, M., Fukuoka, S., Koh, S., Shirakawa, R., et al. (2019). Meibomian gland dysfunction and dry eye are similar but different based on a population-based study: The hirado-takushima study in Japan. *Am. J. Ophthalmol.* 207, 410–418. doi:10.1016/j.ajo.2019.02.024
- Asaoka, R., Murata, H., Hirasawa, K., Fujino, Y., Matsuura, M., Miki, A., et al. (2019). Using deep learning and transfer learning to accurately diagnose early-onset glaucoma from macular optical coherence tomography images. *Am. J. Ophthalmol.* 198, 136–145. doi:10.1016/j.ajo.2018.10.007
- Austin, A., Lietman, T., and Rose-Nussbaumer, J. (2017). Update on the management of infectious keratitis. *Ophthalmology* 124 (11), 1678–1689. doi:10.1016/j.optha.2017.05.012
- Banerjee, A., Kulkarni, S., and Mukherjee, A. (2020). Herpes simplex virus: The hostile guest that takes over your home. *Front. Microbiol.* 11, 733. doi:10.3389/fmicb.2020.00733
- Burlina, P. M., Joshi, N., Pekala, M., Pacheco, K. D., Freund, D. E., and Bressler, N. M. (2017). Automated grading of age-related macular degeneration from color fundus images using deep convolutional neural networks. *JAMA Ophthalmol.* 135 (11), 1170–1176. doi:10.1001/jamaophthalmol.2017.3782
- Cao, K., Verspoor, K., Chan, E., Daniell, M., Sahebajada, S., and Baird, P. N. (2021). Machine learning with a reduced dimensionality representation of comprehensive pentacam tomography parameters to identify subclinical keratoconus. *Comput. Biol. Med.* 138, 104884. doi:10.1016/j.combiomed.2021.104884
- Cao, K., Verspoor, K., Sahebajada, S., and Baird, P. N. (2020). Evaluating the performance of various machine learning algorithms to detect subclinical keratoconus. *Transl. Vis. Sci. Technol.* 9 (2), 24. doi:10.1167/tvst.9.2.24
- Castro-Luna, G., Jiménez-Rodríguez, D., Castaño-Fernández, A. B., and Pérez-Rueda, A. (2021). Diagnosis of subclinical keratoconus based on machine learning techniques. *J. Clin. Med.* 10 (18), 4281. doi:10.3390/jcm10184281
- Chase, C., Elsayy, A., Eleiwa, T., Ozcan, E., Tolba, M., and Abou Shousha, M. (2021). Comparison of autonomous AS-OCT deep learning algorithm and clinical dry eye tests in diagnosis of dry eye disease. *Clin. Ophthalmol.* 15, 4281–4289. doi:10.2147/OPTH.S321764
- Chen, X., Zhao, J., Iselin, K. C., Borroni, D., Romano, D., Gokul, A., et al. (2021). Keratoconus detection of changes using deep learning of colour-coded maps. *B.M.J. Open Ophthalmol.* 6 (1), e000824. doi:10.1136/bmjophth-2021-000824
- Clearfield, E., Muthappan, V., Wang, X., and Kuo, I. C. (2016). Conjunctival autograft for pterygium. *Cochrane Database Syst. Rev.* 2 (2), CD011349. doi:10.1002/14651858.CD011349.pub2
- Craig, J. P., Nelson, J. D., Azar, D. T., Belmonte, C., Bron, A. J., Chauhan, S. K., et al. (2017). TFOS DEWS II report executive summary. *Ocul. Surf.* 15 (4), 802–812. doi:10.1016/j.jtos.2017.08.003
- Craig, J. P., Nichols, K. K., Akpek, E. K., Caffery, B., Dua, H. S., Joo, C. K., et al. (2017). TFOS DEWS II definition and classification report. *Ocul. Surf.* 15 (3), 276–283. doi:10.1016/j.jtos.2017.05.008
- Dai, Q., Liu, X., Lin, X., Fu, Y., Chen, C., Yu, X., et al. (2021). A novel meibomian gland morphology analytic system based on a convolutional neural network. *Ieee. Access* 9, 23083–23094. doi:10.1109/ACCESS.2021.3056234
- de Lacerda, A. G., and Lira, M. (2021). Acanthamoeba keratitis: A review of Biology, pathophysiology and epidemiology. *Ophthalmic Physiol. Opt.* 41 (1), 116–135. doi:10.1111/opo.12752
- Deng, X., Tian, L., Liu, Z., Zhou, Y., and Jie, Y. A. (2021). A deep learning approach for the quantification of lower tear meniscus height. *Biomed. Signal Process. Control* 68, 102655. doi:10.1016/j.bspc.2021.102655
- Deshmukh, M., Liu, Y. C., Rim, T. H., Venkatraman, A., Davidson, M., Yu, M., et al. (2021). Automatic segmentation of corneal deposits from corneal stromal dystrophy images via deep learning. *Comput. Biol. Med.* 137, 104675. doi:10.1016/j.combiomed.2021.104675
- Devalla, S. K., Chin, K. S., Mari, J. M., Tun, T. A., Strouthidis, N. G., Aung, T., et al. (2018). A deep learning approach to digitally stain optical coherence tomography images of the optic nerve head. *Invest. Ophthalmol. Vis. Sci.* 59 (1), 63–74. doi:10.1167/iovs.17-22617
- Dey, D., Slomka, P. J., Leeson, P., Comaniciu, D., Shrestha, S., SenGupta, P. P., et al. (2019). Artificial intelligence in cardiovascular imaging: JACC state-of-the-art review. *J. Am. Coll. Cardiol.* 73 (11), 1317–1335. doi:10.1016/j.jacc.2018.12.054

Conflict of interest

The authors declare that the research was conducted in the absence of any commercial or financial relationships that could be construed as a potential conflict of interest.

Publisher's note

All claims expressed in this article are solely those of the authors and do not necessarily represent those of their affiliated organizations, or those of the publisher, the editors and the reviewers. Any product that may be evaluated in this article, or claim that may be made by its manufacturer, is not guaranteed or endorsed by the publisher.

- Dos Santos, V. A., Schmetterer, L., Stegmann, H., Pfister, M., Messner, A., Schmidinger, G., et al. (2019). CorneaNet: Fast segmentation of cornea OCT scans of healthy and keratoconic eyes using deep learning. *Biomed. Opt. Express* 10 (2), 622–641. doi:10.1364/BOE.10.000622
- Eleiwa, T., Elsayy, A., Özcan, E., and Abou Shousha, M. (2020). Automated diagnosis and staging of Fuchs' endothelial cell corneal dystrophy using deep learning. *Eye Vis. (Lond)* 7, 44. doi:10.1186/s40662-020-00209-z
- Fang, X., Deshmukh, M., Chee, M. L., Soh, Z. D., Teo, Z. L., Thakur, S., et al. (2022). Deep learning algorithms for automatic detection of pterygium using anterior segment photographs from slit-lamp and hand-held cameras. *Br. J. Ophthalmol.* 106 (12), 1642–1647. doi:10.1136/bjophthalmol-2021-318866
- Flaxman, S. R., Bourne, R. A., Resnikoff, S., Ackland, P., Braithwaite, T., Cicinelli, M. V., et al. (2017). Global causes of blindness and distance vision impairment 1990–2020: A systematic review and meta-analysis. *Lancet Glob. Health* 5 (12), e1221–e1234. doi:10.1016/S2214-109X(17)30393-5
- Gao, X., Lin, S., and Wong, T. Y. (2015). Automatic feature learning to grade nuclear cataracts based on deep learning. *Ieee. Trans. Bio Med. Eng.* 62 (11), 2693–2701. doi:10.1109/TBME.2015.2444389
- Gao, X., Wong, D. W., Aryaputera, A. W., Sun, Y., Cheng, C. Y., Cheung, C., et al. (2012). "Automatic pterygium detection on cornea images to enhance computer-aided cortical cataract grading system," in 2012 Annual International Conference of the IEEE Engineering in Medicine and Biology Society, San Diego, CA, USA, 28 August 2012 - 01 September 2012, 4434–4437. doi:10.1109/EMBC.2012.6346950
- Gazzard, G., Saw, S. M., Farook, M., Koh, D., Widjaja, D., Chia, S. E., et al. (2002). Pterygium in Indonesia: Prevalence, severity and risk factors. *Br. J. Ophthalmol.* 86 (12), 1341–1346. doi:10.1136/bjo.86.12.1341
- Ghaderi, M., Sharifi, A., and Jafarzadeh Pour, E. (2021). Proposing an ensemble learning model based on neural network and fuzzy system for keratoconus diagnosis based on pentacam measurements. *Int. Ophthalmol.* 41 (12), 3935–3948. doi:10.1007/s10792-021-01963-2
- Ghosh, A. K., Thammasudjarit, R., Jongkhajornpong, P., Attia, J., and Thakkestian, A. (2022). Deep learning for discrimination between fungal keratitis and bacterial keratitis: DeepKeratitis. *Cornea* 41 (5), 616–622. doi:10.1097/ICO.0000000000002830
- Giannaccare, G., Vigo, L., Pellegrini, M., Sebastiani, S., and Carones, F. (2018). Ocular surface workup with automated noninvasive measurements for the diagnosis of meibomian gland dysfunction. *Cornea* 37 (6), 740–745. doi:10.1097/ICO.0000000000001500
- Gomes, J. A., Tan, D., Rapuano, C. J., Belin, M. W., Ambrósio, R., Jr., Guell, J. L., et al. (2015). Global consensus on keratoconus and ectatic diseases. *Cornea* 34 (4), 359–369. doi:10.1097/ICO.0000000000000408
- Gulshan, V., Peng, L., Coram, M., Stumpe, M. C., Wu, D., Narayanaswamy, A., et al. (2016). Development and validation of a deep learning algorithm for detection of diabetic retinopathy in retinal fundus photographs. *JAMA* 316 (22), 2402–2410. doi:10.1001/jama.2016.17216
- He, K., Zhang, X., Ren, S., and Sun, J. (2016). "Deep residual learning for image recognition," in IEEE Conference on Computer Vision and Pattern Recognition (CVPR), Las Vegas, NV, USA, 27–30 June 2016, 770–778. doi:10.1109/CVPR.2016.90
- Henein, C., and Nanavaty, M. A. (2017). Systematic review comparing penetrating keratoplasty and deep anterior lamellar keratoplasty for management of keratoconus. *Cont. Lens Anterior Eye* 40 (1), 3–14. doi:10.1016/j.clae.2016.10.001
- Herber, R., Pillunat, L. E., and Raiskup, F. (2021). Development of a classification system based on corneal biomechanical properties using artificial intelligence predicting keratoconus severity. *Eye Vis. (Lond)* 8 (1), 21. doi:10.1186/s40662-021-00244-4
- Hosoda, Y., Miyake, M., Meguro, A., Tabara, Y., Iwai, S., Ueda-Arakawa, N., et al. (2020). Keratoconus-susceptibility gene identification by corneal thickness genome-wide association study and artificial intelligence IBM watson. *Commun. Biol.* 3 (1), 410. doi:10.1038/s42003-020-01137-3
- Hung, K. H., Lin, C., Roan, J., Kuo, C. F., Hsiao, C. H., Tan, H. Y., et al. (2022). Application of a deep learning system in pterygium grading and further prediction of recurrence with slit lamp photographs. *Diagn. (Basel)* 12 (4), 888. doi:10.3390/diagnostics12040888
- Hung, N., Shih, A. K., Lin, C., Kuo, M. T., Hwang, Y. S., Wu, W. C., et al. (2021). Using slit-lamp images for deep learning-based identification of bacterial and fungal keratitis: Model development and validation with different convolutional neural networks. *Diagn. (Basel)* 11 (7), 1246. doi:10.3390/diagnostics11071246
- Issarti, I., Consejo, A., Jiménez-García, M., Hershko, S., Koppen, C., and Rozema, J. J. (2019). Computer aided diagnosis for suspect keratoconus detection. *Comput. Biol. Med.* 109, 33–42. doi:10.1016/j.combiomed.2019.04.024
- Jing, D., Liu, Y., Chou, Y., Jiang, X., Ren, X., Yang, L., et al. (2022). Change patterns in the corneal sub-basal nerve and corneal aberrations in patients with dry eye disease: An artificial intelligence analysis. *Exp. Eye Res.* 215, 108851. doi:10.1016/j.exer.2021.108851
- Kamiya, K., Ayatsuka, Y., Kato, Y., Fujimura, F., Takahashi, M., Shoji, N., et al. (2019). Keratoconus detection using deep learning of colour-coded maps with anterior segment optical coherence tomography: A diagnostic accuracy study. *BMJ Open* 9 (9), e031313. doi:10.1136/bmjopen-2019-031313
- Kamiya, K., Ayatsuka, Y., Kato, Y., Shoji, N., Mori, Y., and Miyata, K. (2021a). Diagnosability of keratoconus using deep learning with placido disk-based corneal topography. *Front. Med. (Lausanne)* 8, 724902. doi:10.3389/fmed.2021.724902
- Kamiya, K., Ayatsuka, Y., Kato, Y., Shoji, N., Miyai, T., Ishii, H., et al. (2021b). Prediction of keratoconus progression using deep learning of anterior segment optical coherence tomography maps. *Ann. Transl. Med.* 9 (16), 1287. doi:10.21037/atm-21-1772
- Kato, N., Masumoto, H., Tanabe, M., Sakai, C., Negishi, K., Torii, H., et al. (2021). Predicting keratoconus progression and need for corneal crosslinking using deep learning. *J. Clin. Med.* 10 (4), 844. doi:10.3390/jcm10040844
- Kermany, D. S., Goldbaum, M., Cai, W., Valentim, C. C. S., Liang, H., Baxter, S. L., et al. (2018). Identifying medical diagnoses and treatable diseases by image-based deep learning. *Cell* 172 (5), 1122–1131.e9. doi:10.1016/j.cell.2018.02.010
- Khan, Z. K., Umar, A. I., Shirazi, S. H., Rasheed, A., Qadir, A., and Gul, S. (2021). Image based analysis of meibomian gland dysfunction using conditional generative adversarial neural network. *B.M.J. Open Ophthalmol.* 6 (1), e000436. doi:10.1136/bmjophth-2020-000436
- Kim, J. H., Kim, Y. J., Lee, Y. J., Hyon, J. Y., Han, S. B., and Kim, K. G. (2022). Automated histopathological evaluation of pterygium using artificial intelligence. *Br. J. Ophthalmol.* 106 (12), 1320–1324. doi:10.1136/bjophthalmol-2021-320141
- Koo, T., Kim, M. H., and Jue, M. S. (2021). Automated detection of superficial fungal infections from microscopic images through a regional convolutional neural network. *PLOS ONE* 16 (8), e0256290. doi:10.1371/journal.pone.0256290
- Kovács, I., Mihály, K., Kránitz, K., Juhász, É., Takács, Á., Dienes, L., et al. (2016). Accuracy of machine learning classifiers using bilateral data from a Scheimpflug camera for identifying eyes with preclinical signs of keratoconus. *J. Cataract. Refract. Surg.* 42 (2), 275–283. doi:10.1016/j.jcrs.2015.09.020
- Koyama, A., Miyazaki, D., Nakagawa, Y., Ayatsuka, Y., Miyake, H., Ehara, F., et al. (2021). Determination of probability of causative pathogen in infectious keratitis using deep learning algorithm of slit-lamp images. *Sci. Rep.* 11 (1), 22642. doi:10.1038/s41598-021-02138-w
- Kucur, Ş. S., Holló, G., and Sznitman, R. A. (2018). A deep learning approach to automatic detection of early glaucoma from visual fields. *Plos One* 13 (11), e0206081. doi:10.1371/journal.pone.0206081
- Kundu, G., Shetty, R., Khamar, P., Mullick, R., Gupta, S., Nuijts, R., et al. (2021). Universal architecture of corneal segmental tomography biomarkers for artificial intelligence-driven diagnosis of early keratoconus. *Br. J. Ophthalmol.* 105 (12), 1319–1324. doi:10.1136/bjophthalmol-2021-319309
- Kuo, B. I., Chang, W. Y., Liao, T. S., Liu, F. Y., Liu, H. Y., Chu, H. S., et al. (2020). Keratoconus screening based on deep learning approach of corneal topography. *Transl. Vis. Sci. Technol.* 9 (2), 53. doi:10.1167/tvst.9.2.53
- Kuo, M. T., Hsu, B. W., Yin, Y. K., Fang, P. C., Lai, H. Y., Chen, A., et al. (2020). A deep learning approach in diagnosing fungal keratitis based on corneal photographs. *Sci. Rep.* 10 (1), 14424. doi:10.1038/s41598-020-71425-9
- Lavric, A., and Valentin, P. (2019). KeratoDetect: Keratoconus detection algorithm using convolutional neural networks. *Comput. Intell. Neurosci.* 2019, 8162567. doi:10.1155/2019/8162567
- Lawrence, D. R., Palacios-González, C., and Harris, J. (2016). Artificial intelligence. *Camb. Q. Healthc. Ethics* 25 (2), 250–261. doi:10.1017/S0963180115000559
- Lecun, Y., Bengio, Y., and Hinton, G. (2015). Deep learning. *Nature* 521 (7553), 436–444. doi:10.1038/nature14539
- Lecun, Y., Bottou, L., Bengio, Y., and Haffner, P. (1998). Gradient-based learning applied to document recognition. *Proc. IEEE* 86 (11), 2278–2324. doi:10.1109/5.726791
- Lekhanont, K., Jongkhajornpong, P., Sontichai, V., Anothaisintawee, T., and Nijvipakul, S. (2019). Evaluating dry eye and meibomian gland dysfunction with meibography in patients with stevens-johnson syndrome. *Cornea* 38 (12), 1489–1494. doi:10.1097/ICO.0000000000002025
- Li, D. F., Dong, Y. L., Xie, S., Guo, Z., Li, S. X., Guo, Y., et al. (2021). Deep learning based lesion detection from anterior segment optical coherence tomography images and its application in the diagnosis of keratoconus. *Zhonghua Yan Ke Za Zhi* 57 (6), 447–453. doi:10.3760/cma.j.cn112142-20200818-00540
- Li, Z., Jiang, J., Chen, K., Chen, Q., Zheng, Q., Liu, X., et al. (2021). Preventing corneal blindness caused by keratitis using artificial intelligence. *Nat. Commun.* 12 (1), 3738. doi:10.1038/s41467-021-24116-6
- Lin, A., Rhee, M. K., Akpek, E. K., Amescua, G., Farid, M., Garcia-Ferrer, F. J., et al. (2019). Bacterial keratitis preferred practice Pattern®. *Ophthalmology* 126 (1), P1–P55. doi:10.1016/j.opht.2018.10.018
- Liu, Z., Cao, Y., Li, Y., Xiao, X., Qiu, Q., Yang, M., et al. (2020). Automatic diagnosis of fungal keratitis using data augmentation and image fusion with deep convolutional neural network. *Comput. Methods Programs Biomed.* 187, 105019. doi:10.1016/j.cmpb.2019.105019
- Llorens-Quintana, C., Garaszczuk, I. K., and Szczesna-Iskander, D. H. (2020). Meibomian glands structure in daily disposable soft contact lens wearers: A one-year follow-up study. *Ophthalmic Physiol. Opt.* 40 (5), 607–616. doi:10.1111/opo.12720

- Long, E., Lin, H., Liu, Z., Wu, X., Wang, L., Jiang, J., et al. (2017). An artificial intelligence platform for the multihospital collaborative management of congenital cataracts. *Nat. Biomed. Eng.* 1 (2), 0024. doi:10.1038/s41551-016-0024
- Lo, J., Kriegl, M. F., Tuohy, M. M., Kim, K. H., Prajna, V., Woodward, M. A., et al. (2021). Open-source automatic segmentation of ocular structures and biomarkers of microbial keratitis on slit-lamp photography images using deep learning. *Ieee. J. Biomed. Health Inf.* 25 (1), 88–99. doi:10.1109/JBHI.2020.2983549
- Lv, J., Zhang, K., Chen, Q., Chen, Q., Huang, W., Cui, L., et al. (2020). Deep learning-based automated diagnosis of fungal keratitis with *in vivo* confocal microscopy images. *Ann. Transl. Med.* 8 (11), 706. doi:10.21037/atm.2020.03.134
- Malyugin, B., Sakhnov, S., Izmailova, S., Boiko, E., Pozdeyeva, N., Axenova, L., et al. (2021). Keratoconus diagnostic and treatment algorithms based on machine-learning methods. *Diagn. (Basel)* 11 (10), 1933. doi:10.3390/diagnostics11101933
- Maruoka, S., Tabuchi, H., Nagasato, D., Masumoto, H., Chikama, T., Kawai, A., et al. (2020). Deep neural network-based method for detecting obstructive meibomian gland dysfunction with *in vivo* laser confocal microscopy. *Cornea* 39 (6), 720–725. doi:10.1097/ICO.0000000000002279
- Mas Tur, V., MacGregor, C., Jayaswal, R., O'Brart, D., and Maycock, N. A. (2017). A review of keratoconus: Diagnosis, pathophysiology, and genetics. *Surv. Ophthalmol.* 62 (6), 770–783. doi:10.1016/j.survophthal.2017.06.009
- Mayya, V., Kamath Shevgoor, S., Kulkarni, U., Hazarika, M., Barua, P. D., and Acharya, U. R. (2021). Multi-scale convolutional neural network for accurate corneal segmentation in early detection of fungal keratitis. *J. Fungi (Basel)* 7 (10), 850. doi:10.3390/jof7100850
- Mesquita, R. G., and Figueiredo, E. M. N. (2012). "An algorithm for measuring pterygium's progress in already diagnosed eyes," in 2012 IEEE International Conference on Acoustics, Speech and Signal Processing (ICASSP), Kyoto, Japan, 25–30 March 2012, 733–736. doi:10.1109/ICASSP.2012.6287988
- Mohammadpour, M., Heidari, Z., Hashemi, H., Yaseri, M., and Fotouhi, A. (2022). Comparison of artificial intelligence-based machine learning classifiers for early detection of keratoconus. *Eur. J. Ophthalmol.* 32 (3), 1352–1360. doi:10.1177/11206721211073442
- Nagasato, D., Tabuchi, H., Ohsugi, H., Masumoto, H., Enno, H., Ishitobi, N., et al. (2019). Deep-learning classifier with ultrawide-field fundus ophthalmoscopy for detecting branch retinal vein occlusion. *Int. J. Ophthalmol.* 12 (1), 94–99. doi:10.18240/ijo.2019.01.15
- Niazi, M. K. K., Parwani, A. V., and Gurcan, M. N. (2019). Digital pathology and artificial intelligence. *Lancet Oncol.* 20 (5), e253–e261. doi:10.1016/S1470-2045(19)30154-8
- Papaioannou, L., Miligkos, M., and Papathanassiou, M. (2016). Corneal collagen cross-linking for infectious keratitis: A systematic review and meta-analysis. *Cornea* 35 (1), 62–71. doi:10.1097/ICO.0000000000000644
- Patel, T. P., Prajna, N. V., Farsiou, S., Valikodath, N. G., Niziol, L. M., Dudeja, L., et al. (2018). Novel image-based analysis for reduction of clinician-dependent variability in measurement of the corneal ulcer size. *Cornea* 37 (3), 331–339. doi:10.1097/ICO.0000000000001488
- Peteiro-Barral, D., Remeseiro, B., Méndez, R., and Penedo, M. G. (2017). Evaluation of an automatic dry eye test using MCDM methods and rank correlation. *Med. Biol. Eng. Comput.* 55 (4), 527–536. doi:10.1007/s11517-016-1534-5
- Prabhu, S. M., Chakiat, A., S., S., Vunnavu, K. P., and Shetty, R. (2020). Deep learning segmentation and quantification of meibomian glands. *Biomed. Signal Process. Control* 57 (3), 101776. doi:10.1016/j.bspc.2019.101776
- Rahimy, E. (2018). Deep learning applications in ophthalmology. *Curr. Opin. Ophthalmol.* 29 (3), 254–260. doi:10.1097/ICU.0000000000000470
- Resnikoff, S., Felch, W., Gauthier, T. M., and Spivey, B. (2012). The number of ophthalmologists in practice and training worldwide: A growing gap despite more than 200,000 practitioners. *Br. J. Ophthalmol.* 96 (6), 783–787. doi:10.1136/bjophthalmol-2011-301378
- Resnikoff, S., Lansingh, V. C., Washburn, L., Felch, W., Gauthier, T. M., Taylor, H. R., et al. (2020). Estimated number of ophthalmologists worldwide (international council of ophthalmology update): Will we meet the needs? *Br. J. Ophthalmol.* 104 (4), 588–592. doi:10.1136/bjophthalmol-2019-314336
- Ruiz Hidalgo, I., Rodriguez, P., Rozema, J. J., Ni Dhuhghaill, S., Zakaria, N., Tassignon, M. J., et al. (2016). Evaluation of a machine-learning classifier for keratoconus detection based on Scheimpflug tomography. *Cornea* 35 (6), 827–832. doi:10.1097/ICO.0000000000000834
- Saba, L., Biswas, M., Kuppli, V., Cuadrado Godia, E., Suri, H. S., Edla, D. R., et al. (2019). The present and future of deep learning in radiology. *Eur. J. Radiol.* 114, 14–24. doi:10.1016/j.ejrad.2019.02.038
- Sabeti, S., Kheirkhah, A., Yin, J., and Dana, R. (2020). Management of meibomian gland dysfunction: A review. *Surv. Ophthalmol.* 65 (2), 205–217. doi:10.1016/j.survophthal.2019.08.007
- Saini, J. S., Jain, A. K., Kumar, S., Vikal, S., Pankaj, S., and Singh, S. (2003). Neural network approach to classify infective keratitis. *Curr. Eye Res.* 27 (2), 111–116. doi:10.1076/ceyr.27.2.111.15949
- Sandra Johanna, G. P. S., Antonio, L. A., and Andrés, G. S. (2019). Correlation between type 2 diabetes, dry eye and meibomian glands dysfunction. *J. Optom.* 12 (4), 256–262. doi:10.1016/j.optom.2019.02.003
- Setu, M. A. K., Horstmann, J., Schmidt, S., Stern, M. E., and Steven, P. (2021). Deep learning-based automatic meibomian gland segmentation and morphology assessment in infrared meibography. *Sci. Rep.* 11 (1), 7649. doi:10.1038/s41598-021-87314-8
- Sharma, N., Bagga, B., Singhal, D., Nagpal, R., Kate, A., Saluja, G., et al. (2022). Fungal keratitis: A review of clinical presentations, treatment strategies and outcomes. *Ocul. Surf.* 24, 22–30. doi:10.1016/j.jtos.2021.12.001
- Shi, C., Wang, M., Zhu, T., Zhang, Y., Ye, Y., Jiang, J., et al. (2020). Machine learning helps improve diagnostic ability of subclinical keratoconus using Scheimpflug and OCT imaging modalities. *Eye Vis. (Lond)* 7, 48. doi:10.1186/s40662-020-00213-3
- Smadja, D., Touboul, D., Cohen, A., Doveh, E., Santhiago, M. R., Mello, G. R., et al. (2013). Detection of subclinical keratoconus using an automated decision tree classification. *Am. J. Ophthalmol.* 156 (2), 237–246. e1. doi:10.1016/j.ajo.2013.03.034
- Smolek, M. K., and Klyce, S. D. (1997). Current keratoconus detection methods compared with a neural network approach. *Invest. Ophthalmol. Vis. Sci.* 38 (11), 2290–2299.
- Souza, M. B., Medeiros, F. W., Souza, D. B., Garcia, R., and Alves, M. R. (2010). Evaluation of machine learning classifiers in keratoconus detection from orbscan II examinations. *Clin. (Sao Paulo)* 65 (12), 1223–1228. doi:10.1590/s1807-59322010001200002
- Stapleton, F., Alves, M., Bunya, V. Y., Jalbert, I., Lekhanont, K., Malet, F., et al. (2017). TFOS DEWS II epidemiology report. *Ocul. Surf.* 15 (3), 334–365. doi:10.1016/j.jtos.2017.05.003
- Stegmann, H., Werkmeister, R. M., Pfister, M., Garhöfer, G., Schmetterer, L., and Dos Santos, V. A. (2020). Deep learning segmentation for optical coherence tomography measurements of the lower tear meniscus. *Biomed. Opt. Express* 11 (3), 1539–1554. doi:10.1364/BOE.386228
- Su, T.-Y., Ting, P.-J., Chang, S.-W., and Chen, D.-Y. (2020). Superficial punctate keratitis grading for dry eye screening using deep convolutional neural networks. *I.E.E.E. Sens. J.* 20 (3), 1672–1678. doi:10.1109/JSEN.2019.2948576
- Su, T. Y., Liu, Z. Y., and Chen, D. Y. (2018). Tear film break-up time measurement using deep convolutional neural networks for screening dry eye disease. *Ieee. Sens. J.* 18, 6857–6862. doi:10.1109/JSEN.2018.2850940
- Sullivan, D. A., Dana, R., Sullivan, R. M., Krenzer, K. L., Sahin, A., Arica, B., et al. (2018). Meibomian gland dysfunction in primary and secondary sjögren syndrome. *Ophthalm. Res.* 59 (4), 193–205. doi:10.1159/000487487
- Sun, Q., Deng, L., Liu, J., Huang, H., Yuan, J., Tang, X., et al. (2017). "Convolutional neural network for corneal ulcer area segmentation. Fetal, infant and ophthalmic medical image analysis. OMIA FIFI," in *Lect. Notes comput. Sci.* (Berlin: Springer), 10554.
- Taigman, Y., Yang, M., Ranzato, M. A., and Wolf, L. (2014). "DeepFace: Closing the gap to human-level performance in face verification," in IEEE. Conference on Computer Vision and Pattern Recognition, Columbus, OH, USA, 23–28 June 2014, 1701–1708. doi:10.1109/CVPR.2014.220
- Tan, Z., Chen, X., Li, K., Liu, Y., Cao, H., Li, J., et al. (2022). Artificial intelligence-based diagnostic model for detecting keratoconus using videos of corneal force deformation. *Transl. Vis. Sci. Technol.* 11 (9), 32. doi:10.1167/tvst.11.9.32
- Ting, D. S. W., Cheung, C. Y., Lim, G., Tan, G. S. W., Quang, N. D., Gan, A., et al. (2017). Development and validation of a deep learning system for diabetic retinopathy and related eye diseases using retinal images from multiethnic populations with diabetes. *JAMA* 318 (22), 2211–2223. doi:10.1001/jama.2017.18152
- Ting, D. S. W., Pasquale, L. R., Peng, L., Campbell, J. P., Lee, A. Y., Raman, R., et al. (2019). Artificial intelligence and deep learning in ophthalmology. *Br. J. Ophthalmol.* 103 (2), 167–175. doi:10.1136/bjophthalmol-2018-313173
- Tiwari, M., Piech, C., Baitemirova, M., Prajna, N. V., Srinivasan, M., Lalitha, P., et al. (2022). Differentiation of active corneal infections from healed scars using deep learning. *Ophthalmology* 129 (2), 139–146. doi:10.1016/j.ophtha.2021.07.033
- Tomidokoro, A., Miyata, K., Sakaguchi, Y., Samejima, T., Tokunaga, T., and Oshika, T. (2000). Effects of pterygium on corneal spherical power and astigmatism. *Ophthalmology* 107 (8), 1568–1571. doi:10.1016/s0161-6420(00)00219-0
- Tuft, S., Somerville, T. F., Li, J. O., Neal, T., De, S., Horsburgh, M. J., et al. (2022). Bacterial keratitis: Identifying the areas of clinical uncertainty. *Prog. Retin. Eye Res.* 89, 101031. doi:10.1016/j.preteyeres.2021.101031
- Twa, M. D., Parthasarathy, S., Roberts, C., Mahmoud, A. M., Raasch, T. W., and Bullimore, M. A. (2005). Automated decision tree classification of corneal shape. *Optom. Vis. Sci.* 82 (12), 1038–1046. doi:10.1097/01.opx.0000192350.01045.6f
- Ung, L., Bispo, P. J. M., Shanbhag, S. S., Gilmore, M. S., and Chodosh, J. (2019). The persistent dilemma of microbial keratitis: Global burden, diagnosis, and antimicrobial resistance. *Surv. Ophthalmol.* 64 (3), 255–271. doi:10.1016/j.survophthal.2018.12.003
- Veli, M., and Ozcan, A. (2018). Computational sensing of *Staphylococcus aureus* on contact lenses using 3D imaging of curved surfaces and machine learning. *A.C.S. Nano* 12 (3), 2554–2559. doi:10.1021/acsnano.7b08375

- Venhuizen, F. G., van Ginneken, B., Liefers, B., van Asten, F., Schreur, V., Fauser, S., et al. (2018). Deep learning approach for the detection and quantification of intraretinal cystoid fluid in multivendor optical coherence tomography. *Biomed. Opt. Express* 9 (4), 1545–1569. doi:10.1364/BOE.9.001545
- Vyas, A. H., Mehta, M. A., Kotecha, K., Pandya, S., Alazab, M., and Gadekallu, T. R. (2022). Tear film break up time-based dry eye disease detection using convolutional neural network. *Neural Comput. Appl.*, 1–19. doi:10.1007/s00521-022-07652-0
- Wan, C., Shao, Y., Wang, C., Jing, J., and Yang, W. (2022). A novel system for measuring pterygium's progress using deep learning. *Front. Med. (Lausanne)* 9, 819971. doi:10.3389/fmed.2022.819971
- Wan Zaki, W. M. D., Mat Daud, M., Abdani, S. R., Hussain, A., and Mutalib, H. A. (2018). Automated pterygium detection method of anterior segment photographed images. *Comput. Methods Programs Biomed.* 154, 71–78. doi:10.1016/j.cmpb.2017.10.026
- Wang, F., Ge, Q. M., Shu, H. Y., Liao, X. L., Liang, R. B., Li, Q. Y., et al. (2021). Decreased retinal microvasculature densities in pterygium. *Int. J. Ophthalmol.* 14 (12), 1858–1867. doi:10.18240/ijo.2021.12.08
- Wang, J., Li, S., Yeh, T. N., Chakraborty, R., Graham, A. D., Yu, S. X., et al. (2021). Quantifying meibomian gland morphology using artificial intelligence. *Optom. Vis. Sci.* 98 (9), 1094–1103. doi:10.1097/OPX.0000000000001767
- Wang, J., Yeh, T. N., Chakraborty, R., Yu, S. X., and Lin, M. C. (2019). A deep learning approach for meibomian gland atrophy evaluation in meibography images. *Transl. Vis. Sci. Technol.* 8 (6), 37. doi:10.1167/tvst.8.6.37
- Wang, M., Shen, L. Q., Pasquale, L. R., Petrakos, P., Formica, S., Boland, M. V., et al. (2019). An artificial intelligence approach to detect visual field progression in glaucoma based on spatial pattern analysis. *Invest. Ophthalmol. Vis. Sci.* 60 (1), 365–375. doi:10.1167/iovs.18-25568
- Wang, M. T. M., Vidal-Rohr, M., Muntz, A., Diprose, W. K., Ormonde, S. E., Wolffsohn, J. S., et al. (2020). Systemic risk factors of dry eye disease subtypes: A New Zealand cross-sectional study. *Ocul. Surf.* 18 (3), 374–380. doi:10.1016/j.jtos.2020.04.003
- Watson, S., Cabrera-Aguas, M., and Khoo, P. (2018). Common eye infections. *Aust. Prescr.* 41 (3), 67–72. doi:10.18773/austprescr.2018.016
- Wei, S., Shi, F., Wang, Y., Chou, Y., and Li, X. (2020). A deep learning model for automated sub-basal corneal nerve segmentation and evaluation using *in vivo* confocal microscopy. *Transl. Vis. Sci. Technol.* 9 (2), 32. doi:10.1167/tvst.9.2.32
- Wu, X., Huang, Y., Liu, Z., Lai, W., Long, E., Zhang, K., et al. (2019). Universal artificial intelligence platform for collaborative management of cataracts. *Br. J. Ophthalmol.* 103 (11), 1553–1560. doi:10.1136/bjophthalmol-2019-314729
- Wu, X., Qiu, Q., Liu, Z., Zhao, Y., Zhang, B., Zhang, Y., et al. (2018). Hyphae detection in fungal keratitis images with adaptive robust binary pattern. *Ieee. Access* 6, 13449–13460. doi:10.1109/ACCESS.2018.2808941
- Xie, Y., Zhao, L., Yang, X., Wu, X., Yang, Y., Huang, X., et al. (2020). Screening candidates for refractive surgery with corneal tomographic-based deep learning. *JAMA Ophthalmol.* 138 (5), 519–526. doi:10.1001/jamaophthalmol.2020.0507
- Xu, F., Jiang, L., He, W., Huang, G., Hong, Y., Tang, F., et al. (2021). The clinical value of explainable deep learning for diagnosing fungal keratitis using *in vivo* confocal microscopy images. *Front. Med. (Lausanne)* 8, 797616. doi:10.3389/fmed.2021.797616
- Xu, W., Jin, L., Zhu, P. Z., He, K., Yang, W. H., and Wu, M. N. (2021). Implementation and application of an intelligent pterygium diagnosis system based on deep learning. *Front. Psychol.* 12, 759229. doi:10.3389/fpsyg.2021.759229
- Xu, X., Zhang, L., Li, J., Guan, Y., and Zhang, L. (2020). A hybrid global-local representation CNN model for automatic cataract grading. *Ieee. J. Biomed. Health Inf.* 24 (2), 556–567. doi:10.1109/JBHI.2019.2914690
- Xu, Y., Kong, M., Xie, W., Duan, R., Fang, Z., Lin, Y., et al. (2021). Deep sequential feature learning in clinical image classification of infectious keratitis. *Engineering* 7 (7), 1002–1010. doi:10.1016/j.eng.2020.04.012
- Xu, Z., Feng, R., Jin, X., Hu, H., Ni, S., Xu, W., et al. (2022). Evaluation of artificial intelligence models for the detection of asymmetric keratoconus eyes using Scheimpflug tomography. *Clin. Exp. Ophthalmol.* 50 (7), 714–723. doi:10.1111/ceo.14126
- Yang, J. J., Li, J., Shen, R., Zeng, Y., He, J., Bi, J., et al. (2016). Exploiting ensemble learning for automatic cataract detection and grading. *Comput. Methods Programs Biomed.* 124, 45–57. doi:10.1016/j.cmpb.2015.10.007
- Yeh, C. H., Yu, S. X., and Lin, M. C. (2021). Meibography phenotyping and classification from unsupervised discriminative feature learning. *Transl. Vis. Sci. Technol.* 10 (2), 4. doi:10.1167/tvst.10.2.4
- Yoo, T. K., Choi, J. Y., Kim, H. K., Ryu, I. H., and Kim, J. K. (2021). Adopting low-shot deep learning for the detection of conjunctival melanoma using ocular surface images. *Comput. methods programs Biomed.* 205, 106086. doi:10.1016/j.cmpb.2021.106086
- Yousefi, S., Yousefi, E., Takahashi, H., Hayashi, T., Tampo, H., Inoda, S., et al. (2018). Keratoconus severity identification using unsupervised machine learning. *Plos One* 13 (11), e0205998. doi:10.1371/journal.pone.0205998
- Zéboulon, P., Ghazal, W., and Gatineau, D. (2021). Corneal edema visualization with optical coherence tomography using deep learning: Proof of concept. *Cornea* 40 (10), 1267–1275. doi:10.1097/ICO.0000000000002640
- Zhang, K., Liu, X., Liu, F., He, L., Zhang, L., Yang, Y., et al. (2018). An interpretable and expandable deep learning diagnostic system for multiple ocular diseases: Qualitative study. *J. Med. Internet Res.* 20 (11), e11144. doi:10.2196/11144
- Zhang, Y. Y., Zhao, H., Lin, J. Y., Wu, S. N., Liu, X. W., Zhang, H. D., et al. (2021). Artificial intelligence to detect meibomian gland dysfunction from *in-vivo* laser confocal microscopy. *Front. Med. (Lausanne)* 8, 774344. doi:10.3389/fmed.2021.774344
- Zhang, Z., Wang, H., Wang, S., Wei, Z., Zhang, Y., Wang, Z., et al. (2022a). Deep learning-based classification of infectious keratitis on slit-lamp images. *Ther. Adv. Chronic Dis.* 13, 20406223221136071. doi:10.1177/20406223221136071
- Zhang, Z., Lin, X., Yu, X., Fu, Y., Chen, X., Yang, W., et al. (2022b). Meibomian gland density: An effective evaluation index of meibomian gland dysfunction based on deep learning and transfer learning. *J. Clin. Med.* 11 (9), 2396. doi:10.3390/jcm11092396
- Zheng, Q., Wang, L., Wen, H., Ren, Y., Huang, S., Bai, F., et al. (2022). Impact of incomplete blinking analyzed using a deep learning model with the Keratograph 5M in dry eye disease. *Transl. Vis. Sci. Technol.* 11 (3), 38. doi:10.1167/tvst.11.3.38
- Zhou, Y. W., Yu, Y., Zhou, Y. B., Tan, Y. J., Wu, L. L., Xing, Y. Q., et al. (2020). An advanced imaging method for measuring and assessing meibomian glands based on deep learning. *Zhonghua Yan Ke Za Zhi* 56 (10), 774–779. doi:10.3760/cma.j.cn112142-20200415-00272
- Zou, H. H., Xu, J. H., Zhang, L., Ji, S. F., and Wang, Y. (2019). Assistant diagnose for subclinical keratoconus by artificial intelligence. *Zhonghua Yan Ke Za Zhi* 55 (12), 911–915. doi:10.3760/cma.j.issn.0412-4081.2019.12.008
- Zulkifley, M. A., Abdani, S. R., and Zulkifley, N. H. (2019). Pterygium-net: A deep learning approach to pterygium detection and localization. *Multimed. Tools Appl.* 78 (24), 34563–34584. doi:10.1007/s11042-019-08130-x



OPEN ACCESS

EDITED BY

Yanwu Xu,
Baidu, China

REVIEWED BY

Xiujian Zheng,
Sichuan University, China
Bo Zheng,
Huzhou University, China
Peifang Ren,
Zhejiang University, China

*CORRESPONDENCE

Yongjin Zhou,
✉ yjzhou@szu.edu.cn
Guiqin Liu,
✉ liuguqin1059@163.com
Hua Zhang,
✉ zhanghuawin@sohu.com

[†]These authors have contributed equally to this work and share first authorship

SPECIALTY SECTION

This article was submitted to Molecular and Cellular Pathology, a section of the journal Frontiers in Cell and Developmental Biology

RECEIVED 02 January 2023

ACCEPTED 13 February 2023

PUBLISHED 24 February 2023

CITATION

Zhang Y, Rao J, Wu X, Zhou Y, Liu G and Zhang H (2023), Automatic measurement of exophthalmos based orbital CT images using deep learning. *Front. Cell Dev. Biol.* 11:1135959. doi: 10.3389/fcell.2023.1135959

COPYRIGHT

© 2023 Zhang, Rao, Wu, Zhou, Liu and Zhang. This is an open-access article distributed under the terms of the [Creative Commons Attribution License \(CC BY\)](https://creativecommons.org/licenses/by/4.0/). The use, distribution or reproduction in other forums is permitted, provided the original author(s) and the copyright owner(s) are credited and that the original publication in this journal is cited, in accordance with accepted academic practice. No use, distribution or reproduction is permitted which does not comply with these terms.

Automatic measurement of exophthalmos based orbital CT images using deep learning

Yinghuai Zhang^{1,2†}, Jing Rao^{3,4†}, Xingyang Wu^{3,4}, Yongjin Zhou^{1,2*}, Guiqin Liu^{3,4*} and Hua Zhang^{5*}

¹School of Biomedical Engineering, Health Science Center, Shenzhen University, Shenzhen, China, ²Marshall Laboratory of Biomedical Engineering, Shenzhen, China, ³Shenzhen Eye Hospital, Jinan University, Shenzhen, China, ⁴Shenzhen Eye Institute, Shenzhen, China, ⁵Shenzhen Overseas Chinese Town Hospital, Shenzhen, China

Introduction: Objective, accurate, and efficient measurement of exophthalmos is imperative for diagnosing orbital diseases that cause abnormal degrees of exophthalmos (such as thyroid-related eye diseases) and for quantifying treatment effects.

Methods: To address the limitations of existing clinical methods for measuring exophthalmos, such as poor reproducibility, low reliability, and subjectivity, we propose a method that uses deep learning and image processing techniques to measure the exophthalmos. The proposed method calculates two vertical distances; the distance from the apex of the anterior surface of the cornea to the highest protrusion point of the outer edge of the orbit in axial CT images and the distance from the apex of the anterior surface of the cornea to the highest protrusion point of the upper and lower outer edges of the orbit in sagittal CT images.

Results: Based on the dataset used, the results of the present method are in good agreement with those measured manually by clinicians, achieving a concordance correlation coefficient (CCC) of 0.9895 and an intraclass correlation coefficient (ICC) of 0.9698 on axial CT images while achieving a CCC of 0.9902 and an ICC of 0.9773 on sagittal CT images.

Discussion: In summary, our method can provide a fully automated measurement of the exophthalmos based on orbital CT images. The proposed method is reproducible, shows high accuracy and objectivity, aids in the diagnosis of relevant orbital diseases, and can quantify treatment effects.

KEYWORDS

CT images, deep learning, exophthalmos, orbital diseases, thyroid-associated ophthalmopathy

1 Introduction

The exophthalmos reflects the anterior-posterior position of the eye relative to the orbit (Segni et al., 2002; Ameri and Fenton, 2004) and is associated with various orbital diseases, including Graves' orbitopathy, orbital tumor, and orbital fracture (Burch and Wartofsky, 1993; Bartalena et al., 2000; Alsuhaibani et al., 2011; Guo et al., 2018; Huh et al., 2020; Huang et al., 2022; Ji et al., 2022). Accurate measurement of exophthalmos can assist in the diagnosis

of these related diseases (Segni et al., 2002; Lam et al., 2010) and also quantify the treatment outcome.

Currently, the main clinical methods for measuring exophthalmos can be classified as exophthalmometer and computed tomography (CT) methods. The most widely used method is the Hertel exophthalmometer (Migliori and Gladstone, 1984; Dunskey, 1992), which measures the distance from the lateral orbital rim to the corneal surface in a direction perpendicular to the frontal plane as a quantitative indicator of the degree of exophthalmos (O'Donnell et al., 1999). However, the Hertel exophthalmometer has low inter- and intraobserver reproducibility, which in turn affects the reliability of its results (Frueh et al., 1985; Musch et al., 1985; Dunskey, 1992; Chang et al., 1995; Kim and Choi, 2001; Sleep and Manners, 2002; Ameri and Fenton, 2004). Furthermore, this method is not suitable for subjects with abnormalities, such as severe upper eyelid swelling, ptosis, and hyper-deviated eyes, because it is greatly influenced by facial tissues (Na et al., 2019).

Meanwhile, clinicians using CT scans for diagnosing the degree of exophthalmos measure the relevant distance manually by dragging the mouse after determining physiological structures, such as the outer edge of the orbit and the apex of the anterior surface of the cornea (Nkenke et al., 2003; Bingham et al., 2016; Na et al., 2019). Such a manual method of measuring exophthalmos is not only time-consuming and inefficient but also inevitably subjective to the clinician, resulting in poor reproducibility of the interobserver measurements (Huh et al., 2020). Therefore, an objective, accurate, convenient, and efficient method for measuring exophthalmos is necessary for the timely diagnosis or assessment of treatment outcomes for relevant orbital diseases. The development of image processing and deep learning methods has provided the basis for automatic, objective, efficient, and accurate computer-aided diagnosis, and these methods have been widely applied in a variety of fields—especially in studies related to the diagnosis of ophthalmic diseases (Zhao et al., 2022).

In this paper, we propose an automated method based on image processing and deep learning to measure the vertical distance from the apex of the anterior corneal surface to the lateral orbital rim of both eyes and the longest line of the superior to the inferior orbital rim on the axial and sagittal plane of CT images, respectively. The two distance parameters, related to ocular prominence, can be measured objectively, accurately, and efficiently without relying on the clinician. This method can help clinicians diagnose diseases related to protrusion or depression by measuring the exophthalmos.

2 Materials and methods

2.1 Data

Ocular CT images were collected from 31 subjects in the horizontal position and 43 subjects in the sagittal position at the Shenzhen Eye Hospital and Shenzhen Overseas Chinese Hospital using a Philips Ingenuity core 129—a Dutch computed tomography machine with a CT scan thickness of 0.625 mm using the soft tissue window. For this study, 79 horizontal CT images and 99 sagittal CT

images including the thickest lens were selected by clinicians empirically.

To train a deep learning network model for automatic eye region segmentation, we divided 79 axial CT images from 31 CT sequence images and 99 sagittal CT images from 43 CT sequence images into a training, validation set, and test set in the ratio of 48:8:23 and 48:8:43, respectively. The ratio of the number of eyes in the training set, validation set and test set for axial and sagittal images is 96:16:40 and 96:16:43, respectively.

Two ophthalmology clinician measured the vertical distance of the line from the apex of the anterior surface of the eye to the most protruding point of the orbital rim for 23 images of the axial plane and 43 images of the sagittal plane. A researcher contributed to the annotation of the ground truth using the “polygon selections” and “fill” function of the software ImageJ (National Institutes of Health, Bethesda, MD, United States) to map the mask of the eye region in all CT images for eye region segmentation by U-Net++ networks.

2.2 Overall approach

In this study, we calculated the vertical distance from the apex of the anterior corneal surface to the lateral orbital rim of both eyes on the axial plane of the CT images, as shown in Figure 1. First, the neural network was trained based on the U-Net++ model for segmenting the eye region in the axial plane of the CT images, and then input the remaining CT images not used for training the model into the segmentation model to obtain a mask of the eye. Furthermore, the lateral orbital rim region of both eyes was obtained after a series of image processing steps. Next, the coordinates of the apex of the anterior corneal surface and the most protruding point of the lateral orbital rim of both eyes were extracted. Additionally, the vertical distance of the line from the apex of the anterior corneal surface to the most protruding point of the upper and lower orbital rim was calculated, as shown in Figure 2.

Similarly, the neural network must be trained to segment the eye region based on the U-Net++ model in the sagittal plane of the CT images while processing the CT images to obtain the upper and lower orbital rim regions. After extracting the coordinates of the apex of the anterior corneal surface and the most protruding point of the upper and lower orbital rim, the vertical distance of the line from the apex of the anterior corneal surface to the most protruding point of the upper and lower orbital rim was calculated.

2.3 Segmentation

In order to obtain the best segmentation results, we trained the models commonly used segmentation networks in clinical practice, including FCN32 (Long et al., 2015), SegNet (Badrinarayanan et al., 2017), U-Net (Ronneberger et al., 2015), U-Net++ (Zhou et al., 2018), and Res-U-Net (Zhang et al., 2018), respectively, using the dataset of this paper. The U-Net++ model that achieved the best segmentation performance on the test set was selected for the eye region segmentation.

We implemented the U-Net++ model for eye region segmentation. First, the learning rate and decay rate were set to 0.0001 and 0.99, respectively, Kaiming initialization (He et al.,

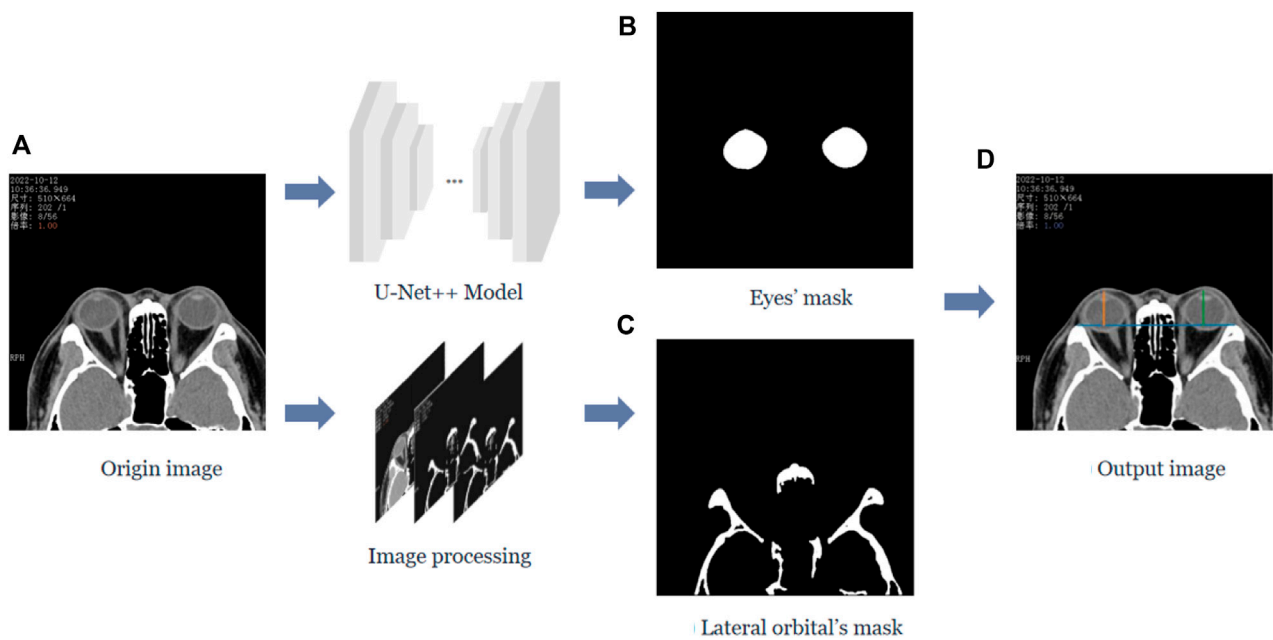


FIGURE 1

Process of calculating the vertical distance from the apex of the anterior surface of the cornea to the lateral orbital rim of both eyes in the axial plane of the CT image. (A) The original axial plane of the CT image, and after the U-Net++ model and Image processing, we can obtain the binary images of the eye region mask shown in (B) and the lateral orbital rim region of both eyes shown in (C), respectively. (D) The line from the apex of the anterior surface of the eye to the apex of the lateral orbital rim is represented by the blue line in (D), and the vertical distance from the apex of the anterior surface of the eye to the apex of the lateral orbital rim represented by the orange and green lines.

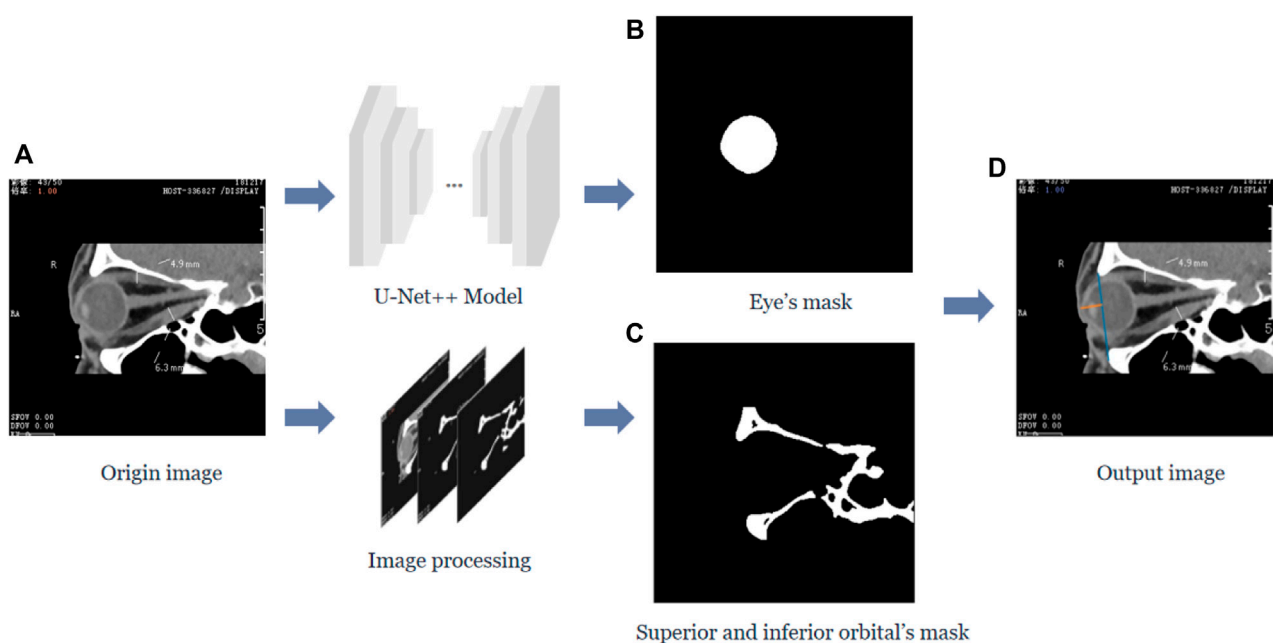


FIGURE 2

The vertical distance from the apex of the anterior surface of the cornea to the longest line between the superior and inferior orbital margins in the sagittal plane of the CT image. (A) Represents the original sagittal CT image, and after the U-Net++ model and Image processing, we obtain the binary images of the eye region mask shown in (B) and the upper and lower orbital rim regions shown in (C), and then after locating the coordinates of the anterior surface apex of the eye and the upper and lower orbital rims, we obtain the line from the apex of the upper and lower orbital rims represented by the blue line in (D) and the vertical distance of the line from the apex of the anterior surface of the cornea to the upper and lower orbital rim most protruding points represented by the orange line.

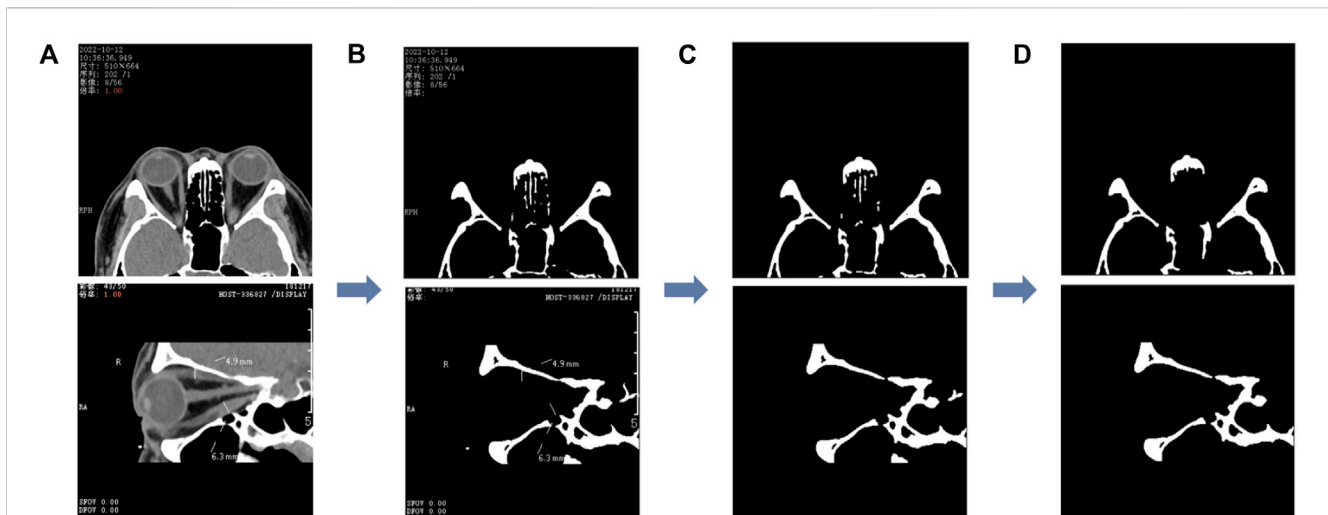


FIGURE 3

Image processing of the segmented orbital rim region. (A) The unprocessed CT image and the binary image in (B) are obtained after the threshold segmentation; the binary image shown in (C) is obtained after the morphological opening operation, and finally, the smaller connected domain is eliminated to obtain the binary image containing the outer edge of the orbit shown in (D). The first row represents the axial CT image and the second row the sagittal CT image.

2015) was used for initializing the weights of the model. Dice loss (Milletari et al., 2016) was used to compare the model segmentation results with the ground truth, and the Adam optimization method (Kingma and Ba, 2014) was applied to minimize the loss value of the network. We inputted the original images and ground truth masks from the training and validation sets to the U-Net++ model. After 200 training iterations of epochs on a server configured with the GPU NVIDIA GeForce GTX 3090TI and using the Pytorch (Paszke et al., 2017) framework, we obtained a network model for automatic eye region segmentation. The formula for Dice loss is shown below.

$$\text{Dice loss} = 1 - (2 * |X \cap Y|) / (|X| + |Y|)$$

X represents the eye area mask produced by the neural network segmentation, and Y represents the ground truth of the eye area mask input to the neural network.

In addition to the orbital region, we must segment the lateral orbital rim regions of both eyes in the axial plane as well as the superior and inferior orbital rim regions in the sagittal plane of the CT images to extract the coordinates of their most protruding points. The orbital rim, i.e., the human orbital bone, shows strong contrast in CT images compared to other tissues, so we can use traditional image processing methods to extract the skeletal region.

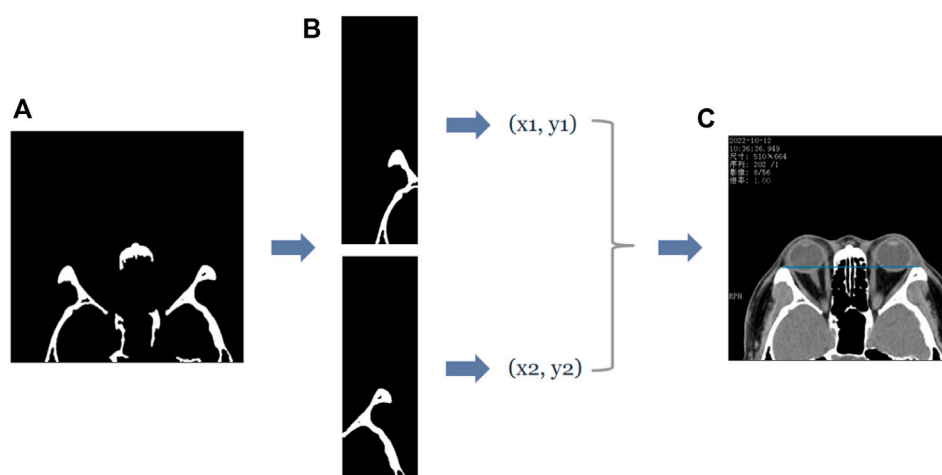
We first performed threshold segmentation separately with a grayscale values' threshold of 200 for the CT images of the two planar views (as in Figure 3A) empirically. After extracting the structures with grayscale values greater than 200 (as in Figure 3B), we eliminated the residual watermark in the CT images, following threshold segmentation, by performing the morphological opening (as in Figure 3C). Finally, after eliminating the smaller connected domains in the images (considered to be noisy), a binary image

containing the lateral orbital rims or the upper and lower orbital rims of both eyes was obtained (as in Figure 3D).

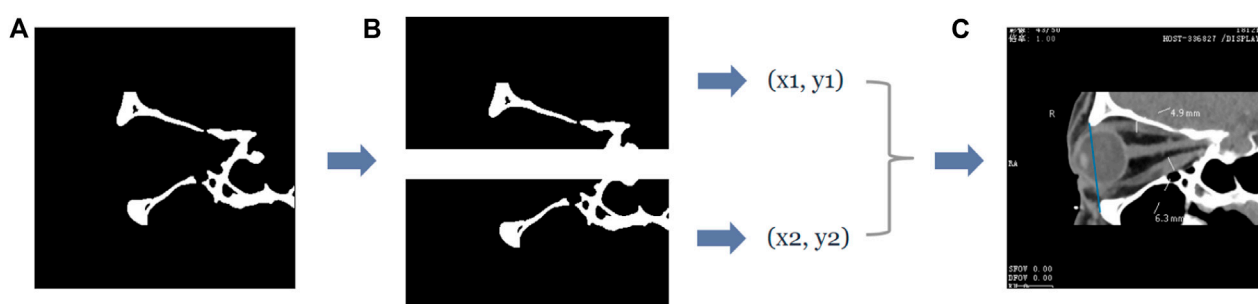
2.4 Distance calculation

In the axial plane of the CT images, the lateral orbital rims of both eyes were located in the leftmost third of the CT image and the rightmost third of the CT image. Furthermore, the most protruding point can be regarded as the pixel point closest to the top, i.e., the pixel point with the smallest y-value in the image coordinate. Therefore, to extract the coordinates of the most protruding point of the lateral orbital rim of both eyes in the axial plane of the CT image, we divided the (d) image in Figure 4 into three subplots: left, middle, and right. First, the images were divided according to the direction of the x-axis in the image coordinates, and then the pixel points were traversed in the left and right images in turn. The pixel point with the smallest y-value in the "white" area of the two subplots was shortlisted as the coordinate of the most protruding point of the lateral orbital rim of both eyes, as shown in Figure 4. The entire process is shown in Figure 4.

In the sagittal plane of the CT images, the upper and lower orbital margins are located in the upper and lower molecular maps of the CT image, respectively—their most protruding point can be regarded as the point closest to the left side of the image, i.e., the pixel point with the smallest x-value in the image coordinates. Therefore, we follow an operation similar to that of the axial plane—the pixel points in the "white" area in the upper and lower submaps are traversed, respectively, and the point with the smallest x-value is recorded as the coordinate of the most protruding point of the upper and lower orbital margins. The entire process is shown in Figure 5.

**FIGURE 4**

The process of obtaining the coordinates of the most protruding point of the lateral orbital rim of both eyes in the axial plane of the CT image. (A) First row of Panel (B), which is the binary image containing the lateral orbital rim region of both eyes. Subsequently, the coordinates of the most protruding points (x1, y1), (x2, y2) of the left and right lateral orbital rims can be determined by traversing the two subgraphs separately, and the straight line passing through the two most protruding points can be visualized by the blue line in (C).

**FIGURE 5**

The process of obtaining the coordinates of the most protruding points of the upper and lower orbital rim in the sagittal plane of the CT image. (A) The second row of Figure 4B, which is the binary image containing the upper and lower orbital rim regions, and extracts the submaps of the upper and lower halves, respectively, to obtain the two submaps as shown in (B). Subsequently, the coordinates of the most protruding points of the superior and inferior orbital rims can be determined by traversing the two subgraphs separately, and then the straight line passing through the two most protruding points can be obtained—the straight line is shown in blue in (C).

After obtaining the coordinates of the lateral orbital rims of both eyes, we obtained the equation of the line passing through the two points of the lateral orbital rims of both eyes. Similarly, we obtained the equation of the line passing through the two points of the upper and lower orbital rims based on the coordinates of the most protruding points of the upper and lower orbital rims in the sagittal plane of the CT image. Subsequently, we traversed the pixel points of the eye region mask output by the eye region segmentation model and recorded the point with the smallest x -value among the mask pixel points as the coordinates of the most protruding point of the anterior corneal surface vertex. From this, we calculated the vertical distance from the apex of the anterior corneal surface to the lateral orbital rim of both eyes in the axial plane of the CT image

and the vertical distance from the apex of the anterior corneal surface to the upper and lower orbital rims in the sagittal plane of the CT image. The results of our automated method and the manual measurements by the physicians were compared.

2.5 Statistical analysis

The Dice coefficient (Dice, 1945), Intersection Over Union (IOU), precision, and recall were used as metrics to evaluate the segmentation performance of the model. The metrics were calculated as shown below.

$$Dice = 2TP / (FP + 2TP + FN)$$

TABLE 1 The mean values (standard deviation) of the Dice Coefficient, IOU, Precision, Recall for segmenting the ocular region model in the axial plane and the sagittal plane of the CT images, respectively.

View	Model	Dice	Recall	Precision	IOU
The axial plane	FCN32	0.8847 (0.0150)	0.8213 (0.0731)	0.9660 (0.0380)	0.7951 (0.0572)
	SegNet	0.9684 (0.0163)	0.9802 (0.0118)	0.9577 (0.0329)	0.9382 (0.0295)
	U-Net	0.9757 (0.0150)	0.9529 (0.0271)	0.9887 (0.0086)	0.9636 (0.0302)
	U-Net++	0.9805 (0.0059)	0.9829 (0.0090)	0.9782 (0.0140)	0.9617 (0.0112)
	Res-U-Net	0.9805 (0.0073)	0.9838 (0.0085)	0.9775 (0.0164)	0.9619 (0.0138)
The sagittal plane	FCN32	0.8425 (0.0587)	0.7487 (0.0878)	0.9729 (0.0335)	0.7319 (0.0813)
	SegNet	0.9570 (0.0376)	0.9506 (0.0517)	0.9662 (0.0463)	0.9200 (0.0650)
	U-Net	0.9770 (0.0135)	0.9804 (0.0170)	0.9740 (0.0224)	0.9553 (0.0248)
	U-Net++	0.9816 (0.0087)	0.9802 (0.0158)	0.9831 (0.0087)	0.9640 (0.0164)
	Res-U-Net	0.9505 (0.0809)	0.9273 (0.1201)	0.9849 (0.0299)	0.9150 (0.1223)

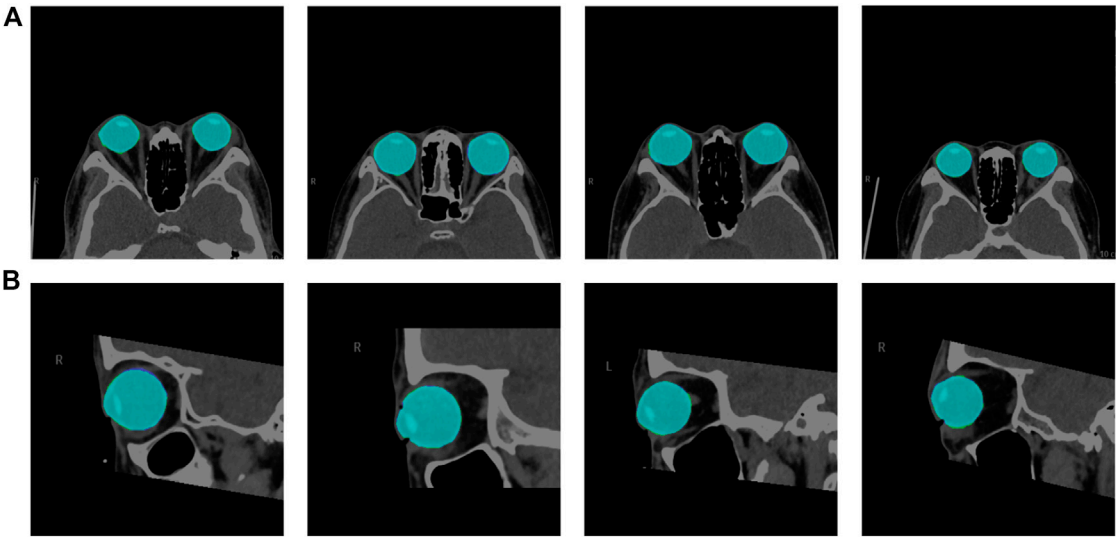


FIGURE 6 Visualization segmentation results of the model used to segment the eye region. Row (A) represents the visual segmentation results of the model in the axial plane of the test set, and row (B) represents the visual segmentation results of the model in the sagittal plane of the test set. The purple and green area represent the segmentation masks predicted by the manual and network, respectively. The light blue area is the overlapping part of both, i.e., the correctly predicted eye area.

$$IOU = TP / (TP + FN + FP)$$
$$Precision = TP / (TP + FP)$$
$$Recall = TP / (TP + FN)$$

The intraclass correlation coefficient (ICC) and the concordance correlation coefficient (CCC) were used to demonstrate the concordance between the results of our automated method and the manual measurements of the physicians. The two-way mixture model and the absolute consistency type were chosen for the calculation of the intra-group correlation coefficients.

3 Results

3.1 Ocular segmentation

We used the segmentation results of 40 eyes in 23 horizontal CT images and 43 eyes in 43 sagittal CT images to test the ability of the model to segment eye region. Table 1 shows the segmentation performance of the five models on the test set data, and Figure 6 shows the visualization of the U-Net++ model segmentation results. From the results, we observe that the region of the eye was segmented accurately in both horizontal and sagittal CT images.

TABLE 2 The mean values (standard deviation) of the Exophthalmometric values between the results measured by the proposed automated method and the manually measured results.

View	Manual method	Automated method
The axial plane	17.83 (2.85)	18.37 (2.67)
The sagittal plane	8.01 (2.79)	8.48 (2.82)

This indicates that this method can accurately locate the vertex coordinates of the anterior surface of the eye.

3.2 Ocular prominence measurement

For testing, we used the vertical distance from the apex of the anterior corneal surface to the most protruding point of the lateral orbital rim of both eyes in 40 eyes from 23 CT images in the axial plane and the vertical distance from the apex of the anterior corneal surface to the most protruding point of the upper and lower orbital rims in 43 eyes from 43 CT images in the

sagittal plane. Table 2 shows the mean values (standard deviation) of the Exophthalmometric values between the results measured by the proposed automated method and the manually measured results. The Bland-Altman plots and the scatter diagram between the computed results of the proposed automated method of ocular prominence measurement on the test set and its corresponding manual measurement by the physician is shown in Figure 7. Figure 8 shows the results of the proposed automated method and the manual measurement by the physician on an axial plane and one sagittal plane of the CT image, respectively. The results of the statistical analysis between the measurements using the two methods on all test sets are shown in Table 3.

From the results of the statistical analysis, it can be observed that although the Bland-Altman plots diagram as well as the mean values of the Exophthalmometric values show a stable error in the results measured by the proposed automated method and the manually measured results, our method is in good agreement with the results of the manual measurement by the physician for both vertical distances. Thus, the accuracy of this method can be verified.

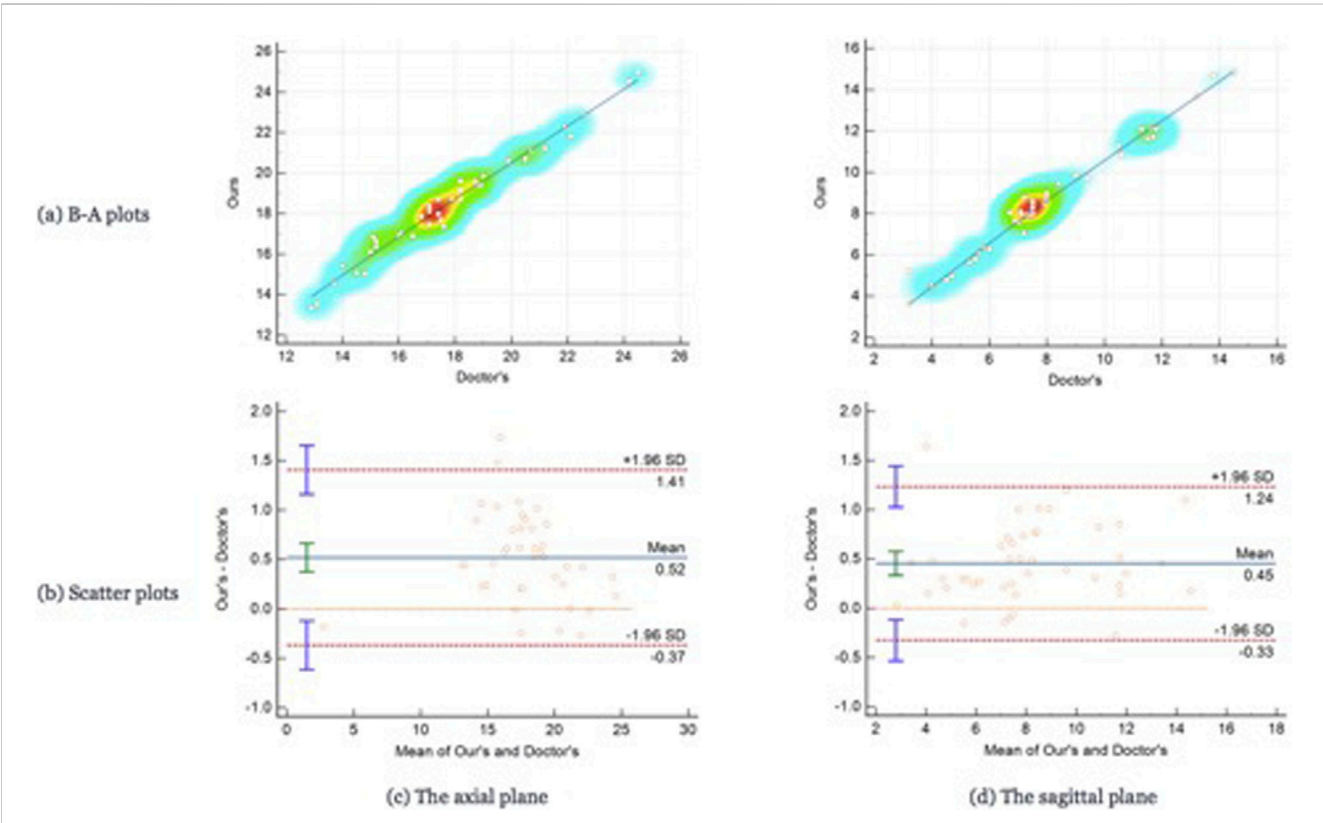


FIGURE 7 The Bland-Altman plots and the scatter plots between the results on the test set using the automated method proposed in this paper. Row (A) represents the Bland-Altman plots and row (B) is the scatter plot, column (C) means the results on the axial plane while column (D) is the results on the sagittal plane. In the scatter plots, the y-axis represents the results calculated by the automated method we proposed in this paper while the x-axis means the results measured by the doctors.

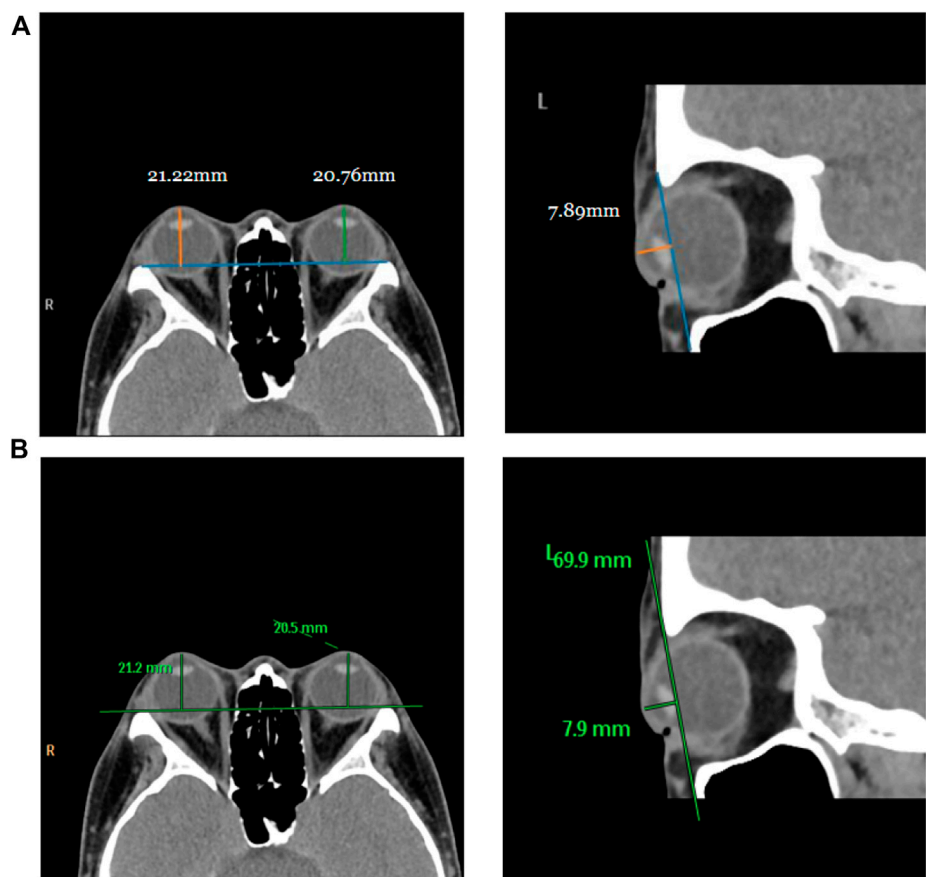


FIGURE 8 Visualization of measurement results of the proposed automated method and the manual measurement method by the physician on the test set. Row (A) represents the visualization result of measurement using the proposed method, and row (B) is the visualization result of manual measurement by the physician on the same image.

TABLE 3 Results of statistical analysis of the concordance correlation coefficient (CCC) and the intraclass correlation coefficient (ICC) between the results measured by the proposed automated method and the manually measured results.

View	CCC	ICC
The axial plane	0.9895	0.9698
The sagittal plane	0.9902	0.9773

4 Discussion

The degree of orbital protrusion is associated with a variety of orbital diseases, and its accurate quantification is important to diagnose certain orbital diseases and determine the effectiveness of their treatment. CT imaging has been used to measure the prominence of the eye because of its high-resolution accuracy and ability to analyze multiple views simultaneously (Kim and Choi, 2001; Nkenke et al., 2003; 2004; Fang et al., 2013). Some studies have shown that CT image-based ocular prominence measurements are more accurate (Hallin and Feldon, 1988; Segni et al., 2002; Nkenke et al., 2003; 2004; Ramli et al., 2015) and

correlate well with measurements using the Hertel ocular prominence meter (Klingenstein et al., 2022). For special subjects such as children and those suffering from ptosis, using CT images to measure ocular prominence is the only feasible method. Currently, the most common clinical method is to manually measure the vertical distance from the apex of the anterior corneal surface to the lateral orbital rim of both eyes on an axial CT image as a measure of ocular prominence (as shown in Figure 9A) (“Axial Globe Position Measurement: A Prospective Multicenter Study by the International Thyroid Eye Disease Society,” 2016; Nkenke et al., 2004). However, when the subject’s head is tilted, using only one plane of view may lead to large errors. In 2019, Na et al. (Na et al., 2019) proposed a method to represent ocular prominence in sagittal CT images by measuring the vertical distance of the longest line connecting the anterior surface apex of the cornea to the superior orbital rim to the inferior orbital rim (as shown in Figure 9B). The method proposed by Park et al. has been validated to be comparable to the Hertel exophthalmometer method with high correlation while being applicable to subjects with horizontal and vertical strabismus. Therefore, a exophthalmos measuring method that combines the two planar views described above would be applicable to a wider population with guaranteed accuracy.

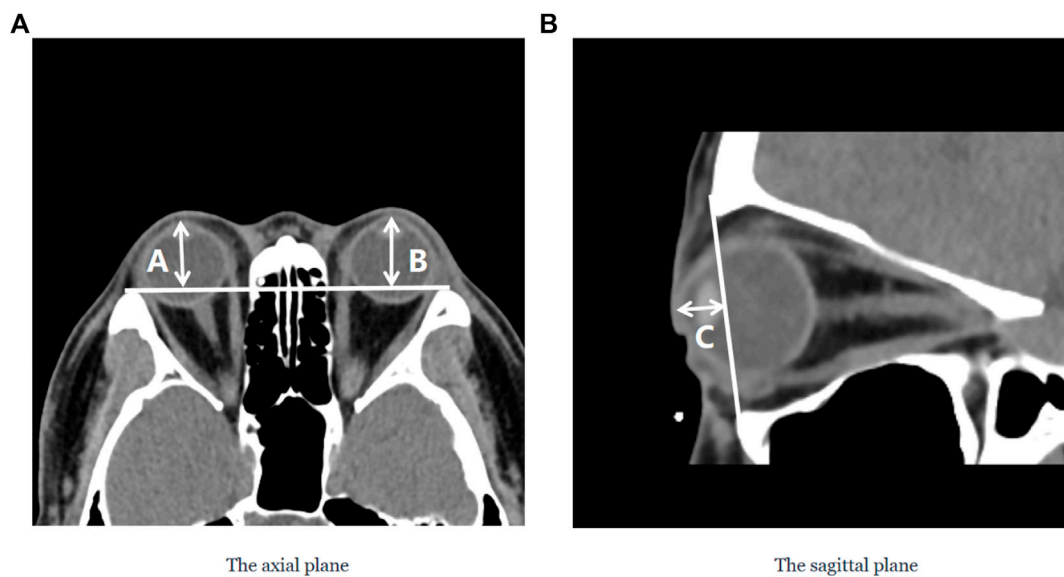


FIGURE 9

Two commonly used clinical parameters for measuring the prominence of the eye based on CT images. (A) The axial plane of the CT image, (A and B) represent the vertical distance from the apex of the anterior corneal surface to the lateral orbital rim of both eyes, respectively; (B) The sagittal plane of the CT image, C represents the vertical distance from the apex of the anterior corneal surface to the longest line of the upper and lower orbital rims.

In this paper, we propose a method based on deep learning and image processing techniques to combine axial and sagittal CT images for the automatic measurement of exophthalmos. The experimental results show that our method can achieve accurate segmentation results with Dice coefficients of 0.976 ± 0.015 and 0.977 ± 0.0135 for the eye region in the axial and sagittal plane of the CT images, respectively, on the dataset used in this paper, as shown in Figure 6. We used image processing techniques to segment the orbital region to achieve accurate localization of the apex of the anterior surface of the eye and the most protruding point of the outer edge of the orbit. Based on the results obtained, the CCC and ICC between the two methods were 0.988 and 0.957 for the axial plane of the CT images, respectively, and 0.990 and 0.965 for the sagittal plane of the CT images, respectively—in our dataset of 23 axial and 43 sagittal CT images, which shows high consistency.

The deep learning and digital image processing methods used in our study can automatically segment the structures of the eye and orbital rim, and locate the apex of the anterior corneal surface and the most protruding point of the orbital rim. The process can then calculate the relevant parameters, ensuring the high accuracy and reproducibility of this method to a certain extent in our dataset. Furthermore, the suggested approach can determine the relevant exophthalmos measurements in both axial and sagittal planes of CT scans, offering medical professionals a multi-dimensional reference for diagnosing orbital disorders in patients displaying abnormal exophthalmos seen only in the axial or sagittal plane. After conducting a PubMed search using the keywords “proptosis” and “CT,” we discovered 57 relevant studies published in the past 20 years. However, all of these studies relied on manual drawings and measurements performed by clinicians or researchers, which can be remedied by implementing the proposed method. Additionally, the full automation of the process in this paper not

only minimizes the impact of subjective factors on measurement results, but also enhances measurement efficiency. On average, the time required to calculate the vertical distance from the anterior corneal surface’s apex to the most protruding point of the lateral orbital rim in axial CT images and the vertical distance from the anterior corneal surface’s apex to the most protruding points of the upper and lower orbital rims in sagittal CT images is 0.9 s and 0.75 s, respectively. This automated method significantly reduces the time and effort required for eye protrusion measurement compared to manual methods.

The work in this paper was performed on 2D CT images, which meets the practical needs of current clinicians for diagnosis (Kim and Choi, 2001), especially in patients with eyelid exophthalmos and other conditions (Na et al., 2019). It is worth mentioning that some research teams have implemented the quantification of ocular prominence on 3D CT images (Guo et al., 2017; 2018; Huh et al., 2020; Willaert et al., 2020), but none of them have been fully automated. However, the mainstream methods in clinical practice are still dominated by the Hertel ocular prominence meter method and the lightweight-based 2D CT image method. The 3D CT image-based ocular prominence measurement method is complex and time-consuming, and we will explore other ocular prominence-related parameters (Kim and Choi, 2001; Campi et al., 2013; Guo et al., 2017; Afanasyeva et al., 2018; Choi and Lee, 2018) in our future work, for automatic measurement and validate their practical feasibility in a clinical setting.

However, the approach in this paper applies to both axial and sagittal CT images and requires the most protruding point of the outer edge of the orbit to determine the measurement of the exophthalmos, which is a limitation in case of some images with incomplete, missing or displaced outer orbit edges.

5 Conclusion

This study introduces an automated approach for assessing eye prominence in both axial and sagittal CT images of the orbit using deep learning and image processing techniques. This method eliminates the need for prior knowledge from clinicians, thereby reducing their workload. On the experimental dataset, the method shows satisfactory efficiency, accuracy, reliability, and reproducibility. This approach has the potential to support the diagnosis and treatment quantification of related orbital diseases.

Data availability statement

The raw data supporting the conclusion of this article will be made available by the authors, without undue reservation.

Author contributions

YHZ conceived and designed the research and wrote the manuscript; JR and XW wrote the manuscript; YJZ, GL, and HZ designed the research, acquired the article information, and revised the manuscript. All authors contributed to the article and have approved the submitted version.

References

- Afanasyeva, D. S., Gushchina, M. B., Gerasimov, M. Y., and Borzenok, S. A. (2018). Computed exophthalmometry is an accurate and reproducible method for the measuring of eyeballs' protrusion. *J. Cranio-Maxillofacial Surg.* 46 (3), 461–465. doi:10.1016/j.jcms.2017.12.024
- Alsuhaibani, A. H., Carter, K. D., Policeni, B., and Nerad, J. A. (2011). Orbital volume and eye position changes after balanced orbital decompression. *Ophthalmic Plastic Reconstr. Surg.* 27 (3), 158–163. doi:10.1097/IOP.0b013e3181ef72b3
- Ameri, H., and Fenton, S. (2004). Comparison of unilateral and simultaneous bilateral measurement of the globe position, using the Hertel exophthalmometer. *Ophthalmic Plastic Reconstr. Surg.* 20, 448–451. doi:10.1097/01.iop.0000143712.42344.8c
- Badrinarayanan, V., Kendall, A., and Cipolla, R. (2017). SegNet: A deep convolutional encoder-decoder architecture for image segmentation. *IEEE Trans. Pattern Analysis Mach. Intell.* 39 (12), 2481–2495. doi:10.1109/TPAMI.2016.2644615
- Bartalena, L., Pinchera, A., and Marcocci, C. (2000). Management of Graves' ophthalmopathy: Reality and perspectives. *Endocr. Rev.* 21 (2), 168–199. doi:10.1210/edrv.21.2.0393
- Bingham, C. M., Sivak-Callcott, J. A., Gurka, M. J., Nguyen, J., Hogg, J. P., Feldon, S. E., et al. (2016). Axial globe position measurement: A prospective multicenter study by the international thyroid eye disease society. *Ophthalmic Plastic Reconstr. Surg.* 32 (2), 106–112. doi:10.1097/IOP.0000000000000437
- Burch, H. B., and Wartofsky, L. (1993). Graves' ophthalmopathy: Current concepts regarding pathogenesis and management. *Endocr. Rev.* 6, 747–793. doi:10.1210/edrv-14-6-747
- Campi, I., Vannucchi, G. M., Minetti, A. M., Dazzi, D., Avignone, S., Covelli, D., et al. (2013). A quantitative method for assessing the degree of axial proptosis in relation to orbital tissue involvement in Graves' orbitopathy. *Ophthalmology* 120 (5), 1092–1098. doi:10.1016/j.ophtha.2012.10.041
- Chang, A. A., Bank, A., Francis, I. C., and Kappagoda, M. B. (1995). Clinical exophthalmometry: A comparative study of the luedde and Hertel exophthalmometers. *Aust. N. Z. J. Ophthalmol.* 23 (4), 315–318. doi:10.1111/j.1442-9071.1995.tb00182.x
- Choi, K. J., and Lee, M. J. (2018). Comparison of exophthalmos measurements: Hertel exophthalmometer versus orbital parameters in 2-dimensional computed tomography. *Can. J. Ophthalmol.* 53 (4), 384–390. doi:10.1016/j.jcjo.2017.10.015
- Dice, L. R. (1945). Measures of the amount of ecologic association between species. *Ecology* 26 (3), 297–302. doi:10.2307/1932409
- Dunsky, I. L. (1992). Normative data for Hertel exophthalmometry in a normal adult black population. *Optometry Vis. Sci.* 69 (7), 562–564. doi:10.1097/00006324-199207000-00009
- Fang, Z. J., Zhang, J. Y., and He, W. M. (2013). CT features of exophthalmos in Chinese subjects with thyroid-associated ophthalmopathy. *Int. J. Ophthalmol.* 6 (2), 146–149. doi:10.3980/j.issn.2222-3959.2013.02.07
- Frueh, B. R., Garber, F., Grill, R., and Musch, D. C. (1985). Positional effects on exophthalmometer readings in Graves' eye disease. *Archives Ophthalmol.* 103 (9), 1355–1356. doi:10.1001/archophth.1985.01050090107043
- Guo, J., Qian, J., and Yuan, Y. (2018). Computed tomography measurements as a standard of exophthalmos? Two-dimensional versus three-dimensional techniques. *Curr. Eye Res.* 43 (5), 647–653. doi:10.1080/02713683.2018.1431285
- Guo, J., Qian, J., Yuan, Y., Zhang, R., and Huang, W. (2017). A novel three-dimensional vector analysis of axial globe position in thyroid eye disease. *J. Ophthalmol.* 2017, 7253898–7253899. doi:10.1155/2017/7253898
- Hallin, E. S., and Feldon, S. E. (1988). Graves' ophthalmopathy: II. Correlation of clinical signs with measures derived from computed tomography. *Br. J. Ophthalmol.* 72 (9), 678–682. doi:10.1136/bjo.72.9.678
- He, K., Zhang, X., Ren, S., and Sun, J. (2015). *Delving deep into rectifiers: Surpassing human-level performance on ImageNet classification*. IEEE Computer Society.
- Huang, X., Ju, L., Li, J., He, L., Tong, F., Liu, S., et al. (2022). An intelligent diagnostic system for thyroid-associated ophthalmopathy based on facial images. *Front. Med.* 9, 920716. doi:10.3389/fmed.2022.920716
- Huh, J., Park, S. J., and Lee, J. K. (2020). Measurement of proptosis using computed tomography based three-dimensional reconstruction software in patients with Graves' orbitopathy. *Sci. Rep.* 10 (1), 14554. doi:10.1038/s41598-020-71098-4
- Ji, Y., Chen, N., Liu, S., Yan, Z., Qian, H., Zhu, S., et al. (2022). Research progress of artificial intelligence image analysis in systemic disease-related ophthalmopathy. *Dis. Markers* 2022, 3406890–3406910. doi:10.1155/2022/3406890
- Kim, I. T., and Choi, J. B. (2001). Normal range of exophthalmos values on orbit computerized tomography in Koreans. *Ophthalmologica* 215 (3), 156–162. doi:10.1159/000050850
- Kingma, D. P., and Ba, J. (2014). "Adam: A method for stochastic optimization," in *International conference on learning representations*.
- Klingenstein, A., Samel, C., Garip-Kübler, A., Hintschich, C., and Müller-Lisse, U. G. (2022). Cross-sectional computed tomography assessment of exophthalmos in comparison to clinical measurement via Hertel exophthalmometry. *Sci. Rep.* 12 (1), 11973. doi:10.1038/s41598-022-16131-4
- Lam, A. K. C., Lam, C. F., Leung, W. K., and Hung, P. K. (2010). Intra-observer and inter-observer variation of Hertel exophthalmometry. *Ophthalmic & Physiological Opt.* 29 (4), 472–476. doi:10.1111/j.1475-1313.2008.00617.x

Funding

This study was supported by Shenzhen Fund for Guangdong Provincial High-level Clinical Key Specialties (SZGSP014), Sanming Project of Medicine in Shenzhen (SZSM202011015), and Science, Technology and Innovation Commission of Shenzhen (GJHZ20190821113605296).

Conflict of interest

The authors declare that the research was conducted in the absence of any commercial or financial relationships that could be construed as a potential conflict of interest.

Publisher's note

All claims expressed in this article are solely those of the authors and do not necessarily represent those of their affiliated organizations, or those of the publisher, the editors and the reviewers. Any product that may be evaluated in this article, or claim that may be made by its manufacturer, is not guaranteed or endorsed by the publisher.

- Long, J., Shelhamer, E., and Darrell, T. (2015). *Fully convolutional networks for semantic segmentation*. (arXiv:1411.4038). arXiv. Available at: <http://arxiv.org/abs/1411.4038>.
- Migliori, M. E., and Gladstone, G. J. (1984). Determination of the normal range of exophthalmometric values for black and white adults. *Am. J. Ophthalmol.* 98 (4), 438–442. doi:10.1016/0002-9394(84)90127-2
- Milletari, F., Navab, N., and Ahmadi, S. A. (2016). “V-Net: Fully convolutional neural networks for volumetric medical image segmentation,” in *2016 fourth international conference on 3D vision (3DV)*.
- Musch, D. C., Frueh, B. R., and Landis, J. R. (1985). The reliability of Hertel exophthalmometry. Observer variation between physician and lay readers. *Ophthalmology* 92 (9), 1177–1180. doi:10.1016/S0161-6420(85)33880-0
- Na, R. P., Moon, J. H., and Lee, J. K. (2019). Hertel exophthalmometer versus computed tomography scan in proptosis estimation in thyroid-associated orbitopathy. *Clin. Ophthalmol.* 13, 1461–1467. doi:10.2147/OPTH.S216838
- Nkenke, E., Benz, M., Maier, T., Wiltfang, J., Holbach, L. M., Kramer, M., et al. (2003). Relative en- and exophthalmometry in zygomatic fractures comparing optical non-contact, non-ionizing 3D imaging to the Hertel instrument and computed tomography. *J. Cranio-Maxillofacial Surg.* 31 (6), 362–368. doi:10.1016/j.jcms.2003.07.001
- Nkenke, E., Maier, T., Benz, M., Wiltfang, J., Holbach, L. M., Kramer, M., et al. (2004). Hertel exophthalmometry versus computed tomography and optical 3D imaging for the determination of the globe position in zygomatic fractures. *Int. J. Oral Maxillofac. Surg.* 33 (2), 125–133. doi:10.1054/ijom.2002.0481
- O'Donnell, N. P., Virdi, M., and Kemp, E. G. (1999). Hertel exophthalmometry: The most appropriate measuring technique. *Br. J. Ophthalmol.* 83 (9), 1096b. doi:10.1136/bjo.83.9.1096b
- Paszke, A., Gross, S., Chintala, S., Chanan, G., Yang, E., Devito, Z., et al. (2017). *Automatic differentiation in PyTorch*.
- Ramli, N., Kala, S., Samsudin, A., Rahmat, K., and Zainal Abidin, Z. (2015). Proptosis—correlation and agreement between Hertel exophthalmometry and computed tomography. *Orbit* 34 (5), 257–262. doi:10.3109/01676830.2015.1057291
- Ronneberger, O., Fischer, P., and Brox, T. (2015). *U-Net: Convolutional networks for biomedical image segmentation*. (arXiv:1505.04597). arXiv. Available at: <http://arxiv.org/abs/1505.04597>.
- Segni, M., Bartley, G. B., Garrity, J. A., Bergstralh, E. J., and Gorman, C. A. (2002). Comparability of proptosis measurements by different techniques. *Am. J. Ophthalmol.* 133 (6), 813–818. doi:10.1016/s0002-9394(02)01429-0
- Sleep, T. J., and Manners, R. M. (2002). Interinstrument variability in hertel-type exophthalmometers. *Ophthalmic Plastic Reconstr. Surg.* 18 (4), 254–257. doi:10.1097/00002341-200207000-00004
- Willlaert, R., Shaheen, E., Deferm, J., Vermeersch, H., Jacobs, R., and Mombaerts, I. (2020). Three-dimensional characterisation of the globe position in the orbit. *Graefes Archive Clin. Exp. Ophthalmol.* 258 (7), 1527–1532. doi:10.1007/s00417-020-04631-w
- Zhang, Z., Liu, Q., and Wang, Y. (2018). Road extraction by deep residual U-net. *IEEE Geoscience Remote Sens. Lett.* 15 (5), 749–753. doi:10.1109/LGRS.2018.2802944
- Zhao, J., Lu, Y., Zhu, S., Li, K., Jiang, Q., and Yang, W. (2022). Systematic bibliometric and visualized analysis of research hotspots and trends on the application of artificial intelligence in ophthalmic disease diagnosis. *Front. Pharmacol.* 13, 930520. doi:10.3389/fphar.2022.930520
- Zhou, Z., Rahman Siddiquee, M. M., Tajbakhsh, N., and Liang, J. (2018). “UNet++: A nested U-net architecture for medical image segmentation,” in *Deep learning in medical image analysis and multimodal learning for clinical decision support*. Editors D. Stoyanov, Z. Taylor, G. Carneiro, T. Syeda-Mahmood, A. Martel, L. Maier-Hein, et al. (Springer International Publishing), 11045, 3–11. doi:10.1007/978-3-030-00889-5_1



OPEN ACCESS

EDITED BY

Yanwu Xu,
Baidu, China

REVIEWED BY

Yiqi Chen,
Zhejiang Provincial People's Hospital,
China
Shi Song Rong,
Massachusetts Eye and Ear Infirmary and
Harvard Medical School, United States
Zou Huan,
Xinqiao Hospital, China

*CORRESPONDENCE

Zhiqing Chen,
✉ chenzhiqing@zju.edu.cn
Juan Ye,
✉ yejuan@zju.edu.cn

[†]These authors contributed equally to this work and share the first authorship.

SPECIALTY SECTION

This article was submitted to Molecular and Cellular Pathology, a section of the journal Frontiers in Cell and Developmental Biology

RECEIVED 02 February 2023

ACCEPTED 27 February 2023

PUBLISHED 08 March 2023

CITATION

Song S, Jin K, Wang S, Yang C, Zhou J, Chen Z and Ye J (2023), Retinal fluid is associated with cytokines of aqueous humor in age-related macular degeneration using automatic 3-dimensional quantification. *Front. Cell Dev. Biol.* 11:1157497. doi: 10.3389/fcell.2023.1157497

COPYRIGHT

© 2023 Song, Jin, Wang, Yang, Zhou, Chen and Ye. This is an open-access article distributed under the terms of the [Creative Commons Attribution License \(CC BY\)](https://creativecommons.org/licenses/by/4.0/). The use, distribution or reproduction in other forums is permitted, provided the original author(s) and the copyright owner(s) are credited and that the original publication in this journal is cited, in accordance with accepted academic practice. No use, distribution or reproduction is permitted which does not comply with these terms.

Retinal fluid is associated with cytokines of aqueous humor in age-related macular degeneration using automatic 3-dimensional quantification

Siyuan Song^{1†}, Kai Jin^{1†}, Shuai Wang^{2,3}, Ce Yang², Jingxin Zhou¹, Zhiqing Chen^{1*} and Juan Ye^{1*}

¹Eye Center, The Second Affiliated Hospital, School of Medicine, Zhejiang University, Hangzhou, China,

²School of Mechanical, Electrical and Information Engineering, Shandong University, Weihai, China,

³School of Cyberspace, Hangzhou Dianzi University, Hangzhou, China

Background: To explain the biological role of cytokines in the eye and the possible role of cytokines in the pathogenesis of neovascular age-related macular degeneration (nAMD) by comparing the correlation between cytokine of aqueous humor concentration and optical coherence tomography (OCT) retinal fluid.

Methods: Spectral-domain OCT (SD-OCT) images and aqueous humor samples were collected from 20 nAMD patient's three clinical visits. Retinal fluid volume in OCT was automatically quantified using deep learning--Deeplabv3+. Eighteen cytokines were detected in aqueous humor using the Luminex technology. OCT fluid volume measurements were correlated with changes in aqueous humor cytokine levels using Pearson's correlation coefficient (PCC).

Results: The patients with intraretinal fluid (IRF) showed significantly lower levels of cytokines, such as C-X-C motif chemokine ligand 2 (CXCL2) ($p = 0.03$) and CXCL11 ($p = 0.009$), compared with the patients without IRF. And the IRF volume was negatively correlated with CXCL2 ($r = -0.407$, $p = 0.048$) and CXCL11 ($r = -0.410$, $p = 0.046$) concentration in the patients with IRF. Meanwhile, the subretinal fluid (SRF) volume was positively correlated with vascular endothelial growth factor (VEGF) concentration ($r = 0.299$, $p = 0.027$) and negatively correlated with interleukin (IL)-36 β concentration ($r = -0.295$, $p = 0.029$) in the patients with SRF.

Conclusion: Decreased level of VEGF was associated with decreased OCT-based retinal fluid volume in nAMD patients, while increased levels of CXCL2, CXCL11, and IL-36 β were associated with decreased OCT-based retinal fluid volume in nAMD patients, which may suggest a role for inflammatory cytokines in retinal morphological changes and pathogenesis of nAMD patients.

KEYWORDS

age-related macular degeneration, cytokine, deep learning, optical coherence tomography, quantitative analysis, retinal fluid

Introduction

As the aging of population in many countries, age-related degenerative diseases pose significant socio-economic challenges. One of the major degenerative diseases affecting the quality of life is age-related macular degeneration (AMD), affecting 8.7% of the global population (Wong et al., 2014). AMD can be neovascular or non-neovascular (Mitchell et al., 2018), of which neovascular AMD (nAMD) can lead to dramatic visual loss due to the destruction of retinal structure in the macular area, and permanent blindness in severe cases (Lim et al., 2012). Chronic inflammation, lipid deposition and oxidative stress are closely related to AMD pathogenesis (Miller, 2013; Fleckenstein et al., 2021). However, the specific association between the retinal morphological changes of AMD and chronic inflammation is still unclear.

Since its introduction, optical coherence tomography (OCT) rapidly became a widely used imaging technique for the diagnosis and treatment of a range of eye diseases affecting the choroid and retina (Huang et al., 1991). OCT imaging is non-invasive and fast to perform, compared with fundus fluorescein angiography (FFA). Compared to traditional fundus photography, OCT imaging could provide 2-3 dimensional structural information about the presence or absence of fluid in the intraretinal, subretinal, and the space below pigment epithelial layer, which are considered proxies for leakage (Wilde et al., 2015). OCT based fluid analyses of intraretinal fluid (IRF), subretinal fluid (SRF), and pigment epithelial detachment (PED) have proven promising for predicting functional deficits in nAMD (Klimescha et al., 2017). Previous studies have shown that retinal fluid change is a reliable OCT biomarker of nAMD (Schmidt-Erfurth et al., 2020; von der Burchard et al., 2018). The identification of retinal fluid based on OCT was subjective and time-consuming, and depended on the experience level of the clinician or observer, lacking an automatic quantification tool.

The emergence of deep learning has filled the gap in OCT imaging interpretation of retinal fluid and nAMD disease surveillance (Jin & Ye, 2022). Many studies have used deep learning technology to automatically detect and quantify baseline features in OCT from patients with AMD, such as IRF and SRF (Schlegl et al., 2018; Moraes et al., 2021). Sophie Riedl et al. related retinal fluid volume to visual acuity and found that the reduction of fluid volume in the retina was associated with visual recovery (Riedl et al., 2022). Quantitative retinal fluid volume has been used in many studies to evaluate the efficacy of anti-VEGF therapy (Schmidt-Erfurth et al., 2020; Michl et al., 2022). The application prospect of deep learning in OCT fluid segmentation makes it possible to quantitatively analyze the association between retinal fluid volume and inflammation.

Abnormal regulation of ocular inflammatory process plays an important role in the pathogenesis of AMD. The primary treatment for nAMD remains anti-vascular endothelial growth factor (VEGF) intravitreal injection, as clinical trials have demonstrated highly effective and tolerable safety profiles (Gillies et al., 2020; Woo et al., 2021; Holekamp et al., 2022). Unfortunately, some patients didn't respond well to anti-VEGF therapy (Brahmah et al., 2018), which may suggest that other inflammatory cytokines play a role in nAMD (Takeda et al., 2009). Aqueous humor and vitreous fluid can more directly and accurately reflect the intraocular inflammation of nAMD than serum. Previous studies have shown that the concentrations of many cytokines, including VEGF, angiogenin, growth-regulated oncogene, interferon γ -inducible protein (IP)-10 and macrophage inflammatory protein-1 β , increased in

aqueous humor and vitreous fluids of nAMD patients compared with normal subjects (Ambati et al., 2013; Agrawal et al., 2019; Tan et al., 2020; Zhou et al., 2020). Studies have shown that intravitreal triamcinolone acetonide can improve visual acuity and fundus performance in patients with nAMD in the short term (Danis et al., 2000). Therefore, understanding the relationship between intraocular cytokines and retinal morphological structure is of great significance for explaining the pathogenesis of AMD and developing new therapeutic strategies. However, few studies have linked retinal fluid to intraocular cytokines (Joo et al., 2021). There has not been a direct quantitative analysis of the association between retinal fluid volume and cytokines.

We aimed to explain the biological role played by cytokines in the eyes, the association between intraocular cytokines and retinal morphological changes, and the possible role of inflammatory cytokines in the pathogenesis of nAMD by quantitatively analyze the association between cytokine concentrations of aqueous humor and retinal fluid volume based on OCT.

Materials and methods

Study design

This study was a cross-sectional study. The Ethical Committee of the Second Affiliated Hospital, Zhejiang University School of Medicine approved the collection and study of human aqueous humor and OCT images. The patient's aqueous humor cytokine data were obtained from another study at our hospital (Chen et al., 2020; Chen et al., 2021). All patients were treated in accordance with the Declaration of Helsinki, and informed consent was obtained from all participants before study participation.

Inclusion/exclusion criteria

20 eyes of 20 consecutive patients with nAMD, who visited the Eye Center at the Second Affiliated Hospital of Zhejiang University (Hangzhou, China) from June 2017 to November 2018, were included in this study. The clinical diagnosis of nAMD was performed by FFA.

The inclusion criteria for this study were as follows: 1) age above 50 years; 2) First treatment; 3) No complications of other eye diseases. Exclusion criteria were: 1) pathological myopia; 2) Treatment history of nAMD, including intravitreal drug injection, photodynamic therapy, and steroid therapy; 3) Previous intraocular surgery, except for cataract surgery (which, for nAMD patients, must have been performed at least 12 months before inclusion); 4) Active inflammation, diabetes, use of immunosuppressive drugs and glucocorticoids, and local and systemic malignancies were excluded from this study.

OCT image collection and annotation

According to the date of three aqueous humor collections, the patients' closest OCT examinations to that date were collected. The days of difference between the two dates was no more than 7 days.

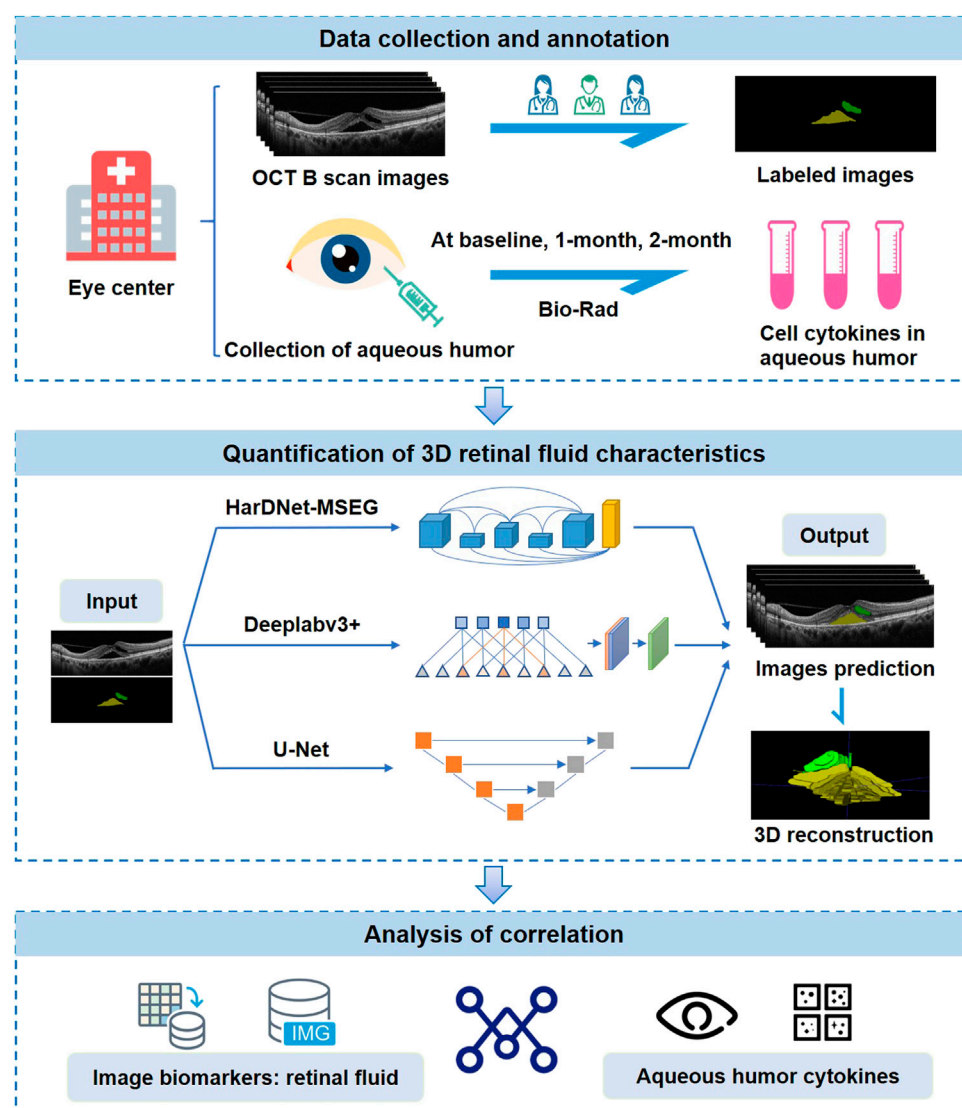


FIGURE 1

Study design. OCT images and aqueous humor samples are collected from eye centers and paired with each other. OCT images are annotated by three ophthalmologists. Retinal fluid volume is automatically segmented and quantified using three deep-learning models. Finally, the correlation between retinal fluid and aqueous humor cytokine levels is analyzed.

Therefore, three aqueous humor samples did not match OCT on the corresponding date. Finally, 57 sets of data matched aqueous humor cytokine data and OCT images were included in the study. All OCT images were taken by a spectral-domain OCT B-scan (RTVue XR, Optovue, Fremont, CA, United States) at 960×405 pixels. One OCT visit consisted of 18 B scan images taken with radiography. We hoped to accurately obtain the volume of retinal fluid in OCT images, so we needed to pursue the accuracy of prediction segmentation of the model, rather than the generalization of the model. Three images were randomly selected from each patient's baseline OCT examination and manually annotated by three ophthalmologists. They are considered experienced and highly trained in OCT fluid identification. IRF and SRF were independently labeled by three ophthalmologists, and inconsistent labels were determined by a majority after discussion.

Aqueous humor sample collection and cytokines measurement

All nAMD patients received intravitreal injection of 0.5 mg ranibizumab for three consecutive months. Aqueous humor samples were collected three times from each patient, at baseline (before the first injection), 1 month (before the second injection), and 2 months (before the third injection). Using Luminex technology (Bio-Rad, Waltham, MA, United States) on a Bio-Plex MAGPIX system, a total of twenty-eight cytokines were detected in aqueous humor by a multiplex cytokine assay Kit (Developed Systems, Minneapolis, MN, United States). Not all cytokines can be detected in every aqueous humor sample. Finally, eighteen cytokines that could be detected in specific numbers were included in the study. To avoid imprecision between trials, cytokines were measured in all patient samples in one trial. Sample concentrations

were calculated using multiparameter standard curves for each cytokine.

Automatic quantification of retinal fluid volume

We selected three deep learning models that have been relatively successful in the field of fluid segmentation—HarDNet-MSEG (Huang et al., 2021), Deeplabv3+ (Chen et al., 2018) and U-Net (Ronneberger et al., 2015) -- to predict the retinal fluid. To train the model for retinal fluid segmentation, we first put 48,694 OCT images with 1,000 labeled images from Second Affiliated Hospital of Xi'an Jiaotong University (Xibei Hospital) into the network for transfer training. As shown in Figure 1, we put 1026 OCT images with 60 labeled images in this study into three deep learning models, and all three models output the predicted images. Then the Deeplabv3+ with the relatively good performance was selected from the three models as the quantitative analysis tool.

3D reconstruction and volumetric algorithm of fluid

To get the 3D segmentation result, we first placed the current 2D segmentation result to the corresponding position in the 3D space, and then used the 3D nearest neighbor interpolation to fill the unknown regions in the 3D space. Because the value of the segmentation result mask had a fixed range and wasn't a continuous value, linear interpolation cannot be selected for the difference method, and the nearest neighbor interpolation was selected.

Statistical analysis

All data were presented as either mean or mean \pm standard deviation (SD). Pearson's Correlation Coefficient (PCC) was used to quantify the correlation between the cytokine of aqueous humor and the OCT-based retinal fluid volume. Kolmogorov-Smirnov test was used to test the normal distribution of all continuous variables. Cytokine's concentrations in the aqueous humor were compared between whether retina fluid presence or not using Student's t-test. Due to the skewed distribution of the fluid volume, the fluid volume was calculated as log base 10 -- lg (fluid volume).

SPSS software (version 25.0) was used for statistical analysis, $p < 0.05$ was considered statistically significant. Statistical maps were drawn by GraphPad Prism 8.

Result

Patient characteristics

A total of 57 sets of matched data from 20 eyes in 20 patients were finally included in the study. As shown in Table 1, the average of nAMD patient's age was 66.65 ± 6.98 years (mean \pm SD). Fourteen of the 20 nAMD cases (70%) were men, and nine of the 20 eyes (45%) were right eyes. And the biomarkers based on OCT were automatically measured by the deep learning model, and fluid volume was quantified.

TABLE 1 Demographic and clinical characteristics of the study population.

Age (mean \pm SD, years)	66.65 \pm 6.98
Gender (n, %)	
Male	14 (70)
Female	6 (30)
Laterality of eye (n, %)	
OD	9 (45)
OS	11 (55)
OCT feature	
IRF volume (mean \pm SD, μm^3)	$1.47 \times 10^7 \pm 5.57 \times 10^7$
lg (IRF volume)	2.54 ± 3.12
SRF volume (mean \pm SD, μm^3)	$3.39 \times 10^7 \pm 5.16 \times 10^7$
lg (SRF volume)	6.78 ± 1.52
Total fluid volume	$4.70 \times 10^7 \pm 9.16 \times 10^7$

IRF, intraretinal fluid; SRF, subretinal fluid.

The average of IRF and SRF volume were $1.47 \times 10^7 \pm 5.57 \times 10^7 \mu\text{m}^3$ and $3.39 \times 10^7 \pm 5.16 \times 10^7 \mu\text{m}^3$ (mean \pm SD). Due to the skewed distribution of the fluid volume, the fluid volume was calculated as log base 10. If the original fluid volume is 0, the logarithm cannot be taken, which was still regarded as 0. So the average of lgIRF (lg μm^3) and lgSRF (lg μm^3) were 2.54 ± 3.12 and 6.78 ± 1.52 (mean \pm SD).

Deep learning model performance

The three model's performance is shown in Table 2. The Deeplabv3+ showed the best performance for IRF segmentation, with the highest dice coefficient and precision of 0.802 and 0.952. The recall rate of Deeplabv3+ reached 0.794, which was not much different from the other two models. HarDNet-MSEG showed the best performance in SRF segmentation, with the dice coefficient and precision respectively reaching the highest values of 0.682 and 0.901. However, HarDNet-MSEG had poor performance in IRF segmentation, whose dice coefficient and precision were only 0.066 and 0.045. Meanwhile, Deeplabv3+ had the highest recall rate of 0.686 on segmental SRF. The dice coefficient and precision of Deeplabv3+ were 0.627 and 0.844, which were better than U-Net. Overall, the Deeplabv3+ model was selected as the tool for automated quantification of retinal fluid volume.

Comparison of intraocular cytokine between retinal fluid presence or absence

Patients with nAMD were subdivided by OCT component on different dates. In the 57 OCT examinations, 24 were found to have IRF presence and 33 were found IRF absence, while 55 were found to have SRF presence and two were found SRF absence. The patients with IRF showed significantly lower levels of inflammatory cytokines, such as C-X-C motif chemokine ligand 2 (CXCL2) ($p = 0.03$) and CXCL11 ($p = 0.009$), compared with the patients without IRF (Table 3). Figures 2A, C shows the results of statistically significant intraocular cytokines in the presence or absence of IRF. This suggested that IRF was sensitive to change in intraocular cytokine concentration.

However, we didn't observe a statistically significant effect of the presence or absence of SRF on intraocular cytokine concentration

TABLE 2 Quantitative results for the performance of three models.

Method	IRF			SRF		
	Dice	Precision	Recall	Dice	Precision	Recall
HarDNet-MSEG	0.066	0.045	0.886	0.682	0.901	0.680
Deeplabv3+	0.802	0.952	0.794	0.627	0.844	0.686
U-Net	0.536	0.642	0.818	0.621	0.798	0.736

IRF, intraretinal fluid; SRF, subretinal fluid. That the bold values indicates, the best performance value of the three models in this vertical column of evaluation indicators.

TABLE 3 Comparison of cytokine in the aqueous humor between patients with IRF or not and correlations between cytokine concentrations and IRF volume.

Cytokine in the aqueous humor (mean ± SD, pg/mL)	IRF			Ig IRF (IRF presence)	
	Presence (n = 24)	Absence (n = 33)	p-value	Pearson's correlation coefficient (95% CI)	p-value
IL-6	3.81 ± 3.74	5.02 ± 6.99	0.452	−0.073 (−0.463 to 0.341)	0.735
uPAR	69.23 ± 26.43	69.39 ± 16.04	0.979	−0.058 (−0.451 to 0.354)	0.790
CXCL10/IP-10/CRG-2	58.79 ± 66.47	115.40 ± 278.26	0.342	−0.175 (−0.541 to 0.246)	0.413
Endoglin	167.4 ± 15.20	173.12 ± 19.29	0.241	−0.086 (−0.473 to 0.329)	0.691
VEGF	33.68 ± 28.26	31.76 ± 21.82	0.777	0.038 (−0.371–0.435)	0.861
CXCL2/Gro β	44.87 ± 4.00	49.41 ± 9.21	0.030	−0.407 (−0.696 to −0.004)	0.048
CCL14/HCC-1	3,108.63 ± 1,109.56	3,154.48 ± 1,053.36	0.877	0.019 (−0.387–0.419)	0.929
CCL22/MDC	45.79 ± 2.60	46.70 ± 2.85	0.226	−0.152 (−0.523 to 0.268)	0.478
CCL21/6Ckine	21.29 ± 10.43	21.79 ± 8.32	0.843	0.110 (−0.307–0.491)	0.610
Thrombospondin-2	555.17 ± 161.62	524.02 ± 214.28	0.559	0.267 (−0.153–0.605)	0.207
CXCL11/I-TAC	16.19 ± 1.48	17.42 ± 1.79	0.009	−0.410 (−0.698 to −0.008)	0.046
Angiopoietin-1	78.88 ± 30.74	90.59 ± 43.90	0.276	0.062 (−0.350–0.454)	0.773
IL-36β/IL-1F8	1.26 ± 0.49	2.07 ± 4.10	0.345	−0.269 (−0.607 to 0.150)	0.203
HGF	328.69 ± 167.21	392.85 ± 392.80	0.463	0.009 (−0.396–0.411)	0.967
FGF acidic	33.45 ± 5.82	33.53 ± 7.33	0.967	−0.329 (−0.647 to 0.086)	0.117
PIGF	3.79 ± 1.21	3.35 ± 0.93	0.138	0.331 (−0.084–0.648)	0.114
ANGPTL4	5,178.5 ± 4,920.62	6,070.91 ± 5,702.11	0.547	0.008 (−0.397–0.410)	0.972
Endostatin	54,268.17 ± 16,879.46	56,772.09 ± 16,854.86	0.589	−0.109 (−0.491 to 0.308)	0.611

That the bold values indicates, $p < 0.05$ for p -values and Pearson's coefficients.

(Table 4). Since the presence of SRF could not be identified in only two of the 57 OCT examinations, this statistical result may not be interpretive.

Associations between intraocular cytokines and retinal fluid volume based on OCT

To further investigate the associations between the volume of IRF/SRF and cytokines of aqueous humor, we performed Pearson's coefficient correlation analysis in patients with IRF/SRF. Because of the skewed normal distribution of retinal fluid volume, we took

logarithm of retinal fluid volume for analysis. Among the eighteen cytokines, the same two cytokines were significantly correlated with IRF volume in the patients with IRF (Table 3). CXCL2 and CXCL11 were statistically significantly correlated with IRF ($p = 0.048$ and $p = 0.046$). Moreover, the IRF volume was negatively correlated with CXCL2 ($r = -0.407$, 95% CI: -0.696 to -0.004) and CXCL11 ($r = -0.410$, 95% CI: -0.698 to -0.008) concentration (Figures 2B, D).

Interestingly, a correlation between aqueous humor cytokines and SRF volume was observed in nAMD patients with SRF (Table 4). VEGF and interleukin (IL)-36β were statistically significantly correlated with SRF volume ($p = 0.027$ and $p = 0.029$). Moreover, the SRF volume was positively correlated with VEGF concentration ($r = 0.299$, 95% CI:

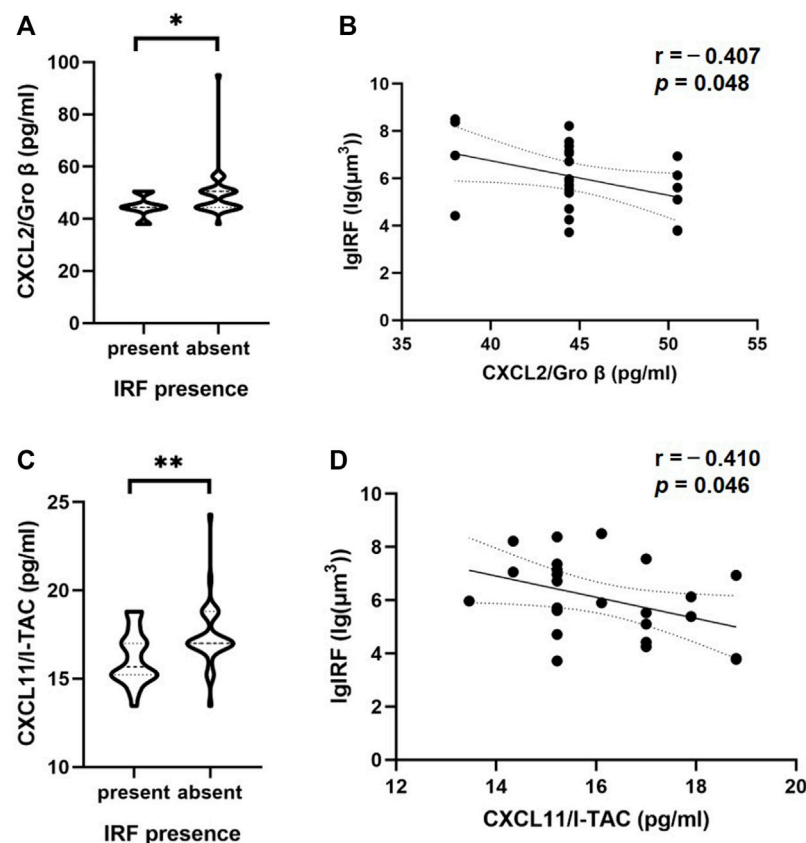


FIGURE 2

Correlations of cytokine in the aqueous humor and IRF based on OCT. The violin plot shows that there were significant differences between CXCL2/Gro β (A), CXCL11/I-TAC (C) and the presence or absence of IRF. (B, D) In patients with IRF, there was a significant inverse correlation between these two cytokines and IRF volume based on Pearson's correlation coefficient. Solid line, linear fitted trend line; Dotted line, 95% confidence interval. * $p < 0.05$, ** $p < 0.01$.

0.036–0.523) and negatively correlated with IL-36 β concentration ($r = -0.295$, 95% CI: -0.520 to -0.032) (Figures 3B, D). At the same time, we observed the classification of these two cytokines in patients with or without SRF (Figures 3A, C).

Discussion

In this study, we investigated the association of OCT-based retinal fluid with various cytokines of aqueous humor. The use of artificial intelligence to automatically analyze OCT images and allow quantification of retinal fluid volume is gaining popularity worldwide. A large number of deep learning models have been developed to quantify fluid volume features in OCT, and the deep learning tool used in our study reported non-inferior model performance in the field of retinal fluid segmentation (Lu et al., 2019; Terry et al., 2021). In previous studies, the central macular thickness based on OCT was associated with cytokine levels by manual measurement (Joo et al., 2021). Joseph R Abraham et al. quantified retinal fluid volume using deep learning in diabetic retinopathy and correlated it with aqueous humor cytokines (Abraham et al., 2021). Two-dimensional images alone cannot accurately measure the characteristics of retinal fluid, so we used SD-OCT volume model to quantitatively analyze the volume of retinal fluid.

Deep learning has significant advantages in quantitative analysis of retinal fluid volume, saving labor cost and time cost. For the first time, we used deep learning to quantify retinal fluid volume in AMD patients and quantitatively associated it with aqueous humor cytokine levels.

The cytokines of aqueous humor and vitreous fluid can better reflect the disease status of the retina than those in serum. Diagnostic sampling of vitreous fluids helps in the diagnosis and treatment of ocular diseases (Funatsu et al., 2006). Obtaining vitreous fluid from a patient's eye is riskier than collecting aqueous humor, which can lead to side effects such as vitreous bleeding and retinal detachment. Significant correlations have been reported between cytokine levels in aqueous humor and vitreous fluids (Butler et al., 2020). In our study, cytokines of aqueous humor rather than serum were measured and associated with retinal fluid volume based on OCT.

The role of VEGF in AMD has been strongly supported in several studies (Lee et al., 2018; Yang et al., 2022). VEGF appears to be a major stimulator of neovascularization growth originating from the retinal and choroidal vasculature (Mameros, 2021). There have been many studies showing significant resolution of SRF after anti-VEGF treatment (Amoaku et al., 2015; Schmidt-Erfurth et al., 2020), suggesting that the reduction of VEGF was associated with SRF shrinkage. These results were consistent with our study, in which we found that decreased VEGF concentration of aqueous humor was associated with reduced SRF

TABLE 4 Comparison of cytokine in the aqueous humor between patients with SRF or not and correlations between cytokine concentrations and SRF volume.

Cytokine in the aqueous humor (mean \pm SD, pg/mL)	SRF			lg SRF (SRF presence)	
	Presence (n = 55)	Absence (n = 2)	p-value	Pearson's correlation coefficient (95% CI)	p-value
IL-6	4.61 \pm 5.95	1.61 \pm 0.00	0.486	0.035 (−0.233–0.297)	0.803
uPAR	69.44 \pm 21.41	66.07 \pm 3.14	0.827	−0.059 (−0.319 to 0.209)	0.668
CXCL10/IP-10/CRG-2	93.99 \pm 221.41	24.84 \pm 12.02	0.666	0.057 (−0.212–0.317)	0.680
Endoglin	170.98 \pm 18.17	163.40 \pm 0.00	0.565	0.001 (−0.265–0.266)	0.996
VEGF	32.21 \pm 25.03	42.55 \pm 11.6	0.570	0.299 (0.036 to 0.523)	0.027
CXCL2/Gro β	47.50 \pm 7.92	47.46 \pm 3.05	0.995	0.011 (−0.255–0.276)	0.934
CCL14/HCC-1	3,150.38 \pm 1,078.57	2,717.00 \pm 961.00	0.584	0.150 (−0.120–0.399)	0.275
CCL22/MDC	46.39 \pm 2.81	44.24 \pm 0.00	0.291	−0.075 (−0.334 to 0.194)	0.585
CCL21/6CKine	21.44 \pm 9.34	25.29 \pm 5.90	0.573	0.027 (−0.240–0.290)	0.848
Thrombospondin-2	537.80 \pm 197.59	518.99 \pm 61.28	0.895	0.048 (−0.221–0.309)	0.730
CXCL11/I-TAC	16.94 \pm 1.79	15.67 \pm 0.44	0.325	−0.011 (−0.275 to 0.256)	0.939
Angiopoietin-1	85.55 \pm 39.89	88.52 \pm 17.78	0.919	0.140 (−0.130–0.391)	0.307
IL-36 β /IL-1F8	1.75 \pm 3.22	1.16 \pm 0.08	0.798	−0.295 (−0.520 to −0.032)	0.029
HGF	370.25 \pm 324.44	244.46 \pm 3.95	0.592	0.055 (−0.214–0.315)	0.692
FGF acidic	33.67 \pm 6.79	28.67 \pm 1.34	0.311	0.009 (−0.257–0.273)	0.951
PIGF	3.54 \pm 1.09	3.26 \pm 0.31	0.720	0.097 (−0.173–0.353)	0.482
ANGPTL4	5,773.27 \pm 5,485.33	3,547.00 \pm 582.00	0.575	−0.098 (−0.354 to 0.172)	0.478
Endostatin	55,843.29 \pm 17,120.05	52,267.00 \pm 8,803.00	0.774	0.090 (−0.179–0.347)	0.512

That the bold values indicates, $p < 0.05$ for p -values and Pearson's coefficients.

volume in nAMD patients with SRF. However, a few studies have reported non-resolution of SRF in the patients with AMD despite anti-VEGF therapy (Hosseini et al., 2021).

The mast cell and macrophage chemokine CXCL2 was found to control the early stages of neutrophil recruitment during tissue inflammation (De Filippo et al., 2013). Md Huzzatul Mursalin et al. found the utility of CXCL2 as a potential target for anti-inflammatory therapy for intraocular inflammation in mice (Mursalin et al., 2021). Retinal pigment epithelium dysfunction caused by abnormal inflammatory responses is associated with the pathogenesis of AMD (Ambati et al., 2013). Previous studies have reported that human retinal pigment epithelium cells produce CXCL11 under inflammatory conditions (Kutty et al., 2015). IL-36 β protected mice from herpes virus infection and had a regulatory effect on immune function (Milora et al., 2017). Our study was the first to show that CXCL2 and CXCL11 concentration in aqueous humor of nAMD patients with IRF is significantly lower than that of patients without IRF. Meanwhile, in patients with IRF, the concentration of CXCL2 and CXCL11 was negatively associated with the volume of IRF based on OCT. We also found that the concentration of IL-36 β was negatively associated with the volume of SRF based on OCT in patients with SRF. The reduction in IRF and SRF volume in some sense represents a reduction in the degree of disease activity. These suggested that chemokines may play a role in

regulating the retinal inflammatory response and macrophage recruitment may partially prevent the deposition of harmful substances in the retina. Appropriate concentration of chemokines can recruit macrophages to gather in the eye, phagocytic harmful substances and reduce inflammatory exudation, so the volume of retinal effusion is reduced.

The pathological environment in the eye, such as ischemia, hypoxia or inflammation, is a pro-angiogenic factor that can lead to the formation of new blood vessels, and corresponding cytokines are involved in these processes. Research into the cytokines and retinal fluid volume associated with AMD pathogenesis may provide new insights into the development of targeted drugs and more effective AMD therapies.

Our study had certain limitations. The number of patients included in the study was only 20 patients, although each patient provided data from three pairs. This was limited by the invasive procedure of obtaining aqueous humor, which can be obtained only in patients receiving anti-VEGF therapy. At the same time, there were fewer data for the absence of SRF, which also led to the statistical results being not meaningful for interpretation.

In summary, changes in cytokine levels after treatment support the notion that the intraocular cytokines other than VEGF were involved in pathogenesis of AMD and morphological changes of retina. Our study suggested that CXCL2, CXCL11 and IL-36 β might be some biomarkers or predictors of response to anti-VEGF therapy

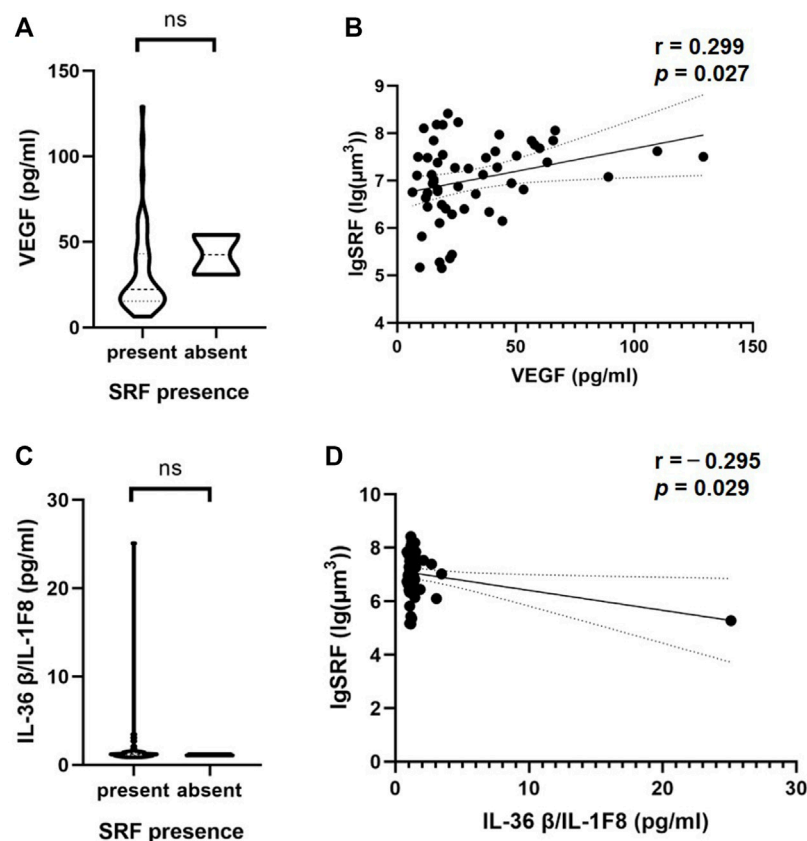


FIGURE 3

Correlations of cytokine in the aqueous humor and SRF based on OCT. The violin plot shows that there were no significant differences between VEGF (A), IL-36 β /IL-1F8 (C) and the presence or absence of SRF. (B, D) In patients with SRF, there was a significant inverse correlation between these two cytokines and SRF volume based on Pearson's correlation coefficient. Solid line, linear fitted trend line; Dotted line, 95% confidence interval. * $p < 0.05$, ** $p < 0.01$.

or corticosteroids, thereby allowing targeted and individualized therapy guided by cytokine levels.

Data availability statement

The raw data supporting the conclusion of this article will be made available by the authors, without undue reservation.

Ethics statement

The studies involving human participants were reviewed and approved by The Ethical Committee of the Second Affiliated Hospital, Zhejiang University School of Medicine. The patients/participants provided their written informed consent to participate in this study.

Author contributions

SS, KJ, ZC, and JY conceived and designed the experiments. SS, JZ, and ZC, collected and provided the data. SW and CY preprocessed the data and developed the deep learning system. KJ and SS analyzed the

results. The first draft of the manuscript was written by SS and all authors commented on previous versions of the manuscript. All authors reviewed and approved the final manuscript.

Funding

Sponsorship for this study was funded by National Key Research and Development Program of China (Grant Number 2019YFC0118400), Zhejiang Provincial Key Research and Development Plan (Grant Number 2019C03020), Natural Science Foundation of China (Grant Number 82201195), Natural Science Foundation of Zhejiang Province (LQ21H120002), the Clinical Medical Research Center for Eye Diseases of Zhejiang Province (2021E50007), and National Natural Science Foundation Regional Innovation and Development Joint Fund (U20A20386).

Conflict of interest

The authors declare that the research was conducted in the absence of any commercial or financial relationships that could be construed as a potential conflict of interest.

Publisher's note

All claims expressed in this article are solely those of the authors and do not necessarily represent those of their affiliated

References

- Abraham, J. R., Wyckoff, C. C., Arepalli, S., Lunasco, L., Yu, H. J., Hu, M., et al. (2021). Aqueous cytokine expression and higher order OCT biomarkers: Assessment of the anatomic-biologic bridge in the IMAGINE DME study. *Am. J. Ophthalmol.* 222, 328–339. doi:10.1016/j.ajo.2020.08.047
- Agrawal, R., Balne, P. K., Wei, X., Bijin, V. A., Lee, B., Ghosh, A., et al. (2019). Cytokine profiling in patients with exudative age-related macular degeneration and polypoidal choroidal vasculopathy. *Invest. Ophthalmol. Vis. Sci.* 60, 376–382. doi:10.1167/iovs.18-24387
- Ambati, J., Atkinson, J. P., and Gelfand, B. D. (2013). Immunology of age-related macular degeneration. *Nat. Rev. Immunol.* 13, 438–451. doi:10.1038/nri3459
- Amoaku, W. M., Chakravarthy, U., Gale, R., Ghanchi, F., Gibson, J., et al. (2015). Defining response to anti-VEGF therapies in neovascular AMD. *Eye Lond Engl.* 29, 721–731. doi:10.1038/eye.2015.48
- Braimah, I. Z., Agarwal, K., Mansour, A., and Chhablani, J. Ziv-aflibercept Study Group (2018). One-year outcome of intravitreal ziv-aflibercept therapy for non-responsive neovascular age-related macular degeneration. *Br. J. Ophthalmol.* 102, 91–96. doi:10.1136/bjophthalmol-2017-310318
- Butler, D. C., Schandl, C., Hyer, M., and Erin Presnell, S. (2020). Aqueous fluid as a viable substitute for vitreous fluid in postmortem chemistry analysis. *J. Forensic Sci.* 65, 508–512. doi:10.1111/1556-4029.14178
- Chen, K., Xu, W., Zheng, J., Shen, Y., Ma, J., and Chen, Z. (2020). Angiogenin, FGF- α , and IL-36 β have higher expression levels in aqueous humor of nAMD patients in comparison to cataract patients. *BMC Ophthalmol.* 20, 431. doi:10.1186/s12886-020-01684-7
- Chen, L.-C., Zhu, Y., Papandreou, G., Schroff, F., and Adam, H. (2018). Encoder-decoder with atrous separable convolution for semantic image segmentation. arXiv.
- Chen, Z., Chen, K., Li, J., Shen, J., and Xu, W. (2021). Elevated levels of endoglin, endostatin, FGF- α , HGF, and thrombospondin-2 in aqueous humor of nAMD patients. *Ocul. Immunol. Inflamm.* 30, 1092–1098. doi:10.1080/09273948.2020.1869785
- Danis, R. P., Ciulla, T. A., Pratt, L. M., and Anliker, W. (2000). Intravitreal triamcinolone acetonide in exudative age-related macular degeneration. *Retina Phila Pa* 20, 244–250. doi:10.1097/00006982-200003000-00004
- De Filippo, K., Dudeck, A., Hasenberg, M., Nye, E., van Rooijen, N., Hartmann, K., et al. (2013). Mast cell and macrophage chemokines CXCL1/CXCL2 control the early stage of neutrophil recruitment during tissue inflammation. *Blood* 121, 4930–4937. doi:10.1182/blood-2013-02-486217
- Fleckenstein, M., Keenan, T. D. L., Guymer, R. H., Chakravarthy, U., Schmitz-Valckenberg, S., Klaver, C. C., et al. (2021). Age-related macular degeneration. *Nat. Rev. Dis. Primer* 7, 31–25. doi:10.1038/s41572-021-00265-2
- Funatsu, H., Yamashita, T., and Yamashita, H. (2006). Vitreous fluid biomarkers. *Adv. Clin. Chem.* 42, 111–166. doi:10.1016/s0065-2423(06)42004-7
- Gillies, M. C., Hunyor, A. P., Arnold, J. J., Guymer, R. H., Wolf, S., Pecher, F. L., et al. (2020). Macular atrophy in neovascular age-related macular degeneration: A randomized clinical trial comparing ranibizumab and aflibercept (rival study). *Ophthalmology* 127, 198–210. doi:10.1016/j.ophtha.2019.08.023
- Holekamp, N. M., Campochiaro, P. A., Chang, M. A., Miller, D., Pieramici, D., Adamis, A. P., et al. (2022). Archway randomized phase 3 trial of the port delivery system with ranibizumab for neovascular age-related macular degeneration. *Ophthalmology* 129, 295–307. doi:10.1016/j.ophtha.2021.09.016
- Hosseini, H., Rabina, G., Pettenkofer, M., Au, A., Chehaibou, I., Heilweil, G., et al. (2021). Clinical characteristics and visual outcomes of non-resolving subretinal fluid in neovascular AMD despite continuous monthly anti-VEGF injections: A long-term follow-up. *Graefes Arch. Clin. Exp. Ophthalmol. Albr. Von. Graefes Arch. Klin. Exp. Ophthalmol.* 259, 1153–1160. doi:10.1007/s00417-020-05024-9
- Huang, C.-H., Wu, H.-Y., and Lin, Y.-L. (2021, January 20): HardNet-MSEG: A simple encoder-decoder polyp segmentation neural network that achieves over 0.9 mean dice and 86 FPS. arXiv.
- Huang, D., Swanson, E. A., Lin, C. P., Schuman, J. S., Stinson, W. G., Chang, W., et al. (1991). Optical coherence tomography. *Science* 254, 1178–1181. doi:10.1126/science.1957169
- Jin, K., and Ye, J. (2022). Artificial intelligence and deep learning in ophthalmology: Current status and future perspectives. *Adv. Ophthalmol. Pract. Res.* 2, 100078. doi:10.1016/j.aopr.2022.100078
- Joo, J.-H., Kim, H., Shin, J.-H., and Moon, S. W. (2021). Aqueous humor cytokine levels through microarray analysis and a sub-analysis based on optical coherence tomography in wet age-related macular degeneration patients. *BMC Ophthalmol.* 21, 399. doi:10.1186/s12886-021-02152-6
- Klimscha, S., Waldstein, S. M., Schlegl, T., Bogunovic, H., Sadeghipour, A., Philip, A. M., et al. (2017). Spatial correspondence between intraretinal fluid, subretinal fluid, and pigment epithelial detachment in neovascular age-related macular degeneration. *Invest. Ophthalmol. Vis. Sci.* 58, 4039–4048. doi:10.1167/iovs.16-20201
- Kutty, R. K., Samuel, W., Abay, R., Cherukuri, A., Nagineni, C. N., Duncan, T., et al. (2015). Resveratrol attenuates CXCL11 expression induced by proinflammatory cytokines in retinal pigment epithelial cells. *Cytokine* 74, 335–338. doi:10.1016/j.cyt.2015.03.016
- Lee, S. H. S., Kim, H. J., Shin, O. K., Choi, J. S., Kim, J., Cho, Y. H., et al. (2018). Intravitreal injection of AAV expressing soluble VEGF receptor-1 variant induces anti-VEGF activity and suppresses choroidal neovascularization. *Invest. Ophthalmol. Vis. Sci.* 59, 5398–5407. doi:10.1167/iovs.18-24926
- Lim, L. S., Mitchell, P., Seddon, J. M., Holz, F. G., and Wong, T. Y. (2012). Age-related macular degeneration. *Lancet* 379, 1728–1738. doi:10.1016/S0140-6736(12)60282-7
- Lu, D., Heisler, M., Lee, S., Ding, G. W., Navajas, E., Sarunic, M. V., et al. (2019). Deep-learning based multiclass retinal fluid segmentation and detection in optical coherence tomography images using a fully convolutional neural network. *Med. Image Anal.* 54, 100–110. doi:10.1016/j.media.2019.02.011
- Marneros, A. G. (2021). Role of inflammasome activation in neovascular age-related macular degeneration. *FEBS J.* 290, 28–36. doi:10.1111/febs.16278
- Michl, M., Fabianska, M., Seeböck, P., Sadeghipour, A., Haj Najeeb, B., Bogunovic, H., et al. (2022). Automated quantification of macular fluid in retinal diseases and their response to anti-VEGF therapy. *Br. J. Ophthalmol.* 106, 113–120. doi:10.1136/bjophthalmol-2020-317416
- Miller, J. W. (2013). Age-related macular degeneration revisited-piecing the puzzle: The LXIX edward jackson memorial lecture. *Am. J. Ophthalmol.* 155, 1–35. doi:10.1016/j.ajo.2012.10.018
- Milora, K. A., Uppalapati, S. R., Sanmiguel, J. C., Zou, W., and Jensen, L. E. (2017). Interleukin-36 β provides protection against HSV-1 infection, but does not modulate initiation of adaptive immune responses. *Sci. Rep.* 7, 5799. doi:10.1038/s41598-017-05363-4
- Mitchell, P., Liew, G., Gopinath, B., and Wong, T. Y. (2018). Age-related macular degeneration. *Lancet* 392, 1147–1159. doi:10.1016/S0140-6736(18)31550-2
- Moraes, G., Fu, D. J., Wilson, M., Khalid, H., Wagner, S. K., Korot, E., et al. (2021). Quantitative analysis of OCT for neovascular age-related macular degeneration using deep learning. *Ophthalmology* 128, 693–705. doi:10.1016/j.ophtha.2020.09.025
- Mursalin, M. H., Coburn, P. S., Miller, F. C., Livingston, E. T., Astley, R., and Callegan, M. C. (2021). C-X-C chemokines influence intraocular inflammation during Bacillus endophthalmitis. *Invest. Ophthalmol. Vis. Sci.* 62, 14. doi:10.1167/iovs.62.14.14
- Riedl, S., Vogl, W.-D., Waldstein, S. M., Schmidt-Erfurth, U., and Bogunović, H. (2022). Impact of intra- and subretinal fluid on vision based on volume quantification in the HARBOR trial. *Ophthalmol. Retina* 6, 291–297. doi:10.1016/j.oret.2021.12.007
- Ronneberger, O., Fischer, P., and Brox, T. (2015): U-Net: Convolutional networks for biomedical image segmentation. arXiv.
- Schlegl, T., Waldstein, S. M., Bogunovic, H., EndstraBer, F., Sadeghipour, A., Philip, A. M., et al. (2018). Fully automated detection and quantification of macular fluid in OCT using deep learning. *Ophthalmology* 125, 549–558. doi:10.1016/j.ophtha.2017.10.031
- Schmidt-Erfurth, U., Vogl, W.-D., Jampol, L. M., and Bogunović, H. (2020). Application of automated quantification of fluid volumes to anti-VEGF therapy of neovascular age-related macular degeneration. *Ophthalmology* 127, 1211–1219. doi:10.1016/j.ophtha.2020.03.010
- Takeda, A., Baffi, J. Z., Kleinman, M. E., Cho, W. G., Nozaki, M., Yamada, K., et al. (2009). CCR3 is a target for age-related macular degeneration diagnosis and therapy. *Nature* 460, 225–230. doi:10.1038/nature08151
- Tan, W., Zou, J., Yoshida, S., Jiang, B., and Zhou, Y. (2020). The role of inflammation in age-related macular degeneration. *Int. J. Biol. Sci.* 16, 2989–3001. doi:10.7150/ijbs.49890
- Terry, L., Trikha, S., Bhatia, K. K., Graham, M. S., and Wood, A. (2021). Evaluation of automated multiclass fluid segmentation in optical coherence tomography images using the pegasus fluid segmentation algorithms. *Transl. Vis. Sci. Technol.* 10, 27. doi:10.1167/tvst.10.1.27
- von der Burchard, C., Treumer, F., Ehlken, C., Koinzer, S., Purtskhvanidze, K., Tode, J., et al. (2018). Retinal volume change is a reliable OCT biomarker for disease activity in neovascular AMD. *Graefes Arch. Clin. Exp. Ophthalmol.* 256, 1623–1629. doi:10.1007/s00417-018-4040-7

- Wilde, C., Patel, M., Lakshmanan, A., Amankwah, R., Dhar-Munshi, S., Amoaku, W., et al. (2015). The diagnostic accuracy of spectral-domain optical coherence tomography for neovascular age-related macular degeneration: A comparison with fundus fluorescein angiography. *Eye* 29, 602–609. doi:10.1038/eye.2015.44
- Wong, W. L., Su, X., Li, X., Cheung, C. M. G., Klein, R., Cheng, C.-Y., et al. (2014). Global prevalence of age-related macular degeneration and disease burden projection for 2020 and 2040: A systematic review and meta-analysis. *Lancet Glob. Health* 2, e106–e116. doi:10.1016/S2214-109X(13)70145-1
- Woo, S. J., Veith, M., Hamouz, J., Ernest, J., Zalewski, D., Studnicka, J., et al. (2021). Efficacy and safety of a proposed ranibizumab biosimilar product vs a reference ranibizumab product for patients with neovascular age-related macular degeneration: A randomized clinical trial. *JAMA Ophthalmol.* 139, 68–76. doi:10.1001/jamaophthalmol.2020.5053
- Yang, S., Li, T., Jia, H., Gao, M., Li, Y., Wan, X., et al. (2022). Targeting C3b/C4b and VEGF with a bispecific fusion protein optimized for neovascular age-related macular degeneration therapy. *Sci. Transl. Med.* 14, eabj2177. doi:10.1126/scitranslmed.abj2177
- Zhou, H., Zhao, X., Yuan, M., and Chen, Y. (2020). Comparison of cytokine levels in the aqueous humor of polypoidal choroidal vasculopathy and neovascular age-related macular degeneration patients. *BMC Ophthalmol.* 20, 15. doi:10.1186/s12886-019-1278-8



OPEN ACCESS

EDITED BY

Weihua Yang,
Jinan University, China

REVIEWED BY

Zhijiang Wan,
Nanchang University, China
Tianming Huo,
Wuhan University, China
Chen-Xing Qi,
Renmin Hospital of Wuhan University,
China

*CORRESPONDENCE

Wensheng Li,
✉ drlws@qq.com
Xin Huang,
✉ 2017103020035@whu.edu.cn

SPECIALTY SECTION

This article was submitted to Molecular
and Cellular Pathology,
a section of the journal
Frontiers in Cell and
Developmental Biology

RECEIVED 07 February 2023

ACCEPTED 08 March 2023

PUBLISHED 17 March 2023

CITATION

Wu Y, Feng Y, Yang J, Fan H, Yu Z, Xie X,
Dai Y, Huang X and Li W (2023), Effects of
exogenous retinoic acid on ocular
parameters in Guinea pigs with form
deprivation myopia.
Front. Cell Dev. Biol. 11:1160897.
doi: 10.3389/fcell.2023.1160897

COPYRIGHT

© 2023 Wu, Feng, Yang, Fan, Yu, Xie, Dai,
Huang and Li. This is an open-access
article distributed under the terms of the
[Creative Commons Attribution License
\(CC BY\)](https://creativecommons.org/licenses/by/4.0/). The use, distribution or
reproduction in other forums is
permitted, provided the original author(s)
and the copyright owner(s) are credited
and that the original publication in this
journal is cited, in accordance with
accepted academic practice. No use,
distribution or reproduction is permitted
which does not comply with these terms.

Effects of exogenous retinoic acid on ocular parameters in Guinea pigs with form deprivation myopia

Yajun Wu^{1,2,3}, Yuliang Feng^{1,2,3}, Jiasong Yang^{1,2,3}, Hua Fan^{2,3},
Zitong Yu^{2,3}, Xiaolin Xie^{2,3}, Yumeng Dai^{2,3}, Xin Huang^{4*} and
Wensheng Li^{1,2,3*}

¹Aier School of Ophthalmology, Central South University, Changsha, Hunan, China, ²Department of Ophthalmology, Shanghai Aier Ophthalmology Hospital, Shanghai, China, ³Shanghai Aier Eye Institute, Shanghai, China, ⁴Department of Ophthalmology, Jiangxi Provincial People's Hospital, The First Affiliated Hospital of Nanchang Medical College, Nanchang, Jiangxi, China

Aim: Myopia is a common chronic eye disease, this study is to investigate the effects of exogenous retinoic acid (RA) on intraocular parameters, especially choroidal thickness (CT) and retinal thickness (RT), in guinea pigs with form deprivation myopia (FDM).

Methods: A total of 80 male guinea pigs were divided randomly into 4 groups: Control, FDM, FDM + RA, and FDM + Citral groups. The FDM + RA group was given 24 mg/kg RA dissolved in 0.4 mL peanut oil; the FDM + Citral group was given citral 445 mg/kg dissolved in 0.4 mL peanut oil; The other two groups were given 0.4 mL peanut oil. After 4 weeks, the refractive error (RE), axial length (AL), and intraocular pressure (IOP) of all guinea pigs were measured, and the parameters of RT and CT were obtained using enhanced depth imaging optical coherence tomography (EDI-OCT).

Results: After 4 weeks, both the RE and AL in the FDM and FDM + RA groups were increased, and the RT and CT in both groups were smaller than those in the Control group ($p < 0.05$). Only the IOP of the right eye in the FDM + RA group increased significantly ($p < 0.05$). The RT of the right eye of the 4 groups was compared: Control group > FDM + Citral group > FDM group > FDM + RA group. Compared with the RT of the left eye and the right eye among the 4 groups, the RT of the right eye in the FDM and FDM + RA groups was significantly less than that in the left eye ($p < 0.05$). Moreover, the CT of the right eye in the Control group was greater than that in the other three groups ($p < 0.0001$). There was no significant difference in the CT among the FDM, FDM + RA, and FDM + Citral groups ($p > 0.05$). In contrast to the RT results, the CT results of the left and right eyes in the FDM + Citral group showed statistically significant differences ($p < 0.05$).

Conclusion: RA participates in the progression of FDM as a regulatory factor. Exogenous RA can increase the RE, AL, and IOP of FDM guinea pigs, and might aggravate the retinal thinning of FDM guinea pigs. Citral can inhibit these changes, but RA might not affect the thickness of the choroid.

KEYWORDS

choroidal thickness, EDI-OCT, form deprivation myopia, Guinea pigs, myopia, retinal thickness, retinoic acid

Introduction

Myopia is the most common refractive error (RE) (Dolgin, 2015), and its incidence is still on the rise (Han et al., 2022), reaching epidemic levels (Medina, 2021). The highest incidence of myopia in the world is in East Asia, where the rate among children alone is as high as 7%–30% (Lee et al., 2022), and the prevalence of myopia in young adults is as high as 80%–90%, among which the prevalence of high myopia (HM) [diopter (D) < −6 or axial length (AL) > 26 mm] is approximately 10%–20% (Morgan et al., 2018). Moreover, among East Asian countries, the prevalence of myopia among students is particularly severe in China, where it is predicted that, by 2050, the prevalence of myopia among children and adolescents aged 3–19 years old might be as high as 84% (Dong et al., 2020). In addition, the prevalence of myopia among high-school students in East and Southeast Asia is approximately 30-times higher than in sub-Saharan Africa (Jonas et al., 2021). The situation of myopia among adolescents is particularly serious, especially in East Asian countries. Adolescents (young people aged 10–19) (Das et al., 2017) are crucial to the future development and progress of a country, and adolescent eye health is related to the national health (Shi et al., 2022), therefore, the high incidence of myopia will bring a burden to society and families. Thus, to slow down or even prevent the high incidence rate of myopia, it is necessary to clarify the mechanism of its occurrence and development, and this is the main direction of myopia research at present.

Retinoic acid (RA) is an acid derivative of vitamin A, which is the one-way oxidation product of photosensitive cells in the eye (Brown et al., 2022a; Brown et al., 2022b), and RA has an important role in eye development. Citral is a competitive inhibitor of the key dehydrogenase required for RA generation. Studies have shown that the retinal RA content of myopia is significantly higher than that of non-myopia (Brown et al., 2022a; Brown et al., 2022b). Also, Wang et al. found that the level of RA and the expression level of Zonula occludens-1 (ZO-1) and occludin in the retinal pigment epithelium (RPE)–choroid complex of lens induced myopia (LIM) guinea pigs were significantly increased, whereas the expression of RA and the proteins of ZO-1 and occludin in LIM guinea pigs treated with RA antagonists were inhibited (Wang et al., 2014). These studies show that RA is involved in myopia regulation. However, the specific role and mechanism of RA in myopia are not clear, as well as its effects on the retina and choroid.

Furthermore, to evaluate the severity of myopia, it is important to obtain relevant ophthalmic indicators. Generally, RE and AL are considered as the most important parameters, and almost all myopia studies will obtain these two parameters, or at least one of them (Tideman et al., 2018; Hughes et al., 2020), also, which will be used as the indicator to evaluate the prevention and control effect of myopia (Chamberlain et al., 2021). The appearance of imaging instruments has provided assistance for the acquisition of ophthalmic parameters. For example, intraocular lens-master (IOL-master), A-scan, and optical coherence tomography (OCT) can be used for the acquisition of AL, of which IOL-master is used widely in clinic, whereas A-scan is used widely in animal research of myopia (Yang et al., 2021). Enhanced depth imaging OCT (EDI-OCT) can be used to acquire choroidal images, compared with ordinary OCT,

which focuses on the retina, and it can improve the quality of choroidal imaging significantly (Sodi et al., 2018a; Sodi et al., 2018b). Thus, EDI-OCT can be used to obtain clear images of the retina and choroid, and the built-in software of its detection system can measure retinal thickness (RT) and choroidal thickness (CT) manually. Moreover, many studies have proved that myopia can also affect RT and CT. Zhang et al. (Zhang et al., 2019) measured the CT of spontaneous myopia guinea pigs, form deprivation myopia (FDM) guinea pigs, and LIM guinea pigs, finding that the CT of the three groups decreased in the myopia stage, but increased in the myopia recovery stage, so they suggested that CT could be used as an early predictor of myopia. Also, Jonas et al. (Jonas et al., 2019) believed that axial myopia could lead to thinning of the retina at the posterior pole, especially around the optic disc, and that AL was related to the RT around the optic disc, but not to the RT of the macula. They believed that axial myopia would cause additional Bruch membrane to be produced in the area behind the equator of the eye, thus causing thinning of the retina around the optic disc, whereas the macular area would not be affected. However, the CT and RT measured in most studies are usually the macular part, not the periphery of the optic disc (Tian et al., 2021).

At present, although it has been known that RA might be involved in the occurrence and development of myopia in guinea pigs, its mechanism is not clear, and no studies have reported the effect of RA on RT and CT in FDM guinea pigs. Therefore, this study intends to explore the effect of RA on the intraocular parameters of guinea pigs with myopia, especially the effects of RA on peripheral RT and CT of the optic disc in FDM guinea pigs by using EDI-OCT.

Materials and methods

Animals

A total of 80 male 2-week-old British guinea pigs [Beijing Weitong Lihua Experimental Animal Technology Co., Ltd., China, production license number: SCXK (Beijing) 2021-0011] were selected. All guinea pigs were kept in a clean environment at a room temperature of 18–29 °C (daily temperature difference ≤4 °C) and relative humidity of 40–70%. Inclusion criteria: 1. male 2-week-old guinea pigs, of body weight 200–220g, and body weight individual value within ± 20% of the mean; 2. The cornea is clear and transparent, the fundus is normal, and there is no obvious anisometropia. Exclusion criteria: 1. Guinea pigs over 2 weeks old; 2. Guinea pigs whose weight is not within the standard range; 3. Guinea pigs with anisometropia >1D, amblyopia, and myopia; 4. There are abnormalities in the eyes, such as corneal trauma or vitreous opacity; 5. Guinea pigs in poor condition and unable to continue the experiment or were injured or died during the experiment.

The breeding environment conforms to the national standard GB14925-2010 of the People's Republic of China. There was one cage for every three guinea pigs, with 12/12 h of light alternating between day and night (light: 07:00 AM to 17:30 PM), all animals drink and eat freely. The relevant contents and procedures involved in this test comply with the relevant provisions of the Institutional Animal Care and Use Committee (IACUC) and have been approved

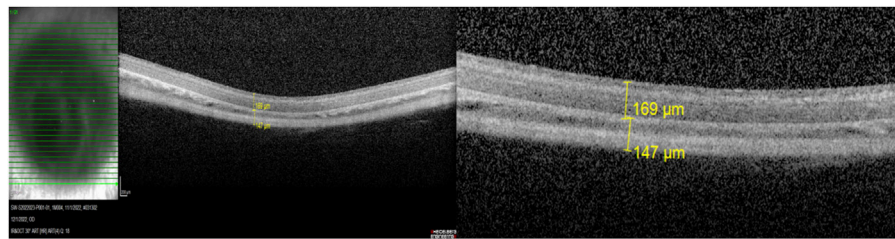


FIGURE 1
Structure of retina and choroid under EDI-OCT.

by the Ethics Committee of West China-Frontier Pharma Tech Co., Ltd., Chengdu, Sichuan, China. The ethics number is: IACUC- SW-S2022022023-P001-01.

Animal grouping and model establishment

There were 4 groups: Control group, FDM group, FDM + RA group, and FDM + Citral group. Guinea pigs were divided randomly according to body weight, with 20 males per group.

The eyes of the control group were not treated. The right eyes of the guinea pigs in the FDM group, the FDM + RA group, and the FDM + Citral group were myopia, and the left eyes were self-control. The white non-toxic No.6 latex balloon is used to make the head cover, which covers the right eye of all FDM guinea pigs but does not compress the cornea and eyelid of the right eye, to ensure that the right eye can blink freely; at the same time, the left eye, mouth, nose, and ears are fully exposed. Wearing of the head cover was checked every 1 day, and any damaged, displaced, and tight head cover was replaced in time to ensure that the right eye of the guinea pig is covered continuously but can blink freely. After 4 weeks, the RE, IOP, and AL of all guinea pigs were measured, and the model was successful if the AL increased and RE decreased. The FDM + RA group was given RA by gavage (24 mg/kg dissolved in 0.4 mL peanut oil, all-trans, Sigma-Aldrich, United States); the FDM + Citral group was given citral by gavage (445 mg/kg dissolved in 0.4 mL peanut oil, mixture of *cis* and *trans*, Macklin, China) (Yu et al., 2021), starting at 10 a.m. each time, for 4 weeks, once every 3 days; the other two groups were given 0.4 mL peanut oil at the same time point.

Retinography and measurement of AL and IOP

RE and AL of all guinea pigs were measured at the beginning of the experiment and 4 weeks later (Since these two data are the key to judge whether guinea pigs successfully induce relative myopia, we measured them before and after induction to determine the degree of myopia). The infrared band-light retinoscope (Suzhou 66 Vision Technology Co., Ltd., China) was used to obtain the RE of all guinea pigs. Compound topical eye drops were used to dilate the eyes. After three times of dosing, the eyes were examined in a dark room 15 min later. The RE in horizontal and vertical positions were detected respectively by an experienced optometrist at the working distance of 50 cm and

0.25 D, and half of the astigmatism was included in the equivalent spherical lens (Luo et al., 2017). OD-1 (Kaixin, Xuzhou, China) small animal A scan was used to measure AL. A tubocaine hydrochloride eye drops (1–2 drops) were placed on the eye surface of all guinea pigs 3 times, each time at an interval of 5 min. The small animal measurement mode was used, and the probe was perpendicular to the pupil area and touched the cornea (avoid pressing), and the value of the waveform contraction in front of the retina was read as AL, accurate to 0.01 mm. The measurement was repeated 3 times, and the average value was taken. The IOP of guinea pigs was measured with TONOVET (TV02) tonometer (Icare, Finland). Each eye was measured 3 times and the average value was taken.

All guinea pigs were kept awake during the examination of RE, AL and IOP.

Measurement of retina and choroid images by EDI-OCT

After 4 weeks, the CT and RT of all guinea pigs were measured using the EDI mode of OCT (Heidelberg, Germany). All guinea pigs were kept awake and their eyes were dilated with compound topical eye drops. After pacifying the guinea pigs, their whole body was wrapped, placed on the OCT examination table, and the eyes to be examined were exposed, so that the anteroposterior diameter of the eyes was consistent with the scanning indicator light source. Then, 31 layers below the optic disc from the bottom to the top was scanned, and the RT and CT of 1 disc diameter (DD) below the optic disc was measured using the manual measurement software provided by the detection system [RT is defined as the inner limiting membrane (ILM) of the retina to the retinal pigment epithelium (RPE), and the highly reflective band width outside the RPE is defined as CT (Sodi et al., 2018a; Sodi et al., 2018b)] (Figure 1).

Statistical analysis

SPSS25.0 (IBM Corp., Armonk, NY, United States) was used for statistical analysis. All results were expressed as mean \pm standard deviation (SD). The comparison of RE, AL, IOP, CT, and RT among the four groups was performed by one-way analysis of variance (ANOVA). The comparison between the left and right eyes among the groups was performed by paired *t*-test. *p* < 0.05 represents a difference with statistical significance.

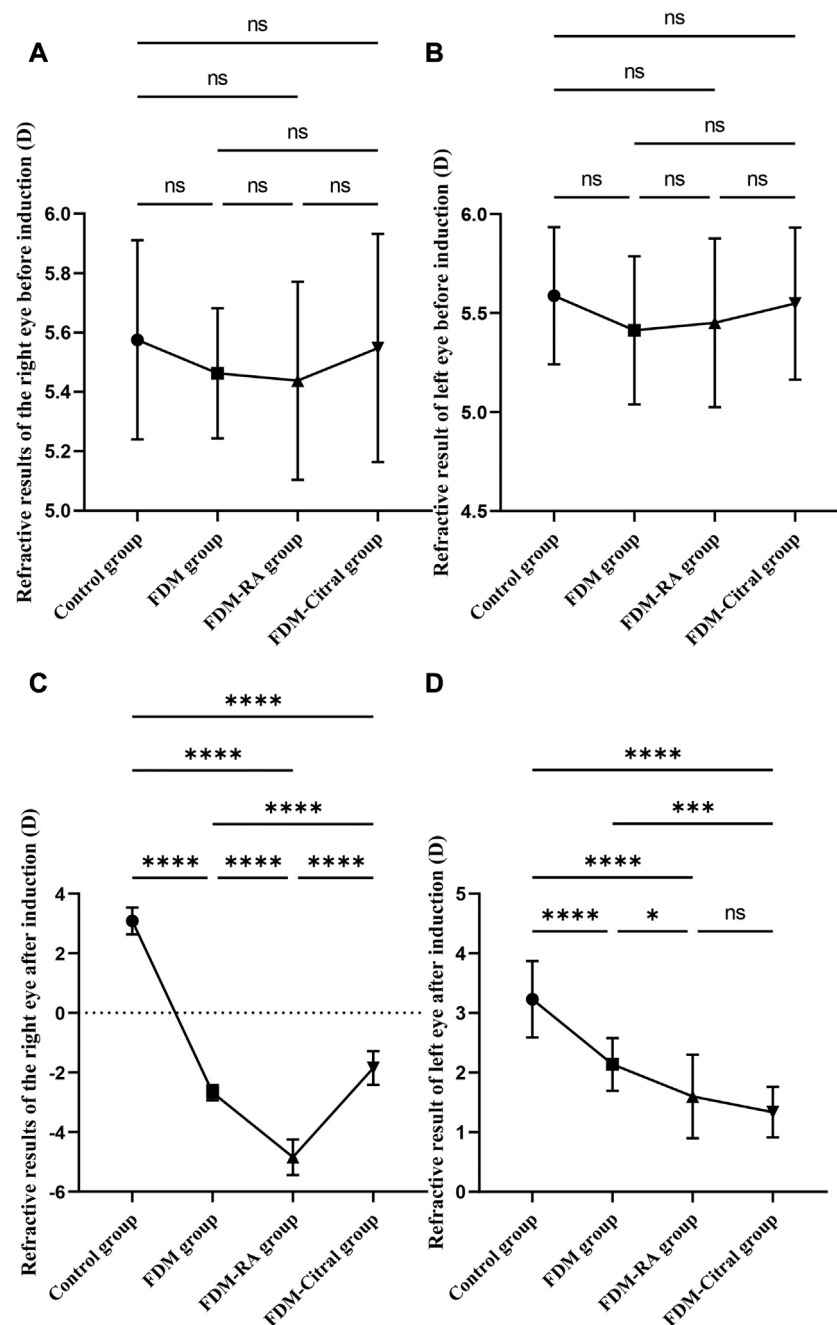


FIGURE 2

Comparative results of RE before and after induction in four groups (D). Note. (A), Comparison of RE in the right eye before induction; (B), Comparison of RE in the left eye before induction; (C), Comparison of RE in the right eye after induction; (D), Comparison of RE in the left eye after induction; (D), diopter; ns means that the difference is not statistically significant; *Indicates $p \leq 0.05$; ** Indicates $p \leq 0.01$; *** Indicates $p \leq 0.001$; **** Indicates $p \leq 0.0001$.

Results

RE results of Guinea pigs in each group

There was no statistical significance in the comparison of RE between the four groups before induction (Figures 2A, B). After 4 weeks of induction, the comparison difference of RE in the right eye of each group was statistically significant, and the FDM + RA group

had the smallest RE (Figure 2C). In the left eye, the comparison difference among other groups was statistically significant except that between FDM group and FDM + Citral group (Figure 2D).

There was no statistically significant difference in RE between the left and right eyes of each group before induction (Figures 3A, C, E, G); The RE in the right eye of the Control group changed from 5.58 ± 0.34 to 3.09 ± 0.45 D, the difference of RE between the left and right eyes was also not statistically significant (Figure 3B); The RE of

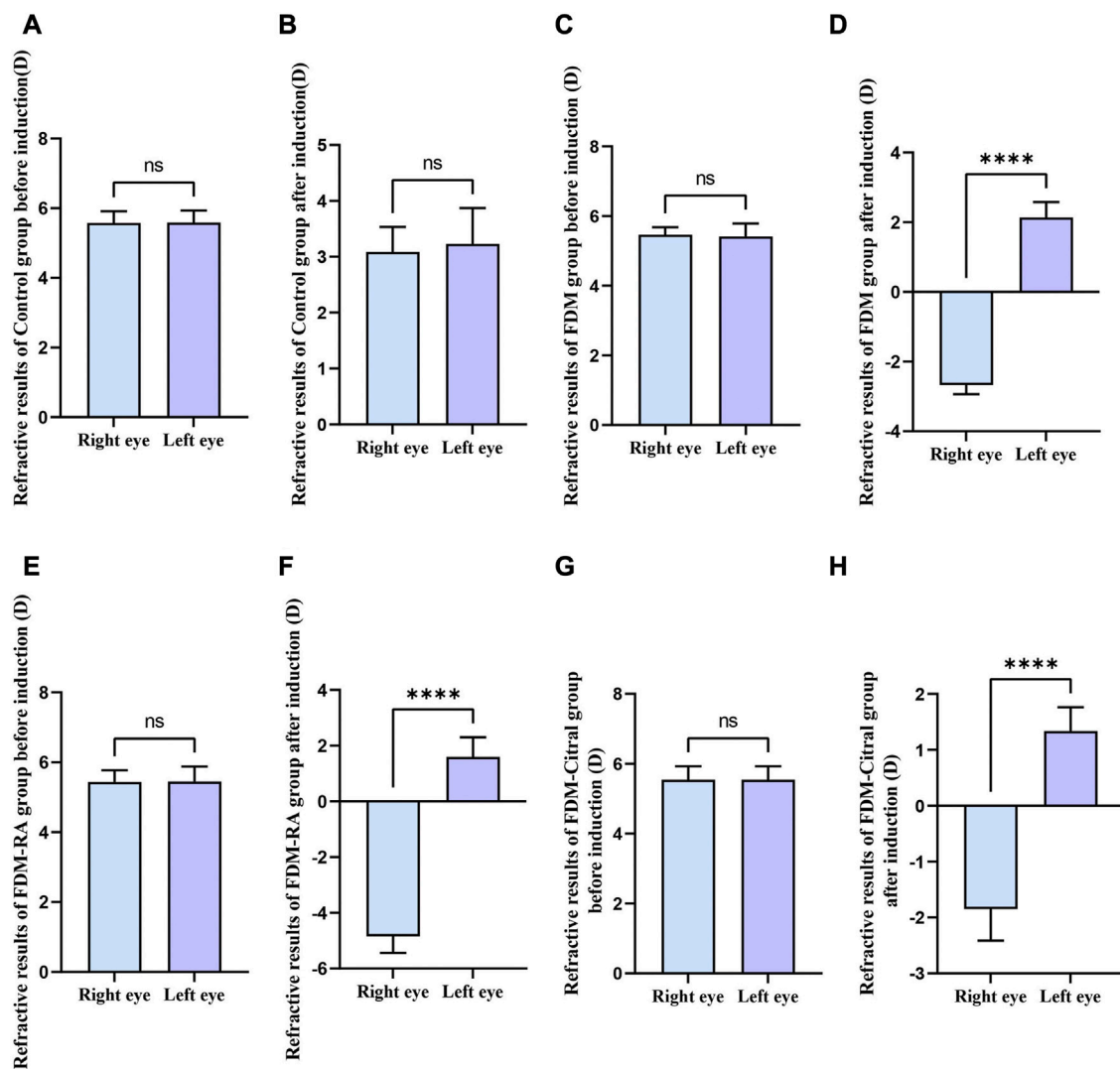


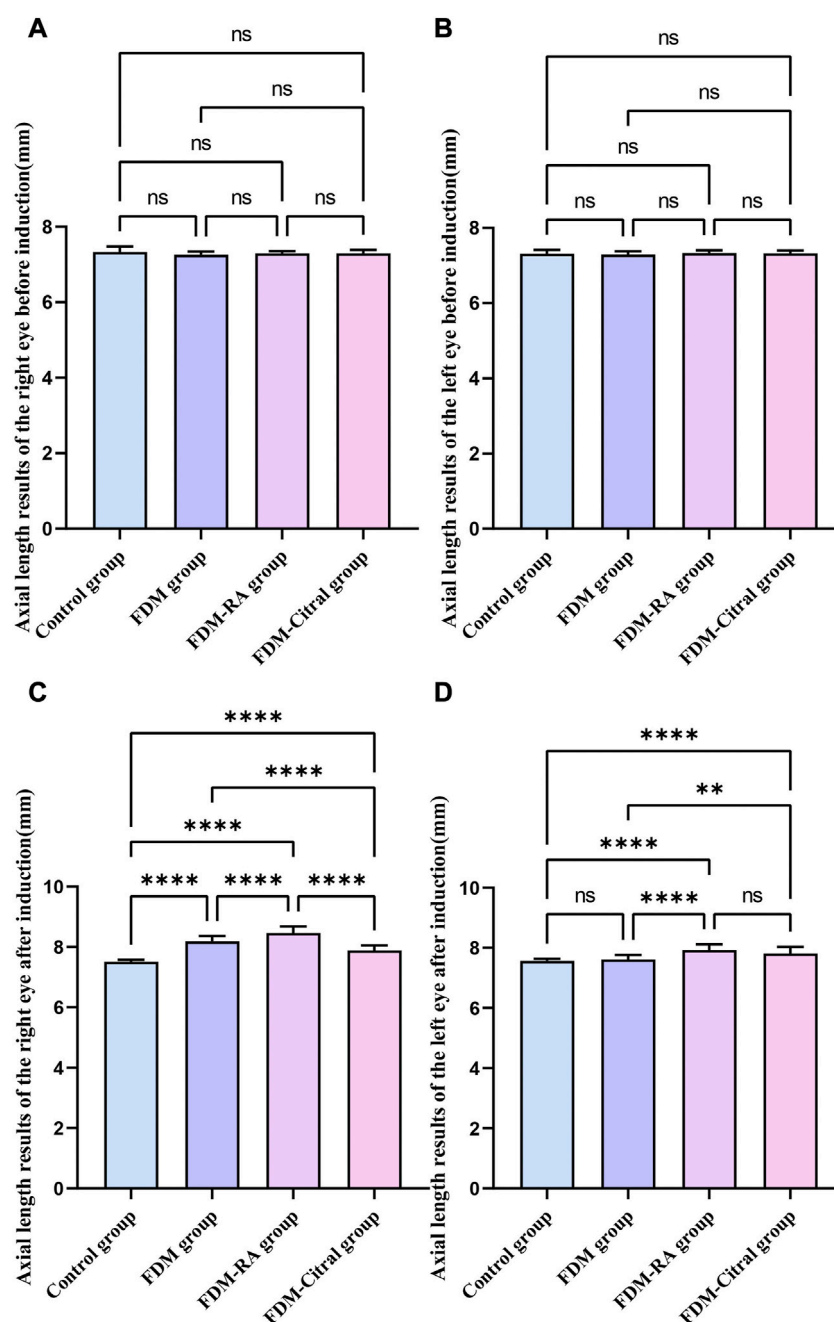
FIGURE 3

Comparison of RE between the left and right eyes before and after induction in each group (D). Note. (A), Comparison of RE between left and right eyes before induction in Control group; (B), Comparison of RE between left and right eyes after induction in Control group; (C), Comparison of RE between left and right eyes before induction in FDM group; (D), Comparison of RE between left and right eyes after induction in FDM group; (E), Comparison of RE between left and right eyes before induction in FDM + RA group; (F), Comparison of RE between left and right eyes after induction in FDM + RA group; (G), Comparison of RE between left and right eyes before induction in FDM + Citral group; (H), Comparison of RE between left and right eyes after induction in FDM + Citral group; (D), diopter; ns means that the difference is not statistically significant; **** Indicates $p \leq 0.0001$.

TABLE 1 RE of left and right eyes of guinea pigs before and after experimental induction (D).

Group (n = 80)	Before induced			T	P	After induced			T	P
	L	R	L-R			L	R	L-R		
Control group	5.59 ± 0.35	5.58 ± 0.34	0.01 ± 0.11	0.11	0.9084	3.23 ± 0.64	3.09 ± 0.45	0.15 ± 0.17	0.83	0.4119
FDM group	5.41 ± 0.37	5.46 ± 0.22	-0.05 ± 0.1	0.52	0.6089	2.14 ± 0.44	-2.68 ± 0.26	4.81 ± 0.11	42.18	<0.0001
FDM + RA group	5.45 ± 0.43	5.44 ± 0.33	0.01 ± 0.12	0.10	0.9182	1.60 ± 0.70	-4.84 ± 0.59	6.44 ± 0.21	31.39	<0.0001
FDM + Citral group	5.55 ± 0.38	5.55 ± 0.38	0.00 ± 0.12	0.00	>0.9999	1.34 ± 0.42	-1.85 ± 0.56	3.19 ± 0.16	20.20	<0.0001
F	0.91	0.83				44.16	958.90			
P	0.4384	0.4796				<0.0001	<0.0001			

Note: R, right eye; L, left eye; D, diopter; RE, refractive error; F, *f* value; P, *p* value; T, *t* value; $p < 0.05$ means statistically significant difference.

**FIGURE 4**

Comparison of AL results of four groups of guinea pigs (mm). Note. (A), Comparison of AL in the right eye before induction; (B), Comparison of AL in the left eye before induction; (C), Comparison of AL in the right eye after induction; (D), Comparison of AL in the left eye after induction; (D), diopter; ns means that the difference is not statistically significant; *Indicates $p \leq 0.05$; ** Indicates $p \leq 0.01$; *** Indicates $p \leq 0.001$; **** Indicates $p \leq 0.0001$.

the right eye of FDM group changed from 5.46 ± 0.22 D to -2.68 ± 0.26 D; The RE of the right eye of FDM + RA group changed from 5.44 ± 0.33 D to -4.84 ± 0.59 D; The RE of the right eye of FDM + Citral group changed from 5.55 ± 0.38 D to -1.85 ± 0.56 D. There was statistically significant difference in RE between the left and right eyes in FDM group (Figure 3D), FDM + RA group (Figure 3F) and FDM + Citral group (Figure 3H). All details are shown in Table 1.

AL results of Guinea pigs in each group

There was no statistical difference in the comparison of bilateral AL between the four groups before induction (Figures 4A, B); After induction, the difference of AL in the right eye between the four groups was statistically significant, and the AL in the FDM + RA group was the largest (Figure 4C); The comparison of left eye AL between the four groups after induction was statistically significant

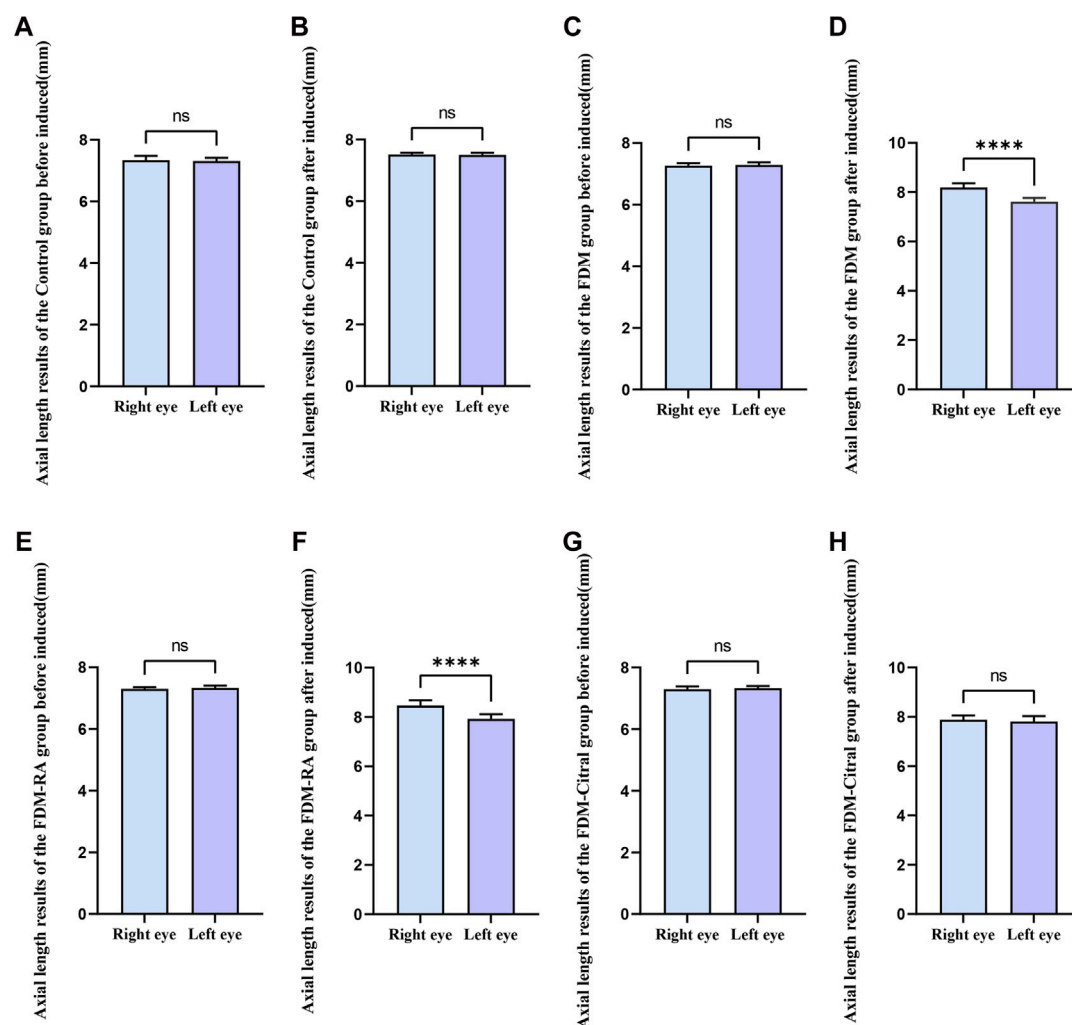


FIGURE 5

Comparison of AL between the left and right eyes in each group (mm). Note. (A), Comparison of AL between left and right eyes before induction in Control group; (B), Comparison of AL between left and right eyes after induction in Control group; (C), Comparison of AL between left and right eyes before induction in FDM group; (D), Comparison of AL between left and right eyes after induction in FDM group; (E), Comparison of AL between left and right eyes before induction in FDM + RA group; (F), Comparison of AL between left and right eyes after induction in FDM + RA group; (G), Comparison of AL between left and right eyes before induction in FDM + Citral group; (H), Comparison of AL between left and right eyes after induction in FDM + Citral group; AL, axial length; ns means that the difference is not statistically significant; **** Indicates $p \leq 0.0001$.

TABLE 2 AL of left and right eyes of guinea pigs before and after experimental induction (mm).

Group (n = 80)	Before induced			T	P	After induced			T	P
	L	R	L-R			L	R	L-R		
Control group	7.31 ± 0.10	7.33 ± 0.15	-0.02 ± 0.04	0.51	0.6154	7.56 ± 0.07	7.58 ± 0.06	-0.01 ± 0.02	0.65	0.5181
FDM group	7.29 ± 0.08	7.26 ± 0.08	0.03 ± 0.03	1.22	0.2304	7.62 ± 0.15	8.19 ± 0.18	-0.57 ± 0.05	11.46	<0.0001
FDM + RA group	7.33 ± 0.07	7.30 ± 0.05	0.03 ± 0.02	1.41	0.1654	7.93 ± 0.19	8.46 ± 0.21	-0.54 ± 0.06	8.41	<0.0001
FDM + Citral group	7.33 ± 0.07	7.30 ± 0.09	0.03 ± 0.03	1.17	0.2510	7.81 ± 0.22	7.88 ± 0.17	-0.07 ± 0.06	1.16	0.2530
F	0.86	1.84				20.94	106.10			
P	0.4678	0.1468				<0.0001	<0.0001			

Note: R, right eye; L, left eye; AL, axial length; FDM, form deprivation myopia; RA, retinoic acid; F, *f* value; P, *p* value; T, *t* value; $p < 0.05$ represents statistically significant difference.

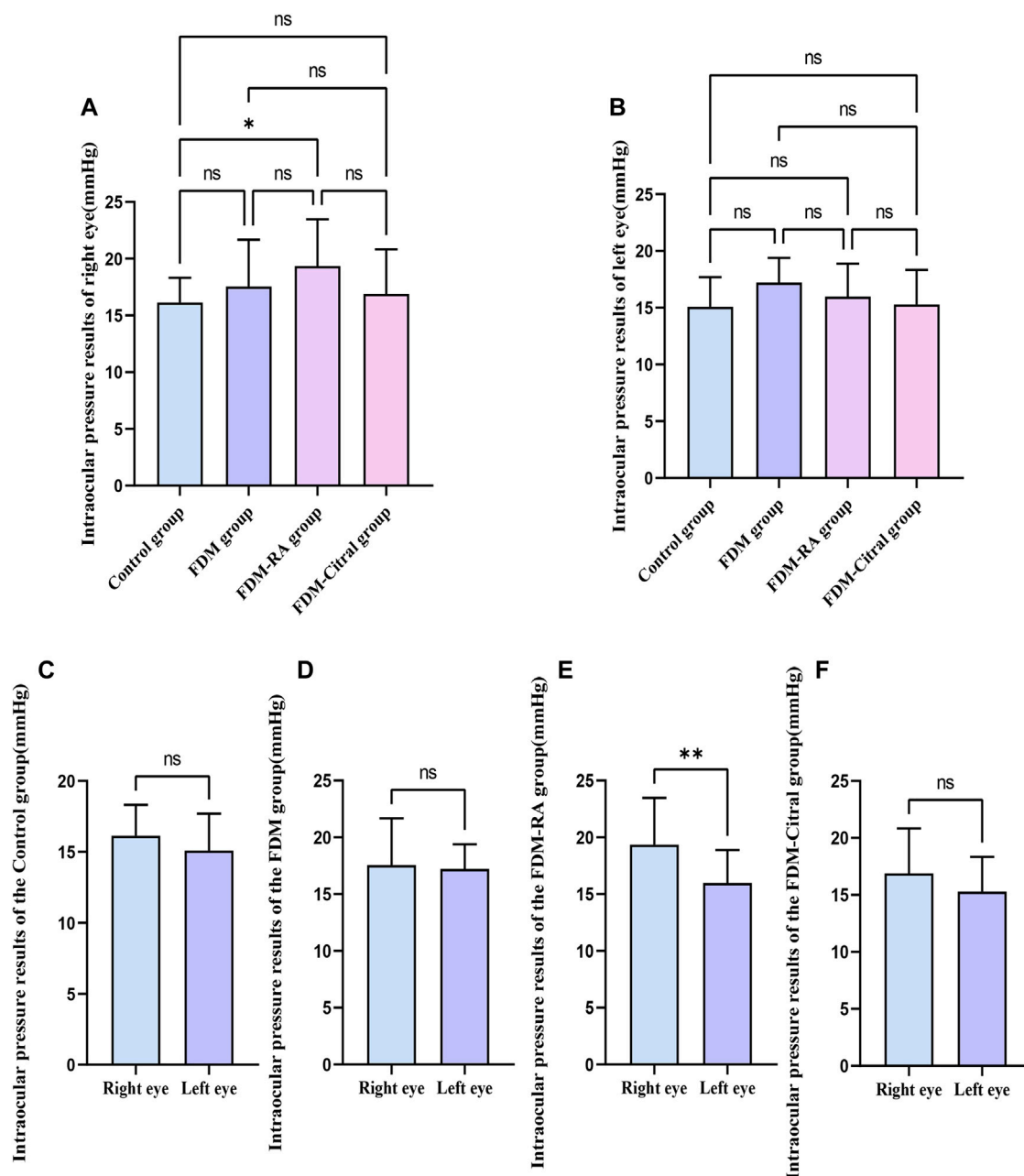


FIGURE 6

Comparison of IOP in each group (mmHg). Note. (A), Comparison of IOP in the right eye; (B), Comparison of IOP in the left eye; (C), Comparison of IOP between left and right eyes in Control group; (D), Comparison of IOP between left and right eyes in FDM group; (E), Comparison of IOP between left and right eyes in FDM + RA group; (F), Comparison of IOP between left and right eyes in FDM + Citral group; IOP, intraocular pressure; ns means that the difference is not statistically significant; *Indicates $p \leq 0.05$; ** Indicates $p \leq 0.01$.

except for the Control group VS. FDM and FDM + RA group VS. FDM + Citral group (Figure 4D).

Before induction, there was no statistical difference in AL between the left and right eyes in each group (Figures 5A, C, E, G); After induction, only the FDM group and FDM + RA group had statistically significant differences in AL between the left and right eyes (Figures 5D, F); There was no statistical difference in AL between the left and right eyes of the Control group and FDM + Citral group (Figures 5B, H); The changes in AL for each group are detailed in Table 2.

The result of IOP after induction

The IOP of the right eye in the FDM + RA group was higher than that in the Control group ($p \leq 0.05$), and the difference between the IOP of the left and right eyes in the FDM-RA group was also statistically significant ($p \leq 0.01$). The IOP of the right eye was greater than that of the left eye, and there was no statistically significant difference between the groups and between the left and right eyes in each group. See Figure 6; Table 3 for details.

TABLE 3 IOP results of left and right eyes of guinea pigs in each group (mmHg).

Group (n = 80)	IOP			T	P
	L	R	L-R		
Control group	15.08 ± 2.60	16.13 ± 2.17	-1.05 ± 0.76	1.38	0.1747
FDM group	17.21 ± 2.18	17.56 ± 4.10	-0.35 ± 0.99	0.35	0.7271
FDM + RA group	15.98 ± 2.90	19.35 ± 4.13	-3.37 ± 1.13	2.99	0.0049
FDM + Citral group	15.29 ± 3.04	16.90 ± 3.93	-1.61 ± 1.04	1.55	0.1277
F	2.73	2.79			
P	0.0491	0.0459			

Note: R, right eye; L, left eye; IOP, intraocular pressure; FDM, form deprivation myopia; RA, retinoic acid; F, *f* value; P, *p* value; T, *t* value; *p* < 0.05 represents statistically significant difference.

CT and RT results of Guinea pigs measured by EDI-OCT

Compared with RT in the right eye of the 4 groups, the Control group > FDM + Citral group > FDM group > FDM + RA group, there was no statistical significance between the FDM group and the FDM + RA group, and the comparison between the other two groups was statistically significant $p < 0.0001$ (Figure 7A). Compared with RT in the left eye of the 4 groups, only the Control group VS. FDM + Citral group and the Control group VS. FDM + RA group showed statistically significant differences ($p < 0.05$), while pairwise comparison among other groups showed no statistically significant differences (Figure 7B). Compared with the CT of the right eye of the 4 groups, the CT of the control group was larger than that of the other three groups, and the difference was statistically significant ($p < 0.0001$), there was no statistical difference between the FDM + Citral group, the FDM group, and the FDM + RA group (Figure 7C); There was no statistically significant difference between the FDM + RA VS. FDM + Citral groups compared with the CT of the left eye in the four groups, and the differences between the other groups were statistically significant (Figure 7D). Detailed data are shown in Tables 4, 5.

There was a statistical difference between FDM group and FDM + RA group in RT of left and right eyes, and RT of right eye was significantly less than that of left eye (Figures 8B, C). There was statistically significant difference between the left and right eye CT of FDM group and FDM + RA group (Figures 8F, G). In FDM + Citral group, there was statistical difference in CT between left and right eyes, and the CT of right eye was significantly smaller than that of left eye (Figure 8H), but not in RT (Figure 8D). There was no difference in CT and RT between the left and right eyes between Control groups (Figures 8A, E).

Discussion

In this study, we discussed the effect of RA on the intraocular parameters of FDM guinea pigs, and, in particular, analyzed the RT and CT measured by EDI-OCT in guinea pigs under different induction factors. We found that the eye axis and refractive degree of young guinea pigs after form deprivation increased.

The AL of the right eye was 0.57 ± 0.05 mm larger than that of the control eye and the right eye was myopia (-2.68 ± 0.26 D), whereas the left eye was still hyperopia (2.14 ± 0.44 D). However, the retina and choroid did decrease correspondingly (RT in the right eye was 34.38 ± 3.24 μ m smaller than that in the left eye, whereas CT was 26.48 ± 2.67 μ m smaller). Moreover, the degree of myopia of FDM guinea pigs treated with RA was more serious, with RE reaching -4.84 ± 0.59 D and AL 8.46 ± 0.21 mm; the RT of the right eye in the FDM + RA group was 118.90 ± 10.30 μ m, which was smaller than that in the FDM group (125.30 ± 8.13 μ m), although the CT results of the two groups were almost the same (102.10 ± 9.01 μ m in FDM group, 102.60 ± 14.10 μ m in FDM + RA group). However, the myopia trend seemed to be alleviated by RA inhibitors. The RE was -1.85 ± 0.56 D, AL was 7.88 ± 0.17 mm, and RT was 146.50 ± 15.29 μ m, however, this did not seem to affect the choroid, its CT was 107.60 ± 12.13 μ m, which is far less than 136.90 ± 12.61 μ m of the control group. Furthermore, we found that RA might aggravate the thinning tendency of the retina in FDM guinea pigs through the results of EDI-OCT. Although there was no statistically significant difference between the RT and CT results of the right eye in the FDM and FDM + RA groups, the RT in the FDM + RA group was the smallest among the four groups, and the RT in the FDM + Citral group was significantly greater than that in the FDM and FDM + RA groups, indicating that RA might aggravate the retinal thinning trend in FDM. This trend was suppressed with RA antagonists. However, RA seemed to have no effect on the change of CT in FDM guinea pigs (there was no statistical difference in CT among the FDM, FDM + RA, and FDM + Citral groups). Also, we found that the IOP of FDM guinea pigs after RA treatment increased and IOP was normal after citral treatment.

RA is present widely in retina and choroid, which is considered to be a key signaling molecule regulating eye growth and might be associated with myopia (Mertz and Wallman, 2000). RA is regulated mainly by retinal aldehyde dehydrogenase 1 and 2 (RALDH1 and RALDH2), which are present in the retina and choroid. Harper et al. found that these two enzymes exist in the choroid and retina of human eyes, especially in the choroid (Harper et al., 2015). However, only RALDH2 changes during the recovery of the experimental myopia model. Summers et al. reported the changes of RALDH2⁺ cells in the choroid of the chick myopia model during the recovery stage of myopia,

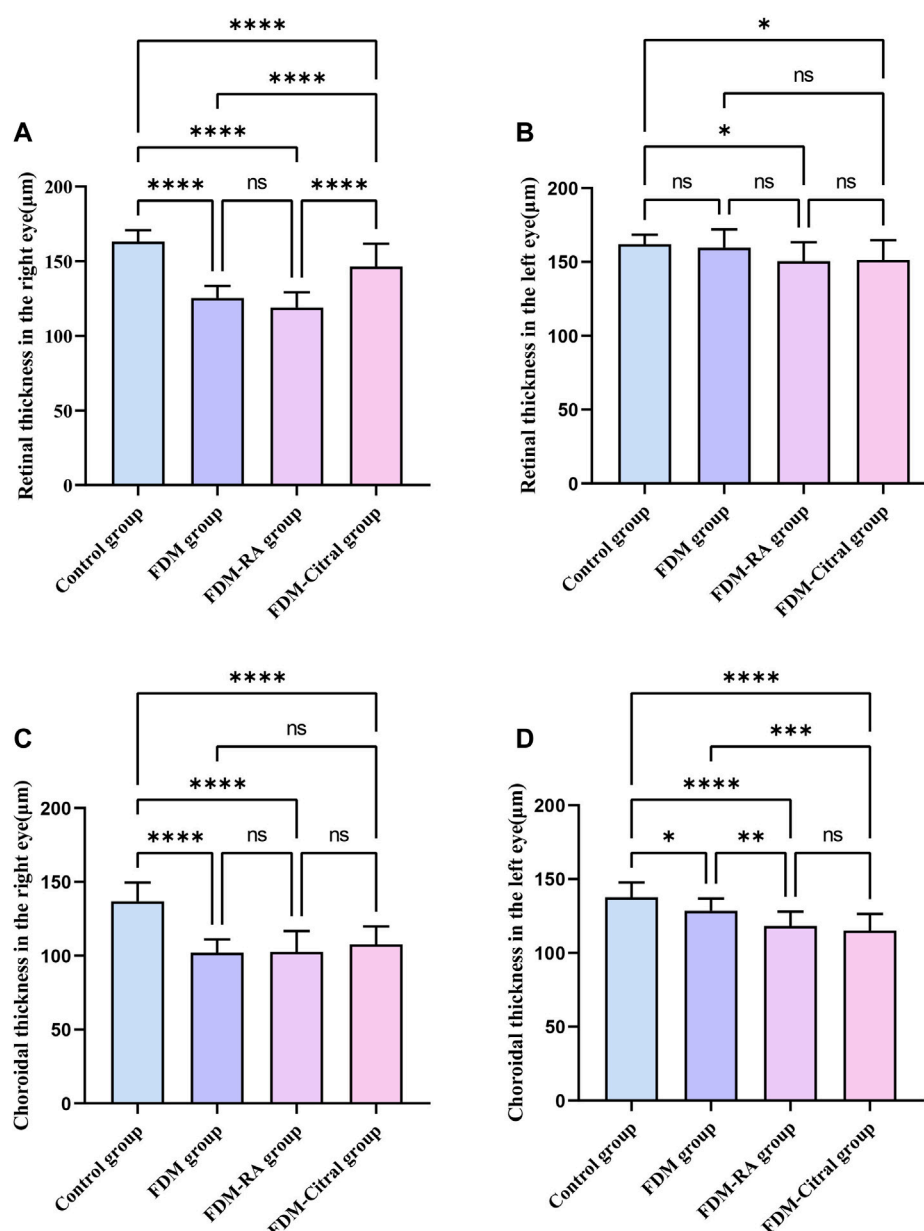


FIGURE 7

Comparative results of CT and RT in each group (μm). Note. (A), Comparison of RT of right eye; (B), Comparison of RT of left eye; (C), Comparison of CT of right eye; (D), Comparison of CT of left eye; ns means that the difference is not statistically significant; *Indicates $p \leq 0.05$; ** Indicates $p \leq 0.01$; *** Indicates $p \leq 0.001$; **** Indicates $p \leq 0.0001$.

finding that the RALDH2⁺ cells existed mainly in the choroid stroma and vascular attachment, and would continue to rise during the recovery stage of myopia. The choroid would also thicken within 4 days of the recovery stage and the trend of RE, AL, and CT increasing was consistent with the change of RALDH2 (Summers et al., 2020). In addition, the phenomenon of CT enlargement in the myopic model has also been reported by Liang et al. who found that the retina and choroid of chicks would thicken within 6 days of form deprivation, and then the thickness of the retina would first return to normal. They found that the concentration of sodium and chlorine in the retina and choroid of myopic eyes was lower than that of normal

eyes, resulting in tissue edema and increased thickness (Liang et al., 2004). Our study found that the retina of FDM guinea pigs may be thickened after 4 weeks of RA induction, but the choroid has no obvious change, and the CT results of FDM + RA group were even larger than those of FDM guinea pigs without RA induction (CT of the FDM group: $102.10 \pm 9.01 \mu\text{m}$; CT of the FDM + RA group: $102.60 \pm 14.10 \mu\text{m}$). We speculated that this might be related to the stage of myopia that the choroid and retina edema occurred during, but the retina first recovered and became thinner with the aggravation of myopia. However, it is not clear whether our phenomenon is related to the mediation of related proteins as other studies have shown.

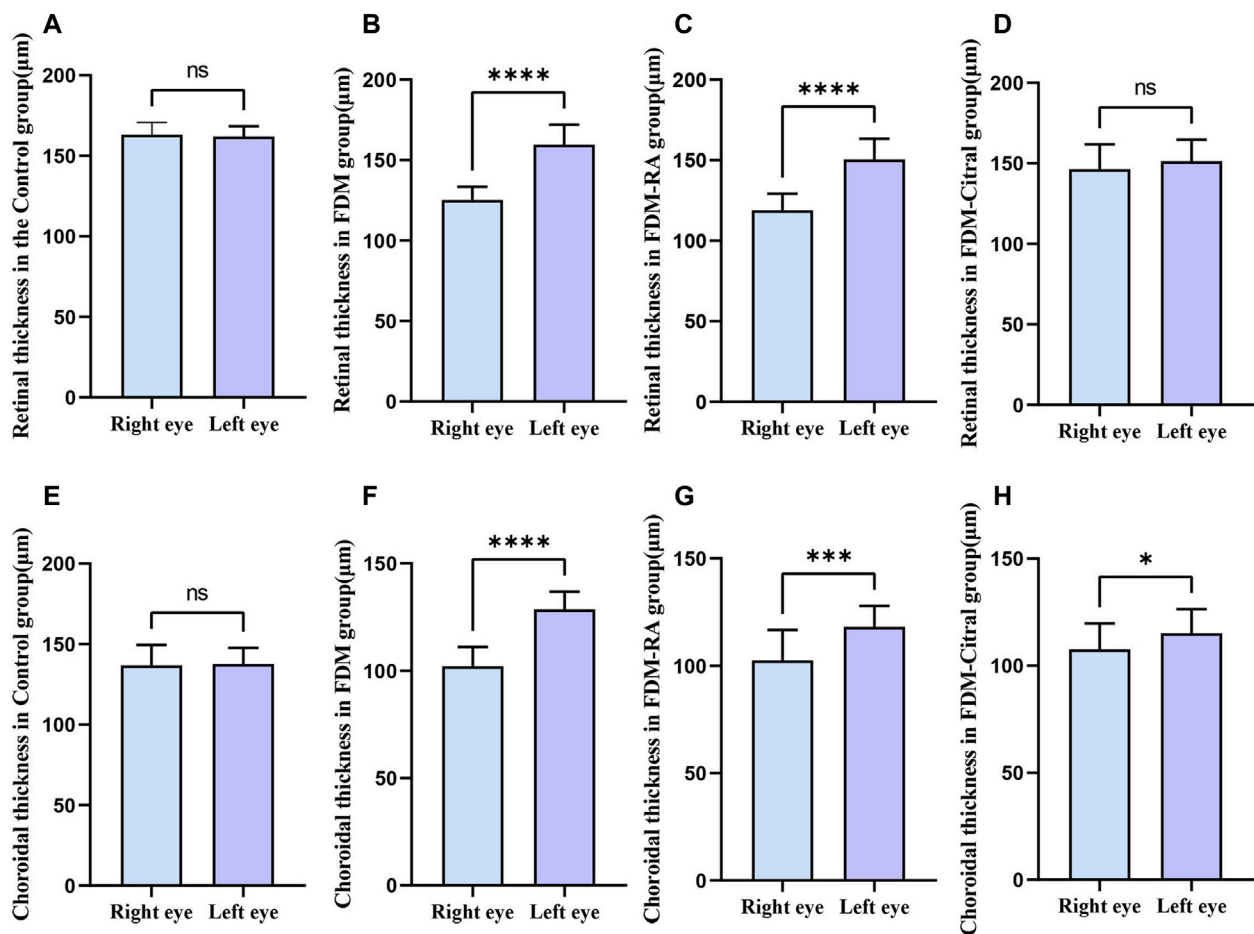


FIGURE 8

Comparison of RT and CT between the left and right eyes in each group (μm). Note. (A), Comparison of RT between left and right eyes in Control group; (B), Comparison of RT between left and right eyes in FDM group; (C), Comparison of RT between left and right eyes in FDM + RA group; (D), Comparison of RT between left and right eyes in FDM + Citral group; (E), Comparison of CT between left and right eyes in Control group; (F), Comparison of CT between left and right eyes in FDM group; (G), Comparison of CT between left and right eyes in FDM + RA group; (H), Comparison of CT between left and right eyes in FDM + Citral group; ns means that the difference is not statistically significant; *Indicates $p \leq 0.05$; ** Indicates $p \leq 0.01$; *** Indicates $p \leq 0.001$; **** Indicates $p \leq 0.0001$.

In fact, in both FDM and LIM models of guinea pigs and chickens, it has been confirmed that all-trans RA (atRA) will increase (Bitzer et al., 2000; Huang et al., 2011), whereas, in hyperopia models, it will decrease,

although the specific mechanism of RA regulating refractive changes is not clear. Also, the significant increase of RALDH2 protein production in the choroid, and the change of its content in the retina might be

TABLE 4 CT results of left and right eyes of guinea pigs in each group measured by EDI-OCT (μm).

Group (n = 80)	CT			T	P
	L	R	L-R		
Control group	137.70 ± 9.92	136.90 ± 12.61	0.85 ± 3.59	0.24	0.8140
FDM group	128.60 ± 8.23	102.10 ± 9.01	26.48 ± 2.67	9.94	<0.0001
FDM + RA group	118.20 ± 9.70	102.60 ± 14.10	15.65 ± 3.83	4.09	0.0002
FDM + Citral group	115.20 ± 11.23	107.60 ± 12.13	7.57 ± 3.45	2.20	0.0335
F	22.69	38.05			
P	<0.0001	<0.0001			

Note: R, right eye; L, left eye; FDM, form deprivation myopia; RA, retinoic acid; CT, choroidal thickness; EDI-OCT, enhanced depth imaging-optical coherence tomography; F, f value; P, p value; T, t value; $p < 0.05$ represents statistically significant difference.

TABLE 5 RT results of left and right eyes of guinea pigs in each group measured by EDI-OCT (μm).

Group ($n = 80$)	RT			T	P
	L	R	L-R		
Control group	162.00 \pm 6.41	163.20 \pm 7.67	-1.15 \pm 2.24	0.51	0.6099
FDM group	159.7 \pm 12.39	125.30 \pm 8.13	34.38 \pm 3.24	10.63	<0.0001
FDM + RA group	150.60 \pm 12.76	118.90 \pm 10.30	31.66 \pm 3.73	8.50	<0.0001
FDM + Citral group	151.40 \pm 13.28	146.50 \pm 15.29	4.91 \pm 4.22	1.16	0.2509
F	5.15	68.09			
P	0.0026	<0.0001			

Note: R, right eye; L, left eye; FDM, form deprivation myopia; RA, retinoic acid; RT, retinal thickness; EDI-OCT, enhanced depth imaging-optical coherence tomography; F, f value; P, p value; T, t value; $p < 0.05$ represents statistically significant difference.

related closely to the formation of myopia. In the LIM model, guinea pigs developed myopia tendency after wearing a -6 D lens for only 2 weeks, and the content of RA and the production of RALDH2 protein also increased. However, in guinea pigs with myopia recovery, the protein was reduced in the retina, but not in the choroid, which is contrary to the results in chicken mentioned earlier (this might be related to the different myopia mechanisms between chickens and guinea pigs). This study suggests that RA in the retina and choroid is involved in the regulation of LIM guinea pigs (Mao et al., 2012). Nevertheless, although both LIM and FDM models form axial myopia, their mechanisms are not completely the same, and the mechanism of RA in FDM guinea pigs might also be different from other types of animal myopia models.

The FDM guinea pig model was selected for our study, which is a commonly used myopia model because of their docile temperament and similar eyeball development to humans (Cheng et al., 2014; Cheng et al., 2015). Studies have reported that the structural changes to the retina of FDM guinea pigs were observed by light and electron microscopy. The depth of the vitreous cavity, retina, and sclera of the RE and AL were thinned after form deprivation, and the activity of superoxide dismutase (SOD) in FDM eyes was reduced significantly. They believed that oxygen free radicals might be related to the formation of FDM (Zi et al., 2020). The results of their study are similar to the changes of intraocular parameters in our FDM group. In addition, we can see that the RE, AL of FDM eyes in guinea pigs are increased compared with those in the FDM group after RA induction. Although the difference of RT comparison results was not statistically significant, there was a decreasing trend. Furthermore, in contrast to the earlier research, we used OCT technology to collect the structure of the retina and choroid of living guinea pigs, which can improve the efficiency of experiments. EDI-OCT can be used clinically to measure CT and RT results of patients (Park et al., 2013). However, animals have poor compliance compared with humans because it is difficult for animals to cooperate closely with instruments for measurement. In addition, eyeballs are often smaller in animals, which is one of the reasons for the difficulty in obtaining intraocular parameters of small animals. Based on the docile characteristics of guinea pigs, in this study, our guinea pigs were awake for OCT scanning, and we also obtained retinal and choroid images successfully, reducing the mortality from anesthesia.

Additionally, we found that the IOP of FDM guinea pigs after RA increased, which has never been reported before. However, myopia is related to glaucoma, and HM is an independent risk factor for glaucoma (Jonas et al., 2020), and, the higher the degree of myopia, the higher the risk of glaucoma. In our study, guinea pigs in the FDM + RA group had the highest degree of myopia in the right eye. We speculated that this might be the reason for the high IOP in this group, although it might also be related to the pharmacological effects of RA.

It should be mentioned that our research has the following limitations. 1. We have not discussed the changes of choroidal blood flow in depth. Optical coherence tomography angiography (OCTA) can determine changes of choroidal blood flow and vascular density, whereas the degree of myopia is correlated negatively with the density of choroidal choriochorionic capillaries (Liu et al., 2021; Li et al., 2022). Unfortunately, our laboratory does not have OCTA instruments. 2. We analyzed the intraocular parameters of RA acting on FDM guinea pigs, but did not further study the pharmacological mechanism. In future research, we will strive to address these limitations.

Conclusion

Morphological deprivation in guinea pigs results in thinning of the retina and choroid. Exogenous RA can aggravate the tendency of myopia in FDM guinea pigs. Meanwhile, exogenous RA can cause an increase of IOP in FDM guinea pigs. However, after RA inhibition, the refractive state and AL of FDM guinea pigs were reduced. At the same time, RA might aggravate retinal thinning in FDM guinea pigs, although it seems to have no obvious effect on choroidal thinning. The study of RA might provide an important breakthrough in understanding the mechanism of myopia.

Data availability statement

The original contributions presented in the study are included in the article/Supplementary Material, further inquiries can be directed to the corresponding authors.

Ethics statement

The animal study was reviewed and approved by the Ethics Committee of West China-Frontier Pharma Tech Co., Ltd., Chengdu, Sichuan, China. The ethics number is: IACUC- SW-S2022022023-P001-01.

Author contributions

YW: mainly responsible for experiment operation and manuscript writing; YF: responsible for the statistics of data; JY: responsible for checking manuscripts and data; HF: responsible for data statistics and chart making; ZY, XX, and YD responsible for proofreading and revising the language of the manuscript; XH: responsible for guiding the design and revision of the study and manuscript; WL: responsible for experimental design and guidance.

Funding

This project was funded by the Science Research Fundation of Aier Eye Hospital Group (Grant No. AF2101D9).

References

- Bitzer, M., Feldkaemper, M., and Schaeffel, F. (2000). Visually induced changes in components of the retinoic acid system in fundal layers of the chick. *Exp. Eye Res.* 70, 97–106. doi:10.1006/exer.1999.0762
- Brown, D. M., Kowalski, M. A., Paulus, Q. M., Yu, J., Kumar, P., Kane, M. A., et al. (2022b). Altered structure and function of murine sclera in form-deprivation myopia. *Invest. Ophthalmol. Vis. Sci.* 63 (13), 13. doi:10.1167/iovs.63.13.13
- Brown, D. M., Mazade, R., Clarkson-Townsend, D., Hogan, K., et al. (2022a). Candidate pathways for retina to scleral signaling in refractive eye growth. *Exp. Eye Res.* 219, 109071. doi:10.1016/j.exer.2022.109071
- Chamberlain, P., Lazon de la Jara, P., Arumugam, B., and Bullimore, M. A. (2021). Axial length targets for myopia control. *Ophthalmic Physiol. Opt.* 41 (3), 523–531. doi:10.1111/opo.12812
- Cheng, Z. Y., Wang, X. P., Schmid, K. L., and Han, X. G. (2014). Inhibition of form-deprivation myopia by a GABA_A receptor antagonist, (1,2,5,6-tetrahydropyridin-4-yl) methylphosphonic acid (TPMPA), in Guinea pigs. *Graefes Arch. Clin. Exp. Ophthalmol.* 252 (12), 1939–1946. doi:10.1007/s00417-014-2765-5
- Cheng, Z. Y., Wang, X. P., Schmid, K. L., Han, Y. F., Han, X. G., Tang, H. W., et al. (2015). GABA_B receptor antagonist CGP46381 inhibits form-deprivation myopia development in Guinea pigs. *Biomed. Res. Int.* 2015, 207312. doi:10.1155/2015/207312
- Das, J. K., Salam, R. A., Thornburg, K. L., Prentice, A. M., Campisi, S., Lassi, Z. S., et al. (2017). Nutrition in adolescents: Physiology, metabolism, and nutritional needs. *Ann. N. Y. Acad. Sci.* 1393 (1), 21–33. doi:10.1111/nyas.13330
- Dolgin, E. (2015). The myopia boom. *Nature* 519 (7543), 276–278. doi:10.1038/519276a
- Dong, L., Kang, Y. K., Li, Y., Wei, W. B., and Jonas, J. B. (2020). Prevalence and time trends of myopia in children and adolescents in China: A systematic review and meta-analysis. *Retina* 40 (3), 399–411. doi:10.1097/IAE.0000000000002590
- Han, X., Liu, C., Chen, Y., and He, M. (2022). Myopia prediction: A systematic review. *Eye (Lond)*. 36 (5), 921–929. doi:10.1038/s41433-021-01805-6
- Harper, A. R., Wiechmann, A. F., Moiseyev, G., Ma, J. X., and Summers, J. A. (2015). Identification of active retinaldehyde dehydrogenase isoforms in the postnatal human eye. *PLOS ONE* 10 (3), e0122008. doi:10.1371/journal.pone.0122008
- Huang, J., Qu, X.-M., and Chu, R.-Y. (2011). Expressions of cellular retinoic acid binding proteins I and retinoic acid receptor- β in the Guinea pig eyes with experimental myopia. *Int. J. Ophthalmol.* 4, 131–136. doi:10.3980/j.issn.2222-3959.2011.02.04
- Hughes, R. P., Vincent, S. J., Read, S. A., and Collins, M. J. (2020). Higher order aberrations, refractive error development and myopia control: A review. *Clin. Exp. Optom.* 103 (1), 68–85. doi:10.1111/cxo.12960
- Jonas, J. B., Ang, M., Cho, P., Guggenheim, J. A., He, M. G., Jong, M., et al. (2021). IMI prevention of myopia and its progression. *Invest. Ophthalmol. Vis. Sci.* 28 (5), 62. doi:10.1167/iovs.62.5.6
- Jonas, J. B., Ohno-Matsui, K., and Panda-Jonas, S. (2019). Myopia: Anatomic changes and consequences for its etiology. *Asia Pac J. Ophthalmol. (Phila)*. 8 (5), 355–359. doi:10.1097/01.APO.0000578944.25956.8b
- Jonas, J. B., Wang, Y. X., Dong, L., and Panda-Jonas, S. (2020). High myopia and glaucoma-like optic neuropathy. *Asia Pac J. Ophthalmol. (Phila)*. 9 (3), 234–238. doi:10.1097/APO.0000000000000288
- Lee, S. S., Lingham, G., Sanfilippo, P. G., Hammond, C. J., Saw, S. M., Guggenheim, J. A., et al. (2022). Incidence and progression of myopia in early adulthood. *JAMA Ophthalmol.* 140 (2), 162–169. doi:10.1001/jamaophthalmol.2021.5067
- Li, Y., Zheng, F., Foo, L. L., Wong, Q. Y., Ting, D., Hoang, Q. V., et al. (2022). Advances in OCT imaging in myopia and pathologic myopia. *Diagn. (Basel)* 12 (6), 1418. doi:10.3390/diagnostics12061418
- Liang, H., Crewther, S. G., Crewther, D. P., and Junghans, B. M. (2004). Structural and elemental evidence for edema in the retina, retinal pigment epithelium, and choroid during recovery from experimentally induced myopia. *Invest. Ophthalmol. Vis. Sci.* 45 (8), 2463–2474. doi:10.1167/iovs.03-1009
- Liu, X., Lin, Z., Wang, F., Peng, X., He, W., Chen, D., et al. (2021). Choroidal thickness and choriocapillaris vascular density in myopic anisometropia. *Eye Vis. (Lond)*. 8 (1), 48. doi:10.1186/s40662-021-00269-9
- Luo, X., Li, B., Li, T., Di, Y., Zheng, C., Ji, S., et al. (2017). Myopia induced by flickering light in Guinea pig eyes is associated with increased rather than decreased dopamine release. *Mol. Vis.* 23, 666–679.
- Mao, J. F., Liu, S. Z., and Dou, X. Q. (2012). Retinoic acid metabolic change in retina and choroid of the Guinea pig with lens-induced myopia. *Int. J. Ophthalmol.* 5 (6), 670–674. doi:10.3980/j.issn.2222-3959.2012.06.04
- Medina, A. (2021). The cause of myopia development and progression: Theory, evidence, and treatment. *Surv. Ophthalmol.* 67, 488–509. doi:10.1016/j.survophthal.2021.06.005
- Mertz, J. R., and Wallman, J. (2000). Choroidal retinoic acid synthesis: A possible mediator between refractive error and compensatory eye growth. *Exp. Eye Res.* 70 (4), 519–527. doi:10.1006/exer.1999.0813
- Morgan, I. G., French, A. N., Ashby, R. S., Guo, X., Ding, X., He, M., et al. (2018). The epidemics of myopia: Aetiology and prevention. *Prog. Retin Eye Res.* 62, 134–149. doi:10.1016/j.preteyeres.2017.09.004
- Park, S. Y., Kim, S. M., Song, Y. M., Sung, J., and Ham, D. I. (2013). Retinal thickness and volume measured with enhanced depth imaging optical coherence tomography. *Am. J. Ophthalmol.* 156 (3), 557–566. doi:10.1016/j.ajo.2013.04.027
- Shi, X., Gao, Z., Leng, L., and Guo, Z. (2022). Temporal and spatial characterization of myopia in China. *Front. Public Health* 10, 896926. doi:10.3389/fpubh.2022.896926

Acknowledgments

Thanks to Aier Eye Group for its funding support; Thanks to WestChina-Frontier PharmaTech Co., Ltd. for providing laboratory facilities and materials for this study.

Conflict of interest

The authors declare that the research was conducted in the absence of any commercial or financial relationships that could be construed as a potential conflict of interest.

The reviewer ZW declared a shared affiliation with the author YW to the handling editor at the time of review.

Publisher's note

All claims expressed in this article are solely those of the authors and do not necessarily represent those of their affiliated organizations, or those of the publisher, the editors and the reviewers. Any product that may be evaluated in this article, or claim that may be made by its manufacturer, is not guaranteed or endorsed by the publisher.

- Sodi, A., Bacherini, D., Lenzetti, C., Caporossi, O., Murro, V., Mucciolo, D. P., et al. (2018a). EDI OCT evaluation of choroidal thickness in stargardt disease. *PLoS One* 13 (1), e0190780. doi:10.1371/journal.pone.0190780
- Sodi, A., Lenzetti, C., Murro, V., Caporossi, O., Mucciolo, D. P., Bacherini, D., et al. (2018b). EDI-OCT evaluation of choroidal thickness in retinitis pigmentosa. *Eur. J. Ophthalmol.* 28 (1), 52–57. doi:10.5301/ejo.5000961
- Summers, J. A., Cano, E. M., Kaser-Eichberger, A., and Schroedl, F. (2020). Retinoic acid synthesis by a population of choroidal stromal cells. *Exp. Eye Res.* 201, 108252. doi:10.1016/j.exer.2020.108252
- Tian, F., Zheng, D., Zhang, J., Liu, L., Duan, J., Guo, Y., et al. (2021). Choroidal and retinal thickness and axial eye elongation in Chinese junior students. *Invest. Ophthalmol. Vis. Sci.* 62 (9), 26. doi:10.1167/iovs.62.9.26
- Tideman, J. W. L., Polling, J. R., Vingerling, J. R., Jaddoe, V. W. V., Williams, C., Guggenheim, J. A., et al. (2018). Axial length growth and the risk of developing myopia in European children. *Acta Ophthalmol.* 96 (3), 301–309. doi:10.1111/aos.13603
- Wang, S., Liu, S., Mao, J., and Wen, D. (2014). Effect of retinoic acid on the tight junctions of the retinal pigment epithelium-choroid complex of Guinea pigs with lens-induced myopia *in vivo*. *Int. J. Mol. Med.* 33 (4), 825–832. doi:10.3892/ijmm.2014.1651
- Yang, Y., Wu, J., Wu, D., Wei, Q., Zhong, T., Yang, J., et al. (2021). Intravitreal brimonidine inhibits form-deprivation myopia in Guinea pigs. *Eye Vis. (Lond)*. 8 (1), 27. Published 2021 Jul 14. doi:10.1186/s40662-021-00248-0
- Yu, M., Liu, W., Wang, B., and Dai, J. (2021). Short wavelength (blue) light is protective for lens-induced myopia in Guinea pigs potentially through a retinoic acid-related mechanism. *Invest. Ophthalmol. Vis. Sci.* 62 (1), 21. doi:10.1167/iovs.62.1.21
- Zhang, S., Zhang, G., Zhou, X., Xu, R., Wang, S., Guan, Z., et al. (2019). Changes in choroidal thickness and choroidal blood perfusion in Guinea pig myopia. *Invest. Ophthalmol. Vis. Sci.* 60 (8), 3074–3083. doi:10.1167/iovs.18-26397
- Zi, Y., Deng, Y., Zhao, J., Ji, M., Qin, Y., Deng, T., et al. (2020). Morphologic and biochemical changes in the retina and sclera induced by form deprivation high myopia in Guinea pigs. *BMC Ophthalmol.* 20 (1), 105. doi:10.1186/s12886-020-01377-1



OPEN ACCESS

EDITED BY

Huiying Liu,
Institute for Infocomm Research
(A*STAR), Singapore

REVIEWED BY

Fan Xu,
People's Hospital of Guangxi Zhuang
Autonomous Region, China
Yitian Zhao,
Ningbo Institute of Materials Technology
and Engineering (CAS), China

*CORRESPONDENCE

Liya Zhang,
✉ 185879076@qq.com
Ying Zhao,
✉ zhaoyingszy@163.com

[†]These authors have contributed equally
to this work and share first authorship

SPECIALTY SECTION

This article was submitted to Molecular
and Cellular Pathology,
a section of the journal
Frontiers in Cell and Developmental
Biology

RECEIVED 17 February 2023

ACCEPTED 20 March 2023

PUBLISHED 28 March 2023

CITATION

Ji Y, Ji Y, Liu Y, Zhao Y and Zhang L (2023),
Research progress on diagnosing retinal
vascular diseases based on artificial
intelligence and fundus images.
Front. Cell Dev. Biol. 11:1168327.
doi: 10.3389/fcell.2023.1168327

COPYRIGHT

© 2023 Ji, Ji, Liu, Zhao and Zhang. This is
an open-access article distributed under
the terms of the [Creative Commons
Attribution License \(CC BY\)](#). The use,
distribution or reproduction in other
forums is permitted, provided the original
author(s) and the copyright owner(s) are
credited and that the original publication
in this journal is cited, in accordance with
accepted academic practice. No use,
distribution or reproduction is permitted
which does not comply with these terms.

Research progress on diagnosing retinal vascular diseases based on artificial intelligence and fundus images

Yuke Ji^{1†}, Yun Ji^{2†}, Yunfang Liu³, Ying Zhao^{2*} and Liya Zhang^{3*}

¹The Laboratory of Artificial Intelligence and Bigdata in Ophthalmology, Affiliated Eye Hospital of Nanjing Medical University, Nanjing, China, ²Affiliated Hospital of Shandong University of traditional Chinese Medicine, Jinan, Shandong, China, ³Department of Ophthalmology, The First People's Hospital of Huzhou, Huzhou, Zhejiang, China

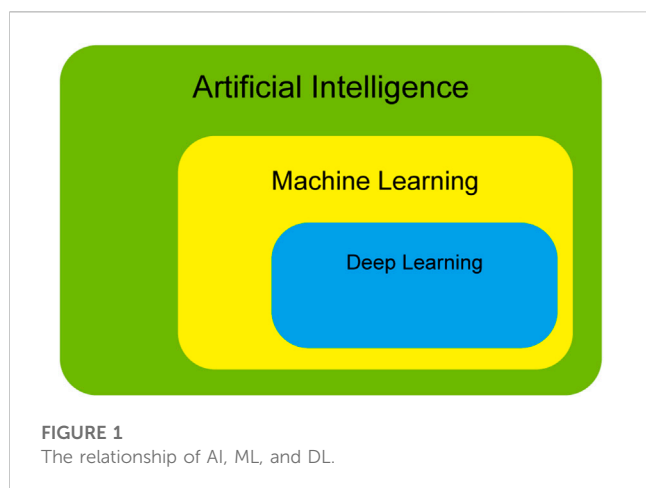
As the only blood vessels that can directly be seen in the whole body, pathological changes in retinal vessels are related to the metabolic state of the whole body and many systems, which seriously affect the vision and quality of life of patients. Timely diagnosis and treatment are key to improving vision prognosis. In recent years, with the rapid development of artificial intelligence, the application of artificial intelligence in ophthalmology has become increasingly extensive and in-depth, especially in the field of retinal vascular diseases. Research study results based on artificial intelligence and fundus images are remarkable and provides a great possibility for early diagnosis and treatment. This paper reviews the recent research progress on artificial intelligence in retinal vascular diseases (including diabetic retinopathy, hypertensive retinopathy, retinal vein occlusion, retinopathy of prematurity, and age-related macular degeneration). The limitations and challenges of the research process are also discussed.

KEYWORDS

artificial intelligence, fundus images, diabetic retinopathy, hypertensive retinopathy, retinal vein occlusion, retinopathy of prematurity, age-related macular degeneration

1 Introduction

In 1956, artificial intelligence (AI) was first proposed. As a branch of computer science, the purpose of AI is to develop and study computer methods to simulate and expand human intelligence and perform complex tasks (Hamet and Tremblay, 2017). Machine learning (ML) is a subfield of AI, where machines learn and mark a large amount of measured data or features through statistical algorithms to use the generated empirical model to complete the task (Deo, 2015). ML can perform the classification task, and the classifier needs to learn to identify the tag features of the research object and then classify the task according to the tag features, which mainly depends on the resolution of the selected features. Deep learning (DL) is a subfield of machine learning, a multilayer neural network, and a machine learning method (LeCun et al., 2015). DL is powerful and can not only perform classification tasks, but also extract features. A single deep learning network can perform two tasks simultaneously, extract the features of a given classification problem, and then classify them. Compared with ML, DL has a special advantage; that is, with the increase in training data, the performance of DL will improve, whereas the performance of ML will reach saturation with the increase in data. The relationship diagrams for AI, ML, and DL are shown in Figure 1.



With the rapid development of computer science in recent years, AI has made significant progress. AI has been applied in the field of medicine, especially in ophthalmology, and the clinical application of AI is particularly extensive. AI has been used to develop AI models for automatic diagnosis, screening, classification and treatment, especially in ophthalmic diseases such as ocular surface diseases (Ji et al., 2022b), anterior segment diseases (Ting et al., 2021), cataracts (Tognetto et al., 2022), glaucoma (Coan et al., 2023), and retinal diseases (Ting et al., 2019).

Retinal vascular disease (RVD) is a major retinal disease. The vascular system of the retina is one of the components of the systemic circulatory system. There are many causes of retinal vascular diseases, including the effects of local eye diseases and systemic diseases on retinal vessels, which can be divided into the following categories: 1) retinal vascular obstructive diseases, such as retinal vein occlusion; 2) the effects of systemic diseases on retinal vessels, such as diabetes and hypertension; 3) retinal vascular inflammatory immune diseases, such as retinal periphlebitis; and 4) retinal vascular abnormalities and developmental abnormalities, such as retinopathy of prematurity. Retinal vascular disease can cause irreversible damage to retinal cells and can seriously affect the vision of patients. If patients are not treated in time, they will experience serious vision loss or blindness. Therefore, for patients with retinal vascular disease, early detection, diagnosis, and treatment are particularly important, but relatively insufficient resources for ophthalmic diagnosis and treatment greatly limit the early diagnosis and treatment of retinal vascular diseases. In recent years, AI has become increasingly used in ophthalmology, especially in image recognition and processing of retinal vascular diseases, which provides a new possibility for early diagnosis and treatment. This review summarizes the research achievements of AI for the diagnosis of retinal vascular diseases in recent years and discusses the limitations and challenges of the research.

2 Basic process of the medical artificial intelligence diagnosis model for research

Using the AI model by Tong et al. (2020), we drew a basic flow chart of the AI research model, as shown in Figure 2. First, the

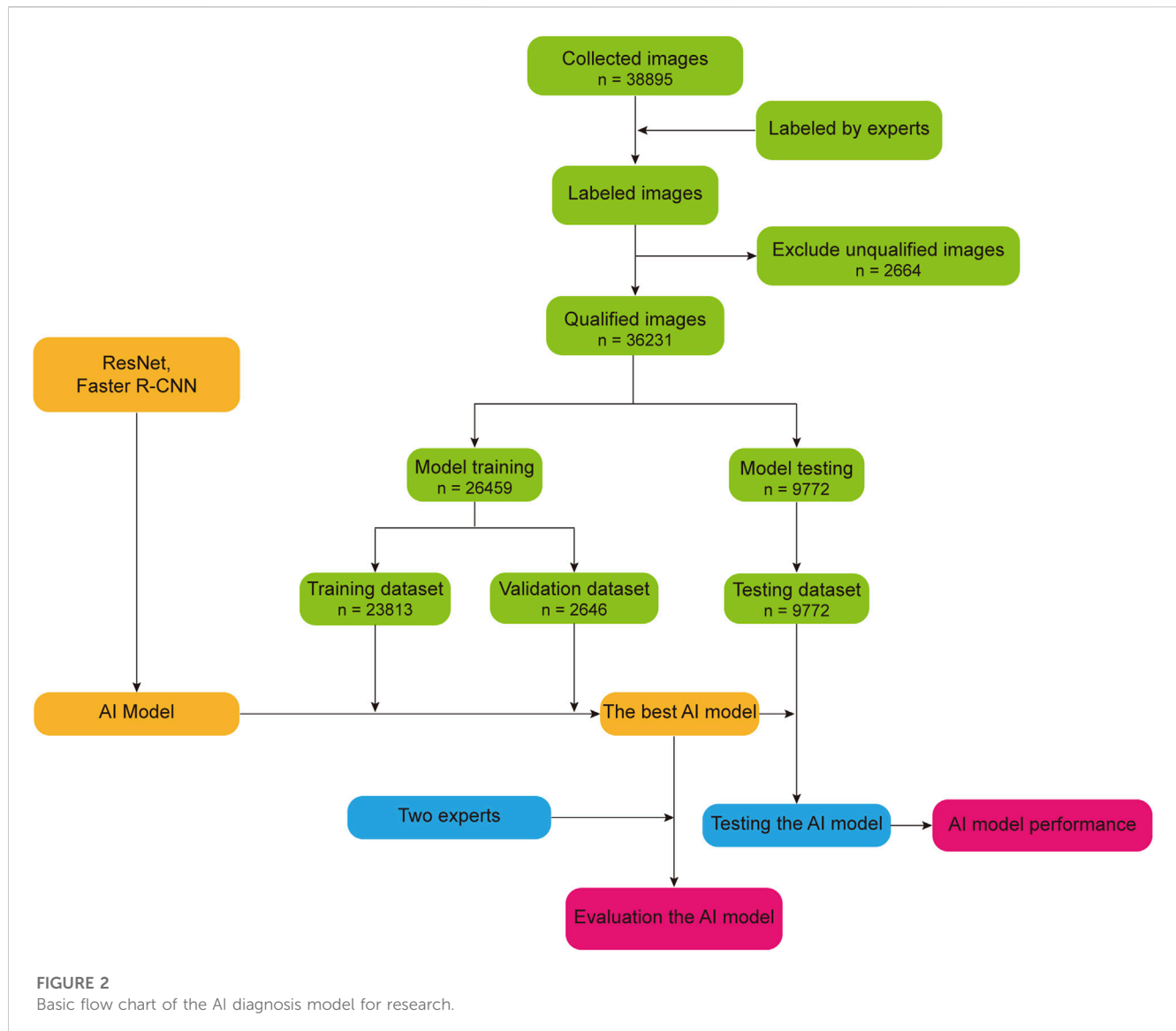
experts mark the collected images, remove the unqualified images in the labeled images, and randomly divide the remaining qualified images into a training dataset, validation dataset, and test dataset according to a certain proportion. Second, the training dataset and validation dataset are used to train and optimize the AI model to obtain the best performing AI model. Finally, we used the test dataset to test the AI model and compare the AI model's performance with the experts.

3 Application of artificial intelligence in retinal vascular diseases

3.1 Application of artificial intelligence in diabetic retinopathy

Diabetes is a common metabolic disease that causes extensive damage to many tissues and organs in the body. Diabetic retinopathy (DR) is one of the most serious microvascular complications of diabetes and a common cause of blindness (Lim et al., 2023). The incidence of DR is primarily related to the course of diabetes and the degree of disease control. The longer the course of diabetes, the higher the incidence of DR (Huang et al., 2023). At present, the pathogenesis of DR is unclear, but glucose metabolism disorder is the root cause of DR (Han et al., 2023). In the early stage of DR, patients with general ocular symptoms can experience various visual impairments with the development of the disease, among which flash sensation and vision loss are the most common (Grauslund, 2022). Clinically, DR is divided into non-proliferative diabetic retinopathy (NPDR) and proliferative diabetic retinopathy (PDR). The most important sign of PDR is retinal neovascularization (Sheng et al., 2022). According to the severity of DR, DR is divided into six stages: stage I, microhemangioma and small hemorrhagic spot; stage II, yellow-white rigid exudation and hemorrhagic spot; stage III, white cotton velvet spot and hemorrhagic spot; stage IV, neovascularization or vitreous hemorrhage; stage V, neovascularization and fiber proliferation; and stage VI, neovascularization and fiber proliferation, accompanied by traction retinal detachment (Mehra et al., 2022; Yang et al., 2022). The treatment of DR mainly includes the following aspects: 1) strict control of blood glucose levels, which can slow the occurrence and progression of DR, 2) laser photocoagulation, 3) vitrectomy and intraocular photocoagulation, and 4) vitreous injection of anti-VEGF drugs (Li F. et al., 2022; Wang et al., 2022).

By analyzing the fundus examination images of DR patients, AI can complete the automatic diagnosis of DR, which is of great significance in improving the diagnostic and work efficiency of doctors. Li X. et al. (2022) constructed an intelligent diagnosis model for DR based on Inception-v4 to assist in the diagnosis of AI. They used 8,739 fundus images for the AI model training and evaluated them using the Messidor-2 dataset. In addition, they compared the performance of the model with that of ophthalmologists. The final results showed that the AUC, sensitivity, and specificity of the model were 0.992, 0.925, and 0.961, respectively, which were better than those of ophthalmologists. To better assist the diagnosis of severe DR, Zhang et al. (2022a) developed an AI model that can diagnose DR automatically on the basis of Inception V3 and applied The



Kaggle public dataset to the development and validation of the AI model. After validation, the sensitivity, specificity, and AUC of the model for diagnosing severe DR were 0.925, 0.907, and 0.968, respectively. [Zhao et al. \(2022\)](#) constructed several DR prediction models using five different machine learning algorithms (Random Forest, Logistic Regression, Extreme Gradient Boosting, Support Vector Machine, K-Nearest Neighbor) and used the eye data of 7,943 patients to train and test the AI model. In addition, they compared different AI models to predict the performance of DR. After testing, the performance of the Extreme Gradient Boosting model was found to be the best, and its AUC, accuracy, sensitivity, specificity were 0.803, 0.889, 0.740, 0.811, respectively.

To build an AI model that can automatically detect DR, [Hassan et al. \(2022\)](#) constructed a DR detection model based on the VGG-16, ResNet-50, and U-Net. They collected 1804 fundus images, used them to train the AI model, and validated the model on external datasets. After validation, the accuracy of the model for the DR diagnosis was 0.9938. [Islam et al. \(2022\)](#) proposed an AI model that can detect DR based on supervised contrastive learning and used the

APTOS 2019 Blindness Detection dataset and Messidor-2 dataset to train and test the AI model. After testing, the accuracy of the DR detection model was 0.9836 and the AUC was 0.9850. Using a deep learning algorithm, [Elgafi et al. \(2022\)](#) proposed an AI model that can detect DR using optical coherence tomography (OCT) images. In this study, 188 OCT images were collected and applied to the training and validation of the AI models. Finally, the accuracy of the model was verified to be 0.9681. By learning the characteristic lesions in the fundus images of DR patients, AI can detect DR, which can facilitate the early detection of DR patients, thereby reducing and improving clinical work pressure.

[Zhang et al. \(2022b\)](#) constructed a deep graph correlation network (DGCN) model through a convolution neural network, which can automatically classify DR without professional labeling. In this study, EyePACS-1 and Messidor-2 datasets were used to train and test the model. Finally, the results showed that the accuracy, sensitivity, and specificity of the model on the EyePACS-1 dataset were 0.899, 0.882, and 0.913, respectively, and the accuracy, sensitivity and specificity of the model on the Messidor-2 dataset

TABLE 1 Research summary of artificial intelligence in diabetes retinopathy.

Year	Country or region	Authors	Task	Dataset (disease images)	AI algorithm	Output
2021	China	Li et al. (2022)	Diagnosis	8,739 images, Messidor-2 dataset (8,379 images)	Inception-v4	AUC = 0.992, Sensitivity = 0.925, Specificity = 0.961
2022	China	Zhang et al. (2022a)	Diagnosis	The Kaggle public dataset (4,192 images)	Inception V3	Sensitivity = 0.925, Specificity = 0.907, AUC = 0.968
2022	China	Zhao et al. (2022)	Diagnosis	7,943 patients' data (1,692 images)	Random Forest, Extreme Gradient Boosting, Logistic Regression, Support Vector Machine and K-Nearest Neighbor	AUC = 0.803, Accuracy = 0.889, Sensitivity = 0.740, Specificity = 0.811
2022	America	Hassan et al. (2022)	Detection	1804 images (920 images)	VGG-16, ResNet-50, U-Net	Accuracy = 0.9938
2022	Bangladesh	Islam et al. (2022)	Detection	APTOS 2019 Blindness Detection dataset, Messidor-2 dataset (5068 images)	Supervised competitive learning	Accuracy = 0.9836, AUC = 0.9850
2022	Egypt	Elgafi et al. (2022)	Detection	188 images (88 images)	Deep learning	Accuracy = 0.9681
2022	China	Zhang et al. (2022b)	Grading	EyePACS-1, Messidor-2 (5849 images)	Deep graph correlation network	EyePACS-1: Accuracy = 0.899, Sensitivity = 0.882, Specificity = 0.913
						Messidor-2: Accuracy = 0.918, Sensitivity = 0.902, Specificity = 0.930
2022	China	Zhang F et al. (2022)	Grading	1,089 images (1,089 images)	ResNet-34, Inception v3	AUC = 0.958, Kappa = 0.860
2021	Israel	Katz et al. (2022)	Grading	6,981 images (6,981 images)	W-net	Accuracy = 0.989

were 0.918, 0.902, and 0.930, respectively. To assist DR classification, [Zhang W. F et al. \(2022\)](#) developed an AI classification model based on ResNet-34 and Inception-v3 and used 1,089 fundus images to train and test the model. After testing, the AUC of the model was 0.958 and the kappa score was 0.860. [Katz et al. \(2022\)](#) constructed an AI model based on W-net, which can automatically classify DR. They collected 6,981 fundus images and used them to train and test the AI model. The final results showed that the accuracy of the model was 0.989. We summarize the above research, as shown in [Table 1](#).

3.2 Application of artificial intelligence in hypertensive retinopathy

Hypertensive retinopathy (HR) is a common retinal vascular disease caused by long-term hypertension ([Ji et al., 2022a](#)). Fundus changes in HR patients are related to age and disease course. The older the age of HR patients, the longer the course of the disease and the higher the incidence of fundus lesions ([Cheung et al., 2022](#)). In the early stage, there is often no obvious change in the fundus of HR patients. With the progression of the disease, the retinal artery gradually changes organically, and the wall of the retina begins to harden, appearing as a copper wire or silver wire ([Di Marco et al., 2022](#)). The diameter of the artery gradually narrows, and the proportion of arteries and veins gradually decreases ([Dziedziak et al., 2022](#)). Retinal hemorrhage, hard exudation, cotton velvet

spots, and other changes occur in the fundus; and optic disc edema may occur in severe cases ([Liu et al., 2021](#); [Badawi et al., 2022](#)). According to the progression and severity of the disease, HR is divided into four grades: grade I, vasoconstriction and narrowing; grade II, arteriosclerosis; grade III, exudation, cotton velvet spots, hemorrhage, and extensive microvascular changes; and grade IV grade III changes and optic disc edema ([Wong and Mitchell, 2004](#); [Tsukikawa and Stacey, 2020](#)). In clinical treatment, lowering blood pressure is the most fundamental means to prevent and treat fundus changes. After the effective control of blood pressure, optic disc edema, retinal edema, hemorrhage, and exudation can be absorbed and eliminated ([Klig, 2008](#); [Del Pinto et al., 2022](#)). If HR patients have complications such as macular edema, treatment such as intravitreal injection of anti-VEGF drugs can significantly improve their vision ([Padhy and Kumar, 2018](#)).

In many studies, AI has been used to screen and diagnose HR, and the AI model constructed in this study showed good screening and diagnostic performance and has the potential for clinical application. [Han et al. \(2021\)](#) constructed an AI model to screen for HR and other common eye diseases based on an anomaly detection algorithm. In this study, 90,499 fundus photos were collected and randomly divided into training, validation, and testing dataset according to a certain proportion, which were used to develop and evaluate the AI model. After testing, the AUC, accuracy, sensitivity, and specificity of the HR diagnosis model were 0.895, 0.8237, 0.8129, and 0.8275, respectively. To assist clinicians in screening HR, [Arsalan et al. \(2021\)](#)

TABLE 2 Research summary of artificial intelligence in hypertensive retinopathy.

Year	Country or region	Authors	Task	Dataset (disease images)	AI algorithm	Output
2021	China	Han et al. (2021)	Screening	90,499 images (26,148 images)	Anonymous detection	AUC = 0.895, Accuracy = 0.8237, Sensitivity = 0.8129, Specificity = 0.8275
2022	Korea	Arsalan et al. (2021)	Screening	DRIVE, STARE, CHASE-DB1 (2051 images)	Dual-stream fusion network, Dual-stream aggregation network	DRIVE: Accuracy = 0.9693, Sensitivity = 0.8268, Specificity = 0.9830, AUC = 0.9842
						CHASE-DB1: Accuracy = 0.9725, Sensitivity = 0.8222, Specificity = 0.9838, AUC = 0.9815
						STARE: Accuracy = 0.9700, Sensitivity = 0.8607, Specificity = 0.9800, AUC = 0.9865
2019	Korea	Arsalan et al. (2019)	Diagnosis	DRIVE, CHASE-DB1, STARE (1960 images)	Convolutional neural networks	Sensitivity = 0.8526, Specificity = 0.9791, Accuracy = 0.9883, AUC = 0.9697
2022	China	Dong et al. (2022)	Diagnosis	120,002 images (8,198 images)	Convolutional neural network	Accuracy = 0.837
2021	Saudi Arabia	Abbas et al. (2021)	Classification	1,400 images (1,000 images)	DenseNet	Sensitivity = 0.905, Specificity = 0.915, Accuracy = 0.926, Matthews correlation coefficient = 0.61, F1-score = 0.92, AUC = 0.915
2017	Pakistan	Akbar et al. (2018)	Classification	INSPIRE-AVR, VICAVR, STARE, and AVRDB (198 images)	Support vector machine, Radial basis function	Accuracy: INSPIRE-AVR = 0.9510, VICAVR = 0.9564, AVRDB = 0.9809, STARE = 0.9593, AVRDB = 0.9750

constructed an AI screening model using a dual-stream fusion network (DSF-Net) and a dual-stream aggregation network (DSA-Net). They evaluated the performance of the model using the DRIVE, STARE, and CHASE-DB1 dataset. After testing, the accuracy, sensitivity, specificity, and AUC value for DRIVE were 0.9693, 0.8268, 0.9830, and 0.9842, respectively; for CHASE-DB1 they were, 0.9725, 0.8222, 0.9838, and 0.9815, respectively; and for STARE they were 0.9700, 0.8607, 0.9800, and 0.9865, respectively. [Arsalan et al. \(2019\)](#) developed a dual-residual-stream-based vessel segmentation network (Vess-Net) model on the basis of convolutional neural networks, which is used to assist HR diagnosis and to train and test on the open datasets of DRIVE, CHASE-DB1, and STARE. Finally, the results showed that the sensitivity, specificity, AUC, and accuracy of the model for diagnosing HR were 0.8526, 0.9791, 0.9883, and 0.9697, respectively. [Dong et al. \(2022\)](#) collected 120,002 fundus photos and used a convolutional neural network to create a retinal AI diagnosis system (RAIDS) for the diagnosis of 10 types of retinal diseases, including HR. They randomly divided 120,002 fundus photos into training, test, and validation datasets and used them in the training and validation of the system. The accuracy of the system in identifying HR was verified to be 0.837.

AI is also used in the classification and grading of HR, which is expected to be used clinically to reduce the pressure on doctors. [Abbas et al. \(2021\)](#) constructed a HYPER-RETINO system based on the DenseNet algorithm to assist in the classification of HR. They collected 1,400 fundus photos and used them for the development and testing of the system. The sensitivity, specificity, accuracy, Matthews correlation coefficient, and AUC of the system were 0.905, 0.915, 0.926, 0.61, and 0.915, respectively. [Akbar et al. \(2018\)](#) constructed an AI model using a DL algorithm (support vector machine and radial basis function) to assist in screening and

grading of HR. The INSPIRE-AVR, VICAVR, STARE, and AVRDB datasets were used to develop, train and test the model. After testing, it was found that the accuracies of the first part of the model on the INSPIRE-AVR, VICAVR, and AVRDB dataset were 0.9510, 0.9564, and 0.9809, respectively, and the accuracies of the second part on the STARE and AVRDB dataset were 0.9593 and 0.9750, respectively. We summarize the above research, as shown in [Table 2](#).

3.3 Application of artificial intelligence in retinal vein occlusion

Retinal vein occlusion (RVO) is one of most common retinal vascular disease, second only to diabetic retinopathy, and more common in older patients ([Ren et al., 2022](#)). The pathogenesis of RVO is related to many factors such as vascular endothelial damage, hemodynamic changes, intraocular pressure, and ocular local compression ([Terao et al., 2022](#); [Trovato Battagliola et al., 2022](#)). In addition, the disease is closely related to arteriosclerosis, cardiovascular and cerebrovascular diseases, hypertension, diabetes, and other risk factors ([Orskov et al., 2022](#); [Tang et al., 2022](#)). According to the location of vein occlusion, RVO is mainly divided into central retinal vein occlusion (CRVO) and branch retinal vein occlusion (BRVO), of which branch occlusion is the most common ([Miao et al., 2022](#)). In the early stage, the symptoms are characterized by a sudden loss of vision to varying degrees; mild patients may have no symptoms or only a little shadow ([Pur et al., 2023](#)), and with the progression of the disease, RVO patients have serious visual impairment ([Zhang X. T et al., 2022](#); [Sood et al., 2022](#)). Typical fundus changes in RVO patients include retinal hemorrhage, tortuous retinal vein dilatation, extensive retinal capillary non-perfusion area, and macular edema ([Irgat and](#)

Ozcara, 2023). Late patients may have complications such as vitreous hemorrhage, traction retinal detachment, and neovascular glaucoma, resulting in severe visual acuity loss and even blindness (Altintas and Ilhan, 2023; Patil et al., 2023). Some commonly used treatment methods in ophthalmology are mainly used to prevent and treat complications such as laser photocoagulation, vitrectomy, vitreous injection of hormones, or anti-VEGF drugs (Ghanchi et al., 2022; Yin et al., 2022).

As an important clinical assistant tool, AI has been widely used in the early screening of retinal vein occlusion, and especially in areas where lacking medical resources, AI can play an important role. To assist in screening for retinal vein occlusion, Chen J. S et al. (2021) constructed an AI screening model using four DL algorithms (ResNet-50, Inception-v3, DenseNet-121, SE-ReNeXt-50). They collected 8,600 color fundus photos and randomly divided them into training, validation, and test dataset according to a certain proportion for the development and testing of AI models. After testing, the Inception-v3 model's performance was the best, and its sensitivity, specificity, F1 score, and AUC were 0.93, 0.99, 0.95, and 0.99, respectively. Nagasato et al. (2019a) constructed two AI models using the VGG-16 and support vector machine algorithms to detect branch retinal vein occlusion. They collected 465 ultrawide-field fundus images for training and validation of AI models and compared the performance of the two models. The final results showed that the detection performance of the VGG-16 model was better than that of support vector machine model, with a sensitivity of 0.940, a specificity of 0.970, and an AUC of 0.976. Nagasato et al. (2018) constructed two screening models for CRVO based on the VGG-16 and support vector machine algorithms. In this study, 363 ultrawide-field fundus images were used to develop and test AI models, and the screening performance of the two AI models was compared. The VGG-16 model had the best screening performance, with a sensitivity of 0.984, specificity of 0.979, and AUC of 0.989. Anitha et al. (2012) constructed an AI diagnosis model based on artificial neural networks to assist in the diagnosis of four retinal diseases, including central retinal vein occlusions. They collected 420 digital retinal images to send and verify their model. The results showed that the model's accuracy, sensitivity, and specificity were 0.977, 0.960, and 0.980, respectively. To assist in the diagnosis of retinal vein occlusion, Kang et al. (2021) developed an AI diagnosis model based on a convolution neural network, and used the examination data of 2,992 eyes to develop and train the model. After testing, the AUC of this model for BRVO was 0.959 and that of CRVO was 0.988. Abitbol et al. (2022) collected 224 ultra-widefield color fundus images and constructed an AI model based on the DenseNet121 network to assist diagnose three types of retinal vascular diseases such as retinal vein occlusion. Finally, the accuracy of the model in the diagnosis of RVO was 0.884, and the AUC was 0.912.

Xu et al. (2022) constructed an AI model based on ResNet18 to assist in the classification of RVO. In their study, 501 fundus images were collected for the development and testing of the model. After testing, the classification accuracy of the model was greater than 0.97, the sensitivity was greater than 0.95, the sensitivity was greater than 0.97, and the F1 score was greater than 0.97. Zhang X. et al. (2022) constructed a VGG-CAM network model based on convolutional neural networks to assist in the diagnosis and classification of RVO. They used a local image database to train

and test the model and compared it with Resnet-34, Inception-V3, and MobileNet network models. After testing, the sensitivity, specificity, Kappa coefficient, and AUC of the model for diagnosing central RVO were 0.99, 0.96, 0.88, and 0.99, respectively, and the sensitivity, specificity, Kappa coefficient, and AUC for diagnosing branch RVO were 0.94, 0.99, 0.97, and 0.99, respectively. In addition, its diagnostic performance was superior to that of other network models. It can be seen that in the clinical classification of retinal vein occlusion, compared with manual classification, automatic classification has lower cost and higher efficiency and can play an important role in clinical practice.

In addition, AI can help clinicians diagnose RVO by identifying and segmenting the characteristic lesions in the images of patients with RVO, thus reducing the workload of clinicians. Tang et al. (2021) constructed an AI model using CE-Net to help segment the non-perfusion area of the retina caused by RVO, thus helping to evaluate RVO severity. They collected 177 fluorescein angiography images for training and testing the AI model and enhanced the performance of the AI model through an adaptive histogram-based data augmentation method. After testing, the accuracy of the model was 0.883. To detect the non-perfusion area caused by RVO in optical coherence tomography angiography (OCTA) images to help diagnose RVO, Nagasato et al. (2019b) constructed an AI model based on VGG-16 and support vector machine and collected 322 OCTA images for AI model training and testing. In addition, they compared the performance of the AI model with the diagnostic abilities of seven ophthalmologists. After testing, the performance of the VGG-16 model was better than support vector machine model and the seven ophthalmologists, and its AUC, sensitivity, and specificity were 0.986, 0.937, and 0.973, respectively. We summarize the above research, as shown in Table 3.

3.4 Application of artificial intelligence in retinopathy of prematurity

Retinopathy of prematurity (ROP), also called retrolental fibroplasia, is a proliferative retinopathy of immature or low birth weight infants (Campbell et al., 2022). Most of the infants were premature with less than 34 weeks of pregnancy, birth weight less than 1,500 g, history of inhalation of high concentrations of oxygen, or stunted low birth weight infants (Sabri et al., 2022). Preterm birth, low birth weight, and inhalation of high concentrations of oxygen are high-risk factors for ROP (Ramanathan et al., 2022). The clinical manifestations of children with ROP vary according to the course of the disease, which is divided into three areas according to the location of the lesion: area I, a circular area with a radius of 2 times the distance from the optic disc to the fovea of the macula (Bai et al., 2022); area II, a circular area centered on the optic disc to the sawtooth margin of the nasal side (Eilts et al., 2023); and area III, the area excluding areas I and II (Nisha et al., 2023). According to the severity of the lesion, it was divided into five stages: stage 1, dividing line stage; stage 2, critical stage; stage 3, increment stage; stage 4, subpanretinal detachment stage; and stage 5, panretinal detachment stage (Gensure et al., 2020). For treatment, stage 1 and stage 2 can disappear naturally, so they should be observed closely (Scruggs et al., 2020); stage 3 should be treated with condensation or photocoagulation to prevent

TABLE 3 Research summary of artificial intelligence in retinal vein occlusion.

Year	Country or region	Authors	Task	Dataset (disease images)	AI algorithm	Output
2021	China	Chen S et al. (2021)	Screening	8,600 images (440 images)	ResNet-50, Inception-v3, DenseNet-121, SE-ReNeXt-50	Sensitivity = 0.93, Specificity = 0.99, F1 = 0.95, AUC = 0.99
2018	Japan	Nagasato et al. (2019a)	Detection	465 images (125 images)	VGG-16, Support vector machine	Sensitivity = 0.940, Specificity = 0.970, AUC = 0.976
2018	Japan	Nagasato et al. (2018)	Screening	363 images (237 images)	VGG-16, Support vector machine	Sensitivity = 0.984, Specificity = 0.979, AUC = 0.989
2011	India	Anitha et al. (2012)	Diagnosis	420 images (95 images)	Artificial neural networks	Accuracy = 0.977, Sensitivity = 0.960, Specificity = 0.980
2021	Taiwan	Kang et al. (2021)	Diagnosis	2,992 eyes (325 eyes)	Convolution neural network	AUC of branch retinal vein occlusion = 0.959; AUC of central retinal vein occlusion = 0.988
2022	France	Abitbol et al. (2022)	Diagnosis	224 images (169 images)	DenseNet121	Accuracy = 0.884, AUC = 0.912
2022	China	Xu et al. (2022)	Classification	501 images (242 images)	ResNet18	Accuracy>0.97 Sensitivity>0.95, F1 score>0.97
2022	China	Zhang et al. (2022a)	Classification	Local image database (Not specified)	Convolutional neural networks	Sensitivity = 0.99, Specificity = 0.96, Kappa coefficient = 0.88, AUC = 0.99
2020	China	Tang et al. (2021)	Division	177 images (177 images)	CE-Net	Accuracy = 0.883
2019	Japan	Nagasato et al.	Detection	322 images (128 images)	VGG-16, Support vector machine	AUC = 0.986, Sensitivity = 0.937, Specificity = 0.973

neovascularization ([Barrero-Castillero et al., 2020](#)); and stage 4 and stage 5 can be treated with a vitrectomy to remove proliferated fibrovascular tissue. Photocoagulation was performed simultaneously ([Morya et al., 2022](#)). Once ROP occurs, it progresses rapidly, and the curative effect in advanced cases is limited; therefore, it is important for children with ROP to be detected and treated early to avoid serious consequences.

To automatically diagnose ROP, [Brown et al. \(2018\)](#) constructed a diagnostic model based on U-Net and Inception version 1, and 5,511 retinal images were used to develop and train the AI model. In addition, they compared the AI model's diagnostic performance with that of eight experts. The final results showed that the sensitivity, specificity, and accuracy of the AI diagnosis model were 0.93, 0.94, 0.91 respectively, whereas the average accuracy of the eight experts was 0.82. This shows that the diagnostic performance of the AI model is superior. [Chen Q. et al. \(2021\)](#) proposed an AI model on the basis of convolution neural network, which can assist the staging diagnosis of ROP. They collected 10,894 fundus images and divided them into training and testing dataset. After testing, the AUROC of the model was 0.99, the AUPRC was 0.98, and the sensitivity was 0.94. [Mao et al. \(2020\)](#) established an AI model that can assist in the diagnosis of ROP based on U-Net and Dense Net and analyzed the progress of ROP. They used 3,311 fundus images to train and verify the AI model. Finally, the results showed that the diagnostic specificity of the model was 0.978, the sensitivity was 0.951, and the sensitivity and specificity for the diagnosis of disease deterioration were 0.924 and 0.974, respectively. [Peng et al. \(2022\)](#) constructed an ADS-Net model based on DenseNet121 to assist doctors in the diagnosis of ROP. In this study, 8,733 fundus images were collected from two datasets

for training and verifying the model. After validation, the accuracy of the model for diagnosing ROP was 0.9776, recall was 0.9714, precision was 0.9835, F1-score was 0.9774, and the kappa coefficient was 0.9552. Based on the above AI research results, it can be found that AI model shows superior performance in automatic diagnosis of ROP by recognizing ophthalmic examination data such as fundus images, and has the potential to be used in clinical diagnosis and treatment, which can greatly improve the work efficiency of clinicians and reduce the work pressure of clinicians.

In recent years, AI model has made a lot of research achievements in assisting the clinical staging and grading diagnosis of ROP. In order to assist in the grading and staging of ROP, [Tong et al. \(2020\)](#) constructed an AI model based on ResNet and faster region-based convolutional neural network (Faster-RCNN). In this study, 36,231 retinal images were collected and randomly divided into training, validation, and testing datasets. In addition, they compared the classification performance of the AI model with two retinal experts. The final results showed that, in terms of ROP classification, the accuracy, sensitivity, specificity, and F1 scores of the model were 0.903, 0.778, 0.932, and 0.761, respectively, which were better than the two retinal experts. In terms of ROP staging, the diagnostic accuracies of stages 1, 2, 3, 4, and 5 were 0.876, 0.942, 0.968, 0.998, and 0.999, respectively. [Peng et al. \(2021\)](#) used ResNet18, DenseNet121, and EfficientNetB2 to create an AI model for ROP staging and used 635 retinal images to train and verify the model. After validation, the recall of the model was 0.905, precision was 0.9092, the F1 score was 0.9043, accuracy was 0.9827, and Kappa was 0.9786. To detect early ROP and staging, [Huang et al. \(2021\)](#) constructed an ROP staging model using a through convolution neural network. They randomly divided

TABLE 4 Research summary of artificial intelligence in retinopathy of prematurity.

Year	Country or region	Authors	Task	Dataset (disease images)	AI algorithm	Output
2018	America	Brown et al. (2018)	Diagnosis	5,511 images (977 images)	U-Net, Inception version 1	Sensitivity = 0.93, Specificity = 0.94, Accuracy = 0.91
2020	America	Chen Q. et al. (2021)	Diagnosis	10,894 images (1945 images)	Convolution neural network	AUROC = 0.99, AUPRC = 0.98, Sensitivity = 0.94
2020	China	Mao et al. (2020)	Diagnosis	3,311 images (1,393 images)	U-Net, Dense Net	Specificity = 0.978, Sensitivity = 0.951
2022	China	Peng et al. (2022)	Diagnosis	8,733 images (3,684 images)	DenseNet121	Accuracy = 0.9776, Recall = 0.9714, Precision = 0.9835, F1-score = 0.9774, Kappa = 0.9552
2020	China	Tong et al. (2020)	Classification	36,231 images (36,231 images)	ResNet, Faster region-based convolutional neural network	Accuracy = 0.903, Sensitivity = 0.778, Specificity = 0.932, F1 score = 0.761
2021	China	Peng et al. (2021)	Classification	635 images (332 images)	ResNet18, DenseNet121, EfficientNetB2	Recall = 0.9055, Precision = 0.9092, F1 score = 0.9043, Accuracy = 0.9827, Kappa = 0.9786
2020	Taiwan	Huang et al. (2021)	Classification	11,372 images (1,279 images)	Convolution neural network	Accuracy = 0.9223, Sensitivity = 0.9614, Specificity = 0.9595, Sensitivity and Specificity of stage 1 ROP = 0.9182, 0.9450, Sensitivity and Specificity of stage 2 ROP = 0.8981, 0.9899
2022	China	Li and Liu (2022)	Classification	18,827 images (3,869 images)	U-Net, Dense Net	Sensitivity of diagnosing = 0.9593, Specificity of diagnosing = 0.9929, Sensitivity and Specificity of stage 1 ROP = 0.9021, 0.9767, Sensitivity and Specificity of stage 2 ROP = 0.9275, 0.9874, Sensitivity and Specificity of stage 3 ROP = 0.9184, 0.9929
2021	India	Agrawal et al. (2021)	Evaluation	4,250 images (2,350 images)	U-Net, Circle Hough Transform	Accuracy = 0.98
2022	China	Wu et al. (2022)	Evaluation	7,796 images (1984 images)	OC-Net, SE-Net	AUC, Accuracy, Sensitivity and Specificity of OC-Net = 0.94, 0.333, 1.00, and 0.075, respectively
						AUC, Accuracy, Sensitivity and Specificity of SE-Net = 0.88, 0.560, 1.00, and 0.353, respectively

11,372 fundus images into training and test datasets and used them to train and test the AI model. The results showed that the accuracy, sensitivity, and specificity of the model were 0.9223, 0.9614, and 0.9595, respectively. The sensitivity and specificity of stage 1 ROP were 0.9182 and 0.9450, respectively; the sensitivity and specificity of stage 2 ROP were 0.8981 and 0.9899, respectively. [Li F. et al. \(2022\)](#) developed an AI model based on U-Net and Dense Net to assist in the diagnosis of children with early ROP in stage 1–3. They collected 18,827 retinal images for training and validation dataset. After validation, the sensitivity and specificity of the model were 0.9593 and 0.9929 for normal images, 0.9021 and 0.9767 for stage 1 ROP, 0.9275 and 0.9874 for stage 2 ROP, 0.9184 and 0.9929 for stage 3 ROP, respectively. AI model has made many achievements in the clinical staging and grading diagnosis of ROP. AI model can help clinicians to grade and stage diagnosis of ROP, which is more conducive to the early diagnosis and treatment of ROP patients.

To detect the blood vessels in areas I, II, and III of children with ROP and to assist in assessing the severity of ROP, [Agrawal et al. \(2021\)](#) built an AI model by combining U-Net and Circle Hough Transform. They collected 4,250 fundus images to develop and test the AI model, all of which were labeled by ROP experts. After testing,

the model's accuracy was 0.98. To predict the occurrence and evaluate the severity of ROP, [Wu et al. \(2022\)](#) constructed an AI prediction model and AI evaluation model based on OC-Net and SE-Net. They collected 7,796 retinal images for training and validation dataset. The results showed that the AUC, accuracy, sensitivity, and specificity of the OC-Net prediction model were 0.94, 0.333, 1.00, and 0.075, respectively. The AUC, accuracy, sensitivity, and specificity of the OC-Net prediction model were 0.88, 0.560, 1.00, and 0.353, respectively. We summarize the above research, as shown in [Table 4](#).

3.5 Application of artificial intelligence in age-related macular degeneration

Age-related macular degeneration (AMD), also known as senile macular degeneration, is common in Europe, the United States, and other developed countries and is the main cause of blindness in the elderly in developed countries. Its incidence increases with age ([Thomas et al., 2021](#)). At present, the etiology and pathogenesis of AMD are not clear, and the related risk factors include age, sex, race, heredity, smoking, malnutrition, metabolic disorders, and retinal light damage

(Lombardo et al., 2022; Tao et al., 2023). Most patients with AMD are more than 50 years old, have both eyes effected at the same time or successively, and have progressive visual impairment. According to clinical manifestations and pathological changes, AMD can be divided into two types: atrophic or non-exudative or dry; exudative or neovascularization or wet (Gale et al., 2023). The main feature of atrophic AMD is progressive RPE atrophy, the main changes of the fundus are vitreous warts and RPE degeneration and atrophy (Zhang et al., 2023), and the characteristic changes of exudative AMD are neovascularization under the RPE, subretinal neovascular membrane, and subretinal hemorrhage (Liberski et al., 2022; Cao et al., 2023). For treatment, because the etiology of AMD is not clear, there is still no specific drug treatment or fundamental effective preventive measures; vitreous injection of anti-VEGF drugs is mainly used for neovascular AMD (Fabre et al., 2022; Galindo-Camacho et al., 2022).

To assist clinicians in diagnosing age-related macular degeneration and distinguishing its different types, AI has carried out a lot of research in this area, with remarkable results. Han et al. (2022) collected 4,749 spectral domain optical coherence tomography (SD-OCT) images and constructed an AI model that can diagnose neovascular age-related macular degeneration using three convolution neural networks (VGG-16, VGG-19, and ResNet). They randomly divided 4,749 images into training and test datasets and used them to develop and verify the model. In addition, they compared the diagnostic performance of the model with that of ophthalmologists. The results showed that the accuracy of the model was 0.874, which was similar to that of ophthalmologists. To distinguish between different types of AMD, Tak et al. (2021) constructed a model based on convolutional neural networks and used 420 Optos wide-field retinal images for training and validation. The classification accuracy of the model was found to be 0.88. Chou et al. (2021) constructed a DL model based on EfficientNet-B3 for the differential diagnosis of neovascular age-related macular degeneration. They collected 699 fundus photographs for training and testing the model. After testing, the model showed good performance with accuracy, sensitivity, specificity, and AUC values of 0.8367, 0.8076, 0.8472, and 0.8857, respectively. Heo et al. (2020) constructed an AI model using the VGG16 model to identify the different types of AMD. In this study, 399 fundus images were used to train and verify the model, and the discrimination performance of the model was compared with that of residents. The accuracy of the model was better than that of the residents, with an accuracy of 0.9086.

In addition to extensive research on the diagnosis and classification of AMD, AI has been used to predict the severity, disease progression, and therapeutic effect in patients with age-related macular degeneration. Ganjdanesh et al. (2022) created a new DL model (LONG-Net) based on ResNet-18 to predict the severity and progression of patients with age-related macular degeneration. They collected approximately 30,000 color fundus photographs for training and verifying the model. The average accuracy of the model was 0.905, and the AUC was 0.762. Song et al. (2022) constructed an AI model that predicted neovascular ANM based on a classified convolution neural network and a complete convolutional neural network algorithm. In total, 671 SD-OCT images were used to train and test the model. The average accuracy of the model was 0.930, the Dice coefficient was 0.873, the sensitivity was 0.873, and the specificity was 0.922. To predict the treatment effect and disease progression in patients with neovascular AMD, Yeh et al. (2022) built an AI prediction model using a new type of deep convolution neural network (Heterogeneous Data Fusion Net).

They collected eye SD-OCT images from 698 patients and used them to train and test the model. In addition, they compared the predictive performance of the model with those of the ResNet50 and AlexNet models. The prediction performance of the model was better than that of ResNet50 and AlexNet, with an AUC value of 0.989, accuracy of 0.936, sensitivity of 0.933, and specificity of 0.938. Yan et al. (2020) developed an AI model based on convolutional neural networks to predict the disease progression in patients with AMD. They collected 31,262 eye OCT images and 52 related mutations. After testing, the AUC value of the model for predicting the disease progression was 0.85.

Holomcik et al. (2022) constructed an AI model on U-Net to automatically segment lesions in fluorescein angiography images of patients with neovascular AMD. They collected 9,268 images to develop and test the model. After testing, the F1 score, accuracy, and recall of the segmented lesion size were 0.65, 0.75, and 0.72, respectively, and the F1 scores, accuracy, and recall of the leakage area were 0.73, 0.80, and 0.78, respectively. He et al. (2022) created a DL model that can detect age-related macular degeneration through the ResNet-50 model and local outlier factor (LOF) algorithm and used the UCSD dataset and Duke dataset to train and test the model. Finally, the accuracy of the model was 0.9987 for the UCSD dataset and 0.9756 for the Duke dataset. We summarize the above research, as shown in Table 5.

4 Limitations and challenges

Based on the referenced studies, AI is widely used in retinal vascular diseases, especially in image recognition and data analysis. Although AI model shows superior performance in assisting the diagnosis, identification, screening, staging and grading of retinal vascular diseases, AI model also faces many limitations and challenges in the research process, which will seriously affect the further research of artificial intelligence in retinal vascular diseases and hinder its clinical application. Below, we list the main limitations and challenges of AI in research on retinal vascular diseases. 1) Image quality in the dataset (Aronson, 2022; Gutierrez et al., 2022): The image quality used in AI research has a significant impact on AI research. The higher the image quality, the better the performance of the AI model. However, the quality of the image is related to a variety of factors, such as shooting equipment, operators, the degree of cooperation of patients and so on. Therefore, high-quality images should be used as much as possible in AI research. 2) Manual annotations of images in the dataset (Hashimoto et al., 2020; Betzler et al., 2022): The images in many studies must be manually annotated, and the accuracy of manual labeling has a significant impact on the performance of the AI model. This requires experts in related diseases to label the images to ensure the validity of the data. 3) Sample size of the dataset (Ji et al., 2022b): The accuracy of the AI model is related to the sample size. The larger the sample size, the higher the accuracy of the AI model. The sample size of the dataset used in some studies was small, which had an impact on the performance of the AI model. Therefore, in the study, the sample size of the dataset should be expanded as much as possible to ensure the accuracy of the AI model. 4) Patient heterogeneity (Galante et al., 2023): Studies on the AI model are likely to be affected by different patient groups. Differences between patients such as age, sex, race, and region affect the performance of the AI model. If only one patient group is included in the data set used in the study, it will seriously affect the

TABLE 5 Research summary of artificial intelligence in age-related macular degeneration.

Year	Country or region	Authors	Task	Dataset (disease images)	AI algorithm	Output
2022	Korea	Han et al. (2022)	Diagnosis	4,749 images (2,624 images)	VGG-16, VGG-19, ResNet	Accuracy = 0.874
2021	America	Tak et al. (2021)	Classification	420 images (420 images)	Convolutional neural networks	Accuracy = 0.88
2021	Taiwan	Chou et al. (2021)	Diagnosis	699 images (491 images)	EfficientNet-B3	Accuracy = 0.8367, Sensitivity = 0.8076, Specificity = 0.8472, AUC = 0.8857
2020	Korea	Heo et al. (2020)	Diagnosis	399 images (399 images)	VGG16	Accuracy = 0.9086
2022	America	Ganjdanesh et al. (2022)	Prediction	30,000 images (30,000 images)	ResNet-18	Accuracy = 0.905, AUC = 0.762
2022	China	Song et al. (2022)	Prediction	671 images (671 images)	Classified convolution neural network, complete convolution neural network	Accuracy = 0.930, Dice coefficients = 0.873, Sensitivity = 0.873, Specificity = 0.922
2022	Taiwan	Yeh et al. (2022)	Prediction	698 images (698 images)	Deep convolution neural network	AUC = 0.989, Accuracy = 0.936, Sensitivity = 0.933, Specificity = 0.938
2020	America	Yan et al. (2020)	Prediction	31,262 images, 52 related mutated genes (31,262 images)	Convolutional neural networks	AUC = 0.85
2022	Austria	Holomcik et al. (2022)	Division	9,268 images (9,268 images)	U-Net	F1 score = 0.65, Accuracy = 0.75, Recall = 0.72
2022	China	He et al. (2022)	Detection	UCSD dataset, Duke dataset (46,421 images)	ResNet-50, Local outlier factor	UCSD: Accuracy = 0.9987
						Duke: Accuracy = 0.9756

accuracy and clinical application of the AI model. 5) Clinical application of the AI model ([Al-Aswad et al., 2022](#); [Wawer Matos et al., 2022](#)): Although in many studies, AI model shows superior performance in external verification datasets, due to the great difference between “real environment” and “research environment”, this will lead to a series of problems in clinical application of AI model, which will affect the performance of AI model. 6) Clinicians’ reserve of AI algorithms and their related knowledge ([Tabuchi, 2022](#); [Yang et al., 2023](#)): AI belongs to a branch of computer science and does not belong to the professional scope of clinicians, which leads to clinicians’ lack of knowledge about AI algorithms, their related knowledge, and lack of explanation, which can easily lead to the “black box phenomenon” and hinder the application of AI in clinical work.

5 Conclusion

At present, the use of AI technology to assist clinicians in the study of ophthalmic images and other ophthalmic examinations is a current major focus. The combination of AI and ophthalmology will greatly improve the diagnosis of ophthalmic diseases, especially retinal vascular diseases based on the analysis of fundus images. The diagnosis model based on AI will be beneficial for the early detection, diagnosis, and treatment of retinal vascular diseases. Although the application of artificial intelligence in the field of ophthalmology has made a lot of research results, but from the overall situation, it is only the beginning. With further developments in computer science and technology, the application of AI in the field of ophthalmology will be more and more widely used in the field of ophthalmology. In addition, with the

deepening of research, in addition to image processing and recognition, other artificial intelligence technologies will also carry out related research in the field of ophthalmology, so as to promote the continuous development of ophthalmology.

Author contributions

YukJ and YunJ conceived and designed the research and wrote the manuscript; YL wrote the manuscript; YZ and LZ designed the research, acquired the article information, and revised the manuscript. All authors contributed to the article and have approved the submitted version.

Funding

This work was supported by Medical Science and Technology Development Project Fund of Nanjing (YKK21262), the Scientific Research Project of the Chinese Medicine Education Association (2022KTM028), and the Medical and health research project of Zhejiang Province (2018PY066).

Conflict of interest

The authors declare that the research was conducted in the absence of any commercial or financial relationships that could be construed as a potential conflict of interest.

Publisher's note

All claims expressed in this article are solely those of the authors and do not necessarily represent those of their affiliated

References

- Abbas, Q., Qureshi, I., and Ibrahim, M. E. A. (2021). An automatic detection and classification system of five stages for hypertensive retinopathy using semantic and instance segmentation in DenseNet architecture. *Sensors (Basel)* 21, 6936. doi:10.3390/s21206936
- Abitbol, E., Miere, A., Excoffier, J. B., Mehanna, C. J., Amoroso, F., Kerr, S., et al. (2022). Deep learning-based classification of retinal vascular diseases using ultra-widefield colour fundus photographs. *BMJ Open Ophthalmol.* 7, e000924. doi:10.1136/bmjophth-2021-000924
- Agrawal, R., Kulkarni, S., Walambe, R., and Kotecha, K. (2021). Assistive framework for automatic detection of all the zones in retinopathy of prematurity using deep learning. *J. Digit. Imaging* 34, 932–947. doi:10.1007/s10278-021-00477-8
- Akbar, S., Akram, M. U., Sharif, M., Tariq, A., and Yasin, U. U. (2018). Arteriovenous ratio and papilledema based hybrid decision support system for detection and grading of hypertensive retinopathy. *Comput. Methods Programs Biomed.* 154, 123–141. doi:10.1016/j.cmpb.2017.11.014
- Al-Aswad, L. A., Ramachandran, R., Schuman, J. S., Medeiros, F., and Eydelman, M. B. Collaborative Community for Ophthalmic Imaging Executive Committee and Glaucoma Workgroup (2022). Artificial intelligence for glaucoma: Creating and implementing artificial intelligence for disease detection and progression. *Ophthalmol. Glaucoma* 5, e16–e25. doi:10.1016/j.ogla.2022.02.010
- Altintas, A. G. K., and Ilhan, C. (2023). Effects of the epiretinal membrane on the outcomes of intravitreal dexamethasone implantation for macular edema secondary to branch retinal vein occlusion. *Arq. Bras. Oftalmol.* 86, 13–19. doi:10.5935/0004-2749.20230011
- Anitha, J., Vijila, C. K., Selvakumar, A. I., Indumathy, A., and Jude Hemanth, D. (2012). Automated multi-level pathology identification techniques for abnormal retinal images using artificial neural networks. *Br. J. Ophthalmol.* 96, 220–223. doi:10.1136/bjophthalmol-2011-300032
- Aronson, J. K. (2022). Artificial intelligence in pharmacovigilance: An introduction to terms, concepts, applications, and limitations. *Drug Saf.* 45, 407–418. doi:10.1007/s40264-022-01156-5
- Arsalan, M., Haider, A., Choi, J., and Park, K. R. (2021). Diabetic and hypertensive retinopathy screening in fundus images using artificially intelligent shallow architectures. *J. Pers. Med.* 12, 7. doi:10.3390/jpm12010007
- Arsalan, M., Owais, M., Mahmood, T., Cho, S. W., and Park, K. R. (2019). Aiding the diagnosis of diabetic and hypertensive retinopathy using artificial intelligence-based semantic segmentation. *J. Clin. Med.* 8, 1446. doi:10.3390/jcm8091446
- Badawi, S. A., Fraz, M. M., Shehzad, M., Mahmood, I., Javed, S., Mosalam, E., et al. (2022). Detection and grading of hypertensive retinopathy using vessels tortuosity and arteriovenous ratio. *J. Digit. Imaging* 35, 281–301. doi:10.1007/s10278-021-00545-z
- Bai, A., Carty, C., and Dai, S. (2022). Performance of deep-learning artificial intelligence algorithms in detecting retinopathy of prematurity: A systematic review. *Saudi J. Ophthalmol.* 36, 296–307. doi:10.4103/sjopt.sjopt_219_21
- Barrero-Castillero, A., Corwin, B. K., Vanderveen, D. K., and Wang, J. C. (2020). Workforce shortage for retinopathy of prematurity care and emerging role of telehealth and artificial intelligence. *Pediatr. Clin. North Am.* 67, 725–733. doi:10.1016/j.pcl.2020.04.012
- Betzler, B. K., Rim, T. H., Sabanayagam, C., and Cheng, C. Y. (2022). Artificial intelligence in predicting systemic parameters and diseases from ophthalmic imaging. *Front. Digit. Health* 4, 889445. doi:10.3389/fdgh.2022.889445
- Brown, J. M., Campbell, J. P., Beers, A., Chang, K., Ostmo, S., Chan, R. V. P., et al. (2018). Automated diagnosis of plus disease in retinopathy of prematurity using deep convolutional neural networks. *JAMA Ophthalmol.* 136, 803–810. doi:10.1001/jamaophthalmol.2018.1934
- Campbell, J. P., Chiang, M. F., Chen, J. S., Moshfeghi, D. M., Nudelman, E., Ruambivonsuk, P., et al. (2022). Artificial intelligence for retinopathy of prematurity: Validation of a vascular severity scale against international expert diagnosis. *Ophthalmology* 129, e69–e76. doi:10.1016/j.ophtha.2022.02.008
- Cao, X., Sanchez, J. C., Patel, T. P., Yang, Z., Guo, C., Malik, D., et al. (2023). Aflibercept more effectively weans patients with neovascular age-related macular degeneration off therapy compared with bevacizumab. *J. Clin. Invest.* 133, e159125. doi:10.1172/JCI159125
- Chen, J. S., Coyner, A. S., Ostmo, S., Sonmez, K., Bajimaya, S., Pradhan, E., et al. (2021a). Deep learning for the diagnosis of stage in retinopathy of prematurity: Accuracy and generalizability across populations and cameras. *Ophthalmol. Retina* 5, 1027–1035. doi:10.1016/j.oret.2020.12.013
- Chen, Q., Yu, W. H., Lin, S., Liu, B. S., Wang, Y., Wei, Q. J., et al. (2021b). Artificial intelligence can assist with diagnosing retinal vein occlusion. *Int. J. Ophthalmol.* 14, 1895–1902. doi:10.18240/ijo.2021.12.13
- Cheung, C. Y., Biousse, V., Keane, P. A., Schiffrin, E. L., and Wong, T. Y. (2022). Hypertensive eye disease. *Nat. Rev. Dis. Prim.* 8, 14. doi:10.1038/s41572-022-00342-0
- Chou, Y. B., Hsu, C. H., Chen, W. S., Chen, S. J., Hwang, D. K., Huang, Y. M., et al. (2021). Deep learning and ensemble stacking technique for differentiating polypoidal choroidal vasculopathy from neovascular age-related macular degeneration. *Sci. Rep.* 11, 7130. doi:10.1038/s41598-021-86526-2
- Coan, L. J., Williams, B. M., Krishna Adithya, V., Upadhyaya, S., Alkafri, A., Czanner, S., et al. (2023). Automatic detection of glaucoma via fundus imaging and artificial intelligence: A review. *Surv. Ophthalmol.* 68, 17–41. doi:10.1016/j.survophthal.2022.08.005
- Del Pinto, R., Mule, G., Vadala, M., Carollo, C., Cottone, S., Agabiti Rosei, C., et al. (2022). Arterial hypertension and the hidden disease of the eye: Diagnostic tools and therapeutic strategies. *Nutrients* 14, 2200. doi:10.3390/nu14112200
- Deo, R. C. (2015). Machine learning in medicine. *Circulation* 132, 1920–1930. doi:10.1161/CIRCULATIONAHA.115.001593
- Di Marco, E., Aiello, F., Lombardo, M., Di Marino, M., Missiroli, F., Mancino, R., et al. (2022). A literature review of hypertensive retinopathy: Systemic correlations and new technologies. *Eur. Rev. Med. Pharmacol. Sci.* 26, 6424–6443. doi:10.26355/eurrev_202209_29742
- Dong, L., He, W., Zhang, R., Ge, Z., Wang, Y. X., Zhou, J., et al. (2022). Artificial intelligence for screening of multiple retinal and optic nerve diseases. *JAMA Netw. Open* 5, e229960. doi:10.1001/jamanetworkopen.2022.9960
- Dziedzic, J., Zaleska-Zmijewska, A., Szaflik, J. P., and Cudnoch-Jedrzejewska, A. (2022). Impact of arterial hypertension on the eye: A review of the pathogenesis, diagnostic methods, and treatment of hypertensive retinopathy. *Med. Sci. Monit.* 28, e935135. doi:10.12659/MSM.935135
- Eilts, S. K., Pfeil, J. M., Poschkamp, B., Krohne, T. U., Eter, N., Barth, T., et al. (2023). Assessment of retinopathy of prematurity regression and reactivation using an artificial intelligence-based vascular severity score. *JAMA Netw. Open* 6, e2251512. doi:10.1001/jamanetworkopen.2022.51512
- Elgafi, M., Sharafelddeen, A., Elnakib, A., Elgarayhi, A., Alghamdi, N. S., Sallah, M., et al. (2022). Detection of diabetic retinopathy using extracted 3D features from OCT images. *Sensors (Basel)* 22, 7833. doi:10.3390/s22207833
- Fabre, M., Mateo, L., Lamaa, D., Baillif, S., Pages, G., Demange, L., et al. (2022). Recent advances in age-related macular degeneration therapies. *Molecules* 27, 5089. doi:10.3390/molecules27165089
- Galante, N., Cotroneo, R., Furci, D., Lodetti, G., and Casali, M. B. (2023). Applications of artificial intelligence in forensic sciences: Current potential benefits, limitations and perspectives. *Int. J. Leg. Med.* 137, 445–458. doi:10.1007/s00414-022-02928-5
- Gale, R. P., Finger, R. P., Eldem, B., Aslam, T., Barratt, J., Daien, V., et al. (2023). The management of neovascular age-related macular degeneration: A systematic literature review of patient-reported outcomes, patient mental health and caregiver burden. *Acta Ophthalmol.* 101, e26–e42. doi:10.1111/aos.15201
- Galindo-Camacho, R. M., Blanco-Llamero, C., Da Ana, R., Fuertes, M. A., Senorans, F. J., Silva, A. M., et al. (2022). Therapeutic approaches for age-related macular degeneration. *Int. J. Mol. Sci.* 23, 11769. doi:10.3390/ijms231911769
- Ganjanesh, A., Zhang, J., Chew, E. Y., Ding, Y., Huang, H., and Chen, W. (2022). LONG-net: Temporal correlation structure guided deep learning model to predict longitudinal age-related macular degeneration severity. *PNAS Nexus* 1, pgab003. doi:10.1093/pnasnexus/pgab003
- Gensure, R. H., Chiang, M. F., and Campbell, J. P. (2020). Artificial intelligence for retinopathy of prematurity. *Curr. Opin. Ophthalmol.* 31, 312–317. doi:10.1097/ICU.0000000000000680
- Ghanchi, F., Bourne, R., Downes, S. M., Gale, R., Rennie, C., Tapply, I., et al. (2022). An update on long-acting therapies in chronic sight-threatening eye diseases of the posterior segment: AMD, DMO, RVO, uveitis and glaucoma. *Eye (Lond)* 36, 1154–1167. doi:10.1038/s41433-021-01766-w
- Grauslund, J. (2022). Diabetic retinopathy screening in the emerging era of artificial intelligence. *Diabetologia* 65, 1415–1423. doi:10.1007/s00125-022-05727-0
- Gutierrez, L., Lim, J. S., Foo, L. L., Ng, W. Y., Yip, M., Lim, G. Y. S., et al. (2022). Application of artificial intelligence in cataract management: Current and future directions. *Eye Vis. (Lond)* 9, 3. doi:10.1186/s40662-021-00273-z

- Hamet, P., and Tremblay, J. (2017). Artificial intelligence in medicine. *Metabolism* 69S, S36–S40. doi:10.1016/j.metabol.2017.01.011
- Han, J., Choi, S., Park, J. I., Hwang, J. S., Han, J. M., Lee, H. J., et al. (2022). Classifying neovascular age-related macular degeneration with a deep convolutional neural network based on optical coherence tomography images. *Sci. Rep.* 12, 2232. doi:10.1038/s41598-022-05903-7
- Han, Y., Li, W., Liu, M., Wu, Z., Zhang, F., Liu, X., et al. (2021). Application of an anomaly detection model to screen for ocular diseases using color retinal fundus images: Design and evaluation study. *J. Med. Internet Res.* 23, e27822. doi:10.2196/27822
- Han, Z., Yang, B., Deng, S., Li, Z., and Tong, Z. (2023). Category weighted network and relation weighted label for diabetic retinopathy screening. *Comput. Biol. Med.* 152, 106408. doi:10.1016/j.combiomed.2022.106408
- Hashimoto, D. A., Witkowski, E., Gao, L., Meireles, O., and Rosman, G. (2020). Artificial intelligence in anesthesiology: Current techniques, clinical applications, and limitations. *Anesthesiology* 132, 379–394. doi:10.1097/ALN.0000000000002960
- Hassan, D., Gill, H. M., Happe, M., Bhatwadekar, A. D., Hajrasouliha, A. R., and Janga, S. C. (2022). Combining transfer learning with retinal lesion features for accurate detection of diabetic retinopathy. *Front. Med. (Lausanne)* 9, 1050436. doi:10.3389/fmed.2022.1050436
- He, T., Zhou, Q., and Zou, Y. (2022). Automatic detection of age-related macular degeneration based on deep learning and local outlier factor algorithm. *Diagn. (Basel)* 12, 532. doi:10.3390/diagnostics12020532
- Heo, T. Y., Kim, K. M., Min, H. K., Gu, S. M., Kim, J. H., Yun, J., et al. (2020). Development of a deep-learning-based artificial intelligence tool for differential diagnosis between dry and neovascular age-related macular degeneration. *Diagn. (Basel)* 10, 261. doi:10.3390/diagnostics10050261
- Holomcik, D., Seeböck, P., Gerendas, B. S., Mylonas, G., Najeeb, B. H., Schmidt-Erfurth, U., et al. (2022). Segmentation of macular neovascularization and leakage in fluorescein angiography images in neovascular age-related macular degeneration using deep learning. *Eye (Lond)*. doi:10.1038/s41433-022-02156-6
- Huang, J., Yeung, A. M., Armstrong, D. G., Battarbee, A. N., Cuadros, J., Espinoza, J. C., et al. (2023). Artificial intelligence for predicting and diagnosing complications of diabetes. *J. Diabetes Sci. Technol.* 17, 224–238. doi:10.1177/19322968221124583
- Huang, Y. P., Basanta, H., Kang, E. Y., Chen, K. J., Hwang, Y. S., Lai, C. C., et al. (2021). Automated detection of early-stage ROP using a deep convolutional neural network. *Br. J. Ophthalmol.* 105, 1099–1103. doi:10.1136/bjophthalmol-2020-316526
- Irgat, S. G., and Ozcara, F. (2023). Afibercept treatment for macular edema with and without serous retinal detachment due to branch retinal vein occlusion. *Arq. Bras. Oftalmol.* 86, 60–67. doi:10.5935/0004-2749.20230019
- Islam, M. R., Abdulrazak, L. F., Nahiduzzaman, M., Goni, M. O. F., Anower, M. S., Ahsan, M., et al. (2022). Applying supervised contrastive learning for the detection of diabetic retinopathy and its severity levels from fundus images. *Comput. Biol. Med.* 146, 105602. doi:10.1016/j.combiomed.2022.105602
- Ji, Y., Chen, N., Liu, S., Yan, Z., Qian, H., Zhu, S., et al. (2022a). Research progress of artificial intelligence image analysis in systemic disease-related ophthalmopathy. *Dis. Markers* 2022, 3406890. doi:10.1155/2022/3406890
- Ji, Y., Liu, S., Hong, X., Lu, Y., Wu, X., Li, K., et al. (2022b). Advances in artificial intelligence applications for ocular surface diseases diagnosis. *Front. Cell. Dev. Biol.* 10, 1107689. doi:10.3389/fcell.2022.1107689
- Kang, E. Y., Yeung, L., Lee, Y. L., Wu, C. H., Peng, S. Y., Chen, Y. P., et al. (2021). A multimodal imaging-based deep learning model for detecting treatment-requiring retinal vascular diseases: Model development and validation study. *JMIR Med. Inf.* 9, e28868. doi:10.2196/28868
- Katz, O., Presil, D., Cohen, L., Nachmani, R., Kirshner, N., Hoch, Y., et al. (2022). Evaluation of a new neural network classifier for diabetic retinopathy. *J. Diabetes Sci. Technol.* 16, 1401–1409. doi:10.1177/19322968211042665
- Klig, J. E. (2008). Ophthalmologic complications of systemic disease. *Emerg. Med. Clin. North Am.* 26, 217–231. doi:10.1016/j.emc.2007.10.003
- Lecun, Y., Bengio, Y., and Hinton, G. (2015). Deep learning. *Nature* 521, 436–444. doi:10.1038/nature14539
- Li, F., Wang, Y., Xu, T., Dong, L., Yan, L., Jiang, M., et al. (2022a). Deep learning-based automated detection for diabetic retinopathy and diabetic macular oedema in retinal fundus photographs. *Eye (Lond)* 36, 1433–1441. doi:10.1038/s41433-021-01552-8
- Li, X., Jiang, Y., Zhang, J., Li, M., Luo, H., and Yin, S. (2022b). Lesion-attention pyramid network for diabetic retinopathy grading. *Artif. Intell. Med.* 126, 102259. doi:10.1016/j.artmed.2022.102259
- Li, P., and Liu, J. (2022). Early diagnosis and quantitative analysis of stages in retinopathy of prematurity based on deep convolutional neural networks. *Transl. Vis. Sci. Technol.* 11, 17. doi:10.1167/tvst.11.5.17
- Libera, S., Wichrowska, M., and Kociński, J. (2022). Aflibercept versus faricimab in the treatment of neovascular age-related macular degeneration and diabetic macular edema: A review. *Int. J. Mol. Sci.* 23, 9424. doi:10.3390/ijms23169424
- Lim, J. I., Regillo, C. D., Sadda, S. R., Ipp, E., Bhaskaranand, M., Ramachandra, C., et al. (2023). Artificial intelligence detection of diabetic retinopathy: Subgroup comparison of the EyeArt system with ophthalmologists' dilated examinations. *Ophthalmol. Sci.* 3, 100228. doi:10.1016/j.xops.2022.100228
- Liu, Y., Li, J., Pan, J., Wang, Y., Mao, G., and Jiang, Z. (2021). Morphological changes in and quantitative analysis of macular retinal microvasculature by optical coherence tomography angiography in hypertensive retinopathy. *Hypertens. Res.* 44, 325–336. doi:10.1038/s41440-020-00583-0
- Lombardo, M., Serrao, S., and Lombardo, G. (2022). Challenges in age-related macular degeneration: From risk factors to novel diagnostics and prevention strategies. *Front. Med. (Lausanne)* 9, 887104. doi:10.3389/fmed.2022.887104
- Mao, J., Luo, Y., Liu, L., Lao, J., Shao, Y., Zhang, M., et al. (2020). Automated diagnosis and quantitative analysis of plus disease in retinopathy of prematurity based on deep convolutional neural networks. *Acta Ophthalmol.* 98, e339–e345. doi:10.1111/aos.14264
- Mehra, A. A., Softing, A., Guner, M. K., Hodge, D. O., and Barkmeier, A. J. (2022). Diabetic retinopathy telemedicine outcomes with artificial intelligence-based image analysis, reflex dilation, and image overread. *Am. J. Ophthalmol.* 244, 125–132. doi:10.1016/j.ajo.2022.08.008
- Miao, J., Yu, J., Zou, W., Su, N., Peng, Z., Wu, X., et al. (2022). Deep learning models for segmenting non-perfusion area of color fundus photographs in patients with branch retinal vein occlusion. *Front. Med. (Lausanne)* 9, 794045. doi:10.3389/fmed.2022.794045
- Morya, A. K., Janti, S. S., Sisodiya, P., Tejaswini, A., Prasad, R., Mali, K. R., et al. (2022). Everything real about unreal artificial intelligence in diabetic retinopathy and in ocular pathologies. *World J. Diabetes* 13, 822–834. doi:10.4239/wjdv13.i10.822
- Nagasato, D., Tabuchi, H., Masumoto, H., Enno, H., Ishitobi, N., Kameoka, M., et al. (2019a). Automated detection of a nonperfusion area caused by retinal vein occlusion in optical coherence tomography angiography images using deep learning. *PLoS One* 14, e0223965. doi:10.1371/journal.pone.0223965
- Nagasato, D., Tabuchi, H., Ohsugi, H., Masumoto, H., Enno, H., Ishitobi, N., et al. (2018). Deep neural network-based method for detecting central retinal vein occlusion using ultrawide-field fundus ophthalmoscopy. *J. Ophthalmol.* 2018, 1875431. doi:10.1155/2018/1875431
- Nagasato, D., Tabuchi, H., Ohsugi, H., Masumoto, H., Enno, H., Ishitobi, N., et al. (2019b). Deep-learning classifier with ultrawide-field fundus ophthalmoscopy for detecting branch retinal vein occlusion. *Int. J. Ophthalmol.* 12, 94–99. doi:10.18240/ijo.2019.01.15
- Nisha, K. L., Ganapathy, S., Puthumangalathu Savithri, S., Idaguri, M., Mohanachandran, P., Vinekar, A., et al. (2023). A novel method to improve inter-clinician variation in the diagnosis of retinopathy of prematurity using machine learning. *Curr. Eye Res.* 48, 60–69. doi:10.1080/02713683.2022.2139847
- Orskov, M., Vorum, H., Bjerregaard Larsen, T., Vestergaard, N., Lip, G. Y. H., Bek, T., et al. (2022). A review of risk factors for retinal vein occlusions. *Expert Rev. Cardiovasc Ther.* 20, 761–772. doi:10.1080/14779072.2022.2112667
- Padhy, S., and Kumar, V. (2018). Dramatic response to intravitreal Bevacizumab in hypertensive retinopathy. *Indian J. Ophthalmol.* 66, 1494–1495. doi:10.4103/ijo.IJO_214_18
- Patil, N. S., Mihalache, A., Dhoot, A. S., Popovic, M. M., Muni, R. H., and Kertes, P. J. (2023). The impact of residual retinal fluid following intravitreal anti-vascular endothelial growth factor therapy for diabetic macular edema and macular edema secondary to retinal vein occlusion: A systematic review. *Ophthalmic Surg. Lasers Imaging Retina* 54, 50–58. doi:10.3928/23258160-20221122-01
- Peng, Y., Chen, Z., Zhu, W., Shi, F., Wang, M., Zhou, Y., et al. (2022). ADS-net: Attention-awareness and deep supervision based network for automatic detection of retinopathy of prematurity. *Biomed. Opt. Express* 13, 4087–4101. doi:10.1364/BOE.461411
- Peng, Y., Zhu, W., Chen, Z., Wang, M., Geng, L., Yu, K., et al. (2021). Automatic staging for retinopathy of prematurity with deep feature fusion and ordinal classification strategy. *IEEE Trans. Med. Imaging* 40, 1750–1762. doi:10.1109/TMI.2021.3065753
- Pur, D. R., Krance, S., Pucchio, A., Bassi, A., Miranda, R. N., and Felfeli, T. (2023). Emerging applications of bioinformatics and artificial intelligence in the analysis of biofluid markers involved in retinal occlusive diseases: A systematic review. *Graefes Arch. Clin. Exp. Ophthalmol.* 261, 317–336. doi:10.1007/s00417-022-05769-5
- Ramanathan, A., Athikar, S. E., and Lam, G. C. (2022). Artificial intelligence for the diagnosis of retinopathy of prematurity: A systematic review of current algorithms. *Eye (Lond)*. doi:10.1038/s41433-022-02366-y
- Ren, X., Feng, W., Ran, R., Gao, Y., Lin, Y., Fu, X., et al. (2022). Artificial intelligence to distinguish retinal vein occlusion patients using color fundus photographs. *Eye (Lond)*. doi:10.1038/s41433-022-02239-4
- Sabri, K., Ellis, A. L., Lee, E. Y., Dutta, S., and Vinekar, A. (2022). Retinopathy of prematurity: A global perspective and recent developments. *Pediatrics* 150, e2021053924. doi:10.1542/peds.2021-053924
- Scruggs, B. A., Chan, R. V. P., Kalpathy-Cramer, J., Chiang, M. F., and Campbell, J. P. (2020). Artificial intelligence in retinopathy of prematurity diagnosis. *Transl. Vis. Sci. Technol.* 9, 5. doi:10.1167/tvst.9.2.5
- Sheng, B., Chen, X., Li, T., Ma, T., Yang, Y., Bi, L., et al. (2022). An overview of artificial intelligence in diabetic retinopathy and other ocular diseases. *Front. Public Health* 10, 971943. doi:10.3389/fpubh.2022.971943
- Song, X., Xu, Q., Li, H., Fan, Q., Zheng, Y., Zhang, Q., et al. (2022). Automatic quantification of retinal photoreceptor integrity to predict persistent disease activity in

neovascular age-related macular degeneration using deep learning. *Front. Neurosci.* 16, 952735. doi:10.3389/fnins.2022.952735

Sood, G., Samanta, R., Kumawat, D., Agrawal, A., and Singh, A. (2022). Clinical profile and retinal nerve fibre layer thickness of optic disc oedema patients at a tertiary care institute in North India. *Ther. Adv. Ophthalmol.* 14, 25158414211072634. doi:10.1177/25158414211072634

Tabuchi, H. (2022). Understanding required to consider AI applications to the field of ophthalmology. *Taiwan J. Ophthalmol.* 12, 123–129. doi:10.4103/tjo.tjo_8_22

Tak, N., Reddy, A. J., Martel, J., and Martel, J. B. (2021). Clinical wide-field retinal image deep learning classification of exudative and non-exudative age-related macular degeneration. *Cureus* 13, e17579. doi:10.7759/cureus.17579

Tang, Y., Cheng, Y., Wang, S., Wang, Y., Liu, P., and Wu, H. (2022). Review: The development of risk factors and cytokines in retinal vein occlusion. *Front. Med. (Lausanne)* 9, 910600. doi:10.3389/fmed.2022.910600

Tang, Z., Zhang, X., Yang, G., Zhang, G., Gong, Y., Zhao, K., et al. (2021). Automated segmentation of retinal nonperfusion area in fluorescein angiography in retinal vein occlusion using convolutional neural networks. *Med. Phys.* 48, 648–658. doi:10.1002/mp.14640

Tao, T., Xu, H., Ma, X., Cheng, Y., Shi, X., Sun, Y., et al. (2023). Analysis of systemic and serum risk factors in patients with age-related macular degeneration and polypoidal choroidal vasculopathy. *Ophthalmol. Ther.* 12, 1033–1044. doi:10.1007/s40123-023-00650-y

Terao, R., Fujino, R., and Ahmed, T. (2022). Risk factors and treatment strategy for retinal vascular occlusive diseases. *J. Clin. Med.* 11, 6340. doi:10.3390/jcm11216340

Thomas, C. J., Mirza, R. G., and Gill, M. K. (2021). Age-related macular degeneration. *Med. Clin. North Am.* 105, 473–491. doi:10.1016/j.mcna.2021.01.003

Ting, D. S. J., Foo, V. H., Yang, L. W. Y., Sia, J. T., Ang, M., Lin, H., et al. (2021). Artificial intelligence for anterior segment diseases: Emerging applications in ophthalmology. *Br. J. Ophthalmol.* 105, 158–168. doi:10.1136/bjophthalmol-2019-315651

Ting, D. S. W., Pasquale, L. R., Peng, L., Campbell, J. P., Lee, A. Y., Raman, R., et al. (2019). Artificial intelligence and deep learning in ophthalmology. *Br. J. Ophthalmol.* 103, 167–175. doi:10.1136/bjophthalmol-2018-313173

Tognetto, D., Giglio, R., Vinciguerra, A. L., Milan, S., Rejdak, R., Rejdak, M., et al. (2022). Artificial intelligence applications and cataract management: A systematic review. *Surv. Ophthalmol.* 67, 817–829. doi:10.1016/j.survophthal.2021.09.004

Tong, Y., Lu, W., Deng, Q. Q., Chen, C., and Shen, Y. (2020). Automated identification of retinopathy of prematurity by image-based deep learning. *Eye Vis. (Lond)* 7, 40. doi:10.1186/s40662-020-00206-2

Trovato Battagliola, E., Pacella, F., Malvasi, M., Scalinci, S. Z., Turchetti, P., Pacella, E., et al. (2022). Risk factors in central retinal vein occlusion: A multi-center case-control study conducted on the Italian population: Demographic, environmental, systemic, and ocular factors that increase the risk for major thrombotic events in the retinal venous system. *Eur. J. Ophthalmol.* 32, 2801–2809. doi:10.1177/11206721211064469

Tsukikawa, M., and Stacey, A. W. (2020). A review of hypertensive retinopathy and chorioretinopathy. *Clin. Optim. (Auckl)* 12, 67–73. doi:10.2147/OPTO.S183492

Wang, R., Zuo, G., Li, K., Li, W., Xuan, Z., Han, Y., et al. (2022). Systematic bibliometric and visualized analysis of research hotspots and trends on the application of artificial intelligence in diabetic retinopathy. *Front. Endocrinol. (Lausanne)* 13, 1036426. doi:10.3389/fendo.2022.1036426

Wawer Matos, P. A., Reimer, R. P., Rokohl, A. C., Caldeira, L., Heindl, L. M., and Grosse Hokamp, N. (2022). Artificial intelligence in ophthalmology - status quo and future perspectives. *Semin. Ophthalmol.*, 1–12. doi:10.1080/08820538.2022.2139625

Wong, T. Y., and Mitchell, P. (2004). Hypertensive retinopathy. *N. Engl. J. Med.* 351, 2310–2317. doi:10.1056/NEJMra032865

Wu, Q., Hu, Y., Mo, Z., Wu, R., Zhang, X., Yang, Y., et al. (2022). Development and validation of a deep learning model to predict the occurrence and severity of retinopathy of prematurity. *JAMA Netw. Open* 5, e2217447. doi:10.1001/jamanetworkopen.2022.17447

Xu, W., Yan, Z., Chen, N., Luo, Y., Ji, Y., Wang, M., et al. (2022). Development and application of an intelligent diagnosis system for retinal vein occlusion based on deep learning. *Dis. Markers* 2022, 4988256. doi:10.1155/2022/4988256

Yan, Q., Weeks, D. E., Xin, H., Swaroop, A., Chew, E. Y., Huang, H., et al. (2020). Deep-learning-based prediction of late age-related macular degeneration progression. *Nat. Mach. Intell.* 2, 141–150. doi:10.1038/s42256-020-0154-9

Yang, D., Ran, A. R., Nguyen, T. X., Lin, T. P. H., Chen, H., Lai, T. Y. Y., et al. (2023). Deep learning in optical coherence tomography angiography: Current progress, challenges, and future directions. *Diagn. (Basel)* 13, 326. doi:10.3390/diagnostics13020326

Yang, Z., Tan, T. E., Shao, Y., Wong, T. Y., and Li, X. (2022). Classification of diabetic retinopathy: Past, present and future. *Front. Endocrinol. (Lausanne)* 13, 1079217. doi:10.3389/fendo.2022.1079217

Yeh, T. C., Luo, A. C., Deng, Y. S., Lee, Y. H., Chen, S. J., Chang, P. H., et al. (2022). Prediction of treatment outcome in neovascular age-related macular degeneration using a novel convolutional neural network. *Sci. Rep.* 12, 5871. doi:10.1038/s41598-022-09642-7

Yin, S., Cui, Y., Jiao, W., and Zhao, B. (2022). Potential prognostic indicators for patients with retinal vein occlusion. *Front. Med. (Lausanne)* 9, 839082. doi:10.3389/fmed.2022.839082

Zhang, G., Sun, B., Chen, Z., Gao, Y., Zhang, Z., Li, K., et al. (2022a). Diabetic retinopathy grading by deep graph correlation network on retinal images without manual annotations. *Front. Med. (Lausanne)* 9, 872214. doi:10.3389/fmed.2022.872214

Zhang, G., Sun, B., Zhang, Z., Wu, S., Zhuo, G., Rong, H., et al. (2022b). Hypermixed convolutional neural network for retinal vein occlusion classification. *Dis. Markers* 2022, 1730501. doi:10.1155/2022/1730501

Zhang, W. F., Li, D. H., Wei, Q. J., Ding, D. Y., Meng, L. H., Wang, Y. L., et al. (2022c). The validation of deep learning-based grading model for diabetic retinopathy. *Front. Med. (Lausanne)* 9, 839088. doi:10.3389/fmed.2022.839088

Zhang, X., Li, F., Li, D., Wei, Q., Han, X., Zhang, B., et al. (2022d). Automated detection of severe diabetic retinopathy using deep learning method. *Graefes Arch. Clin. Exp. Ophthalmol.* 260, 849–856. doi:10.1007/s00417-021-05402-x

Zhang, X. T., Zhong, Y. F., Xue, Y. Q., Li, S. Q., Wang, B. Y., Zhang, G. Q., et al. (2022e). Clinical features of central retinal vein occlusion in young patients. *Ophthalmol. Ther.* 11, 1409–1422. doi:10.1007/s40123-022-00534-7

Zhang, Y., Gan, Y., Zeng, Y., Zhuang, X., Zhang, X., Ji, Y., et al. (2023). Incidence and multimodal imaging characteristics of macular neovascularisation subtypes in Chinese neovascular age-related macular degeneration patients. *Br. J. Ophthalmol.* 2022, 322392. doi:10.1136/bjo-2022-322392

Zhao, Y., Li, X., Li, S., Dong, M., Yu, H., Zhang, M., et al. (2022). Using machine learning techniques to develop risk prediction models for the risk of incident diabetic retinopathy among patients with type 2 diabetes mellitus: A cohort study. *Front. Endocrinol. (Lausanne)* 13, 876559. doi:10.3389/fendo.2022.876559



OPEN ACCESS

EDITED BY

Weihua Yang,
Jinan University, China

REVIEWED BY

Zhenping Xia,
Suzhou University of Science and
Technology, China
Weitong Hao,
Second Hospital of Tianjin Medical
University, China
Zhongpai Gao,
Ull America, United States

*CORRESPONDENCE

Yan Wang,
✉ wangyan7143@vip.sina.com,
✉ ophwangyan@tmu.edu.cn
Gang Luo,
✉ gang_luo@meei.harvard.edu

[†]These authors have contributed equally
to this work and share first authorship

RECEIVED 25 February 2023

ACCEPTED 04 April 2023

PUBLISHED 13 April 2023

CITATION

Cheng W, Li L, Luo G and Wang Y (2023),
Using a smartphone app in the
measurement of posture-related pupil
center shift on centration during corneal
refractive surgery.
Front. Cell Dev. Biol. 11:1174122.
doi: 10.3389/fcell.2023.1174122

COPYRIGHT

© 2023 Cheng, Li, Luo and Wang. This is
an open-access article distributed under
the terms of the [Creative Commons
Attribution License \(CC BY\)](https://creativecommons.org/licenses/by/4.0/). The use,
distribution or reproduction in other
forums is permitted, provided the original
author(s) and the copyright owner(s) are
credited and that the original publication
in this journal is cited, in accordance with
accepted academic practice. No use,
distribution or reproduction is permitted
which does not comply with these terms.

Using a smartphone app in the measurement of posture-related pupil center shift on centration during corneal refractive surgery

Wenbo Cheng^{1†}, Li Li^{2†}, Gang Luo^{3*} and Yan Wang^{4*}

¹Department of Ophthalmology, The First Affiliated Hospital of Xinjiang Medical University, Urumqi, Xinjiang, China, ²Department of Ophthalmology, Fujian Provincial Hospital South Branch, Fujian Provincial Hospital, Fuzhou, Fujian, China, ³Schepens Eye Research Institute, Massachusetts Eye and Ear, Harvard Medical School, Boston, MA, United States, ⁴Tianjin Eye Hospital, Tianjin Eye Institute, Tianjin Key Lab of Ophthalmology and Visual Science, Clinical College of Ophthalmology, Tianjin Medical University, Nankai University, Tianjin, China

Purpose: Pupil center is an important anchor point in corneal refractive surgery, which may affect by body position. This study investigated the feasibility of using a smartphone application in measurement of posture-related pupil center shifts.

Methods: Images of undilated eyes were captured for 25 participants (age: 18–38 years) at a distance of 40 cm in four body positions (seated, supine, right lateral, and left lateral) under controlled lighting conditions. During taking images, a smartphone application was used to guide positioning without head rotation and tilt. From the images, the location of the pupil center and pupil diameter with respect to the limbus boundary were measured.

Results: According to the data obtained by the smartphone application, pupil center was located slightly nasal and superior to the limbus center in the seated position, and it shifted more nasally and superiorly ($p < 0.001$, OD 0.54 ± 0.11 mm, OS 0.57 ± 0.14 mm) in the supine position. When body position switched between left and right lateral positions, the pupil centers of both eyes shifted along the direction of gravity ($p < 0.05$), and no significant shift occurred along the longitudinal axis. Moreover, pupil constriction was observed when the body position changed from seated to supine position ($p < 0.001$, OD 0.64 ± 0.57 mm, OS 0.63 ± 0.58 mm).

Conclusion: Posture-related pupil center shift may be larger than the error tolerance of centration in corneal refractive surgery, which might be difficult to measure by the existing instruments. An accessible application is necessary for evaluating the shift of pupil center and guiding centration during the surgery.

KEYWORDS

pupil, shift, centration, posture, cornea refractive surgery

Introduction

First postulated by Snellen in 1869, corneal refractive surgery has more recently become an alternative to dependence on contact lenses or spectacles for use in routine daily activities. Although there are several types of corneal refractive surgery, most involve laser vision correction (LVC), such as laser *in situ* keratomileusis (LASIK), laser epithelial keratomileusis (LASEK), femtosecond laser *in situ* keratomileusis (FS-LASIK), and small incision lenticule extraction

TABLE 1 Subject characteristics.

Characteristics	All subjects included in this study (%) (<i>n</i> = 25)
Sex	
Female	10 (40.0)
Male	15 (60.0)
Ethnicity	
Caucasian	7 (28.0)
Asian	17 (68.0)
African American	1 (4.0)

(SMILE). Regardless of the treatment, centration remains a critical step during refractive procedures. Decentration of ablation may be associated with a significant increase in higher-order aberrations (HOAs) (Bueeler et al., 2003), decreases in quality of vision and contrast sensitivity, diplopia (Yap and Kowal, 2001), and night vision disturbances (Mrochen et al., 2001). Thus, proper centration of the treatment is essential during corneal refractive procedures.

The pupil center is widely utilized to determine centration during several corneal refractive procedures, such as LASIK and FS-LASIK. However, the location of the pupil center may shift. Yang (Yang et al., 2002) measured the location of the pupil center under photopic, mesopic and pupil dilation conditions, noting consistent temporal shifts in this location relative to the geometric corneal center as the pupil dilated. Another study (Mathur et al., 2014) reported that luminance and accommodation influence pupil size, although only the luminance change significantly affected the location of the pupil center. Moreover, some evidence suggests that changes in body position also induce pupil center shifts. Using wavefront measurements, Liu (Liu et al., 2013) observed such shifts between the seated-dilated state and the supine-undilated state during laser ablation, suggesting that the pupil center shifts temporally and superiorly. However, it was unable to determine whether changes in pupil diameter or body position induced a shift in the pupil center.

Before corneal refractive surgery, necessary examinations need be done in the seated position to check the pupil center location relative to the corneal center for perfect centration during the surgery. However, the surgery must be applied in the supine position due to the technical limitation, which may cause decentration by position-related pupil center shifts. Position-related pupil center shifts are hard to be measured by existing instruments, so this study turned to AI technology.

Therefore, a smartphone application is designed for investigating the pupil center shifts associated with 4 different body positions in this preliminary study. Although lateral body positions are not relevant to refractive surgery, the position were included to help postulate whether the pupil center shift may be related to gravity.

Materials and methods

Participants

The present study was conducted between July 2018 and May 2019, approved by the institutional review boards of each institution

and conducted in accordance with the tenets of the Declaration of Helsinki. Informed consent was obtained from each participant following a detailed explanation of the nature and possible consequences of the study. Twenty-five individuals aged 18–38 years participated (Table 1). Inclusion criteria were as follows: 1) age \geq 18 years, 2) clear corneas with no signs of opacity, and 3) absence of other ocular conditions. Exclusion criteria were as follows: 1) any corneal and iris anomalies, such as keratoconus or iritis, and 2) use of any ophthalmic or systemic medications.

Measurement of pupil shifts in different body positions

Participants were asked to take four positions (seated, supine, right lateral, and left lateral), staring directly at the smartphone camera flash. A photo was captured including both eyes, using a smartphone application at a distance of 40 cm under the same illuminant condition. An apparatus was made to ensure that the distance and location were kept constant during image capture (Figure 1). Participants were instructed to hold the device, place their chin on the chinrest, and maintain contact between their forehead and the forehead bar during the experiment, even in lateral positions.

The smartphone application was designed for images taken to guide positioning and minimize head rotation and tilt. A pair of alignment boxes were plotted on the screen, the distance between them can be adjusted according to the pupil distance of each Participant (Figure 1). When taking images, eyes should be included in boxes with the eyelid margin parallel to horizontal borders. For good quality images, the limbus and pupil should be seen clearly, so that the boundaries can be marked without ambiguity.

Image analysis

Image J (Rawak Software, Inc., Germany) was used to mark the limbus and pupil rim, from which their centers were determined (Figure 2). Because that the limbus is a fixed biological landmark, the shifts in pupil center were calculated with respect to limbus center. We also measured pupil and limbus diameters in pixels, and then converted those measures to millimeters assuming the iris diameter is 11.8 mm for all eyes (Bergmanson and Martinez, 2017). The vector shift of the pupil center was calculated as the square root of the sum of the squares of the horizontal and vertical shifts.

Data analysis

Analysis was conducted using SPSS (version 23.0; IBM Corp., Chicago, IL, United States). The results are expressed as the mean \pm standard deviation (SD). The normality of all data distributions was confirmed using the Kolmogorov-Smirnov test (all $p > 0.05$) prior to further analyses. A two-tailed test was used to compare the magnitudes of the horizontal and vertical shifts of the pupil centers in all eyes. The paired-samples *t*-test was used to evaluate whether shifts were significantly different between right and left

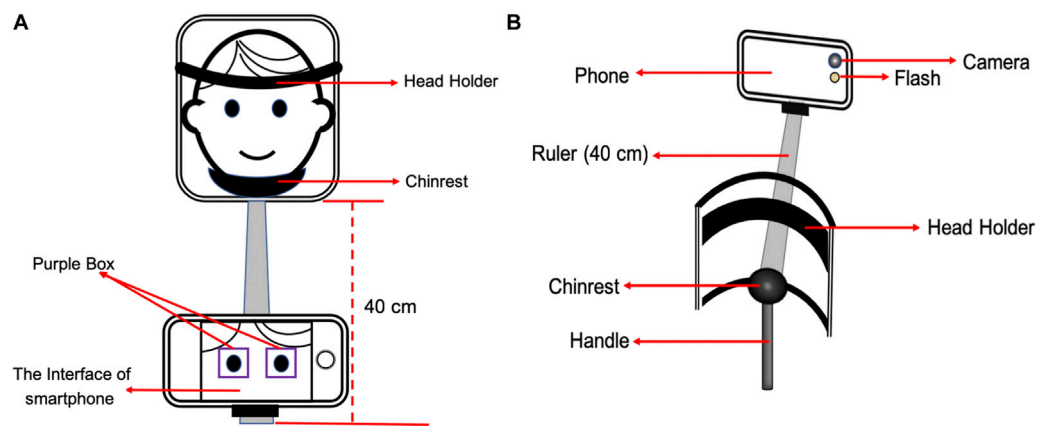


FIGURE 1

The device was made to fix the smartphone on the same location at 40 cm from the face. Subjects were asked to hold the device and focused on the camera flash during the whole process, putting the chin on the chinrest and sticking the forehead to the head holder (A, B). A pair of purple boxes were plotted on the screen to help guide positioning without head rotation (A).

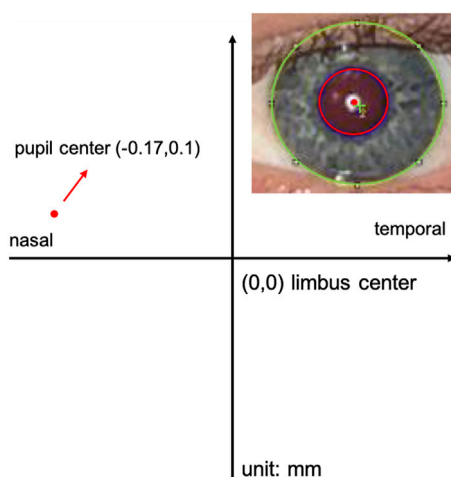


FIGURE 2

A good quality image is processed using Image J. The limbus and pupil of one eye can be accurately marked by Image J. Limbus center was considered as Origin (0, 0), and marked by green cross. Pupil center was marked by red dot.

eyes. Repeated-measures one-way analyses of variance (ANOVA) with Bonferroni correction were used to evaluate differences between pupil diameters at each position. The level of statistical significance was set at $p < 0.05$.

Results

Pupil center location in the seated and supine positions

The location of the pupil center in the seated position is shown in Figure 3. They are slightly superior and nasal relative to the limbus

centers. Considering the limbus center as the origin (0,0), the average location of the right pupil center was at $(0.14 \pm 0.09, 0.10 \pm 0.13 \text{ mm})$, and the location of the left pupil center was at $(-0.17 \pm 0.10, 0.06 \pm 0.10 \text{ mm})$ (Table 2). The off-center amplitude was almost the same for the two eyes ($p = 0.997$, $0.21 \pm 0.10 \text{ mm}$ for the right eye and $0.21 \pm 0.07 \text{ mm}$ for the left eye).

The pupil center was more nasally and superiorly when the position changed from seated to supine. On average, the right pupil center shifted to $(0.42 \pm 0.12, 0.32 \pm 0.12 \text{ mm})$, and the left pupil center shifted to $(-0.48 \pm 0.14, 0.27 \pm 0.14 \text{ mm})$. The off-center amplitude was almost the same for both eyes ($p = 0.335$, $0.54 \pm 0.11 \text{ mm}$ for the right eye and $0.57 \pm 0.14 \text{ mm}$ for the left eye).

In terms of the shift of each pupil, the right eyes shifted nasally by $0.28 \pm 0.14 \text{ mm}$ and superiorly by $0.21 \pm 0.17 \text{ mm}$ ($p < 0.001$), and the left eyes shifted similarly, nasally by $-0.31 \pm 0.15 \text{ mm}$ and superiorly by $0.21 \pm 0.15 \text{ mm}$ ($p < 0.001$), when body position changed from seated to supine. Overall, the shift amplitude was about the same for both eyes ($0.38 \pm 0.16 \text{ mm}$ for the right eye and $0.40 \pm 0.15 \text{ mm}$ for the left eye, $p = 0.579$).

Pupil center shifts in the lateral position

The results of pupil shift in lateral position are shown in Figure 4 and Table 2. When the body position changed from the seated to right lateral position, the X coordinates of both pupil centers shifted to the right side ($0.10 \pm 0.14 \text{ mm}$ for the right eyes, $p = 0.011$, and $0.26 \pm 0.18 \text{ mm}$ for the left eyes, $p < 0.001$). Similarly, When the body position changed from the seated to left lateral position, the X coordinates of both pupil centers significantly shifted to the left side ($0.21 \pm 0.15 \text{ mm}$ for right eyes, $p < 0.001$, and $0.13 \pm 0.09 \text{ mm}$ for the left eyes, $p < 0.001$). Interestingly, the nasal shift was larger than temporal shift for both left and right later positions ($p < 0.001$). In other words, the pupil in the upper position dropped down significantly more than the pupil in the lower position, when the bodies lied on one side. No significant shift was observed for the Y coordinates ($p > 0.101$).

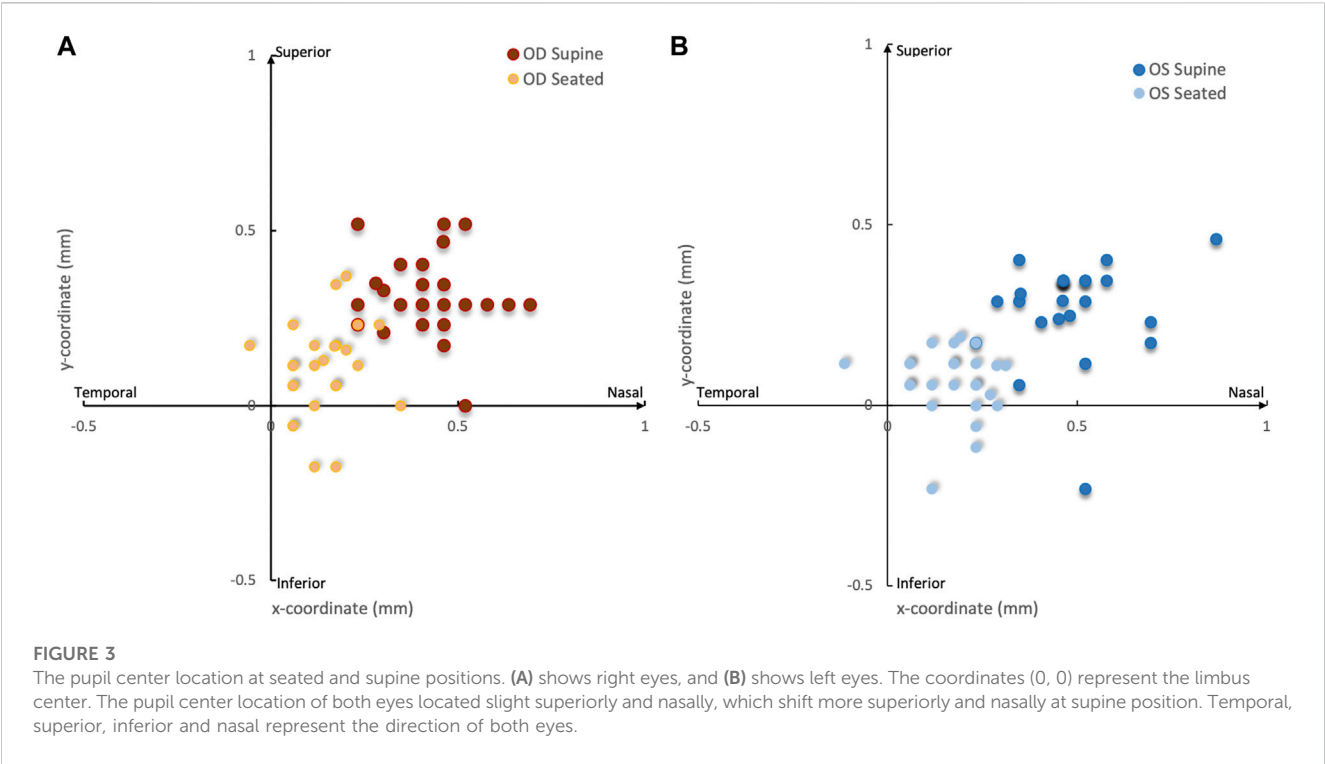


TABLE 2 The pupil center location at different positions.

Body position	Eye	X coordinate	Y coordinate	Amplitude
		Mean ± SD (mm)		
Seated	OD	0.14 ± 0.09	0.10 ± 0.13	0.21 ± 0.10
	OS	−0.17 ± 0.10	0.06 ± 0.10	0.21 ± 0.07
Supine	OD	0.42 ± 0.12	0.32 ± 0.12	0.54 ± 0.11
	OS	−0.48 ± 0.14	0.27 ± 0.14	0.57 ± 0.14
Supine-Seated	OD	0.28 ± 0.14 (<i>p</i> < 0.001)	0.21 ± 0.17(<i>p</i> < 0.001)	0.38 ± 0.16 (<i>p</i> < 0.001)
	OS	−0.31 ± 0.15(<i>p</i> < 0.001)	0.21 ± 0.15(<i>p</i> < 0.001)	0.40 ± 0.15 (<i>p</i> < 0.001)
Right lateral-seated	OD	−0.10 ± 0.14 (<i>p</i> = 0.011)	0.03 ± 0.15 (<i>p</i> = 0.373)	0.19 ± 0.13 (<i>p</i> < 0.001)
	OS	−0.26 ± 0.18 (<i>p</i> < 0.001)	0.02 ± 0.13 (<i>p</i> = 0.727)	0.31 ± 0.14 (<i>p</i> < 0.001)
Left lateral-seated	OD	0.21 ± 0.15 (<i>p</i> < 0.001)	0.06 ± 0.21 (<i>p</i> = 0.101)	0.28 ± 0.18 (<i>p</i> < 0.001)
	OS	0.13 ± 0.09 (<i>p</i> = 0.001)	0.04 ± 0.16 (<i>p</i> = 0.294)	0.21 ± 0.10 (<i>p</i> < 0.001)

OD, right eyes; OS, left eyes. Supine-seated position, shifts of pupil center from seated to supine position; right lateral-seated position, shifts of pupil center from seated to right lateral position; left lateral-seated position, shifts of pupil center from seated to left lateral position.

Changes in pupil diameter in different positions

Interestingly, the pupil diameter in supine position was significantly than all the other positions (Figure 5). For instance, the pupil constricted by 0.64 ± 0.57 mm in the right eyes and by 0.63 ± 0.58 mm in the left eyes ($p < 0.001$) when the body position changed from seated to supine. There were no significant differences observed between the seated and right/left lateral positions ($p > 0.05$).

Discussion

This study aimed to investigate the feasibility of using a smartphone application in measurement of posture-related pupil center location and pupil diameter. According to the data obtained by the application, the pupil center was located slightly nasally and superiorly with respect to the limbus center when participants were in the seated position (Liu et al., 2013). Interestingly, the pupil center shifted more nasally and

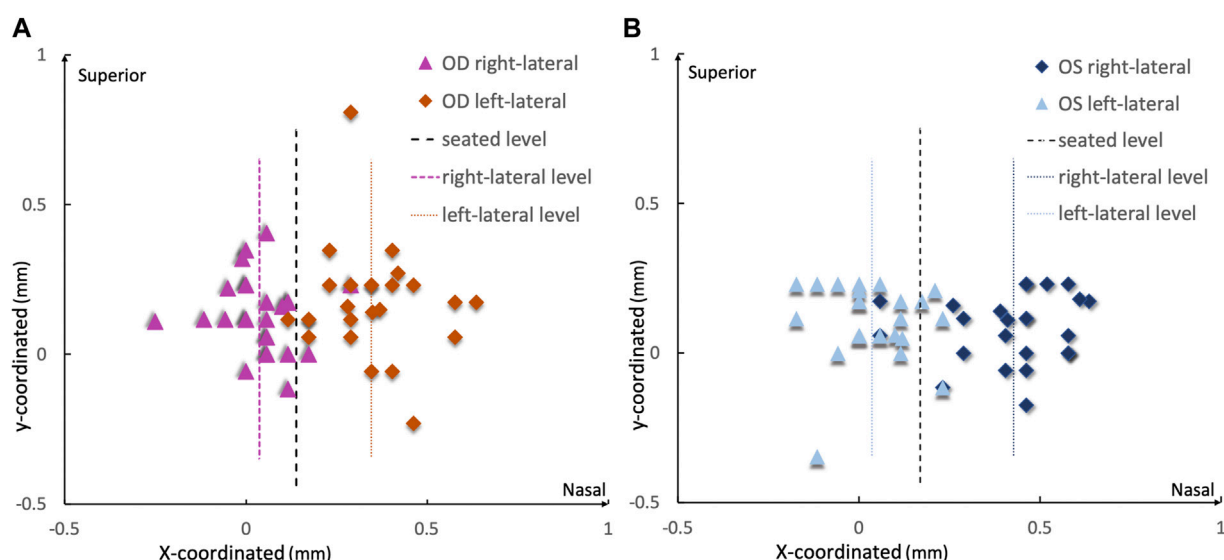


FIGURE 4

The pupil center shift at lateral position [(A) for right eyes and (B) for left eyes]. The coordinates (0, 0) represent the limbus center. When changed from seated to right lateral, pupil centers of both eyes shift to the right, which means nasal for left eyes and temporal for right eyes. Similarly, when switched from seated to left lateral, pupil centers of both eyes shift to the left, which means nasal for right eyes and temporal for left eyes. The dotted lines represent the average shifts at each position.

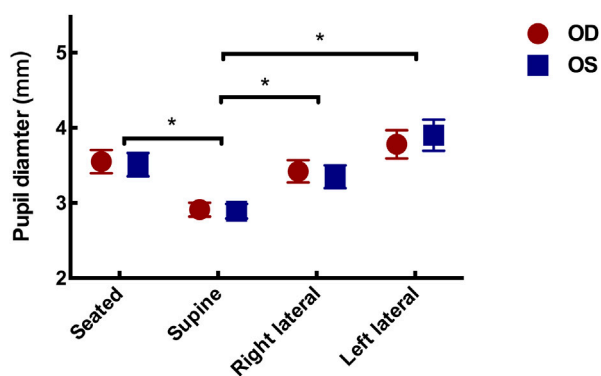


FIGURE 5

Pupil diameter change in different positions. The horizontal pupil diameter became constricting when the position changed from seated to supine ($p = 0.09$ for right eye, and 0.08 for left eye).

superiorly when participants were in the supine position, which is the body position of patients in corneal refractive surgery. To investigate what might cause the shift, we also measured the pupil center location in lateral body positions. The pupil center shift due to different changes in the body position suggests that gravity might play a role—the pupils in both eyes shift down if one sits up (from supine position), shift to left in left lateral position, and shift right in right lateral position. It has been shown that gravity can influence vertical eye position and movements as a whole (Pierrot-Deseilligny, 2009), but we are not aware of any previous work showing gravity's impact on sub-structures inside the eyes. It is even more mysterious that the gravity seemed to affect two eyes

differently—it pulls the two pupils in temporal direction (i.e., in opposite direction) when one sits up in addition to pulling them in inferior direction, and it pulls the pupils nasally more than temporally in lateral body positions.

Moreover, it was also found that the pupil constricted when the body position changed from seated or lateral to supine. A previous study (Yang et al., 2002) showed that pupil size change may be associated with pupil center shift—when pupil diameter changed from 7.58 mm (dilated condition) to 4.06 mm (photopic condition), the pupil center shifted inferio-nasally by approximately 0.183 mm with respect to the limbus center. In our study, the pupil constriction due to body position change was much smaller than that in Yang's study (Yang et al., 2002) only from 3.5 to 2.9 mm. However, but the pupil center shifted more (about 0.4 mm) and in superior-nasal direction rather than inferio-nasal direction (Figure 3). The difference suggests that the mechanism behind the shift may be different. In other words, the pupil center shift observed in this study was associated with body position, not due to pupil size change.

Our findings may have implications to corneal refractive surgery, in which centration of the treatment zone is key to optimizing visual outcomes, and the pupil center is always used to determine centration or as an important reference point. Since the location of the pupil center may be variable depending on body position, it is a question whether the centration in treatment should be based on upright or supine position. Previous studies (Porter et al., 2006) have reported that decentration during LASIK procedures increases the risk of HOAs postoperatively, which cannot be well explained by an inconsistency between preoperative aberration measurements over a dilated pupil and surgical correction over an undilated pupil. A study by Liu et al. (2015) found that the postoperative refractive outcomes would decrease if the deviation between corneal vertex and lenticule

center was more than 0.3 mm. Because the deviation due to body position change may reach 0.4 mm, as we found in this study, we speculate that the pupil center shift induced by changes in body position may contribute to the increased risk of postoperative HOAs. Further studies are warranted to confirm if body position should be taken into consideration when determining the treatment center.

Interestingly, the pupil diameter became smaller in the supine position than in the other body positions under similar illumination conditions. Because the images were captured under the same photopic conditions with the room lights on and the phone camera fixed at the same location, changes in pupil diameter were unlikely to have been influenced by changes in illumination. Non-luminance-mediated (Joshi et al., 2016) changes in pupil diameter have been associated with some neuronal activities, possibly because the supine position evokes pupillary constriction in both eyes. However, there was no significant difference in pupil diameter in lateral positions. Further studies are required to determine the relationship between pupil diameter and body position.

Limitations

The present study possesses some limitations of note. The pupil location and pupil diameter were normalized by each participant's iris diameter, rather than measured directly. To help readers better understand the level of pupil shift, the iris diameter for all eyes was approximated to 12 mm, and the pupil shift was scaled linearly using the iris diameter as a reference. Such an approximation may cause 4% standard deviation in the pupil shift estimation due to the variability in iris diameter (11.8 ± 0.5 mm) (Hashemi et al., 2015). To improve accuracy, future studies should measure individual's iris size if it is used as a reference. Another limitation is that the participants fell within a narrow age range (18–38 years). Therefore, we could not investigate the effect of age with a small sample in this preliminary study. Adolescents and older adults should be included in future studies.

Conclusion

Our findings demonstrated that the smartphone application is feasible for evaluating the posture-related shift of pupil center and guiding centration during the surgery. According to the data, the pupil center shifted nasally and superiorly when the body position changed from seated to supine. Non-luminance-mediated pupillary constriction also occurred at the same time. Posture-related pupil center shift may be larger than the error tolerance of centration in corneal refractive surgery, which may affect postoperative visual quality following corneal refractive surgery or any treatment using the pupil center as a reference. Further studies need to confirm if the

shifts in pupil center location that may occur with changes in body position should be taken into consideration.

Data availability statement

The raw data supporting the conclusion of this article will be made available by the authors, without undue reservation.

Ethics statement

The studies involving human participants were reviewed and approved by Schepens Eye Research Institute. Written informed consent for participation was not required for this study in accordance with the national legislation and the institutional requirements.

Author contributions

Concept and design (CD), data acquisition (DA), data analysis/interpretation (DI), drafting manuscript (DM), statistical analysis (SA), critical revision (CR) of manuscript, supervision (SV). WC: DA, DI, DM, SA; LL: DA, DI, DM, SA; GL: CD, CR, SV; YW: CD, CR, SV. WC and LL contributed equally to this work. The authors read and approved the final manuscript.

Acknowledgments

We would like to thank the participants for their time and effort in making this study possible.

Conflict of interest

The authors declare that the research was conducted in the absence of any commercial or financial relationships that could be construed as a potential conflict of interest.

The reviewer WH declared a shared parent affiliation, with the author YW to the handling editor at the time of the review.

Publisher's note

All claims expressed in this article are solely those of the authors and do not necessarily represent those of their affiliated organizations, or those of the publisher, the editors and the reviewers. Any product that may be evaluated in this article, or claim that may be made by its manufacturer, is not guaranteed or endorsed by the publisher.

References

- Bergmanson, J. P., and Martinez, J. G. (2017). Size does matter: What is the corneo-limbal diameter? *Clin. Exp. optometry* 100, 522–528. doi:10.1111/cxo.12583
- Bueeler, M., Mrochen, M., and Seiler, T. (2003). Maximum permissible lateral decentration in aberration-sensing and wavefront-guided corneal ablation. *J. cataract Refract. Surg.* 29, 257–263. doi:10.1016/s0886-3350(02)01638-3

- Hashemi, H., Khabazkhoob, M., Emamian, M. H., Shariati, M., Yekta, A., and Fotouhi, A. (2015). White-to-white corneal diameter distribution in an adult population. *J. Curr. Ophthalmol.* 27, 21–24. doi:10.1016/j.joco.2015.09.001
- Joshi, S., Li, Y., Kalwani, R. M., and Gold, J. I. (2016). Relationships between pupil diameter and neuronal activity in the locus coeruleus, colliculi, and cingulate cortex. *Neuron* 89, 221–234. doi:10.1016/j.neuron.2015.11.028
- Liu, M., Sun, Y., Wang, D., Zhang, T., Zhou, Y., Zheng, H., et al. (2015). Decentration of optical zone center and its impact on visual outcomes following SMILE. *Cornea* 34, 392–397. doi:10.1097/ICO.0000000000000383
- Liu, Y. L., Yeh, P. T., Huang, J. Y., Wang, I. J., Chen, W. L., Hu, F. R., et al. (2013). Pupil centroid shift and cyclotorsion in bilateral wavefront-guided laser refractive surgery and the correlation between both eyes. *J. Formos. Med. Assoc.* 112, 64–71. doi:10.1016/j.jfma.2012.02.028
- Mathur, A., Gehrmann, J., and Atchison, D. A. (2014). Influences of luminance and accommodation stimuli on pupil size and pupil center location. *Investigative Ophthalmol. Vis. Sci.* 55, 2166–2172. doi:10.1167/iops.13-13492
- Mrochen, M., Kaemmerer, M., Mierdel, P., and Seiler, T. (2001). Increased higher-order optical aberrations after laser refractive surgery: A problem of subclinical decentration. *J. Cataract Refract. Surg.* 27, 362–369. doi:10.1016/s0886-3350(00)00806-3
- Pierrot-Deseilligny, C. (2009). Effect of gravity on vertical eye position. *Ann. N. Y. Acad. Sci.* 1164, 155–165. doi:10.1111/j.1749-6632.2009.03864.x
- Porter, J., Yoon, G., Lozano, D., Wolfing, J., Tumber, R., Macrae, S., et al. (2006). Aberrations induced in wavefront-guided laser refractive surgery due to shifts between natural and dilated pupil center locations. *J. Cataract Refract. Surg.* 32, 21–32. doi:10.1016/j.jcrs.2005.10.027
- Yang, Y., Thompson, K., and Burns, S. A. (2002). Pupil location under mesopic, photopic, and pharmacologically dilated conditions. *Investigative Ophthalmol. Vis. Sci.* 43, 2508–2512.
- Yap, E. Y., and Kowal, L. (2001). Diplopia as a complication of laser *in situ* keratomileusis surgery. *Clin. Exp. Ophthalmol.* 29, 268–271. doi:10.1046/j.1442-9071.2001.00418.x



OPEN ACCESS

EDITED BY

Yanwu Xu,
Baidu, China

REVIEWED BY

Lixia Lou,
Department of Ophthalmology, College
of Medicine, The Second Affiliated
Hospital of Zhejiang University, China
Yaqi Wang,
Zhejiang University of Media and
Communications, China

*CORRESPONDENCE

Yiqi Chen,
✉ eyedoctor-chen@outlook.com
Lijun Shen,
✉ slj@mail.eye.ac.cn[†]These authors have contributed equally
to this work

RECEIVED 13 February 2023

ACCEPTED 10 April 2023

PUBLISHED 20 April 2023

CITATION

Shen Y, Ye X, Tao J, Zhao C, Xu Z, Mao J,
Chen Y and Shen L (2023), Quantitative
assessment of retinal microvascular
remodeling in eyes that underwent
idiopathic epiretinal membrane surgery.
Front. Cell Dev. Biol. 11:1164529.
doi: 10.3389/fcell.2023.1164529

COPYRIGHT

© 2023 Shen, Ye, Tao, Zhao, Xu, Mao,
Chen and Shen. This is an open-access
article distributed under the terms of the
[Creative Commons Attribution License
\(CC BY\)](https://creativecommons.org/licenses/by/4.0/). The use, distribution or
reproduction in other forums is
permitted, provided the original author(s)
and the copyright owner(s) are credited
and that the original publication in this
journal is cited, in accordance with
accepted academic practice. No use,
distribution or reproduction is permitted
which does not comply with these terms.

Quantitative assessment of retinal microvascular remodeling in eyes that underwent idiopathic epiretinal membrane surgery

Yingjiao Shen^{1†}, Xin Ye^{1†}, Jiwei Tao¹, Chenhao Zhao¹, Zhaokai Xu¹,
Jianbo Mao², Yiqi Chen^{2*} and Lijun Shen^{1,2*}¹National Clinical Research Center for Ocular Diseases, Eye Hospital, Wenzhou Medical University, Wenzhou, China, ²Department of Ophthalmology, Zhejiang Provincial People's Hospital, Hangzhou, China**Purpose:** To explore the surgical outcomes of the macular microvasculature and visual function in eyes with idiopathic epiretinal membrane (iERM) using spectral-domain optical coherence tomography angiography (SD-OCTA).**Methods:** This observational, cross-sectional study included 41 participants who underwent iERM surgery with a 3-month (3M) follow-up. Forty-one healthy eyes formed the control group. The assessments included best-corrected visual acuity (BCVA) and mean sensitivity (MS) by microperimetry and SD-OCTA assessment of vessel tortuosity (VT), vessel density (VD), foveal avascular zone, and retinal thickness (RT).**Results:** The findings showed statistically significant differences in VT, foveal avascular zone parameters, RT, BCVA, and MS between the iERM and control groups ($p < 0.05$). After iERM surgery, the macular VT, SCP VD, and RT decreased significantly ($p < 0.01$) while the DCP VD increased ($p = 0.029$). The BCVA improved significantly ($p < 0.001$) and was associated with the MS ($rs = -0.377$, $p = 0.015$). MS was associated with the SCP VD and RT at 3M (SCP VD $rs = 0.511$, $p = 0.001$; RT $rs = 0.456$, $p = 0.003$). In the superior quadrant, the MS improved significantly ($p < 0.001$) and the improvement of MS was associated with the reduction of VT ($\beta = -0.330$, $p = 0.034$).**Conclusion:** Microcirculatory remodeling and perfusion recovery were observed within 3 months after iERM surgery. VT was a novel index for evaluating the morphology of the retinal microvasculature in eyes with iERM and was associated with MS in the superior quadrant.

KEYWORDS

idiopathic epiretinal membrane, optical coherence tomography angiography, vessel tortuosity, vitrectomy, microvascular remodeling

Introduction

Idiopathic epiretinal membrane (iERM) is a common macular disease characterized by abnormal glial proliferation in the vitreoretinal interface. Proliferative cells in the macular area, migrating along the surface of the internal limiting membrane (ILM), can cause wrinkling and retinal traction (Fung et al., 2021). The contraction of the iERM is responsible for the additional thickening, folding, or puckering, along with vascular distortion, and the

traction on the retina can alter the morphology of the fovea, leading to clinical symptoms such as metamorphopsia, blurred vision, and decreased visual acuity (Steel and Lotery, 2013). Pars plana vitrectomy, followed by peeling of the membrane and ILM, is the recommended therapy for treating iERM, which can normalize the wrinkled retinal surface and thickened macula (Far et al., 2021).

Optical coherence tomography (OCT) is widely applied in the assessment and diagnosis of macular diseases. However, OCT cannot be used to visualize retinal blood flow (Koustenis et al., 2017). OCT angiography (OCTA), a newly introduced imaging modality based on OCT, is used extensively because of its non-invasiveness in visualizing the retinal vessels. It provides a detailed en-face view of each capillary layer. In addition, the high resolution of the capillary network facilitates better visualization of the retinal vasculature in multiple layers and more reliable assessments of vascular features. Previous reports have described OCTA-derived indexes, including foveal avascular zone (FAZ) parameters, vessel density (VD), and fractal dimension (Kim and Park, 2021; Mao et al., 2021).

Normal retinal blood vessels are straight or slightly curved but may become dilated and tortuous in several conditions, including angiogenesis, high blood flow, and blood vessel congestion (Hart et al., 1999). Therefore, vessel tortuosity (VT) was also a meaningful indicator of microvascular evaluation, which could infer the severity and the progression of many retinopathies. Previous studies evaluated VT in sickle cell retinopathy (SCR), (Alam et al., 2019), diabetic retinopathy (DR) (Alam et al., 2020; Alam et al., 2021), and familial retinal arteriolar tortuosity (FRAT) (Saraf et al., 2019), among others. However, few studies have evaluated VT in eyes with iERM. Additionally, sensitivity based on microperimetry is a good functional parameter, but it is rarely used in research on microperimetry assessment for iERM. In contrast with automated perimetry, it demonstrates better reliability and retest-variability (Pfau et al., 2021). Only a few studies have combined OCTA with microperimetry to evaluate retinal changes in eyes with iERM (Feng et al., 2021; D'Aloisio et al., 2021). Therefore, we aimed to explore the changes in retinal microvascular architecture and visual function in the macular region in iERM patients using OCTA images.

Materials and methods

We examined 41 eyes of 41 patients affected by iERM that were admitted to the Affiliated Eye Hospital of Wenzhou Medical University between January 2019 and December 2021. All patients underwent 23-gauge pars plana vitrectomy combined with iERM peeling and non-foveal-sparing ILM peeling by a senior surgeon (SLJ). Patients with mild cataract who were older than 55 years old also underwent phacoemulsification and intraocular lens implantation. Matched for age, 41 healthy eyes of 41 healthy participants were used as controls. This study used anonymous retrospective data and did not require active patient participation or informed consent. All procedures adhered to the tenets of the Declaration of Helsinki. The study was reviewed and approved by the Medical Ethics Committee of the Affiliated Eye Hospital of Wenzhou Medical University.

Before and after surgery, all enrolled patients received a comprehensive ophthalmic evaluation, including the assessment of best-corrected visual acuity (BCVA), slit-lamp biomicroscopy,

indirect fundus ophthalmoscopy, OCTA, and microperimetry. The criteria for inclusion were: 1) diagnosis of iERM by retinal experts based on the results of fundus examination, OCT, and OCTA; and 2) no previous history of vitreoretinal prior surgery. The criteria for exclusion were: 1) previous history of ocular diseases such as retinal vascular occlusions, retinal detachment, trauma, high myopia, and uveitis; 2) previous history of systemic disorders, including systemic hypertension and diabetes; and 3) poor image quality (signal strength index less than 5) due to poor image fixation or obvious opacity in refracting media, such as severe cataract and leukoplakia.

Image acquisition

All images were acquired with spectral-domain OCTA (SD-OCTA) (Optovue, Fremont, CA, United States). All the OCTA images had a field of view of 6 mm × 6 mm. Retinal vasculature was assessed within two horizontal retinal slabs of the OCTA, including the superficial capillary plexus (SCP) and deep capillary plexus (DCP), spanning from the ILM to the superficial inner plexiform layer and from the deep inner plexiform layer to the outer plexiform layer, respectively. For each eye, three 6 × 6-mm OCTA volume scans were acquired at baseline, 1 month (1M), and 3 months (3M) after surgery.

Image processing

The primary indicators included: 1) VT; 2) SCP VD; 3) retinal thickness (RT); 4) DCP VD; 5) FAZ area (FAZA), perimeter (FAZp), and acircularity index (AI). While analyzing the former three parameters, we considered the temporal, superior, nasal, and inferior sectors of a circular zone with a diameter of 6 mm. VD, RT, FAZA, and FAZp were obtained from the built-in image analysis software of the OCTA device. FAZ AI was calculated as the measured FAZp divided by the perimeter of the regular circle with the same FAZA.

To calculate VT, we exported the OCTA images of SCP (Figure 1A) and used ImageJ for further feature extraction and image analysis. According to the method described previously (Lee et al., 2018), we converted the original images to 8-bit grayscale images and used the “Trainable Weka Segmentation” plugin to binarize the vessels. After image binarization, using the “Skeletonize” plugin and acquiring a thin track of vessels with a 1-pixel diameter (Figure 1B). The “Analyze skeleton” plugin in ImageJ was used for the calculation of the length of vessels, including the actual length of each branch and the imaginary straight length between the two branch nodes (Figure 1C). VT was calculated as shown in Figure 1D. If needed, manual segmentation was performed to assess the entire retina to prevent segmentation errors. Images with poor quality, such as those with poor contrast due to poor image fixation or media opacities, were excluded. When erroneous segmentation results were caused by poor image quality, we discarded the analysis for obvious failure cases.

Functional assessment

Microperimetry was performed with MP-3 (NIDEK, Gamagori, Japan) at the baseline and 1M and 3M postoperatively. All patients

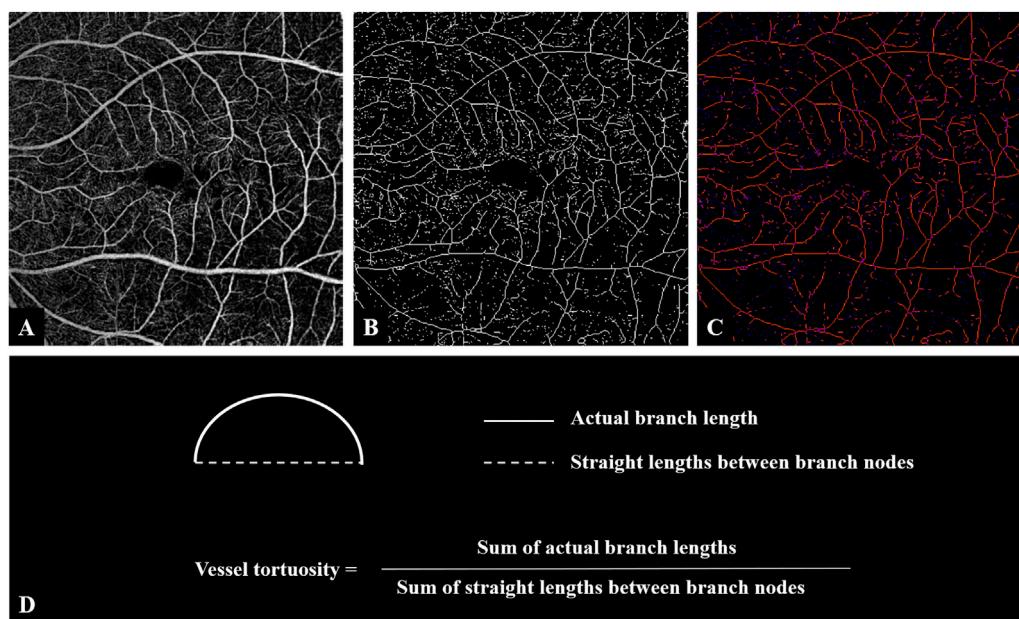


FIGURE 1

Image processing steps for analyzing vessel tortuosity. (A) OCTA image of the superficial retinal layer of an eye with iERM. (B) Binarized vessel was skeletonized. (C) The vessel branches and the branch nodes were obtained and the lengths of both actual branches and the imaginary straight lines between nodes were generated. (D) Vessel tortuosity was calculated as the sum of the branch lengths divided by the sum of the lengths of the imaginary straight lines. Abbreviations: iERM, idiopathic epiretinal membrane; OCTA, optical coherence tomography angiography.

underwent the examination under dim-light conditions. The fixation target of MP-3 was a red ring with a diameter of 1 with a white monochromatic background at 31.4 abs. The fovea was marked by a blue star. An automatic eye tracker was used with a customized grid of 61 points covering the central 20° centered on the fovea (approximately 6 mm × 6 mm range). The retinal sensitivities were approximately 0–36 dB. In this study, the mean sensitivity (MS) of all 61 points and the MS of the four quadrants of the 15 points were calculated. BCVA was performed using a Snellen chart, and trained optometrists recorded measurements before and after the surgery. For statistical analysis, BCVA was converted to a logarithm of the minimal angle of resolution (logMAR).

Statistical analysis

All statistical analyses were performed using SPSS v26.0 (SPSS for Windows, Chicago, IL, United States). All quantitative variables were described as mean ± standard deviation (SD). A Shapiro–Wilk test was performed to evaluate the departure of each variable from a normal distribution. The independent-sample t-test was performed for the difference in age between the groups. The Chi-squared test was performed for the difference in sex between the groups. The Wilcoxon signed-rank and Kruskal–Wallis H tests were used to compare the parameters. Spearman’s Rho correlation coefficient was used to evaluate the correlations between the anatomical and functional parameters. Multivariate linear regression was used to analyze the correlations between the functional and anatomical variables. $p < 0.05$ was considered statistically significant.

Results

We included 41 eyes of 41 patients diagnosed with iERM as the iERM group and 41 healthy eyes of 41 persons as the control group. During vitrectomy, 39 of 41 eyes were treated by phacoemulsification for cataracts. One eye was pseudophakic. One eye did not undergo cataract surgery because the patient was relatively young with no apparent cataract. No statistically significant differences were found in age ($p = 1.000$) and sex ($p = 0.557$) between the iERM and control groups (see Table 1).

Microvascular remodeling

At baseline, the iERM group had a higher VT, smaller FAZa, smaller FAZp, larger FAZ AI, and greater RT than the control group (VT 1.1165 ± 0.0226 vs. 1.1072 ± 0.0129 , $p = 0.047$; FAZa $0.07 \pm 0.10 \text{ mm}^2$ vs. $0.30 \pm 0.11 \text{ mm}^2$, $p < 0.001$; FAZp $1.04 \pm 0.53 \text{ mm}$ vs. $2.12 \pm 0.38 \text{ mm}$, $p < 0.001$; FAZ AI 1.25 ± 0.20 vs. 1.12 ± 0.06 , $p < 0.001$; RT $359.93 \pm 52.58 \mu\text{m}$ vs. $284.44 \pm 15.91 \mu\text{m}$, $p < 0.001$). No significant differences were found in the SCP VD and DCP VD (SCP VD $48.06\% \pm 5.96\%$ vs. $48.51\% \pm 3.76\%$, $p = 0.856$; DCP VD $45.14\% \pm 6.43\%$ vs. $48.06\% \pm 5.37\%$, $p = 0.078$) (see Table 1).

Compared to the baseline values, there were significant reductions in VT, SCP VD, and RT in the macular region during the 3-month follow-up (VT, from 1.1165 ± 0.0226 to 1.0978 ± 0.0239 , $p < 0.001$; SCP VD, from $48.06\% \pm 5.96\%$ to $45.17\% \pm 4.11\%$, $p = 0.002$; RT, from $359.93 \pm 52.58 \mu\text{m}$ to $298.24 \pm 26.87 \mu\text{m}$, $p < 0.001$). The DCP VD of the macular region increased from $45.14\% \pm$

TABLE 1 Comparison of baseline parameters between the iERM (N = 41) and control (N = 41) groups.

Baseline parameter	iERM group	Control group	<i>p</i> -value
Age (year)	66.20 ± 8.68	66.20 ± 8.74	1.000
Sex (M/F)	8/33	6/35	0.557
Anatomical parameters			
VT	1.1165 ± 0.0226	1.1072 ± 0.0129	0.047
SCP VD (%)	48.06 ± 5.96	48.51 ± 3.76	0.856
DCP VD (%)	45.14 ± 6.43	48.06 ± 5.37	0.078
FAZa (mm ²)	0.07 ± 0.10	0.30 ± 0.11	< 0.001
FAZp (mm)	1.04 ± 0.53	2.12 ± 0.38	< 0.001
FAZ AI	1.25 ± 0.20	1.12 ± 0.06	< 0.001
RT (μm)	359.93 ± 52.58	284.44 ± 15.91	< 0.001
Functional parameters			
MS (dB)	22.27 ± 3.87	26.18 ± 1.93	< 0.001
BCVA (logMAR)	0.49 ± 0.38	0.01 ± 0.04	< 0.001

Bold font indicates statistically significance ($p < 0.05$).

Abbreviations: iERM, idiopathic epiretinal membrane; VT, vessel tortuosity; VD, vessel density; SCP, superficial capillary plexus; DCP, deep capillary plexus; FAZ, foveal avascular zone; FAZa, FAZ area; FAZp, FAZ perimeter; FAZ AI, FAZ acircularity index; RT, retinal thickness; MS, mean sensitivity; BCVA, best-corrected visual acuity; logMAR, logarithm of the minimal angle of resolution.

TABLE 2 Comparison of functional and anatomical parameters of the macular region at baseline and 3 months (3M) after surgery in eyes with iERM.

Parameters	Baseline	3M	<i>p</i> -value
Anatomical parameters			
VT	1.1165 ± 0.0226	1.0978 ± 0.0239	< 0.001
SCP VD (%)	48.06 ± 5.96	45.17 ± 4.11	0.002
DCP VD (%)	45.14 ± 6.43	48.32 ± 4.86	0.029
FAZa (mm ²)	0.07 ± 0.10	0.08 ± 0.05	0.053
FAZp (mm)	1.04 ± 0.53	1.17 ± 0.38	0.140
FAZ AI	1.25 ± 0.20	1.19 ± 0.13	0.228
RT (μm)	359.93 ± 52.58	298.24 ± 26.87	<0.001
Functional parameters			
MS (dB)	22.27 ± 3.87	22.79 ± 2.63	0.451
BCVA (logMAR)	0.49 ± 0.38	0.22 ± 0.26	<0.001

Bold font indicates statistically significance ($p < 0.05$).

Abbreviations: iERM, idiopathic epiretinal membrane; VT, vessel tortuosity; VD, vessel density; SCP, superficial capillary plexus; DCP, deep capillary plexus; FAZ, foveal avascular zone; FAZa, FAZ area; FAZp, FAZ perimeter; FAZ AI, FAZ acircularity index; RT, retinal thickness; MS, mean sensitivity; BCVA, best-corrected visual acuity; logMAR, logarithm of the minimal angle of resolution.

6.43% to 48.32% ± 4.86% over 3 months ($p = 0.029$). No significant differences were found in the FAZa ($p = 0.053$), FAZp ($p = 0.140$), and FAZ AI ($p = 0.228$) at 3M relative to the baseline (see [Table 2](#); [Figure 2](#)).

The VT, SCP VD, and RT were divided into four quadrants in the macular area for further analysis at baseline, 1M, and 3M. At 1M, VT decreased significantly in the superior, nasal, and inferior quadrants (all $p < 0.05$). At 3M, VT also significantly decreased in the superior, nasal, and inferior quadrants (all $p < 0.01$). However, there was no significant improvement in the temporal quadrant at 1M or 3M ($p = 0.785$, $p = 0.134$, respectively). The SCP VD decreased significantly in four quadrants at 1M and 3M (all $p < 0.05$). Within 3 months, RT showed a steady decline for the entire

macular area and all quadrants (all $p < 0.01$) (see [Table 3](#); [Figures 2A–C](#); [Supplementary Table S1](#)).

At baseline, there were no significant differences in VT ($p = 0.114$) and RT ($p = 0.139$) across the four quadrants. The SCP VD of the temporal quadrant was the lowest among the four quadrants ($p < 0.001$). At 3M, there were significant differences in VT, SCP VD, and RT across the different quadrants ($p < 0.001$; $p < 0.001$; $p < 0.001$). Pairwise comparisons were made among the four quadrants. The VT of the temporal quadrant was more tortuous than that of the superior ($p < 0.001$) and inferior ($p < 0.001$) quadrants. There were no significant differences between the VTs of the temporal and nasal quadrants ($p = 0.542$). Compared to the other three quadrants, the SCP VD of the

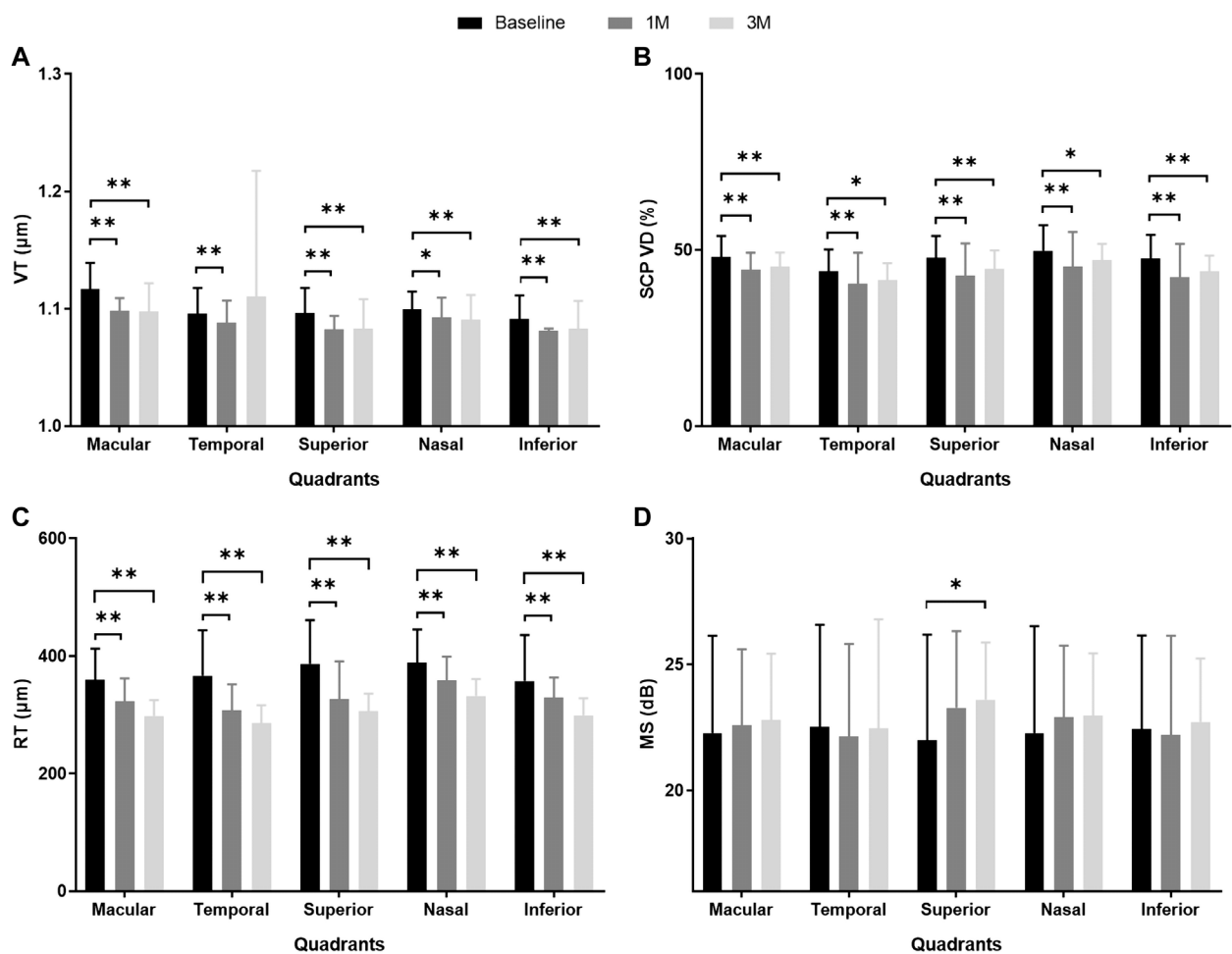


FIGURE 2

MS and anatomical parameters of the macular region in eyes with iERM observed at baseline and 1 month (1M) and 3 months (3M) after vitreoretinal surgery. (A) VT; (B) SCP VD (%); (C) RT (μm); (D) MS (dB). ** $p < 0.01$, * $p < 0.05$. Abbreviations: iERM, idiopathic epiretinal membrane; VT, vessel tortuosity; SCP, superficial capillary plexus; VD, vessel density; RT, retinal thickness; MS, mean sensitivity.

temporal quadrant was the lowest (superior $p = 0.002$; nasal $p < 0.001$; inferior $p = 0.015$). The RT of the temporal quadrant was thinner than that of the superior ($p = 0.007$) and nasal ($p < 0.001$) quadrants (see Table 3).

Functional improvement

At baseline, the iERM group had worse MS and BCVA than those of the control group (MS 22.27 ± 3.87 dB vs. 26.18 ± 1.93 dB, $p < 0.001$; BCVA 0.49 ± 0.38 logMAR vs. 0.01 ± 0.04 logMAR, $p < 0.001$; see Table 1). During the 3-month follow-up after iERM surgery, the BCVA significantly improved to 0.22 ± 0.26 logMAR ($p < 0.001$). The MS of the macular region showed no difference after iERM surgery ($p = 0.451$), but there was a trend of increase (see Table 2; Figure 2D).

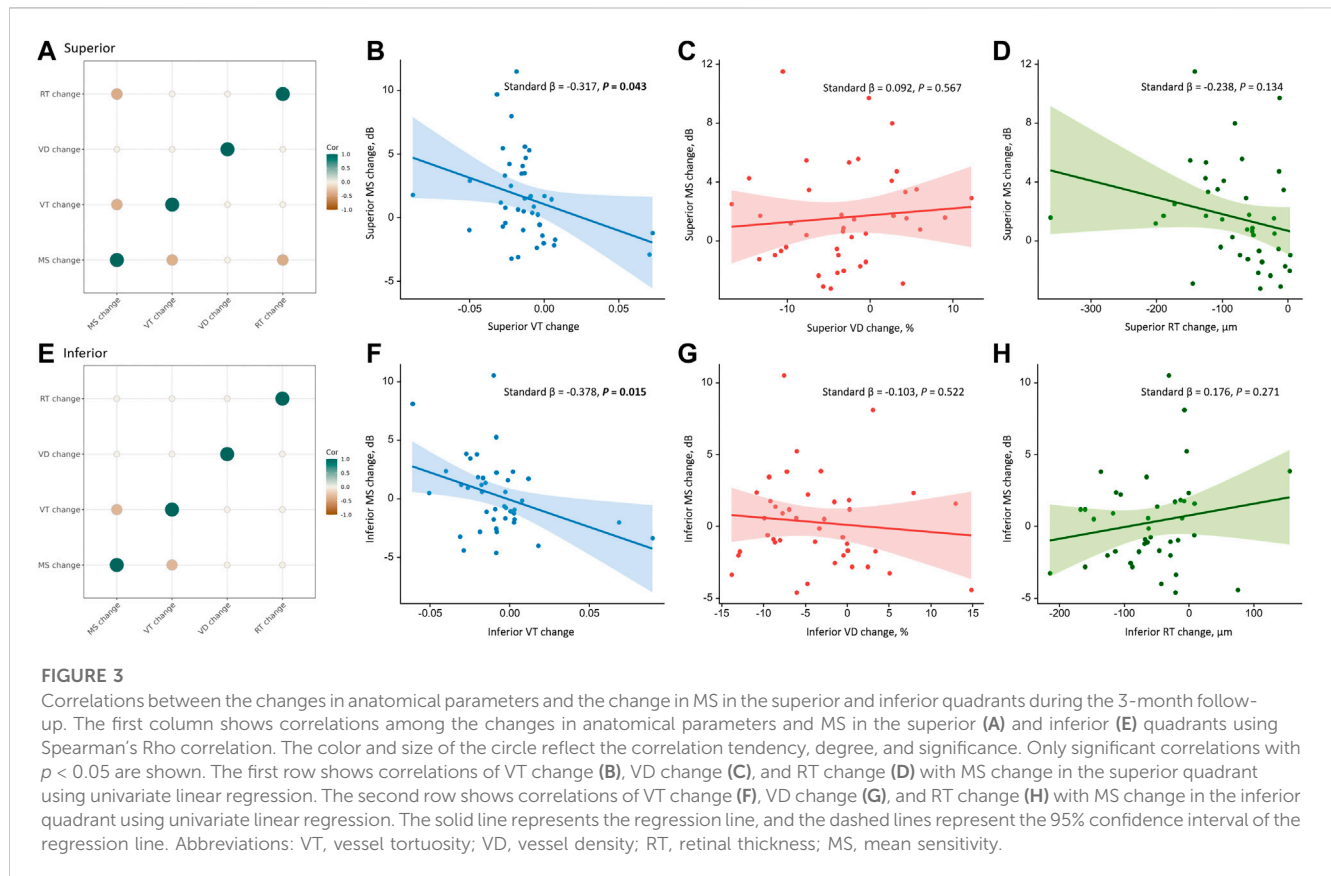
The MS of the superior quadrant significantly improved after iERM surgery (1M $p = 0.043$; 3M $p = 0.010$). In the three other quadrants, MS showed a trend of increase but with no significant

difference (see Table 2; Figure 2D). Among the four quadrants, there was no significant difference in MS at baseline ($p = 0.860$) and 3M ($p = 0.400$) (see Table 3).

Correlations between functional and anatomical parameters

We assessed the correlations between the functional and anatomical parameters of the macular region at 3M. There was a significant correlation between the BCVA and the MS at M3 ($r_s = -0.377$, $p = 0.015$). The BCVA was associated with SCP VD, but not VT and RT at M3 (VT $r_s = -0.253$, $p = 0.111$; SCP VD $r_s = -0.554$, $p < 0.001$; RT $r_s = -0.076$, $p = 0.635$). MS was associated with SCP VD and RT but not VT at M3 (VT $r_s = 0.077$, $p = 0.634$; SCP VD $r_s = 0.511$, $p = 0.001$; RT $r_s = 0.456$, $p = 0.003$) (see Supplementary Table S2).

We further analyzed the correlations between the changes in MS and anatomical parameters in different quadrants during the



3-month follow-up after iERM surgery (see Figure 3). Using Spearman's Rho correlation, a greater increase in MS was associated with greater reductions of VT and RT in the superior quadrant (VT, $r_s = -0.397$, $p = 0.010$; RT, $r_s = -0.409$, $p = 0.008$). In the inferior quadrant, a greater increase in MS was associated with a greater reduction of VT ($r_s = -0.349$, $p = 0.025$). No correlation was found between the changes in VD and MS in the macular region and four quadrants (all $p > 0.05$) (see Table 4). Among the anatomical parameters, changes in VT were related to changes in VD in the temporal quadrant ($r_s = 0.350$, $p = 0.025$; see Supplementary Figure S1E). No significant correlations were found between the changes in VT, RT, and VD in the macular, superior, nasal, and inferior quadrants (all $p > 0.05$; see Supplementary Figure S1).

Univariate linear regression showed that an improvement in MS was associated with the reduction of VT in the superior (standard $\beta = -0.317$, $p = 0.043$) and inferior (standard $\beta = -0.378$, $p = 0.015$) quadrants, but not the macular region and temporal and nasal quadrants (all $p > 0.05$). Using multivariate linear regression, the improvement of MS was associated with the reduction of VT in the temporal (standard $\beta = -0.322$, $p = 0.044$), superior (standard $\beta = -0.330$, $p = 0.034$), and inferior (standard $\beta = -0.480$, $p = 0.003$) quadrants but not in the macular region and nasal quadrant (all $p > 0.05$). No correlation was found between the changes in SCP VD and RT with MS in the macular region and four quadrants (all $p > 0.05$) (see Table 5).

Discussion

Our study assessed the impact of iERM surgery on retinal microvasculature. We showed that surgery may improve the structure of the retinal microcirculation over 3 months or even 1 month. We quantified and analyzed the vascular tortuosity of the retina in iERM using SD-OCTA. Previous studies have demonstrated that VT may be useful in differentiating the progression of DR (Klein et al., 2018; Alam et al., 2021). However, research examining VT in eyes with iERM has been limited. To our knowledge, this is the first study on vascular tortuosity and sensitivity in four quadrants before and after surgery for iERM. To obtain a more detailed and visually intuitive view, we focused on the microvascular characteristics of SCP. Additionally, the traction of ERM may alter the OCTA signal quality of DCP status, and it is necessary to prevent ERM-related projection artifacts.

Surgical treatment for ERM can release traction in the vitreoretinal interface, leading to vascular restoration and remodeling. Tangential and vertical macular tractions from ERM were considered the reason for vessel translocation and tortuosity (Yagi et al., 2012), which was supported by our observations that the VT in the eyes with iERM was higher than those in healthy eyes. With the release of tractional force generated from the ERM after removing preretinal tissue, the surgery facilitates the recovery of the main retinal vessels and capillaries to their original position. The VT significantly decreased after surgical treatment in this study, which may have contributed to the improvement of macular microcirculation. Consistent with the study by Miyazawa et al.

TABLE 3 Comparison of MS and anatomical parameters of different quadrants at baseline and 3 months (3M) after surgery in eyes with iERM.

Parameters	Baseline	3M	P_1 -value
VT			
Temporal	1.0957 ± 0.0219	1.1105 ± 0.1070	0.134
Superior	1.0962 ± 0.0214	1.0831 ± 0.0249	<0.001
Nasal	1.0993 ± 0.0153	1.0906 ± 0.0212	0.001
Inferior	1.0914 ± 0.0199	1.0830 ± 0.0236	0.001
P_2 -value	0.114	<0.001	
SCP VD (%)			
Temporal	44.02 ± 6.18	41.48 ± 4.75	0.024
Superior	47.72 ± 6.31	44.56 ± 5.36	0.007
Nasal	49.82 ± 7.26	47.11 ± 4.68	0.013
Inferior	47.57 ± 6.77	43.98 ± 4.42	0.001
P_2 -value	<0.001	<0.001	
RT (μm)			
Temporal	366.81 ± 76.93	286.33 ± 30.33	<0.001
Superior	387.06 ± 74.05	306.71 ± 29.51	<0.001
Nasal	388.79 ± 56.41	332.34 ± 28.68	<0.001
Inferior	357.69 ± 78.07	299.42 ± 28.97	<0.001
P_2 -value	0.076	<0.001	
MS (dB)			
Temporal	22.52 ± 4.05	22.46 ± 4.33	0.717
Superior	22.00 ± 4.18	23.61 ± 2.26	0.010
Nasal	22.27 ± 4.25	22.98 ± 2.46	0.488
Inferior	22.43 ± 3.72	22.72 ± 2.52	0.928
P_2 -value	0.860	0.400	

P_1 -value was obtained from the comparison of parameters at baseline and 3 months postoperatively.

P_2 -value was obtained from the comparison of parameters for the four quadrants.

Bold font indicates statistically significance ($p < 0.05$).

Abbreviations: iERM, idiopathic epiretinal membrane; VT, vessel tortuosity; VD, vessel density; SCP, superficial capillary plexus; RT, retinal thickness; MS, mean sensitivity.

(Miyazawa et al., 2022), more linearized vessels were found postoperatively.

Previous study demonstrated that FAZ would be enlarged and rounded after surgery (Hirata et al., 2019; Ersoz et al., 2021). This study obtained consistent results, and we suggested that the changes in FAZ were also manifestations of vascular restoration and remodeling after the release of traction. The formation of iERM may cause the centripetal contraction of retinal layers, accompanied by vascular displacement and contortion, which may contribute to the reduction of the FAZ area and the progressive deterioration of the standard circular shape of the FAZ. Our patients show more extensive AI than the controls, with smaller FAZa and FAZp. After ERM surgery, we still observed a decrease in AI yielding a more circular shape, although this was not statistically significant. Therefore, FAZ can reflect surgical efficacy at the end of peripheral blood circulation. Removing the retinal pucker can facilitate revascularization and resolve central vessel crowding and deformation.

Notably, there were different anatomic remodeling patterns among the four quadrants in the macular area. We found that VT and MS showed no significant improvement postoperatively in the temporal quadrant (see Figures 4A, B). A reason may be that the nerve fiber layer was thinner, and the ganglion cells were fewer in the

temporal retina than in other areas, which seemed more vulnerable to mechanical damage such as ILM peeling. Beyond that, the temporal blood vessels located at the end of retinal microcirculation may be more susceptible to the loss of structural support after membrane removal. As a result, the vessel network of the temporal region may be more disorganized, which may affect functional recovery. Conversely, the nasal macular area, localized at the proximal end to the optic disc, may be relatively stable and less influenced due to the high stability of the optic disc.

The most pronounced effect of VT was observed in the superior quadrant after treatment (see Figures 4C, D). The change in MS was associated with the change in VT in the superior and inferior quadrants using multivariate linear regression. However, the MS only improved significantly in the superior quadrant. Several studies have reported functional and structural asymmetries in the superior and inferior retina. In terms of functionality, the superior macular region may be more active. Some authors have found that the amplitudes of electroretinograms and the contrast sensitivity of the intermediate spatial frequencies are larger in the superior macular region than in the inferior macular region (Miyake et al., 1989; Silva et al., 2010), which suggests functional superiority of the upper retina. Secondly, there were anatomic differences between the superior and inferior retina. Earlier

TABLE 4 Correlation between the change in MS and anatomical parameters in different quadrants during the 3-month follow-up after iERM surgery using Spearman's Rho correlation.

Quadrant	Anatomical parameters	rs	p-value
Macular	VT change	−0.130	0.418
	SCP VD change	−0.022	0.892
	RT change	−0.032	0.844
Temporal	VT change	0.009	0.955
	SCP VD change	0.085	0.596
	RT change	−0.007	0.963
Superior	VT change	−0.397	0.010
	SCP VD change	0.180	0.259
	RT change	−0.409	0.008
Nasal	VT change	0.151	0.347
	SCP VD change	−0.098	0.540
	RT change	−0.107	0.504
Inferior	VT change	−0.349	0.025
	SCP VD change	−0.114	0.478
	RT change	0.202	0.205

Bold font indicates statistically significance ($p < 0.05$).

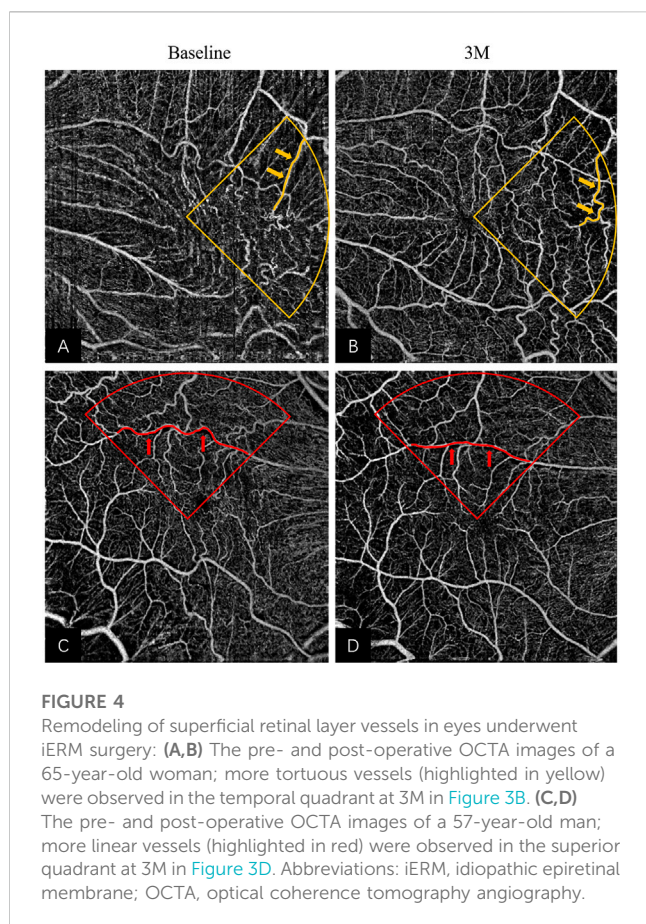
Abbreviations: iERM, idiopathic epiretinal membrane; VT, vessel tortuosity; VD, vessel density; SCP, superficial capillary plexus; RT, retinal thickness; MS, mean sensitivity.

TABLE 5 Correlation between the change in MS and anatomical parameters in different quadrants during the 3-month follow-up after iERM surgery using multivariate linear regression.

Quadrant	Anatomical parameters	Standard β	p-value	Adjusted R-square
Macular	VT change	−0.020	0.905	−0.076
	SCP VD change	−0.063	0.707	
	RT change	−0.003	0.988	
Temporal	VT change	−0.322	0.044	0.052
	SCP VD change	0.171	0.281	
	RT change	−0.057	0.716	
Superior	VT change	−0.330	0.034	0.104
	SCP VD change	0.064	0.672	
	RT change	−0.255	0.098	
Nasal	VT change	−0.067	0.691	−0.063
	SCP VD change	−0.099	0.555	
	RT change	−0.067	0.684	
Inferior	VT change	−0.480	0.003	0.195
	SCP VD change	−0.274	0.076	
	RT change	0.261	0.080	

Bold font indicates statistically significance ($p < 0.05$).

Abbreviations: iERM, idiopathic epiretinal membrane; VT, vessel tortuosity; VD, vessel density; SCP, superficial capillary plexus; RT, retinal thickness; MS, mean sensitivity.



studies found ganglion cell and rod density were higher in the upper retina (Curcio and Allen, 1990; Curcio et al., 1990) and a recent study indicated that the blood flow in the superior retina was higher than that of the inferior retina (Tomita et al., 2020). Similar to these findings, our results showed appreciable MS improvement only in the superior quadrant. Taken together, the superior retina may show better vascular morphological restoration and blood flow reperfusion.

Our study presented a novel index for evaluating structural remodeling and blood flow perfusion. Additionally, we found the RT became thinner after surgery; however, the tortuosity of vessels in SCP reduced, which may also be the reason for the VD reduction in SCP. With the distorted and disorganized vessels tending to be normal, the resistance in the superficial vascular bed reduced, and the density decreased subsequently. Furthermore, the perfusion increased in DCP, suggesting the recovery of the anomalous tortuous capillaries dragged by the ERM and the improvement of blood flow in deep layers. Notably, the sensitivity improved after surgery, and MS was positively associated with RT and SCP VD 3 months after surgery. These may be because of retinal microstructural restoration and vascular perfusion after resolving the force exerted by the ERM, followed by the improvement of cell function. Several researchers have shown improvement of MS and BCVA in eyes with iERM postoperatively (Osada et al., 2020; Feng et al., 2021; Blautain et al., 2022). Consistent with these previous studies, visual acuity improved significantly and was associated with MS

postoperatively in this study. As an example, [Supplementary Figure S2](#) shows the images of a patient with iERM who had vessel remodeling in SCP and improved MS. However, the MS only showed a slight but non-statistically significant upward trend, which may be due to the limited sample size. Furthermore, anatomical features may recover relatively quickly, while visual function may demonstrate a chronic recovery course. This has already received our attention and will be further perfected and supplemented in subsequent studies.

There were several limitations of this study. First, the sample size was limited. Second, we only reported short-term outcomes, and long-term changes should be explored. Third, we focused on the vessels of the SCP to prevent or minimize artifacts, and future research on the microvascular characteristics of DCP is required.

Conclusion

This study showed microvascular remodeling and perfusion recovery with a decrease in VT. BCVA improved significantly after iERM surgery and was associated with MS. In the superior macular quadrant, the reduction of VT was associated with the improvement of MS. Thus, VT may be a novel index for the morphology of the retinal microvasculature.

Data availability statement

The original contributions presented in the study are included in the article/[Supplementary Material](#), further inquiries of source data can be directed to the corresponding authors.

Ethics statement

The studies involving human participants were reviewed and approved by The Affiliated Eye Hospital of Wenzhou Medical University. Written informed consent for participation was not required for this study in accordance with the national legislation and the institutional requirements.

Author contributions

LS had full access to all the data in the study and will take responsibility for the integrity of the data and the accuracy of the data analysis. Study concept and design: YS, XY, and LS. Acquisition, analysis, or interpretation of data: YS, XY, JT, CZ, and ZX. Drafting of the manuscript: YS, XY, and YC. Critical revision of the manuscript for important intellectual content: LS and YC. Study supervision: LS.

Acknowledgments

We thank all participants for their contribution to the present study.

Conflict of interest

The authors declare that the research was conducted in the absence of any commercial or financial relationships that could be construed as a potential conflict of interest.

Publisher's note

All claims expressed in this article are solely those of the authors and do not necessarily represent those of their affiliated

organizations, or those of the publisher, the editors and the reviewers. Any product that may be evaluated in this article, or claim that may be made by its manufacturer, is not guaranteed or endorsed by the publisher.

Supplementary material

The Supplementary Material for this article can be found online at: <https://www.frontiersin.org/articles/10.3389/fcell.2023.1164529/full#supplementary-material>

References

- Alam, M., Le, D., Lim, J. I., Chan, R. V. P., and Yao, X. (2019). Supervised machine learning based multi-task artificial intelligence classification of retinopathies. *J. Clin. Med.* 8, 872. doi:10.3390/jcm8060872
- Alam, M., Le, D., Lim, J. I., and Yao, X. (2021). Vascular complexity analysis in optical coherence tomography angiography of diabetic retinopathy. *Retina* 41, 538–545. doi:10.1097/IAE.0000000000002874
- Alam, M., Zhang, Y., Lim, J. I., Chan, R. V. P., Yang, M., and Yao, X. (2020). Quantitative optical coherence tomography angiography features for objective classification and staging of diabetic retinopathy. *Retina* 40, 322–332. doi:10.1097/IAE.0000000000002373
- Blautain, B., Glacet-Bernard, A., Blanco-Garavito, R., Toutée, A., Jung, C., Ortolí, M., et al. (2022). Long-term follow-up of retinal sensitivity assessed by microperimetry in patients with internal limiting membrane peeling. *Eur. J. Ophthalmol.* 32, 539–545. doi:10.1177/1120672121997300
- Curcio, C. A., and Allen, K. A. (1990). Topography of ganglion cells in human retina. *J. Comp. Neurol.* 300, 5–25. doi:10.1002/cne.903000103
- Curcio, C. A., Sloan, K. R., Kalina, R. E., and Hendrickson, A. E. (1990). Human photoreceptor topography. *J. Comp. Neurol.* 292, 497–523. doi:10.1002/cne.902920402
- D'Aloisio, R., Carpineto, P., Aharrh-Gnama, A., Iafigliola, C., Cerino, L., Di Nicola, M., et al. (2021). Early vascular and functional changes after vitreoretinal surgery: A comparison between the macular hole and epiretinal membrane. *Diagn. (Basel)* 11, 1031. doi:10.3390/diagnostics11061031
- Ersoz, M. G., Hocaoglu, M., Sayman Muslubas, I., Arf, S., and Karacorlu, M. (2021). Quantitative assessment of the foveal avascular zone using optical coherence tomography angiography before and after surgery for idiopathic epiretinal membrane. *Retina* 41, 54–59. doi:10.1097/IAE.0000000000002794
- Far, P. M., Yeung, S. C., Ma, P. E., Hurley, B., Kertes, P., You, Y., et al. (2021). Effects of internal limiting membrane peel for idiopathic epiretinal membrane surgery: A systematic review of randomized controlled trials. *Am. J. Ophthalmol.* 231, 79–87. doi:10.1016/j.ajo.2021.04.028
- Feng, J., Yang, X., Xu, M., Wang, Y., Shi, X., Zhang, Y., et al. (2021). Association of microvasculature and macular sensitivity in idiopathic macular epiretinal membrane: Using oct angiography and microperimetry. *Front. Med. (Lausanne)* 8, 655013. doi:10.3389/fmed.2021.655013
- Fung, A. T., Galvin, J., and Tran, T. (2021). Epiretinal membrane: A review. *Clin. Exp. Ophthalmol.* 49, 289–308. doi:10.1111/ceo.13914
- Hart, W. E., Goldbaum, M., Côté, B., Kube, P., and Nelson, M. R. (1999). Measurement and classification of retinal vascular tortuosity. *Int. J. Med. Inf.* 53, 239–252. doi:10.1016/s1386-5056(98)00163-4
- Hirata, A., Nakada, H., Mine, K., Masumoto, M., Sato, T., and Hayashi, K. (2019). Relationship between the morphology of the foveal avascular zone and the degree of aniseikonia before and after vitrectomy in patients with unilateral epiretinal membrane. *Graefes Arch. Clin. Exp. Ophthalmol.* 257, 507–515. doi:10.1007/s00417-019-04245-x
- Kim, J., and Park, K. H. (2021). Temporal changes of parafoveal microvasculature after epiretinal membrane surgery: An optical coherence tomography angiography study. *Retina* 41, 1839–1850. doi:10.1097/iae.0000000000003132
- Klein, R., Lee, K. E., Danforth, L., Tsai, M. Y., Gangnon, R. E., Meuer, S. E., et al. (2018). The relationship of retinal vessel geometric characteristics to the incidence and progression of diabetic retinopathy. *Ophthalmology* 125, 1784–1792. doi:10.1016/j.ophtha.2018.04.023
- Koustenis, A., Jr., Harris, A., Gross, J., Januleviciene, I., Shah, A., and Siesky, B. (2017). Optical coherence tomography angiography: An overview of the technology and an assessment of applications for clinical research. *Br. J. Ophthalmol.* 101, 16–20. doi:10.1136/bjophthalmol-2016-309389
- Lee, H., Lee, M., Chung, H., and Kim, H. C. (2018). Quantification of retinal vessel tortuosity in diabetic retinopathy using optical coherence tomography angiography. *Retina* 38, 976–985. doi:10.1097/IAE.0000000000001618
- Mao, J., Xu, Z., Lao, J., Chen, Y., Xu, X., Wu, S., et al. (2021). Assessment of macular microvasculature features before and after vitrectomy in the idiopathic macular epiretinal membrane using a grading system: An optical coherence tomography angiography study. *Acta Ophthalmol.* 99, e1168–e1175. doi:10.1111/aos.14753
- Miyake, Y., Shiroyama, N., Horiguchi, M., and Ota, I. (1989). Asymmetry of focal erg in human macular region. *Invest. Ophthalmol. Vis. Sci.* 30, 1743–1749.
- Miyazawa, K., Sakimoto, S., Kanai, M., Shiraki, A., Takahashi, S., Shiraki, N., et al. (2022). Vascular tortuosity analysis in eyes with epiretinal membrane imaged by optical coherence tomography angiography. *BMC Ophthalmol.* 22, 198. doi:10.1186/s12886-022-02420-z
- Osada, U., Kunikata, H., Yasuda, M., Hashimoto, K., Nishiguchi, K. M., and Nakazawa, T. (2020). Association of retinal vessel density with retinal sensitivity in surgery for idiopathic epiretinal membrane. *Graefes Arch. Clin. Exp. Ophthalmol.* 258, 1911–1920. doi:10.1007/s00417-020-04754-0
- Pfau, M., Jolly, J. K., Wu, Z., Denniss, J., Lad, E. M., Guymer, R. H., et al. (2021). Fundus-controlled perimetry (microperimetry): Application as outcome measure in clinical trials. *Prog. Retin Eye Res.* 82, 100907. doi:10.1016/j.preteyeres.2020.100907
- Saraf, S. S., Tyring, A. J., Chen, C. L., Le, T. P., Kalina, R. E., Wang, R. K., et al. (2019). Familial retinal arteriolar tortuosity and quantification of vascular tortuosity using swept-source optical coherence tomography angiography. *Am. J. Ophthalmol. Case Rep.* 14, 74–78. doi:10.1016/j.ajoc.2019.03.001
- Silva, M. F., Mateus, C., Reis, A., Nunes, S., Fonseca, P., and Castelo-Branco, M. (2010). Asymmetry of visual sensory mechanisms: Electrophysiological, structural, and psychophysical evidences. *J. Vis.* 10, 26. doi:10.1167/10.6.26
- Steel, D. H., and Lotery, A. J. (2013). Idiopathic vitreomacular traction and macular hole: A comprehensive review of pathophysiology, diagnosis, and treatment. *Eye (Lond)* 27 (1), S1–S21. doi:10.1038/eye.2013.212
- Tomita, R., Iwase, T., Ueno, Y., Goto, K., Yamamoto, K., Ra, E., et al. (2020). Differences in blood flow between superior and inferior retinal hemispheres. *Invest. Ophthalmol. Vis. Sci.* 61, 27. doi:10.1167/iovs.61.5.27
- Yagi, T., Sakata, K., Funatsu, H., and Hori, S. (2012). Evaluation of perifoveal capillary blood flow velocity before and after vitreous surgery for epiretinal membrane. *Graefes Arch. Clin. Exp. Ophthalmol.* 250, 459–460. doi:10.1007/s00417-011-1618-8



OPEN ACCESS

EDITED BY

Yanwu Xu,
Baidu, China

REVIEWED BY

Jinhai Huang,
Fudan University, China
Yifan Xiang,
Sun Yat-sen University, China
Tae Keun Yoo,
B&VIIT Eye center/Refractive surgery & AI
Center, Republic of Korea
Qi Dai,
Wenzhou Medical University, China

*CORRESPONDENCE

Qin Jiang,
✉ jqin710@vip.sina.com
Keran Li,
✉ kathykeran860327@126.com

[†]These authors share first authorship

RECEIVED 27 February 2023

ACCEPTED 17 April 2023

PUBLISHED 28 April 2023

CITATION

Wang S, Ji Y, Bai W, Ji Y, Li J, Yao Y,
Zhang Z, Jiang Q and Li K (2023),
Advances in artificial intelligence models
and algorithms in the field of optometry.
Front. Cell Dev. Biol. 11:1170068.
doi: 10.3389/fcell.2023.1170068

COPYRIGHT

© 2023 Wang, Ji, Bai, Ji, Li, Yao, Zhang,
Jiang and Li. This is an open-access
article distributed under the terms of the
[Creative Commons Attribution License
\(CC BY\)](https://creativecommons.org/licenses/by/4.0/). The use, distribution or
reproduction in other forums is
permitted, provided the original author(s)
and the copyright owner(s) are credited
and that the original publication in this
journal is cited, in accordance with
accepted academic practice. No use,
distribution or reproduction is permitted
which does not comply with these terms.

Advances in artificial intelligence models and algorithms in the field of optometry

Suyu Wang^{1,2†}, Yuke Ji^{1,2†}, Wen Bai^{1,2†}, Yun Ji³, Jiajun Li^{1,2},
Yujia Yao^{1,2}, Ziran Zhang^{1,2}, Qin Jiang^{1,2*} and Keran Li^{1,2*}

¹Department of Ophthalmology, The Affiliated Eye Hospital of Nanjing Medical University, Nanjing, China,

²The Fourth School of Clinical Medicine, Nanjing Medical University, Nanjing, China, ³Affiliated Hospital of Shandong University of Traditional Chinese Medicine, Jinan, Shandong, China

The rapid development of computer science over the past few decades has led to unprecedented progress in the field of artificial intelligence (AI). Its wide application in ophthalmology, especially image processing and data analysis, is particularly extensive and its performance excellent. In recent years, AI has been increasingly applied in optometry with remarkable results. This review is a summary of the application progress of different AI models and algorithms used in optometry (for problems such as myopia, strabismus, amblyopia, keratoconus, and intraocular lens) and includes a discussion of the limitations and challenges associated with its application in this field.

KEYWORDS

artificial intelligence, optometry, myopia, strabismus, amblyopia, corneal conus, artificial lens

1 Introduction

Artificial intelligence (AI) is a relatively new technology that endows machines with human behavior, thinking, and emotional abilities and can liberate human beings from tedious physical and mental labor and assist in the production and development of fields such as the economy, culture, and social life. AI, as a subfield of computer science, simulates human intelligence using algorithms that are developed using computers to engage in human work (Nuzzi et al., 2021). Machine learning (ML) is a research field of AI, which is a technology that allows computer systems to learn automatically from data and improve performance. Deep learning (DL) is a research field of ML, which is a representation learning algorithm based on artificial neural network. The relationship between AI, ML, and DL is shown in Figure 1. Current, commonly used AI algorithms include ML, DL, artificial neural networks, deep neural networks (DNNs), convolutional neural networks (CNNs), and migration learning. Over the past few years, the great development of computer science and technology has led to accelerated evolution in the field of AI, accelerating its application in medicine, especially ophthalmology. The first ophthalmic AI device, IDx-DR, was approved for listing with landmark significance on 11 April 2018, opening a new chapter on the combination of AI with ophthalmology. Since then, the application of AI in the ophthalmology has entered a new stage of development, leading to a series of satisfactory research results in the diagnosis, classification, recognition, and screening of ophthalmic diseases, such as diabetic retinopathy (Deepa et al., 2022; Hardas et al., 2022; Zhang et al., 2022), age-related macular degeneration (Glaret Subin and Muthukannan, 2022; Sotoudeh-Paima et al.,

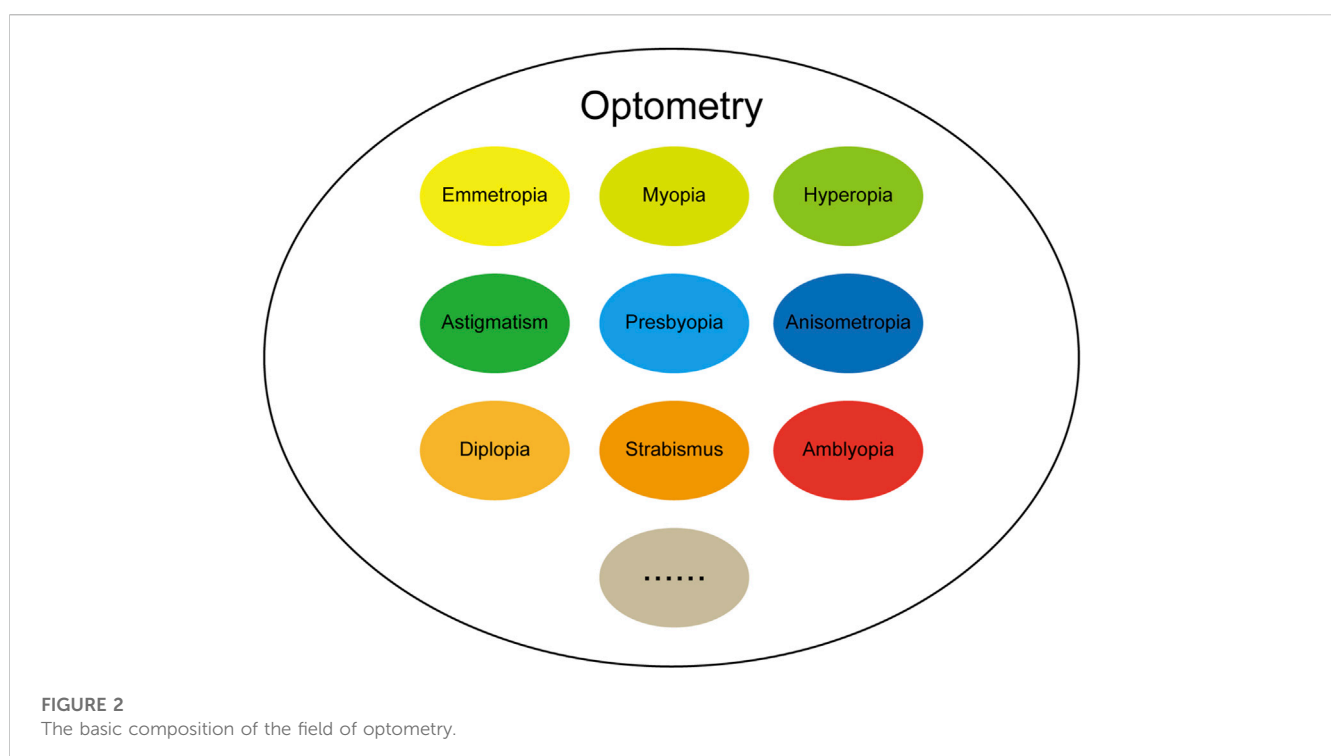


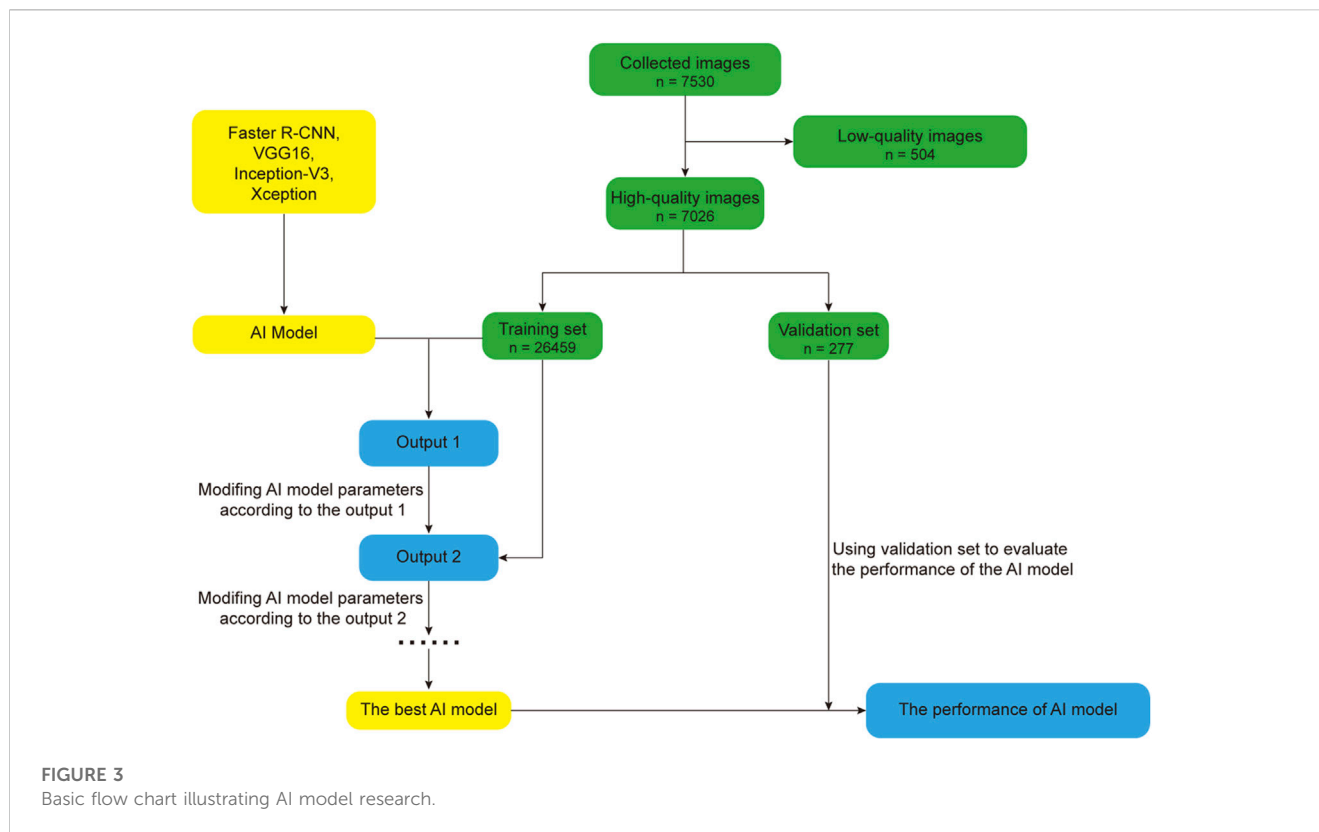
2022; Wang et al., 2022), retinopathy of prematurity (Coyner et al., 2022; Li et al., 2022; Wu et al., 2022), glaucoma (Dong et al., 2022; Li et al., 2022; Xiong et al., 2022), and retinal vein occlusion (Miao et al., 2022; Ren et al., 2022; Zhang et al., 2022).

The term optometry originated in the ancient Greek words *optos* (“see”) and *metron* (“measure”), indicating that it is closely related to “eyes” and “vision.” At the beginning of the 20th century, visual optics was defined as “studying the philosophy of light and vision,” and included a deep understanding of the connotation of the relationship between “light” and “vision”; By the middle of the 20th century, people understood optical vision as “the art of determining the visual state of normal people or correcting the abnormal state through glasses,” and the understanding and correction of vision became more specific. After hundreds of years of evolution and development, optometry has since developed rapidly. In terms of composition, the field of optometry mainly includes emmetropia, myopia, hyperopia, presbyopia, astigmatism, anisometropia, strabismus, amblyopia and so on, as shown in Figure 2. The continuous increase in the application of AI in the ophthalmology in recent years has achieved many remarkable research results. Here, we aimed to review the recent research results of using AI in the field of ophthalmic optometry over the past few years, with the challenges and limitations of AI in optometry applications discussed.

2 Application of AI models and algorithms in the field of optometry

In this section, we mainly review the research progress of AI in the field of optometry in the past 5 years. AI has carried out a lot of research in the field of optometry, especially in the diagnosis, screening and treatment of diseases. In recent years, with the continuous development and improvement of AI technology, the research of AI in the field of optics has become more in-depth and extensive. In order to better describe the basic flow of AI research, we





take the DL model in [Zheng et al. \(2021\)](#) as an example, the basic flow of AI model research is illustrated in [Figure 3](#). The process of developing an AI model involves deleting low-quality images and randomly dividing the remaining high-quality images into training and verification sets, with which the training set is optimized to obtain the best possible AI model and the performance is verified using the verification set.

2.1 Application of AI models and algorithms in myopia

Myopia is a type of ametropia in which parallel light is focused on the front of the retina through the intraocular refractive medium and thus a clear image is not formed on the retina. The problem occurs mainly during childhood and early adulthood ([Morgan et al., 2018](#)). Although there is still much to learn about the etiology of myopia, the general consensus is that genetic, environmental, and biochemical variables play a role in the development of myopia. Myopia in children is mostly caused by a decline in outdoor playtime and an increase in time spent staring at screens. The mechanism of myopia progression mainly includes: 1) accommodative lag, 2) retinal peripheral defocus theory, 3) scleral thinning and ocular axial lengthening caused by extracellular matrix remodeling, 4) changes in the level of retinal nerve growth factor and inflammatory factors, *etc.* According to recent studies, alterations in the choroid's thickness and function are also variables in the evolution of myopia. The choroid may operate as a barrier to the diffusion of endogenous growth hormones that encourage axial elongation. Adults over 50 can also develop nuclear myopia due

to cataracts ([Amirsolaimani et al., 2017](#); [Bullimore and Brennan, 2019](#); [Wong et al., 2021](#)). The issue is thus a public health problem of widespread concern. High and pathological myopia can significantly increase the incidence of retinal detachment, myopic macular degeneration, macular choroidal neovascularization, and other diseases. According to statistics, more than 150 million people worldwide suffer from moderate to severe visual impairment due to uncorrected ametropia ([Baird et al., 2020](#); [Blindness G.B.D., 2021](#)). At present, the main treatment methods are drug therapy (such as atropine eye drops), instrumental correction (such as frame glasses and keratoscopes), and surgical treatment (such as femtosecond pulsed or excimer lasers) ([Li and Yam, 2019](#); [Weiss and Park, 2019](#); [Tsai et al., 2021](#)). However, the complex causes and the large number of people affected renders large-scale screening and stratified analysis of myopia difficult, and the serious complications that are associated with the problem are generally not detected early enough for suitable intervention. It is therefore important that high-risk groups for high myopia are accurately identified and treated in a timely and effective manner to delay the progression of the disease. The development of AI for medical use has led to remarkable results in myopia prediction, diagnosis, screening, follow-up, and treatment ([Gunasekaran et al., 2021](#)). It can achieve effective data management and analysis, deeply excavating the inherent mechanisms by which myopia develops, and the big data storage function associated with AI is conducive to the accumulation of numerous individual experiences, thus playing an important auxiliary role in diagnosis and classification.

One development in the use of AI to diagnose myopia was made by [Varadarajan et al. \(2018\)](#), who constructed a DL model based on a residual network and a soft-attention layer and used it to analyze

226 870 fundus images. The model can predict spherical diopters, cylindrical diopters, and equivalent spherical equivalents by analyzing millions of parameters such as picture pixel values to judge the ametropia situation. A total of 39 757 fundus images were used to validate the model. The results showed average absolute errors of 0.56 D and 0.91 D, respectively, for the two data sets, realizing a technical leap in accurately predicting refractive errors from retinal fundus images. [Lin et al. \(2018\)](#) established an AI model that can predict myopia in children on the basis of a random forest algorithm using refractive data for 132 457 children from the electronic medical record database at eight eye centers, which were applied to training and verification. The model predicts myopia in children under 18 years of age by analyzing data such as age, spherical equivalent, and the annual myopia progression rate. The results showed an AUC between 0.940 and 0.985 for high myopia within 3 years, 0.856 and 0.901 within 5 years, and 0.801 and 0.837 within 8 years, indicating that the model can accurately predict the incidence of high myopia in school-age children at specific points in the future. In a studying the prediction of axial myopia, [Tang et al. \(2020\)](#) used six different ML algorithms to build an AI model that can predict axial length in children and optimized the AI model using cross-sectional datasets. The axial length for the children was predicted by analyzing variables such as sex, age, central corneal thickness, spherical equivalent error, K-means, and the black-and-white corneal diameter for 1,011 myopic children aged 6–18 years old. The results indicated that robust linear regression model had the best prediction result for eye-axis length, with an R^2 of 0.87, proving that the algorithm could be used to estimate the physiological components of eye axis growth and provide data support for separating non-physiological components from eye axis elongation for other therapeutic methods. To better predict adolescent myopia, [Yang et al. \(2020\)](#) used a support vector machine to establish a prediction model for juvenile myopia, using data from 3,112 pupils (including heredity, eye habit, environment, and diet) and constructed a dataset for training and testing the model using univariate and multivariate correlation analyses. The results showed an accuracy, specificity, sensitivity, and AUC of 0.93, 0.94, 0.94, and 0.98, respectively, for predicting myopia, proving that the model can comprehensively analyze several causes of myopia and can be used to help formulate myopia prevention and control policies. These studies indicate that AI has opened up a novel prediction model for myopia prediction through image and related data analysis that has high accuracy, is feasible for clinical application, and provides new ideas for myopia prevention and control. [Foo et al. \(2023\)](#) developed a deep learning system to identify children at risk of developing high myopia. In this study three distinct algorithms were derived (image, clinical and mix models) to predict the development of high myopia in adolescents after 5 years. 7,456 baseline fundus images were used for training and verification, 821 images with clinical data for external validation. Results showed that this DLS achieved a high accuracy with AUC all above 0.90, and can prevent the progression and complications of myopia in adulthood, help ophthalmologists to make clinical decisions.

Through analyzing eye images, AI can thus assist in the diagnosis and classification of myopia, improving the diagnostic efficiency and aiding ophthalmologists in screening for large-scale myopia while also facilitating the long-term follow-up of patients

with high myopia, reducing the heavy burden caused by visual impairment and even blindness that can result from myopia. [Sogawa et al. \(2020\)](#) constructed several models using different DL algorithms (VGG16, VGG19, DenseNet121, InceptionV3 and ResNet50) and used them to analyze 910 eye optical coherence tomography (OCT) images. The experimental results showed that the AUC, sensitivity, and specificity for the DL model were 0.970, 0.906, and 0.942; the average correct classification rate for high myopia, myopic choroidal neovascularization, and retinoschisis images of 0.889 shows the feasibility of using these algorithm models in screening for single diseases and provides support for preventing vision loss in patients with myopic macular degeneration. To assist diagnosis of myopia in the clinical, [Yang et al. \(2020\)](#) constructed an AI diagnosis model using deep convolutional neural networks (DCNNs) and the VGG-Face algorithm. In this study, the eye appearance images of 2,350 children aged 6–18 years were collected from three angles; front, side, 45° anterior side, and spherical equivalent refraction was used to determine the refraction state of each eye from the images. The AUC, sensitivity, and specificity of the model for the diagnosis of myopia were 0.9270, 0.8113, and 0.8642, respectively, after training and verification, rendering vision screening possible without the need for examination, thus providing a more convenient method for routine vision screening. [Hemelings et al. \(2021\)](#) used the CNN to construct a DL model that can diagnose pathological myopia and used 1,200 color fundus images for the model training and testing. The final results showed that the AUC of the model for the diagnosis of pathological myopia was 0.9867. [Li et al. \(2023\)](#) collected 1,200 retinal fundus images to train a novel deep learning model on the basis of MyopiaDETR algorithm. This model using 2D fundus images as input, which can diagnose and discriminate different kinds of myopia such as normal myopia (NM), high myopia (HM) and pathological myopia (PM) through the analysis of the images. Besides, it has significant advantages over the traditional algorithms in terms of the accuracy and speed of the diagnosis. The results showed excellent localization and classification performance in the diagnosis of PM, reaching AP50 of 0.8632. [Li et al. \(2022\)](#) collected 412 OCT macular images of patients with high myopia and constructed an AI model based on the InceptionResnetV2 algorithm to identify four visual threats: retinoschisis, macular hole, retinal detachment, and pathological myopic choroidal neovascularization. The results showed an AUC of between 0.961 and 0.999 for the model, with both sensitivity and specificity reaching >0.90. These results show that AI is particularly accurate in diagnosing myopia and its complications and indicate that it can play an important role in large-scale myopia screening.

Refractive surgery, which can be divided into corneal refractive surgery and intraocular refractive surgery, is used to correct refractive errors in adult patients with stable myopia. At present, corneal refractive surgery comprises laser epithelial keratomileusis (LASEK), laser *in situ* keratomileusis (LASIK), and small-incision lens extraction (SMILE). Intraocular surgery includes lens implantation and cataract surgery. Some progress has also been made in the application of AI to preoperative screening and surgical planning for refractive surgery. [Xie et al. \(2020\)](#) constructed a DL model based on the InceptionResNetV2 algorithm used

6,465 corneal tomography images (including axial curvature, anterior corneal topography, posterior corneal topography, and corneal thickness) to train and test the model to screen potentially suitable patients for refractive surgery, with a screening accuracy of 0.947. Yoo et al. (2020) developed an ML model based on a multiclass XGBoost model that can select the best refractive surgery for patients with myopia. The algorithm can automatically extract 80 features from corneal topography and convert the numbers from the image into textual data. Eye examination data were collected from 18 480 myopic patients who planned to undergo refractive surgery and divided into the LASEK, LASIK, SMILE, and contraindication groups. The results showed accuracies of 0.810 and 0.789 for the internal and external verification datasets, respectively, indicating that it can synthesize ophthalmic data and select the most suitable operation plan at expert level. Wan et al. (2023) constructed a Deep learning model on basis of Resnet50 and XG Boost algorithms, aiming to Predict the early postoperative visual acuity after small-incision lenticule extraction surgery. In this study, 10,176 laser scanning images from the surgical videos were collected for training, and patients were classified by good or poor recovery. The results turned out with the accuracy of 0.96, AUC value of the DL model was 0.962–0.998. This model enables accurate prediction of early postoperative vision and complications only through surgical videos and pictures, which has an important influence on the application of AI in refractive surgery.

Contact lens Contact lens is a common adjuvant therapeutic tool in the field of optometry, includes rigid contact lens, soft contact lens and Orthokeratology (OK). Orthokeratology is a crucial component of clinical myopia management since it is a successful myopia control strategy. Nowadays, Orthokeratology (OK) is second only to muscarinic antagonists in terms of effectiveness in reducing childhood myopia. AI-assisted contact lens therapy is gradually becoming popular. In order to predict the curvature of orthokeratology lens, Fan et al. (2022) construct a machine learning model based on Linear Regression (Robust), Support Vector Machines (linear), Bagged Trees, Gaussian processes algorithms. Using sex, age, horizontal visible iris diameter (HVID), spherical refraction (SER), anterior chamber depth (ACD), axial length (AL) etc., of 1,271 patients with myopia as input variables, to estimate the alignment curve (AC) curvature of orthokeratology lens. Results indicated that the linear SVM and Gaussian process machine learning models achieves best performance, the R-squared values for the output AC1K1, AC1K2 and AC2K1 values were 0.91, 0.84, and 0.73. Prediction of orthokeratology lens curvature based on the ML model can reduce the number of lens trials, improve efficiency and accuracy, and reduce the probability of cross-infection caused by the test lens. By analyzing the clinical data of 1,037 Chinese myopic adolescents, Fan et al. (2021), developed a ML model on basis of Support vector machines (SVMs), Gaussian processes, Linear Regression (Robust) algorithms. This model is able to predict the return zone depth (RZD) and landing zone angle (LZA) of four quadrants of corneal refractive therapy (CRT) lenses under different combinations of age, sex and ocular parameters. Results showed that this model achieved higher accuracy, and is easier to use and faster to implement compared to the traditional sliding card method.

To predict the treatment effect of orthokeratology, Fang et al. (2023) developed a ML model based on Logistic least absolute shrinkage and selection operator (LASSO) regression algorithm. The study collected the ocular parameters and clinical characteristics of 91 patients undergoing ortho-k treatment. It turned out that factors such as, lens wearing time, age, axial length, outdoor activity time, and white-to-white distance were strongly associated with treatment effects, with AUC values 0.949 and C-statistic of the predictive model was 0.821. This demonstrates how the ML model-based prediction of contact lens efficacy can help clinicians make clinical judgments and select more suitable treatment alternatives for patients. The above studies are summarized in Table 1.

Myopia as a common refractive problem exists widely in adolescents and adults. Myopia tends to progress rapidly in adolescence. Variable degrees of fundus changes will also be present in individuals with high myopia in addition to vision loss, floaters, and flash sensations. The risk of retinal detachment, hiatus, fundus hemorrhage, and neovascularization is significantly higher than it is in healthy individuals. Therefore, early prediction and diagnosis of different types of myopia are of great significance for myopia treatment and prevention of complications. The prediction, classification diagnosis and auxiliary treatment of myopia based on artificial intelligence can greatly improve the diagnosis and treatment efficiency and accuracy of clinicians, and play an important role in the large-scale screening of myopia.

2.2 Application of AI models and algorithms in strabismus

Strabismus refers to any clinical phenomenon of visual axis deviation that can be caused by binocular abnormalities, neuromuscular abnormalities in eye movement control, or various other mechanical limitations (Sousa de Almeida et al., 2015). Strabismus can be divided into different types according to fusion state, eye movement and fixation, eye position, and age of occurrence (Castanes, 2003; Mojon-Azzi et al., 2011), and is commonly associated with visual development in children. Studies have shown that a prevalence of is 2%–4% for strabismus in children worldwide, which is significantly higher than observed in adults (Chia et al., 2010). One of the main issues with strabismus is that it can lead to abnormal visual functions such as strabismic amblyopia and seriously endanger the physical and mental health of infants and children, rendering timely diagnosis and treatment particularly important (Kelkar et al., 2015; Debert et al., 2016). At present, the common examination methods for strabismus in clinics include masking and cover-uncover tests, alternate cover tests, prism and cover tests, corneal reflection methods, synoptophore examinations, diagnostic strabismus tests, and eye movement traction tests (Chia et al., 2007; Wang et al., 2018; Yoo et al., 2019). Traditional strabismus diagnosis methods usually require manual examination by ophthalmologists, which is time-consuming and labor-intensive with subjective results. The application of AI technology in strabismus amblyopia has achieved much and is thus expected to improve the current state of diagnosis and treatment for strabismus amblyopia.

TABLE 1 Application summary of different AI models and algorithms used in myopia.

Authors	Task	Sample size	AI algorithms	Output
Varadarajan et al. (2018)	Prediction	266627 images	Residual network, Soft-attention layer	Average absolute error of two datasets = 0.56 D, 0.91 D
Lin et al. (2018)	Prediction	132 457 individuals	Random forest	AUC for 3 years = 0.940–0.985
				AUC for 5 years = 0.856–0.901
				AUC for 8 years = 0.801–0.837
Tang et al. (2020)	Prediction	1,011 individuals	Linear Regression (linear)	R2 of robust linear expression model = 0.87
			Linear Regression (Robust)	
			SVM (linear)	
			SVM (Quadratic)	
			SVM (Cubic)	
			Bagged Trees	
Yang et al. (2020)	Prediction	3,112 individuals	SVM	Accuracy = 0.93
				Specificity = 0.94
				Sensitivity = 0.94
				AUC = 0.98
Foo et al. (2023)	Prediction	7,456 images	image, clinical and mix (image + clinical) models	Image models
				AUC of Primary dataset = 0.93–0.95
				AUC of Test dataset = 0.91–0.93
				Clinical models
				AUC of Primary dataset = 0.90–0.97
				AUC of Test dataset = 0.93–0.94
				Mixed (image + clinical) models: AUC of Primary dataset = 0.97
				Test dataset = 0.97–0.98
Sogawa et al. (2020)	Classification	910 images	VGG16	AUC = 0.970
			VGG19	Sensitivity = 0.906
			DenseNet121	Specificity = 0.942
			InceptionV3ResNet50	Accuracy = 0.889
Yang et al. (2020)	Diagnosis	2,350 individuals	DCNN	AUC = 0.9270, sensitivity = 0.8113
			VGG-Face	specificity = 0.8642
Hemelings et al. (2021)	Diagnosis	1,200 images	CNN	AUC = 0.9867
Li et al. (2023)	Diagnosis	1,200 images	MyopiaDETR	A PAP50 = 0.8632
Li et al. (2022)	Classification	412 images	InceptionResnetV2	AUC = 0.961–0.999
				Sensitivity >0.90, Specificity >0.90
Xie et al. (2020)	Screening	6,465 images	InceptionResNetV2	Accuracy = 0.947
Yoo et al. (2020)	Surgery	18,480 individuals	Multiclass XGBoost	Accuracy of internal validation dataset = 0.81
				Accuracy of external validation datasets = 0.789
Wan et al. (2023)	Prediction	10176 images	Resnet50	Accuracy = 0.96
			XG Boost	AUC = 0.962–0.998

(Continued on following page)

TABLE 1 (Continued) Application summary of different AI models and algorithms used in myopia.

Authors	Task	Sample size	AI algorithms	Output
Fan et al. (2021)	Prediction	1,271 individuals	Linear Regression (Robust)	R-squared values for the output AC1K1, AC1K2 and AC2K1 values = 0.91, 0.84, 0.73
			SVM (linear)	
			Bagged Trees	
			Gaussian processes	
Fan et al. (2021)	Prediction	1,037 individuals	SVM (SVMs)	R values for the nasal, temporal, superior and inferior LZA = 0.843, 0.693, 0.866, 0.762, RZD = 0.970, 0.964, 0.975, 0.964
			Gaussian processes	
			Linear Regression (Robust)	
Fang et al. (2023)	Prediction	91 individuals	Logistic least absolute shrinkage and selection operator (LASSO) regression	AUC = 0.949
				95%CI:0.815, 0.827

Kang et al. (2022) constructed a DL model based on the U-Net network that can segment the cornea and scleral limbus and then classify the segmented eye region to realize automatic strabismus detection using 828 gaze photographs of strabismus patients with different eye positions used to train and verify the model. After verification, an accuracy of 0.9984 was obtained for corneal segmentation using the model, with a sensitivity of 0.9747, specificity of 0.9990, diameter similarity coefficient (DSC) of 0.9688, while the accuracy of limbal segmentation was 0.9992, with a sensitivity of 0.9563, specificity of 0.9996, and DSC of 0.9571. To develop a DL system that can assist in diagnosing strabismus, Mao et al. constructed a system based on InceptionResNetV2 using 5,797 corneal light reflection photos to develop, train, and verify the system (Mao et al., 2021). The system diagnoses strabismus by identifying different gaze states in reflective corneal photos. After training and testing, the experimental results showed sensitivity, specificity, and AUC of 0.991, 0.983 and 0.998 respectively, for the system. Another app that was developed by de Figueiredo et al. (2021) based on the Resnet50 neural network can diagnose strabismus by identifying the different gaze positions of patients. The app was developed using gaze photos from 110 patients and the overall accuracy in the diagnosis of strabismus was between 0.42 and 0.92, with precision between 0.28 and 0.84. The above studies show that the AI model performs well in the auxiliary diagnosis of strabismus and has the potential for clinical application, where it may improve the accuracy of strabismus diagnosis and reduce the work pressure of clinicians.

Zheng et al. (2021) used a convolutional neural network and three deep convolution neural networks (Faster R-CNN, VGG16, Inception-V3, and Xception) to construct a DL model that can detect strabismus through the gaze of children using 7,530 primary gaze photos to develop, train, and verify the model. After external verification, a sensitivity of 0.940 was with a specificity of 0.993, AUC of 0.990, and accuracy of 0.950, for the model, which is better than that acquired by clinicians. Chen et al. (2018) constructed a DL model that can recognize strabismus using six different convolution neural networks (AlexNet, VGG-S, VGG-M, VGG-16, VGG-F, VGG-19). They collected gaze deviation images from 42 subjects and used them to train and verify the model. The results indicated

that VGG-S had the best performance in recognizing strabismus, with a specificity of 0.960 and sensitivity of 0.941. Huang et al. (2022) constructed a strabismus screening and classification method based on the ResNet-12 network and used positive facial images from 60 subjects to train and test. This method identifies eye position in frontal facial images to diagnose strabismus and resulted in accuracy, sensitivity, and specificity for screening and classification values of 0.805, 0.768, and 0.842, respectively. To better assist in strabismus screening, Huang et al. (2021) constructed a DL model for strabismus screening based on the convolution neural network with 60 frontal facial images for training and verification. The experimental results showed that sample mean and standard deviation values for normal images of 1.073 ± 0.014 and 0.039 , respectively, while those for strabismus images were 1.924 ± 0.169 and 0.472 , respectively. The results of the above AI model in strabismus screening and recognition indicate that AI will likely be applied to strabismus screening in the future. The development of remote diagnosis methods for strabismus also overcomes limitations surrounding spatial distance, which is also significant for early detection and treatment in ophthalmopathy.

Liu et al. (2019) developed a DL model based on a support vector machine that can predict the time it will take for a patient to achieve visual function following strabismus surgery from the deviation angle of the eye position 1 day and 6 months after the operation. In this study, using the surgical data of 132 patients to train and test the model and a prediction accuracy of 0.821 was achieved. To aid patients with strabismus in selecting the best surgical treatment strategy, Almeida et al. (2015) proposed an AI method based on support vector regression, with the clinical data of 88 strabismus patients used to train and verify the method. This method can be used to decide the best surgical treatment strategies for strabismus patients according to the deviation degree, deviation type, visual acuity data, diopter, and fundus examination data of strabismus patients. Finally, the results showed that the average error in the proposed surgical treatment strategy was 0.5 mm for recoil and 0.7 for resection for medial rectus surgery while the mean error was 0.6 for recoil and 0.8 for resection in lateral rectus surgery, indicating that this method is feasible for use in planning strabismus surgery. Lou et al. (2022) constructed a novel recurrent residual CNN with global attention gate based on GAR2U-Net to automatically evaluate

TABLE 2 Application summary of different AI models and algorithms used for strabismus.

Authors	Task	Sample size	AI algorithms	Output
Kang et al. (2022)	Diagnosis	828 images	U-Net	Accuracy = 0.9984
				Sensitivity = 0.9747
				Specificity = 0.9990
				DSC = 0.9688
Mao et al. (2021)	Diagnosis	5,797 images	InceptionResNetV2	Sensitivity = 0.991
				Specificity = 0.983
				AUC = 0.998
de Figueiredo et al. (2021)	Diagnosis	110 individuals	Resnet50	Accuracy = 0.42–0.92
				Precision = 0.28–0.84
Zheng et al. (2021)	Detection	7,530 images	Faster R-CNN	Sensitivity = 0.940
			VGG16	Specificity = 0.993
			Inception-V3,Xception	AUC = 0.990
				Accuracy = 0.950
Chen et al. (2018)	Detection	42 individuals	AlexNet	Specificity = 0.960
			VGG-F	
			VGG-M	
			VGG-S	Sensitivity = 0.941
			VGG-16	
			VGG-19	
Huang et al. (2022)	Detection	60 individuals	ResNet-12	Accuracy = 0.805
				Sensitivity = 0.768
				Specificity = 0.842
Huang et al. (2021)	Detection	60 images	CNN	The sample mean and standard deviation of normal images = $1.073 \pm 0.014, 0.039$
				The sample mean and standard deviation of strabismus images = $1.924 \pm 0.169, 0.472$
Liu et al. (2019)	Prediction	132 individuals	SVM	Accuracy = 0.821
Almeida et al. (2015)	Prediction	88 individuals	Support Vector Regression	The average error for recoil = 0.5 mm
				The average error for resection = 0.7 mm
				The mean error for recoil = 0.6 mm
				The mean error for resection = 0.8 mm
Lou et al. (2022)	Prediction	106 eyes	GAR2U-Net	Kendall's tau: 0.721; 95% confidence interval: 0.652 to 0.779; $p < 0.001$

the Inferior oblique overaction (IOOA). This study included 106 eyes of 72 consecutive patients, and the height difference between the inferior corneal limbus of both eyes were measured. The results showed significant correlations measurements and clinical gradings. The new method allows for objective, accurate and reproducible IOOA measurements and has obvious advantages such as low cost, easy acquisition and wide measurement range compared with conventional methods. The above studies are summarized in Table 2.

Strabismus as a common eye disease, if not timely diagnosis and treatment, may lead to significant vision loss or even blindness. More importantly, strabismus will bring serious psychological burden to patients, resulting in many adverse consequences. Therefore, it is very important for timely diagnosis and treatment of strabismus. The above AI studies show that AI can play an important role in the diagnosis of strabismus. It can not only diagnose strabismus without ophthalmologist, but also significantly reduce the cost of diagnosis.

2.3 Application of AI models and algorithms in keratoconus

Keratoconus (KC) is a non-inflammatory corneal disease characterized by thinning of the corneal stroma, anterior protrusion, and irregular astigmatism. Thinning occurs in or near the center of the cornea, with subtemporal thinning the most common (Romero-Jiménez et al., 2013; Sharif et al., 2018). The prevalence rate of KC is approximately 1/2000–1/500, and it usually occurs during puberty, generally in one eye, with early symptoms including blurred vision and photophobia. Visual acuity declines progressively as the disease progresses, with irregular corneal astigmatism, monocular diplopia, and even irreversible vision loss observed (Jones-Jordan et al., 2013; Mostovoy et al., 2018; Flockerzi et al., 2021). The etiology and causes of this disease have not yet been clarified; however, studies have suggested that it may be related to structural changes in the corneal collagen tissue (Kankariya et al., 2013). Early diagnosis of KC is difficult, and is generally made by comprehensive analysis of the corneal topography and biomechanical characteristics during evaluation (Randleman et al., 2008; Santodomingo-Rubido et al., 2022). Currently, contact lenses, corneal cross-linking treatment, keratoplasty, and several other methods are used to treat the disorder (Godefrooij et al., 2017; Röck et al., 2018; Ferdi et al., 2019); however, corneal transplantation can lead to rejection, complicated cataracts, iris atrophy, secondary glaucoma, and other problems (Shah et al., 2010). Therefore, the early detection of KC and timely intervention are of great significance in controlling the progress of the disease and maintaining good vision. AI models that are useful in diagnosing KC have so far been established using SVM, decision tree, CNN, multilayer perception neural networks (MLPNN), and feed forward neural networks (FNN), all of which have been found helpful in the early diagnosis of KC (artificial intelligence and corneal diseases, 2022).

Combining corneal topography with AI was found useful in improving the accuracy of KC diagnosis. Using three types of convolution neural networks (ResNet152, VGG16Net, Inception v3), Kuo et al. (2020) constructed a DL model that can diagnose KC and 359 corneal topographic maps were used to train and verify the model. The results showed sensitivities and specificities of >0.90 for all the CNN models, of which ResNet152 exhibited the best diagnostic performance with an AUC value of 0.995. Al-Timemy et al. (2021) constructed an AI model that can diagnose KC based on the hybrid DL algorithm using 3,794 corneal images (divided into normal cornea, suspected KC, and keratoconus). According to data describing the anterior and posterior eccentricity, anterior and posterior sagittal arc, and corneal thickness, corneal features were extracted for training and verification of the AI model, with results indicating AUC values of 0.99 and 0.93 and accuracies of 0.988 and 0.815, respectively, for KC. Compared with the previous single CNN model, which is sometimes highly sensitive to slight disturbances in the pixels comprising the input image, the hybrid algorithm provides more reliable results. Zéboulon et al. (2020) established an ML model based on a CNN to diagnose KC. They collected 3,000 corneal topography maps (normal corneal topography, KC topography, and corneal topography with a history of refractive surgery) and

used the data of anterior corneal height map, posterior corneal height map, anterior keratometry map, and corneal thickness map for training and testing. After testing, the results showed that the accuracy of the model was as high as 0.993 in diagnosing KC, and thus has potential for application in clinical practice. Kamiya et al. (2021) constructed a DL model for diagnosing normal corneas and KC based on the VGG-16 neural network, using 519 corneal topographic images that were coded by color to train and test the model. The results showed that the model performed well in diagnosing KC, with an accuracy of 0.966, sensitivity of 0.988, and specificity of 0.944. Using CNNs, Kato et al. (2021) constructed an AI model that could predict the progress of KC. In this study, 274 corneal tomography images were collected and before and after anterior keratogram and corneal thickness images combined to form the training set and test set of DL model. measured to form the training and test sets for the DL model. The results showed that AUC, sensitivity, and specificity values of 0.81, 0.78, and 0.70, respectively, for predicting KC progression. The above research results illustrate the usefulness of using AI for the auxiliary diagnosis of KC, for which it can significantly improve the accuracy of a diagnosis, save time, and provide the best treatment for patients.

AI can help ophthalmologists effectively distinguish KC from normal corneas and classify diseases by analyzing the corneal shape and thickness, among other parameters. In order to assist KC classification, Feng et al. (2021) created a DL algorithm (KerNet algorithm). They used 854 corneal images together with original data such as the anterior and posterior surface curvature, anterior and posterior surface topography, and corneal thickness to form a numerical matrix for the training and verification of the algorithm. The results showed that the algorithm could achieve better results than the most advanced methods in detecting and classifying KC, especially subclinical KC, with an accuracy of 0.95. To distinguish KC from subclinical KC and normal cornea, Abdelmotaal et al. (2020) constructed a DL model based on a CNN and collected 3,218 corneal images for training and testing. The model can be realized using a single image for highly accurate KC classification, with an average of 0.983, and the fact that less computing resources are required renders this model advantageous in terms of applicability to large-scale disease screening without sufficient data. Atila et al. (2021) constructed some DL models using a variety of algorithms (random forest classifier, Gaussian naive Bayes classifier, K neighbors classifier, logistic regression, linear discriminant analysis, decision tree classifier, and support vector machine) for the classification of KC. They used 12 242 corneal topography maps to compare the classification performance of the different DL models. The results indicated that random forest had the best classification performance, with an accuracy as high as 0.95. Cao et al. (2020) constructed an AI model that can distinguish subclinical KC from non-KC based on a variety of DL algorithms (random forest, decision tree, logistic regression, support vector machine, linear discriminant analysis, multilayer perceptron neural network, lasso regression, and k-nearest neighbor). Corneal parameters of 49 subclinical KC and 39 control eyes were analyzed, with diagnostic results showing an AUC of 0.97 for the random forest random forest model. This indicates that selecting a combination of important parameters

TABLE 3 Application summary of different AI models and algorithms in keratoconus.

Authors	Task	Sample size	AI algorithms	Output
Kuo et al. (2020)	Diagnosis	359 images	ResNet152	AUC = 0.995
			VGG16Net	
			Inception v3	
Al-Timemy et al. (2021)	Diagnosis	3,794 images	unsupervised machine learning	AUC = 0.99, 0.93
				Accuracy = 0.988, 0.815
Zéboulon et al. (2020)	Diagnosis	3,000 images	CNN	Accuracy = 0.993
Kamiya et al. (2021)	Diagnosis	519 images	VGG-16	Accuracy = 0.966, Sensitivity = 0.988, Specificity = 0.944
Kato et al. (2021)	Prediction	274 images	CNN	AUC = 0.81
				Sensitivity = 0.78
				Specificity = 0.70
Feng et al. (2021)	Classification	854 images	KerNet	Accuracy = 0.95
Abdelmotaal et al. (2020)	Detection	3,218 images	CNN	Accuracy = 0.983
Aatila et al. (2021)	Classification	12242 images	Random forest classifier	Accuracy = 0.95
			Gaussian naive bayes classifier	
			K neighbors classifier	
			Logistic regression	
			Linear discriminant analysis	
			Decision tree classifier	
			SVM	
Cao et al. (2020)	Classification	88 images	Random forest, Decision tree, Logistic regression, Support vector machine	Accuracy = 0.97
			Linear discriminant analysis	
			Multilayer perceptron neural network	
			Lasso regression	
			K-nearest neighbor	

from a larger set of parameters would lead to more objective and effective KC screening when constructing a ML model, rendering it a useful tool in clinical practice. The above studies are summarized in [Table 3](#).

Late keratoconus often leads to severe vision loss or even blindness in patients. Early and timely treatment can effectively alleviate the progression of keratoconus and protect patients' vision. Therefore, for patients with keratoconus, early diagnosis and timely treatment are very important. The above AI studies show that AI has carried out a lot of research in the diagnosis, classification and prediction of keratoconus, and the AI model has shown good performance. AI model can provide great help to doctors in the clinical diagnosis of keratoconus, and automatically complete the relevant diagnosis and treatment work, so as to reduce the workload of doctors, which has important clinical significance to improve the efficiency of doctors.

2.4 Application of AI models and algorithms in the preoperative measurement and effect prediction of intraocular lenses

An intraocular lens (IOL) is a special lens made of synthetic materials that can replace the human lens ([Lundström et al., 2018](#)). The development of cataract surgery and the demand for high visual quality has meant that cataract surgery has evolved from visual rehabilitation to accurate refractive surgery with high visual quality ([Piovella et al., 2019](#)). The choice of intraocular lens has also gradually diversified from unifocal to functional intraocular lenses ([Simon et al., 2014](#)). The postoperative visual acuity of patients depends to a large extent on accurate biometric and IOL diopter calculations prior to operating. However, the changes that occur in the intraocular structure of some patients before surgery renders calculation of the IOL diopter difficult, and postoperative

complications can easily occur in surgery for issues such as high myopia (Savini and Hoffer, 2018; Yao et al., 2021). In addition, the abnormal position of the IOL that can result from various factors will seriously affect visual quality after surgery (Wang et al., 2022). In recent years, IOL calculation methods based on AI have shown good performance and been proved able to effectively improve the accuracy of IOL diopter calculations (Wang et al., 2016; Melles et al., 2019; Nemeth et al., 2022). At the same time, a variety of methods such as slit-lamp photography, slit-lamp video photography, and OCT can be combined to determine the location of the IOL (Mura et al., 2010; Omoto et al., 2022).

Using AI in designing the IOL calculation formula can improve the accuracy of the calculation according to the characteristics of different patients so that better visual quality can be obtained following surgery. Mori et al. (2021) constructed an ML model based on a support vector regression algorithm to adapt the diopter calculation method for intraocular lens in a specific patient population to improve the accuracy of the calculation. By analyzing the clinical data for 11 611 eyes with a single monofocal IOL implantation model, the constants of the SRK/T and Haigis formulas were optimized and the support vector regression algorithm was used to adapt the SRK/T, Haigis, Hill-RBF, and Barrett Universal II formulas. The results showed a smaller average error in the optimized formula for calculating the IOL diopter than that obtained using the other formulas ($p < 0.001$). To improve the accuracy in calculating the IOL degree for high myopia, Wei et al. (2020) developed an AI calculation model based on the XGBoost regression algorithm. They collected data from 1,564 high myopia eyes for training and verification and combined a constant IOL diopter with the Barrett Universal II formula and other data, they developed a new IOL calculation method. The results showing significant decreases in the median absolute and median square errors as compared to those obtained under the BUII formula ($p \leq 0.001$), and the proportion of eyes with prediction errors within $\pm 0.25D$ increased significantly. Cabeza-Gil et al. (2020) proposed two intraocular lens calculation models based on the DNN algorithm to calculate the biomechanical stability of IOL which were then verified using data from 37,161 cases. Six parameters (length, width, thickness, opening angle of the haptic, tactility, and haptic-optic junction in the reference data) were used to enhance the consistency of patient characteristics so as to improve the success rate of the operation. The results showed Pearson's r values of 0.995 and 0.992 for the two models; indicating good performance. Clarke and Kapelner (2020) designed a more accurate diopter calculation model for the intraocular lens, Bayesian Additive Regression Trees (BART), which was based on the ML algorithm. They collected measurement subsets based on the specific characteristics of patients and their eyes. The results showed an average absolute error of 0.204 D, proving that the diopter of the intraocular lens calculated by this model was more accurate than that obtained by other commonly used formulas.

The calculation formula for the IOL has undergone several generations of evolution at different times. The first-generation formula is based only on regression data, while the second-generation formula includes the influencing factor of axis length and the third-generation formula refers to optics and IOL position factors. Methods for formula optimization are now more abundant,

and combined with artificial intelligence, the accuracy of IOL calculation has been much improved. Guillaume et al. (2021) constructed an ML model based on the multiple linear regression algorithm to improve the IOL formula and constructed the new PEARL-DGS formula to calculate the diopter of IOLs by analyzing the data of 4,242 intraocular lens implants. The examination data of another 677 eyes were collected and compared with the K6 and Olsen, EVO 2.0, RBF 3.0, and BUII formulas, with results showing the smallest calculation error when using the PEARL-DGS formula with an error range of $\pm 0.382 D$, which indicates that completely retraining the formula, rather than the conventional constant adjustment, can allow adaption to the habits of doctors and the characteristics of specific patient groups. Ladas et al. (2021) constructed an AI model based on DL algorithms (extreme gradient boosting, support vector regression, artificial neural network) to optimize the existing diopter calculation formula for intraocular lens and develop a new hybrid formula based on AI. They analyzed the eye data of 1,391 patients who underwent IOL implantation, with the factor axial length, anterior chamber depth, lens thickness, sex, age, and postoperative significant diopter considered, and determined both the average absolute error in each IOL formula and the number of eyes that predicted diopter within 0.5 D. After AI optimization, the average percentage of eyes within $\pm 0.5 D$ predicted by the SRK formula increased to 14%, the Holladay 1 formula increased by 9.3% and the LSF formula increased by 5.3% ($p < 0.05$), while in terms of average absolute error, the predicted diopter of optimized SRK formula decreased to 0.14 D, the Holladay 1 formula decreased to 0.08D and the LSF formula decreased to 0.04D.

In the process of intraocular lens implantation, the influence that location and the size of the anterior and posterior space have on visual quality and postoperative complications can easily be ignored. An IOL localization method based on AI can effectively solve this problem. Schwarzenbacher et al. (2022) used a CNN to construct a DL model that can automatically divide the IOL, Retrolental, and Berger's space and analyze the spatial resolution to accurately locate the target structure. In the study, a total of 92 eye OCT images were used to train and verify the model, with results indicating Precision, Recall, and Dice scores of 0.97, 0.90, and 0.93, respectively, indicating that the model has high accuracy in locating the IOL. This is the first time that this type of algorithm has been proposed to automatically segment the posterior structure of the anterior segment. To evaluate the position of the IOL in three-dimensional space, Xin et al. (2020) constructed an AI evaluation model based on a region-based fully convolutional network (R-FCN), with 86 AS-OCT images used to train and verify the model. The results showed an evaluation efficiency of 0.910 for the model, with intraclass correlation coefficients (ICC) of 0.867 and 0.901 for reliability and repeatability, respectively, evaluating the location of the IOL in a three-dimensional space to provide data support for the design of a better functional IOL. The above studies are summarized in Table 4.

Intraocular lens implantation is a common method of ocular surgery. Patients' postoperative visual acuity is highly correlated with their accurate preoperative biometric features and IOL diopter calculation. AI-based IOL diopter calculation can effectively improve the accuracy and help solve some cases with complicated intraocular structure. In addition, artificial

TABLE 4 Application of different AI models and algorithms in intraocular lens calculation and postoperative prediction.

Authors	Task	Sample size	AI algorithms	Output
Mori et al. (2021)	Optimization	11611 eyes	Support vector regression	The average calculation error of IOL diopter calculated by the optimized formula is smaller than that of other formulas ($p < 0.001$)
Wei et al. (2020)	Design	1,564 eyes	XGBoost regression	Median absolute errors and median square errors decreased significantly ($p < 0.001$)
Cabeza-Gil et al. (2020)	Design	37161 individuals	DNN	Pearson's r of two models = 0.995 and 0.992
Clarke and Kapelner (2020)	Design	5,331 eyes	Bayesian Additive Regression Trees	The average absolute error = 0.204 D
Debellemanière et al. (2021)	Optimization	4,919 eyes	Multiple linear regression	The error range = ± 0.382 D
Ladas et al. (2021)	Optimization	1,391 eyes	Support vector regression	The accuracy rate of each calculation formula is improved after optimization
			Extreme gradient boosting	
			ANN	
Schwarzenbacher et al. (2022)	Location	92 images	CNN	Precision = 0.97
				Recall = 0.90
				Dice score = 0.93
Xin et al. (2020)	Assessment	86 images	Region-based fully convolutional network	Intragroup correlation coefficient of reliability = 0.867
				Intragroup correlation coefficient of repeatability = 0.901

intelligence can assist in determining the location of IOL implantation, which plays an important role in improving patients' visual quality and reducing postoperative complications.

2.5 Application of AI models and algorithms in amblyopia

Amblyopia is a decrease in monocular or binocular best-corrected visual acuity that leads to abnormal visual experiences (monocular strabismus, anisometropia, high ametropia, and form deprivation) during visual development (Kates and Beal, 2021). Factors that cause amblyopia include ametropia, strabismus, anisometropia, ptosis, lens opacity, and form deprivation (Paff et al., 2010; Rajavi et al., 2012; Barrett et al., 2013). According to its etiology, amblyopia is mainly divided into strabismic, anisometropic, ametropic, and form deprivation amblyopia (Maurer and K. S., 2018; Birch, 2013). Amblyopia can be mild, moderate, or severe. The main manifestations of amblyopia are lower than normal best-corrected visual acuity, crowding, paracentric fixation, prolonged PVEP latency, and decreased amplitude of visual evoked potentials (Lempert, 2006; Hess and Thompson, 2015). At present, the main treatment strategy for amblyopia is to remove the factors that cause deprivation as soon as possible, with cataract treatment, complete ptosis correction, the use of appropriate corrective glasses, covering healthy eyes, and optical drug suppression therapy all used (Birch et al., 2021; Boniquet-Sanchez and Sabater-Cruz, 2021; Meier and Tarczy-Hornoch, 2022). According to the law of visual development, early detection, diagnosis, and intervention are particularly important for patients with amblyopia, and can significantly improve the therapeutic effects (Holmes and Levi, 2018).

Murali et al. (2020) constructed a DL model based on a CNN for screening the risk factors for amblyopia in children. This model can identify biological characteristics such as corneal light reflection, iris center position, pupil radius, and ratio of eye radius to iris diameter from the facial image, allowing easy screening of the risk factors in children. They collected facial images of 54 participants to train and test the model, with results indicating an accuracy of 0.796, sensitivity of 0.882, specificity of 0.756, and an F-score of 0.732. Murali et al. (2021) collected facial images of 654 participants (randomly divided into training and verification sets) and constructed a DL model that could screen and identify the risk factors of amblyopia in children based on a convolution neural network. After verification, the values of 0.908, 0.836, and 0.859, respectively, for accuracy, sensitivity, and specificity indicate that the use of DL to analyze photographic images is an effective alternative method for screening risk factors in children with amblyopia. The above studies show that using AI to recognize the biological features of children's facial images allows accurate detection of the risk factors for amblyopia, which is of great significance for amblyopic children. The above studies are summarized in Table 5.

Amblyopia is a common eye disease in children. For amblyopic children, the therapeutic effect is closely related to age, and the younger the age, the better the therapeutic effect. In addition, early treatment not only has a short course of treatment, but also has a significantly higher cure rate. Therefore, it is particularly important to screen the risk factors of amblyopia in children. Through the above research, we can see that AI shows a good performance in the screening of risk factors of amblyopia in children. Its use in the screening of risk factors of amblyopia in children can not only save manpower, material and financial resources, but also is of great significance for the early treatment of children with amblyopia.

TABLE 5 Application summary of different AI models and algorithms in amblyopia.

Authors	Task	Sample size	AI algorithms	Output
Murali et al. (2020)	Detection	54 images	CNN	Accuracy = 0.796
				Sensitivity = 0.882
				Specificity = 0.756
				F-Score = 0.732
Murali et al. (2021)	Detection	654 images	CNN	Accuracy = 0.908
				Sensitivity = 0.836
				Specificity = 0.945
				F-Score = 0.859

3 Limitations and challenges

As can be seen from the above studies, AI has been widely used in optometry. Many AI models and algorithms have shown superior performance in the diagnosis, identification, screening, prediction, and treatment of disease with satisfactory results achieved. However, there remain many challenges and limitations that are likely to seriously affect further research and the application of AI in the field of optometry. For example, 1) The quality of the image in the data set (Ting et al., 2019; Xie et al., 2020). The datasets used in some studies are public, and include many poor-quality images. Because the research results of the AI model are closely related to image quality, this issue will significantly impact the AI model, resulting in inaccurate results. 2) Sample size (Chen et al., 2018; Huang et al., 2021; Gutierrez et al., 2022; Huang et al., 2022). The small sample size in some studies is likely to affect the stability of the AI model, affecting the reliability of the results. For example, in some AI studies of strabismus, amblyopia and other diseases, the sample size in the data set is small, which will have a certain impact on the performance of the final AI model. 3) External verification of the algorithm (Wawer Matos et al., 2022; Wong et al., 2022). Some AI models have excellent performance in training and verification; however, there is a huge gap between the “real environment” and the “research environment”, which may lead to performance degradation and produce unstable results when such AI models are applied to clinical diagnosis and treatment. For example, in the research of strabismus, keratoconus and other diseases, many AI models are verified only on external data sets, but not in the “real environment.” 4) Validity of the datasets (Ting et al., 2019; Ng et al., 2021). The images used in many studies need to be annotated, with strict requirements for labeling. The validity of the data used is particularly important for the research results of an AI model. For example, in some studies, the task of image annotation is completed by residents, which may be difficult to ensure the accuracy of image annotation, thus affecting the performance of the AI model. 5) Interpretability of AI algorithms (Al-Aswad et al., 2022; Betzler et al., 2022). Because AI belongs to a subfield of computer science, many clinical medical staff have little AI-related knowledge, which leads to incorrect interpretation in the process of clinical application, resulting in the so-called “black box phenomenon.” 6) AI model may lead to medical legal problems (Ji et al., 2022). No

one is perfect, and artificial intelligence cannot be 100% accurate. When the diagnosis of the AI model is wrong or even has serious consequences, how to determine its behavior? Who should bear the consequences? These will become some thorny medical legal issues. 7) The privacy and security of patients (Murdoch, 2021). Medical data focus on patients' health, disease status, biological genes and other information, once leaked, the consequences are unimaginable. The privacy security problems of medical artificial intelligence are as follows: do patients fully get their informed consent in the process of data collection? In the event of a privacy leak, who will be held responsible? Who has the right to get information about a patient's health or disease? These are all important and urgent problems to be solved. 8) The lack of legal protection related to AI technology. In recent years, the rapid development of AI technology has greatly changed our lives. However, the legislative process for artificial intelligence is relatively slow. Artificial intelligence needs to have corresponding laws and regulations in all aspects of research and development, development and production process, and stipulate the ownership of responsibility and the direction of development; artificial intelligence (especially deep learning) if there is no legal escort, will seriously affect its development and application.

4 Conclusion

Through the above AI research, it can be found that many research achievements have been made in the application of AI in the field of optics, and the application prospect is very broad, which can bring reform and progress to the field of optics in many aspects. Intelligent systems based on different AI algorithms can help ophthalmologists better diagnose and treat diseases in the field of optometry according to patients' eye clinical data and personal data, which has important clinical significance. But for clinical medical staff, only this is far from enough. Because this shallow clinical application plays a more auxiliary role, such as reducing the repetitive physical labor of clinical medical personnel, improving the accuracy of diagnosis and so on. If we want to fully apply AI to ophthalmic clinic, AI must have more functions. It can not only complete the assigned tasks, but also develop more technologies and methods according to the characteristics of each task. In addition, AI

also needs to pay more attention to those unsolved technologies and challenges, so as to better promote the clinical application of AI in ophthalmology.

As mentioned in this review, AI can complete specified tasks by building algorithm models and DL networks, particularly image recognition, classification, diagnosis, and data analysis. Although there are still several challenges associated with AI modeling, it can provide doctors with objective clinical decisions, laying the foundation for accurate treatment. There is an urgent need for future research into the unknown aspects of target diseases, which combined with application, could instigate targeted and high-quality research. Simultaneously, the introduction and application of a number of standardized norms are that can further improve the quality of AI medical research and promote AI products will provide great advantages in the diagnosis and treatment of optometry-related diseases as soon as possible.

5 Resource identification initiative

PubMed (RRID:SCR_004846).

Author contributions

SW and YJ carried out the studies and drafted the manuscript. WB participated in data collection. KL and QJ participated in the study design and guidance. All authors read and approved the final manuscript.

References

- Aatila, M., Lachgar, M., Hamid, H., and Kartit, A. (2021). Keratoconus severity classification using features selection and machine learning algorithms. *Comput. Math. Methods Med.* 2021, 9979560. doi:10.1155/2021/9979560
- Abdelmotaal, H., Mostafa, M. M., Mostafa, A. N. R., Mohamed, A. A., and Abdelazeem, K. (2020). Classification of color-coded Scheimpflug camera corneal tomography images using deep learning. *Transl. Vis. Sci. Technol.* 9, 30. doi:10.1167/tvst.9.13.30
- Al-Aswad, L. A., Ramachandran, R., Schuman, J. S., Medeiros, F., and Eydelman, M. B., and Collaborative Community for Ophthalmic Imaging Executive Committee and Glaucoma Workgroup (2022). Artificial intelligence for glaucoma: Creating and implementing artificial intelligence for disease detection and progression. *Ophthalmol. Glaucoma*, 5, e16–e25. doi:10.1016/j.ogla.2022.02.010
- Almeida, J. D., Silva, A. C., Teixeira, J. A., Paiva, A. C., and Gattass, M. (2015). Surgical planning for horizontal strabismus using Support Vector Regression. *Comput. Biol. Med.* 63, 178–186. doi:10.1016/j.cmpbiomed.2015.05.025
- Al-Timemy, A. H., Mosa, Z. M., Alyasser, Z., Lavric, A., Lui, M. M., Hazarbasanov, R. M., et al. (2021). A hybrid deep learning construct for detecting keratoconus from corneal maps. *Transl. Vis. Sci. Technol.* 10, 16. doi:10.1167/tvst.10.14.16
- Amirsolaimani, B., Peyman, G., Schwiegerling, J., Bablumyan, A., and Peyghambarian, N. (2017). A new low-cost, compact, auto-phoropter for refractive assessment in developing countries. *Sci. Rep.* 7, 13990. doi:10.1038/s41598-017-14507-5
- Baird, P. N., Saw, S. M., Lanca, C., Guggenheim, J. A., Smith, E. L., Zhou, X., et al. (2020). Myopia. *Nat. Rev. Dis. Prim.* 6, 99. doi:10.1038/s41572-020-00231-4
- Barrett, B. T., Bradley, A., and Candy, T. R. (2013). The relationship between anisometropia and amblyopia. *Prog. Retin. Eye Res.* 36, 120–158. doi:10.1016/j.preteyres.2013.05.001
- Betzler, B. K., Rim, T. H., Sabanayagam, C., and Cheng, C. Y. (2022). Artificial intelligence in predicting systemic parameters and diseases from ophthalmic imaging. *Front. Digit. Health.* 4, 889445. doi:10.3389/fdgh.2022.889445
- Birch, E. E., Kelly, K. R., and Wang, J. (2021). Recent advances in screening and treatment for amblyopia. *Ophthalmol. Ther.* 10, 815–830. doi:10.1007/s40123-021-00394-7
- Birch, E. E. (2013). Amblyopia and binocular vision. *Prog. Retin. Eye Res.* 33, 67–84. doi:10.1016/j.preteyres.2012.11.001
- Boniquet-Sanchez, S., and Sabater-Cruz, N. (2021). Current management of amblyopia with new technologies for binocular treatment. *Vis. (Basel)* 5, 31. doi:10.3390/vision5020031
- Bullimore, M. A., and Brennan, N. A. (2019). Myopia control: Why each diopter matters. *Optom. Vis. Sci.* 96, 463–465. doi:10.1097/OPX.0000000000001367
- Cabeza-Gil, I., Ríos-Ruiz, I., and Calvo, B. (2020). Customised selection of the haptic design in C-loop intraocular lenses based on deep learning. *Ann. Biomed. Eng.* 48, 2988–3002. doi:10.1007/s10439-020-02636-4
- Cao, K., Verspoor, K., Sahebjada, S., and Baird, P. N. (2020). Evaluating the performance of various machine learning algorithms to detect subclinical keratoconus. *Transl. Vis. Sci. Technol.* 9, 24. doi:10.1167/tvst.9.2.24
- Castanes, M. S. (2003). Major review: The underutilization of vision screening (for amblyopia, optical anomalies and strabismus) among preschool age children. *Binocul. Vis. Strabismus Q.* 18, 217–232.
- Chen, Z., Fu, H., Lo, W. L., and Chi, Z. (2018). Strabismus recognition using eye-tracking data and convolutional neural networks. *J. Healthc. Eng.* 2018, 7692198. doi:10.1155/2018/7692198
- Chia, A., Roy, L., and Seenyen, L. (2007). Comitant horizontal strabismus: An Asian perspective. *Br. J. Ophthalmol.* 91, 1337–1340. doi:10.1136/bjo.2007.116905
- Chia, A., Dirani, M., Chan, Y. H., Gazzard, G., Au Eong, K. G., Selvaraj, P., et al. (2010). Prevalence of amblyopia and strabismus in young Singaporean Chinese children. *Invest. Ophthalmol. Vis. Sci.* 51, 3411–3417. doi:10.1167/iops.09-4461
- Clarke, G. P., and Kapelner, A. (2020). The bayesian additive regression trees formula for safe machine learning-based intraocular lens predictions. *Front. Big Data.* 3, 572134. doi:10.3389/fdata.2020.572134
- Coyner, A. S., Oh, M. A., Shah, P. K., Singh, P., Ostmo, S., Valikodath, N. G., et al. (2022). External validation of a retinopathy of prematurity screening model using artificial intelligence in 3 low- and middle-income populations. *JAMA Ophthalmol.* 140, 791–798. doi:10.1001/jamaophthalmol.2022.2135
- de Figueiredo, L. A., Dias, J. V. P., Polati, M., Carricondo, P. C., and Debert, I. (2021). Strabismus and translational intelligence app: Optimizing diagnostic and accuracy. *Transl. Vis. Sci. Technol.* 10, 22. doi:10.1167/tvst.10.7.22

Funding

This study was supported by the National Natural Science Foundation of China (82171080, 82101155), Nanjing Medical Science and Technology Development Project (YKK19157), and Postgraduate Research & Practice Innovation Program of Jiangsu Province (JX10413973).

Acknowledgments

The authors would like to thank the Affiliated Eye Hospital of Nanjing Medical University for supporting the research work.

Conflict of interest

The authors declare that the research was conducted in the absence of any commercial or financial relationships that could be construed as a potential conflict of interest.

Publisher's note

All claims expressed in this article are solely those of the authors and do not necessarily represent those of their affiliated organizations, or those of the publisher, the editors and the reviewers. Any product that may be evaluated in this article, or claim that may be made by its manufacturer, is not guaranteed or endorsed by the publisher.

- Debellemière, G., Dubois, M., Gauvin, M., Wallerstein, A., Brenner, L. F., Rampat, R., et al. (2021). The PEARL-DGS formula: The development of an open-source machine learning-based thick IOL calculation formula. *Am. J. Ophthalmol.* 232, 58–69. doi:10.1016/j.ajo.2021.05.004
- Debert, I., Miller, J. M., Danh, K. K., and Scott, A. B. (2016). Pharmacologic injection treatment of comitant strabismus. *J. AAPOS.* 20, 106–111. doi:10.1016/j.jaapos.2015.11.011
- Deepa, V., Sathish Kumar, C., and Cherian, T. (2022). Automated grading of diabetic retinopathy using CNN with hierarchical clustering of image patches by Siamese network. *Phys. Eng. Sci. Med.* 45, 623–635. doi:10.1007/s13246-022-01129-z
- Dong, L., He, W., Zhang, R., Ge, Z., Wang, Y. X., Zhou, J., et al. (2022). Artificial intelligence for screening of multiple retinal and optic nerve diseases. *JAMA Netw. Open.* 5, e229960. doi:10.1001/jamanetworkopen.2022.9960
- Fan, Y., Yu, Z., Peng, Z., Xu, Q., Tang, T., Wang, K., et al. (2020). Machine learning based strategy surpasses the traditional method for selecting the first trial Lens parameters for corneal refractive therapy in Chinese adolescents with myopia. *CONTACT LENS ANTERIO* 44 (3), 101330. doi:10.1016/j.clae.2020.05.001
- Fan, Y., Yu, Z., Tang, T., Liu, X., Xu, Q., Peng, Z., et al. (2021). Machine learning algorithm improves accuracy of ortho-K lens fitting in vision shaping treatment. *CONTACT LENS ANTERIO* 45 (3), 101474. doi:10.1016/j.clae.2021.101474
- Fang, J., Zheng, Y., Mou, H., Shi, M., Yu, W., and Du, C. (2023). Machine learning for predicting the treatment effect of orthokeratology in children. *Front. Pediatr.* 10, 1057863. doi:10.3389/fped.2022.1057863
- Feng, R., Xu, Z., Zheng, X., Hu, H., Jin, X., Chen, D. Z., et al. (2021). KerNet: A novel deep learning approach for keratoconus and sub-clinical keratoconus detection based on raw data of the pentacam hr system. *IEEE J. Biomed. Health Inf.* 25, 3898–3910. doi:10.1109/JBHI.2021.3079430
- Ferdi, A. C., Nguyen, V., Gore, D. M., Allan, B. D., Rozema, J. J., and Watson, S. L. (2019). Keratoconus natural progression: A systematic review and meta-analysis of 11 529 eyes. *Ophthalmology* 126, 935–945. doi:10.1016/j.ophtha.2019.02.029
- Flockerzi, E., Xanthopoulos, K., Goebels, S. C., Zemova, E., Razafimino, S., Hamon, L., et al. (2021). Keratoconus staging by decades: A baseline abcd classification of 1000 patients in the homburg keratoconus center. *Br. J. Ophthalmol.* 105, 1069–1075. doi:10.1136/bjophthalmol-2020-316789
- Foo, L. L., Lim, G. Y. S., Lanca, C., Wong, C. W., Hoang, Q. V., Zhang, X. J., et al. (2023). Deep learning system to predict the 5-year risk of high myopia using fundus imaging in children. *NPJ Digit. Med.* 6 (1), 10. doi:10.1038/s41746-023-00752-8
- GBD 2019 Blindness and Vision Impairment Collaborators, Vision Loss Expert Group of the Global Burden of Disease Study (2021). Trends in prevalence of blindness and distance and near vision impairment over 30 years: An analysis for the Global Burden of Disease Study. *Vision Impairment, and S. Lancet Glob. Health.* 9, e130–e143. doi:10.1016/S2214-109X(20)30425-3
- Glaret Subin, P., and Muthukannan, P. (2022). Optimized convolution neural network based multiple eye disease detection. *Comput. Biol. Med.* 146, 105648. doi:10.1016/j.compbiomed.2022.105648
- Godefrooi, D. A., Mangen, M. J., Chan, E., O'Bart, D. P. S., Imhof, S. M., de Wit, G. A., et al. (2017). Cost-effectiveness analysis of corneal collagen crosslinking for progressive keratoconus. *Ophthalmology* 124, 1485–1495. doi:10.1016/j.ophtha.2017.04.011
- Gunasekeran, D. V., Tseng, R. M. W. W., Tham, Y. C., and Wong, T. Y. (2021). Applications of digital health for public health responses to COVID-19: A systematic scoping review of artificial intelligence, telehealth and related technologies. *NPJ Digit. Med.* 4, 40. doi:10.1038/s41746-021-00412-9
- Gutierrez, L., Lim, J. S., Foo, L. L., Ng, W. Y., Yip, M., Lim, G. Y. S., et al. (2022). Application of artificial intelligence in cataract management: Current and future directions. *Eye Vis. (Lond).* 9, 3. doi:10.1186/s40662-021-00273-z
- Hardas, M., Mathur, S., Bhaskar, A., and Kalla, M. (2022). Retinal fundus image classification for diabetic retinopathy using SVM predictions. *Phys. Eng. Sci. Med.* 45, 781–791. doi:10.1007/s13246-022-01143-1
- Hemelings, R., Elen, B., Blaschko, M. B., Jacob, J., Stalmans, I., and De Boever, P. (2021). Pathological myopia classification with simultaneous lesion segmentation using deep learning. *Comput. Methods Programs Biomed.* 199, 105920. doi:10.1016/j.cmpb.2020.105920
- Hess, R. F., and Thompson, B. (2015). Amblyopia and the binocular approach to its therapy. *Vis. Res.* 114, 4–16. doi:10.1016/j.visres.2015.02.009
- Holmes, J. M., and Levi, D. M. (2018). Treatment of amblyopia as a function of age. *Vis. Neurosci.* 35, E015. doi:10.1017/S0952523817000220
- Huang, X., Lee, S. J., Kim, C. Z., and Choi, S. H. (2021). An automatic screening method for strabismus detection based on image processing. *PLOS ONE* 16, e0255643. doi:10.1371/journal.pone.0255643
- Huang, X., Lee, S. J., Kim, C. Z., and Choi, S. H. (2022). An improved strabismus screening method with combination of meta-learning and image processing under data scarcity. *PLOS ONE* 17, e0269365. doi:10.1371/journal.pone.0269365
- Ji, Y., Chen, N., Liu, S., Yan, Z., Qian, H., Zhu, S., et al. (2022). Research progress of artificial intelligence image analysis in systemic disease-related ophthalmopathy. *Dis. Markers* 2022, 3406890. doi:10.1155/2022/3406890
- Jones-Jordan, L. A., Walline, J. J., Sinnott, L. T., Kymes, S. M., and Zadnik, K. (2013). Asymmetry in keratoconus and vision-related quality of life. *Cornea* 32, 267–272. doi:10.1097/ICO.0b013e31825697c4
- Kamiya, K., Ayatsuka, Y., Kato, Y., Shoji, N., Mori, Y., and Miyata, K. (2021). Diagnosability of keratoconus using deep learning with Placido disk-based corneal topography. *Front. Med. (Lausanne)* 8, 724902. doi:10.3389/fmed.2021.724902
- Kang, L., Ballouz, D., and Woodward, M. A. (2022). Artificial intelligence and corneal diseases. *Curr. Opin. Ophthalmol.* doi:10.1097/ICU.0000000000000885
- Kang, Y. C., Yang, H. K., Kim, Y. J., Hwang, J. M., and Kim, K. G. (2022). Automated mathematical algorithm for quantitative measurement of strabismus based on photographs of nine cardinal gaze positions. *Biomed. Res. Int.* 2022, 9840494. doi:10.1155/2022/9840494
- Kankariya, V. P., Kymionis, G. D., Diakonis, V. F., and Yoo, S. H. (2013). Management of pediatric keratoconus - evolving role of corneal collagen cross-linking: An update. *Indian J. Ophthalmol.* 61, 435–440. doi:10.4103/0301-4738.116070
- Kates, M. M., and Beal, C. J. (2021). Amblyopia. *JAMA.* 325, 408. doi:10.1001/jama.2020.5741
- Kato, N., Masumoto, H., Tanabe, M., Sakai, C., Negishi, K., Torii, H., et al. (2021). Predicting keratoconus progression and need for corneal crosslinking using deep learning. *J. Clin. Med.* 10, 844. doi:10.3390/jcm10040844
- Kelkar, J. A., Gopal, S., Shah, R. B., and Kelkar, A. S. (2015). Intermittent exotropia: Surgical treatment strategies. *Indian J. Ophthalmol.* 63, 566–569. doi:10.4103/0301-4738.167109
- Kuo, B. I., Chang, W. Y., Liao, T. S., Liu, F. Y., Liu, H. Y., Chu, H. S., et al. (2020). Keratoconus screening based on deep learning approach of corneal topography. *Transl. Vis. Sci. Technol.* 9, 53. doi:10.1167/tvst.9.2.53
- Ladas, J., Ladas, D., Lin, S. R., Devgan, U., Siddiqui, A. A., and Jun, A. S. (2021). Improvement of multiple generations of intraocular lens calculation formulae with a novel approach using artificial intelligence. *Transl. Vis. Sci. Technol.* 10, 7. doi:10.1167/tvst.10.3.7
- Lempert, P. (2006). Relationship between anisometropia, patient age, and the development of amblyopia. *Am. J. Ophthalmol.* 142, 891–892. author reply 891–891; author reply 892. doi:10.1016/j.ajo.2006.07.059
- Li, F. F., and Yam, J. C. (2019). Low-concentration atropine eye drops for myopia progression. *Asia Pac. J. Ophthalmol. (Phila.)* 8, 360–365. doi:10.1097/APO.0000000000000256
- Li, F., Su, Y., Lin, F., Li, Z., Song, Y., Nie, S., et al. (2022). A deep-learning system predicts glaucoma incidence and progression using retinal photographs. *J. Clin. Invest.* 132, e157968. doi:10.1172/JCI157968
- Li, J., Huang, K., Ju, R., Chen, Y., Li, M., Yang, S., et al. (2022). Evaluation of artificial intelligence-based quantitative analysis to identify clinically significant severe retinopathy of prematurity. *Retina* 42, 195–203. doi:10.1097/IAE.0000000000003284
- Li, Y., Feng, W., Zhao, X., Liu, B., Zhang, Y., Chi, W., et al. (2022). Development and validation of a deep learning system to screen vision-threatening conditions in high myopia using optical coherence tomography images. *Br. J. Ophthalmol.* 106, 633–639. doi:10.1136/bjophthalmol-2020-317825
- Li, M., Liu, S., Wang, Z., Li, X., Yan, Z., Zhu, R., et al. (2023). MyopiaDETR: End-to-end pathological myopia detection based on transformer using 2D fundus images. *Front. Neurosci.* 17, 1130609. doi:10.3389/fnins.2023.1130609
- Lin, H., Long, E., Ding, X., Diao, H., Chen, Z., Liu, R., et al. (2018). Prediction of myopia development among Chinese school-aged children using refraction data from electronic medical records: A retrospective, multicentre machine learning study. *PLOS Med.* 15, e1002674. doi:10.1371/journal.pmed.1002674
- Liu, Y., Liu, C., Zhang, W., Chen, X., and Zhao, K. (2019). Model of a support vector machine to assess the functional cure for surgery of intermittent exotropia. *Sci. Rep.* 9, 8321. doi:10.1038/s41598-019-38969-x
- Lou, L., Huang, X., Sun, Y., Cao, J., Wang, Y., Zhang, Q., et al. (2022). Automated photographic analysis of inferior oblique overaction based on deep learning. *Quant. Imag. Med. Surg.* 13 (1), 329–338. doi:10.21037/qims-22-467
- Lundström, M., Dickman, M., Henry, Y., Manning, S., Rosen, P., Tassignon, M. J., et al. (2018). Risk factors for refractive error after cataract surgery: Analysis of 282 811 cataract extractions reported to the European Registry of Quality Outcomes for cataract and refractive surgery. *J. Cataract. Refract. Surg.* 44, 447–452. doi:10.1016/j.jcrs.2018.01.031
- Mao, K., Yang, Y., Guo, C., Zhu, Y., Chen, C., Chen, J., et al. (2021). An artificial intelligence platform for the diagnosis and surgical planning of strabismus using corneal light-reflection photos. *Ann. Transl. Med.* 9, 374. doi:10.21037/atm-20-5442
- Maurer, D., and McKEE, S. P. (2018). Classification and diversity of amblyopia. *Vis. Neurosci.* 35, E012. doi:10.1017/S0952523817000190
- Meier, K., and Tarczy-Hornoch, K. (2022). Recent treatment advances in amblyopia. *Annu. Rev. Vis. Sci.* 8, 323–343. doi:10.1146/annurev-vision-100720-022550

- Melles, R. B., Kane, J. X., Olsen, T., and Chang, W. J. (2019). Update on intraocular lens calculation formulas. *Ophthalmology* 126, 1334–1335. doi:10.1016/j.ophtha.2019.04.011
- Miao, J., Yu, J., Zou, W., Su, N., Peng, Z., Wu, X., et al. (2022). Deep learning models for segmenting non-perfusion area of color fundus photographs in patients with branch retinal vein occlusion. *Front. Med. (Lausanne)* 9, 794045. doi:10.3389/fmed.2022.794045
- Mojon-Azzi, S. M., Kunz, A., and Mojon, D. S. (2011). The perception of strabismus by children and adults. *Graefes Arch. Clin. Exp. Ophthalmol.* 249, 753–757. doi:10.1007/s00417-010-1555-y
- Morgan, I. G., French, A. N., Ashby, R. S., Guo, X., Ding, X., He, M., et al. (2018). The epidemics of myopia: Aetiology and prevention. *Prog. Retin. Eye Res.* 62, 134–149. doi:10.1016/j.preteyeres.2017.09.004
- Mori, Y., Yamauchi, T., Tokuda, S., Minami, K., Tabuchi, H., and Miyata, K. (2021). Machine learning adaptation of intraocular lens power calculation for a patient group. *Eye Vis. (Lond)* 8, 42. doi:10.1186/s40662-021-00265-z
- Mostovoy, D., Vinker, S., Mimouni, M., Goldich, Y., Levartovsky, S., and Kaiserman, I. (2018). The association of keratoconus with blepharitis. *Clin. Exp. Optom.* 101, 339–344. doi:10.1111/cxo.12643
- Mura, J. J., Pavlin, C. J., Condon, G. P., Belovay, G. W., Kranemann, C. F., Ishikawa, H., et al. (2010). Ultrasound biomicroscopic analysis of iris-sutured foldable posterior chamber intraocular lenses. *Am. J. Ophthalmol.* 149, 245–252. doi:10.1016/j.ajo.2009.08.022
- Murali, K., Krishna, V., Krishna, V., and Kumari, B. (2020). Application of deep learning and image processing analysis of photographs for amblyopia screening. *Indian J. Ophthalmol.* 68, 1407–1410. doi:10.4103/ijo.IJO_1399_19
- Murali, K., Krishna, V., Krishna, V., Kumari, B., Raveendra Murthy, S., Vidhya, C., et al. (2021). Effectiveness of Kanna photoscreener in detecting amblyopia risk factors. *Indian J. Ophthalmol.* 69, 2045–2049. doi:10.4103/ijo.IJO_2912_20
- Murdoch, B. (2021). Privacy and artificial intelligence: Challenges for protecting health information in a new era. *BMC Med. Ethics* 22 (1), 122. doi:10.1186/s12910-021-00687-3
- Nemeth, G., Kemeny-Beke, A., and Modis, L., Jr. (2022). Comparison of accuracy of different intraocular lens power calculation methods using artificial intelligence. *Eur. J. Ophthalmol.* 32, 235–241. doi:10.1177/1120672121994720
- Ng, W. Y., Zhang, S., Wang, Z., Ong, C. J. T., Gunasekaran, D. V., Lim, G. Y. S., et al. (2021). Updates in deep learning research in ophthalmology. *Clin. Sci. (Lond.)* 135, 2357–2376. doi:10.1042/CS20210207
- Nuzzi, R., Boscia, G., Marolo, P., and Ricardi, F. (2021). The impact of artificial intelligence and deep learning in eye diseases: A review. *Front. Med. (Lausanne)* 8, 710329. doi:10.3389/fmed.2021.710329
- Omoto, M., Sugawara, K., Torii, H., Yotsukura, E., Masui, S., Shigeno, Y., et al. (2022). Investigating the prediction accuracy of recently updated intraocular lens power formulas with artificial intelligence for high myopia. *J. Clin. Med.* 11, 4848. doi:10.3390/jcm11164848
- Paff, T., Oudesluys-Murphy, A. M., Wolterbeek, R., Swart-van den Berg, M., de Nie, J. M., Tijssen, E., et al. (2010). Screening for refractive errors in children: The plusoptix S08 and the Retinomax K-plus2 performed by a lay screener compared to cycloplegic retinoscopy. *J. AAPOS* 14, 478–483. doi:10.1016/j.jaapos.2010.09.015
- Piovella, M., Colonval, S., Kapp, A., Reiter, J., Van Cauwenberge, F., and Alfonso, J. (2019). Patient outcomes following implantation of a trifocal toric IOL: Twelve-month prospective multicentre study. *Eye (Lond.)* 33, 144–153. doi:10.1038/s41433-018-0076-5
- Rajavi, Z., Parsafar, H., Ramezani, A., and Yaseri, M. (2012). Is noncycloplegic photorefractometry applicable for screening refractive amblyopia risk factors? *J. Ophthalmic Vis. Res.* 7, 3–9.
- Randleman, J. B., Woodward, M., Lynn, M. J., and Stulting, R. D. (2008). Risk assessment for ectasia after corneal refractive surgery. *Ophthalmology* 115, 37–50. doi:10.1016/j.ophtha.2007.03.073
- Ren, X., Feng, W., Ran, R., Gao, Y., Lin, Y., Fu, X., et al. (2022). Artificial intelligence to distinguish retinal vein occlusion patients using color fundus photographs. *Eye (Lond)* 2022. doi:10.1038/s41433-022-02239-4
- Röck, T., Bartz-Schmidt, K. U., and Röck, D. (2018). Trends in corneal transplantation at the university eye hospital in Tübingen, Germany over the last 12 years: 2004–2015. *PLOS ONE* 13, e0198793. doi:10.1371/journal.pone.0198793
- Romero-Jiménez, M., Santodomingo-Rubido, J., and González-Méjome, J. M. (2013). The thinnest, steepest, and maximum elevation corneal locations in noncontact and contact lens wearers in keratoconus. *Cornea* 32, 332–337. doi:10.1097/ICO.0b013e318259c98a
- Santodomingo-Rubido, J., Carracedo, G., Suzuki, A., Villa-Collar, C., Vincent, S. J., and Wolffsohn, J. S. (2022). Keratoconus: An updated review. *Cont. Lens Anterior Eye* 45, 101559. doi:10.1016/j.clae.2021.101559
- Savini, G., and Hoffer, K. J. (2018). Intraocular lens power calculation in eyes with previous corneal refractive surgery. *Eye Vis. (Lond)* 5, 18. doi:10.1186/s40662-018-0110-5
- Schwarzenbacher, L., Seeböck, P., Schartmüller, D., Leydolt, C., Menapace, R., and Schmidt-Erfurth, U. (2022). Automatic segmentation of intraocular lens, the retrolental space and Berger's space using deep learning. *Acta Ophthalmol.* 100, e1611–e1616. doi:10.1111/aos.15141
- Shah, A. K., Terry, M. A., Shamie, N., Chen, E. S., Phillips, P. M., Hoar, K. L., et al. (2010). Complications and clinical outcomes of descemet stripping automated endothelial keratoplasty with intraocular lens exchange. *Am. J. Ophthalmol.* 149, 390–397. doi:10.1016/j.ajo.2009.11.002
- Sharif, R., Bak-Nielsen, S., Hjortdal, J., and Karamichos, D. (2018). Pathogenesis of keratoconus: The intriguing therapeutic potential of prolactin-inducible protein. *Prog. Retin. Eye Res.* 67, 150–167. doi:10.1016/j.preteyeres.2018.05.002
- Simon, S. S., Chee, Y. E., Haddadin, R. I., Veldman, P. B., Borboli-Gerogiannis, S., Brauner, S. C., et al. (2014). Achieving target refraction after cataract surgery. *Ophthalmology* 121, 440–444. doi:10.1016/j.ophtha.2013.09.022
- Sogawa, T., Tabuchi, H., Nagasato, D., Masumoto, H., Ikuno, Y., Ohsugi, H., et al. (2020). Accuracy of a deep convolutional neural network in the detection of myopic macular diseases using swept-source optical coherence tomography. *PLOS ONE* 15, e0227240. doi:10.1371/journal.pone.0227240
- Sotoudeh-Paima, S., Jodeiri, A., Hajizadeh, F., and Soltanian-Zadeh, H. (2022). Multi-scale convolutional neural network for automated AMD classification using retinal OCT images. *Comput. Biol. Med.* 144, 105368. doi:10.1016/j.combiomed.2022.105368
- Sousa de Almeida, J. D., Silva, A. C., Teixeira, J. A., Paiva, A. C., and Gattass, M. (2015). Computer-aided methodology for syndromic strabismus diagnosis. *J. Digit. Imaging* 28, 462–473. doi:10.1007/s10278-014-9758-0
- Tang, T., Yu, Z., Xu, Q., Peng, Z., Fan, Y., Wang, K., et al. (2020). A machine learning-based algorithm used to estimate the physiological elongation of ocular axial length in myopic children. *Eye Vis. (Lond)* 7, 50. doi:10.1186/s40662-020-00214-2
- Ting, D. S. W., Pasquale, L. R., Peng, L., Campbell, J. P., Lee, A. Y., Raman, R., et al. (2019). Artificial intelligence and deep learning in ophthalmology. *Br. J. Ophthalmol.* 103, 167–175. doi:10.1136/bjophthalmol-2018-313173
- Ting, D. S. W., Peng, L., Varadarajan, A. V., Keane, P. A., Burlina, P. M., Chiang, M. F., et al. (2019). Deep learning in ophthalmology: The technical and clinical considerations. *Prog. Retin. Eye Res.* 72, 100759. doi:10.1016/j.preteyeres.2019.04.003
- Tsai, H. R., Chen, T. L., Wang, J. H., Huang, H. K., and Chiu, C. J. (2021). Is 0.01% atropine an effective and safe treatment for myopic children? A systemic review and meta-analysis. *J. Clin. Med.* 10, 3766. doi:10.3390/jcm10173766
- Varadarajan, A. V., Poplin, R., Blumer, K., Angermueller, C., Ledsam, J., Chopra, R., et al. (2018). Deep learning for predicting refractive error from retinal fundus images. *Invest. Ophthalmol. Vis. Sci.* 59, 2861–2868. doi:10.1167/iovs.18-23887
- Wan, Q., Yue, S., Tang, J., Wei, R., Tang, J., Ma, K., et al. (2023). Prediction of early visual outcome of small-incision lenticule extraction (SMILE) based on deep learning. *Ophthalmol. Ther.* 12 (2), 1263–1279. doi:10.1007/s40123-023-00680-6
- Wang, W., Yan, W., Fotis, K., Prasad, N. M., Lansingh, V. C., Taylor, H. R., et al. (2016). Cataract surgical rate and socioeconomic status: A global study. *Invest. Ophthalmol. Vis. Sci.* 57, 5872–5881. doi:10.1167/iovs.16-19894
- Wang, K. J., Chang, Q. L., Man, F. Y., Ding, J., Wang, J. H., Xian, J. F., et al. (2018). Congenital monocular strabismus fixus. *J. Pediatr. Ophthalmol. Strabismus* 55, 363–368. doi:10.3928/01913913-20180620-02
- Wang, L., Jin, G., Zhang, J., Chen, X., Tan, X., Wang, W., et al. (2022). Clinically significant intraocular lens decentration and tilt in highly myopic eyes: A swept-source optical coherence tomography study. *Am. J. Ophthalmol.* 235, 46–55. doi:10.1016/j.ajo.2021.08.017
- Wang, W., Li, X., Xu, Z., Yu, W., Zhao, J., Ding, D., et al. (2022). Learning Two-Stream CNN for multi-modal age-related macular degeneration categorization. *IEEE J. Biomed. Health Inf.* 26, 4111–4122. doi:10.1109/JBHI.2022.3171523
- Wawer Matos, P. A., Reimer, R. P., Rokohl, A. C., Caldeira, L., Heindl, L. M., and Große Hokamp, N. (2022). Artificial intelligence in ophthalmology - Status quo and future perspectives. *Semin. Ophthalmol.* 38, 226–237. doi:10.1080/08820538.2022.2139625
- Wei, L., Song, Y., He, W., Chen, X., Ma, B., Lu, Y., et al. (2020). Accuracy improvement of IOL power prediction for highly myopic eyes with an XGBoost machine learning-based calculator. *Front. Med. (Lausanne)* 7, 592663. doi:10.3389/fmed.2020.592663
- Weiss, R. S., and Park, S. (2019). Recent updates on myopia control: Preventing progression 1 diopter at a time. *Curr. Opin. Ophthalmol.* 30, 215–219. doi:10.1097/ICU.0000000000000571
- Wong, C. W., Tsai, A., Jonas, J. B., Ohno-Matsui, K., Chen, J., Ang, M., et al. (2021). Digital screen time during the COVID-19 pandemic: Risk for a further myopia boom? *Am. J. Ophthalmol.* 223, 333–337. doi:10.1016/j.ajo.2020.07.034

- Wong, D. Y. L., Lam, M. C., Ran, A., and Cheung, C. Y. (2022). Artificial intelligence in retinal imaging for cardiovascular disease prediction: Current trends and future directions. *Curr. Opin. Ophthalmol.* 33, 440–446. doi:10.1097/ICU.0000000000000886
- Wu, Q., Hu, Y., Mo, Z., Wu, R., Zhang, X., Yang, Y., et al. (2022). Development and validation of a deep learning model to predict the occurrence and severity of retinopathy of prematurity. *JAMA Netw. Open.* 5, e2217447. doi:10.1001/jamanetworkopen.2022.17447
- Xie, Y., Zhao, L., Yang, X., Wu, X., Yang, Y., Huang, X., et al. (2020). Screening candidates for refractive surgery with corneal tomographic-based deep learning. *JAMA Ophthalmol.* 138, 519–526. doi:10.1001/jamaophthalmol.2020.0507
- Xin, C., Bian, G. B., Zhang, H., Liu, W., and Dong, Z. (2020). Optical coherence tomography-based deep learning algorithm for quantification of the location of the intraocular lens. *Ann. Transl. Med.* 8, 872. doi:10.21037/atm-20-4706
- Xiong, J., Li, F., Song, D., Tang, G., He, J., Gao, K., et al. (2022). Multimodal machine learning using visual fields and peripapillary circular OCT scans in detection of glaucomatous optic neuropathy. *Ophthalmology* 129, 171–180. doi:10.1016/j.ophtha.2021.07.032
- Yang, X., Chen, G., Qian, Y., Wang, Y., Zhai, Y., Fan, D., et al. (2020). Prediction of myopia in adolescents through machine learning methods. *Int. J. Environ. Res. Public Health.* 17, 463. doi:10.3390/ijerph17020463
- Yang, Y., Li, R., Lin, D., Zhang, X., Li, W., Wang, J., et al. (2020). Automatic identification of myopia based on ocular appearance images using deep learning. *Ann. Transl. Med.* 8, 705. doi:10.21037/atm.2019.12.39
- Yao, Y., Lu, Q., Wei, L., Cheng, K., Lu, Y., and Zhu, X. (2021). Efficacy and complications of cataract surgery in high myopia. *J. Cataract. Refract. Surg.* 47, 1473–1480. doi:10.1097/j.jcrs.0000000000000664
- Yoo, Y. J., Yang, H. K., Seo, J. M., Kim, K. G., and Hwang, J. M. (2019). Infrared photographs with a selective wavelength filter to diagnose small-angle esotropia in young children. *Graefes Arch. Clin. Exp. Ophthalmol.* 257, 645–650. doi:10.1007/s00417-019-04240-2
- Yoo, T. K., Ryu, I. H., Choi, H., Kim, J. K., Lee, I. S., Kim, J. S., et al. (2020). Explainable machine learning approach as a tool to understand factors used to select the refractive surgery technique on the expert level. *Transl. Vis. Sci. Technol.* 9, 8. doi:10.1167/tvst.9.2.8
- Zéboulon, P., Debellemannière, G., Bouvet, M., and Gatineau, D. (2020). Corneal topography raw data classification using a convolutional neural network. *Am. J. Ophthalmol.* 219, 33–39. doi:10.1016/j.ajo.2020.06.005
- Zhang, G., Sun, B., Zhang, Z., Wu, S., Zhuo, G., Rong, H., et al. (2022). Hypermixed convolutional neural network for retinal vein occlusion classification. *Dis. Markers.* 2022, 1730501. doi:10.1155/2022/1730501
- Zhang, W. F., Li, D. H., Wei, Q. J., Ding, D. Y., Meng, L. H., Wang, Y. L., et al. (2022). The validation of deep learning-based grading model for diabetic retinopathy. *Front. Med. (Lausanne).* 9, 839088. doi:10.3389/fmed.2022.839088
- Zheng, C., Yao, Q., Lu, J., Xie, X., Lin, S., Wang, Z., et al. (2021). Detection of referable horizontal strabismus in children's primary gaze photographs using deep learning. *Transl. Vis. Sci. Technol.* 10, 33. The following formatting styles are meant as a guide, as long as the full citation is complete and clear, Frontiers referencing style will be applied during typesetting.



OPEN ACCESS

EDITED BY

Huiying Liu,
Institute for Infocomm Research
(A*STAR), Singapore

REVIEWED BY

Yongbin Ouyang,
Jinling Institute of Technology, China
Guangming Wan,
First Affiliated Hospital of Zhengzhou
University, China
Huihui Fang,
Baidu, China

*CORRESPONDENCE

Guofan Cao,
✉ caoguofan587@163.com

RECEIVED 24 February 2023

ACCEPTED 24 April 2023

PUBLISHED 04 May 2023

CITATION

Zhang L, Tang L, Xia M and Cao G (2023),
The application of artificial intelligence in
glaucoma diagnosis and prediction.
Front. Cell Dev. Biol. 11:1173094.
doi: 10.3389/fcell.2023.1173094

COPYRIGHT

© 2023 Zhang, Tang, Xia and Cao. This is
an open-access article distributed under
the terms of the [Creative Commons
Attribution License \(CC BY\)](https://creativecommons.org/licenses/by/4.0/). The use,
distribution or reproduction in other
forums is permitted, provided the original
author(s) and the copyright owner(s) are
credited and that the original publication
in this journal is cited, in accordance with
accepted academic practice. No use,
distribution or reproduction is permitted
which does not comply with these terms.

The application of artificial intelligence in glaucoma diagnosis and prediction

Linyu Zhang^{1,2}, Li Tang¹, Min Xia^{1,2} and Guofan Cao^{1,2*}

¹The Affiliated Eye Hospital of Nanjing Medical University, Nanjing, China, ²The Fourth School of Clinical Medicine, Nanjing Medical University, Nanjing, China

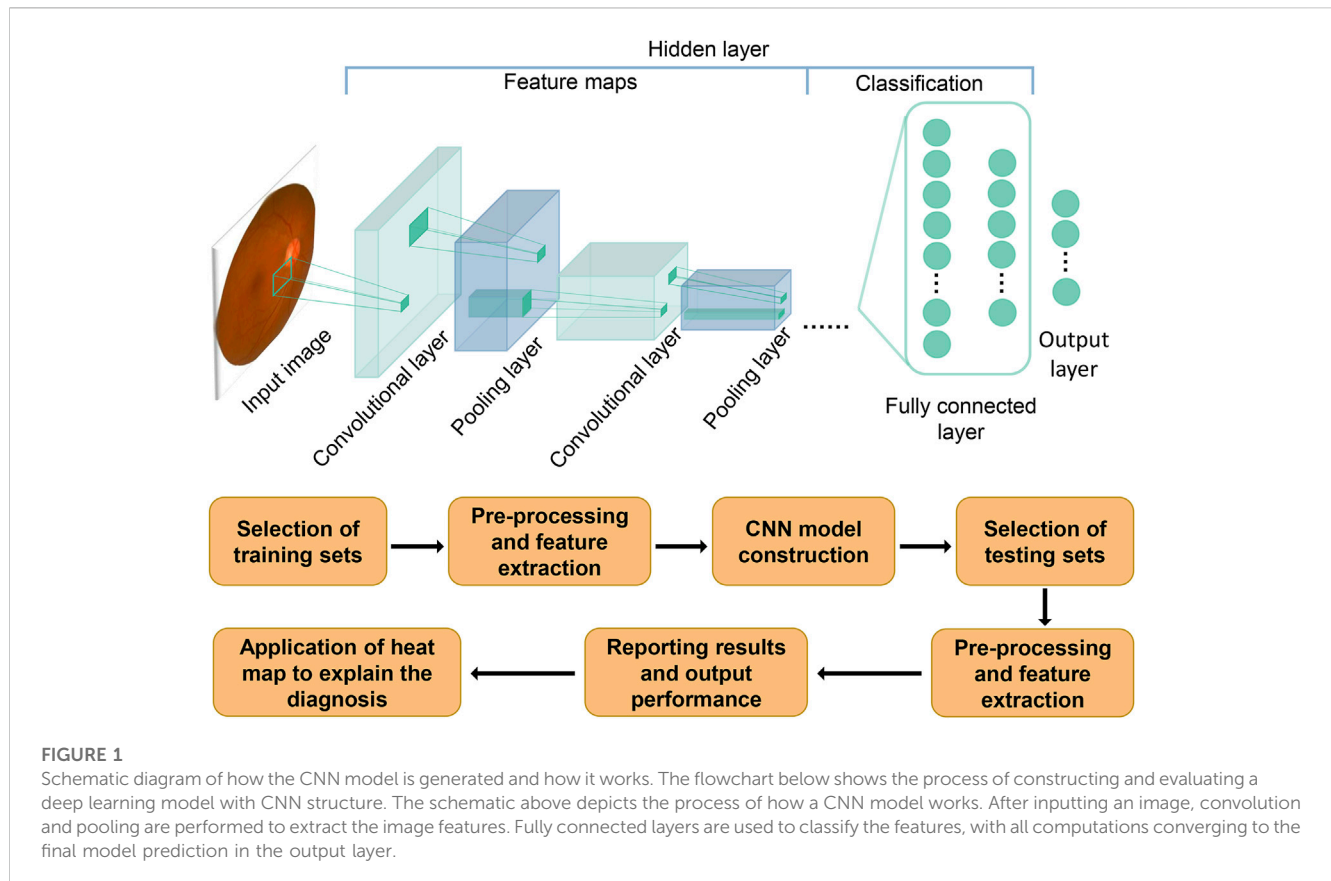
Artificial intelligence is a multidisciplinary and collaborative science, the ability of deep learning for image feature extraction and processing gives it a unique advantage in dealing with problems in ophthalmology. The deep learning system can assist ophthalmologists in diagnosing characteristic fundus lesions in glaucoma, such as retinal nerve fiber layer defects, optic nerve head damage, optic disc hemorrhage, etc. Early detection of these lesions can help delay structural damage, protect visual function, and reduce visual field damage. The development of deep learning led to the emergence of deep convolutional neural networks, which are pushing the integration of artificial intelligence with testing devices such as visual field meters, fundus imaging and optical coherence tomography to drive more rapid advances in clinical glaucoma diagnosis and prediction techniques. This article details advances in artificial intelligence combined with visual field, fundus photography, and optical coherence tomography in the field of glaucoma diagnosis and prediction, some of which are familiar and some not widely known. Then it further explores the challenges at this stage and the prospects for future clinical applications. In the future, the deep cooperation between artificial intelligence and medical technology will make the datasets and clinical application rules more standardized, and glaucoma diagnosis and prediction tools will be simplified in a single direction, which will benefit multiple ethnic groups.

KEYWORDS

Glaucoma, artificial Intelligence, visual field, optical coherence tomography, fundus photographs

1 Introduction

Glaucoma alludes to a chronic neurodegenerative disease that is associated with progressive loss of optic disc edge, retinal nerve fiber layer (RNFL) thinning and ganglion cell damage. It has been the second most common cause of blindness globally (Davis et al., 2016; GBD, 2019 Blindness and Vision Impairment Collaborators, 2021). The number of people with glaucoma (aged 40–80 years) worldwide was estimated to be 76.0 million in 2020 and 111.8 million in 2040 (Tham et al., 2014). Because of the progressive and insidious nature of glaucoma, early diagnosis is extremely vital to prevent disease progression and permanent vision loss. However, identifying glaucoma is a complicated process that requires multiple examinations and clinical expertise, which would be time-consuming and labor-intensive. In resource-constrained and geopolitically disadvantaged places, this process is beset by several challenges, such as a lack of healthcare infrastructure, inadequate follow-up, and poor therapy adherence (Nduaguba and Lee, 2006; Santos Martins et al., 2021). Considering that many potential glaucoma patients are at risk of



future vision persecution or even blindness, early identification of glaucoma and improvement of diagnostic practices are topics that modern ophthalmologists are constantly striving for. The emergence of artificial intelligence (AI) technology and its integration with ophthalmology has solved this problem to some extent.

AI is expected to equip ophthalmologists with revolutionary automated methods for diagnosing and managing ocular illnesses. It is a multidisciplinary science that allows machines to simulate human cognitive processes such as learning, reasoning, problem solving, information processing, social awareness, and general intelligence (Hamet and Tremblay, 2017). It has the powerful data processing capability to analyze data and predict development trends autonomously. For autonomous diagnosis of characteristic fundus lesions of glaucoma, such as retinal nerve fiber layer defects, optic nerve head injury, and optic disc hemorrhage, it has unique advantages. Artificial intelligence encompasses machine learning, which learns and improves itself automatically from data, without the need for human-written programs to specify rules and logic. Machine learning in turn includes deep learning (DL). Deep learning, a development of machine learning within the field of AI, analyzes data using layered algorithmic frameworks. The architecture was inspired by the biological neural networks of animal brains (LeCun et al., 2015; Thompson et al., 2020). DL has relatively mature applications in bioengineering and smart medicine, and there are already successful cases in ophthalmology. In 2018 the U.S. Food and Drug Administration approved the first fully autonomous AI algorithm IDx-DR for the detection of diabetic retinopathy (Abramoff et al., 2018), which has

greatly advanced the development and dissemination of DL in the clinical setting. Recently, DL is evolving day by day, new network structures convolutional neural networks (CNN) have already made prominent contributions in a number of disciplines including dermatology (Combalia et al., 2022), cardiovascular disease risk prediction (Padmanabhan et al., 2019), radiology and ophthalmology (Setio et al., 2016; Xu et al., 2020b; Benet and Pellicer-Valero, 2022). Promising to provide ophthalmologists with novel tools for the diagnosis and treatment of ocular diseases. Figure 1 depicts a schematic diagram of a deep learning model with CNN structure to process images. With these technical conditions, ophthalmologists can greatly reduce the cumbersome process during diagnosis and treatment, decrease manpower resources for interpreting auxiliary examinations, and increase the ability to capture subtle lesions that are not discernible to human eyes.

Enhanced computing power expanded storage capacity, and compilation of medical data allow for broader applications and more accurate diagnostic methods for AI technology in the direction of disease screening and ancillary test judgment. In ophthalmology, due to the reliance on ancillary examination images and the requirement for various diagnostic evidence, AI is uniquely positioned to analyze and interpret glaucoma intraocular pressure, visual field (VF), optical coherence tomography (OCT) and retinal fundus images (Devalla et al., 2020). Detection systems using AI can overcome the stress of the healthcare resource shortage due to an aging population (Chan et al., 2016), provide mass screening at low cost, especially for regions lacking medical care

professionals, and can provide full-cycle health monitoring for patients in a high-quality and efficient manner (Balyen and Peto, 2019). The current functional and structural tests commonly used in glaucoma diagnosis include VF detection, retinal fundus photography and OCT, so in this review article we detail the combination of these tests with AI for glaucoma diagnosis and prediction, as well as some of the other techniques under development for their current applications in research and clinical practice. We further explore the limitations and potential challenges, as well as the prospects for future applications in the hope of providing new perspectives for scholars in this field to contemplate.

2 Diagnostic model of glaucoma

2.1 Visual fields

In the clinical setting, VFs are widely used as the gold standard for diagnosing whether a patient is glaucomatous, and the Standard Automated Perimetry (SAP) remains the primary tool for diagnosing and tracking functional changes in the disease. SAP assessment of functional impairment rates is extremely important for establishing patient prognosis and treatment aggressiveness. However, this test is often influenced by a variety of subjective factors, such as patient attention fatigue or poor doctor-patient cooperation, which can readily influence the ultimate judgment of disease progression. AI systems combined with some advanced testing devices for review, such as the frequency-doubling perimetry, Humphrey Matrix 24-2 test, short-wavelength automated perimetry, and Heidelberg edge perimetry, can yield accuracy gains at lower cost and higher efficiency. Deep learning models use VFs collected from various healthcare facilities, commonly use total deviation plots, mean deviation values, and pattern deviation probability plots. Data samples with excessive false-positive and false-negative rates were excluded when collecting this VF information. Additional features of glaucoma patients were also collected as an assist and the plots were processed to make lesion features more susceptible to detection. The relevant information is extracted and used as variables in the classifiers to train algorithms for diagnosing or predicting glaucoma conditions. A few models also incorporate numerical pattern deviation plots and numerical displays to assist in training. Results obtained can be compared with clinicians' judgments to verify their validity.

In 2014 (Asaoka et al., 2014) developed a Random Forests machine-learning method in order to distinguish the VFs of preperimetric open angle glaucoma eyes. After achieving good results in the area under the receiver operating characteristic curve (ROC) and significant total deviation differences with this method, studies combining AI with VF detection to diagnose glaucoma are beginning to gain traction. After that, other researchers developed a CNN system using the vision geometrical group (VGG) network structure (Li et al., 2018a). The VGG network is first pre-trained on the ImageNet dataset, then the output dimension of the penultimate layer is modified with the last layer output two-dimensional (2D) vector, and all parameters of the network are initialized and updated. The network is compared with the results of rule-based methods (like Advanced Glaucoma

Intervention Study criteria and Glaucoma Staging System criteria) and non-deep machine learning algorithms (like random forest). With an accuracy of 0.876, specificity of 0.826, and sensitivity of 0.932, the CNN far exceeded several other types of AI visual field algorithms, showing good glaucomatous VF discrimination. The results demonstrate the advantages of the CNN algorithm for applications. However, one thing to note is that this study only used pattern deviation images as input objects and early glaucoma may not be identified, and the capabilities of DL models need to be expanded to diagnose more types of glaucoma.

Convolutional long short-term memory neural networks for glaucoma progression detection have also been trained and combined with clinical data (Dixit et al., 2021). This neural network extracts spatiotemporal features of glaucoma progression, and the researchers used a longitudinal dataset containing VF as well as clinical data to improve the evaluation of the model. The researchers utilized two machine learning models that defined progression using algorithms such as VF index slope, pointwise linear regression, and mean deviation slope. And one was trained using clinical data containing information such as cup-to-disc ratio, intraocular pressure and central corneal thickness. The long short-term memory neural network had an accuracy of 91%–93%, and the model trained using clinical data showed a higher AUC than the model trained using only the VF dataset. Creating clinically accessible diagnostic interfaces and windows is also essential. Huang et al. (Huang et al., 2022) developed a fine-grained grading deep learning system and an interactive diagnostic aid interface has been created for clinical implementation. Two DL models Humphrey Field Analyzer (HFA) data (FGG-H) and Octopus data (FGG-O) were constructed both using the Residual Neural Network (ResNet) structure, where the FGG-O was initialized with the final parameters of FGG-H preprocessed with HFA data from the Harvard dataset, and they added identity mapping over CNN to grade glaucoma with high accuracy. The fine-grained grading deep learning system achieves almost the same accuracy as ophthalmology clinicians and provides a user-friendly interface for patients and physicians to perform the test. In addition, a smartphone application-based DL system has been developed (Li et al., 2020a), which applies optical character recognition techniques to extract data points in the VF and uses CNN models to modify the original ResNet18 to detect changes in the VF, resulting in the “iGlaucoma” mobile software. The DL system outperformed 6 ophthalmologists for different patterns in all three test sets and recognition pattern deviation probability map regions, showing its promise for clinical applicability.

Glaucoma diagnosis by VF measurement has become a common practice in clinical, and AI will have considerable potential in the field of automated VF measurement. However, the clinical generality of DL models from different studies, as well as the size of external test datasets and manual screening methods, affect the application of DL.

2.2 Fundus image

Artificial intelligence applied to fundus photography is a hot topic for researchers recently, because this methodology is able to perform targeted screening in different areas with simple devices, which makes the detection of early fundus lesions more convenient.

Thus its mode of combining with AI for diagnosis has received attention from the initial detection of diabetic retinopathy (Gulshan et al., 2016; Abràmoff et al., 2018), and gradually applied to the diagnosis of glaucoma. AI focuses on problems including segmentation and detection of the optic nerve head, optic disc and RNFL to achieve accurate analyses of glaucoma fundus photographs. The early role of AI in glaucoma was comparatively simple, such as robust algorithms for quickly locating the optic disc region (Wang et al., 2017). This efficient kernelized least squares classifier extracts optic disc locations using vascular alignment, and its detection results on two digital retinal image datasets show that it has high Geometric Dilution Precision and speed. Then more DL systems and multi-integrated CNN models came out of the woodwork.

Among the numerous neural network structures for diagnosing glaucoma fundus photographs, the one more widely used is the ResNet structure. This DL model classifies fundus photographs with anatomical features of the upper and lower portions of the optic disc which are commonly used when diagnosing, with reduced training time. In 2018, (Christopher et al., 2018) used the transfer learning ResNet architecture to generate a DL algorithm that identifies glaucomatous optic neuropathy (GON). A subsequent study (Li et al., 2020b) using a DL model relying on ResNet101 demonstrated that identifying color fundus images with the neuroretinal rim region, RNFL defect areas (superior or inferior) and combining it with medical history information could better identify GON. However, several false negative results still affect the accuracy of the assay, e.g., pathologic or high myopia, age-related macular degeneration and diabetic retinopathy (Li et al., 2018b). The deep residual learning algorithm ResNet10 developed by Shibata et al. (2018) verified the accuracy of diagnosing glaucoma in high myopic eyes. It obtained an AUC value of 97.1% in the “G” (glaucoma) and “N” (normal eyes) groups and 96.4% in the “mG” (high myopia and glaucoma) and “mN” (high myopia and non-glaucoma) groups, which is markedly stronger than the residents (AUC 72.6%–91.2%). Recently, this network architecture has also been used in primary open-angle glaucoma (Fan et al., 2022). Experts took advantage of VF and optic disc information from 1,636 participants collected by the ocular hypertension treatment study over an average of 10 years to train the ResNet50 model and achieve high specificity on the test set beyond the study endpoint committee. To facilitate patient applications, DL algorithms have also been developed for smartphones using ResNet6 (Nakahara et al., 2022), which requires an accompanying D-Eye lens for fundus photo capture. Although it has some effectiveness in advanced glaucoma, its usage requires the flash to be continuously lit for 1 min against a dilated eye, which needs to be updated.

Several other neural network structures with different characteristics have also been employed for glaucoma detection. Deep convolutional neural algorithms in the Inception-v3 architecture identify optic nerve head features and GON from fundus images to facilitate early glaucoma referral diagnostic decisions (Phene et al., 2019). This algorithm was trained on individual pathological features and GON wholeness based on 86,618 fundus photographs and demonstrated AUCs between 0.855 and 0.945 on three test sets. Distinct from the traditional U-Net network, the SA module, namely, Scale-Attention Deep Learning Network, is inserted into the bridging connection to

capture more scale features to interpret different structures and functions in retinal tissues (Hu et al., 2021). It can effectively segment 2D small sample retinal fundus images in order to determine glaucomatous fundus lesions. Another cycle generative adversarial network (CycleGAN) (Yoo et al., 2022) can connect information from the retro-ocular segment to the pre-ocular segment for detecting closed-angle glaucoma and has found that shallow anterior chamber depth is characterized by brighter areas around the optic disc and macula. Alternatively, one may choose to skillfully apply CycleGAN in combination with U-Net for retinal lesion localization (Zhang et al., 2022), where CycleGAN generates more available images and U-Net acts as a generator against the discriminator to generate the optimal solution, collaborating with the classifier to distinguish the domain of the input image. This demonstrates that a combination of different AI tools can improve diagnostic performance.

The ensemble model with its superior performance over the single model is now also highly preferred. Compared to a single model, the ensemble model combines the advantages of different AI image analyses as well as complements each other's shortcomings. In 2020, (Ko et al., 2020) built an ensemble model TVGH-CNN merging a VGGNet-based CNN model and an SVM classifier to detect GON. For the easy-to-miss features of AI based on optic disc segmentation, such as increased vertical CorelDRAW and thinning of the upper and lower neuroretinal edges, it is possible to select a model via confidence scores, with SVM selected for low confidence in CNN, to achieve mid-to-late stage diagnosis of glaucoma. It achieved 95.0% accuracy and 94.2% specificity in the Drishti GS dataset. However, the classification accuracy is low and the generalizability is not high. But this method of assigning confidence scores provides a new way of thinking about the integration of models. Modeling several different neural networks to form an integrated system to automatically grade the severity of glaucoma is also a way forward for an ensemble system (Cho et al., 2021). Recently, a study has utilized a multimodal model to analyze the vertical cup-to-disc ratio and mean RNFL thickness to identify glaucoma in a myopic population (Lim et al., 2022). Where random forest, SVM, logistic regression, Ada-boost, k-nearest neighbors and a dense neural network were linked, and the images were categorized with the Xception model. This DL system was followed up with a web page for screening and telemedicine, covering a sizeable glaucoma suspect population.

Artificial intelligence scholars have focused on the convenience and trustworthiness of fundus photography, which can be implemented in less medically privileged areas, and have explored the possibilities of the combination of two technologies for accurate and efficient glaucoma diagnosis. This technology is now evolving from a single neural network to an ensemble model. Simple optic disc segmentation and vascular localization can determine whether disease is present or absent in GON detection and RNFL thickness measurement for grading glaucoma and identifying new fundus features.

2.3 OCT

Compared to fundus imaging, OCT has superior sensitivity and specificity. Recent innovations in OCT equipment have brought

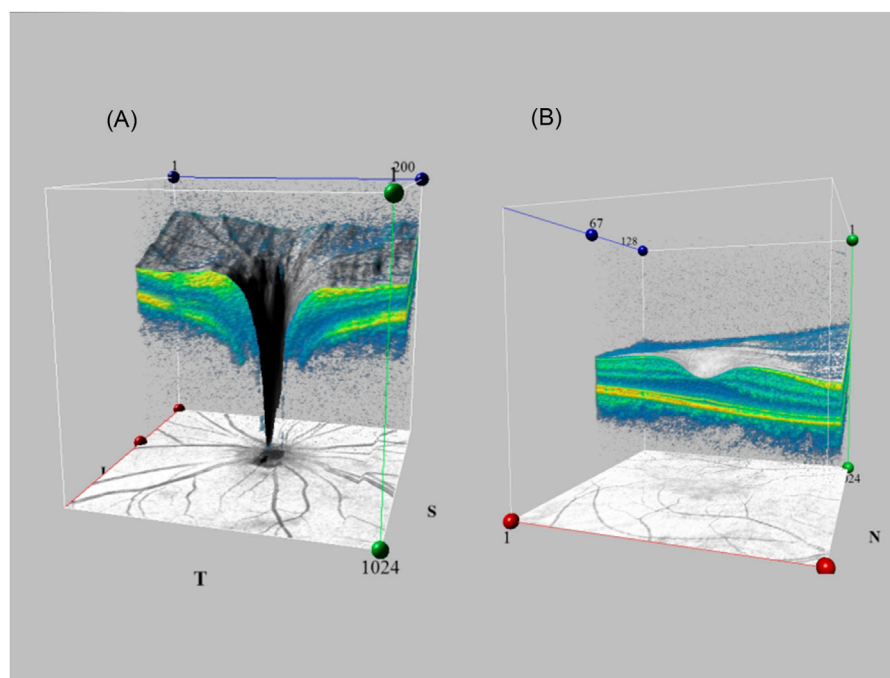


FIGURE 2

SD-OCT utilizes 3D capabilities for fundus scanning. Generating 3D fundus images by volume scanning and linear scanning of the feature site (A). Optic disc region (B). Macular region.

high-quality analytical data to the development of AI. Spectral domain OCT (SD-OCT) and scanning source OCT (SS-OCT) have improved axial resolution, enabling faster and more accurate acquisition of morphological features at the posterior end of the eye. Anterior segment OCT (AS-OCT) allows assessment of atrial angle opening and closing, anterior chamber depth as well as iris and lens to obtain biometric parameters (Ran et al., 2021). In contrast to traditional machine learning models, the DL model does not require segmentation and it can use the raw OCT data to classify and identify areas of lesion that are not readily detectable to humans.

Nowadays SD-OCT is widely used in ophthalmology. A three-dimensional (3D) deep learning algorithm allows combination with SD-OCT to scan degeneration of the glaucomatous optic nerve head. Figure 2 shows the SD-OCT performing fundus scans using 3D capabilities. The first 3D deep learning system (Ran et al., 2019) which utilizes ResNet structures for glaucomatous lesion analyses in optic nerve head volume data collected by SD-OCT. Compared to 2D models, it uses 3D deep learning algorithms to obtain better results. Its diagnosis relies on accurate segmentation of the retinal layers, as well as quantification of the RNFL and macular ganglion cell complex. Later scholars (Noury et al., 2022) attempted to formulate a 3D convolutional neural network and trained it to discriminate glaucoma on datasets from Stanford University, Hong Kong, India, and Nepalese sources, responding to its good judgment in OCT images of different ethnic groups. For glaucoma diagnosis, the lamina cribrosa region is highlighted. This is consistent with clinical parameters like cup diameter/volume or rim area/volume. Other scholars wanted to develop a multi-task 3D deep learning model to detect GON and other fundus lesions

like myopia in relation to glaucoma diagnosis (Ran et al., 2022). ResNet architecture was developed with multi-input CNNs and multi-channel variational autoencoders, which were applied for internal and external validation, with results outperforming RNFL thickness. CNNs have been trained before by using the macular RNFL thickness and ganglion cell complex layer thickness on images (Asaoka et al., 2019), which performed better than random forest and SVM. Rather than being limited by errors in manual classification of subjective markers, it saves even more manpower and time (Medeiros et al., 2021). Subsequently, researchers have attempted to develop a model for predicting the development of glaucoma by combining fundus photographs with OCT in a “machine-to-machine” model (Medeiros et al., 2019). This model continues to use the ResNet34 architecture to consecutively predict the mean RNFL thickness, achieving a mean absolute error (MAE) of 7.39 μm . RNFL thickness values for all sectors “CNNA” combined with temporal sectors “CNNT” using SD-OCT circle scans can also be used to measure the central 10° visual field map in glaucoma patients (Kamalipour et al., 2023). Or AI can use the additional information collected by SD-OCT to form an overall DL model to evaluate visual function, such as ganglion cell layer, ganglion cell-inner plexiform layer, inner plexiform layer and macular ganglion cell layer (Christopher et al., 2021). Lee et al. (Lee et al., 2020a) developed a hybrid deep learning model algorithm that utilized Inception-ResNet-v2 to extract features and paired it with SVM for regression and classification problems. The results with red-free RNFL photographs measurement macular ganglion cell-inner plexiform layer thickness showed a correlation coefficient of $r = 0.739$ and a consistency metric of $\text{MAE} = 4.76 \mu\text{m}$ with the true

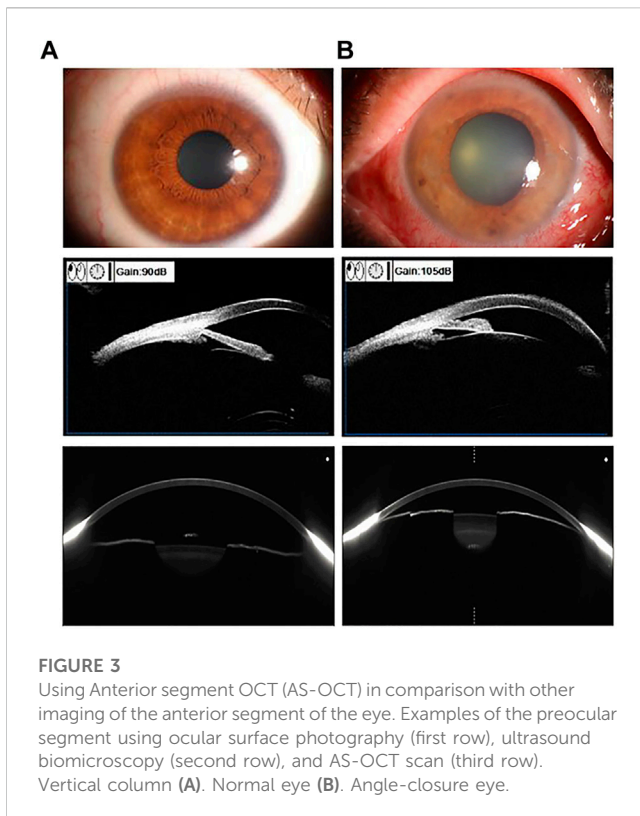


FIGURE 3

Using Anterior segment OCT (AS-OCT) in comparison with other imaging of the anterior segment of the eye. Examples of the preocular segment using ocular surface photography (first row), ultrasound biomicroscopy (second row), and AS-OCT scan (third row). Vertical column (A). Normal eye (B). Angle-closure eye.

measurements. This suggests that hybrid DL models also hold good promise for applications in OCT.

Traditional detection of the preocular segment using AS-OCT depends on the ophthalmologist's refinement of the image and identification of the scleral spur. Artificial intelligence can automatically perform the extraction of features from AS-OCT such as thick peripheral iris roll, plateau iris and expanded lens vault in the anterior segment and reduce the errors caused by manual recognition through feature extraction. This AI system can detect anterior chamber angles more accurately than other auto-angle closure detection systems. Figure 3 shows the comparison of AS-OCT with other imaging modalities of the anterior segment. By placing long short-term memory neural networks, which captures temporal information in images, in the last pooling layer of a trained ResNet model (Hao et al., 2022), a DL model was constructed to process image data and investigate the relationship between dynamic iris changes and primary angle-closure glaucoma. Xu et al. (Xu et al., 2019) formulated three competing multiclass CNNs to compute binary probabilities of atrial angle closure (Shaffer class 0 or 1). In the end the ResNet18 classifier obtained superior performance. It helps clinical judgment of angle opening and closing by using accurate calculation power, which saves time and improves accuracy. The DL model also allows for the development of an automated digital gonioscopy system to simulate static and dynamic gonimetry at a level not inferior to that of a clinician (Li et al., 2022b). Alternatively, a sliding window-based regression task for locating the anterior atrial angle can be created to automatically perform angle detection using three parallel sub-networks to process data and extract image features (e.g., anterior segmental allostructure, iris structure, atrial

angle structure) from the AS-OCT output. The Chinese American Eye Study has utilized this theory to develop a DL model for detecting the atrial angle that has been tested in communities of different ethnicities (Randhawa et al., 2021). AS-OCT combined with AI can also analyze features that are not noticed by humans to facilitate the adoption of unsupervised learning. For example, setting the latent space size of the β -variational autoencoder to 6 and the beta value to 53 in the study by Shon et al. (2022a); Shon et al., 2022b) enables the extraction of low-dimensional latent variables, which can then be converted into shallow and understandable features.

As the machines are updated, new features are being created to fill the gaps in the development of modern OCT, which can be combined with a variety of ophthalmic examination instruments to detect multiple diseases simultaneously and even explore the pathogenesis of glaucoma in the microscopic cellular world. For example, an hybrid deep learning model can be linked with a single wide-field OCT for quadrant analysis to differentiate glaucoma (Muhammad et al., 2017), the custom DL architecture LightOCT can classify various diseases of the eye in public datasets (Butola et al., 2020), and SS-OCT is combined with a DL model to detect peripheral anterior adhesions (Yang et al., 2021). Zadeh et al. (Soltanian-Zadeh et al., 2021) used adaptive optical AO-OCT with weakly supervised deep learning WeakGCSEg to automatically segment cells in order to study the cellular level characteristics of retinal ganglion cells, using click-points weak supervision to generate a fast, high-throughput detection system.

From the perspective of public health, OCT belongs to a category of expensive testing equipment, which is not as widely tested everywhere on a large scale as fundus imaging. But because of its precision, it is ideally suited to provide AI with more specific ocular features, and because of the addition of AI, it also makes OCT technology more labor efficient. They complement each other. In the future, it is likely that SD-OCT with its universality and AS-OCT with its immediacy will have a large market share in the field of glaucoma research. But other OCT techniques will receive more attention and exploration on the strength of their unique ability to retrieve information. Table 1 shows the deep learning studies for glaucoma diagnosis using OCT images as input.

3 Prediction models in glaucoma

Keeping track of a patient's progress can be of great significance in preventing blindness and delaying the condition. Glaucoma requires close monitoring of longitudinal case information by doctors and timely medical intervention to salvage the nerve and VF damage caused by high intraocular pressure. Although prediction and diagnosis are similar by virtue of the detection tools, the conception of the DL model extraction, analysis and output content is not identical. They target different sites and severity of lesions in different periods of glaucoma, and the methods of analyses used are not uniform. It is widely known that glaucoma is closely related to VF, so the prediction of glaucoma in all aspects is largely focused on the prediction of VF as well. However, it has undergone some processes to be perfected. Some researchers (Eslami et al., 2023) investigated the accuracy of the previously emerged CNN model and recurrent neural network

TABLE 1 Summary table of deep learning studies for glaucoma diagnosis with OCT images as input.

References	Year	Model	Dataset		Aim	Result
Ran et al.	2019	ResNet	GON/No GON		detect GON	Primary validation: AUROC: 0.969, sensitivity: 89%, specificity: 96%, accuracy: 91%
	—	—	Training, testing, and primary validation dataset	2926/1951	—	External validation: AUROC: 0.893–0.897, sensitivities: 78%–90%, specificities: 79%–86%, accuracies: 80%–86%
	—	—	External validation dataset	1434/610	—	—
Noury et al.	2022	DiagFind	Glaucoma/Non-glaucoma		manifest glaucoma	AUC: perimetric glaucoma
						Stanford: 0.91
						Hong Kong: 0.80
						India: 0.94
						Nepal: 0.87
	—	—	Training	1022/542	—	—
	—	—	Validation	142/61	—	—
	—	—	Test	453/241	—	—
	—	—	External validation dataset	1642/1035	—	—
Ran et al.	2022	ResNet	yes GON and yes MF/no GON and yes MF/yes GON and no MF/no GON and no MF		GON	AUROC
					MF	GON: Internal validation 0.949
						External testing dataset 0.890–0.950
	—	—	Training	1679/890/629/721	—	MF: 0.855–0.896
	—	—	Tuning	195/163/32/70	—	—
	—	—	Internal validation	205/114/36/99	—	—
	—	—	External testing dataset	1347/515/677/777	—	—
	Asaoka et al.	2019	Deep learning	Glaucoma/Non-glaucoma		early glaucoma
Pretraining: 93.7%						
Without pretraining: 76.6%–78.8%						
			Pretraining	1371/193	—	—
			Training	94/84	—	—
			Test	114/82	—	—
Medeiros et al.	2021	ResNet50	86 123		progressive glaucomatous changes over time	AUC: 0.86
Medeiros et al.	2019	ResNet34	Normal/Suspect/Glaucoma		quantify glaucomatous structural damage	MAE: 7.39 μm
						AUC: predictions: 0.944
						actual measurements: 0.940
	—	—	Training	3982/13 410/9136	—	—
	—	—	Test	877/3345/2070	—	—
Kamalipour et al.	2023	CNN _A	Normal/Suspect/Glaucoma		estimate central 10° visual field	MAE
						CNN _A : 4.04 dB

(Continued on following page)

TABLE 1 (Continued) Summary table of deep learning studies for glaucoma diagnosis with OCT images as input.

References	Year	Model	Dataset		Aim	Result				
	—	CNN _T	Training and Validation	174/367/623	—	—				
	—	LR	Test	20/71/110	—	—				
Christopher et al.	2021	ResNet50	10-2 Visual Field/24-2 Visual Field		estimating visual function	10-2				
						R ² MD:0.82				
						PSD: 0.69				
						MAE MD: 1.9 dB				
	—	—	Training	2131/277	—	24-2				
						R ² MD:0.79				
						PSD: 0.68				
—	—	Test	2674/325	—	MAE MD: 2.1 dB					
Lee et al.	2020a	HDLM	Normal/Suspect/Glaucoma		predicts macular ganglion cell-inner plexiform layer thickness	MAE: 4.76 μm				
	—	—	292/109/388		—	—				
Hao et al.	2022	ResNet + LSTM	Glaucoma/Non-glaucoma		angle-closure screening	AUC				
						Casia dataset: Images 0.766; Original videos 0.820; Aligned videos 0.905.				
	—	—	159/210		—	Zeiss dataset: Images 0.767; Original videos 0.837; Aligned videos 0.919				
Xu et al.	2019	ResNet18	Open angle/Closed angle		detect gonioscopic angle closure and primary angle closure disease	AUC: gonioscopic angle: 0.928				
						disease: 0.952				
	—	—	Cross-validation	1632/1764	—	—				
	—	—	Test	311/329	—	—				
Li et al.	2022b	ResNet34	Task I/Task II		Task I (1) narrow iridocorneal angles	Task I				
						AUC: 0.943, sensitivity: 0.867, and specificity: 0.878				
	—	—	Training	4515/378	Task II (2) peripheral anterior synechiae	Task II				
	—	—	Internal validation	1101/376	—	AUC: 0.902, sensitivity: 0.900, and specificity: 0.890				
	—	—	External testing	2222/102	—	—				
	Randhawa et al.	2021	ResNet18	Open angle/Closed angle		detect gonioscopic angle closure	AUC: 0.894–0.922			
—							—	CHES train	1764/1632	—
—							—	CHES test	329/311	—
—							—	Singapore	570/9595	—
—							—	USC	66/234	—
Shon et al.	2022a	β-VAE	Training	1692	extract a low-dimensional latent structure	mean values of visual field index: 86.4%				
						mean deviation: −5.33 dB				

(Continued on following page)

TABLE 1 (Continued) Summary table of deep learning studies for glaucoma diagnosis with OCT images as input.

References	Year	Model	Dataset		Aim	Result
	—	—	Validation	419	—	—
Shon et al.	2022b	VAE	Training	1692	Analysis the latent structure	Among the symmetrical latent variables, the first three and the last demonstrated easily recognized features.
	—	—	Validation	419	—	—
Muhammad et al.	2017	HDLM	Glaucoma/Health or suspects		Distinguish glaucoma eyes	accuracy: 63.7%–93.1%
	—	—	57 eye/45 eye		—	—
Butola et al.	2020	LightOCT	Choroidal neovascularization/Diabetic macular edema/Drusen/Normal		Distinguish glaucoma eyes	accuracy: 96%
	—	—	Training	27 206/11 349/8617/51 140	—	—
	—	—	Test	250/250/250/250	—	—
Yang et al.	2021	InceptionResNetV2	Open angle/Closed angle		detect the static gonioscopic angle closure and peripheral anterior synechia	static gonioscopic angle closure AUC: 0.963 sensitivity: 0.929 specificity: 0.877
	—	—	Training	3 4705/1 5945	—	appositional from synechial angle closure AUC: 0.873 Sensitivity: 0.846 Specificity 0.764
	—	—	Validation	8037/3254	—	—
	—	—	Test	7860/3024	—	—
	2021	WeakGCSEg	Training samples/Testing samples		Cell-level quantitative features of retinal ganglion cells	WeakGCSEg is on par with or superior to human experts and is superior to other state-of-the-art networks.
	—	—	Subject 1 (IU/IU)	Healthy: 7:14/1:2	—	—
	—	—	Subject 2 (IU/IU)	Healthy: 7:14/1:1	—	—
Soltanian-Zadeh et al.	—	—	Subject 3 (FDA/FDA)	Healthy: 3:4-5/1:1-2	—	—
	—	—		Glaucoma: 4:8/1:2	—	—
	—	—	Subject 4 (IU/FDA)	Healthy: 8:16/4:6	—	—
	—	—	FDA/IU	Healthy: 4:6/8:16	—	—
	—	—	IU + FDA/IU + FDA)	Healthy: 9:16-17/9:16-17	—	—

● ResNet residual network; GON, glaucomatous optic neuropathy; AUROC, area under the receiver operating characteristic; AUC, area under curve; MF, myopic features; MAE mean absolute error; CNN, convolutional neural network; LR, ordinary least squares linear regression models; MD, mean deviation; PSD, pattern standard deviation; HDLM, hybrid deep learning method; LSTM, long short-term memory; CHES, the Chinese American Eye Study; USC, the University of Southern California; VAE variational auto-encoder; IU, the Indiana University; FDA, the U.S. food and drug administration.

model in predicting VF changes over time. Although exerting some power, both models showed errors in predicting patients with severe glaucoma, like grossly underestimating the degree of deterioration in VFs loss and working poor in patients with large changes in VFs at baseline and follow-up. These may affect the clinical applicability. The generalized Variational

Autoencoder DL model (Berchuck et al., 2019) ameliorates these problems to some extent. It uses a lower dimensional latent space representation of a higher dimensional VF image to output a resultant prediction via an arbitrary non-linear mapping. It was learned and tested on 29,161 VFs with good results.

In subsequent studies, the researchers predicted the course of glaucoma by using various auxiliary tests in the AI analyses to predict VF changes. In previous years, scholars first used fundus photographs to predict the progression of glaucoma (Thakur et al., 2020). They found the AUC predicted from fundus photographs 4–7 years before onset was 0.77, 1–3 years predicted 0.88, and 0.95 for post-onset diagnosis. The closer to the time of onset the more obvious the lesion is the easier it is to detect by AI. Additional studies (Lee et al., 2020b) have transformed qualitative structural data (optic disc photograph) into quantitative functional data (standard automated perimetry, mean deviation), predicting standard automated VF measurements from single-field optic disc photographs. A neural architecture search network (NASNet) was used to extract fundus features and predict VF progression. There are other studies that have used machine-to-machine approaches, such as (Lee et al., 2021) who trained deep learning algorithms in OCT images to predict longitudinal changes in RNFL thickness on fundus images to explore whether it could predict the future development of glaucomatous VFs. A longitudinal survival model was used for this retrospective cohort study, controlling for other confounding factors (e.g., age, mean intraocular pressure, etc.), and the DL system still accurately predicted regression in glaucoma. The ResNet6 architecture allows the exploitation of a multiple linear regression model that, after pre-training on a larger dataset followed by fine-tuning and transfer learning, can also perform well on a smaller training set, achieving a smaller mean absolute error, which is advantageous when applied to VF prediction for fundus imaging. These technologies will also gradually come into our lives, with a glaucoma prediction system for smartphones already in development (Li et al., 2022a).

The application of OCT images to predict glaucoma also focuses on the evaluation of the VFs. Predicting changes in the HFA 10–2 visual field based on macular retinal layer thickness measured by SD-OCT, and HFA 24–2 test values, both ResNet and VGG algorithms can be applied (Christopher et al., 2020; Asano et al., 2021). It is also possible to analyze RNFL, ganglion cell layer and inner plexiform layer, outer segment and retinal pigment epithelium using the unsupervised learning pattern-based regularization method to determine the 10° central field of view (Hashimoto et al., 2021). Or use tensor regression (CNN-TR) (Xu et al., 2020a) to develop a model with higher-order multiple regression to reduce the number of parameters and improve accuracy. It replaces fully connected neural networks and vectorisation operations and has the relative advantage of predicting the central 10° field of view. In addition to SD-OCT, SS-OCT can also be employed. SS-OCT (Park et al., 2020) combined with the Inception architecture allows for VF prediction, but with decreasing accuracy as glaucoma progresses. [Supplementary Table S1](#) summarizes the deep learning studies used for glaucoma prediction.

At the current stage, prediction of structures and functions is not yet complete and multimodal detection tools are still being bred. To get a better trend, it is necessary to combine structure and function, collect more clinically relevant data from patients and incorporate multiple perspectives to analyze the outlook for disease progression. For future clinical applications, it may be more promising to investigate early prediction before the onset of the disease.

4 Limitations and further advancements

4.1 Limitations

With the introduction of artificially intelligent diagnostic and predictive models, our review opens a door to a new approach to the detection of glaucoma. The logic behind studying these technologies is that they allow for direct clinical diagnosis, the timely identification of patients requiring referral or surgical intervention is critical for glaucoma specialists, and AI can assist with such steps to reduce the loss of vision and VFs in patients. Today's epidemic of SARS-CoV-2 and the crowding of medical resources are challenging the healthcare system, requiring AI to combine with medicine to facilitate each other's development and provide more sophisticated technology for increased medical needs. Visualization of the AI analysis reveals that its segmentation and judgments are often in most of the same locations as those used by ophthalmologists in their diagnoses, but also in some of the features that have not been identified by humans. This will be a key component of future developments, which will better reveal the pathological mechanisms of disease and obtain more information from the raw images. Yet the growth of AI in recent years has also revealed a number of problems.

- 1) Standard dataset creation It is about whether AI can be developed or even have practical effects. Firstly, the dataset is homogeneous in terms of features. Because the datasets being used are publicly available (Camara et al., 2022), the classification of images lacks specificity that is often consistent with homogeneous diseases or populations, making it difficult to ensure the fairness of the validated results. Secondly, the utilization of clinical data is very low. Although there have been some studies that have utilized clinical features of disease with some personalization, AI still has low usage of clinical records, resulting in little information for grading prognosis of diseases. Third, the quality of images varies. Public datasets are often created for large-scale disease screening or treatment evaluation, and their images may be all-encompassing but lack classification and labeling. The quality of photography also varies, with no uniform standards to regulate it. Private datasets tended to be difficult to access and had insufficient images (<10,000). Finally, the AI developed by different datasets lacks comparability. DL models trained and tested with large datasets are not necessarily more accurate than with small datasets (Zheng et al., 2019). Moreover, transfer learning without adjustment is likely to fail in the real world, and the AUC is not as reliable and will be higher in smaller datasets.
- 2) Standardized norms and guidelines Any medical instrument must undergo multiple rounds of experimental validation and production of manuals for reference before it can be clinically applied. So does AI. However, we only hear the call of the market, but do not see the preparation for it. Although some countries have already proposed specifications (Bossuyt et al., 2003), an international consensus standard is needed to face the rapidly evolving AI systems. The definition of criteria for accuracy and specificity, the uniformity of testing, the fixed population to

which it can be applied, and the long-term follow-up system make up a complete evaluation system.

- 3) Single and simple usage Glaucoma is a complex neurodegenerative disease that requires both structural and functional evidence for a definitive diagnosis. The numerous and lengthy tests are burdens for both doctors and patients, and AI has not yet evolved to a point where a definitive diagnosis can be made with simple one method; it can only improve on one of the existing tests to a certain extent, which is the direction to be considered in the future.
- 4) Multi-ethnic applications Although technology has no borders, people of different nationalities have different physiques. How the invented AI can serve more people to expand its popularity, if it has good sensitivity and specificity in different people, requires more cross-border, multi-center experimental studies.
- 5) Black Box Theory In clinical work, it is difficult to gain patients' trust if they cannot understand the treatment tools, and only conclusions can be drawn about the new disease features explored by CNNs, without complete clarity of the inference process. The "black box" nature of AI makes it uninterpretable, and even with the application of feature visualization techniques such as Class Activation Mapping, the completed analysis process of a CNN is still not available. This is the area that needs to continue exploration.

4.2 Further advancements

Anything that develops faces more than one type of problem, but this is exactly the prospect necessary for growth. There are already some scientific answers to the questions we discussed, for example, for dataset updates, articles have been reported using Generative Adversarial Networks to modify synthetic real images to enrich existing datasets without compromising patient privacy. Regarding image quality it has also been reported that CycleGAN's tool can eliminate artifact interference. The existing research in AI shows that there is a great interest in new disease features perceived by DL models, which may be an important clue to investigate the source of the disease and deserves to be studied in depth. In response to the issues raised, dataset optimization, including the establishment of multicenter, large sample, and high validity datasets is the determined growth prospect. Simplification of the existing diagnostic methods in a single way, so that the created AI system serves more diverse people is also a development direction to be worked on. Uniform rules and guidelines for assisted development require global consultation and exchange of ideas. Apart from the aforementioned, we believe that the development of telemedicine and virtual reality technology will become a hot prospect for ophthalmology and even the whole medical field under the conditions of today's social communication networks and electronic equipment hardware. There has been some progress in the research of AI and telemedicine (Nikolaidou and Tsaousis, 2021), and the integration with virtual reality technology (Ma et al., 2022) is still on the rise. In addition, glaucoma is a genetically linked genetic disorder and should be subject to early genetic screening and referral for further precise diagnosis and intervention. Genetic

diagnosis combined with AI technology development is another way to obtain critical evidence that improves diagnostic efficiency and allows for better patient prognosis. These fields of research will certainly bring the technology of AI for glaucoma diagnosis and prediction to maturity and canonicalization.

5 Conclusion

Artificial intelligence is evolving rapidly in the field of ophthalmology, and since previous reviews on glaucoma with AI are not perfect, we have written this targeted review to explore the development of AI models in the field of glaucoma diagnosis and prediction in recent years, especially the revolution of DL models. We present the current state of research and found that scholars have mainly used HFA, fundus photography and OCT, which are commonly used in ophthalmology to collect image data. Using network structures such as ResNet, VGG, U-Net, Inception, CycleGAN and ensemble convolutional neural that can explore deeply to extract image features. Dataset quality, uniform rules and guidelines, single and simple usage, multi-ethnic applications and black box effect will be the critical issues to be addressed. Issues such as genetic screening for glaucoma and telemedicine could be promising opportunities.

Author contributions

LZ conceived, organized, and wrote the manuscript; GC reviewed and revised the manuscript; LT and MX collected the original images and other materials for the article. All authors contributed to the article and approved the submitted version.

Conflict of interest

The authors declare that the research was conducted in the absence of any commercial or financial relationships that could be construed as a potential conflict of interest.

Publisher's note

All claims expressed in this article are solely those of the authors and do not necessarily represent those of their affiliated organizations, or those of the publisher, the editors and the reviewers. Any product that may be evaluated in this article, or claim that may be made by its manufacturer, is not guaranteed or endorsed by the publisher.

Supplementary material

The Supplementary Material for this article can be found online at: <https://www.frontiersin.org/articles/10.3389/fcell.2023.1173094/full#supplementary-material>

References

- Abrahamoff, M. D., Lavin, P. T., Birch, M., Shah, N., and Folk, J. C. (2018). Pivotal trial of an autonomous AI-based diagnostic system for detection of diabetic retinopathy in primary care offices. *NPJ Digit. Med.* 1, 39. doi:10.1038/s41746-018-0040-6
- Asano, S., Asaoka, R., Murata, H., Hashimoto, Y., Miki, A., Mori, K., et al. (2021). Predicting the central 10 degrees visual field in glaucoma by applying a deep learning algorithm to optical coherence tomography images. *Sci. Rep.* 11 (1), 2214. doi:10.1038/s41598-020-79494-6
- Asaoka, R., Iwase, A., Hirasawa, K., Murata, H., and Araie, M. (2014). Identifying "preperimetric" glaucoma in standard automated perimetry visual fields. *Invest. Ophthalmol. Vis. Sci.* 55 (12), 7814–7820. doi:10.1167/iov.14-15120
- Asaoka, R., Murata, H., Hirasawa, K., Fujino, Y., Matsuura, M., Miki, A., et al. (2019). Using deep learning and transfer learning to accurately diagnose early-onset glaucoma from macular optical coherence tomography images. *Am. J. Ophthalmol.* 198, 136–145. doi:10.1016/j.ajo.2018.10.007
- Balyen, L., and Peto, T. (2019). Promising artificial intelligence-machine learning-deep learning algorithms in ophthalmology. *Asia Pac. J. Ophthalmol. (Phila)* 8 (3), 264–272. doi:10.22608/apo.2018479
- Benet, D., and Pellicer-Valero, O. J. (2022). Artificial intelligence: The unstoppable revolution in ophthalmology. *Surv. Ophthalmol.* 67 (1), 252–270. doi:10.1016/j.survophthal.2021.03.003
- Berchuck, S. I., Mukherjee, S., and Medeiros, F. A. (2019). Estimating rates of progression and predicting future visual fields in glaucoma using a deep variational autoencoder. *Sci. Rep.* 9 (1), 18113. doi:10.1038/s41598-019-54653-6
- Bossuyt, P. M., Reitsma, J. B., Bruns, D. E., Gatsonis, C. A., Glasziou, P. P., Irwig, L. M., et al. (2003). Towards complete and accurate reporting of studies of diagnostic accuracy: The STARD Initiative. *Ann. Intern. Med.* 138 (1), 40–44. doi:10.7326/0003-4819-138-1-200301070-00010
- Butola, A., Prasad, D. K., Ahmad, A., Dubey, V., Kaiser, D., Srivastava, A., et al. (2020). Deep learning architecture "LightOCT" for diagnostic decision support using optical coherence tomography images of biological samples. *Biomed. Opt. Express* 11 (9), 5017–5031. doi:10.1364/boe.395487
- Camara, J., Rezende, R., Pires, I. M., and Cunha, A. (2022). Retinal glaucoma public datasets: What do we have and what is missing? *J. Clin. Med.* 11 (13), 3850. doi:10.3390/jcm11133850
- Chan, E. W., Li, X., Tham, Y. C., Liao, J., Wong, T. Y., Aung, T., et al. (2016). Glaucoma in asia: Regional prevalence variations and future projections. *Br. J. Ophthalmol.* 100 (1), 78–85. doi:10.1136/bjophthalmol-2014-306102
- Cho, H., Hwang, Y. H., Chung, J. K., Lee, K. B., Park, J. S., Kim, H. G., et al. (2021). Deep learning ensemble method for classifying glaucoma stages using fundus photographs and convolutional neural networks. *Curr. Eye Res.* 46 (10), 1516–1524. doi:10.1080/02713683.2021.1900268
- Christopher, M., Belghith, A., Bowd, C., Proudfoot, J. A., Goldbaum, M. H., Weinreb, R. N., et al. (2018). Performance of deep learning architectures and transfer learning for detecting glaucomatous optic neuropathy in fundus photographs. *Sci. Rep.* 8 (1), 16685. doi:10.1038/s41598-018-35044-9
- Christopher, M., Bowd, C., Belghith, A., Goldbaum, M. H., Weinreb, R. N., Fazio, M. A., et al. (2020). Deep learning approaches predict glaucomatous visual field damage from OCT optic nerve head en face images and retinal nerve fiber layer thickness maps. *Ophthalmology* 127 (3), 346–356. doi:10.1016/j.ophtha.2019.09.036
- Christopher, M., Bowd, C., Proudfoot, J. A., Belghith, A., Goldbaum, M. H., Rezapour, J., et al. (2021). Deep learning estimation of 10-2 and 24-2 visual field metrics based on thickness maps from macula OCT. *Ophthalmology* 128 (11), 1534–1548. doi:10.1016/j.ophtha.2021.04.022
- Combalia, M., Codella, N., Rotemberg, V., Carrera, C., Dusza, S., Gutman, D., et al. (2022). Validation of artificial intelligence prediction models for skin cancer diagnosis using dermoscopy images: The 2019 international skin imaging collaboration grand challenge. *Lancet Digit. Health* 4 (5), e330–e339. doi:10.1016/s2589-7500(22)00021-8
- Davis, B. M., Crawley, L., Pahlitzsch, M., Javaid, F., and Cordeiro, M. F. (2016). Glaucoma: The retina and beyond. *Acta Neuropathol.* 132 (6), 807–826. doi:10.1007/s00401-016-1609-2
- Devalla, S. K., Liang, Z., Pham, T. H., Boote, C., Strouthidis, N. G., Thiery, A. H., et al. (2020). Glaucoma management in the era of artificial intelligence. *Br. J. Ophthalmol.* 104 (3), 301–311. doi:10.1136/bjophthalmol-2019-315016
- Dixit, A., Yohannan, J., and Boland, M. V. (2021). Assessing glaucoma progression using machine learning trained on longitudinal visual field and clinical data. *Ophthalmology* 128 (7), 1016–1026. doi:10.1016/j.ophtha.2020.12.020
- Eslami, M., Kim, J. A., Zhang, M., Boland, M. V., Wang, M., Chang, D. S., et al. (2023). Visual field prediction: Evaluating the clinical relevance of deep learning models. *Ophthalmol. Sci.* 3 (1), 100222. doi:10.1016/j.xops.2022.100222
- Fan, R., Bowd, C., Christopher, M., Brye, N., Proudfoot, J. A., Rezapour, J., et al. (2022). Detecting glaucoma in the ocular hypertension study using deep learning. *JAMA Ophthalmol.* 140 (4), 383–391. doi:10.1001/jamaophthalmol.2022.0244
- GBD 2019 Blindness and Vision Impairment Collaborators (2021). Causes of blindness and vision impairment in 2020 and trends over 30 years, and prevalence of avoidable blindness in relation to VISION 2020: The right to sight: An analysis for the global burden of disease study. *Lancet Glob. Health* 9 (2), e144–e160. doi:10.1016/s2214-109x(20)30489-7
- Gulshan, V., Peng, L., Coram, M., Stumpe, M. C., Wu, D., Narayanaswamy, A., et al. (2016). Development and validation of a deep learning algorithm for detection of diabetic retinopathy in retinal fundus photographs. *Jama* 316 (22), 2402–2410. doi:10.1001/jama.2016.17216
- Hamet, P., and Tremblay, J. (2017). Artificial intelligence in medicine. *Metabolism* 69s, S36–S40. doi:10.1016/j.metabol.2017.01.011
- Hao, L., Hu, Y., Xu, Y., Fu, H., Miao, H., Zheng, C., et al. (2022). Dynamic analysis of iris changes and a deep learning system for automated angle-closure classification based on AS-OCT videos. *Eye Vis. (Lond)* 9 (1), 41. doi:10.1186/s40662-022-00314-1
- Hashimoto, Y., Asaoka, R., Kiwaki, T., Sugiura, H., Asano, S., Murata, H., et al. (2021). Deep learning model to predict visual field in central 10° from optical coherence tomography measurement in glaucoma. *Br. J. Ophthalmol.* 105 (4), 507–513. doi:10.1136/bjophthalmol-2019-315600
- Hu, J., Wang, H., Wang, J., Wang, Y., He, F., and Zhang, J. (2021). SA-net: A scale-attention network for medical image segmentation. *PLoS One* 16 (4), e0247388. doi:10.1371/journal.pone.0247388
- Huang, X., Jin, K., Zhu, J., Xue, Y., Si, K., Zhang, C., et al. (2022). A structure-related fine-grained deep learning system with diversity data for universal glaucoma visual field grading. *Front. Med. (Lausanne)* 9, 832920. doi:10.3389/fmed.2022.832920
- Kamalipour, A., Moghimi, S., Khosravi, P., Jazayeri, M. S., Nishida, T., Mahmoudinezhad, G., et al. (2023). Deep learning estimation of 10-2 visual field map based on circumpapillary retinal nerve fiber layer thickness measurements. *Am. J. Ophthalmol.* 246, 163–173. doi:10.1016/j.ajo.2022.10.013
- Ko, Y. C., Wey, S. Y., Chen, W. T., Chang, Y. F., Chen, M. J., Chiou, S. H., et al. (2020). Deep learning assisted detection of glaucomatous optic neuropathy and potential designs for a generalizable model. *PLoS One* 15 (5), e0233079. doi:10.1371/journal.pone.0233079
- LeCun, Y., Bengio, Y., and Hinton, G. (2015). Deep learning. *Nature* 521 (7553), 436–444. doi:10.1038/nature14539
- Lee, J., Kim, Y. K., Ha, A., Sun, S., Kim, Y. W., Kim, J. S., et al. (2020a). Macular ganglion cell-inner plexiform layer thickness prediction from red-free fundus photography using hybrid deep learning model. *Sci. Rep.* 10 (1), 3280. doi:10.1038/s41598-020-60277-y
- Lee, J., Kim, Y. W., Ha, A., Kim, Y. K., Park, K. H., Choi, H. J., et al. (2020b). Estimating visual field loss from monoscopic optic disc photography using deep learning model. *Sci. Rep.* 10 (1), 21052. doi:10.1038/s41598-020-78144-1
- Lee, T., Jammal, A. A., Mariottoni, E. B., and Medeiros, F. A. (2021). Predicting glaucoma development with longitudinal deep learning predictions from fundus photographs. *Am. J. Ophthalmol.* 225, 86–94. doi:10.1016/j.ajo.2020.12.031
- Li, F., Wang, Z., Qu, G., Song, D., Yuan, Y., Xu, Y., et al. (2018a). Automatic differentiation of Glaucoma visual field from non-glaucoma visual field using deep convolutional neural network. *BMC Med. Imaging* 18 (1), 35. doi:10.1186/s12880-018-0273-5
- Li, Z., He, Y., Keel, S., Meng, W., Chang, R. T., and He, M. (2018b). Efficacy of a deep learning system for detecting glaucomatous optic neuropathy based on color fundus photographs. *Ophthalmology* 125 (8), 1199–1206. doi:10.1016/j.ophtha.2018.01.023
- Li, F., Song, D., Chen, H., Xiong, J., Li, X., Zhong, H., et al. (2020a). Development and clinical deployment of a smartphone-based visual field deep learning system for glaucoma detection. *NPJ Digit. Med.* 3, 123. doi:10.1038/s41746-020-00329-9
- Li, F., Yan, L., Wang, Y., Shi, J., Chen, H., Zhang, X., et al. (2020b). Deep learning-based automated detection of glaucomatous optic neuropathy on color fundus photographs. *Graefes Arch. Clin. Exp. Ophthalmol.* 258 (4), 851–867. doi:10.1007/s00417-020-04609-8
- Li, F., Su, Y., Lin, F., Li, Z., Song, Y., Nie, S., et al. (2022a). A deep-learning system predicts glaucoma incidence and progression using retinal photographs. *J. Clin. Invest.* 132 (11), e157968. doi:10.1172/jci157968
- Li, F., Yang, Y., Sun, X., Qiu, Z., Zhang, S., Tun, T. A., et al. (2022b). Digital gonioscopy based on three-dimensional anterior-segment OCT: An international multicenter study. *Ophthalmology* 129 (1), 45–53. doi:10.1016/j.ophtha.2021.09.018
- Lim, W. S., Ho, H. Y., Ho, H. C., Chen, Y. W., Lee, C. K., Chen, P. J., et al. (2022). Use of multimodal dataset in AI for detecting glaucoma based on fundus photographs assessed with OCT: Focus group study on high prevalence of myopia. *BMC Med. Imaging* 22 (1), 206. doi:10.1186/s12880-022-00933-z
- Ma, M. K. I., Saha, C., Poon, S. H. L., Yiu, R. S. W., Shih, K. C., and Chan, Y. K. (2022). Virtual reality and augmented reality-emerging screening and diagnostic techniques in ophthalmology: A systematic review. *Surv. Ophthalmol.* 67 (5), 1516–1530. doi:10.1016/j.survophthal.2022.02.001

- Medeiros, F. A., Jammal, A. A., and Thompson, A. C. (2019). From machine to machine: An OCT-trained deep learning algorithm for objective quantification of glaucomatous damage in fundus photographs. *Ophthalmology* 126 (4), 513–521. doi:10.1016/j.ophtha.2018.12.033
- Medeiros, F. A., Jammal, A. A., and Mariottoni, E. B. (2021). Detection of progressive glaucomatous optic nerve damage on fundus photographs with deep learning. *Ophthalmology* 128 (3), 383–392. doi:10.1016/j.ophtha.2020.07.045
- Muhammad, H., Fuchs, T. J., De Cuir, N., De Moraes, C. G., Blumberg, D. M., Liebmann, J. M., et al. (2017). Hybrid deep learning on single wide-field optical coherence tomography scans accurately classifies glaucoma suspects. *J. Glaucoma* 26 (12), 1086–1094. doi:10.1097/jgj.0000000000000765
- Nakahara, K., Asaoka, R., Tanito, M., Shibata, N., Mitsuhashi, K., Fujino, Y., et al. (2022). Deep learning-assisted (automatic) diagnosis of glaucoma using a smartphone. *Br. J. Ophthalmol.* 106 (4), 587–592. doi:10.1136/bjophthalmol-2020-318107
- Nduaguba, C., and Lee, R. K. (2006). Glaucoma screening: Current trends, economic issues, technology, and challenges. *Curr. Opin. Ophthalmol.* 17 (2), 142–152. doi:10.1097/01.icu.00000193088.75432.c9
- Nikolaidou, A., and Tsaousis, K. T. (2021). Teleophthalmology and artificial intelligence as game changers in ophthalmic care after the COVID-19 pandemic. *Cureus* 13 (7), e16392. doi:10.7759/cureus.16392
- Noury, E., Mannil, S. S., Chang, R. T., Ran, A. R., Cheung, C. Y., Thapa, S. S., et al. (2022). Deep learning for glaucoma detection and identification of novel diagnostic areas in diverse real-world datasets. *Transl. Vis. Sci. Technol.* 11 (5), 11. doi:10.1167/tvst.11.5.11
- Padmanabhan, M., Yuan, P., Chada, G., and Nguyen, H. V. (2019). Physician-friendly machine learning for glaucoma detection and identification of novel diagnostic areas in diverse real-world datasets. *Transl. Vis. Sci. Technol.* 11 (5), 11. doi:10.1167/tvst.11.5.11
- Padmanabhan, M., Yuan, P., Chada, G., and Nguyen, H. V. (2019). Physician-friendly machine learning for glaucoma detection and identification of novel diagnostic areas in diverse real-world datasets. *Transl. Vis. Sci. Technol.* 11 (5), 11. doi:10.1167/tvst.11.5.11
- Park, K., Kim, J., Kim, S., and Shin, J. (2020). Prediction of visual field from swept-source optical coherence tomography using deep learning algorithms. *Graefes Arch. Clin. Exp. Ophthalmol.* 258 (11), 2489–2499. doi:10.1007/s00417-020-04909-z
- Phene, S., Dunn, R. C., Hammel, N., Liu, Y., Krause, J., Kitade, N., et al. (2019). Deep learning and glaucoma specialists: The relative importance of optic disc features to predict glaucoma referral in fundus photographs. *Ophthalmology* 126 (12), 1627–1639. doi:10.1016/j.ophtha.2019.07.024
- Ran, A. R., Cheung, C. Y., Wang, X., Chen, H., Luo, L. Y., Chan, P. P., et al. (2019). Detection of glaucomatous optic neuropathy with spectral-domain optical coherence tomography: A retrospective training and validation deep-learning analysis. *Lancet Digit. Health* 1 (4), e172–e182. doi:10.1016/s2559-7500(19)30085-8
- Ran, A. R., Tham, C. C., Chan, P. P., Cheng, C. Y., Tham, Y. C., Rim, T. H., et al. (2021). Deep learning in glaucoma with optical coherence tomography: A review. *Eye (Lond)* 35 (1), 188–201. doi:10.1038/s41433-020-01191-5
- Ran, A. R., Wang, X., Chan, P. P., Chan, N. C., Yip, W., Young, A. L., et al. (2022). Three-dimensional multi-task deep learning model to detect glaucomatous optic neuropathy and myopic features from optical coherence tomography scans: A retrospective multi-centre study. *Front. Med. (Lausanne)* 9, 860574. doi:10.3389/fmed.2022.860574
- Randhawa, J., Chiang, M., Porporato, N., Pardeshi, A. A., Dredge, J., Apolo Aroca, G., et al. (2021). Generalisability and performance of an OCT-based deep learning classifier for community-based and hospital-based detection of gonioscopic angle closure. *Br. J. Ophthalmol.* 107, 511–517. doi:10.1136/bjophthalmol-2021-319470
- Santos Martins, T. G. D., de Azevedo Costa, A. L. F., and Schor, P. (2021). Comment on: "Do we have enough ophthalmologists to manage vision-threatening diabetic retinopathy? A global perspective. *Eye (Lond)* 35 (2), 690–691. doi:10.1038/s41433-020-0903-3
- Setio, A. A., Ciompi, F., Litjens, G., Gerke, P., Jacobs, C., van Riel, S. J., et al. (2016). Pulmonary nodule detection in CT images: False positive reduction using multi-view convolutional networks. *IEEE Trans. Med. Imaging* 35 (5), 1160–1169. doi:10.1109/tmi.2016.2536809
- Shibata, N., Tanito, M., Mitsuhashi, K., Fujino, Y., Matsuura, M., Murata, H., et al. (2018). Development of a deep residual learning algorithm to screen for glaucoma from fundus photography. *Sci. Rep.* 8 (1), 14665. doi:10.1038/s41598-018-33013-w
- Shon, K., Sung, K. R., Kwak, J., Lee, J. Y., and Shin, J. W. (2022a). Development of cumulative order-preserving image transformation based variational autoencoder for anterior segment optical coherence tomography images. *Transl. Vis. Sci. Technol.* 11 (8), 30. doi:10.1167/tvst.11.8.30
- Shon, K., Sung, K. R., Kwak, J., Shin, J. W., and Lee, J. Y. (2022b). Development of a β -variational autoencoder for disentangled latent space representation of anterior segment optical coherence tomography images. *Transl. Vis. Sci. Technol.* 11 (2), 11. doi:10.1167/tvst.11.2.11
- Soltanian-Zadeh, S., Kurokawa, K., Liu, Z., Zhang, F., Saeedi, O., Hammer, D. X., et al. (2021). Weakly supervised individual ganglion cell segmentation from adaptive optics OCT images for glaucomatous damage assessment. *Optica* 8 (5), 642–651. doi:10.1364/optica.418274
- Thakur, A., Goldbaum, M., and Yousefi, S. (2020). Predicting glaucoma before onset using deep learning. *Ophthalmol. Glaucoma* 3 (4), 262–268. doi:10.1016/j.ogla.2020.04.012
- Tham, Y. C., Li, X., Wong, T. Y., Quigley, H. A., Aung, T., and Cheng, C. Y. (2014). Global prevalence of glaucoma and projections of glaucoma burden through 2040: A systematic review and meta-analysis. *Ophthalmology* 121 (11), 2081–2090. doi:10.1016/j.ophtha.2014.05.013
- Thompson, A. C., Jammal, A. A., and Medeiros, F. A. (2020). A review of deep learning for screening, diagnosis, and detection of glaucoma progression. *Transl. Vis. Sci. Technol.* 9 (2), 42. doi:10.1167/tvst.9.2.42
- Wang, R., Zheng, L., Xiong, C., Qiu, C., Li, H., Hou, X., et al. (2017). Retinal optic disc localization using convergence tracking of blood vessels. *Multimedia Tools Appl.* 76 (22), 23309–23331. doi:10.1007/s11042-016-4146-z
- Xu, B. Y., Chiang, M., Chaudhary, S., Kulkarni, S., Pardeshi, A. A., and Varma, R. (2019). Deep learning classifiers for automated detection of gonioscopic angle closure based on anterior segment OCT images. *Am. J. Ophthalmol.* 208, 273–280. doi:10.1016/j.ajo.2019.08.004
- Xu, L., Asaoka, R., Kiwaki, T., Murata, H., Fujino, Y., Matsuura, M., et al. (2020a). Predicting the glaucomatous central 10-degree visual field from optical coherence tomography using deep learning and tensor regression. *Am. J. Ophthalmol.* 218, 304–313. doi:10.1016/j.ajo.2020.04.037
- Xu, X., Wang, C., Guo, J., Gan, Y., Wang, J., Bai, H., et al. (2020b). MSCS-DeepLN: Evaluating lung nodule malignancy using multi-scale cost-sensitive neural networks. *Med. Image Anal.* 65, 101772. doi:10.1016/j.media.2020.101772
- Yang, Y., Wu, Y., Guo, C., Han, Y., Deng, M., Lin, H., et al. (2021). Diagnostic performance of deep learning classifiers in measuring peripheral anterior synechia based on swept source optical coherence tomography images. *Front. Med. (Lausanne)* 8, 775711. doi:10.3389/fmed.2021.775711
- Yoo, T. K., Ryu, I. H., Kim, J. K., Lee, I. S., and Kim, H. K. (2022). A deep learning approach for detection of shallow anterior chamber depth based on the hidden features of fundus photographs. *Comput. Methods Programs Biomed.* 219, 106735. doi:10.1016/j.cmpb.2022.106735
- Zhang, Z., Ji, Z., Chen, Q., Yuan, S., and Fan, W. (2022). Joint optimization of CycleGAN and CNN classifier for detection and localization of retinal pathologies on color fundus photographs. *IEEE J. Biomed. Health Inf.* 26 (1), 115–126. doi:10.1109/jbhi.2021.3092339
- Zheng, C., Johnson, T. V., Garg, A., and Boland, M. V. (2019). Artificial intelligence in glaucoma. *Curr. Opin. Ophthalmol.* 30 (2), 97–103. doi:10.1097/icu.0000000000000552



OPEN ACCESS

EDITED BY

Weihua Yang,
Jinan University, China

REVIEWED BY

Xiaodan Sui,
Shandong Normal University, China
Rongchang Zhao,
Central South University, China

*CORRESPONDENCE

Quanyong Yi,
✉ quanyong_yi@163.com
Yitian Zhao,
✉ yitian.zhao@nimte.ac.cn

†These authors have contributed equally
to this work and share first authorship

RECEIVED 07 March 2023

ACCEPTED 24 April 2023

PUBLISHED 05 May 2023

CITATION

Zhang J, Sha D, Ma Y, Zhang D, Tan T,
Xu X, Yi Q and Zhao Y (2023), Joint
conditional generative adversarial
networks for eyelash artifact removal in
ultra-wide-field fundus images.
Front. Cell Dev. Biol. 11:1181305.
doi: 10.3389/fcell.2023.1181305

COPYRIGHT

© 2023 Zhang, Sha, Ma, Zhang, Tan, Xu, Yi
and Zhao. This is an open-access article
distributed under the terms of the
[Creative Commons Attribution License
\(CC BY\)](https://creativecommons.org/licenses/by/4.0/). The use, distribution or
reproduction in other forums is
permitted, provided the original author(s)
and the copyright owner(s) are credited
and that the original publication in this
journal is cited, in accordance with
accepted academic practice. No use,
distribution or reproduction is permitted
which does not comply with these terms.

Joint conditional generative adversarial networks for eyelash artifact removal in ultra-wide-field fundus images

Jiong Zhang^{1,2†}, Dengfeng Sha^{1,3†}, Yuhui Ma¹, Dan Zhang⁴,
Tao Tan⁵, Xiayu Xu^{6,7}, Quanyong Yi^{2*} and Yitian Zhao^{1,2*}

¹Cixi Institute of Biomedical Engineering, Ningbo Institute of Materials Technology and Engineering, Chinese Academy of Sciences, Ningbo, China, ²The Affiliated Ningbo Eye Hospital of Wenzhou Medical University, Ningbo, China, ³Faculty of Electrical Engineering and Computer Science, Ningbo University, Ningbo, China, ⁴School of Cyber Science and Engineering, Ningbo University of Technology, Ningbo, China, ⁵Faulty of Applied Sciences, Macao Polytechnic University, Macao, Macao SAR, China, ⁶The Key Laboratory of Biomedical Information Engineering of Ministry of Education, School of Life Science and Technology, Xi'an Jiaotong University, Xi'an, China, ⁷Zhejiang Research Institute of Xi'an Jiaotong University, Hangzhou, China

Background: Ultra-Wide-Field (UWF) fundus imaging is an essential diagnostic tool for identifying ophthalmologic diseases, as it captures detailed retinal structures within a wider field of view (FOV). However, the presence of eyelashes along the edge of the eyelids can cast shadows and obscure the view of fundus imaging, which hinders reliable interpretation and subsequent screening of fundus diseases. Despite its limitations, there are currently no effective methods or datasets available for removing eyelash artifacts from UWF fundus images. This research aims to develop an effective approach for eyelash artifact removal and thus improve the visual quality of UWF fundus images for accurate analysis and diagnosis.

Methods: To address this issue, we first constructed two UWF fundus datasets: the paired synthetic eyelashes (PSE) dataset and the unpaired real eyelashes (uPRE) dataset. Then we proposed a deep learning architecture called Joint Conditional Generative Adversarial Networks (JcGAN) to remove eyelash artifacts from UWF fundus images. JcGAN employs a shared generator with two discriminators for joint learning of both real and synthetic eyelash artifacts. Furthermore, we designed a background refinement module that refines background information and is trained with the generator in an end-to-end manner.

Results: Experimental results on both PSE and uPRE datasets demonstrate the superiority of the proposed JcGAN over several state-of-the-art deep learning approaches. Compared with the best existing method, JcGAN improves PSNR and SSIM by 4.82% and 0.23%, respectively. In addition, we also verified that eyelash artifact removal via JcGAN could significantly improve vessel segmentation performance in UWF fundus images. Assessment via vessel segmentation illustrates that the sensitivity, Dice coefficient and area under curve (AUC) of ResU-Net have respectively increased by 3.64%, 1.54%, and 1.43% after eyelash artifact removal using JcGAN.

Conclusion: The proposed JcGAN effectively removes eyelash artifacts in UWF images, resulting in improved visibility of retinal vessels. Our method can facilitate

better processing and analysis of retinal vessels and has the potential to improve diagnostic outcomes.

KEYWORDS

retina, ultra-wide-field fundus images, artifact removal, conditional GAN, vessel segmentation

1 Introduction

Ultra-Wide-Field (UWF) fundus images are a new type of retinal colour fundus image with ultra wide angle characteristics, which can cover 200° [Patel et al. \(2020\)](#) of the retinal fundus in a single image. It has significant advantages over conventional colour fundus images in screening and detecting retina-related diseases such as diabetic retinopathy. However, the imaging characteristics of UWF fundus images often lead to problems with eyelash artefacts in UWF fundus images. As shown in [Figure 1](#), eyelash artefacts obscure the site of the lesion and some of the blood vessels, making it difficult to clearly distinguish key information. In the diagnosis of clinical disease, eyelash artefacts are a serious problem in terms of image quality and pose a significant diagnostic challenge to physicians [Kornberg et al. \(2016\)](#); [Ajlan et al. \(2020\)](#).

To reduce the effect of eyelash artifacts, some physical methods are often applied to the UWF imaging acquisition. These methods include manually pulling up the eyelid, retracting eyelashes via cotton bud [Cheng et al. \(2008\)](#), holding down eyelashes via disposable eyelid speculum (EzSpec) [Inoue et al. \(2013\)](#) and expanding eyelids with the eyelid clasper [Ozawa et al. \(2020\)](#), etc. Although these methods can reduce the appearance of eyelash artifacts to a certain extent, they are not able to completely solve the problem of eyelash artifacts, and these methods bring new challenges during surgical inspections [Inoue et al. \(2013\)](#). Therefore, eyelash artifact has always plagued doctors as a problem with the interpretation of UWF images. In recent years, researchers have found that eyelash artifact is a serious interference problem in the study of UWF images such as lesion detection and blood vessel segmentation [Yoo et al. \(2020\)](#); [Li et al. \(2020, 2019\)](#), as shown in [Figure 1](#). Given the adverse effects of eyelash artifacts on both clinical diagnosis and computer vision tasks, it is necessary to develop an automatic and effective method for removing eyelash artifacts from UWF images.

To the best of our knowledge, there is no automatic algorithm that has been proposed for eyelash artifact removal of UWF images. The main reason is that it is difficult to obtain corresponding image pairs eyelashes/eyelashes-free, and super-sized images are very important for model design and training strategy is no small challenge. At present, the task of removing shadow occlusion [Fan et al. \(2019\)](#) in natural image processing is similar to the task of removing eyelash artifacts in UWF images, both of which are dedicated to removing occlusion artifacts and recovering occluded information [Chen et al. \(2021\)](#). However, compared with natural images, it is more difficult to remove eyelash artifacts in UWF images [Matsui et al. \(2019\)](#). For example, the features of eyelash artifacts are complex and diverse, with large differences, and the structures of blood vessels and lesions are relatively small. Hence, the difficulties of fully automatic UWF image eyelash removal methods: On the one hand, relying on an

image acquisition process like natural images, it is impossible to obtain paired UWF images (i.e., images with eyelashes and corresponding eyelash-free labels) for supervised learning. On the other hand, eyelash artifacts in UWF images are usually highly complex and diverse, which makes it difficult to preserve some fine structures such as blood vessels/lesions in the eyelash artifact area for further analysis. Most of the UWF images currently available contain eyelashes, only a small part contains no eyelashes at all and a few contain few eyelashes, and there are no matching image pairs of eyelashes/eyelashes-free at all. Secondly, when designing the model, it is necessary to take into account the removal of eyelashes and the recovery of the information occluded by the eyelashes [Mackenzie et al. \(2007\)](#), and what method to use for training large-size images is also a problem that needs to be considered.

In response to the problems raised above, this paper proposes a Joint Conditional Generative Adversarial Network (JcGAN) to remove eyelash artifacts from UWF images and constructs two UWF image datasets: synthetic eyelashes (SEL) and real eyelashes (REL). The joint conditional generative adversarial network (See [Figure 2](#)) adopts the combination of conditional adversarial network and adversarial network and uses two sets of data sets as input to train the same generator, which not only trains the generator to remove synthetic eyelashes but also trains the generator to remove real eyelashes ability. Connect a background refinement module after the generator to ensure background integrity.

The proposed method extends considerably our previous work [Sha et al. \(2022\)](#), which was trained only on the paired samples with synthetic eyelash artifacts generated from the proposed Eyelash Growing Model. In this work, we first extended our synthetic dataset in a manner contrary to Eyelash Growing Model, where paired samples were obtained by manually erasing eyelash artifacts from real UWF images. Secondly, we have collected an unpaired dataset, which consists of real UWF images with and without eyelash artifacts. In order to fully utilize the unpaired samples and thus further enhance the generalization performance on real UWF images with eyelash artifacts, we have also improved the architecture by introducing one additional discriminator into the generative adversarial network, which shares the generator with the original one. Different from the original discriminator, the additional discriminator aims at distinguishing between real samples without eyelash artifacts and the ones generated from real samples with eyelash artifacts. To this end, the additional discriminator could constrain the generator to improve the performance of eyelash artifact removal on the real UWF images. Overall, the contributions of our work can be summarized as follows:

- For the first time in the UWF fundus imaging field, we construct two datasets for eyelash artifact removal, which respectively consist of paired images with/without synthetic eyelash artifacts and unpaired images with/without real eyelash artifacts.

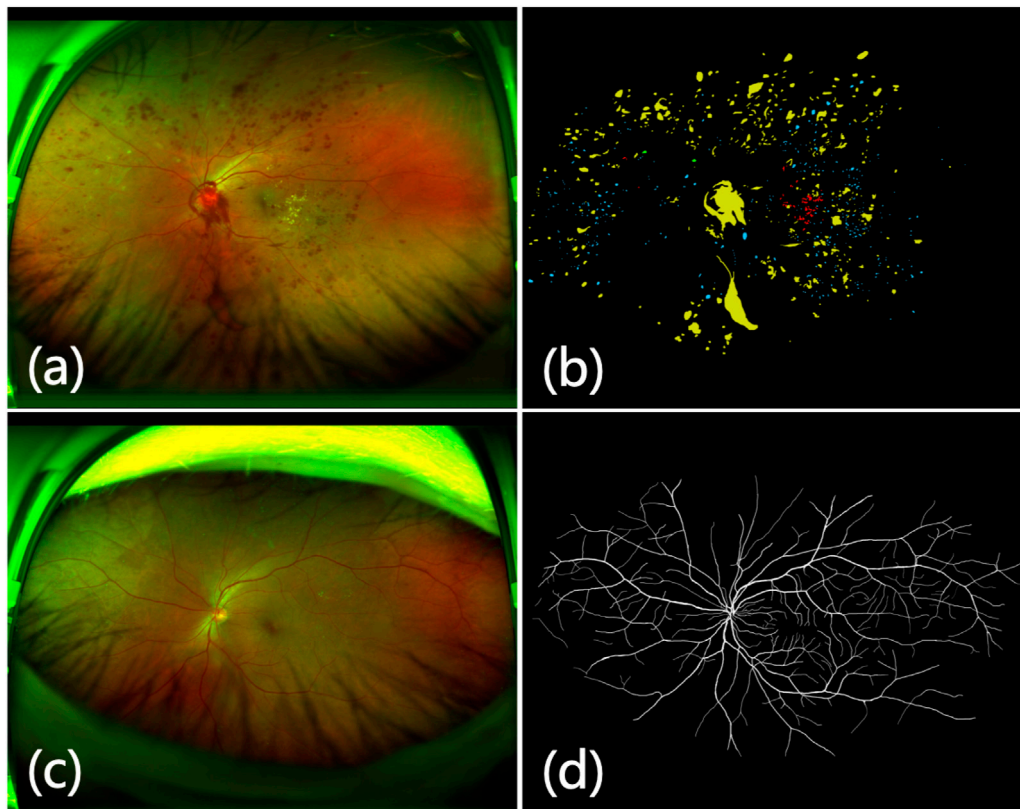


FIGURE 1

Detailed illustration of eyelash artifacts obscuring lesions and blood vessels. **(A)** The eyelash artifact obscures the lesion information. **(B)** Ground truth of the lesion in **(A)**. **(C)** The eyelash artifact obscures the vessel information. **(D)** Ground truth of the vessel in **(C)**

- We develop a deep learning architecture called Joint conditional Generative Adversarial Networks (JcGAN), which adopts one shared generator with two discriminators for jointly removing real and synthetic eyelash artifacts and utilizes a background refinement module to refine background information.

- We apply the proposed JcGAN on the datasets for eyelash artifact removal. Both quantitative and qualitative results demonstrate the superiority of the proposed JcGAN in eliminating eyelash artifacts and its performance gains to the vessel segmentation task.

2 Related works

2.1 GAN and CGAN

Generative Adversarial Network (GAN) was first proposed by Ian Goodfellow [Goodfellow et al. \(2014\)](#). It is a framework for estimating generative models through an adversarial process, including a generative model G that captures data distribution and a discriminant model D that estimates the probability that samples come from training data rather than G -generated data. The training goal of generative model G is to generate images similar to the target domain to greatly increase the error probability of discriminant model D , while the training goal of discriminant

model D is to greatly reduce the probability of discriminatory errors. A minimax game process is the so-called generative confrontation. The generative adversarial model is only a mapping from the source domain to the target domain, and cannot specify a fixed target, which is caused by the lack of target guidance. Conditional generative adversarial network (CGAN) [Mirza and Osindero \(2014\)](#) is to add prior conditions to both the generator and the discriminator based on the generative adversarial network, so that a conditional model is formed into the guidance of additional conditions. This extra condition is diverse, it can be class labels or other patterns of data, guided by the extra condition, we can generate a fixed single target for the generator.

2.2 Eyelash artifact removal from UWF images

Since the availability of UWF images, the range of fundus examinations has been greatly improved and the efficiency of fundus screening has been increased, providing an efficient method of screening for a wide range of eye diseases. However, the existence of eyelash artifacts has increased the difficulty of automatic UWF image examination. At present, methods of removing eyelash artifacts from UWF images are limited to physical avoidance methods of the shooting process. [Inoue et al.](#)

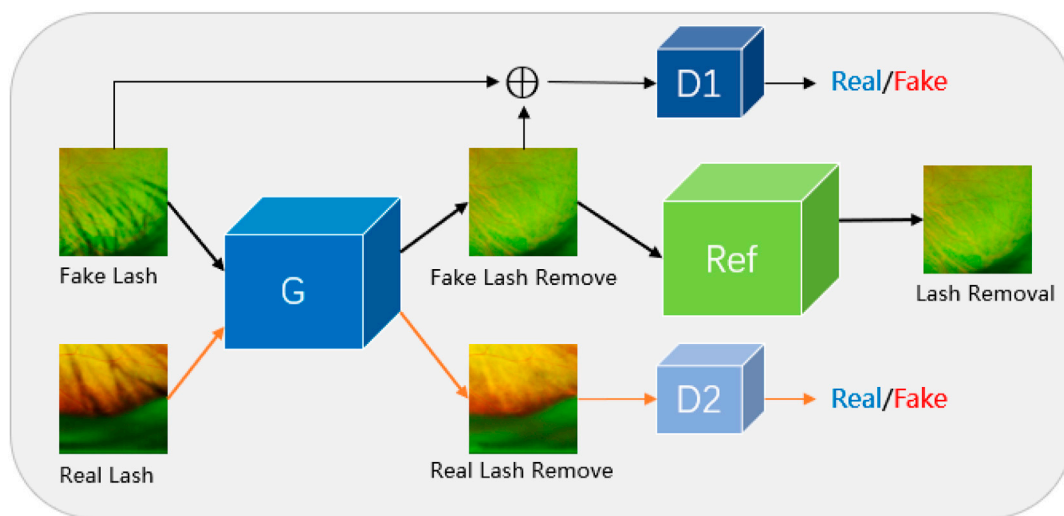


FIGURE 2

We propose Joint Conditional Generative Adversarial Networks (JcGAN) for eyelash artifact removal from UWF images. The network includes a generator G, two discriminators D1 and D2 and a background refinement module called Ref. The generator G and the discriminator D1 form a conditional generative adversarial network that takes the synthetic eyelashes (SEL) dataset as input. The generator G and the discriminator D2 form a generative adversarial network that takes the real eyelashes (REL) dataset as input.

(2013) have invented a disposable eyelid mirror (EzSpec), a flexible translucent speculum that keeps the eye open to misalignment and covers a wider eyelash area, but the use process requires topical anesthesia, which is expensive and not universal. Ozawa et al. (2020) invented an eyelid clamp to circumvent the problem of eyelash artifacts during UWF images to capture. It is a face-worn tool that keeps the eyes open by applying pressure in the eyelid area, but the avoidance effect of eyelash artifacts is not obvious. In addition, there are some small ways to avoid eyelashes in the process of taking UWF images, such as using tape to stick eyelashes, using cotton swabs to converge eyelashes, or pulling up eyelashes directly by hand, etc. However, these methods The effect of avoiding eyelashes is not obvious, and it is not easy to operate and control. Therefore, the problem of eyelash artifacts in UWF images has always been a disturbing factor of UWF images.

2.3 Shadow removal

The problem of eyelash artifact occlusion in UWF images is similar to the problem of shadow removal of natural images. However, the automatic algorithm for eyelash artifact removal of UWF images has not been studied before, while the automatic removal algorithms for the task of natural image shadow removal have been extensively explored. In general, image shadow removal algorithms can be divided into traditional methods and deep learning based methods. The traditional methods were developed based on image gradient Finlayson et al. (2005); Gryka et al. (2015), lighting information Yang et al. (2012); Zhang et al. (2015), and region attributes Guo et al. (2012). Deep learning based methods mainly include supervised learning models Zhang et al. (2019); Liu et al. (2020) and unsupervised learning models Hu et al. (2019b).

Previous methods remove shadows by modeling the image as a combination of shadow and shadow-free components Arbel and Hel-Or (2010); Finlayson et al. (2009, 2002), or by shifting colors from shadow-free to shadow regions Shor and Lischinski (2008); Wu and Tang (2005); Xiao et al. (2013). Due to the limitations of the underlying models in those methods, they are usually unable to handle shadows in complex real-world scenes Khan et al. (2015). Following that, researchers explored statistical modeling methods to discover and remove shadows using features such as intensity Gong and Cosker (2014), color Guo et al. (2012), texture Khan et al. (2014), and gradient Finlayson et al. (2005); Gryka et al. (2015). However, these handcrafted features are hard to represent the complex features of shadows. Therefore, Khan et al. (2015) propose a method of using a convolutional neural network (CNN) to detect shadows and then using a Bayesian model to remove shadows. Qu et al. (2017) develop three sub-networks to extract features of multiple views separately, and embedded all sub-networks into a complete framework for shadow removal. Wang et al. (2018) used one conditional generative adversarial network (CGAN) to detect shadows and another CGAN to remove shadows. Hu et al. (2019a) explore orientation-aware spatial context methods to detect and remove shadows. However, these methods are trained in paired images, which are limited by paired datasets. To get rid of the dependence on paired data, Hu et al. (2019b) propose a Mask Shadow GAN framework based on Cycle GAN Zhu et al. (2017), which utilizes unpaired data to learn the mapping from unshadowed domains to shadowed domains and *vice versa*. Of course. Later Liu et al. (2021) develop the LG Shadow Net framework to improve the Mask Shadow GAN Hu et al. (2019b) by introducing a brightness-guided strategy that uses the learned brightness features to guide the learning of shadow removal.

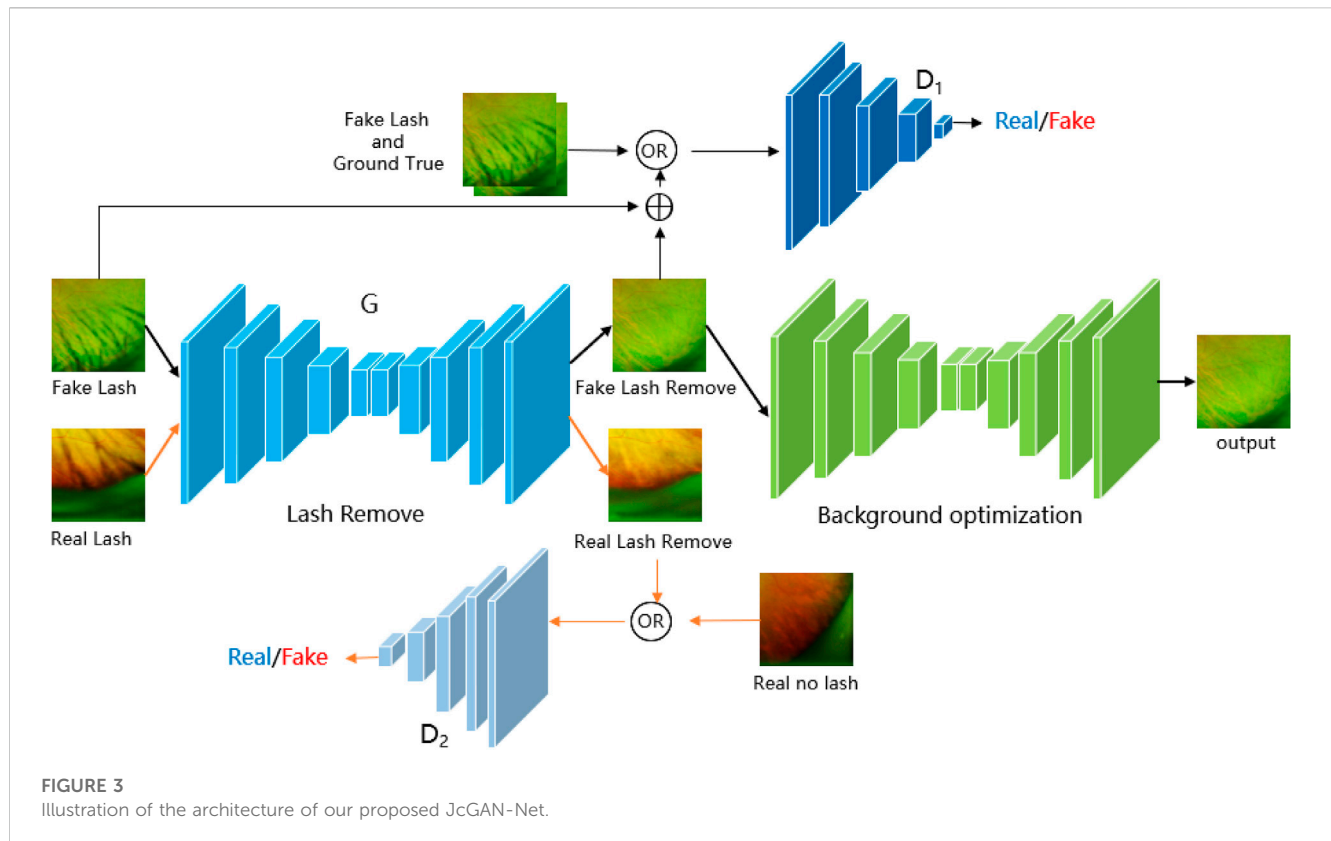


FIGURE 3
Illustration of the architecture of our proposed JcGAN-Net.

3 Datasets

To the best of our knowledge, there is no research using deep learning methods for eyelash artifact removal of UWF images. Also, there is no publicly available dataset on eyelash artifacts in UWF images. This paper constructs two new datasets of eyelash artifacts in UWF images. The first is the paired synthetic eyelashes (PSE) dataset and the second are the unpaired real eyelashes (uPRE) dataset. Table 1 presents the details of the two datasets. All data used in this paper were collected from the affiliated Ningbo Eye Hospital of Wenzhou Medical University and Ningbo People's Hospital at Ningbo, China. The acquisition device was an Optos fundus camera (Optos PLC, Dunfermline, Scotland). Prior to examination, written informed consents were obtained from subjects in accordance to the tenets of Declaration of Helsinki. The PSE dataset consists of 7025 pairs of eyelash and eyelash-free images with a size of 1024×1024 , where the eyelashes are from the eyelash growing model Sha et al. (2022). We used 5975 pairs of images as the training set and 1050 pairs of images as the test set. The uPRE dataset includes 3687 each of eyelash images and eyelash-free images with a size of 1024×1024 , where the eyelashes are from the patients themselves. We used 3037 pairs of images as the training set and 650 pairs of images as the test set.

3.1 Paired synthetic eyelashes dataset

In practice, it is difficult to obtain paired eyelash/eyelash-free UWF images by controlling the eyelash variables during image

acquisition, as is in the case of ISTD Wang et al. (2018). Previously, we proposed an eyelash growing model in the DelashNet Sha et al. (2022) method to solve the above problem. Since the lash removal performance can be easily affected by the reliability of the eyelash growing model, we additionally set up more realistic data pairs into the training set to better guide the model. To this end, we respectively adopted forward and reverse synthesis methods to generate the pairwise dataset for eyelash artifact removal. For the forward synthesis method, the eyelash growing model was developed to simulate eyelash features and generate synthetic eyelashes, followed by a fusion procedure to combine eyelash-free UWF images. For the reverse synthesis method, *Photoshop* is used to manually erase eyelash artifacts from UWF images and thus generate eyelash-free images. The forward synthesis method fails to simulate the complicated characteristics of eyelash artifacts, thus hinders the model's capability of identifying and eliminating real eyelash artifacts. Conversely, the reverse synthesis method preserves the authenticity of the eyelash artifacts, but this process may distort the background. The paired data generated in the above two ways construct the Paired Synthetic Eyelashes (PSE) Dataset in this work.

3.2 Unpaired real eyelashes dataset

A UWF image contains both eyelash information and eyelash-free information. Therefore, UWF image patches with eyelashes and without eyelashes can be separately obtained by cropping the entire image. We cropped the large size (3900×3072) UWF images into

TABLE 1 Details of the two datasets PSE and uPRE.

Datasets	Amount	Content of images	Type
PSE	7025	eyelash/eyelash-free	pair
uPRE	3687	eyelash/eyelash-free	unpair

several small-size patches for training. The cropped patch size is also an important issue that needs to be considered. If the size is too small, less global information can be preserved. While if the size is too large, it will be impossible to achieve high computational efficiency. Therefore, we finally use patch size of 1024×1024 for data training. Although the data with eyelashes and without eyelashes are not completely matched, the construction basis of this real data set is still of great significance to our follow-up model design.

4 Proposed method

In this section, we introduce the proposed architecture called JcGAN, for eyelash artifact removal in UWF fundus images. The overall framework of JcGAN is illustrated in Figure 3. It adopts one shared generator with two discriminators and learns to translate those images with eyelash artifacts into artifact-free ones via adversarial training jointly with paired and unpaired samples. JcGAN also introduce an additional background refinement module into an end-to-end process, in order to further restore background information obscured by eyelash artifacts.

4.1 Architecture

Our JcGAN consists of two generative adversarial networks with one shared generator G and an additional background refinement module (BRM), as shown in Figure 3. The generator G tries to generate the corresponding artifact-free image from the input image with synthetic or real eyelash artifacts, and the discriminator D_1 (D_2) attempts to distinguish between real artifact-free images and the ones generated from synthetic (real) samples. In order to further restore background details covered by eyelash artifacts, the background refinement module (BRM) is applied to refine the generated results from the generator G via end-to-end training.

Both the generator G and background refinement module (BRM) adopts the same U-shape structure, which contains eight encoder-decoder layers with symmetric skip connections (Ronneberger et al. (2015)). All encoder layers employ 4×4 convolution with stride 2 followed by Batch Normalization (BN) and Leaky ReLU, except the last encoder layer with ReLU instead and no BN. For the first seven decoder layers, we utilize 4×4 transposed convolution with stride 2 followed by BN and ReLU. The last decoder layer also removes BN and outputs the final result through Tanh function.

For both discriminators D_1 and D_2 , we construct a network with five 4×4 convolutional layers, where stride is set to 2 in the first three layers and 1 in the last two layers. BN is used in the 2nd-

4th layers. All layers introduce Leaky ReLU except the last layer. Finally, the discriminator network outputs a confidence map via Sigmoid function, where each pixel represents the probability that the corresponding local region of the input image is identified as coming from a real artifact-free sample.

4.2 Loss function

In order to effectively constrain the proposed JcGAN, we employ the joint adversarial training strategy to optimize the architecture end-to-end based on both paired and unpaired samples. Finally, we construct the loss function including conditional adversarial loss, unconditional adversarial loss and refinement loss.

- **Conditional adversarial loss** For a synthetic pair of corruption/artifact-free samples (x_p/y_p), the generator G takes x_p and random noise vector z as input and attempts to produce the fake result (denoted as $G(z, x_p)$) which is close to y_p as possible, while the discriminator D_1 attempts to classify between the real pair (x_p, y_p) and the fake pair ($x_p, G(z, x_p)$). Through the competition between G and D_1 , JcGAN can learn the mapping from corruption images to the corresponding artifact-free ones. Thus the conditional adversarial loss \mathcal{L}_{ca} can be expressed as:

$$\mathcal{L}_{ca}(G, D_1) = E_{x_p, y_p \sim P_{PSE}(x_p, y_p)} [\log D_1(x_p, y_p)] + E_{x_p \sim P_{PSE}(x_p), z \sim p_z(z)} [\log(1 - D_1(x_p, G(z, x_p)))] \quad (1)$$

In addition, we also introduce L1 distance to further minimize the discrepancy between the generated image $G(z, x_p)$ and the real artifact-free image y_p :

$$\mathcal{L}_1(G) = E_{x_p, y_p \sim P_{PSE}(x_p, y_p), z \sim p_z(z)} \|y_p - G(z, x_p)\|_1 \quad (2)$$

- **Unconditional adversarial loss** For unpaired corruption/artifact-free samples (x_u/y_u), the generator G also takes x_u as input and attempts to produce the fake result (denoted as $G(z, x_u)$), while the discriminator D_2 attempts to identify whether one given image is real or fake artifact-free image. The competition between G and D_2 could promote the perceptual quality of generated images from G . Therefore, the unconditional adversarial loss \mathcal{L}_{uca} can be denoted as:

$$\mathcal{L}_{uca}(G, D_2) = E_{y_u \sim P_{uPRE}(y_u)} [\log D_2(y_u)] + E_{x_u \sim P_{uPRE}(x_u), z \sim p_z(z)} [\log(1 - D_2(G(z, x_u)))] \quad (3)$$

- **Refinement loss** In order to constrain background refinement module (denoted as R) to produce refined artifact-free results more precisely, we adopt L1 distance as refinement loss:

$$\mathcal{L}_{ref}(G, R) = E_{x_p, y_p \sim P_{PSE}(x_p, y_p), z \sim p_z(z)} \|y_p - R(G(z, x_p))\|_1 \quad (4)$$

Finally, the total loss function of the proposed JcGAN is defined as:

$$\mathcal{L}_{total}(G, D_1, D_2, R) = \mathcal{L}_{ca}(G, D_1) + \mathcal{L}_1(G) + \mathcal{L}_{uca}(G, D_2) + \mathcal{L}_{ref}(G, R) \quad (5)$$

where λ_1 and λ_2 represent the weighted parameters of L1 distance and refinement loss.

TABLE 2 The values of the PSNR and SSIM tests of our 3×3 groups.

Methods	PSNR			SSIM		
	PSE1	PSE2	PSE	PSE1	PSE2	PSE
PSE1+uPRE	39.270	37.488	40.125	0.9640	0.9304	0.9585
PSE2+uPRE	35.935	38.972	38.073	0.9475	0.9253	0.9462
PSE + uPRE	40.182	38.943	43.692	0.9652	0.9353	0.9729

5 Experimental setup

In this section, we describe the experimental setups, including the evaluation metrics, data ablation, module ablation and comparative experiments.

5.1 Implementation settings

The proposed JcGAN was implemented with PyTorch library, and the experiments were conducted on two NVIDIA GPUs (Tesla V100 with 32 GB). All training images were resized to 1024×1024 , and a random horizontal flipping was applied for data augmentation. Adam optimization was applied to train the model, with epochs of 200, the initial learning rate of 0.0002 and batch size of 15. The weighted parameters in the final objective function were experimentally set as: $\lambda_1 = 100$ and $\lambda_2 = 10$.

5.2 Evaluation criteria

We verify the synthetic data and real data separately. For synthetic paired data, the traditional image enhancement [Maini and Aggarwal \(2010\)](#) evaluation criteria are used to calculate PSNR and SSIM [Hore and Ziou \(2010\)](#):

- Peak Signal to Noise Ratio (PSNR);

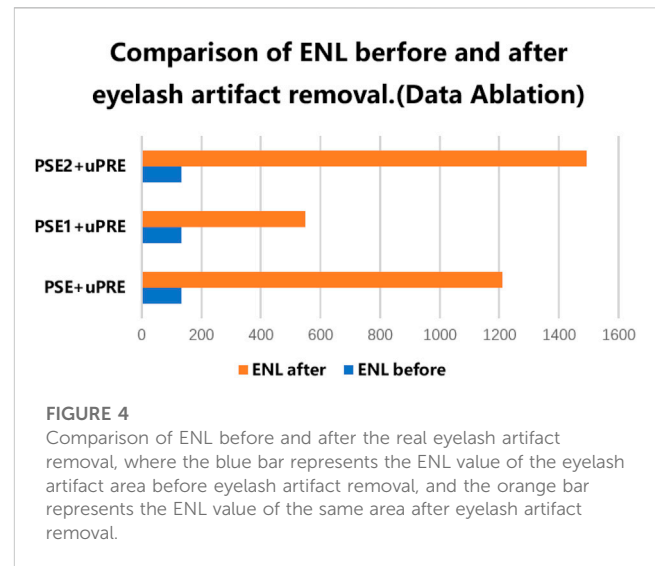
$$PSNR = 10 \times \log \left(\frac{(2^n - 1)^2}{MSE} \right) \quad (6)$$

where MSE [Sara et al. \(2019\)](#) is the mean squared error between the original image and the processed image.

- Structural Similarity (SSIM);

$$SSIM(x, y) = \frac{(2\mu_x\mu_y + c_1)(2\delta_{xy} + c_2)}{(\mu_x^2 + \mu_y^2 + c_1)(\delta_x^2 + \delta_y^2 + c_2)} \quad (7)$$

where μ_x is the mean of x , μ_y is the mean of y , δ_x is the variance of x , δ_y is the variance of y , and δ_{xy} is the covariance of x and y . $c_1 = (\kappa_1 L)^2$, $c_2 = (\kappa_2 L)^2$ is a constant used to maintain stability. L is the dynamic range of pixel values. $\kappa_1 = 0.01$, $\kappa_2 = 0.02$. Structural similarity ranges from -1 to 1 . When the two images are identical, the value of SSIM is equal to 1 . For the real unpaired data, we use the equivalent numbers of looks in the local area to evaluate the smoothness of the processed image. Additionally, we use the



performance on the validation vessel segmentation task as an indirect evaluation metric.

- Equivalent numbers of looks (ENL) [Vespe and Greidanus \(2012\)](#);

$$ENL = \frac{\mu^2}{\delta^2} \quad (8)$$

where μ is the mean of the local area of the image, δ is the variance of the local area of the image. ENL is commonly used to measure the speckle suppression of different SAR/OCT image filters. When the ENL value is bigger, it indicates the image is smoothed well.

- Resunet was used to train a vessel segmentation network, which was indirectly validated by the effect on vessel segmentation performance before and after eyelash artifact removal.

5.3 Data ablation

As mentioned above, two datasets including PSE and uPRE are used for evaluation. The PSE dataset consists of two parts, PSE part 1 (PSE1) from the eyelash growing model and PSE part 2 (PSE2) from manual erasure. PSE1 is characterized by the fact that the synthetic eyelashes can only approximate the key information of the real eyelashes to some extent, but cannot completely model the real eyelashes. PSE2 is used to compensate PSE1 by including paired eyelash information from realistic UWF images. To verify the effectiveness of the two data generation approaches, we conduct the data ablation experiments as follows. We designed three experiments to verify the performance of the three dataset combinations respectively. (i) The combination of PSE1 dataset and uPRE dataset. (ii) The combination of PSE2 dataset and uPRE dataset. (iii) The combination of PSE dataset and uPRE dataset.

We used the data of the above three combinations to train three models. For each model, we also tested the three sets of data: PSE1,

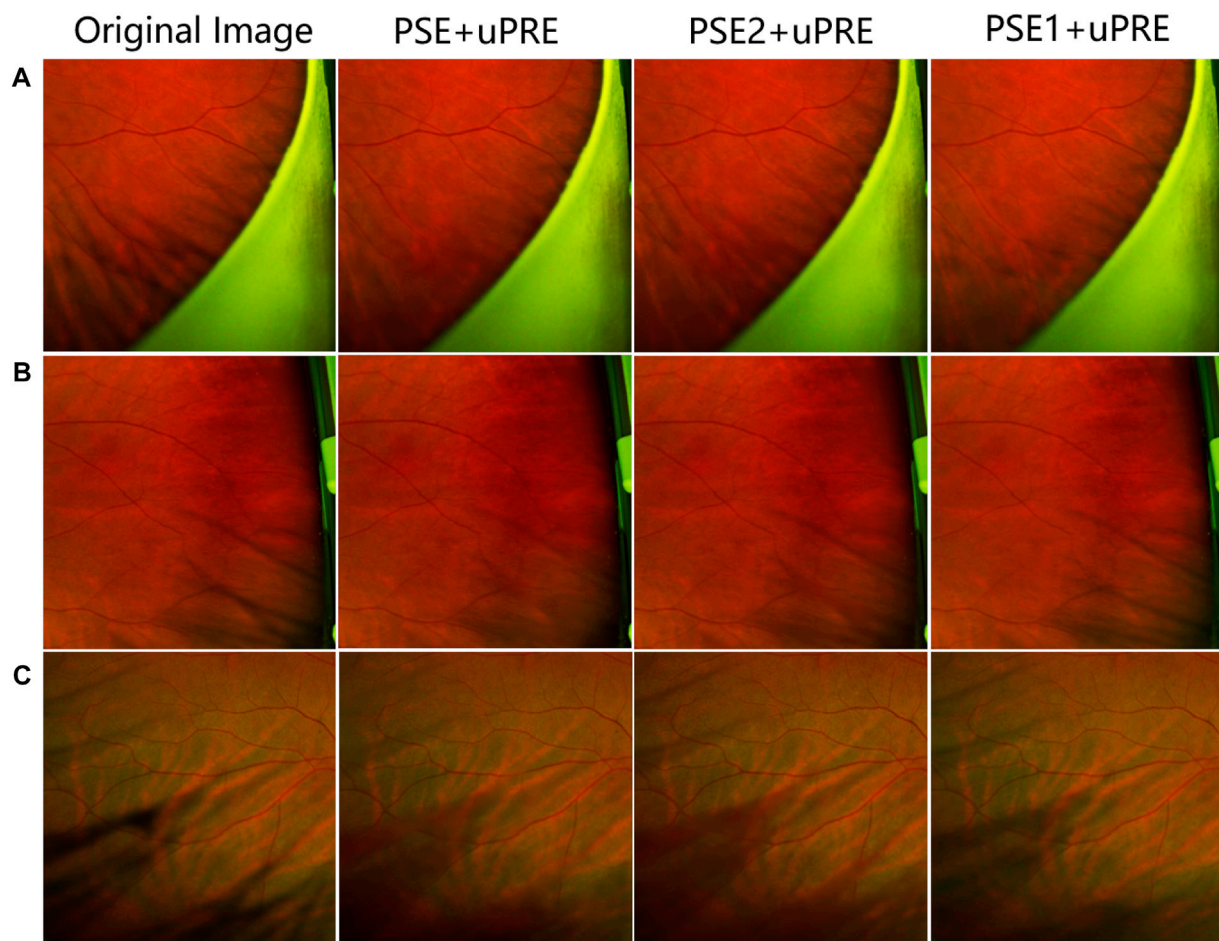


FIGURE 5

Visual representation of a data ablation experiment. (A–C) represent three different pictures, the first column shows the original picture, the second column shows the test results of PSE + uPRE training, and the third column shows the test results of PSE2 + uPRE training, the fourth column shows the test results of the PSE1 + uPRE training.

PSE2 and PSE. Therefore, in the experiment of data ablation, we have completed a total of 3×3 data testing. Table 2 shows the values of the PSNR and SSIM of the 3×3 groups. The results show that the training method using the third data combination achieves the best results. The results show that the model trained on the PSE + uPRE data achieves the best results. First of all, the PSE1 does not simulate all the information of real eyelashes. Adding the PSE2 reduce the effects of lacking of synthetic eyelashes. Second, the ground truth from PSE2 data has limitations with inaccurate backgrounds. Adding accurate ground truth from the PSE1 can compensate this issue in the PSE2. At the same time, we use the uPRE dataset to verify the effects of the three models. As shown in Figure 4, the ENL results of the real data have been improved to a certain extent.

As shown in Figure 4, all three different data resulted in improved ENL after eyelash removal, among which the combination of PSE2+uPRE achieved the largest improvement, and the combination of PSE + uPRE achieved the second rank. For the test results of synthetic eyelashes data, the combination of PSE + uPRE achieved the best results, which met our expectations. While for the test results of the real eyelash data, the combination of

PSE + uPRE has not achieved the best results in the test of real eyelash data. We know that ENL only calculates the local area of eyelash artifact. Therefore, in order to fully verify the performance of these three sets of data, it is necessary to compare them in a larger area.

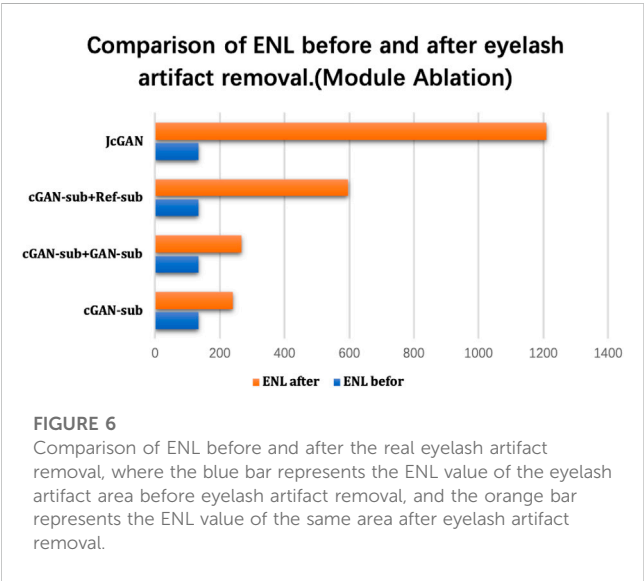
Figure 5 shows the test results on three sets of training data. From the figure, we can see that the results of the PSE + uPRE training data are significantly better than the results of the other two groups. It removes most of the artifacts and preserves the background much better. Thus, we take the PSE1+PSE2 data as the final PSE dataset.

5.4 Module ablation

The JcGAN proposed in this paper includes three sub-nets: a conditional generative adversarial Mirza and Osindero (2014) sub-net (cGAN-sub) composed of generator G and discriminator D1, a generative adversarial Goodfellow et al. (2014) sub-net (GAN-sub) composed of generator G and discriminator D2, and a background refinement sub-net (Ref-sub). To verify the contributions of each

TABLE 3 The values of PSNR and SSIM tested on the PSE dataset for the module ablation experiments.

Methods	PSNR	SSIM
cGAN-sub	39.1357	0.9519
cGAN-sub + Ref-sub	42.1008	0.9640
cGAN-sub + GAN-sub	40.8884	0.9697
JcGAN	43.6922	0.9729



sub-net to the overall JcGAN network, we design module ablation experiments as follows.

According to the combination of different sub-net, we conduct a total of four module ablation experiments. 1) The conditional generative adversarial sub-net (cGAN-sub) is used as the baseline of the JcGAN network framework. Hence, we first design experiments to train the conditional generative adversarial sub-net to verify the effectiveness of the baseline module. 2) Based on the conditional generative adversarial sub-net (cGAN-sub), we separately add the background refinement sub-net (Ref-sub) to verify the utility of the background refinement sub-net on model performance. 3) Based on the conditional generative adversarial sub-net (cGAN-sub), we separately add the generative adversarial sub-net (GAN-sub) to verify the utility of the generative adversarial sub-net on model performance. 4) Finally, we add a generative adversarial sub-net (GAN-sub) and a background refinement sub-net (Ref-sub) on the baseline, i.e., our complete JcGAN network framework, to verify the effectiveness of all sub-networks.

After completing the above four experiments, we use the PSE dataset and the uPRE dataset to verify the results respectively. Table 3 shows the PSNR and SSIM values on the PSE dataset.

It is obvious from Table 3 that our method achieves competitive performance on the PSE dataset. The baseline of our model (cGAN-sub) has achieved significant breakthroughs in PSNR and SSIM values. The value of PSNR is as high as 39.1357, which is due to the

TABLE 4 The values of PSNR and SSIM tested on the PSE Dataset for the comparative experiments.

Methods	PSNR	SSIM
Pix2Pix	34.1901	0.9281
Mask-ShadowGAN	37.2841	0.9462
CycleGAN	37.8026	0.9442
ST-CGAN	41.6814	0.9707
JcGAN	43.6922	0.9729

high resolution Takahashi et al. (2019) of UWF images. Initially, we design Ref-sub as a background refinement sub-network in the overall framework of JcGAN, in order to ensure that the background occluded Audet and Cooperstock (2007) by eyelash artifacts can be fully recovered while eyelash artifacts are removed. Now, after adding Ref-sub on the basis of cGAN-sub, the values of PSNR and SSIM are further improved, which shows that Ref-sub plays an active role. After verifying the effectiveness of cGAN-sub and Ref-sub, we further verify the effectiveness of GAN-sub. Adding GAN-sub on the basis of cGAN-sub means that the joint idea of our JcGAN network is applied. The two datasets train the same generator alternatively so that this generator has the ability to remove synthetic eyelashes and real eyelashes. As shown in the results, our joint strategy achieve competitive performance on the PSE dataset. Finally, the test results of the JcGAN network also show that each sub-network in our whole framework plays an active role, and combining the three sub-networks can produce the best results.

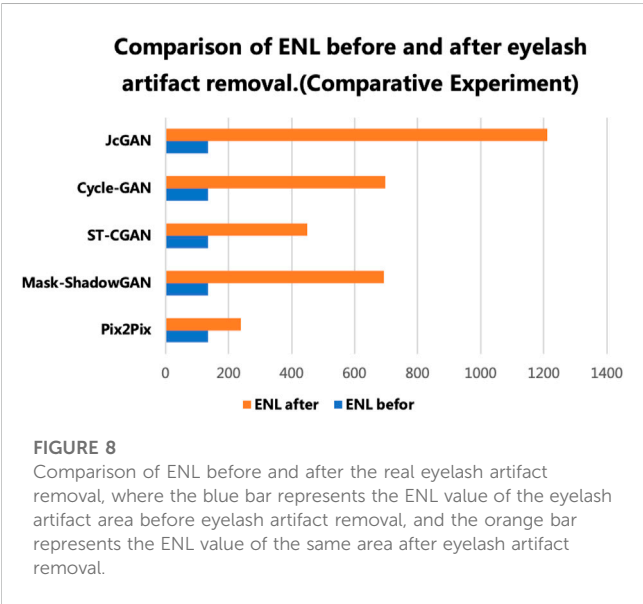
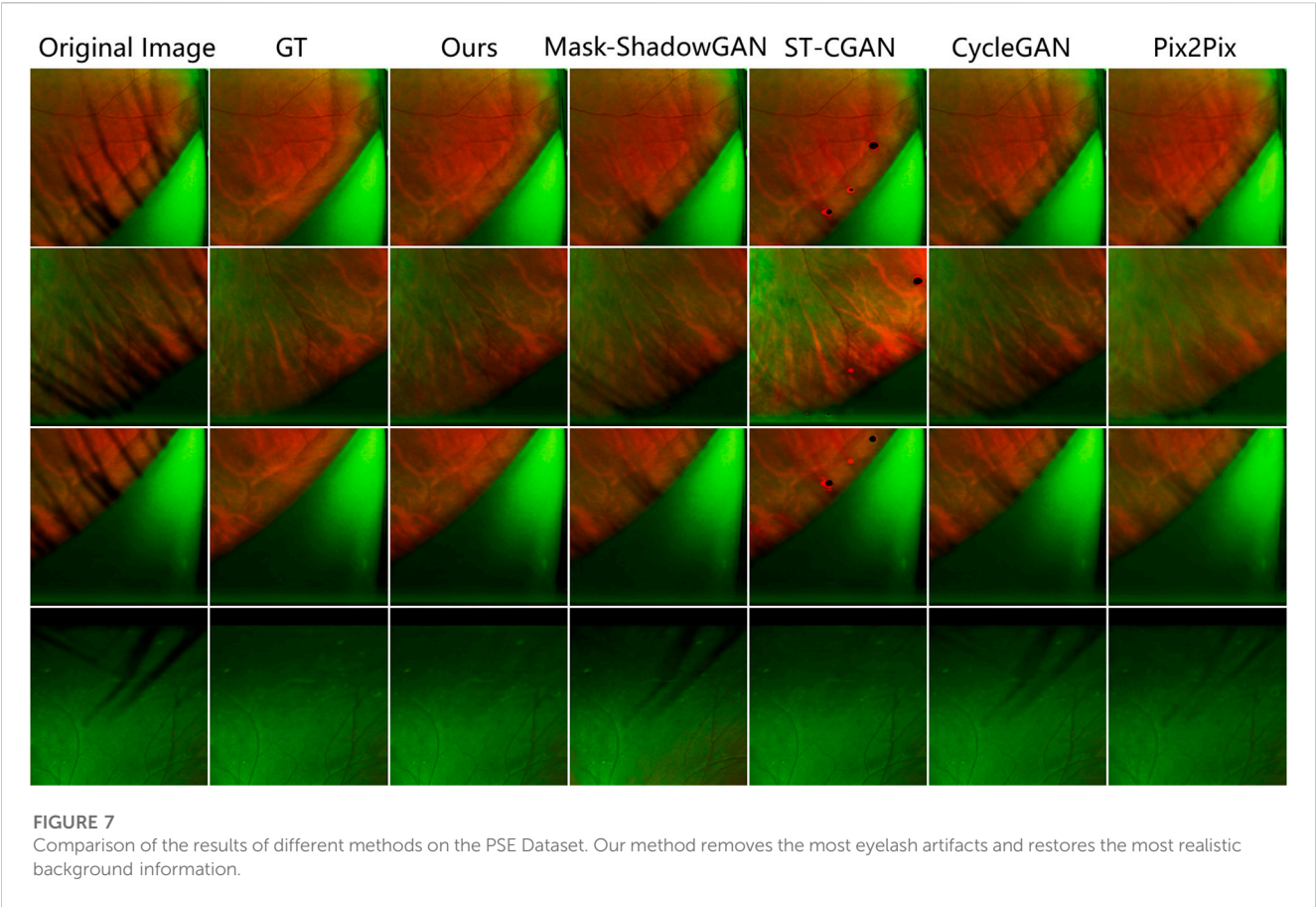
After being evaluated on the PSE Dataset, we also validate our method on the uPRE dataset. We used the local area of eyelash artifact removal to calculate the ENL value. Figure 6 shows the ENL values of the eyelash occluded area before and after eyelash artifact removal.

As shown in Figure 6, the combination of different sub-networks improves the value of ENL. In particular, the addition of the Ref-sub subnet has greatly improved the value of ENL. This shows that our Ref-sub sub-network effectively recovers the background of the eyelash artifact part. The JcGAN network framework improves the value of ENL the most, which also strongly proves that our joint strategy is also successful in the artifact removal of real eyelashes.

6 Discussion

6.1 Comparative analysis

To verify the effectiveness of our method, we selected several methods similar to ours for comparative experiments. Currently, no deep learning method has been proposed for artifact removal in ultra-widefield fundus images. Therefore, we selectively choose several classical GAN network related methods Pix2Pix Isola et al. (2017) and cycleGAN Zhu et al. (2017) and some natural image shadow removal methods ST-CGAN Wang et al. (2018) and Mask-ShadowGAN Hu et al. (2019b) as comparison methods in our



analysis. We trained the above methods sequentially and tested each method using PSE dataset and uPRE dataset, as shown in Table 4. The results show that our method achieves remarkable performance on the PSE Dataset. Our proposed JcGAN method achieves a high PSNR value of 43.6922 and a SSIM value of 0.9729, the highest among all methods. Compared with the best existing

method, JcGAN improves PSNR and SSIM by 4.82% and 0.23%, respectively. At the same time, we compare the visual effects of the PSE Dataset test, and our method also achieves the best results, as shown in Figure 7. From Figure 7 we can see that our method achieves the best results in both eyelash artifact removal and background restoration. Compared with our method, none of the other methods completely remove eyelash artifacts. Among them, ST-CGAN has problems in the process of background recovery, which leads to information loss in the test image. Similarly, we perform the results validation of different methods on the uPRE dataset. We calculated the position ENL value of the local area of the eyelash artifact removal part for different methods. A comparison of ENL value results for different methods on the uPRE Dataset is shown in Figure 8. From Figure 8, we can see that our method JcGAN achieves the largest improvement in ENL value, which shows that our method restores the smooth background in the region removed for eyelash artifacts. Figure 9 shows a visual comparison of the results of different methods on the REL dataset.

6.2 Application to UWF image segmentation

To verify that our proposed eyelash artifact removal algorithm can promote better processing and analysis of retinal vessels, a dedicated experiment for vessel segmentation in UWF images is performed. The corresponding segmentation results are shown in Figure 10, and sensitivity (SEN), Dice and area under curve (AUC)

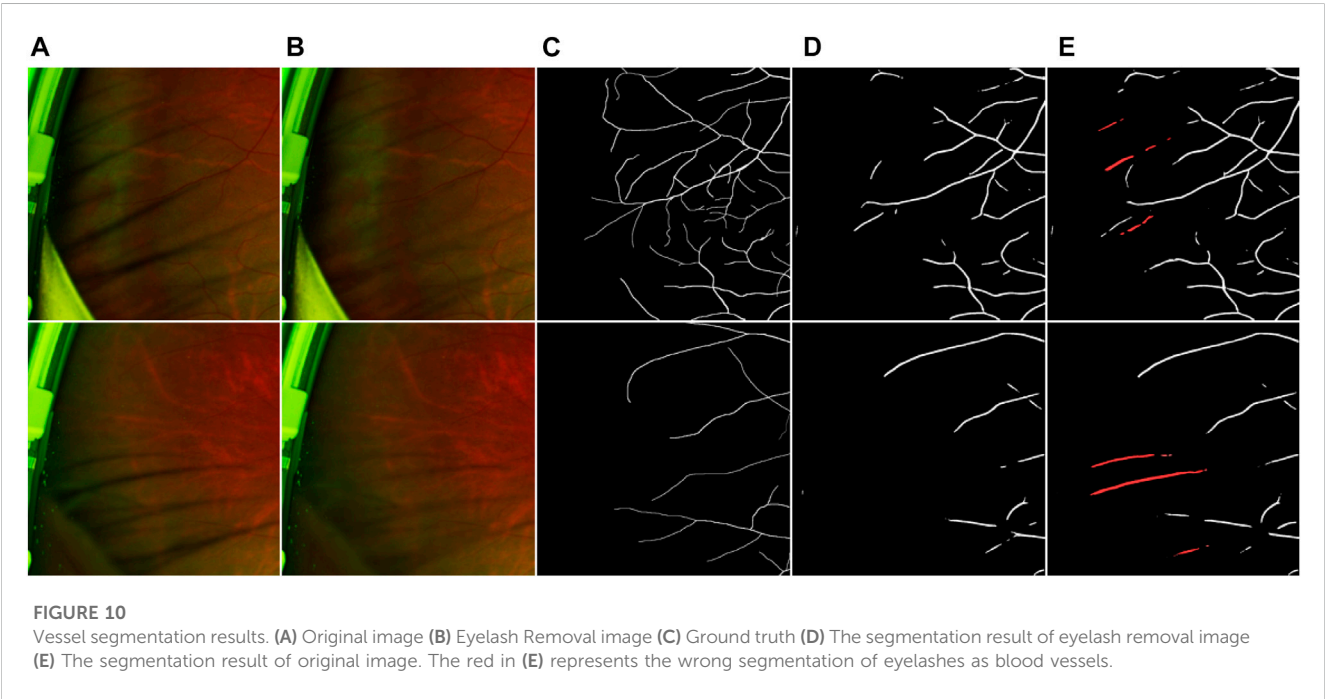
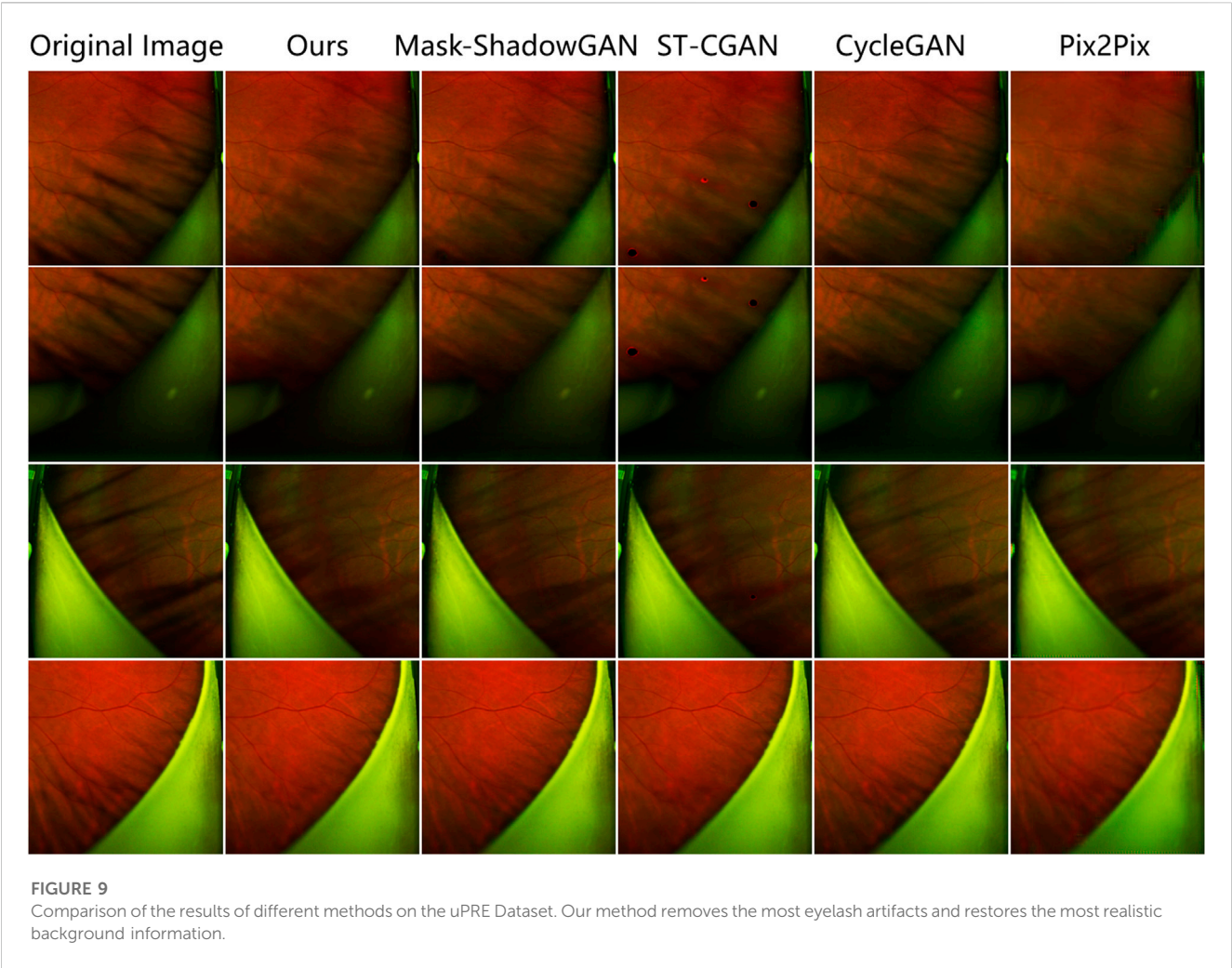


TABLE 5 The results of the eyelashes removal image and the original image on the blood vessel segmentation index.

Methods	ResU-net		
	SEN	Dice	AUC
Original image	0.4663	0.5124	0.8783
Eyelash Removal image	0.4833	0.5203	0.8909

are shown in Table 5. ResU-Net Diakogiannis et al. (2020) is adopted as the segmentation network. 406 eyelash-free images are used to train ResU-Net. For the trained segmentation model, the original image with eyelashes and the image processed by JcGAN are used for testing respectively. Assessment via vessel segmentation illustrates that the SEN, Dice and AUC of ResU-Net have respectively increased by 3.64%, 1.54%, and 1.43% after eyelash artifact removal using JcGAN, as shown in Table 5. As shown in Figure 10; Table 5, the eyelash-removed images have better performance on the vessel segmentation task than the original images. The images processed by our JcGAN network successfully solved the problem that eyelashes were incorrectly segmented as blood vessels, and improved the overall segmentation performance.

6.3 Summary

Artifacts caused by eyelash occlusions hinder high-quality inspection on retinopathy at wide range in UWF fundus images. In this work, we tackle the issue of eyelash artifacts existing in UWF fundus images with deep learning technique for the first time. We firstly collect UWF fundus images and construct two eyelash datasets called paired synthetic eyelashes (PSE) and unpaired real eyelashes (uPRE) respectively. Based on the two datasets, we have proposed a deep learning approach called Joint conditional Generative Adversarial Networks (JcGAN) to eliminate eyelash artifacts in UWF fundus images. The proposed JcGAN could jointly learn the mapping from images with real or synthetic eyelash artifacts to artifact-free ones via two generative adversarial networks with a shared generator. In addition, a background refinement module is trained with the generator in an end-to-end manner to further recover the detailed information of regions corrupted by eyelash artifacts. The experimental results on both PSE and uPRE dataset show that our eyelash artifact removal approach have achieved the best performance. Compared with other deep learning methods, our JcGAN can remove eyelash artifacts more effectively and achieve higher visual effect. Furthermore, JcGAN can significantly facilitate vessel segmentation in UWF fundus images due to the improved visibility of vessels obscured by eyelash artifacts. In the future, we will consider exploring a more appropriate method to construct paired synthetic eyelash samples and introducing prior knowledge of eyelash artifacts into the deep learning model. Furthermore, we will apply our approach to lesion segmentation tasks (e.g., identifying hemorrhages and exudates) as a preprocessing procedure to verify the effectiveness of eyelash artifact removal.

Data availability statement

The raw data supporting the conclusion of this article will be made available by the authors, without undue reservation.

Ethics statement

The studies involving human participants were reviewed and approved by the Ethics committee of Cixi Institute of Biomedical Engineering, Ningbo Institute of Materials Technology and Engineering, Chinese Academy of Sciences. The patients/participants provided their written informed consent to participate in this study.

Author contributions

JZ: conceptualization, supervision, writing-original draft, project administration, writing-review and editing; DS: writing-original draft, investigation, validation; YM: methodology, visualization, writing-review and editing; DZ: investigation, writing-review and editing; TT: formal analysis, writing-review and editing; XX: methodology, writing-review and editing; QY: resources, data curation, conceptualization, writing-review and editing; YZ: supervision, project administration, formal analysis, writing-review and editing.

Funding

This work was supported in part by the National Natural Science Foundation Program of China under Grants (62103398 and 61906181), in part by the Zhejiang Provincial Natural Science Foundation (LQ23F010002, LZ23F010002, LR22F020008, LZ19F010001, and LQ21F010007), in part by the Ningbo Natural Science Foundation (2022J143, 2022JCGY010608), in part by the Youth Innovation Promotion Association CAS (2021298), the Research Startup Fund of Ningbo University of Technology (2022KQ29), and in part by 2025 S&T Megaprojects (2019B10033, 2019B10061, and 2021Z054).

Conflict of interest

The authors declare that the research was conducted in the absence of any commercial or financial relationships that could be construed as a potential conflict of interest.

Publisher's note

All claims expressed in this article are solely those of the authors and do not necessarily represent those of their affiliated organizations, or those of the publisher, the editors and the reviewers. Any product that may be evaluated in this article, or claim that may be made by its manufacturer, is not guaranteed or endorsed by the publisher.

References

- Ajlan, R. S., Barnard, L. R., and Mainster, M. A. (2020). *Nonconfocal ultra-widefield scanning laser ophthalmoscopy: Polarization artifacts and diabetic macular edema*, 40. Philadelphia, Pa: Retina, 1374.
- Arbel, E., and Hel-Or, H. (2010). Shadow removal using intensity surfaces and texture anchor points. *IEEE Trans. pattern analysis Mach. Intell.* 33, 1202–1216. doi:10.1109/TPAMI.2010.157
- Audet, S., and Cooperstock, J. R. (2007). Shadow removal in front projection environments using object tracking. In *2007 IEEE conference on computer vision and pattern recognition*, IEEE, 1–8.
- Chen, Z., Long, C., Zhang, L., and Xiao, C. (2021). “Canet: A context-aware network for shadow removal,” in *Proceedings of the IEEE/CVF international conference on computer vision*, 4743–4752.
- Cheng, S. C., Yap, M. K., Goldschmidt, E., Swann, P. G., Ng, L. H., and Lam, C. S. (2008). Use of the optomap with lid retraction and its sensitivity and specificity. *Clin. Exp. Optometry* 91, 373–378. doi:10.1111/j.1444-0938.2007.00231.x
- Diakogiannis, F. I., Waldner, F., Caccetta, P., and Wu, C. (2020). Resunet-a: A deep learning framework for semantic segmentation of remotely sensed data. *ISPRS J. Photogrammetry Remote Sens.* 162, 94–114. doi:10.1016/j.isprsjprs.2020.01.013
- Fan, H., Han, M., and Li, J. (2019). Image shadow removal using end-to-end deep convolutional neural networks. *Appl. Sci.* 9, 1009. doi:10.3390/app9051009
- Finlayson, G. D., Drew, M. S., and Lu, C. (2009). Entropy minimization for shadow removal. *Int. J. Comput. Vis.* 85, 35–57. doi:10.1007/s11263-009-0243-z
- Finlayson, G. D., Hordley, S. D., and Drew, M. S. (2002). “Removing shadows from images,” in *European conference on computer vision* (Springer), 823–836.
- Finlayson, G. D., Hordley, S. D., Lu, C., and Drew, M. S. (2005). On the removal of shadows from images. *IEEE Trans. pattern analysis Mach. Intell.* 28, 59–68. doi:10.1109/TPAMI.2006.18
- Gong, H., and Cosker, D. (2014). “Interactive shadow removal and ground truth for variable scene categories,” in *Bmvc* (Nottingham, UK: BMVA Press), 1–11.
- Goodfellow, I., Pouget-Abadie, J., Mirza, M., Xu, B., Warde-Farley, D., Ozair, S., et al. (2014). Generative adversarial nets. *Adv. neural Inf. Process. Syst.* 27.
- Gryka, M., Terry, M., and Brostow, G. J. (2015). Learning to remove soft shadows. *ACM Trans. Graph. (TOG)* 34, 1–15. doi:10.1145/2732407
- Guo, R., Dai, Q., and Hoiem, D. (2012). Paired regions for shadow detection and removal. *IEEE Trans. pattern analysis Mach. Intell.* 35, 2956–2967. doi:10.1109/TPAMI.2012.214
- Hore, A., and Ziou, D. (2010). “Image quality metrics: Psnr vs. ssim,” in *2010 20th international conference on pattern recognition (IEEE)*, 2366–2369.
- Hu, X., Fu, C.-W., Zhu, L., Qin, J., and Heng, P.-A. (2019a). Direction-aware spatial context features for shadow detection and removal. *IEEE Trans. pattern analysis Mach. Intell.* 42, 2795–2808. doi:10.1109/TPAMI.2019.2919616
- Hu, X., Jiang, Y., Fu, C.-W., and Heng, P.-A. (2019b). “Mask-shadowgan: Learning to remove shadows from unpaired data,” in *Proceedings of the IEEE/CVF international conference on computer vision*, 2472–2481.
- Inoue, M., Yanagawa, A., Yamane, S., Arakawa, A., Kawai, Y., and Kadonosono, K. (2013). Wide-field fundus imaging using the optos optomap and a disposable eyelid speculum. *JAMA Ophthalmol.* 131, 226. doi:10.1001/jamaophthalmol.2013.750
- Isola, P., Zhu, J.-Y., Zhou, T., and Efros, A. A. (2017). “Image-to-image translation with conditional adversarial networks,” in *Proceedings of the IEEE conference on computer vision and pattern recognition*, 1125–1134.
- Khan, S. H., Bannamoun, M., Soheli, F., and Togneri, R. (2014). “Automatic feature learning for robust shadow detection,” in *2014 IEEE conference on computer vision and pattern recognition (IEEE)*, 1939–1946.
- Khan, S. H., Bannamoun, M., Soheli, F., and Togneri, R. (2015). Automatic shadow detection and removal from a single image. *IEEE Trans. pattern analysis Mach. Intell.* 38, 431–446. doi:10.1109/TPAMI.2015.2462355
- Kornberg, D. L., Klufas, M. A., Yannuzzi, N. A., Orlin, A., D’Amico, D. J., and Kiss, S. (2016). “Clinical utility of ultra-widefield imaging with the optos optomap compared with indirect ophthalmoscopy in the setting of non-traumatic rhegmatogenous retinal detachment,” in *Seminars in ophthalmology* (Taylor & Francis), 31, 505–512.
- Li, Z., Guo, C., Nie, D., Lin, D., Zhu, Y., Chen, C., et al. (2019). A deep learning system for identifying lattice degeneration and retinal breaks using ultra-widefield fundus images. *Ann. Transl. Med.* 7, 618. doi:10.21037/atm.2019.11.28
- Li, Z., Guo, C., Nie, D., Lin, D., Zhu, Y., Chen, C., et al. (2020). Development and evaluation of a deep learning system for screening retinal hemorrhage based on ultra-widefield fundus images. *Transl. Vis. Sci. Technol.* 9, 3. doi:10.1167/tvst.9.2.3
- Liu, D., Long, C., Zhang, H., Yu, H., Dong, X., and Xiao, C. (2020). “Arshadowgan: Shadow generative adversarial network for augmented reality in single light scenes,” in *Proceedings of the IEEE/CVF conference on computer vision and pattern recognition*, 8139–8148.
- Liu, Z., Yin, H., Mi, Y., Pu, M., and Wang, S. (2021). Shadow removal by a lightness-guided network with training on unpaired data. *IEEE Trans. Image Process.* 30, 1853–1865. doi:10.1109/TIP.2020.3048677
- Mackenzie, P. J., Russell, M., Ma, P. E., Isbister, C. M., and Maberley, D. A. (2007). Sensitivity and specificity of the optos optomap for detecting peripheral retinal lesions. *Retina* 27, 1119–1124. doi:10.1097/IAE.0b013e3180592b5c
- Maini, R., and Aggarwal, H. (2010). *A comprehensive review of image enhancement techniques*. arXiv preprint arXiv:1003.4053.
- Matsui, Y., Ichio, A., Sugawara, A., Uchiyama, E., Suimon, H., Matsubara, H., et al. (2019). “Comparisons of effective fields of two ultra-widefield ophthalmoscopes, optos 200tx and clarus 500,” in *BioMed research international* 2019.
- Mirza, M., and Osindero, S. (2014). *Conditional generative adversarial nets*. arXiv preprint arXiv:1411.1784.
- Ozawa, N., Mori, K., Katada, Y., Tsubota, K., and Kurihara, T. (2020). Efficacy of the newly invented eyelid clasper in ultra-widefield fundus imaging. *Life* 10, 323. doi:10.3390/life10120323
- Patel, S. N., Shi, A., Wibbelsman, T. D., and Klufas, M. A. (2020). Ultra-widefield retinal imaging: An update on recent advances. *Ther. Adv. Ophthalmol.* 12, 2515841419899495. doi:10.1177/2515841419899495
- Qu, L., Tian, J., He, S., Tang, Y., and Lau, R. W. (2017). “Deshadownet: A multi-context embedding deep network for shadow removal,” in *Proceedings of the IEEE conference on computer vision and pattern recognition*, 4067–4075.
- Ronneberger, O., Fischer, P., and Brox, T. (2015). “U-net: Convolutional networks for biomedical image segmentation,” in *International Conference on Medical image computing and computer-assisted intervention* (Springer), 234–241.
- Sara, U., Akter, M., and Uddin, M. S. (2019). Image quality assessment through fsim, ssim, mse and psnr—A comparative study. *J. Comput. Commun.* 7, 8–18. doi:10.4236/jcc.2019.73002
- Sha, D., Ma, Y., Zhang, D., Zhang, J., and Zhao, Y. (2022). “Delashnet: A deep network for eyelash artifact removal in ultra-wide-field fundus images,” in *Proceedings of the 5th international conference on control and computer vision*, 107–112.
- Shor, Y., and Lischinski, D. (2008). “The shadow meets the mask: Pyramid-based shadow removal,” in *Computer graphics forum* (Wiley Online Library), 27, 577–586.
- Takahashi, H., Tanaka, N., Shinohara, K., Yokoi, T., Yoshida, T., Uramoto, K., et al. (2019). Ultra-widefield optical coherence tomographic imaging of posterior vitreous in eyes with high myopia. *Am. J. Ophthalmol.* 206, 102–112. doi:10.1016/j.ajo.2019.03.011
- Vespe, M., and Greidanus, H. (2012). Sar image quality assessment and indicators for vessel and oil spill detection. *IEEE Trans. Geoscience Remote Sens.* 50, 4726–4734. doi:10.1109/tgrs.2012.2190293
- Wang, J., Li, X., and Yang, J. (2018). “Stacked conditional generative adversarial networks for jointly learning shadow detection and shadow removal,” in *Proceedings of the IEEE conference on computer vision and pattern recognition*, 1788–1797.
- Wu, T.-P., and Tang, C.-K. (2005). A bayesian approach for shadow extraction from a single image. In *Tenth IEEE Int. Conf. Comput. Vis. (ICCV’05) Volume 1 (IEEE)*, vol. 1, 480–487.
- Xiao, C., She, R., Xiao, D., and Ma, K.-L. (2013). 32. Wiley Online Library, 207–218. Fast shadow removal using adaptive multi-scale illumination transfer. *Comput. Graph. Forum*
- Yang, Q., Tan, K.-H., and Ahuja, N. (2012). Shadow removal using bilateral filtering. *IEEE Trans. Image Process.* 21, 4361–4368. doi:10.1109/TIP.2012.2208976
- Yoo, T. K., Ryu, I. H., Kim, J. K., Lee, I. S., Kim, J. S., Kim, H. K., et al. (2020). Deep learning can generate traditional retinal fundus photographs using ultra-widefield images via generative adversarial networks. *Comput. Methods Programs Biomed.* 197, 105761. doi:10.1016/j.cmpb.2020.105761
- Zhang, L., Zhang, Q., and Xiao, C. (2015). Shadow remover: Image shadow removal based on illumination recovering optimization. *IEEE Trans. Image Process.* 24, 4623–4636. doi:10.1109/TIP.2015.2465159
- Zhang, S., Liang, R., and Wang, M. (2019). Shadowgan: Shadow synthesis for virtual objects with conditional adversarial networks. *Comput. Vis. Media* 5, 105–115. doi:10.1007/s41095-019-0136-1
- Zhu, J.-Y., Park, T., Isola, P., and Efros, A. A. (2017). “Unpaired image-to-image translation using cycle-consistent adversarial networks,” in *Proceedings of the IEEE international conference on computer vision*, 2223–2232.



OPEN ACCESS

EDITED BY

Weihua Yang,
Jinan University, China

REVIEWED BY

Libin Lu,
Wuhan Polytechnic University, China
Qiankun Zuo,
Hubei University of Economics, China
Kangkang Liu,
Sun Yat-Sen University, China
Ming-Jie Luo,
Sun Yat-Sen University, China

*CORRESPONDENCE

Le Gao,
✉ le.gao@nscg-gz.cn
Jin Hong,
✉ hongjin@gdph.org.cn

RECEIVED 29 March 2023

ACCEPTED 24 April 2023

PUBLISHED 09 May 2023

CITATION

Su H, Gao L, Lu Y, Jing H, Hong J, Huang L
and Chen Z (2023), Attention-guided
cascaded network with pixel-
importance-balance loss for retinal
vessel segmentation.
Front. Cell Dev. Biol. 11:1196191.
doi: 10.3389/fcell.2023.1196191

COPYRIGHT

© 2023 Su, Gao, Lu, Jing, Hong, Huang
and Chen. This is an open-access article
distributed under the terms of the
[Creative Commons Attribution License
\(CC BY\)](https://creativecommons.org/licenses/by/4.0/). The use, distribution or
reproduction in other forums is
permitted, provided the original author(s)
and the copyright owner(s) are credited
and that the original publication in this
journal is cited, in accordance with
accepted academic practice. No use,
distribution or reproduction is permitted
which does not comply with these terms.

Attention-guided cascaded network with pixel-importance-balance loss for retinal vessel segmentation

Hexing Su¹, Le Gao^{1*}, Yichao Lu¹, Han Jing¹, Jin Hong^{2,3*},
Li Huang¹ and Zequn Chen⁴

¹Faculty of Intelligent Manufacturing, Wu Yi University, Jiangmen, China, ²Guangdong Provincial Key Laboratory of South China Structural Heart Disease, Guangdong Provincial People's Hospital (Guangdong Academy of Medical Sciences), Southern Medical University, Guangzhou, China, ³Medical Research Institute, Guangdong Provincial People's Hospital (Guangdong Academy of Medical Sciences), Southern Medical University, Guangzhou, China, ⁴Faculty of Social Sciences, Lingnan University, Hongkong, China

Accurate retinal vessel segmentation from fundus images is essential for eye disease diagnosis. Many deep learning methods have shown great performance in this task but still struggle with limited annotated data. To alleviate this issue, we propose an Attention-Guided Cascaded Network (AGC-Net) that learns more valuable vessel features from a few fundus images. Attention-guided cascaded network consists of two stages: the coarse stage produces a rough vessel prediction map from the fundus image, and the fine stage refines the missing vessel details from this map. In attention-guided cascaded network, we incorporate an inter-stage attention module (ISAM) to cascade the backbone of these two stages, which helps the fine stage focus on vessel regions for better refinement. We also propose Pixel-Importance-Balance Loss (PIB Loss) to train the model, which avoids gradient domination by non-vascular pixels during backpropagation. We evaluate our methods on two mainstream fundus image datasets (i.e., DRIVE and CHASE-DB1) and achieve AUCs of 0.9882 and 0.9914, respectively. Experimental results show that our method outperforms other state-of-the-art methods in performance.

KEYWORDS

retinal vessel segmentation, deep learning, attention mechanism, U-net, pixel-wise loss

1 Introduction

Retinal vessel analysis is a non-invasive and cost-effective test that ophthalmologists and other specialists routinely use (Chatziralli et al., 2012; Ji et al., 2023). Physicians can diagnose and track many diseases (e.g., macular degeneration, hypertension, diabetes) by looking at morphologic information related to retinal vessels (e.g., curvature, length, and width) because these diseases cause morphologic changes in the retinal vessels (Olafsdottir et al., 2011). The segmentation of retinal vessels is an essential foundation for the quantitative analysis of fundus images. Since manual segmentation is time-consuming, labor-intensive, and relies on professionals' subjective judgment, many researchers have turned to computer-aided intervention to achieve automatic retinal vessel segmentation (Zhao et al., 2022a; Zhao et al., 2022b).

Automatic retinal vessel segmentation is an important research problem in the field of computer vision, and its main purpose is to separate vascular and non-vascular regions from

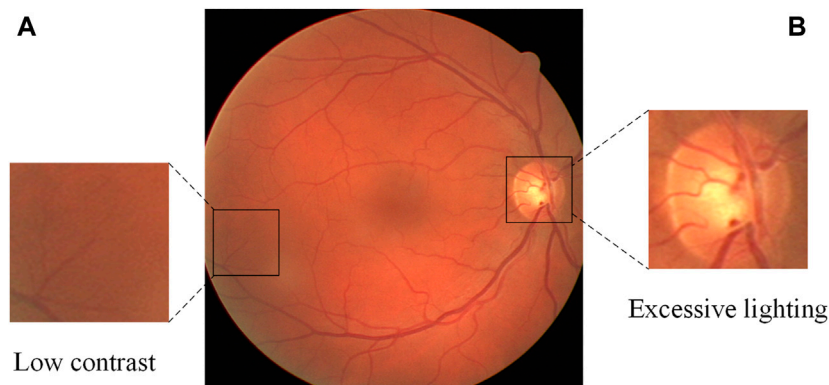


FIGURE 1

A fundus retinal image from the DRIVE database, containing thin blood vessels with low contrast (A) and over-illuminated optic disc (B).

fundus images. Solving this problem is of great significance for clinical diagnosis and research in the field of ophthalmology. Because it can promote the early detection and treatment of eye diseases, and provide clinicians with a fast, accurate, and reliable analysis method. However, due to the complexity and variability of fundus images, finding every vessel without introducing too many false positives is difficult, especially for thin vessels. When improper imaging illumination, sensor noise, and other factors are considered, things become even more complicated because vital vessel information may be lost as a result. In Figure 1, for example, there is usually over-illumination near the optic disc, causing some vessels near the optic disc to lose feature information. Thin vessels are typically found in darker, lower contrast areas, and their width is only one or a few pixels when compared to thick vessels, so they are easily overlooked. To address these challenges, many methods for automatic retinal vessel segmentation have been proposed in the past few decades. For example, the blood vessel tracking method (Yin et al., 2012; Tolia and Panas, 1998; Chutatape et al., 1998) begins by selecting a starting point in the fundus image and utilizes a specific tracking strategy to progressively extend along the blood vessel path, culminating in a comprehensive segmentation of the blood vessels. The method based on morphology (Sazak et al., 2019; Zana and Klein, 2001) performs some morphological operator processing (such as erosion, dilation, opening and closing operations, etc.) on the fundus image to realize the segmentation of blood vessels. In addition, methods based on traditional machine learning (Ricci and Perfetti, 2007; Staal et al., 2004; Lupascu et al., 2010) manually extract vascular features (such as shape, texture, etc.), and send these features to classifiers (such as support vector machines, decision trees, etc.) for training to achieve segmentation. Although these traditional retinal vessel segmentation methods have certain advantages and applicability, there are still limitations in the processing of fundus image noise, generalization, etc.

Due to the powerful feature extraction ability of the convolutional neural network, it has gradually become the mainstream method for segmentation tasks (Khandouzi et al., 2022). Fully convolutional network (Long et al., 2015) is a pioneering work using a convolutional neural network in

image segmentation. It discards the fully connected layers of the Very deep convolutional networks (Simonyan and Zisserman, 2014), and the entire network uses convolution operations for feature extraction, followed by upsampling of the feature maps to restore the original resolution. However, FCN is not sensitive to the details of objects in the image, resulting in the loss of edge details of many objects. Subsequently, based on the idea of an encoder-decoder structure, Ronneberger et al. (2015) proposed U-Net, which made up for the lack of details of FCN to a certain extent by using skip connection operation, and gradually became the mainstream model in the field of medical image segmentation. In recent years, many U-Net based variants (Jin et al., 2019; Guo et al., 2021a; Alom et al., 2019; Guo et al., 2021b; Wang et al., 2020b; Wu et al., 2021; Zhang et al., 2019) for the task of retinal vessel segmentation have emerged, but they suffer from insufficient vessel information and features due to the limited number of fundus images with dense annotations in the public dataset [e.g., DRIVE (Staal et al., 2004), CHASE_DB1 (Owen et al., 2009)]. In this case, some studies (Wang et al., 2020a; Xia et al., 2018; Li et al., 2020) have shown that the coarse-to-fine segmentation architecture is beneficial for extracting more vascular information from limited fundus images. However, these works simply transfer vessel feature maps (such as concatenation or addition) between coarse and fine stages, which makes the fine stage unable to align vessel regions for better refinement and leads to suboptimal performance. To address this problem, we propose an Attention-Guided Cascaded Network (AGC-Net), which can learn more valuable vascular information from limited retinal fundus images. AGC-Net consists of two identical U-shaped backbones for coarse and fine representation learning. Specifically, the coarse-stage backbone generates a rough vessel probability map from the fundus image. In contrast, the fine-stage backbone acts as a post-processing module to further refine missing vessel details from this map. This coarse-to-fine representation learning can allow those misclassified pixels to be corrected, especially those blood vessel pixels whose predicted probability value is slightly lower than the segmentation threshold (usually taken as 0.5). Then, we incorporate an inter-stage attention module (ISAM) to

cascade the two-stage backbone in AGC-Net. ISAM uses a multi-scale spatial attention mechanism to promote fine-stage backbone focus on vessel regions for better refinement.

Furthermore, deep learning-based segmentation models are typically trained using pixel-wise loss (e.g., Cross Entropy Loss). It creates a loss by comparing the per-pixel difference between the vessel probability map generated by the segmentation model and the Ground Truths labeled by human experts and then uses that loss for gradient computation and backpropagation. In the pixel-wise loss, each pixel is treated with equal importance (i.e., the loss weights are all 1.0) and the loss is calculated separately for each pixel. However, when the ratio of background pixels and blood vessel pixels in the retinal image is seriously unbalanced (the ratio is about 8:2), pixel-wise loss makes the optimization of the segmentation results severely affected by the background, which leads to inaccurate blood vessel segmentation. To prevent the gradient from being dominated by many background pixels during backpropagation, we propose a Pixel-Importance-Balance Loss (PIB Loss) for training the blood vessel segmentation model. It scales the loss weights for each pixel according to the number of vessels around them. Our primary contributions are as follows:

1. We propose AGC-Net, a deep learning-based segmentation model for retinal vessel segmentation that aims to improve segmentation results from limited fundus data by allowing misclassified pixels to be corrected.
2. We propose ISAM to cascade two backbones in AGC-Net, which intends to enable the fine-stage backbone to focus more effectively on vascular regions for better refinement.
3. We propose PIB Loss for training vessel segmentation model, which can prevent the gradient from being dominated by many background pixels during backpropagation.

The remainder of this paper is structured as follows. [Section 2](#) reviews the studies related to retinal image vessel segmentation. [Section 3](#) describes our method. Data and experimental details are described in [Section 4](#). [Section 5](#) evaluates our approach quantitatively and qualitatively and presents experimental results. Finally, in [Section 6](#), we conclude.

2 Related works

In the past decades, many automatic retinal segmentation algorithms have been proposed, and they can be broadly classified into three categories.

The first class of algorithms is designed using traditional computer vision methods for vessel segmentation and is based on the inherent morphological prior knowledge of retinal vessels. For example, threshold-based methods ([Roychowdhury et al., 2015](#); [Zardadi et al., 2016](#)), filter-based methods ([Mendonca and Campilho, 2006](#); [Fraz et al., 2012a](#); [Zhang et al., 2015](#)) and vessel tracking-based methods ([Nayebifar and Moghaddam, 2013](#); [Vázquez et al., 2013](#)). [Roychowdhury et al. \(2015\)](#) designed an iterative adaptive thresholding method to improve the robustness of vessel segmentation. [Oliveira et al. \(2016\)](#) enhanced the vessels by combining three filters: the matched filter, the Gabor Wavelet filter, and Frangi's filter. [Zhang et al. \(2010\)](#) detected blood vessels by

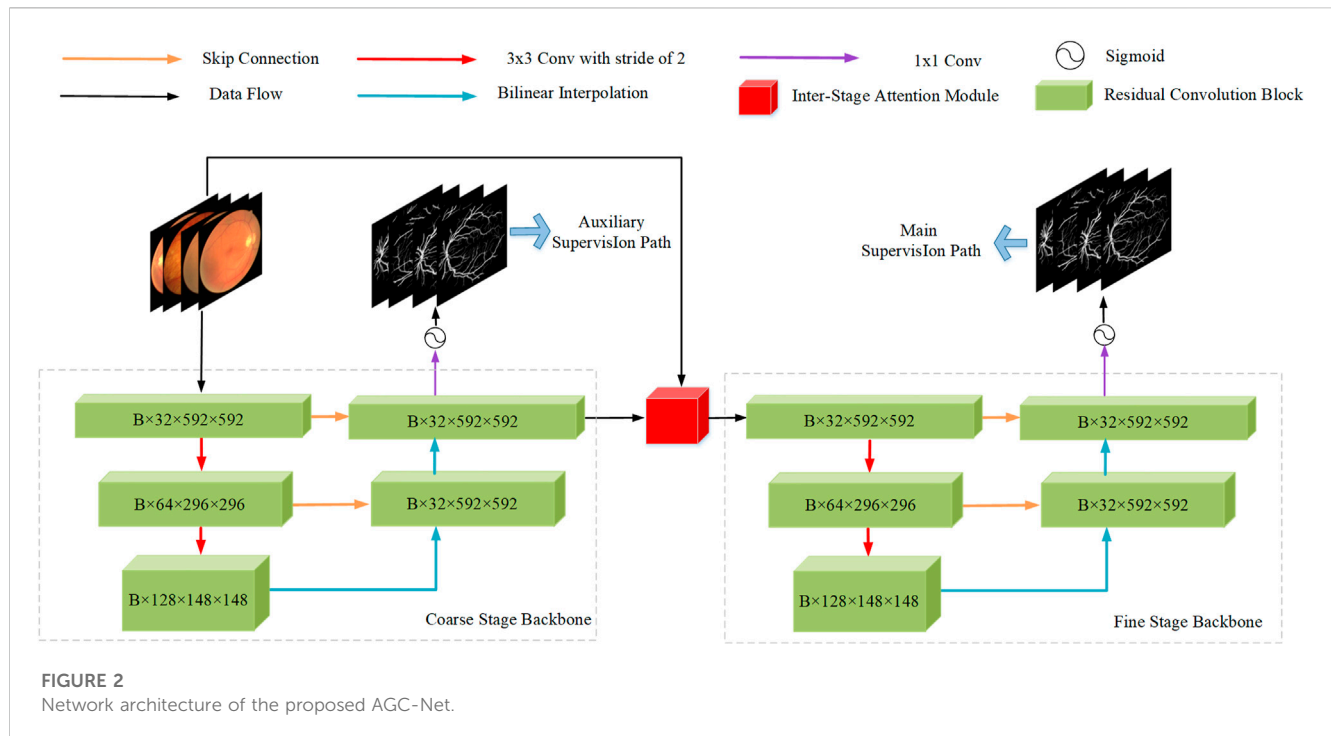
thresholding the response of the retinal image to the matched filter and later adjusted the threshold by the image's response to the first-order derivative of Gaussian. [Nayebifar and Moghaddam \(2013\)](#) used least-cost matching, global graph optimization, and Dijkstra's algorithm to track vessels as a way to ensure vessel continuity. Traditional algorithms based on morphological priors are relatively simple in principle, but they are unsupervised methods that lack label constraints with annotations and produce less accurate vessel segmentation results.

The second class of algorithms is based on traditional machine learning approaches, identifying blood vessel pixels by feeding manually designed features to a trained classifier. [Staal et al. \(2004\)](#) created feature vectors from blood vessel centerlines and then classified them using a k-nearest neighbor classifier. Simple feature vectors were created based on the texture, local intensity, spatial properties, and geometry of blood vessels, and some researchers ([Fraz et al., 2012b](#); [Memari et al., 2017](#); [Lupascu et al., 2010](#)) tried to use ensemble learning methods (e.g., Bagging and Boosting) to classify blood vessel pixels. [Ricci et al. \(2004\)](#) used linear detectors and support vector machines to complete the segmentation representation of blood vessels. The performance of traditional machine learning-based methods is heavily influenced by manually designed features. However, these features are typically defined empirically, resulting in bias and poor generalization performance.

The third class of algorithms is the deep learning-based approach, which automatically extracts blood vessel features rather than manually designed features through powerful convolutional neural networks. U-Net ([Ronneberger et al., 2015](#)) has become the most widely used model in the medical field of image segmentation, and several U-Net variants have made significant progress in retinal vessel segmentation. [Alom et al. \(2019\)](#) used the idea of recurrent neural networks and proposed a recurrent convolution in U-Net instead of a normal convolution to effectively accumulate more vessel features. [Jin et al. \(2019\)](#) integrated deformable convolution into U-Net. This convolution operation can adaptively adjust the receptive field according to the scale and shape of blood vessels to better capture various retinal blood vessels. SA-UNet ([Guo et al., 2021b](#)) and CAR-UNet ([Guo et al., 2021a](#)), proposed by Guo et al., respectively introduce attention mechanisms of spatial dimension and channel dimension in U-Net to improve the vessel segmentation performance of U-Net. IterNet ([Li et al., 2020](#)) and CTF-Net ([Wang et al., 2020a](#)) have shown that vessel segmentation performance can be improved based on cascades using multiple U-Nets, and we will implement a similar strategy in our method.

3 Methodology

This study aims to accurately segment retinal vessels in fundus images using deep learning methods. Inspired by IterNet ([Li et al., 2020](#)) and CBAM ([Woo et al., 2018](#)), we propose our model AGC-Net by combining their advantages. As shown in [Figure 2](#), the model is implemented based on a U-shape architecture and consists of three main ideas: residual convolution block, inter-stage attention module, and cascaded refinement structure design. In addition, we



also propose PIB Loss for model training. We detail the proposed model and loss function below.

3.1 Network architecture

Figure 2 shows our proposed AGC-Net vessel segmentation model. The model consists of a representation learning cascade of coarse and fine stages and aims to use the fine stage as a post-processing module to give pixels misclassified by the coarse stage a chance to relearn. Specifically, first, the fundus image passes through the backbone of the coarse stage to generate a rough vessel prediction probability map as an intermediate output. Then, ISAM (See Figure 4) uses a multi-scale attention mechanism on this intermediate output to generate feature maps of enhanced vessel regions. Finally, feature maps of enhanced vessel regions and fundus images are concatenated as the input of the fine-stage backbone to generate the final refined vessel segmentation map.

Both stages are equipped with a U-shaped backbone for their respective learning tasks. The U-backbone is an encoder and decoder structure that generates multi-scale vessel feature maps to identify vessels of different lengths. Specifically, the encoder extracts the vascular features of the fundus image through a residual convolution block (See Figure 3). Each block includes a convolutional layer, a batch normalization layer, and a ReLU activation layer, and we use residual connections to speed up the convergence of the model. To obtain a larger receptive field, downsampling is necessary. This operation is implemented by a convolution with stride 2. At each downsampling stage, the size of the feature map is halved, and the number of channels is doubled. Since too much downsampling will lose the spatial information of vessels, there are only two downsampling stages in the backbone,

each with 32, 64, and 128 channels. In the decoder part, we upsample the vessel feature map by bilinear interpolation and compensate for the lost spatial information of the vessel by skip connections to receive the feature map of the encoder. Finally, through a 1×1 convolution and a Sigmoid layer, we get the final vessel segmentation.

Since AGC-Net is composed of two backbone network cascades, it may suffer from the gradient disappearance problem due to the increase in network depth. In response to this problem, inspired by DSN (Lee et al., 2015), in addition to adding the main supervision path to the network's final output, we also add an auxiliary supervision path to the intermediate output of the backbone in the coarse stage. During training, the loss functions of these two supervised paths are weighted into the overall loss function, which helps gradient backpropagation back to shallower layers and speeds up model convergence. Specifically, we compare the predicted probability maps outputted from the backbone of the two stages with the ground truth and compute the loss for backpropagation using the PIB loss (see Section 5.3), as shown in the following figure:

$$Loss = Loss_{main} + \gamma Loss_{auxl}$$

$$Loss_{main} = PIB(PM_f, GT)$$

$$Loss_{auxl} = PIB(PM_c, GT)$$

where $Loss_{main}$ and $Loss_{auxl}$ are the losses generated by the backbone of the fine stage and coarse stage, respectively, and the weight λ represents the trade-off between the two losses, which we set as 1.0 in the experiments. PIB represents the proposed PIB loss, and PM_f , PM_c and GT are respectively the predicted probability map of the coarse stage, the predicted probability map of the fine stage, and the ground truths.

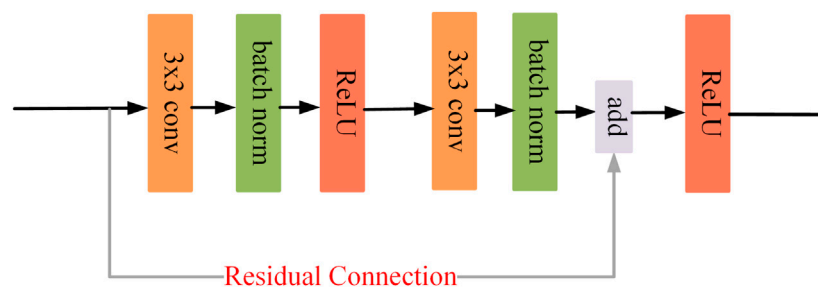


FIGURE 3
Residual convolution block.

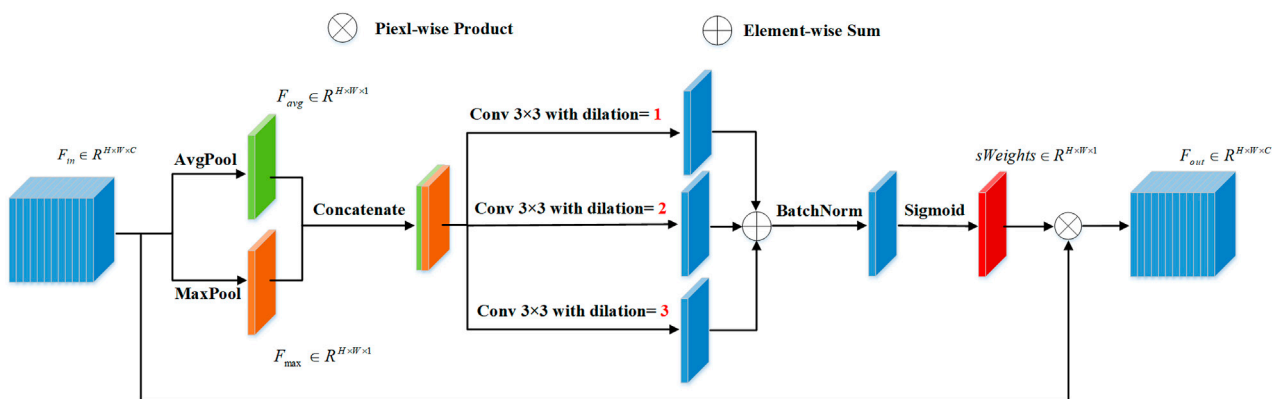


FIGURE 4
Diagram of the proposed Inter-Stage Attention Module (ISAM).

3.2 Inter-stage attention module

ISAM is proposed to enhance the vessel region of the intermediate output, which can facilitate the fine-stage backbone to focus on vessel regions for better refinement.

As shown in Figure 4, we assume that the ISAM has an input resolution of $F_{in} \in R^{H \times W \times C}$, we first apply average and maximum pooling operations to F_{in} along the channel axis to obtain spatial feature descriptors $F_{avg} \in R^{H \times W \times 1}$ and $F_{max} \in R^{H \times W \times 1}$, as shown in the following equation:

$$F_{avg} \in R^{H \times W \times 1} = avgPool(F_{in})$$

$$F_{max} \in R^{H \times W \times 1} = maxPool(F_{in})$$

Subsequently, to enhance the vessel region of F_{in} , we concatenate these two spatial feature descriptors and use 3×3 convolution kernels with different dilation rates to model the neighborhood relationship of pixels. We add the results of the modeling and then use the sigmoid operation to generate the attention map $sWeights \in R^{H \times W \times 1}$, as shown below:

$$sWeights = \sigma \left(BN \left(\varphi_{3,rate=1}([F_{avg}; F_{max}]) + \varphi_{3,rate=2}([F_{avg}; F_{max}]) + \varphi_{3,rate=3}([F_{avg}; F_{max}]) \right) \right)$$

Among them, σ represents Sigmoid activation, BN represents Batch Normalization, and $\varphi_{3,rate=N}$ represents the 3×3 convolution with a dilation rate of N . It is worth mentioning that in the above process, the purpose of using convolution operations with different dilation rates is to integrate multi-scale context information when calculating the importance of pixels, to better encode the emphasized or suppressed positions. Finally, we obtain the ISAM output $F_{out} \in R^{H \times W \times C}$ based on the obtained spatial attention map and scaled feature map F_{in} , as shown in the following equation:

$$F_{out} = sWeights \otimes F_{in}$$

where \otimes denotes pixel-wise product.

3.3 Pixel-importance-balance loss

There are three types of pixels in fundus images: background, thick vessels, and thin vessels. Their proportions in the fundus image vary from high to low. To balance the contributions of these three types of pixels in loss computation, we scale their loss weights according to the number of vessel pixels in their neighborhood. Specifically, for background

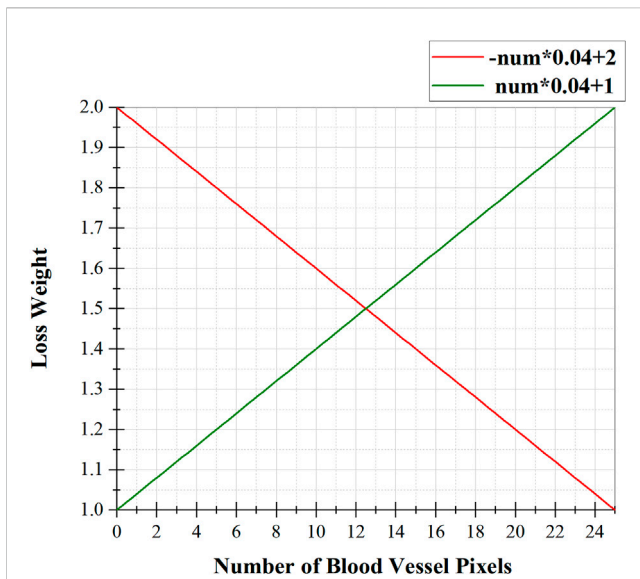


FIGURE 5

The relationship between the loss weight of a pixel and the number of blood vessel pixels around it, where the red function is used for vessel pixels and the green function is used for background pixels.

pixels, we think that only background pixels near blood vessels need to be emphasized, as this can force the model to keep the predicted blood vessel thickness consistent with the thickness in the ground truth. Therefore, the loss weights of background pixels should be proportional to the number of blood vessel pixels in their neighborhood. As for blood vessel pixels, if they belong to thick blood vessels, they will be surrounded by more blood vessel pixels in the fundus image, and fewer if they belong to thin blood vessels. Therefore, to balance the contributions of these two kinds of vessel pixels, the loss weights of vessel pixels should be inversely proportional to the number of vessel pixels in their neighborhood.

Algorithm 1 shows the calculation process of loss weights for different types of pixels in PIB loss. Firstly, the background pixels and vessel pixels of the Ground Truth are represented by 0 and 1. Secondly, the importance loss weight for each pixel is calculated as follows: with the pixel as the center, the number of pixels with value 1 (i.e., the number of surrounding vessel pixels) present in a box separated by 2 pixels is counted as *num*. Thirdly, if the pixel belongs to a vessel, it is converted into a loss weight by an inverse proportional function $-num \cdot 0.04 + 2$ (see Figure 5, red line), which emphasizes thin blood vessels; if the pixel belongs to the background, it is converted into loss weights by a direct proportional function $num \cdot 0.04 + 1$ (see Figure 5, green line), as shown below:

$$\text{Loss weight}(Y_{ij}) = \begin{cases} -\left(\sum_{p=i-2}^{i+2} \sum_{q=j-2}^{j+2} Y_{pq}\right) \cdot 0.04 + 2 & \text{if } y_{ij} = 1 \\ \left(\sum_{p=i-2}^{i+2} \sum_{q=j-2}^{j+2} Y_{pq}\right) \cdot 0.04 + 1 & \text{if } y_{ij} = 0 \end{cases}$$

Finally, the obtained loss weights are combined with the Cross Entropy, as shown below:

$$\text{PIB Loss}(P, Y) = \begin{cases} -\sum \text{weight}(Y_{ij}) \cdot \log(P_{ij}) & \text{if } Y_{ij} = 1 \\ -\sum \text{weight}(Y_{ij}) \cdot \log(1 - P_{ij}) & \text{if } Y_{ij} = 0 \end{cases}$$

```

Input: GroundTruth Y
Output: loss weight W
/* iterate over each pixel */
1 for  $Y_{ij}$  in Y do
    /* Count the number of blood vessel pixels at a distance of two
    pixels around  $Y_{ij}$  */
    2  $num \leftarrow 0$ ;
    3 for  $p = i - 2$  to  $i + 2$  do
    4     for  $q = j - 2$  to  $j + 2$  do
    5         if  $Y_{pq} = 1$  then
    6              $num \leftarrow num + 1$ ;
    7         end
    8     end
    9 end
    /* Convert num to loss weight by whether  $Y_{ij}$  belongs to blood vessel
    or background */
    10 if  $Y_{pq} = 1$  then
    11      $W_{ij} = -num \cdot 0.04 + 2$ ;
    12 end
    13 else
    14      $W_{ij} = num \cdot 0.04 + 1$ ;
    15 end
    16 end
    17 return W

```

Algorithm 1. Loss weight calculation process of Our PIB Loss.

4 Experimental configuration

4.1 Dataset and augmentation

We evaluate the proposed method using two publicly available datasets (DRIVE¹ and CHASE_DB1²). Specific information about these two databases is shown in Table 1. It should be noted that the original size of the two datasets is not suitable for our network, so we adjusted its size by zero padding around it, but the size was cropped to the initial size during evaluation. (See Table 1, Crop size). For the DRIVE dataset, the official data division is adopted, which means 20 training images were used for model training and 20 test images were used for performance evaluation. The CHASE_DB1 dataset has no official data division, so we follow the previous work (Alom et al., 2019; Wang et al., 2020b), using the first 20 images for model training, and the remaining 8 images for model evaluation. Furthermore, since the number of training images is limited to 20, some data augmentation methods are required. We use four data augmentation methods (see Table 1, Augmentation methods) for both datasets to generate randomly modified samples during the training process.

4.2 Evaluation metrics

To evaluate our method, we compare the segmentation results to the corresponding Ground Truths and classify the outcomes of each pixel comparison into True Positive (TP), False Positive (FP), False Negative (FN), and True Negative (TN). The model's performance is

1 DRIVE: <http://www.isi.uu.nl/Research/Databases/DRIVE/>

2 CHASE_DB1: <https://blogs.kingston.ac.uk/retinal/chasedb1/>

TABLE 1 The specific information of DRIVE and CHASE_DB1 datasets.

Datasets	DRIVE	CHASE_DB1
Form	A diabetic retinal disease screening study in the Netherlands	Comprehensive health study of 200 primary schools in the United Kingdom
Imaging equipment	Canon CR5 non-mydratic 3CCD camera	NIDEK NM-200D Handy Fundus Camera
Total number	40	28
Train/Test number	20/20	20/8
Resolution (pixel)	584 × 565	999 × 960
Pad size	592 × 592	1008 × 1008
Augmentation methods	1) Random horizontal and vertical flip. 2) Random rotation. 3) color jittering.	

then evaluated using sensitivity (SE), F1 score (F1), and accuracy (ACC), which are defined as:

$$SE = \frac{TP}{TP + FN}$$

$$SP = \frac{TN}{TN + FP}$$

$$ACC = \frac{TP + TN}{TP + TN + FP + FN}$$

$$F1 = \frac{2TP}{2TP + FP + FN}$$

The closer the value of these evaluation metrics are to 1, the better the prediction. Furthermore, receiver operating characteristic (ROC) curves and the area under the ROC curve (AUC) were used to evaluate the performance of our model. The ROC curve was calculated as the variation of the TP and FP rate for different values of a changing threshold.

4.3 Implementation details

Our method is built on the PyTorch³ framework and all experiments were run on an NVIDIA RTX3090 with 24 GB of memory. We did not use any pre-trained models, and the entire training process was end-to-end without any post-processing. For the hyperparameter settings, the batch size was set to 2 for both datasets, and the network was optimized using an Adam (Kingma and Ba, 2014) optimizer with an initial learning rate of 1e-3. The total number of learning epochs was set to 200, and a learning rate decay by the factor 0.1 was performed at epochs 150 and 190. We used the best epoch of results for testing.

5 Results and discussions

5.1 Segmentation performance on two databases

Figure 6 shows the training process of AGC-Ne in DRIVE and CHASE_DB1, where the blue line represents the loss change curve

on the training set, and the orange line represents the loss change curve on the test set. We can observe that on the two data sets, the loss of AGC-Net on the training set and the test set can converge well, and the loss of the test set can be comparable to that of the training set. This shows that AGC-Net can adapt well to unseen data and has good generalization ability.

We present in Figure 7 some test images of the two datasets, their ground truth values, and the predictions generated by AGC-Net using these images. As can be seen from the figure, AGC-Net detects most retinal vessels on fundus images, including thin vessels with low contrast and thick vessels with over-illumination. Furthermore, the vessel thickness in our model predictions is consistent with the ground truth. Most of the spatial information of retinal vessels is preserved, such as vessel connectivity, bifurcations, and edges.

We also quantitatively evaluate AGC-Net on the two datasets separately. Table 2 presents the five metric values of our method on the two datasets. The table shows that on the two data sets, the SE, SP, ACC, F1, and AUC of AGC-Net can reach 0.8251/0.8499, 0.9844/0.9854, 0.9704/0.9767, 0.8301/0.8213 and 0.9881/0.9917 respectively. This demonstrates that our proposed AGC-Net model can generate accurate and meaningful retinal vessel segmentation, providing doctors valuable auxiliary diagnostic information in clinical practice.

5.2 Ablation studies

As shown in Figure 2, AGC-Net can be regarded as a segmentation network composed of Cascade Design (CD), Auxiliary Supervision (AS), Inter-Stage Attention Module (ISAM), and Pixel-Importance-Balance Loss (PIBL). In this section, we conduct ablation studies to verify the effectiveness of these crucial components in AGC-Net and evaluate the impact of each component on the vessel segmentation results. We use Res-UNet (Xiao et al., 2018) with an initial channel number of 32 and only two downsampling stages as a baseline and gradually add the above crucial components. All experiments are performed with the same hyperparameter configuration. Table 3 shows the quantitative comparison of network configurations that incorporate different crucial components.

From Index 2 in Table 3, we can see that when we simply add another backbone to the baseline for cascading, SE, ACC, F1, and AUC all suffer a decline. This shows that adding the cascade

³ <https://pytorch.org/>

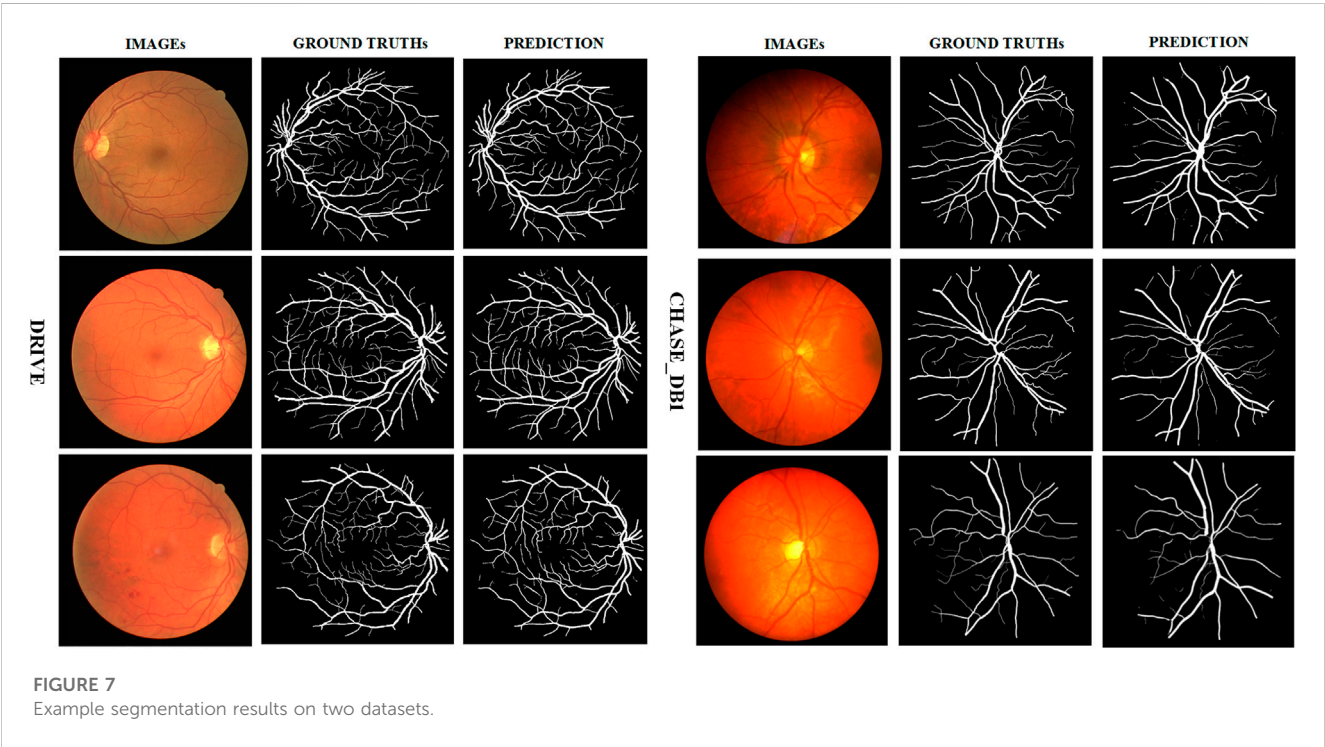
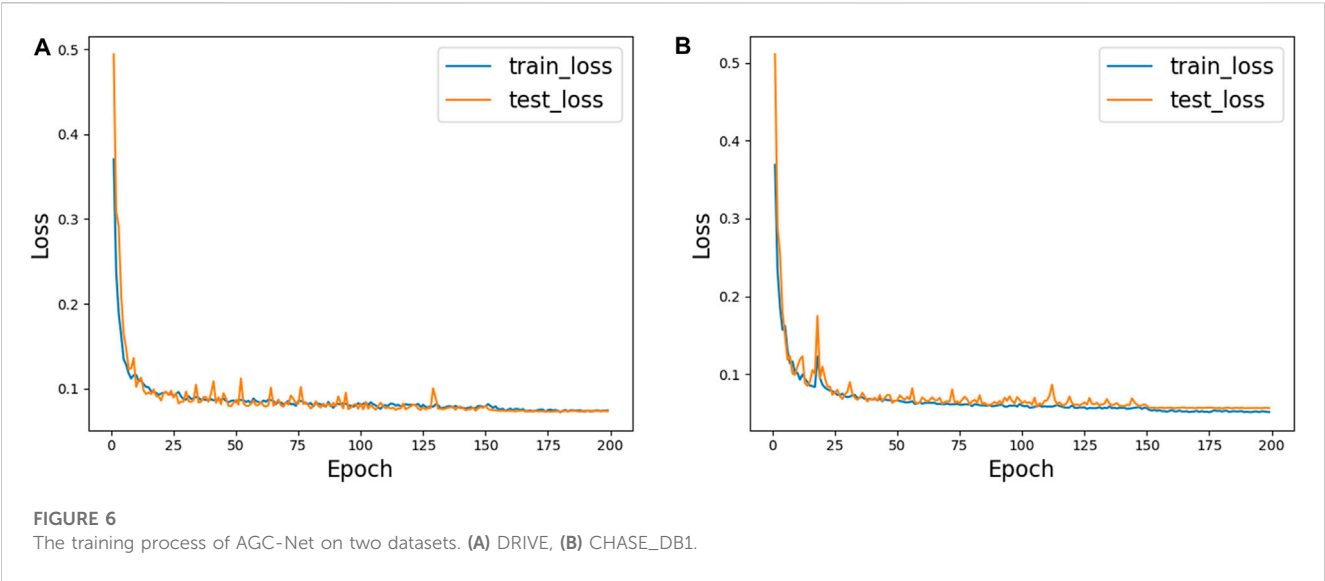


TABLE 2 Performance of the proposed AGC-Net on DRIVE and CHASE_DB1 datasets.

Datasets	SE	SP	ACC	F1	AUC
DRIVE	0.8251	0.9844	0.9704	0.8301	0.9881
CHASE_DB1	0.8499	0.9854	0.9767	0.8213	0.9917

design will bring optimization problems caused by increased network depth. That is, the gradient cannot be backpropagated well. As seen in Index 3, this problem can be solved after we add

auxiliary supervision. Adding auxiliary supervision enables the cascaded design to further improve the baseline performance, among which SE, ACC, F1, and AUC are increased by 0.72%, 0.05%, 0.33%, and 0.08% compared with the baseline, respectively. Then, if we continue to add ISAM, by comparing index 3 and index 4 in the table, we find that SE, ACC and F1 continue to grow by 0.44%, 0.01%, and 0.13%, respectively. And when we don't add ISAM but use PIB loss to train the network with index 3, by comparing index 3 and index 5 in the table, the SE and F1 of the network also improve, increasing by 2.81% and 0.16%, respectively, but SP and ACC have a slight

TABLE 3 Ablation studies with different network configurations.

Index	Baseline	CD	AS	ISAM	PIBL	SE (%)	SP (%)	ACC (%)	F1 (%)	AUC (%)
1	√					78.95	98.75	97.01	82.27	98.72
2	√	√				78.36	98.78	96.99	82.00	98.66
3	√	√	√			79.67	98.73	97.06	82.60	98.80
4	√	√	√	√		80.11	98.70	97.07	82.73	98.80
5	√	√	√		√	81.79	98.48	97.02	82.76	98.80
6	√	√	√	√	√	82.51	98.44	97.04	83.01	98.81

Baseline: Res-UNet; CD, Cascade Design; AS, Auxiliary Supervision; ISAM, Inter-Stage Attention Module; and PIBL, Pixel-Importance-Balance Loss. The value in bold is the highest value under that metric.

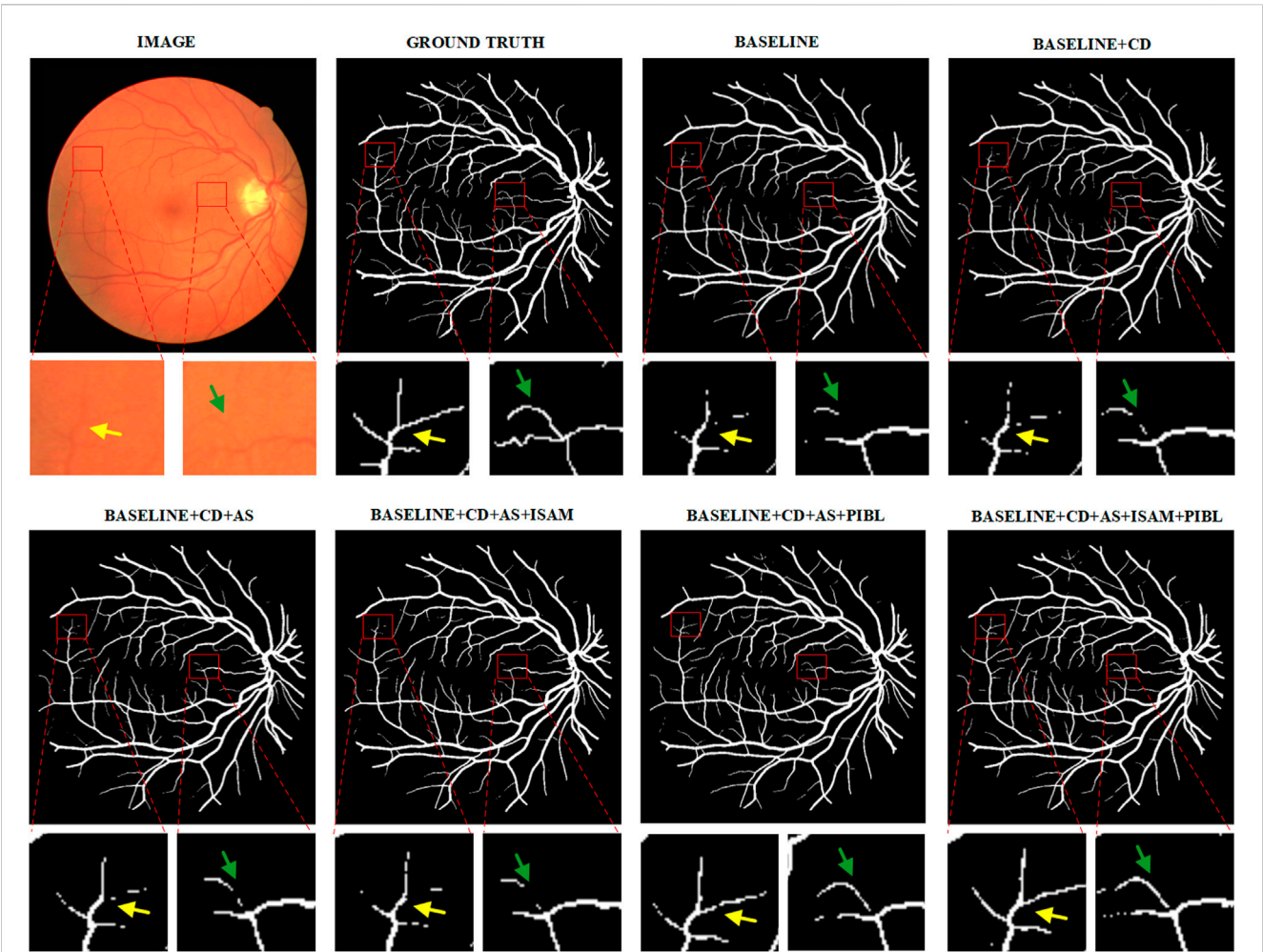
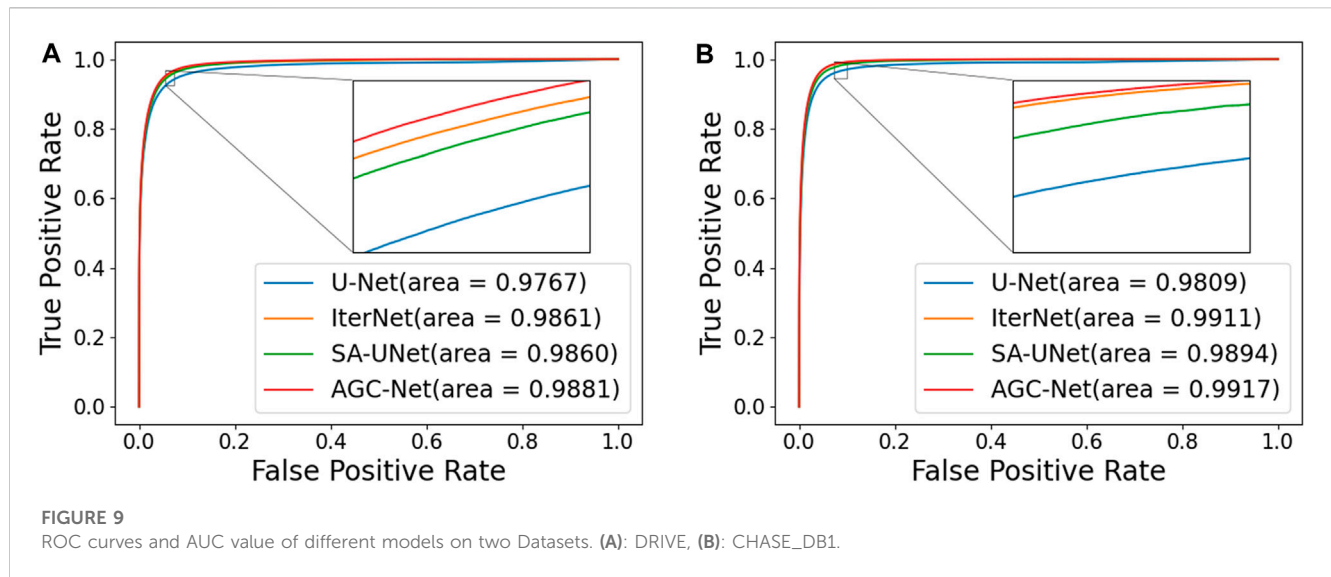


FIGURE 8 Example segmentation results for different network configurations on the DRIVE dataset. Baseline: Res-UNet; CD, Cascade Design; AS, Auxiliary Supervision; ISAM, Inter-Stage Attention Module, and PIBL, Pixel-Importance-Balance Loss.

drop. Finally, when we use both ISAM and PIB loss, SE, F1 and AUC reach the highest values of 82.51, 83.01, and 98.81 in Table 3, which are 3.56%, 0.74%, and 0.09% higher than the baseline, respectively. This is higher than the improvement obtained by adding ISAM or PIB loss alone, which shows that the two are compatible with each other and can promote performance improvement. But the SP reached the lowest value of 98.44%. The highest SE and the lowest SP reflect that



our method further enhances the vessel extraction ability but inevitably introduces some false positives, which is acceptable (Moccia et al., 2018).

Furthermore, we plot some heatmaps generated using Grad-CAM (Selvaraju et al., 2017) in [Supplementary Figure S1](#). In the heatmap, the redder the region's color, the more the network pays attention to the feature of the region when predicting blood vessels. From [Supplementary Figure S1](#), we can observe that the blood vessel area has been emphasized after adding ISAM to the network. This demonstrates that ISAM can promote fine-stage backbones in the network to focus on vascular regions and perform better refinement.

We present example segmentation results of different network configurations in ablation studies in [Figure 8](#) and further zoom in on some vessel regions under each image for qualitative comparison. As can be seen from the figure, the baseline after adding all the important components works best for the effect of vessel segmentation. This shows the necessity of every critical component.

5.3 Comparison with the state-of-the-art methods

In this section, we compare the proposed method with some popular vessel segmentation methods, including U-Net (Ronneberger et al., 2015), IterNet (Li et al., 2020), and SA-UNet (Guo et al., 2021b). To test the results of these vessel segmentation methods, we used their public codes on the DRIVE and CHASE_DB1 datasets for training and evaluation. The Receiver Operating Characteristic (ROC) curves and AUC values of the four models on the two datasets are shown in [Figure 9](#). The figure shows that compared with the suboptimal method, the AUC values obtained by AGC-Net have increased by 0.20% and 0.03% on the two data sets, respectively. Considering that these popular methods already have high performance (i.e., AUC values very close to 1.0), this improvement means that many vessel pixels can now be correctly classified.

In addition, we also compare some state-of-the-art methods in the literature, including R2UNet (Alom et al., 2019), DUNet (Jin et al.,

2019), NFN+ (Wu et al., 2020), CAR-UNet (Guo et al., 2021a), RVSegNet (Wang et al., 2020b), SCS-Net (Wu et al., 2021), AG-Net (Zhang et al., 2019) and FR-UNet (Liu et al., 2022). Only the four methods in the previous paragraph come from our reproduced results, and the results of all other methods come from the corresponding papers. The results on the DRIVE dataset are listed in [Table 4](#). Among all the compared methods, our method ranks second in ACC, F1 and AUC, and is very close to the first-ranked method (FR-UNet). Specifically, among these metrics, for the ACC value, our method achieves 0.9704, which is only 0.01% lower than FR-UNet. In addition, the AUC value and F1 value reached 0.9881 and 0.8301, respectively. In all comparison methods, same as FR-UNet, these two values exceed the values of 0.98 and 0.83. For the other two metrics SE and SP, the results obtained by AGC-Net are also comparable to other state-of-the-art methods. SE is usually interpreted as the model's ability to correctly detect all vascular regions in retinal images. The SE obtained by our method can reach 0.8251, which is 1.05% lower than FR-UNet (0.8356). Nevertheless, this is still much higher than some other methods based on coarse-to-fine architectures [such as NFN+ (0.7796), CAR-UNet (0.8135) and IterNet (0.7921)]. The difference between AGC-Net and other methods based on coarse-to-fine architecture is that we use ISAM to enhance the container area of the intermediate output, which enables the backbone of the fine stage to better refine the container, resulting in higher SE value. SP is often interpreted as the localization ability of retinal vessel segmentation models. This ability refers to the ability to unerringly identify non-vascular regions as blood vessels. The SP of our method can reach 0.9844, which is 0.3% lower than the top-ranked IterNet (0.9874). We believe this is due to our method detecting more blood vessels, but inevitably introducing some false positives. Since the goal of the retinal vessel segmentation task is to detect as many vessels as possible, a relatively low SP is acceptable.

[Table 5](#) shows the results of the different methods on the CHASE_DB1 dataset. It should be noted that the data partitioning methods of DUNet and NFN+ are different from ours. Therefore, for the sake of fairness, we do not compare the results of these two methods. Unlike the case on the DRIVE dataset, on this dataset, our proposed AGC-Net exceeds FR-UNet and achieves 0.9767, 0.8213, and 0.9917 in ACC, F1 and AUC, respectively, which are the best results among all

TABLE 4 Performance comparison of the DRIVE dataset.

Method	Year	SE	SP	ACC	F1	AUC
U-Net Ronneberger et al. (2015)	2015	0.7776	0.9867	0.9681	0.8108	0.9766
R2UNet Alom et al. (2019)	2018	0.7792	0.9813	0.9556	0.8171	0.9784
DUNet Jin et al. (2019)	2019	0.7963	0.9800	0.9566	0.8237	0.9802
AG-Net Zhang et al. (2019)	2019	0.8100	0.9848	0.9692	—	0.9856
IterNet Li et al. (2020)	2019	0.7921	0.9874	0.9699	0.8244	0.9861
NFN+ Wu et al. (2020)	2020	0.7796	0.9813	0.9582	0.8295	0.9830
RVSeg-Net Wang et al. (2020b)	2020	0.8107	0.9845	0.9681	—	0.9817
SCS-Net Wu et al. (2021)	2021	0.8289	0.9838	0.9697	—	0.9837
SA-UNet Guo et al. (2021b)	2021	0.8264	0.9823	0.9687	0.8224	0.9861
CAR-UNet Guo et al. (2021a)	2022	0.8135	0.9849	0.9699	—	0.9852
FR-UNet Liu et al. (2022)	2022	0.8356	0.9837	0.9705	0.8316	0.9889
AGC-Net (Our)	2023	0.8251	0.9844	0.9704	0.8301	0.9881

The value in bold is the highest value under that metric.

TABLE 5 Performance comparison on the CHASE_DB1 dataset.

Method	Year	SE	SP	ACC	F1	AUC
U-Net Ronneberger et al. (2015)	2015	0.7961	0.9863	0.9746	0.7974	0.9808
R2UNet Alom et al. (2019)	2018	0.7756	0.9820	0.9634	0.7928	0.9815
AG-Net Zhang et al. (2019)	2019	0.8186	0.9848	0.9743	—	0.9863
IterNet Li et al. (2020)	2019	0.8141	0.9878	0.9766	0.8165	0.9910
RVSeg-Net Wang et al. (2020b)	2020	0.8069	0.9836	0.9726	—	0.9833
SCS-Net Wu et al. (2021)	2021	0.8365	0.9839	0.9744	—	0.9867
SA-UNet Guo et al. (2021b)	2021	0.8651	0.9814	0.9740	0.8076	0.9893
CAR-UNet Guo et al. (2021a)	2022	0.8439	0.9839	0.9751	—	0.9898
FR-UNet Liu et al. (2022)	2023	0.8798	0.9814	0.9748	0.8151	0.9913
AGC-Net (Our)	2023	0.8499	0.9854	0.9767	0.8213	0.9917

The value in bold is the highest value under that metric.

compared methods. Among these metrics, the AUC value best reflects the comprehensive performance of the model segmentation. In this experiment, our method reached 0.9917, which is very close to 1.0, which shows the good robustness of AGC-Net. For the ACC and F1 values, our method outperforms FR-UNet by 0.19% and 0.62%, respectively. FR-UNet is a segmentation framework that maintains full-resolution representation learning to retain more spatial information lost due to downsampling. However, the fundus images on the CHASE_DB1 dataset are already of high resolution (999×960) and have sufficient spatial information, which makes the advantage of FR-UNet on this dataset diminished. In addition, we can observe that some segmentation methods based on the same coarse-to-fine architecture also have higher ACC values than FR-UNet (0.9748), such as IterNet (0.9766) and CAR-UNet (0.9751). This suggests that for some high-

resolution fundus images, a segmentation method based on the coarse-to-fine architecture may be a better choice. For the SE metric, AGC-Net achieves 0.8499, which ranks third among all compared methods and outperforms other methods based on coarse-to-fine architecture. This is because we designed a more reasonable loss function and used ISAM to promote the fine stage to achieve better refinement.

Through qualitative comparisons on the two datasets, we find that both AGC-Net can guarantee the improvement of comprehensive segmentation performance and maintain a high SE without introducing too many false positives. Therefore, compared to other methods, we believe that AGC-Net can better cope with the vessel segmentation task.

Especially when we compare the segmentation results of different methods in [Figure 10](#), the advantages of AGC-Net are

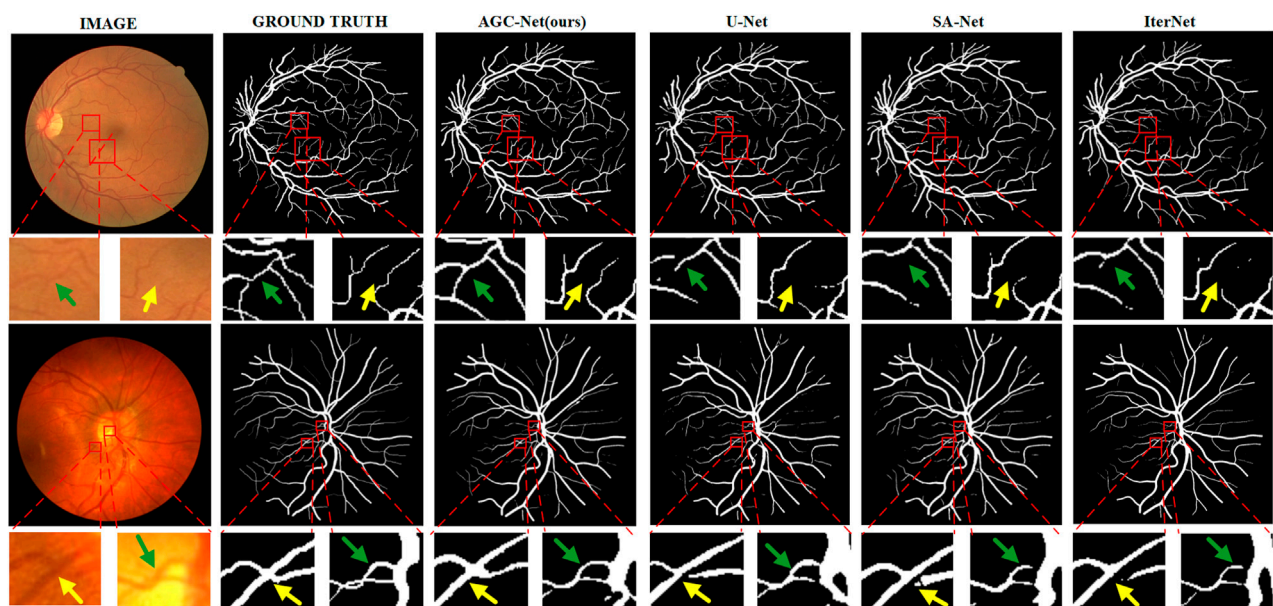


FIGURE 10

Example segmentation results of different models on two datasets. From left to right are image, ground truth, prediction result of AGC-Net, prediction result of U-Net, prediction result of SA-UNet, and prediction result of IterNet. From top to bottom are the DRIVE dataset and the CHASE-DB1 dataset.

more prominent. It can be seen from the figure that the blood vessel segmentation results obtained by other methods lack sufficient semantic information, and the blood vessels are broken. The segmentation result of our method is closer to the ground truth, as it identifies some blood vessels that other methods cannot identify, including over-illuminated blood vessels and low-contrast thin blood vessels, and the connectivity of blood vessels is better. There are three reasons for the superior performance of AGC-Net on visual effects: First, the fine stage in the AGC-Net framework gives those misclassified vessel pixels a chance to be corrected. Second, ISAM improves the degree of attention of the fine-stage backbone to the vessel region, which achieves a better refinement effect. Third, the PIB loss scales the loss weights per pixel so that certain key pixels contribute more to the gradient. The advantages of AGC-Net in qualitative comparison with other methods can provide doctors or experts with more useful vascular information in practical applications. This can facilitate early detection and treatment of eye diseases.

For the problem of imbalance between foreground pixels and background pixels in fundus images, PIB Loss is very effective. We recommend that other researchers use PIB Loss to improve performance when training blood vessel segmentation models. If other researchers are designing a segmentation model based on a coarse-to-fine architecture, we suggest using ISAM to improve the refinement effect of the fine stage.

5.4 Limitations

Although our method performs very well compared to other methods, several limitations exist. First, the proposal of PIB

Loss can significantly alleviate the problem of an unbalanced ratio of foreground pixels and background pixels in fundus images. However, due to the selection of pixel distance (we fixed it as a box with a distance of 2 pixels in the method) coupled with the proportional function, PIB Loss still needs to be flexible enough. This limit exploring the effect of pixel distances of 3 or more pixels on experimental results. In future work, we plan to decouple the pixel distance and proportional function of PIB Loss and explore the impact of more pixel distances on experiments. Second, although our method has segmented more blood vessels than other methods, there are still breaks or unrecognized phenomena for some extremely small blood vessels. This is attributed to the amount of training data being too small (usually only around 20 capacity), which leads to poor generalization on these extremely small blood vessels. We plan to explore more effective data augmentation techniques in future work.

6 Conclusion

Our paper presents a novel method for segmenting retinal vessels, which are essential for diagnosing and treating eye diseases. The proposed method designs a coarse-to-fine network with a two-stage strategy: the first stage generates a rough vessel prediction map, and the second stage corrects the misclassified pixels in this map. The coarse-to-fine network uses a novel inter-stage attention module to adjust the importance of vessel regions in the intermediate output for better refinement. In addition, we design a novel PIB loss for network training to address the problem of pixel ratio imbalance in fundus images. PIB avoids the gradient being dominated by many background

pixels by scaling the loss weight of each pixel, which is of great help to improve the blood vessel segmentation effect. We evaluated our method on two public datasets and found that it outperformed several state-of-the-art methods with high performance.

Data availability statement

The original contributions presented in the study are included in the article/[Supplementary Material](#), further inquiries can be directed to the corresponding authors.

Author contributions

HS: Algorithm design and draft writing. LG: Investigate and analyze experimental feasibility. JH: Review and editing. LH: Participate in the design and implementation of experiments. YL: Handling article logic and Figure drawing. HJ: Data collection and processing. ZC: Text proofreading.

Funding

This project is supported by the “Wu Yi University Hong Kong Macao Joint Research: 2019WGALH23,” the “Guangdong Province

Teaching Reform Project: GDJX2020009,” and the “Wuyi University Teaching Reform Project: JX2020052.”

Conflict of interest

The authors declare that the research was conducted in the absence of any commercial or financial relationships that could be construed as a potential conflict of interest.

Publisher's note

All claims expressed in this article are solely those of the authors and do not necessarily represent those of their affiliated organizations, or those of the publisher, the editors and the reviewers. Any product that may be evaluated in this article, or claim that may be made by its manufacturer, is not guaranteed or endorsed by the publisher.

Supplementary Material

The Supplementary Material for this article can be found online at: <https://www.frontiersin.org/articles/10.3389/fcell.2023.1196191/full#supplementary-material>

References

- Alom, M. Z., Yakopcic, C., Hasan, M., Taha, T. M., and Asari, V. K. (2019). Recurrent residual U-Net for medical image segmentation. *J. Med. Imaging* 6 (1), 014006. doi:10.1117/1.JMI.6.1.014006
- Chatziralli, I. P., Kanonidou, E. D., Kerytopoulos, P., Dimitriadis, P., and Papazisis, L. E. (2012). The value of funduscopy in general practice. *open Ophthalmol. J.* 6, 4–5. doi:10.2174/1874364101206010004
- Chutatape, O., Zheng, L., and Krishnan, S. M. (1998). “Retinal blood vessel detection and tracking by matched Gaussian and Kalman filters,” in *Proceedings of the 20th annual international conference of the IEEE engineering in medicine and Biology society (IEEE)*, 20, 3144–3149. doi:10.1109/IEMBS.1998.746160
- Fraz, M. M., Barman, S. A., Remagnino, P., Hoppe, A., Basit, A., Uyyanonvara, B., et al. (2012). An approach to localize the retinal blood vessels using bit planes and centerline detection. *Comput. methods programs Biomed.* 108 (2), 600–616. doi:10.1016/j.cmpb.2011.08.009
- Fraz, M. M., Remagnino, P., Hoppe, A., Uyyanonvara, B., Rudnicka, A. R., Owen, C. G., et al. (2012). An ensemble classification-based approach applied to retinal blood vessel segmentation. *IEEE Trans. Biomed. Eng.* 59 (9), 2538–2548. doi:10.1109/TBME.2012.2205687
- Guo, C., Szemeyeni, M., Hu, Y., Wang, W., Zhou, W., and Yi, Y. (2021). “Channel attention residual u-net for retinal vessel segmentation,” in *ICASSP 2021-2021 IEEE international conference on acoustics, speech and signal processing (ICASSP) (IEEE)*, 1185–1189. doi:10.1109/ICASSP39728.2021.9414282
- Guo, C., Szemeyeni, M., Yi, Y., Wang, W., Chen, B., and Fan, C. (2021). “Sa-unet: Spatial attention u-net for retinal vessel segmentation,” in *2020 25th international conference on pattern recognition (ICPR) (IEEE)*, 1236–1242. doi:10.1109/ICPR48806.2021.9413346
- Ji, Y., Ji, Y., Liu, Y., Zhao, Y., and Zhang, L. (2023). Research progress on diagnosing retinal vascular diseases based on artificial intelligence and fundus images. *Front. Cell. Dev. Biol.* 11, 1168327. doi:10.3389/fcell.2023.1168327
- Jin, Q., Meng, Z., Pham, T. D., Chen, Q., Wei, L., and Su, R. (2019). DUNet: A deformable network for retinal vessel segmentation. *Knowledge-Based Syst.* 178, 149–162. doi:10.1016/j.knsys.2019.04.025
- Khandouzi, A., Ariafar, A., Mashayekhpour, Z., Pazira, M., and Baleghi, Y. (2022). Retinal vessel segmentation, a review of classic and deep methods. *Ann. Biomed. Eng.* 50 (10), 1292–1314. doi:10.1007/s10439-022-03058-0
- Kingma, D. P., and Ba, J. (2014). *Adam: A method for stochastic optimization*. arXiv preprint arXiv:1412.6980.
- Lee, C. Y., Xie, S., Gallagher, P., Zhang, Z., and Tu, Z. (2015). “Deeply-supervised nets,” in *Proceedings of the 18th International Conference on Artificial Intelligence and Statistics (AISTATS) 2015, San Diego, CA (JMLR: W&CP)*, Vol. 38.
- Li, L., Verma, M., Nakashima, Y., Nagahara, H., and Kawasaki, R. (2020). “Internet: Retinal image segmentation utilizing structural redundancy in vessel networks,” in *Proceedings of the IEEE/CVF winter conference on applications of computer vision*, 3656–3665.
- Liu, W., Yang, H., Tian, T., Cao, Z., Pan, X., Xu, W., et al. (2022). Full-resolution network and dual-threshold iteration for retinal vessel and coronary angiograph segmentation. *IEEE J. Biomed. Health Inf.* 26 (9), 4623–4634. doi:10.1109/JBHI.2022.3188710
- Long, J., Shelhamer, E., and Darrell, T. (2015). “Fully convolutional networks for semantic segmentation,” in *Proceedings of the IEEE conference on computer vision and pattern recognition*, 3431–3440.
- Lupascu, C. A., Tegolo, D., and Trucco, E. (2010). Fabc: Retinal vessel segmentation using AdaBoost. *IEEE Trans. Inf. Technol. Biomed.* 14 (5), 1267–1274. doi:10.1109/TITB.2010.2052282
- Memari, N., Ramli, A. R., Bin Saripan, M. I., Mashohor, S., and Moghbel, M. (2017). Supervised retinal vessel segmentation from color fundus images based on matched filtering and AdaBoost classifier. *PLoS one* 12 (12), e0188939. doi:10.1371/journal.pone.0188939
- Mendonça, A. M., and Campilho, A. (2006). Segmentation of retinal blood vessels by combining the detection of centerlines and morphological reconstruction. *IEEE Trans. Med. Imaging* 25 (9), 1200–1213. doi:10.1109/TMI.2006.879955
- Moccia, S., De Momi, E., El Hadji, S., and Mattos, L. S. (2018). Blood vessel segmentation algorithms—Review of methods, datasets and evaluation metrics. *Comput. methods programs Biomed.* 158, 71–91. doi:10.1016/j.cmpb.2018.02.001
- Nayebifar, B., and Moghaddam, H. A. (2013). A novel method for retinal vessel tracking using particle filters. *Comput. Biol. Med.* 43 (5), 541–548. doi:10.1016/j.combiomed.2013.01.016
- Olafsdottir, O. B., Hardarson, S. H., Gottfredsdottir, M. S., Harris, A., and Stefánsson, E. (2011). Retinal oximetry in primary open-angle glaucoma. *Investigative Ophthalmol. Vis. Sci.* 52 (9), 6409–6413. doi:10.1167/iov.10-6985
- Oliveira, W. S., Teixeira, J. V., Ren, T. I., Cavalcanti, G. D., and Sijbers, J. (2016). Unsupervised retinal vessel segmentation using combined filters. *PLoS one* 11 (2), e0149943. doi:10.1371/journal.pone.0149943

- Owen, C. G., Rudnicka, A. R., Mullen, R., Barman, S. A., Monekosso, D., Whincup, P. H., et al. (2009). Measuring retinal vessel tortuosity in 10-year-old children: Validation of the computer-assisted image analysis of the retina (CAIAR) program. *Investigative Ophthalmol. Vis. Sci.* 50 (5), 2004–2010. doi:10.1167/iovs.08-3018
- Ricci, E., and Perfetti, R. (2007). Retinal blood vessel segmentation using line operators and support vector classification. *IEEE Trans. Med. Imaging* 26 (10), 1357–1365. doi:10.1109/TMI.2007.898551
- Ronneberger, O., Fischer, P., and Brox, T. (2015). U-net: Convolutional networks for biomedical image segmentation. In *Medical image computing and computer-assisted intervention—MICCAI 2015: 18th international conference*, Munich, Germany. Springer International Publishing, 234–241. doi:10.1007/978-3-319-24574-4_28
- Roychowdhury, S., Koozekanani, D. D., and Parhi, K. K. (2015). Iterative vessel segmentation of fundus images. *IEEE Trans. Biomed. Eng.* 62 (7), 1738–1749. doi:10.1109/TBME.2015.2403295
- Sazak, Ç., Nelson, C. J., and Obara, B. (2019). The multiscale bowler-hat transform for blood vessel enhancement in retinal images. *Pattern Recognit.* 88, 739–750. doi:10.1016/j.patcog.2018.10.011
- Selvaraju, R. R., Cogswell, M., Das, A., Vedantam, R., Parikh, D., and Batra, D. (2017). “Grad-cam: Visual explanations from deep networks via gradient-based localization,” in *Proceedings of the IEEE international conference on computer vision*, 618–626.
- Simonyan, K., and Zisserman, A. (2014). *Very deep convolutional networks for large-scale image recognition*. Oxford, United Kingdom: Cornell University. arXiv preprint arXiv:1409.155.
- Staal, J., Abramoff, M. D., Niemeijer, M., Viergever, M. A., and Van Ginneken, B. (2004). Ridge-based vessel segmentation in color images of the retina. *IEEE Trans. Med. Imaging* 23 (4), 501–509. doi:10.1109/TMI.2004.825627
- Tolias, Y. A., and Panas, S. M. (1998). A fuzzy vessel tracking algorithm for retinal images based on fuzzy clustering. *IEEE Trans. Med. Imaging* 17 (2), 263–273. doi:10.1109/42.700738
- Vázquez, S. G., Cancela, B., Barreira, N., Penedo, M. G., Rodríguez-Blanco, M., Pena Seijo, M., et al. (2013). Improving retinal artery and vein classification by means of a minimal path approach. *Mach. Vis. Appl.* 24, 919–930. doi:10.1007/s00138-012-0442-4
- Wang, K., Zhang, X., Huang, S., Wang, Q., and Chen, F. (2020). Ctf-net: Retinal vessel segmentation via deep coarse-to-fine supervision network. In *2020 IEEE 17th international symposium on biomedical imaging*. IEEE, 1237–1241. doi:10.1109/ISBI45749.2020.9098742
- Wang, W., Zhong, J., Wu, H., Wen, Z., and Qin, J. (2020). “Rvseg-net: An efficient feature pyramid cascade network for retinal vessel segmentation,” in *Medical image computing and computer assisted intervention—MICCAI 2020: 23rd international conference*, Lima, Peru (Springer International Publishing), 23, 796–805. doi:10.1007/978-3-030-59722-1_77
- Woo, S., Park, J., Lee, J. Y., and Kweon, I. S. (2018). “Cbam: Convolutional block attention module,” in *Proceedings of the European conference on computer vision* (Berlin, Germany: Springer), 3–19.
- Wu, H., Wang, W., Zhong, J., Lei, B., Wen, Z., and Qin, J. (2021). Scs-net: A scale and context sensitive network for retinal vessel segmentation. *Med. Image Anal.* 70, 102025. doi:10.1016/j.media.2021.102025
- Wu, Y., Xia, Y., Song, Y., Zhang, Y., and Cai, W. (2020). NFN+: A novel network followed network for retinal vessel segmentation. *Neural Netw.* 126, 153–162. doi:10.1016/j.neunet.2020.02.018
- Xia, H., Zhuge, R., and Li, H. (2018). “Retinal vessel segmentation via a coarse-to-fine convolutional neural network,” in *2018 IEEE international conference on bioinformatics and biomedicine (BIBM)* (IEEE), 1036–1039. doi:10.1109/BIBM.2018.8621352
- Xiao, X., Lian, S., Luo, Z., and Li, S. (2018). “Weighted res-unet for high-quality retina vessel segmentation,” in *2018 9th international conference on information technology in medicine and education (ITME)* (IEEE), 327–331. doi:10.1109/ITME.2018.00080
- Yin, Y., Adel, M., and Bourennane, S. (2012). Retinal vessel segmentation using a probabilistic tracking method. *Pattern Recognit.* 45 (4), 1235–1244. doi:10.1016/j.patcog.2011.09.019
- Zana, F., and Klein, J. C. (2001). Segmentation of vessel-like patterns using mathematical morphology and curvature evaluation. *IEEE Trans. image Process.* 10 (7), 1010–1019. doi:10.1109/83.931095
- Zardadi, M., Mehrshad, N., and Razavi, S. M. (2016). Unsupervised segmentation of retinal blood vessels using the human visual system line detection model. *J. Inf. Syst. Telecommun. (JIST)* 2 (14), 1. doi:10.7508/jist.2016.02.008
- Zhang, B., Zhang, L., Zhang, L., and Karray, F. (2010). Retinal vessel extraction by matched filter with first-order derivative of Gaussian. *Comput. Biol. Med.* 40 (4), 438–445. doi:10.1016/j.compbiomed.2010.02.008
- Zhang, L., Fisher, M., and Wang, W. (2015). Retinal vessel segmentation using multi-scale textons derived from keypoints. *Comput. Med. Imaging Graph.* 45, 47–56. doi:10.1016/j.compmedimag.2015.07.006
- Zhang, S., Fu, H., Yan, Y., Zhang, Y., Wu, Q., Yang, M., et al. (2019). “Attention guided network for retinal image segmentation,” in *Medical image computing and computer assisted intervention—MICCAI 2019: 22nd international conference* (Shenzhen, China: Springer International Publishing), 1 22, 797–805. doi:10.1007/978-3-030-32239-7_88
- Zhao, J., Lu, Y., Qian, Y., Luo, Y., and Yang, W. (2022). Emerging trends and research foci in artificial intelligence for retinal diseases: Bibliometric and visualization study. *J. Med. Internet Res.* 24 (6), e37532. doi:10.2196/37532
- Zhao, J., Lu, Y., Zhu, S., Li, K., Jiang, Q., and Yang, W. (2022). Systematic bibliometric and visualized analysis of research hotspots and trends on the application of artificial intelligence in ophthalmic disease diagnosis. *Front. Pharmacol.* 13, 930520. doi:10.3389/fphar.2022.930520



OPEN ACCESS

EDITED BY

Weihua Yang,
Jinan University, China

REVIEWED BY

Bilian Ke,
Shanghai General Hospital, China
Gangjin Kang,
The Affiliated Hospital of Southwest
Medical University, China
Fan Li,
Zhongshan People's Hospital (ZSPH),
China

*CORRESPONDENCE

Jin Yuan,
✉ yuanjincornea@126.com
Peng Xiao,
✉ xiaopengaddis@hotmail.com

[†]These authors have contributed equally
to this work

RECEIVED 29 March 2023

ACCEPTED 02 May 2023

PUBLISHED 11 May 2023

CITATION

Zhang J, Luo Z, Wang G, Huang Y, Fei K,
Liu Y, Li J, Yuan J and Xiao P (2023),
Oxygen-saturation-related functional
parameter as a biomarker for diabetes
mellitus—extraction method and
clinical validation.
Front. Cell Dev. Biol. 11:1195873.
doi: 10.3389/fcell.2023.1195873

COPYRIGHT

© 2023 Zhang, Luo, Wang, Huang, Fei,
Liu, Li, Yuan and Xiao. This is an open-
access article distributed under the terms
of the [Creative Commons Attribution
License \(CC BY\)](https://creativecommons.org/licenses/by/4.0/). The use, distribution or
reproduction in other forums is
permitted, provided the original author(s)
and the copyright owner(s) are credited
and that the original publication in this
journal is cited, in accordance with
accepted academic practice. No use,
distribution or reproduction is permitted
which does not comply with these terms.

Oxygen-saturation-related functional parameter as a biomarker for diabetes mellitus—extraction method and clinical validation

Jinze Zhang[†], Zhongzhou Luo[†], Gengyuan Wang,
Yuancong Huang, Keyi Fei, Yushuang Liu, Jiaxiong Li, Jin Yuan*
and Peng Xiao*

State Key Laboratory of Ophthalmology, Zhongshan Ophthalmic Center, Sun Yat-sen University,
Guangdong Provincial Key Laboratory of Ophthalmology and Visual Science, Guangdong Provincial
Clinical Research Center for Ocular Diseases, Guangzhou, China

Purpose: To develop a computational method for oxygen-saturation-related functional parameter analysis of retinal vessels based on traditional color fundus photography, and to explore their characteristic alterations in type 2 diabetes mellitus (DM).

Methods: 50 type 2 DM patients with no-clinically detectable retinopathy (NDR) and 50 healthy subjects were enrolled in the study. An optical density ratio (ODR) extraction algorithm based on the separation of oxygen-sensitive and oxygen-insensitive channels in color fundus photography was proposed. With precise vascular network segmentation and arteriovenous labeling, ODRs were acquired from different vascular subgroups, and the global ODR variability (ODR_v) was calculated. Student's t-test was used to analyze the differences of the functional parameters between groups, and regression analysis and receiver operating characteristic (ROC) curves were used to explore the discrimination efficiency of DM patients from healthy subjects based on these functional parameters.

Results: There was no significant difference in the baseline characteristics between the NDR and healthy normal groups. The ODRs of all vascular subgroups except the micro venule were significantly higher ($p < 0.05$, respectively) while ODR_v was significantly lower ($p < 0.001$) in NDR group than that in healthy normal group. In the regression analysis, the increased ODRs except micro venule and decreased ODR_v were significantly correlated with the incidence of DM, and the C-statistic for discrimination DM with all ODR is 0.777 (95% CI 0.687–0.867, $p < 0.001$).

Conclusion: A computational method to extract the retinal vascular oxygen-saturation-related optical density ratios (ODRs) with single color fundus photography was developed, and increased ODRs and decreased ODR_v of retinal vessels could be new potential image biomarkers of DM.

KEYWORDS

fundus photography, diabetes mellitus, retina vessel segmentation, oxygen saturation level, light reflection analysis

1 Introduction

The eye is a structurally advanced optical organ with a complex vascular network. The maintenance of retinal function is critically dependent on the normal functioning of the blood-retinal barrier (Kaur et al., 2008; O'Leary and Campbell, 2023). Fundus diseases and related systematic diseases can cause functional changes in the fundus such as ischemia and hypoxia, which can damage the blood-retinal barrier, leading to retinal vascular permeability changes, hemorrhage, exudation, neovascularization, and other lesions (Pournaras et al., 2008; Ascunce et al., 2023; Monickaraj et al., 2023). Diabetes mellitus (DM) is a common endocrine metabolic disease with its microvascular complications in the eye that can result in diabetic retinopathy (DR), which is the leading cause of blindness in working-age people (Bourne et al., 2021; Steinmetz et al., 2021). Hypoxia is considered to be the core pathogenesis of DR besides of hyperglycemia in retinal blood vessels caused by DM (Hardarson, 2013). Hypoxia along with hyperglycemia stimulate vascular endothelium and eventually lead to vascular endothelial cell dysfunction, which in turn leads to the occurrence of DR. (Hardarson and Stefánsson, 2012; Khoobehi et al., 2013). Therefore, it is equally important to detect retinal oxygen saturation as well as blood glucose in DM patients, which can help to prompt the potential occurrence of DR and avoid further visual impairment.

Retinal vessel is the only vascular system in the body that can be observed *in vivo* (Hanssen et al., 2022), and non-invasive imaging technique is the first choice for retinal vascular oxygen saturation measurement. Nevertheless, there are only limited imaging instruments available to measure retinal oxygen saturation, in which dual-wavelength retinal oximetry is a promising technique. By measuring the light of different wavelengths reflected from the eye, it takes advantage of the light absorption variations between oxyhemoglobin and hemoglobin, and a calculation can be made that correlates directly to the retinal vascular oxygenation (Beach, 2014; Jeppesen and Bek, 2019; Garg et al., 2021). Previous studies using retinal oximetry have found that the oxygen saturation of retinal vessels in DR is significantly higher than that in normal subjects, and increases with the severity of DR (Hardarson and Stefánsson, 2012; Khoobehi et al., 2013; Jørgensen and Bek, 2014). Retinal oximetry has also been used to monitor retinal oxygen saturation in other eye diseases such as central retinal vein occlusion (CRVO) and glaucoma, showing varying degrees of increase in retinal oxygen saturation (Stefánsson et al., 2019). However, despite its potential, retinal oximetry is not widely used in ophthalmology clinics due to its recent commercialization.

Traditional color fundus cameras are the most commonly used equipment for fundus examination and disease screening (Karlsson et al., 2021). Their broad-spectrum cameras use complementary metal-oxide semiconductor (CMOS) or charge couple device (CCD) photoreceptors covered with red-green-blue (RGB) filters (Malvar et al., 2004). Thus, oxygen-sensitive and insensitive wavelengths reflected from retina vessels, which corresponds to different oxyhemoglobin and hemoglobin light absorptions, are generally received in the red and green channels, respectively, allowing for the estimation of blood oxygen function by extracting light absorption information from these channels.

In this study, we aim to develop a computational method for analyzing oxygen-saturation-related functional parameters with

traditional color fundus photography based on precise vessel segmentation and light absorption analysis, providing an easy-to-apply image analysis algorithm for traditional color fundus cameras. With that, we also explore the characteristic alterations of retinal vascular oxygen function in type 2 DM patients to look for new potential image biomarkers for the monitoring of DM.

2 Methods

2.1 Ethics

This was a retrospective observational study. The project underwent a formal administrative review and was determined to be methodologically validated according to the institutional policy of Zhongshan Ophthalmic Center, Sun Yat-sen University. Therefore, this study was considered not to be a human subject's study, but the study was still reviewed by Institutional Review Board to avoid information leakage during data processing (protocol number: 2017KYPJ104).

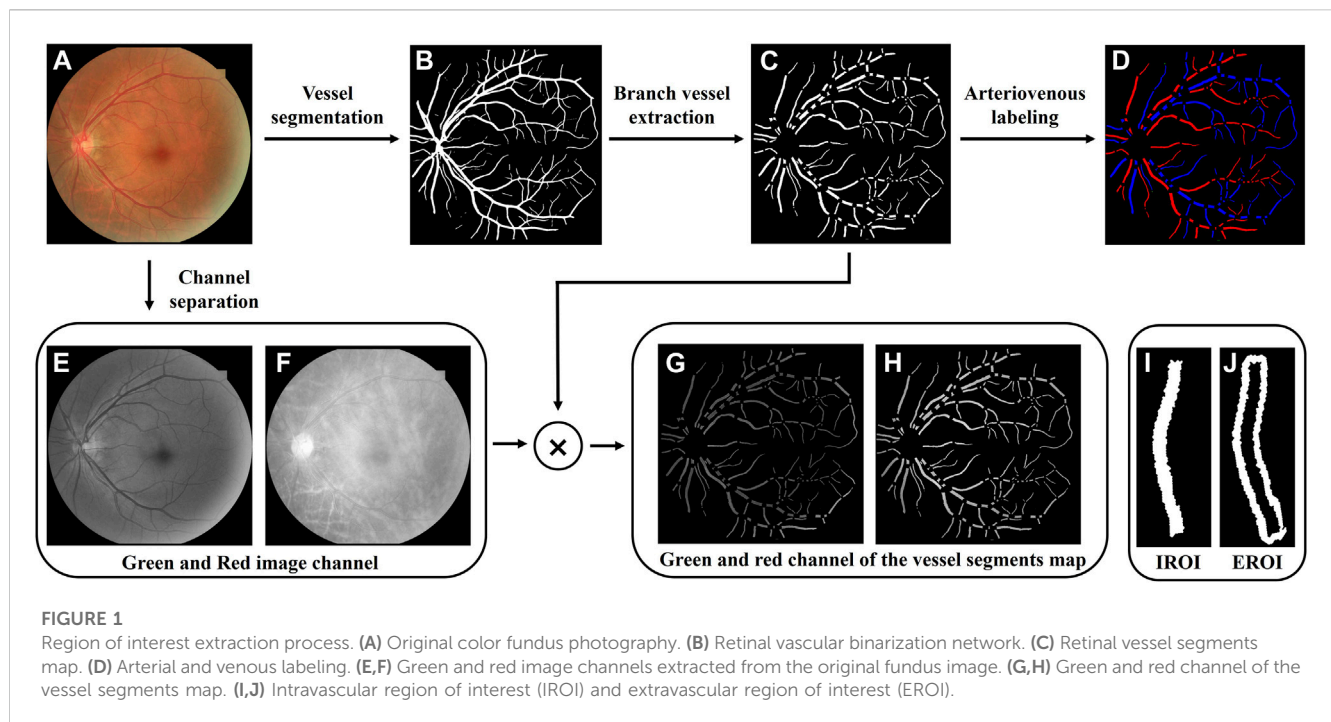
2.2 Population

We included 50 patients with type 2 diabetes mellitus (DM) and a normal group of 50 age- and sex-matched healthy normal subjects between 1 January 2019 and 15 May 2021. All the subjects were adults. We extracted the age and sex information of the subjects from the medical records for intergroup matching and determined whether the subjects are patients with type 2 DM or not. To assess the existence of diabetic retinopathy, standard seven-fields fundus photographs were obtained with a mydriasis-free digital fundus camera (RetiCam 3100, SYSEYE, China). Patients with clinically detectable retinopathy, or with a history of ocular disease, inflammation, trauma, or any intraocular surgery were excluded. Further exclusion criteria include related systemic diseases, such as Alzheimer's disease, hypertension or lung disease. The healthy normal group should also meet the above exclusion criteria in addition to no diabetes.

2.3 Vessel segmentation and labeling

Only the 50° fundus photography centered on the macula are analyzed. Figure 1 shows the flowchart for the processing of the region of interest (ROI) of retinal vessels. To extract the retinal vascular network, we employed an intelligent automatic vascular segmentation method, details of which are available in our earlier publication (Wang et al., 2021; 2023). Briefly, the original fundus color photographs (Figure 1A) were processed with an enhanced U-net by employing a multipath attention network model (MA-net) for improved vessel segmentation, achieving an area under the curve (AUC) of 0.9838 for segment accuracy (Wang et al., 2023). Blood vessel junctions on the obtained retinal vascular binarization network (Figure 1B) were detected then through a convolution method on vessel skeleton, facilitating the vessel segments extraction (Figure 1C). The arteriovenous labeling of the segmented vessels was further processed based on an intra-image regularization classifier (Figure 1D) (Xu et al., 2017).

To ensure the calculation of the oxygen-saturated-related functional parameter of retinal vessels, the red and green



channels (Figures 1E,F) composing the original fundus color photography were extracted through channel separation. By multiplying them with the binarized vessel segments map, oxygen-sensitive and insensitive wavelengths reflected from the retinal vascular areas were obtained (Figures 1G,H), of which each vessel segment was marked as the intravascular regions of interest (IROI, Figure 1I). To obtain the light reflection information of the retinal background around the vessel segment, a range of one vessel diameter is extended outward along the blood vessel segment outlines, which was marked as the extravascular region of interest (EROI, Figure 1J).

2.4 Optical density ratio extraction

According to the EROI and IROI of blood vessels, the optical density (OD) values were calculated for every three pixels along the vascular central line (Formula 1), the red channel is used as the oxygen sensitive channel, and the green channel represents the oxygen insensitive channel, and the optical density ratio (ODR) of the two is defined as the blood oxygen-saturation-related parameter (Formula 2) (Tiedeman et al., 1998; Beach et al., 1999).

$$OD = \log_{10} \frac{O_{EROI}}{O_{IROI}} \quad (1)$$

$$ODR = \frac{OD_{red}}{OD_{green}} \quad (2)$$

In order to study the differences of different types of blood vessels, all branch vessels output ODR according to the labeling of arteries and veins, and distinguish between main and micro vessels referring to the setting of commercial retinal oximeter (Stefánsson et al., 2017), i.e., ≥ 6 pixel diameter (1 pixel $\approx 12.69 \mu\text{m}$ in this study)

was defined as main vessels and < 6 pixel diameter was defined as micro vessels. Finally, ODR outputs the results according to all vessels (All), all arteriole (A), main arteriole (main A), micro arteriole (mic A), all venule (V), main venule (main V), and micro venule (mic V).

In addition to the ODR of each vascular subgroup, we also average the absolute value of the difference of ODR between all adjacent blocks of pixels and define it as ODR variability (ODR_v , Formula 3).

$$ODR_v = \frac{\sum |ODR_n - ODR_{n-1}|}{n - 1} \quad (3)$$

2.5 Statistical analysis

Student's t-test or chi-square test used to compare the differences between Normal and DM groups. All data were recorded as mean \pm standard deviation (SD). Data distribution was analyzed by the Kolmogorov-Smirnov test to determine normally distributed data ($P > 0.05$). Logistics regression was used to analyze the relationship between ODR and DM in each vascular subgroup and to generate ROC curve to evaluate the diagnostic efficiency of retinal vascular function parameters. All statistical analyses were performed using SPSS software (25.0; IBM Corporation, Armonk, NY). GraphPad Prism 9.0 was used for data visualization.

3 Results

There is no difference in the age and sex between the 50 healthy volunteers in Normal group and the 50 patients in DM group (Table 1).

TABLE 1 Clinical parameters and ODR of study subjects.

	Normal	DM	T-statistic	<i>p</i> value
No, of subject	50	50		
Age, yrs	43.4 (4.5)	43.9 (4.8)	−0.555	0.58
Sex, female, no (%)	23 (46%)	24 (48%)	NA	0.55
Duration of diabetes, yrs	/	4.16 (4.03)		
Fasting plasma glucose, mmol/L	/	8.89 (4.55)		
Optical density ratio, ODR				
All vessels	0.711 (0.060)	0.754 (0.082)	−3.037	0.03
All arteriole	0.713 (0.057)	0.755 (0.083)	−2.997	0.04
All venule	0.709 (0.063)	0.754 (0.082)	−3.037	0.03
Main arteriole	0.728 (0.056)	0.773 (0.083)	−3.199	0.02
Main venule	0.717 (0.058)	0.761 (0.082)	−3.092	0.03
Micro arteriole	0.634 (0.068)	0.672 (0.096)	−2.263	0.026
Micro venule	0.599 (0.082)	0.627 (0.117)	−1.405	0.164
Variability (ODR _v)	0.273 (0.025)	0.236 (0.059)	3.915	<0.001

a. Student's t-test or chi-square test used to compare difference between groups.

TABLE 2 Variables in the equation of the logistics regression.

	OR	95% CI		<i>p</i> value
		Lower	Upper	
All vessels	1.885	1.214	2.925	0.005
All arteriole	1.863	1.201	2.891	0.006
All venule	1.884	1.215	2.923	0.005
Main arteriole	1.953	1.252	3.046	0.020
Main venule	1.908	1.227	2.968	0.004
Micro arteriole	1.604	1.047	2.455	0.030
Micro venule	1.334	0.889	2.002	0.166
Variability	0.381	0.210	0.693	0.002

a. Logical regression was used to analyze the relationship between ODR, and DM, in each vascular subgroup and variability.

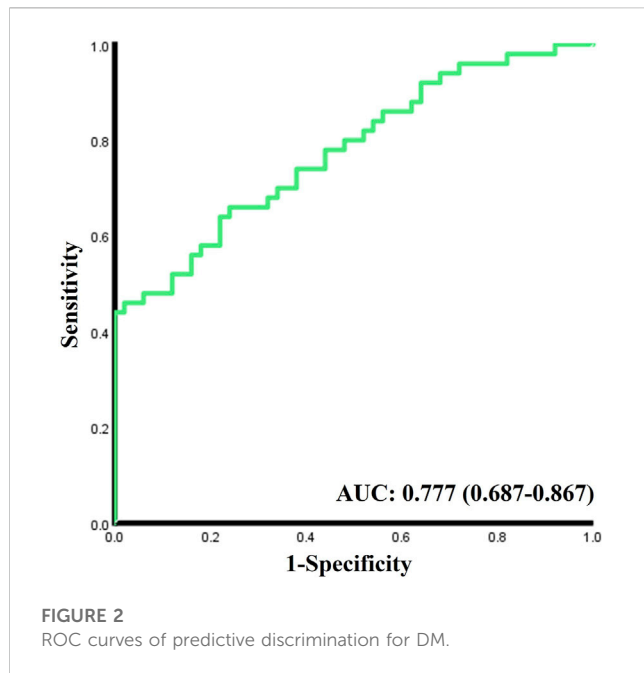
Table 1 alsodemonstrates the ODR for all vascular subgroups, ODR_v, as well as the t-statistic and *p*-values. In both healthy normal group and DM group, A ODR is higher than V ODR (mean ± SD, A vs. V, Normal: 0.713 ± 0.057 vs. 0.708 ± 0.063; DM: 0.755 ± 0.083 vs. 0.754 ± 0.082), main A ODR is higher than main V ODR (Normal: 0.728 ± 0.056 vs. 0.717 ± 0.058; DM: 0.773 ± 0.083 vs. 0.761 ± 0.082) and micro A is higher than micro V ODR (Normal: 0.634 ± 0.068 vs. 0.599 ± 0.082; DM: 0.672 ± 0.096 vs. 0.627 ± 0.117), which means that ODR is positively correlated with blood oxygen saturation. Compared to Normal group, ODR is significantly increased in all vascular subgroups except micro venular in DM group (*p* < 0.05, respectively). ODR_v is significantly decreased in DM group (*p* < 0.001).

As shown in the logistics regression results in Table 2, higher ODRs are significantly associated with the occurrence of DM,

especially in main A (OR 1.953, 95% CI 1.252-3.046) and main V (OR 1.908, 95% CI 1.227-2.968), and also in micro A (OR 1.604, 1.047-2.455). While Lower ODR_v (OR 0.381, 95% CI 0.210-0.693) is significantly associated with the occurrence of DM. The C-statistic for the discrimination of DM from the healthy normal group combining all the acquired oxygen-saturation-related functional parameters is 0.777 (95% CI 0.687-0.867, *p* < 0.001) (Figure 2).

4 Discussion

In this study, we present a computational approach for extracting oxygen-saturation-related functional parameters through precise vascular segmentation and light reflection



channel analysis using single traditional color fundus photography. By applying this method to the comprehensive analysis of the fundus images acquired from normal individuals and patients with type 2 diabetes, we revealed that the retinal vascular ODRs were increased while the ODR variability was reduced significantly in DM patients, providing new potential image biomarkers for the management of DM.

The successful extraction of retinal vascular ODRs with color fundus photography offers a new protocol for retinal vascular function evaluation, providing additional quantitative functional information based on the most commonly used fundus imaging tools in clinical settings. Compared to the current existed retinal oximetry, which only reveals oxygen saturation level in main retinal vessels and requires subjects to withstand long light exposure time (Hardarson, 2013), our method achieves information in microvascular level without any additional hardware implementation, which ensures its convenience and accessibility with greatly reduced cost. These advantages suggest extensive potential application value in the diagnosis and screening of retinal diseases.

In our study, we have shown that the increase of proposed oxygen-saturation-related ODRs were statistically significant at the stage of DM, which could be related to the stronger affinity of glycosylated hemoglobin to oxygen in DM (Graham et al., 1980; van Kampen and Zijlstra, 1983). Indeed, former studies using retinal oximetry have found obvious increase in retinal oxygen saturation level during DR, especially in proliferative DR, but no significant change was shown in DM stage before (Khoobei et al., 2013). This indicates that our newly proposed ODRs might be more sensitive parameters than that of commercial retinal oximetry in finding alterations in blood oxygen function. Moreover, our exploration of ODR in the

microvascular groups revealing significant increase in micro arterioles of DM patients further proves the high sensitivity of our method.

We have proposed and analyzed the ODR variability for the first time on the basis of extracted ODR of the full retinal vascular network and found it to be significantly decreased in DM patients compared to normal subjects. While glycosylated hemoglobin has higher affinity to oxygen (Graham et al., 1980), it damps the oxygen-release capacity (Ditzel, 1972) of retinal blood, results in reduced oxygen saturation variations. Studies have also found that the retinal blood flow velocity increases in DM patients (Landa et al., 2011), meaning less oxygen release time of blood in retinal vessels, further reduced the ODR variability.

Our method suffers limited retinal vessel resolution and imaging depth due to the physical nature of fundus photography. Only the superficial retinal vessels can be analyzed without 3-dimensional (3D) illustration. The same limitations also exist in current commercial retinal oximetry. Recently, visible-light optical coherence tomography based techniques for retinal oxygen saturation measurement have been gradually proposed (Pi et al., 2020; Poddar and Basu, 2020), achieving high resolution 3D imaging of retinal vascular oxygen function information (Pi et al., 2020), although most of these studies are still in laboratorial stage.

Our attempt to distinguish DM from normal subjects with all the extracted functional ODR parameters showed a relative low C statistic result (AUC = 0.777), which is not sufficient for DM diagnosis or screening. Since our previous study found that the morphological parameters of retinal vessels in DM patients also changed significantly (Li et al., 2021), further combining functional and morphological parameters of retinal blood vessels and multi-center studies or follow-up studies may help us better understand the changes in retinal blood vessel characteristics during the occurrence and development of DM and even DR, so as to diagnose DM or DR More accurately. Furthermore, applying our method to other eye diseases related to retinal vascular oxygen function alterations such as glaucoma (Vandewalle et al., 2014), central retinal vein occlusion (Hardarson and Stefánsson, 2010), age-related macular degeneration (Geirsdottir et al., 2014), etc. in the future would further demonstrate the reliability and universality of our method.

Data availability statement

The raw data supporting the conclusions of this article are available from the corresponding authors upon reasonable request.

Ethics statement

The studies involving human participants were reviewed and approved by Institutional Review Board of Zhongshan Ophthalmic Center, Sun Yat-sen University. The patients/participants provided their written informed consent to participate in this study.

Author contributions

JZ and ZL: Conceptualization, methodology, software, and writing—original draft. GW and YH: methodology and writing—review and editing. KF, YL, and JL: Investigation and data collection and writing—review and editing. JY and PX: Conceptualization, writing—review and editing, and supervision. All authors read and approved the final manuscript. All authors listed have made a substantial, direct, and intellectual contribution to the work and approved it for publication.

Funding

This work was supported by the National Natural Science Foundation of China (Nos. 82230033 and 82271133), the Department of Science and Technology of Guangdong Province (Nos. 2021TX06Y127 and 2021TQ06Y137), and the Basic and

Applied Basic Research Foundation of Guangdong Province (No. 2022A1515011486).

Conflict of interest

The authors declare that the research was conducted in the absence of any commercial or financial relationships that could be construed as a potential conflict of interest.

Publisher's note

All claims expressed in this article are solely those of the authors and do not necessarily represent those of their affiliated organizations, or those of the publisher, the editors and the reviewers. Any product that may be evaluated in this article, or claim that may be made by its manufacturer, is not guaranteed or endorsed by the publisher.

References

- Ascunce, K., Dhodapkar, R. M., Huang, D., and Hafler, B. P. (2023). Innate immune biology in age-related macular degeneration. *Front. Cell Dev. Biol.* 11, 1118524. doi:10.3389/fcell.2023.1118524
- Beach, J. M., Schwenzer, K. J., Srinivas, S., Kim, D., and Tiedeman, J. S. (1999). Oximetry of retinal vessels by dual-wavelength imaging: Calibration and influence of pigmentation. *J. Appl. Physiol.* 86, 748–758. doi:10.1152/jappl.1999.86.2.748
- Beach, J. (2014). Pathway to retinal oximetry. *Trans. Vis. Sci. Tech.* 3, 2. doi:10.1167/tvst.3.5.2
- Bourne, R., Steinmetz, J. D., Flaxman, S., Briant, P. S., Taylor, H. R., Resnikoff, S., et al. (2021). Trends in prevalence of blindness and distance and near vision impairment over 30 years: An analysis for the global burden of disease study. *Lancet Glob. Health* 9, e130–e143. doi:10.1016/S2214-109X(20)30425-3
- Ditzel, J. (1972). Impaired oxygen release caused by alterations of the metabolism in the erythrocytes in diabetes. *Lancet* 1, 721–723. doi:10.1016/S0140-6736(72)90233-4
- Garg, A. K., Knight, D., Lando, L., and Chao, D. L. (2021). Advances in retinal oximetry. *Transl. Vis. Sci. Technol.* 10, 5. doi:10.1167/tvst.10.2.5
- Geirsdottir, A., Hardarson, S. H., Olafsdottir, O. B., and Stefánsson, E. (2014). Retinal oxygen metabolism in exudative age-related macular degeneration. *Acta Ophthalmol.* 92, 27–33. doi:10.1111/aos.12294
- Graham, J. J., Ryall, R. G., and Wise, P. H. (1980). Glycosylated haemoglobin and relative polycythaemia in diabetes mellitus. *Diabetologia* 18, 205–207. doi:10.1007/BF00251917
- Hanssen, H., Streese, L., and Vilser, W. (2022). Retinal vessel diameters and function in cardiovascular risk and disease. *Prog. Retin Eye Res.* 91, 101095. doi:10.1016/j.preteyeres.2022.101095
- Hardarson, S. H. (2013). Retinal oximetry. *Acta Ophthalmol.* 91, 1–47. doi:10.1111/aos.12086
- Hardarson, S. H., and Stefánsson, E. (2010). Oxygen saturation in central retinal vein occlusion. *Am. J. Ophthalmol.* 150, 871–875. doi:10.1016/j.ajo.2010.06.020
- Hardarson, S. H., and Stefánsson, E. (2012). Retinal oxygen saturation is altered in diabetic retinopathy. *Br. J. Ophthalmol.* 96, 560–563. doi:10.1136/bjophthalmol-2011-300640
- Jeppesen, S. K., and Bek, T. (2019). The retinal oxygen saturation measured by dual wavelength oximetry in larger retinal vessels is influenced by the linear velocity of the blood. *Curr. Eye Res.* 44, 46–52. doi:10.1080/02713683.2018.1524015
- Jørgensen, C., and Bek, T. (2014). Increasing oxygen saturation in larger retinal vessels after photocoagulation for diabetic retinopathy. *Invest. Ophthalmol. Vis. Sci.* 55, 5365–5369. doi:10.1167/iovs.14-14811
- Karlsson, R. A., Jonsson, B. A., Hardarson, S. H., Olafsdottir, O. B., Halldorsson, G. H., and Stefánsson, E. (2021). Automatic fundus image quality assessment on a continuous scale. *Comput. Biol. Med.* 129, 104114. doi:10.1016/j.compbiomed.2020.104114
- Kaur, C., Foulds, W. S., and Ling, E. A. (2008). Blood-retinal barrier in hypoxic ischaemic conditions: Basic concepts, clinical features and management. *Prog. Retin Eye Res.* 27, 622–647. doi:10.1016/j.preteyeres.2008.09.003
- Khoobehi, B., Firn, K., Thompson, H., Reinoso, M., and Beach, J. (2013). Retinal arterial and venous oxygen saturation is altered in diabetic patients. *Invest. Ophthalmol. Vis. Sci.* 54, 7103–7106. doi:10.1167/iovs.13-12723
- Landa, G., Amde, W., Haileselassie, Y., and Rosen, R. B. (2011). Cilioretinal arteries in diabetic eyes are associated with increased retinal blood flow velocity and occurrence of diabetic macular edema. *Retina* 31, 304–311. doi:10.1097/IAE.0b013e3181e91108
- Li, M., Wang, G., Xia, H., Feng, Z., Xiao, P., and Yuan, J. (2021). Retinal vascular geometry detection as a biomarker in diabetes mellitus. *Eur. J. Ophthalmol.* 112067212110334, 1710–1719. doi:10.1177/11206721211033488
- Malvar, H. S., He, L.-W., and Cutler, R. (2004). “High-quality linear interpolation for demosaicing of Bayer-patterned color images,” in 2004 IEEE International Conference on Acoustics, Speech, and Signal Processing, Montreal, Canada, May 2004 (IEEE), 485–488.
- Monickaraj, F., Acosta, G., Cabrera, A. P., and Das, A. (2023). Transcriptomic profiling reveals chemokine CXCL1 as a mediator for neutrophil recruitment associated with blood-retinal barrier alteration in diabetic retinopathy. *Diabetes*, db220619. doi:10.2337/db22-0619
- O'Leary, F., and Campbell, M. (2023). The blood-retina barrier in health and disease. *FEBS J.* 290, 878–891. doi:10.1111/febs.16330
- Pi, S., Hormel, T. T., Wei, X., Cepurna, W., Wang, B., Morrison, J. C., et al. (2020). Retinal capillary oximetry with visible light optical coherence tomography. *Proc. Natl. Acad. Sci. U.S.A.* 117, 11658–11666. doi:10.1073/pnas.1918546117
- Poddar, R., and Basu, M. (2020). Characterization and oxygen saturation study of human retinal blood vessels evaluated by spectroscopic Optical Coherence Tomography Angiography. *Opt. Laser Technol.* 122, 105886. doi:10.1016/j.optlastec.2019.105886
- Pournaras, C. J., Rungger-Brändle, E., Riva, C. E., Hardarson, S. H., and Stefánsson, E. (2008). Regulation of retinal blood flow in health and disease. *Prog. Retin Eye Res.* 27, 284–330. doi:10.1016/j.preteyeres.2008.02.002
- Stefánsson, E., Olafsdottir, O. B., Einarsdottir, A. B., Eliasdottir, T. S., Eysteinnsson, T., Vehmeijer, W., et al. (2017). Retinal oximetry discovers novel biomarkers in retinal and brain diseases. *Invest. Ophthalmol. Vis. Sci.* 58, BIO227–BIO233. doi:10.1167/iovs.17-21776
- Stefánsson, E., Olafsdottir, O. B., Eliasdottir, T. S., Vehmeijer, W., Einarsdottir, A. B., Bek, T., et al. (2019). Retinal oximetry: Metabolic imaging for diseases of the retina and brain. *Prog. Retin. Eye Res.* 70, 1–22. doi:10.1016/j.preteyeres.2019.04.001
- Steinmetz, J. D., Bourne, R. R. A., Briant, P. S., Flaxman, S. R., Taylor, H. R. B., Jonas, J. B., et al. (2021). Causes of blindness and vision impairment in 2020 and trends over 30 years, and prevalence of avoidable blindness in relation to VISION 2020: The right to

sight: An analysis for the global burden of disease study. *Lancet Glob. Health* 9, e144–e160. doi:10.1016/S2214-109X(20)30489-7

Tiedeman, J. S., Kirk, S. E., Srinivas, S., and Beach, J. M. (1998). Retinal oxygen consumption during hyperglycemia in patients with diabetes without retinopathy. *Ophthalmology* 105, 31–36. doi:10.1016/s0161-6420(98)71029-1

Van Kampen, E. J., and Zijlstra, W. G. (1983). Spectrophotometry of hemoglobin and hemoglobin derivatives. *Adv. Clin. Chem.* 23, 199–257. doi:10.1016/s0065-2423(08)60401-1

Vandewalle, E., Abegão Pinto, L., Olafsdottir, O. B., De Clerck, E., Stalmans, P., Van Calster, J., et al. (2014). Oximetry in glaucoma: Correlation of metabolic change with structural and functional damage. *Acta Ophthalmol.* 92, 105–110. doi:10.1111/aos.12011

Wang, G., Huang, Y., Ma, K., Duan, Z., Luo, Z., Xiao, P., et al. (2023). Automatic vessel crossing and bifurcation detection based on multi-attention network vessel segmentation and directed graph search. *Comput. Biol. Med.* 155, 106647. doi:10.1016/j.combiomed.2023.106647

Wang, G., Li, M., Yun, Z., Duan, Z., Ma, K., Luo, Z., et al. (2021). A novel multiple subdivision-based algorithm for quantitative assessment of retinal vascular tortuosity. *Exp. Biol. Med. (Maywood)* 246, 2222–2229. doi:10.1177/15353702211032898

Xu, X., Ding, W., Abramoff, M. D., and Cao, R. (2017). An improved arteriovenous classification method for the early diagnostics of various diseases in retinal image. *Comput. Methods Programs Biomed.* 141, 3–9. doi:10.1016/j.cmpb.2017.01.007



OPEN ACCESS

EDITED BY

Weihua Yang,
Jinan University, China

REVIEWED BY

Yu Ji,
The First Affiliated Hospital of Nanchang
University, China
Bing Lin Huang,
Jiangxi University of Chinese Medicine,
China

*CORRESPONDENCE

Xin Huang,
✉ huangxin5921@126.com
Baojun Xie,
✉ xiebj@126.com

RECEIVED 26 February 2023

ACCEPTED 25 April 2023

PUBLISHED 12 May 2023

CITATION

Wen Z, Kang Y, Zhang Y, Yang H, Zhao Y,
Huang X and Xie B (2023), Disrupted
dynamic amplitude of low-frequency
fluctuations in patients with active
thyroid-associated ophthalmopathy.
Front. Cell Dev. Biol. 11:1174688.
doi: 10.3389/fcell.2023.1174688

COPYRIGHT

© 2023 Wen, Kang, Zhang, Yang, Zhao,
Huang and Xie. This is an open-access
article distributed under the terms of the
[Creative Commons Attribution License
\(CC BY\)](https://creativecommons.org/licenses/by/4.0/). The use, distribution or
reproduction in other forums is
permitted, provided the original author(s)
and the copyright owner(s) are credited
and that the original publication in this
journal is cited, in accordance with
accepted academic practice. No use,
distribution or reproduction is permitted
which does not comply with these terms.

Disrupted dynamic amplitude of low-frequency fluctuations in patients with active thyroid-associated ophthalmopathy

Zhi Wen¹, Yan Kang^{2,3}, Yu Zhang¹, Huaguang Yang¹, Yilin Zhao¹,
Xin Huang^{4*} and Baojun Xie^{1*}

¹Department of Radiology, Renmin Hospital of Wuhan University, Wuhan, China, ²State Key Laboratory of Magnetic Resonance and Atomic and Molecular Physics, National Center for Magnetic Resonance in Wuhan, Wuhan Institute of Physics and Mathematics, Innovation Academy for Precision Measurement Science and Technology, Chinese Academy of Sciences, Wuhan, China, ³University of Chinese Academy of Sciences, Beijing, China, ⁴Department of Ophthalmology, Jiangxi Provincial People's Hospital, The First Affiliated Hospital of Nanchang Medical College, Nanchang, Jiangxi, China

Purpose: Thyroid-associated ophthalmopathy (TAO) is an autoimmune disease that affects the orbit and is the most prevalent extra-thyroidal complication of Graves' disease. Previous neuroimaging studies have focused on abnormal static regional activity and functional connectivity in patients with TAO. However, the characteristics of local brain activity over time are poorly understood. This study aimed to investigate alterations in the dynamic amplitude of low-frequency fluctuation (dALFF) in patients with active TAO and to distinguish patients with TAO from healthy controls (HCs) using a support vector machine (SVM) classifier.

Methods: A total of 21 patients with TAO and 21 HCs underwent resting-state functional magnetic resonance imaging scans. dALFFs were calculated in conjunction with sliding window approaches to assess dynamic regional brain activity and to compare the groups. Then, we used SVM, a machine learning algorithm, to determine whether dALFF maps may be used as diagnostic indicators for TAO.

Results: Compared with HCs, patients with active TAO showed decreased dALFF in the right calcarine, lingual gyrus, superior parietal lobule, and precuneus. The SVM model showed an accuracy of 45.24%–47.62% and area under the curve of 0.35–0.44 in distinguishing TAO from HCs. No correlation was found between clinical variables and regional dALFF.

Conclusion: Patients with active TAO showed altered dALFF in the visual cortex and the ventral and dorsal visual pathways, providing further details on the pathogenesis of TAO.

KEYWORDS

thyroid-associated ophthalmopathy, active phase, visual dysfunction, dynamic amplitude of low-frequency fluctuation, support vector machine

1 Introduction

Thyroid-associated ophthalmopathy (TAO), commonly known as Graves' ophthalmopathy, is an autoimmune disease that affects the orbit and is the most prevalent extra-thyroidal complication of Graves' disease. The main pathological changes of TAO were extraocular muscle swelling and periorbital fat increase. Although the pathogenesis is not fully understood, the thyroid-stimulating hormone receptor (TSHR) is considered the main target of the autoimmune reaction (Hiromatsu et al., 2014). The activation of autoantibodies against TSHR mediates inhibiting, interfering with, or stimulating intracellular signal transduction. In patients with TAO, an over-expression of TSHR is observed in the thyroid, extraocular muscles, and retrobulbar tissue, particularly in orbital fibroblasts, leading to extraocular muscle swelling, expansion of the orbital adipose tissue, and high intraocular pressure. Long-lasting orbital edema causes the extraocular muscles to fibrose and/or atrophy, which results in restrictive strabismus (Weiler, 2017). The swelling of extraocular muscles directly compresses the optic nerve at the orbital apex. The orbital fat expands, resulting in overt exophthalmos, which may lead to stretching and injury of the optic nerve. Compression and circulatory obstruction of optic nerve fibers may lead to denervated atrophy (Bartalena et al., 2021; Song et al., 2022).

The course of TAO includes an active and an inactive phase (Weiler, 2017). In the active stage, TAO has severe inflammatory lymphocyte infiltration, edema, and fibroblast proliferation in orbital tissues (Hiromatsu et al., 2014) and presents typical eye symptoms, including exophthalmos and diplopia, which can lead to retinal damage, optic neuropathy, and even blindness in severe cases (Bartalena et al., 2021). Active immunosuppression intervention may be helpful to limit the destructive and fibrotic consequences of the immune cascade and release aggravation of eye symptoms. In the chronic stage, orbital residual fibrosis persists, and there is little response to medical treatment that requires surgery. Therefore, understanding the pathological mechanism of active TAO is helpful to save vision at an early stage.

Neuroimaging studies demonstrated that the abnormal brain structural and functional changes were associated with the visual and cognitive impairments in TAO. For example, diffusion tensor imaging studies showed significantly decreased fractional anisotropy (FA) in the optic nerve in TAO that correlated negatively with visual field defects and positively with clinical activity scores (CAS) (Ozkan et al., 2015), "NO SPECS" classification, and extraocular muscle thickness (Lee et al., 2018). Compared with healthy controls (HCs), patients with active TAO had cortical thinning in the left lateral occipital sulcus, left fusiform gyrus, right precuneus, right superior frontal cingulate, right superior periparietal gyrus, right paracentral gyrus, right postcentral gyrus, and right insula (Silkiss and Wade, 2016) but increased gray matter volume (GMV) in the right inferior frontal gyrus, left superior frontal gyrus (SFG), left orbital SFG, left orbital middle frontal gyrus, left precuneus, and left postcentral gyrus (Luo et al., 2022). Resting-state functional MRI (rs-fMRI) studies demonstrated decreased amplitudes of low-frequency fluctuations (ALFFs) in the left middle occipital gyrus (MOG), superior occipital gyrus, and precuneus (Chen et al., 2021c), decreased fractional ALFF (fALFF) in the right calcarine, and increased fALFF in the right inferior temporal gyrus and left

posterior cingulate cortex in active TAO relative to HCs (Zhu et al., 2022). The microvascular density of the optic nerve head was negatively correlated with fALFF in the right calcarine, while it was positively correlated with fALFF in the posterior cingulate cortex (Zhu et al., 2022). Another study found decreased regional homogeneity in the right MOG and the right angular gyrus, reduced ALFF in the right superior occipital gyrus and bilateral precuneus, decreased voxel-mirrored homotopic connectivity (VMHC) between calcarine, angular gyri, and MOG, and decreased functional connectivity between the calcarine/lingual gyri and the contralateral middle temporal gyrus (MTG) (Qi et al., 2021, 2022; Wen et al., 2022). There are a few neuroimaging results focused on the neural activity differences between active and inactive TAO. A direct comparison of the active and inactive phases of TAO found increased GMV in the right MTG, left SFG, and left precuneus (Luo et al., 2022), as well as increased ALFF in bilateral precuneus (Chen et al., 2021c). ALFF values in the bilateral precuneus were positively correlated with CAS and mini-mental state examination (MMSE) scores and negatively correlated with disease duration (Chen et al., 2021c). Moreover, in the hyperthyroid condition, gray matter volumes were increased in the right cerebellum lobule VI and decreased in the bilateral visual cortex and cerebellum lobules I–IV, the ALFF was decreased in the right posterior cingulate cortex, and the FC was increased in the bilateral anterior insula, posterior insula, and cerebellum anterior lobe, compared to the euthyroid condition, again suggesting a crucial role for the cerebellum in the mediation of TH effects (Gobel et al., 2020). Thus, these studies have demonstrated that patients with active TAO may provide evidence of the pathological mechanisms underlying active TAO.

fMRI can non-invasively measure neuronal activity, deepening our understanding of visual processing and perception. Previous studies assumed that the BOLD signal was static during the fMRI scanning. However, recent research has proposed that neural activity is dynamic over time (Liu and Duyn, 2013). Evidence from task-based fMRI and electrophysiology research showed that functional activities and connectivity may show dynamic changes in the time scale of several seconds to several minutes (Liegeois et al., 2017). Compared with static analysis by using the average functional activity or connectivity, dynamic analysis is helpful to observe the details in static analysis and can provide a deeper understanding of the basic mechanism of brain activity and connectivity. The ALFF method calculates the power within the effective frequency range (0.01–0.08 Hz) of each voxel in the brain and reflects the spontaneous activity of neurons at rest (Biswal et al., 2010). Dynamic ALFF (dALFF) is an extension of ALFF, which studies the temporal variability of brain activity and provides information on the changes in ALFF with time by combining the sliding window method. The decrease in dALFF represents functional impairment, while the increase in dALFF represents unstable neural activity. The support vector machine (SVM) model is a focused area of machine learning in recent years and shows its advantages in small samples, especially when the sample size is far less than the feature dimension. Combining dALFF and SVM classification analysis has been applied in various disease conditions, such as comitant exotropia (Chen et al., 2022a), transient ischemic attack (Ma et al., 2021), and

Parkinson's disease (Zhang et al., 2019), and showed good performance to distinguish patients and healthy controls.

Our hypotheses show that the dynamic changes in spontaneous brain activity may present a disease-related pattern in patients with TAO. In the present study, we aimed to investigate dynamic alterations in local resting-state metrics and to explore whether dALFF could be used as a diagnostic tool for TAO.

2 Methods

2.1 Ethics approval

This cross-sectional study was approved by the Research Ethics Committee of Jiangxi Provincial People's Hospital and adhered to the guidelines of the Declaration of Helsinki. All patients with TAO and HCs provided written informed consent before participation.

2.2 Participants

The pool of patients with TAO and HCs was identical to that reported in previous studies (Qi et al., 2021, 2022; Wen et al., 2022). A total of 21 patients with TAO (seven females' mean age, 54.17 ± 4.83 years) were enrolled from the Departments of Ophthalmology and Endocrinology, Jiangxi Provincial People's Hospital.

Patients in the active phase of TAO who were right-handed were included in the TAO group. The diagnosis of TAO was made by two experienced ophthalmologists according to the diagnostic criteria for Graves' ophthalmopathy (Bartley and Gorman, 1995), measuring visual acuity, visual field, color vision, and the pupil reflex. The disease activity of TAO was evaluated according to the modified 7-point Mourits' CAS, and the active phase was defined by a CAS equal to or greater than 3 (Bartalena et al., 2021). The exclusion criteria for the TAO and HC groups were as follows: (1) severe TAO with dysthyroid optic neuropathy; (2) symptoms caused by other ocular diseases, such as glaucoma, vitreous hemorrhage, high myopia, strabismus, cataract, and optic neuritis; (2) history of eye trauma or surgery; (3) history of neurological and psychiatric disorders; (4) alcohol or drug abuse; and (5) contraindications to MRI, such as claustrophobia or implanted pacemakers.

A total of 21 HCs (seven females' mean age: 55.17 ± 5.37 years) matched for age, sex, handedness, and educational level were also recruited. HCs were psychologically healthy, with no history of TAO, and had normal or corrected-to-normal vision. The exclusion criteria for the TAO and HC groups were as follows: (1) symptoms caused by other ocular diseases, such as glaucoma, vitreous hemorrhage, high myopia, and strabismus; (2) history of eye trauma or surgery; (3) history of neurological and psychiatric disorders; (4) alcohol or drug abuse; and (5) contraindications to MRI, such as claustrophobia or implanted pacemakers.

2.3 Clinical assessment

All patients underwent comprehensive eye examinations that included measuring intraocular pressure (IOP), eyeball protrusion, best-corrected visual acuity (BCVA), and

performing slit lamp examinations and retinal funduscopy. In addition, the TAO duration was confirmed by self-reports from patients and was determined as the interval between the onset of TAO-related clinical symptoms and the date of the MRI examination.

2.4 MRI data acquisition

MRI scanning was performed on a 3-T MR scanner (Discovery 750W System; GE Healthcare, Chicago, IL, United States) with an 8-channel head coil. Foam pads were placed on both sides of the jaw to limit head movements, and earplugs were used to attenuate noise during scanning. During data acquisition, all participants were asked to close their eyes, stay awake, and not to think about anything in particular.

High-resolution T1-weighted images covering the whole brain were acquired with a magnetization-prepared rapid gradient echo (MPRAGE) sequence, with the following parameters: repetition time (TR) = 8.5 ms, echo time (TE) = 3.3 ms, flip angle = 12° , slice thickness = 1.0 mm, slice gap = 0 mm, voxel size = $1 \times 1 \times 1 \text{ mm}^3$, field of view (FOV) = $240 \times 240 \text{ mm}^2$, matrix size = 256×256 , and sagittal slice number = 176. rs-fMRI involved a gradient-recalled echo (GRE) planar imaging sequence, with the following parameters: TR = 2000 ms, TE = 25 ms, flip angle = 90° , FOV = $240 \times 240 \text{ mm}^2$, matrix size = 64×64 , voxel size = $3.6 \times 3.6 \times 3.6 \text{ mm}^3$, axial slice number = 35, and volume numbers = 240. T2-weighted imaging and T2 fluid-attenuated inversion recovery images were acquired to exclude brain lesions. The total scanning time for each subject was 15 min.

2.5 fMRI data preprocessing

rs-fMRI data were preprocessed using the toolbox for Data Processing & Analysis of Brain Imaging (DPABI; <http://www.rfmri.org/dpabi>) and Statistical Parametric Mapping 8 (SPM8, <http://www.fil.ion.ucl.ac.uk>) implemented in MATLAB (2013a; MathWorks, Natick, MA, United States). Preprocessing included the following steps: (1) Original DICOM-format files were converted into the NIFTI format. (2) The first 10 time points for each subject were removed due to the signal reaching equilibrium and the participants adapting to scanning noise. (3) Slice-timing and motion correction were performed; subjects with a maximum displacement of less than 1.5 mm in any cardinal direction (x, y, z) and a maximum spin (x, y, z) of less than 1.5 were included in the following analysis. (4) Each T1 image was co-registered to the mean functional image and was segmented into gray matter, white matter, and cerebrospinal fluid using the Diffeomorphic Anatomical Registration Through Exponentiated Lie Algebra approach (Ashburner, 2007). (5) Functional images were normalized to the Montreal Neurological Institute space, resampled with a voxel size of $3 \times 3 \times 3 \text{ mm}$, and smoothed with a Gaussian kernel with a full-width at half maximum of 6 mm. This was followed by (6) detrending and (7) applying a temporal filter (0.01–0.08 Hz) to reduce the influence of low-frequency drift and high-frequency noise. Subsequently, the images were used to compute the dALFF maps.

2.6 Calculation of dALFF

To obtain ALFF values, the time series for each voxel were transformed to the frequency domain using a fast Fourier transform, and the power spectrum was then obtained using DPABI software. The square root of the power spectrum was z-transformed using Fisher's r-to-z transformation to reduce the global effects of variability across participants.

The sliding window method was applied to evaluate the dALFF for each participant using the Temporal Dynamic Analysis (TDA) toolkit in DPABI software. The sliding window length affected the dALFF: the minimum window length should be larger than $1/f_{\min}$, where f_{\min} is the minimum frequency of time series (Leonardi and Van De Ville, 2015). Liao et al. (2019) also found that when the step size of the sliding window is fixed, the variance of dALFF decreases with the increase in the sliding window length; when the window length is kept at 50 TRs, the variance of dALFF is constant with the increase in the step size. Previous studies have shown that a window length of 50 TRs (100 s) is the optimal parameter to keep a balance between capturing rapidly shifting dynamic activity and achieving reliable brain activity estimation. Therefore, we chose 50 TRs as the sliding window length and 1 TRs as the step size to calculate the dALFF of each participant, which is in accordance with the methods of Liu et al. (2021) and Cui et al. (2020). The ALFF map was computed within each window, generating a set of ALFF maps for each participant. The standard deviation (SD) divided by the global mean value of the ALFF at each voxel across each window was calculated to assess the temporal variability of the ALFF, which is defined as dALFF.

2.7 Validation analysis

To verify our findings on the dALFF variability obtained using a sliding window length of 50 times the TR, we performed auxiliary analyses with different sliding window lengths. We recalculated the main results using window lengths of 30 and 80 times the TR, which is in accordance with the methods of Liu et al. (2021) and Cui et al. (2020).

2.8 Support vector machine analysis

We performed machine learning analyses using the SVM algorithm to determine whether dALFF maps can be used as potential diagnostic indicators of TAO. Using the Pattern Recognition for Neuroimaging Toolbox (Schrouff et al., 2013), the dALFF values of brain regions that differed between the groups were used as classification features. Then, leave-one-out cross-validation (LOOCV) was used to validate the SVM classifier. The accuracy, sensitivity, and specificity were used to quantify the performance of classification methods. The receiver operating characteristic curves and the corresponding areas under the curve (AUCs) were generated to assess the classification efficiency.

2.9 Statistical analysis

SPSS software (v22.0; IBM Corp., Armonk, NY, United States) was used to analyze clinical variables. p -values <0.05 were

considered statistically significant. One-sample t -tests were performed in the Statistical Parametric Mapping software to assess the intragroup z -values of dALFF maps. Then, with age, sex, and total intracranial volume as covariates, the individual z -maps were entered into a two-sample t -test to identify differences between groups. The Gaussian random field method (Worsley et al., 1996) was used to correct for multiple comparisons, with a cluster-level $p < 0.05$ as statistically significant, corresponding to a two-tailed voxel level of $p < 0.01$.

2.10 Correlation analysis

Pearson correlation analysis was applied to determine the relationship between mean dALFF values and clinical factors in TAO, such as the severity of the disease, BCVA, and IOP. p -values below 0.05 were considered statistically significant.

3 Results

3.1 Demographics and disease characteristics

Sex, age, and educational level did not significantly differ between the TAO and HC groups ($p = 1$, $p = 0.75$, and $p = 0.86$, respectively). In comparison with HCs, the TAO group showed significantly worse BCVA ($p < 0.05$) and higher IOP ($p < 0.001$) in both eyes. Table 1 lists demographic and disease characteristics of the study sample.

3.2 dALFF in TAO and HC groups

Setting the window length to 50 TR and the sliding step to 1 TR produced the main findings. Then, these were validated using different sliding window lengths. The spatial distributions of mean dALFF in the TAO and HC groups with window lengths of 30x, 50x, and 80x TR are shown in Figure 1.

With a window length of $\times 50$ TR and a sliding step of 1 TR, patients with TAO had significantly lower dALFF in two locations in the right hemisphere (calcarine gyrus [Brodmann's area (BA) 17,18] and lingual gyrus [BA 18]), compared with HCs (Table 2, Figure 2B). Similarly, with window lengths of $\times 30$ and $\times 80$ TR, patients with TAO showed significantly lower dALFF in three locations in the right hemisphere (calcarine gyrus [BA 17,18], precuneus [BA 7], and superior parietal lobule (SPL; BA 7]) compared with HCs (Table 2, Figure 2A, Figure 2C).

3.3 Support vector machine classification

Setting the window length to $\times 30$, $\times 50$, or $\times 80$ TR with a sliding step of 1 TR, the SVM classification of dALFF achieved overall accuracies of 45.24%, 47.62%, and 45.24% and AUCs of 0.44, 0.37, and 0.35, respectively, for distinguishing between patients with TAO and HCs (Figure 3).

TABLE 1 Characteristics of participants in TAO and HC groups.

Condition	TAO group	HC group	t	p
Gender (male/female)	14/7	14/7	N/A	1
Age (years)	54.17 ± 4.83	55.17 ± 5.37	−0.348	0.75
Duration (months)	11.25 ± 4.42	-	-	-
Education	11.17 ± 2.64	11.42 ± 1.95	−0.269	0.86
BCVA-OD	0.67 ± 0.35	1.14 ± 0.15	−4.462	0.026*
BCVA-OS	0.64 ± 0.29	1.06 ± 0.23	−4.297	0.023*
IOP-OD	25.81 ± 2.35	15.33 ± 1.20	−5.554	<0.001*
IOP-OS	25.62 ± 2.32	15.10 ± 1.11	−5.560	<0.001*

Notes: Independent sample *t*-test for the normally distributed continuous data (means ± SD). Chi-squared test for sex. **p* < 0.05 indicated statistically significant. TAO, thyroid-associated ophthalmopathy; HC, healthy control; BCVA, best-corrected visual acuity; OD, oculus dexter; OS, oculus sinister; IOP, intraocular pressure.

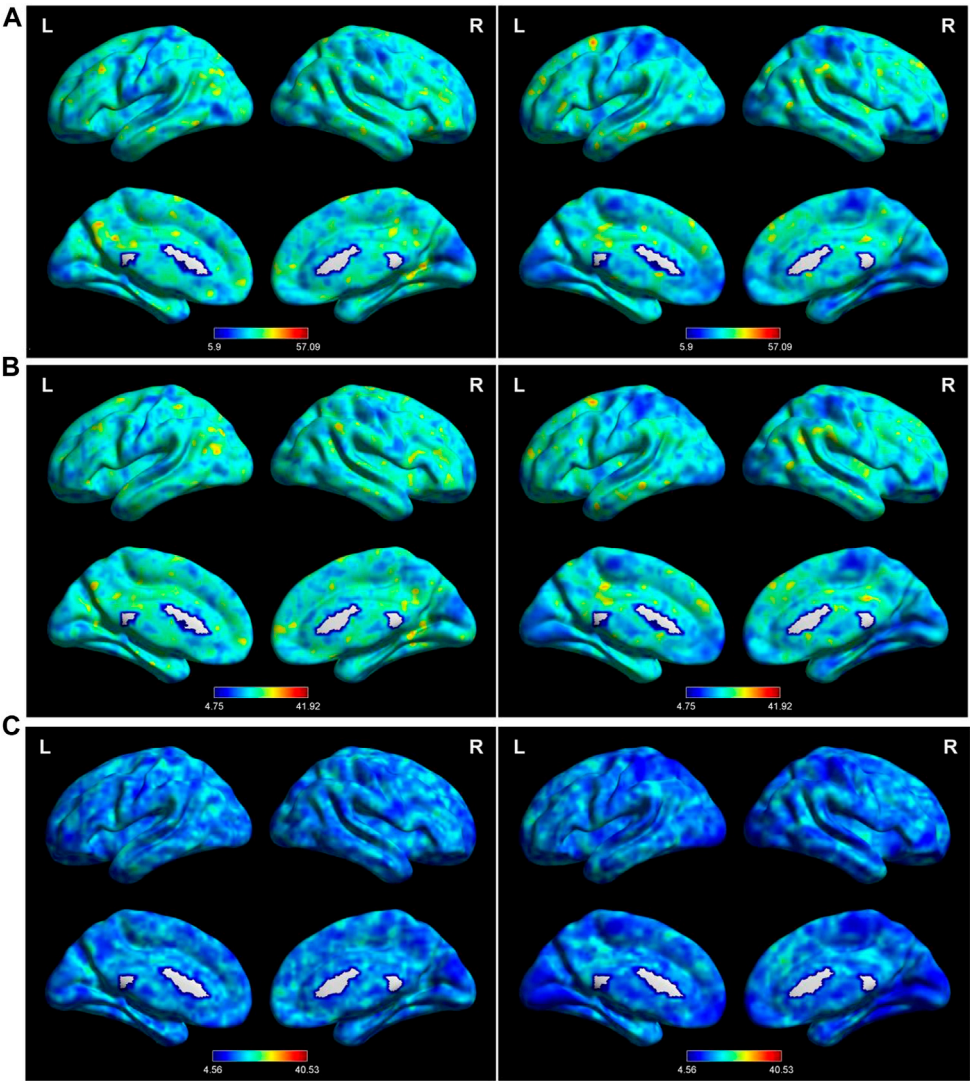


FIGURE 1 Distribution of dALFF using the following three distinct sliding window parameter settings in the typical frequency band (0.01–0.08 Hz) in TAO (left column) and HC (right column) groups: (A) window length of 30 TRs (60 s), (B) window length of 50 TRs (100 s), and (C) window length of 80 TRs (160 s). dALFF, dynamic amplitude of low-frequency fluctuation; TAO, thyroid-associated ophthalmopathy; HC, healthy control; L, left; R, right.

TABLE 2 Brain regions with significant differences in dALFF values between TAO and HC groups (voxel-level $p < 0.01$ for Gaussian random field correction, cluster-level $p < 0.05$).

Region	Brodmann's areas	Side	MNI coordinate			Peak T	Cluster size
			x	y	z		
TAO < HC, with a window size of 30 TRs and sliding step of 1 TR							
Calcarine	17, 18	R	21	−87	0	−3.30	40
Superior parietal lobule	7	R	30	−57	60	−4.42	47
Precuneus	7	R	9	−66	63	−3.60	40
TAO < HC, with a window size of 50 TRs and sliding step of 1 TR							
Calcarine	17, 18	R	21	−75	12	−3.79	50
Lingual gyrus	18	R	34	−60	0	−3.41	40
TAO < HC, with a window size of 80 TRs and sliding step of 1 TR							
Calcarine	17, 18	R	21	−75	12	−3.63	40
Superior parietal lobule	7	R	27	−81	51	−3.40	11
Precuneus	7	R	6	−72	57	−3.91	36

dALFF, dynamic amplitude of low-frequency fluctuation; TAO, thyroid-associated ophthalmopathy; HC, healthy control; MNI, Montreal Neurological Institute; GFR, Gaussian random field theory; TR, time of repetition; R, right.

3.4 Correlation analysis

There was no correlation between mean dALFF values and disease duration, BCVA, or IOP in patients with TAO.

4 Discussion

This study used dALFF analysis to investigate the temporal variability in local brain activity in patients with TAO. Compared with HCs, patients with TAO exhibited decreased dALFF in several posterior brain regions in the right hemisphere such as the calcarine gyrus (BA 17,18) and lingual gyrus (BA 18). We used other sliding window lengths to verify our findings and found that the temporal variability of dALFF in the right calcarine was highly reproducible across different window lengths. In addition, dALFF in the right precuneus (BA 7) and right SPL (BA 7) in TAO was reduced by using window lengths equal to 30 and 80 TRs. Unfortunately, the dALFF variability in these regions could not be used to classify patients with TAO and HCs, achieving an accuracy of 45.24%–47.62% and AUC of 0.35–0.44, because AUCs of 0.5–0.7 indicate low accuracy and 0.7–0.9 represents higher accuracy. Indeed, no correlation was found between the clinical variables and the dALFF of these brain regions. Nonetheless, the present study emphasized the significance of considering dynamic local brain activity in TAO.

We found that the spatial pattern of temporal variability of dALFF in the right calcarine was highly reproducible across different window lengths. The calcarine is regarded as the part of the primary visual cortex (V1). On the one hand, it receives visual inputs from the retina via thalamic relays and is associated with visual field defects and blurred vision. On the other hand, it receives visual information from the lateral geniculate body and is the core component of binocular vision, creating depth perception (Weiler, 2017). Dysfunction in the primary visual cortex is a common finding among various eye diseases such as glaucoma

(Chen et al., 2022b), diabetic retinopathy (Huang et al., 2021), exotropia and amblyopia (Liang et al., 2016; Chen J. et al., 2021), and optic neuropathy (Sujanthan et al., 2022). Compared with HCs, patients with active TAO demonstrated decreased fALFF in the right calcarine (Zhu et al., 2022) and decreased FC between hemispheric calcarine gyri (Qi et al., 2022; Wen et al., 2022). The microvascular density of the optic nerve head has been negatively correlated with fALFF in the right calcarine (Zhu et al., 2022). Patients with TAO and in the euthyroid status showed decreased fALFF in the bilateral calcarine (Chen et al., 2021d) and decreased VMHC in lingual gyri/calcarine (Chen et al., 2021b). The VMHC of the lingual gyri/calcarine was positively correlated with visual acuity (Chen et al., 2021b). Moreover, patients with hyperthyroidism and without orbital symptoms showed reduced GMV in the bilateral calcarine, suggesting a preclinical stage of TAO (Zhang et al., 2014). However, no particular differences were observed in the calcarine gyrus in patients with inactive TAO, relative to HCs or patients with active TAO (Chen et al., 2021c; Luo et al., 2022). In the present study, patients with active TAO consistently demonstrated decreased dALFF variability in the right calcarine (BA 17, 18); findings obtained from three different sliding window values of $\times 30$, $\times 50$, and $\times 80$ TRs were in line with the aforementioned studies. Altogether, static and dynamic dysfunctions of the calcarine might be promising indicators in TAO, which may be associated with impaired retinal projection and binocular fusion.

The visual pathway consists of ventral and dorsal streams. The ventral stream originates from V1 and projects to the inferior temporal cortex. The lingual gyrus is a key hub in the ventral stream and is commonly known as the ventral occipitotemporal region (lingual, fusiform, and parahippocampal gyri) and participates in face recognition (Dinkelacker et al., 2011). In the present study, dALFF was lower in the right lingual gyrus in active TAO patients than that in HCs, which is consistent with the previous finding of reduced FC between the contralateral MTG and bilateral calcarine/lingual gyri (Wen et al., 2022). This suggested that the ventral stream, which processes faces, was impaired (Reisch et al., 2022).

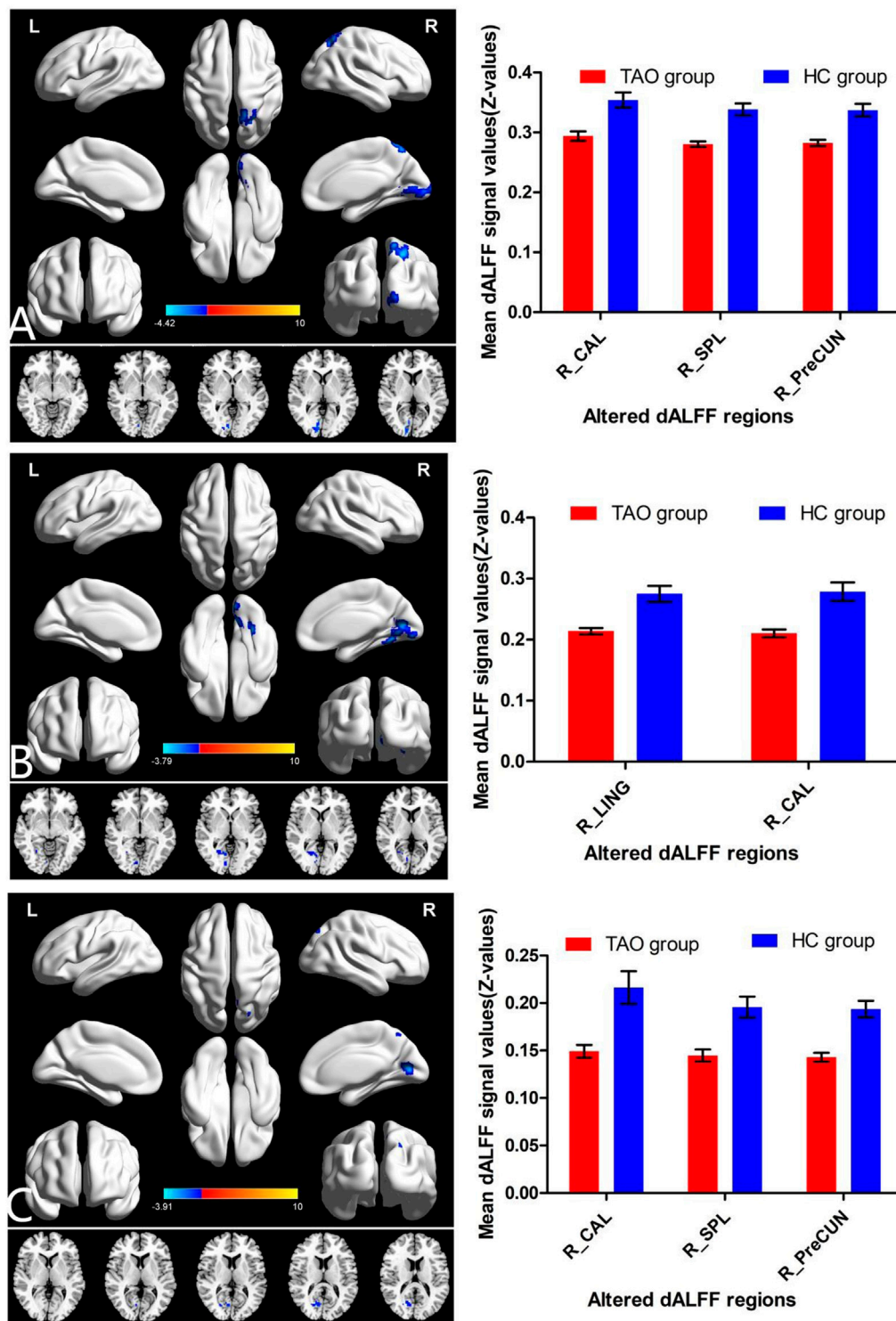


FIGURE 2

Brain regions with significant differences in dALFF between TAO and HC groups using the following three distinct sliding window parameter settings: (A) window length of 30 TRs (60 s), (B) window length of 50 TRs (100 s), and (C) window length of 80 TRs (160 s). The histogram shows the mean and standard deviation of dALFF values in these regions in TAO and HC groups. dALFF, dynamic amplitude of low-frequency fluctuation; TAO, thyroid-associated ophthalmopathy; HC, healthy control; LING, lingual gyrus; CAL, calcarine; PreCun, precuneus; SPL, superior parietal lobule; TR, time of repetition; L, left; R, right.

The dorsal visual stream starts from V1 and projects to the posterior parietal cortex, which is important for binocular vision fusion, and has predominant advantages in decoding the disparities

present in 3D images. The SPL forms the association cortex of the parietal lobe and is responsible for visual-motor coordination (Wolpert et al., 1998). Located medial to the SPL, the precuneus

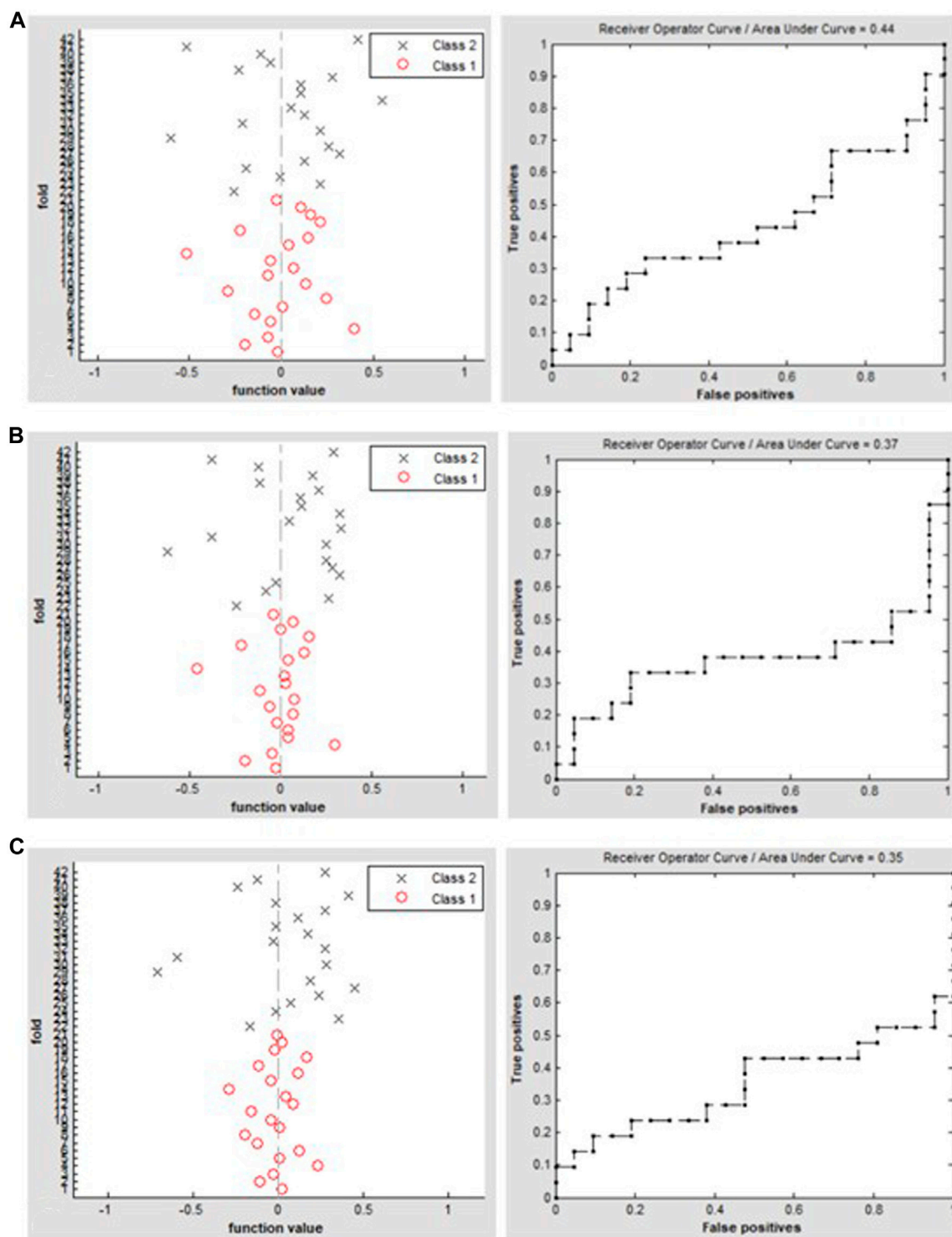


FIGURE 3

Classification results using SVM based on dALFF values using the following three distinct sliding window parameter settings: (A) window length of 30 TRs (60 s), (B) window length of 50 TRs (100 s), and (C) window length of 80 TRs (160 s). The left column of images shows a 10-fold in the class 1 (TAO group) and class 2 (HC group), and the right column shows the ROC curve of the SVM classifier with AUC values of 0.44, 0.37, and 0.35, respectively. dALFF, dynamic amplitude of low-frequency fluctuation; TAO, thyroid-associated ophthalmopathy; HC, healthy control; ROC, receiver operating characteristic; SVM, support vector machine; AUC, area under the curve.

is a component of the dorsal stream as well as the default mode network. It receives visual information from cortical area V5, which plays an important role in visuospatial imagination and plot memory extraction (Cavanna and Trimble, 2006). Most previous imaging studies have shown that the structure and function of the precuneus changed in TAO. However, there have been inconsistencies in the results. Compared with HCs, the right precuneus of patients with active TAO was atrophied, which indicated cognitive impairment (Silkiss and Wade, 2016). In contrast, compared with HCs and patients with inactive TAO, the GMV of the left precuneus of patients with active TAO was increased. The GMV of the right precuneus was positively correlated with CAS, left exophthalmos, and quality of life in thyroid eye disease (TED-QOL), while it was negatively correlated with right eye visual acuity (Luo et al., 2022). Qi et al. (2021) found that ALFF of the bilateral precuneus was lower in patients with active TAO, while Chen et al. (2021c) did not find differences between patients with active TAO and HCs. The ALFF in the right precuneus in TAO was positively correlated with CAS and MMSE scores but negatively correlated with disease duration (Chen et al., 2021c). Our study found decreased dALFF in the right precuneus and speculated that it was related to the slow processing speed of visual spatial information. In future studies, more attention needs to be paid to the importance of the precuneus in TAO.

In the present study, the SVM classification was adopted, and dALFF was used as a feature to distinguish patients with active TAO from HCs. Unfortunately, the dALFF variability in these regions only achieved an accuracy of 45.24%–47.62% and AUCs of 0.35–0.44, indicating poor accuracy. Hence, which indicator could be most sensitive to detecting TAO-related brain changes has to be determined yet.

There were some limitations to the present study. First, the sample size was small. Second, this study recruited patients with active TAO to explore TAO-specific brain functional changes without controlling for levels of thyroid hormones. Changes in thyroid hormone have short- and long-term effects on brain function (Gobel et al., 2020). Other studies that recruited patients with TAO and in a hematologically euthyroid state (Chen et al., 2021d; Jiang et al., 2022; Zhou et al., 2022), or those that performed longitudinal monitoring of thyroid hormone levels, may provide additional evidence for understanding the role of thyroid hormones in the visual and cognitive impairments seen in TAO.

In conclusion, this study found that in the pathogenesis of TAO, the dALFF in visual cortex and ventral and dorsal pathways decreased. This might indicate that patients with TAO may need to consider neuroprotective therapy in the future.

References

- Ashburner, J. (2007). A fast diffeomorphic image registration algorithm. *Neuroimage* 38 (1), 95–113. doi:10.1016/j.neuroimage.2007.07.007
- Bartolena, L., Kahaly, G. J., Baldeschi, L., Dayan, C. M., Eckstein, A., Marcocci, C., et al. (2021). The 2021 European Group on Graves' orbitopathy (EUGOGO) clinical practice guidelines for the medical management of Graves' orbitopathy. *Eur. J. Endocrinol.* 185 (4), G43–G67. doi:10.1530/EJE-21-0479
- Bartley, G. B., and Gorman, C. A. (1995). Diagnostic criteria for Graves' ophthalmopathy. *Am. J. Ophthalmol.* 119 (6), 792–795. doi:10.1016/s0002-9394(14)72787-4
- Biswal, B. B., Mennes, M., Zuo, X. N., Gohel, S., Kelly, C., Smith, S. M., et al. (2010). Toward discovery science of human brain function. *Proc. Natl. Acad. Sci. U. S. A.* 107 (10), 4734–4739. doi:10.1073/pnas.0911855107
- Cavanna, A. E., and Trimble, M. R. (2006). The precuneus: A review of its functional anatomy and behavioural correlates. *Brain* 129 (3), 564–583. doi:10.1093/brain/awl004
- Chen, J., Jin, H., Zhong, Y. L., and Huang, X. (2021a). Abnormal low-frequency oscillations reflect abnormal eye movement and stereovision in patients with comitant exotropia. *Front. Hum. Neurosci.* 15, 754234. doi:10.3389/fnhum.2021.754234

Data availability statement

The raw data supporting the conclusion of this article will be made available by the authors, without undue reservation.

Ethics statement

The studies involving human participants were reviewed and approved by the Research Ethics Committee of Jiangxi Provincial People's Hospital. The patients/participants provided their written informed consent to participate in this study.

Author contributions

BX designed the study. YK wrote the protocol. ZW and XH collected the clinical and MRI data. ZW, YK, YuZ, YLZ, and HY analyzed the MRI data and drafted the manuscript. All authors contributed to the article and approved the submitted version.

Funding

This work was supported by the Natural Science Foundation of Jiangxi Province (Grant No. 20212BAB216058), Jiangxi Provincial Health Technology Project (Grant Nos 202210012 and 202310114), Jiangxi Provincial Traditional Chinese Technology Project (Grant No. 2022B840), and Fundamental Research Funds for the Central Universities (Grant No. 2042018kf0178).

Conflict of interest

The authors declare that the research was conducted in the absence of any commercial or financial relationships that could be construed as a potential conflict of interest.

Publisher's note

All claims expressed in this article are solely those of the authors and do not necessarily represent those of their affiliated organizations, or those of the publisher, the editors, and the reviewers. Any product that may be evaluated in this article, or claim that may be made by its manufacturer, is not guaranteed or endorsed by the publisher.

- Chen, R. B., Ye, S. Y., Pei, C. G., and Zhong, Y. L. (2022a). Altered temporal dynamics of the amplitude of low-frequency fluctuations in comitant exotropia patients. *Front. Hum. Neurosci.* 16, 944100. doi:10.3389/fnhum.2022.944100
- Chen, R. B., Zhong, Y. L., Liu, H., and Huang, X. (2022b). Machine learning analysis reveals abnormal functional network hubs in the primary angle-closure glaucoma patients. *Front. Hum. Neurosci.* 16, 935213. doi:10.3389/fnhum.2022.935213
- Chen, W., Hu, H., Wu, Q., Chen, L., Zhou, J., Chen, H. H., et al. (2021b). Altered static and dynamic interhemispheric resting-state functional connectivity in patients with thyroid-associated ophthalmopathy. *Front. Neurosci.* 15, 799916. doi:10.3389/fnins.2021.799916
- Chen, W., Wu, Q., Chen, L., Zhou, J., Chen, H. H., Xu, X. Q., et al. (2021d). Aberrant brain voxel-wise resting state fMRI in patients with thyroid-associated ophthalmopathy. *J. Neuroimaging* 31 (4), 773–783. doi:10.1111/jon.12858
- Chen, W., Wu, Q., Chen, L., Zhou, J., Chen, H. H., Xu, X. Q., et al. (2021c). Disrupted spontaneous neural activity in patients with thyroid-associated ophthalmopathy: A resting-state fMRI study using amplitude of low-frequency fluctuation. *Front. Hum. Neurosci.* 15, 676967. doi:10.3389/fnhum.2021.676967
- Cui, Q., Sheng, W., Chen, Y., Pang, Y., Lu, F., Tang, Q., et al. (2020). Dynamic changes of amplitude of low-frequency fluctuations in patients with generalized anxiety disorder. *Hum. Brain Mapp.* 41 (6), 1667–1676. doi:10.1002/hbm.24902
- Dinkelacker, V., Gruter, M., Klaver, P., Gruter, T., Specht, K., Weis, S., et al. (2011). Congenital prosopagnosia: Multistage anatomical and functional deficits in face processing circuitry. *J. Neurol.* 258 (5), 770–782. doi:10.1007/s00415-010-5828-5
- Gobel, A., Gottlich, M., Reinwald, J., Rogge, B., Uter, J. C., Heldmann, M., et al. (2020). The influence of thyroid hormones on brain structure and function in humans. *Exp. Clin. Endocrinol. Diabetes* 128 (6–07), 432–436. doi:10.1055/a-1101-9090
- Hiromatsu, Y., Eguchi, H., Tani, J., Kasaoka, M., and Teshima, Y. (2014). Graves' ophthalmopathy: Epidemiology and natural history. *Intern Med.* 53 (5), 353–360. doi:10.2169/internalmedicine.53.1518
- Huang, X., Wen, Z., Qi, C. X., Tong, Y., and Shen, Y. (2021). Dynamic changes of amplitude of low-frequency fluctuations in patients with diabetic retinopathy. *Front. Neurol.* 12, 611702. doi:10.3389/fneur.2021.611702
- Jiang, W. H., Chen, H. H., Chen, W., Wu, Q., Chen, L., Zhou, J., et al. (2022). Altered long- and short-range functional connectivity density in patients with thyroid-associated ophthalmopathy: A resting-state fMRI study. *Front. Neurol.* 13, 902912. doi:10.3389/fneur.2022.902912
- Lee, H., Lee, Y. H., Suh, S. I., Jeong, E. K., Baek, S., and Seo, H. S. (2018). Characterizing intraorbital optic nerve changes on diffusion tensor imaging in thyroid eye disease before dysthyroid optic neuropathy. *J. Comput. Assist. Tomogr.* 42 (2), 293–298. doi:10.1097/RCT.0000000000000680
- Leonardi, N., and Van De Ville, D. (2015). On spurious and real fluctuations of dynamic functional connectivity during rest. *Neuroimage* 104, 430–436. doi:10.1016/j.neuroimage.2014.09.007
- Liang, M., Xie, B., Yang, H., Yu, L., Yin, X., Wei, L., et al. (2016). Distinct patterns of spontaneous brain activity between children and adults with anisometropic amblyopia: A resting-state fMRI study. *Graefes Arch. Clin. Exp. Ophthalmol.* 254 (3), 569–576. doi:10.1007/s00417-015-3117-9
- Liao, W., Li, J., Ji, G. J., Wu, G. R., Long, Z., Xu, Q., et al. (2019). Endless fluctuations: Temporal dynamics of the amplitude of low frequency fluctuations. *IEEE Trans. Med. Imaging* 38 (11), 2523–2532. doi:10.1109/TMI.2019.2904555
- Liegeois, R., Laumann, T. O., Snyder, A. Z., Zhou, J., and Yeo, B. T. T. (2017). Interpreting temporal fluctuations in resting-state functional connectivity MRI. *Neuroimage* 163, 437–455. doi:10.1016/j.neuroimage.2017.09.012
- Liu, J., Bu, X., Hu, X., Li, H., Cao, L., Gao, Y., et al. (2021). Temporal variability of regional intrinsic neural activity in drug-naïve patients with obsessive-compulsive disorder. *Hum. Brain Mapp.* 42 (12), 3792–3803. doi:10.1002/hbm.25465
- Liu, X., and Duyn, J. H. (2013). Time-varying functional network information extracted from brief instances of spontaneous brain activity. *Proc. Natl. Acad. Sci. U. S. A.* 110 (11), 4392–4397. doi:10.1073/pnas.1216856110
- Luo, L., Wen, H., Gao, L., Li, R., Wang, S., Wang, Z., et al. (2022). Morphological brain changes between active and inactive phases of thyroid-associated ophthalmopathy: A voxel-based morphometry study. *Brain Res.* 1790, 147989. doi:10.1016/j.brainres.2022.147989
- Ma, H., Huang, G., Li, M., Han, Y., Sun, J., Zhan, L., et al. (2021). The predictive value of dynamic intrinsic local metrics in transient ischemic attack. *Front. Aging Neurosci.* 13, 808094. doi:10.3389/fnagi.2021.808094
- Ozkan, B., Anik, Y., Katre, B., Altintas, O., Gencturk, M., and Yuksel, N. (2015). Quantitative assessment of optic nerve with diffusion tensor imaging in patients with thyroid orbitopathy. *Ophthalmic Plast. Reconstr. Surg.* 31 (5), 391–395. doi:10.1097/IOP.0000000000000359
- Qi, C. X., Wen, Z., and Huang, X. (2022). Reduction of interhemispheric homotopic connectivity in cognitive and visual information processing pathways in patients with thyroid-associated ophthalmopathy. *Front. Hum. Neurosci.* 16, 882114. doi:10.3389/fnhum.2022.882114
- Qi, C. X., Wen, Z., and Huang, X. (2021). Spontaneous brain activity alterations in thyroid-associated ophthalmopathy patients using amplitude of low-frequency fluctuation: A resting-state fMRI study. *Neuroreport* 32 (18), 1416–1422. doi:10.1097/WNR.0000000000001745
- Reisch, L. M., Wegrzyn, M., Mielke, M., Mehlmann, A., Woermann, F. G., Bien, C. G., et al. (2022). Face processing and efficient recognition of facial expressions are impaired following right but not left anteromedial temporal lobe resections: Behavioral and fMRI evidence. *Neuropsychologia* 174, 108335. doi:10.1016/j.neuropsychologia.2022.108335
- Schrouff, J., Rosa, M. J., Rondina, J. M., Marquand, A. F., Chu, C., Ashburner, J., et al. (2013). PRoNTTo: Pattern recognition for neuroimaging toolbox. *Neuroinformatics* 11 (3), 319–337. doi:10.1007/s12021-013-9178-1
- Silkiss, R. Z., and Wade, A. R. (2016). Neuroanatomic variations in Graves' dysthyroid ophthalmopathy as studied with MRI. *Trans. Am. Ophthalmol. Soc.* 114, T9.
- Song, C., Luo, Y., Yu, G., Chen, H., and Shen, J. (2022). Current insights of applying MRI in Graves' ophthalmopathy. *Front. Endocrinol. (Lausanne)* 13, 991588. doi:10.3389/fendo.2022.991588
- Sujanthan, S., Shmuel, A., and Mendola, J. D. (2022). Resting-state functional MRI of the visual system for characterization of optic neuropathy. *Front. Hum. Neurosci.* 16, 943618. doi:10.3389/fnhum.2022.943618
- Weiler, D. L. (2017). Thyroid eye disease: A review. *Clin. Exp. Optom.* 100 (1), 20–25. doi:10.1111/cxo.12472
- Wen, Z., Wan, X., Qi, C. X., and Huang, X. (2022). Local-to-Remote brain functional connectivity in patients with thyroid-associated ophthalmopathy and assessment of its predictive value using machine learning. *Int. J. Gen. Med.* 15, 4273–4283. doi:10.2147/IJGM.S353649
- Wolpert, D. M., Goodbody, S. J., and Husain, M. (1998). Maintaining internal representations: The role of the human superior parietal lobe. *Nat. Neurosci.* 1 (6), 529–533. doi:10.1038/2245
- Worsley, K. J., Marrett, S., Neelin, P., Vandal, A. C., Friston, K. J., and Evans, A. C. (1996). A unified statistical approach for determining significant signals in images of cerebral activation. *Hum. Brain Mapp.* 4 (1), 58–73. doi:10.1002/(SICI)1097-0193(1996)4:1<58::AID-HBM4>3.0.CO;2-O
- Zhang, C., Dou, B., Wang, J., Xu, K., Zhang, H., Sami, M. U., et al. (2019). Dynamic alterations of spontaneous neural activity in Parkinson's disease: A resting-state fMRI study. *Front. Neurol.* 10, 1052. doi:10.3389/fneur.2019.01052
- Zhang, W., Song, L., Yin, X., Zhang, J., Liu, C., Wang, J., et al. (2014). Grey matter abnormalities in untreated hyperthyroidism: A voxel-based morphometry study using the DARTEL approach. *Eur. J. Radiol.* 83 (1), e43–e48. doi:10.1016/j.ejrad.2013.09.019
- Zhou, J., Chen, W., Wu, Q., Chen, L., Chen, H. H., Liu, H., et al. (2022). Reduced cortical complexity in patients with thyroid-associated ophthalmopathy. *Brain Imaging Behav.* 16 (5), 2133–2140. doi:10.1007/s11682-022-00683-0
- Zhu, P., Liu, Z., Lu, Y., Wang, Y., Zhang, D., Zhao, P., et al. (2022). Alterations in spontaneous neuronal activity and microvascular density of the optic nerve head in active thyroid-associated ophthalmopathy. *Front. Endocrinol. (Lausanne)* 13, 895186. doi:10.3389/fendo.2022.895186



OPEN ACCESS

EDITED BY

Xiaomeng Li,
Hong Kong University of Science and
Technology, Hong Kong, SAR China

REVIEWED BY

Yongjin Zhou,
Shenzhen University, China
Qiang Ao,
Sichuan University, China

*CORRESPONDENCE

Weihua Yang,
✉ benben0606@139.com
Shaochong Zhang,
✉ zhangshaochong@gzzoc.com
Yan Lou,
✉ ylou04@cmu.edu.cn

RECEIVED 14 April 2023

ACCEPTED 02 May 2023

PUBLISHED 15 May 2023

CITATION

Feng H, Chen J, Zhang Z, Lou Y, Zhang S
and Yang W (2023), A bibliometric
analysis of artificial intelligence
applications in macular edema: exploring
research hotspots and Frontiers.
Front. Cell Dev. Biol. 11:1174936.
doi: 10.3389/fcell.2023.1174936

COPYRIGHT

© 2023 Feng, Chen, Zhang, Lou, Zhang
and Yang. This is an open-access article
distributed under the terms of the
[Creative Commons Attribution License
\(CC BY\)](https://creativecommons.org/licenses/by/4.0/). The use, distribution or
reproduction in other forums is
permitted, provided the original author(s)
and the copyright owner(s) are credited
and that the original publication in this
journal is cited, in accordance with
accepted academic practice. No use,
distribution or reproduction is permitted
which does not comply with these terms.

A bibliometric analysis of artificial intelligence applications in macular edema: exploring research hotspots and Frontiers

Haiwen Feng¹, Jiaqi Chen¹, Zhichang Zhang², Yan Lou^{2*},
Shaochong Zhang^{3*} and Weihua Yang^{3*}

¹Department of Software Engineering, School of Software, Shenyang University of Technology, Shenyang, Liaoning, China, ²Department of Computer, School of Intelligent Medicine, China Medical University, Shenyang, Liaoning, China, ³Shenzhen Eye Institute, Shenzhen Eye Hospital, Jinan University, Shenzhen, China

Background: Artificial intelligence (AI) is used in ophthalmological disease screening and diagnostics, medical image diagnostics, and predicting late-disease progression rates. We reviewed all AI publications associated with macular edema (ME) research Between 2011 and 2022 and performed modeling, quantitative, and qualitative investigations.

Methods: On 1st February 2023, we screened the Web of Science Core Collection for AI applications related to ME, from which 297 studies were identified and analyzed (2011–2022). We collected information on: publications, institutions, country/region, keywords, journal name, references, and research hotspots. Literature clustering networks and Frontier knowledge bases were investigated using bibliometrix-BiblioShiny, VOSviewer, and CiteSpace bibliometric platforms. We used the R “bibliometrix” package to synopsise our observations, enumerate keywords, visualize collaboration networks between countries/regions, and generate a topic trends plot. VOSviewer was used to examine cooperation between institutions and identify citation relationships between journals. We used CiteSpace to identify clustering keywords over the timeline and identify keywords with the strongest citation bursts.

Results: In total, 47 countries published AI studies related to ME; the United States had the highest H-index, thus the greatest influence. China and the United States cooperated most closely between all countries. Also, 613 institutions generated publications - the Medical University of Vienna had the highest number of studies. This publication record and H-index meant the university was the most influential in the ME field. Reference clusters were also categorized into 10 headings: retinal Optical Coherence Tomography (OCT) fluid detection, convolutional network models, deep learning (DL)-based single-shot predictions, retinal vascular disease, diabetic retinopathy (DR), convolutional neural networks (CNNs), automated macular pathology diagnosis, dry age-related macular degeneration (DARMD), class weight, and advanced DL architecture systems. Frontier keywords were represented by diabetic macular edema (DME) (2021–2022).

Conclusion: Our review of the AI-related ME literature was comprehensive, systematic, and objective, and identified future trends and current hotspots. With increased DL outputs, the ME research focus has gradually shifted from manual ME examinations to automatic ME detection and associated symptoms. In

this review, we present a comprehensive and dynamic overview of AI in ME and identify future research areas.

KEYWORDS

bibliometric analysis, deep learning, artificial intelligence, macular edema, ophthalmology, machine learning

1 Introduction

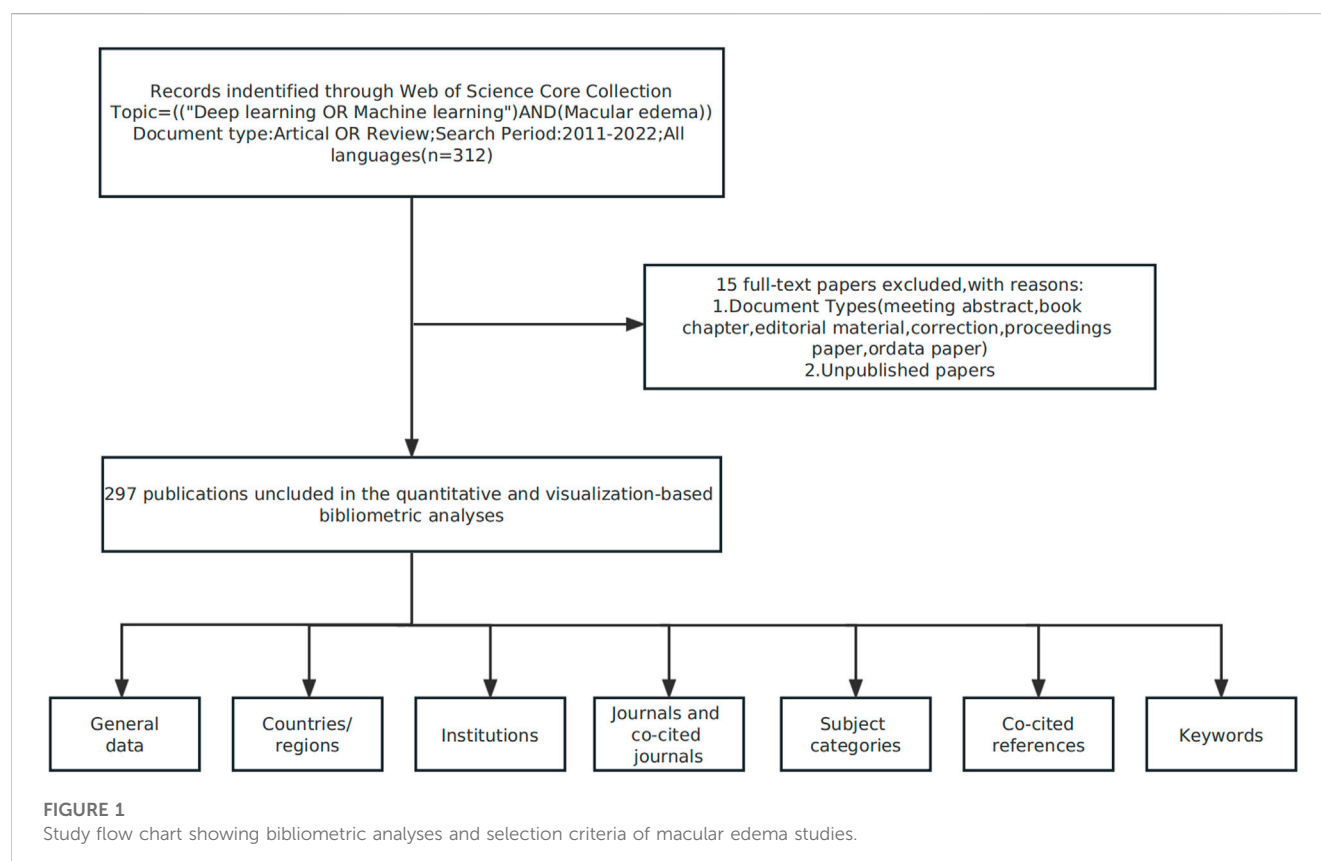
Macular edema (ME) is a common, critical disease caused by retinal vein occlusion, diabetic retinopathy (DR), chronic uveitis, and eye injury, of which, macular lesions are the leading cause of disease. Clinically significant ME is manifested by retinal thickening which impacts the macula center, is defined by central retinal thickness $>250\text{--}300\text{ }\mu\text{m}$, and examined using Optical Coherence Tomography (OCT) (Hee et al., 1995). ME also involves fluid accumulation in retinal layers which is a common morphological manifestation in different retinal diseases (Daruich et al., 2018). Therefore, it is vital to quantitatively analyze ME research areas, the disease *status quo*, and future prospects related to disease progression.

Bibliometrics is used to analyze different knowledge carriers using mathematics and statistics (Cancino et al., 2017). It evaluates development trends in target disciplines/scientific fields by analyzing database and document characteristics to identify research hotspots and key research directions. In recent years, bibliometric analysis have been successfully used in orthopedics, ophthalmology, and gynecology (Qiu et al., 2018; Huang et al., 2020;

He J. et al., 2021). Additionally, the approach is invaluable for writing guidelines, making clinical decisions, and importantly, treating different diseases. However, bibliometric analyses related to ME in ophthalmology remains under-studied (Narotsky et al., 2012; Seriwala et al., 2015; Khan et al., 2016), therefore, we systematically investigated this research area to characterize the *status quo* and identify research hotspots.

2 Materials and methods

On 1st February 2023, we downloaded data from the Web of Science Core Collection (2011–2022) using: “machine learning” OR “deep learning” OR “convolutional neural network*” OR “CNN*” OR “Recurrent neural network*” OR “RNN” OR “Fully Convolutional Network*” OR “FCN*” search terms. The parallel search subject was ME and relevant studies included basic information on: authors, abstracts, keywords, titles, institutions, journals, countries/regions, and references. Indexed database studies were included, but meeting abstracts, book chapters, data papers, proceedings, editorials,



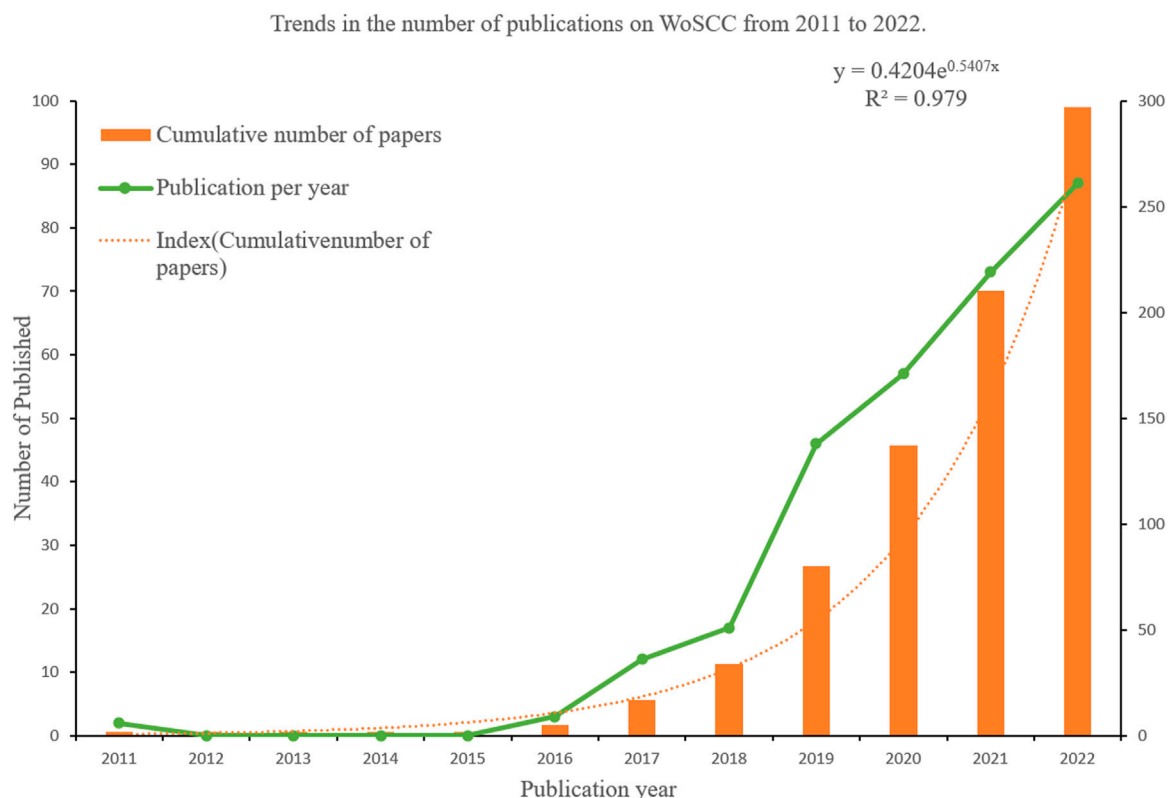


FIGURE 2

Macular edema publications; publication trends between 2011 and 2022 (publication years).

and repeat articles, and unpublished studies containing limited data were excluded. A summary of this process is shown (Figure 1).

We also examined publication characteristics: keywords, institutions, countries/regions, and journals. We also used the H-index which evaluates the scientific value of research and measures author/journal scientific productivity (Eyre-Walker and Stoletzki, 2013). To represent collaborative networks across journals/institutes/countries/keywords and facilitate co-occurrence investigations, we used R language bibliometrics software (Massimo Aria and Corrado Cuccurullo), CiteSpace (Drexel University, PA, United States), and VOSviewer (Leiden University, Holland). The R language bibliometric package is widely used in statistical computation and graphics (Aria and Cuccurullo, 2017) and was used to extract the top 10 keywords and cluster them into themes/evolution/hierarchical clustering/topic trends. From collaborative data, we used the VOSviewer to provide a comprehensive and detailed view of bibliometric maps. We also generated a cooperation relationship diagram between institutions and also a reference relationship diagram between foresight to analyze cooperation outputs between institutions and reference relationships between disciplines. CiteSpace was used to investigate knowledge from the literature and visualize data (Chen, 2004). We also generated knowledge maps, performed discipline evolution analyses, and determined burst keywords (BKs) to identify recurrent keywords.

3 Results

3.1 Study distribution (year of publication)

We observed that AI in ME research commenced in 2011. From 2011 to 2022, we identified 297 papers and identified AI-associated ME publication trends (Figure 2). While this type of research emerged in 2011, it fell silent from 2012 to 2015. However, from 2016, in-depth learning approaches combined with ophthalmology led to increased ME research outputs, and paper outputs increased year on year suggesting an important research trend had been established.

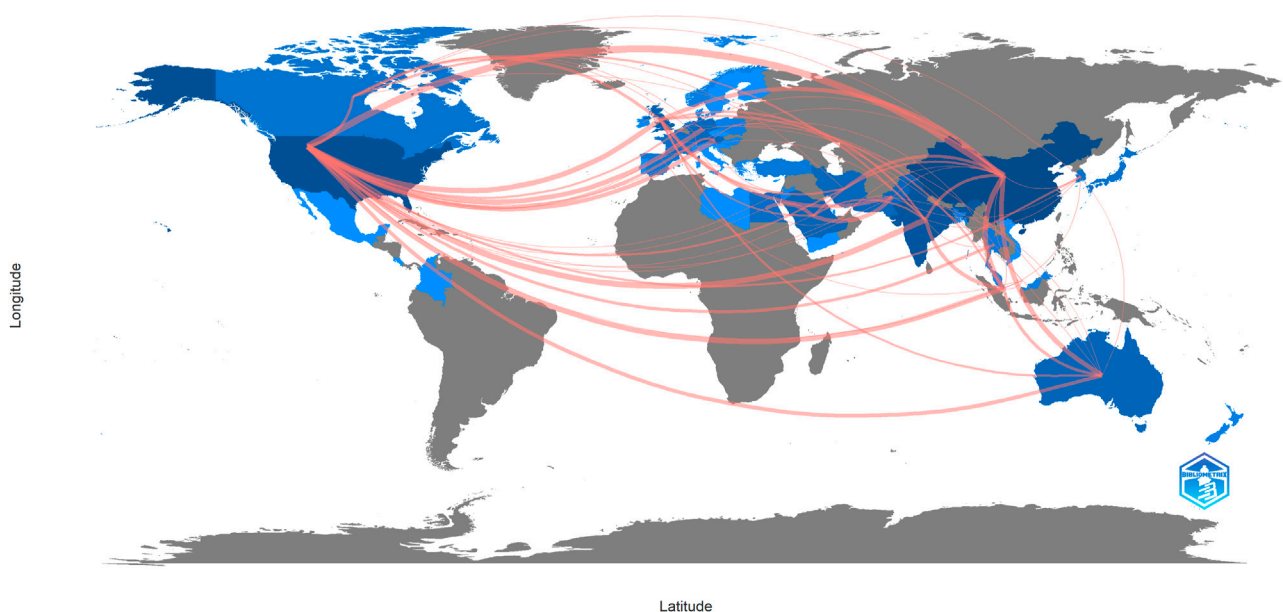
3.2 Institutes/countries/regions

Forty-seven countries/regions published ME studies - the top 10 countries (Table 1) and collaborations (Figures 3, 4) are indicated. China published the most studies (101), then the United States (73), India (48), and the United Kingdom (23). Some countries (United States, China, and the United Kingdom) showed high centrality (dark blue—Figure 3) suggesting important regional roles in/contributions to ME research. H index is a mixed quantitative index, which can be used to evaluate the quantity and level of academic output of a country or institution. Because the United States has the highest H-index, it has the greatest influence in the field of macular edema.

TABLE 1 Top ten institutions and countries/regions.

Rank	Countries/Regions	Count	Citations	H-index	Institutions	Count	H-index
1	China	101	3,286	23	Medical University Of Vienna	15	11
2	United States	73	7,302	28	National University Of Singapore	12	10
3	India	48	4,026	14	University Of California System	12	7
4	England	23	1,419	10	Singapore National Eye Center	11	9
5	Singapore	21	718	11	Shanghal Jiao Tong University	10	6
6	Saudi Arabia	18	157	7	Egyptian Knowledge Bank EKB	9	3
7	Australia	17	613	8	Indian Institute Of Technology System IIT System	9	7
8	Austria	17	1,011	11	Isfahan University Medical Science	9	5
9	Pakistan	15	157	8	Shantou University	9	4
10	Iran	14	349	7	Cleveland Clinic Foundation	8	6

Country Collaboration Map

**FIGURE 3**

Collaboration map showing how countries/regions contributed to/collaborated on macular edema publications.

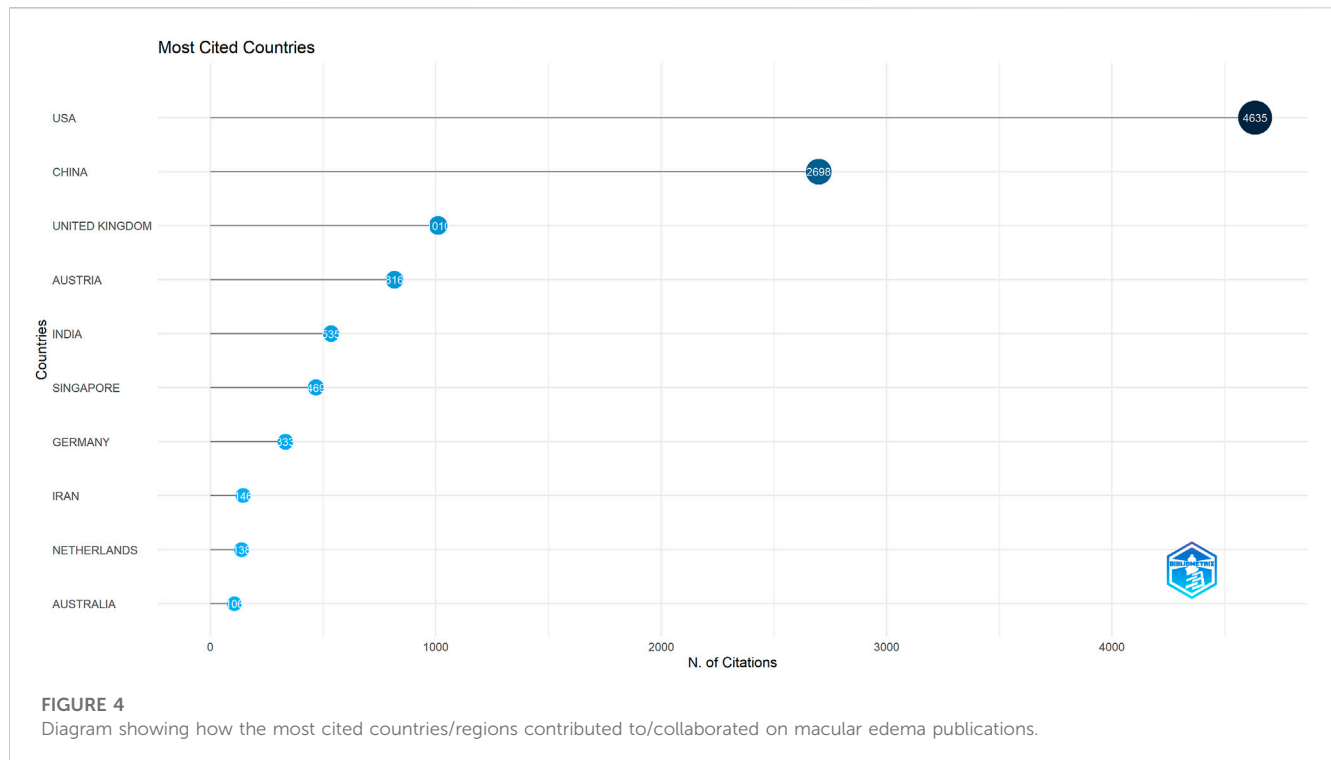
In total, 613 institutes generated ME publications; the top ten are shown (Table 1). Institutions are also outlined (Figure 5). The Medical University of Vienna had the most publications (15), followed by the National University of Singapore (12), the University of California (12), and the Singapore National Eye Center (11).

We also cataloged research institutions with outstanding contributions to the ME field (Figure 5) using VOSviewer. Regional institutional distributions showed distinct aggregation effects, indicating that academic research was concentrated to a few countries. From a literature perspective, most institutions were based in universities and scientific research institutions and generally reflected the ME research status. A possible reason

could be that the ME research field is highly academic in nature and not currently economically feasible, thus enterprises and other institutions may currently eschew the field. The Medical University of Vienna and the National University of Singapore were major prominent organizations which had significant ME research outputs.

3.3 Journals

Across all academic fields, knowledge exchange in/between fields is often reflected in reference relationships between



academic journals. Citing papers are knowledge frontiers, while referenced papers are knowledge bases. As indicated (Figure 6; Table 2), the major journals contributing to ME research included, *Biomed Opt Express*, *Ieee T Med Imaging*, *Ophthalmology*, *Med Image Anal*, and *Invest Ophth Vis Sci*—with high centrality, these were the most popular journals publishing ME research.

A journal dual-map overlay (Figure 7) showed citing (left) and cited (right) journals, while citation associations were indicated by colored lines—these investigations demonstrated that studies in computer/medicine/molecular journals were typically cited in ophthalmology/mathematics/clinical journals.

3.4 References

Reference analysis is an important index in bibliometric—typically, often-cited studies significantly impact certain research areas. Therefore, we used Citespace to cluster references from data to generate a reference clustering diagram (with a timeline) to analyze ME research.

A co-citation reference network was used to assess the relevance of studies (Figure 8). Cluster setting: g-index $K = 5$ and #years/slice = 1. The modularity Q score was 0.8306 (>0.5), thus the network was adequately split into loosely coupled clusters. The weighted mean silhouette score was 0.9621 (>0.5), thus cluster homogeneity was reasonable.

Index items, as cluster markers, were extracted from studies. The largest clusters were cluster #0 “retinal oct fluid detection” (Lee et al., 2017; Venhuizen et al., 2018; Girish et al., 2019), cluster #1 “convolutional network model” (Gargeya and Leng, 2017; Porwal et al., 2020; Singh and Gorantla, 2020; Dai et al., 2021), cluster #2 “deep learning-based single-shot prediction” (Rasti et al., 2018; Das et al., 2019; Tsuji et al., 2020), cluster #3 “retinal vascular disease”

(Karri et al., 2017; Ehlers et al., 2019; Figueiredo et al., 2020; Rasti et al., 2020), cluster #4 “diabetic retinopathy” (Ting et al., 2017; Raumviboonsuk et al., 2019; Ting et al., 2019), cluster #5 “convolutional neural network” (Keremany et al., 2018; Hwang et al., 2019), cluster #6 “automated macular pathology diagnosis” (Chang and Lin, 2011), cluster #7 “dry age-related macular degeneration” (Kafieh et al., 2013; Srinivasan et al., 2014a; Rathke et al., 2014; Karri et al., 2016), cluster #8 “class weight” (Wan et al., 2018; Li et al., 2019b; Huang et al., 2019), and cluster #9 “recent advanced deep learning architecture” (Schmidt-Erfurth et al., 2018; Bogunovic et al., 2019; Gu et al., 2019; Lu et al., 2019).

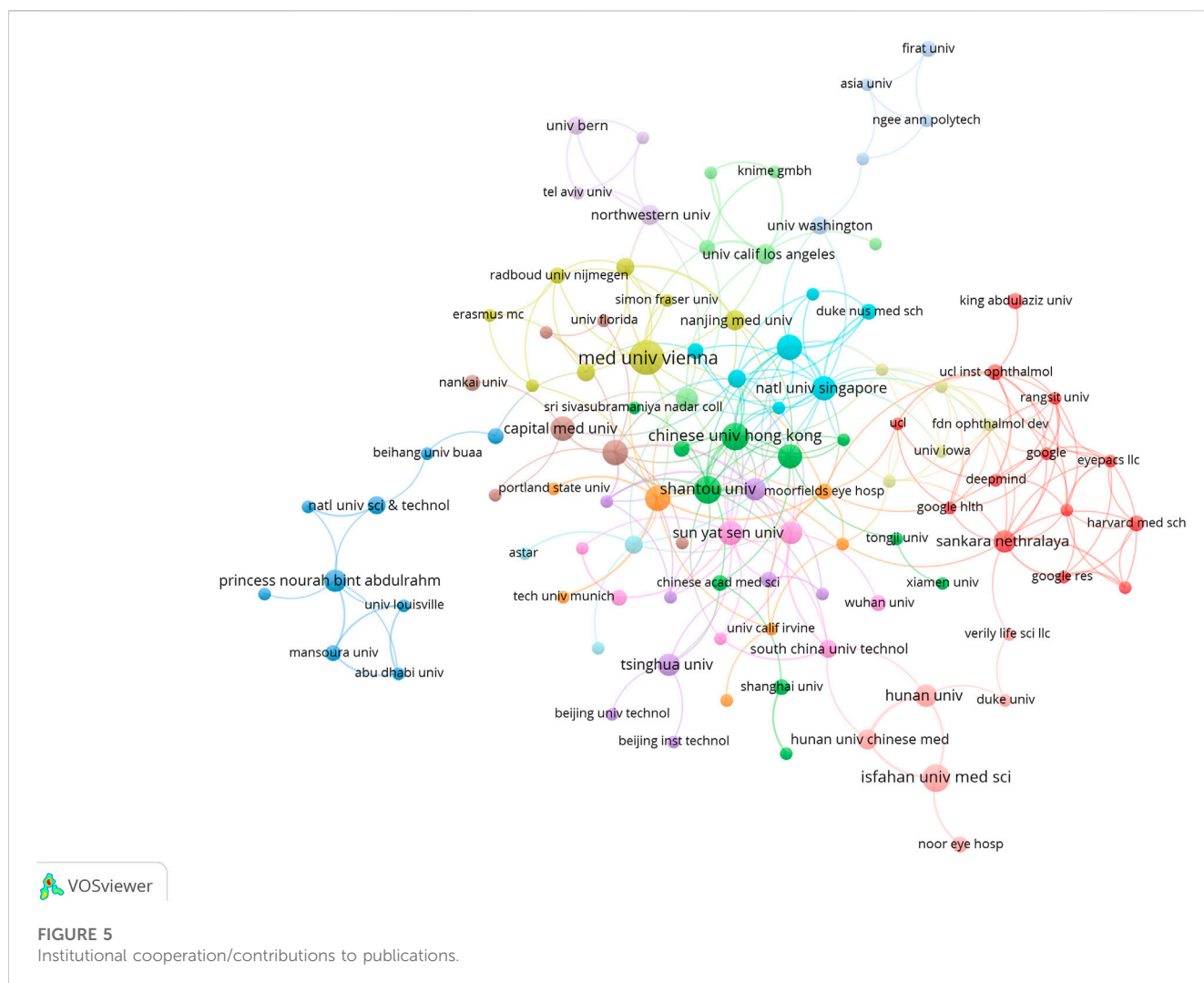
3.5 Keywords

Keyword analyses help summarize research themes and explore research hotspots and trends in a given field. The top 20 keywords from ME studies are shown (Table 3). Temporal trend/hotspot shifts (from seven keywords with the strongest citation burst) in 2016–2019; BKs were Image Analysis (2016–2019), OCT Imaging (2017–2019), Layer Segmentation (2017–2019), and Age Related Macular Degeneration (AMD) (2017–2019). BKs in 2020–2022 were validation (2020), system (2020), and the hotspot, Diabetic Macular Edema (DME) (2021–2022). (Figure 9).

4 Discussion

4.1 General data

Between 2011 and 2022, 297 ME studies, conforming to inclusion/exclusion criteria and search terms, were identified.



China generated the most studies (101, 34.007%), with the United States in second place (73, 24.579%). Two of the top ten institutions were in China. The most common ME publication journal, and the major contributor to ME research, was BIOMEDICAL OPTICS EXPRESS. The top study (cited 2,936 times) was by Gulshan et al. in JAMA-JOURNAL OF THE AMERICAN MEDICAL ASSOCIATION (Gulshan et al., 2016). The second top study (cited 1,474 times) was by Kermany et al. in CELL (Kermany et al., 2018).

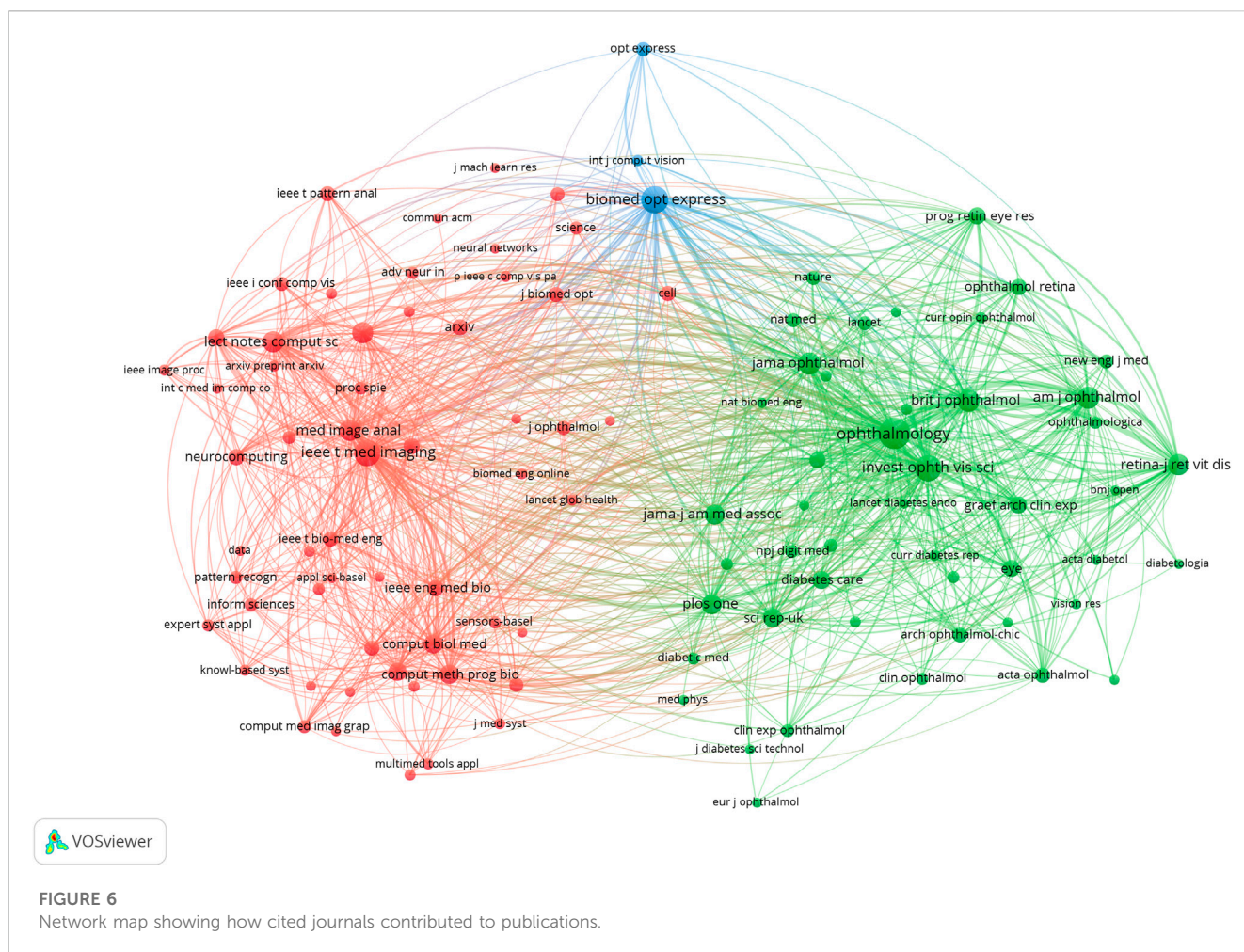
4.2 Knowledge base

Previously DL-related technologies and associations with ME generated several major achievements. When co-cited references were clustered (Figure 8), key clustering nodes were used to identify knowledge bases in ME research: #0 “retinal oct fluid detection,” #1 “convolutional network model,” #2 “deep learning-based single-shot prediction,” #3 “retinal vascular disease,” #4 “diabetic retinopathy,” #5 “convolutional neural network,” #6 “automated macular pathology diagnosis,” #7 “dry age-related macular degeneration,” #8 “class weight,” and

#9 “recent advanced deep learning architecture.” In the following sections, we outline knowledge bases according to different clusters.

#0 “Retinal OCT fluid detection”; Lee et al. (2017) generated a model formulated on encoding and decoding mechanism and outlined improved segmentation intraretinal fluid (IRF) methods, which showed good IRF segmentation results in OCT images. Roy et al. (2017) developed an AI approach (Relay Net) which segmented multiple retinal layers and generated fluid bag descriptions in OCT eye images. The model displayed excellent performance in object segmentation. Fundus dropsy can lead to ME. These methods were used to segment retinal fundus dropsy and automatically detected ME in OCT and affected segmented parts.

#1 “Convolutional network model”; Gargeya and Leng. (2017) designed a convolution network model to facilitate automatic DR recognition. Abramoff et al. (2016) compared this convolutional network with other automatic detection methods (IDx-DR X2.1) to automatically detect DR, mainly evaluating the analysis software that IDx-DR X2.1 runs on the server maintained and controlled by IDx. Porwal et al. (2020) generated a dataset for



Indian populations with DR which provided normal retinal and typical DR structures at pixel levels. Image information was also provided for DR and DME severity, and facilitated image algorithm development and evaluations for early DR detection. DR is one of the most common diabetic microvascular complications. Retinal microvascular leakage and occlusions caused by chronic progressive diabetes causes different fundus diseases. DR is one of the main inducements of ME. Importantly, automated DR screening combined with a convolutional network model can effectively and economically prevent ME.

#2 “Deep learning-based single-shot prediction”; [Rasti et al. \(2018\)](#) used a DL-based single-shot prediction method (MCME) to predict macular OCT categories. The model performed category predictions based on minimum preprocessing requirements and helped to automatically classify macular OCT in clinical settings. The method by [Srinivasan et al. \(2014b\)](#) automatically detected diabetic ME and DARMD in OCT images. Using Histogram of Oriented Gradient descriptors and SVMs to classify spectral domain-OCT images, the method may be used to remotely diagnose some ophthalmic diseases.

#3 “Retinal vascular disease”; [Karri et al. \(2017\)](#) used a DL technique to identify DME or DARMD in retinal vascular

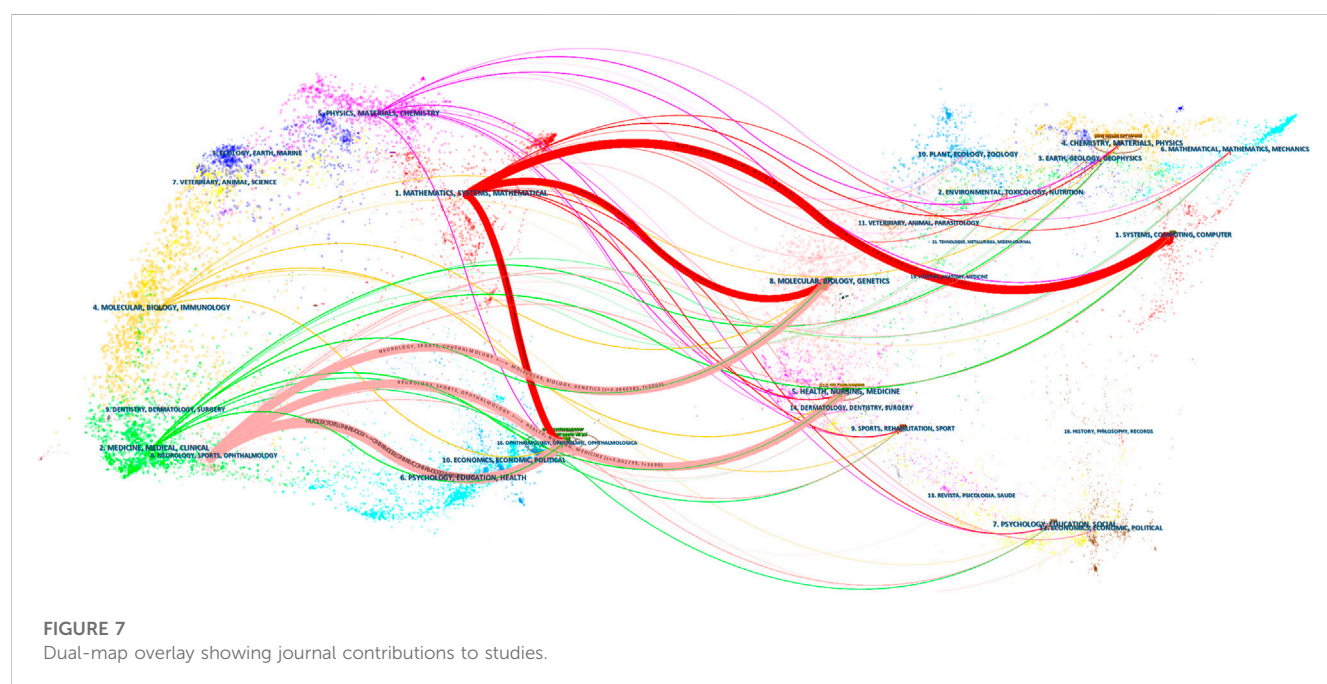
diseases from OCT images. The strategy used transfer learning and the pre-trained GoogLeNet as a classification model to allow for faster convergence with less data. [Li et al. \(2019a\)](#) combined four classification models to automatically detect four retinal vascular diseases in OCT images: choroidal neovascularization, DME, DRUSEN, and NORMAL. The method had a classification accuracy = 0.973, which met or exceeded ophthalmologist expectations.

#4 “Diabetic retinopathy”; a DL system by [Ting et al. \(2017\)](#) was used to rapidly and accurately screen DR and related eye diseases. [Abramoff et al. \(2018\)](#) diagnostically evaluated an autonomous AI system (mtmDR) to automatically detect DR and DME; the approach improved early DR detection rates and reduced pain induced by vision loss and blindness. Thus, to some extent, these methods helped limit ME.

#5 “CNN” is one of the representative DL algorithms ([Gu et al., 2018](#)). [Gulshan et al. \(2016\)](#) developed a CNN algorithm to detect DR in retinal fundus images and detect referential diagnostic retinopathy. [Kermany et al. \(2018\)](#) formulated an effective transfer learning algorithm which processed medical images and identified key pathology traits in images. The algorithm was primarily used to analyze retinal OCT images, while combination with a CNN helped clinicians effectively diagnose ME.

TABLE 2 Top ten macular edema artificial intelligence citations.

Rank	Source titles	Title of References	Count	Interpretation of findings
1	Jama-Journal Of The American Medical Association	Development and Validation of a Deep Learning Algorithm for Detection of Diabetic Retinopathy in Retinal Fundus Photographs	2,919	Detecting diabetic retinopathy (DR) using deep learning (DL)
2	Cell	Identifying Medical Diagnoses and Treatable Diseases by Image-Based Deep Learning	1,465	Using an artificial intelligence (AI) algorithm for retinal optical coherence tomography (OCT) image diagnoses
3	Nature Medicine	Clinically applicable deep learning for diagnosis and referral in retinal disease	952	Establishing a referral recommendation framework based on DL algorithms for retinal diseases which endanger vision
4	Investigative Ophthalmology and Visual Science	Improved Automated Detection of Diabetic Retinopathy on a Publicly Available Dataset Through Integration of Deep Learning	460	Using a convolutional network method to automatically detect DR when compared with other automated detection methods (IDx DR X2.1)
5	Biomedical Optics Express	Automatic segmentation of nine retinal layer boundaries in OCT images of non-exudative AMD patients using deep learning and graph search	306	A new framework automatically segmenting nine-layer boundaries in retinal OCT images
6	Biomedical Optics Express	ReLayNet: retinal layer and fluid segmentation of macular optical coherence tomography using fully convolutional networks	297	A Relay Net strategy to segment multiple retinal layers and delineate fluid pockets in OCT images
7	Progress In Retinal and Eye Research	Artificial intelligence in retina	278	Introducing AI to the retina
8	Ophthalmology	Fully Automated Detection and Quantification of Macular Fluid in OCT Using Deep Learning	233	A DL method which automatically detects and quantifies intra retinal cystic and subretinal fluid
9	Biomedical Optics Express	Deep-learning based, automated segmentation of macular edema in optical coherence tomography	181	A segmentation method based on DL and segmented intraretinal fluid
10	Progress in Retinal and Eye Research	Deep learning in ophthalmology: The technical and clinical considerations	171	Technologies and considerations are outlined for the construction of DL algorithms in ophthalmological/clinical settings



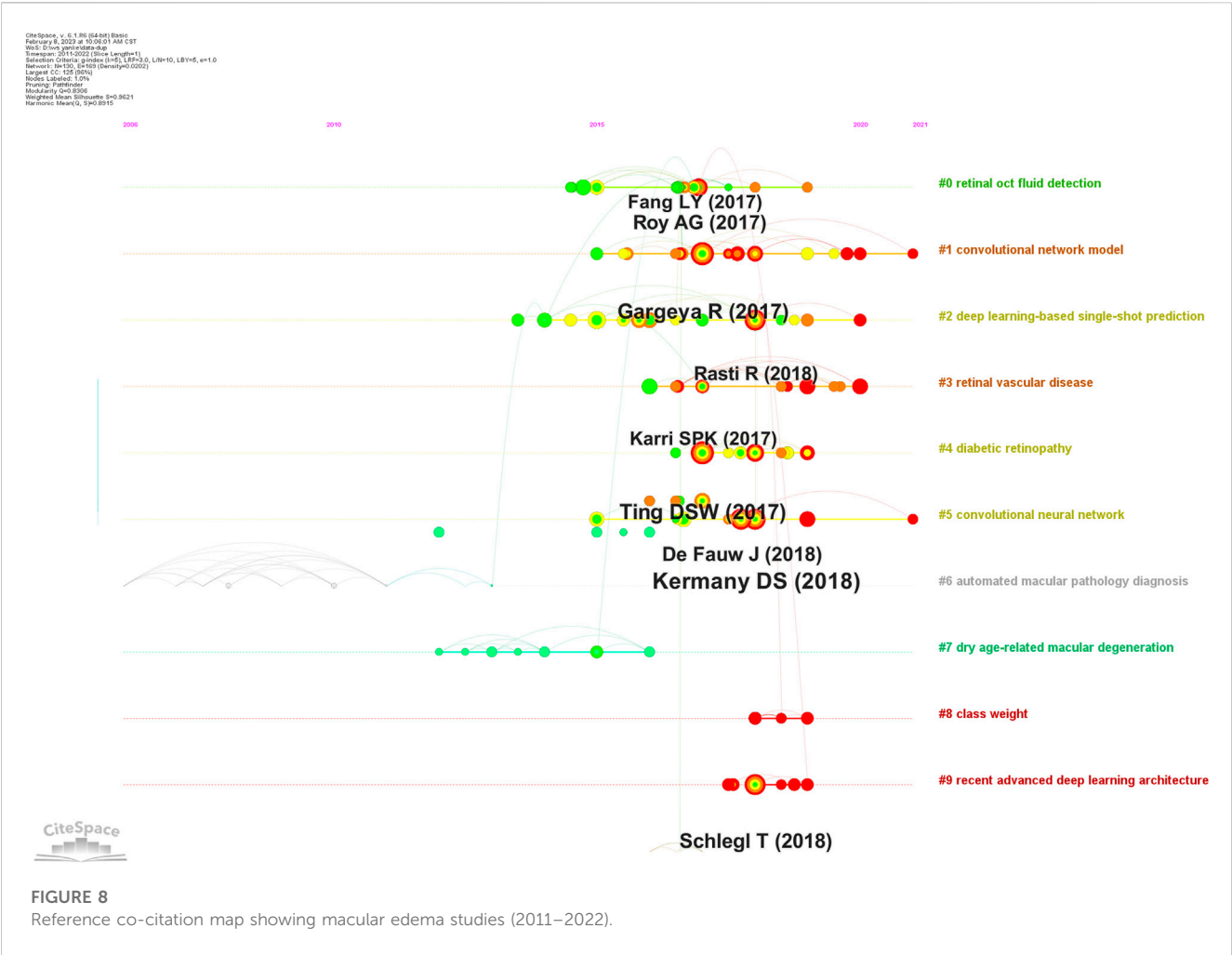


TABLE 3 The top 20 keywords and associated strength data.

Rank	Keyword	Occurrence	Link strength	Rank	Keyword	Occurrence	Link strength
1	Optical coherence tomography	110	356	11	Diabetic-retinopathy	35	108
2	Diabetic macular edema	94	329	12	Automated detection	32	138
3	Deep learning	87	337	13	Images	32	106
4	Macular edema	75	226	14	Artificial intelligence	30	136
5	Diabetic retinopathy	62	225	15	Ranibizumab	30	86
6	Degeneration	57	208	16	Retina	28	120
7	Classification	52	196	17	Prevalence	26	85
8	Segmentation	50	182	18	Fluid	25	86
9	Retinopathy	48	212	19	Diseases	24	113
10	Validation	37	156	20	Machine learning	24	96

#6 “Automated macular pathology diagnosis”; [Chang and Lin \(2011\)](#) introduced a software package for SVM algorithms—the LIBSVM library—which is one of the most widely used SVM software programs. The algorithm effectively supported automatic macular pathological diagnoses using SVM.

Top 7 Keywords with the Strongest Citation Bursts

Keywords	Year	Strength	Begin	End	2011 - 2022
image analysis	2016	2.09	2016	2019	
oct image	2017	2.97	2017	2019	
layer segmentation	2017	2.55	2017	2019	
amd	2017	2.43	2017	2019	
validation	2018	2.47	2020	2020	
system	2020	2.2	2020	2020	
diabetic macular edema (dme)	2019	2.13	2021	2022	

FIGURE 9

Keywords with the strongest citation bursts in macular edema studies (2011–2022).

#7 “Dry age-related macular degeneration”; [Chiu et al. \(2015\)](#) designed a method to automatically segment diabetic ME in OCT images. The authors first estimated fluid and retinal layer positions using a classification method based on kernel regression, and then used classification estimates to accurately segment retinal layer boundaries using dynamic programming frameworks and graph theory. The method was the first to be validated, fully-automated, seven-layered, and fluid segmented for analyzing severe real-world DME images. [Karri et al. \(2016\)](#) generated a structured learning algorithm which enhanced layer specific-edge detection in OCT retinal images. Simultaneously, the algorithm identified layers and corresponding edges so that layer-specific edge computation were calculated to within 1 s.

#8 “Class weight”; [Huang et al. \(2019\)](#) formulated a layer-guided CNN to classify OCT retinal images. The method was divided into; 1), a segmentation network (ReLayNet) extracted segmentation maps from retinal layers, and 2), two disease related layers (RPE-BrM and ILM-RPE) were taken from layer segmentation graphs. The network may be applied to other retinal diseases (macular hole and macular telangiectasia) and also retinopathy detection and segmentation.

#9 “Recent advances in deep learning architecture”; [Bogunovic et al. \(2019\)](#) reviewed the standards and models used in retinal OCT fluid detection and segmentation, and showed that >50% of clinical teams selected UNet and its derivative model structure as a basic network architecture to segment OCT images. [Schlegel et al. \(2018\)](#) generated a DL strategy to automatically quantify and detect subretinal fluid (SRF) and intra-retinal cystic fluid (IRC). The method included a CNN with encoder/decoder architecture, which identified IRC and SRF. In the ME research field, codec structures (similar to UNet) have become popular DL network architecture approaches.

4.3 Frontiers and hotspots

Keywords typically highlight research ideas, while BKs reflect research frontiers and trends. Citespace captured BKs and

identified ME research frontiers; e.g., DME in 2021–2022. We forecast these words will highlight future research frontiers ME research.

DME represents retinal thickening or hard exudative deposition caused by extracellular fluid accumulation in the optic disc diameter, in the macular fovea. OCT image are important tools for diagnosing diabetic macular disease, and AI-related methods for identifying and segmenting disease related ME diabetes in OCT image are key modalities for clinicians who treat and screen diseases and help reduce medical costs.

When AI correlation methods were used to assess OCT images, ([Sunija et al., 2021](#); [Nazir et al., 2021](#); [Tayal et al., 2021](#); [Wu et al., 2021](#); [Atteia et al., 2021](#)) used DL to automatically recognize ME-related lesions in OCT images. Similarly, He et al. provided accurate image support for doctors when diagnosing ME by layering retinas in images.

[Sunija et al. \(2021\)](#) used a lightweight DL algorithms to determine if patients had DME from OCT images. The algorithm network comprised six deep CNN layers and had accuracy and recall rates of 99.69% and 99.69%, respectively.

[He Y. et al. \(2021\)](#) formulated a unified framework for segmenting structured layer surfaces which generated continuous structured and smooth layer surfaces, with ordered topology, in an end-to-end DL strategy. DME was effectively observed by layering the retinal surface, and generating sub-pixel surface positions in single feed-forward propagation with full connection layers, thereby improving segmentation accuracy.

[Nazir et al. \(2021\)](#) proposed an automatic DR and DME screening method. The algorithm used DenseNet-100 as the basic CNN architecture and was greatly improved. The approach also extracted representative information from low-intensity/noisy images and accurately classified them.

The diagnostic method by [Tayal et al. \(2021\)](#) automatically detected DME and used three different CNN models (five, seven, and nine layer approaches) to classify and recognize four eye diseases. The strategy generated high F1 scores, accuracy and sensitivity outputs, and greatly reduced detection times.

Wu et al. (2021) developed a DL model to detect morphological DME patterns based on OCT images using a VGG-16 network strategy. The model was trained using ME manifestations in OCT images (diffused retinal thickening, cystoid ME, and serous retinal detachment) and greatly facilitated disease diagnostics.

Atteia et al. (2021) formulated a transfer-based stacked autoencoder neural network system, which used four standard pre-training depth networks to extract information from small input datasets. With a maximum classification accuracy = 96.8% and specificity = 95.5%, the approach allowed clinicians to automatically detect and diagnose DME.

5 Conclusion

We performed a bibliometric investigation of ME research related to DL, machine learning, FCN, CNN, RNN, and other AI fields. We identified the ME knowledge base, future trends, and current research hotspots. The knowledge base included: retinal OCT fluid detection, convolutional network models, DL-based single-shot predictions, retinal vascular disease, DR, CNNs, automated macular pathology diagnosis, DARMD, class weight, and recent advances in DL architecture. DME was also identified as a future research trend and Frontier. The current research focuses on disease classification in OCT images, segmentation and segmentation of disease regions based on OCT images.

Our study had some limitations; we only identified studies between 2011 and 2022, therefore, some research may have been missed, thus we possibly and inadvertently introduced publication bias into our investigation which impacted our conclusion.

Data availability statement

The datasets presented in this study can be found in online repositories. The names of the repository/repositories and accession number(s) can be found in the article/[Supplementary Material](#).

References

- Abramoff, M. D., Lavin, P. T., Birch, M., Shah, N., and Folk, J. C. (2018). Pivotal trial of an autonomous AI-based diagnostic system for detection of diabetic retinopathy in primary care offices. *NPJ Digit. Med.* 1, 39. doi:10.1038/s41746-018-0040-6
- Abramoff, M. D., Lou, Y., Erginay, A., Clarida, W., Amelon, R., Folk, J. C., et al. (2016). Improved automated detection of diabetic retinopathy on a publicly available dataset through integration of deep learning. *Invest. Ophthalmol. Vis. Sci.* 57 (13), 5200–5206. doi:10.1167/iov.16-19964
- Aria, M., and Cuccurullo, C. (2017). Bibliometrix: An R-tool for comprehensive science mapping analysis. *J. Inf.* 11 (4), 959–975. doi:10.1016/j.joi.2017.08.007
- Atteia, G., Abdel Samee, N., and Zohair Hassan, H. (2021). DFTSA-Net: Deep feature transfer-based stacked autoencoder network for DME diagnosis. *Entropy (Basel)* 23 (10), 1251. doi:10.3390/e23101251
- Bogunovic, H., Venhuizen, F., Klimscha, S., Apostolopoulos, S., Bab-Hadiashar, A., Bagci, U., et al. (2019). Retouch: The retinal OCT fluid detection and segmentation benchmark and challenge. *IEEE Trans. Med. Imaging* 38 (8), 1858–1874. doi:10.1109/TMI.2019.2901398
- Cancino, C., Merigó, J. M., Coronado, F., Dessouky, Y., and Dessouky, M. (2017). Forty years of computers and industrial engineering: A bibliometric analysis. *Comput. Industrial Eng.* 113, 614–629. doi:10.1016/j.cie.2017.08.033
- Chang, C.-C., Lin, C.-J., McQuoid, D. R., Messer, D. F., Taylor, W. D., Singh, K., et al. (2011). Reduction of dorsolateral prefrontal cortex gray matter in late-life depression. *Psychiatry Res.* 193 (3), 1–6. doi:10.1016/j.psychres.2011.01.003
- Chen, C. (2004). Searching for intellectual turning points: Progressive knowledge domain visualization. *Proc. Natl. Acad. Sci. U. S. A.* 101, 5303–5310. doi:10.1073/pnas.0307513100
- Chiu, S. J., Allingham, M. J., Mettu, P. S., Cousins, S. W., Izatt, J. A., and Farsiu, S. (2015). Kernel regression based segmentation of optical coherence tomography images with diabetic macular edema. *Biomed. Opt. Express* 6 (4), 1172–1194. doi:10.1364/BOE.6.001172
- Dai, L., Wu, L., Li, H., Cai, C., Wu, Q., Kong, H., et al. (2021). A deep learning system for detecting diabetic retinopathy across the disease spectrum. *Nat. Commun.* 12 (1), 3242. doi:10.1038/s41467-021-23458-5
- Daruich, A., Matet, A., Moulin, A., Kowalczyk, L., Nicolas, M., Sellam, A., et al. (2018). Mechanisms of macular edema: Beyond the surface. *Prog. Retin Eye Res.* 63, 20–68. doi:10.1016/j.preteyeres.2017.10.006
- Das, V., Dandapat, S., and Bora, P. K. (2019). Multi-scale deep feature fusion for automated classification of macular pathologies from OCT images. *Biomed. Signal Process. Control* 54, 101605. doi:10.1016/j.bspc.2019.101605
- Ehlers, J. P., Jiang, A. C., Boss, J. D., Hu, M., Figueiredo, N., Babiuch, A., et al. (2019). Quantitative ultra-widefield angiography and diabetic retinopathy severity: An

Author contributions

WY, SZ, ZZ, HF, and YL conceived the research and designed the research method. HF and JC have prepared and standardized the contents and chapters. JC searched the references cited in the article. All authors contributed to the article and approved the submitted version.

Funding

Supported by the Shenzhen Fund for Guangdong Provincial High-level Clinical Key Specialties (SZGSP014), Sanming Project of Medicine in Shenzhen (SZSM202011015) and Shenzhen Science and Technology Planning Project (KCXFZ20211020163813019).

Conflict of Interest

The authors declare that the research was conducted in the absence of any commercial or financial relationships that could be construed as a potential conflict of interest.

Publisher's note

All claims expressed in this article are solely those of the authors and do not necessarily represent those of their affiliated organizations, or those of the publisher, the editors and the reviewers. Any product that may be evaluated in this article, or claim that may be made by its manufacturer, is not guaranteed or endorsed by the publisher.

Supplementary material

The Supplementary Material for this article can be found online at: <https://www.frontiersin.org/articles/10.3389/fcell.2023.1174936/full#supplementary-material>

- assessment of panretinal leakage index, ischemic index and microaneurysm count. *Ophthalmology* 126 (11), 1527–1532. doi:10.1016/j.optha.2019.05.034
- Eyre-Walker, A., and Stoletzki, N. (2013). The assessment of science: The relative merits of post-publication review, the impact factor, and the number of citations. *PLoS Biol.* 11 (10), e1001675. doi:10.1371/journal.pbio.1001675
- Figueiredo, N., Srivastava, S. K., Singh, R. P., Babiuch, A., Sharma, S., Rachitskaya, A., et al. (2020). Longitudinal panretinal leakage and ischemic indices in retinal vascular disease after aflibercept therapy: The PERMEATE study. *Ophthalmol. Retina* 4 (2), 154–163. doi:10.1016/j.oret.2019.09.001
- Gargeya, R., and Leng, T. (2017). Automated identification of diabetic retinopathy using deep learning. *Ophthalmology* 124 (7), 962–969. doi:10.1016/j.optha.2017.02.008
- Girish, G. N., Thakur, B., Chowdhury, S. R., Kothari, A. R., and Rajan, J. (2019). Segmentation of intra-retinal cysts from optical coherence tomography images using a fully convolutional neural network model. *IEEE J. Biomed. Health Inf.* 23 (1), 296–304. doi:10.1109/JBHI.2018.2810379
- Gu, J., Wang, Z., Kuen, J., Ma, L., Shahroudy, A., Shuai, B., et al. (2018). Recent advances in convolutional neural networks. *Pattern Recognit.* 77, 354–377. doi:10.1016/j.patcog.2017.10.013
- Gu, Z., Cheng, J., Fu, H., Zhou, K., Hao, H., Zhao, Y., et al. (2019). CE-Net: Context encoder network for 2D medical image segmentation. *IEEE Trans. Med. Imaging* 38 (10), 2281–2292. doi:10.1109/TMI.2019.2903562
- Gulshan, V., Peng, L., Coram, M., Stumpe, M. C., Wu, D., Narayanaswamy, A., et al. (2016). Development and validation of a deep learning algorithm for detection of diabetic retinopathy in retinal fundus photographs. *JAMA* 316 (22), 2402–2410. doi:10.1001/jama.2016.17216
- He, J., He, L., Geng, B., and Xia, Y. (2021a). Bibliometric analysis of the top-cited articles on unicompartmental knee arthroplasty. *J. Arthroplasty* 36 (5), 1810–1818.e3. doi:10.1016/j.arth.2020.11.038
- He, Y., Carass, A., Liu, Y., Jedynak, B. M., Solomon, S. D., Saidha, S., et al. (2021b). Structured layer surface segmentation for retina OCT using fully convolutional regression networks. *Med. Image Anal.* 68, 101856. doi:10.1016/j.media.2020.101856
- Hee, M. R., Puliafito, C. A., Wong, C., Duker, J. S., Reichel, E., Rutledge, B., et al. (1995). Quantitative assessment of macular edema with optical coherence tomography. *Arch. Ophthalmol.* 113 (8), 1019–1029. doi:10.1001/archophth.1995.01100080071031
- Huang, L., He, X., Fang, L., Rabbani, H., and Chen, X. (2019). Automatic classification of retinal optical coherence tomography images with layer guided convolutional neural network. *IEEE Signal Process. Lett.* 26 (7), 1026–1030. doi:10.1109/lsp.2019.2917779
- Huang, X., Liu, X., Shang, Y., Qiao, F., and Chen, G. (2020). Current trends in research on bone regeneration: A bibliometric analysis. *Biomed. Res. Int.* 2020, 8787394. doi:10.1155/2020/8787394
- Hwang, D. K., Hsu, C. C., Chang, K. J., Chao, D., Sun, C. H., Jheng, Y. C., et al. (2019). Artificial intelligence-based decision-making for age-related macular degeneration. *Theranostics* 9 (1), 232–245. doi:10.7150/thno.28447
- Kafieh, R., Rabbani, H., Abramoff, M. D., and Sonka, M. (2013). Intra-retinal layer segmentation of 3D optical coherence tomography using coarse grained diffusion map. *Med. Image Anal.* 17 (8), 907–928. doi:10.1016/j.media.2013.05.006
- Karri, S. P., Chakraborti, D., and Chatterjee, J. (2016). Learning layer-specific edges for segmenting retinal layers with large deformations. *Biomed. Opt. Express* 7 (7), 2888–2901. doi:10.1364/BOE.7.002888
- Karri, S. P., Chakraborty, D., and Chatterjee, J. (2017). Transfer learning based classification of optical coherence tomography images with diabetic macular edema and dry age-related macular degeneration. *Biomed. Opt. Express* 8 (2), 579–592. doi:10.1364/BOE.8.000579
- Kermany, D. S., Goldbaum, M., Cai, W., Valentim, C. C. S., Liang, H., Baxter, S. L., et al. (2018). Identifying medical diagnoses and treatable diseases by image-based deep learning. *Cell* 172 (5), 1122–1131. doi:10.1016/j.cell.2018.02.010
- Khan, M. S., Ullah, W., Riaz, I. B., Bhulani, N., Manning, W. J., Tridandapani, S., et al. (2016). Top 100 cited articles in cardiovascular magnetic resonance: A bibliometric analysis. *J. Cardiovasc. Magn. Reson.* 18 (1), 87. doi:10.1186/s12968-016-0303-9
- Lee, C. S., Tying, A. J., Deruyter, N. P., Wu, Y., Rokem, A., and Lee, A. Y. (2017). Deep-learning based, automated segmentation of macular edema in optical coherence tomography. *Biomed. Opt. Express* 8 (7), 3440–3448. doi:10.1364/BOE.8.003440
- Li, F., Chen, H., Liu, Z., Zhang, X.-d., Jiang, M.-s., Wu, Z.-z., et al. (2019a). Deep learning-based automated detection of retinal diseases using optical coherence tomography images. *Biomed. Opt. Express* 10 (12), 6204–6226. doi:10.1364/boe.10.006204
- Li, F., Chen, H., Liu, Z., Zhang, X., and Wu, Z. (2019b). Fully automated detection of retinal disorders by image-based deep learning. *Graefes Arch. Clin. Exp. Ophthalmol.* 257 (3), 495–505. doi:10.1007/s00417-018-04224-8
- Lu, D., Heisler, M., Lee, S., Ding, G. W., Navajas, E., Sarunic, M. V., et al. (2019). Deep-learning based multiclass retinal fluid segmentation and detection in optical coherence tomography images using a fully convolutional neural network. *Med. Image Anal.* 54, 100–110. doi:10.1016/j.media.2019.02.011
- Narotsky, D., Green, P. H., and Lebwohl, B. (2012). Temporal and geographic trends in celiac disease publications: A bibliometric analysis. *Eur. J. Gastroenterol. Hepatol.* 24 (9), 1071–1077. doi:10.1097/MEG.0b013e328355a4ab
- Nazir, T., Nawaz, M., Rashid, J., Mahum, R., Masood, M., Mehmood, A., et al. (2021). Detection of diabetic eye disease from retinal images using a deep learning based CenterNet model. *Sensors (Basel)* 21 (16), 5283. doi:10.3390/s21165283
- Porwal, P., Pachade, S., Kokare, M., Deshmukh, G., Son, J., Bae, W., et al. (2020). IDRiD: Diabetic retinopathy - segmentation and grading challenge. *Med. Image Anal.* 59, 101561. doi:10.1016/j.media.2019.101561
- Qiu, Y., Yang, W., Wang, Q., Yan, S., Li, B., and Zhai, X. (2018). Osteoporosis in postmenopausal women in this decade: A bibliometric assessment of current research and future hotspots. *Arch. Osteoporos.* 13 (1), 121. doi:10.1007/s11657-018-0534-5
- Rasti, R., Allingham, M. J., Mettu, P. S., Kavusi, S., Govind, K., Cousins, S. W., et al. (2020). Deep learning-based single-shot prediction of differential effects of anti-VEGF treatment in patients with diabetic macular edema. *Biomed. Opt. Express* 11 (2), 1139–1152. doi:10.1364/BOE.379150
- Rasti, R., Rabbani, H., Mehridehnavi, A., and Hajizadeh, F. (2018). Macular OCT classification using a multi-scale convolutional neural network ensemble. *IEEE Trans. Med. Imaging* 37 (4), 1024–1034. doi:10.1109/TMI.2017.2780115
- Rathke, F., Schmidt, S., and Schnorr, C. (2014). Probabilistic intra-retinal layer segmentation in 3-D OCT images using global shape regularization. *Med. Image Anal.* 18 (5), 781–794. doi:10.1016/j.media.2014.03.004
- Raumviboonsuk, P., Krause, J., Chotcomwongse, P., Sayres, R., Raman, R., Widner, K., et al. (2019). Deep learning versus human graders for classifying diabetic retinopathy severity in a nationwide screening program. *NPJ Digit. Med.* 2, 25. doi:10.1038/s41746-019-0099-8
- Roy, A. G., Conjeti, S., Karri, S. P. K., Sheet, D., Katouzian, A., Wachinger, C., et al. (2017). ReLayNet: Retinal layer and fluid segmentation of macular optical coherence tomography using fully convolutional networks. *Biomed. Opt. Express* 8 (8), 3627–3642. doi:10.1364/BOE.8.003627
- Schlegl, T., Waldstein, S. M., Bogunovic, H., Endstrasser, F., Sadeghipour, A., Philip, A. M., et al. (2018). Fully automated detection and quantification of macular fluid in OCT using deep learning. *Ophthalmology* 125 (4), 549–558. doi:10.1016/j.optha.2017.10.031
- Schmidt-Erfurth, U., Sadeghipour, A., Gerendas, B. S., Waldstein, S. M., and Bogunovic, H. (2018). Artificial intelligence in retina. *Prog. Retin Eye Res.* 67, 1–29. doi:10.1016/j.preteyeres.2018.07.004
- Seriwala, H. M., Khan, M. S., Shuaib, W., and Shah, S. R. (2015). Bibliometric analysis of the top 50 cited respiratory articles. *Expert Rev. Respir. Med.* 9 (6), 817–824. doi:10.1586/17476348.2015.1103649
- Singh, R. K., and Gorantla, R. (2020). DMENet: Diabetic macular edema diagnosis using hierarchical ensemble of CNNs. *PLoS One* 15 (2), e0220677. doi:10.1371/journal.pone.0220677
- Srinivasan, P. P., Heflin, S. J., Izatt, J. A., Arshavsky, V. Y., and Farsiu, S. (2014a). Automatic segmentation of up to ten layer boundaries in SD-OCT images of the mouse retina with and without missing layers due to pathology. *Biomed. Opt. Express* 5 (2), 348–365. doi:10.1364/BOE.5.000348
- Srinivasan, P. P., Kim, L. A., Mettu, P. S., Cousins, S. W., Comer, G. M., Izatt, J. A., et al. (2014b). Fully automated detection of diabetic macular edema and dry age-related macular degeneration from optical coherence tomography images. *Biomed. Opt. Express* 5 (10), 3568–3577. doi:10.1364/BOE.5.003568
- Sunija, A. P., Kar, S., S. G., Gopi, V. P., and Palanisamy, P. (2021). OctNET: A lightweight CNN for retinal disease classification from optical coherence tomography images. *Comput. Methods Programs Biomed.* 200, 105877. doi:10.1016/j.cmpb.2020.105877
- Tayal, A., Gupta, J., Solanki, A., Bisht, K., Nayyar, A., and Masud, M. (2021). DL-CNN-based approach with image processing techniques for diagnosis of retinal diseases. *Multimed. Syst.* 28 (4), 1417–1438. doi:10.1007/s00530-021-00769-7
- Ting, D. S. W., Cheung, C. Y., Lim, G., Tan, G. S. W., Quang, N. D., Gan, A., et al. (2017). Development and validation of a deep learning system for diabetic retinopathy and related eye diseases using retinal images from multiethnic populations with diabetes. *JAMA* 318 (22), 2211–2223. doi:10.1001/jama.2017.18152
- Ting, D. S. W., Pasquale, L. R., Peng, L., Campbell, J. P., Lee, A. Y., Raman, R., et al. (2019). Artificial intelligence and deep learning in ophthalmology. *Br. J. Ophthalmol.* 103 (2), 167–175. doi:10.1136/bjophthalmol-2018-313173
- Tsuji, T., Hirose, Y., Fujimori, K., Hirose, T., Oyama, A., Saikawa, Y., et al. (2020). Classification of optical coherence tomography images using a capsule network. *BMC Ophthalmol.* 20 (1), 114. doi:10.1186/s12886-020-01382-4
- Venhuizen, F. G., van Ginneken, B., Liefers, B., van Asten, F., Schreur, V., Fauser, S., et al. (2018). Deep learning approach for the detection and quantification of intraretinal cystoid fluid in multivendor optical coherence tomography. *Biomed. Opt. Express* 9 (4), 1545–1569. doi:10.1364/BOE.9.001545
- Wan, S., Liang, Y., and Zhang, Y. (2018). Deep convolutional neural networks for diabetic retinopathy detection by image classification. *Comput. Electr. Eng.* 72, 274–282. doi:10.1016/j.compeleceng.2018.07.042
- Wu, Q., Zhang, B., Hu, Y., Liu, B., Cao, D., Yang, D., et al. (2021). Detection of morphologic patterns of diabetic macular edema using a deep learning approach based on optical coherence tomography images. *Retina* 41 (5), 1110–1117. doi:10.1097/IAE.0000000000002992



OPEN ACCESS

EDITED BY

Yanwu Xu,
Baidu, China

REVIEWED BY

Yi Shao,
Nanchang University, China
Wei Lin,
Shandong Academy of Medical Sciences
(SDAMS), China
Qi Zhang,
The First Affiliated Hospital of Chongqing
Medical University, China

*CORRESPONDENCE

Liang Hu,
✉ huliang@eye.ac.cn,
Wei Chen,
✉ chenweimd@wmu.edu.cn,
Qinxiang Zheng,
✉ qinxiangzheng@wmu.edu.cn

[†]These authors have contributed equally
to this work

RECEIVED 03 April 2023

ACCEPTED 07 June 2023

PUBLISHED 15 June 2023

CITATION

Huang B, Fei F, Wen H, Zhu Y, Wang Z,
Zhang S, Hu L, Chen W and Zheng Q
(2023), Impacts of gender and age on
meibomian gland in aged people using
artificial intelligence.
Front. Cell Dev. Biol. 11:1199440.
doi: 10.3389/fcell.2023.1199440

COPYRIGHT

© 2023 Huang, Fei, Wen, Zhu, Wang,
Zhang, Hu, Chen and Zheng. This is an
open-access article distributed under the
terms of the [Creative Commons
Attribution License \(CC BY\)](#). The use,
distribution or reproduction in other
forums is permitted, provided the original
author(s) and the copyright owner(s) are
credited and that the original publication
in this journal is cited, in accordance with
accepted academic practice. No use,
distribution or reproduction is permitted
which does not comply with these terms.

Impacts of gender and age on meibomian gland in aged people using artificial intelligence

Binge Huang^{1†}, Fangrong Fei^{2†}, Han Wen¹, Ye Zhu¹,
Zhenzhen Wang¹, Shuwen Zhang¹, Liang Hu^{1*}, Wei Chen^{1*} and
Qinxiang Zheng^{1*}

¹School of Ophthalmology and Optometry, Eye Hospital, Wenzhou Medical University, Wenzhou, China,

²Zhejiang Provincial Center for Disease Control and Prevention, Hangzhou, China

Purpose: To evaluate the effects of age and gender on meibomian gland (MG) parameters and the associations among MG parameters in aged people using a deep-learning based artificial intelligence (AI).

Methods: A total of 119 subjects aged ≥ 60 were enrolled. Subjects completed an ocular surface disease index (OSDI) questionnaire, received ocular surface examinations including Meibography images captured by Keratograph 5M, diagnosis of meibomian gland dysfunction (MGD) and assessment of lid margin and meibum. Images were analyzed using an AI system to evaluate the MG area, density, number, height, width and tortuosity.

Results: The mean age of the subjects was 71.61 ± 7.36 years. The prevalence of severe MGD and meibomian gland loss (MGL) increased with age, as well as the lid margin abnormalities. Gender differences of MG morphological parameters were most significant in subjects less than 70 years old. The MG morphological parameters detected by AI system had strong relationship with the traditional manual evaluation of MGL and lid margin parameters. Lid margin abnormalities were significantly correlated with MG height and MGL. OSDI was related to MGL, MG area, MG height, plugging and lipid extrusion test (LET). Male subjects, especially the ones who smoke or drink, had severe lid margin abnormalities, and significantly decreased MG number, height, and area than the females.

Conclusion: The AI system is a reliable and high-efficient method for evaluating MG morphology and function. MG morphological abnormalities developed with age and were worse in the aging males, and smoking and drinking were risk factors.

KEYWORDS

meibomian glands, meibomian gland dysfunction, meibography, artificial intelligence, aging

1 Introduction

Meibomian gland dysfunction (MGD) is a chronic and diffuse disease in the meibomian glands (MG), which is the major type of evaporative dry eye disease (DED) and commonly seen in eye clinic. It is characterized by terminal duct obstruction with or without the abnormality of the glandular secretion, and usually accompanied by different levels of meibomian gland loss (MGL) (Nelson et al., 2011). Among the diverse intrinsic and external factors contributing to MGD, aging is a major one due to the development of meibomian glands atrophy with structural and functional abnormalities (Schaumborg et al.,

2011; Yeotikar et al., 2016; Arita et al., 2017). Furthermore, the sex hormone receptor has been found in ocular surface, through which sex hormone regulates metabolism, gene expression and tear secretion (Schirra et al., 2005; Suzuki et al., 2008; Versura et al., 2015). Some population-based studies have found that the prevalence of MGD in males is higher than that in females at any age (Viso et al., 2011; Siak et al., 2012; Hashemi et al., 2017; Hashemi et al., 2021). And abnormal lid margin and MG morphology are more common in aging males (Den et al., 2006). The effect of hormones on the ocular surface is still controversial, since the deficiency of estrogen promotes the occurrence of dry eye disease in females (Grasso et al., 2021; Hat et al., 2023). To analyze the influence of gender on the MGs, we evaluated the MG morphology and MGL level of different genders in the current study, and the risk factors of smoking and drinking were also taken into consideration.

At present, there has been many studies on MGD in the elderly, but few on the changes of MG parameters. Nowadays the clinical diagnosis of MGD still lacks objective evaluations, and depends on the subjective judgment. Recently, the technology of meibography has been constantly developed, and is able to provide objective means to evaluate MG status using artificial intelligence (AI) (Adil et al., 2019; Deng et al., 2021; Xiao et al., 2021; Liu et al., 2022; Zhang et al., 2022). In order to obtain objective results, we evaluated the relationship of MG parameters identified by AI with age and gender in the current study. We enrolled the aged people on a hospital-based group. After collecting meibography and eye surface examination, the deep learning model developed in our early study (Liu et al., 2022; Zhang et al., 2022) was used to identify gland parameters, including gland area, area density, number, height, width and tortuosity. The associations between AI-reported MG parameters and traditional values of MGL, lid margin abnormalities were assessed, as well as the age and gender effects on MGD.

2 Materials and methods

2.1 Subjects

In this prospective cross-sectional study, a total of 119 subjects aged at ≥ 60 years were recruited from the outpatient department of the Eye Hospital of Wenzhou Medical University between September 2020 and May 2021. The exclusion criteria included: ocular or systemic diseases associated with dry eye disease such as Sjögren's syndrome, graft *versus* host disease, collagen angiopathy, except MGD; any active eye disease such as infection and acute glaucoma; a previous history of ophthalmologic surgery; structure abnormality of the eyelid, conjunctiva and cornea; history of contact lens wear within 6 months; history of systemic or ocular medication treatment within 6 months such as hormones, antiallergic drugs, immunosuppressants, except artificial tears without preservatives. The whole procedure of the study was approved by the Institutional Review Board of Wenzhou Medical University and adhered to the tenets of the Declaration of Helsinki (No. 2020-096-K-83), and the written informed consent was obtained from all subjects before participating in the study.

All the subjects were examined by Bing Huang. Only the right eyes were evaluated. The examinations were conducted in sequence: 1) completing an ocular surface disease index (OSDI) questionnaire; 2) noninvasive meibography by Keratograph 5M (K5M; Oculus Optikgeräte GmbH, Wetzlar, Germany); 3) slit-lamp biomicroscopy including diagnosis and staging of MGD and assessment of lid margin and meibum.

2.2 Diagnosis and staging of MGD

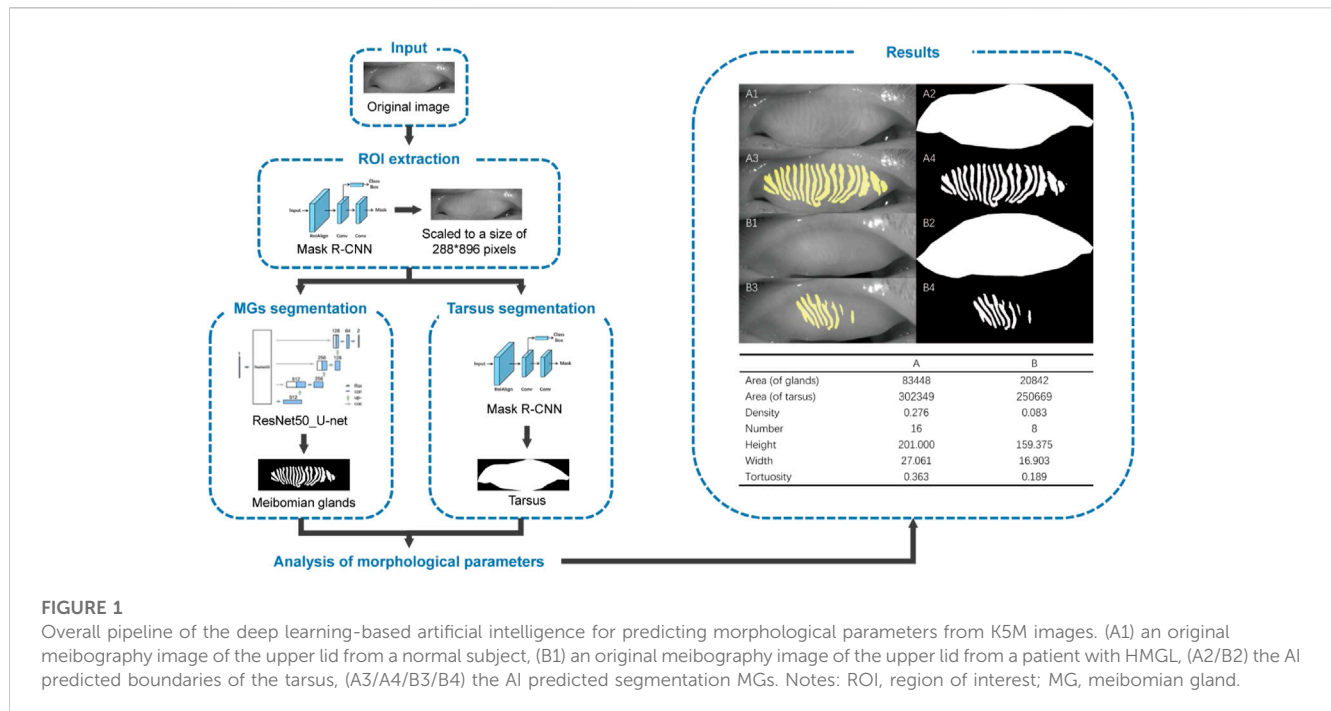
The subjects were diagnosed with normal, asymptomatic MGD and MGD based on the "Expert consensus of diagnosis and treatment of meibomian gland dysfunction in China (2017)" (China branch of Asian dry eye Association et al., 2017), in which subjects with asymptomatic MGD were not diagnosed as MGD. Patients with MGD were divided into 3 stages according to condition of lid margin, meibomian gland orifices and meibum based on the clinical judgment of the same ophthalmologist.

2.3 Meibography collection and MG parameters detection

Meibography images of the upper and lower lids were conducted by the noncontact infrared camera system in the K5M. The MGL score was graded according to the meibography results as 0 (no loss of meibomian glands), 1 (area loss was less than one third of the total meibomian gland area), 2 (area loss was between one third and two thirds), and 3 (area loss was more than two thirds). Both of the upper and lower lid were examined and the total summing score was used for analysis. And the participants were then divided into two groups depending on the score of MGL: the low MGL group (LMGL) with meiboscore <3 , and the high MGL group (HMGL) with meiboscore ≥ 3 . Images of upper lid were analyzed based on a novel MG morphology analytic system we developed recently (Zhang et al., 2022). This AI system automatically segmented MGs and quantitatively analyzed the MGs' morphological features (gland area, density, number, height, width and tortuosity).

2.4 Lid margin and meibum assessment

The lid margin and meibum examinations were conducted according to the Arita R et al.'s grading methods (Arita et al., 2016). Lid margin telangiectasia was graded as 0 (no sign of telangiectasia), 1 (mild sign), 2 (moderate sign affecting $<1/2$ of the lid margin) and 3 (severe sign affecting $\geq 1/2$ of the lid margin). Lid margin irregularity on the mucocutaneous junction was graded as 0 (marx line (ML) does not touch the meibomian orifice (MO)), 1 (parts of ML touch MOs), 2 (ML crosses MOs), 3 (ML touches the lid margin side of MOs). Lid margin thickness was assessed as 0 (no thickening), 1 (mild thickening) and 2 (severe thickening). MO plugging was graded as 0 (no sign of plugging), 1 (mild covering on the MOs), 2 (moderate plugging and hunch), 3 (severe plugging or atrophy). Lipid extrusion test (LET) was used to evaluate the degree of ease with which meibum could be expressed and the scores of LET at the central area of both upper and lower lid were added together:



grade 0, clear meibum readily expressed; grade 1, cloudy meibum expressed with mild pressure; grade 2, cloudy meibum expressed with more than moderate pressure; 3, meibum could not be expressed even with strong pressure (Shimazaki et al., 1998). The meibum quality from the 8 MOs at the central area of the lower lid was assessed: grade 0, clear meibum expressed with digital pressure; grade 1, cloudy meibum expressed; grade 2, cloudy meibum expressed with granules; 3, thick meibum expressed. The scores of the 8 MOs were summed for analysis.

2.5 Statistical analysis

Statistical analysis was performed using the SPSS statistics 26.0 (IBM corp., Armonk, NY, USA). Values were expressed as the mean \pm standard deviation (SD) or range or median (interquartile range [IQR]). Normal distribution of data was tested using Shapiro Wilk test. Independent sample *t*-test and one-way ANOVA with LSD correction were used for comparison when the variance was homogeneous, or otherwise the Mann-Whitney U rank test. Spearman correlation analysis was conducted to evaluate the strengths of correlation between the parameters. Differences in prevalence among categorical variables were compared using the Chi Square test. Two-tailed $p < 0.05$ was considered as a statistically significant difference.

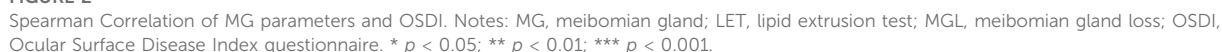
3 Results

A total of 119 aging subjects (119 eyes; 46 males, 73 females) were identified. The mean age of the participants was 71.61 ± 7.36 (mean \pm standard deviation) years (range: 60–89 years). 95.8% subjects were initially diagnosed with dry eye syndrome based on

the OSDI score (26.98 ± 10.27 points) (Grubbs et al., 2014). There was no significant difference between genders (male: 26.780 ± 12.220 , female: 27.110 ± 8.905 , $p = 0.873$) in OSDI score. Figure 1 shows the workflow of the deep learning model for predicting morphological parameters from K5M images and provides two typical cases of predicted meibomian gland segmentation and parameters estimation for the upper lids. The tarsus segmentation model was based on Mask R-CNN (He et al., 2020). The ResNet50_U-net was reported previously (Zhang et al., 2022).

3.1 The associations between MG parameters

The correlations between the AI reported meibomian gland morphology parameters (MG area, density, number, height, width and tortuosity), lid margin parameters (telangiectasia, irregularity, thickening, plugging and LET), meibum score, MGL and OSDI score were evaluated (Figure 2). Among the MG morphology parameters, the MG height showed the strongest correlation with all the lid margin parameters ($r < -0.212$, $p < 0.020$); MG area was relevant with plugging ($r = -0.19$, $p = 0.038$); MG density was relevant with irregularity ($r = -0.185$, $p = 0.044$), thickening ($r = -0.165$, $p = 0.008$) and LET ($r = -0.164$, $p = 0.032$). OSDI score had relations with MGL ($r = 0.261$, $p = 0.004$), MG area ($r = -0.205$, $p = 0.025$), MG height ($r = -0.233$, $p = 0.011$), plugging ($r = 0.255$, $p = 0.005$) and LET ($r = 0.240$, $p = 0.009$), but not significant with MG density ($r = -0.170$, $p = 0.064$). Furthermore, we found MGL were highly correlated with MG area ($r = -0.686$, $p < 0.001$), density ($r = -0.689$, $p < 0.001$), number ($r = -0.531$, $p < 0.001$), height ($r = -0.707$, $p < 0.001$), tortuosity ($r = 0.193$, $p = 0.036$), telangiectasia ($r = 0.262$, $p = 0.004$), irregularity ($r = 0.368$,



	60-69 (N = 52)	70-79 (N = 50)	80-89 (N = 17)	R	P
Morphological parameters					
Area	44580.596 ± 20039.422	43229.740 ± 22284.460	33976.235 ± 21592.014	−0.100	0.280
Density	0.154 ± 0.065	0.140 ± 0.068	0.127 ± 0.073	−0.102	0.269
Number	15.620 ± 3.986	14.880 ± 5.583	12.120 ± 5.555	−0.208	0.023
Height	134.103 ± 36.834	131.940 ± 45.13	116.180 ± 39.801	−0.113	0.220
Width	20.072 ± 3.899	20.897 ± 3.822	21.446 ± 4.360	0.145	0.116
Tortuosity	0.312 ± 0.071	0.321 ± 0.166	0.280 ± 0.070	−0.078	0.396
Lid margin abnormality parameters					
Telangiectasia	0.870 ± 0.627	1.460 ± 0.908	1.410 ± 0.795	0.229	0.012
Irregularity	0.730 ± 1.012	1.180 ± 0.873	1.290 ± 1.105	0.341	<0.001
Thickening	0.250 ± 0.519	0.600 ± 0.670	0.470 ± 0.514	0.266	0.003
Plugging	0.750 ± 0.837	1.280 ± 1.031	1.650 ± 1.115	0.291	0.001
LET	1.400 ± 1.287	1.500 ± 1.298	1.060 ± 1.435	−0.020	0.831
Others					
Meibum Score	9.310 ± 5.147	9.420 ± 5.897	11.880 ± 5.611	0.114	0.215
MGL	2.810 ± 1.522	3.380 ± 1.772	3.530 ± 1.700	0.235	0.010

frontiersin.org

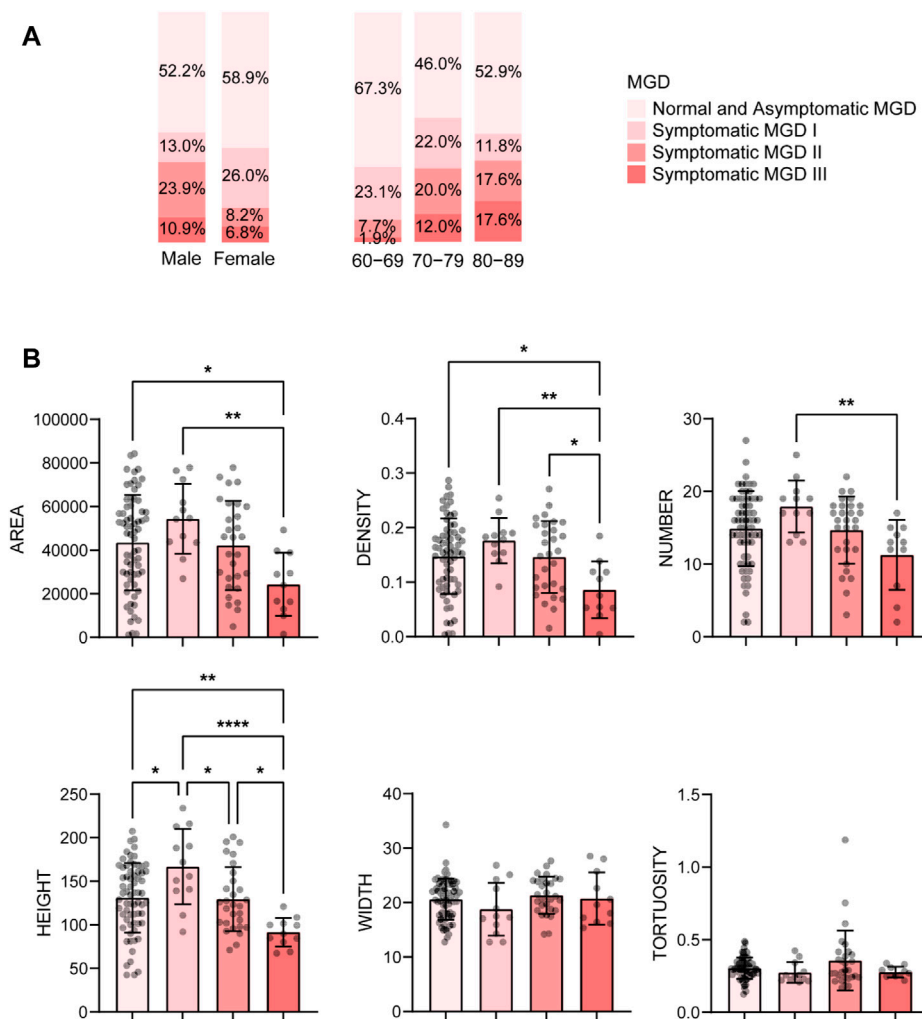


FIGURE 3

Percent of different severity of MGD in different gender and age groups (A) and mean \pm standard deviation of MG morphological parameters in each severity group (B). Notes: MGD, meibomian gland dysfunction. * $p < 0.05$; ** $p < 0.01$; *** $p < 0.001$; **** $p < 0.0001$.

$p < 0.001$), thickening ($r = 0.301$, $p < 0.001$), plugging ($r = 0.374$, $p < 0.001$), LET ($r = 0.300$, $p < 0.001$), meibum score ($r = 0.208$, $p = 0.023$). Thus, AI system is able to output reliable MG morphology parameters, which have strong association with the traditional manual evaluation of MGL and lid margin parameters but are more efficient and objective.

3.2 Age was a risk factor for MGD and MGL

Among the meibomian gland parameters, the number of MGs degenerated with age significantly, which decreased from 15.62 ± 3.99 in subjects aged 60-69 years to 12.12 ± 5.56 in those aged 80-89 years ($r = -0.208$, $p = 0.023$) (Table 1). And the MGL level and parameters of the lid margin including the telangiectasia, irregularity, thickening and plugging, also aggravated with age with significant correlations ($r \geq 0.229$, $p \leq 0.012$) (Table 1).

With age grows, the severity of MGD increases. The percentage of severe MGD (level II and III) was highest in subjects aged 80-

89 years (9.6% in 60-69, 32.0% in 70-79, 35.2% in 80-89, see Figure 3A), and the MG parameters including gland area, density, number and height, decreased with the MGD level increased (Figure 3B). Besides, there was a strong correlation between MGD severity and age ($r = 0.350$, $p < 0.001$), and the proportion of HMGL subjects also increased with age (Figure 4A). The mean age of patients with LMGL was 69.49 ± 6.61 , and the mean age of patients with HMGL was 73.1 ± 7.54 ($p = 0.008$). And the gland area, density, number and height, were much lower in HMGL subjects than the LMGL group ($p < 0.001$) (Figure 4B).

3.3 MG morphology differs in aging males and females

AI found that there were significant differences in MG number, height, and area between the aging males and females, and the values were all much lower in the male group ($p < 0.001$) (Figure 5). Correspondingly, the MGL and lid margin parameters including

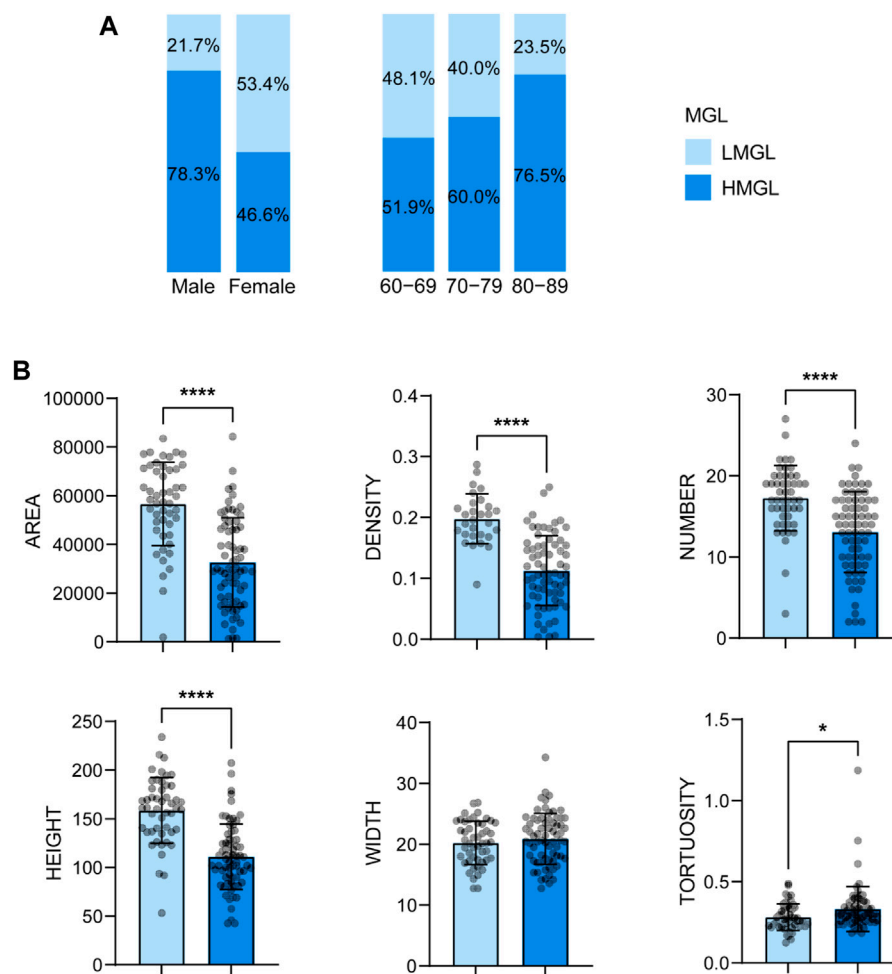


FIGURE 4
Percent of HMGL and LMGL in different gender and age groups (A) and mean \pm standard deviation of MG morphological parameters in each severity group (B). Notes: MGL, meibomian gland loss; LMGL, low MGL; HMGL, high MGL. * $p < 0.05$; ** $p < 0.01$; *** $p < 0.001$; **** $p < 0.0001$.

telangiectasia, irregularity, thickening, plugging, were also severely higher in the males ($p \leq 0.034$) (Figure 5). Among the 46 male subjects, 22 (47.8%) were diagnosed with MGD, of which 34.8% were moderate or severe; of the 73 female subjects, 30 (41.1%) were MGD, in which 15.0% were moderate or severe (Figure 3A). The severity of male MGD was significantly higher than that of female (Chi square test: $\chi^2 = 7.899$, $p = 0.048$). These results demonstrated that the MG morphology and function were significantly worse in aging males compared with the females. And with the severity of MGD increases, the AI reported values of MG area, density, number and height decreases significantly ($p < 0.05$).

Besides, the ratio of HMGL subjects was much higher in males (36/46, 78.26%) than that in the females (34/73, 46.6%) (Chi square test: $\chi^2 = 11.696$, $p = 0.001$) (Figure 4A). And in different age groups, the differences in MG morphology, lid margin parameters and MGL level were significant between the males and females, and they were the most marvelous in the 70-79 years age groups (Figure 6).

Then we found that smoking and drinking were both risk factors associated with the worse MG presentations in the males. The aging males who smoke showed significant higher levels of lid margin

thickening ($p = 0.006$) and plugging ($p < 0.001$), and the ones who drinks presented greater meibum score ($p = 0.006$) (Figure 7).

4 Discussion

Although many standardized grading scales have been developed to assess the morphology severity of MGs at present (Arita et al., 2009; Daniel et al., 2019; Wang et al., 2022), the scores are based on the subjective judgment of the examiner. AI has been found of excellent accuracy, efficiency and consistency to evaluate MG parameters, helping to diagnosis and even preclinical diagnosis of MGD (Fasanella et al., 2016; Xiao et al., 2021; Zhang et al., 2021). The current study explored the influence of age and gender on MG morphology and correlations among MG parameters in the elderly based on an AI system.

Recently, the development and combination of meibography and AI technology have provided the possibility for objective and efficient identification of MG parameters (Deng et al., 2021). K5M is a non-invasive infrared meibography used routinely in clinical to evaluate

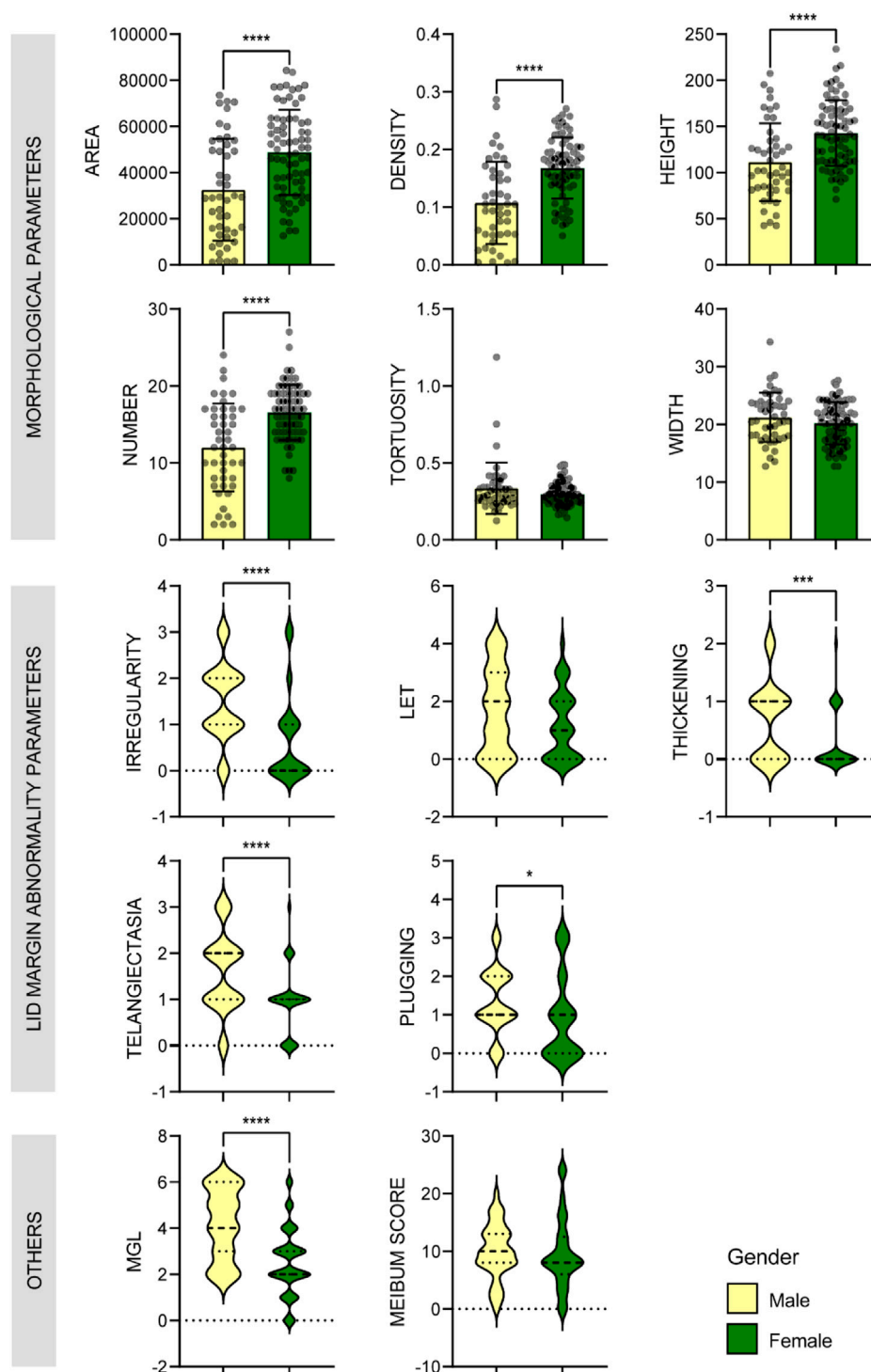


FIGURE 5

Comparison of MG parameters between male and female groups. Bar plots with mean \pm standard deviation were used to show scale variables and violin plots were used to show ordinal variables. * $p < 0.05$; ** $p < 0.01$; *** $p < 0.001$; **** $p < 0.0001$.

morphology of MGs. It could generate the MG results in 1 min without any discomfort. Koh et al. (Koh et al., 2012) firstly reported an algorithm to output MG results from K5M images in 2012, incorporating a deep learning model to differentiate healthy and unhealthy MGs to help diagnoses of MGD. Nowadays AI has been

consistently developed and is able to detect various MG parameters and minimize the influence of artifacts (Maruoka et al., 2020; Deng et al., 2021). In the current study, we applied a deep learning model, which was reported previously (Liu et al., 2022; Zhang et al., 2022) to segment MGs from images and compute MG parameters. The

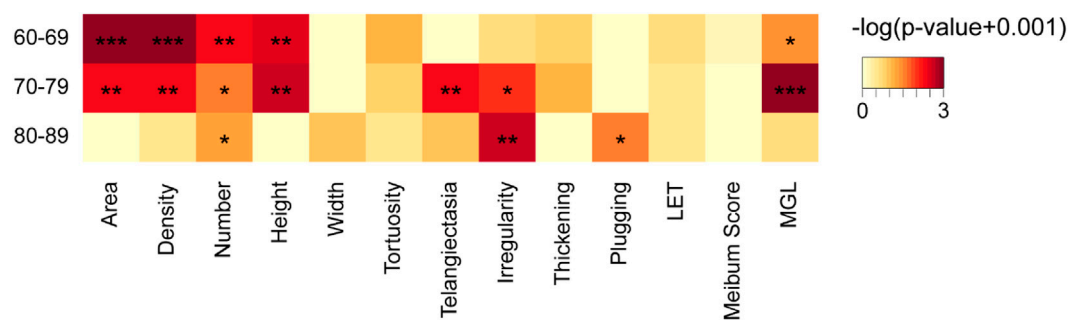


FIGURE 6

Comparison of meibomian gland and ocular surface parameters of males and females in different age groups. * $p < 0.05$; ** $p < 0.01$; *** $p < 0.001$.

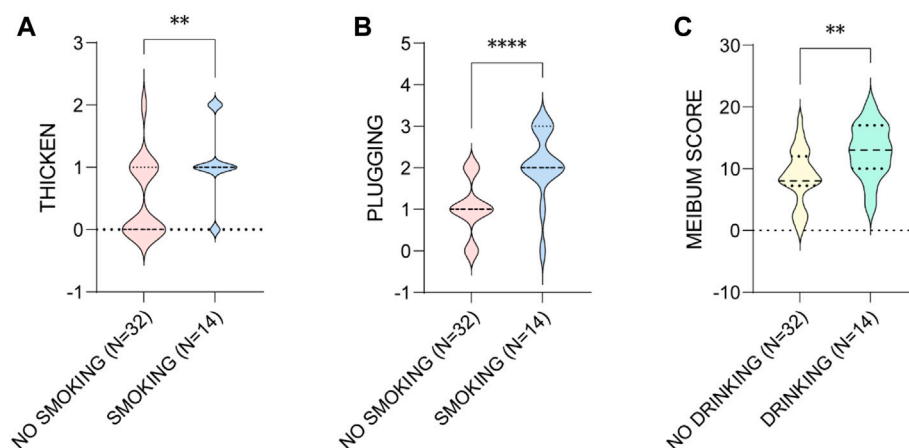


FIGURE 7

The influence of smoking on the (A) thickening of MGs and (B) the plugging of MOs, and (C) drinking on the meibum score in aging males. * $p < 0.05$; ** $p < 0.01$; *** $p < 0.001$; **** $p < 0.0001$.

proposed MG density can diagnose MGD with high sensitivity and specificity. The results show that the area, density, number and height of MGs present strong negative correlation coefficient with the subjective parameter of MGL, indicating that the AI generated MG parameters are reliable consistent with the traditional evaluation of MGL. In addition, the values of MG area, density, number and height were uniformly associated with the severity of MGD. However, there was a discrepancy in our results that the MG morphological parameters of normal and asymptomatic MGD group were lower than those of mild MGD group. It was possible that some patients with significant abnormal morphology of MG or MGL, may report no symptoms and were diagnosed as non-MGD.

The decreases in MG height, width and number lead to MGL, and lid margin abnormalities are also associated with MGL development (Arita et al., 2008; Ha et al., 2021). Our results found that, lid margin telangiectasia, irregularity, thickening, plugging and LET were significantly correlated with MG height and MGL level but not MG width or number, demonstrating that the MG height might be more sensitive to reflect MGL in patients with abnormal lid margin. In addition, we found MG density may have

higher correlation with the change of lid margin parameters than MG area. These results indicate that the MG height and density have more clinical significance than other parameters, and may be helpful for the diagnosis and severity assessment of MGD.

The OSDI is a 12-item questionnaire designed to assess ocular symptoms related to dry eye disease and their effect on vision function. Our results found that OSDI was associated to MGL, MG area, MG height, lid margin plugging and LET. However, it was of no difference between the males and females, but the MG parameters and the severity of MGD and MGL were significantly different between them. The reasons for these discrepancies are unclear. Daniel et al. (Daniel et al., 2019, Daniel et al., 2020) found no morphological features of MG related to OSDI in patients with moderate to severe dry eye disease. Adil et al. (Adil et al., 2019) also found OSDI did not correlate with any MG morphologic parameter in MGD patients, however the OSDI at different meibogrades had statistical differences. Their results were not contradictory to ours on the base of different design and subjects.

Sex hormones modulate gene expression in MGs and play an important role in ocular surface health (Schirra et al., 2005; Suzuki

et al., 2008). Epidemiological data shows the prevalence rates of MGD ranging from 39% to 68% in Asia, and mainly in the elderly and male (Siak et al., 2012; Alghamdi et al., 2016; Hashemi et al., 2017). In the current study, the prevalence of symptomatic MGD and HMGL in aging males were much higher than that in the females. And most of the MG parameters of aging males were worse than those of the females. Studies have shown that androgens promote meibum secretion, which leads to higher incidence of dry eye disease in women and obstructive MGD in older men (Schirra et al., 2005). The effect of estrogen on the ocular surface is still controversial. It is generally accepted that excessive exposure and deficiency of estrogen promote the occurrence of dry eye disease (Schirra et al., 2009; Versura et al., 2015). So we speculated that the habits of smoking and drinking may play a more important role on MGD and MGL development, since the subjects who smoke in the male group had significant higher levels of lid margin thickening and plugging, and the ones who drinks had greater meibum score. None of the females in the current study had the habit of smoking or drinking. Similarly, it was reported that smoking index was significantly correlated with the scores of lid margin abnormality and meibum (Wang et al., 2016), and smoking is associated with dry eye and MGD (Carreira et al., 2022).

Several previous studies have reported the prevalence of MGD increases with age (Siak et al., 2012; Alghamdi et al., 2016; Hashemi et al., 2017), which was consistent with our results. And in the aging people over 60 years old, MG function became severely worse with age climbs, especially for the lid margin abnormalities, MGL level and MG number, which was in accordance with previous reports (Arita et al., 2008; Ban et al., 2013). In addition, the sample size of the current study could be enlarged in the following investigations to exert stronger conclusions, and we aim to improve the AI system to reduce the impact of artifacts and exploring more MG parameters of clinical value in the next step.

Collectively, the AI system is a reliable and fast method for evaluating MG parameters. Using this method, we found gender and age influenced various MG parameters, and were risk factors for the health of MGs in the elderly.

Data availability statement

The raw data supporting the conclusions of this article will be made available by the authors, without undue reservation.

References

- Adil, M. Y., Xiao, J., Olafsson, J., Chen, X., Lagali, N. S., Raeder, S., et al. (2019). Meibomian gland morphology is a sensitive early indicator of meibomian gland dysfunction. *Am. J. Ophthalmol.* 200, 16–25. doi:10.1016/j.ajo.2018.12.006
- Alghamdi, Y. A., Mercado, C., McClellan, A. L., Batawi, H., Karp, C. L., and Galor, A. (2016). Epidemiology of meibomian gland dysfunction in an elderly population. *Cornea* 35 (6), 731–735. doi:10.1097/ico.0000000000000815
- Arita, R., Fukuoka, S., and Morishige, N. (2017). New insights into the morphology and function of meibomian glands. *Exp. Eye Res.* 163, 64–71. doi:10.1016/j.exer.2017.06.010
- Arita, R., Itoh, K., Inoue, K., and Amano, S. (2008). Noncontact infrared meibography to document age-related changes of the meibomian glands in a normal population. *Ophthalmology* 115 (5), 911–915. doi:10.1016/j.ophtha.2007.06.031
- Arita, R., Itoh, K., Maeda, S., Maeda, K., Furuta, A., Fukuoka, S., et al. (2009). Proposed diagnostic criteria for obstructive meibomian gland dysfunction. *Ophthalmology* 116 (11), 2058–2063. doi:10.1016/j.ophtha.2009.04.037
- Arita, R., Minoura, I., Morishige, N., Shirakawa, R., Fukuoka, S., Asai, K., et al. (2016). Development of definitive and reliable grading scales for meibomian gland dysfunction. *Am. J. Ophthalmol.* 169, 125–137. doi:10.1016/j.ajo.2016.06.025
- Ban, Y., Shimazaki-Den, S., Tsubota, K., and Shimazaki, J. (2013). Morphological evaluation of meibomian glands using noncontact infrared meibography. *Ocul. Surf.* 11 (1), 47–53. doi:10.1016/j.jtos.2012.09.005
- Carreira, A. R., Rodrigues-Barros, S., Silva, J. C., de Almeida, M. F., Machado, I., Cardoso, J. N., et al. (2022). Tobacco effects on ocular surface, meibomian glands, and corneal epithelium and the benefits of treatment with a lipid-based lubricant. *Graefes Arch. Clin. Exp. Ophthalmol.* 261, 171–184. doi:10.1007/s00417-022-05778-4

Ethics statement

The studies involving human participants were reviewed and approved by Wenzhou Medical University. The patients/participants provided their written informed consent to participate in this study. Written informed consent was obtained from the individual(s) for the publication of any potentially identifiable images or data included in this article.

Author contributions

BH and FF: Conceptualization, Methodology, Investigation, Formal Analysis, Writing–Original Draft; HW: Data Curation, Writing–Original Draft; YZ: Methodology; ZW: Formal Analysis; SZ: Visualization; LH: Resources, Supervision, Writing–Review and Editing; WC: Funding Acquisition, Supervision; QZ: Conceptualization, Resources, Supervision, Writing–Review and Editing. All authors contributed to the article and approved the submitted version.

Acknowledgments

We thank Mr. Qi Dai from the Eye Hospital of Wenzhou Medical University for his technical assistance with the deep learning model.

Conflict of interest

The authors declare that the research was conducted in the absence of any commercial or financial relationships that could be construed as a potential conflict of interest.

Publisher's note

All claims expressed in this article are solely those of the authors and do not necessarily represent those of their affiliated organizations, or those of the publisher, the editors and the reviewers. Any product that may be evaluated in this article, or claim that may be made by its manufacturer, is not guaranteed or endorsed by the publisher.

- China branch of Asian dry eye Association Ocular Surface Tear Disease Group of Ophthalmology Specialized Committee of the Cross-Strait Medical Exchange Association (2017). Expert consensus of diagnosis and treatment of meibomian gland dysfunction in China (2017). *Chin. J. Ophthalmol.* 53, 657–661.
- Daniel, E., Maguire, M. G., Pistilli, M., Bunya, V. Y., Massaro-Giordano, G. M., Smith, E., et al. (2019). Grading and baseline characteristics of meibomian glands in meibography images and their clinical associations in the Dry Eye Assessment and Management (DREAM) study. *Ocul. Surf.* 17 (3), 491–501. doi:10.1016/j.jtos.2019.04.003
- Daniel, E., Pistilli, M., Ying, G. S., Bunya, V. Y., Massaro-Giordano, M., Asbell, P. A., et al. (2020). Association of meibomian gland morphology with symptoms and signs of dry eye disease in the Dry Eye Assessment and Management (DREAM) study. *Ocul. Surf.* 18 (4), 761–769. doi:10.1016/j.jtos.2020.07.014
- Den, S., Shimizu, K., Ikeda, T., Tsubota, K., Shimmura, S., and Shimazaki, J. J. C. (2006). Association between meibomian gland changes and aging, sex, or tear function. *Cornea* 25 (6), 651–655. doi:10.1097/01.icc.0000227889.11500.6f
- Deng, Y., Wang, Q., Luo, Z., Li, S., Wang, B., Zhong, J., et al. (2021). Quantitative analysis of morphological and functional features in meibography for meibomian gland dysfunction: Diagnosis and grading. *EClinicalMedicine* 40, 101132. doi:10.1016/j.eclinm.2021.101132
- Fasanella, V., Agnifili, L., Mastropasqua, R., Brescia, L., Di Staso, F., Ciancaglini, M., et al. (2016). *In vivo* laser scanning confocal microscopy of human meibomian glands in aging and ocular surface diseases. *Biomed. Res. Int.* 2016, 7432131. doi:10.1155/2016/7432131
- Grasso, A., Di Zazzo, A., Giannaccare, G., Sung, J., Inomata, T., Shih, K. C., et al. (2021). Sex hormones related ocular dryness in breast cancer women. *J. Clin. Med.* 10 (12), 2620. doi:10.3390/jcm10122620
- Grubbs, J. R., Jr., Tolleson-Rinehart, S., Huynh, K., and Davis, R. M. (2014). A review of quality of life measures in dry eye questionnaires. *Cornea* 33 (2), 215–218. doi:10.1097/ico.0000000000000038
- Ha, M., Kim, J. S., Hong, S. Y., Chang, D. J., Whang, W. J., Na, K. S., et al. (2021). Relationship between eyelid margin irregularity and meibomian gland dropout. *Ocul. Surf.* 19, 31–37. doi:10.1016/j.jtos.2020.11.007
- Hashemi, H., Asharilous, A., Aghamirsalim, M., Yekta, A., Pourmatin, R., Sajjadi, M., et al. (2021). Meibomian gland dysfunction in geriatric population: Tehran geriatric eye study. *Int. Ophthalmol.* 41 (7), 2539–2546. doi:10.1007/s10792-021-01812-2
- Hashemi, H., Rastad, H., Emamian, M. H., and Fotouhi, A. (2017). Meibomian gland dysfunction and its determinants in Iranian adults: A population-based study. *Cont. Lens Anterior Eye* 40 (4), 213–216. doi:10.1016/j.clae.2017.05.003
- Hat, K., Planinic, A., Jezek, D., and Kastelan, S. (2023). Expression of androgen and estrogen receptors in the human lacrimal gland. *Int. J. Mol. Sci.* 24 (6), 5609. doi:10.3390/ijms24065609
- He, K., Gkioxari, G., Dollar, P., and Girshick, R. (2020). Mask R-CNN. *IEEE Trans. Pattern Anal. Mach. Intell.* 42 (2), 386–397. doi:10.1109/tpami.2018.2844175
- Koh, Y. W., Celik, T., Lee, H. K., Petznick, A., and Tong, L. (2012). Detection of meibomian glands and classification of meibography images. *J. Biomed. Opt.* 17 (8), 086008. doi:10.1117/1.JBO.17.8.086008
- Liu, X., Fu, Y., Wang, D., Huang, S., He, C., Yu, X., et al. (2022). Uneven index: A digital biomarker to prompt demodex blepharitis based on deep learning. *Front. Physiol.* 13, 934821. doi:10.3389/fphys.2022.934821
- Maruoka, S., Tabuchi, H., Nagasato, D., Masumoto, H., Chikama, T., Kawai, A., et al. (2020). Deep neural network-based method for detecting obstructive meibomian gland dysfunction with *in vivo* laser confocal microscopy. *Cornea* 39 (6), 720–725. doi:10.1097/ico.0000000000002279
- Nelson, J. D., Shimazaki, J., Benitez-del-Castillo, J. M., Craig, J. P., McCulley, J. P., Den, S., et al. (2011). The international workshop on meibomian gland dysfunction: Report of the definition and classification subcommittee. *Invest. Ophthalmol. Vis. Sci.* 52 (4), 1930–1937. doi:10.1167/iov.10-6997b
- Schaumberg, D. A., Nichols, J. J., Papas, E. B., Tong, L., Uchino, M., and Nichols, K. K. (2011). The international workshop on meibomian gland dysfunction: Report of the subcommittee on the epidemiology of, and associated risk factors for, MGD. *Invest. Ophthalmol. Vis. Sci.* 52 (4), 1994–2005. doi:10.1167/iov.10-6997e
- Schirra, F., Seitz, B., Knop, N., and Knop, E. (2009). Sex hormones and dry eye. *Ophthalmologie* 106 (11), 988–994. doi:10.1007/s00347-009-2005-2
- Schirra, F., Suzuki, T., Richards, S. M., Jensen, R. V., Liu, M., Lombardi, M. J., et al. (2005). Androgen control of gene expression in the mouse meibomian gland. *Invest. Ophthalmol. Vis. Sci.* 46 (10), 3666–3675. doi:10.1167/iov.05-0426
- Shimazaki, J., Goto, E., Ono, M., Shimmura, S., and Tsubota, K. (1998). Meibomian gland dysfunction in patients with Sjögren syndrome. *Ophthalmology* 105 (8), 1485–1488. doi:10.1016/s0161-6420(98)98033-2
- Siak, J. J., Tong, L., Wong, W. L., Cajucom-Uy, H., Rosman, M., Saw, S. M., et al. (2012). Prevalence and risk factors of meibomian gland dysfunction: The Singapore Malay eye study. *Cornea* 31 (11), 1223–1228. doi:10.1097/ICO.0b013e31823f0977
- Suzuki, T., Schirra, F., Richards, S. M., Jensen, R. V., and Sullivan, D. A. (2008). Estrogen and progesterone control of gene expression in the mouse meibomian gland. *Invest. Ophthalmol. Vis. Sci.* 49 (5), 1797–1808. doi:10.1167/iov.07-1458
- Versura, P., Giannaccare, G., and Campos, E. C. (2015). Sex-steroid imbalance in females and dry eye. *Curr. Eye Res.* 40 (2), 162–175. doi:10.3109/02713683.2014.966847
- Viso, E., Gude, F., and Rodríguez-Ares, M. T. (2011). The association of meibomian gland dysfunction and other common ocular diseases with dry eye: A population-based study in Spain. *Cornea* 30 (1), 1–6. doi:10.1097/ICO.0b013e3181da5778
- Wang, J., Bao, J., Song, W., Li, S., Hao, Y., Tian, L., et al. (2022). Assessment of eyelid pressure using a novel pressure measurement device in patients with moderate-to-severe dry eye disease. *Front. Med. (Lausanne)* 9, 833576. doi:10.3389/fmed.2022.833576
- Wang, S., Zhao, H., Huang, C., Li, Z., Li, W., Zhang, X., et al. (2016). Impact of chronic smoking on meibomian gland dysfunction. *PLoS One* 11 (12), e0168763. doi:10.1371/journal.pone.0168763
- Xiao, P., Luo, Z., Deng, Y., Wang, G., and Yuan, J. (2021). An automated and multiparametric algorithm for objective analysis of meibography images. *Quant. Imaging Med. Surg.* 11 (4), 1586–1599. doi:10.21037/qims-20-611
- Yeotikar, N. S., Zhu, H., Markoulli, M., Nichols, K. K., Naduvilath, T., and Papas, E. B. (2016). Functional and morphologic changes of meibomian glands in an asymptomatic adult population. *Invest. Ophthalmol. Vis. Sci.* 57 (10), 3996–4007. doi:10.1167/iov.15-18467
- Zhang, Y. Y., Zhao, H., Lin, J. Y., Wu, S. N., Liu, X. W., Zhang, H. D., et al. (2021). Artificial intelligence to detect meibomian gland dysfunction from *in-vivo* laser confocal microscopy. *Front. Med. (Lausanne)* 8, 774344. doi:10.3389/fmed.2021.774344
- Zhang, Z., Lin, X., Yu, X., Fu, Y., Chen, X., Yang, W., et al. (2022). Meibomian gland density: An effective evaluation index of meibomian gland dysfunction based on deep learning and transfer learning. *J. Clin. Med.* 11 (9), 2396. doi:10.3390/jcm11092396



OPEN ACCESS

EDITED BY

Weihua Yang,
Jinan University, China

REVIEWED BY

Wangting Li,
Shenzhen Eye Hospital, China
Cheng Wan,
Nanjing University of Aeronautics and
Astronautics, China
Lucia Ballerini,
University of Edinburgh, United Kingdom

*CORRESPONDENCE

Wen Bin Wei,
✉ weiwenbintr@163.com

RECEIVED 27 February 2023

ACCEPTED 09 June 2023

PUBLISHED 21 June 2023

CITATION

Shi XH, Dong L, Zhang RH, Zhou DJ,
Ling SG, Shao L, Yan YN, Wang YX and
Wei WB (2023), Relationships between
quantitative retinal microvascular
characteristics and cognitive function
based on automated artificial
intelligence measurements.
Front. Cell Dev. Biol. 11:1174984.
doi: 10.3389/fcell.2023.1174984

COPYRIGHT

© 2023 Shi, Dong, Zhang, Zhou, Ling,
Shao, Yan, Wang and Wei. This is an open-
access article distributed under the terms
of the [Creative Commons Attribution
License \(CC BY\)](https://creativecommons.org/licenses/by/4.0/). The use, distribution or
reproduction in other forums is
permitted, provided the original author(s)
and the copyright owner(s) are credited
and that the original publication in this
journal is cited, in accordance with
accepted academic practice. No use,
distribution or reproduction is permitted
which does not comply with these terms.

Relationships between quantitative retinal microvascular characteristics and cognitive function based on automated artificial intelligence measurements

Xu Han Shi^{1,2,3}, Li Dong^{1,2,3}, Rui Heng Zhang^{1,2,3}, Deng Ji Zhou⁴,
Sai Guang Ling⁴, Lei Shao^{1,2,3}, Yan Ni Yan^{1,2,3}, Ya Xing Wang⁵ and
Wen Bin Wei^{1,2,3*}

¹Beijing Tongren Eye Center, Beijing Key Laboratory of Intraocular Tumor Diagnosis and Treatment, Beijing Tongren Hospital, Capital Medical University, Beijing, China, ²Beijing Ophthalmology and Visual Sciences Key Lab, Beijing Tongren Hospital, Capital Medical University, Beijing, China, ³Medical Artificial Intelligence Research and Verification Key Laboratory of the Ministry of Industry and Information Technology, Beijing Tongren Hospital, Capital Medical University, Beijing, China, ⁴EVision Technology (Beijing) Co., Ltd., Beijing, China, ⁵Beijing Ophthalmology and Visual Science Key Laboratory, Beijing Tongren Eye Center, Beijing Tongren Hospital, Beijing Institute of Ophthalmology, Capital Medical University, Beijing, China

Introduction: The purpose of this study is to assess the relationship between retinal vascular characteristics and cognitive function using artificial intelligence techniques to obtain fully automated quantitative measurements of retinal vascular morphological parameters.

Methods: A deep learning-based semantic segmentation network ResNet101-UNet was used to construct a vascular segmentation model for fully automated quantitative measurement of retinal vascular parameters on fundus photographs. Retinal photographs centered on the optic disc of 3107 participants (aged 50–93 years) from the Beijing Eye Study 2011, a population-based cross-sectional study, were analyzed. The main parameters included the retinal vascular branching angle, vascular fractal dimension, vascular diameter, vascular tortuosity, and vascular density. Cognitive function was assessed using the Mini-Mental State Examination (MMSE).

Results: The results showed that the mean MMSE score was 26.34 ± 3.64 (median: 27; range: 2–30). Among the participants, 414 (13.3%) were classified as having cognitive impairment (MMSE score < 24), 296 (9.5%) were classified as mild cognitive impairment (MMSE: 19–23), 98 (3.2%) were classified as moderate cognitive impairment (MMSE: 10–18), and 20 (0.6%) were classified as severe cognitive impairment (MMSE < 10). Compared with the normal cognitive function group, the retinal venular average diameter was significantly larger ($p = 0.013$), and the retinal vascular fractal dimension and vascular density were significantly smaller (both $p < 0.001$) in the mild cognitive impairment group. The retinal arteriole-to-venular ratio ($p = 0.003$) and vascular fractal dimension ($p = 0.033$) were significantly decreased in the severe cognitive impairment group compared to the mild cognitive impairment group. In the multivariate analysis, better cognition (i.e., higher MMSE score) was significantly associated with higher retinal vascular fractal dimension ($b = 0.134$, $p = 0.043$) and higher retinal

vascular density ($b = 0.152$, $p = 0.023$) after adjustment for age, best corrected visual acuity (BCVA) (logMAR) and education level.

Discussion: In conclusion, our findings derived from an artificial intelligence-based fully automated retinal vascular parameter measurement method showed that several retinal vascular morphological parameters were correlated with cognitive impairment. The decrease in retinal vascular fractal dimension and decreased vascular density may serve as candidate biomarkers for early identification of cognitive impairment. The observed reduction in the retinal arteriole-to-venular ratio occurs in the late stages of cognitive impairment.

KEYWORDS

artificial intelligence, deep learning, retinal vascular, cognitive function, cognitive impairment

Introduction

Cognitive impairment is the most common neurodegenerative disorder. Severe cognitive impairment that leads to Alzheimer's disease and dementia ultimately manifests as an extensive loss of cognitive ability and imposes a tremendous burden on patients, economies, healthcare systems, and society (Prince et al., 2013; Alzheimer's Association, 2022). The prevalence of cognitive impairment is high globally, its pathogenesis is complex, and there are no effective treatments currently available. However, evidence-based preventative methods to delay the development and progression of the disease have been proposed. Therefore, it is particularly important to diagnose and prevent cognitive impairments at an early stage (Yu et al., 2020). Currently, the diagnosis of cognitive impairment relies on the detection of serum and protein biomarkers, examination of cerebrospinal fluid (CSF), and positron emission tomography (PET) scans. As a result of their high cost, high level of risk to patients posed by invasive procedures, high level of technical difficulty, and considerable time costs, these diagnostic procedures are not appropriate for early large-scale screening of the disease (Jack et al., 2018; Polanco et al., 2018; Fish et al., 2019). Consequently, it is essential to discover effective, noninvasive, easy-to-implement, and cost-efficient biomarkers that can identify individuals with cognitive impairment in its early stages to allow timely interventions to prevent or delay the onset of dementia.

Vascular diseases are a risk factor for cognitive impairment (Reitz et al., 2011; Ngolab et al., 2019). Previous studies have demonstrated that vascular risk factors affecting the cerebral microcirculation may also play a significant role in cognitive impairment (Czakó et al., 2020; Sur et al., 2020). In the majority of cases characterized by cognitive impairment, variations in cerebral microvascular characteristics, such as increased tortuosity and arteriolar narrowing, and their association with degenerative changes have been reported (Liesz, 2019; O'Neill et al., 2021). There are many similarities between the retina and the brain, including their physiological characteristics, embryological origins, cellular resemblances, precise neuron cell layers, and microvasculature (Xie et al., 2023). As a window to the brain, the retina offers an excellent opportunity for researchers to investigate the pathogenesis of numerous ophthalmic and neurodegenerative diseases (Snyder et al., 2021; Zhang et al., 2021). Accumulating reports of retinal imaging utilizing various imaging techniques have revealed a correlation between retinal vascular alterations and the incidence of cognitive impairment (Patton et al., 2005;

Ravi Teja et al., 2017; Ngolab et al., 2019; Wu et al., 2020). However, it has been determined that some of the findings of these reports are inconsistent, and so the relationship between retinal vascular parameters (e.g., retinal vascular diameter, retinal vascular tortuosity, etc.) and cognitive function remains controversial. We therefore conducted a study to further clarify the relationship between retinal vascular parameters and cognitive function.

Retinal fundus photography is a valuable technique for the quick assessment of retinal vascular characteristics. In the last two decades, computer programs developed for medical imaging have made it possible to perform a number of computer-based measurements on retinal fundus photography and ultimately demonstrate a relationship between retinal vascular changes and clinical characteristics (Cheung et al., 2011a; Dervenis et al., 2019). With the help of computer-assisted analysis programs, characteristics of the retinal vasculature, including fractal dimension, tortuosity, and vessel caliber, can be assessed quantitatively (Cheung et al., 2011b). Nevertheless, until recently, the majority of quantitative measurements have been carried out with the assistance of semiautomated retinal vessel measurements software, such as SIVA, IVAN, and VAMPIRE (Trucco et al., 2015; Chan et al., 2017; Czakó et al., 2020). These methods involve manual input and adjustment by qualified technicians, are time-consuming and prone to error, and are therefore inefficient (McGrory et al., 2018; Mautuit et al., 2022).

In recent years, deep learning algorithms have proven superior performance in assessing diabetic retinopathy and other retinal characteristics (Ting et al., 2017; Dong et al., 2022). In this study, we developed a deep learning model to perform fully automated segmentation of retinal vessels and quantitatively evaluate retinal vessel parameters, including retinal vessel diameter, retinal vessel curvature, retinal vessel fractal dimension, retinal vessel density, etc. We described retinal vascular characteristics that may serve as candidate biomarkers for the early identification of cognitive impairment as well as for the progression of the disease.

Materials and methods

Study population

The Beijing Eye Study 2011 is a cross-sectional population-based study that was conducted in five communities in the urban district in

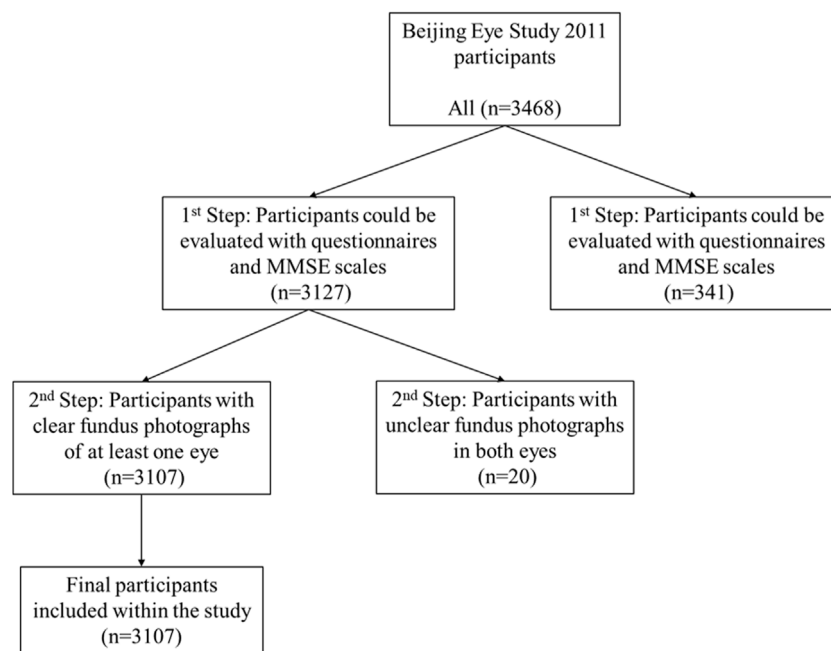


FIGURE 1
A flow chart of participant inclusion and exclusion criteria.

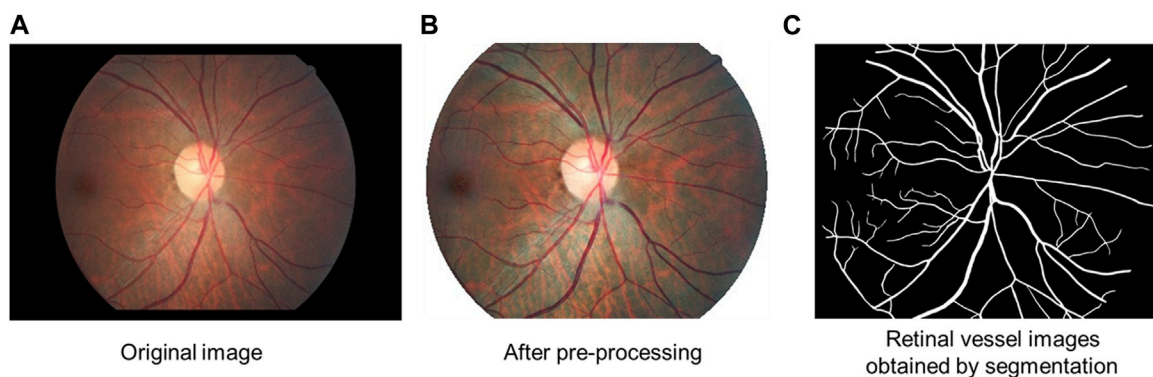


FIGURE 2
Diagram of retinal vessel segmentation. (A) Original image. (B) Image after pre-processing: regions of interest (ROI) were extracted, denoised, normalized, and enhanced. (C) Retinal vessel images obtained by segmentation.

northern central Beijing and in three communities in the village area in southern Beijing. A detailed description of the population and the design of the study has been provided previously (Liu et al., 2010; Yan et al., 2015). Among 4,403 eligible individuals, 3,468 individuals [response rate: 78.8%; females: 1,963 (56.6%); mean age: 64.6 ± 9.8 years; median age: 64 years; age range: 50–93 years] participated in the study. The Medical Ethics Committee of Beijing Tongren Hospital approved the study protocol, and all participants gave informed written consent in accordance with the Declaration of Helsinki. The ethics committee confirmed that all methods were performed in accordance with the relevant guidelines and regulations.

Ophthalmic and general examinations

All examinations were conducted in the communities at either schoolhouses or community houses. Participants in the study were interviewed by trained research technicians and completed standardized questionnaires. The interview included standardized questions on demographics and socioeconomic factors, such as age, sex, education level, current smoking status, and systemic disease histories, such as arterial hypertension, diabetes mellitus, cardiovascular disease, and infarction (including both myocardial infarction and brain infarction). The education levels of participants were classified as “illiteracy,” “partial illiteracy with knowledge of

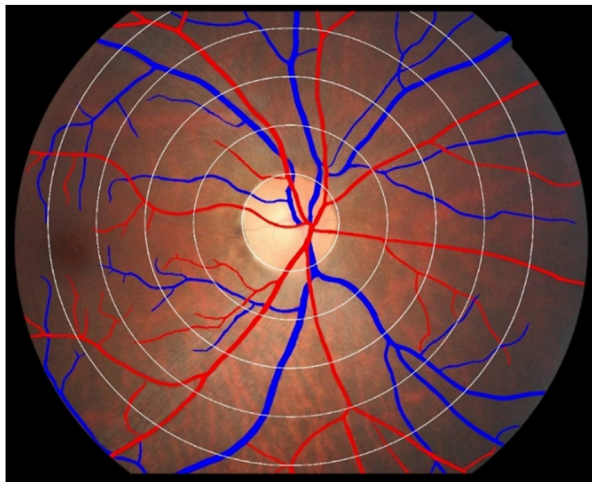


FIGURE 3
Identification of retinal arteries and veins.

some Chinese words,” “primary school education,” “middle school education,” and “college or higher education.”

The ophthalmic examination included measurement of best corrected visual acuity (BCVA) (logMAR), slit lamp-assisted biomicroscopy of the anterior segment of the eye, and fundus photographs centered on the optic disc (nonstereoscopic photograph of 45° of the central fundus; fundus camera type CR6-45NM; Canon Inc., Tokyo, Japan).

Cognitive function was assessed as a cognitive function score using the Mini-Mental State Examination (MMSE) (Folstein et al., 1975; Crum et al., 1993). The MMSE is a widely used and validated screening tool for detecting cognitive impairment. In clinical practice, it exhibits moderate to high sensitivity and specificity. It is particularly useful when comparing individuals across a wide age range (Folstein et al., 1975; Tombaugh and McIntyre, 1992). Cognitive impairment was defined as an MMSE score < 24, in line with previous studies that have demonstrated good sensitivity and specificity at this cut point. Further grading of cognitive impairment was performed. Mild cognitive impairment was

defined as an MMSE score ranging between 19 and 23 points, moderate cognitive impairment was defined as an MMSE score ranging between 10 and 18 points, and severe cognitive impairment was defined as an MMSE score < 10 (Folstein et al., 1975; Tombaugh and McIntyre, 1992; Liew et al., 2009; Jonas et al., 2018).

A patient was included if he or she could be evaluated with questionnaires and MMSE scales. The exclusion criteria were as follows: unclear bilateral fundus photographs of the eyes (inability to clearly visualize the optic disc and retinal vasculature) that could not be analyzed; and inability to evaluate the patient with questionnaires and MMSE scales (Figure 1). The data of all the right eyes were included in the current study. If a clear fundus photograph of the right eye could not be obtained, the data from the left eye were included.

Quantitative measurements of retinal vascular parameters based on artificial intelligence automatic analysis technology

Participants' color fundus photographs centered on the optic disc were analyzed. Included in the measurements were the retinal vascular branching angle, vascular fractal dimension, vascular average diameter, vascular average tortuosity, and retinal vascular density; the vascular average diameter and vascular average tortuosity were analyzed further in the annular regions 0.5–1.0 papillary diameter (PD) (C1), 1.0–1.5 PD (C2), 1.5–2.0 PD (C3), and 2.0–2.5 PD (C4) from the optic disc border. The vascular fractal dimension indicates the branching complexity of the retinal vascular network, reflecting the distribution of blood throughout the entire retinal circulation, with larger values indicating branching complexity (Liew et al., 2008). The retinal vascular average tortuosity indicates the degree of bend in retinal vessels. A smaller value indicates a flatter retinal vessel (Vilela et al., 2021). The annular area close to the optic disc provides a better measure of the diameter of the central retinal arterioles and venules. The annular region further from the optic disc, where there are more retinal vascular branches, can better demonstrate the branching complexity of the retinal vascular network and the degree of curvature of the retinal vessels.

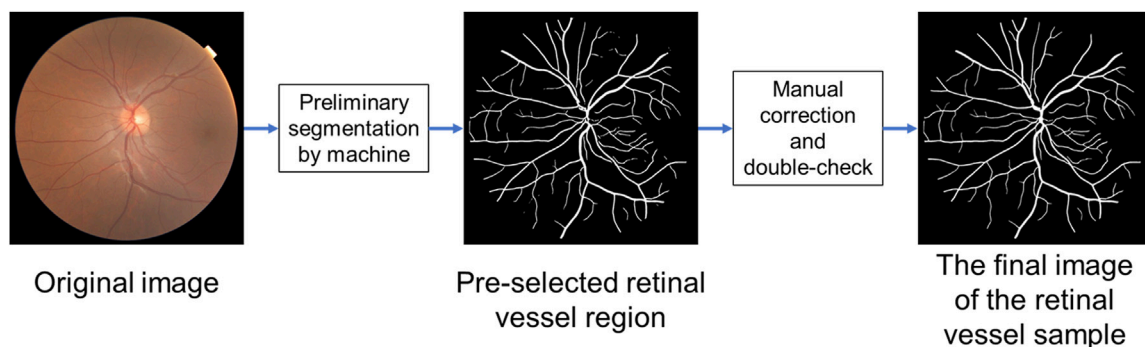


FIGURE 4
The process of labeling fundus photographs.

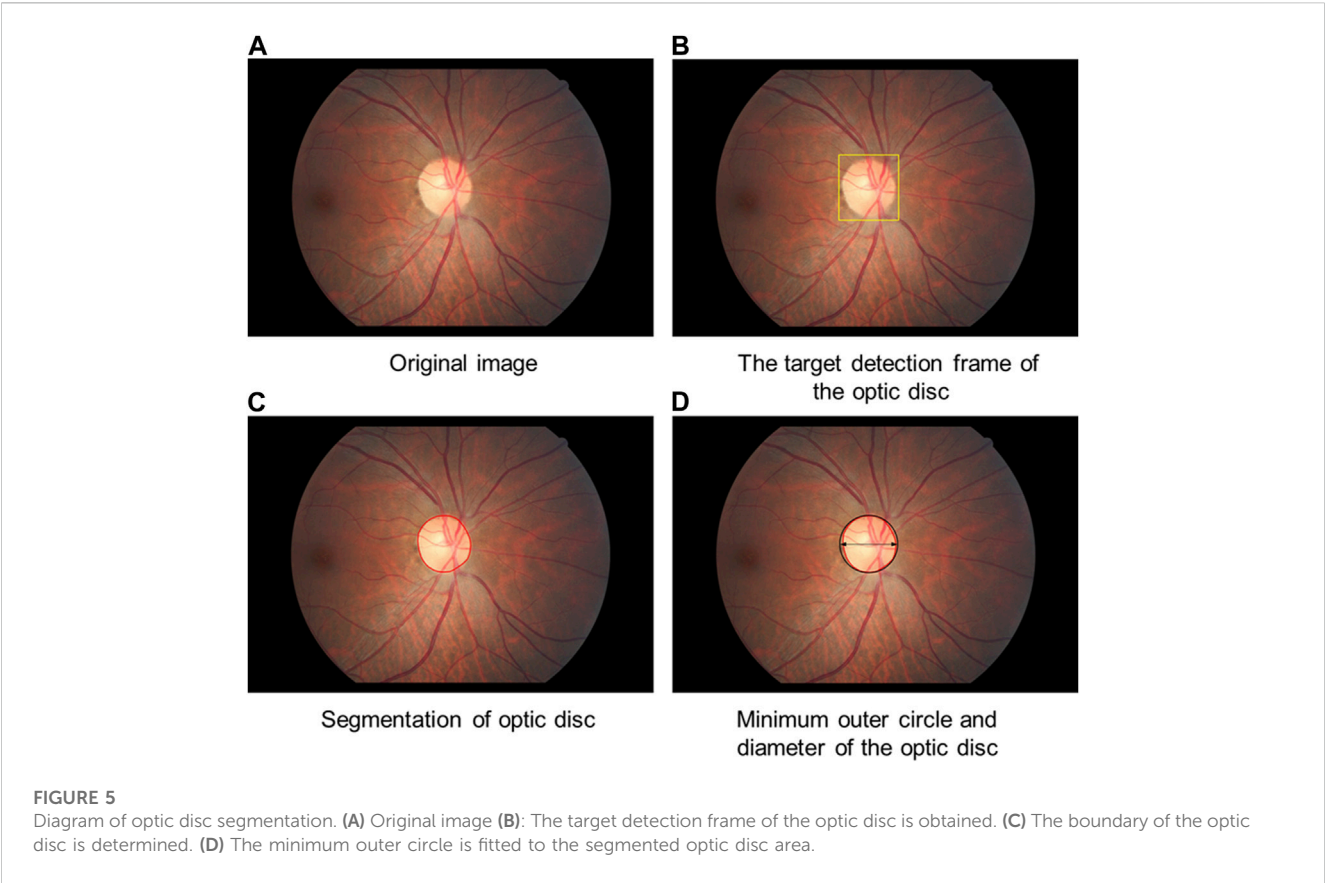


TABLE 1 Results of retinal vascular and optic disc segmentation accuracy evaluation.

Category	Accuracy (Acc)	Sensitivity	Specificity	Intersection ratio (IoU)	DICE
Retinal vascular segmentation	0.966	0.888	0.974	0.711	0.832
Optic disc segmentation	0.998	0.969	0.999	0.939	0.972

In this study, we developed a computer image processing method using deep learning and computer vision technology to automatically segment retinal vessels and optic disc features on color fundus images based on the principle of human visual bionics and then extracted the centerline of blood vessels. Through the fusion of deep learning and computer vision technology, morphological parameters such as vascular diameter, vascular tortuosity, vascular fractal dimension, vascular branching angle, and vascular density can be calculated.

Preprocessing of images

To enhance the fundus images, regions of interest (ROI) were extracted, denoised, normalized, and enhanced (Xu et al., 2019; Shao et al., 2021). After the channel separation of the image, the threshold segmentation method was used on the red (R) channel to obtain the preselected ROI. The threshold for the ROI preselection area was used as 1/3 of the average grey value of the R channel. Afterward, the preselected

area was filtered based on its location, area, roundness, and other attributes. In order to filter the area, we selected the largest area in the ROI preselection area. Then, the boundary was determined using morphological operations (image opening operations) to obtain the final ROI. On the color fundus image, this area represented the effective fundus retinal imaging area, which reduced the interference of invalid areas such as the background on the subsequent feature recognition and segmentation process. In the following step, the noise was removed by applying a low-pass filter (median filtering) to reduce the noise resulting from the camera's imaging procedures. Furthermore, the color, brightness, and size of the images were normalized by mean calibration and resampling to minimize the variability between images. Mean calibration means adjusting the mean value of brightness and color of each image to the mean of the statistical values of all images. Resampling is the linear difference method used to scale all images to a uniform size. Additionally, the images were enhanced using the contrast-limited adaptive histogram equalization (CLAHE) algorithm, which enhanced the retinal features on the images (Figure 2B).

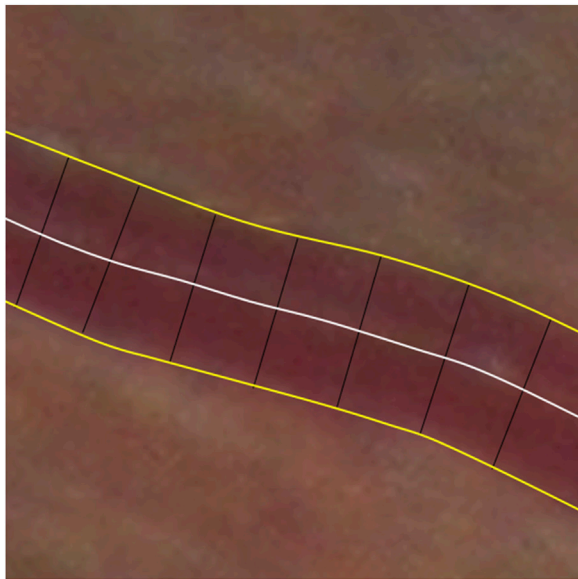


FIGURE 6
Schematic diagram of vascular diameter measurement.

Segmentation of retinal vessels

In this study, we use a deep learning-based semantic segmentation network ResNet101-UNet to construct a retinal vessel segmentation model, which adopts a cross-layer connectivity architecture and is capable of extracting vessel features at different scales (Ronneberger et al., 2015). A semiautomatic machine-assisted annotation method is employed to annotate the sample. First, the color image is converted into grayscale according to the following formula.

$$Gray = R \times 0.299 + G \times 0.587 + B \times 0.144$$

And then the resulting grayscale image is segmented using the Otsu algorithm to obtain the dark region. As a next step, the segmented dark region is filtered based on the brightness and morphology of the blood vessels on the fundus image to obtain the preselected blood vessel region. For the extracted retinal vascular regions, we used a trained deep learning semantic segmentation model to distinguish between arteries and veins. Arterial vessels and venous vessels are distinguished and identified by the corresponding vessel color and brightness, as well as the connection and topological relationship between the vessels. Two senior attending ophthalmologists then manually corrected the segmentation, with one performing the initial correction and the other reviewing and performing any additional correction, to obtain the final image of the blood vessel sample (Figures 3, 4).

The labeled 755 case samples were divided into training and validation sets at a ratio of 655:100. The training set is input into the ResNet101-UNet network for model training, and the loss value of the network model is calculated with the validation set. The model parameters are adjusted and optimized according to the loss value. The training is stopped when the loss value no longer decreases to

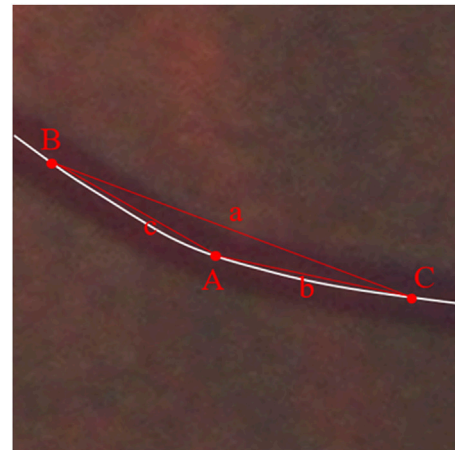


FIGURE 7
Schematic diagram of vascular tortuosity measurement. The curvature of each retinal vessel at a certain interval was measured and the average curvature to the points on the centerline of the vessel was calculated as the vascular average tortuosity.

obtain the final vessel segmentation model. This model is then used to segment the blood vessels (Figure 2).

Optic disc segmentation

In this study, optic disc segmentation was divided into two steps. First, the optic disc is detected using the deep learning object detection method to determine its location. The object detection model consists of single shot detection (SSD), and the backbone of the network structure is ResNet50. The model is trained with 2,000 training samples from the publicly available online Kaggle competition dataset to obtain the optic disc detection model and to ultimately obtain the object detection frame of the optic disc. The center point of the object detection frame is used as the center point of the optic disc. Afterward, the boundary of the optic disc is determined based on the visual attention mechanism. The center point determined by optic disc localization is used as the origin for performing a polar coordinate transformation on the fundus image. On the polar coordinate image, the edge detection operator is employed to determine the edge of the optic disc in polar coordinates. Then, the image is inversely transformed to finally obtain the edge of the optic disc in the image coordinate system to achieve detailed segmentation of the optic disc. Finally, the minimum outer circle is fitted to the segmented optic disc area. The center of the outer circle is used to locate the center point of the final optic disc, and the diameter of the optic disc is defined by the diameter of the outer circle (Figure 5).

Accuracy evaluation of retinal vessel segmentation and optic disc segmentation

A sample of 100 manually annotated and reviewed color fundus images was used for the test, with each fundus image

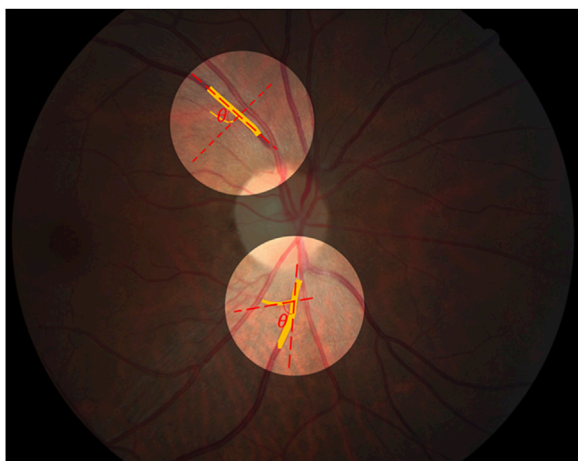


FIGURE 8
Schematic diagram of vascular branch angle measurement.

labeled separately for the retinal vessels and optic disc. Each manually annotated image was reviewed and corrected by two physicians, one for initial annotation or correction and the other for review and further correction. The automatic segmentation results of the model were compared with the manual annotation results. In units of pixels, accuracy (Acc), sensitivity, specificity, intersection over union (IoU), and DICE coefficients were calculated according to the following formulas. The results are shown in Table 1.

$$Acc = \frac{TP + TN}{TP + TN + FP + FN}$$

$$Sensitivity = \frac{TP}{TP + FN}$$

$$Specificity = \frac{TN}{TN + FP}$$

$$IoU = \frac{TP}{TP + FP + FN}$$

$$DICE = \frac{2 \times TP}{FP + 2 \times TP + FN}$$

Note:

TP (True Positives): The prediction indicates that the sample is positive, and the prediction is accurate.

TN (True Negatives): The prediction indicates that the sample is negative, and the prediction is accurate.

FP (False Positives): The prediction indicates that the sample is positive, but the prediction is incorrect.

FN (False Negatives): The prediction indicates that the sample is negative, but the prediction is incorrect.

Calculation of vascular fractal dimension

This study focuses on calculating the vascular fractal dimension. The fractal dimension was calculated on the segmented images. The fundus images were divided into several grids with different edge lengths (ϵ). In the grid corresponding to each edge length, the number of grid boxes intersecting retinal vessels was calculated as (N). The number of grid boxes intersecting with retinal vessels in each case and the inverse of its side length was fitted to a straight line in logarithm form, and the resulting slope of the line was the fractal dimension, which is calculated as follows.

$$dim_{box} = \lim_{\epsilon \rightarrow 0} \frac{\log N(\epsilon)}{\log (1/\epsilon)}$$

TABLE 2 Participant summary characteristics.

Patient characteristics	ALL (n = 3107)	Normal cognition (n = 2693)	Cognitive impairment (n = 414)	p-value
Age (years, Mean \pm SD)	64.18 \pm 9.75	63.41 \pm 9.37	69.15 \pm 10.69	<0.001
Male, n (%)	1,351 (43.5%)	1,235 (45.9%)	116 (28.0%)	<0.001
BCVA (logMAR) (Mean \pm SD)	0.94 \pm 0.22	0.97 \pm 0.19	0.76 \pm 0.27	<0.001
Education, middle school, college or higher, n (%)	2,216 (74.1%)	2,172 (83.5%)	44 (11.3%)	<0.001
Currently smoking, yes, n (%)	628 (21.0%)	530 (20.4%)	98 (25.3%)	0.027
BMI (kg/m ² , Mean \pm SD)	25.59 \pm 3.85	25.53 \pm 3.77	26.01 \pm 4.30	0.035
Hypertension, yes, n (%)	1,426 (50.7%)	1,190 (48.6%)	236 (64.8%)	<0.001
Diabetes, yes, n (%)	362 (13.8%)	322 (13.9%)	40 (12.9%)	0.644
Cardiovascular disease, yes, n (%)	507 (18.3%)	434 (17.8%)	73 (21.2%)	0.128
Infarction, yes, n (%)	204 (6.9%)	172 (6.7%)	32 (8.6%)	0.173
MMSE score (Mean \pm SD)	26.36 \pm 3.64	27.43 \pm 1.98	19.36 \pm 4.21	<0.001

Values are n (%) for categorical variables and mean \pm SD for continuous variables. p values were calculated by independent samples t and chi-squared tests.

Abbreviations: BCVA, best corrected visual acuity; BMI, body mass index; MMSE, mini-mental state examination; SD, standard deviation.

p < 0.05 was considered statistically significant.

The bold values are to highlight p < 0.05.

TABLE 3 Retinal vascular characteristics stratified by cognitive function.

Characteristics	All (N = 3107)	Normal cognition (n = 2693, 86.7%)	Mild cognitive impairment (n = 296, 9.5%)	Moderate cognitive impairment (n = 98, 3.2%)	Severe cognitive impairment (n = 20, 0.6%)	p-value	Post hoc comparisons	Post hoc p-value
Retinal vascular average diameter (um), mean ± SD	59.703 ± 4.457	59.475 ± 4.100	60.890 ± 5.871	61.697 ± 6.542	64.120 ± 7.396	<0.001	Normal cognition vs. Mild cognitive impairment	<0.001
							Normal cognition vs. Moderate cognitive impairment	0.001
							Normal cognition vs. Severe cognitive impairment	0.038
Retinal arteriolar average diameter (um), mean ± SD	49.348 ± 3.798	49.314 ± 3.601	49.527 ± 5.091	49.898 ± 4.493	48.843 ± 4.537	0.246	—	
Retinal venular average diameter (um), mean ± SD	70.359 ± 5.834	70.157 ± 5.577	71.373 ± 6.784	71.887 ± 8.121	75.858 ± 7.534	<0.001	Normal cognition vs. Mild cognitive impairment	0.013
							Normal cognition vs. Severe cognitive impairment	0.006
Arteriole-to-venular ratio, mean ± SD	0.704 ± 0.059	0.705 ± 0.056	0.698 ± 0.073	0.694 ± 0.072	0.648 ± 0.071	<0.001	Normal cognition vs. Severe cognitive impairment	0.001
							Mild cognitive impairment vs. Severe cognitive impairment	0.003
							Moderate cognitive impairment vs. Severe cognitive impairment	0.036
Retinal vascular fractal dimension, mean ± SD	1.512 ± 0.098	1.521 ± 0.074	1.471 ± 0.166	1.434 ± 0.206	1.401 ± 0.242	<0.001	Normal cognition vs. Mild cognitive impairment	<0.001
							Normal cognition vs. Moderate	<0.001
							Normal cognition vs. Severe	<0.001
							Mild cognitive impairment vs. Moderate cognitive impairment	0.001
							Mild cognitive impairment vs. Severe cognitive impairment	0.033
Retinal vascular branching angle (°), mean ± SD	55.484 ± 9.457	55.646 ± 9.458	54.660 ± 9.049	53.311 ± 10.129	54.496 ± 10.634	0.058	—	
*Retinal vascular tortuosity, mean ± SD	0.794 ± 0.163	0.788 ± 0.160	0.840 ± 0.173	0.797 ± 0.187	0.881 ± 0.213	<0.001	Normal cognition vs. Mild cognitive impairment	<0.001
							Mild cognitive impairment vs. Moderate cognitive impairment	0.047

(Continued on following page)

TABLE 3 (Continued) Retinal vascular characteristics stratified by cognitive function.

Characteristics	All (N = 3107)	Normal cognition (n = 2693, 86.7%)	Mild cognitive impairment (n = 296, 9.5%)	Moderate cognitive impairment (n = 98, 3.2%)	Severe cognitive impairment (n = 20, 0.6%)	p-value	Post hoc comparisons	Post hoc p-value
Retinal vascular density, mean ± SD	0.086 ± 0.020	0.088 ± 0.018	0.079 ± 0.027	0.071 ± 0.026	0.067 ± 0.029	<0.001	Normal cognition vs. Mild cognitive impairment	<0.001
							Normal cognition vs. Moderate cognitive impairment	<0.001
							Normal cognition vs. Severe cognitive impairment	0.001
							Mild cognitive impairment vs. Moderate cognitive impairment	0.001

Values are n (%) for categorical variables and mean ± SD for continuous variables. p values were calculated by the Kruskal–Wallis test.

Abbreviations: SD, standard deviation.

*Tortuosity values were multiplied by 1000 to be shown in Table.

p < 0.05 was considered statistically significant.

The bold values are to highlight p < 0.05.

Calculation of retinal vascular density

The retinal vascular density is a quantitative representation of the state and coverage of fundus blood flow and has important clinical significance for detecting the occurrence, progression, and diagnosis of fundus diseases. Retinal vascular density refers to the retinal vascular area per unit fundus area; that is, in a certain area, the ratio of the area of the retinal vasculature to the area of the fundus on the photograph can be expressed as:

$$\rho = \frac{S'}{S}$$

where S' is the extraction area of the retinal vasculature and S is the area of the fundus.

Measurement of retinal vascular average diameter

Using the retinal vessel image obtained by segmentation, a bidirectional morphological erosion operation was applied based on the vessel boundary to determine the vessel centerline. At a certain step interval along the vessel centerline, the straight line orthogonal to the tangent line to a point on the centerline could be found. The orthogonal straight line intersects the vessel boundary at two points. The Euclidean distance d between those two points was calculated, and d is the vascular diameter corresponding to the point. The vessel diameter is calculated at 5-pixel intervals in the vessel direction. The average retinal vascular diameter refers to the average of the vascular diameters corresponding to the points on the centerline. With the center of the optic disc as the reference origin and the diameter of the optic disc as the reference distance, the average value of the vascular diameter corresponding to the points on the centerline of the vessels in different regions was calculated, which was taken as the average vascular diameter value of

the region. Finally, the optic disc diameter of 1.5 mm was used as a reference for unit conversion of the vascular diameter values (Figure 6).

Measurement of retinal vascular tortuosity

The curvature corresponding to each point on the centerline of the vessel was calculated based on the following formula.

Points B and C are identified on either side of point A such that their distances on the line from point A are equal, i.e., $\widehat{AB} = \widehat{AC}$. R_A is the radius of the external circle of $\triangle ABC$ composed of points A, B, and C, and C_A is the curvature of the vessel at point A (Figure 7).

$$R_A = \frac{a}{2 \sin A}$$

$$C_A = \frac{1}{R_A}$$

The curvature is calculated for each point on the vessel except for 25 pixels at the ends of the vessel (as the conditions for calculation are not met). The average curvature to the points on the centerline of the vessel was calculated as the vascular average tortuosity. Retinal vascular tortuosity was calculated as the average of the curvatures of each retinal vessel at a certain interval for all the extracted retinal vessels. Using the center of the optic disc as the reference origin and the diameter of the optic disc as the reference distance, the average tortuosity in different regions (C1, C2, C3, and C4 as mentioned above) was calculated (Figure 7).

Measurement of retinal vascular branching angle

In this study, the branching angle of the vessel was calculated as the average angle between the main vessel and the branch vessels. Within a

TABLE 4 Retinal vascular characteristics stratified by cognitive function in individuals with and without hypertension.

Characteristics	All (<i>n</i> = 3107)	Normal cognition (<i>n</i> = 2693, 86.7%)	Mild cognitive impairment (<i>n</i> = 296, 9.5%)	Moderate cognitive impairment (<i>n</i> = 98, 3.2%)	Severe cognitive impairment (<i>n</i> = 20, 0.6%)	<i>p</i> -value
With hypertension	<i>n</i> = 1426	<i>n</i> = 1190, 83.5%	<i>n</i> = 176, 12.3%	<i>n</i> = 49, 3.4%	<i>n</i> = 11, 0.8%	
Retinal vascular average diameter (μm), mean ± SD	59.860 ± 4.638	59.527 ± 4.253	61.125 ± 5.758	62.649 ± 6.137	64.807 ± 8.099	<0.001
Retinal arteriolar average diameter (μm), mean ± SD	49.074 ± 3.926	49.043 ± 3.664	49.099 ± 5.239	49.936 ± 4.573	48.310 ± 5.307	0.171
Retinal venular average diameter (μm), mean ± SD	70.625 ± 6.083	70.343 ± 5.803	71.581 ± 7.006	73.105 ± 7.583	76.247 ± 7.691	0.001
Arteriole-to-venular ratio, mean ± SD	0.698 ± 0.060	0.700 ± 0.056	0.688 ± 0.077	0.688 ± 0.080	0.637 ± 0.078	0.014
Retinal vascular fractal dimension, mean ± SD	1.502 ± 0.109	1.512 ± 0.081	1.456 ± 0.187	1.461 ± 0.144	1.338 ± 0.313	<0.001
Retinal vascular branching angle (°), mean ± SD	55.540 ± 9.568	55.691 ± 9.571	54.587 ± 8.879	55.058 ± 11.135	54.524 ± 12.958	0.485
*Retinal vascular tortuosity, mean ± SD	0.809 ± 0.170	0.801 ± 0.168	0.857 ± 0.183	0.828 ± 0.165	0.844 ± 0.179	<0.001
Retinal vascular density, mean ± SD	0.083 ± 0.021	0.085 ± 0.019	0.077 ± 0.028	0.072 ± 0.023	0.062 ± 0.033	<0.001
Without hypertension	<i>n</i> = 1,389	<i>n</i> = 1,261, 90.8%	<i>n</i> = 90, 6.5%	<i>n</i> = 32, 2.3%	<i>n</i> = 6, 0.4%	
Retinal vascular average diameter (μm), mean ± SD	59.549 ± 4.110	59.431 ± 3.954	60.995 ± 4.945	59.591 ± 5.867	62.352 ± 6.990	0.010
Retinal arteriolar average diameter (μm), mean ± SD	49.639 ± 3.594	49.565 ± 3.515	50.486 ± 4.363	50.051 ± 4.071	50.266 ± 3.930	0.072
Retinal venular average diameter (μm), mean ± SD	70.076 ± 5.523	70.002 ± 5.330	71.030 ± 6.323	69.625 ± 8.846	73.740 ± 8.657	0.375
Arteriole-to-venular ratio, mean ± SD	0.711 ± 0.057	0.710 ± 0.056	0.715 ± 0.069	0.704 ± 0.057	0.686 ± 0.064	0.323
Retinal vascular fractal dimension, mean ± SD	1.525 ± 0.067	1.528 ± 0.059	1.501 ± 0.099	1.462 ± 0.162	1.514 ± 0.032	<0.001
Retinal vascular branching angle (°), mean ± SD	55.672 ± 9.361	55.814 ± 9.376	55.192 ± 9.237	51.322 ± 8.153	55.064 ± 10.638	0.067
*Retinal vascular tortuosity, mean ± SD	0.776 ± 0.153	0.773 ± 0.149	0.810 ± 0.158	0.756 ± 0.214	0.919 ± 0.260	0.013
Retinal vascular density, mean ± SD	0.090 ± 0.018	0.090 ± 0.017	0.084 ± 0.024	0.073 ± 0.025	0.084 ± 0.013	<0.001

Values are *n* (%) for categorical variables and mean ± SD for continuous variables. *p* values were calculated by the Kruskal–Wallis test.

Abbreviations: SD, standard deviation.

*Tortuosity values were multiplied by 1000 in order to be shown in Table.

p < 0.05 was considered statistically significant.

The bold values are to highlight *p* < 0.05.

distance of 2 PD from the optic disc boundary, the retina was divided into upper and lower halves using the optic disc as a reference, and the vessel with the largest diameter was taken as the main vessel in each half. Based on the centerline of the vessel, the number of neighboring pixels corresponding to each pixel point on the centerline of the main vessel was calculated based on the 8-neighborhood algorithm, and the point with three neighboring pixels was selected as the branching point. Using the branching point as the starting point, a point 10 pixels away from the branching point was extracted from the centerline of the main vessel and the centerline of the corresponding branch vessel, and a straight line was fitted to each of them, after which the angle between

the two lines was measured and calculated as the angle at the branching point. All the angles on the main vessel within 2 PD from the optic disc boundary were obtained, and the average value of all the angles were calculated and output as the retinal vascular branching angle (Figure 8).

Statistical analysis

Statistical analyses were performed in Statistical Package for Social Science (SPSS, version 25.0, IBM Corp., Armonk, New York,

TABLE 5 Retinal vascular characteristics stratified by cognitive function in different sexes.

Characteristics	All (<i>n</i> = 3107)	Normal cognition (<i>n</i> = 2693, 86.7%)	Mild cognitive impairment (<i>n</i> = 296, 9.5%)	Moderate cognitive impairment (<i>n</i> = 98, 3.2%)	Severe cognitive impairment (<i>n</i> = 20, 0.6%)	<i>p</i> -value
Male	<i>n</i> = 1351	<i>n</i> = 1235, 91.4%	<i>n</i> = 81, 6.0%	<i>n</i> = 27, 2.0%	<i>n</i> = 8, 0.6%	
Retinal vascular average diameter (um), mean ± SD	59.786 ± 4.372	59.647 ± 4.203	60.571 ± 4.876	63.175 ± 6.883	63.185 ± 8.586	0.008
Retinal arteriolar average diameter (um), mean ± SD	49.223 ± 3.720	49.201 ± 3.620	49.728 ± 4.628	49.186 ± 4.702	47.731 ± 5.537	0.329
Retinal venular average diameter (um), mean ± SD	70.418 ± 5.650	70.312 ± 5.562	70.625 ± 5.499	74.154 ± 8.033	73.531 ± 8.367	0.104
Arteriole-to-venular ratio, mean ± SD	0.702 ± 0.056	0.702 ± 0.055	0.705 ± 0.058	0.669 ± 0.080	0.656 ± 0.101	0.031
Retinal vascular fractal dimension, mean ± SD	1.516 ± 0.080	1.521 ± 0.060	1.480 ± 0.129	1.386 ± 0.289	1.411 ± 0.158	<0.001
Retinal vascular branching angle (°), mean ± SD	56.347 ± 8.983	56.361 ± 8.953	56.433 ± 9.261	54.739 ± 8.774	58.795 ± 13.472	0.904
*Retinal vascular tortuosity, mean ± SD	0.784 ± 0.151	0.781 ± 0.148	0.832 ± 0.180	0.769 ± 0.155	0.816 ± 0.170	0.027
Retinal vascular density, mean ± SD	0.086 ± 0.019	0.087 ± 0.018	0.078 ± 0.025	0.069 ± 0.024	0.059 ± 0.033	<0.001
Female	<i>n</i> = 1756	<i>n</i> = 1458, 83.0%	<i>n</i> = 215, 12.2%	<i>n</i> = 71, 4.0%	<i>n</i> = 12, 0.7%	
Retinal vascular average diameter (um), mean ± SD	59.639 ± 4.522	59.327 ± 4.006	61.010 ± 6.212	61.175 ± 6.387	64.799 ± 6.755	<0.001
Retinal arteriolar average diameter (um), mean ± SD	49.446 ± 3.856	49.411 ± 3.583	49.449 ± 5.267	50.161 ± 4.421	49.652 ± 3.727	0.427
Retinal venular average diameter (um), mean ± SD	70.313 ± 5.974	70.026 ± 5.587	71.656 ± 7.204	71.088 ± 8.058	77.551 ± 6.758	<0.001
Arteriole-to-venular ratio, mean ± SD	0.706 ± 0.060	0.708 ± 0.057	0.695 ± 0.078	0.703 ± 0.067	0.642 ± 0.043	<0.001
Retinal vascular fractal dimension, mean ± SD	1.510 ± 0.109	1.520 ± 0.085	1.468 ± 0.178	1.452 ± 0.164	1.394 ± 0.293	<0.001
Retinal vascular branching angle (°), mean ± SD	54.807 ± 9.762	55.032 ± 9.833	53.968 ± 8.894	52.775 ± 10.607	52.152 ± 8.547	0.120
*Retinal vascular tortuosity, mean ± SD	0.801 ± 0.172	0.794 ± 0.169	0.843 ± 0.170	0.806 ± 0.197	0.928 ± 0.237	<0.001
Retinal vascular density, mean ± SD	0.087 ± 0.021	0.088 ± 0.019	0.080 ± 0.028	0.071 ± 0.027	0.073 ± 0.025	<0.001

Values are *n* (%) for categorical variables and mean ± SD for continuous variables. *p* values were calculated by the Kruskal–Wallis test.

Abbreviations: SD, standard deviation.

*Tortuosity values were multiplied by 1000 in order to be shown in Table.

p < 0.05 was considered statistically significant.

The bold values are to highlight *p* < 0.05.

United States) and GraphPad Prism 9.4.0 (GraphPad Software, San Diego, CA, United States). Population summary measures and retinal vascular parameters are described using the mean and SD for continuous variables or frequencies and percentages for categorical variables. Independent samples *t*-tests and chi-squared tests were used to compare the differences in participant characteristics between participants with and without cognitive impairment. The Kruskal–Wallis test was used to determine the differences in retinal vascular parameters in the whole area and four annular zones among the four

groups. Then, *post hoc* multiple comparisons (Bonferroni correction) were performed to determine pairwise differences. Furthermore, we included a multivariate linear regression analysis to test associations between the MMSE score and retinal vascular parameters. The MMSE score was defined as a dependent parameter, and the parameters that were significantly associated with MMSE were appropriately selected as independent parameters. All *p* values were two-sided, and *p* < 0.05 indicated statistical significance. Ninety-five percent confidence intervals are presented.

TABLE 6 Retinal vascular characteristics stratified by cognitive function in different age groups.

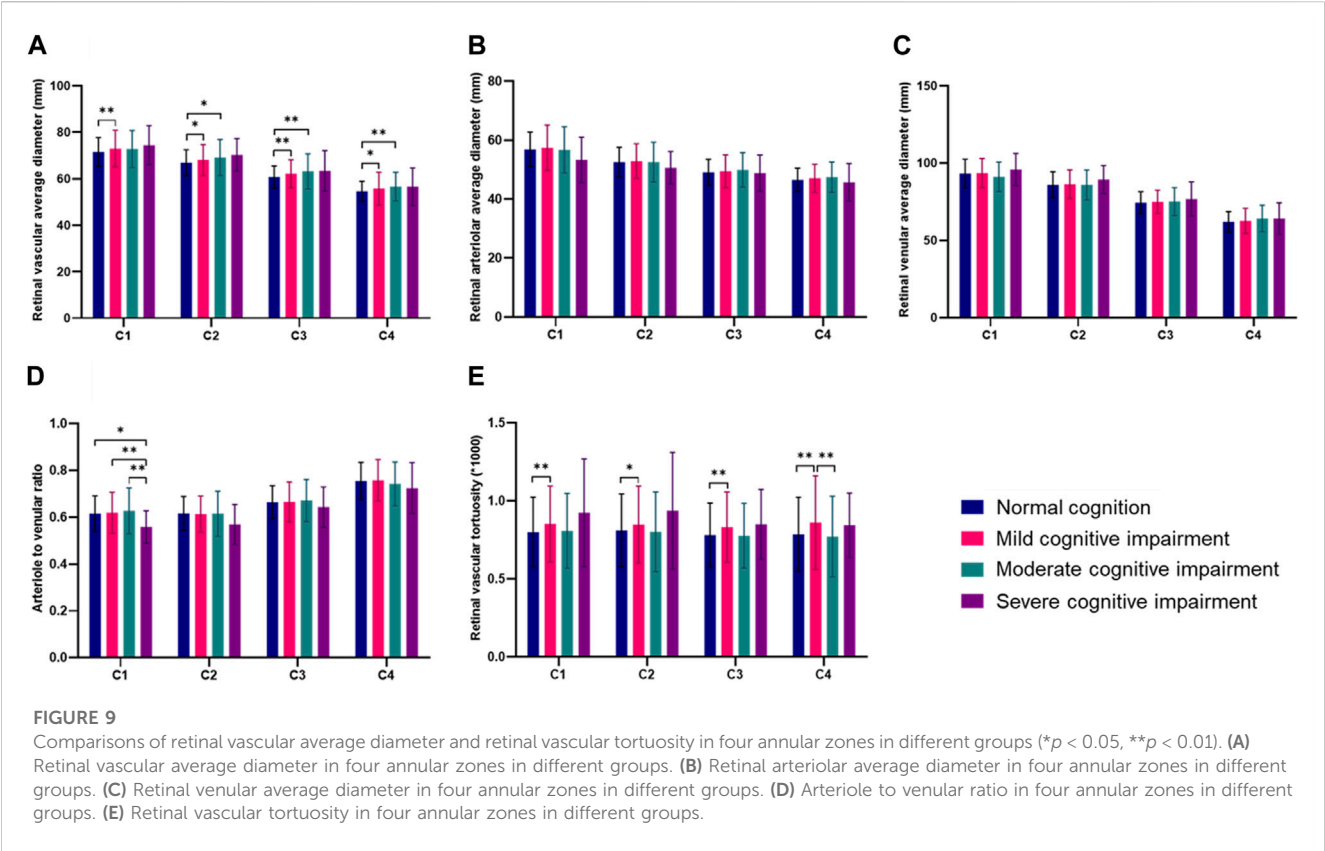
Characteristics	All (<i>n</i> = 3107)	Normal cognition (<i>n</i> = 2693, 86.7%)	Mild cognitive impairment (<i>n</i> = 296, 9.5%)	Moderate cognitive impairment (<i>n</i> = 98, 3.2%)	Severe cognitive impairment (<i>n</i> = 20, 0.6%)	<i>p</i> -value
Age: 50–64 years	<i>n</i> = 1692	<i>n</i> = 1540, 91.0%	<i>n</i> = 127, 7.5%	<i>n</i> = 23, 1.4%	<i>n</i> = 2, 0.1%	
Retinal vascular average diameter (um), mean ± SD	58.743 ± 3.499	58.714 ± 3.443	59.179 ± 4.137	58.580 ± 3.422	55.784 ± 1.233	0.316
Retinal arteriolar average diameter (um), mean ± SD	48.950 ± 3.089	48.951 ± 3.066	49.149 ± 3.279	47.800 ± 3.509	48.397 ± 3.236	0.554
Retinal venular average diameter (um), mean ± SD	69.480 ± 4.934	69.446 ± 4.952	69.865 ± 4.700	70.073 ± 5.085	64.631 ± 0.453	0.158
Arteriole-to-venular ratio, mean ± SD	0.707 ± 0.051	0.707 ± 0.052	0.706 ± 0.048	0.683 ± 0.042	0.749 ± 0.055	0.120
Retinal vascular fractal dimension, mean ± SD	1.543 ± 0.046	1.544 ± 0.044	1.537 ± 0.070	1.537 ± 0.042	1.542 ± 0.012	<0.001
Retinal vascular branching angle (°), mean ± SD	55.730 ± 9.026	55.799 ± 9.065	55.152 ± 8.614	54.666 ± 8.751	50.626 ± 11.496	0.739
*Retinal vascular tortuosity, mean ± SD	0.805 ± 0.164	0.801 ± 0.162	0.841 ± 0.164	0.874 ± 0.248	0.756 ± 0.062	0.011
Retinal vascular density, mean ± SD	0.095 ± 0.013	0.095 ± 0.012	0.094 ± 0.017	0.092 ± 0.018	0.092 ± 0.003	0.736
Age: 65–79 years	<i>n</i> = 1188	<i>n</i> = 999, 84.1%	<i>n</i> = 137, 11.5%	<i>n</i> = 44, 3.7%	<i>n</i> = 8, 0.7%	
Retinal vascular average diameter (um), mean ± SD	60.671 ± 4.780	60.357 ± 4.528	62.212 ± 5.726	62.915 ± 5.702	62.460 ± 5.407	<0.001
Retinal arteriolar average diameter (um), mean ± SD	49.838 ± 4.349	49.768 ± 4.147	50.034 ± 5.620	50.971 ± 4.473	49.580 ± 4.185	0.146
Retinal venular average diameter (um), mean ± SD	71.239 ± 6.308	71.034 ± 6.119	72.073 ± 6.970	72.752 ± 8.020	74.997 ± 5.738	0.044
Arteriole-to-venular ratio, mean ± SD	0.702 ± 0.065	0.703 ± 0.061	0.697 ± 0.084	0.700 ± 0.083	0.663 ± 0.059	0.162
Retinal vascular fractal dimension, mean ± SD	1.489 ± 0.103	1.497 ± 0.083	1.446 ± 0.172	1.427 ± 0.167	1.499 ± 0.020	<0.001
Retinal vascular branching angle (°), mean ± SD	55.236 ± 9.869	55.384 ± 9.856	54.403 ± 9.059	53.644 ± 12.144	57.308 ± 11.674	0.569
*Retinal vascular tortuosity, mean ± SD	0.783 ± 0.161	0.774 ± 0.158	0.844 ± 0.175	0.777 ± 0.125	0.867 ± 0.241	<0.001
Retinal vascular density, mean ± SD	0.079 ± 0.021	0.080 ± 0.019	0.072 ± 0.027	0.064 ± 0.025	0.079 ± 0.010	<0.001
Age: ≥80 years	<i>n</i> = 227	<i>n</i> = 154, 67.8%	<i>n</i> = 32, 14.1%	<i>n</i> = 31, 13.7%	<i>n</i> = 10, 4.4%	
Retinal vascular average diameter (um), mean ± SD	61.904 ± 6.775	61.411 ± 5.337	62.182 ± 9.757	62.473 ± 8.682	67.447 ± 8.044	0.083
Retinal arteriolar average diameter (um), mean ± SD	49.812 ± 5.085	50.039 ± 4.311	48.860 ± 8.164	50.103 ± 4.802	48.287 ± 5.361	0.886
Retinal venular average diameter (um), mean ± SD	72.423 ± 8.019	71.639 ± 6.668	74.626 ± 10.879	72.111 ± 10.095	79.119 ± 7.393	0.024
Arteriole-to-venular ratio, mean ± SD	0.689 ± 0.073	0.697 ± 0.063	0.664 ± 0.100	0.694 ± 0.077	0.612 ± 0.060	0.005
Retinal vascular fractal dimension, mean ± SD	1.407 ± 0.198	1.441 ± 0.134	1.318 ± 0.260	1.364 ± 0.290	1.294 ± 0.313	0.002
Retinal vascular branching angle (°), mean ± SD	54.839 ± 10.512	55.798 ± 10.767	53.426 ± 11.209	51.689 ± 8.007	52.389 ± 9.990	0.174

(Continued on following page)

TABLE 6 (Continued) Retinal vascular characteristics stratified by cognitive function in different age groups.

Characteristics	All (n = 3107)	Normal cognition (n = 2693, 86.7%)	Mild cognitive impairment (n = 296, 9.5%)	Moderate cognitive impairment (n = 98, 3.2%)	Severe cognitive impairment (n = 20, 0.6%)	p-value
*Retinal vascular tortuosity, mean ± SD	0.765 ± 0.158	0.747 ± 0.131	0.814 ± 0.199	0.762 ± 0.193	0.921 ± 0.213	0.039
Retinal vascular density, mean ± SD	0.062 ± 0.025	0.066 ± 0.023	0.048 ± 0.027	0.062 ± 0.022	0.051 ± 0.034	0.004

Values are n (%) for categorical variables and mean ± SD for continuous variables. *p* values were calculated by Kruskal–Wallis test.
Abbreviations: SD, standard deviation.
*Tortuosity values were multiplied by 1000 to be shown in Table.
p < 0.05 was considered statistically significant.
The bold values are to highlight *p* < 0.05.



Results

Demographic characteristics

Among the 3,468 participants, 3,107 individuals (89.6%) [1,351 (43.5%) male] for whom fundus photographs centered on the optic disc and measurements of cognitive function were available were included in the current study. Participants had a mean age of 64.18 ± 9.75 years (median: 63 years; range: 50–93 years) and 74.1% had an education level classified as middle school education or college or higher education. The characteristics of the study population are summarized in detail in Table 2. Participants with cognitive impairment were more likely to be older, female, and a current

smoker and to have lower BCVA (logMAR), less education, a higher BMI, and a higher prevalence of hypertension than participants without cognitive impairment.

Retinal vascular characteristics in participants with different cognitive functions

The mean MMSE score was 26.34 ± 3.64 (median: 27; range: 2–30). Out of the 3,107 study participants, 414 (13.3%) individuals were classified as having cognitive impairment with an MMSE score < 24. A total of 296 (9.5%) of these individuals were

TABLE 7 Associations (multivariate analysis) between the cognitive function score and retinal vascular parameters.

Parameter	Regression coefficient B	Standard error	Standardized coefficient beta	t	95% CI	p value
*Retinal vascular average diameter	−0.097	0.055	−0.027	−1.756	−0.206~0.011	0.079
*Retinal arteriolar average diameter	−0.053	0.052	−0.015	−1.023	−0.156~0.049	0.307
*Retinal venular average diameter	−0.022	0.053	−0.006	−0.416	−0.126~0.082	0.677
*Arteriole-to-venular ratio	−0.032	0.052	−0.009	−0.619	−0.134~0.070	0.536
*Retinal vascular fractal dimension	0.134	0.066	0.034	2.028	0.004~0.263	0.043
*Retinal vascular branching angle	0.009	0.051	0.003	0.173	−0.091~0.109	0.863
*Retinal vascular tortuosity	−0.048	0.052	−0.014	−0.925	−0.150~0.054	0.355
*Retinal vascular density	0.152	0.067	0.042	2.282	0.021~0.283	0.023

Abbreviations: CI, confidence interval.
*The retinal vascular parameters were transformed into standardized Z-scores before inclusion in regression models.
Adjustment: age, education, best corrected visual acuity (logMAR).
 $p < 0.05$ was considered statistically significant.
The bold values are to highlight $p < 0.05$.

classified as having mild cognitive impairment (MMSE score range: 19–23), 98 (3.2%) individuals were classified as having moderate cognitive impairment (MMSE score range: 10–18), and 20 (0.6%) individuals were classified as having severe cognitive impairment (MMSE score < 10).

Retinal vascular characteristics of the participants with different cognitive functions are detailed in Table 3. Between the normal cognition group and the mild cognitive impairment group, significant differences existed in retinal vascular average diameter ($p < 0.001$), retinal venular average diameter ($p = 0.013$), retinal vascular fractal dimension ($p < 0.001$), retinal vascular tortuosity ($p < 0.001$), and retinal vascular density ($p < 0.001$). Comparison of the different stages of cognitive impairment showed there were significant differences in the arteriole-to-venular ratio (mild cognitive impairment vs. severe cognitive impairment, $p = 0.003$; moderate cognitive impairment vs. severe cognitive impairment, $p = 0.036$), retinal vascular fractal dimension (mild cognitive impairment vs. moderate cognitive impairment, $p = 0.001$; mild cognitive impairment vs. severe cognitive impairment, $p = 0.033$), and retinal vascular density (mild cognitive impairment vs. moderate cognitive impairment, $p = 0.001$).

To further analyses the relationship between retinal vascular parameters and cognitive function in individuals with different sexes, ages and hypertensive status, we conducted subgroup analyses to assess the relationship between retinal vascular parameters and cognitive impairment in individuals with and without hypertension, in individuals of different sexes, and in individuals of different age groups. The results are described in detail in Tables 4–6, respectively.

Regional characteristics of retinal vascular alterations

The retinal vascular average diameter and retinal vascular tortuosity in four annular zones were further analyzed. Among the four annuli, the retinal vascular average diameter and retinal

vascular tortuosity were significantly larger in the mild cognitive impairment group than in the normal cognition group (Figures 9A, E). In the C1 annuli, the arteriole-to-venular ratio was significantly lower in the severe cognitive impairment group than in the other three groups (Figure 9D). No significant differences in retinal arteriolar average diameter and venular average diameter were found within the four annuli (Figures 9B, C).

Correlation between retinal vascular parameters and MMSE score

In the multivariate analysis, we first used the MMSE score as a dependent variable and all significantly associated systemic parameters ($p < 0.05$) as independent variables. Since the MMSE was affected by demographic factors, mostly by age and educational level, both parameters were included in the multivariate analysis in the present study (Jonas et al., 2018).

Second, we removed those parameters indicating a high degree of collinearity and parameters that were no longer significantly associated with the MMSE score ($p > 0.05$), including sex ($p = 0.258$), hypertension ($p = 0.635$), infarction ($p = 0.708$), current smoking ($p = 0.417$) and BMI ($p = 0.121$). After adjustment for age, BCVA (logMAR), and education level, a better MMSE score was significantly associated with a higher retinal vascular fractal dimension and higher retinal vascular density. For every 1 SD increase in the retinal vascular fractal dimension, the MMSE score increased by 0.134 points. (B = 0.134, 95% CI: 0.004~0.263, $p = 0.043$). For every 1 SD increase in the retinal vascular density, the MMSE score increased by 0.152 points. (B = 0.152, 95% CI: 0.021~0.283, $p = 0.023$) (Table 7).

Discussion

In this study, we performed fully automated retinal vessel segmentation and quantitative measurement of retinal vascular

parameters on color fundus photographs using artificial intelligence algorithms. With our fully automated quantitative results, this study demonstrated that alterations in retinal vascular parameters such as retinal vascular diameter, vascular fractal dimension, and vascular curvature are associated with cognitive impairment in a population-based cohort.

Previously, most of the quantitative measurements used for the analysis of retinal vascular parameters were semiautomated by computer-aided analysis programs, such as SIVA, IVAN, and VAMPIRE (Cheung et al., 2011b; Ong et al., 2013; McGorry et al., 2018; Mautuit et al., 2022). These methods require manual labeling and correction of the segmentation of the optic disc and retinal vessels. It takes a trained operator 20–30 min to correct the segmentation of each fundus image, and inevitably subjective bias will be introduced (Cheung et al., 2021b; Cheung et al., 2022). A variety of deep learning models for retinal vessel segmentation have emerged in recent years, and different deep learning models for vessel segmentation have sensitivities of approximately 0.72–0.95, specificities of 0.80–0.98, and accuracies of 0.91–0.98 (Chen et al., 2021). These studies, however, did not perform simultaneous quantitative measurements on the basis of vessel segmentation. Cheung et al. (2021b) developed a Singapore I Vessel Analyzer deep-learning system (SIVA-DLS) to automatically measure retinal vessel caliber. However, this system cannot detect other valuable retinal vascular parameters, such as vascular fractal dimension and retinal vascular tortuosity, at the same time. Shi et al. (2022) performed a meaningful study, in which they developed an artificial intelligence system for fully automated vessel segmentation and quantification of the retinal microvasculature. Sixteen basic parameters were included in the study. However, parameters such as vascular fractal dimension and vessel density, which are also of great importance, were not included. Wiseman et al. (2023) quantified retinal vessel density (VD) and branching complexity on optical coherence tomography angiography (OCTA). They found that retinal microvascular abnormalities exhibited on OCTA were associated with cerebral small vessel disease.

In this study, we constructed a vessel segmentation model based on the deep learning semantic segmentation network ResNet101-UNet, which can complete the process of optic disc segmentation and retinal vessel segmentation in a few seconds. This model is effective in reducing human error and has good sensitivity, specificity, and accuracy. In addition, based on retinal vessel segmentation, a fully automated detection method can then be used to quantitatively analyze the characteristics of the retinal microvascular system, deeply integrating deep learning and computer vision technologies to extract morphological information about all the vasculature in color fundus photographs, providing accurate measurements of retinal vascular branching angle, vascular fractal dimension, vascular average diameter, vascular average tortuosity, and other parameters.

Because age-related eye conditions (such as age-related macular degeneration and glaucoma) are common in older individuals, we intentionally included fundus photographs of patients with concomitant eye disease to increase applicability. Moreover, excluding eyes with these conditions may also introduce selection bias, as research indicates that cognitively impaired patients are more likely to have age-related macular degeneration and glaucoma (Lee et al., 2019; Cheung et al., 2021a).

In previous studies, research on the relationship between retinal vessel diameter and cognitive impairment has yielded mixed results. Liew et al. (2009) analyzed fundus photographs of the Blue Mountains Eye Study population and revealed that retinal venular dilation was associated with significant cognitive impairment, particularly in older persons with hypertension. In contrast, the Circulatory Risk in Communities Study reported that generalized arteriolar narrowing and a total number of retinal abnormalities may be useful markers for identifying persons at higher risk of disabling dementia (Jinnouchi et al., 2017). Recently, fully automated measurements of retinal arteriolar and venular calibers from retinal fundus images were estimated by Cheung et al. (2022) using a deep-learning system. They indicated that narrower retinal arteriolar caliber and wider retinal venular caliber are associated with an increased risk of cognitive decline. However, another study based on the Northern Ireland Cohort for the Longitudinal Study of Aging (NICOLA) showed that there were no associations between central retinal venular measures and mild cognitive impairment (O'Neill et al., 2021). The different findings may be due to inconsistent approaches to the definition of cognitive impairment or inconsistencies in the range of fundus photographs used to measure retinal vascular parameters.

Our study showed that the average retinal vascular diameter was increased in the cognitive impairment group compared to those with normal cognitive function. Separate analyses of retinal arteriolar average diameter and venular average diameter revealed that retinal arteriolar average diameter was not associated with cognitive impairment. In addition, the increase in retinal vascular average diameter mainly occurred in the venules. Evidence suggests that cognitive decline and related diseases may be associated with a wider retinal venular diameter (Yim-Lui Cheung et al., 2010; Simen et al., 2011), which is indicative of systemic inflammation, endothelial dysfunction, and abnormal blood-brain barriers (Nguyen and Wong, 2006; Wong et al., 2006).

In the present study, we found that retinal vascular fractal dimension and retinal vascular density may be more relevant candidate biomarkers for the early diagnosis of cognitive impairment than retinal vascular diameter. In individuals with cognitive impairment, the retinal vascular fractal dimension is decreased, and retinal vascular density is reduced. Similarly, Cheung et al. (2014) observed that Alzheimer's disease (AD) patients had sparser retinal microvascular networks than controls, suggesting that retinal microvascular function is impaired in AD individuals. Ong et al. (2014) also indicated that reduced retinal arteriolar and venular fractal dimensions are associated with an increased risk of mild and moderate cognitive impairment. In a recent study, Xie et al. (2023) evaluated the association between changes in retinal microvasculature and Alzheimer's disease and mild cognitive impairment using deep segmentation of OCTA images. They also revealed that the mild cognitive impairment group in their study had a reduced vascular fractal dimension compared with the control group. We performed a multiple linear regression analysis and found that retinal fractal dimension and retinal vascular density were positively correlated with the MMSE score. For every 1 SD increase in retinal fractal dimension, the MMSE increased by 0.134 points, and for every 1 SD increase in retinal vessel density, the MMSE increased by 0.152 points.

We analyzed the underlying reasons for the decrease in retinal vascular fractal dimension and retinal vascular density in a cognitively dysfunctional population. The fractal dimension of the retinal vasculature is an indicator of the complexity of the vascular branches, reflecting the distribution of blood throughout the retinal circulation, with larger values indicating a more complex distribution. When the fractal dimension of retinal vessels decreases, the sparse distribution of retinal vessels may represent the same alterations in the microvasculature of the brain (Nadal et al., 2020), indicating inadequate cerebral blood perfusion, which triggers activity in hypoxia-induced pathways that leads to pathological changes in tau, ultimately leading to the development and progression of cognitive impairment and even Alzheimer's disease (Koike et al., 2011; Sabayan et al., 2012; Love and Miners, 2016).

We performed a *post hoc* test to compare pairs of the group with normal cognitive function and the groups with different stages of cognitive impairment. The results showed that there were significant differences in retinal venous diameter, vascular tortuosity, retinal vascular fractal dimension, and vascular density between the normal and mildly cognitively dysfunctional groups. On the other hand, between groups with different degrees of cognitive impairment, the severe cognitive impairment group had a reduced arteriole-to-venular ratio and a decreased retinal vascular fractal dimension compared to the mild and moderate cognitive impairment groups. These findings suggest that alterations in retinal venular average diameter, retinal vascular tortuosity, retinal vascular fractal dimension, and retinal vascular density may be early indicators of cognitive impairment, while reduced arteriole-to-venular ratio and decreased fractal dimension may be indicators of the progression of cognitive impairment.

We performed a zonation analysis on the retinal vascular parameters. Within the four annular regions C1–C4, the average vascular diameter, as well as the vascular tortuosity, were significantly different between the normal cognitive function group and the mild cognitive impairment group, suggesting that an increase in these two parameters within each region may occur in the early stages of cognitive impairment. Within the C1 zone, compared to that in the severe cognitive impairment group, the arteriole-to-venular ratio was significantly greater in the normal cognitive function group, the mild cognitive impairment group, and the moderate cognitive impairment group. The significant decrease in the arteriole-to-venular ratio in the severe cognitive impairment group suggested that the decrease in the arteriole-to-venular ratio of the central retinal vessels around the optic disc occurred late in the progression of cognitive impairment.

Our research has several advantages. First, computer intelligence-assisted measurement of vascular characteristics was used in this study to explore the relationship between retinal vascular characteristics and cognitive impairment based on the numerical indicators obtained. Compared with previous computer-aided detection of retinal vessels, the greatest breakthrough of this study is the automatic detection and segmentation of retinal vessels followed by the automatic calculation of vascular characteristic parameters, thus realizing a fully automated process of vascular parameter measurement. The fully automated process saves considerable time, reduces manpower

costs, and avoids the subjective errors introduced by manual measurement or machine-assisted manual measurement. Second, we included data from population-based studies with large samples. In addition, we selected fundus images centered on the optic disc, which provide valuable information on the nasal vessels of the retina. Furthermore, we graded cognitive impairment and investigated the retinal vasculature in different regions to identify more accurate candidate biomarkers for early identification and late progression of cognitive impairment.

Potential limitations should be mentioned. First, it should be noted that 45° photographs of the central fundus were used for this study. The photographs included a limited area, which rendered it impossible to measure the peripheral vessels that are more susceptible to variations. Second, in the zonation analysis, we only performed the annular zones and did not divide them by quadrant, which may have yielded some meaningful results. We have only performed a zonal analysis of retinal vascular diameter and vascular tortuosity, without including retinal vascular fractal dimension and vascular density, which might have provided more meaningful information. Moreover, as this was a cross-sectional study, it was not possible to determine a potential causal relationship between the alterations in retinal vascular parameters and the decline in cognitive function.

In conclusion, we developed a vascular segmentation model based on deep learning algorithms to fully automate the quantitative measurement of retinal vascular parameters on fundus photographs. In this study, we demonstrated that an assessment of retinal vascular parameters with this model provided information on the risk of cognitive decline. The decrease in retinal vascular fractal dimension and decreased vascular density may serve as candidate biomarkers for early identification of cognitive impairment. The reduction in the retinal arteriole-to-venular ratio occurs in the late stages of cognitive impairment.

Data availability statement

The raw data supporting the conclusion of this article will be made available by the authors, without undue reservation.

Ethics statement

The studies involving human participants were reviewed and approved by The Medical Ethics Committee of Beijing Tongren Hospital. The patients/participants provided their written informed consent to participate in this study.

Author contributions

XS, LD, and WW: design of the study. DZ and SL: development of the algorithm. LS, YY, and YW: gathering the data. XS and RZ: performing the data analysis. XS, LD, and DZ: drafting the first version of the manuscript. All authors contributed to the article and approved the submitted version.

Funding

This study was supported by the National Natural Science Foundation of China (82220108017 and 82141128), the Capital Health Research and Development of Special (2020-1-2052), and the Science and Technology Project of Beijing Municipal Science and Technology Commission (Z201100005520045 and Z181100001818003).

Conflict of interest

Authors DZ and SL were employed by EVision Technology (Beijing) Co., Ltd.

References

- Alzheimer's Association (2022). Alzheimer's disease facts and figures. *Alzheimer's Dementia J. Alzheimer's Assoc.* 18 (4), 700–789. doi:10.1002/alz.12638
- Chan, V. T. T., Tso, T. H. K., Tang, F., Tham, C., Mok, V., Chen, C., et al. (2017). Using retinal imaging to study dementia. *J. Vis. Exp. JoVE* 129, 56137. doi:10.3791/56137
- Chen, C., Chuah, J. H., Ali, R., and Wang, Y. (2021). Retinal vessel segmentation using deep learning: A review. *IEEE Access* 9, 111985–112004. doi:10.1109/access.2021.3102176
- Cheung, C. Y., Mok, V., Foster, P. J., Trucco, E., Chen, C., and Wong, T. Y. (2021a). Retinal imaging in Alzheimer's disease. *J. Neurology, Neurosurg. Psychiatry* 92 (9), 983–994. doi:10.1136/jnnp-2020-325347
- Cheung, C. Y., Tay, W. T., Mitchell, P., Wang, J. J., Hsu, W., Lee, M. L., et al. (2011b). Quantitative and qualitative retinal microvascular characteristics and blood pressure. *J. Hypertens.* 29 (7), 1380–1391. doi:10.1097/HJH.0b013e328347266c
- Cheung, C. Y., Wong, W. L. E., Hilal, S., Kan, C. N., Gyanwali, B., Tham, Y. C., et al. (2022). Deep-learning retinal vessel calibre measurements and risk of cognitive decline and dementia. *Brain Commun.* 4 (4), fcac212. doi:10.1093/braincomms/fcac212
- Cheung, C. Y., Xu, D., Cheng, C.-Y., Sabanayagam, C., Tham, Y.-C., Yu, M., et al. (2021b). A deep-learning system for the assessment of cardiovascular disease risk via the measurement of retinal-vessel calibre. *Nat. Biomed. Eng.* 5 (6), 498–508. doi:10.1038/s41551-020-00626-4
- Cheung, C. Y.-L., Ong, Y. T., Ikram, M. K., Ong, S. Y., Li, X., Hilal, S., et al. (2014). Microvascular network alterations in the retina of patients with Alzheimer's disease. *Alzheimer's Dementia J. Alzheimer's Assoc.* 10 (2), 135–142. doi:10.1016/j.jalz.2013.06.009
- Cheung, C. Y.-L., Zheng, Y., Hsu, W., Lee, M. L., Lau, Q. P., Mitchell, P., et al. (2011a). Retinal vascular tortuosity, blood pressure, and cardiovascular risk factors. *Ophthalmology* 118 (5), 812–818. doi:10.1016/j.ophtha.2010.08.045
- Crum, R. M., Anthony, J. C., Bassett, S. S., and Folstein, M. F. (1993). Population-based norms for the Mini-Mental State Examination by age and educational level. *JAMA* 269 (18), 2386–2391. doi:10.1001/jama.269.18.2386
- Czakó, C., Kovács, T., Ungvari, Z., Csizsar, A., Yabluchanskiy, A., Conley, S., et al. (2020). Retinal biomarkers for Alzheimer's disease and vascular cognitive impairment and dementia (VCID): Implication for early diagnosis and prognosis. *GeroScience* 42 (6), 1499–1525. doi:10.1007/s11357-020-00252-7
- Derveniz, N., Coleman, A. L., Harris, A., Wilson, M. R., Yu, F., Anastasopoulos, E., et al. (2019). Factors associated with retinal vessel diameters in an Elderly population: The Thessaloniki eye study. *Investigative Ophthalmol. Vis. Sci.* 60 (6), 2208–2217. doi:10.1167/jovs.18-26276
- Dong, L., He, W., Zhang, R., Ge, Z., Wang, Y. X., Zhou, J., et al. (2022). Artificial intelligence for screening of multiple retinal and optic Nerve diseases. *JAMA Netw. Open* 5 (5), e229960. doi:10.1001/jamanetworkopen.2022.9960
- Fish, P. V., Steadman, D., Bayle, E. D., and Whiting, P. (2019). New approaches for the treatment of Alzheimer's disease. *Bioorg. Med. Chem. Lett.* 29 (2), 125–133. doi:10.1016/j.bmcl.2018.11.034
- Folstein, M. F., Folstein, S. E., and McHugh, P. R. (1975). "Mini-mental state". A practical method for grading the cognitive state of patients for the clinician. *J. Psychiatric Res.* 12 (3), 189–198. doi:10.1016/0022-3956(75)90026-6
- Jack, C. R., Bennett, D. A., Blennow, K., Carrillo, M. C., Dunn, B., Haeberlein, S. B., et al. (2018). NIA-AA Research Framework: Toward a biological definition of Alzheimer's disease. *Alzheimer's Dementia J. Alzheimer's Assoc.* 14 (4), 535–562. doi:10.1016/j.jalz.2018.02.018
- Jinnouchi, H., Kitamura, A., Yamagishi, K., Kiyama, M., Imano, H., Okada, T., et al. (2017). Retinal vascular changes and prospective risk of disabling dementia: The circulatory risk in communities study (CIRCS). *J. Atheroscler. Thrombosis* 24 (7), 687–695. doi:10.5551/jat.37291
- Jonas, J. B., Wei, W. B., Zhu, L. P., Xu, L., and Wang, Y. X. (2018). Cognitive function and Ophthalmological diseases: The Beijing eye study. *Sci. Rep.* 8 (1), 4816. doi:10.1038/s41598-018-23314-5
- Koike, M. A., Garcia, F. G., Kitazawa, M., Green, K. N., and Laferla, F. M. (2011). Long term changes in phospho-APP and tau aggregation in the 3xTg-AD mice following cerebral ischemia. *Neurosci. Lett.* 495 (1), 55–59. doi:10.1016/j.neulet.2011.03.034
- Lee, C. S., Larson, E. B., Gibbons, L. E., Lee, A. Y., Mccurry, S. M., Bowen, J. D., et al. (2019). Associations between recent and established ophthalmic conditions and risk of Alzheimer's disease. *Alzheimer's Dementia J. Alzheimer's Assoc.* 15 (1), 34–41. doi:10.1016/j.jalz.2018.06.2856
- Liesz, A. (2019). The vascular side of Alzheimer's disease. *Sci. (New York, N.Y.)* 365 (6450), 223–224. doi:10.1126/science.aay2720
- Liew, G., Mitchell, P., Wong, T. Y., Lindley, R. I., Cheung, N., Kaushik, S., et al. (2009). Retinal microvascular signs and cognitive impairment. *J. Am. Geriatrics Soc.* 57 (10), 1892–1896. doi:10.1111/j.1532-5415.2009.02459.x
- Liew, G., Wang, J. J., Cheung, N., Zhang, Y. P., Hsu, W., Lee, M. L., et al. (2008). The retinal vasculature as a fractal: Methodology, reliability, and relationship to blood pressure. *Ophthalmology* 115 (11), 1951–1956. doi:10.1016/j.ophtha.2008.05.029
- Liu, H. H., Xu, L., Wang, Y. X., Wang, S., You, Q. S., and Jonas, J. B. (2010). Prevalence and progression of myopic retinopathy in Chinese adults: The Beijing eye study. *Ophthalmology* 117 (9), 1763–1768. doi:10.1016/j.ophtha.2010.01.020
- Love, S., and Miners, J. S. (2016). Cerebral Hypoperfusion and the Energy Deficit in Alzheimer's disease. *Brain Pathol. (Zurich, Switz.)* 26 (5), 607–617. doi:10.1111/bpa.12401
- Mautuit, T., Cunnac, P., Cheung, C. Y., Wong, T. Y., Hogg, S., Trucco, E., et al. (2022). Concordance between SIVA, IVAN, and VAMPIRE software tools for Semi-automated analysis of retinal vessel caliber. *Diagn. (Basel, Switz.)* 12 (6), 1317. doi:10.3390/diagnostics12061317
- Mcgrory, S., Taylor, A. M., Pellegrini, E., Ballerini, L., Kirin, M., Doubal, F. N., et al. (2018). Towards Standardization of quantitative retinal vascular parameters: Comparison of SIVA and VAMPIRE measurements in the Lothian Birth cohort 1936. *Transl. Vis. Sci. Technol.* 7 (2), 12. doi:10.1167/tvst.7.2.12
- Nadal, J., Deverdun, J., De Champfleury, N. M., Carriere, I., Creuzot-Garcher, C., Delcourt, C., et al. (2020). Retinal vascular fractal dimension and cerebral blood flow, a pilot study. *Acta Ophthalmol.* 98 (1), e63–e71. doi:10.1111/aos.14232
- Ngolab, J., Honma, P., and Rissman, R. A. (2019). Reflections on the utility of the retina as a biomarker for Alzheimer's disease: A Literature review. *Neurology Ther.* 8 (2), 57–72. doi:10.1007/s40120-019-00173-4
- Nguyen, T. T., and Wong, T. Y. (2006). Retinal vascular manifestations of metabolic disorders. *Trends Endocrinol. Metabolism TEM* 17 (7), 262–268. doi:10.1016/j.tem.2006.07.006
- O'Neill, R. A., Maxwell, A. P., Paterson, E. N., Kee, F., Young, I., Hogg, R. E., et al. (2021). Retinal microvascular parameters are not significantly associated with mild cognitive impairment in the Northern Ireland Cohort for the Longitudinal Study of Ageing. *BMC Neurol.* 21 (1), 112. doi:10.1186/s12883-021-02137-4
- Ong, Y.-T., De Silva, D. A., Cheung, C. Y., Chang, H.-M., Chen, C. P., Wong, M. C., et al. (2013). Microvascular structure and network in the retina of patients with ischemic stroke. *Stroke* 44 (8), 2121–2127. doi:10.1161/STROKEAHA.113.001741

- Ong, Y.-T., Hilal, S., Cheung, C. Y.-L., Xu, X., Chen, C., Venketasubramanian, N., et al. (2014). Retinal vascular fractals and cognitive impairment. *Dementia Geriatric Cognitive Disord. Extra* 4 (2), 305–313. doi:10.1159/000363286
- Patton, N., Aslam, T., Macgillivray, T., Pattie, A., Deary, I. J., and Dhillon, B. (2005). Retinal vascular image analysis as a potential screening tool for cerebrovascular disease: A rationale based on homology between cerebral and retinal microvasculatures. *J. Anat.* 206 (4), 319–348. doi:10.1111/j.1469-7580.2005.00395.x
- Polanco, J. C., Li, C., Bodea, L.-G., Martinez-Marmol, R., Meunier, F. A., and Götz, J. (2018). Amyloid- β and tau complexity - towards improved biomarkers and targeted therapies. *Nat. Rev. Neurol.* 14 (1), 22–39. doi:10.1038/nrneurol.2017.162
- Prince, M., Bryce, R., Albanese, E., Wimo, A., Ribeiro, W., and Ferri, C. P. (2013). The global prevalence of dementia: A systematic review and metaanalysis. *Alzheimer's Dementia J. Alzheimer's Assoc.* 9 (1), 63–75. doi:10.1016/j.jalz.2012.11.007
- Ravi Teja, K. V., Tos Berendschot, T., Steinbusch, H., Carroll Webers, A. B., Praveen Murthy, R., and Mathuranath, P. S. (2017). Cerebral and retinal Neurovascular changes: A biomarker for Alzheimer's disease. *J. Gerontology Geriatric Res.* 6 (4), 447. doi:10.4172/2167-7182.1000447
- Reitz, C., Brayne, C., and Mayeux, R. (2011). Epidemiology of Alzheimer disease. *Nat. Rev. Neurol.* 7 (3), 137–152. doi:10.1038/nrneurol.2011.2
- Ronneberger, O., Fischer, P., and Brox, T. (2015). *U-net: Convolutional networks for biomedical image segmentation*. Springer, 234–241.
- Sabayan, B., Jansen, S., Oleksik, A. M., Van Osch, M. J. P., Van Buchem, M. A., Van Vliet, P., et al. (2012). Cerebrovascular hemodynamics in Alzheimer's disease and vascular dementia: A meta-analysis of transcranial Doppler studies. *Ageing Res. Rev.* 11 (2), 271–277. doi:10.1016/j.arr.2011.12.009
- Shao, L., Zhang, Q. L., Long, T. F., Dong, L., Zhang, C., Da Zhou, W., et al. (2021). Quantitative assessment of fundus Tesselated density and associated factors in fundus images using artificial intelligence. *Transl. Vis. Sci. Technol.* 10 (9), 23. doi:10.1167/tvst.10.9.23
- Shi, D., Lin, Z., Wang, W., Tan, Z., Shang, X., Zhang, X., et al. (2022). A deep learning system for fully automated retinal vessel measurement in high Throughput image analysis. *Front. Cardiovasc. Med.* 9, 823436. doi:10.3389/fcvm.2022.823436
- Simen, A. A., Bordner, K. A., Martin, M. P., Moy, L. A., and Barry, L. C. (2011). Cognitive dysfunction with aging and the role of inflammation. *Ther. Adv. Chronic Dis.* 2 (3), 175–195. doi:10.1177/2040622311399145
- Snyder, P. J., Alber, J., Alt, C., Bain, L. J., Bouma, B. E., Bouwman, F. H., et al. (2021). Retinal imaging in Alzheimer's and neurodegenerative diseases. *Alzheimer's Dementia J. Alzheimer's Assoc.* 17 (1), 103–111. doi:10.1002/alz.12179
- Sur, S., Lin, Z., Li, Y., Yasar, S., Rosenberg, P., Moghekar, A., et al. (2020). Association of cerebrovascular reactivity and Alzheimer pathologic markers with cognitive performance. *Neurology* 95 (8), e962–e972. doi:10.1212/WNL.0000000000010133
- Ting, D. S. W., Cheung, C. Y.-L., Lim, G., Tan, G. S. W., Quang, N. D., Gan, A., et al. (2017). Development and validation of a deep learning system for diabetic retinopathy and related eye diseases using retinal images from multiethnic populations with diabetes. *JAMA* 318 (22), 2211–2223. doi:10.1001/jama.2017.18152
- Tombaugh, T. N., and McIntyre, N. J. (1992). The mini-mental state examination: A comprehensive review. *J. Am. Geriatrics Soc.* 40 (9), 922–935. doi:10.1111/j.1532-5415.1992.tb01992.x
- Trucco, E., Giachetti, A., Ballerini, L., Relan, D., and Macgillivray, T. (2015). *Morphometric measurements of the retinal vasculature in fundus images with Vampire. Biomedical image Understanding, methods and Applications*.
- Vilela, M. A., Amaral, C. E., and Ferreira, M. A. T. (2021). Retinal vascular tortuosity: Mechanisms and measurements. *Eur. J. Ophthalmol.* 31 (3), 1497–1506. doi:10.1177/1120672120979907
- Wiseman, S. J., Zhang, J.-F., Gray, C., Hamid, C., Valdés Hernández, M. D. C., Ballerini, L., et al. (2023). Retinal capillary microvessel morphology changes are associated with vascular damage and dysfunction in cerebral small vessel disease. *J. Cereb. Blood Flow Metabolism Official J. Int. Soc. Cereb. Blood Flow Metabolism* 43 (2), 231–240. doi:10.1177/0271678X221135658
- Wong, T. Y., Islam, F. M. A., Klein, R., Klein, B. E. K., Cotch, M. F., Castro, C., et al. (2006). Retinal vascular caliber, cardiovascular risk factors, and inflammation: The multi-ethnic study of atherosclerosis (MESA). *Investigative Ophthalmol. Vis. Sci.* 47 (6), 2341–2350. doi:10.1167/iovs.05-1539
- Wu, H., Wang, C., Chen, C., Xu, X., Zhu, Y., Sang, A., et al. (2020). Association between retinal vascular Geometric changes and cognitive impairment: A systematic review and meta-analysis. *J. Clin. Neurology (Seoul, Korea)* 16 (1), 19–28. doi:10.3988/jcn.2020.16.1.19
- Xie, J., Yi, Q., Wu, Y., Zheng, Y., Liu, Y., Macerollo, A., et al. (2023). Deep segmentation of OCTA for evaluation and association of changes of retinal microvasculature with Alzheimer's disease and mild cognitive impairment. *Br. J. Ophthalmol.* 3. doi:10.1136/bjo-2022-321399
- Xu, Y., Wang, Y., Liu, B., Tang, L., Lv, L., Ke, X., et al. (2019). The diagnostic accuracy of an intelligent and automated fundus disease image assessment system with lesion quantitative function (SmartEye) in diabetic patients. *BMC Ophthalmol.* 19(1), 184. doi:10.1186/s12886-019-1196-9
- Yan, Y. N., Wang, Y. X., Xu, L., Xu, J., Wei, W. B., and Jonas, J. B. (2015). Fundus Tesselation: Prevalence and associated factors: The Beijing eye study 2011. *Ophthalmology* 122 (9), 1873–1880. doi:10.1016/j.ophtha.2015.05.031
- Yim-Lui Cheung, C., Wong, T. Y., Lamoureux, E. L., Sabanayagam, C., Li, J., Lee, J., et al. (2010). C-reactive protein and retinal microvascular caliber in a multiethnic Asian population. *Am. J. Epidemiol.* 171 (2), 206–213. doi:10.1093/aje/kwp357
- Yu, J.-T., Xu, W., Tan, C.-C., Andrieu, S., Suckling, J., Evangelou, E., et al. (2020). Evidence-based prevention of Alzheimer's disease: Systematic review and meta-analysis of 243 observational prospective studies and 153 randomised controlled trials. *J. Neurology, Neurosurg. Psychiatry* 91 (11), 1201–1209. doi:10.1136/jnnp-2019-321913
- Zhang, Y., Wang, Y., Shi, C., Shen, M., and Lu, F. (2021). Advances in retina imaging as potential biomarkers for early diagnosis of Alzheimer's disease. *Transl. Neurodegener.* 10 (1), 6. doi:10.1186/s40035-021-00230-9



OPEN ACCESS

EDITED BY

Weihua Yang,
Jinan University, China

REVIEWED BY

Lianqun Wu,
Fudan University, China
Yumei Xue,
Beihang University, China
Lingjia Liu,
Tianjin Medical University Eye Hospital,
China

*CORRESPONDENCE

Jiawen Lin,
✉ ljw@fzu.edu.cn
Ying Xue,
✉ 502873740@qq.com

[†]These authors share first authorship

RECEIVED 30 March 2023

ACCEPTED 22 May 2023

PUBLISHED 21 June 2023

CITATION

Li L, Lai T, Zou J, Guo L, Lin Z, Lin J and Xue Y (2023), Effects of orthokeratology lenses on tear film and tarsal glands and control of unilateral myopia in children. *Front. Cell Dev. Biol.* 11:1197262. doi: 10.3389/fcell.2023.1197262

COPYRIGHT

© 2023 Li, Lai, Zou, Guo, Lin, Lin and Xue. This is an open-access article distributed under the terms of the [Creative Commons Attribution License \(CC BY\)](#). The use, distribution or reproduction in other forums is permitted, provided the original author(s) and the copyright owner(s) are credited and that the original publication in this journal is cited, in accordance with accepted academic practice. No use, distribution or reproduction is permitted which does not comply with these terms.

Effects of orthokeratology lenses on tear film and tarsal glands and control of unilateral myopia in children

Li Li^{1,2,3,4†}, Taichen Lai⁵, Jing Zou⁵, Linling Guo⁵, Zhiming Lin⁶, Jiawen Lin^{6*} and Ying Xue^{1,2*}

¹Shengli Clinical Medical College of Fujian Medical University, Fuzhou, China, ²Ophthalmology Department, Fujian Provincial Hospital South Branch, Fujian Provincial Hospital, Fuzhou, China, ³Division of Ophthalmology, Department of Surgery, University of Melbourne, Melbourne, VIC, Australia, ⁴Centre for Eye Research Australia, Royal Victorian Eye and Ear Hospital, Melbourne, VIC, Australia, ⁵Department of Clinical Medicine, Fujian Medical University, Fuzhou, China, ⁶College of Computer and Big Data, Fuzhou University, Fuzhou, China

Introduction: To investigate the effects of an orthokeratology lens on the tear film and tarsal glands and myopia control in children with unilateral myopia using an intelligent analysis model.

Methods: We retrospectively reviewed the medical records from November 2020 to November 2022 of 68 pediatric patients with unilateral myopia in Fujian Provincial Hospital who had been wearing an orthokeratology lens for more than 1 year. The 68 myopic eyes were included in the treatment group, while the 68 healthy, untreated contralateral eyes were included in the control group. Tear film break-up times (TBUTs) were compared between the two groups at various intervals, and an intelligent analysis model was used to compare the deformation coefficients of 10 meibomian glands in the central area and the different positions of the glands in the two groups after 12 months of treatment. Changes in axial length and equivalent spherical power were also compared between the groups before and after 12 months of treatment.

Results: In the treatment group, TBUTs differed significantly between 1 and 12 months after treatment, although no significant differences from baseline were observed at 3 or 6 months. No significant differences in TBUTs were observed at any time point in the control group. After 12 months of treatment, significant between-group differences were observed for glands 2, 3, 4, 5, 6, 7, 8, and 10 (numbered from the temporal to nasal regions). The treatment group also exhibited significant differences in deformation coefficients at different detection positions in the central region, with glands 5 and 6 exhibiting the highest deformation coefficients. Increases in axial length and equivalent spherical power were significantly greater in the control group than in the treatment group after 12 months of treatment.

Discussion: Wearing orthokeratology lenses at night can effectively control myopia progression in children with unilateral myopia. However, long-term use of these lenses may lead to meibomian gland deformation and impact tear film function, and the extent of deformation may vary at different positions in the central region.

KEYWORDS

myopia, orthokeratology lens, tear film, tarsal gland, artificial intelligence

1 Introduction

In recent decades, technological advancements have introduced a variety of electronic products and children's toys that are viewed within a close range and have become ubiquitous in daily life. The childhood developmental period is a critical window for both cognitive and physical growth. Increased emphasis on educational attainment has resulted in a high frequency of close-range eye behaviors (e.g., reading, mobile device usage, and computer usage). When coupled with improper reading and writing postures, this can lead both eyes to develop different degrees of myopia during eye development. Accordingly, one eye may develop myopia earlier than the other, resulting in unilateral myopia. Children with unilateral myopia present with overload of the myopic eye when viewing near objects, which can aggravate the progression of myopia and lead to symptoms of ocular fatigue due to decreased coordination between the eyes. If the difference in the refractive error between the two eyes is greater than 2.5 D, fine motor impairments can be observed, and children can find it difficult to adapt to wearing frame glasses, thereby affecting quality of life.

The orthokeratology lens, which is a reverse geometry lens made of highly gas permeable rigid material, is worn by patients on the corneal surface during sleep. The central region of the cornea is flattened by the positive pressure of the base curve at the central region of the lens, allowing epithelial cells to accumulate at the reverse curve through migration, thereby effectively halting the development of myopia. At present, the orthokeratology lens is an effective method for controlling disease progression in children with low to moderate myopia, and the strategy has recently gained attention given the relative comfort of the lens and low risk of complications (Müller et al., 2016). In addition to delaying myopia progression during adolescence, several studies have demonstrated (Ren et al., 2016; Xie and Guo, 2016) that orthokeratology lenses help to control the rapid growth of the eye axis and negate the need for frame glasses. However, long-term use of an orthokeratology lens may exert detrimental effects on the tear film and tarsal glands via mechanical irritation or hypoxic interference.

To address this gap in knowledge and determine the effectiveness of myopia control, the present retrospective study was designed to investigate the effects of orthokeratology lenses on the tear film and tarsal glands in children with unilateral myopia. To achieve this aim, we analyzed complete data of pediatric patients treated at our hospital who had been wearing an orthokeratology lens in one eye continuously for more than 12 months using an intelligent analysis model.

2 Materials and methods

2.1 General information

We reviewed the medical records from November 2020 to November 2022 of 68 pediatric patients with unilateral myopia treated in the Department of Ophthalmology of Fujian Provincial

Hospital. The myopic eyes of patients treated using an orthokeratology lens were included in the treatment group (68 eyes), in which the mean spherical equivalent was -1.92 ± 1.21 D, whereas the healthy, untreated contralateral eyes were included in the control group (68 eyes), in which the mean spherical equivalent was $+1.06 \pm 0.68$ D. The inclusion criteria were as follows: a) age of 8–14 years, b) more than 1 year of complete data for review, c) diagnosis of unilateral myopia with a spherical equivalent of -1.00 to 6.00 D in the myopic eye, d) best corrected visual acuity ≥ 5.0 in both eyes, and e) normal intraocular pressure and fundus in both eyes. The exclusion criteria were as follows: a) organic eye disease; b) corneal diseases, moderate or severe allergic conjunctivitis, dry eye disease, or keratoconus; c) poor compliance and/or inability to be followed up according to medical advice; d) combined use of other myopia interventions, such as low-dose atropine and defocus lenses; and e) contraindications to orthokeratology lens use. The risks and potential complications of wearing the orthokeratology lens were explained in detail to the patients and guardians before treatment, and consent was obtained for fitting. The study was approved by the Ethics Committee (K2020-03-124) of the hospital, and the parents or guardians of the enrolled patients signed an informed consent form.

2.2 Methods

2.2.1 Fitting for the orthokeratology lens

All patients underwent appropriate eye examinations prior to enrolment and fitting, including naked eye vision examination, best corrected visual acuity, mydriatic retinophotoscopy, specular microscopy, corneal topography, IOLMaster examination, slit lamp examination, tear film break-up time (TBUT) estimation, and infrared photography of the tarsal glands. Patients eligible for the orthokeratology lens were screened with reference to the inclusion criteria. A suitable trial orthokeratology lens was selected for try-on and evaluation based on the corneal diameter and corneal topography of each patient. After 30 min of trial fitting, the dynamic and static fit of the lens was evaluated, and the parameters of the trial lens were adjusted until the ideal fit was achieved. A lens with ideal fit was defined as a well-centered lens with 1–2 mm of mobility when blinking, with all curves stained to standard. All patients were instructed by the same optometrist on the standard methods of lens removal, placement, and care. The minimum and maximum durations of nighttime lens wear were set to 8 h and 10 h, respectively.

2.2.2 Method of constructing an intelligent model for the tarsal glands

UNet++ was introduced to construct a tarsal gland segmentation model and provide a workflow for automatic gland segmentation, as shown in Figure 1. We considered tarsal gland segmentation as a binary classification problem at each pixel of an image. Tarsal gland segmentation was divided into two stages (training and segmentation) and included the following three modules.

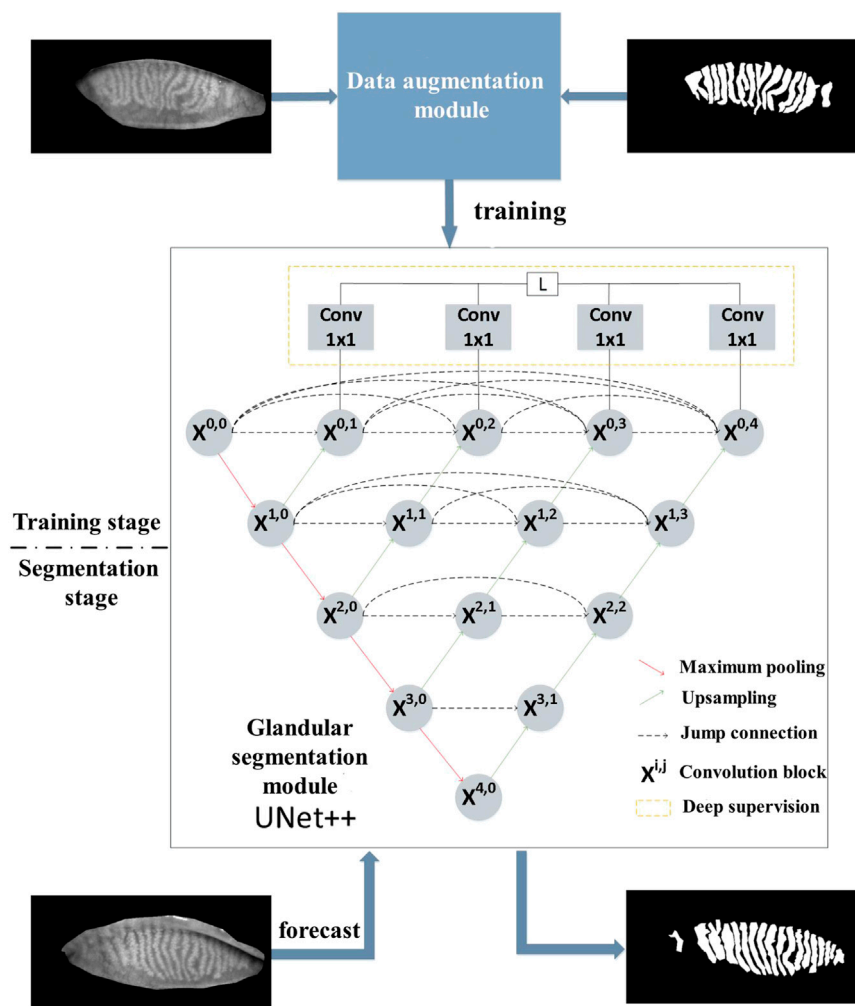


FIGURE 1
The procedure for meibomian gland segmentation based on UNet++.

2.2.2.1 Data augmentation module

In this module, an automatic data augmentation strategy was introduced to randomly select N of 11 types of data augmentation methods (e.g., cropping, flipping, cutting, translation, rotation, equalization, contrast adjustment, brightness adjustment), following which the corresponding magnitude of transformation, M , for these N types was selected. Eventually, we set N to 2 and the selection range for M to 1–10 based on experimental findings. The data augmentation module used for this study did not require a manually designed data augmentation strategy, could provide adequate data samples for the gland segmentation model, and enhanced the generalizability of the model.

2.2.2.2 Gland segmentation module

The infrared images of the tarsal glands were grayscale images, which do not contain rich semantic information. Our preliminary analyses indicated that it would be inappropriate to use a complex network model. Proposed in 2015, the UNet model (Ronneberger et al., 2015) was designed specifically for

application in medical image segmentation. UNet uses hop connections to merge the superficial and deep semantic feature maps to overcome the information loss caused by subsampling, thereby significantly improving the accuracy of medical image segmentation. UNet++ is an improved version of UNet in which the hop connections have been redesigned to further reduce the semantic gap in merging the features between encoder and decoder. This module was used to introduce the UNet++ model as the main network for automatic gland segmentation.

2.2.2.3 Gland analysis module

After segmenting the tarsal glands, a small portion of the automatically segmented images can be processed again to capture missed areas or select additional areas using the editing tool in the software. After perfecting the tarsal gland images, the parameters of the gland model were analyzed, and the deformation coefficients of the glands (reflecting the degree of gland deformation) were automatically calculated. The deformation coefficient was calculated as follows:

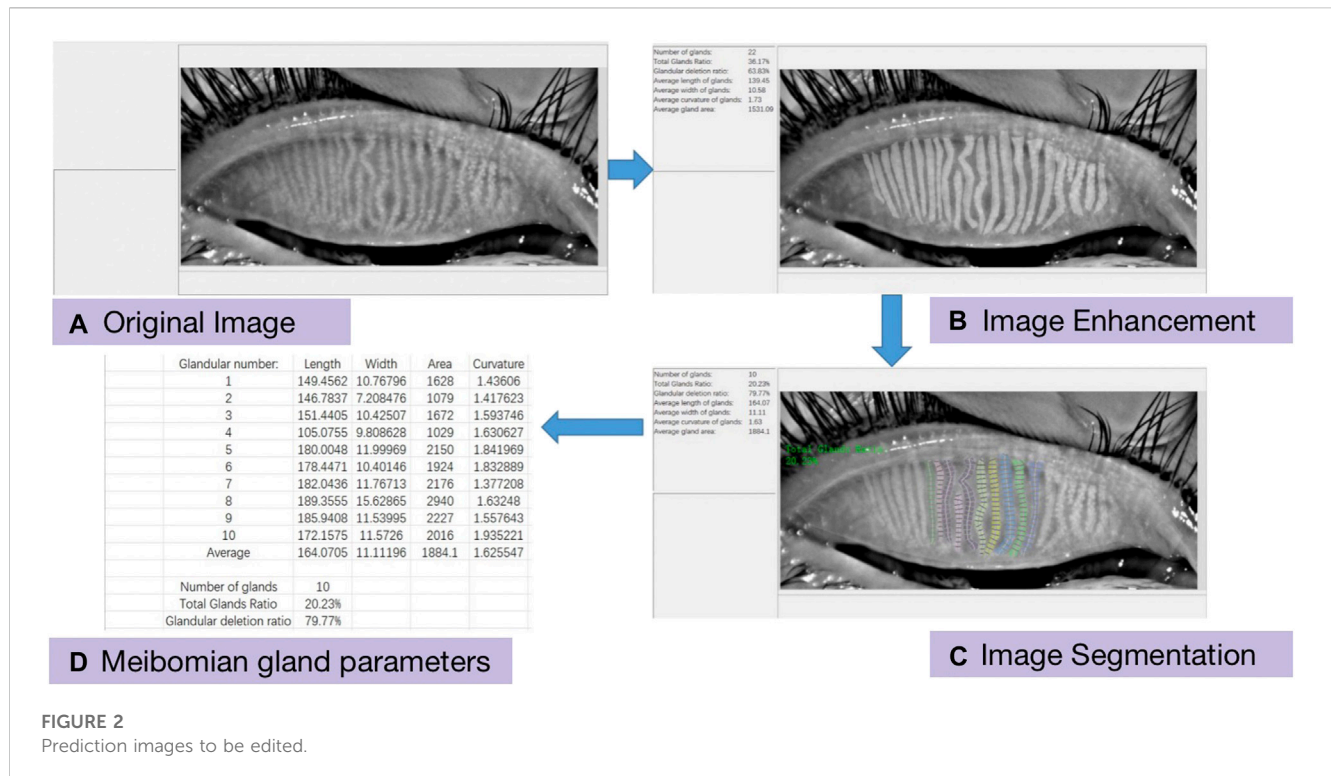


FIGURE 2
Prediction images to be edited.

$$\frac{p_a \times p_b}{\text{length}(\text{central})^2} \times \left(\frac{\sqrt{\sum_{i=1}^n (w_i - w_{avg})^2}}{n} + 1 \right)$$

The formula for calculating the deformation coefficient of the gland was established and improved upon based on the arc-string ratio model (Figure 2). Here, p_a refers to the length of the left side of the gland, p_b refers to the length of the right side of the gland, w_i refers to the diameter of the gland taken after each step, w_{avg} refers to the average diameter of the gland, length (central) refers to the length of the central line, n refers to the number of diameters taken by the gland, the minimum value of the formula is 1, and the deformation coefficients are dimensionless units.

2.3 Observational indicators

All enrolled patients underwent an eye examination before treatment (when the custom-made orthokeratology lens arrived), which was considered the starting point of the observation period. Follow-ups were conducted 1, 3, 6, and 12 months after initiating treatment. Indicators evaluated in this study included TBUT, axial length, and spherical equivalent, as well as adverse reactions during the treatment period.

2.3.1 TBUT

The inferior conjunctival sacs of both eyes were lightly touched with a fluorescein sodium strip that had been moistened with saline. The patient was asked to blink three times to allow the cornea to make full contact with the

fluorescein, and the corneal condition was observed under cobalt blue light with a slit lamp. During the examination, the patient was advised not to blink until a black spot appeared on the cornea. The time taken for the first black spot to appear during the examination was recorded, and the measurement was repeated three times to obtain an average value.

2.3.2 Tarsal gland deformation coefficient

Changes in the morphology of each tarsal gland were analyzed using the intelligent model. In this study, the deformation coefficients of 10 glands in the central regions of the upper eyelids of both eyes were calculated after 12 months of treatment. Using the midline of the overall tarsal gland area of each patient's upper eyelid as the center, values were calculated for five glands extending towards the nasal and temporal sides, respectively, resulting in a total of 10 glands for analysis. The 10 glands were numbered such that the first tarsal gland at the temporal side was considered gland 1, while the first tarsal gland on the nasal side was considered gland 10.

2.3.3 Axial length

IOLMaster was used to examine axial length, and the measurement was repeated five times to obtain an average value.

2.3.4 Spherical equivalent

The patients were administered 1% compound tropicamide eye drops to fully paralyze the ciliary muscle. Treated eyes underwent optometry using an automatic computerized refractometer while the orthokeratology lens was in place, while control eyes underwent the same assessment on the

TABLE 1 Patient information.

Patient information		Number of cases
Sex	Female	38
	Male	30
Residence	Urban	52
	Rural	16
Myopic eye	Right	29
	Left	39
Premature infant	Yes	10
	No	58
Family history of unilateral myopia	Yes	4
	No	64

naked eye. The measurement was repeated five times to obtain an average spherical equivalent value.

2.4 Statistical analysis

Data were statistically analyzed using SPSS 22.0 software. Independent samples t-tests were used to compare the average values of the two groups at each time point. Paired t-tests were used to compare the average values of the same group at different time points. Paired samples t-tests were also used to evaluate the deformation coefficients of the 10 tarsal glands in the central region in the two groups after 12 months of treatment. A one-way analysis of variance (ANOVA) was used to evaluate the deformation coefficients of the tarsal glands at different examination locations in each of the two groups. The measurement data of both groups were expressed as mean \pm standard deviation ($x \pm s$), whereas the count data were expressed as proportions (%). A difference was considered statistically significant when $p < 0.05$.

3 Results

Data were retrospectively analyzed for 68 patients (30 boys, 38 girls; mean age: 11.12 ± 0.76 years; age range: 8–14 years). The characteristics of the included patients are summarized in Table 1.

3.1 TBUT

In the treatment group, there were no statistically significant differences in TBUT from baseline at 3 or 6 months after treatment ($p > 0.05$). However, TBUTs differed significantly between 1 and 12 months after treatment ($p < 0.05$). No significant differences in TBUT from baseline were observed at any time point in the control group ($p > 0.05$) (Table 2).

3.2 Differences in Deformation Coefficients of 10 glands in the central regions of the upper eyelids between the Two Groups

Significant between-group differences in deformation coefficients were observed for glands 2, 3, 4, 5, 6, 7, 8, and 10 in the central region ($p < 0.05$). In all cases, deformation coefficients were higher in the treatment group than in the control group (Table 3).

3.3 Differences in Deformation Coefficients of 10 glands in the central regions of the upper eyelids at Different Examination Sites

3.3.1 Treatment group

Within the treatment group, significant differences in gland deformation coefficients were observed across different examination sites. Deformation coefficients for glands 5 and 6 were higher than those for glands 3 and 4, while deformation coefficients for glands 3 and 4 were higher than those for glands 1, 2, 8, 9, and 10 (Table 4; Figure 3).

TABLE 2 Comparison of tear film break-up time before and at 1, 3, 6, and 12 months after treatment initiation in the treatment and control groups.

Time point	Group	TBUT		t	p
		Pre-treatment	Post-treatment		
1 month	Treatment group	10.50 ± 1.40	6.50 ± 0.97	45.445	.000
	Control group	10.98 ± 1.62	10.12 ± 1.5	0.764	.272
3 months	Treatment group	10.50 ± 1.40	10.00 ± 0.82	1.785	.079
	Control group	10.98 ± 1.62	10.58 ± 1.81	.268	.725
6 months	Treatment group	10.50 ± 1.40	9.67 ± 1.5	1.132	.128
	Control group	10.98 ± 1.62	10.77 ± 1.87	.000	1.000
12 months	Treatment group	10.50 ± 1.40	7.17 ± 1.36	29.807	.000
	Control group	10.98 ± 1.62	10.85 ± 1.35	.000	1.000

Data are expressed as mean \pm standard deviation.
TBUT, tear film break-up time.

TABLE 3 Differences in gland deformation coefficients between the groups.

		Paired difference					t	Significance (two-tailed)
		Average value	Standard deviation	Standard error of the mean	95% confidence interval for difference			
					Upper limit	Lower limit		
Pair 1	Deformation coefficient of gland 1 in the treatment group—deformation coefficient of gland 1 in the control group	0.121	0.384	0.064	−0.009	0.251	1.888	0.067
Pair 2	Deformation coefficient of gland 2 in the treatment group—deformation coefficient of gland 2 in the control group	0.420	1.016	0.169	0.076	0.764	2.481	0.018
Pair 3	Deformation coefficient of gland 3 in the treatment group—deformation coefficient of gland 3 in the control group	1.207	1.544	0.257	0.685	1.730	4.691	0.000
Pair 4	Deformation coefficient of gland 4 in the treatment group—deformation coefficient of gland 4 in the control group	2.195	2.919	0.487	1.208	3.183	4.512	0.000
Pair 5	Deformation coefficient of gland 5 in the treatment group—deformation coefficient of gland 5 in the control group	4.563	3.536	0.589	3.367	5.759	7.744	0.000
Pair 6	Deformation coefficient of gland 6 in the treatment group—deformation coefficient of gland 6 in the control group	4.960	5.345	0.891	3.152	6.769	5.569	0.000
Pair 7	Deformation coefficient of gland 7 in the treatment group—deformation coefficient of gland 7 in the control group	2.205	2.062	0.344	1.508	2.903	6.417	0.000
Pair 8	Deformation coefficient of gland 8 in the treatment group—deformation coefficient of gland 8 in the control group	0.634	1.165	0.194	0.240	1.028	3.266	0.002
Pair 9	Deformation coefficient of gland 9 in the treatment group—deformation coefficient of gland 9 in the control group	0.077	0.439	0.073	−0.072	0.225	1.049	0.301
Pair 10	Deformation coefficient of gland 10 in the treatment group—deformation coefficient of gland 10 in the control group	0.268	0.343	0.057	0.151	0.384	4.677	0.000

3.3.2 Control group

Within the control group, significant differences in gland deformation coefficients were also observed at different examination sites ($p < 0.05$). The deformation coefficient of gland 6 was higher than the deformation coefficients for glands 1, 2, 3, 4, 5, 7, 8, 9, and 10, while the deformation coefficients for glands 3, 5, and 8 were higher than the deformation coefficient for gland 10 (Table 5; Figure 4).

3.4 Axial length

In both groups, axial length increased with time after treatment. However, after 12 months of treatment, the degree of increase in axial length was significantly lower in the treatment group (0.15 ± 0.13 mm) than in the control group (0.39 ± 0.23 mm) ($p < 0.05$) (Table 6).

3.5 Spherical equivalent

After 12 months of treatment, the spherical equivalent increased in 20 eyes (29.4%) in the treatment group, whereas it increased in 58 eyes (85.3%) in the control group, and the difference in the spherical equivalent between the two groups was statistically significant ($p < 0.05$) (Table 7).

4 Discussion

The prevalence of myopia among school-age children in East Asia is extremely high compared with other regions. The prevalence of myopia among school-age children in East Asia is extremely high compared with other regions (Grzybowski A et al., 2020). In clinical practice, most affected children present with bilateral myopia. However, poor eye habits and other

TABLE 4 Differences in gland deformation coefficients at different detection sites in the treatment group.

Examination site	Average value	Standard deviation	95% confidence interval for the average value		F	Significance	Least significant difference (LSD)
			Upper limit	Lower limit			
Gland 1	1.983	0.454	1.830	2.137	29.003	0.000	5, 6 > 3, 4 > 1, 2, 8, 9, 10
Gland 2	2.179	0.963	1.853	2.505			
Gland 3	3.285	1.270	2.855	3.714			
Gland 4	4.120	2.894	3.141	5.099			
Gland 5	6.608	3.424	5.449	7.767			
Gland 6	7.447	4.500	5.925	8.970			
Gland 7	4.176	2.136	3.453	4.899			
Gland 8	2.684	1.248	2.261	3.106			
Gland 9	1.852	0.469	1.693	2.011			
Gland 10	1.890	0.457	1.736	2.045			

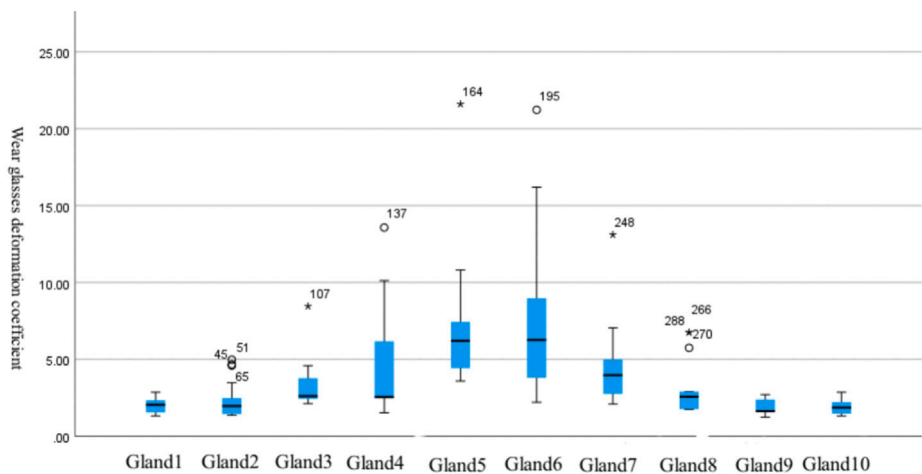


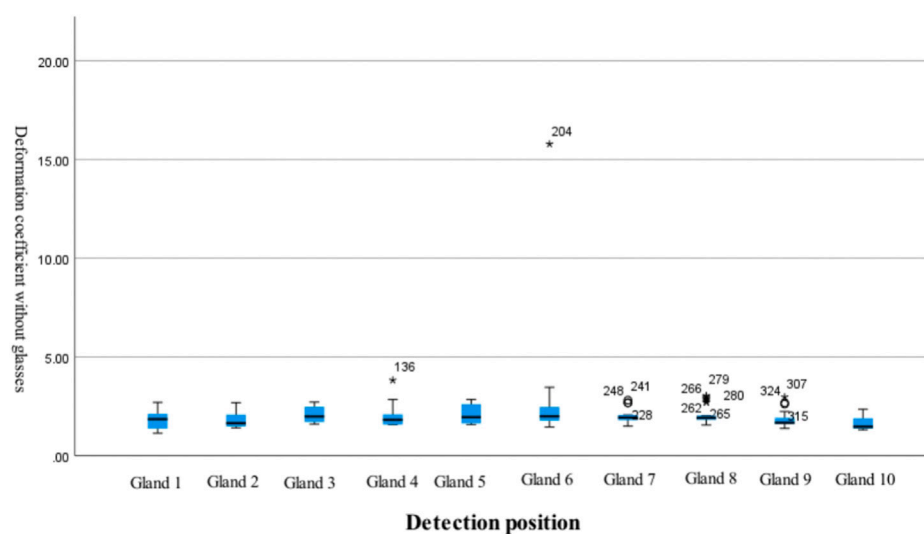
FIGURE 3 Differences in gland deformation coefficients at different detection locations in the treatment group.

environmental factors (e.g., masking the eyes on one side when writing and tilting the body when reading/writing) can lead to inconsistencies in the distance between each eye and the viewing material. Such factors may also contribute to differences in visual acuity between the eyes (Shi et al., 2021) and an increase in the number of adolescents with unilateral myopia presenting with anisometropia. For children who have unilateral myopia with anisometropia, differences in refractive error can lead to contradictory eye adjustments and an imbalance in image size. At present, the two most common correction materials are frame glasses and orthokeratology lenses. While frame glasses are widely accepted by patients and parents in clinical practice given their convenience and low cost, correction with frame glasses is

associated with problems such as imbalanced visual quality and difficulty in fusion, which will continue to increase the refractive error of myopia. In contrast, the orthokeratology lens exerts its effects via nighttime wear. In addition to controlling the rate of increase in the refractive error of myopia, orthokeratology lenses can reduce the overall refractive error of myopic eyes and improve both visual quality and fusion function in the two eyes during adolescence. Therefore, orthokeratology lens treatment has become the preferred correction method for adolescents who have unilateral myopia with anisometropia. Some studies have also shown that orthokeratology lenses are the best means to control myopia among the available non-surgical treatment methods (Walline et al., 2020).

TABLE 5 Differences in gland deformation coefficients at different detection sites in the control group.

Examination site	Average value	Standard deviation	95% confidence interval for the average value		F	Significance	Least significant difference (LSD)
			Upper limit	Lower limit			
Gland 1	1.862	0.404	1.726	1.999	3.011	0.002	6 > 1,2,3,4,5,7,8,9,10;3, 5, 8 > 10
Gland 2	1.759	0.335	1.646	1.873			
Gland 3	2.077	0.426	1.933	2.222			
Gland 4	1.925	0.447	1.773	2.076			
Gland 5	2.045	0.411	1.906	2.184			
Gland 6	2.487	2.328	1.699	3.274			
Gland 7	1.971	0.275	1.878	2.063			
Gland 8	2.050	0.437	1.902	2.197			
Gland 9	1.775	0.359	1.653	1.897			
Gland 10	1.622	0.284	1.527	1.718			

**FIGURE 4**

Differences in gland deformation coefficients at different detection locations in the control group.

TABLE 6 Axial length before and after treatment in the two groups at 12 months.

		Change within 12 months of treatment
Increase in axial length	Treatment group	0.14 ± 0.08
	Control group	0.42 ± 0.17
	t	-11.393
	p	<0.01

Data are expressed as mean ± standard deviation.

TABLE 7 Spherical equivalent before and after treatment in the two groups at 12 months.

		Change within 12 months of treatment
Change in spherical equivalent	Treatment group	0.04 ± 0.16
	Control group	0.56 ± 0.36
	t	−10.168
	p	<0.01

Data are expressed as mean ± standard deviation.

Despite these results, Yang et al. (2021) find that Short-term OOK may reduce the stability of the tear film and increase damage to the corneal epithelium. Long-term OOK could induce ocular inflammation through the disruption of meibomian glands. However, Na et al. (2016) reported no significant changes in tear film stability after treatment with an orthokeratology lens. While TBUT was the main observational indicator in their study, the results were largely influenced by the subjective nature of the examinations and patient cooperation. To ensure more objective analyses, each patient/parent was informed of the examination precautions and the standard of cooperation required during examination. In the current study, the treatment group exhibited a significant reduction in TBUT from baseline at 1 month after treatment. This may be because the initial shaping begins in the early stage of lens wear, in which the corneal epithelial cells begin to migrate and distribute. This in turn leads to an uneven corneal surface, which affects the uniform distribution of tear film and reduces tear film stability. In contrast, TBUTs at 3 and 6 months after treatment initiation did not significantly differ from baseline. This may have been due to improvements in tear film stability following stabilization of the corneal shape, resulting in restoration of tear film function during treatment. However, some studies have found that long-term use of an orthokeratology lens may lead to altered tarsal gland function (Walline et al., 2020). Others have similarly concluded (Zhu and Huang, 2016; Zhou et al., 2019) that wearing an orthokeratology lens for 1 year exerts certain effects on the tarsal glands and that the frequency with which tear film function is examined should be increased. Gad et al. (2019) also noted that changes in the number and function of goblet cells and changes in the inflammatory response of the ocular surface may contribute to decreased tear film stability during long-term treatment with an orthokeratology lens. These findings are in accordance with the significant change in the TBUT after 12 months of treatment in our patients.

In clinical practice, although children undergoing long-term treatment with an orthokeratology lens often present no significant atrophy of the tarsal glands, other morphological changes such as distortion may emerge. Lin et al. (2020) recently reported significant correlations of tarsal gland tortuosity with the meiboscore and meibum expressibility score, suggesting that changes in the morphology of the tarsal glands can affect their function. However, at present, clinical examinations do not allow for a more accurate quantitative assessment of the tarsal glands. Therefore, we constructed an intelligent analysis model based on deep learning methods to analyze the deformation coefficients of the tarsal glands after processing and segmenting the infrared photographic report. After a preliminary test of this method, Our

team, Lin et al. (2022), found that the average accuracy of the algorithm was 94.31%, with an average sensitivity of 82.15%, an average specificity of 96.13%, and an average intersection ratio of 65.55%. Based on this tarsal gland segmentation algorithm, we developed a quantitative tarsal gland analysis model that can quantitatively analyze data from each tarsal gland in the upper eyelid. However, in the current study, data were collected for only 10 tarsal glands in the central region of the upper eyelid, mainly because it is easier to collect complete data for the upper eyelid than for the lower eyelid, and the images are clearer. Further, The glands in the central region play a major role in maintaining the stability of the microenvironment at the ocular surface.

After 12 months of treatment with an orthokeratology lens, we observed significant between-group differences in the deformation coefficients of the 10 tarsal glands in the central region, with the deformation coefficients being significantly higher in the treatment group than in the control group. This result suggests that long-term use of an orthokeratology lens exerts certain effects on tarsal gland morphology. In addition, although there were certain differences between the 10 tarsal glands at different sites in both groups, the box plots indicated that the average deformation coefficients of the 10 glands in the central region were closer to each other in the control group. In the treatment group, the average deformation coefficients of the glands near the center were significantly higher than those of the glands near the periphery. This may be related to the positioning of the orthokeratology lens at the central cornea. Yu et al. (2022) reported increased atrophy of the meibomian glands in the lower eyelid in children wearing orthokeratology lenses. During sleep, a certain amount of pressure is exerted not only on the cornea but also on the tarsal glands owing to the mechanics of the orthokeratology lens, which may lead to morphological changes in the glands closer to the central area. In the future, based on the results of this study, for children with OK lenses, it is recommended that additional images of the tarsal gland be taken at the time of outpatient follow-up and that the main focus be on morphological changes of the tarsal gland in the central region.

The refractive error of the human eye is closely related to both corneal curvature and axial length. An increase in negative refractive error is mainly related to an increase in axial length when the corneal curvature remains unchanged (Alhussain et al., 2022). In this study, both the treatment and control groups exhibited an increase in axial length after 12 months. After 12 months of treatment with an orthokeratology lens, the average increase in axial length in the treatment group was 0.15 ± 0.13 mm, which was significantly less than that in the control group. The smaller change in axial length in the treatment group may be explained by a reduction in the average corneal curvature in the central region of the cornea through

positive pressure exerted by the base curve of the lens. Light passing through the central region is then better concentrated at the fovea of the macula. The siphon principle of the reverse curve causes the corneal epithelial cells to migrate and accumulate at the reverse curve region, and the incident rays passing through this region are focused in front of the peripheral retina. This then forms a myopic defocus that inhibits the increase in axial length. Although the rate of increase in axial length was slower in the treatment group than in the control group of the present study, axial length was significantly longer in the treatment group than in the control group at each time point during the 12-month treatment period. This suggests that for the same patient, the axial length increases with an increase in negative refractive error, provided that the difference in corneal curvature between the two eyes is insignificant.

In clinical practice, orthokeratology lenses are usually replaced each year. If each parameter (including corneal topography positioning, corneal condition, and changes in the eye axis) remains stable at this time, many parents will choose to have their child fitted for a new orthokeratology lens. Therefore, the change in spherical equivalent after pupil dilation following use of the lens is often used to assess myopia control after 1 year of treatment. For this reason, we also chose to compare changes in the spherical equivalent after lens use between the treatment and control groups. While eyes in the control group were not initially myopic, as the treatment group wore the orthokeratology lens for a long period of time, the changes in spherical equivalent became much higher in the control group than in the treatment group. This finding is in accordance with the significantly greater increase in axial length observed in the control group.

This study has some limitations. Given the retrospective nature of the analysis, we were unable to evaluate infrared photographic data of the tarsal glands when the patients first wore the orthokeratology lens, and the abnormal morphological changes in the tarsal glands of the ipsilateral eyes before and after 1 year of wearing the lens were not further compared. These relationships should be examined in future studies.

5 Conclusion

In children with anisometropia, unilateral treatment with an orthokeratology lens was effective in controlling increases in axial length and negative refractive error in the myopic eye, thereby delaying the progression of myopia. Increases in axial length and negative refractive error were greater in the contralateral non-myopic eyes. The TBUT of myopic eyes tended to decrease with long-term use of the orthokeratology lens. Using an intelligent model to analyze the deformation coefficients, we found that long-term orthokeratology lens use significantly influenced morphological changes in the 10 tarsal glands in the central region, exerting a relatively greater effect on the glands closer to the central region. Given these results, children undergoing single-eye treatment with an orthokeratology lens should be closely followed up for changes in spherical equivalent, axial length, tarsal gland morphology, and tear film function in both eyes to ensure that any abnormalities are detected and addressed using appropriate interventions in a timely manner. This will not only help to control the increase in the axial length of the non-

myopic eye as early as possible but also ensure better comfort and reduce the likelihood of complications with long-term use.

Data availability statement

The raw data supporting the conclusion of this article will be made available by the authors, without undue reservation.

Ethics statement

The studies involving human participants were reviewed and approved by the Ethics Committee (K2020-03-124) of the Fujian Provincial Hospital. Written informed consent to participate in this study was provided by the participants' legal guardian/next of kin.

Author contributions

Concept and design: LL and YX. Intelligent model design: JL and ZL. Acquisition, analysis, or interpretation of data: TL, ZL, JZ, and LG. Drafting of the manuscript: LL. Statistical analysis: LL, TL, and YX. Administrative, technical, or material support: All authors. Methodology: LL, JL, and YX. All authors contributed to the article and approved the submitted version.

Funding

The work was supported by Natural Science Foundation of Fujian Province, China [grant number: 2020J011084] to LL.

Acknowledgments

Thanks to Yanqing Fan, Qian Yang, and Conghui Chen for their contributions to patient education, management, and follow-up communication.

Conflict of interest

The authors declare that the research was conducted in the absence of any commercial or financial relationships that could be construed as a potential conflict of interest.

Publisher's note

All claims expressed in this article are solely those of the authors and do not necessarily represent those of their affiliated organizations, or those of the publisher, the editors and the reviewers. Any product that may be evaluated in this article, or claim that may be made by its manufacturer, is not guaranteed or endorsed by the publisher.

References

- Alhussain, S. H. A., Mallen, E. A. H., Strang, N. C., and Jonuscheit, S. (2022). The role of peripheral ocular length and peripheral corneal radius of curvature in determining refractive error. *J. Optom.* 15 (2), 129–137. doi:10.1016/j.optom.2021.02.001
- Gad, A., Vingrys, A. J., Wong, C. Y., Jackson, D. C., and Downie, L. E. (2019). Tear film inflammatory cytokine upregulation in contact lens discomfort. *Ocul. Surf.* 17, 89–97. doi:10.1016/j.jtos.2018.10.004
- Grzybowski, A., Kanclerz, P., Tsubota, K., Lanca, C., and Saw, S. M. (2020). A review on the epidemiology of myopia in school children worldwide. *BMC Ophthalmol.* 14 (1), 27. doi:10.1186/s12886-019-1220-0
- Lin, J., Lin, Z., Lai, T., Guo, L., Zou, J., Li, L., et al. (2022). Potential of fluorescent nanoprobe in diagnosis and treatment of Alzheimer's disease. *Int. J. Ophthalmol.* 22, 1191–1211. doi:10.2217/nnm-2022-0022
- Lin, X., Fu, Y., Li, L., Chen, C., Chen, X., Mao, Y., et al. (2020). A novel quantitative index of meibomian gland dysfunction, the meibomian gland tortuosity. *Transl. Vis. Sci. Technol.* 9, 34. doi:10.1167/tvst.9.9.34
- Müller, T. M., Lavy, I., Baydoun, L., Lie, J. T., Dapena, I., and Melles, G. R. (2016). Case report of Quarter-Descemet membrane endothelial keratoplasty for Fuchs endothelial dystrophy. *Cornea* 36, 104–107. doi:10.1097/ICO.0000000000001008
- Na, K. S., Yoo, Y. S., Hwang, H. S., Mok, J. W., Kim, H. S., and Joo, C. K. (2016). The influence of overnight orthokeratology on ocular surface and meibomian glands in children and adolescents. *Eye Contact Lens* 42, 68–73. doi:10.1097/ICL.0000000000000196
- Ren, Q. J., Yue, H., and Zhou, Q. (2016). Effects of orthokeratology lenses on the magnitude of accommodative lag and accommodative convergence/accommodation. *Zhong Nan Da Xue Xue Bao Yi Xue Ban.* 41, 169–173. doi:10.11817/j.jissn.1672-7347.2016.02.009
- Ronneberger, O., Fischer, P., and Brox, T. (2015). “U-net: Convolutional networks for biomedical image segmentation,” in *Medical image computing and computer-assisted intervention – miccai 2015* (Cham: Springer).
- Shi, H., Fu, J., Liu, X., Wang, Y., Yong, X., Jiang, L., et al. (2021). Influence of the interaction between parental myopia and poor eye habits when reading and writing and poor reading posture on prevalence of myopia in school students in Urumqi, China. *BMC Ophthalmol.* 21, 299–9. doi:10.1186/s12886-021-02058-3
- Walline, J. J., Lindsley, K. B., Vedula, S. S., Cotter, S. A., Mutti, D. O., Ng, S. M., et al. (2020). Interventions to slow progression of myopia in children. *Cochrane Database Syst. Rev.* 1, CD004916. doi:10.1002/14651858.CD004916.pub4
- Xie, P., and Guo, X. (2016). Chinese experiences on orthokeratology. *Eye Contact Lens* 42, 43–47. doi:10.1097/ICL.0000000000000190
- Yang, L., Zhang, L., Jian Hu, R., Yu, P. P., and Jin, X. (2021). The influence of overnight orthokeratology on ocular surface and dry eye-related cytokines IL-17A, IL-6, and PGE2 in children. *Cont. Lens Anterior Eye* 44 (1), 81–88. doi:10.1016/j.clae.2020.04.001
- Yu, H., Yuan, Y., Wu, W., Zeng, W., Tong, L., Zhang, Y., et al. (2022). Orthokeratology lens wear for 2 years in children did not alter tear film lipid thickness by non-invasive interferometry. *Front. Med. (Lausanne)* 9, 821106. doi:10.3389/fmed.2022.821106
- Zhou, Z., Siddiquee, M. M. R., Tajbakhsh, N., and Liang, J. (2019). UNet++: Redesigning skip connections to exploit multiscale features in image segmentation. *IEEE Trans. Med. Imaging* 39, 1856–1867. doi:10.1109/TMI.2019.2959609
- Zhu, J., and Huang, Z. P. (2016). Effects of wearing orthokeratology lens on tear film and visual quality in adolescent patients with myopia. *Int. J. Ophthalmol.* 16, 2099–2102.



OPEN ACCESS

EDITED BY

Wei Chi,
Sun Yat-sen University, China

REVIEWED BY

Xianjun Zhu,
Sichuan Academy of Medical Sciences
and Sichuan Provincial People's Hospital,
China
Gilbert Yong San Lim,
SingHealth, Singapore

*CORRESPONDENCE

Qinxiang Zheng,
✉ zhengqinxiang@aliyun.com
Jiewei Jiang,
✉ jiangjw924@126.com
Wei Chen,
✉ chenweimd@wmu.edu.cn

[†]These authors have contributed equally
to this work

RECEIVED 30 March 2023

ACCEPTED 20 July 2023

PUBLISHED 28 July 2023

CITATION

Xie H, Li Z, Wu C, Zhao Y, Lin C, Wang Z,
Wang C, Gu Q, Wang M, Zheng Q, Jiang J
and Chen W (2023), Deep learning for
detecting visually impaired cataracts
using fundus images.
Front. Cell Dev. Biol. 11:1197239.
doi: 10.3389/fcell.2023.1197239

COPYRIGHT

© 2023 Xie, Li, Wu, Zhao, Lin, Wang,
Wang, Gu, Wang, Zheng, Jiang and Chen.
This is an open-access article distributed
under the terms of the [Creative
Commons Attribution License \(CC BY\)](#).
The use, distribution or reproduction in
other forums is permitted, provided the
original author(s) and the copyright
owner(s) are credited and that the original
publication in this journal is cited, in
accordance with accepted academic
practice. No use, distribution or
reproduction is permitted which does not
comply with these terms.

Deep learning for detecting visually impaired cataracts using fundus images

He Xie^{1†}, Zhongwen Li^{2†}, Chengchao Wu³, Yitian Zhao^{2,4},
Chengmin Lin⁵, Zhouqian Wang¹, Chenxi Wang¹, Qinyi Gu¹,
Minye Wang¹, Qinxiang Zheng^{1,2*}, Jiewei Jiang^{3*} and
Wei Chen^{1,2*}

¹National Clinical Research Center for Ocular Diseases, Eye Hospital, Wenzhou Medical University, Wenzhou, China, ²Ningbo Eye Hospital, Wenzhou Medical University, Ningbo, China, ³School of Electronic Engineering, Xi'an University of Posts and Telecommunications, Xi'an, China, ⁴Cixi Institute of Biomedical Engineering, Ningbo Institute of Materials Technology and Engineering, Chinese Academy of Sciences, Ningbo, China, ⁵Department of Ophthalmology, Wenzhou Hospital of Integrated Traditional Chinese and Western Medicine, Wenzhou, China

Purpose: To develop a visual function-based deep learning system (DLS) using fundus images to screen for visually impaired cataracts.

Materials and methods: A total of 8,395 fundus images (5,245 subjects) with corresponding visual function parameters collected from three clinical centers were used to develop and evaluate a DLS for classifying non-cataracts, mild cataracts, and visually impaired cataracts. Three deep learning algorithms (DenseNet121, Inception V3, and ResNet50) were leveraged to train models to obtain the best one for the system. The performance of the system was evaluated using the area under the receiver operating characteristic curve (AUC), sensitivity, and specificity.

Results: The AUC of the best algorithm (DenseNet121) on the internal test dataset and the two external test datasets were 0.998 (95% CI, 0.996–0.999) to 0.999 (95% CI, 0.998–1.000), 0.938 (95% CI, 0.924–0.951) to 0.966 (95% CI, 0.946–0.983) and 0.937 (95% CI, 0.918–0.953) to 0.977 (95% CI, 0.962–0.989), respectively. In the comparison between the system and cataract specialists, better performance was observed in the system for detecting visually impaired cataracts ($p < 0.05$).

Conclusion: Our study shows the potential of a function-focused screening tool to identify visually impaired cataracts from fundus images, enabling timely patient referral to tertiary eye hospitals.

KEYWORDS

artificial intelligence, deep learning, visual impairment, cataracts, fundus images

Abbreviations: DLS; Deep learning system, ROC; Receiver operating characteristic curve, WHO; World Health Organization, LOCS; Lens Opacities Classification System, ZEHWZ; Zhejiang Eye Hospital at Wenzhou, ZEHZH; Zhejiang Eye Hospital at Hangzhou, NEH; Ningbo Eye Hospital, BCDVA; Best corrected decimal visual acuity, CNN; Convolutional neural network, ADAM; Adaptive Estimation of Moments, t-SNE; t-distributed stochastic neighbour embedding; GradCAM, Gradient-weighted Class Activation Mapping; CIs, Confidence intervals; AUC, Area under the curve.

1 Introduction

Worldwide, the incidence of visual impairment is increasing (GBD, 2019 Blindness and Vision Impairment Collaborators, 2021), which is an important public health problem, with cataracts being the leading cause of visual impairment (Flaxman et al., 2017). According to recent research, among the 2.2 billion people who suffer from visual impairment worldwide, 134 million are blind, and 571 million have moderate-to-severe visual impairment in 2020 due to cataracts (Bourne et al., 2017; Flaxman et al., 2017). In low- and middle-income countries, especially in Southeast Asia and Africa, cataracts lead to higher rates of visual impairment than in high-income countries due to limited healthcare and financial resources (Lam et al., 2015). The World Health Organization (WHO) has adopted a 30 percent increase in effective coverage of cataract surgery as a new global target for eye care by 2030 (WHO, 2021). Therefore, there is an urgent need to facilitate and expedite cataract screening capabilities, especially for underserved populations.

Traditional cataract screening requires a professional ophthalmologist to assess the lens through a slit-lamp microscope (Gali et al., 2019) and grading methods based on the lens opacity classification system LOCS II (Chylack et al., 1989) or LOCS III (Chylack et al., 1993) (Lens Opacities Classification System, LOCS) and Wisconsin cataract grading system (Wong et al., 2013), which limits the efficiency of large-scale cataract screening. A simple and effective model for screening and referral remains a key challenge for the sustainable implementation of cataract screening programs. To enhance community screening for retinal disease in some countries (Lian et al., 2016; Verbraak et al., 2019), they have implemented telemedicine or artificial intelligence analysis of fundus images acquired by non-specialists. Grading the assessment of cataracts by fundus images may also be an effective solution. Abdul-Rahman used Fourier analysis to quantify optical degradation in fundus images, which was shown to be correlated well with the LOCS III (Abdul-Rahman et al., 2008).

Several studies have developed deep learning systems (DLSs) to grade the severity of cataracts based on the blurriness of fundus images. According to the visibility of the optic disk or retinal vessels of the fundus images, they classified cataracts into 3, four or 5 grades (Xiong et al., 2017; Zhang et al., 2019; Xu et al., 2020; Yue Zhou and Li, 2020). Considering that visual acuity is one of the most common indicators for evaluating the impact of cataracts on patients, it would be more meaningful to establish a visual function-based cataract grading system (WHO, 2020). This functional cataract screening program is more targeted for cataract patients, which can reduce the excessive referral of people with mild visual impairment and reduce the pressure on tertiary eye hospitals.

In this study, we developed a visual function-based DLS for populations based on fundus images, especially for the screening of visually impaired cataracts. In addition, we used images taken by different types of fundus cameras from three institutions to evaluate the effectiveness and generalizability of the system.

2 Materials and Methods

2.1 Image datasets

In this retrospectively study, a total of 6,997 fundus images (4,346 subjects) collected from Zhejiang Eye Hospital at Wenzhou (ZEHWZ) between September 2020 and March 2021 were used to develop the DLS. The ZEHWZ dataset included cataract patients whose best corrected decimal visual acuity (BCDVA) was good (>0.6) within 1 month after cataract surgery and non-cataract patients without refractive media opacities. The fundus images were captured without mydriasis before surgery. The exclusion criteria were traumatic cataracts, congenital cataracts and lens dislocation, corneal diseases, asteroid hyalosis, vitreous haemorrhage, and severe retinal and optic nerve diseases. Poor quality and unreadable images were also excluded: images out of focus; images underexposed; images overexposed; incomplete images with more than 1/3 peripheral halo.

Two additional datasets, including 1,398 fundus images obtained from two other institutions retrospectively, adopted the same inclusion criteria and exclusion criteria as ZEHWZ for external testing. One was derived from the inpatient department at Zhejiang Eye Hospital at Hangzhou (ZEHHZ), consisting of 1,097 images from 730 individuals; the other was derived from outpatient clinics and the inpatient department at Ningbo Eye Hospital (NEH), consisting of 301 images from 169 individuals.

This study adhered to the principles of the Declaration of Helsinki and was approved by the Ethics Committee of Zhejiang Eye Hospital at Wenzhou (Number, 2022-008-K-06-01). Due to the retrospective study design and the use of fully anonymized fundus images, the need for informed patient consent was waived by the review committee.

2.2 Criteria of cataract classification

The diagnosis of each fundus image was diagnosed by two cataract specialists based on the previous medical records and the results of the ophthalmology examination. If there was a difference between the two cataract specialists, there would be a third senior cataract specialists for diagnosis. All fundus images with a definitive diagnosis were screened for quality control. Poor quality and unrecognizable images were excluded.

All fundus images were classified into three categories: non-cataracts, mild cataracts, and visually impaired cataracts. Non-cataracts were defined as patients with transparent lenses and without refractive media opacities. Mild cataracts were defined as cataracts with mild vision impairment with BCDVA ≥ 0.3 , and visually impaired cataracts were defined as cataracts with moderate-to-severe vision impairment or blindness with BCDVA < 0.3 . Typical examples of non-cataract and cataract fundus images are displayed in Figure 1.

2.3 Image preprocessing

During image preprocessing, each image was uniformly scaled down to 224×224 pixels, and the pixel values were normalized

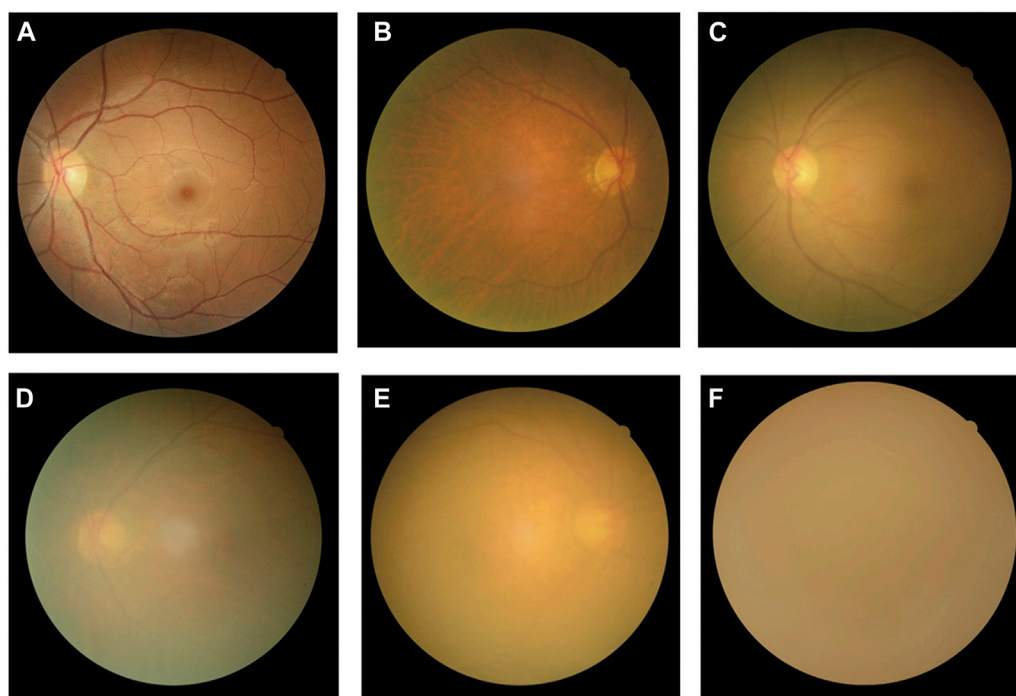


FIGURE 1

Typical examples of fundus images of non-cataracts, mild cataracts, and visually impaired cataracts (A) Non-cataracts (B) The cataract with BCDVA = 0.8 (C) The cataract with BCDVA = 0.5 (D) The cataract with BCDVA = 0.3 (E) The cataract with BCDVA = 0.1 (F) The cataract with BCDVA = HM/BE.

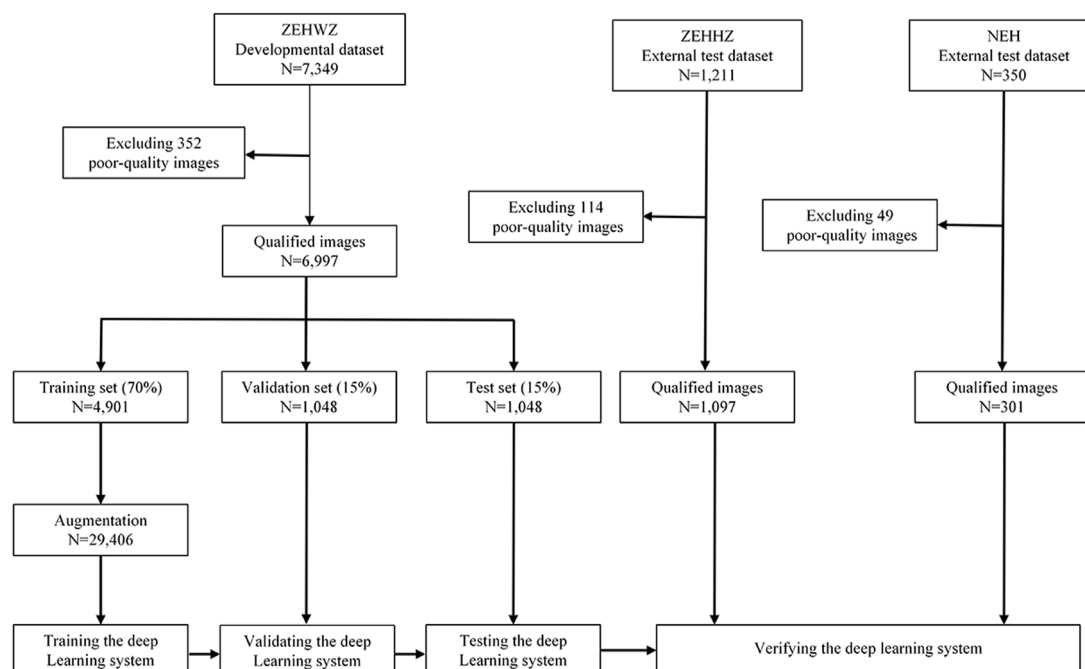


FIGURE 2

Flow chart for the development and evaluation of the DLS. ZEHWS = Zhejiang Eye Hospital at Wenzhou; ZEHHS = Zhejiang Eye Hospital at Hangzhou; NEH = Ningbo Eye Hospital.

between 0 and 1. Then, data augmentation techniques were applied to increase the diversity of the dataset and thereby alleviate the overfitting problem during deep learning training. The new samples were generated by a simple transformation of the original image, simulating “real world” acquisition conditions. Random cropping, rotation of 90°, and horizontal and vertical flipping were applied to the images of the training dataset to increase the sample size to six times the original size (from 4,901 to 29,406).

2.4 Development and evaluation of the DLS

The fundus images drawn from the ZEHWZ dataset were randomly divided into training, validation, and internal test datasets at a ratio of 70%:15%:15%. The training and validation datasets were used to develop the system, and the test dataset was used to evaluate the performance of the system. Images from the same person were only assigned to a single dataset to prevent deep learning leaks and biased evaluations.

To find the best deep learning model for distinguishing non-cataracts, mild cataracts, and visually impaired cataracts, three convolutional neural network (CNN) architectures (DenseNet121, Inception-v3, and ResNet50) were compared. The parameters of the CNN were initialized with weights pretrained for ImageNet classification.

The deep learning models were trained using PyTorch (version 1.6.0) as the backend. Using the Adaptive Estimation of Moments (ADAM) optimizer, the initial learning rate was 0.001, β_1 was 0.9, β_2 was 0.999, and the weight decay was $1e-4$. Each model was trained for 80 epochs. During the training, the validation loss was evaluated on the validation dataset after each epoch and used as a reference for model selection. Each time the validation loss was reduced, the model state and corresponding weight matrix were saved. The model state with the lowest validation loss was saved as the final state of the model for the test dataset.

The diagnostic performance of the three-class classification model was then evaluated on two independent external test datasets. The development and evaluation process of the system is shown in Figure 2. Using the t-distributed stochastic neighbour embedding (t-SNE) technique, the embedding features of each class learned by the model were displayed in a two-dimensional space.

2.5 Visualization heatmap

To understand which areas of fundus images were most likely to be used by deep learning models to generate decisions for this system, we use the Gradient-weighted Class Activation Mapping (GradCAM) technique to generate heatmaps. This technique uses the gradients of any target concept, flowing into the final convolutional layer to produce a localization map highlighting the important regions in the image for predicting the concept (Ramprasaath et al., 2020). Hotter colours represent the regions with more contribution to the predicted output, while cooler colours may indicate relatively less contribution to the predicted output. Using this method, heatmaps were generated to illustrate the basic principles of DLSs in differentiating between non-cataracts, mild cataracts, and visually impaired cataracts.

2.6 Characteristics of misclassification by the deep learning system

A senior cataract specialists who had not been involved in the initial diagnosis reviewed the characteristics of all images misclassified by the DenseNet121 algorithm and analysed the possible causes of misclassification in combination with the corresponding BCDVA.

2.7 DLS versus cataract specialists

To assess our DLS in the context of cataract detection, we recruited two cataract specialists with 3 and 10 years of clinical experience. The ZEHHZ dataset was employed to compare the performance of the best system (DenseNet121) to that of the cataract specialists with the reference standard. The system and specialists independently classified each image into one of the following three categories: non-cataracts, mild cataracts, and visually impaired cataracts. Notably, to reflect the level of experience of the cataract specialists in normal clinical practice, they were not told that they were competing with an AI-based system to avoid competition bias.

2.8 Statistical analysis

The performance of the deep learning system for the classification of non-cataracts, mild cataracts, and visually impaired cataracts was evaluated by employing the one-versus-rest tactic and calculating the AUC, sensitivity, specificity, and accuracy. Statistical analysis was performed using Python 3.7.8 (Wilmington, Delaware, United States of America). The 95% confidence intervals (CIs) for sensitivity, specificity, and accuracy were calculated by the Wilson scoring method using the Stats model package (version 0.11.1), and those for the area under the receiver operating characteristic (ROC) curve (AUC) were calculated using an empirical bootstrap procedure with 1,000 repetitions. We plotted the receiver operating characteristic (ROC) curve to demonstrate the capability of the system by plotting the ratio of true positive cases (sensitivity) to false positive cases (1-specificity) using the Scikit-learn (version 0.23.2) and Matplotlib (version 3.3.1) packages; a larger AUC indicated better performance. Unweighted Cohen's kappa coefficients were calculated to compare the results of the system to a reference standard. Differences in sensitivity, specificity, and accuracy between systems and the cataract specialists were analysed using the McNemar test. All statistical tests were two-sided with a significance level of 0.05.

3 Results

3.1 Characteristics of the datasets

After removing 515 poor-quality images, a total of 8,395 qualified images (3,569 images of non-cataracts, 3,245 images of mild cataracts, and 1,581 images of visually impaired cataracts) from 5,245 individuals were used to develop

TABLE 1 Summary of datasets.

Item	ZEHWZ dataset			ZEHHZ dataset	NEH dataset
Total no. of images	7,349			1,211	350
Total no. of qualified images	6,997			1,097	301
No. of subjects	4,346			730	169
Age, mean/range (years)	46.54/5–92			50.70/3–92	48.04/4–87
No. (%) of women	2,333/53.68			425/58.22	99/58.58
Camera model	Canon CR-2 PLUS AF (Japan)			Canon CR-2 (Japan)	RetiCam 3,100 (China)
	Training Set (70%) 4,901	Validation Set (15%) 1,048	Test Set (15%) 1,048		
Non-cataracts No. (%)	2,141 (43.68)	458 (43.70)	458 (43.70)	405 (36.92)	107 (35.55)
Mild cataracts No. (%)	1808 (36.89)	387 (36.93)	387 (36.93)	560 (51.05)	103 (34.22)
Visually impaired cataracts No. (%)	952 (19.42)	203 (19.37)	203 (19.37)	132 (12.03)	91 (30.23)

ZEHWZ = zhejiang eye hospital at wenzhou; ZEHHZ = zhejiang eye hospital at hangzhou; NEH, ningbo eye hospital.

and externally evaluate the DLS. Further information on the datasets from ZEHWZ, ZEHHZ, and NEH is summarized in Table 1.

3.2 Performance of different deep learning algorithms on the internal test dataset

This study used three classical deep learning algorithms, DenseNet121, ResNet50, and Inception-v3, to train the models. The t-SNE technique showed that the features of each category learned by the DenseNet121 algorithm were more separable than those learned by ResNet50 and Inception-v3 (Figure 3A). The performance of the three algorithms on the internal test dataset is shown in Figures 3B,C, which indicates that the best algorithm was DenseNet121. More information, including the accuracy, sensitivity, and specificity of the algorithms, is presented in Table 2.

The best algorithm achieved an AUC of 0.999 (95% confidence interval [CI], 0.998–1.000), a sensitivity of 98.3% (95% CI, 97.1–99.5), and a specificity of 98.8% (95% CI, 97.9–99.7) in detecting non-cataracts. The best algorithm discriminated mild cataracts from non-cataracts and visually impaired cataracts with an AUC of 0.958 (95% CI, 0.946–0.968), a sensitivity of 83.2% (95% CI, 79.5–86.9), and a specificity of 94.1% (95% CI, 92.3–95.9). The best algorithm discriminated visually impaired cataracts from non-cataracts and mild cataracts with an AUC of 0.956 (95% CI, 0.944–0.968), a sensitivity of 84.7% (95% CI, 79.8–89.7), and a specificity of 93.1% (95% CI, 91.4–94.8). Based on the reference standard of the internal test dataset, the unweighted Cohen's kappa coefficient of the best algorithm, DenseNet121, was 0.845 (0.817–0.873).

3.3 Performance of the different deep learning algorithms on the external test datasets

The performance of the DenseNet121, ResNet50, and Inception-v3 algorithms for cataract validation on the external test dataset is

shown in Figure 4, confirming that DenseNet121 achieved the best performance. The t-SNE technique also indicated that the features of each category learned by the DenseNet121 algorithm were more separable than those learned by Inception-v3 and ResNet50 (Figure 4A–D).

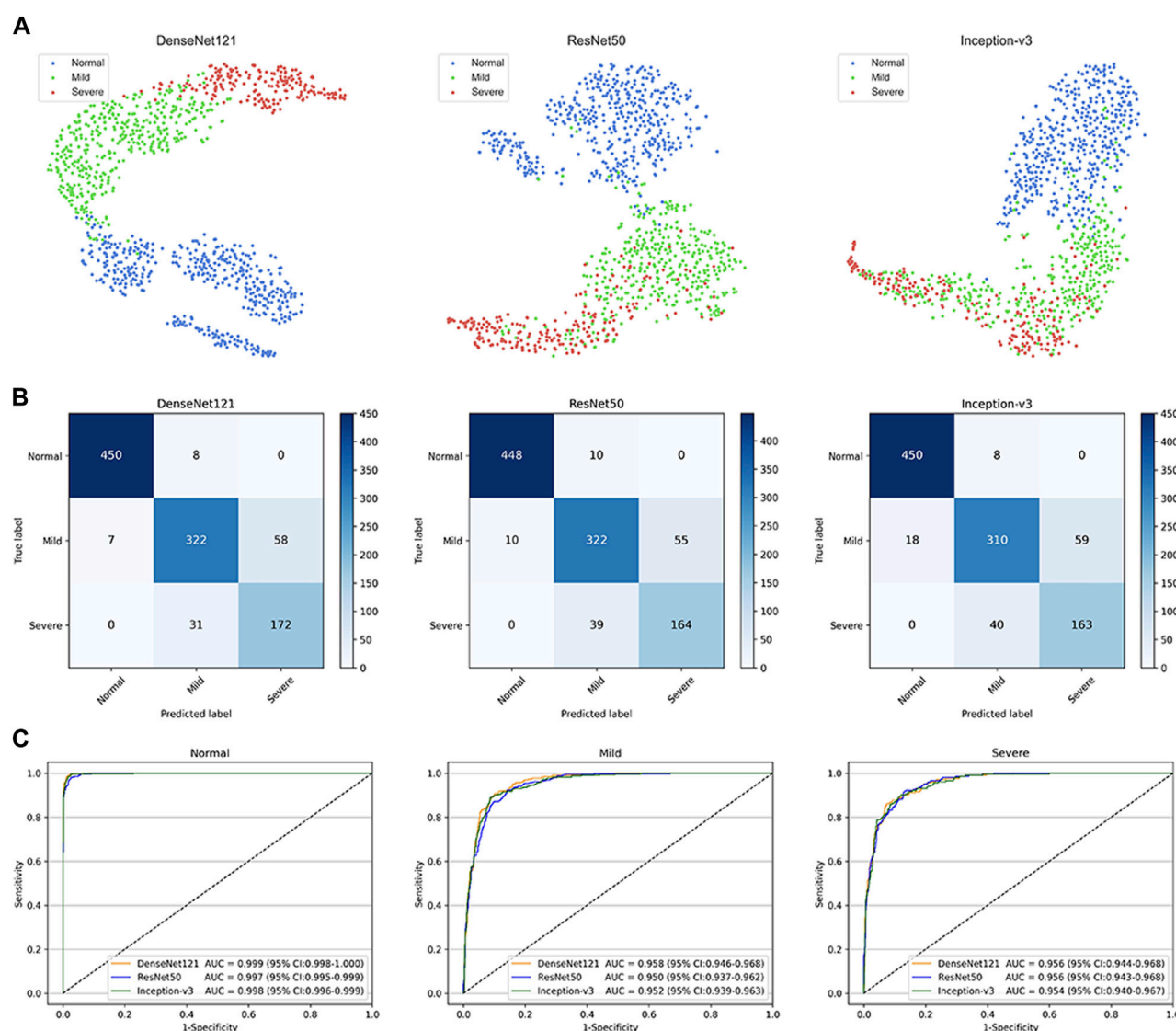
For the ZEHHZ dataset, the system based on DenseNet121 achieved AUCs of 0.998 (95% CI, 0.996–0.999), 0.938 (95% CI, 0.924–0.951), and 0.937 (95% CI, 0.918–0.953) in the classification of non-cataracts, mild cataracts, and visually impaired cataracts, respectively. In the NEH dataset, the system based on DenseNet121 achieved AUCs of 0.998 (95% CI, 0.995–1.000), 0.966 (95% CI, 0.946–0.983), and 0.977 (95% CI, 0.962–0.989) in the classification of non-cataracts, mild cataracts, and visually impaired cataracts, respectively.

The details on the classification performance of the three algorithms with the external datasets are shown in Table 2. In the ZEHHZ dataset, the accuracies of the best algorithm (DenseNet121) in the detection of non-cataracts, mild cataracts, and visually impaired cataracts were 97.3% (95% CI, 96.3–98.2), 85.5% (95% CI, 83.4–87.6), and 88.2% (95% CI, 86.3–90.1), respectively. In the NEH dataset, the accuracies of the best algorithm in the detection of non-cataracts, mild cataracts, and visually impaired cataracts were 98.7% (95% CI, 97.4–100.0), 89.7% (95% CI, 86.3–93.1), and 91.0% (95% CI, 87.8–94.3), respectively.

Based on the reference standards of the ZEHHZ and NEH datasets, the unweighted Cohen's kappa coefficients of the best algorithm, DenseNet121, were 0.762 (0.728–0.796) and 0.845 (0.793–0.897), respectively.

3.4 Heatmaps

We use heatmaps to provide insights into regions of the fundus images that might influence the algorithm's prediction. Based on the heatmaps shown in Figure 5, we observed that the regions highlighted by the algorithm matched well with the clear features on the fundus image. For the fundus images of the non-cataracts, the region highlighted by the heatmaps was relatively consistent: large

**FIGURE 3**

Performance of deep learning algorithms in the internal test dataset from Zhejiang Eye Hospital at Wenzhou (A) Visualization by t-distributed stochastic neighbour embedding (t-SNE) of the separability for the features learned by deep learning algorithms. Different coloured point clouds represent the different categories (B) Confusion matrices describing the accuracies of three deep learning algorithms (C) Receiver operating characteristic curves indicating the performance of each algorithm for detecting non-cataracts, mild cataracts, and visually impaired cataracts. "Normal" indicates non-cataracts. "Mild" indicates mild cataract. "Severe" indicates visually impairing cataract.

range, circular, and centred. For the fundus images of mild cataracts, the regions highlighted by the heatmaps are smaller, eccentric, oval, and around the optic disk. For the fundus images of visually impaired cataracts, the regions highlighted by the heatmaps are irregular. Figure 5 shows typical heatmaps of non-cataracts, mild cataracts, and visually impaired cataracts, respectively.

3.5 Classification errors

In the internal and external test datasets, a total of 293 images (11.98% of the total 2,446) were inconsistent with the diagnostic reference standard by the DenseNet121 algorithm. In the non-cataracts group (970 images), 38 images (3.92%) were

misclassified as mild cataracts by the system, 89.47% (34 images) of which were misclassified due to dark shooting, the region highlighted by the heatmaps was eccentric and oval, as the mild cataracts, for the images were slightly darker, slightly defocused or surrounded by the halo. In the mild cataracts group (1,050 images), 11 images (1.05%) were misclassified as non-cataracts by the system due to clarity of the fundus images, most of the patients are early cortical or nuclear cataracts, the highlighted region of the heatmaps show large range, circular, and centred, as the non-cataracts. 167 (15.90%) images were misclassified as visually impaired cataracts by the system, of which 65.27% images had relatively poor BCDVA (BCDVA < 0.5) with blurred fundus images and 10.78% had good BCDVA (BCDVA between 0.8–1.0) with advanced cortical opacity, whose fundus images were blurred, the highlighted region of the

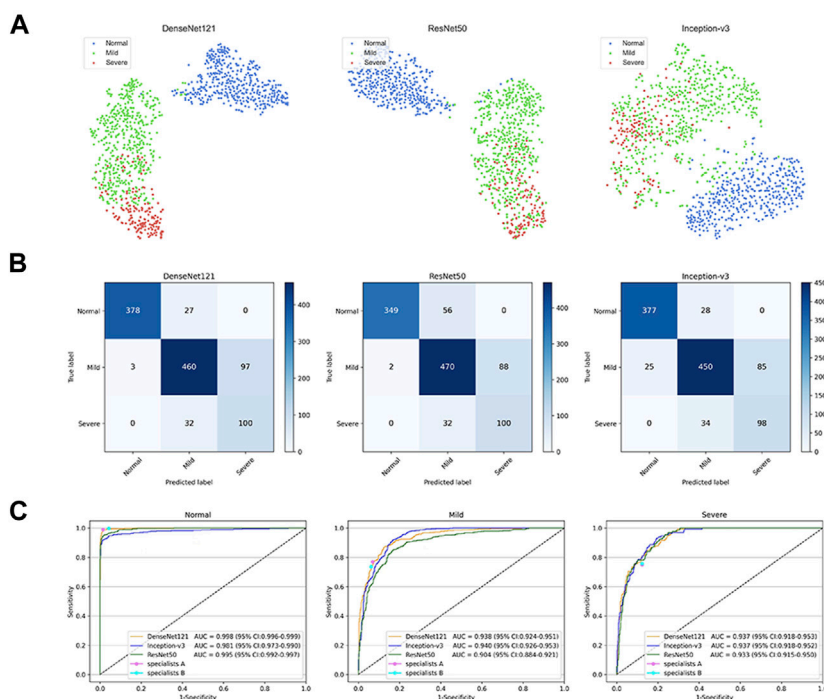
TABLE 2 Performance of three deep learning algorithms in the internal and external test datasets.

One-vs.-rest classification	ZEHWZ internal test dataset			ZEHHZ external test dataset			NEH external test dataset		
	Sensitivity (95% CI)	Specificity (95% CI)	Accuracy (95% CI)	Sensitivity (95% CI)	Specificity (95% CI)	Accuracy (95% CI)	Sensitivity (95% CI)	Specificity (95% CI)	Accuracy (95% CI)
Normal vs mild + severe									
DenseNet121	98.3% (97.1–99.5)	98.8% (97.9–99.7)	98.6% (97.8–99.3)	93.3% (90.9–95.8)	99.6% (99.1–100.0)	97.3% (96.3–98.2)	97.2% (94.1–100.0)	99.5% (98.5–100.0)	98.7% (97.4–100.0)
ResNet50	97.8% (96.5–99.2)	98.3% (97.3–99.3)	98.1% (97.3–98.9)	86.2% (82.8–89.5)	99.7% (99.3–100.0)	94.7% (93.4–96.0)	96.3% (92.7–99.9)	99.0% (97.5–100.0)	98.0% (96.4–99.6)
Inception-v3	98.3% (97.1–99.5)	96.9% (95.6–98.3)	97.5% (96.6–98.5)	93.1% (90.6–95.6)	96.4% (95.0–97.8)	95.2% (93.9–96.4)	94.4% (90.0–98.8)	92.3% (88.5–96.0)	93.0% (90.1–95.9)
Mild vs normal + severe									
DenseNet121	83.2% (79.5–86.9)	94.1% (92.3–95.9)	90.1% (88.3–91.9)	82.1% (79.0–85.3)	89.0% (86.4–91.7)	85.5% (83.4–87.6)	87.4% (81.0–93.8)	90.9% (86.9–94.9)	89.7% (86.3–93.1)
ResNet50	83.2% (79.5–86.9)	92.6% (90.6–94.6)	89.1% (87.2–91.0)	83.9% (80.9–87.0)	83.6% (80.5–86.7)	83.8% (81.6–86.0)	88.3% (82.2–94.5)	88.9% (84.5–93.3)	88.7% (85.1–92.3)
Inception-v3	80.1% (76.1–84.1)	92.7% (90.8–94.7)	88.1% (86.1–90.0)	80.4% (77.1–83.6)	88.5% (85.8–91.2)	84.3% (82.2–86.5)	72.8% (64.2–81.4)	88.4% (83.9–92.8)	83.1% (73.3–89.3)
Severe vs normal + mild									
DenseNet121	84.7% (79.8–89.7)	93.1% (91.4–94.8)	91.5% (89.8–93.2)	75.8% (68.4–83.1)	89.9% (88.1–91.8)	88.2% (86.3–90.1)	83.5% (75.9–91.1)	94.3% (91.1–97.4)	91.0% (87.8–94.3)
ResNet50	80.3% (74.8–85.8)	93.0% (91.3–94.7)	90.6% (88.8–92.3)	74.2% (66.8–81.7)	91.2% (89.4–93.0)	89.2% (87.3–91.0)	81.3% (73.3–89.3)	93.8% (90.6–97.1)	90.0% (86.6–93.4)
Inception-v3	80.8% (75.4–86.2)	93.5% (91.8–95.2)	91.0% (89.3–92.8)	75.8% (68.4–83.1)	90.9% (89.1–92.7)	89.1% (87.2–90.9)	80.2% (72.0–88.4)	95.2% (92.4–98.1)	90.7% (87.4–94.0)

ZEHWZ = zhejiang eye hospital at wenzhou; ZEHHZ = zhejiang eye hospital at hangzhou; NEH = ningbo eye hospital.

“Normal” indicates non-cataracts. “Mild” indicates mild cataracts. “Severe” indicates visually impaired cataracts.

ZEHHZ external test dataset



NEH external test dataset

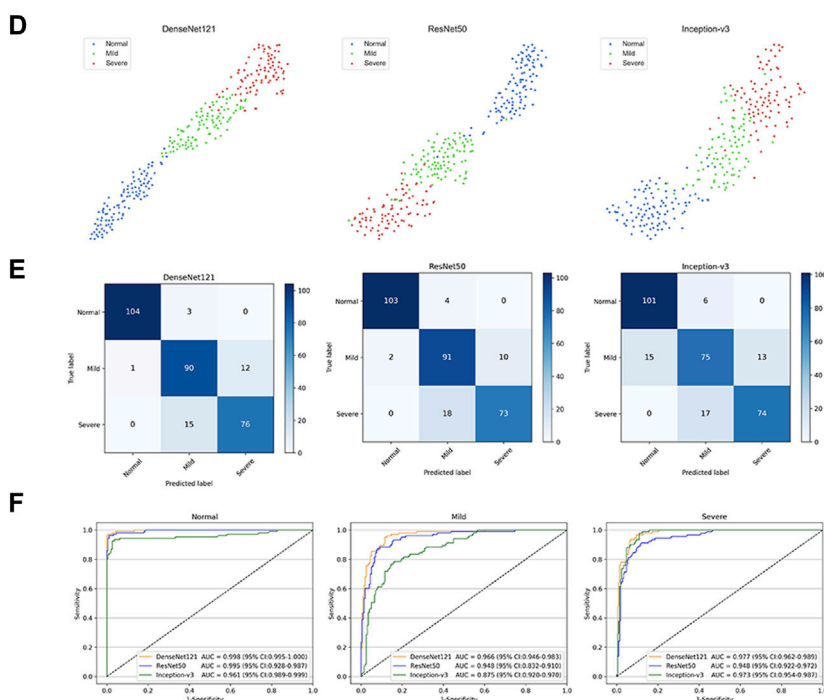


FIGURE 4

Confusion matrices and receiver operating characteristic (ROC) curves for three deep learning algorithms performance in two external test datasets. The t-distributed stochastic neighbour embedding (t-SNE) (A–D) presenting the separability for the features learned by deep learning algorithms in ZEHHZ and NEH external test datasets. Confusion matrices (B–E) describing the accuracies of two deep learning algorithms in the ZEHHZ and NEH external test datasets. ROC curves (C–F) indicating the performance of each algorithm for discriminating among non-cataracts, mild cataracts, and visually impaired cataracts in the ZEHHZ and NEH external test datasets. The performance of two cataract specialists were also indicated (C). ZEHHZ, Zhejiang Eye Hospital at Hangzhou. NEH, Ningbo Eye Hospital. “Normal” indicates non-cataracts. “Mild” indicates mild cataract. “Severe” indicates visually impaired cataract.

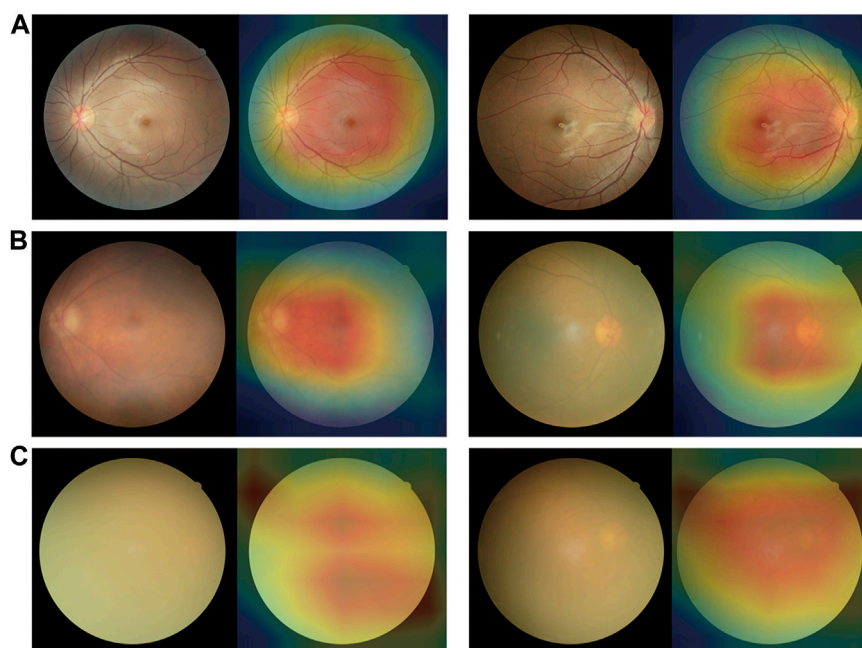
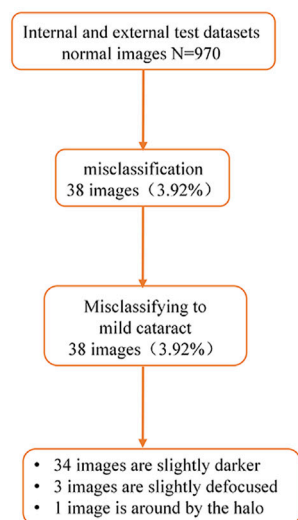


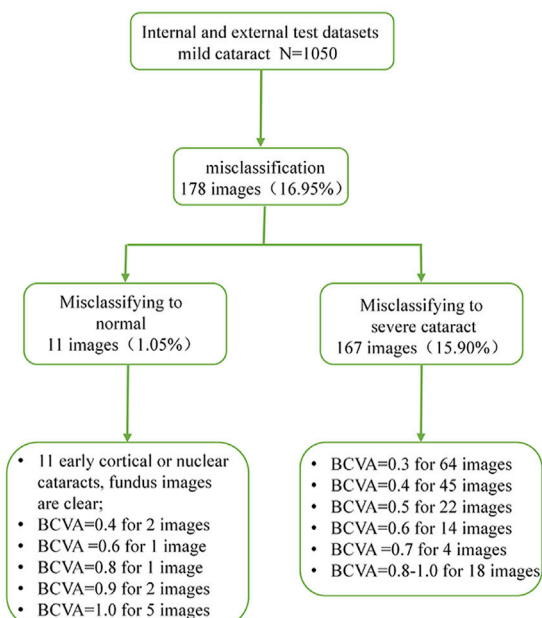
FIGURE 5

Saliency maps highlighting regions that the algorithm focuses on when making classification (A) Non-cataracts (B) mild cataracts (C) visually impaired cataracts. Each category is shown in a pair of an original image (left) and a corresponding heatmap (right). In these heatmaps, hotter areas (i.e., reds and oranges) are indicative of regions with increased contributions towards the predicted output, and colder regions (blues and greens) might be indicative of relatively less contribution. For each subgroup, each set of two images (from two different eyes) consistently shows the same region or feature highlighted by the algorithm.

A The misclassification of "normal"



B The misclassification of "mild cataract"



C The misclassification of "severe cataract"

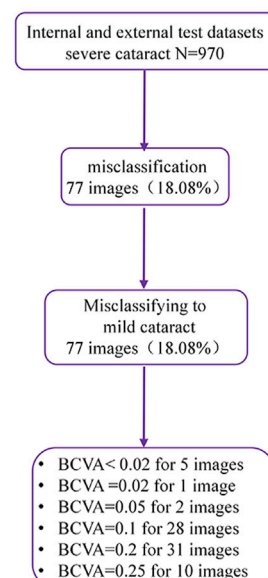


FIGURE 6

Details of deep learning system error classification in internal and external test datasets. (A) The misclassification of the non-cataracts group; (B) The misclassification of the mild cataracts group; (C) The misclassification of the visually impaired cataracts group.

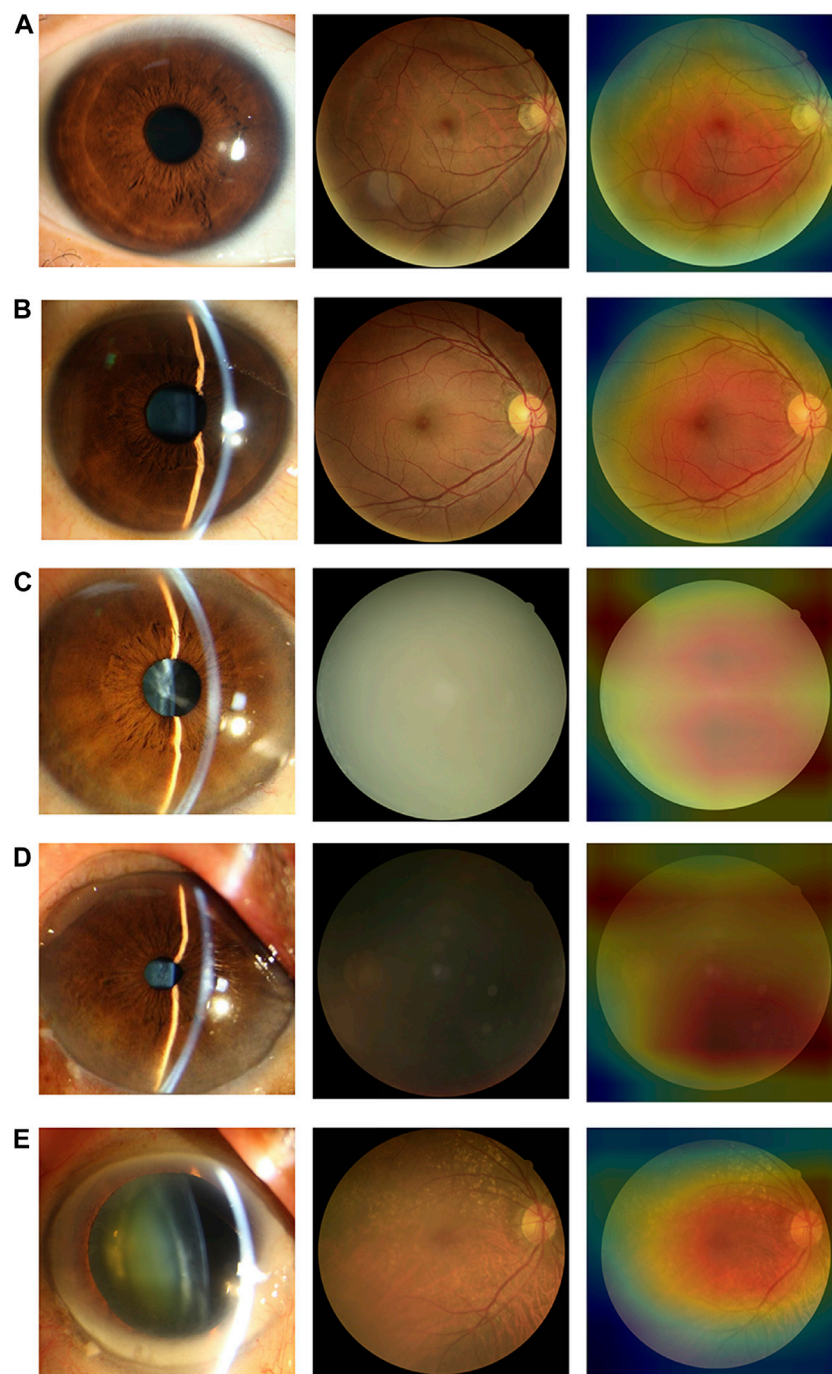


FIGURE 7

Typical examples of misclassified images by the DLS **(A)** Images of “non-cataract” incorrectly classified as “mild cataract”. The fundus image was around by the halo **(B)** Images of “mild cataract” incorrectly classified as “non-cataract”. The patient had cataracts in the early stage, BCDVA = 1.0 **(C)** Images of “mild cataract” incorrectly classified as “visually impaired cataract”. The patient had advanced cortical opacity, BCDVA = 0.6 **(D)** Images of “mild cataract” incorrectly classified as “visually impaired cataract”. Patients with small pupils reduced the amount of light entering their eyes (BCDVA = 0.4) **(E)** Images of “visually impaired cataract” incorrectly classified as “mild cataract”. The patient had a small-scale posterior subcapsular area, BCDVA = 0.16.

heatmaps was irregular, as the visually impaired cataracts. In the visually impaired cataracts group (426 images), 77 images (18.08%) were systematically misclassified as mild cataracts, the heatmaps show the characteristic of the mild cataracts: smaller, eccentric, oval, and around the optic disk, because among these classification errors,

most cataracts' BCDVAs were not too bad (89.61% of the Images had BCDVA ≥ 0.1). The misclassification BCDVA situation of the DLS is shown in Figure 6. Figure 7 shows typical example of misclassified images of “non-cataract” incorrectly classified as “mild cataract”, misclassified images of “mild cataract”

TABLE 3 Performance comparison of DenseNet121 with cataract specialists in the ZEHHZ dataset.

	DenseNet121	Specialists A	Specialists B	P1	P2
Normal vs mild + severe					
Sensitivity (95% CI)	93.3% (90.9–95.8)	99.0% (98.0–100.0)	99.8% (99.3–100.0)	0.000	0.000
Specificity (95% CI)	99.6% (99.1–100.0)	98.6% (97.7–99.4)	95.8% (94.3–97.3)	0.065	0.000
Accuracy (95% CI)	97.3% (96.3–98.2)	98.7% (98.1–99.4)	97.3% (96.3–98.2)	0.014	1.000
Mild vs normal + severe					
Sensitivity (95% CI)	82.1% (79.0–85.3)	77.0% (73.5–80.5)	73.6% (69.9–77.2)	0.001	0.000
Specificity (95% CI)	89.0% (86.4–91.7)	93.1% (91.0–95.3)	93.9% (91.8–95.9)	0.002	0.000
Accuracy (95% CI)	85.5% (83.4–87.6)	84.9% (82.7–87.0)	83.5% (81.3–85.7)	0.576	0.074
Severe vs normal + mild					
Sensitivity (95% CI)	75.8% (68.4–83.1)	75.0% (67.6–82.4)	75.8% (68.4–83.1)	1.000	1.000
Specificity (95% CI)	89.9% (88.1–91.8)	87.7% (85.6–89.7)	87.7% (85.6–89.7)	0.005	0.006
Accuracy (95% CI)	88.2% (86.3–90.1)	86.1% (84.1–88.2)	86.2% (84.2–88.3)	0.012	0.019

ZEHHZ = Zhejiang Eye Hospital at Hangzhou. P1 refers to the *p*-value that was calculated between the deep learning system and cataract specialist A using the two-sided McNemar test. P2 refers to the *p*-value that was calculated between the deep learning system and cataract specialist B using the two-sided McNemar test. Cataract specialist A has 3 years of clinical experience. Cataract specialist B has 10 years of clinical experience. “Normal” indicates non-cataracts. “Mild” indicates mild cataract. “Severe” indicates visually impairing cataract.

incorrectly classified as “non-cataract”, images of “mild cataract” incorrectly classified as “visually impaired cataract”, and images of “visually impaired cataract” incorrectly classified as “mild cataract”, respectively.

3.6 Comparison of the deep learning system and cataract specialists

In the ZEHHZ dataset, for the classification of non-cataracts, mild cataracts, and visually impaired cataracts, the cataract specialist with 3 years of experience achieved accuracies of 98.7% (98.1–99.4), 84.9% (82.7–87.0), and 86.1% (84.1–88.2), respectively, the senior cataract specialist with 10 years of experience achieved accuracies of 97.3% (96.3–98.2), 83.5% (81.3–85.7) and 86.2% (84.2–88.3), respectively, and the DLS achieved accuracies of 97.3% (96.3–98.2), 85.5% (83.4–87.6) and 88.2% (86.3–90.1), respectively. Our system had comparable performance to that of cataract specialists in classifying non-cataracts and mild cataracts and had better performance in classifying visually impaired cataracts ($p < 0.05$) (Table 3 and Figure 4C).

4 Discussion

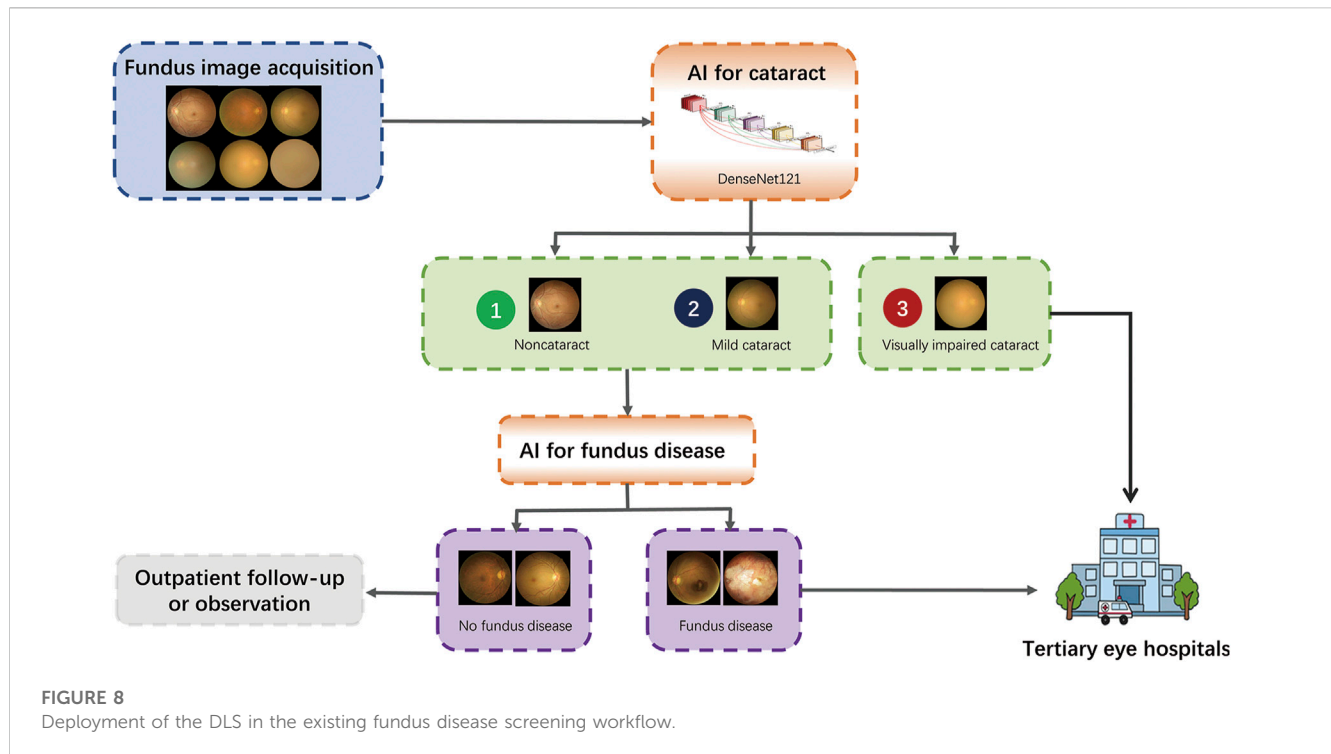
We developed a single-modality DLS using only fundus images to detect both mild cataracts and visually impaired cataracts in the general population. Our main finding was that the system based on a convolutional neural network could discriminate among non-cataracts, mild cataracts, and visually impaired cataracts, and the DenseNet121 algorithm had the best performance. In the internal and two external test datasets, the AUCs of the system based on the best algorithm were 0.998–0.999, 0.938–0.966, and 0.937–0.977, respectively, which demonstrated the broad generalizability of our system. In addition, the unweighted Cohen’s kappa coefficients were 0.762–0.845, which showed good consistency between the outcomes of the DLS and the reference standard,

further substantiating the effectiveness of our system. Moreover, our system has better performance in classifying visually impaired cataracts than cataract specialists.

The visual function-centric DLS in this study can serve as a simple, automated, and comprehensive cataract screening deployment tool. This system only needs to input fundus images and does not require other time-consuming and labour-intensive professional ophthalmic operations to obtain the severity of the patients’ cataract and the range of the best corrected visual acuity. Its simplicity can be used as an effective tool for community screening options, especially in resource-poor regions. It can not only screen for cataracts and but also can tell patients about their eye health. Moreover, visually impaired cataracts can be screened out and referred to tertiary eye hospitals.

With the increase in fundus disease-based primary care programs and community screening programs (Lin et al., 2021; Ruamviboonsuk et al., 2022), fundus photography is a routine examination procedure, and the cataract algorithm of this study can be used as an add-on algorithm to these existing devices with minimal additional cost to achieve more disease screening functions. In addition, the blurring of some fundus images caused by severe cataracts is a common cause of ungradable fundus disease (Scanlon et al., 2005). Our algorithm can screen out the fundus images of non-cataracts and mild cataracts because the fundus images of these two groups have relatively high definition, which can improve the accuracy of intelligent screening of fundus diseases and reduce the burden of unnecessary manual classification, enabling more effective referrals and improving the capacity of the existing screening programs for eye diseases. The visually impaired cataracts selected by the algorithm can be referred to a tertiary eye hospital for treatment. The workflow is shown in Figure 8.

Most of the previous studies on deep learning algorithms for cataracts based on fundus images focused on the artificial classification of the blurriness of the fundus images (Xiong et al., 2017; Zhang et al., 2019; Xu et al., 2020; Yue Zhou and Li, 2020). The annotations are subjective, and there is no accurate corresponding clinical guiding significance. In these studies, the application of these



algorithms did not meet the actual situation and needs of the communities, and most of the previous studies did not consider the state of visual function. Recently, [Tham et al. \(2022\)](#) developed an algorithm for the automatic detection of visually significant cataracts with an AUC of 0.916–0.966. However, their algorithm can only distinguish visually significant cataracts from mild cataracts in cataract patients, but our algorithm can further classify non-cataracts from cataracts, which is of great significance for cataract screening and eye health guidance in communities. At the same time, our algorithm can also distinguish mild cataracts from non-cataracts. Although the patients only need regular follow-up and observation, we can give them some suggestions for controlling and delaying the progression of cataracts, for numerous studies had found that the risk factors for cataract formation had been associated with lifestyle and systemic diseases, include smoking, ultra-violet light exposure, alcohol intake, nutritional status, diabetes mellitus, hypertension, obesity, chronic kidney disease and autoimmune disease ([Ang and Afshari, 2021](#)). Therefore, we can advise the patients to choose a healthy lifestyle and control systemic diseases, such as controlling blood sugar well. In addition, in our research, we compared three different CNN algorithms: DenseNet121, ResNet50, and Inception-v3. Among them, Densenet121 is the most accurate algorithm. It has a variety of advantages used in their study when compared to two other algorithms: alleviating the vanishing-gradient problem, strengthening feature propagation, encouraging feature reuse, and substantially improving parameter efficiency ([Huang et al., 2019](#)).

Reducing false negative misclassification of visually impaired cataracts is critical to avoid missing cataract patients who should be referred to tertiary eye centres for surgical intervention. A total of 18.08% (77/970) of visually impaired cataracts were misclassified as mild cataracts. Analysis of the misclassified fundus images found

that 89.61% (69/77) of them had moderate visual impairment ($0.1 \leq \text{BCDVA} < 0.3$). The optometry to get BCDVA is subjective and requires the patient's cooperation. Some cataract patients with relatively poor visual acuity might give up their efforts to see some small optotypes. Therefore, the actual visual acuity of the patients may be slightly better than the checked visual acuity. Additionally, this misclassification may be caused by a small-scale posterior subcapsular cataract. This type of cataract has a greater impact on visual acuity, while its small-scale turbidity has less impact on the quality of fundus images ([Stifter et al., 2005](#)). Reducing false positive cataract results for visually impaired cataracts is also an important consideration in community screening programs to avoid unnecessary referrals. In this study, 65.27% (109/178) of patients incorrectly diagnosed with cataracts had $\text{BCDVA} < 0.5$. In some countries, the population in need of cataract surgery is defined as having $\text{BCDVA} < 0.5$, with cataracts as the main cause of vision impairment or blindness ([WHO, 2021](#)). Referral of these patients would not waste medical resources. Some patients with advanced cortical opacity have poor contrast sensitivity, although their visual acuity is good ([Maraini et al., 1994](#)). Therefore, these false positives may still need to be referred to a tertiary eye centre and cannot be completely considered incorrect referrals.

This study has several limitations. First, we did not investigate the influence of corneal diseases and vitreous haemorrhage on fundus images. However, the incidence of spontaneous vitreous haemorrhage and corneal opacity in the general population is low, 0.007% ([Manuchehri and Kirkby, 2003](#)) and 3.7% ([Mukhija et al., 2020](#)), respectively. If the patient has corneal opacity or vitreous haemorrhage, he or she must go to the hospital for further examination, and the recommendation given by the system would still apply. Second, the optometry is affected by patient

compliance. Therefore, misclassification due to subjective measurement errors cannot be completely ruled out.

We developed and evaluated a novel single-modality, fundus image-based DLS for the detection of cataracts, especially visually impaired cataracts. The performance of the DLS is comparable to that of the experienced cataract specialist, indicating that this DLS can not only be used to screen cataract patients but also facilitate a timelier and more accurate referral of visually impaired cataract patients from communities to tertiary eye hospitals.

Data availability statement

The raw data supporting the conclusion of this article will be made available by the authors, without undue reservation.

Ethics statement

The studies involving human participants were reviewed and approved by This study adhered to the principles of the Declaration of Helsinki and was approved by the Ethics Committee of Zhejiang Eye Hospital at Wenzhou (Number, 2022-008-K-06-01). Due to the retrospective study design and the use of fully anonymized fundus images, the need for informed patient consent was waived by the review committee. Written informed consent from the participants' legal guardian/next of kin was not required to participate in this study in accordance with the national legislation and the institutional requirements. Written informed consent was not obtained from the individual(s) for the publication of any potentially identifiable images or data included in this article.

Author contributions

Conception and design: HX, ZL, QZ, JJ, and WC. Funding obtainment: WC. Provision of study data: WC and HX. Collection

and assembly of data: CW, ZW, CL, QG, and MW. Data analysis and interpretation: HX, ZL, JJ, CW, WC, and YZ. Manuscript writing: All authors contributed to the article and approved the submitted version.

Funding

This study received funding from the National Key R&D Programme of China (grant no. 2019YFC0840708), the National Natural Science Foundation of China (grant no. 81970770), the Medical Health Science and Technology Project of Zhejiang Provincial Health Commission (2019KY466), the National Natural Science Foundation of China (grant no. 62276210), the Natural Science Basic Research Program of Shaanxi (grant no. 2022JM-380) and the Wenzhou Science and Technology Foundation (grant no. Y20211005). The funding organizations played no role in the study design, data collection and analysis, decision to publish, or preparation of the manuscript.

Conflict of interest

The authors declare that the research was conducted in the absence of any commercial or financial relationships that could be construed as a potential conflict of interest.

Publisher's note

All claims expressed in this article are solely those of the authors and do not necessarily represent those of their affiliated organizations, or those of the publisher, the editors and the reviewers. Any product that may be evaluated in this article, or claim that may be made by its manufacturer, is not guaranteed or endorsed by the publisher.

References

- Abdul-Rahman, A. M., Molteno, T., and Molteno, A. C. (2008). Fourier analysis of digital retinal images in estimation of cataract severity. *Clin. Exp. Ophthalmol.* 36 (7), 637–645. doi:10.1111/j.1442-9071.2008.01819.x
- Ang, M. J., and Afshari, N. A. (2021). Cataract and systemic disease: A review. *Clin. Exp. Ophthalmol.* 49 (2), 118–127. doi:10.1111/ceo.13892
- Bourne, R. R. A., Flaxman, S. R., Braithwaite, T., Cicinelli, M. V., Das, A., Jonas, J. B., et al. (2017). Magnitude, temporal trends, and projections of the global prevalence of blindness and distance and near vision impairment: A systematic review and meta-analysis. *Lancet Glob. health* 5 (9), e888–e897. doi:10.1016/S2214-109X(17)30293-0
- Chylack, L. T., Jr., Leske, M. C., McCarthy, D., Khu, P., Kashiwagi, T., and Sperduto, R. (1989). Lens opacities classification system II (LOCS II). *Archives Ophthalmol.* 107 (7), 991–997. doi:10.1001/archophth.1989.01070020053028
- Chylack, L. T., Jr., Wolfe, J. K., Singer, D. M., Leske, M. C., Bullimore, M. A., Bailey, I. L., et al. (1993). The lens opacities classification system III. The longitudinal study of cataract study group. *Archives Ophthalmol.* 111 (6), 831–836. doi:10.1001/archophth.1993.01090060119035
- Flaxman, S. R., Bourne, R. R. A., Resnikoff, S., Ackland, P., Braithwaite, T., Cicinelli, M. V., et al. (2017). Global causes of blindness and distance vision impairment 1990–2020: A systematic review and meta-analysis. *Lancet Glob. health* 5 (12), e1221–e1234. doi:10.1016/S2214-109X(17)30393-5
- Gali, H. E., Sella, R., and Afshari, N. A. (2019). Cataract grading systems: A review of past and present. *Curr. Opin. Ophthalmol.* 30 (1), 13–18. doi:10.1097/ICU.0000000000000542
- GBD 2019 Blindness and Vision Impairment Collaborators (2021). Trends in prevalence of blindness and distance and near vision impairment over 30 years: An analysis for the global burden of disease study. *Lancet Glob. health* 9 (2), e130–e143. doi:10.1016/S2214-109X(20)30425-3
- Huang, G., Liu, Z., Pleiss, G., Van Der Maaten, L., and Weinberger, K. (2019). Convolutional networks with dense connectivity. *IEEE Trans. Pattern Anal. Mach. Intell.* 44, 8704–8716. doi:10.1109/TPAMI.2019.2918284
- Lam, D., Rao, S. K., Ratna, V., Liu, Y., Mitchell, P., King, J., et al. (2015). *Cataract. Nat. Rev. Dis. Prim.* 1, 15014. doi:10.1038/nrdp.2015.14
- Lian, J. X., Gangwani, R. A., McGhee, S. M., Chan, C. K., Lam, C. L., Primary Health Care, G., et al. (2016). Systematic screening for diabetic retinopathy (DR) in Hong Kong: Prevalence of DR and visual impairment among diabetic population. *Br. J. Ophthalmol.* 100 (2), 151–155. doi:10.1136/bjophthalmol-2015-307382
- Lin, D., Xiong, J., Liu, C., Zhao, L., Li, Z., Yu, S., et al. (2021). Application of comprehensive artificial intelligence retinal Expert (CARE) system: A national real-world evidence study. *Lancet Digit. Health* 3 (8), e486–e495. doi:10.1016/S2589-7500(21)00086-8

- Manuchehri, K., and Kirkby, G. (2003). Vitreous haemorrhage in elderly patients: Management and prevention. *Drugs Aging* 20 (9), 655–661. doi:10.2165/00002512-200320090-00003
- Maraini, G., Rosmini, F., Graziosi, P., Tomba, M. C., Bonacini, M., Cotichini, R., et al. (1994). Influence of type and severity of pure forms of age-related cataract on visual acuity and contrast sensitivity. Italian American Cataract Study Group. *Invest. Ophthalmol. Vis. Sci.* 35 (1), 262–267.
- Mukhija, R., Gupta, N., Vashist, P., Tandon, R., and Gupta, S. K. (2020). Population-based assessment of visual impairment and pattern of corneal disease: Results from the CORE (corneal opacity rural epidemiological) study. *Br. J. Ophthalmol.* 104 (7), 994–998. doi:10.1136/bjophthalmol-2019-314720
- Ramprasaath, R., Selvaraju, M. C., Das, A., Vedantam, R., Parikh, D., and Batra, D. (2020). Grad-CAM: Visual explanations from deep networks via gradient-based localization. *Int. J. Comput. Vis.* 128, 336–359. doi:10.1007/s11263-019-01228-7
- Ruamviboonsuk, P., Tiwari, R., Sayres, R., Nganthavee, V., Hemarat, K., Kongprayoon, A., et al. (2022). Real-time diabetic retinopathy screening by deep learning in a multisite national screening programme: A prospective interventional cohort study. *Lancet Digit. Health* 4 (4), e235–e244. doi:10.1016/S2589-7500(22)00017-6
- Scanlon, P. H., Foy, C., Malhotra, R., and Aldington, S. J. (2005). The influence of age, duration of diabetes, cataract, and pupil size on image quality in digital photographic retinal screening. *Diabetes Care* 28 (10), 2448–2453. doi:10.2337/diacare.28.10.2448
- Stifter, E., Sacu, S., Benesch, T., and Weghaupt, H. (2005). Impairment of visual acuity and reading performance and the relationship with cataract type and density. *Invest. Ophthalmol. Vis. Sci.* 46 (6), 2071–2075. doi:10.1167/iovs.04-0890
- Tham, Y. C., Goh, J. H. L., Anees, A., Lei, X., Rim, T. H., Chee, M. L., et al. (2022). Detecting visually significant cataract using retinal photograph-based deep learning. *Nat. Aging* 2, 264–271. doi:10.1038/s43587-022-00171-6
- Verbraak, F. D., Abramoff, M. D., Bausch, G. C. F., Klaver, C., Nijpels, G., Schlingemann, R. O., et al. (2019). Diagnostic accuracy of a device for the automated detection of diabetic retinopathy in a primary care setting. *Diabetes Care* 42 (4), 651–656. doi:10.2337/dc18-0148
- WHO (2020). Discussion Paper Proposed global targets for 2030 on integrated people-centred eye care World Health Organization. Available at: https://cdn.who.int/media/docs/default-source/blindness-and-visual-impairment/discussion-paper-eye-care-indicators-and-proposed-targets-11-11-20.pdf?sfvrsn=ff4dad2_2.
- WHO (2021). Integrated people-centred eye care, including preventable vision impairment and blindness Global targets for 2030. World Health Organization Available at: https://apps.who.int/gb/ebwha/pdf_files/WHA74/A_9-en.pdf.
- Wong, W. L., Li, X., Li, J., Cheng, C. Y., Lamoureux, E. L., Wang, J. J., et al. (2013). Cataract conversion assessment using lens opacity classification system III and Wisconsin cataract grading system. *Invest. Ophthalmol. Vis. Sci.* 54 (1), 280–287. doi:10.1167/iovs.12-10657
- Xiong, L., Li, H., and Xu, L. (2017). An approach to evaluate blurriness in retinal images with vitreous opacity for cataract diagnosis. *J. Healthc. Eng.* 2017, 5645498. doi:10.1155/2017/5645498
- Xu, X., Zhang, L., Li, J., Guan, Y., and Zhang, L. (2020). A hybrid global-local representation CNN model for automatic cataract grading. *IEEE J. Biomed. Health Inf.* 24 (2), 556–567. doi:10.1109/JBHI.2019.2914690
- Yue Zhou, G. L., and Li, H. (2020). Automatic cataract classification using deep neural network with discrete state transition. *IEEE Trans. Med. Imaging* 39 (2), 436–446. doi:10.1109/TMI.2019.2928229
- Zhang, H., Niu, K., Xiong, Y., Yang, W., He, Z., and Song, H. (2019). Automatic cataract grading methods based on deep learning. *Comput. methods programs Biomed.* 182, 104978. doi:10.1016/j.cmpb.2019.07.006

Frontiers in Cell and Developmental Biology

Explores the fundamental biological processes of life, covering intracellular and extracellular dynamics.

The world's most cited developmental biology journal, advancing our understanding of the fundamental processes of life. It explores a wide spectrum of cell and developmental biology, covering intracellular and extracellular dynamics.

Discover the latest Research Topics

[See more](#) →

Frontiers

Avenue du Tribunal-Fédéral 34
1005 Lausanne, Switzerland
frontiersin.org

Contact us

+41 (0)21 510 17 00
frontiersin.org/about/contact

